Cover Picture

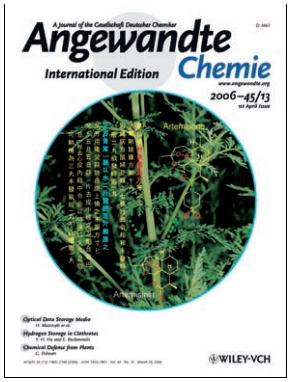

Richard K. Haynes,* Burkhard Fugmann, Jörg Stetter, Karl Rieckmann, Hans-Dietrich Heilmann, Ho-Wai Chan, Man-Ki Cheung, Wai-Lun Lam, Ho-Ning Wong, Simon L. Croft, Livia Vivas, Lauren Rattray, Lindsay Stewart, Wallace Peters, Brian L. Robinson, Michael D. Edstein, Barbara Kotecka, Dennis E. Kyle, Bernhard Beckermann, Michael Gerisch, Martin Radtke, Gabriele Schmuck, Wolfram Steinke, Ute Wollborn, Karl Schmeer, and Axel Römer

Qing hao su, or artemisinin, is the active compound isolated from the herb *Artemisia annua* (qīng hāo) shown in the cover picture. The Chinese text shown describing its use in Chinese medicine dates back to 340 AD. Derivatives of artemisinin are currently used for the treatment of malaria. In their Communication on page 2082 ff., R. K. Haynes et al. describe the preparation and superior efficacy of the new derivative artemisone against the malaria parasite. (Chinese text verified by Prof. Chun-Tao Che.)

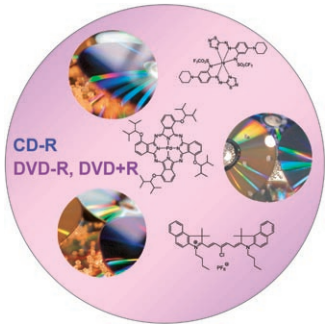

Optical Data Storage Media
In their Review on page 2016 ff., H. Mustroph et al. explain the principles of the widespread CD und DVD technologies. These media rely heavily upon the development of new organic dyes.

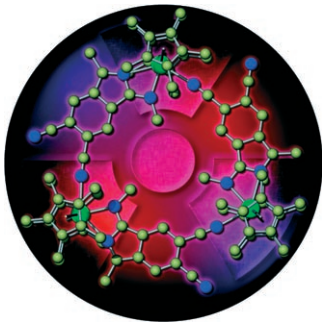

Cyclization and Self-Assembly
J. L. Kiplinger, D. E. Morris, and co-workers present complexes with a triangle of actinide metal centers linked by 5,6-dicyano-1-methyl-3-(*N*-methylamino)isoindolyl ligands in their Communication on page 2036 ff.

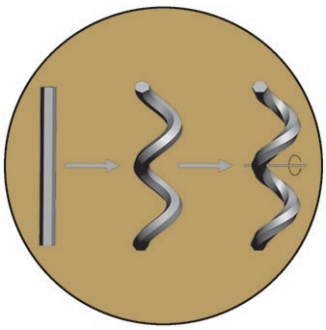

Chiral Mesostructures
Mesostructured fibers of MCM-41, which were prepared in the presence of an achiral surfactant by a simple dilute synthesis system, are surprisingly chiral. The details of these findings are given by Tang et al. in their Communication on page 2088 ff.

Contents

VIP ***The following Communications have been judged by at least two referees to be "very important papers" and will be published online at www.angewandte.org soon:***

*A. Kaminaga, V. Vanag, I. Epstein**
A Reaction-Diffusion Memory Device

*V. Stamenkovic, B. S. Moon, K. J. Mayrhofer, P. Ross, N. Markovic, J. Rossmeisl, J. Greeley, J. Nørskov**
Changing the Activity of Electrocatalysts for Oxygen Reduction by Tuning the Surface Electronic Structure

J. Blumberger, B. Ensing, M. Klein*
Formamide Hydrolysis in Alkaline Aqueous Solution: Insights from Ab Initio Metadynamics Calculations

G. Dolphin, P. Dumy, J. Garcia**
Control of Amyloid β-Peptide Protofibril Formation by a Designed Template Assembly

J. M. B. v. Colbe, W. Schmidt, M. Felderhoff, B. Bogdanovic, F. Schüth**
Hydrogen Isotope Scrambling on Doped Sodium Alanate

W. Zhao, Y. Gao, S. Kandadai, M. Brook, Y. Li**
DNA Polymerization on Gold Nanoparticles through Rolling Circle Amplification: Towards Scaffolds for Three-Dimensional Periodical Nanoassemblies

News

Organic Chemistry: Buchwald Awarded ——— **2004**

Bioinorganic Chemistry: Wieghardt Receives Prize ——— **2004**

Materials Science: Meijer Honored ——— **2004**

Books

Multiphase Homogeneous Catalysis — B. Cornils, W. A. Herrmann, I. T. Horváth, W. Leitner, S. Mecking, H. Olivier-Bourbigou, D. Vogt — *reviewed by O. Walter* ——— **2005**

Boronic Acids — Dennis G. Hall — *reviewed by S. Marsden* ——— **2005**

Highlights

Chemical Defense

G. Pohnert* ——— **2008 – 2010**

Genetic Engineering Renders Plants Attractive to "Bodyguards"

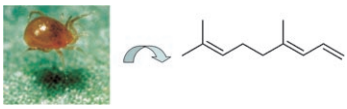

A continuous cry for help is let out by transgenic *Arabidopsis thaliana* plants that are modified to produce volatile terpenoid derivatives, such as dimethylnonatriene, which are well-known attractants for predatory mites or "bodyguards" (see picture). Such transgenic plants are important in ecological experiments to obtain insights into indirect chemical defense strategies.

Hydrogen Storage

Y. H. Hu,* E. Ruckenstein — **2011 – 2013**

Clathrate Hydrogen Hydrate—A Promising Material for Hydrogen Storage

Captured and caged: The capture of H_2 in H_2O cages to give clathrate hydrogen hydrate is a recent breakthrough in the development of hydrogen storage materials. Pure H_2 hydrate is stabilized only under high pressures (typically 220 MPa at 249 K). However, inclusion of THF as a second guest allows stabilization of the resultant clathrate at pressures of only 5 MPa at 279.6 K (see picture; THF blue, H_2 red).

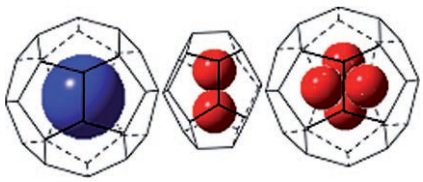

WILEY InterScience DISCOVER SOMETHING GREAT
© 2006 Wiley-VCH Verlag GmbH & Co. KGaA, Weinheim

Reviews

Improvements in play-back quality of stored information and the rapidly increasing demand for media with greater storage capacity have led to a very fast development in optical storage media (CD, DVD) in the last 20 years. The most successful systems are those based on organic dyes. This Review describes the general developments in this area and discusses the optical and thermal properties of the dyes and dye layers in more detail.

Data Storage Media

H. Mustroph,* M. Stollenwerk, V. Bressau ——— **2016 – 2035**

Current Developments in Optical Data Storage with Organic Dyes

Communications

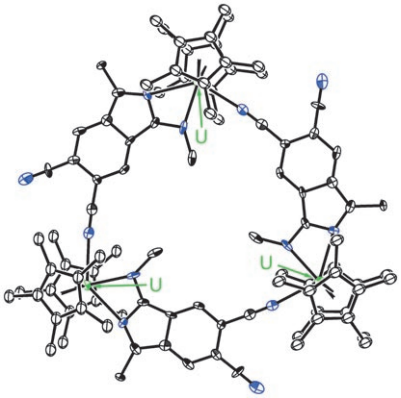

Heavy metal triangles: A class of actinide metallomacrocycles has been prepared in which three $(C_5Me_5)_2An$ (An = Th, U) fragments are coordinated by three 5,6-dicyano-1-methyl-3-(*N*-methylamino)-isoindolyl bridging ligands (N blue). The tetravalent actinide centers form a triangular array in the products obtained through an unprecedented actinide-mediated cyclization of 1,2,4,5-tetracyanobenzene and subsequent self-assembly.

Actinide Supramolecular Chemistry

J. L. Kiplinger,* J. A. Pool, E. J. Schelter, J. D. Thompson, B. L. Scott, D. E. Morris* ——— **2036 – 2041**

Actinide-Mediated Cyclization of 1,2,4,5-Tetracyanobenzene: Synthesis and Characterization of Self-Assembled Trinuclear Thorium and Uranium Macrocycles

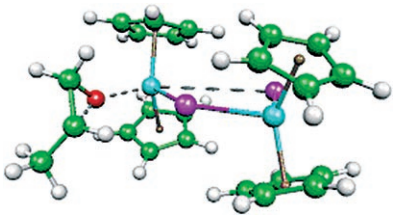

Steric effects govern the catalytic reductive epoxide ring opening. This is the result of combined experimental and theoretical studies, which revealed interesting features of the catalyst structure, substrate binding, transition state (see picture), and reaction energies. In light of these, highly selective conditions for the ring opening can be proposed.

Catalyzed Ring Opening

K. Daasbjerg,* H. Svith, S. Grimme,* M. Gerenkamp, C. Mück-Lichtenfeld, A. Gansäuer,* A. Barchuk, F. Keller ——— **2041 – 2044**

Elucidation of the Mechanism of Titanocene-Mediated Epoxide Opening by a Combined Experimental and Theoretical Approach

For the USA and Canada:
ANGEWANDTE CHEMIE International Edition (ISSN 1433-7851) is published weekly by Wiley-VCH PO Box 191161, D 69451 Weinheim, Germany. Air freight and mailing in the USA by Publications Expediting Inc. 200 Meacham Ave., Elmont, NY 11003. Periodicals postage paid at Jamaica NY 11431. US POSTMASTER: send address changes to *Angewandte Chemie*, Wiley-VCH, 111 River Street, Hoboken, NJ 07030. Annual subscription price for institutions: US$ 5685/5168 (valid for print and electronic / print or electronic delivery); for individuals who are personal members of a national chemical society prices are available on request. Postage and handling charges included. All prices are subject to local VAT/sales tax.

© 2006 Wiley-VCH Verlag GmbH & Co. KGaA, Weinheim

The best in chemistry –

for more than a hundred years

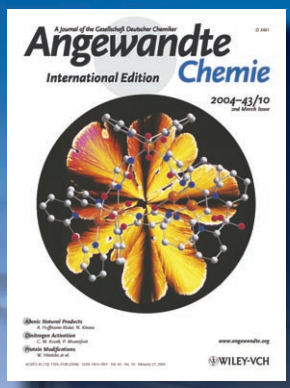

A Journal of the Gesellschaft Deutscher Chemiker

Angewandte
International Edition **Chemie**

www.angewandte.org

1888: ***The beginning of a success story***

Constant Innovations

1962: *First issue of the International Edition*
1976: *Graphical abstracts*
1979: *Cover pictures*
1988: *Centenary of Angewandte*
1989: *Routine use of color*
1991: *New section: Highlights*
1992: *Computerized editorial tracking system*
1995: *Internet service for readers*
1998: *Regular press service; full-text online*
2000: *New section: Essays; EarlyView: Communications available online ahead of the printed version*
2001: *New section: Minireviews*
2002: *Online submission of manuscripts*
2003: *Weekly publication; new section: News; new layout*
2004: *Backfiles (1962-1997); ManuscriptXpress: Online system for authors and referees*

Angewandte's advisors...

Robert Langer
Massachusetts Institute of Technology

»***Angewandte Chemie*** *is one of the top chemistry journals in the world. As such, I try to publish there frequently and am honored to be a member of its International Advisory Board.*«

Angewandte Chemie International Edition *is a journal of the German Chemical Society (GDCh)*

GDCh

WILEY InterScience® DISCOVER SOMETHING GREAT

WILEY-VCH

1841404_gu

Peeling off the layers: Boron nitride nanotubes (BNNTs) can be successfully peeled upon heating in dimethyl sulfoxide solution. The peeled BN shells can be reassembled into nanotubes branching from BNNT trunks to form Y-junction BNNTs (see TEM images).

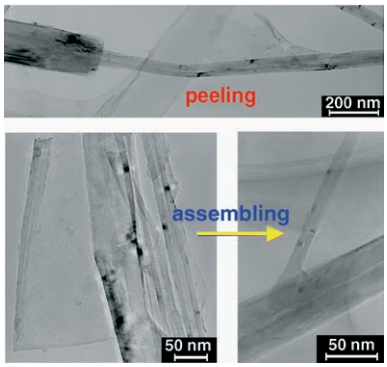

BN Nanotubes

Q. Huang,* Y. Bando, C. Zhi, D. Golberg, K. Kurashima, F. Xu, L. Gao **2044 – 2047**

Chemical Peeling and Branching of Boron Nitride Nanotubes in Dimethyl Sulfoxide

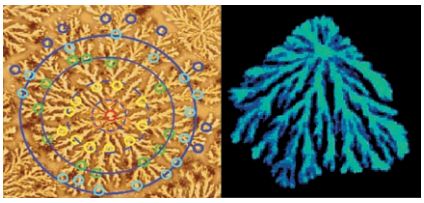

Light fingered: Highly photoluminescent (PL) polycrystalline dendrites have been grown by a controlled thermodynamic process from CdSe/ZnS core/shell quantum dots (see PL image, left) and quantum rods (see confocal PL image, right). In these dendrites, energy transfer takes place from the fingers to the core region.

Nanotechnology

A. Sukhanova, A. V. Baranov, T. S. Perova, J. H. M. Cohen, I. Nabiev* **2048 – 2052**

Controlled Self-Assembly of Nanocrystals into Polycrystalline Fluorescent Dendrites with Energy-Transfer Properties

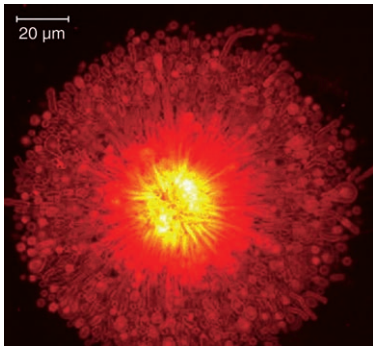

Implications for the nervous system: The formation of polymeric myelin structures was studied at the copolymer/water interface and then elaborated in a dispersed phase. Sun-like structures formed with a complex multilamellar core and a corona made of short myelins. Myelin growth is solvent-promoted, in a strong analogy to natural myelins, which have membranes with a higher proportion of fluidizing molecules such as cholesterol.

Polymer Membranes

G. Battaglia,* A. J. Ryan* **2052 – 2056**

Neuron-Like Tubular Membranes Made of Diblock Copolymer Amphiphiles

Double take: Paired carceroisomers of a resorcin[4]arene-based C_{4v} carceplex with an included DMF molecule are formed when a non-interacting second guest (CH_3CN) exists in excess. The two most stable carceroisomers of the carceplex with an included molecule each of DMF and CH_3CH (see picture) were observed in a 2:1 ratio at 25 °C in $CDCl_3$ by ^1H NMR spectroscopy, and their spatial arrangements were studied by ^1H-^1H ROESY experiments.

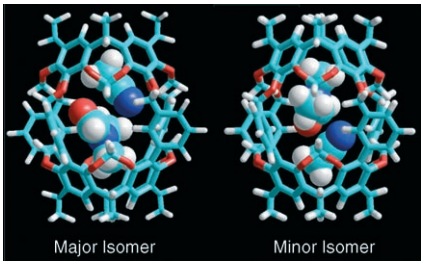

Host–Guest Chemistry

C. Ihm, E. Jo, J. Kim, K. Paek* **2056 – 2059**

Paired Carceroisomers

© 2006 Wiley-VCH Verlag GmbH & Co. KGaA, Weinheim

Contents

Platinum Carbonyl Clusters

C. Femoni, F. Kaswalder, M. C. Iapalucci, G. Longoni,* M. Mehlstäubl, S. Zacchini, A. Ceriotti _____ **2060 – 2062**

Synthesis and Crystal Structure of $[NBu_4]_2[Pt_{24}(CO)_{48}]$: An Infinite 1D Stack of $\{Pt_3(CO)_6\}$ Units Morphologically Resembling a CO-Insulated Platinum Cable

Pieces of eight: Upon crystallization, $[NBu_4]_2[Pt_{24}(CO)_{48}]$ self-assembles into infinite one-dimensional stacks of $\{Pt_3(CO)_6\}$ units arranged in layers separated by $[NBu_4]^+$ ions. Close examination of the $\{Pt_3(CO)_6\}$ stacks, which resemble CO-insulated platinum cables (see picture; CO ligands omitted), shows them to be composed of alternating blocks of seven $\{Pt_3(CO)_6\}$ units and single $\{Pt_3(CO)_6\}$ units.

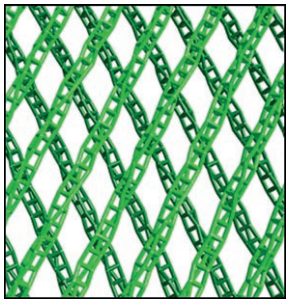

Solvent Effects

C. P. Price, G. D. Glick, A. J. Matzger* _____ **2062 – 2066**

Dissecting the Behavior of a Promiscuous Solvate Former

Take any partner: Benzodiazepine derivative Bz-423 (see picture) can be described as an indiscriminate solvate former as it cocrystallizes with a diverse array of small molecules. This behavior was investigated by analysis of the packing efficiency of these crystal forms relative to that of unsolvated Bz-423 and an appropriate model compound.

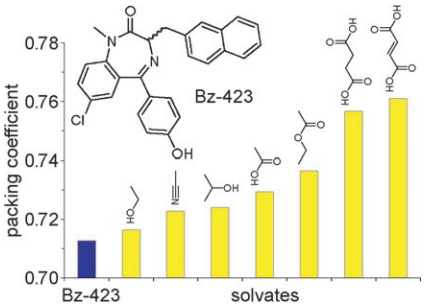

Computational Chemistry

D. A. R. S. Latino, J. Aires-de-Sousa* _____ **2066 – 2069**

Genome-Scale Classification of Metabolic Reactions: A Chemoinformatics Approach

On the map: A Kohonen self-organizing map distributes 3468 metabolic reactions over a 2D surface according to their similarity (neurons activated by reactions of the same enzyme class are identically colored). No specification of the reaction center was used. General agreement with EC numbers was observed. Red = oxidoreductases, dark blue = transferases, green = hydrolases, yellow = lyases, light blue = isomerases, pink = ligases.

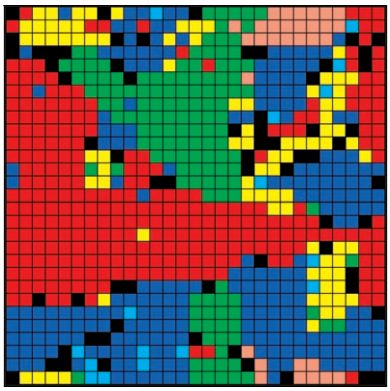

Computational Chemistry

S. X. Tian,* J. Yang _____ **2069 – 2072**

Effects of Intramolecular Hydrogen Bonding on the Ionization Energies of Proline

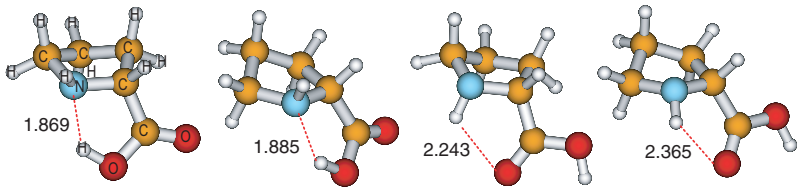

Ab initio studies show the influence of intramolecular hydrogen bonding on the ionization energies of proline conformers (see picture). These results were used to assign the UV photoelectron spectrum.

© 2006 Wiley-VCH Verlag GmbH & Co. KGaA, Weinheim

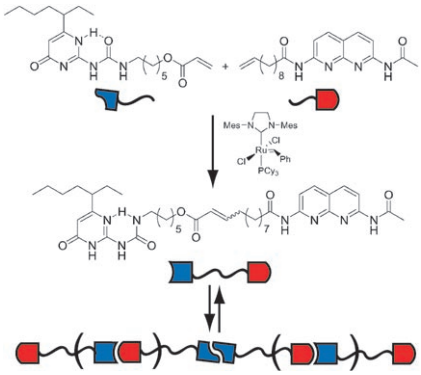

Two become one: An AB-type monomer containing both 2-ureido-4[1*H*]-pyrimidinone and 2,7-diamido-1,8-naphthyridine quadruple hydrogen-bonding moieties is obtained by selective olefin cross metathesis. This monomer addresses the issue of stoichiometric imbalance in the self-assembly of AA + BB-type supramolecular polymers. Moreover, as the linker between both motifs is quite flexible, this monomer exists as a monocycle at low concentrations.

Self-Assembly

O. A. Scherman, G. B. W. L. Ligthart, R. P. Sijbesma,* E. W. Meijer* ——— **2072 – 2076**

A Selectivity-Driven Supramolecular Polymerization of an AB Monomer

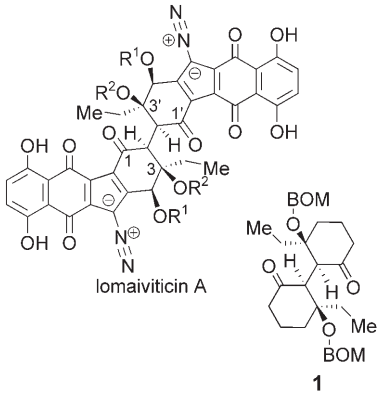

1

Models incorporated: Two model systems representing the core structures of antitumor compounds lomaiviticins A and B have been prepared through a temporary bridge strategy (the structures of lomaiviticin A and its model core structure **1** are shown; BOM = benzyloxymethyl). A feature of the approach is a stereocontrolled Michael addition of dimethyl malonate to a dimeric enone.

Natural Products

K. C. Nicolaou,* R. M. Denton, A. Lenzen, D. J. Edmonds, A. Li, R. R. Milburn, S. T. Harrison ——— **2076 – 2081**

Stereocontrolled Synthesis of Model Core Systems of Lomaiviticins A and B

Artemisinin—the next generation: Efficacies of artemisone against the malaria parasite are substantially greater than those of the current artemisinin "gold standard", artesunate. Also, in contrast to most current artemisinins it displays low lipophilicity and negligible neuro- and cytotoxicity in in vitro and in vivo assays. Thus, the drug offers promise for use in artemisinin-based combination therapy.

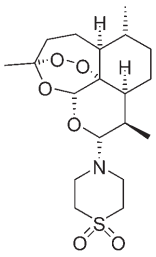

Antimalarial Drugs

R. K. Haynes,* B. Fugmann, J. Stetter, K. Rieckmann, H.-D. Heilmann, H.-W. Chan, M.-K. Cheung, W.-L. Lam, H.-N. Wong, S. L. Croft, L. Vivas, L. Rattray, L. Stewart, W. Peters, B. L. Robinson, M. D. Edstein, B. Kotecka, D. E. Kyle, B. Beckermann, M. Gerisch, M. Radtke, G. Schmuck, W. Steinke, U. Wollborn, K. Schmeer, A. Römer ——— **2082 – 2088**

Artemisone—A Highly Active Antimalarial Drug of the Artemisinin Class

Straightening out chirality: Chiral mesostructured silica nanofibers of MCM-41 with one (see TEM image, the arrows indicate periodic fringes) and two twist axes were fabricated from a simple dilute synthesis system without any chiral additives. A continuous transformation from a chiral mesostructure to an achiral straight mesostructure was observed, thus demonstrating an interesting relationship between these two seemingly different structures.

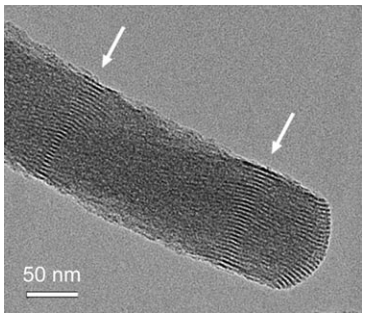

Mesoporous Materials

VIP

B. Wang, C. Chi, W. Shan, Y. H. Zhang, N. Ren, W. L. Yang, Y. Tang* **2088 – 2090**

Chiral Mesostructured Silica Nanofibers of MCM-41

© 2006 Wiley-VCH Verlag GmbH & Co. KGaA, Weinheim

Contents

Cyclization Sequence

J. Barluenga,* A. Diéguez, A. Fernández, F. Rodríguez, F. J. Fañanás ‒ **2091 – 2093**

Gold- or Platinum-Catalyzed Tandem Cycloisomerization/Prins-Type Cyclization Reactions

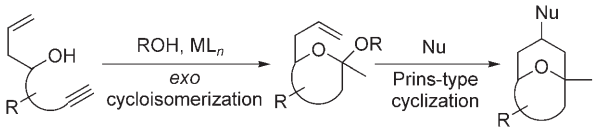

Straightforward and efficient: Functionalized eight-membered carbocycles are easily obtained from simple allyl-substituted 5-hexyn-1-ol derivatives by a catalytic tandem sequence involving a 6-*exo* cycloisomerization followed by a Prins-type cyclization (see scheme).

Gas-Phase studies

C. Denekamp,* Y. Sandlers **2093 – 2096**

Electrophilicity–Nucleophilicity Scale Also in the Gas Phase

Changing the state: The electrophilicity of benzhydryl cations (see formula) towards neutral amine nucleophiles in the gas phase was determined. It was found that the kinetics of electrophile–nucleophile gas-phase reactions correlate well with values known in solution although the actual electrophilicity parameters are considerably smaller in the gas phase.

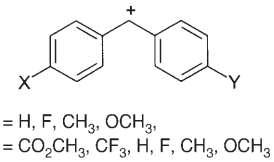

Asymmetric Synthesis

A. Blanc, F. D. Toste* ——— **2096 – 2099**

Enantioselective Synthesis of Cyclic Ethers through a Vanadium-Catalyzed Resolution/Oxidative Cyclization

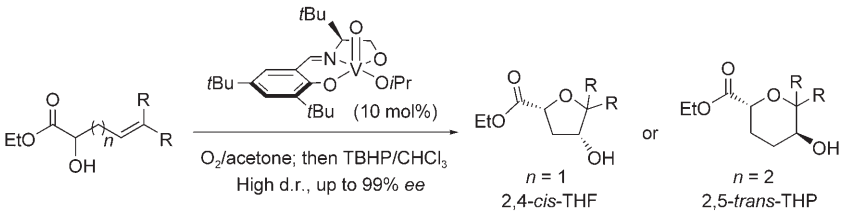

Two steps, one catalyst: A vanadium(v)–oxo complex with a tridentate Schiff base as an additional ligand catalyzes the title reaction which transforms racemic bishomoallylic α-hydroxyesters into *trans*-tetrahydropyrans (THPs) and *cis*-tetrahydrofurans (THFs). This synthetic method provides an efficient asymmetric synthesis of cyclic ethers as demonstrated by the first enantioselective synthesis of (−)-pantofuranoid E. TBHP = *tert*-butylhydroperoxide.

Chirality

N. Mercier,* A.-L. Barres, M. Giffard, I. Rau, F. Kajzar, B. Sahraoui **2100 – 2103**

Conglomerate-to-True-Racemate Reversible Solid-State Transition in Crystals of an Organic Disulfide-Based Iodoplumbate

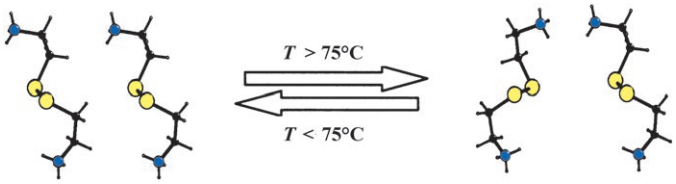

Switch over: All the disulfide moieties in the cations of an iodoplumbate display the same chiral conformation in a single crystal; however, during a phase transition (75 °C) half of these molecules undergo a conformational change, from the left- to the right-handed helical form, and a true racemate is formed. This transition is reversible, and thus this compound can act as a second harmonic generation switch.

© 2006 Wiley-VCH Verlag GmbH & Co. KGaA, Weinheim

The missing link: Chiral catenanes have been obtained by including prochiral phosphorus centers in both rings of a [2]catenane moiety. These compounds, which also contain stereogenic carbon atoms, have been prepared by the well known copper(I) template synthesis and have been isolated as enantiomerically pure, single diastereoisomers.

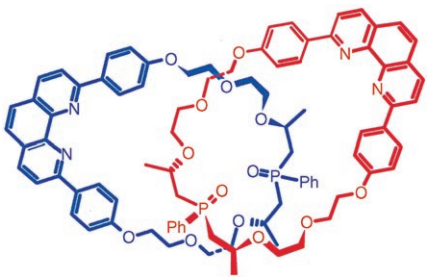

Template Synthesis

A. Theil, C. Mauve, M.-T. Adeline, A. Marinetti,* J.-P. Sauvage **2104 – 2107**

Phosphorus-Containing [2]Catenanes as an Example of Interlocking Chiral Structures

---

Breaking the rule: The metal-carbide endofullerene $Sc_2C_2@C_{68}$ was isolated and characterized (see picture). It has a valence state $(Sc^{3+})_2(C_2)^{2-}@C_{68}{}^{4-}$, and its carbon cage does not comply with the isolated-pentagon rule (IPR). This result, in combination with previous work on $Sc_3N@C_{68}$, shows that different non-IPR C_{68} cages can be synthesized by using different endohedral clusters as templates.

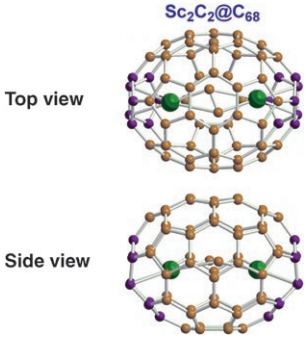

Fullerenes

Z.-Q. Shi, X. Wu, C.-R. Wang,* X. Lu,* H. Shinohara* **2107 – 2111**

Isolation and Characterization of $Sc_2C_2@C_{68}$: A Metal-Carbide Endofullerene with a Non-IPR Carbon Cage

---

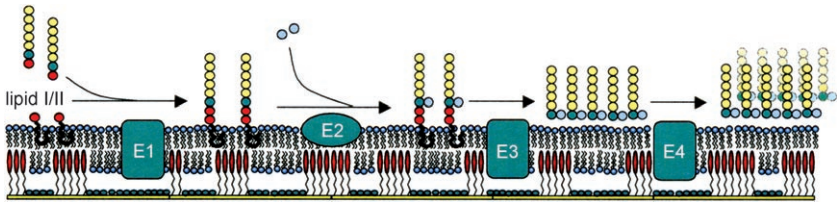

At the end of its tether: Solid-supported tethered lipid bilayers that present native versions of the peptidoglycan precursors lipid I and lipid II are used to compare the binding of vancomycin and ramoplanin. Through the use of *E. coli* inner membranes, the resulting "proteolipid layer" contains the full range of intrinsic and extrinsic proteins found in vivo, thus allowing the in vitro biosynthesis of a peptidoglycan cell wall. E = enzyme.

Lipid Bilayers

M. J. Spencelayh, Y. Cheng, R. J. Bushby, T. D. H. Bugg, J.-j. Li, P. J. F. Henderson, J. O'Reilly, S. D. Evans* **2111 – 2116**

Antibiotic Action and Peptidoglycan Formation on Tethered Lipid Bilayer Membranes

---

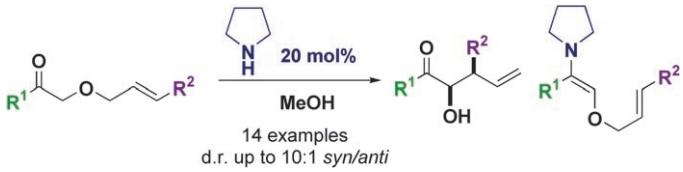

Simple secondary amine organocatalysts induce a general [2,3] Wittig rearrangement via an enamine under extremely mild conditions. The organocatalytic rearrangement gives good diastereoselectivities over a range of substrates and generates the *syn* isomer, which is contrary to what would be expected from the conventional [2,3]-reaction.

Organocatalysis

A. McNally, B. Evans, M. J. Gaunt* **2116 – 2119**

Organocatalytic Sigmatropic Reactions: Development of a [2,3] Wittig Rearrangement through Secondary Amine Catalysis

© 2006 Wiley-VCH Verlag GmbH & Co. KGaA, Weinheim

Contents

Metallaboranes

F. de Montigny, R. Macias, B. C. Noll, T. P. Fehlner* ——— **2119 – 2122**

Molybdenum-Mediated Alkyne Incorporation into an Iridaborane Framework—Release of the Iridacarborane from the Molybdenum Coordination Sphere through a Dissociative Equilibrium

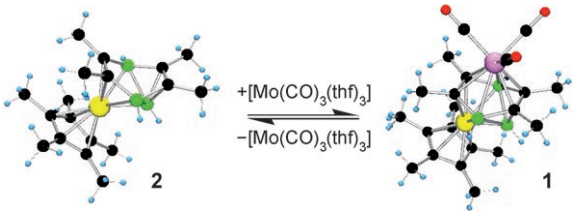

Chaperone service: An iridacarborane–$Mo(CO)_3$ coordination equilibrium follows the insertion of two 2-butyne units into iridaborane $[(Cp^*IrH)B_4H_9]$ to give $[Cp^*Ir(B_3H_3C_4Me_4)\{Mo(CO)_3\}]$ (**1**; yellow Ir, green B, magenta Mo, black C, red O, cyan H); a reduced binding affinity frees the iridacarborane $[Cp^*Ir(B_3H_3C_4Me_4)]$ (**2**).

Microporous Materials

F. Stallmach,* S. Gröger, V. Künzel, J. Kärger, O. M. Yaghi, M. Hesse, U. Müller* ——— **2123 – 2126**

NMR Studies on the Diffusion of Hydrocarbons on the Metal-Organic Framework Material MOF-5

On the move: High intracrystalline mobilities and fast exchange between the crystal and the surrounding gas phase were found in NMR studies on the diffusion of methane, ethane, *n*-hexane, and benzene in large crystals of the metal-organic framework MOF-5 (see SEM image). The results support future use of metal-organic framework materials as tailorable sorbents for fast gas processing and gas-storage materials in industry.

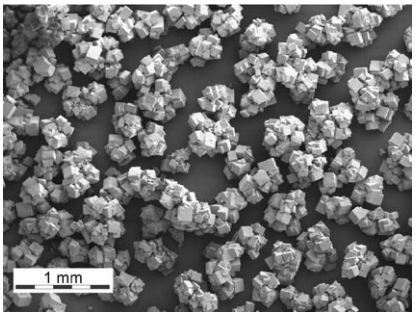

Switchable Biostructures

D. Strohbach, N. Novak, S. Müller* ——— **2127 – 2129**

Redox-Active Riboswitching: Allosteric Regulation of Ribozyme Activity by Ligand-Shape Control

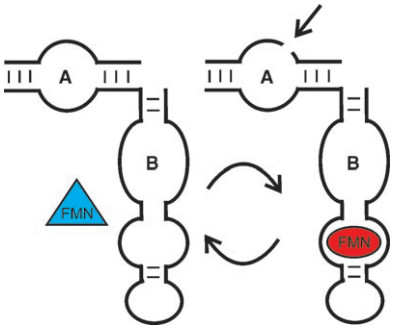

On and off: A flavine mononucleotide (FMN) dependent hairpin ribozyme can sense the oxidative state of its environment. Although oxidized FMN is planar and thus binds to the allosteric domain of the ribozyme, binding is interrupted by reduction of FMN due to the change from planar to rooflike geometry reflected in dramatically decreased ribozyme activity.

Asymmetric Polymerization

I. Hilker, G. Rabani, G. K. M. Verzijl, A. R. A. Palmans, A. Heise* **2130 – 2132**

Chiral Polyesters by Dynamic Kinetic Resolution Polymerization

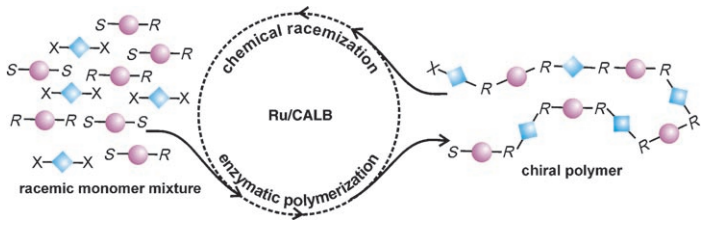

Problem resolved: Enzymatic polymerization was combined with an in situ Ru-catalyzed racemization process. The reaction mixture comprises a racemic mixture of a chiral diol and dimethyl adipate. Because of the high stereoselectivity of the enzyme *Candida antarctica* lipase B (CALB), the *S*-configured stereocenters of the chiral diol are practically nonreactive. Polycondensation was achieved by concurrent racemization of the *S*- into the *R*-configured centers.

© 2006 Wiley-VCH Verlag GmbH & Co. KGaA, Weinheim

All good things come in fours: Thermal metal–metal borylene transfer from the terminal borylene complexes $[(OC)_5M{=}BN(SiMe_3)_2]$ (M = Cr, W) leads to the new tetranuclear rhodium complex $[Rh_4\{\mu\text{-}BN(SiMe_3)_2\}_2(\mu\text{-}Cl)_4(\mu\text{-}CO)(CO)_4]$ (see structure), which is the first doubly borylene-bridged transition-metal complex. In the solid state, the tetranuclear units aggregate (dashed lines), giving a rare example of a neutral chain of rhodium atoms.

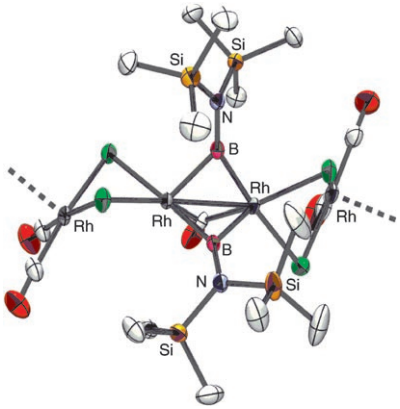

Coordination Chemistry

H. Braunschweig,* M. Forster, K. Radacki ——— 2132 – 2134

Borylene Transfer under Thermal Conditions: Synthesis and Structure of a Tetrarhodium Bisborylene Complex

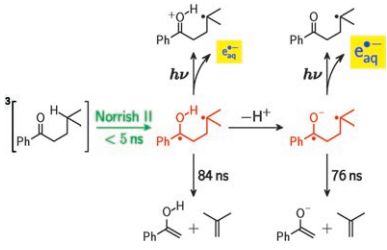

Extremely little is known about the factors governing the efficiency of photoionizations. The comparison of propiophenone and γ-methylvalerophenone highlights that a spontaneous intramolecular transformation accompanied by small structural and electronic changes—the conversion of a triplet moiety into a radical (anion) moiety by a Norrish II reaction—can have a pronounced effect on the electron yield.

Photochemistry

M. Goez,* V. Zubarev ——— 2135 – 2138

Efficient Photoionization of a Norrish II Diradical

Clamping down: A new class of aspartic protease inhibitors that target the malarial protease family Plasmepsin are reported. These ligands utilize a novel "diamine clamp" to engage the catalytic dyad. They are potent inhibitors of plasmepsins I, II, and IV, while retaining good selectivity against the closely related human cathepsins D and E.

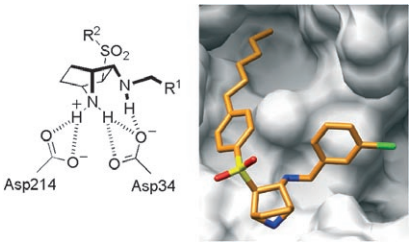

Enzyme Inhibitors

F. Hof, A. Schütz, C. Fäh, S. Meyer, D. Bur, J. Liu, D. E. Goldberg, F. Diederich* ——— 2138 – 2141

Starving the Malaria Parasite: Inhibitors Active against the Aspartic Proteases Plasmepsins I, II, and IV

The issues for March 2006 appeared online on the following dates
Issue 9: February 13 · Issue 10: February 21 · Issue 11: March 1 · Issue 12: March 6

Sources

Product and Company Directory

You can start the entry for your company in "Sources" in any issue of *Angewandte Chemie*.

If you would like more information, please do not hesitate to contact us.

Wiley-VCH Verlag – Advertising Department
Tel.: 0 62 01 - 60 65 65
Fax: 0 62 01 - 60 65 50
E-Mail: MSchulz@wiley-vch.de

Service

Keywords ——— *2142*

Authors ——— *2143*

Preview ——— *2147*

 © 2006 Wiley-VCH Verlag GmbH & Co. KGaA, Weinheim

Awarded...

ACS Creativity Award to S. L. Buchwald

Stephen L. Buchwald (Massachusetts Institute of Technology (MIT), Cambridge, USA) receives the 2006 American Chemical Society (ACS) Award for Creative Work in Synthetic Organic Chemistry. He is honored for his important contributions to the development of transition-metal-catalyzed coupling methods.

S. Buchwald

Buchwald studied chemistry at Brown University (Providence, RI, USA) and Columbia University and completed his PhD in 1982 at Harvard University under the guidance of J. R. Knowles on the mechanism of phosphoryl transfer in chemistry and biochemistry. He then carried out postdoctoral research in the group of R. H. Grubbs at the California Institute of Technology on titanocene reagents and the mechanism of Ziegler–Natta catalysis. In 1984 he joined MIT as an assistant professor and was appointed Camille Dreyfus Professor of Chemistry in 1997. The research interests of his group include new methods for C–C, C–N, and C–O bond formation, as well as asymmetric conjugate reductions. He recently reported on the formation of palladacycles during Pd-catalyzed C–N bond-forming reactions in *Angewandte Chemie*.[1a] He is a member of the editorial board of *Advanced Synthesis & Catalysis* and recently discussed industrial-scale palladium-catalyzed coupling reactions of aryl halides with amines therein.[1b]

K. Wieghardt Receives ACS Award

The ACS Award in Inorganic Chemistry for 2006 is presented to Karl Wieghardt (Max Planck Institute for Bioinorganic Chemistry, Mülheim/Ruhr, Germany). The prize is rarely awarded outside of the USA, and this is only the second time that it is awarded to a German (H. W. Roesky was the prizewinner in 2004). Wieghardt is recognized for his work in the area of bioinorganic chemistry, focused in particular on metalloproteins and preparing models of their active sites. He recently reported in *Angewandte Chemie* on [(cyclam-acetato)Fe(N)]$^+$, an iron(v) species with a ground-state spin of $S = 1/2$.[2a]

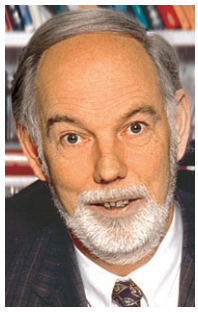

K. Wieghardt

Wieghardt studied chemistry at the Universities of Hamburg and Heidelberg and completed his PhD under the guidance of H. Siebert at Heidelberg in 1969. He carried out postdoctoral research with A. G. Sykes at the University of Leeds (UK) during 1972–73, before returning to Germany to complete his habilitation at Heidelberg (1974). He subsequently joined the University of Hannover as an associate professor. In 1981 he accepted a position at the University of Bochum and remained there until 1994, when he joined the Max Planck Society. Wieghardt serves on the editorial board of *Chemistry – A European Journal* and is a co-editor of the *Handbook of Metalloproteins*.[2b]

ACS Award to E. W. Meijer

Bert Meijer (Technische Universiteit Eindhoven, The Netherlands) receives the ACS Award in Polymer Chemistry 2006 for his work in the area of macromolecular organic chemistry and biomedicinal chemistry. Meijer is interested in the design, synthesis, and characterization of supramolecular systems with emphasis on chiral structures, dendrimers, π-conjugated oligomers, and polymers, as well as hydrogen-bonded architectures and their application in functional materials. He recently reported in *Angewandte Chemie* on the direct visualization of efficient energy transfer in single oligo(*p*-phenylenevinylene) vesicles.[3]

Meijer studied chemistry at the University of Groningen (The Netherlands) and completed his PhD there in 1982 working in the group of H. Wynberg. During 1982–89 he was a research chemist in the field of functional organic materials at Philips Research Laboratories in Eindhoven, and during 1989–92 he was head of the "New Materials" department at DSM Research in Geleen. Since 1991 he is Professor of Organic Chemistry at the Eindhoven University of Technology, and since 1995 he is also Adjunct Professor in Macromolecular Chemistry at Nijmegen University. Meijer is a member of the international advisory board of *Angewandte Chemie* and serves on the editorial boards of *Advanced Materials* and *Chemistry – A European Journal*, among others.

E. W. Meijer

[1] a) E. R. Strieter, S. L. Buchwald, *Angew. Chem.* **2006**, *118*, 939; *Angew. Chem. Int. Ed.* **2006**, *45*, 925; b) S. L. Buchwald, C. Mauger, G. Mignani, U. Scholz, *Adv. Synth. Catal.* **2006**, *348*, 23.

[2] a) N. Aliaga-Alcalde, S. DeBeer George, B. Mienert, E. Bill, K. Wieghardt, F. Neese, *Angew. Chem.* **2005**, *117*, 2968; *Angew. Chem. Int. Ed.* **2005**, *44*, 2908; b) *Handbook of Metalloproteins* (Eds.: A. Messerschmidt, R. Huber, T. Poulos, K. Wieghardt), Wiley, New York, **2001**.

[3] F. J. M. Hoeben, I. O. Shklyarevskiy, M. J. Pouderoijen, H. Engelkamp, A. P. H. J. Schenning, P. C. M. Christianen, J. C. Maan, E. W. Meijer, *Angew. Chem.* **2006**, *118*, 1254; *Angew. Chem. Int. Ed.* **2006**, *45*, 1232.

DOI: 10.1002/anie.200600708

InterScience © 2006 Wiley-VCH Verlag GmbH & Co. KGaA, Weinheim

Chemical Defense

DOI: 10.1002/anie.200504082

Genetic Engineering Renders Plants Attractive to "Bodyguards"

*Georg Pohnert**

Keywords:
biosynthesis · chemical defense · gene technology · terpenoids

It is observed in everyday life that certain plants are able to defend themselves by means of chemicals. Their bitter or pungent taste leads to both humans and other herbivores avoiding their consumption. Chemists associate a plant's defense system with elaborate structures of toxic natural products, which stimulate developments in pharmacy, synthesis, and analytics. These compounds are readily accessible by extraction because they are mostly stored in the plant tissue. However, the full and often more subtle potential of defense reactions can only be observed if the plant is regarded in its ecological context. Upon herbivory, some plants can activate rapid transformations that result in the formation of highly repellent or toxic metabolites.[1] Other plants are even able to recognize a threat through chemical indicators and subsequently react by the up-regulation of the de novo biosynthesis of defensive metabolites.[2]

Besides relying on the direct action of defensive chemicals, plants can even recruit "bodyguards" for their protection. Such an indirect defense can, for example, be facilitated through airborne chemical signals as is found in cucumbers. Once infected with an herbivorous spider mite, cucumber leaves emit a bouquet of mainly terpenoid volatiles. This blend of volatiles then attracts the predatory mite *Phytoseiulus persimilis*, which consumes the herbivores and thus relieves the plant from the nuisance.[3] These types of interactions are also commercially interesting, and *P. persimilis* has become one of the mainstays of greenhouse-integrated pest management programs for the control of spider mites.

Intense ecological, chemical, and biochemical research was carried out on these so-called tritrophic interactions between plants, herbivores, and predatory or parasitic insects.[4–6] However, advances in molecular biology have only recently provided new tools that allow the investigation of chemical defenses in more detail.[5] *Arabidopsis thaliana* is the first plant whose genome was fully sequenced and annotated, and pioneering molecular biological work has subsequently been performed with this model organism.

In contrast to other plants, *A. thaliana* releases only minor amounts of terpenoid volatiles. It therefore represents a good tool for metabolic engineering approaches that are aimed to elucidate the influence of individual metabolites on the indirect chemical defense. One volatile compound of *A. thaliana* is the C16-homoterpene 4,8,12-trimethyl-1,3(*E*),7(*E*),11-tridecatetraene (TMTT). In contrast, the homologue C11-sesquiterpene 4,8-dimethyl-1,3(*E*),7-nonatriene (DMNT), which is induced after herbivory in several other plant species, is not detected.[7] The biosynthesis of TMTT and DMNT follows similar pathways from geranylgeranyl diphosphate and farnesyl diphosphate, respectively. These precursors are rearranged to geranyllinalool or nerolidol and sub sequently broken down to the C16 or C11 hydrocarbons, respectively (Scheme 1).[8,9] As nerolidol also cannot be detected in *A. thaliana*, the lack of a central enzyme for the generation of this DMNT precursor is likely.

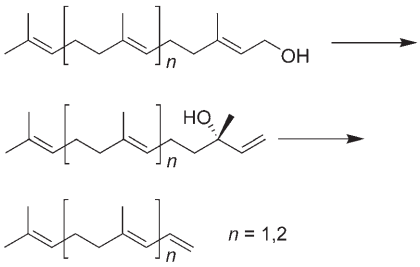

Scheme 1. Biosynthesis of DMNT ($n=1$) and TMNT ($n=2$) takes place through nerolidol ($n=1$) and geranyllinalool ($n=2$), respectively.

In an attempt to generate nerolidol-releasing transgenic plants, Kappers et al. introduced FaNES1, a gene encoding for a strawberry linalool/nerolidol synthase, into *A. thaliana*.[10] However, the expression of FaNES1 in the plastids of *A. thaliana* did not result in a significant release of new volatiles. For a successful strategy it is a prerequisite that the new enzyme makes contact with its substrates. Consequently, several previous attempts to generate terpene-emitting plants also failed as the introduced enzymes were not located in the correct cellular compartments. As *A. thaliana* contains a farnesyl diphosphate synthase with a mitochondrial signal, this cellular compartment was finally selected for the expression of the linalool/nerolidol synthase. Investigation of volatiles of such transgenic plants revealed that nine out of 12 transform-

[*] Prof. Dr. G. Pohnert
Ecole Polytechnique Féderale de Lausanne (EPFL)
Institute of Chemical Sciences and Engineering
Laboratory of Chemical Ecology
1015 Lausanne (Switzerland)
Fax: (+41) 21-693-9305
E-mail: georg.pohnert@epfl.ch

WILEY InterScience DISCOVER SOMETHING GREAT
© 2006 Wiley-VCH Verlag GmbH & Co. KGaA, Weinheim

ants produced up to 30 times more nerolidol compared to those where FaNES1 was targeted to plastids. As well as nerolidol, five of the nine transformants released DMNT also. This unexpected formation of product might be explained with the unspecific action of TMTT-synthesizing enzymes present in *A. thaliana* that accept nerolidol as substrate as well.[10] This simple genetic manipulation demonstrates that the plant is only one gene away from the release of a secondary metabolite that could carry important information to potential bodyguards. However, in contrast to the induced formation of volatile indicators of herbivory, nerolidol and DMNT were released continuously by the transgenic plants. Interestingly, this constitutive volatile production did not interfere significantly with the growth and development of *A. thaliana*. The flowering stems in transgenic plants appeared at the same time as those in the wild type, although the basal rosette leaves in the former were slightly retarded (Figure 1).[10]

Ecologists thus have in hand a useful tool for the further investigation of indirect chemical defenses. Two sets of transgenic plants that release either nerolidol alone or a blend of nerolidol and DMNT provided the basis for a series of behavioral experiments with the predatory mite *P. persimilis*. These experiments were aimed to test the influence of the volatiles on potential bodyguards. A significant attraction of the mite to transgenic DMNT- and nerolidol-emitting *A. thaliana* could be observed. The same result was found with plants that produce only nerolidol, while no preference was observed for the wild-type plants that do not release any of these metabolites. When mites were placed in the middle of a circle of alternating transgenic and wild-type plants, significantly more predators first visited the plants that emitted volatiles (Figure 1). Thus, one single additional gene can make an important difference for a potential indirect chemical defense.

These experiments clearly demonstrate that transgenic plants are very valuable for experiments that probe the influence of single metabolites. Nevertheless, if such an approach would be applied to for example, crop protection, it could be expected that the artificially generated "constitutive indirect defense strategy" that guides bodyguards to healthy as well as infected plants would not be successful. Animals will learn fast that the continuously emitted smell of the plant does not indicate a benefit and that these volatiles are thus of no use for the location of prey. To adapted insects the plants would therefore probably not be more attractive than their non-smell-emitting counterparts. It can thus only be speculated if and how similar strategies could be applied for crop protection in the future.

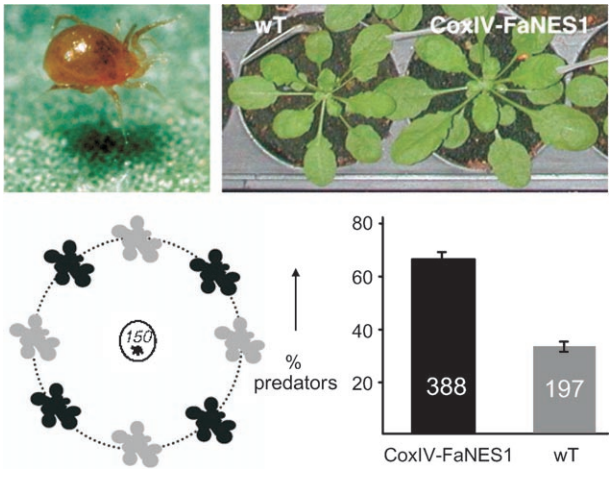

Figure 1. Wild-type (wT) and genetically modified (CoxIV-FaNES1) plants have similar developmental rates (top right). The predatory mite *Phytoseiulus persimilis* (top left) significantly prefers volatile-emitting plants if placed in the middle of an alternating arrangement of wild-type (black) and transgenic (gray) plants. The numbers in bars indicate the number of predators that chose the respective plants in repeated experiments. (Figure reproduced with permission from Science magazine and Andermatt BIOCONTROL AG.)

The induced defense processes in plants also can be modified by genetic engineering. Progress in this direction has already been obtained with transgenic plants, in which central enzymes of the hormonal system have been genetically manipulated. Plants that are deficient in the expression or reception of hormones belonging to the group of jasmonates were not able to produce defense compounds on demand. In laboratory experiments, these plants were indeed more susceptible to attack by herbivores.[11,12] Even field experiments with genetically engineered native tobacco (*Nicotiana attenuata*), which is deficient in a certain lipoxygenase involved in the production of jasmonic acid, allowed the significance of induced defenses to be monitored.[13] The reduced production of induced volatiles in hormone-deficient plants was correlated with a reduced resistance to attack by the specialist herbivore *Manduca sexta*. In addition, novel herbivores rarely found on wild type *N. attenuata* were now able to feed on the modified plant. Induced defenses thus influence not only the degree of herbivore feeding but even the composition of the herbivore community.[13]

These first investigations confirm the value of genetically modified plants with altered metabolite production or even completely changed hormonal regulations for ecological investigations of the role of chemical defenses. This field of molecular chemical ecology is still emerging, and interesting insights into complex ecological interactions can be expected from these or similar approaches in the near future.

[1] U. Wittstock, J. Gershenzon, *Curr. Opin. Plant Biol.* **2002**, *5*, 300–307.
[2] R. Karban, I. T. Baldwin, *Induced Responses to Herbivory*, University of Chicago Press, Chicago, IL, **1997**.
[3] J. Takabayashi, M. Dicke, S. Takahashi, M. A. Posthumus, T. A. Vanbeek, *J. Chem. Ecol.* **1994**, *20*, 373–386.
[4] J. Takabayashi, M. Dicke, M. A. Posthumus, *J. Chem. Ecol.* **1994**, *20*, 1329–1354.
[5] A. Kessler, I. T. Baldwin, *Annu. Rev. Plant Biol.* **2002**, *53*, 299–328.
[6] M. Dicke, J. J. A. van Loon, *Entomol. Exp. Appl.* **2000**, *97*, 237–249.

 © 2006 Wiley-VCH Verlag GmbH & Co. KGaA, Weinheim

[7] R. M. P. Van Poecke, M. A. Posthumus, M. Dicke, *J. Chem. Ecol.* **2001**, *27*, 1911 – 1928.
[8] W. Boland, A. Gäbler, *Helv. Chim. Acta* **1989**, *72*, 247 – 253.
[9] A. Gäbler, W. Boland, U. Preiss, H. Simon, *Helv. Chim. Acta* **1991**, *74*, 1773 – 1789.
[10] I. F. Kappers, A. Aharoni, T. van Herpen, L. L. P. Luckerhoff, M. Dicke, H. J. Bouwmeester, *Science* **2005**, *309*, 2070 – 2072.
[11] S. Berger, *Planta* **2002**, *214*, 497 – 504.
[12] R. Halitschke, I. T. Baldwin, *Plant J.* **2003**, *36*, 794 – 807.
[13] A. Kessler, R. Halitschke, I. T. Baldwin, *Science* **2004**, *305*, 665 – 668.

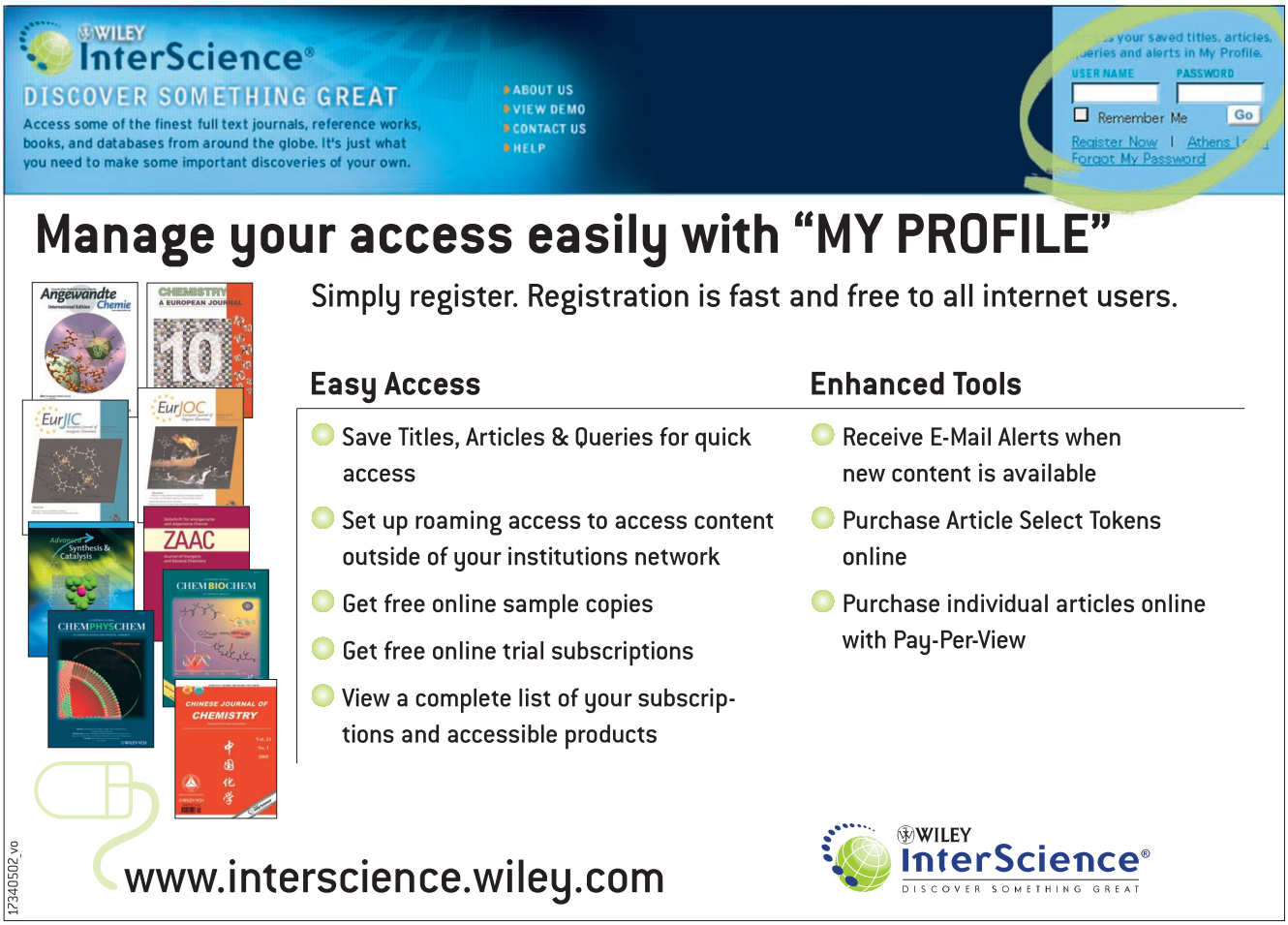

 © 2006 Wiley-VCH Verlag GmbH & Co. KGaA, Weinheim

Hydrogen Storage

DOI: 10.1002/anie.200504149

Clathrate Hydrogen Hydrate—A Promising Material for Hydrogen Storage

Yun Hang Hu and Eli Ruckenstein*

Keywords:
cage compounds · clathrates · hydrates · hydrogen · water

Hydrogen is viewed as a promising clean fuel of the future. A low-cost hydrogen storage technology that provides a high storage capacity and fast kinetics is a critical factor in the development of a hydrogen economy for transportation. The technologies to store hydrogen can be classified into three types: compression, liquefaction, and storage in a solid material.[1,2] Compressing hydrogen requires a very high pressure to obtain enough hydrogen fuel for a reasonable driving cycle of 400–500 km, which in turn leads to safety issues related to tank rupture in case of accidents.[2] The large amount of energy consumed during liquefaction and the continuous boil-off of hydrogen limit the possible use of liquid-hydrogen storage technology.[1] Therefore, attention is currently focused on solid storage materials.

In general, the storage of hydrogen in solid materials is achieved by one of two processes: chemical reactions, in which the hydrogen reacts with the solid material to form new compounds, and adsorption, in which the hydrogen is adsorbed on the solid material. Materials for the storage of hydrogen through chemical reactions include metals,[3] complex hydrides,[4] and nitrides.[5] Materials with relatively high hydrogen storage capacities usually have a hydrogen-releasing temperature of over 100 °C (some even higher than 200 °C) as a consequence of the high energy needed to break chemical bonds. On the other hand, the release temperature of hydrogen is usually low if hydrogen is stored in a solid material by adsorption,[6,7] however, such materials have lower storage capacities.

A new type of hydrates, namely the clathrate hydrogen hydrates, were recently reported,[8–12] opening a new direction for hydrogen storage. Storage of H_2 in this type of material is carried out by capturing the hydrogen in H_2O cages rather than through chemical reaction or adsorption.

Hydrogen-bonded H_2O frameworks can generate polyhedron cages around guest molecules to form solid clathrate hydrates.[13–15] There are three common types of gas hydrate structures: 1) the sI hydrate, which consists of 46 water molecules that form two pentagonal dodecahedron (5^{12}) and six tetrakaidecahedron ($5^{12}6^2$) cages in a unit cell; 2) the sII hydrate, which consists of 136 water molecules that form sixteen 5^{12} and eight $5^{12}6^4$ cages in a unit cell; and 3) the sH hydrate, which consists of 36 water molecules that form three 5^{12}, two $4^35^66^3$, and one $5^{12}6^8$ cages in a unit cell. The type of crystalline structure that forms depends on the size of the guest molecule; for example, CH_4 and C_2H_6 generate the sI hydrate, C_3H_8 gives rise to the sII hydrate, and the larger guest molecules, such as cyclopentane in the presence of methane, result in the sH hydrate.[15]

In contrast to other gases, the hydrogen molecule with its diameter of 2.72 Å was initially thought to be too small to support a clathrate structure. However, this point of view was challenged by recent experimental results.[8–12] Mao et al. reported that mixtures of H_2 and H_2O can crystallize into an sII clathrate with a molar ratio of H_2 to H_2O of approximately 1:2.[8] When a mixture of H_2 and H_2O was compressed at a pressure of 180–220 MPa and cooled to 249 K, a single solid compound was formed. Furthermore, energy-dispersive X-ray diffraction (EDXD) measurements indicated that the solid compound has a face-centered cubic unit cell with $a = 17.047 \pm 0.010$ Å, in excellent agreement with the archetypal sII clathrate.[16]

As the H_2/H_2O ratio in the hydrate is 0.45 ± 0.05, the 24 cages must be multiply occupied by H_2 clusters to accommodate 61 ± 7 molecules of H_2. By comparing the size of the H_2 clusters and the volume of the cage cavities, Mao et al. proposed that two molecules of H_2 were located in each of the 5^{12} cages and four molecules of H_2 were located in each of the $5^{12}6^4$ cages (Figure 1 A).[8] This means that the hydrogen hydrate can reversibly store about 5.3 wt % hydrogen (excluding the hydrogen atoms of H_2O).[9]

Raman spectroscopy showed that the roton peaks for hydrogen in the clathrate were similar in frequency to those of pure hydrogen, indicating that the hydrogen molecules in the clathrate cages were still in free rotational states.[8] This indicates that the hydrogen molecules in the clathrate remain unbonded to each other or to water. However, a substantial softening and splitting of the vibron peaks of hydrogen indicate some intermolecular interactions.

The stability of type sII hydrogen clathrate was investigated using a statistical mechanical model in conjunction

[*] Prof. Y. H. Hu, Prof. E. Ruckenstein
Department of Chemical and Biological Engineering
State University of New York at Buffalo
Buffalo, NY 14260 (USA)
Fax: (+1) 716-645-3822
E-mail: yhu@buffalo.edu

© 2006 Wiley-VCH Verlag GmbH & Co. KGaA, Weinheim

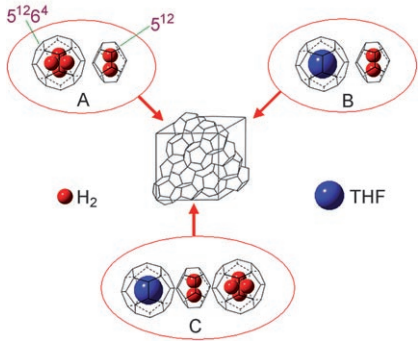

Figure 1. Clathrate hydrate with the sII structure, which contains 136 molecules of water that form sixteen 5^{12} and eight $5^{12}6^4$ cages per unit cell: A) pure hydrogen hydrate, in which H_2 occupies all cages; B) H_2/THF hydrate, in which H_2 occupies the smaller 5^{12} cages and THF occupies the larger $5^{12}6^4$ cages; and C) H_2/THF hydrate, in which H_2 is located in both the smaller 5^{12} and larger $5^{12}6^4$ cages and THF occupies the larger $5^{12}6^4$ cages.

with first-principle quantum chemistry calculations.[12] It was found that the stability of the hydrogen clathrate is mainly due to the dispersive interactions between the molecules of H_2 and the water molecules that form the cage walls. Furthermore, the theoretical analysis showed that the hydrogen molecules undergo essentially free rotations inside the clathrate cages,[12] consistent with the experimental results provided by Raman spectroscopy.[8]

A limitation of this example is that the hydrogen clusters can be stabilized in a clathrate hydrate only at extremely high pressures (typically 220 MPa at 249 K).[8,9] To store H_2 at lower pressures, Sloan and co-workers introduced a second guest component into the hydrogen hydrate.[10] They found that by introducing tetrahydrofuran (THF) into the larger cavities, the clathrate could be stabilized at pressures of 5 MPa at 279.6 K as compared to 300 MPa at 280 K for pure H_2 hydrate.[10] This observation is a very meaningful result and challenges the current theory, which suggests that hydrogen is *excluded* from the clathrate framework in the presence of a second guest component.[17,18]

X-ray powder diffraction (XRPD) data showed that the H_2/THF hydrate has the crystalline structure of the sII hydrate;[10] that is, it has the same structure as reported for the pure H_2 hydrate by Mao et al.[8] Furthermore, on the basis of Raman spectroscopy measurements Sloan and co-workers suggested that all or most of the large cages of the binary clathrate hydrate are filled with THF. In contrast, the H_2 molecules most likely occupy to a significant extent only the small cages (Figure 1B). Although the inclusion of THF molecules, which almost completely fill the larger cavities, decreases considerably the synthesis pressure, their presence also leads to a significant decrease in the capacity of hydrogen storage.

In another study, Lee et al. found by tuning the H_2/THF composition that the hydrogen guest can enter both in the larger and the smaller cages, thus increasing the hydrogen storage capacity to approximately 4 wt% at modest pressures.[11] Lee et al. carried out a number of experiments at a H_2 pressure of 12 MPa and temperature of 277.3 K. When the THF concentration was in the range of 2.0 to 5.56 mol%, H_2 and THF molecules occupied the smaller and larger cages, respectively, leading to a storage capacity of 2.09 wt% H_2. However, a further decrease in the concentration of THF was found to enhance the H_2 capacity, such that a maximum storage capacity of about 4 wt% H_2 was finally reached at a concentration of 0.15 mol% THF. In this case, H_2 occupied not only all the small cages but also some of the larger ones (Figure 1C). However, at a lower THF concentration (0.1 mol%), a hydrogen-containing hydrate was no longer formed under the conditions used (12 MPa H_2 and 277.3 K).

Other additives, such as 1,3-dioxolane, 2,5-dihydrofuran, and tetrahydropyran, can have similar effects on the formation of hydrogen hydrate as THF, but none of these performs as well as THF.[19]

In summary, the successful synthesis of hydrogen hydrates is a breakthrough in the development of materials for hydrogen storage. While very different from conventional hydrogen storage materials, the hydrogen hydrates, which are neither flammable nor corrosive, provide a safe and environmentally friendly material to store hydrogen. However, it still remains a challenge to employ hydrogen hydrates as practical materials for hydrogen storage. The synthesis of hydrogen hydrates mentioned above is a relatively slow process because their formation is controlled by diffusion through a bulk solid phase. The slow kinetics may create difficulties to recharge hydrogen onboard for fuel cell vehicles. However, an extremely fast method of clathrate synthesis was recently reported that allows the formation of hydrogen hydrate to be completed in minutes.[20] Permanent cooling, which is necessary to keep hydrogen hydrates stable, may be another issue. When the cooling fails, the material will release large amounts of hydrogen in a rather short time, which may lead to safety problems. Another challenge is to increase the hydrogen capacity of the hydrogen hydrates. The maximum hydrogen capacity is 5.3 wt% for the sII structure of the hydrogen hydrate at a high synthesis pressure and 4 wt% at a modest pressure. Thus, to achieve higher capacities, new structures of hydrogen hydrates are required.

Published online: February 21, 2006

[1] A. Züttel, *Naturwissenschaften* **2004**, *91*, 157.
[2] M. Fichtner, *Adv. Eng. Mater.* **2005**, *7*, 443.
[3] "Hydride Storage", G. Sandrock in *Handbook of Fuel Cells*, (Eds.: W. Vielstich, A. Lamm, H. A. Gasteiger), Wiley, New York, **2003**, p. 101.
[4] B. Bogdanovic, M. Schwickardi, *J. Alloys Compd.* **1997**, *253*, 1.
[5] Y. H. Hu, E. Ruckenstein, *J. Phys. Chem. A* **2003**, *107*, 9737.
[6] A. M. Seayad, D. M. Antonelli, *Adv. Mater.* **2004**, *16*, 765.
[7] N. L. Rosi, J. Eckert, M. Eddaoudi, D. T. Vodak, J. Kim, M. O'Keefe, O. M. Yaghi, *Science* **2003**, *300*, 1127.
[8] W. L. Mao, H. K. Mao, A. F. Goncharov, V. V. Struzhkin, Q. Guo, J. Hu, J. Shu, R. J. Hemley, M. Somayazulu, Y. Zhao, *Science* **2002**, *297*, 2247.
[9] W. L. Mao, H. K. Mao, *Proc. Natl. Acad. Sci. USA* **2004**, *101*, 708.
[10] L. J. Florusse, C. J. Peters, J. Schoonman, K. C. Hester, C. A. Koh, S. F. Dec, K. N. Marsh, E. D. Sloan, *Science* **2004**, *306*, 469.
[11] H. Lee, J. Lee, D. Y. Kim, J. Park, Y. Seo, H. Zeng, I L. Moudrakovskl, C. I. Ratcliffe, J. A. Ripmeester, *Nature* **2005**, *434*, 743.
[12] S. Patchkovskii, J. S. Tse, *Proc. Natl. Acad. Sci. USA* **2003**, *100*, 14645.
[13] E. D. Sloan, *Clathrate Hydrates of Natural Gases*, 2nd ed., Dekker, New York, **1997**.

 © 2006 Wiley-VCH Verlag GmbH & Co. KGaA, Weinheim

[14] J. S. Loveday, R. J. Nelmes, M. Guthrie, S. A. Belmonte, D. R. Allan, D. D. Klug, J. S. Tse, Y. P. Handa, *Nature* **2001**, *410*, 661.
[15] a) C. A. Koh, *Chem. Soc. Rev.* **2002**, *31*, 157; b) P. Englezos, J. D. Lee, *Korean J. Chem. Eng.* **2005**, *22*, 671.
[16] T. C. W. Mak, R. K. McMullan, *J. Chem. Phys.* **1965**, *42*, 2732.
[17] G. D. Holder, J. L. Stephenson, J. J. Joyce, V. T. John, V. A. Kamath, *Ind. Eng. Chem. Process Des. Dev.* **1983**, *22*, 170.
[18] S. X. Zhang, G. J. Chen, C. F. Ma, L. Y. Yang, T. M. Guo, *J. Chem. Eng. Data* **2000**, *45*, 908.
[19] C. J. Peters, L. J. Rovetto, J. Schoonman, *Proceedings of the International Conference on Gas Hydrates*, Trondheim, Norway **2005**, paper 5031, p. 1644.
[20] M. Greenblatt, D. He, R. J. Hemley, M. V. Lobanov, K. A. Lokshin, W. L. Mao, H. K. Mao, Y. Zhao, *Proceedings of the International Conference on Gas Hydrates*, Trondheim, Norway, **2005**, paper 5024, p. 1601.

The definitive work in electrochemistry

Encyclopedia of Electrochemistry

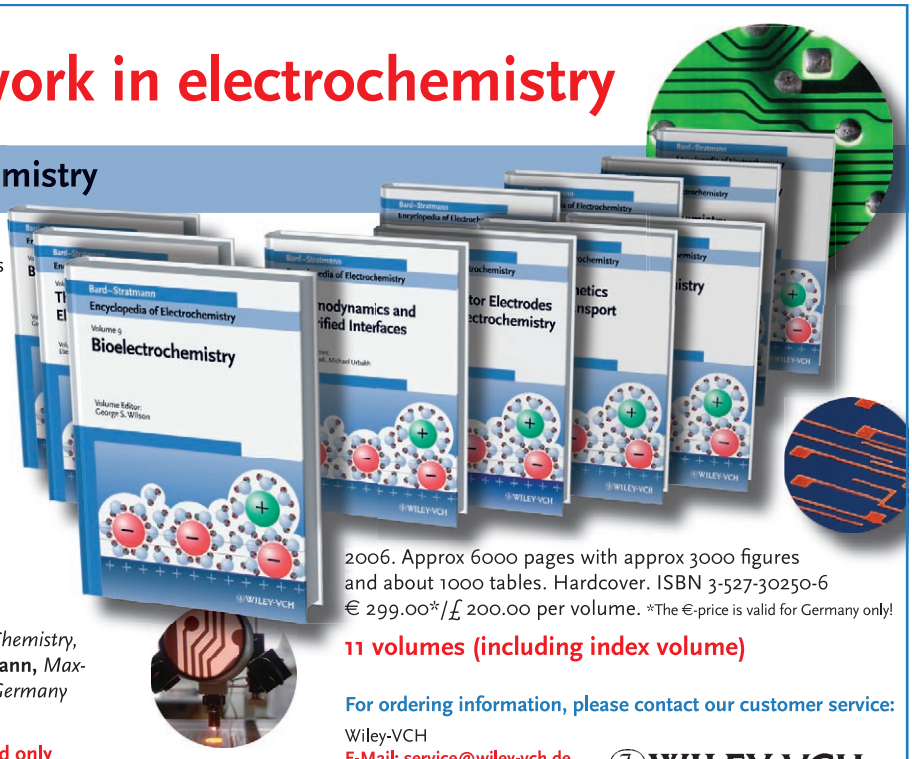

Available Volumes:
1: Thermodynamics and Electrified Interfaces
2: Interfacial Kinetics and Mass Transport
3: Instrumentation and Electroanalytical Chemistry
4: Corrosion and Oxide Films
6: Semiconductor Electrodes and Photoelectrochemistry
8: Organic Electrochemistry
9: Bioelectrochemistry

Forthcoming Volumes *(completed Fall 2006)*:
5: Electrochemical Engineering
7: Inorganic Electrochemistry
10: Modified Electrodes
11: Index

Editors-in-Chief: **Allen J. Bard,** *Department of Chemistry, University of Texas, Austin, USA*/ **Martin Stratmann,** *Max-Planck-Institute for Iron Research, Duesseldorf, Germany*

Stay up-to-date in electrochemistry
- a total of 11 volumes makes this **the first and only** complete reference on electrochemistry
- covering **all aspects**, from fundamental research to applications in industry
- **easy access** to electrochemical topics

www.wiley-vch.de/bard/eoe

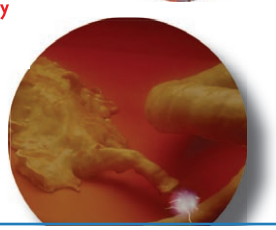

2006. Approx 6000 pages with approx 3000 figures and about 1000 tables. Hardcover. ISBN 3-527-30250-6
€ 299.00*/£ 200.00 per volume. *The €-price is valid for Germany only!

11 volumes (including index volume)

For ordering information, please contact our customer service:

Wiley-VCH
E-Mail: service@wiley-vch.de
www.wiley-vch.de

John Wiley & Sons, Inc.
E-Mail: custserv@wiley.com
www.wiley.com

John Wiley & Sons, Ltd.
E-Mail: cs-books@wiley.co.uk
www.wiley.com

WILEY-VCH
WILEY
WILEY InterScience® DISCOVER SOMETHING GREAT

1872504_gu

 © 2006 Wiley-VCH Verlag GmbH & Co. KGaA, Weinheim

DOI: 10.1002/anie.200502820

Data Storage Media

Current Developments in Optical Data Storage with Organic Dyes

Heinz Mustroph, Manfred Stollenwerk, and Volker Bressau*

Keywords:
CD · DVD · dyes/pigments · materials science · optical data storage

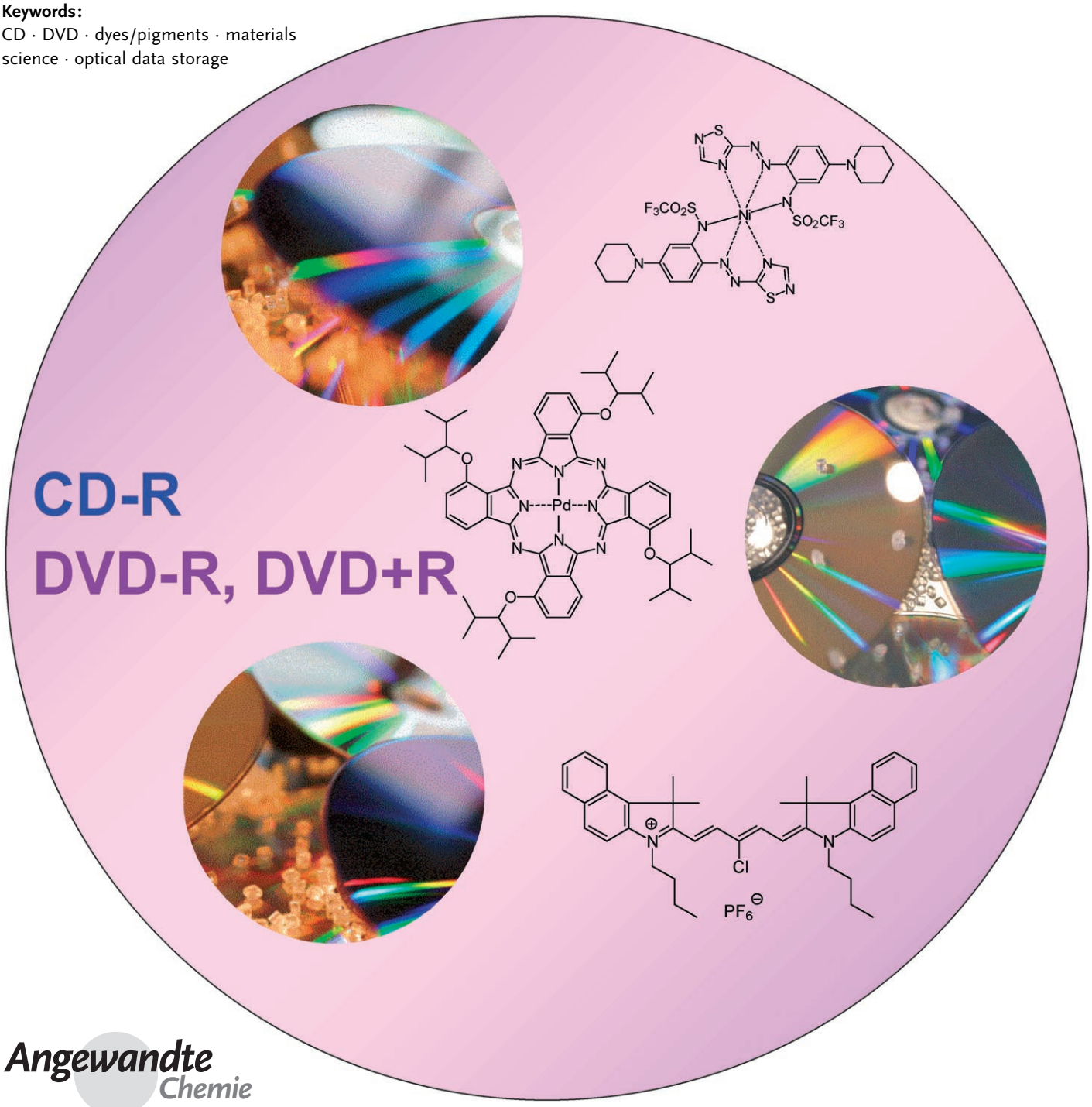

© 2006 Wiley-VCH Verlag GmbH & Co. KGaA, Weinheim

The main motivation for the development of digital data storage has been the improvement in play-back quality and the increase in storage capacity. In 1982 Philips and Sony introduced the first technically and economically successful system based on this—the compact disc (CD) and a compatible player. A very broad diversity of optical data recording formats are available today, and a difference is drawn between prerecorded, recordable, and rewritable media. This Review gives an overview of the systems used, the main features of production, and then concentrates on the properties of the organic dyes that are used in recordable systems. Dyestuffs chemistry has gained the reputation of having become a mature field of activity. Is this prejudice or a justified swan song for dyestuffs chemistry? When applications in optical data storage are considered, it is evident that even today progresses such as CD-R and DVD/R would not be feasible without functional dyes.

From the Contents

1. Introduction 2017
2. Optical Data Stores 2018
3. Production of Recordable Optical Data Stores 2022
4. Influences on the Recordability and the Readability of Recordable Discs 2024
5. Dyes 2027
6. Summary and Outlook 2032

1. Introduction

Media that are able to store signals in any form whatsoever are generally described as data storage systems. In the case of analogue data storage, for example, sound (magnetic tape, records), pictures (camera film), or sound and picture (movies, video tape), deterioration occurs on repeated playing, thus leading to hissing and crackling during play-back. This loss does not occur with digital storage, and so the improvement in play-back quality is a significant driving force for the development of digital data storage.

Naturally, application software for computers and data are stored digitally. The increasing diversity of information has meant that the demand for portable storage media with high storage capacity has increased, both professionally and privately. Whereas in 1985 the 5 1/4-inch disc with 360 kByte disc space was state of the art, the introduction of the DVD has resulted in the capacity increasing 13 000-fold in less than 20 years. Thus, a second important reason for the introduction of digital media is the increase in storage capacity. Optical storage media have played a major part in this development. The success of these storage media is founded both on the high storage capacity and the compatibility of the formats developed later with the drives already installed as well as on the low costs per MByte (Figure 1).

At the outset of the success story lies a small silvery disc 16 g in weight, with a diameter of 12 cm and a thickness of 1.2 mm—the compact disc (CD). Philips and Sony began the development of this digital recording system for sound at the end of the 1970s. No-one imagined the success when the two firms presented their new system, which consisted of the compact disc (at that time all CDs were produced by PolyGram in Langenhagen, near Hanover) and player in 1982. Within a few years, CD-audio had won through dramatically. Important advantages compared to phonograph records were the extraordinary purity of sound and simple handling. In 1990, just a few years after the introduction of CD-audio onto the market, 28 % of all households in the USA already possessed a CD player. Thus, the CD-audio was the first commercially successful optical data storage system, and it has stimulated the development of further systems. In addition to the digital storage of music and speech, this form has also allowed the digital storage of application software and data for computers. These data stores are called CD-ROM (read only memories) and came onto the market three years later. A recommended review of their technical development has been published recently.[1]

In 1989 an article on the then known recordable optical data stores was published in this Journal,[2] followed shortly

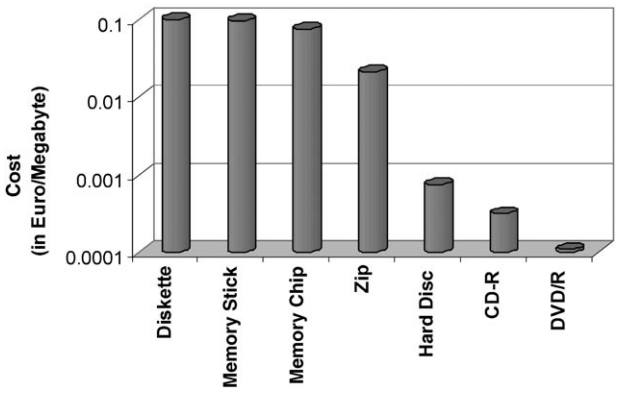

Figure 1. Comparison of the costs for different storage media.

[*] Dr. H. Mustroph
FEW Chemicals GmbH
ChemiePark Bitterfeld Wolfen
Technikumstrasse 1, 06766 Wolfen (Germany)
Fax: (+49) 3494-63-8099
E-mail: mustroph@few.de
Dr. M. Stollenwerk
STEAG HamaTech AG
Ferdinand-von-Steinbeis-Ring 10, 75447 Sternenfels (Germany)
V. Bressau
STEAG ETA-Optik Gesellschaft für optische Meßtechnik mbH
Borsigstrasse 78–80, 52525 Heinsberg (Germany)

© 2006 Wiley-VCH Verlag GmbH & Co. KGaA, Weinheim

afterwards by a review that summarized in particular the state of the art of recordable storage media (write once read many; WORM).[3] In the intervening years both the pure read-only stores as well as the recordable and rewritable stores have developed at a rapid pace. The present Review gives an overview of the systems used, the main features of the production of recordable optical data media, and then concentrates on the properties of the organic dyes and dye layers that are used in the recordable systems. In the conclusion a perspective of future developments is given.

2. Optical Data Stores

The first attempts at the storage of video sequences on compact discs date back to the 1960s. However, attempts were made at analogue storage. Mention is made here of the Video Disc of Philips, which stored the film as small individual pictures on the disc. Philips marketed the Video Disc in 1978, but it was not a success: the storage capacity was too small for good picture reproduction and the semiconductor laser used had a durability of about one hundred operating hours.[1] Further development towards the CD with digital data storage, as we know it now, was then carried out primarily by Philips and Sony.

A broad diversity of optical data media formats is available today. A difference is drawn between the prerecorded, the recordable (-R), and the rewritable (-RW) media. Whereas the content (for example, music or computer data) is fixed during manufacture in the case of the prerecorded CD, the data can be "burnt" onto the discs by the user in the case of recordable media. Figure 2 gives an overview of the different formats that will be described more closely in the following sections.

2.1. The Development of Optical Data Stores with Prerecorded Information

2.1.1. Prerecorded CD

After the prototype of a player for CDs was introduced in 1979, and Sony and Philips had agreed on a standard, the CD was officially marketed in 1982—originally as CD-audio for playing back audio signals. The data are stored bit by bit (binary digit) as depressions (pits) and regions without

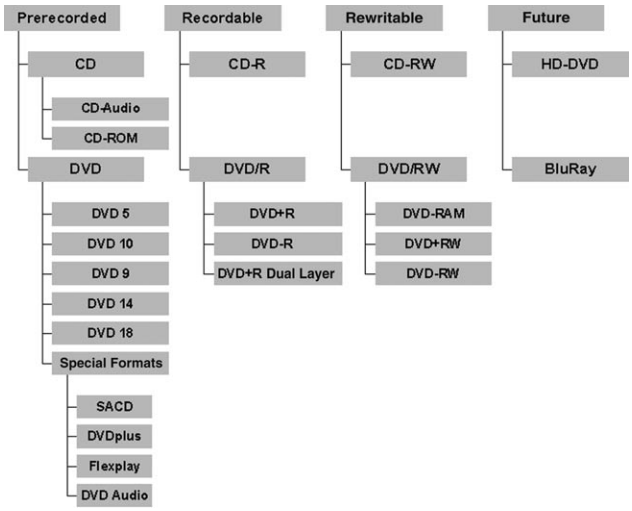

Figure 2. Overview of the important optical data media formats and their breakdown into prerecorded, recordable (-R), and rewritable (-RW) media.

depressions (lands). The pits are ideally $\lambda/4$ deep. In this way, the phase shift of the laser light reflected from the bottom of the pit relative to that reflected from the land is $\lambda/2$ and interferes destructively with the incident beam so that the intensity of the reflected laser beam is greatly reduced.[4] This decrease in the intensity of the reflected laser light relative to that reflected from the land is measured with photodiodes. Together with the information on the length of the pits and the land, the binary information is thus determined and a digital-analogue converter produces an electrical signal. For play-back, a CD can in principle rotate at a constant frequency (constant angular velocity; CAV) or the frequency of rotation is so controlled that the relative velocity between the reading laser and the disc remains constant even with varying radii (constant linear velocity; CLV). At constant rotational velocity the pit length must be adjusted from the inside outwards, while at constant linear velocity the speed of rotation is dependent upon the radius. The CD operates with constant linear velocity and thus with identical pit lengths.

Pivotal for success was the world-wide compatibility of the CD, irrespective of who produced the discs or the drives for the players. This compatibility was guaranteed by the compilation of the data coding and the physical properties

Heinz Mustroph was born in 1951, studied chemistry at the Humboldt-Universität zu Berlin, and gained his doctorate at the Universität Leipzig. In 1975 he joined the research department of Filmfabrik Wolfen and in 1992 became manager of research. Since 1995 he has been general manager of FEW Chemicals GmbH in Wolfen. His current research interests include dyestuffs chemistry as well as photochemistry and structure–color relationships of dyes.

Manfred Stollenwerk was born in Aachen in 1965 and studied physics at the RWTH Aachen. After gaining his Diploma (1991) he was research associate at the Institut für Kunststoffverarbeitung at the RWTH Aachen and gained his doctorate in 1996 on plasma-supported coating of plastics from the gas phase. His dissertation received many awards. Since 1996 he has occupied several positions at STEAG HamaTech AG, Sternenfels, recently general manager for recordable media equipment.

 © 2006 Wiley-VCH Verlag GmbH & Co. KGaA, Weinheim

of the CD in a book, the contents of which all producers had to follow. The book for CD-audio had a red jacket and, therefore, since its publication has been known as the "Red Book".[5] The introduction of the CD-ROM for computer applications followed in 1985. The specification was published in a book with a yellow jacket—the "Yellow Book".[6] The specifications were extended in subsequent years and a few, not very successful, special formats were also developed (for example, CD + G, CDV, and CD-I).

CD-audio and CD-ROM consist essentially of a 1.2-mm thick substrate of polycarbonate (Figure 3). The substrate is produced by injection molding and already contains the data in the form of pits and lands. Finally a reflecting layer of aluminum (ca. 50 nm) is prepared by sputter technology and sealed with a UV-cured lacquer.

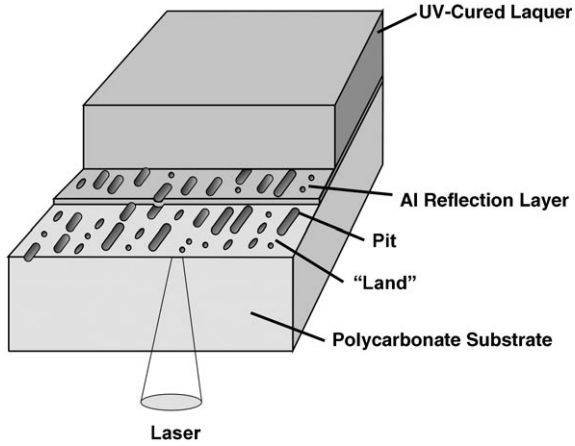

Figure 3. Design of CD-audio/ROM (schematic).

2.1.2. *Prerecorded DVD*

With up to 700 MB memory capacity, the CD achieved a great leap in storage capacity over floppy discs. However, this memory capacity is still insufficient for the storage of movies, and it was therefore apparent for the need to develop a new format with more memory capacity. A higher storage capacity is possible by reduction of 1) the size of the pits and lands, 2) the data track, and 3) the track pitch, as well as by 4) the enlargement of the aperture angle of the objective.[4] The implementation of the first three points requires shorter laser wavelengths for read-out, while the fourth necessitates a reduction in the distance between the objective and the object, which in the case of the optical recording material is determined by the thickness of the substrate d. The aperture angle becomes larger as the separation decreases. The product $n\sin\alpha$ (where α is the half aperture angle of the objective) is known as the numerical aperture (NA). The resolution limit is directly dependent upon the wavelength λ of the laser beam and indirectly upon the numerical aperture.

A laser wavelength of 780 nm is used to read the data from the CD, whereas a wavelength of 650 nm is used with DVD, thus enabling smaller pit structures and narrower tracks to be used in the latter case. These changes lead to a physical increase in the capacity by a factor of 4.54 compared to a CD. Furthermore, the coding of the data is improved (factor of 1.49) and the DVD exhibits a somewhat larger area (factor of 1.02). All the effects together give rise to a capacity of 4700 MB for a single-layer DVD (also called DVD 5).

The experience obtained with CDs showed that a unified standard was necessary for global success of new storage media. Many companies, mainly Japanese with the exception of Philips, had pursued their own developments for a new storage format with higher capacity and were protected with patents. On December 12 1995, the final format for DVD (digital versatile disc) with a storage capacity up to 17 GB was agreed upon in the "DVD Forum", an association on which the most important companies are represented. The forum defines both the video standard and the requirements for DVD-ROM applications. Table 1 gives an overview of the significant differences between CD and DVD.

Table 1: Comparison between CD and DVD 5 (single layer).

	CD (74 min)	DVD 5 (single layer)
thickness [mm]	1.2	2×0.6
diameter [mm]	120	120
laser wavelength [nm]	780	650
numerical aperture	0.45	0.60
laser spot diameter [μm]	0.87	0.54
track separation [μm]	1.6	0.74
minimal pit length [μm]	0.84	0.40
recording speed (CLV) [$m\,s^{-1}$]	1.21	3.49
data rate [$MBit\,s^{-1}$]	1.2288	11.08
effective storage capacity [MByte]	682	4700

Volker Bressau was born in 1970 and studied chemical engineering with the core subject nuclear chemistry at the FH Aachen, Department Jülich, with Prof. Dr. W. Kullbach. After two years at Kurita Europe GmbH in the water chemistry department, he joined Fuji Magnetics GmbH in 1996 working on process qualification and optimization of recordable CD and DVD. Since 2000 he has been product manager of STEAG ETA-Optik GmbH in Heinsberg responsible for the world-wide application of inline measurement instruments for quality testing of optical data media of all formats.

Such high capacities can be achieved by the use of several layers as illustrated in Figure 4. A DVD consists basically of two half discs (or layers) each 0.6-mm thick that are bonded together by a UV-cured lacquer. DVD 5 consists of only one active side (polycarbonate with a reflecting layer of aluminum) that is bonded with an inactive half disc (dummy disc). In the case of DVD 10, two active discs are bonded together, which leads to double the capacity. DVD 10 must be turned for complete playing, a feature that finds little acceptance amongst consumers. This disadvantage is not found with DVD 9: It too consists of two information layers that can, however, be read out from one side. For this purpose it is necessary to keep the reflecting layer of the lower half disc

© 2006 Wiley-VCH Verlag GmbH & Co. KGaA, Weinheim

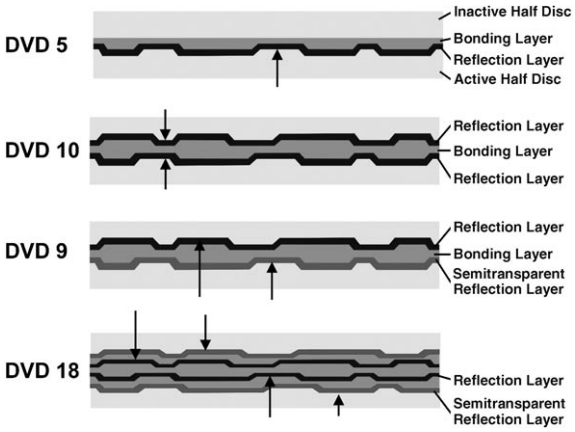

Figure 4. Principal layer construction of the different DVD formats.

(L0) semitransparent whilst the upper half disc (L1) is highly reflective. The upper half disc L1 is read by the laser penetrating L0 as well as the semitransparent reflecting layer and the bonding layer. This arrangement requires a production process that guarantees a bubble-free bonding layer. Still higher capacities can be achieved by three (DVD 14) or even four layers (DVD 18). These formats have thus far, however, only a small market share and are difficult to produce.

2.1.3. *Special Formats*

In addition to the standard formats described, there are a few special developments that were only able to occupy niche positions in the market.

- The SACD (super audio compact disc) is a combination of a CD and a DVD. The format may be played both on a CD player and also in a special SACD player with improved tone quality.
- The DVD-plus format is also a combination of a DVD and a CD. However, the disc must be rotated in compliance with the desired format. Thus, the music can be played from the CD side in a normal CD player and the video sequence contained on the DVD side can be played in a DVD player.
- Flexplay allows "self-destruction" of the DVD within a certain time after opening the package by chemical decomposition of the reflecting layer. Consumers can obtain this Flexplay DVD in supermarkets for a lower price than a normal DVD, but it is playable for a limited time only. Flexplay is thus in direct competition with DVD rentals.
- The DVD-audio contains solely audio information and requires a special audio DVD player. The tone quality is clearly better, however, than that obtained with a normal audio CD player.[7]

2.1.4. *The Next Formats*

The storage capacity of a DVD is still too low for high-resolution television formats (high-density television; HDTV). The pit structures must be much smaller for larger storage capacities to be achieved. For this reason the development of optical data media with higher capacity is closely associated with the availability of semiconductor lasers that have shorter emission wavelengths. In addition, the demands on the mechanical and optical properties of the polycarbonate increases.[8] The new formats BluRay and HD-DVD (high-definition-DVD, previously known as advanced optical disc, AOD) currently under discussion have storage capacities of 25 GB and 15 GB, respectively.[9–11] Both formats use blue laser diodes ($\lambda = 405$ nm) to play and record the data. Otherwise these formats have little in common (Figure 5).

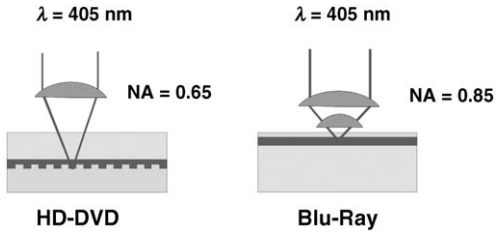

Figure 5. Design of an HD-DVD and BluRay disc (schematic).

HD-DVD is similar to a normal DVD but constructed with smaller pit/land structures. Thus, it consists of two layers, both with a thickness of 0.6 mm. The BluRay disc consists of a 1.1-mm thick support substrate upon which a 0.1-mm thick layer is situated that contains the data. This arrangement gives a numerical aperture of 0.85 (near field) compared with 0.65 with HD-DVD (far field). Which of the two formats will capture the greatest market share is currently unclear.[12] There are powerful demands within the industry to come to an agreement on a common format, but it remains to be seen whether it will be possible to bring the two groups to a consensus.

2.2. *Rewritable Data Stores*

2.2.1. *Rewritable CD*

Soon after the introduction of the prerecorded CDs, consumers started to demand optical data stores with which personal data could be recorded. Although recordable data media dominate the current market, the rewritable CD was the first to be fully developed for the market. In the 1980s a number of different recording principles for rewritable optical discs, the content of which could be erased and rewritten, were proposed.[2] In practice only two have prevailed: those based upon magnetooptical effects and the interchange between amorphous and crystalline phases.

The rotation of the plane of polarization of a polarizable light ray by a magnetic field is known as the magnetooptical effect. It is principally on this basis that pits in reflection (magnetooptical Kerr effect) or in transmission (magneto-optical Faraday effect) are produced. In magnetooptical storage media the active information layer consists of alloys of rare earth metals and transition metals that are magnetized vertically to the plate surface. On "writing", this layer is heated by a laser beam and undergoes polarity reversal by an

 © 2006 Wiley-VCH Verlag GmbH & Co. KGaA, Weinheim

external magnetic field. The pits thus produced retain the new orientation of the magnetic field on cooling. The Kerr effect (differences in the reflection through differential rotation of the plane of polarization of the reflected light) is used in playing back such a "written" disc. Erasure of the information occurs in a similar manner when the original magnetic orientation is reset by a change in the direction of the external magnetic field.[13] The corresponding rewritable CD was developed by Sony and Philips and introduced to the market in 1989 as CD-MO. However, they are not compatible with CD-audio and CD-ROM, and have therefore only been able to achieve a small market share. In 2004 the turnover was only 5 million CD-MO/year.[14] Sony used the technology of magnetooptical CD to introduce the minidisc (MD) for sound and data recording in 1992. Minidiscs currently occupy a niche position in the market.

More universally useable are the rewritable discs that are based on the phase change from the crystalline to the amorphous state. Both phases show a reflection of different intensity, by which means binary data can be read out. This format was developed as the CD-RW (rewritable) in 1996.[15] The actual information layer is an alloy of Sb-Te with an admixture of Ag and In. For thermal reasons this alloy is embedded between two ZnS-SiO_2 buffer layers that act as heat sinks. Above these comes a reflecting layer of AgCr. All these layers must be applied by sputtering (the buffer layers can even be applied by high-frequency sputtering). As with a prerecorded CDs, the layers are protected by a UV-cured lacquer (Figure 6).

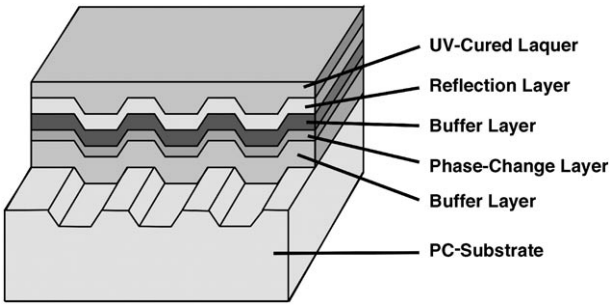

Figure 6. Design of a CD-RW (schematic).

The walls of the pre-grooves of the CD-RW are waved (wobble) with a constant frequency modulation of 22.05 kHz so that the burner can recognize where the laser is located and can control the speed of rotation when recording in the as yet empty pre-grooves. This type of addressing is called absolute time in pre-groove (ATIP). At the same time the ATIP code controls the recording strategy to be used. CD-RW are compatible with the prerecorded CD, but the lower reflection means they are only partially readable in very old CD players.

2.2.2. *Rewritable DVD*

As with CDs, developments followed the prerecorded DVD format that also led to being able to record a DVD.[16] The independent approaches in different companies (again with the corresponding patents and claims for patent licenses) have led to a whole series of different formats. One of the first onto the market in 1997 was the DVD-RAM, which was mainly promoted by a group of Japanese producers led by Matsushita (trade name Panasonic). The DVD-RAM was considered above all to be a storage medium for the computer market. They were delivered in sealed cartridges to protect them from damage. The pit/land structure and the use of a cartridge makes this format incompatible with the prerecorded DVD. Consequently this format has thus far only made an impact in Japan.

In addition to the DVD-RAM, two other rewritable media have largely established themselves in the market place: the DVD-RW ("DVD minus RW") and DVD + RW ("DVD plus RW").[16–19] The essential difference between these two formats lies in the way the data is addressed. Similar to the CD-RW, the DVD + RW developed by Philips and Sony have a wavelike structure in the walls of the pre-grooves with a frequency modulation of 817.4 kHz so that the burner can recognize where the laser is located and can control the speed of rotation when recording in the still empty pre-grooves. This type of addressing is called address in pre-groove (ADIP). Since Philips and Sony hold the patents for this method Pioneer chose another form of addressing for the DVD-RW. Here the wobble signal has a frequency of 140.6 kHz and the positions of the sectors are determined by additional land/pre-pits. Both formats can be written with all current conventional burners and read out with all equipment. Both formats are called DVD/RW in the subsequent discussions.

As with the CD-RW, all three rewritable DVD formats use the crystalline–amorphous phase change induced by local heating for storage of information. Very high investment in production plant is necessary for the production of rewritable media (CD-RW and DVD/RW). At the same time these plants have a comparably low productivity. The associated higher media prices of these formats have meant that they have only been able to capture approximately 5% of the market share of recordable media.[20]

2.3. *Recordable Data Stores*

2.3.1. *Recordable CD (CD-R)*

Work was being undertaken to develop an optical recording technique for recordable media as early as the 1980s. The first product was the previously described WORM. It was based on a dye layer that had a strong absorption at 780 nm—the wavelength of the laser.[2,3,21,22] The laser radiation is absorbed by the dye in the layer when it is electronically excited, after which the absorbed laser radiation is converted into heat, and the dye destroyed by the heat generated. The resulting differences in reflection can then be read by a laser of lower intensity. Despite all the efforts, WORM was not a commercial success: there was no generally binding standard, WORM media of different manufacturers were not compatible, and special hardware was required in each case for burning and play-back. For these reasons the system and the

 © 2006 Wiley-VCH Verlag GmbH & Co. KGaA, Weinheim

apparatus remained very expensive, and despite an actually existing demand it did not win through.

Surprisingly, in 1989 the Japanese company Taiyo Yuden introduced a recordable CD (CD-R) that was completely compatible with the CD standard and could be read in normal CD-ROM and CD-audio drives.[23–28] The difference compared to WORM was that the reflection at a metal surface was exploited, in the same way as with CD, but only a weakly absorbing dye layer (see Section 4.2). The schematic design of a CD-R and a DVD-R is shown in Figure 7. The spiral groove (pre-groove) that guides the laser during read-out and recording is situated in an injection-molded polycarbonate substrate (thickness for CD-R: 1.2 mm, for DVD-R: 0.6 mm). The actual information medium is the dye layer upon which

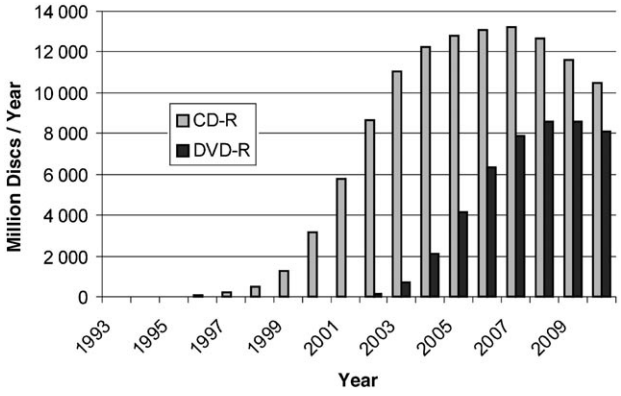

Figure 8. Worldwide consumption of CD-R and DVD/R.

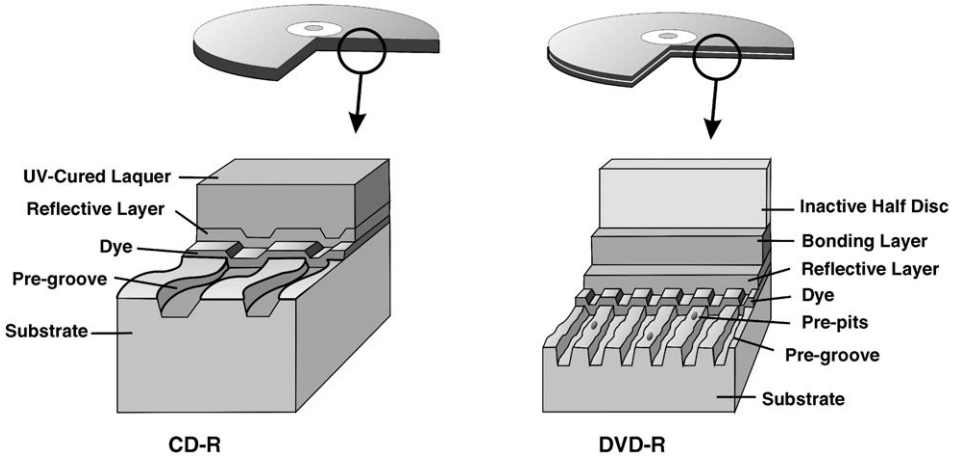

Figure 7. Design of a CD-R and DVD-R (schematic).

there is a metal layer. The surface of the CD-R is formed by a protective lacquer.

The recordable CD as we know it today was introduced in 1991. One of the first applications in 1992 was the Photo-Disc from Kodak for the storage of photographs. The specification of the CD-R is governed by the "orange book".[29] The consumption of CD-R rose steeply from 1996 as a result of its compatibility with the prerecorded CD and the rapid decrease in the price of both the burners and the discs (Figure 8). The production and the operation of the CD-R is described in more detail in Section 3.

2.3.2. *Recordable DVD (DVD/R)*

As with recordable CDs, it is also the recordable DVD format that has won the greatest market share by far. The reasons for this are the successful customer acceptance of single recordable media for the CD-R and the low price. In the case of the recordable DVD there are also two different formats: the DVD + R ("plus R") and DVD-R ("minus R").[30–32] As with the DVD/RW, there are also two significant differences in the way the data are addressed. In the actual production process these are of lesser importance, and for this reason DVD + R and DVD-R are generally known together under the name DVD/R. In analogy to DVD 5, a second polycarbonate half disc without information content is also attached in the case of the DVD/R (Figure 7).

At the beginning of 2004 Philips introduced DVD + R Dual Layer as new format.[33] The disc is constructed in a similar way to DVD 9 and consists of two recordable layers. The capacity of 8.5 GB is about twice as large as that of a single-layer DVD + R. Since the data of both active half discs have to be recorded and read from one side, the production steps for the preparation of the L1 layer are very complicated and only a low level of productivity can be achieved. Whether it will achieve any significant share of the market cannot be assessed at this time.

3. Production of Recordable Optical Data Stores

3.1. Production of CD-R

Figure 9 shows the schematic representation of the equipment for the production of CD-R. Production begins with injection molding of the CD-R substrate that already includes the pre-groove. For this purpose a "stamper" is attached to the mold of the injection-molding machine that contains a negative of the pre-groove. Up to three injection-molding machines are operated at the same time to decrease the cycle time.

On removal from the injection-molding machine the CD-R substrates have a temperature of about 110 °C, and so must next be adequately cooled. The dye is applied ("dye coating") after cooling. The dye is dissolved in a highly volatile solvent and is applied to the polycarbonate substrate by spin coating. The thickness of the layer in the pre-groove of the CD-R after spinning is about 150 nm and 40 nm on the land (see also Section 4.2). The correct setting of these layer thicknesses is critical for the quality of the complete CD-R. The solvent must always evaporate at the same rate to ensure a reproducible layer thickness. This is achieved by stabilization

 © 2006 Wiley-VCH Verlag GmbH & Co. KGaA, Weinheim

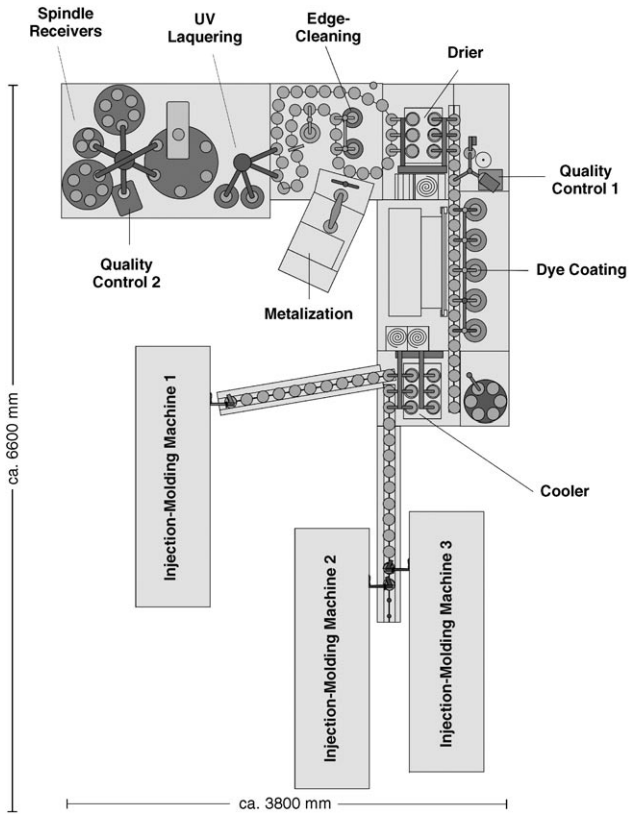

Figure 9. Main components of a production system for the manufacture of CD-R.

of the climate in the region of the dye coating to a constant temperature of ± 0.2 K and a relative humidity of $\pm 5\%$ by an external air-conditioning unit. The substrates are inspected for defects after application of the dye layer. Classical rejection criteria are imperfections in the dye layer, dust, or errors in the substrate such as too high birefringence or mechanical deviations (tilt). Modern systems also measure the thickness of the dye layer of each disc optically and correct the parameters of the spin coating in a closed-loop function so that a constant layer thickness distribution of the dye is always achieved.

After application of the dye layer the residual solvent must be evaporated completely. This takes place in the drier, where the substrates are heated to temperatures (according to process) of between 60 and 110 °C for 12–30 minutes. Opinions differ within the industry as to whether the drying process has other actions on the layer, in addition to pure evaporation, that lead to other layer properties. After drying, a silver layer is applied by argon sputtering which serves as a reflector and also acts as a heat sink during the recording of the pits. Measurement of the layer thickness enables the sputter process to be controlled so that a constant layer thickness is achieved.

The dye solution is applied up to the edge of the disc during dye coating. This process can lead to permeation of moisture at the edge and thus to destruction of the CD-R. Thus, the edge must be cleaned prior to finishing the CD-R. This is carried out in the edge cleaning station where a solvent washes the dye from the edge, and the silver metal layer acts as a mask. The outer edge of the substrate was not metalized, therefore the solvent can rinse off the dye; the rest of the disc is protected from attack by the solvent by the metal layer. The next step in CD-R production is the application of the UV-cured lacquer layer by spin coating. The lacquer distribution and the adjustment of the layer thickness is carried out by adjustment of the spinning program, with curing by irradiation with UV light. The last step is again quality control for detection of optical defects, when the discs are tested mainly for their mechanical properties, for errors in the metal layer, and errors in the protective lacquer. Depending upon the results of the quality control, the discs are then mounted on different spindle receivers. They are then printed and where appropriate packed in a separate plant.

The technology of CD-R production has made considerable progress since 1997. Whereas approximately 7000 CD-R could be produced in a CD-R production plant every 24 hours in 1997, this production capacity of a system since 2000 is about 48 000 CD-R in 24 hours—and this is with considerably increased demands on the quality of the discs produced.

3.2. The Production of DVD/R

It must be noted that in the production of DVD/R two half discs (L0 and L1) have to be produced. For this purpose two injection-molding machines are used. A production system for the manufacture of DVD/R is illustrated in Figure 10. During the injection process the pre-groove is formed in the L0 half disc with the stamper, the L1 half disc does not contain a pre-groove and only serves for later completion of the DVD/R. The L1 half disc is therefore called the "dummy disc".

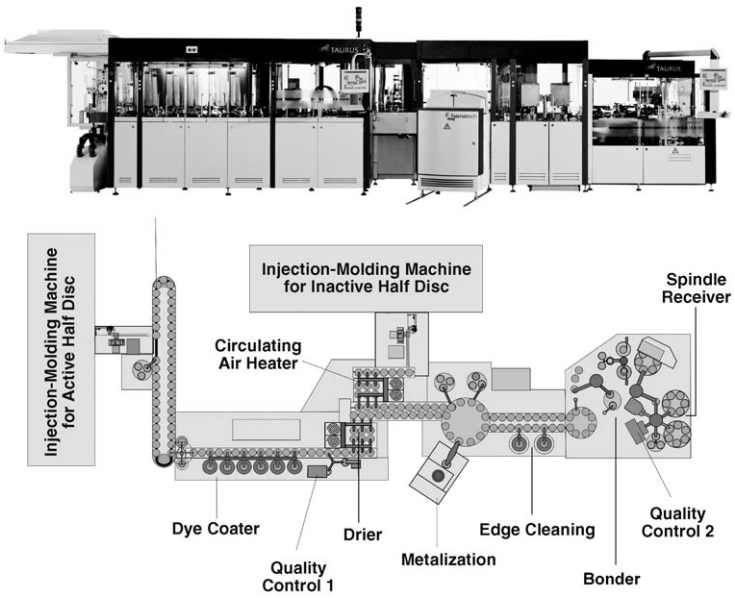

Figure 10. Production system for the manufacture of DVD/R and its main components.

© 2006 Wiley-VCH Verlag GmbH & Co. KGaA, Weinheim

Figure 11 shows sections of atomic force microscope images (AFM images) of a DVD + R L0 substrate and a DVD-R L0 substrate compared with a CD-R substrate. The main construction is identical in all three formats. The pre-groove has a U-shaped structure with a depth of about 180 nm

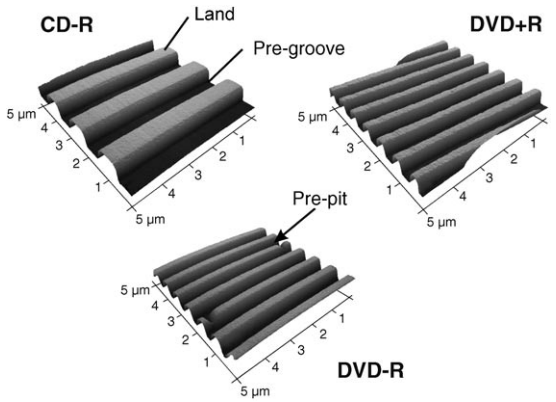

Figure 11. AFM images of a CD-R, DVD-R, and DVD + R (without dye). See text for the heights of the structures.

in the CD-R format and about 160 nm in the DVD/R formats. The width of the pre-groove at half height is about 670 nm (flank angle 50°) in the CD-R and about 350 nm in the DVD/R (flank angle 60°). As with the rewritable CDs, the DVD-R also has a further structure in the land compared with the DVD + R, the so-called pre-pits (Section 2.2.2).

The requirement for molding finer structures in DVD/R results in the temperatures of the molds during DVD/R injection being about 125 °C, which is about 20 °C higher than in CD-R production. Together with the smaller thickness of the DVD/R, which results in easier deformation, special cooling is required after removal from the injection-molding machine.[34]

After cooling, the DVD/R production steps up to and including metalization are identical to those in the production of CD-R. However, only the L0 half disc is processed. The L1 half disc is produced separately and fed in, but it too passes through an air heater that is identical in construction to the drier for the active L0 half disc. This procedure is necessary so that the half discs experience the same temperature procedures. Only then is it guaranteed that, after combination, the two half discs behave identically during climatic changes and do no lead to deformation of the DVD/R, as with a bimetal.

The last production step in DVD/R production is the combination of the L0 and L1 half discs. In the so-called bonding a UV-cured lacquer is introduced between the two half discs, which after spinning is cured in UV light. This process step plays a pivotal role in determining the mechanical properties of the completed DVD/R. Different methods to generate this adhesive layer have been developed in industry. One method is, for example, the gap-dispense method, in which the curable lacquer is introduced into the space between the two half discs and then the two half discs are brought together. The lacquer is then distributed very evenly without air inclusions by the capillary forces that act upon it between the two half discs. The exact thickness of the bonding layer is determined by the spinning program. Currently more than 20000 DVD/R can be produced every 24 hours in a DVD/R production plant.

4. Influences on the Recordability and the Readability of Recordable Discs

4.1. Recording Mechanism

The required compatibility with prerecorded CD means that differences in the reflection between the recorded and nonrecorded regions must also be produced by the recording process in CD-R. The intensity of the interference has a significant influence on the quality of play-back, which is characterized by the carrier to noise ratio (CNR). Reliable play-back requires that the CNR must be greater than 47 dB to lie within the CD-R standard. Moreover, the length of the pits may only vary within a narrow range so that the data can be played back without error. Deviations from this are termed "jitter" and may only be a maximum of 35 ns.

The conceptions originally expressed on the recording process[23] were verified experimentally and the fraction of individual partial contributions to the difference of the optical wavelengths have been investigated in more detail.[35] During the recording process the dye layer absorbs the laser radiation and converts it into heat with destruction of the dye molecules. In addition, the polycarbonate melts through the heat produced and the silver mirror is deformed. Thus, differences in optical wavelengths are produced in the recorded regions (written marks) by:

- the formation of a bump at the polycarbonate/dye interface through the melting of the polycarbonate,
- the formation of a hole (pit) at the dye/metallic mirror interface through destruction of the dye and
- bubble formation at the dye/metallic mirror interface through the development of gases during decomposition of the dye.[35]

The total deformed region corresponds to the pit in the molded CD and has a lower reflection because of the destructive interference of the laser beam. It was estimated from the difference in the individual refractive indices and the respective layer thicknesses that a pit would be most efficient, followed by a bubble, whereas a bump should have the smallest effect.[35] Subsequent work has not confirmed this gradation. It was possible to show that there are two important temperature thresholds: the glass transition temperature (T_g) of the polycarbonate (ca. 140 °C) and the decomposition temperature of the dye.[36] The precise formation of the bump and the decomposition of the dye are critical for CNR and jitter (Figure 12).[37,38] These interrelationships found in CD-R also apply in principle to the recording of DVD/R.

 © 2006 Wiley-VCH Verlag GmbH & Co. KGaA, Weinheim

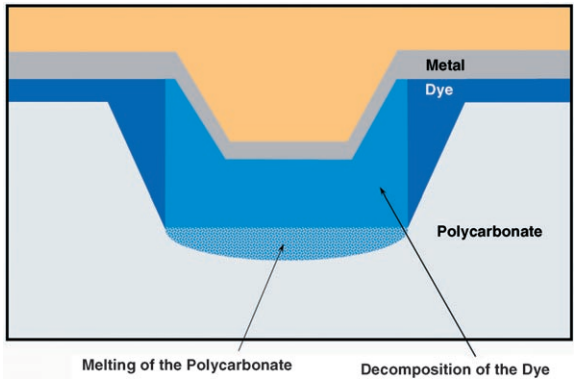

Figure 12. Effects in the formation of the recorded regions in a CD-R (schematic).

4.2. Optical Properties of the Dye Layer

The recordability and readability of recordable optical data media depend critically upon the material properties and layer thickness distribution of the dyes used: after application of the sputter layer, the thin dye layer must have the necessary reflection at the recording/read-out wavelength, while the absorption must be sufficient to ensure the recordability by laser light (see also Section 4.1).

In general the intensity of incident light is divided into absorption, reflection, and transmission for thin, light-transparent layers. Thin dye layers on a flat substrate produce pronounced interference effects that are based on partial reflections at the substrate/dye and dye/air interfaces (Figure 13) which can be exploited in a targeted manner in recordable optical data media.

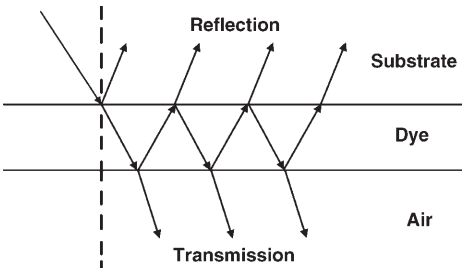

Figure 13. Breakdown of incident light into reflection and transmission in a thin dye layer on a planar substrate.

The interaction of solids with electromagnetic radiation is described by the dielectric function, from which the reflection and absorption in thin dye layers can be calculated. The dielectric function is linked to the complex refractive index $N = n + ik$, where n represents the real part of the complex refractive index and ik the imaginary part. Independent of the layer thicknesses, the optical properties of a dye can be described on the basis of the wavelength-dependent refractive index n and the absorption index k (the absorption coefficient $\alpha = 4\pi k/\lambda$ is determined by k so that k represents a measure of how much electromagnetic radiation is absorbed). In-phase addition of the partial reflections results in pronounced minima and maxima being obtained in the reflections as a function of the thickness of the dye minima with destructive interference, maxima are obtained with constructive interference (Figure 14).

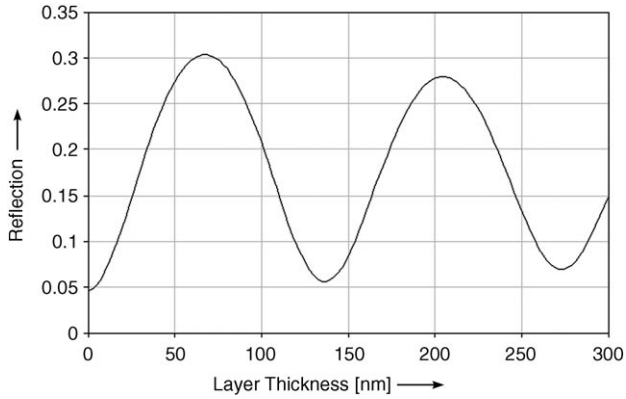

Figure 14. Modulation of the reflection ($\lambda = 650$ nm; $n = 2.37$; $k = 0.054$) by interference as a function of the thickness of the dye layer.

The strength of the partial reflections is dependent upon the difference in the refractive indices at the substrate/dye and dye/air interfaces: the greater the refractive index of the dye the greater the partial reflection and thus the modulation of the reflection with layer thickness (Figure 15). The

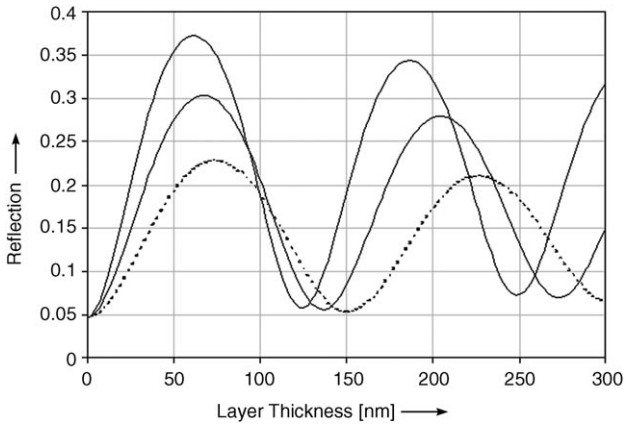

Figure 15. Influence of the refractive index n and the thickness of the dye layer at 650 nm and $k = 0.054$ on reflection. —— $n = 2.57$; —— $n = 2.37$; ----- $n = 2.17$.

modulations in the reflection for three different refractive indices n of the dye are illustrated. The modulation increases significantly at higher values of n. Moreover, the period, that is the distance between two neighboring maxima, decreases sharply with increasing values of n, since the geometric thickness d becomes smaller for the same optical path ($n \times d$).

The sequence of reflection maxima as a function of layer thickness is also superimposed by an exponential dampening as a function of k. The dampening of the reflection increases significantly at larger values of k (Figure 16) so that there is a

 © 2006 Wiley-VCH Verlag GmbH & Co. KGaA, Weinheim

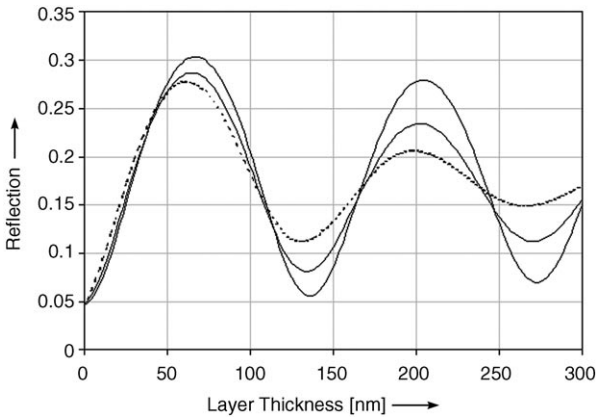

Figure 16. Influence of the absorption index k and the thickness of the dye layer on the reflection at 650 nm and $n = 2.37$. —— $k = 0.054$; —— $k = 0.162$; ----- $k = 0.324$.

limit above which k cannot be increased further by increasing the laser absorption.

Absorption and reflection in the dye layer are not only dependent on the thickness of the layer, but are highly dependent upon the wavelength. Figure 17 shows the behav-

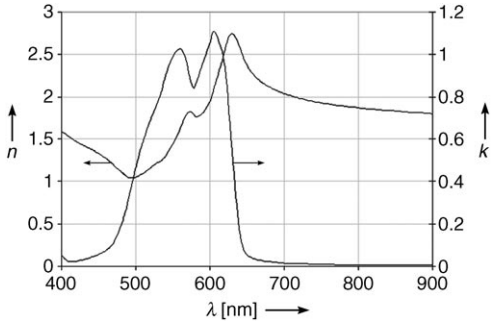

Figure 17. Reflection (n) and absorption index (k) of a DVD/R dye as a function of wavelength.

ior of n and k as a function of the wavelength for a typical DVD/R dye. The refractive index n reaches its maximum at about 650 nm, while the absorption index k takes on a small value.

However, the dye layer does not exist as an even layer upon a planar substrate in the case of CD-R or DVD-R. In fact the substrate is furnished with the pre-groove in which most of the dye is located (Figure 18). Therefore two layer thicknesses have to be considered: "dye on land" and "dye in groove". For a CD-R or DVD/R layer system the dye/air

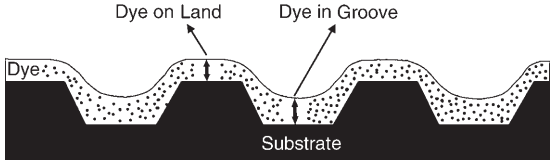

Figure 18. Distribution of the dye on a structured substrate with grooves and land (schematic).

interface is replaced by the dye/full reflector (for example, Ag alloy) interface. It is important that the reflection on the land differs significantly from the reflection in the pre-groove since only in this way does the recording/read-out head receive a tracking signal. With known material data (n and k) and known pre-groove geometry, a suitable process window in respect to reflection may be derived from Figure 19.

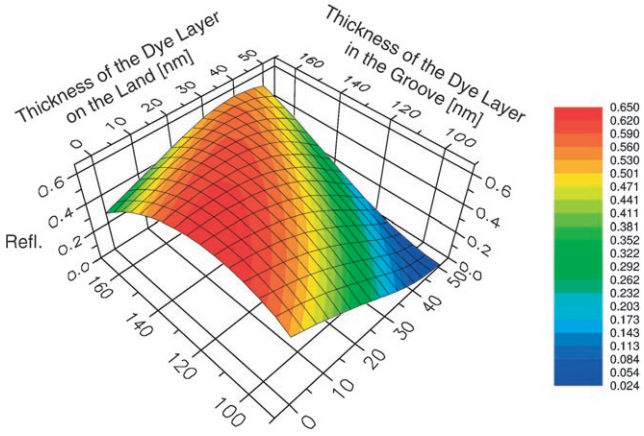

Figure 19. Relationship of the reflection of DVD/R at $\lambda = 650$ nm as a function of the thickness of the dye layer on the land and in a groove.

In Figure 19 the reflection in the pre-groove is represented as a function of the layer thickness distribution.[39,40] At the same time it must also be noted that the reflection in the pre-groove is also influenced by the dye thickness on the land since the focus of the recording/read-out head is significantly greater than the width of the pre-groove and so the dye on the land is also partially registered. However, these details cannot be discussed more closely within the scope of this article.[39,40]

4.3. Thermal Properties of the Dye Layer

The thermal properties of the dye for CD-R and DVD/R have a considerable influence upon the formation of the recorded areas (written marks) and thus the quality of the pit–land structures obtained. At the same time the recording process itself evades direct experimental observation. Significant insights can be achieved, however, by investigation of the recorded regions with different microscopic techniques[35–38] and the assistance of model calculations.[41–43] As already discussed, the exact development of the bump in the polycarbonate and the destruction of the dye are pivotal for CNR and jitter. It follows from this that the first requirement is that the decomposition point of the dye must lie far enough above the glass transition point of the polycarbonate that the polycarbonate melts during recording.[37,38,44] The precise lower limit of the decomposition point is not known; however, experimental experience does show that even dyes with a decomposition point of about 200 °C lead to good results. On the other hand the decomposition point cannot be allowed to rise unrestrainedly. Large pits are formed if the resulting temperature reaches a critical point at which the threshold for

 © 2006 Wiley-VCH Verlag GmbH & Co. KGaA, Weinheim

thermal stress is exceeded, and this possibly leads to destruction of the pre-groove profile, which in turn leads to a higher error rate.[37,44] Secondly the dye must be thermally stable up to its decomposition point, and thirdly it must have a well-defined decomposition threshold; decomposition over a wide temperature range leads to less-sharp edges at the pits and thus to increased jitter values. The heat of reaction from the decomposition of the dye itself has little influence.[48] A fourth important point is the formation of decomposition products and the associated outgassing. Formation of many gaseous decomposition products leads to delamination, and the silver separates from the polycarbonate.

Thermal decomposition behavior becomes more important with faster burning speeds. Higher burning speeds are achieved with greater laser performance and a corresponding shortening of the laser pulse so that more energy hits the dye in less time. Pits or lands of nine different lengths are used in a CD-R (I_3 to I_{11}), with the length measured in time units T (3 T–11 T; T = 230 ns). The length of the pits remain the same, even at higher burning speeds, although the time for burning is correspondingly shortened. For example, a value of T of 230 ns is reduced formally to 4.4 ns at a 52-fold burning speed! With DVD/R, which operates with more different pit lengths (3 T–11 T and 14 T; T = 38.2 ns), T is reduced to 2.4 ns at a 16-fold recording speed. Consequently the demands on the dynamics of thermal decomposition of the dye described above are increased still more. The influence of thermal properties of DVD/R dyes has been comprehensively investigated with azo–metal complexes.[45–47]

The decomposition point and decomposition range can be determined in a preliminary test by differential scanning calorimetry (DSC) and the fraction of highly volatile components can be determined by thermogravimetric analysis (TGA). Thus, these two methods allow for a preselection of dyes from a thermal standpoint. However, these alone are not sufficient for optimization of the dyes.

The heat formed is conducted in both a radial and a lateral direction to the metal, dye, and polycarbonate layers.[36] Since the thermal conductivity of the metal layer is much greater than that of the other two layers, a strong temperature gradient is formed. When a pit is recorded the heat also diffuses to the site at which the next pit is to be recorded (preheat), which leads to preheating so that the edge of the newly recorded pit is not sharply defined. The second effect of heat diffusion proceeds in a similar manner. When the next pit is recorded the heat diffuses back to the previously recorded pit and disrupts the cooling process (postheat).[49] Both effects intensify at higher burning speeds, and heat transfer occurs particularly when a 3 T pit lies between two 11 T lands or a 3 T land lies between two 11 T pits and leads to higher error rates since the boundaries between the pit and the land become blurred.[50,51] In the first case the 3 T pit is insufficiently defined by the removal of the heat, and secondly there is additional melting of the polycarbonate at the edges of the 3 T land through the heat of the 11 T pit. One possibility to prevent this process to a large extent is to have a reduced thermal conductivity of the dye layer. This effect is countered with respect to the burner by using a specifically balanced recording strategy with which the recording performance of the laser and the respective time interval of the laser pulse are synchronized.[49]

4.4. Additional Influences

In addition to the optical and thermal properties of the dyes and the respective optimized recording strategy, the compatibility of CD-R and DVD/R are also highly dependent upon the quality of the substrate, the pre-groove geometry (depth, width, flank angle), and the extent of filling of the pre-groove with dye. Therefore, the recording strategy, the geometry of the pre-groove, and the coating program are optimized in respect to a certain dye to meet all the demands. These additional influences are only mentioned here for completeness. A detailed discussion is beyond the scope of this article.

5. Dyes

The absorption of the color layer determines the sensitivity and the reflection of the read-out of the signal. The higher the absorption is in the region of the wavelength of the recording laser, the more laser light is absorbed. Furthermore, the better the laser beam is reflected by the land, the more precisely the signal can be read out, since the difference in the reflection of the laser beam between the pit and the land is increased (see also Section 4.2).

Not every pathway that aims to increase absorption leads to success. The absorption at 780 nm (650 nm) with the same dye is a function of the layer thickness. An increase in the absorption with increased layer thicknesses cannot be realized in practice. Thicker dye layers lead to more diffuse forms at the pits, which has an increased negative impact as recording speeds increase. There is also a greater accumulation of heat between the pits (see also Section 4.3) which has an effect on jitter and modulation amplitude. Moreover, thick dye layers also require more energy for decomposition. The solution to this problem lies in the target-oriented modification of the dye structures through which the absorption of the dye is shifted bathochromically so that more laser light is absorbed at the wavelength of the recording laser. However, even this pathway is not unconditionally available since a higher absorption reduces reflection (see also Section 4.2). Therefore optimization of the dyes must include both properties.

As described in Section 4.2, reflection is proportional to the real part of the refractive index n. A high value of n is in turn only achieved with dyes that have a large molar decadic extinction coefficient ε in solution.[35,52,53] Only dyes with $\varepsilon > 200\,000\ \mathrm{L\,cm^{-1}\,mol^{-1}}$ for CD-R and $\varepsilon > 100\,000\ \mathrm{L\,cm^{-1}\,mol^{-1}}$ for DVD/R achieve the necessary refractive indices in the layer. Thus, azo dyes, anthraquinones, formazans, naphthaquinones, and dithiolate complexes, for example, are excluded, but nevertheless are frequently patented.

Dyes, depending upon their chemical structure, are crystalline or amorphous in the solid state or are in a transitional state.[54] Larger and irregular dye particles lead

© 2006 Wiley-VCH Verlag GmbH & Co. KGaA, Weinheim

not only to decomposition over a wide temperature range, but also to light scattering at the particle surfaces, which reduces reflection. Therefore, a thin dye layer surface is sought that is made up of small homogeneously distributed, almost equally sized, and as far as possible amorphous particles.

The knowledge on these dyes and their behavior in layer formation is concentrated in patent specifications, and there are few scientific publications on this topic. One thing is certain, the intermolecular π–π interactions increase with increasing polarizabilty of the dyes, such that the tendency towards the formation of aggregates increases. According to the present state of knowledge it is assumed that the dye layer represents a transition state between the amorphous and the "precrystalline" state.[55] Two main absorption bands are generated in the solid layer (Figure 20). The long wavelength

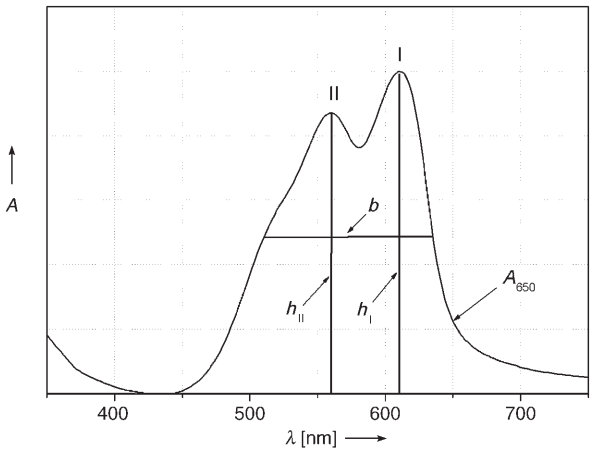

Figure 20. Parameters for the interpretation of the absorption spectrum of a thin dye layer (I: monomer band, II: dimer band, h_I: height of the monomer band, h_{II}: height of the dimer band, b: half band width of the whole band).

band (I) is assigned to the absorption of the monomer, and the second (II) to that of the "associate".[55] The difference between the two absorption maxima of about 1400 cm^{-1} suggests, however, that here it is a dimer band.[56] The fraction of dimer is determined by the structure of the dye and any additives that are present for stabilization of a particular state. It is known that dimerization (aggregation) in solution can be reduced by steric hindrance, or even almost totally prevented.[57] Similar structural effects also act in the solid dye layer. The greater is the steric hindrance to dimerization by sterically demanding substituents, the smaller is the short wavelength band and the half-band width of the total band. It will be shown in the following section how the tendency towards dimerization and crystallization was reduced by targeted structure variations.

Organic dyes exhibit a large structural diversity[58–63] and thus, especially with the dyes, there is a plethora of patents from the a wide-range of companies. Patents that claim dyes that do not adhere to the criterion of molar decadic extinction coefficients in solution are not cited in this Review. The three classes of dye described in the following section substantially fulfill this point. However, because of the enormous number of patents it is not easy to identify any advance over the previously described state of the art. We have from the outset, therefore, abandoned a complete review of patents and have attempted to make a selection and assess the fundamental patents that have stood at the outset of each respective development and which have later made an impression on technical development.

5.1. Cyanine Dyes

Cyanine dyes have excellent optical and thermal properties and have already been used in WORM.[2,3,21,22,52] Diverse chemical structures derived from known photosensitizers in silver halide photography have been patented.[64–69] However, only the derivatives of indolenine are of any practical use. The first reason for this is the aggregation behavior of the dye in the pure layer. Cyanine dyes that have benzoxazole, benzthiazole, or quinoline groups as end groups readily form dimers or aggregates. This effect is specifically exploited in the sensitization of silver halide.[65–71] This property is disruptive in optical data storage and leads to the effects described in the previous section. On the basis of the parameters outlined in Figure 20, this structural effect can be illustrated by a comparison of the spectra of films of dyes **1** and **2**. The absorption spectra of both dyes in MeOH do not

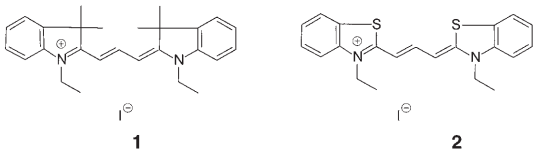

1 **2**

differ critically, but in the spectra of the films the relative intensity of the shortwave band of dye **1** is significantly lower than that of **2** and the half band width of the whole band of **2** is larger (Figure 21). On the basis of these observations it can be concluded that **1** forms less dimer than **2** in the solid layer. The cause of this are the two methyl groups in the 3-position

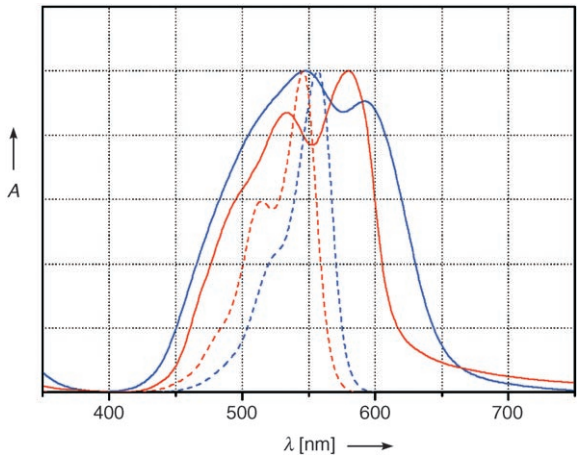

Figure 21. Absorption spectra of the dye **1** (red curve) and **2** (blue curve) in MeOH (----) and of thin dye film **1** (——).

 © 2006 Wiley-VCH Verlag GmbH & Co. KGaA, Weinheim

of the indolenine that lead to steric hindrance of dimerization. Moreover, dyes from indolenine are readily soluble in organic solvents and are thermally more stable than those with other end groups.[3]

The dye used in the first CD-R patent of Tayo Yuden was **3**.[24] A variety of further pentamethine cyanines were later

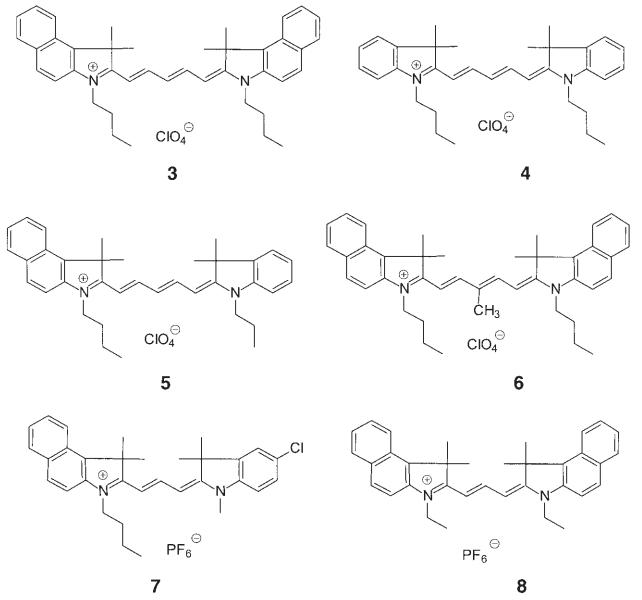

used to optimize the optical and thermal properties.[26–28] For example, **4** and **5** were developed to increase the reflectivity. A *meso*-methyl group in the polymethine chain of **6** also reduces the tendency towards dimerization. A further possibility to reduce dimerization by steric hindrance is through the introduction of a nitro group in the indolenine and benzoindolenine moiety.[55] After the ground-breaking publication on CD-R,[23] a series of further investigations on the thermal and optical properties of cyanines for CD-R and especially for DVD/R followed that resulted in the well-known correlations between dye structure and thermal and optical properties.[53,72–76] Pentamethine cyanines, such as **3**–**6**, are used for CD-R, and the corresponding trimethine cyanines **7** and **8** are used for DVD/R, because of their absorption (Table 2).

In addition, a wide range of possible anions are available for the cyanines, but few are suitable for use in optical data storage. Initially, when gold was used for the reflection layers, dyes with iodine as the anion were used most commonly. This was no longer an option when silver layers were used since reactions with the surface of the silver layer occurred, thus resulting in poorer reflection. The type of anion also influences the long-term stability of the amorphous dye layer. The sensitive heptamethine cyanine **9** was chosen for a

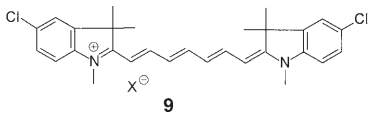

systematic investigation: amorphous dye layers were prepared on polycarbonate and the reflection measured at 60 °C and 90 % relative humidity.[77] After 30 days under these conditions the dye layers with perchlorate and hexafluorophosphate counterions remained effectively stable. Measurement of the angle of contact with dye layers on glass showed there was an influence of the anion on the hydrophilicity of the surface of the dye layer. The more hydrophobic the layer surface is, the more stable is the amorphous dye layer and the smaller are the changes in reflection. Consequently a possible mechanism proposed for the deterioration of the reflection is that water molecules are adsorbed on the surface and induce crystallization which then extends to the whole dye layer.[77] This effect occurs less extensively with penta- and trimethine cyanines, but the dye cation and the ion selected should still be as hydrophobic as possible. That is also one of the reasons why the nitrogen atom is preferably substituted with propyl or butyl groups, and dyes with perchlorate or hexafluorophosphate as the anion are mainly used today with CD-R and DVD/R.[78]

As well as their many advantages, cyanines have the disadvantage of relatively low light stability. Under the influence of light and oxygen they are destroyed by singlet oxygen formed photochemically.[79] Quenchers are thus added to the cyanine layers to inhibit formation of singlet oxygen. Nitrosoanilines such as **10** were initially used for this purpose.[80] The long-established quinone diimonium salts[81] such as **11** and ammenium salts[82] such as **12** are very effective. Nickel dithiolate complexes are also effective,[83–86] but are usually poorly soluble. They were consequently modified to

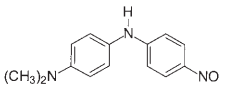

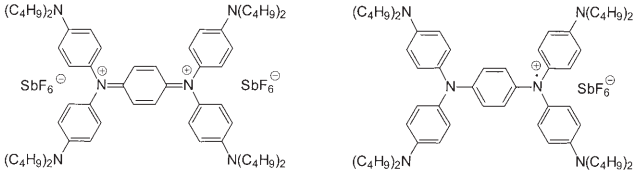

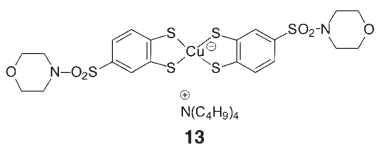

Table 2: Absorption maxima and molar decadic extinction coefficients of penta- und trimethinecyanines in MeOH solution.

Dye	λ_{max} [nm]	ε [L cm^{-1} mol^{-1}]
3	680	225 000
4	643	240 000
5	661	230 000
6	667	230 000
7	569	130 000
8	586	120 000

© 2006 Wiley-VCH Verlag GmbH & Co. KGaA, Weinheim

improve solubility, as with, for example, **13** (patent example from ref. [86]). The stabilizing action of tetracyanoquinodimethanes has also been described, which act as powerful electron acceptors and quench the excited singlet state of the cyanines.[87,88] Furthermore, azo–metal complexes[89–93] and formazan–metal complexes[94] are suitable for improving light stability. Thus, a broad palette of oxygen scavengers are available, which makes it possible to produce highly light-stable layers in CD-R and DVD/R, even with cyanine dyes.

5.2. Phthalocyanines

Copper complexes of phthalocyanines are used to a large extent as blue pigments, and their halogen derivatives are excellent green pigments.[58–63,95] In addition to halogen substitution, the absorption spectrum can also be influenced by the central metal atom, and thus a series of possibilities are available for modifying the absorption behavior.[95] The commercial success of these dyes as pigments rests on three properties: their high extinction coefficients ($>200\,000\ \mathrm{L\,cm^{-1}\,mol^{-1}}$) and narrow absorption bands result in them producing brilliant blue to green tones; they are extraordinarily light stable, and largely insensitive to chemical influences. The pigments are almost insoluble in organic solvents and hence are not suitable for the preparation of CD-R by spin coating.

It has been known for a considerable time that the solubility of phthalocyanines can be increased, in principle, by the addition of *tert*-butyl groups.[96] Long-chain, branched alkyl residues were consequentially introduced in the initial phase of the development of phthalocyanines for CD-R to increase the solubility and prevent crystallization in the layer.[97,98] In addition to alkyl groups, aryl and alkoxy derivatives as well as aryl and alkylthio derivatives were utilized. Such compounds have not been used technically because of the considerable synthetic effort needed and the associated costs. The breakthrough was achieved by chemists at Mitsui who seized upon a synthesis[99] published in 1982.[97,100] 3-Nitrophthalodinitrile (**14**), which can be readily transformed into alkoxyphthalodinitrile **15,** was commercially available. The phthalocyanines can be prepared directly from **15** or via the diiminoisoindoline **16**. The four isomeric phthalocyanines **17**–**20** are formed if **15** is used. The isomeric ratio can be modified according to the reaction conditions, and **17** and **18** can be obtained as the main components in the ratio 60:40 to 40:60.[100] Isomer **17** is readily soluble in organic solvents, while **18** is not, and thus the aim is to get a high fraction of the readily soluble isomer **17** and, in particular, to avoid the poorly soluble isomer **18**. The fraction of **17** can be increased to 85–95 % by starting from the diiminoisoindoline **16**.[100]

Branched alkyl chains, such as isomer **21** (patent example 2 in ref. [100]), lead to particularly good solubility and amorphous dye layers. Fine adjustment of the absorption in the layer is achieved with halogen derivatives (especially by bromine substitution).[98,101] The solubility was dramitically improved and the absorption spectrum was shifted into the desired range through bromine substitution. A relatively high

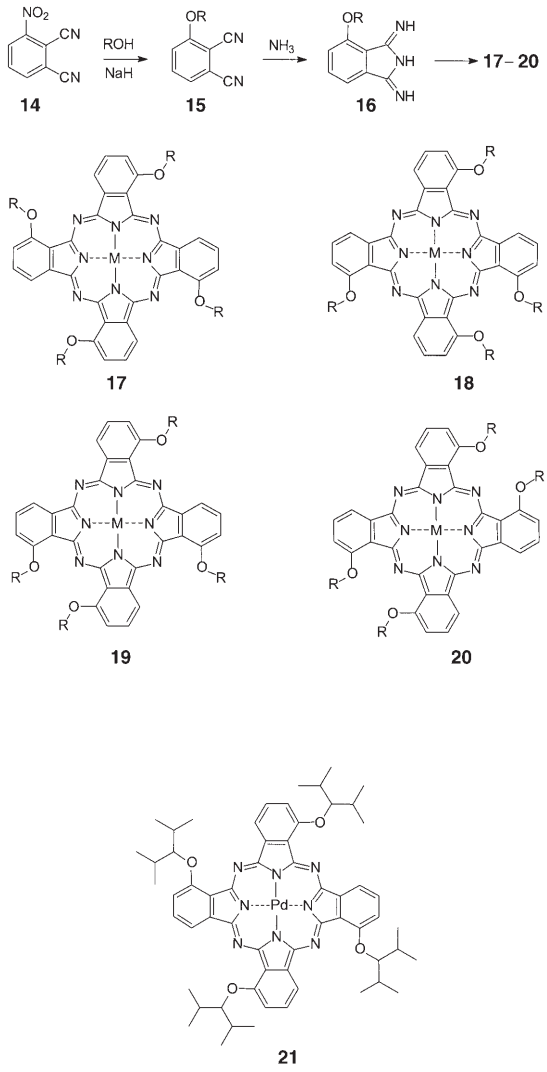

decomposition point remained as a disadvantage, which necessitates considerable laser performance and causes deformation in pit formation, which in turn leads to high jitter values. The chemists at Mitsui were successful in reducing the decomposition temperature of the phthalocyanines and thus critically improving the jitter values by the addition of metallocenes (for example, ferrocene).[101] Thus, phthalocyanines were successfully developed which, together with the cyanines, are suitable for the production of CD-R.

This chemistry was modified and patented a few years later: modification of the synthesis conditions enabled a fraction of at least 90 %[102] and 80 %[103] of the two isomers **17** and **19**, respectively, to be obtained in the total isomer mixture. A method for the bromination of alkoxy substituted phthalocyanines was also claimed,[104] and ferrocene was bonded chemically to the phthalocyanines.[105–107] The phthalocyanines have captured the greatest market share by far in CD-R production. In addition to the advantages in stability, the availability of a complete process package, including a universal stamper, in particular, have brought this about.

The absorption maxima of the metal-free phthalocyanine **22** ($\lambda_{max}=698$ nm, $\varepsilon=162\,200\ \mathrm{L\,cm^{-1}\,mol^{-1}}$ in 1-chloronaph-

 © 2006 Wiley-VCH Verlag GmbH & Co. KGaA, Weinheim

thalene) and the metal phthalocyanenes such as the copper complex **23** ($\lambda_{max} = 678$ nm, $\varepsilon = 218\,800\ L\,cm^{-1}\,mol^{-1}$ in 1-chloronaphthaline) lie above 650 nm in solution so they are

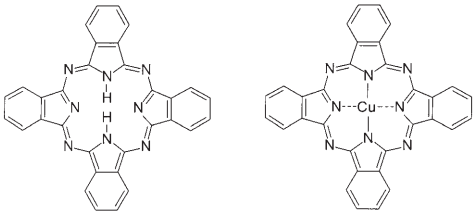

22 **23**

not suitable for use in recordable DVD. Dipyrromethene–metal chelates were developed to exploit the advantage of the light stability of metal complexes. The experience obtained for the inhibition of crystallization by introducing sterically demanding substituents into the phthalocyanines was exploited.[108] However, they have currently not achieved widespread use.

5.3. Azo–Metal Complexes

The complexation of a metal ion influences the absorption spectrum, the charge status, solubility, and stability of azo dyes. The main objective here is the increase in light stability. Complex formation with azo dyes is usually achieved through a substituent (for example, OH, NH_2, $NHSO_2R$, COOH, SO_3H) located in the *ortho* position to the azo group that can be transformed into the anionic form and thus act as an electron donor. A second bond is formed with the β-nitrogen atom of the azo group, so that the azo dyes capable of forming complexes are at least bidentate ligands. However, complexes with two chelate rings are not very stable; thus an additional electron donor is usually introduced into the *ortho′* position so that a third bond is formed when the ligand becomes tridentate. Such substituents can be either electrically neutral (for example, heterocyclic −N=, carbonyl O=, organic sulfide −S−) or anionic. Most azo–metal complexes exhibit the disadvantage of a low extinction coefficient and a broad absorption band which leads to a dull color tone on dyeing and makes them totally unsuitable for use as dyes in CD-R and DVD/R. Thus, a fundamental requirement is the search for a method to increase their extinction coefficients. Moreover, most azo–metal complexes have a low solubility in organic solvents.

The absorption spectrum is determined by the structure of the azo–metal complexes and various isomer phenomena. Optical isomerism (enantioisomerism) has no influence here since, apart from their action on polarized light, enantiomorphic compounds otherwise exhibit identical properties. Geometric isomerism enhances the width of the total absorption band. In azo–metal complexes *E*/*Z* isomerism occurs in quadratic-planar structures and facial–meridional (*fac*–*mer*) isomerism occurs in octahedral structures.[63,109] Bond isomerism (N_α,N_β isomerism) occurs in both the planar[110,111] and the octahedral structure.[112,113] If the third substituent is, for example, an OH group, N_α,N_β isomers are formed with different combinations of 5/6 and 6/5 chelate rings, such as in **24**–**26**, which exhibit different absorption spectra.[113]

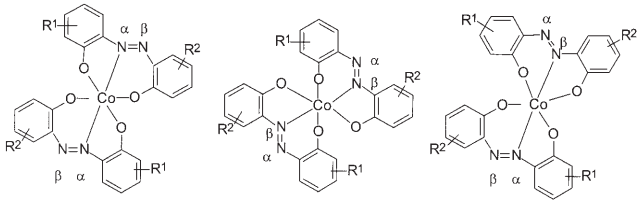

α,α Form **24** β,β Form **25** α,β Form **26**

This was a first starting point. Unlike azo–metal complexes with hydroxy groups in the *ortho* and *ortho′* positions, those with a nitrogen heterocycle are fixed in 5/5 or 5/6 chelate rings depending upon the *ortho* substituents, as in **27** and **28**, respectively, so that N_α,N_β isomerism cannot occur.[114]

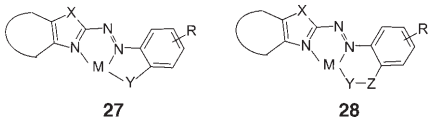

27 **28**

In spite of this, azo–metal complexes with *ortho*-hydroxy groups and cobalt(III) and chromium(III) centers give broad absorption spectra with relatively low extinction coefficients, which is attributed to deformation of the ligands.[114] The mere introduction of a carboxy group reduces this deformation and brings about higher extinction coefficients.[114] Comparable values are obtained by exchanging the carboxy group with a sulfo group.[115] The extinction coefficients of such complexes are about $50\,000\ L\,cm^{-1}\,mol^{-1}$, but are still far from the target value. Furthermore, their solubility in organic solvents is too low. In respect to the improvement in solubility, nickel complexes have, in particular, proved to be preferred variants. However, extinction coefficients of above $50\,000\ L\,cm^{-1}\,mol^{-1}$ are barely achieved with nickel complexes of 1-(2-thiazolylazo)-2-naphthalene[116] or 1-(2-pyridylazo)-2-naphthalene.[117]

The pivotal impetus came from analytical chemistry. Substitution with an amino group in the *para* position to the azo group as, for example, in **29** and **30**, leads to an increase in the extinction coefficients and stability.[118] The absorption maximum is shifted bathochromically and the extinction coefficient is increased if the hydroxy group is replaced by a carboxy group (in **31** and **32**; Table 3). Insertion of a sulfo group (for example, **33** and **34**) affords azo–metal complexes with good solubility in organic solvents and average light and climatic stability which are suitable for use in CD-R.[119–122] Weaknesses in climatic stability result from the relatively good water solubility of azo–metal complexes with sulfo groups.

This principle was initially followed with azo–metal complexes for DVD/R, and azo–metal complexes with hydroxy, carboxy, sulfo, and alkyl sulfonamido groups in the

 © 2006 Wiley-VCH Verlag GmbH & Co. KGaA, Weinheim

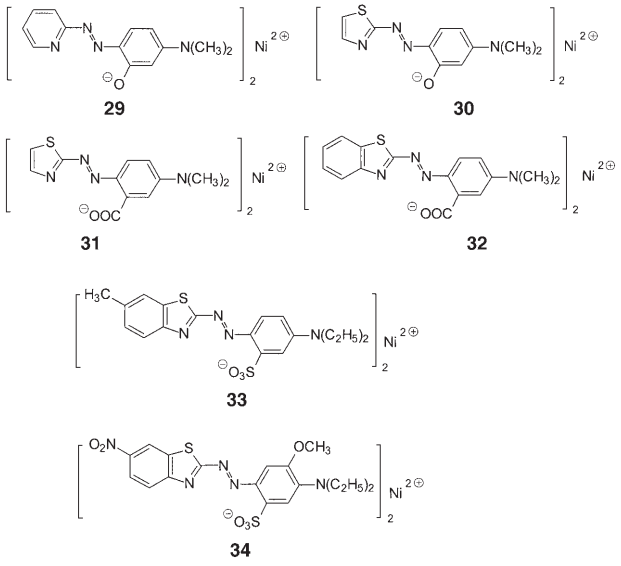

Table 3: Absorption maxima and molar decadic extinction coefficients of azo–metal complexes in solution.

Dye	λ_{max} [nm]	ε [$\times 10^{-3}$ L cm^{-1} mol^{-1}]	Ref.
29	545	98.0	[118a]
30	558	69.0	[118a]
31	610	95.0	[118b]
32	640	120.0	[118b]
33	646	106.0	[119]
34	688	150.0	[119]

ortho position were patented.[123] Success was then achieved in the synthesis of alkyl sulfonamides that were substituted with fluorine on the alkyl group—a land mark discovery.[124] Azo–metal complexes prepared from them have unusually high extinction coefficients (for example, **35**: $\lambda_{max} = 577$ nm $\varepsilon = 157\,000$ L cm^{-1} mol^{-1} in chloroform; **36**: $\lambda_{max} = 582$ nm $\varepsilon = 118\,000$ L cm^{-1} mol^{-1} in chloroform)[125] and for this reason

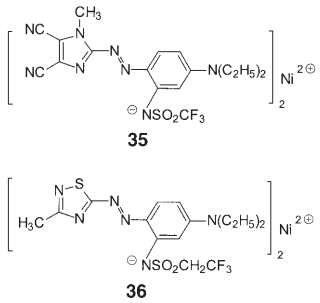

high refraction indices n as solid dye layers, which leads to excellent reflection values. The fluoroalkyl sulfonamide substituents also effect a thermal decomposition of the respective azo–metal complexes within an extremely narrow range. Unlike the azo–metal complexes with sulfo groups, they also have good light and climatic stability[125] Thus far, this pivotal innovation has not been appreciated outside the industry, as two publications on azo–metal complexes show they are barely suitable as dyes for DVD/R.[126,127] Irrespective of their end use, a rewarding research field has opened up for fundamental investigations on structure, further interesting properties, and other possible applications of these novel azo–metal complexes.

6. Summary and Outlook

The introduction of CD-audio onto the market 23 years ago initiated a technical development that has influenced many aspects of our daily life and will continue to affect it in the future. Without question, the near future will see a further increase in storage capacity—BluRay and HD-DVD are two formats that are on the threshold of market launch.

It was the aim of this Review to present the current state of progress in optical data storage (especially the recordable version). This technology is multidisciplinary and requires the active cooperation of dyestuffs chemists, physicists, materials scientists, technicians, and electronic engineers. Only a few areas have seen such a rapid advance in technology as in optical data storage. A fundamentally new optical data media format with millions of applications will be brought from basic research to market maturity every 3–5 years. While the respective new formats of optical data media have already become mass-produced products, the demands on chemistry and production methods will continuously intensify as a result of higher recording speeds and stricter quality demands in ever shorter cycles. The increase in recording speed from single speed (1×) to the maximum possible speed of 52× in CD-R took almost 12 years; with DVD/R this development from 1× to the maximum possible speed of 16× was realized within 3 years. Moreover, for commercial success, the producers of optical data media require complete process solutions including the stamper with the respective production codes which guarantee the compatibility of the produced media with the installed burners.

From the materials side, this development is also substantially dependent upon the dye. To the general public, dyestuffs chemistry has the reputation of being a mature field. The examples presented here show impressively how today, 150 years after the synthesis of aniline purple by William Henry Perkin, dyestuffs chemistry still has to solve new and exacting problems. Other advanced technologies, such as organic light-emitting diodes (OLED), ink-jet and thermotransfer printing as well as electrophotography[128] and fluorescence markers in diagnostics,[129] require constant new developments on the part of dyestuffs chemistry. The next challenge is waiting in the field of data storage with the recordable BluRay disc and HD-DVD. Moreover, a new, highly promising method for reversible storage of information is provided by the photorefractive effect based on organic dyes.[130]

We thank our colleagues Dr. Steffen Ernst, Dr. Jürgen Mistol, Dr. Knut Reiner (all of FEW), Dr. Torsten Dippell (STEAG HamaTech), and Dr. Wilbert Windeln (ETA-Optik) for stimulating discussions and critical review of the manuscript.

 © 2006 Wiley-VCH Verlag GmbH & Co. KGaA, Weinheim

We also thank Tilman Rieseweber (STEAG HamaTech) for the AFM images.

Received: August 9, 2005

[1] J.-J. Wanègue, *Opt. Disc Syst.* **2003**, *5*, 42 – 52; J.-J. Wanègue, **2003**, *6*, 52 – 66.
[2] M. Emmelius, G. Pawlowski, H. W. Vollmann, *Angew. Chem.* **1989**, *101*, 1475 – 1502; *Angew. Chem. Int. Ed. Engl.* **1989**, *28*, 1445 – 1471.
[3] F. Matsui in *Infrared Absorbing Dyes* (Ed.: M. Matsuoka), Plenum, New York, **1990**, pp. 117 – 140.
[4] D. G. Stinson, *J. Imaging Sci. Technol.* **1998**, *42*, 39 – 48.
[5] *Red Book, System Description CD-Audio*, Royal Philips Electronics, Eindhoven, Latest Version: May **1999**, http://www.licensing.philips.com/information/cd/.
[6] *Yellow Book, System Description CD-ROM*, Royal Philips Electronics, Eindhoven, Latest Version: May **1999**, http://www.licensing.philips.com/information/cd/.
[7] S. Harvey, *Medialine* **2003**, *8*, 20 – 21.
[8] F. Bruder, *Macromol. Mater. Eng.* **2001**, *286*, 685 – 690.
[9] a) M. Fidler, *Mediaware* **2004**, *2*, 14; b) W. Lieberfarb, *Mediaware* **2004**, *2*, 15; c) P. Tinner, *Mediaware* **2004**, *2*, 16; d) K. Hammen, *Mediaware* **2004**, *2*, 18; e) D. DallaVarde, *Mediaware* **2004**,*2*, 20; M. Mitchell, *Mediaware* **2004**, *2*, 21.
[10] F. Yokogawa, S. Ohsawa, T. Iida, Y. Araki, K. Yamamoto, Y. Moriyama, *Jpn. J. Appl. Phys. Part 1* **1998**, *37*, 2176 – 2178.
[11] T. Higuchi, H. Koyanagi, *Jpn. J. Appl. Phys. Part 1* **2000**, *39*, 933 – 936.
[12] T. P. Keegan, *Medialine* **2002**, *7*, 22.
[13] M. Mansuripur, *The Physical Priciples of Magneto-optical Recording*, Cambridge University Press, Cambridge, **1995**.
[14] J. Freeman, *Strategic Marketing Decisions Cooperation OpTMIS Media Forecast* **2005**, http://www.smdcorp.com.
[15] Y. Kageyama, H. Iwasaki, M. Harigaya, Y. Ide, *Jpn. J. Appl. Phys. Part 1* **1996**, *35*, 500 – 501.
[16] R. van Woudenberg, *Jpn. J. Appl. Phys. Part 1* **1998**, *37*, 2159 – 2162.
[17] K. Nagata, T. Saimi, S. Furukawa, K. Nishiuchi, N. Yamada, N. Akahira, *Jpn. J. Appl. Phys. Part 1* **1998**, *37*, 2236 – 2240.
[18] E. Muramatsu, A. Yamaguchi, K. Horikawa, M. Kato, S Taniguchi, S. Jinno, M. Yamaguchi, H. Kudo, *Jpn. J. Appl. Phys. Part 1* **1998**, *37*, 2257 – 2258.
[19] M. Yamaguchi, T. Togashi, S. Jinno, H. Kudo, E. Muramatsu, S. Taniguchi, A. Inoue, *Jpn. J. Appl. Phys. Part 1* **1999**, *38*, 1806 – 1810.
[20] *Understanding Solutions* **2004**, *5*, 107 – 111.
[21] J. E. Kuder, *J. Imaging Sci.* **1988**, *32*, 51 – 56.
[22] M. Matsuoka in *Near-Infrared Dyes for High Technology Applications* (Eds.: S. Daehne, U. Resch-Genger, O. S. Wolfbeis), Kluver, Dordrecht, **1998**, pp. 203 – 231.
[23] E. Hamada, Y. Shin, T. Ishiguro, *Proc. SPIE-Int. Soc. Opt. Eng.* **1989**, *1078*, 80 – 87.
[24] E. Hamada, Y. Arai, Y. Shin, T. Ishiguro (Taiyo Yuden Co., Ltd.) US 4940618, **1989**.
[25] Y. Arai, Y. Shin, T. Ishiguro, E. Hamada (Taiyo Yuden Co., Ltd.) US 5009818, **1989**.
[26] Y. Takagisi, K. Ootaguro, E. Hamada, T. Fujii, (Taiyo Yuden Co., Ltd.) US 5080946, **1990**.
[27] E. Hamada, Y. Arai, Y. Shin, T. Ishiguro (Taiyo Yuden Co., Ltd.) US 5090009, **1989**.
[28] E. Hamada, Y. Arai, Y. Tagagisi, T. Ishiguro (Taiyo Yuden Co., Ltd.) US 5213955, **1990**.
[29] *Orange Book, System Description CD-R*, Part II, *Vol. 2*, Royal Philips Electronics, Eindhoven, Version 1.2, April **2002**, http://www.licensing.philips.com/information/cd/.
[30] E. Hamada, T. Fujii, Y. Tomizawa, S. Iimura, *Jpn. J. Appl. Phys. Part 1* **1997**, *36*, 593 – 594.
[31] K. S. Min, Y. J. Huh, S. K. Shim, *Jpn. J. Appl. Phys. Part 1* **1999**, *38*, 1675 – 1678.
[32] E. Muramatsu, A. Shirota, K. Horikawa, M. Kato, S Taniguvhi, A. Inour, *Jpn. J. Appl. Phys. Part 1* **2001**, *40*, 1798 – 1802.
[33] Philips Intellectual Property & Standards, *Mediaware* **2004**, *2*, 11 – 12.
[34] J. Heermann, T. Langetepe, *Medialine* **2004**, *9*, 48 – 50.
[35] A. H. Holtslag, E. F. McCord, G. H. Werumeus Buning, *Jpn. J. Appl. Phys. Part 1* **1992**, *31*, 484 – 493.
[36] J. S. Kim, K. S Min, *Korean J. Chem. Eng.* **1997**, *14*, 407 – 411.
[37] Y. J. Huh, S. H. Kim, T. Y. Nam, S. C. Kim, *Jpn. J. Appl. Phys. Part 1* **1997**, *36*, 403 – 409.
[38] Y. J. Huh, S. H. Kim, S. C. Kim, *Jpn. J. Appl. Phys. Part 1* **1997**, *36*, 7233 – 7238.
[39] R. Hertling, W. Schaudig, W. Windeln (Steag Hama Tech AG) US 6744521, **1999**.
[40] R. Hertling (Steag ETA-Optik GmbH) US 6753971, **2000**.
[41] B. J. Bartholomeusz, *Appl. Opt.* **1992**, *31*, 909 – 918.
[42] J. S. Kim, T. Y. Nam, Y. J. Huh, *Korean J. Chem. Eng.* **1997**, *14*, 88 – 92.
[43] R. Gade, U. W. Grummt, *J. Phys. D* **2000**, *33*, 2560 – 2567.
[44] E. R. Meinders, B. Tieke, *Jpn. J. Appl. Phys. Part 1* **2003**, *42*, 834 – 840.
[45] Y. Suzuki, M. Horie, Y. Okamoto, Y. Kurose, S. Maeda, *Jpn. J. Appl. Phys. Part 1* **1998**, *37*, 2084 – 2088.
[46] Y. Suzuki, Y. Okamoto, Y. Kurose, S. Maeda, *Jpn. J. Appl. Phys. Part 1* **1999**, *38*, 1669 – 1674.
[47] Y. Suzuki, Y. Ookijima, H. Takeshima, S. Maeda, *Jpn. J. Appl. Phys. Part 1* **2001**, *40*, 1588 – 1589.
[48] S. Y. Suh, D. L. Anderson, *Appl. Opt.* **1984**, *23*, 3965 – 3971.
[49] B. Tieke, G. R. Langereis, E. R. Meinders, J. G. F. Kablau, R. Woudenberg, R. A. J. van Kollenburg, *Jpn. J. Appl. Phys. Part 1* **2002**, *41*, 1735 – 1738.
[50] T. Fujii, T. Tajima, R. Negishi, I. Okitsu, Y. Tomizawa, T. Matsuda, E. Hamada, *Jpn. J. Appl. Phys. Part 1* **2000**, *39*, 779 – 784.
[51] E. Hamada, Y. Takagishi, T. Yoshizawa, T. Fujii, R. Negishi, T. Nakajima, *Jpn. J. Appl. Phys. Part 1* **2000**, *39*, 785 – 788.
[52] R. Hurditch in *Colour Science '98. Vol. 1: Dye and Pigment Chemistry* (Ed.: J. Griffiths), University of Leeds, **1999**, pp. 202 – 216.
[53] S. Sun, P. Chen, S. Zhou, Z. Qian, D. Zheng, O. Tsuneki, H. Masaaki, *Imaging Sci. J.* **1999**, *47*, 113 – 117.
[54] D. Horn, J. Rieger, *Angew. Chem.* **2001**, *113*, 4460 – 4492; *Angew. Chem. Int. Ed.* **2001**, *40*, 4330 – 4361.
[55] T. Tajima, T. Fujii, Y. Tomizawa, E. Hamada (Taiyo Yuden Co., Ltd.) US 6291045, **1999**.
[56] W. West, S. Pearce, *J. Phys. Chem.* **1965**, *69*, 1894 – 1903.
[57] a) H. Langhals, R. Ismael, O. Yürük, *Tetrahedron* **2000**, *56*, 5435 – 5441; b) F. Würthner, R. Sens, K.-H. Etzbach, G. Seybold, *Angew. Chem.* **1999**, *111*, 1753 – 1757; *Angew. Chem. Int. Ed.* **1999**, *38*, 1649 – 1652; c) F. Würthner, S. Yao, *Angew. Chem.* **2000**, *112*, 2054 – 2057; *Angew. Chem. Int. Ed.* **2000**, *39*, 1978 – 1981; d) F. Würthner, S. Yao, T. Debaerdemaeker, R. Wortmann, *J. Am. Chem. Soc.* **2002**, *124*, 9431 – 9447.
[58] J. Griffiths, *Colour and Constitution of Organic Molecules*, Academic Press, London, **1976**.
[59] J. Fabian, H. Hartmann, *Light Absorption of Organic Colorants*, Springer, Berlin, **1980**.
[60] P. F. Gordon, P. Gregory, *Organic Chemistry in Colour*, Springer, Berlin, **1983**.
[61] R. M. Christie, *Colour Chemistry*, The Royal Society of Chemistry, Cambridge, **2001**.
[62] P. Bamsfield, *Chromic Phenomena*, The Royal Society of Chemistry, Cambridge, **2001**.

 © 2006 Wiley-VCH Verlag GmbH & Co. KGaA, Weinheim

[63] H. Zollinger, *Color Chemistry*, 3rd ed., Verlag Helvetica Chimica Acta, Zürich, **2003**.

[64] F. Hamer, *The Chemistry of Heterocyclic Compounds*, vol. 18, *The Cyanine Dyes and Related Compounds* (Ed.: A. Weissberger), Wiley-Interscience, New York, **1964**.

[65] L. G. S. Brooker in *The Theory of the Photographic Process*, 3rd ed. (Eds.: C. E. K. Mees, T. H. James), Macmillan, New York, **1966**, pp. 198 – 232.

[66] D. M. Sturmer, D. W. Heseltine in *The Theory of the Photographic Process*, 4th ed. (Ed.: T. H. James), Macmillan, New York, **1977**, pp. 194 – 234.

[67] D. M. Sturmer in *The Chemistry of Heterocyclic Compounds*, vol. 30 (Eds.: A Weissberger, E. C. Taylor), Wiley-Interscience, New York, **1977**, pp. 441 – 587.

[68] D. M. Sturmer in *Kirk-Othmer Encyclopedia of Chemical Technology*, 3rd ed., vol. 7, Wiley-Interscience, New York, **1979**, pp. 335 – 358.

[69] G. Bach, S Daehne in *Second Supplements to the 2nd Edition of Rodd's Chemistry of Carbon Compounds*, vol. IV B (Ed.: M. Sainsbury), Elsevier, Amsterdam, **1997**, pp. 383 – 481.

[70] F. Dietz, *J. Signalaufzeichnungsmater.* **1973**, *1*, 157 – 180, 237 – 252, 381 – 382.

[71] A. Herz, *Adv. Colloid Interface Sci.* **1977**, *8*, 237 – 298..

[72] E. Hamada, T. Fujii, Y. Tomizawa, S. Imura, *Jpn. J. Appl. Phys. Part 1* **1997**, *36*, 593 – 594.

[73] P. Chen, J. Zhao, D. S. Zheng, T. Okasaki, M. Hayami, *J. Inf. Rec.* **1997**, *23*, 585 – 592.

[74] S. Sun, P. Chen, D. Zheng, T. Okasaki, M. Hayami, *Proc. SPIE-Int. Soc. Opt. Eng.* **1998**, *3562*, 11 – 16.

[75] S. Sun, P. Chen, D. Zheng, T. Okasaki, M. Hayami, *Imaging Sci. J.* **1998**, *46*, 99 – 102.

[76] J.-P. Zhang, S.-Y. Zhou, P. Chen, O. Tsuneki, H. Masaaki, *Dyes Pigm.* **2001**, *51*, 93 – 101.

[77] Y. Inagaki, M. Yabe, *J. Soc. Photogr. Sci. Technol. Jpn.* **2003**, *66*, 597 – 600.

[78] Y. Takagishi, T. Matsumoto, Y. Shin, E. Hamada (Taiyo Yuden Co., Ltd.) EP 895230, **1998**.

[79] a) G. W. Byers, S. Gross, P. M. Henrichs, *Photochem. Photobiol.* **1976**, *23*, 37 – 43; b) J. Li, P. Chen, J. Zhao, D. Zheng, T. Okasaki, M. Hayami, *Chin. Chem. Lett.* **1997**, *8*, 711 – 714.

[80] K. Ootaguro, E. Hamada, Y. Takagisi (Taiyo Yuden Co., Ltd.) US 5318882, **1991**.

[81] P. V. Susi, (American Cyanamid Co.) US 3637769, **1963**.

[82] P. V. Susi, N. A. Weston (American Cyanamid Co.) US 3484467, **1963**.

[83] H. Nakazumi, E. Hamada, T. Ishiguro, H. Shiozaki, T. Kitao, *J. Soc. Dyers Colour.* **1989**, *105*, 26 – 29.

[84] K. Namba, A. Kuroiwa, S. Nakagawa, (TDK Co.), US 5741623, **1992**.

[85] K. Namba, M. Shinkai, T. T. Inoue, S. Kitagawa (TDK Co.), EP 458257, **1991**.

[86] K. Namba, S. Kitagawa, M. Shinkai, M. Suzuki, S. Kimura, K. Hiraku (TDK Co.) US 6071672, **1998**.

[87] S. Morishima, K. Wariishi, M. Shibata, T. Ishida, H. Kubo, *Jpn. J. Appl. Phys. Part 1* **1999**, *38*, 1634 – 1637.

[88] S. Morishima, K. Wariishi, T. Ishida, M. Shibata (Fuji Photo Film Co., Ltd.) US 5879772, **1997**.

[89] S. Maeda, S. Imamura, K. Matsuhashi, T. Tsukahara (Mitsubishi Kasei Co.) US 5330542, **1991**.

[90] S. Maeda, S. Imamura, K. Matsuhashi, T. Tsukahara (Mitsubishi Kasei Co.) US 5389419, **1994**.

[91] D. D. Chapman, R. Goswami, C. A. Kovacs (Eastman Kodak Co.) US 5500325, **1995**.

[92] D. D. Chapman, R. Goswami, C. A. Kovacs (Eastman Kodak Co.) US 5821029, **1997**.

[93] D. D. Chapman, C. A. Kovacs (Eastman Kodak Co.) EP 961266, **1998**.

[94] a) M. P. Cunningham, S. Evans (Eastman Kodak Co.) US 5547728, **1995**; b) D. D. Chapman, M. P. Cunningham, R. Goswami (Eastman Kodak Co.) US 5731054, **1996**; c) D. D. Chapman, M. P. Cunningham, R. Goswami (Eastman Kodak Co.) US 5773193, **1996**.

[95] a) R. M. Christie, *Dyes Pigm.* **1995**, *27*, 35 – 43; b) *Phthalocyanines. Properties and Applications*, Vol. *1* (Eds.: C. C. Leznoff, A. B. P. Lever), VCH, Weinheim, **1989**; *Phthalocyanines. Properties and Applications*, Vol. *2 and 3* (Eds.: C. C. Leznoff, A. B. P. Lever), VCH, Weinheim, **1993**; *Phthalocyanines. Properties and Applications*, Vol. *4* (Eds.: C. C. Leznoff, A. B. P. Lever), VCH, Weinheim, **1996**; c) N. B. McKeown, *Phthalocyanine Materials. Synthesis, Structure and Function*, Cambridge University Press, Cambridge, **1998**; d) P. Erk, H. Hengelsberg in *Porphyrin Handbook*, vol. 19 (Eds.: K. M. Kadish, K. M. Smith, R. Guilard), Elsevier Science, San Diego, **2003**, pp. 105 – 149.

[96] a) E. A. Luk'yanets, S. A. Mikhalenko, E. I. Kovshev, *Zh. Obshch. Khim.* **1971**, *41*, 934 – 935; b) E. I. Kovshev, E. A. Luk'yanets, *Zh. Obshch. Khim.* **1972**, *42*, 696 – 699.

[97] H. Itoh, K. Enomoto, T. Oguchi, T. Nishizawa (Mitsui Toatsu Chemicals Inc.) US 5124067, **1989**.

[98] H. Itoh, K. Enomoto, T. Oguchi, T. Nishizawa (Mitsui Toatsu Chemicals Inc.) US 5024926, **1990**.

[99] T. W. Hall, S. Greenberg, C. R. McArthur, B. Khouw, C. C. Leznoff, *Nouv. J. Chim.* **1982**, *6*, 653 – 658.

[100] T. Oguchi, K. Sugimoto, S. Aihara, H. Itoh, M. Matsumoto, T. Masaoka, M. Nakamura (Mitsui Toatsu Chemicals Inc.) US 5220010, **1991**.

[101] T. Koike, H. Umehara, Y. Inatomi, T. Tsuda, S. Hirose (Mitsui Toatsu Chemicals Inc.) US 5492744, **1993**.

[102] H. Wolleb (Ciba-Geigy Co.) US 5663326, **1995**.

[103] H. Wolleb (Ciba Speciality Chemicals Co.) US 5817804, **1997**.

[104] H. Wolleb (Ciba-Geigy Co.) US 5594128, **1995**.

[105] H. Wolleb, A. Wolleb, B. Schmidhalter, J.-L. Budry (Ciba Speciality Chemicals Co.) US 6399768, **1999**.

[106] H. Wolleb, A. Wolleb, B. Schmidhalter, J.-L. Budry (Ciba Speciality Chemicals Co.) US 6790593, **2001**.

[107] J. Beyrich, R. Blattner, J.-L. Budry, W. Freitag, C. Morton, G. A. Murphy, B. Schmidhalter, M. Schulz, H. Spahni, C. Stern, A. Wolleb, H. Wolleb, R. Zoelper (Ciba Speciality Chemicals Co.) US 2004/0132990, **2002**.

[108] T. Misawa, K. Sugimoto, T. Nishimoto, H. Tsukajara, T. Tsuda, K. Takuma, H. Umehara (Mitsui Chemicals Inc.) US 6060606, **1999**.

[109] A. Lycka, *Annu. Rep. NMR Spectrosc.* **2000**, *38*, 1 – 57.

[110] H. Pfitzner, *Angew. Chem.* **1972**, 84, 351 – 352; *Angew. Chem. Int. Ed. Engl.* **1972**, *11*, 312 – 313.

[111] E. Steiner, C. Mayer, G. Schetty, *Helv. Chim. Acta* **1976**, *59*, 364 – 376.

[112] G. Schetty, E. Steiner, *Helv. Chim. Acta* **1972**, *55*, 1509 – 1532.

[113] G. Schetty, E. Steiner, *Helv. Chim. Acta* **1974**, *57*, 2149 – 2172.

[114] G. Schetty, *Helv. Chim. Acta* **1968**, *51*, 505 – 509.

[115] G. Schetty, *Helv. Chim. Acta* **1968**, *51*, 509 – 512.

[116] M. Adachi, T. Bredow, K. Jug, *Dyes Pigm.* **2004**, *63*, 225 – 230.

[117] K. Ohshita, H. Wada, G. Nakagawa, *Anal. Chim. Acta* **1982**, *140*, 291 – 300.

[118] a) S. Shibata, M. Furukawa, K. Toei, *Anal. Chim. Acta* **1973**, *66*, 397 – 409; b) M. Furukawa, *Anal. Chim. Acta* **1980**, *140*, 281 – 289.

[119] T. Murayama, S. Maeda, C. Fukabori, T. Nagao (Mitsubishi Kasei Co.) US 5298608, **1991**.

[120] T. Ochiai, Y. Kurose, T. Nagao, T. Tsukahara, S. Imamura (Mitsubishi Chemical Co.) US 5447823, **1993**.

[121] T. Ochiai, Y. Kurose, T. Nagao, T. Tsukahara, S. Imamura (Mitsubishi Chemical Co.) US 5532342, **1995**.

 © 2006 Wiley-VCH Verlag GmbH & Co. KGaA, Weinheim

[122] S. Wang, S. Shen, H. Xu, D. Gu, J. Yin, X. Tang, *Dyes Pigm.* **1999**, *42*, 173 – 177.
[123] Y. Suzuki, M. Horie, S. Maeda, Y. Kurose, Y. Okamoto (Mitsubishi Chemical Co.) US 6214519, **1998**.
[124] Y. Okamoto, Y. Kurose, S. Maeda, Y. Suzuki (Mitsubishi Chemical Co.) US 6225023, **1998**.
[125] Y. Okamoto, Y. Kurose, S, Maeda, Y. Suzuki (Mitsubishi Chemical Co.) US 6284877, **2000**.
[126] S. Wang, S. Shen, H. Xu, *Dyes Pigm.* **2000**, *44*, 195 – 198.
[127] H. Park, E.-R. Kim, D. J. Kim, H. Lee, *Bull. Chem. Soc. Jpn.* **2002**, *75*, 2067 – 2070.
[128] *High-Technology Applications of Organic Colorants* (Ed.: P. Gregory), Plenum, New York, **1991**; *Chemistry and Technology of Printing and Imaging Systems* (Ed.: P. Gregory), Blackie Academic, Glasgow, **1996**.
[129] a) A. Mayer, S. Neunhofer, *Angew. Chem.* **1994**, *106*, 1097 – 1126; *Angew. Chem. Int. Ed. Engl.* **1994**, *33*, 1044 – 1072; b) O. Mader, K. Reiner, H.-J. Egelhaaf, R. Fischer, R. Brock, *Bioconjugate Chem.* **2004**, *15*, 70 – 78.
[130] F. Würthner, R. Wortmann, K. Meerholz, *ChemPhysChem* **2002**, *3*, 17 – 31.

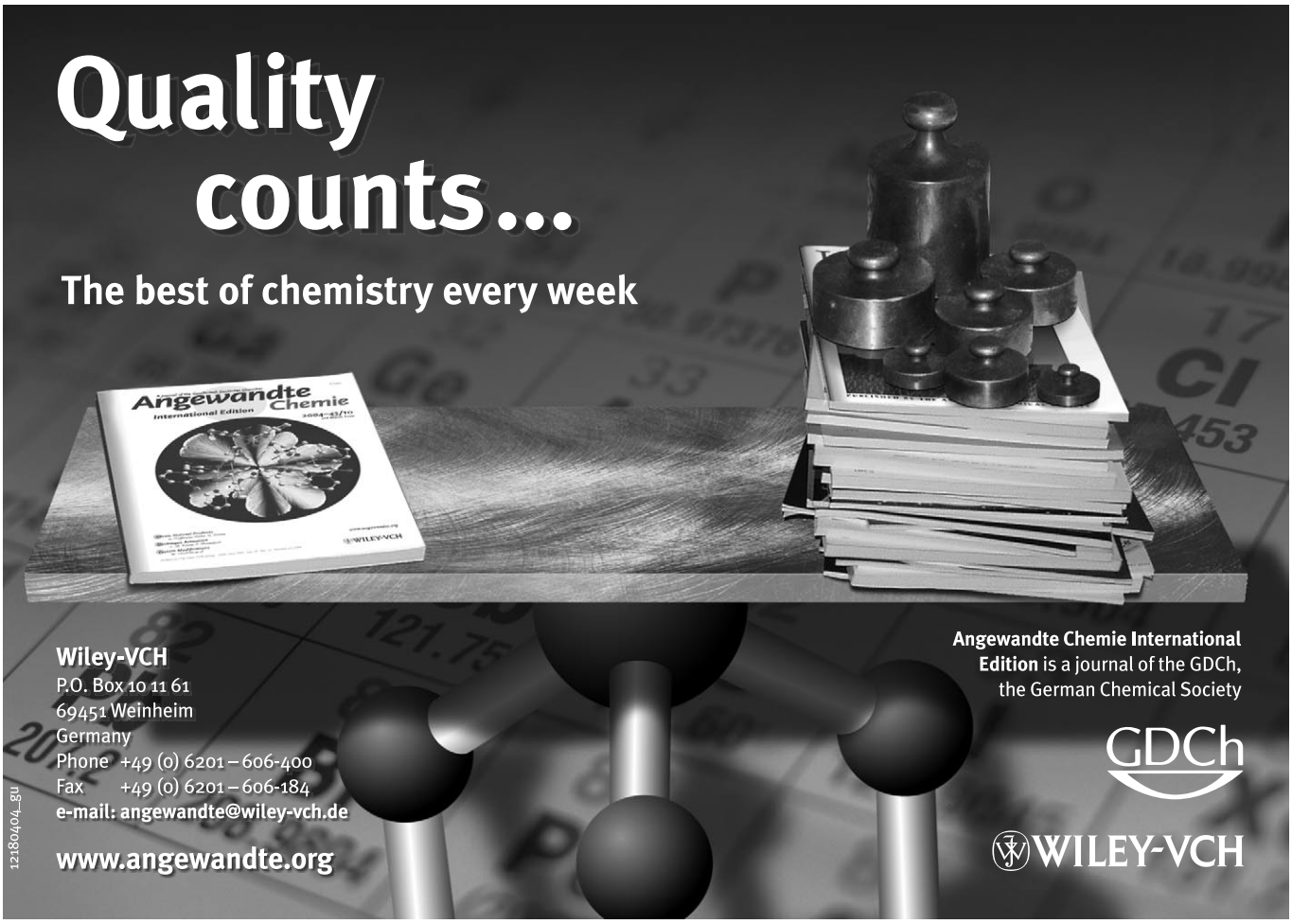

© 2006 Wiley-VCH Verlag GmbH & Co. KGaA, Weinheim

Communications

DOI: 10.1002/anie.200504306

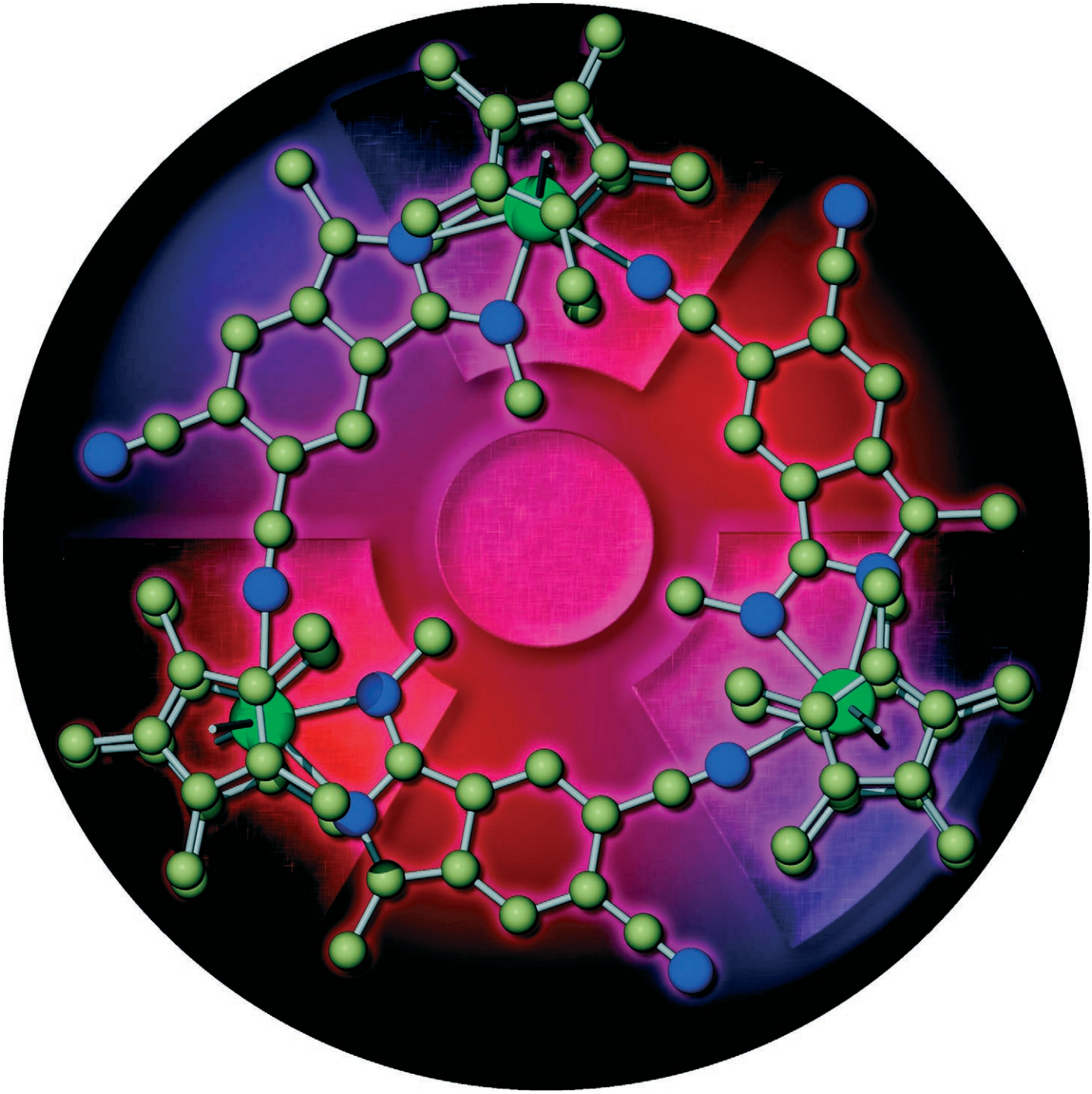

A class of actinide metallomacrocycles with three $(C_5Me_5)_2An$ (An = Th, U) fragments coordinated by three bridging 5,6-dicyano-1-methyl-3-(*N*-methylamino)isoindolyl ligands is presented in the Communication by J. L. Kiplinger, D. E. Morris and coworkers on the following pages. They are the result of an actinide-mediated cyclization of 1,2,4,5-tetracyanobenzene and self-assembly.

WILEY InterScience DISCOVER SOMETHING GREAT
© 2006 Wiley-VCH Verlag GmbH & Co. KGaA, Weinheim

Actinide Supramolecular Chemistry

DOI: 10.1002/anie.200504306

Actinide-Mediated Cyclization of 1,2,4,5-Tetracyanobenzene: Synthesis and Characterization of Self-Assembled Trinuclear Thorium and Uranium Macrocycles**

Jaqueline L. Kiplinger, Jaime A. Pool, Eric J. Schelter, J. D. Thompson, Brian L. Scott, and David E. Morris**

The large ionic radii of the actinides coupled with the high nodality of the 5f orbitals creates a unique platform for reactivity patterns that are not available to the d transition metals. An illustration of this is provided by the uranyl chloride condensation reaction of phthalonitrile to give 20-membered, pentadentate "superphthalocyanine" macrocycles.[1] This contrasts the chemistry of the transition metal ions, which template the formation of tetradentate phthalocyanines.

We recently reported that benzonitrile inserts into the uranium–carbon bonds in complexes of the type $[(C_5Me_5)_2UR_2]$ (where $R = CH_2Ph$, CH_3) to afford monometallic ketimide complexes **1**[2] with enhanced covalency in the

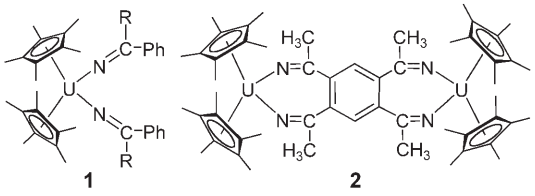

1 **2**

uranium–ketimide linkages.[3] Intrigued by the prospect of preparing bimetallic actinide complexes possessing bridging ketimide ligands (such as the proposed structure **2**) that might promote metal–metal interactions, we investigated the reactivity between uranium and thorium alkyl complexes and 1,2,4,5-tetracyanobenzene.

We now report that the reaction between 1,2,4,5-tetracyanobenzene and $[(C_5Me_5)_2An(CH_3)_2]$ (**3**, An = Th, U) does not afford the anticipated bimetallic actinide complexes. Instead, 24-membered, cyclic trinuclear thorium(IV) and uranium(IV) triangular macrocycles are formed by sequential nitrile-coupling chemistry and self-assembly. The actinide-mediated cyclization features the unprecedented coupling of a nitrile with a ketimide functional group and represents a new entry into the synthesis of supramolecular assemblies containing organometallic actinide components.

Addition of one equivalent of 1,2,4,5-tetracyanobenzene to a THF solution of **3a** or **3b** at ambient temperature affords the corresponding trinuclear actinide macrocycle **4a** (61%) or **4b** (47%) as dark purple crystalline solids [Eq. (1)].

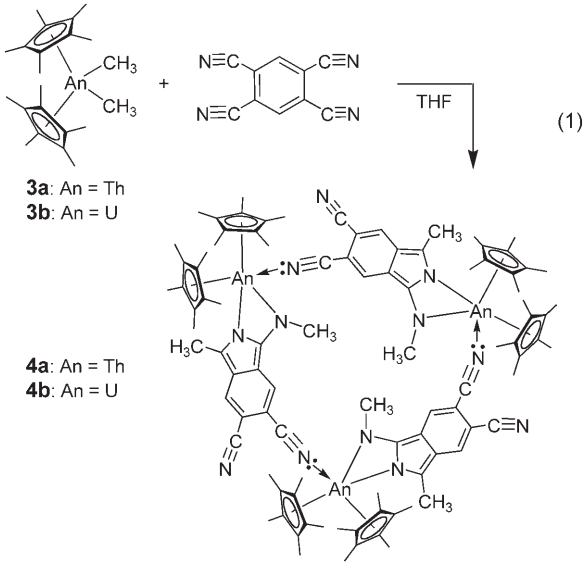

3a: An = Th
3b: An = U

4a: An = Th
4b: An = U

(1)

Diagnostic spectroscopic data indicate that in the absence of light the structures maintain their integrity and high symmetry in solution. For example, NMR spectroscopy clearly establishes that the addition of strong donor ligands (e.g., pyridine, CH_3CN, or THF) to C_6D_6 solutions of **4** does not disrupt the trinuclear macrocycles within 2 h at room temperature. The ^1H NMR spectrum of the diamagnetic thorium(IV) macrocycle **4a** revealed clean formation of one compound with two downfield singlets at $\delta = 8.50$ and 7.55 ppm corresponding to the two aryl protons, two singlets at $\delta = 3.78$ and 2.61 ppm for the two different methyl groups, and a signal at $\delta = 2.04$ ppm for the C_5Me_5 ligands. A nearly identical ^1H NMR spectrum is observed for the uranium derivative **4b** except that the relatively sharp signals are paramagnetically shifted, which is typical for $5f^2$ uranium(IV) species.

Cooling of a concentrated THF/diethyl ether solution of **4b** to −35 °C produced dark purple needles suitable for a single crystal X-ray diffraction study (Figure 1).[4] The analysis revealed a triangular array of uranium atoms (U–U distance 10.92 Å) bridged by three unusual 5,6-dicyano-1-methyl-3-(*N*-methylamino)isoindolyl ligands. The macrocycle has C_{3h} symmetry; each 9-coordinate uranium atom adopts a typical bent-metallocene geometry, with an average $U-C_{C_5Me_5}$ bond length of 2.78(1) Å and a $C_5Me_{5(cent)}$-U-$C_5Me_{5(cent)}$ bond angle of 134.8°. These values are well within the range typically found in $(C_5Me_5)_2U^{IV}$ complexes.[2,3a] Each isoindolyl

[*] Dr. J. L. Kiplinger, Dr. J. A. Pool, Dr. E. J. Schelter, Dr. J. D. Thompson, Dr. B. L. Scott, Dr. D. E. Morris
Los Alamos National Laboratory
Los Alamos, NM 87545 (USA)
Fax: (+1) 505-667-9905
E-mail: kiplinger@lanl.gov
demorris@lanl.gov

[**] For financial support we acknowledge Los Alamos National Laboratory (Director's Postdoctoral Fellowship to J.A.P.), the LANL G. T. Seaborg Institute (Postdoctoral Fellowship to E.J.S.), the LANL LDRD Program, and the Division of Chemical Sciences, Office of Basic Energy Sciences.

Supporting information for this article is available on the WWW under http://www.angewandte.org or from the author.

 © 2006 Wiley-VCH Verlag GmbH & Co. KGaA, Weinheim

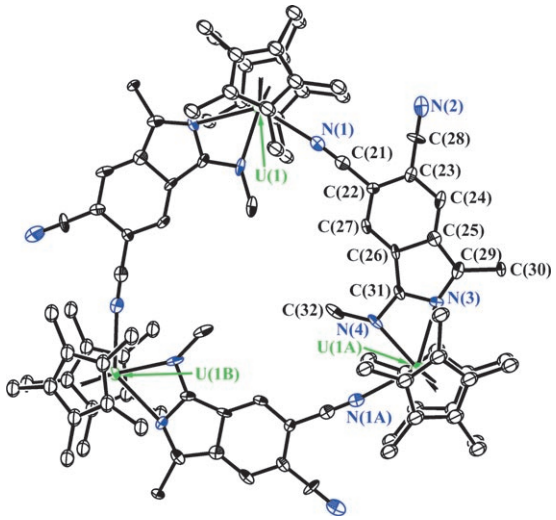

Figure 1. Molecular structure of complex **4b** (thermal ellipsoids at the 30% probability level). Selected distances [Å] and angles [°]: U(1)-N(1) 2.469(14), U(1A)-N(3) 2.464(10), U(1A)-N(4) 2.236(12), N(4)-C(32) 1.496(19), N(4)-C(31) 1.356(18), N(3)-C(31) 1.360(16), N(3)-C(29) 1.361(17), N(1)-C(21) 1.136(17), N(2)-C(28) 1.144(17), C(29)-C(30) 1.528(18), C(29)-C(25) 1.411(19), C(25)-C(24) 1.396(19), C(25)-C(26) 1.466(16), C(26)-C(31) 1.444(18), C(26)-C(27) 1.388(16), C(22)-C(27) 1.381(16), C(22)-C(23) 1.435(16), C(22)-C(21) 1.422, C(23)-C(28) 1.306(18), C(23)-C(24) 1.391(17), $C_5Me_{5(cent)}$-U = 2.425, U-C_{ave} = 2.78(1); N(4)-U(1A)-N(1A) 75.9(4), N(4)-U(1A)-N(3) 58.1(4), N(1A)-U(1A)-N(3) 134.1(3), U(1)-N(1)-C(21) 174.2(11), C(23)-C(28)-N(2) 197.2(18), $C_5Me_{5(cent)}$-U-$C_5Me_{5(cent)}$ 134.8.

ligand bridges two uranium(IV) centers: one is bound in an η^2-(*N*,*N*′) fashion through one U–N σ bond to the *N*-methylamide moiety (U(1A)-N(4)) and one U–N σ interaction to the nitrogen of the isoindole ring (U(1A)-N(3)), while one of the two nitrile groups coordinates to a second uranium center (U(1)-N(1)). The U(1A)–N(4) amide bond length of 2.236(12) Å is comparable to that of other structurally characterized uranium(IV) amide complexes.[5] Although actinide isoindolyl complexes are not known, the U(1A)–N(3) bond length of 2.464(10) Å is in good agreement with U–N bond lengths reported for σ-bonded uranium(IV) pyrrolyl[6] and pyrazolyl[7] complexes.

The U(1)–N(1) bond is substantially shorter (about 0.1–0.2 Å) than expected for neutral[8] or cationic[9] uranium(IV)–nitrile dative interactions and indicates that the uranium–nitrile linkages holding together the trinuclear framework of **4b** are rather robust. Transition metal nitrile complexes exhibit a shortening of the M–N bond, which has been attributed to better orbital overlap that arises from the sp hybridization of the nitrogen atom of the nitrile group.[10a] In complex **4b**, the U(1)-N(1)-C(21) bond angle (174.1(11)°) shows a slight deviation from linearity and the N(1)–C(21) bond (1.136(17) Å) exhibits a small shortening compared to the uncoordinated nitrile group (N(2)-C(28) = 1.144(17) Å) in the molecule.[10] The thorium(IV) macrocycle **4a** is isostructural to **4b**, however, because of the poor quality of the crystallographic data only connectivity could be established.

The formation of **4** is proposed to occur by the mechanism depicted in Scheme 1. Nitrile insertion into an actinide–methyl bond of complexes **3** would lead to the formation of the ketimide complexes **5**. As described earlier, this reaction has ample precedent.[2,11] We suggest that the actinide center in **5** mediates the coupling of the newly formed ketimide functional group with the *ortho* nitrile group, which would generate the isoindole skeleton and afford complexes **6**. Subsequent 1,2-methyl migration would give complexes **7**, which contain the 5,6-dicyano-1-methyl-3-(*N*-methylamino)-isoindolyl ligand. Finally, self-assembly of three molecules of **7** would yield the observed trinuclear products **4**.

This mechanism is quite distinct from that of the well-known actinide and transition metal ion templated condensation reactions of phthalonitrile compounds, which yield monometallic phthalocyanine complexes.[1,12] The formation of an actinide ketimide complex (**5**) seems to be the crucial step in the synthesis of the unique 5,6-dicyano-1-methyl-3-(*N*-methylamino)isoindolyl ligand. Numerous examples of metal-mediated nitrile coupling reactions with compounds such as amines,[13a] imines,[13b] ketones,[13c] alkynes,[13d] amidines,[13e] oximes,[13f] and other nitriles[13g] are known. However, to the best of our knowledge, the coupling of a nitrile with a

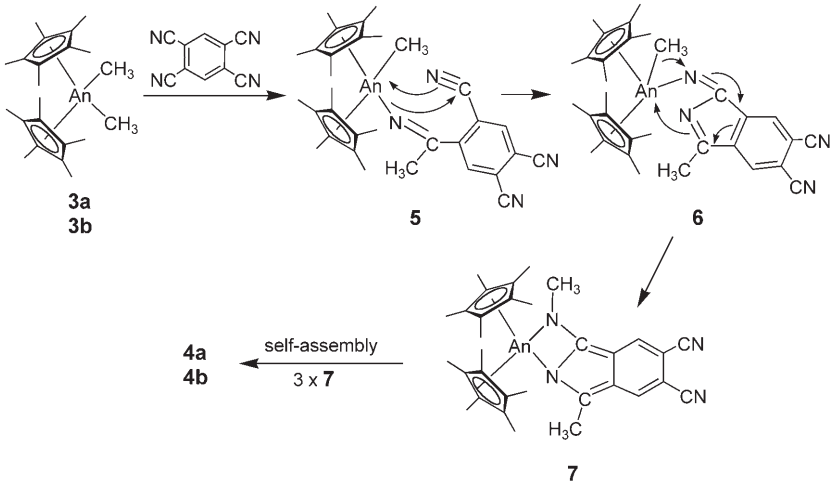

Scheme 1. Proposed mechanism for the formation of the trinuclear actinide macrocycles **4**.

ketimide functional group has not been observed with transition metals, once again highlighting the differences between transition metals and the actinides.

The use of actinide centers as highly directional building blocks in well-defined supramolecular multimetallic assemblies has been limited due to their flexible and unpredictable coordination behavior.[14–16] Some degree of success has been realized using the linear uranyl moiety $(O{\equiv}U{\equiv}O)^{2+}$ as a building block for the construction of triangular $[UO_2L]_3^{6-}$ and square $[UO_2L]_4^{8-}$ metallamacrocycles with L =

 © 2006 Wiley-VCH Verlag GmbH & Co. KGaA, Weinheim

(2*R*,3*R*,4*S*,5*S*)-tetrahydrofurantetracarboxylic acid.[15] However, the preparation of complexes **4** together with recently reported polymetallic uranium–nitrogen macrocycles, $[\{(C_5Me_4R)_2U(\mu\text{-}N)U(\mu\text{-}N_3)(C_5Me_4R)_2\}_4]$ (R = Me, H),[16] clearly demonstrates that actinide bent-metallocene frameworks are also able to function as linker units and direct the formation of discrete actinide supramolecular structures.

Metal–metal communication in the macrocycles **4** was assessed using a combination of voltammetry, UV/vis/NIR absorption spectroscopy, and magnetic susceptibility. In contrast to the monometallic $[(C_5Me_5)_2U\{N{=}C(Ph)(R)\}_2]$ (R = Ph, CH_2Ph, CH_3) systems that show clean, chemically reversible one-electron waves attributable to both a U^V/U^{IV} oxidation step and a U^{IV}/U^{III} reduction step,[2,3a,b] the voltammetric response of **4b** entails at least eight ill-resolved voltammetric waves of varying degrees of chemical and electrochemical reversibility (see Supporting Information). Three of these are oxidation waves in the potential range from ≈ 0 to -1.0 V (vs $[(C_5H_5)_2Fe]^+/[(C_5H_5)_2Fe]^0$), and five are reduction waves in the potential range from -1.5 to -3.0 V. Correlation of waves between **4a** and **4b** reveals that all oxidation waves are commensurate between the two, whereas the voltammogram of **4b** shows two well-defined, chemically reversible reduction waves (-1.8 and -2.7 V) not observed for **4a**, with the latter having a significantly larger peak current than the former. These waves are attributed to U^{IV}/U^{III} redox transformations for two or all three metal centers in the macrocycle **4b**.

The electronic absorption spectral data for **4a** and **4b** are shown in Figure 2. The hallmark f–f transitions common to uranium(IV) species are evident in the NIR region of the spectra. The energy range for these transitions is comparable to that of the other uranium(IV) bent metallocene complexes,[2,3] and the number of bands is similar to that seen in monometallic uranium(IV) bis(ketimide) and mono(imido) complexes. If, in fact, there were significant metal–metal coupling in **4b**, one might anticipate splitting of degenerate f orbital-based electronic states on adjacent metal centers due to this coupling giving rise to a larger number of f–f electronic transitions than in a monometallic system.

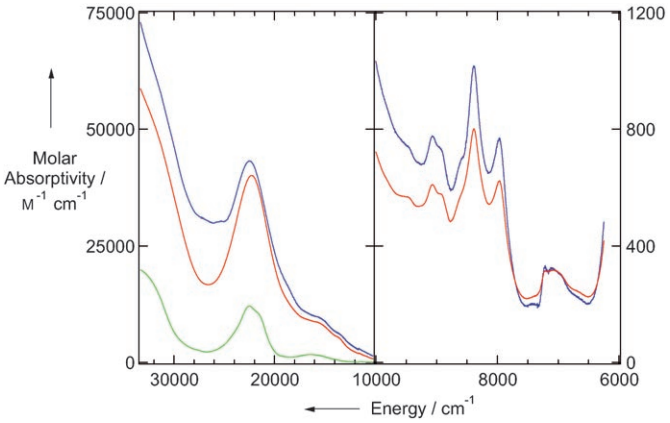

Figure 2. Room-temperature electronic absorption spectral data for **4a** in toluene (——) and **4b** in toluene (——) and THF (——). Molar absorptivities are expressed as per mol of trimetallic species, not per mol of metal.

No electronic absorption bands are observed in the spectrum of **4a** in the NIR region as expected for the $6d^05f^0$ electronic configuration of this molecule. This complex does give three intense, well-resolved bands in the visible and near ultraviolet regions ($E_{max} \approx 16300$, 22500, and > 33300 cm^{-1}) that arise from ligand-based n–π* and π–π* transitions on the indole and/or nitrile functional groups.[17] The UV/Vis spectral region for complex **4b** is dominated by an additional, more-intense band ($E_{max} = 22290$ cm^{-1} in toluene; 22500 cm^{-1} in THF) that overlies and obscures the band at 22500 cm^{-1}. This additional electronic transition in complex **4b** is assigned to a ligand-to-metal charge transfer (LMCT) transition similar to that seen in numerous pyrrole and pyrazole complexes of transition metals such as iron,[18] copper,[19] and ruthenium.[20]

In the present case, the terminal metal orbital for the LMCT transition is an f orbital. The assignment as a CT transition is supported by the energy shift observed on going from a low-dielectric solvent (toluene) to a higher-dielectric solvent (THF). The presence of an LMCT transition in energetic proximity to the f–f electronic transitions provides an explanation for the substantially enhanced intensity in the f–f bands for **4b** similar to that proposed previously for the monometallic uranium bis(ketimide) complexes: coupling of the f–f states with the CT state through a common f orbital.[3b] Such coupling is facilitated by a stronger covalent interaction with the ketimide ligand due to both σ and π donor interactions. A similar observation for the macrocycle **4b** suggests that the interaction of the indole unit with the metal center is also unusually strong providing added stabilization that could help to explain the formation and existence of this unusual supramolecular construct.

Temperature-dependent magnetic susceptibility data were collected for **4b** in the temperature range from 1.8 to 350 K and the data are shown in Figure 3. The χT vs T response shows a strong, non-Curie temperature dependence with a high-temperature value of 1.11 emu K mol^{-1} and a low-temperature value that approaches zero, while the χ vs T data increase monotonically with decreasing temperature and approach a finite value at low temperatures. The strong

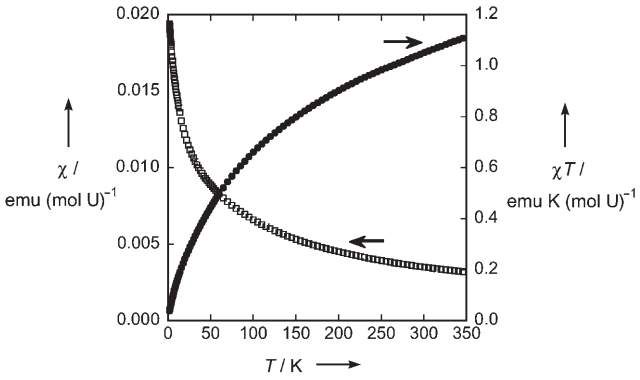

Figure 3. Temperature-dependent magnetic susceptibility data for **4b** per mol uranium(IV).

 © 2006 Wiley-VCH Verlag GmbH & Co. KGaA, Weinheim

temperature dependence in the data for **4b** is the result of the depopulation of electronic crystal-field states resulting from the $^3H_4$ ground manifold of the uranium(IV) ions and is consistent with magnetic behavior reported for such complexes.[21] The high-temperature value attained in the χT vs T data for **4b** is significantly less than the expected value for a uranium(IV) free ion predicted by the Curie law for $S=1$, $L=5$, and $J=4$ (1.60 emu K mol^{-1}).

This disparity implies that the overall crystal-field splitting in **4b** is $> kT$ at the high-temperature limit in this experiment. At each uranium(IV) ion of **4b**, a singlet crystal-field state lies lowest in energy with residual paramagnetism observed at low temperature attributed to temperature-independent contributions (Van Vleck paramagnetism).[21] Treatment of the high-temperature $1/\chi$ vs T data (see Supporting Information) between 350 and 200 K yields a Weiss constant, θ, of -159 K for **4b**. The temperature dependence of the susceptibility of **4b** from depopulation of crystal-field states of the uranium(IV) ions precludes the use of the Weiss constant for determining magnetic coupling of the uranium(IV) ions in this complex. While a signature of magnetic coupling between excited states of the uranium(IV) ions may be present within the Weiss constant, it is ultimately masked by the strong temperature dependence of the other primary effect.

In summary, a new class of actinide metallomacrocycles has been prepared in which three $(C_5Me_5)_2An$ (An = Th, U) fragments are coordinated by three 5,6-dicyano-1-methyl-3-(*N*-methylamino)isoindolyl bridging ligands. The tetravalent actinide centers have been combined to form an uncommon triangular geometry following the unprecedented actinide-mediated cyclization of 1,2,4,5-tetracyanobenzene and self-assembly. Voltammetric data show at least two well-separated uranium(IV) reduction waves indicative of some metal–metal interaction. However, neither optical nor magnetic data exhibit traditional indications of any significant metal–metal coupling. The optical data, in particular the enhanced f–f transition intensities, do reflect the unusually strong metal–indole interaction in these actinide complexes. This strong interaction is a likely origin for their formation and a potential springboard for the design of additional new multimetallic actinide systems tailored for enhanced metal–metal communication.

Experimental Section

All manipulations were performed in a recirculating Vacuum Atmospheres Model HE-553-2 inert atmosphere (N_2 or He) drybox with a MO-40-2 Dri-Train.

4a: 1,2,4,5-Tetracyanobenzene (0.171 g, 0.962 mmol) was dissolved in 10 mL of THF and slowly added with stirring to a 125-mL Erlenmeyer flask charged with **3a** (0.394 g, 0.740 mmol) and 30 mL of THF. The resulting dark purple reaction mixture was stirred for 2 h and then the volatiles were removed under reduced pressure. The resulting oil was washed three times with approximately 10 mL of diethyl ether to give **4a** as a dark purple crystalline solid. Analytically pure samples of **4a** were obtained by recrystallization from diethyl ether at −35 °C (0.321 g, 0.151 mmol, 61.0 %). ^{1}H NMR (C_6D_6, 21 °C): $\delta = 2.04$ (s, 90 H, C_5Me_5), 2.61 (s, 9 H, CH_3), 3.78 (s, 9 H, NCH_3), 7.55 (s, 3 H, H_{Ar}), 8.50 ppm (s, 3 H, H_{Ar}). ^{13}C{^{1}H} NMR (C_6D_6, 21 °C): $\delta =$ 10.1 ($C_5\mathit{Me}_5$), 14.1 (CH_3), 22.5 (NCH_3), 79.8, 95.6, 113.7, 117.1, 119.9, 125.9, 129.4, 134.9, 136.7, 153.4 (C≡N, C_{Ar}), 125.7 ppm (C_5Me_5). C,H,N analysis (%) calcd for $C_{100}H_{124}N_{12}OTh_3$: C 54.44; H 5.67; N 7.62; found: C 54.37; H 5.74; N 7.49.

4b: The synthesis of complex **4b** was performed in an analogous manner to that of **4a**, using 1,2,4,5-tetracyanobenzene (0.173 g, 0.973 mmol) and **3b** (0.403 g, 0.748 mmol) to give **4b** as a dark purple crystalline solid (0.252 g, 0.117 mmol, 47.0 %). ^{1}H NMR (C_6D_6, 21 °C): $\delta = -31.64$ (s, 9 H, CH_3), 5.78 (s, 3 H, H_{Ar}), 6.02 (s, 90 H, C_5Me_5), 6.72 (s, 3 H, H_{Ar}), 24.21 ppm (s, 9 H, CH_3). C,H,N analysis (%) calcd for $C_{104}H_{134}N_{12}O_2U_3$: C 55.61; H 5.88; N 7.32; found: C 55.43; H 5.48; N 7.17.

Received: December 3, 2005
Published online: February 21, 2006

Keywords: metallomacrocycles · self-assembly · tetracyanobenzene · thorium · uranium

[1] a) V. W. Day, T. J. Marks, W. A. Wachter, *J. Am. Chem. Soc.* **1975**, *97*, 4519–4527; b) T. J. Marks, D. R. Stojakovic, *J. Am. Chem. Soc.* **1978**, *100*, 1695–1705.

[2] K. C. Jantunen, C. J. Burns, I. Castro-Rodriguez, R. E. Da Re, J. T. Golden, D. E. Morris, B. L. Scott, F. L. Taw, J. L. Kiplinger, *Organometallics* **2004**, *23*, 4682–4692.

[3] a) J. L. Kiplinger, D. E. Morris, B. L. Scott, C. J. Burns, *Organometallics* **2002**, *21*, 3073–3075; b) D. E. Morris, R. E. Da Re, K. C. Jantunen, I. Castro-Rodriguez, J. L. Kiplinger, *Organometallics* **2004**, *23*, 5142–5153; c) R. E. Da Re, K. C. Jantunen, J. T. Golden, J. L. Kiplinger, D. E. Morris, *J. Am. Chem. Soc.* **2005**, *127*, 682–689.

[4] Crystal structure data for **4b**·2 THF ($C_{104}H_{130}N_{12}O_2U_3$): hexagonal; crystal size: $0.44\times0.06\times0.01$ mm^3; $a = 20.1663(16)$, $b = 20.1663(16)$, $c = 17.693(3)$ Å; $V = 6231.4(13)$ Å^3; $Z = 2$; $\rho_{calc} = 1.178$ Mg m^{-3}; $2\theta_{max} = 50.64°$; ω scans; $T = 141(2)$ K; $\lambda = 0.71073$ Å; 60244 reflections, 3928 unique ($R_{int} = 0.1632$); $R_1 = 0.0393$ ($I > 2\sigma(I)$), $wR_2 = 0.0873$; Lorentzian-polarization and absorption corrections performed with SADABS 2.03; $\mu = 3.927$ mm^{-1}; max/min transmission: 0.9618 and 0.2769; 127 parameters; full-matrix, least squares on F^2. Structure was solved and refined using SHELXTL 5.10. All hydrogen atom positions were treated as idealized contributions. CCDC-290125 contains the supplementary crystallographic data for this paper. These data can be obtained free of charge from The Cambridge Crystallographic Data Centre via www.ccdc.cam.ac.uk/data_request/cif.

[5] a) T. Straub, W. Frank, G. J. Reiss, M. S. Eisen, *J. Chem. Soc. Dalton Trans.* **1996**, 2541–2546; b) R. G. Peters, B. P. Warner, C. J. Burns, *Organometallics* **1999**, *18*, 2587–2589; c) B. D. Stubbert, C. L. Stern, T. J. Marks, *Organometallics* **2003**, *22*, 4836–4838.

[6] I. Korobkov, S. Gambarotta, G. P. A. Yap, *Organometallics* **2001**, *20*, 2552–2559.

[7] C. W. Eigenbrot, K. N. Raymond, *Inorg. Chem.* **1982**, *21*, 2653–2660.

[8] F. A. Cotton, D. O. Marler, W. Schwotzer, *Acta Crystallogr. Sect. C* **1984**, *40*, 1186–1188.

[9] a) H. Aslan, K. Yünlü, R. D. Fischer, G. Bombieri, F. Benetollo, *J. Organomet. Chem.* **1988**, *354*, 63–76; b) J. C. Berthet, P. Thuéry, M. Ephritikhine, *Inorg. Chem.* **2005**, *44*, 1142–1146.

[10] a) J. W. Lauher, J. A. Ibers, *Inorg. Chem.* **1975**, *14*, 640–645; b) B. N. Storhoff, H. C. Lewis, Jr., *Coord. Chem. Rev.* **1977**, *23*, 1–29.

[11] a) A. Dormund, A. Aaliti, A. El Bouadili, C. Moise, *J. Organomet. Chem.* **1987**, *329*, 187–199; b) A. Dormund, A. Aaliti, A. El Bouadili, C. Moise, *Inorg. Chim. Acta* **1987**, *139*, 171–176.

 © 2006 Wiley-VCH Verlag GmbH & Co. KGaA, Weinheim

[12] a) M. Nicolau, B. Cabezón, T. Torres, *Coord. Chem. Rev.* **1999**, *190–192*, 231 – 243; b) T. Inabe, H. Tajima, *Chem. Rev.* **2004**, *104*, 5503 – 5533.
[13] a) S. Du, J. A. Kautz, T. D. McGrath, F. G. A. Stone, *J. Chem. Soc. Dalton Trans.* **2002**, 1553 – 1558; b) D. A. Garnovskii, V. Y. Kukushkin, M. Haukka, G. Wagner, A. J. L. Pombeiro, *J. Chem. Soc. Dalton Trans.* **2001**, 560 – 566; c) G. A. Molander, C. N. Wolfe, *J. Org. Chem.* **1998**, *63*, 9031 – 9036; d) M. Etienne, C. Carfagna, P. Lorente, R. Mathieu, D. de Montauzon, *Organometallics* **1999**, *18*, 3075 – 3086; e) N. A. Bokach, T. V. Kuznetsova, S. A. Simanova, M. Haukka, A. J. L. Pombeiro, V. Y. Kukushkin, *Inorg. Chem.* **2005**, *44*, 5152 – 5160; f) V. Y. Kukushkin, I. V. Ilichev, G. Wagner, J. J. R. Fraústo da Silva, A. J. L. Pombeiro, *J. Chem. Soc. Dalton Trans.* **1999**, 3047 – 3052; g) Y. C. Tsai, F. H. Stephens, K. Meyer, A. Mendiratta, M. D. Gheorghiu, C. C. Cummins, *Organometallics* **2003**, *22*, 2902 – 2913.
[14] a) R. M. Yeh, A. M. Davis, K. N. Raymond in *Comprehensive Coordination Chemistry II, Vol 7* (Eds.: M. Fujita, A. Powell, C. A. Creutz), Elsevier, Amsterdam, **2004**, pp. 327 – 355, and references therein; b) J. C. G. Bünzli, C. Piguet, *Chem. Rev.* **2002**, *102*, 1897 – 1928.
[15] P. Thuéry, C. Villiers, J. Jaud, M. Ephritikhine, B. Masci, *J. Am. Chem. Soc.* **2004**, *126*, 6838 – 6839.
[16] W. J. Evans, S. A. Kozimor, J. W. Ziller, *Science* **2005**, *309*, 1835 – 1838.
[17] N. Kobayashi, T. Ishizaki, K. Ishii, H. Konami, *J. Am. Chem. Soc.* **1999**, *121*, 9096 – 9110.
[18] R. E. Shepherd, *J. Am. Chem. Soc.* **1976**, *98*, 3329 – 3335.
[19] E. Bernarducci, W. F. Schwindinger, J. L. Hughey, K. Kroghjespersen, H. J. Schugar, *J. Am. Chem. Soc.* **1981**, *103*, 1686 – 1691.
[20] S. Baitalik, U. Florke, K. Nag, *Inorg. Chem.* **1999**, *38*, 3296 – 3308.
[21] a) K. P. Mortl, J. P. Sutter, S. Golhen, L. Ouahab, O. Kahn, *Inorg. Chem.* **2000**, *39*, 1626 – 1627; b) K. C. Jantunen, R. J. Batchelor, D. B. Leznoff, *Organometallics* **2004**, *23*, 2186 – 2193; c) E. A. Boudreaux, L. N. Mulay, *Theory and Applications of Molecular Paramagnetism*, Wiley, New York, **1976**.

 © 2006 Wiley-VCH Verlag GmbH & Co. KGaA, Weinheim

Catalyzed Ring Opening

DOI: 10.1002/anie.200504176

Elucidation of the Mechanism of Titanocene-Mediated Epoxide Opening by a Combined Experimental and Theoretical Approach**

Kim Daasbjerg, Heidi Svith, Stefan Grimme,* Mareike Gerenkamp, Christian Mück-Lichtenfeld, Andreas Gansäuer,* Andriy Barchuk, and Florian Keller*

Titanocene-mediated[1] and -catalyzed epoxide ring opening[2] continues to be a highly pertinent synthetic transformation in organic chemistry. However, despite its preparative usefulness nothing is known about its mechanism. Herein, we present a study to elucidate this mechanism by a combination of electrochemical, kinetic, computational, and synthetic methods.

The determination of catalyst composition and the kinetics of the ring opening are the essential experimental basis for any mechanistic discussion. Thus, Zn-reduced THF solutions of $[Cp_2TiCl_2]$ (**1**; Cp = cyclopentadiene), **2**, and **3**[3] were first analyzed by cyclic voltammetry, a technique uniquely suited for the investigation of redox-active species.[4]

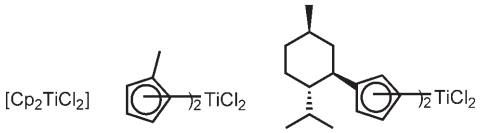

1 **2** **3**

The solution derived from **1** consists of two species, $[Cp_2TiCl]$ (**1b**) and the dimer $[Cp_2TiCl]_2$ (**1a**), which are in rapid equilibrium ($K = 3000\,M^{-1}$).[5] Herein, we demonstrate

[*] Prof. Dr. K. Daasbjerg, H. Svith
Department of Chemistry
University of Aarhus
Langelandsgade 140, 8000 Aarhus C (Denmark)
Fax: (+45) 8919-6199
E-mail: kdaa@chem.au.dk

Prof. Dr. S. Grimme, Dr. M. Gerenkamp, Dr. C. Mück-Lichtenfeld
Organisch-Chemisches Institut
Westfälische Wilhelms-Universität
Corrensstrasse 40, 49149 Münster (Germany)
Fax: (+49) 251-83-36515
E-mail: grimmes@uni-muenster.de

Prof. Dr. A. Gansäuer, A. Barchuk, F. Keller
Kekulé-Institut für Organische Chemie und Biochemie
Universität Bonn
Gerhard-Domagk-Strasse 1, 53127 Bonn (Germany)
Fax: (+49) 228-73-4760
E-mail: andreas.gansaeuer@uni-bonn.de

[**] We are indebted to the Danish Natural Science Research Council, the Deutsche Forschungsgemeinschaft, and the Fonds der Chemischen Industrie for generous financial support.

Supporting information for this article is available on the WWW under http://www.angewandte.org or from the author.

 © 2006 Wiley-VCH Verlag GmbH & Co. KGaA, Weinheim

that for **2** the dimer **2a** remains an important constituent ($K = 1000\,\text{M}^{-1}$), but to a noticeably lesser extent. The presence of the bulkier ligand in **3** makes the monomer **3b** the only species detectable by cyclic voltammetry ($K < 100\,\text{M}^{-1}$, as deduced from digital simulations; see Supporting Information). For 2-mM Zn-reduced solutions of **1**, **2**, and **3**, this implies that the dimer/monomer ratio is 1.5, 0.8, and < 0.15, respectively.

Kinetic analysis of the opening of **4**[2a] with Zn-reduced solutions of **1**, **2**, and **3** was then carried out (Table 1). The rate

Table 1: Rate constants k [$\text{M}^{-1}\,\text{s}^{-1}$] of the reductive ring opening of **4** with Zn-reduced THF solutions of **1**–**3**.

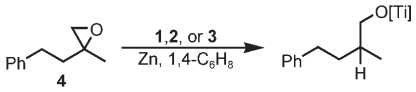

catalyst	k(monomer)	k(dimer)
1	0.5	1.4
2	1.3	3.9
3	0.8	–

constants, k, were extracted by monitoring the disappearance of the Ti^{III} species with a UV dip-probe in the presence of an excess of **4** (see Supporting Information). As in the synthetic work, 1,4-cyclohexadiene (1,4-C_6H_8) was added in order to chemically reduce the radical intermediate formed upon electron-transfer-mediated ring opening. The kinetics were unaffected by the concentration of 1,4-C_6H_8. Thus, electron transfer is the rate-controlling step of the overall reduction. This renders any mechanism with a quick and reversible ring opening before radical trapping unlikely.

To establish the nature of the reductant, with specific emphasis on the influence of the monomer/dimer distribution, kinetic traces were recorded at different Ti^{III} concentrations in the range 1–8 mM. In the case of **3** no effect was observed on the extracted pseudo-first-order rate constants, thus indicating that the monomer is the only reducing agent. This is consistent with the cyclic voltammetry studies, where no dimer constituent could be detected. Also, the reaction rate is relatively low in this case ($k = 0.8\,\text{M}^{-1}\,\text{s}^{-1}$), which can be attributed to larger steric constraints during substrate binding or in the transition state (TS). In contrast, in the case of **1** and **2** the Zn-reduced solutions contain appreciable amounts of the dimer, and the reaction rate is strongly affected by the Ti^{III} concentration. This was interpreted as though both monomer and dimer have a measurable reactivity towards **4** under these conditions, in agreement with the kinetic analysis of the reaction between Zn-reduced **1** and benzaldehyde or benzyl chloride.[5]

By numerically fitting the decay curves pertaining to the concentration of Ti^{III} (see Supporting Information) we established that the dimers ($k = 1.4$ and $3.9\,\text{M}^{-1}\,\text{s}^{-1}$ for **1** and **2**, respectively) open **4** faster than the corresponding monomers ($k = 0.5$ and $1.3\,\text{M}^{-1}\,\text{s}^{-1}$). For an employed concentration of Ti^{III} of 10 mM for instance, this implies that 84% and 75% of **4** will be opened by the dimers, respectively.

An important question at this point pertains to the actual structure of the dimer. Both **1a** and **2a** have no vacant coordination site and should be unable to complex **4**. We therefore propose the half-open structure **1′a** as the species responsible for epoxide binding to **1** (Scheme 1), with a

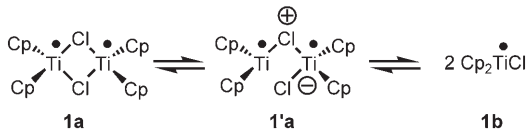

Scheme 1. Dimeric (**1a** or **1′a**) and monomeric species (**1b**) present in Zn-reduced THF solutions of **1**.

similar structure in the case of **2**. Complex **1′a** is a highly Lewis acidic intermediate in the formation of **1a** according to the principle of activation of electrophiles through dimeric association.[6]

On the basis of the above experimental results, we turned our attention towards calculations to gain further insight into the reaction mechanism. Activation and reaction energies were determined along with the structures of all pertinent intermediates and transition states by density functional theory (DFT) calculations[7] with the BP functional and a TZVP basis set. The [Cp_2TiCl]-derived complexes, which are valuable models for higher-substituted titanocenes, were investigated first. As model compounds for the epoxide we focused on the simpler propene oxide (**5**) and isobutene oxide (**6**) rather than **4**.

The results concerning the binding of **5** and **6** with [Cp_2TiCl] to afford the corresponding complexes **7** and **8** (see Table 2) proved to be interesting as there is a binding-energy difference in favor of **7** by about 4 kcal mol^{-1}. The calculations show that this is because the hydrogen atom at the substituted carbon atom of the epoxide part in **7** cannot be replaced by a second methyl group (giving **8**) without causing geometrical changes: For steric reasons the epoxide has to be rotated by 90° in **8** compared to **7** in order to enable complexation by titanium. Despite this structural change the Ti–O bond length in **8** is slightly shorter than in **7**. Illustrations of complexes **7** and **8** are given in Figure 1.

All activation energies, $\Delta E^{\neq}$, are in the range 7.0–9.4 kcal mol^{-1}, thus indicating that radical generation should be facile at room temperature, in agreement with the experimental results. It should also be noted that $\Delta E^{\neq}$ for the formation of **7a** and **8a** is lower than for **7b** and **8b**, and that the higher-substituted radicals are the thermodynami-

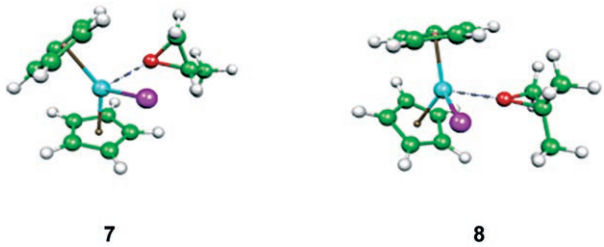

Figure 1. DFT-calculated structures of **7** and **8**.

 © 2006 Wiley-VCH Verlag GmbH & Co. KGaA, Weinheim

cally favored products. These results are summarized in Table 2.

Table 2: Reaction and activation energies [kcal mol^{-1}] of the ring opening of **7** (R^1 = Me, R^2 = H) and **8** (R^1 = R^2 = Me) by **1b**.

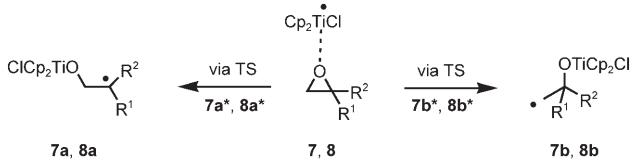

7a, 8a **7, 8** **7b, 8b**

ΔE(**7**)		$\Delta E^{\neq}$ (**7**)		ΔE(**8**)		$\Delta E^{\neq}$ (**8**)	
a	**b**	**a**	**b**	**a**	**b**	**a**	**b**
−4.0	−1.8	8.2	9.4	−8.5	−1.3	7.0	9.0

In all transition-state structures (i.e., **7a**$^{\neq}$, **7b**$^{\neq}$, **8a**$^{\neq}$, and **8b**$^{\neq}$) the spin density on the evolving radical center is lower (approximately 0.3) than on titanium (approximately 0.7), thereby suggesting that radical stability should not be as important an issue as steric effects. Steric effects have also been found to be significant in other titanocene-catalyzed reactions.[8] In the less-favored transition-state structures **7b**$^{\neq}$ and **8b**$^{\neq}$ the methyl group of the epoxide part is indeed in closer proximity to one of the cyclopentadienyl ligands (see Figure 2 for a comparison of **7a**$^{\neq}$ and **7b**$^{\neq}$). Thus, substituted cyclopentadienyl ligands should increase the steric effects.

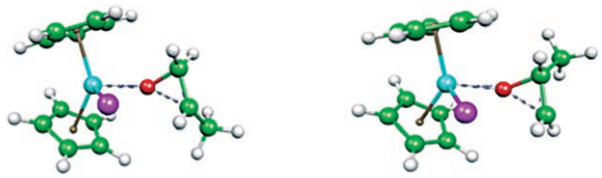

7a* **7b***

Figure 2. DFT-calculated structures of **7a**$^{\neq}$ and **7b**$^{\neq}$.

The calculations with $[Cp_2TiCl]_2$ did not provide a stable complex with propene oxide (**5**) if $[Cp_2TiCl]_2$ was assumed to be in its closed structure **1a**. However, the half-open structure **1′a** was found to readily complex **5** to give **9**, with the second Cp_2TiCl unit pointing away from the other titanocene unit. Binding of isobutene oxide (**6**) with **1′a** is less favorable as the epoxide in this case has to be rotated by 90°, which is in keeping with the results obtained for the binding of **6** with the monomer **1b** (see Supporting Information for details of all structures).

Ring opening to **9a** proceeds with $\Delta E = -6.4$ kcal mol^{-1} and $\Delta E^{\neq} = 6.3$ kcal mol^{-1} and to **9b** with $\Delta E = -4.6$ kcal mol^{-1} and $\Delta E^{\neq} = 7.5$ kcal mol^{-1} (Table 3). It is noteworthy that these activation energies are around 2 kcal mol^{-1} lower than those calculated for the corresponding reactions of **1b**. As the calculations do not include solvent effects, they reproduce the experimental finding of a higher reactivity of the dimer reasonably well.

Table 3: Ring opening of **5** by **1′a**.

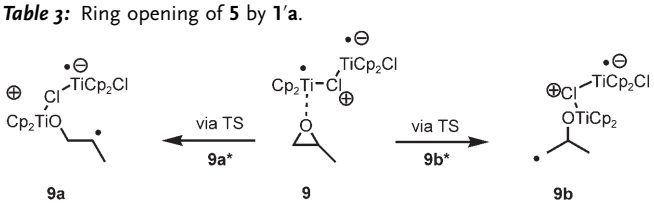

9a **9** **9b**

	ΔE [kcal mol^{-1}]	$\Delta E^{\neq}$ [kcal mol^{-1}]
9a	−6.4	6.3
9b	−4.6	7.5

Although **7** and **9** are energetically quite different, the differences in reaction and activation energies of secondary and primary radical generation from these species are surprisingly similar. Moreover, all complexes originating from **7** and **9** are structurally very similar at the reaction center. The calculated activation energies were therefore used to compare the predicted (88:12 for both **7a**:**7b** and **9a**:**9b**, and 97:3 for **8a**:**8b** at 25 °C) and experimentally determined selectivity of epoxide ring opening.

Ring opening of **10**, which is a nonvolatile analogue of **5**, with **1** proceeds with a regioselectivity of between 88:12 and 90:10 in the presence of γ-terpinene or *tert*-butyl acrylate as trapping agents (Scheme 2). As the agreement between

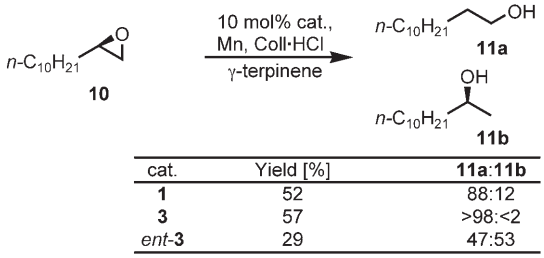

cat.	Yield [%]	**11a**:**11b**
1	52	88:12
3	57	>98:<2
ent-**3**	29	47:53

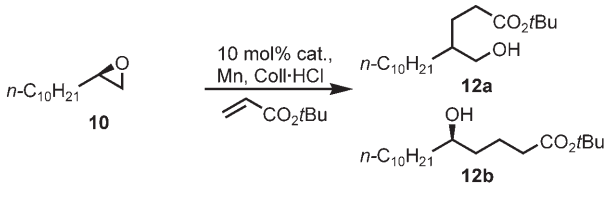

cat.	Yield [%]	**12a**:**12b**
1	73	90:10
2	87	93:7
3	61	>98:<2
ent-**3**	27	67:33

Scheme 2. Reagent control in the ring opening of **10**. Coll = collidine.

theory and experiment is excellent and independent of the trapping reagent, our mechanistic proposal, including the irreversibility of the ring opening, is strongly supported.

Substituted catalysts **2** and **3** were investigated in the reaction of **10** next. The presence of the methyl groups in **2** results in a slightly but noticeably higher selectivity of ring opening, as expected if selectivity is dominated by steric factors in the transition state. Further evidence for this hypothesis was obtained from the reaction of (*R*)-**10** with both

 © 2006 Wiley-VCH Verlag GmbH & Co. KGaA, Weinheim

enantiomers of **3**. As anticipated for an irreversible ring opening, matched and mismatched cases for its regioselectivity were observed in the formation of **11a** and **11b** or **12a** and **12b**. Gratifyingly, in both matched cases complete selectivity of epoxide opening was combined with higher yields of the products (Scheme 2).

In summary, we have developed a comprehensive picture of the titanocene-mediated epoxide ring opening through electron transfer. The investigations were carried out by a combination of synthetic organic, physical organic, and computational techniques, and have resulted in unique insights into the reaction at a molecular level. We have been able to determine that the identity of the most reactive Ti^{III} species is the dimer in its half-open structure and that the selectivity of the ring opening is governed by steric effects. Moreover, in light of these results it becomes possible to develop novel reactions.

Received: November 23, 2005

Keywords: cyclic voltammetry · density functional calculations · homogeneous catalysis · titanium · transition states

[1] T. V. RajanBabu, W. A. Nugent, *J. Am. Chem. Soc.* **1994**, *116*, 986 – 997.

[2] a) A. Gansäuer, H. Bluhm, M. Pierobon, *J. Am. Chem. Soc.* **1998**, *120*, 12849 – 12859; b) A. Gansäuer, T. Lauterbach, S. Narayan, *Angew. Chem.* **2003**, *115*, 5714 – 5731; *Angew. Chem. Int. Ed.* **2003**, *42*, 5556 – 5573.

[3] E. Cesarotti, H. B. Kagan, R. Goddard, C. Krüger, *J. Organomet. Chem.* **1978**, *162*, 297 – 309.

[4] S. U. Pedersen, K. Daasbjerg in *Electron Transfer in Chemistry*, *Vol. 1* (Ed.: V. Balzani), Wiley-VCH, Weinheim, **2001**, pp. 422 – 502.

[5] a) R. J. Enemærke, J. Larsen, T. Skrydstrup, K. Daasbjerg, *J. Am. Chem. Soc.* **2004**, *126*, 7853 – 7864; b) R. J. Enemærke, G. H. Hjøllund, J. Larsen, T. Skrydstrup, K. Daasbjerg, *Organometallics* **2005**, *24*, 1252 – 1262.

[6] E.-i. Negishi, *Chem. Eur. J.* **1999**, *5*, 411 – 420.

[7] Computational details: All DFT calculations were performed with the TURBOMOLE program package.[7a] The geometries and energies were obtained with the BP functional[7b,c] and a polarized valence triple-ξ basis set (TZVP)[7d] using unrestricted wavefunctions. The transition state was obtained using an eigenvector-following algorithm.[7e] Spin densities for the transition state were calculated using the Mulliken population analysis scheme. a) TURBOMOLE 5.6: R. Ahlrichs, M. Bär, H.-P. Baron, R. Bauernschmitt, S. Böcker, M. Ehrig, K. Eichkorn, S. Elliot, F. Furche, F. Haase, M. Häser, H. Horn, C. Huber, U. Huniar, M. Kattanek, C. Kölmel, M. Kollwitz, K. May, C. Ochsenfeld, H. Öhm, A. Schäfer, U. Schneider, O. Treutler, M. von Armin, F. Weigend, P. Weis, H. Weiss, Universität Karlsruhe, **2003**; b) A. D. Becke, *Phys. Rev. B* **1988**, *38*, 3098 – 3100; c) J. P. Perdew, *Phys. Rev. B* **1986**, *33*, 8822 – 8824; d) A. Schäfer, C. Huber, R. Ahlrichs, *J. Chem. Phys.* **1994**, *100*, 5829 – 5835; e) EF routine in MOPAC6: J. Baker, *J. Comput. Chem.* **1986**, *7*, 385 – 395.

[8] a) A. Gansäuer, B. Rinker, M. Pierobon, S. Grimme, M. Gerenkamp, C. Mück-Lichtenfeld, *Angew. Chem.* **2003**, *115*, 3815 – 3818; *Angew. Chem. Int. Ed.* **2003**, *42*, 3687 – 3690; b) A. Gansäuer, B. Rinker, N. Ndene-Schiffer, M. Pierobon, S. Grimme, M. Gerenkamp, C. Mück-Lichtenfeld, *Eur. J. Org. Chem.* **2004**, 2337 – 2351.

 © 2006 Wiley-VCH Verlag GmbH & Co. KGaA, Weinheim

BN Nanotubes

DOI: 10.1002/anie.200504351

Chemical Peeling and Branching of Boron Nitride Nanotubes in Dimethyl Sulfoxide**

Qing Huang, Yoshio Bando, Chunyi Zhi, Dmitri Golberg, Keiji Kurashima, Fangfang Xu, and Lian Gao*

In a similar manner to carbon nanotubes (CNTs), multiwalled boron nitride nanotubes (BNNTs) comprise a series of coaxial cylindrical graphite-like shells in which B and N atoms alternately substitute for C atoms.[1] The excellent mechanical and thermal properties of BNNTs, in particular their high resistance to oxidization, make them an advantageous constituent part of composite materials that can be used at elevated temperatures. The electrical properties of BNNTs are independent of the atomic structure of the tube which is of prime importance for the fabrication of reproducible and reliable micro- and nanodevices.[1a] Recently, theoretical and experimental data revealed that the band gap of BNNTs with different diameters can be effectively tuned by applying a transverse electric field,[2] a result that will undoubtedly broaden their range of applications. Thus, it is indispensable to develop methods to modify the geometry and configuration of BNNTs to promote their integration into various nanodevices. Cumings et al. successfully performed such manipulation with CNTs under a transmission electron microscope and demonstrated ultralow friction between tubular shells,[3] while Collins et al. tuned the conduction of CNTs using a similar method.[4] Sharpened multiwalled CNTs can also be obtained under extreme oxidation conditions.[5] However, the insulating character and high resistance to oxidation of BNNTs preclude the use of these preexisting methods. It is therefore imperative to explore novel suitable approaches for the engineering of BNNTs.

Hexagonal BN is a well-known layer-structured material with delocalized out-of-plane π orbitals and weak van der Waals interactions between layers. The hydrolysis of BN is expected to take place preferably from the rim of BN shells by the addition of hydroxide ions and protons to B and N atoms, respectively. However, BNNTs synthesized by chemical vapor

[*] Dr. Q. Huang, Prof. Dr. Y. Bando, Dr. C. Zhi, Prof. Dr. D. Golberg, K. Kurashima
Advanced Materials Laboratory and Nanomaterials Laboratory
National Institute for Materials Science
Namiki 1-1, Tsukuba, Ibaraki 305-0044 (Japan)
Fax: (+81) 298-51-6280
E-mail: huang.qing@nims.go.jp
Dr. F. Xu, Prof. Dr. L. Gao
Shanghai Institute of Ceramics
Chinese Academy of Sciences
Dingxi Road 1295, Shanghai 200050 (P.R. China)

[**] Q.H. acknowledges Y. Uemura for experimental support.

Supporting information for this article is available on the WWW under http://www.angewandte.org or from the author.

WILEY InterScience DISCOVER SOMETHING GREAT
© 2006 Wiley-VCH Verlag GmbH & Co. KGaA, Weinheim

deposition (CVD) do not react to moisture and are hydrophobic owing to their seamless cylindrical structure, which minimizes the number of dangling B–N bonds, and/or a weak surface electrostatic potential (SEP) on their outer shells.[6]

Herein, we demonstrate that BNNTs can be effectively peeled in solution in the polar solvent dimethyl sulfoxide (DMSO) under solvothermal conditions. The cycloaddition of DMSO to BNNTs is suggested to weaken the B–N covalent bonds and ease the hydrolysis process. Interestingly, peeled shells are found to form Y junctions with trunk tubes, providing the first example that Y-junction BNNTs can be fabricated through a chemical method.

Figure 1a shows a transmission electron microscopy (TEM) image of a thick BNNT whose outer shells have been peeled off. Some traces of the peeled layers can be distinguished on the sidewalls (indicated with an arrow). At least 20% of the BNNTs were peeled as verified by TEM. The sharp variation in contrast between the original and peeled domains of the BNNT implies that the etching rate is so fast that some cavities may form within a trunk BNNT (Figure 1b). This result is in line with previous calculations, which suggested that the interior surface has a highly positive SEP value and is more reactive.[6a] Polygonal caps at the ends of the tube tips (Figure 1c) were most typical in the present tubes. A solvothermal reaction over 24 h resulted in the thinnest protruding BNNT with a wall thickness of 2 nm (Figure 1d).

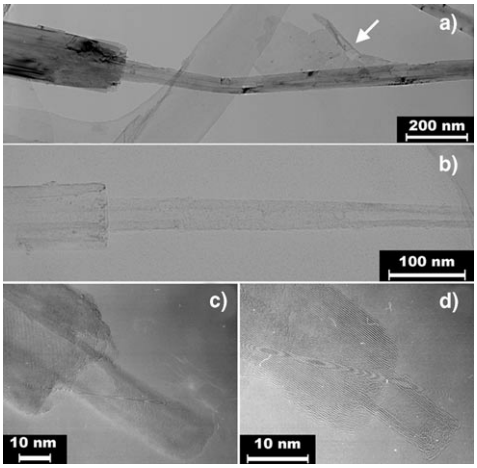

Figure 1. TEM images of peeled BNNTs with different diameters (d) and wall thicknesses (w). a) $d = 56$ nm, $w = 20$ nm; b) $d = 32$ nm, $w = 9$ nm; c) $d = 16.6$ nm, $w = 5$ nm; d) $d = 7.8$ nm, $w = 2$ nm.

BNNTs without protruding segments were etched to a large extent at the ends of their tips (Figure 2a). The explosive tip-end morphology validates the remarkable reactivity of the open ends of BNNTs with highly positive SEP.[6] Importantly, a tiny BNNT indicated by the arrow in Figure 2a was found to stem from the etched BNNT and construct a novel Y-junction tube. It is evident that a part of the new BN walls originate from a trunk BN, whereas some shells within the trunk tube are broken (see Figure 2b and Supporting Information). Such characteristics of a junction preclude the possibility of its formation during CVD. In fact,

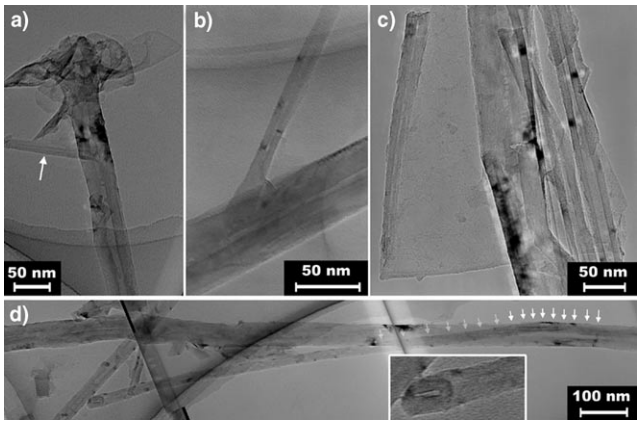

Figure 2. TEM images showing a) etching at the tip ends, b) a typical Y-junction BNNT, c) an intermediate stage in the rolling up process, and d) Y-junction BNNTs with a long branch (inset: enlarged TEM image highlighting the branch cross-section).

no Y junctions were observed in the as-produced BNNTs.[7] Figure 2c displays the mechanism of formation of Y junctions: they are formed through the rolling up of peeled BN shells. From the high-resolution TEM image of a rolled BN shell edge (Figure 3), the inner diameter of a BNNT branch (1.6 to 2.6 nm) is much smaller than that of the trunk (12 nm). The thickness of the newly rolled shells is approximately 3 nm, as shown in the upper left inset. The circular highlighted area reveals that the surface of BN experiences a large extent

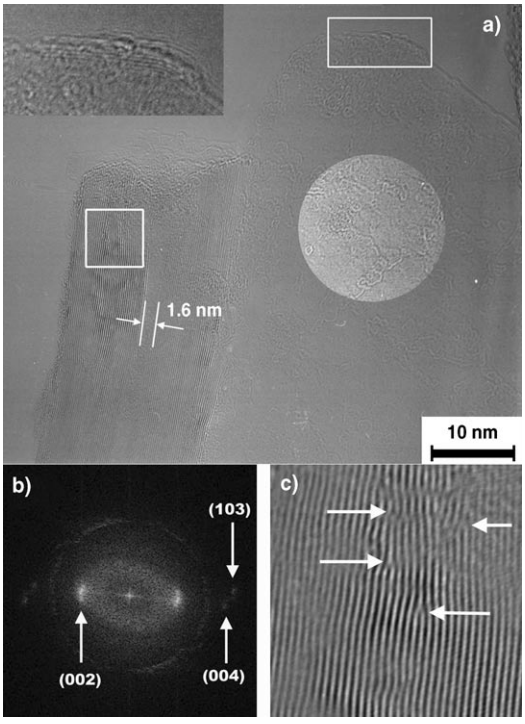

Figure 3. a) High-resolution TEM (HRTEM) image revealing the morphology of a rolled-up BNNT branch (inset: enlarged view of the 3-nm-thick edge area). b) Fourier transform pattern of the newly formed BNNT, suggesting the folding mechanism. c) Enlarged HRTEM image displaying some Frank dislocations in a tube wall.

 © 2006 Wiley-VCH Verlag GmbH & Co. KGaA, Weinheim

of etching. The Fourier transform image of the BNNT branch depicts two additional 2*mm* symmetry breaking (103) diffraction spots. This observation suggests that the nanotubes are formed through folding a faceted BN plane.[8] Some Frank-type dislocations with Burgers vectors of 1/2[0001] are distinct. They may be due to the structural imperfection of the peeled shells. A BNNT branch as long as 1 μm forms within a Y junction (Figure 2d). A rectangle-like cross-section (wall thickness of ca. 7 nm) and a narrow inner tube channel confirm the proposed folding mechanism. The Y junctions in CNTs prepared by template and pyrolysis methods have been studied intensively, and, for example, they revealed excellent rectifying properties.[9] However, such junctions have rarely been observed in BNNTs. Thus, the present BNNT Y junctions may be of interest with respect to their chemical and physical properties.

On the one hand, numerous peeled BN films were observed in the product. On the other hand, no obvious etching was found in the BNNTs that were hydrothermally treated in the absence of DMSO. This control experiment shows that although a hydrolysis reaction is thermodynamically possible it has slow kinetics in BNNTs as a result of strong B–N 2pπ–2pπ bonds that envelope the outer surface. The role of DMSO is thus crucial to weaken B–N covalent bonds and to accelerate the hydrolysis. Su theoretically predicted that the cycloaddition of polar $(CH_3)_2X$ (X = C, Si) molecules to sidewalls of BNNTs may be thermodynamically favorable and could open a B–N bond through nucleophilic attack on X and electrophilic attack on N.[10] DMSO, with a similar molecular structure to $(CH_3)_2X$ (here, X = S=O), contains electrophilic S and O atoms that are more electronegative than the above-mentioned X (C, Si) atoms. In fact, Abell and Kirby found that polar DMSO can destabilize the P–O ester bond of the *p*-nitrophenyl phosphate dianion by nucleophilic attack and accelerate its hydrolysis by a magnitude of 10^6.[11] It is therefore reasonable to assume that DMSO molecules may be added to the sidewalls of BNNTs through nucleophilic attack of O on B and electrophilic attack of S on N, as shown in Scheme 1. The delocalization of electrons for the B–N 2pπ–2pπ overlapping bonds is thus enhanced. In other words, a trigonal-planar sp^2 hybrid orbital will transform into a pyramidal sp^3 hybrid orbital. The larger curvature and numerous defects in the vicinity of a tube cap undoubtedly enhance the electronic localization and increase ionization energies.[6b] The newly formed sp^3 orbitals of B and N atoms allow additional chemical bonding with OH^- and H^+ ions dissociated from H_2O by DMSO. IR analysis shows that the vibration peaks corresponding to S=O (1060 cm^{-1}), S–C (619 cm^{-1}), C–H (3184 cm^{-1}), N–H (3428 cm^{-1}), and B–OH (1132 cm^{-1}) groups remain after solvothermal reaction (Figure 4). This result indicates that DMSO bonds to the walls of BNNTs. Moreover, the E_{1u}(EO) transverse optic mode (798 cm^{-1}) and multiphonon absorption processes (2336, 2361, 2530 cm^{-1}) of the BNNTs are clearly enhanced and is possibly related to the relaxed interactions between BNNT walls and weakened B–N bonds.

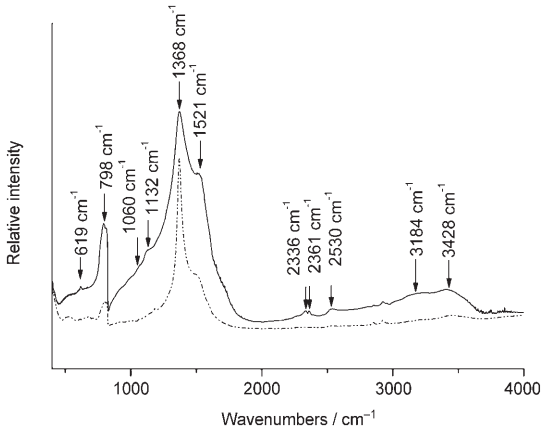

Figure 4. IR spectrum showing the characteristic vibration peaks of N–H, C–H, B–OH, S–C, and S=O groups in the treated BNNTs (——). The IR spectrum of the starting BNNTs (-----) is also provided for reference.

By electron energy loss spectroscopy (EELS) within the core loss regions, the sp^2 or sp^3 hybrid states of a BN material can be qualitatively evaluated through comparing the intensity ratio of π* and σ* peaks. The π* peaks at all sites (trunk, junctions, branches, and peeled sheet) in the treated sample decreased (Figure 5) relative to the EEL spectra of the original BNNTs.[7] This implies an increase in the sp^3 hybrid orbital ratio in accord with our previous assumption. As the 1s-to-π* transition is parallel to the *c* axis,[12] the peeled sheets that lie parallel to the incident beam display more-intense π* peaks. Interestingly, the π* peak becomes stronger for the BNNT branches. This observation may indicate that somehow the branches reassemble to minimize the defective surface

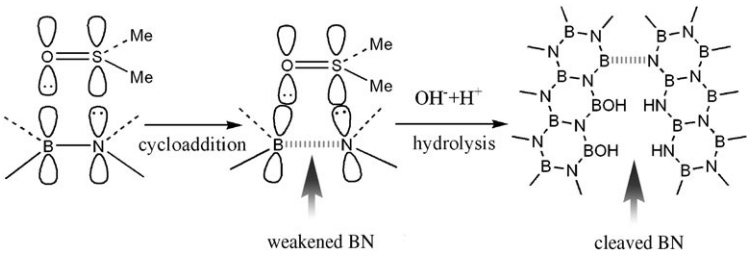

Scheme 1. Molecular orbital representation of the cycloaddition of DMSO on BNNTs followed by hydrolysis.

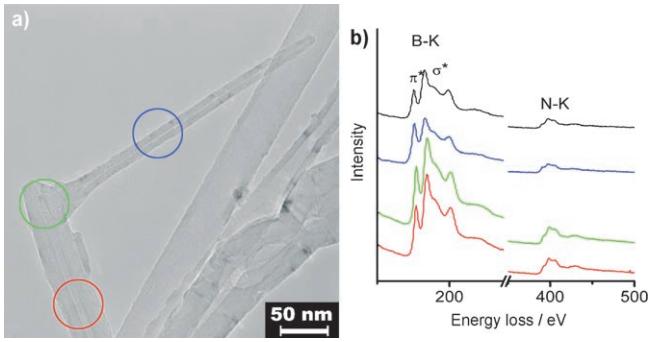

Figure 5. a) TEM image showing a branched BNNT. b) EEL spectra obtained from a BNNT trunk (red), junction (green), branch (blue), and peeled BN sheets (black).

© 2006 Wiley-VCH Verlag GmbH & Co. KGaA, Weinheim

and numerous dangling sp^3 bonds. In other words, an original outside surface inversely becomes an inner surface after the roll up, as depicted in Figure 3.

The reassembly of peeled BN shells into Y-junction nanotubes is of special interest. Note that most H^+ ions dissociated from H_2O are strongly bonded to polar DMSO to form a $[(DMSO)H]^+$ complex.[13] Thus, the driving force behind the rolling up of the tube is, most likely, hydrogen deficiency of the outermost BN shells which induces a high surface tension. This high surface tension could be reduced by shell bending as in the case of the formation of TiO_2 nanotubes.[14] Also note that some BNNTs branches have the ends of their tips capped (see Figure 5a and Supporting Information). Therefore, there should exist some $(BOH)_x(NH)_y$ precursors peeled from BNNTs within the product. These precursors may condense and deposit on the BNNT trunks through lip–lip interactions or π–π stacking.[15] The etched sidewalls of BNNT trunks have a great number of defects, which provide the nucleation sites for the growth of BNNT branches. Recently, this self-catalytic growth mechanism was proposed for carbon nanotubes.[16] Zhu et al. also proposed a similar self-assembly mechanism to account for the formation of tube-in-tube CNT nanostructures.[17] We have also been able to fabricate BNNTs with diameters smaller than 10 nm when a hexagonal BN powder was treated under the same solvothermal conditions.[18]

In summary, peeled BNNTs and Y junctions were obtained through solvothermal reactions in DMSO solution. A cycloaddition reaction between DMSO and the BNNTs is proposed to weaken the B–N bonds and consequently cleave the shells. The mechanism of formation of Y-junction BNNTs is explained in terms of roll-up and self-catalyst processes. These findings broaden the chemistry of BNNTs and should stimulate further studies on the engineering of BNNTs. For instance, BNNTs functionalized with sulfur-containing DMSO molecules may anchor some catalyst metals (Pt, Pd, Ru, Au, Ag, etc.) on the sidewalls, and thus act as a prospective catalyst support. Moreover, as reported previously,[2] Y-junction BNNTs composed of two segments with varying diameters are promising for electromechanical and optoelectronic devices.

Experimental Section

BNNTs were prepared by the CVD method and used without additional purification.[7] The as-synthesized BNNTs were straight with diameters ranging from 20 to 100 nm. BNNTs (10 mg) were added to a mixture of H_2O/DMSO (1 mL/40 mL) and sonicated for 30 min. Then, the mixture was sealed in a 60-mL teflon-lined stainless-steel autoclave and heated at 180 °C for 6 h. The products were rinsed several times with acetone and deionized water before characterization.

TEM and EELS measurements were performed using a field-emission (300 kV) transmission electron microscope (JEOL JEM-3000F). IR transmission measurements were conducted with a Fourier transform infrared spectrometer (JEOL JIR-7000).

Received: December 7, 2005
Published online: February 21, 2006

Keywords: boron · hydrolysis · nanostructures · nanotubes · nitrides

[1] a) A. Rubio, J. L. Corkill, M. L. Cohen, *Phys. Rev. B* **1994**, *49*, 5081; b) N. G. Chopra, R. J. Luyken, K. Cherrey, V. H. Crespi, M. L. Cohen, S. G. Louie, A. Zettl, *Science* **1995**, *269*, 966; c) D. Golberg, Y. Bando, M. Eremets, K. Takemura, K. Kurashima, H. Yusa, *Appl. Phys. Lett.* **1996**, *69*, 2045; d) W. Q. Han, Y. Bando, K. Kurashima, T. Sato, *Appl. Phys. Lett.* **1998**, *73*, 3085; e) X. Blase, A. De Vita, J. C. Charlier, R. Car, *Phys. Rev. Lett.* **1998**, *80*, 1666.
[2] a) K. H. Khoo, M. S. C. Mazzoni, S. G. Louie, *Phys. Rev. B* **2004**, *69*, 201401; b) M. Ishigami, J. D. Sau, S. Aloni, M. L. Cohen, A. Zettl, *Phys. Rev. Lett.* **2005**, *94*, 056804.
[3] a) J. Cumings, P. G. Collins, A. Zettl, *Nature* **2000**, *406*, 586; b) J. Cumings, A. Zettl, *Science* **2000**, *289*, 602.
[4] P. G. Collins, M. S. Arnold, P. Avouris, *Science* **2001**, *292*, 706.
[5] a) J. Y. Chang, A. Ghule, J. J. Chang, S. H. Tzing, Y. C. Ling, *Chem. Phys. Lett.* **2002**, *363*, 583; b) J. Y. Chang, B. Lo, M. L. Jeng, S. H. Tzing, Y. C. Ling, *Appl. Phys. Lett.* **2004**, *85*, 2613.
[6] a) Z. Peralta-Inga, P. Lane, J. S. Murray, S. Boyd, M. E. Grice, C. J. O'Connor, P. Politzer, *Nano Lett.* **2003**, *3*, 21; b) P. Politzer, P. Lane, M. C. Concha, J. S. Murray, *Microelectron. Eng.* **2005**, *81*, 485.
[7] C. Y. Zhi, Y. Bando, C. Tang, D. Golberg, *Solid State Commun.* **2005**, *135*, 67.
[8] A. Celik-Aktas, J. M. Zuo, J. F. Stubbins, C. Tang, Y. Bando, *Acta Crystallogr. Sect. A* **2005**, *61*, 533.
[9] a) J. Li, C. Paradopoulos, J. Xu, *Nature* **1999**, *402*, 254; b) C. Paradopoulos, A. Rakitin, J. Li, A. S. Vedeneev, J. M. Xu, *Phys. Rev. Lett.* **2000**, *85*, 3476; c) B. C. Satishkumar, P. J. Thomas, A. Govindaraj, C. N. R. Rao, *Appl. Phys. Lett.* **2000**, *77*, 2530.
[10] M. D. Su, *J. Phys. Chem. B* **2005**, *109*, 21647.
[11] K. W. Y. Abell, A. J. Kirby, *Tetrahedron Lett.* **1986**, *27*, 1085.
[12] N. D. Browing, J. Yuan, L. M. Brown, *Ultramicroscopy* **1991**, *38*, 291.
[13] M. Calligaris, O. Carugo, *Coord. Chem. Rev.* **1996**, *153*, 83.
[14] S. Zhang, L. M. Peng, Q. Chen, G. H. Du, G. Dawson, W. Z. Zhou, *Phys. Rev. Lett.* **2003**, *91*, 256103.
[15] a) M. B. Nardelli, C. Brabec, A. Maiti, C. Roland, J. Bernholc, *Phys. Rev. Lett.* **1998**, *80*, 313; b) R. Chen, Y. Zhang, D. Wang, H. Dai, *J. Am. Chem. Soc.* **2001**, *123*, 3838.
[16] Z. Zhu, Y. Lu, S. Bai, T. Hu, L. Li, J. Zheng, *J. Am. Chem. Soc.* **2005**, *127*, 15698.
[17] Z. Zhu, D. Su, G. Weinberg, R. Schlogel, *Nano lett.* **2004**, *4*, 2255.
[18] Q. Huang, Y. Bando, C. Zhi, D. Goldberg, K. Kurashima, F. Xu, L. Gao, unpublished results.

 © 2006 Wiley-VCH Verlag GmbH & Co. KGaA, Weinheim

Nanotechnology

DOI: 10.1002/anie.200503016

Controlled Self-Assembly of Nanocrystals into Polycrystalline Fluorescent Dendrites with Energy-Transfer Properties**

*Alyona Sukhanova, Alexander V. Baranov, Tatiana S. Perova, Jacques H. M. Cohen, and Igor Nabiev**

Recent advances in polycrystalline and single-crystal inorganic and organic optoelectronic devices have attracted much attention.[1–3] Among the numerous types of nanometer-scale building blocks, colloidal semiconductor nanocrystals are of special interest because they permit the construction of ordered assemblies for use in optoelectronics, photonics, and biosensing. Self-assembly processes which make it possible to obtain structures with a high level of ordering are of special interest.[4] Thermodynamically driven self-organization processes are especially appealing because their potential for large-scale production requires very little investment in infrastructure. Colloidal self-assembly of nanocrystals allows the formation of patterns ranging from nanowires[5,6] to ordered 2D or 3D superlattices of nanocrystals[7–9] and percolated networks.[10–12] It is important that the properties of the nanocrystals that are essential for the arrangement process, including their size, shape,[13,14] surface protection, stabilization, and charge,[15] can be controlled along with the electronic structure of each nanocrystal. Dendritelike photoluminescent nanostructures are of particular interest as a consequence of their ability to compete with organic dendrimers as color-selectable chromophores in light-emitting and artificial light-harvesting systems.[16–20] The main advantages of nanocrystal-based dendrites over organic ones are their broad absorption bands with much higher extinction coefficients, as well as the possibility of efficient inter-nanocrystal energy transfer in nanocrystal-based solids.[7,21–23]

The results reported here represent the first example of the controlled thermodynamically driven growth of highly photoluminescent polycrystalline dendrites from CdSe/ZnS core/shell nanocrystal quantum dots (QDs) and quantum rods (QRs). Although the dendrites are formed spontaneously during the growth front nucleation, their size and the nanocrystal ordering along the direction of the dendrite branch growth can be controlled. Control of the shape and concentration of the dendritic nanocrystal building blocks and of the water evaporation temperature during dendrite growth allows dendrites of the desired size and crystallinity, as well as optical and energy-transfer properties, to be obtained.

The experiments were carried out in 7 μL droplets of water solutions of water-solubilized CdSe/ZnS core/shell QDs and QRs at concentrations of 0.1–1.0 mg mL^{-1}. QDs with diameters of 4 nm and QRs with diameters of 4 nm and lengths of 25 nm were synthesized, solubilized in water with DL-Cys,[21,24] and applied to microscope slides coated with aminoalkylsilane. Supersaturation was achieved by gradually evaporating water in an ambient atmosphere between 20 and 50 °C. In other cases, the saturated vapor pressure was controlled to change the rate of water evaporation (see Supporting Information for details).

At a relatively low (0.2–0.4 mg mL^{-1}) concentration of the nanocrystals, the QRs (Figure 1a,b) and QDs (Figure 1c,d)

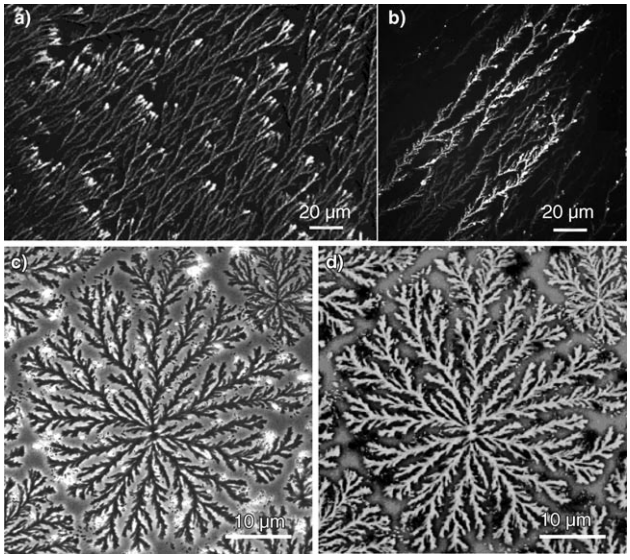

Figure 1. Phase contrast (a,c) and fluorescent (b,d) images of dendrites formed by water-solubilized CdSe/ZnS QRs (a,b) and by QDs (c,d) upon their drying-mediated self-assembly at room temperature at 0.3 mg mL^{-1} concentration.

formed dendrites that were considerably different in terms of both size and structure. In these cases, the QD or QR dendrite expands in the lateral plane to approximately 40 μm and 400 μm, respectively, with thicknesses not exceeding 0.3 μm (Figure 2c). Two types of dendrite structures were identified in different regions of the evaporating droplet. The brightest, most dense, highly organized asymmetric dendrites were

[*] Dr. A. Sukhanova, Prof. J. H. M. Cohen, Prof. I. Nabiev
EA n°3798 Détection et Approches Thérapeutiques Nanotechnologiques dans les Mécanismes Biologiques de Défense
Université de Reims Champagne-Ardenne
51100 Reims (France)
Fax: (+33) 3-2691-8127
E-mail: igor.nabiev@univ-reims.fr
Dr. A. V. Baranov
Vavilov State Optical Institute
199034 St. Petersburg (Russia)
Dr. T. S. Perova
Trinity College
Dublin 2 (Ireland)

[**] I.N. and A.S. thank the Ligue National Contre le Cancer and NATO Collaborative Linkage Grants for financial support. A.S. is grateful to the FEBS for providing a long-term fellowship. A.B. acknowledges partial support from RFBR grants nos. 04-02-16175 and 05-02-16212.

Supporting information for this article is available on the WWW under http://www.angewandte.org or from the author.

WILEY InterScience DISCOVER SOMETHING GREAT
© 2006 Wiley-VCH Verlag GmbH & Co. KGaA, Weinheim

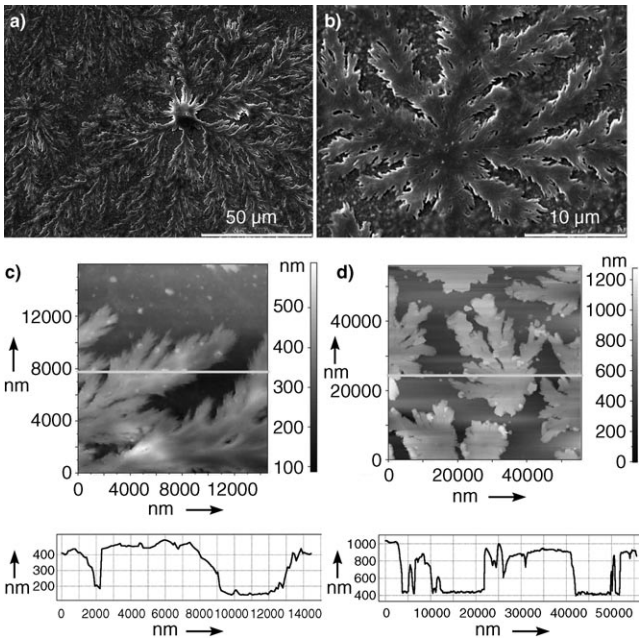

Figure 2. Scanning electron microscopy (a, b) and atomic force microscopy (AFM) (c, d) images of dendrites formed by evaporation of a droplet of water-solubilized CdSe/ZnS QDs at concentrations of 0.1 mg mL^{-1} (a) and 0.6 mg mL^{-1} (b) at room temperature. The panels below (c) and (d) show the typical thicknesses of dendrites formed near the edges of the droplet at lower (c) and higher (d) concentrations of the QD solution in the drying droplet.

observed near the edge of the droplet, and less bright, rougher, and more symmetrical structures with a thickness gradually decreasing from about 0.3 μm to 0.1 μm were formed closer to the center. Typically, QD dendrites had a distinct highly photoluminescent core corresponding to the center of crystallization and six–ten branches growing from the center with up to four–five generations, whereas the self-assembly of QRs under the same conditions yielded completely asymmetric, long, denser dendrites with two–three branches growing from the core towards the droplet center (Figure 1). An increase in the water evaporation temperature from 25 °C to 50 °C or an increase in the concentration of the nanocrystals from 0.1 to 1 mg mL^{-1} caused essentially the same effect: the dendrite lateral sizes gradually decreased and their thickness increased (Figure 2), followed by disordering of dendrite structures, eventually transforming them into isolated islands or disks.

The self-ordering of nanocrystals into dendritelike polycrystalline structures within a droplet of colloidal suspension drying on a polar surface has been intensively studied,[10,25,26] and can be described in terms of strongly non-equilibrium crystal growth. The freezing-in of local orientation fluctuations of the building blocks at the growth-front nucleation takes place and the concentration of free nanocrystals in the suspension decreases as the nanostructures grow.[25] These structures are generated as a result of the interplay between the ordering effect of crystallization, the disordering effect of local orientation fluctuations of the nanocrystals, and the freezing of the domain edges after solvent evaporation.[10,25,26]

The key parameter is the relationship between the mobility of the nanocrystals in solution and the rate of evaporation (v_{ev}). The mobility of the nanocrystals is determined by both the translational (v_t) and the orientational (v_{or}) diffusion rates. The translational diffusion rate, together with the concentration, controls the number of building blocks moving as a result of either capillary[27] or van der Waals forces to the growth front, thereby forming new grains. The orientational diffusion rate controls the block alignment along the crystallographic axes of the grains. The evaporation rate is directly related to the freezing rate because of the very low mobility of the nanocrystals on a dry surface. The v_t/v_{ev} and v_{or}/v_{ev} ratios are very large under near-equilibrium, quasi-steady conditions ($v_{ev} \rightarrow 0$), and result, for example, in the self-organization of spherical CdTe nanocrystals into single-crystal structures, such as nanowires.[5,6] Far from equilibrium, at high evaporation or freezing rates, various structures can be formed, including dendritelike crystalline or polycrystalline structures.[10,25] Moreover, at appropriate concentrations, the larger the v_t/v_{or} ratio, the more prevalent is the polycrystalline growth of the structures.[25]

Importantly, the mobility of the nanocrystals and the evaporation rate can be controlled experimentally by varying the temperature, size of the nanocrystals, and their initial concentration in the droplet. These factors determine the optimal conditions for the growth of the polycrystalline nanocrystal dendrites, as depicted in Equation (1).

$$v_t(v_{or}) \leq v_{ev} \text{ and } v_t > v_{or} \quad (1)$$

The formation of various types of dendrites can be understood from simple considerations based on model calculations.[10,25] When the nanocrystal concentration is sufficient, a thick polycrystalline border consisting of totally disordered nanocrystals is created at the initial stage of the droplet drying. At this moment, numerous building blocks arrive at the crystallization front and individual nanocrystals have no time for alignment relative to each other before the next block arrives. As the border is formed, the nanocrystal concentration decreases as the growth front moves to the center, thus providing time for the nanocrystals to align and for ordered dendrites to form. However, a subsequent decrease in the density of the nanocrystals decreases the rate of their delivery to the dendrite growth front until it becomes comparable with the rate of solvent evaporation. This impedes alignment of individual nanocrystals, which results in dendrites with a disordered alignment of the nanocrystals.

According to the extended microscopic solvability criterion, the dynamically selected morphology is the fastest-growing one.[28] In other words, if more than one dendrite morphology is possible, only the fastest one is nonlinearly stable and, hence, observable. The difference in morphology between QD and QR dendrites probably results from the stronger dipole–dipole interaction between QRs than between QDs, as well as the shape anisotropy of the QRs leading to higher v_t/v_{or} values.

To characterize the crystalline structure and optical properties of the luminescent dendrites formed at low nano-

 © 2006 Wiley-VCH Verlag GmbH & Co. KGaA, Weinheim

crystal concentrations at room temperature we analyzed their birefringence properties and polarization of the photoluminescence (PL). The faceting and birefringence are macroscopic evidence for both the ordering of the nanocrystals into the array and the net alignment of their unique optical axes within a regular pattern. Birefringence images of QD dendrites located close to the edge of the droplet showed a fourfold symmetry of uniaxial hexagonal nanocrystals so oriented that their optical axes were perpendicular to the direction of growth of the dendrite branch (Figure 3a). In regions closer to the center, there were dendrites with a clear twofold symmetry of the birefringence pattern typical for biaxial crystals (Figure 3c,d), whereas the dendrites located in the center of the droplet showed no polarization twisting like the thick layer of totally disordered QDs or QRs on a glass surface. Interestingly, the dendrites with similar thicknesses located near the edge and near the center of the droplet considerably differed in birefringence, which indicates different levels of nanocrystal ordering.

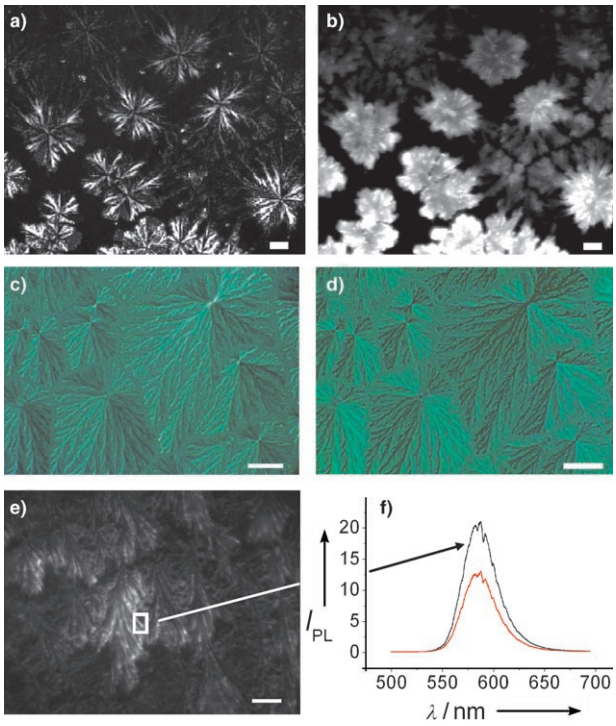

Figure 3. The fourfold symmetry of birefringence (a) and fluorescence (b) images of QD dendrites located near the edge of the droplet and the twofold symmetry of the birefringence pattern of QD dendrites near the center (c, d) recorded under crossed polarizer axes differing by 45° under an optical microscope. Panel (e) shows the difference in the polarized fluorescence images of QR dendrites recorded at the polarizer axes perpendicular and parallel to the axis of polarization of exciting light. Panel (f) shows the fluorescence spectra recorded from the indicated area with the polarizer of the of PL emission parallel (black curve) and perpendicular (red curve) to the axis of the polarization of exciting light. Scale bar: 10 μm.

Both individual QDs and QD solids depolarized band-edge PL excited through high-energy transitions, while the PL from nanocrystals self-assembled into single-crystal structures is expected to be noticeably polarized. Polarized PL is also expected in the cases of strong interaction between the electronic subsystems of assembled nanocrystals. Our polarized PL measurements showed that the band-edge PL from the various types of QD dendrites displaying a birefringence pattern is practically depolarized; therefore, they had a polycrystalline structure formed from weakly, if at all, interacting QDs. Conversely, the fingers of QR dendrites exhibited a pronounced polarization of fluorescence (Figure 3e,f), which indicated that QR axes were preferably orientated along the direction of dendrite growth. We conclude that the ordering of the QR building blocks can be varied by changing the growth conditions (temperature and concentration) in order to create QR dendrites with desired structural and optical properties.

Steady-state and time-resolved PL measurements showed that some dendrite structures have optical properties that suggest energy transfer from the photoexcited periphery to the dendrite core. Typically, the PL spectra of individual dendrites recorded under excitation with a defocused laser beam exhibited a pronounced red shift, asymmetry, and broadening compared with the PL spectra of diluted solutions of nanocrystals, or nanocrystals in water applied from chloroform solution at low coverage density to the slide (Figure 4a,e). These modifications of the inhomogeneously broadened PL band of the nanocrystal within the dendrites and its temporal behavior may indicate energy transfer in densely packed solids as a result of the inter-nanocrystal coupling.[7,22,23,29]

Strong PL signals from the dendrites allowed us to reconstruct their 3D luminescent images by using confocal microscopy. As an example, Figure 4b shows a typical 3D image of a QR dendrite with a z-thickness of about 0.3 μm as well as a distinct shift in the PL emission wavelength from the fingers to the core (presented in different colors). The PL image of one of the studied dendrites built from the QDs is shown in Figure 4c. To obtain information about the distribution of the nanocrystal bandgap energies along the dendrite we performed the measurements of the PL spectra from different local parts of the dendrite. The small circles of different colors in Figure 4c indicate local regions within the QD dendrite where micro-PL spectra were measured with a lateral resolution of about 1 μm. Here, concentric circles roughly mark successive "generations" of the dendrite, and normalized PL bands averaged over the spectra from all spots of the same dendrite generation are shown in Figure 4e using the same color for each generation as in Figure 4c. These spectra exhibit a red-shift of about 12 nm, thus indicating a reduction in the bandgap energy as the areas probed by the beam are moved from the periphery to the center of the dendrite (Figure 4e). Quantitative comparison of the intensities of PL bands with different peak energies is difficult, since the excited volumes within the QD dendrite are unknown. Nevertheless, the integrated intensities of the PL from the cores of the dendrites were at least four times higher than those of their peripheral parts. Evidently the PL bands thus obtained correspond to spectral components of inhomogeneously broadened PL spectrum of this individual dendrite.

 © 2006 Wiley-VCH Verlag GmbH & Co. KGaA, Weinheim

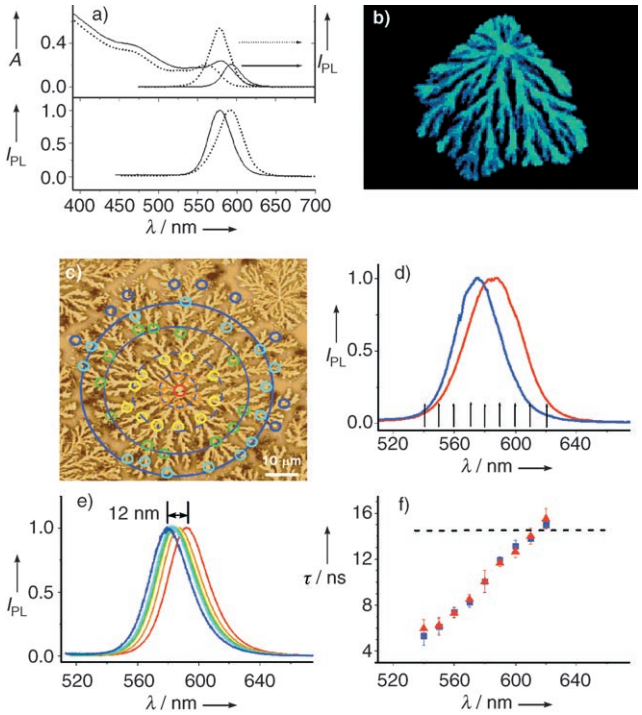

Figure 4. Optical properties of water-solubilized CdSe/ZnS QDs, QRs, and nanocrystal-based dendrites. a) Top: the absorption and PL spectra of QDs (dotted lines) and QRs (solid lines) in diluted aqueous solutions; bottom: the PL spectrum of QDs applied to the slide at low surface density from a chloroform solution (solid line) and the PL spectrum of the QD dendrites (dotted line). b) The confocal PL microscopy image of a dendrite constructed from QRs. The different colors show the energy transfer from the dendrite fingers to the core region. c) The PL image of the dendrite built from the QDs. Small circles of different colors indicate local regions of the dendrite from which micro-PL spectra were recorded. Concentric circles indicate approximately successive "generations" of the dendrite. d) The averaged PL spectrum from the whole dendrite (red line) showing the red shift and asymmetrical broadening when compared with a diluted aqueous solution of QDs (blue line). e) Normalized PL bands; each is averaged over the spectra from all the spots marked with the same color in (c) for a particular generation. f) The mean decay time of the PL of the dendrite as a function of the detection wavelength indicated in (d) by the arrows. The dotted line shows the mean decay time of non-interacting QDs in diluted aqueous solution, where aggregation is negligible.

The intensities of the PL signals recorded from different local dendrite spots were insufficient for time-resolved PL measurements. To perform these measurements, the diode laser beam was focused to a spot 30–50 μm in diameter, which was comparable in size with the dendrites, and yielded a PL spectrum which was a superposition of the spectra of different local elements of the dendrite (Figure 4d). The PL decays were then measured with a spectral width of the detected PL of about 4 nm at different wavelengths (indicated with arrows in Figure 4d) and analyzed to estimate the PL decay time of the nanocrystals at various fundamental transition energies. For noninteracting QDs in dilute solutions, where nanocrystal aggregation is negligible, a biexponential PL decay was observed with a mean decay time of about 15 ns and almost independent of the wavelength of detection (Figure 4f). Indeed, wavelength-independent PL decay was also found for nanocrystals applied at a low surface density from a chloroform solution to the slide. Although the PL of the dendrites also exhibit biexponential PL decay times, which agrees with the data on the PL decay in QD solids,[22] the PL transition energies of QDs within QD dendrites and the PL decay times are anticorrelated (Figure 4f). This observation, together with the red-shift of the dendrite PL band, compared with that of the system of isolated QDs, indicates an inhomogeneously broadened nanosystem with energy transfer between elements that have higher and lower energy transitions.[22] Evidently, the polycrystalline QD dendrites are a special case of QD solids with energy transfer between the QD building blocks.

The simple size-selective precipitation of nanocrystals[30,31] upon the slow evaporation of the water may first lead to crystallization of the bigger nanocrystals, followed by a gradual decrease in the size of the nanocrystals in the dendritic arms consecutive to the evolution of the crystallization process. The variation in the size of the nanocrystals may produce the observed batochromic shift in the PL from the periphery to the center of the dendrites if the size-selective precipitation takes place in our conditions.[22,32] Otherwise, the simple size-selective precipitation should be certainly affected by the growth-front nucleation formed during the solvent evaporation. Moreover, the above described inhomogeneous broadening of the dendrite optical spectra may certainly be caused not only by the initial size distribution of the nanocrystals followed by the size-dependent crystallization but also by the interaction of close-packed nanocrystals within the dendrite and by the changes of the dynamics of the electronic excitations of the nanocrystals as a result of energy transfer.

A detailed physical explanation of the described optical effects is not possible without analysis of a large variety of parameters contributing to the dendrite growth and remains to be defined. However, the presented data show that some of the described nanocrystal-based dendrites demonstrate a decrease in the bandgap energies from the periphery to the core which is energetically favorable for the transport of photoexcitation energy. This phenomenon resembles the so-called energy funnel widely discussed in the optics of molecular dendrimers[18–20] and of the multiple layers of CdTe nanocrystals with an energy-gap gradient.[23] The high efficiency of the FRET between close-packed nanocrystals with slightly different fundamental optical transition energies is also favorable for effective energy transport from the strongly light-absorbing periphery to the core of the dendrites. Hence, the nanocrystal dendrites certainly deserve further investigation as promising nanostructures for use in artificial light-harvesting and light-emitting systems. It should also be noted that nucleation-controlled aggregation with strong crystallographic anisotropy forming dendrites is not a rare phenomenon. Similar dendrite structures were recently observed by us upon drying aqueous suspensions of CdTe nanocrystals (see the Supporting Information) and during crystallization of $FeSO_4$ in an aqueous solution film. In addition, the optical activity of semiconductor fluorescent

 © 2006 Wiley-VCH Verlag GmbH & Co. KGaA, Weinheim

nanocrystals makes them promising tools for monitoring the self-assembly processes in nature and technology.

Received: August 24, 2005
Revised: December 12, 2005
Published online: February 27, 2006

Keywords: dendrites · nanostructures · nanotechnology · quantum dots · self-assembly

[1] T. H. Lee, R. M. Dickson, *Proc. Natl. Acad. Sci. USA* **2003**, *100*, 3043 – 3046.
[2] A. H. Mueller, M. A. Petruska, M. Achermann, D. J. Werder, E. A. Akhadov, D. D. Koleske, M. A. Hoffbauer, V. I. Klimov, *Nano Lett.* **2005**, *5*, 1039 – 1044.
[3] A. Hepp, H. Heil, W. Weise, M. Ahles, R. Schmechel, H. von Seggern, *Phys. Rev Lett.* **2003**, *91*, 157406.
[4] G. M. Whitesides, B. Grzybowski, *Science* **2002**, *295*, 2418 – 2421.
[5] Z. Tang, N. A. Kotov, M. Giersig, *Science* **2002**, *297*, 237 – 240.
[6] Y. Volkov, S. Mitchell, N. Gaponik, Y. P. Rakovich, J. F. Donegan, D. Kelleher, A. L. Rogach, *ChemPhysChem* **2004**, *5*, 1600 – 1602.
[7] C. B. Murray, C. R. Kagan, M. G. Bawendi, *Science* **1995**, *270*, 1335 – 1338.
[8] C. B. Murray, C. R. Kagan, M. G. Bawendi, *Annu. Rev. Mater. Sci.* **2000**, *30*, 545 – 610.
[9] D. V. Talapin, E. V. Shevchenko, A. Kornowski, N. Gaponik, M. Haase, A. L. Rogach, H. Weller, *Adv. Mater.* **2001**, *13*, 1868 – 1871.
[10] E. Rabani, D. R. Reichman, P. L. Geissler, L. E. Brus, *Nature* **2003**, *426*, 271 – 274.
[11] C. Stowell, B. A. Korgel, *Nano Lett.* **2001**, *1*, 595 – 600.
[12] P. Moriarty, M. D. Taylor, M. Brust, *Phys. Rev. Lett.* **2002**, *89*, 248303.
[13] X. Peng, L. Manna, W. Yang, J. Wickham, E. Scher, A. Kadavanich, A. P. Alivisatos, *Nature* **2000**, *404*, 59 – 61.
[14] F. Kim, J. H. Song, P. Yang, *J. Am. Chem. Soc.* **2002**, *124*, 14316 – 14317.
[15] T. K. Sau, C. J. Murphy, *Langmuir* **2005**, *21*, 2923 – 2929.
[16] J. M. J. Frechet, *Science* **1994**, *263*, 1710 – 1715.
[17] D. L. Jiang, T. Aida, *Nature* **1997**, *388*, 454 – 456.
[18] V. Balzani, P. Ceroni, M. Maestri, C. Saudan, V. Vicinelli, *Top. Curr. Chem.* **2003**, *228*, 159 – 191.
[19] M. I. Ranasinghe, Y. Wang, T. Goodson, *J. Am. Chem. Soc.* **2003**, *125*, 5258 – 5259.
[20] D.-J. Heijs, V. A. Malyshev, J. Knoester, *J. Chem. Phys.* **2004**, *121*, 4884 – 4892.
[21] R. Wargnier, A. V. Baranov, V. G. Maslov, V. Stsiapura, M. Artemyev, M. Pluot, A. Sukhanova, I. Nabiev, *Nano Lett.* **2004**, *4*, 451 – 457.
[22] C. B. Murray, C. R. Kagan, M. G. Bawendi, *Phys. Rev. B* **1996**, *54*, 8633 – 8643.
[23] T. A. Klar, T. Franzl, A. L. Rogach, J. Feldmann, *Adv. Mater.* **2005**, *17*, 769 – 773.
[24] A. Sukhanova, J. Devy, L. Venteo, H. Kaplan, M. Artemyev, V. Oleinikov, D. Klinov, M. Pluot, J. H. M. Cohen, I. Nabiev, *Anal. Biochem.* **2004**, *324*, 60 – 67.
[25] L. Granasy, T. Pusztai, T. Borzsonyi, J. A. Warren, J. F. Douglas, *Nat. Mater.* **2004**, *3*, 645 – 650.
[26] S. Narayanan, J. Wang, X. M. Lin, *Phys. Rev Lett.* **2004**, *93*, 135503.
[27] P. A. Kralchevsky, N. D. Denkov, *Curr. Opin. Colloid Interface Sci.* **2001**, *6*, 383 – 401.
[28] E. Ben-Jacob, P. Garik, *Nature* **1990**, *343*, 523 – 530.
[29] L.-S. Li, J. Hu, W. Yang, A. P. Alivisatos, *Nano Lett.* **2001**, *1*, 349 – 351.
[30] N. Gaponik, D. V. Talapin, A. L. Rogach, K. Hoppe, E. V. Shevchenko, A. Kornowski, A. Eychmuller, H. Weller, *J. Phys. Chem. B* **2002**, *106*, 7177 – 7185.
[31] C. B. Murray, D. J. Norris, M. G. Bawendi *J. Am. Chem. Soc.* **1993**, *115*, 8706 – 8715.
[32] D. V. Talapin, A. L. Rogach, A. Kornowski, M. Haase, H. Weller, *Nano Lett.* **2001**, *1*, 207 – 211.

 © 2006 Wiley-VCH Verlag GmbH & Co. KGaA, Weinheim

Polymer Membranes

DOI: 10.1002/anie.200503334

Neuron-Like Tubular Membranes Made of Diblock Copolymer Amphiphiles**

Giuseppe Battaglia and Anthony J. Ryan**

The complexity and the functionalities of biological membranes have been recently mimicked[1–5] by synthetic block copolymer amphiphiles. The entirely artificial nature of these polymeric membranes allows an extensive variety of chemistry to be applied to the design of mechanically and chemically enhanced[2] micro- and nanostructures with a tunable range of dimensions and membrane thicknesses.[6] In analogy with biological membranes, polymer membranes have also been found to generate more complex architectures.[7] Myelins are very long (up to a few meters) multilamellar tubules that connect the neuronal cells and together with them make up the intricate network essential for the function of the nervous system and brain.

Studies of the water–solid amphiphile interface have revealed that myelins form upon dissolution of membrane-forming synthetic amphiphiles.[8–12] Indeed, whilst the morphology of water–amphiphile mixtures is strongly dependent on the concentration, several studies have reported how membrane-forming amphiphiles assemble into different morphologies as a function of the water/amphiphile ratio.[13–16]

[*] Dr. G. Battaglia
Department of Engineering Materials
The Kroto Research Institute North Campus
University of Sheffield
Broad Lane, Sheffield, S3 7HQ (UK)
Fax: (+44) 114-222-5945
E-mail: g.battaglia@sheffield.ac.uk
Prof. A. J. Ryan
Department of Chemistry
University of Sheffield
Dainton Building, Brook Hill Sheffield, S3 7HF (UK)
Fax: (+44) 114-222-9389
E-mail: tony.ryan@sheffield.ac.uk

[**] The authors thank Dr. Shao-min Mai for the synthesis of the copolymer and the ICI Strategic Technology Group for financial support.

WILEY InterScience DISCOVER SOMETHING GREAT
© 2006 Wiley-VCH Verlag GmbH & Co. KGaA, Weinheim

The common factor in all these studies, however, is the membrane structure, which arises from the balance between hydrophilic and hydrophobic interactions.[17,18] The formation of surfactant-driven tubules is also responsible for the explosive nature of mixing[19] in fast polymerizations; the myelins that form are responsible for mass transport on timescales shorter than that of the normal diffusion mechanisms.

In the present contribution, the poly(ethylene oxide)–copoly(butylene oxide) copolymer $E_{16}B_{22}$ was selected to study the formation of myelins and their stabilization. Macroscopically, $E_{16}B_{22}$ copolymer films are observed to swell very quickly when placed in contact with water. At the interface with water, the mutual diffusion of copolymer toward water and water toward the bulk copolymer generates a concentration gradient. We studied the swelling of $E_{16}B_{22}$ by confocal laser scanning microscopy (CLSM; Figure 1). The copolymer was mixed with a small amount (0.1–0.2 % w/w) of the amphiphilic fluorescent dye rhodamine B octadecyl ester perchlorate. The images were recorded using three different channels on the microscope system: two set for rhodamine emission ($\lambda_{em} \geq 560$ nm) at two different sensitivities and one for differential interference contrast (DIC). The bulk copolymer swells and generates a range of different structures on going from high concentrations (lamellae) to low concentrations (vesicles). The transition from swollen lamellar stacks to vesicles occurs via a sequence of swollen multilamellar tubules, myelins. Such structures can grow very long and have different morphologies, and some of them can grow helically, as shown in Figure 1 c–e. In Figure 1 b both the thickness of the swollen film, L (the distance from the swollen lamellae to the last vesicle formed at the water front, Figure 1 a) and a typical contour length for the myelin growth, MG (Figure 1 d), are plotted against time.

The swelling was found to be proportional to the square root of time; the experimental data were fitted by Equation (1), where t_0 is the time at which the swelling starts, L_0 is

$$L(t) = k_m\sqrt{(t-t_0)} + L_0 \quad (1)$$

the initial length of the film (in the specific experiment found to be 71.5 μm (dry copolymer)), and k_m is a proportionality constant related to the diffusion velocity (here found to be 27.21 μm min$^{-1/2}$ (0.45 μm s$^{-1/2}$)).

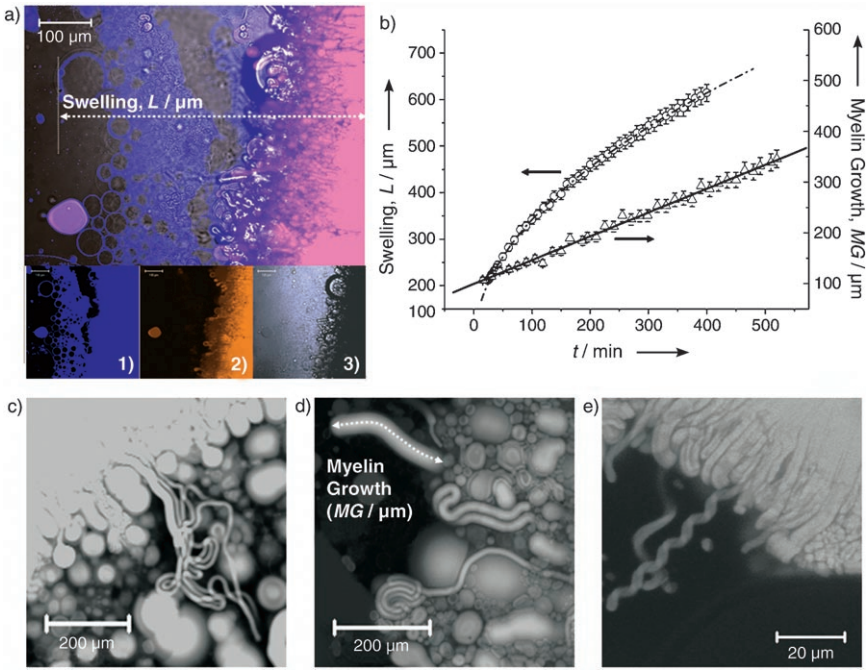

Figure 1. a) Images recorded by composite confocal laser scanning microscopy at the interface of water and a film of $E_{16}B_{22}$ (prestained with rhodamine B octadecyl ester perchlorate) showing the evolution from swollen lamellar structure to vesicles. The micrographs have been taken using three different channels: 1) high sensitivity and 2) low sensitivity set on rhodamine emission, 3) DIC transmission mode and combined to give the master. b) The graph shows the swelling length, L, from (a) and the myelin growth, MG, from (d) over time; ○: swelling length L, (–•–•–): $L(t) = 27.21\,t^{1/2} + 71.5$, △: myelin growth MG, (——): $MG(t) = 0.47\,t$. c)–e) Confocal micrographs showing different myelin morphologies.

Equation (1) is the result of the application of the random-walk model in describing diffusional processes. Einstein in his work[20] on Brownian motion derived the diffusion equation using the random-walk model, in other words, by assuming that the direction of motion of a particle is "forgotten" after a certain time and that the mean-square displacement during this time is finite. The overall swelling of the present copolymer follows the same principle, and the fact that the actual myelin growth is linearly proportional to time (gradient of 0.47 mm μin^{-1} indicating a typical random-walk growth) supports the argument of diffusional growth. Using the same method as in reference [7], and assuming a myelin fraction of the cross-sectional area as close-packed tubes of $\gamma = 0.907$, we calculate the collective diffusive coefficient to be $D_{col} = 0.5\,\gamma k_m^2 = 9.33 \times 10^{-14}$ m^2 s^{-1}. The value calculated here is three orders of magnitude smaller than the value reported for the nonionic surfactant triethylene glycol monotridecyl ether ($C_{12}E_3$) in water ($D = 8.5 \times 10^{-11}$ m^2 s^{-1}). The difference obviously arises because $E_{16}B_{22}$ has a higher molecular weight (2300 g mol^{-1}), and hence lower mobility, than the nonionic surfactant (318 g mol^{-1}).

Myelins have always been considered as "kinetic instabilities", in other words, as an expression of the dynamic interface instability resulting from the reorganization of the amphiphilic membranes in an excess of solvent. Buchanan et al.[9] proposed that the nearly immiscible, fully swollen, lamellar phase of a surfactant takes the form of myelins because of the aggregative diffusion of the surfactant towards the solvent to establish equilibrium with the inward diffusion

 © 2006 Wiley-VCH Verlag GmbH & Co. KGaA, Weinheim

of the solvent. At the very beginning, when the bulk lamellar film is placed in contact with water, its surface starts to wrinkle. This can be a result of a mutual increase of the equilibrium area per polar head-group when the film is in pure water and the fluctuations caused by unbinding[21,22] of the membranes when the film is in excess water. Similar[23] surface-roughening behavior has been observed when a surface-active molecule is formed by reaction at the smooth interface between two incompatible polymers. In Figure 2a

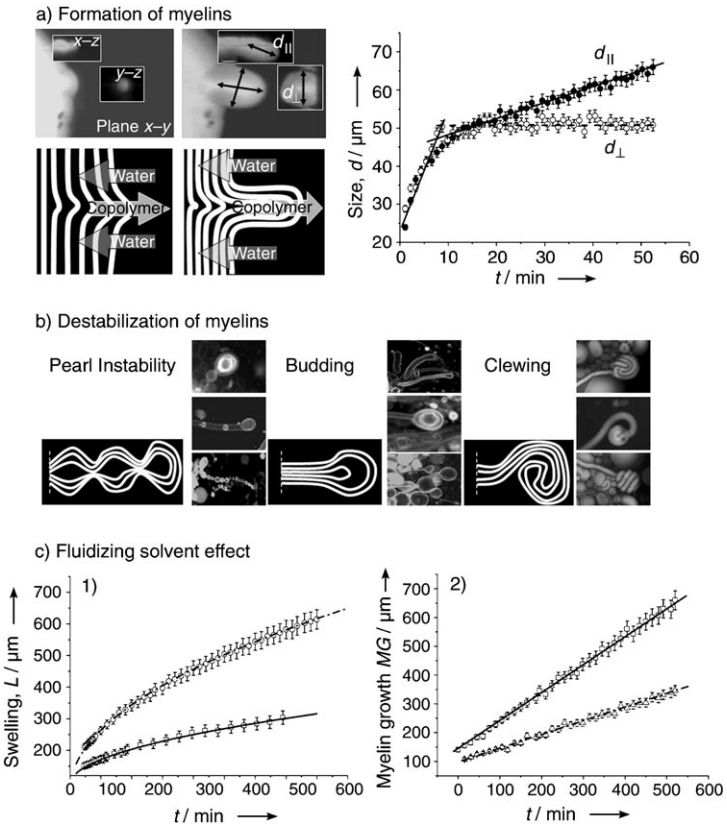

Figure 2. a) Early stage of myelin formation; the plot shows the evolution of dimensions parallel (●) and perpendicular (○) to the myelin growth over time. b) Mechanisms for the destabilization of myelins by conversion into unilamellar and multilamellar vesicles. c) Swelling and myelin growth with and without chloroform. The fits show respectively a decrease in the collective diffusion in the presence of chloroform and an increase in the myelin growth rate: 1) ○: $E_{16}B_{22}$ swelling, (–•–•): $L(t) = 27.21\,t^{1/2} + 71.5$, □: $E_{16}B_{22}$/$CHCl_3$ swelling, (——): $L(t) = 11.21\,t^{1/2} + 91.5$; 2) △: $E_{16}B_{22}$ myelin growth, (–•–•): $MG(t) = 0.47\,t$, □: $E_{16}B_{22}$/$CHCl_3$ myelin growth, (——): $MG(t) = 0.98\,t$.

the initial evolution with time of such wrinkles was measured. The dimensions parallel $d_\parallel$ and perpendicular $d_\perp$ to the growth were plotted versus time. It is evident that at a very early stage the growth rates are almost equal for both dimensions, leading to an almost hemispherical structure. However, in less than 10 min, the growth stops in the perpendicular direction, whereas the parallel direction continues its linear growth, and as a consequence myelin formation is observed. According to Buchanan et al.,[9] myelins are made of a lamellar phase that is already fully swollen and thus in local equilibrium with the surrounding solvent. Water, entering the lamellar phase at the roots, feeds the myelins, which grow backward into the surrounding water phase.

As observed in Figure 1, $E_{16}B_{22}$ swelling and assembly depends strongly on the concentration profile and therefore on the topology of the swollen copolymer. Depending on the position in the film, the swollen copolymers assemble into different structures that are stable at that concentration. Therefore, most of the myelins grow up to a point where they destabilize, generating spherical aggregates, most of which are unilamellar or multilamellar vesicles. In Figure 2b, three different destabilization mechanisms are shown: pearl instability, budding, and clewing. The first two occur when the myelins are in an excess of water, and they generally lead to the formation of unilamellar vesicles or concentric multilamellar vesicles (onions). Clewing, however, occurs at interface between swollen lamellae and the vesicle-formation zone. In most of the cases, the myelins grow from high to low concentrations. Moreover the growth seems to follow a pseudo-random walk with an occasional path-reversal back into the high concentration zone. As a consequence, the myelins start clewing and generate lumps of multilamellar aggregates.

Myelin formation can be been enhanced by adding chloroform, a fluidizing solvent, to the starting amphiphilic film (1:1 w/w), and this causes a quantitative change in the swelling mechanism. As showed in Figure 2c, the swelling of copolymer/chloroform still follows a typical diffusion growth; however, the presence of chloroform slows the copolymer swelling. The collective diffusion coefficient in the presence of chloroform was found to be $D_{col} = 1.74 \times 10^{-14}\ m^2 s^{-1}$. This difference results from the hydrophobic membrane becoming more hydrophobic in the presence of chloroform and therefore less water-permeable. Moreover, the myelin formation is observed very promptly and with much higher number density. The myelins are longer and much smaller in diameter than those under chloroform-free conditions. In the absence of water, chloroform is a good solvent for both of the blocks, but the presence of water, which is a preferential solvent for poly(ethylene oxide), drives the partition of chloroform from poly(ethylene oxide) to poly(butylene oxide). The initial effect of the solvent, though, is to increase the mobility of the polymer; this is seen as a reduction viscosity that is directly proportional to the of the polymer volume fraction. Once myelin formation occurs, the hydrophobic domain will become further enriched in solvent and increasingly mobile, thereby accounting for the narrower diameter and faster growth (Figure 2c). Furthermore, the myelins, once they reach the low concentration zone, destabilize to form vesicles as was observed in chloroform-free conditions, and the destabilization, in this case, seems to occur exclusively through pearl instability and budding. No clewing phenomena are observed.

Myelins have thus far been observed only at the interface between solid amphiphiles and water. Myelins can take up few hours to form and any change in the interface that stabilizes the concentration gradient will result in a destabilization of the myelins in favor of more stable structures such as unilamellar and multilamellar vesicles. This leads to the conclusion that myelins are kinetic instabilities that occur

 © 2006 Wiley-VCH Verlag GmbH & Co. KGaA, Weinheim

only when an amphiphile is dissolved in water in the absence of any extra energy input such as mechanical forces (stirring, sonication, extrusion) or electrical fields. Nevertheless, myelins and their formation are essential for the existence and functioning of the nerve cells and therefore of our brain.

Because copolymer myelination is enhanced by addition of solvent, we dissolved two different mixtures of copolymer and chloroform (1:1 and 3:2 w/w) up to a copolymer concentration in water of 1% w/w. The result is the formation of a multiphase system composed of an oil-in-water emulsion (bottom) and a copolymer vesicle dispersion (top). Microscopic examination of the emulsion revealed very surprising results: The emulsion is made of sun-like aggregates (Figure 3) that we have named *myelinsomes* (from the Greek *soma*: body). At a chloroform content of 50% w/w, (Figure 1a–c) the myelins that make the corona are short and fatter than those at a chloroform content of 40% w/w (Figure 1d,e). The core in both cases (Figure 1c,d) is a very complex cellular structure made of interconnected amphiphilic membranes. If

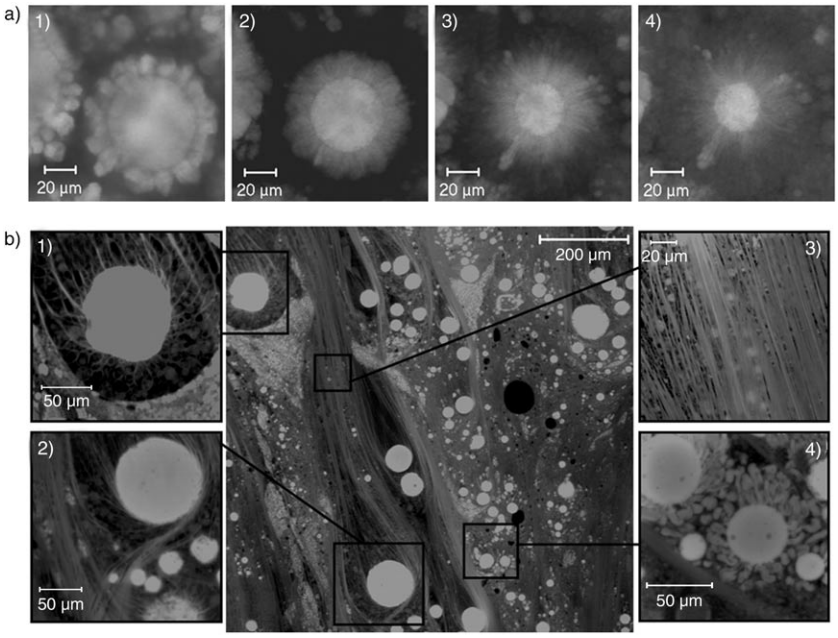

Figure 4. a) Myelinsomes swelling upon dilution in water. b) Formation of a neuron-like network after dilution with water in ratio 1:1.

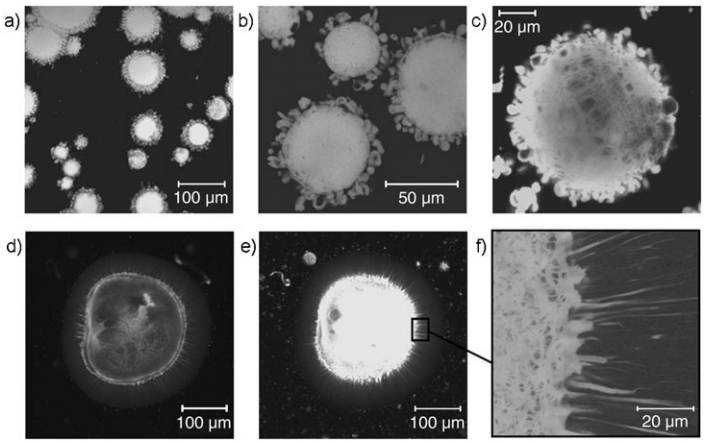

Figure 3. a–c) Myelinsomes formed by $E_{16}B_{22}$/chloroform in water with composition 1:1 w/w consisting of a core made of an amphiphilic membrane network and a corona made of myelins; d,e) Myelinsomes at compositions of 3:2 w/w; f) magnification of the myelin corona.

the composition of the mixture remains unchanged, these myelinsomes are very stable, and even after several days no morphological changes were observed. This is understandable in the context of block copolymer amphiphiles forming non-ergodic structures[7,24] in water because the amphiphile cannot be exchanged between discrete objects as a consequence of their inherently low solubility as single molecules.

Upon dilution with water, however, the myelins of these sun-like aggregates started to grow (Figure 4a). At fourfold dilution, the myelins grew very quickly and after 10 min they started to destabilize and form vesicles. When the dilution ratio was lower, typically twofold, the myelins grew indefinitely. As soon as the water/amphiphile ratio was changed (by dilution), rapid myelin growth (with its concomitant vesicle-forming mechanisms) was observed to occur again.

Obviously, this "zoo" of morphologies cannot be at equilibrium, and the non-ergodic structures are trapped metastable states. As soon as the thermodynamic conditions change, the system readjusts by growing myelins and budding off vesicles. Crucially, however, as soon as vesicular or myelin structures become isolated, they are essentially fixed in their amphiphile population.

Figure 4b shows the eventual result of such growth. The myelins reached lengths of over a millimeter yet remained attached to the multilamellar core. The growth can even be directionally controlled by applying a concentration gradient obtained by placing the diluting water beside the slurry. The different sections of Figure 4b show representative structures at different magnifications. In pictures 1 and 2 of Figure 4b the cores and starting point of the myelins are shown. Some of them display pearl instabilities at the myelin root, while others seem to grow very smoothly from the root on. In picture 3 a bunch of myelins is shown, and some vesicles seem to have been trapped by the growing myelins. In picture 4 some myelinsomes that are not completely swollen are also found trapped in the myelin network.

These results demonstrate controlled myelination and the formation of myelin structures with directionality, specifically, the growth of a myelin along a concentration gradient. The micrograph in Figure 4b shows striking similarity to nerves cells, whereas other structures, for example in Figure 2, show some of the budding and fission features of the crenullated membranes of the Golgi apparatus and the endoplasmic reticulum.[25]

 © 2006 Wiley-VCH Verlag GmbH & Co. KGaA, Weinheim

One of the advantages of studying higher molecular weight amphiphiles is that their dynamics are much slower than those of naturally occurring lipids or nonionic surfactants. Furthermore, the intrinsically low solubility of the single molecules and the formation of more entangled and potentially thicker membranes leads to the formation of long-lived metastable structures. The slower growth kinetics observed herein can be of benefit for the understanding the fundamental processes of myelin growth. The swollen amphiphile layer grows with thickness that depends on $t^{1/2}$, that is, classical Fickian diffusion, whereas individual myelins have a linear growth rate, indicating a random walk. In analogy to naturally occurring membranes containing cholesterol,[26,27] the benefit that chloroform has on the efficacy of myelination can be interpreted as a fluidification of the hydrophobic membrane. In particular, cholesterol is found in much greater proportions[25] in nerve-cell membranes than in other biological membranes, and it has been found to have a crucial role in myelination.[28]

These fundamental studies of the kinetics and mechanism of myelin formation demonstrate clearly the large effect on the structures resulting from a small change in the hydrophobe dynamics, shedding light on the membrane composition in the nervous system. Furthermore, the demonstration of the oriented growth of myelins in a concentration gradient has great potential application in the design and engineering of controlled tubular structures for scaffolds in tissue engineering. Finally, we have presented a method for growing oriented insulating tubes and foresee using such morphologies in molecular electronics application.

Received: September 20, 2005
Published online: February 22, 2006

Keywords: amphiphiles · block copolymers · myelins · self-assembly · vesicles

[1] A. V. Kabanov, T. K. Bronich, V. A. Kabanov, K. Yu, A. Eisenberg, *J. Am. Chem. Soc.* **1998**, *120*, 9941.
[2] B. M. Discher, Y.-Y. Won, D. S. Ege, J. C.-M. Lee, F. S. Bates, D. E. Discher, D. A. Hammer, *Science* **1999**, *284*, 1143.
[3] D. E. Discher, A. Eisenberg, *Science* **2002**, *297*, 967.
[4] Y. Zhou, D. Yan, *Angew. Chem.* **2005**, *117*, 3287; *Angew. Chem. Int. Ed.* **2005**, *44*, 3223.
[5] Y. Zhou, D. Yan, *Angew. Chem.* **2004**, *116*, 4896; *Angew. Chem. Int. Ed.* **2004**, *43*, 5004.
[6] G. Battaglia, A. J. Ryan, *J. Am. Chem. Soc.* **2005**, *127*, 8757.
[7] S. Jain, F. S. Bates, *Science* **2003**, *300*, 460.
[8] M. Buchanan, J. Arrault, M. E. Cates, *Langmuir* **1998**, *14*, 7371.
[9] M. Buchanan, S. U. Egelhaaf, M. E. Cates, *Langmuir* **2000**, *16*, 3718.
[10] M. Buchanan, L. Starrs, S. U. Egelhaaf, M. E. Cates, *Phys. Rev. E* **2000**, *62*, 6895.
[11] M. Haran, A. Chowdhury, C. Manohar, J. Bellare, *Colloids Surf. A* **2002**, *205*, 21.
[12] K. Suzuki, H. Masuhara, *Langmuir* **2005**, *21*, 537.
[13] G. J. T. Tiddy, *Phys. Rep.* **1980**, *57*, 1.
[14] W. Helfrich, *J. Phys. Condens. Matter* **1994**, *6*, A79.
[15] G. Battaglia, A. J. Ryan, *Nat. Mater.* **2005**, *4*, 869.
[16] G. Battaglia, A. J. Ryan, *Macromolecules* **2006**, *39*, 798.
[17] C. Tanford, *Proc. Natl. Acad. Sci. USA* **1979**, *76*, 4175.
[18] J. Israelachivili, H. Wennerstrom, *Nature* **1996**, *379*, 219.
[19] S.-P. Lyu, J. J. Cernohous, F. S. Bates, C. W. Macosko, *Macromolecules* **1999**, *32*, 106.
[20] A. Einstein, *Ann. Phys.* **1906**, *19*, 371.
[21] S. Leibler, R. Lipowsky, *Phys. Rev. B* **1987**, *35*, 7004.
[22] R. Lipowsky, S. Leibler, *Phys. Rev. Lett.* **1986**, *56*, 2541.
[23] S. C. Machuga, H. L. Midje, J. S. Peanasky, C. W. Macosko, W. E. Ranz, *AIChE J.* **1988**, *34*, 1057.
[24] S. Jain, F. S. Bates, *Macromolecules* **2004**, *37*, 1511.
[25] B. Alberts, A. Johnson, J. Lewis, M. Raff, K. Roberts, P. Walter, *Molecular Biology of the Cell*, 5th ed., Garland Science, New York, **2002**.
[26] J. Lemmich, K. Mortensen, J. H. Ipsen, T. Hønger, R. Bauer, O. G. Mouritsen, *Eur. Biophys. J.* **1997**, *25*, 293.
[27] H. Ohvo-Rekila, B. Ramstedt, P. Leppimaki, J. P. Slotte, *Prog. Lipid Res.* **2002**, *41*, 66.
[28] G. Saher, B. Brugger, C. Lappe-Siefke, W. Mobius, R.-i. Tozawa, M. C. Wehr, F. Wieland, S. Ishibashi, K.-A. Nave, *Nat. Neurosci.* **2005**, *8*, 468.

 © 2006 Wiley-VCH Verlag GmbH & Co. KGaA, Weinheim

Host–Guest Chemistry

DOI: 10.1002/anie.200503441

Paired Carceroisomers**

*Chaesang Ihm, Eunhee Jo, Jaheon Kim, and Kyungsoo Paek**

New types of stereoisomers in a confined cavity, such as those provided by container molecules or molecular capsules, are stimulating research targets because of their potential to undergo molecular spin and act as a molecular switch for data storage devices and molecular electronics.[1] D_{4h}- and C_{4v}-symmetric container hosts composed of two resorcin[4]arene moieties could give pseudohelical stereoisomers (so-called twistomers[2]) stabilized by the constrictive binding environment of the host.[3] Reinhoudt and co-workers coined the term carceroisomer[4] for C_{4v}-symmetric carcerands composed

[*] Dr. C. Ihm, E. Jo, Prof. J. Kim, Prof. K. Paek
Department of Chemistry and CAMDRC
Soongsil University
Seoul 156-743 (Korea)
Fax: (+82) 2-822—2362
E-mail: kpaek@ssu.ac.kr
Dr. C. Ihm, Prof. K. Paek
Center for Bioactive Molecular Hybrids
Yonsei University
Seoul 120-749 (Korea)

[**] Molecular Engineering, Part 11. Financial support from the Ministry of Commerce, Industry, and Energy of Korea (No. 10022953), as well as the Center for Bioactive Molecular Hybrids, Yonsei University (2005) is gratefully acknowledged. We thank Sang Beom Choi for help with the X-ray data analysis.

Supporting information for this article is available on the WWW under http://www.angewandte.org or from the author.

WILEY InterScience DISCOVER SOMETHING GREAT
© 2006 Wiley-VCH Verlag GmbH & Co. KGaA, Weinheim

of two different hemispheres and/or having unsymmetrical pillars in which the opposite orientations of unsymmetrical guests along the long (C_4) axis form stereoisomers. Rebek and co-workers have also used the terms social isomers[5] and constellation isomers[6] for molecular capsules containing two different guests in 1:1 and 1:2 ratios, respectively.

The facile control over these new types of stereoisomers by energy-saving methods at ambient temperature could lead to an efficient multispin data-storage system. For an applicable method of control, the equilibrium should shift from one side to the other side completely and reversibly. The thermal or electronic energies, steric effects, hydrogen-bonding interactions, dipole–dipole interactions, or van der Waals interactions between the host and guest, as well as between the guests, have been the usual controlling concepts. Here we report the first control of carceroisomers by using a secondary guest, which can enter and escape reversibly through the portals of a carcerand.

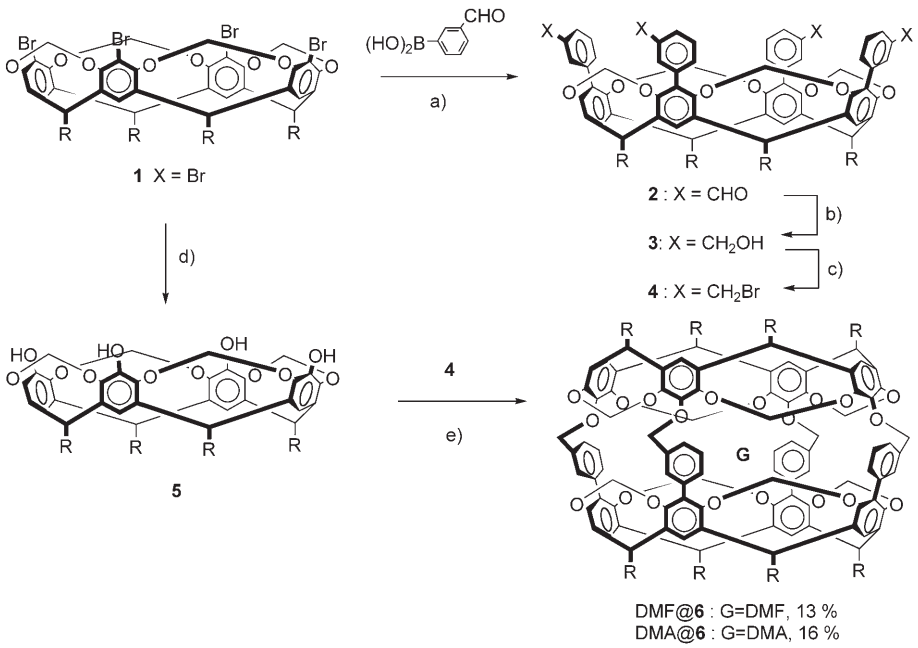

Scheme 1. Synthesis of carceplex DMF@**6** and DMA@**6** (R = $(CH_2)_6CH_3$). a) $[Pd(PPh_3)_4]$, THF, KF, reflux, 86%; b) LiAlH, THF, RT, 89%. c) PBr_3, toluene/diethyl ether, RT, 90%; d) 1. *n*BuLi/−78 °C, 2. $B(OMe)_3$, 3. H_2O_2, NaOH, 52%; e) G(solvent), K_2CO_3, 90 °C. G = guest.

The synthesis of the carceplexes started with a Suzuki coupling reaction between tetrabromide **1** and *meta*-formylphenylboronic acid which gave aldehydic cavitand **2** in 86% yield (Scheme 1). Subsequent transformations of cavitand **2** into hydroxy cavitand **3**, and then to bromocavitand **4** were accomplished in yields of 89 and 90%, respectively. The shell-closing reaction between bromocavitand **4** and tetrol **5**[7] in *N*,*N*-dimethylformamide (DMF) or *N*,*N*-dimethylacetamide (DMA) gave carceplexes DMF@**6** and DMA@**6** in yields of 13 and 16%, respectively. The free carcerand **6** could not be isolated, and also could not be obtained by heating these carceplexes up to 230 °C for 3 days. All the new compounds were fully characterized by ^{1}H NMR spectroscopy, MALDI-TOF mass spectrometry, and elemental analyses. The spacial arrangements between the host and guests in the carceroisomers were studied by ^{1}H-^{1}H ROESY measurements (500 MHz, $CDCl_3$, 25 °C). The crystal structure of the major carceroisomer of carceplex DMA@**6** was also solved.

The formation of carceroisomers in carceplex DMF@**6** on addition of acetonitrile was evident by ^{1}H NMR spectroscopic analysis (Figure 1). The three resonances of DMF in carceplex DMF@**6** in $CDCl_3$ at 25 °C appear as singlets at $\delta = 6.53$ ppm for HC=O, $\delta = 1.14$ ppm for *cis*-NCH_3, and $\delta = -0.26$ ppm for *trans*-NCH_3 (Figure 1a). The addition of 2% CH_3CN resulted in four new resonances between $\delta = -0.4$ and -2.2 ppm, two of which arose from resolution of the *trans*-NCH_3 resonance (Figure 1b). The ratio of these four resonances at $\delta = -0.41$, -1.21, -1.73, and -2.11 ppm was saturated at 1:2:2:1 upon addition of more than 20% CH_3CN (Figure 1c). The two upfield resonances ($\delta = -1.73$ and -2.11 ppm) in 20% $CD_3CN/CDCl_3$ solution disappeared, which implies that these missing resonances correspond to incarcerated CH_3CN and the remaining two signals at $\delta = -0.41$ and -1.21 ppm correspond to the *trans*-NCH_3 groups of two paired carceroisomers. Therefore, the secondary guest (acetonitrile) assisted the formation of carceroisomers of (DMF + CH_3CN)@**6** in a 1:2 ratio in 20% $CH_3CN/CDCl_3$ at 25 °C, and the four signals of the two guests are paired as $\delta = -0.41$ and

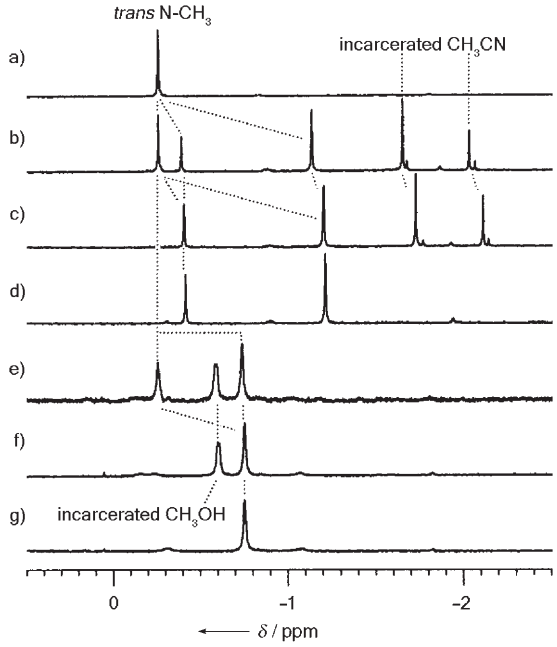

Figure 1. Changes in the partial ^{1}H NMR spectra (400 MHz) of carceplex DMF@**6** by the addition of acetonitrile or methanol at 25 °C; a) in $CDCl_3$, b) in 2% $CH_3CN/CDCl_3$, c) in 20% $CH_3CN/CDCl_3$, d) in 20% $CD_3CN/CDCl_3$, e) in 0.3% $CH_3OH/CDCl_3$, f) in 2% $CH_3OH/CDCl_3$, and g) in 2% $CD_3OD/CDCl_3$.

 © 2006 Wiley-VCH Verlag GmbH & Co. KGaA, Weinheim

−2.11 ppm for the minor carceroisomer, and $\delta = -1.21$ and −1.73 ppm for the major carceroisomer. The resonance for *trans*-NCH_3 ($\delta = -0.26$ ppm) shifted to $\delta = -0.74$ ppm and appeared as a singlet when MeOH was added, and a new singlet resonance for complexed MeOH at $\delta = -0.59$ ppm appeared (Figure 1e). These two resonances were saturated in a 1:1 ratio as the concentration of MeOH was increased (Figure 1f), and the whole spectrum indicates that the C_{4v} symmetry of (DMF + MeOH)@**6** remained unchanged until −90 °C. The results imply that the complexed DMF and CH_3OH tumble rapidly along the long C_4 axis—even at −90 °C on the ^{1}H NMR spectroscopic timescale. Other small guests such as acetaldehyde, acetic acid, ethanol, propanol, or nitromethane could not be complexed by carceplex DMF@**6**.

Figure 2 shows the proposed orientations of guests in the two most stable carceroisomers of (DMF + CH_3CN)@**6**. We

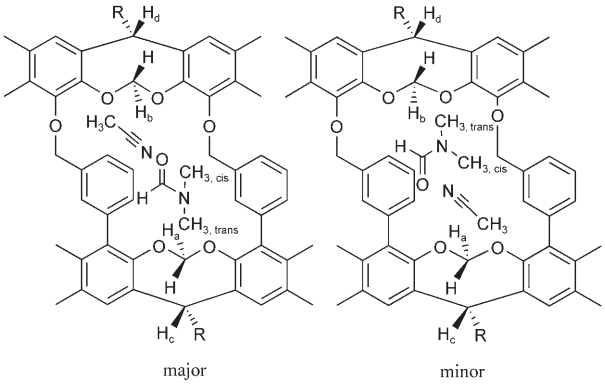

Figure 2. The proposed orientation of the guests in two paired carceroisomers.

call them the major and minor carceroisomers. Figure 3 shows the ^{1}H-^{1}H ROESY spectrum of (DMF + CD_3CN)@**6** in $CDCl_3$ at 25 °C. It is clear from the large NOE effects

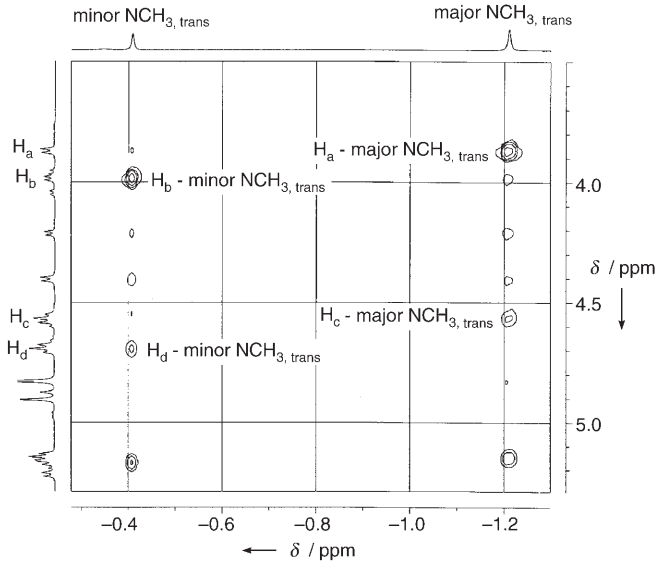

Figure 3. Partial 2D ROESY spectrum (500 MHz) of (DMF + CD_3CN)@**6** dissolved in $CDCl_3$ at 25 °C.

between *trans*-NCH_3 and H_a and H_c in the major carceroisomer, and between *trans*-NCH_3 and H_b and H_d in the minor carceroisomer, that these proposed orientations in Figure 2 correspond to the two most stable carceroisomers of (DMF + CH_3CN)@**6** in $CDCl_3$ at 25 °C. Figure 4 shows the energy-

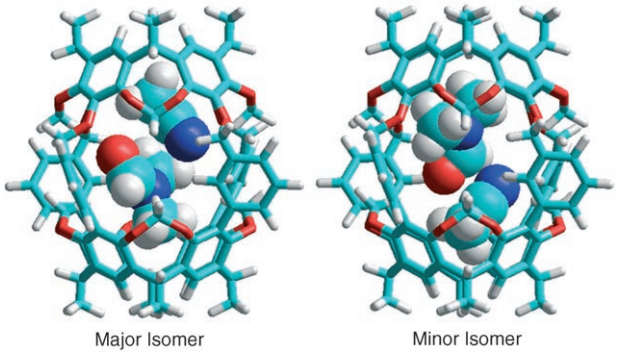

Figure 4. Energy-minimized structures of two carceroisomers of (DMF + CH_3CN)@**6** by HyperChem (MM + force field; the heptyl groups have been substituted by methyl groups for clarity).

minimized structures of these two carceroisomers, which also correspond to the proposed conformations and shows the pairwise dipole complementarity between the -C≡N and O=C moieties of two paired guests. Carceplex DMA@**6** cannot accommodate any additional small molecules, and its carceroisomers can only be observed by ^{1}H NMR spectroscopy below −90 °C. The crystal structure in Figure 5 shows the major carceroisomer of DMA@**6**, in which the two methyl groups of *cis*-NCH_3 and CH_3−C=O are aligned along the C_4 axis.[8] The two clearest planes, made of eight *meta*-oxygen atoms of each hemisphere, are tilted 16.2°, and the four *meta*-phenyl groups incorporated on the pillars partially wrap around the cavity. This arrangement results from the tendency to minimize the vacancy and, consequently, maximize the van der Waals interaction between the host and guest. The northern hemisphere is more polar than the southern hemisphere (12 versus 8 oxygen atoms around each rim of the hemispheres), but the cavity volume of the southern hemisphere seems slightly larger than that of the northern hemisphere. When the temperature was lowered to 183 K, the resonance for *trans*-NCH_3 ($\delta = -0.11$ ppm) was split into a pair of singlets at $\delta = -0.31$ and −0.66 ppm, and the CH_3C=O resonance ($\delta = -1.18$ ppm) was split into a pair of singlets at $\delta = -1.39$ and −1.74 ppm. The ratio of these four resonances was 1:2:2:1. From the coalescence temperature of 203 K for these paired singlets, the energy barrier ($\Delta G^{\circ}_{203\,K}$) for the free tumbling of carceroisomers of DMA@**6** was calculated to be 9.4 kcal mol^{-1} in CD_2Cl_2.

The association constants were obtained directly from the ^{1}H NMR spectra, and the thermodynamic parameters for the complexation of MeOH and CH_3CN by carceplex DMF@**6** were obtained therefrom. The thermodynamic parameters determined for MeOH are $\Delta G^{\circ}_{263} = -10.9$ kJ mol^{-1}, $\Delta H^{\circ} = -37.0$ kJ mol^{-1}, and $\Delta S^{\circ} = -99.1$ J mol^{-1} K^{-1} and those for

 © 2006 Wiley-VCH Verlag GmbH & Co. KGaA, Weinheim

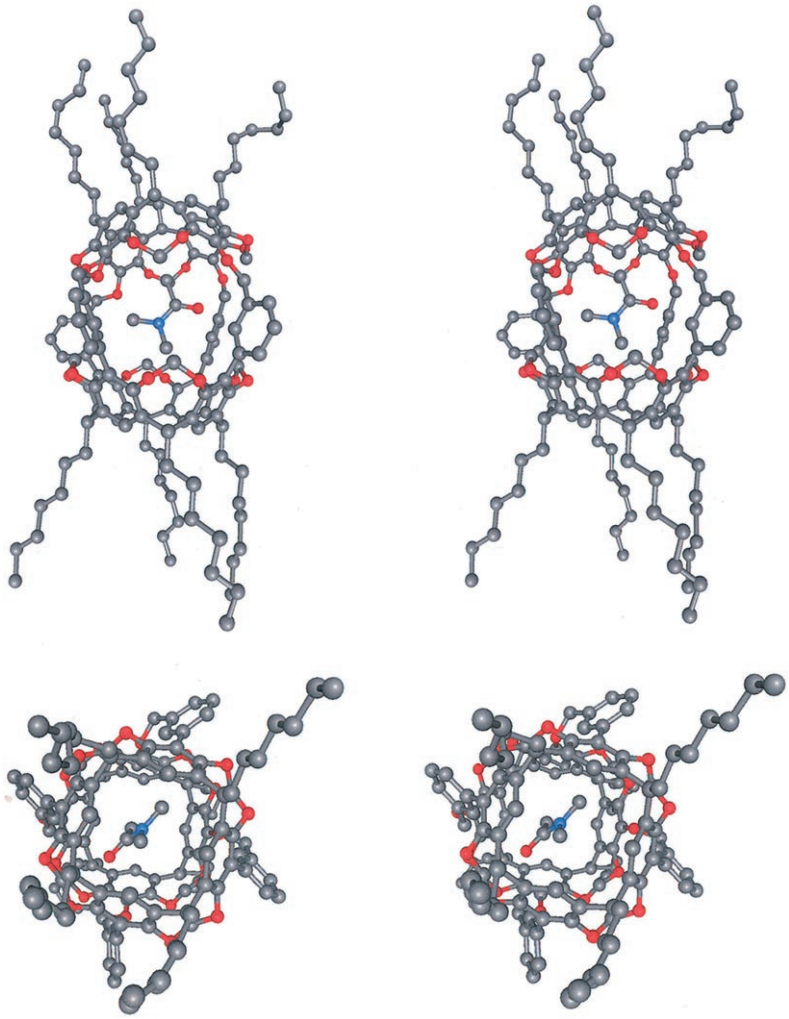

Figure 5. Stereoviews of the single-crystal structure of carceplex DMA@**6** (top: side view; bottom: top view).

CH_3CN are $\Delta G^{\circ}_{263} = -4.2\ kJ\,mol^{-1}$, $\Delta H^{\circ} = -22.7\ kJ\,mol^{-1}$, and $\Delta S^{\circ} = -71.8\ J\,mol^{-1}\,K^{-1}$. These values indicate that this paired complexation is enthalpically driven in both cases.

In conclusion, resorcin[4]arene-based carceplexes which possess a C_{4v}-symmetric cavity were synthesized and characterized. The fast movement of the first guest (DMF) was hindered by the reversible incarceration of the non-interacting second guest (CH_3CN), which results in a new kind of paired carceroisomers. The two most stable carceroisomers of (DMF + CH_3CN)@**6** were observed in a 1:2 ratio at 25 °C in $CDCl_3$ by ^1H NMR spectroscopy when an excess of CH_3CN existed. The orientations of the guests inside carcerand **6** were studied by 2D ROESY NMR experiments and by crystal-structure analysis. Such phenomena of novel stereoisomerism may offer an opportunity for the development of unprecedented molecular devices for high-density information storage.

Keywords: calixarenes · carcerands · host–guest systems · inclusion compounds · isomers

[1] a) D. J. Cram, J. M. Cram, *Container Molecules and Their Guests, Monographs in Supramolecular Chemistry, Vol. 4* (Ed.: J. F. Stoddart), The Royal Society of Chemistry, Cambridge, **1994**; b) J. Rebek, Jr., *Angew. Chem.* **2005**, *117*, 2104; *Angew. Chem. Int. Ed.* **2005**, *44*, 2068.

[2] a) R. G. Chapman, J. C. Sherman, *J. Am. Chem. Soc.* **1999**, *121*, 1962; b) K. Paek, H. Ihm, S. Yun, H. C. Lee, *Tetrahedron Lett.* **1999**, *40*, 8905; c) K. Paek, H. Ihm, S. Yun, H. C. Lee, K. T. No, *J. Org. Chem.* **2001**, *66*, 5736.

[3] D. J. Cram, M. T. Blanda, K. Paek, C. B. Knobler, *J. Am. Chem. Soc.* **1992**, *114*, 7765.

[4] a) P. Timmerman, W. Verboom, F. C. J. M. van Veggel, J. P. M. van Duynhoven, D. N. Reinhoudt, *Angew. Chem.* **1994**, *106*, 2437; *Angew. Chem. Int. Ed. Engl.* **1994**, *33*, 2345; b) B.-H. Huisman, D. M. Rudkevich, F. C. J. M. van Veggel, D. N. Reinhoudt, *J. Am. Chem. Soc.* **1996**, *118*, 3523; c) A. M. A. van Wageningen, P. Timmermann, J. P. M. van Duynhoven, W. Verboom, F. C. J. M. van Veggel, D. N. Reinhoudt, *Chem. Eur. J.* **1997**, *3*, 639.

[5] A. Shivanyuk, J. Rebek, Jr., *J. Am. Chem. Soc.* **2002**, *124*, 12074.

[6] a) M. Yamanaka, J. Rebek, Jr., *Angew. Chem.* **2003**, *115*, 708; *Angew. Chem. Int. Ed.* **2003**, *42*, 684; b) M. Yamanaka, J. Rebek, Jr., *Proc. Natl. Acad. Sci. USA* **2004**, *101*, 2669.

[7] J. C. Sherman, C. B. Knobler, D. J. Cram, *J. Am. Chem. Soc.* **1991**, *113*, 2194.

[8] Crystals of DMA@**6** suitable for X-ray analysis were grown in DMF/CH_2Cl_2 solution. Crystal data: $C_3H_7NO@C_{149}H_{178}O_{20}\cdot CH_2Cl_2$, $M_r = 2446.94$, triclinic, space group $P\bar{1}$, $T = 173(2)$ K, $a = 13.4924(8)$, $b = 23.7915(14)$, $c = 23.8264(14)$ Å, $\alpha = 64.437(1)$, $\beta = 73.875(1)$ $\gamma = 80.239(1)$°, $V = 6617.3(7)$ Å^3, $Z = 2$, $\rho_{calcd} = 1.194\ g\,cm^{-3}$, $\mu(Mo_{K\alpha}) = 0.119\ mm^{-1}$, $F(000) = 2628$. A total of 41261 reflections were measured, of which 29768 were unique ($R_{int} = 0.093$). Data collection was performed by the Bruker SMART CCD diffractometer. The crystal was mounted on a glass capillary, and flash-frozen under a cold nitrogen stream. The frame data were integrated using SANIT-PLUS and absorption correction was applied using SADABS. The structure was solved by direct methods (Bruker-XS) and subsequent difference Fourier analyses, and refined by full-matrix least-squares methods based on F^2 (Bruker-XL). All non-hydrogen atoms were refined anisotropically, and hydrogen atoms were generated and refined at their ideal positions using AFIX instructions. The final R values were converged to $R_1 = 0.0887$, $wR_2 = 0.1768$ for 9085 observed reflections with $I > 2\sigma(I)$. CCDC-285228 contains the supplementary crystallographic data for this paper. These data can be obtained free of charge from The Cambridge Crystallographic Data Centre via www.ccdc.cam.ac.uk/data_request/cif.

Received: September 29, 2005
Published online: February 22, 2006

 © 2006 Wiley-VCH Verlag GmbH & Co. KGaA, Weinheim

Platinum Carbonyl Clusters

DOI: 10.1002/anie.200503495

Synthesis and Crystal Structure of $[NBu_4]_2[Pt_{24}(CO)_{48}]$: An Infinite 1D Stack of $\{Pt_3(CO)_6\}$ Units Morphologically Resembling a CO-Insulated Platinum Cable**

Cristina Femoni, Francesco Kaswalder, Maria Carmela Iapalucci, Giuliano Longoni, Marita Mehlstäubl, Stefano Zacchini, and Alessandro Ceriotti*

The so-called "platinum carbonyl", which probably consists of $[Pt_{3n}(CO)_{6n}]^{2-}$ oligomers with an average n value of approximately 10, was reported several years ago.[1,2] To date only discrete $[Pt_{3n}(CO)_{6n}]^{2-}$ oligomers with $n = 1$–5 have been selectively synthesized and characterized.[2–7] 1D molecular metal wires,[8,9] and 1D and 2D superclusters[10,11] are interesting in themselves as low-dimensional molecular materials with possible applications in molecular electronics and nanolithography.[12–14] The recent improvement of the synthesis of "platinum carbonyl"[7] prompted a reinvestigation of the chemistry of the $[Pt_{3n}(CO)_{6n}]^{2-}$ oligomers with $n = 6$–10. Herein, we report the synthesis of the $n = 8$ oligomer $[Pt_{24}(CO)_{48}]^{2-}$, which was selectively obtained as a $[NBu_4]^+$ salt by the oxidation of $[Pt_6(CO)_{12}]^{2-}$ in THF, according to Equation (1).

$$4\,[Pt_6(CO)_{12}]^{2-} + 2\,SbCl_3 \rightarrow [Pt_{24}(CO)_{48}]^{2-} + 2\,Sb + 6\,Cl^- \qquad (1)$$

The $[NBu_4]_2[Pt_{24}(CO)_{48}]$ salt immediately separates from the reaction solution as a dark amorphous precipitate. Extraction of the precipitate with acetone gives a green-brown solution. The infrared (IR) spectrum of the solution has carbonyl absorption bands at 2070 and 1885 cm^{-1}, which are hardly diagnostic of the species present in solution, as all of the $[Pt_{3n}(CO)_{6n}]^{2-}$ ($n = 6$–10) oligomers generate carbonyl absorption bands in the range 2060–2075 cm^{-1} for terminal and 1875–1890 cm^{-1} for edge-bridging carbonyl groups. Electrospray ionization mass spectrometric (ESI-MS) analysis of $[NBu_4]_2[Pt_{24}(CO)_{48}]$ reveals a distribution of oligomers centered at $n = 5$, with peaks of lesser intensity at $n = 4$ and $n = 6$. The observed distribution is narrower than the bell-shaped distribution of $n = 3$–10 oligomers, centered at $n = 6$ or 7, exhibited by "platinum carbonyl".[7] The absence of the expected molecular peak for the $[Pt_{24}(CO)_{48}]^{2-}$ ion and the observed distribution of oligomers with $n = 4$–6 is clearly due to fragmentation processes occurring during the ESI-MS analysis, because the IR spectrum of the injected solution does not show the characteristic carbonyl absorptions of oligomers with $n = 4$–6.[2]

The nature of the $[NBu_4]_2[Pt_{24}(CO)_{48}]$ compound was clarified by single-crystal X-ray analysis.[15] The unit cell contains four $[Pt_{24}(CO)_{48}]^{2-}$ ions and eight $[NBu_4]^+$ ions. As shown in Figure 1, the molecular structure of the

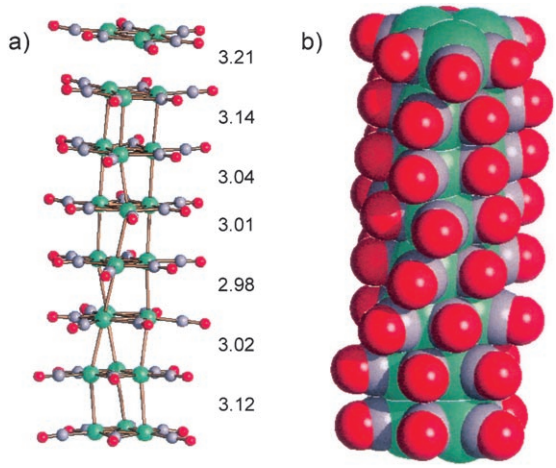

Figure 1. a) Ball-and-stick and b) space-filling models of the molecular structure of the $[Pt_{24}(CO)_{48}]^{2-}$ ion. In (a), the weak Pt–Pt contacts between the $\{Pt_3(CO)_6\}$ monomer and the $\{Pt_{21}(CO)_{42}\}$ heptamers above and below it are not shown as bonds. The interplane distances [Å] between the $\{Pt_3(CO)_6\}$ units are indicated. See text for details. Pt green, O red, C gray.

$[Pt_{24}(CO)_{48}]^{2-}$ ion is closely related to that of the previously reported $[Pt_{15}(CO)_{30}]^{2-}$ oligomer,[5] but it also has some new features. The $[Pt_{24}(CO)_{48}]^{2-}$ oligomer consists of a sequence of eight $\{Pt_3(CO)_6\}$ units stacked with a clock- or anticlockwise twist of 3–26° between consecutive units. The twist probably allows the minimization of repulsive intra- and intermolecular nonbonding interactions between the carbonyl groups of consecutive units and of adjacent oligomers. This twist is also responsible for the Pt–Pt contacts between neighboring $\{Pt_3(CO)_6\}$ units being longer than the distance between the Pt_3 planes of these units. The Pt–Pt bond distances within the individual $\{Pt_3(CO)_6\}$ units fall in the narrow range of 2.666(2)–2.679(2) Å. In contrast, the Pt–Pt contacts between neighboring $\{Pt_3(CO)_6\}$ units are spread over a wider range of 3.024(2)–3.307(2) Å. The shortest interplane distances occur between the inner $\{Pt_3(CO)_6\}$ units. The interplane distances become longer towards the top and bottom of the stack, like in an accordion (Figure 1). The longest Pt–Pt contacts between neighboring $\{Pt_3(CO)_6\}$ units (3.292(2)–3.307(2) Å) are those involving the top $\{Pt_3(CO)_6\}$ unit, and these are deliberately not shown as bonds in Figure 1. The Pt–Pt contacts and the interplane distances (3.21 Å) between this unit and the $\{Pt_{21}(CO)_{42}\}$ stacks above and below it are the same. Thus, the pseudo-1D $[Pt_{24}(CO)_{48}]^{2-}$ molecular ions are arranged in infinite chains composed of alternating

[*] Dr. C. Femoni, F. Kaswalder, Prof. M. C. Iapalucci, Prof. G. Longoni, M. Mehlstäubl, Dr. S. Zacchini
Dipartimento di Chimica Fisica ed Inorganica
viale Risorgimento 4, 40136 Bologna (Italy)
Fax: (+39) 051-209-3690
E-mail: longoni@ms.fci.unibo.it
Prof. A. Ceriotti
Dipartimento di Chimica Inorganica, Metallorganica ed Analitica
via G. Venezian 21, 20133 Milano (Italy)

[**] We thank the EU (Project No.: NMP4-CT-2004–500355, NAIMO) for financing.

InterScience
© 2006 Wiley-VCH Verlag GmbH & Co. KGaA, Weinheim

$\{Pt_{21}(CO)_{42}\}$ moieties and single $\{Pt_3(CO)_6\}$ units (see below). The chains can be described as molecular cables consisting of CO-insulated platinum wires. As shown in Figure 2a, layers of parallel $[Pt_{24}(CO)_{48}]^{2-}$ chains are intercalated by layers of $[NBu_4]^+$ ions. The overall texture resulting from the overlapping layers of chains is illustrated in Figure 2b.

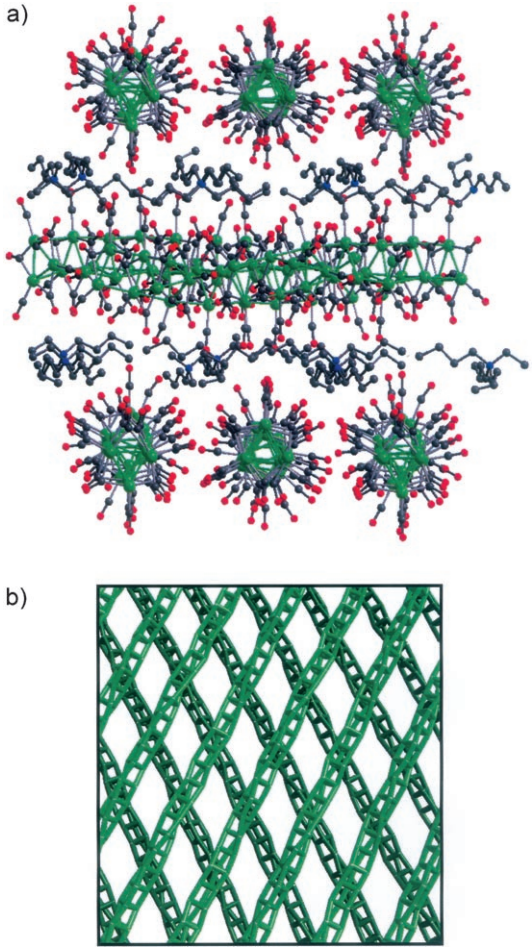

Figure 2. a) View of the crystal structure of $[NBu_4]_2[Pt_{24}(CO)_{48}]$, emphasizing the layers of $[Pt_{24}(CO)_{48}]^{2-}$ chains separated by layers of $[NBu_4]^+$ ions. Pt green, O red, N blue, C gray. H atoms are omitted for clarity. b) Two superimposed layers of $[Pt_{24}(CO)_{48}]^{2-}$ chains. CO ligands are omitted for clarity.

The formation of infinite platinum chains based on stacked $\{Pt_3(CO)_6\}$ units was predicted by Hoffmann and co-workers several years ago.[18] The possibility that such 1D chains could show Peierls distortions, owing to a partial filling of the energy band arising from the overlap of the cyclopropenyl-like LUMOs of the $\{Pt_3(CO)_6\}$ units along the pseudo-C_3 axis was also advanced. Within the frame of Peierls distortion theory applied to linear chains,[19,20] a $^1/_8$-filled energy band should give rise to octamers of $\{Pt_3(CO)_6\}$ units stabilized by two electrons (that is, discrete $[Pt_{24}(CO)_{48}]^{2-}$ ions). The experimentally found ordered sequence of heptamers sandwiching $\{Pt_3(CO)_6\}$ monomers seems to be due to another phenomenon. It seems likely that the solid-state infinite-chain structure of $[Pt_{24}(CO)_{48}]^{2-}$, with its alternation of six shorter (2.98–3.14 Å) and two longer (3.21 Å) interplane distances, represents a snapshot of the intermolecular exchange of $\{Pt_3(CO)_6\}$ units, as detected in solution by ^{195}Pt NMR spectroscopy for mixtures of $[Pt_{3n}(CO)_{6n}]^{2-}$ ($n = 3$, 4) ions.[21,22] Semi-empirical extended Hückel molecular orbital (EHMO) calculations on two idealized $[Pt_{12}(CO)_{24}]^{2-}$ ions (calculations on two $[Pt_{21}(CO)_{42}]^{2-}$ ions were beyond the capabilities of our facilities), kept 6.42 Å apart, and a $\{Pt_3(CO)_6\}$ monomer shuttling between the two, yield an electronic energy minimum when the monomer is located halfway between the two ions (3.21 Å). The energy of this configuration is 0.1 eV lower than that for the system when the $\{Pt_3(CO)_6\}$ shuttle is docked on one of the two $[Pt_{12}(CO)_{24}]^{2-}$ ions. This result supports the conclusion that the 1D chains in the solid-state structure of $[NBu_4]_2[Pt_{24}(CO)_{48}]$ result from the intermolecular exchange of $\{Pt_3(CO)_6\}$ units between $[Pt_{24}(CO)_{48}]^{2-}$ oligomers.

The self-assembly of $[Pt_{24}(CO)_{48}]^{2-}$ into 1D chains resembling a CO-insulated platinum cable upon crystallization of $[NBu_4]_2[Pt_{24}(CO)_{48}]$ makes this salt a promising precursor for patterning surfaces with platinum nanowires.[23] Moreover, the morphological resemblance of the chains to wires may lead to semiconducting or conducting behavior for this and related salts. The combined influence of the negative charge per $\{Pt_3(CO)_6\}$ unit, the length of the $[Pt_{3n}(CO)_{6n}]^{2-}$ oligomer, and the size of the counterion on the Pt–Pt distance between stacked oligomers is currently under investigation.

Received: October 3, 2005
Published online: February 22, 2006

Keywords: carbonyl ligands · chain structures · cluster compounds · platinum · structure elucidation

[1] G. Booth, J. Chatt, P. Chini, *J. Chem. Soc. Chem. Commun.* **1965**, 639–640.
[2] G. Longoni, P. Chini, *J. Am. Chem. Soc.* **1976**, *98*, 7225–7231.
[3] A. Ceriotti, G. Longoni, M. Marchionna, *Inorg. Synth.* **1989**, *26*, 316–319.
[4] M. J. D'Aniello, C. J. Carr, M. G. Zammit, *Inorg. Synth.* **1989**, *26*, 319–323.
[5] J. C. Calabrese, L. F. Dahl, P. Chini, G. Longoni, S. Martinengo, *J. Am. Chem. Soc.* **1974**, *96*, 2614–2616.
[6] L. Bengtsson-Kloo, M. C. Iapalucci, G. Longoni, S. Ulvenlund, *Inorg. Chem.* **1998**, *37*, 4335–4343.
[7] C. Femoni, F. Kaswalder, M. C. Iapalucci, G. Longoni, M. Mehlstäubl, S. Zacchini, *Chem. Commun.* **2005**, 5769–5771.
[8] J. K. Bera, K. R. Dunbar, *Angew. Chem.* **2002**, *114*, 4633–4637; *Angew. Chem. Int. Ed.* **2002**, *41*, 4453–4457.
[9] G. M. Finnis, E. Canadell, C. Campana, K. R. Dunbar, *Angew. Chem.* **1996**, *108*, 2946–2948; *Angew. Chem. Int. Ed. Engl.* **1996**, *35*, 2772–2774.
[10] T. Nakajima, A. Ishiguro, Y. Wakatsuki, *Angew. Chem.* **2001**, *113*, 1096–1099; *Angew. Chem. Int. Ed.* **2001**, *40*, 1066–1067.
[11] C. E. Plechnik, S. Liu, X. Chen, E. A. Meyers, S. G. Shore, *J. Am. Chem. Soc.* **2004**, *126*, 204–213.
[12] R. L. Carroll, C. B. Gorman, *Angew. Chem.* **2002**, *114*, 4556–4579; *Angew. Chem. Int. Ed.* **2002**, *41*, 4378–4400.
[13] G. Schmid, U. Simon, *Chem. Commun.* **2005**, 697–710.
[14] D. Wouters, U. S. Schubert, *Angew. Chem.* **2004**, *116*, 2534–2550; *Angew. Chem. Int. Ed.* **2004**, *43*, 2480–2495.

 © 2006 Wiley-VCH Verlag GmbH & Co. KGaA, Weinheim

[15] Crystal data for $[NBu_4]_2[Pt_{24}(CO)_{48}]$: orthorhombic, $Pna2_1$, $a=21.515(3)$, $b=24.311(3)$, $c=22.257(3)$ Å, $V=11\,641(2)$ Å^3, $Z=4$, $\rho=3.715\,g\,cm^{-3}$, graphite-monochromatized $Mo_{K\alpha}$ radiation ($\lambda=0.71073$ Å), $R_1=0.0547$, $wR_2=0.0948$ (for 20518 I_o, $I_o>2\sigma(I_o)$). Data were collected at 100 K, and corrected for Lorentz-polarization and absorption (empirical, SADABS[16]). The structures were solved by direct methods and refined by full-matrix least-squares procedures (SHELX97[17]). CCDC-285211 contains the supplementary crystallographic data for this paper. These data can be obtained free of charge from The Cambridge Crystallographic Data Centre via www.ccdc.cam.ac.uk/data_request/cif.
[16] G. M. Sheldrick, SADABS, Universität Göttingen, Germany.
[17] G. M. Sheldrick, SHELX97, Universität Göttingen, Germany.
[18] D. J. Underwood, R. Hoffmann, K. Tatsumi, A. Nakamura, Y. Yamamoto, *J. Am. Chem. Soc.* **1985**, *107*, 5968 – 5980.
[19] M.-H. Whangbo, *Acc. Chem. Res.* **1983**, *16*, 95 – 101.
[20] J. K. Burdett in *Chemical Bonding in Solids*, Oxford University Press, New York, **1995**.
[21] C. Brown, B. T. Heaton, P. Chini, A. Fumagalli, G. Longoni, *J. Chem. Soc. Chem. Commun.* **1977**, 309 – 310.
[22] C. Brown, B. T. Heaton, A. D. C. Towl, P. Chini, A. Fumagalli, G. Longoni, *J. Organomet. Chem.* **1979**, *181*, 233 – 254.
[23] H. Remita, B. Keita, K. Torigoe, J. Belloni, L. Nadjo, *Surf. Sci.* **2004**, *572*, 301 – 308.

 © 2006 Wiley-VCH Verlag GmbH & Co. KGaA, Weinheim

Solvent Effects

DOI: 10.1002/anie.200503533

Dissecting the Behavior of a Promiscuous Solvate Former**

*Christopher P. Price, Gary D. Glick, and Adam J. Matzger**

Solvate formation is a common occurrence among organic, organometallic, and inorganic compounds. Its impact on the stability and bioavailability of pharmaceuticals has led to considerable investigation of solvated drug substances.[1] Some compounds display indiscriminate solvate formation, while others are considerably more selective. Significantly, the structural features that lead to one behavior or another have not been identified. Hence, empirical approaches are required for the discovery of solvates. Two situations can readily be envisaged that would tend to favor solvate formation. First, compounds in which potential intermolecular interactions, such as hydrogen bonding, are not well satisfied in the unsolvated form generally incorporate solvent molecules to provide strong intermolecular interactions and often solvate selectively based on functionality. The other limiting case is solvent inclusion to decrease void space in the crystal. Most compounds have contributions from both of these driving forces, which can be viewed as lowering the crystal free energy primarily through electrostatic and van der Waals interactions, respectively.

Readily solvated pharmaceuticals have received attention in the literature, two prominent examples are sulfathiazole and gossypol. Sulfathiazole is an antibacterial sulfa-drug known to crystallize in over 100 solvates/cocrystals and five solvent-free polymorphs.[2–6] It forms solvates with many solvents; however, there are some notable exceptions, which include hydrocarbon and halogenated solvents. Solvated sulfathiazole forms a diverse set of crystal structures, as well as several isostructural solvates. In some cases, the role of the solvent is to fill void space in the lattice (e.g., acetonitrile, dioxane), while in other crystals the solvent satisfies specific intermolecular interactions (e.g., *N*-formyl piperidine). Gossypol is a natural product that has been used as a male contraceptive and it forms solvates/cocrystals with nearly 100 molecules.[7] Solvates can be generated from nearly every common organic solvent. It does, however, crystallize in a solvent-free form from ligroin and mixtures of hexane and diethyl ether. Like sulfathiazole, gossypol forms isostructural solvates, in which the solvent fills a cavity in the structure (e.g., carbon tetrachloride, *m*-xylene), as well as solvates with specific hydrogen-bonding interactions between gossypol and the included solvent (e.g., acetic acid, 2-propanol).

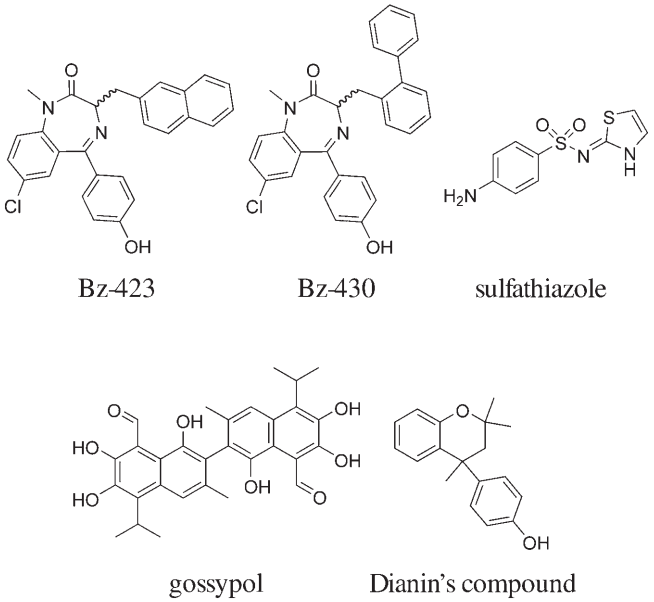

To learn more about the factors that lead to solvate formation in pharmaceuticals, we investigated the crystallization of Bz-423, a 1,4-benzodiazepin-2-one. Bz-423 specifi-

[*] C. P. Price, Prof. G. D. Glick, Prof. A. J. Matzger
Department of Chemistry
University of Michigan
Ann Arbor, MI 48109–1055 (USA)
Fax: (+1) 734-615-8553
E-mail: matzger@umich.edu

[**] Supported in part by the National Institutes of Health Grant R01 AI47450. We thank GMP | Immunotherapeutics for samples of Bz-423 and Bz-430 and Jeff W. Kampf for the crystal structure determination.

Supporting information for this article is available on the WWW under http://www.angewandte.org or from the author.

InterScience
© 2006 Wiley-VCH Verlag GmbH & Co. KGaA, Weinheim

cally attenuates autoimmune disease in the best animal models of systemic lupus erythematosus.[8–10] In the process of selecting a crystalline form for ultimate dosage, a remarkable property of this compound was revealed: all crystals of Bz-423 obtained from common solvents were solvates. Furthermore, solvents that did not lead to crystalline materials (e.g., acetone, benzene, diethyl ether, 2,2,4,4,6,8,8-heptamethyl nonane, heptane, hexanes, pyridine, triethylamine, 2,2,4-trimethylpentane, CH_2Cl_2, THF) yielded amorphous forms, typically with included solvent as judged by Raman spectroscopy.

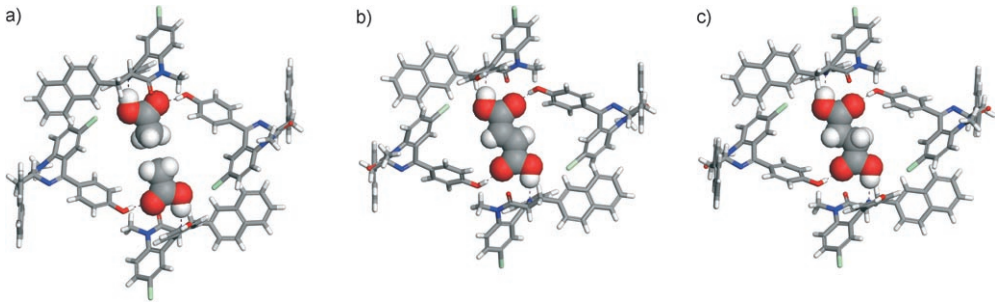

Figure 2. Isomorphous hydrogen-bonding motif found in the crystal structure of Bz-423 with a) acetic acid, b) fumaric acid, and c) succinic acid.

Cocrystals of acetonitrile, acetic acid, dibutyl ether, ethanol, ethyl acetate, methanol, 1-propanol, 2-propanol, toluene, and 1,2,4-trichlorobenzene with Bz-423 were readily formed by evaporation from pure solution. Crystal structures of the acetonitrile, ethanol, ethyl acetate, 2-propanol, and acetic acid solvates were determined to ascertain whether these forms were isomorphous, perhaps with the solvent occupying channels or other regular vacancies in the lattice.[11] However, these are structurally distinct with different modes of interaction between Bz-423 molecules and the solvent (Figure 1). The acetonitrile solvate, for example, forms hydrogen bonds with the phenolic hydroxy group of Bz-423, whereas ethanol and 2-propanol both accept a hydrogen bond from the hydroxy group and act as a donor with the carbonyl group of Bz-423. In contrast, ethyl acetate forms no strong hydrogen bonds with Bz-423. However, not all of the forms differ substantially in structure, carboxylic acids, including the Bz-423/acetic acid (1:1), the Bz-423/fumaric acid (2:1), and Bz-423/succinic acid (2:1) cocrystals, are isostructural with essentially identical hydrogen-bonding patterns (Figure 2), and each is nearly isostructural with the Bz-423/acetonitrile solvate (1:1). The Bz-423/ethanol (1:1) and Bz-423/2-propanol (1:1) solvates are also nearly isostructural, with both possessing identical hydrogen-bonding patterns.

To test the hypothesis that the particular combination of functionality found in Bz-423 drives the solvation behavior, the crystallization of Bz-430, which contains a biphenyl unit in place of the naphthalene ring, was scrutinized. This compound does not display a propensity toward solvate formation despite being crystallized from acetonitrile, benzene, ethyl acetate, methanol, CH_2Cl_2, and THF (see the Supporting Information). This finding suggests that functionality-driven solvation, in which solvent inclusion is favored by enhanced satisfaction of intermolecular interactions, does not explain the observed behavior of Bz-423. In addition, Bz-423 cocrystallizes with a wide variety of solvents, with many different structures being formed, and displays an inability to form unsolvated crystals from common solvents. These observations suggest that Bz-423, in contrast to Bz-430, does not pack efficiently with itself.

One measure of how tightly a molecule packs in a crystal lattice is packing efficiency, measured by the packing coefficient C_k.[12] This quantity reflects the percentage of void space in molecular crystals. A solvent-free reference form was required to assess the effect of solvent inclusion on the packing efficiency of Bz-423. This reference form was achieved by dissolving the Bz-423/methanol solvate in polyethylene glycol dimethyl ether ($x_n = 11$) at elevated temperature overnight to yield solvent-free single crystals. The packing coefficient of this structure was calculated using the equation developed by Kitaigorodskii.[13] Because the packing coefficient relates the volume of the unit cell to the volume of molecules in the cell, the molecular volume of each nonequivalent molecule in the crystal must be calculated.[14] The volume of each isolated species was determined for the solvates and then added together according to stoichiometry.

Consistent with the notion of inefficient packing in the unsolvated form, the packing coefficients of the Bz-423 solvate structures, as well as Bz-430, were all higher than that of the solvent-free form (Figure 3). This observation indicates that Bz-423 fills space more efficiently with a solvent molecule present than in pure form. The increased packing efficiency of solvated Bz-423 offers an attractive explanation for why the molecule will not crystallize as a solvent-free form from small-molecule solvents. To explore if this hypothesis

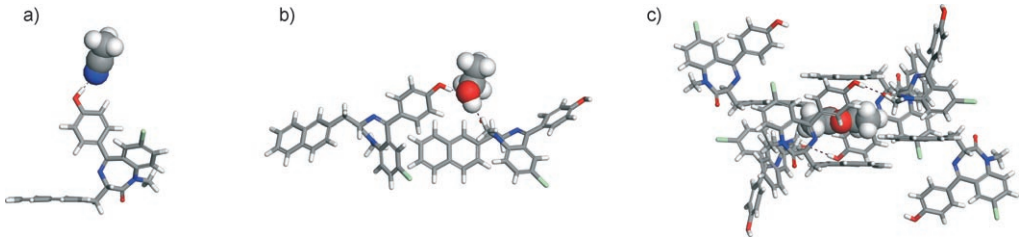

Figure 1. Modes of interaction between Bz-423 and the included a) acetonitrile, b) ethanol, and c) ethyl acetate solvent molecules extracted from the respective crystal structures.

 © 2006 Wiley-VCH Verlag GmbH & Co. KGaA, Weinheim

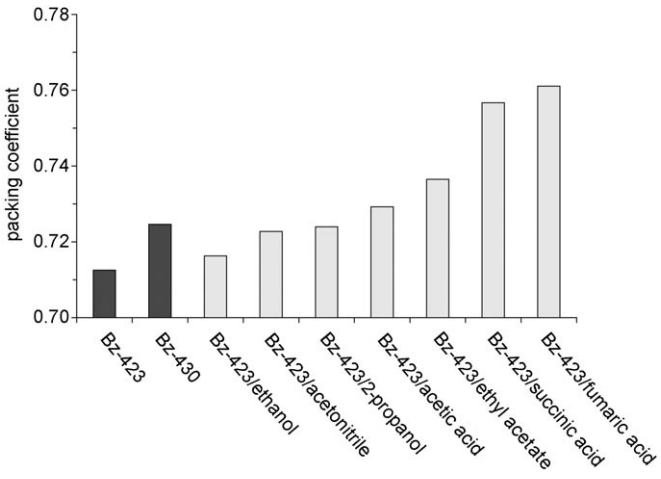

Figure 3. Comparison of the packing coefficients of the Bz-423 solvates, solvent-free Bz-423, and Bz-430.

generally holds for other pharmaceuticals prone to solvate formation, solvent-free and solvated crystal structures of sulfathiazole and gossypol culled from the Cambridge Structural Database (CSD) were analyzed and their packing coefficients were calculated.[15] In both cases, the presence of polymorphism as well as variation of the temperature of the data collection complicates the analysis somewhat. In addition, although there are over 100 solvates/cocrystals of sulfathiazole, few of the crystal structures are available in the CSD.[16] The packing coefficients of the five polymorphs and three solvates were calculated (Figure 4). These solvates pack with efficiencies that are intermediate between the most and least dense solvent-free polymorph of this pharmaceutical. A similar analysis on gossypol, which encompasses two solvent-free polymorphs and 31 solvates, finds that the packing coefficients for all solvates are intermediate between the more and less dense polymorphs of the solvent-free compound (Figure 5). The presence of relatively close-packed polymorphs for both sulfathiazole and gossypol offers a potential explanation for why, in contrast to Bz-423, these compounds can readily give rise to unsolvated forms.

It is instructive to contrast the behavior of the pharmaceuticals described above with Dianin's compound, a derivative of 1,2-benzopyran that has been studied extensively as a host material.[17–22] This molecule forms isomorphous solvates with a diverse array of solvents, and in each and every structure the solvent resides in the same pocket. A solvent-free crystal form of Dianin's compound was obtained from dodecane, a solvent too large to occupy the lattice vacancies. Packing coefficients were calculated for the structures found in the CSD, and the solvates were revealed to pack more efficiently than the solvent-free crystal (Figure 6). Like Bz-423, Dianin's compound solvates many different solvents, thus increasing its packing efficiency, but unlike Bz-423 it forms isomorphous structures in all structurally characterized

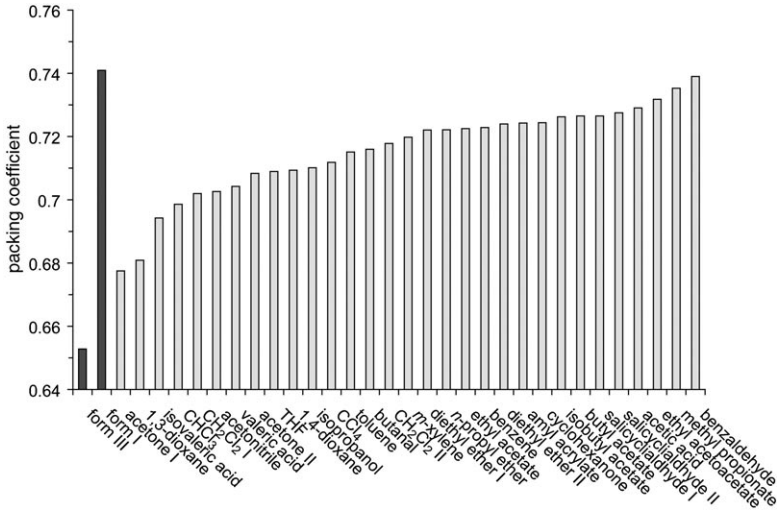

Figure 5. Comparison of the packing coefficients of the gossypol solvates and polymorphs taken from the CSD.

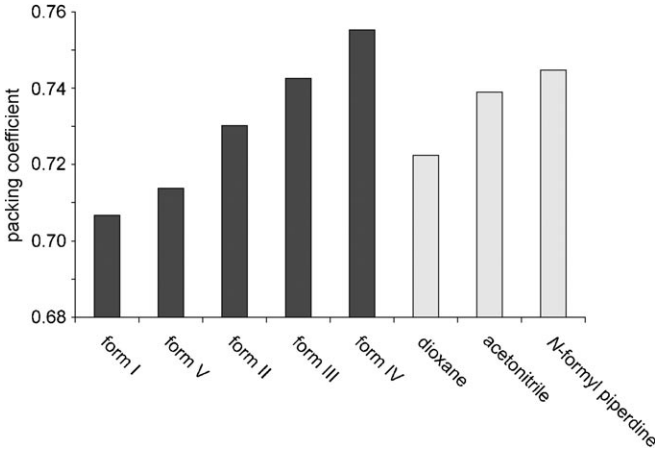

Figure 4. Comparison of the packing coefficients of the sulfathiazole solvates and polymorphs taken from the CSD.

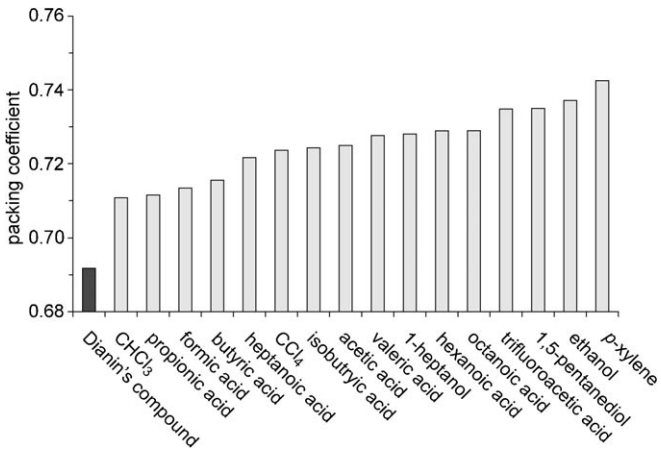

Figure 6. Comparison of the packing coefficients of the Dianin's compound solvates and solvent-free form taken from the CSD.

 © 2006 Wiley-VCH Verlag GmbH & Co. KGaA, Weinheim

solvates. This suggests that the inefficiency of crystal packing for Bz-423 arises from a confluence of multiple small voids rather than a well-defined cavity or channel structure. Predicting such behavior in new compounds will require a comparison to reference packing coefficients derived from data for structural relatives. This approach will aid in the evaluation of the tendency of a particular compound to form solvates.[23]

Received: October 5, 2005
Published online: February 22, 2006

Keywords: benzodiazepines · packing efficiency · solid-state structures · solvates · supramolecular chemistry

[1] For recent examples of studies that employ crystal engineering of pharmaceutical solvates/cocrystals, see: a) I. D. H. Oswald, D. R. Allan, P. A. McGregor, W. D. S. Motherwell, S. Parsons, C. R. Pulham, *Acta Crystallogr. Sect. B* **2002**, *58*, 1057 – 1066; b) R. D. B. Walsh, M. W. Bradner, S. Fleischman, L. A. Morales, B. Moulton, N. Rodríguez-Hornedo, M. J. Zaworotko, *Chem. Commun.* **2003**, 186 – 187; c) J. F. Remenar, S. L. Morissette, M. L. Peterson, B. Moulton, J. M. MacPhee, H. R. Guzmán, Ö. Almarsson, *J. Am. Chem. Soc.* **2003**, *125*, 8456 – 8457; d) S. G. Fleischman, S. S. Kuduva, J. A. McMahon, B. Moulton, R. D. B. Walsh, N. Rodríguez-Hornedo, M. J. Zaworotko, *Cryst. Growth Des.* **2003**, *3*, 909 – 919; e) Ö. Almarsson, M. B. Hickey, M. L. Peterson, S. L. Morissette, S. Soukasene, C. McNulty, M. Tawa, J. M. MacPhee, J. F. Remenar, *Cryst. Growth Des.* **2003**, *3*, 927 – 933; f) S. L. Childs, L. J. Chyall, J. T. Dunlap, V. N. Smolenskaya, B. C. Stahly, G. P. Stahly, *J. Am. Chem. Soc.* **2004**, *126*, 13335 – 13342; g) J. A. McMahon, J. A. Bis, P. Vishweshwar, T. R. Shattock, O. L. McLaughlin, M. J. Zaworotko, *Z. Kristallogr.* **2005**, *220*, 340 – 350; h) A. V. Trask, W. D. S. Motherwell, W. Jones, *Cryst. Growth Des.* **2005**, *5*, 1013 – 1021.

[2] G. J. Kruger, G. Gafner, *Acta Crystallogr. Sect. B* **1971**, *27*, 326 – 333.

[3] G. J. Kruger, G. Gafner, *Acta Crystallogr. Sect. B* **1972**, *28*, 272 – 283.

[4] F. V. Babilev, V. K. Bel'skii, Y. A. Simonov, A. P. Arzamastsev, *Khim. Farm. Zh.* **1987**, *21*, 1275 – 1280.

[5] D. S. Hughes, M. B. Hursthouse, T. Threlfall, S. Tavener, *Acta Crystallogr. Sect. C* **1999**, *55*, 1831 – 1833.

[6] A. L. Bingham, D. S. Hughes, M. B. Hursthouse, R. W. Lancaster, S. Tavener, T. L. Threlfall, *Chem. Commun.* **2001**, 603 – 604.

[7] M. Gdaniec, B. T. Ibragimov, S. A. Talipov in *Comprehensive Supramolecular Chemistry, Vol. 6* (Eds.: D. D. MacNicol, F. Toda, R. Bishop), Elsevier Sciences, London, **1996**, pp. 117 – 145.

[8] N. B. Blatt, J. J. Bednarski, R. E. Warner, F. Leonetti, K. M. Johnson, A. Boitano, R. Yung, B. C. Richardson, K. J. Johnson, J. A. Ellman, A. W. Opipari, G. D. Glick, *J. Clin. Invest.* **2002**, *110*, 1123 – 1132.

[9] J. J. Bednarski, R. E. Warner, T. Rao, F. Leonetti, R. Yung, B. C. Richardson, K. J. Johnson, J. A. Ellman, A. W. Opipari, G. D. Glick, *Arthritis Rheum.* **2003**, *46*, 757 – 766.

[10] K. M. Johnson, X. N. Chen, A. Boitano, L. Swenson, A. W. Opipari, G. D. Glick, *Chem. Biol.* **2005**, *12*, 485 – 496.

[11] Crystal data: a) solvent-free Bz-423; $C_{27}H_{21}ClN_2O_2$, colorless plate crystal of dimensions $0.28 \times 0.20 \times 0.04$ mm was analyzed at 123(2) K, orthorhombic, space group *Pbca* (no. 61), $a = 14.835(3)$, $b = 14.999(3)$, $c = 19.901(4)$ Å, $V = 4528.4(14)$ Å^3, $Z = 8$, $\rho_{calcd} = 1.323$ g cm^{-3}, $\mu(Mo_{K\alpha}) = 0.200$ mm^{-1}, $F(000) = 1840$, 3789 unique reflections between $2.90° \le 2\theta \le 24.81°$, $T_{max} = 0.99$, $T_{min} = 0.95$, $R_1 = 0.0378$, $R_w = 0.0780$; b) Bz-430: $C_{29}H_{23}ClN_2O_2$ colorless plate crystal of dimensions $0.12 \times 0.04 \times 0.02$ mm was analyzed at 123(2) K, monoclinic, space group $P2_1/c$ (no. 14), $a = 9.7205(8)$, $b = 19.3671(17)$, $c = 12.8434(10)$, $\beta = 104.870(3)°$, $V = 2336.9(3)$ Å^3, $Z = 4$, $\rho_{calcd} = 1.327$ g cm^{-3}, $\mu(Mo_{K\alpha}) = 0.193$ mm^{-1}, $F(000) = 967$, 2554 unique reflections between $3.02° \le 2\theta \le 21.18°$, $R_1 = 0.0424$, $R_w = 0.0892$; c) Bz-423/acetic acid solvate: $C_{27}H_{21}ClN_2O_2 \cdot C_2H_4O_2$, colorless plate crystal of dimensions $0.36 \times 0.24 \times 0.10$ mm was analyzed at 123(2) K, monoclinic, space group $P2_1/c$ (no. 14), $a = 9.261(2)$, $b = 13.649(3)$, $c = 19.753(4)$ Å, $\beta = 97.623(4)°$, $V = 2474.9(9)$ Å^3, $Z = 4$, $\rho_{calcd} = 1.345$ g cm^{-3}, $\mu(Mo_{K\alpha}) = 0.193$ mm^{-1}, $F(000) = 1048$, 4629 unique reflections between $2.97° \le 2\theta \le 25.65°$, $T_{max} = 0.98$, $T_{min} = 0.93$, $R_1 = 0.0428$, $R_w = 0.0881$; d) Bz-423/acetonitrile solvate: $C_{27}H_{21}ClN_2O_2 \cdot C_2H_3N$, colorless plate crystal of dimensions $0.25 \times 0.14 \times 0.05$ mm was analyzed at 153(2) K, monoclinic, space group $P2_1/c$ (no. 14), $a = 9.310(11)$, $b = 13.7802(17)$, $c = 19.082(2)$ Å, $\beta = 93.634(2)°$, $V = 2443.2(5)$ Å^3, $Z = 4$, $\rho_{calcd} = 1.310$ g cm^{-3}, $\mu(Mo_{K\alpha}) = 0.181$ mm^{-1}, $F(000) = 920$, 5610 unique reflections between $1.82° \le 2\theta \le 27.51°$, $T_{max} = 0.99$, $T_{min} = 0.96$, $R_1 = 0.0352$, $R_w = 0.0976$; e) Bz-423/ethanol solvate: $C_{27}H_{21}ClN_2O_2 \cdot C_2H_6O$, colorless plate crystal of dimensions $0.32 \times 0.18 \times 0.08$ mm was analyzed at 153(2) K, orthorhombic, space group *Pbca* (no. 61), $a = 14.7352(11)$, $b = 15.3206(11)$, $c = 22.1937(17)$ Å, $V = 5010.3(6)$ Å^3, $Z = 8$, $\rho_{calcd} = 1.291$ g cm^{-3}, $\mu(Mo_{K\alpha}) = 0.186$ mm^{-1}, $F(000) = 2048$, 5769 unique reflections between $1.84° \le 2\theta \le 27.57°$, $T_{max} = 0.98$, $T_{min} = 0.96$, $R_1 = 0.0901$, $R_w = 0.2224$; f) Bz-423/ethyl acetate solvate $2C_{27}H_{21}ClN_2O_2 \cdot C_4H_8O_2$: colorless block crystal of dimensions $0.50 \times 0.26 \times 0.14$ mm was analyzed at 123(2) K, monoclinic, space group $P2_1/n$ (no. 14), $a = 16.208(2)$ $b = 9.2803(12)$, $c = 16.937(2)$ Å, $\beta = 110.161(2)°$, $V = 2391.5(5)$ Å^3, $Z = 4$, $\rho_{calcd} = 1.347$ g cm^{-3}, $\mu(Mo_{K\alpha}) = 0.195$ mm^{-1}, $F(000) = 1020$, 5930 unique reflections between $3.07° \le 2\theta \le 28.30°$, $T_{max} = 0.97$, $T_{min} = 0.91$, $R_1 = 0.0350$, $R_w = 0.0933$; g) Bz-423/fumaric acid cocrystal: $2C_{27}H_{21}ClN_2O_2 \cdot C_4H_4O_4$, colorless plate crystal of dimensions $0.30 \times 0.24 \times 0.08$ mm was analyzed at 123(2) K, monoclinic, space group $P2_1/c$ (no. 14), $a = 9.0653(13)$, $b = 13.7215(19)$, $c = 18.753(3)$ Å, $\beta = 93.236(3)°$, $V = 2329.0(6)$ Å^3, $Z = 4$, $\rho_{calcd} = 1.423$ g cm^{-3}, $\mu(Mo_{K\alpha}) = 0.205$ mm^{-1}, $F(000) = 1040$, 5797 unique reflections between $2.86° \le 2\theta \le 28.37°$, $T_{max} = 0.98$, $T_{min} = 0.94$, $R_1 = 0.0412$, $R_w = 0.0886$; h) Bz-423/2-propanol solvate: $C_{27}H_{21}ClN_2O_2 \cdot C_3H_8O$, colorless plate crystal of dimensions $0.40 \times 0.36 \times 0.12$ mm was analyzed at 123(2) K, orthorhombic, space group *Pbca* (no. 61), $a = 14.418(3)$, $b = 15.779(3)$, $c = 22.625(4)$ Å, $V = 5147.3(16)$ Å^3, $Z = 8$, $\rho_{calcd} = 1.293$ g cm^{-3}, $\mu(Mo_{K\alpha}) = 0.183$ mm^{-1}, $F(000) = 2112$, 4420 unique reflections between $2.11° \le 2\theta \le 24.78°$, $T_{max} = 0.98$, $T_{min} = 0.93$, $R_1 = 0.0339$, $R_w = 0.0805$; i) Bz-423/succinic acid cocrystal: $2C_{27}H_{21}ClN_2O_2 \cdot C_4H_6O_4$, colorless plate block of dimensions $0.44 \times 0.22 \times 0.20$ mm was analyzed at 123(2) K, monoclinic, space group $P2_1/c$ (no. 14), $a = 9.1098(14)$, $b = 13.834(2)$, $c = 18.715(2)$ Å, $\beta = 92.223(3)°$, $V = 2356.8(6)$ Å^3, $Z = 4$, $\rho_{calcd} = 1.409$ g cm^{-3}, $\mu(Mo_{K\alpha}) = 0.203$ mm^{-1}, $F(000) = 1044$, 5860 unique reflections between $2.86° \le 2\theta \le 28.40°$, $T_{max} = 0.96$, $T_{min} = 0.92$, $R_1 = 0.0335$, $R_w = 0.0882$. Intensity data were collected on a Bruker SMART CCD-based X-ray diffractometer ($Mo_{K\alpha} = 0.71073$ Å). The structures were solved by direct methods and refined using the SHELXTL (v6.10 for structures (d) and (e) and v6.12 for all others) software package. All non-hydrogen atoms were refined anisotropically with hydrogen atoms generated at idealized positions and constrained to ride on their parent atoms. CCDC-285005–285013 contain the supplementary crystallographic data for this paper. These data can be obtained free of charge from The Cambridge Crystallographic Data Centre via www.ccdc.cam.ac.uk/data_request/cif.

[12] A. I. Kitaigorodskii, *Organic Chemical Crystallography*, Consultants Bureau, New York, **1961**.

 © 2006 Wiley-VCH Verlag GmbH & Co. KGaA, Weinheim

[13] Packing coefficient is calculated by using the following equation: $C_k = Z V_{mol} V_{cell}^{-1}$, where V_{mol} is the molecular volume (Å^3), V_{cell} is the volume of the unit cell (Å^3), and Z is the number of molecules in the unit cell.
[14] Molecular volume was calculated with Spartan'04 (Wavefunction Inc.), which employs van der Waals radii in the calculation of molecular volume of 1.75 Å for carbon, 1.78 Å for chlorine, 1.30 Å for fluorine, 1.20 Å for hydrogen, 1.55 Å for nitrogen, 1.52 Å for oxygen, and 1.82 Å for sulfur atoms. For the packing efficiency of the crystal structures of sulfathiazole solvates not found in the CSD (see reference [16]) and for disordered solvate structures, models of sulfathiazole and the various solvent molecules were constructed in Spartan '04 and the equilibrium geometry for each was calculated by using molecular mechanics (MMFF). After geometric minimization, the C–H, N–H, and O–H bonds were normalized to 1.083 Å for C–H and 0.983 Å for O–H and N–H and the molecular volume was calculated. A list of the structures that possess disordered solvent molecules can be found in the Supporting Information.
[15] Crystal structures of two-component systems containing organic solvent molecules (liquid under ambient conditions) and possessing 3D coordinates were selected from the CSD for each compound. The C–H, O–H, and N–H bonds in each structure were normalized and the molecular volume was calculated (see reference [14]). CSD reference codes for the structures used in the paper: sulfathiazole, SUTHAZ01, SUTHAZ02, SUTHAZ03, SUTHAZ04, SUTHAZ05, BABYIN, BABYOT, and FURDIF; gossypol, AWEXUV, BEMLOU03, BEMLOU12, CUVKEJ20, CUVKUZ20, CUVLAG10, DUBVUR, GOSPOL01, JEGWAT, JIDROD, JIDTIZ10, JIDTOF01, JIDTOF10, JIDVEX10, JIDWEY01, JINFAN, KIVCAT, LOQSEP, RIDNOH, RIDNUN, VAYJUA, VEVMOY, VEVNUF01, VEVRIX, VEVROD, VEVRUJ, VEVSEU, VEVTOF, VEVVUN01, VEVWUO, VEVXAV, VIGVUC, and YEWMUI; Dianin's compound, BEGSUC, DIANCH, DIANET, DIANHP13, HUSXOI, HUSXUO, HUSYAV, HUSYEZ, HUSYID, HUSYOJ, HUSYUP, HUSZAW, HUSZEA, HUSZIE, OBEQUH, PEPTIN, and SIHJEY01; references for these can be found in the Supporting Information.
[16] For a number of sulfathiazole solvates not found in the CSD, unit-cell constants, and stoichiometry have been reported; see the Supporting Information of reference [6]. The packing coefficients for the acetone, cyclohexanol, cyclohexanone, piperidine, propionitrile, propylene carbonate, sulfolane, and THF solvates were calculated from these data with the caveat that the geometries of both sulfathiazole and the solvent must be assumed, thus making these values somewhat less reliable than those derived from 3D structures. The calculated packing coefficients of these structures range from 0.684 (cyclohexanol) to 0.746 (sulfolane), with an average value of 0.713, which is intermediate to the packing coefficients of the most and least dense polymorphs of sulfathiazole.
[17] J. L. Flippen, J. Karle, I. L. Karle, *J. Am. Chem. Soc.* **1970**, *92*, 3749 – 3754.
[18] L. Pang, E. A. C. Lucken, G. Bernardinelli, *J. Am. Chem. Soc.* **1990**, *112*, 8754 – 8764.
[19] F. Imashiro, M. Yoshimura, T. Fujiwara, *Acta Crystallogr. Sect. C* **1998**, *54*, 1357 – 1360.
[20] G. D. Enright, C. I. Ratcliffe, J. A. Ripmeester, *Mol. Phys.* **1999**, *97*, 1193 – 1196.
[21] J. G. Selbo, J. M. Desper, C. J. Eckhardt, *J. Inclusion Phenom. Macrocyclic Chem.* **2003**, *45*, 73 – 78.
[22] R. W. H. Small, *Acta Crystallogr. Sect. B* **2003**, *59*, 141 – 148.
[23] For rigid molecules, the packing coefficient may be conveniently extracted from the cell parameters and a knowledge of the chemical structure facilitating prescreening studies utilizing only indexed powder X-ray diffraction data.

 © 2006 Wiley-VCH Verlag GmbH & Co. KGaA, Weinheim

Computational Chemistry

DOI: 10.1002/anie.200503833

Genome-Scale Classification of Metabolic Reactions: A Chemoinformatics Approach**

*Diogo A. R. S. Latino and João Aires-de-Sousa**

Dedicated to Professor Johann Gasteiger

Catalytic functions of proteins are generally described by the EC numbers assigned to the catalyzed chemical reactions.[1,2] The EC number is simultaneously employed as an identifier of reactions, enzymes, and enzyme genes, thus linking metabolic and genomic information. Although chemically meaningful and well established, the EC numbers are based on rules that are often ambiguous and heterogeneous among the different types of reactions. Their use for diversity analysis of metabolic reactions (the reactome) is limited. In the context of genome-scale reconstruction of metabolic pathways, the definition of reaction similarity, and the automatic classification of enzymatic reactions in terms of EC numbers, are crucial for the similarity-based proposal of enzyme sequences from their functions.[3–5]

In the last 20 years, several methods for the representation and classification of reactions have been put forward,[6–16] which were mostly based on the physicochemical properties of the reaction center[6–9] or on codes of the reaction center.[3,10–14] Chen and Gasteiger have explored Kohonen neural networks to define a space of chemical reactions on a map, with the physicochemical properties of the reaction center as the numerical representation of the reaction.[15] Recently, the same method was applied to classify the metabolic reactions of subclass EC 3.1 on the basis of the physicochemical properties of the reactants.[16]

Herein, we report mapping of the reactome into a self-organizing map (SOM)[17,18] to classify metabolic reactions, to

[*] D. A. R. S. Latino, Prof. J. Aires-de-Sousa
CQFB and REQUIMTE, Departamento de Química
Faculdade de Ciências e Tecnologia
Universidade Nova de Lisboa
2929-516 Caparica (Portugal)
Fax: (+351) 21-294-8550
E-mail: jas@fct.unl.pt

[**] D.A.R.S.L. acknowledges the Fundação para a Ciência e Tecnologia (Lisbon, Portugal) for financial support under a PhD grant (SFRH/BD/18347). Molecular Networks GmbH (Erlangen, Germany) is acknowledged for access to the PETRA program.

WILEY InterScience DISCOVER SOMETHING GREAT
© 2006 Wiley-VCH Verlag GmbH & Co. KGaA, Weinheim

assign EC numbers from the molecular structures of the substrates and products, and to define a metric in the space of metabolic reactions. Each reaction is represented numerically, without assignment of the reaction center, by the difference between molecular descriptors of the products and the substrates.[19]

The chemical reactivity of a compound is related to its propensity for bond breaking and bond making, which mainly depends on the physicochemical properties of the bonds. Gasteiger et al.[20–22] proposed that seven empirical physicochemical properties are particularly relevant in predicting the reactivity of a chemical bond toward heterolytic cleavage: difference in total charge, difference in π charge, difference in σ electronegativity, bond polarity, resonance stabilization of charges generated by heterolysis, effective bond polarizability, and bond dissociation energy. These encode charge-distribution effects,[23,24] inductive effects,[25] resonance effects,[24] polarizability effects,[26] and bond dissociation energies,[27] and are calculated by empirical procedures implemented in the program PETRA.[28] To use all this information for an entire molecule, and at the same time have a fixed-length representation, we first map all the bonds of a molecule into a Kohonen SOM—a MOLMAP (molecular map of atom-level properties).

A Kohonen SOM distributes objects over a 2D surface (a grid of neurons) in such a way that objects bearing similar features are mapped onto the same or adjacent neurons.[17,18] We trained a 15×15 SOM with a diversity of bonds randomly selected from covering the chemical space of the metabolic compounds, each bond described by the above-mentioned seven physicochemical properties. Then the bonds of one molecule were submitted to the trained SOM (SOM A in Scheme 1), each bond activating one neuron. The pattern of activated neurons is a map of reactivity features of that molecule (MOLMAP)—a fingerprint of the bonds available in the structure.[19] For easier computational processing, the pattern of activated neurons is encoded numerically. Each neuron is given a value equal to the number of times it was activated by bonds of the molecule. The map (a matrix) is then transformed into a vector by concatenation of columns

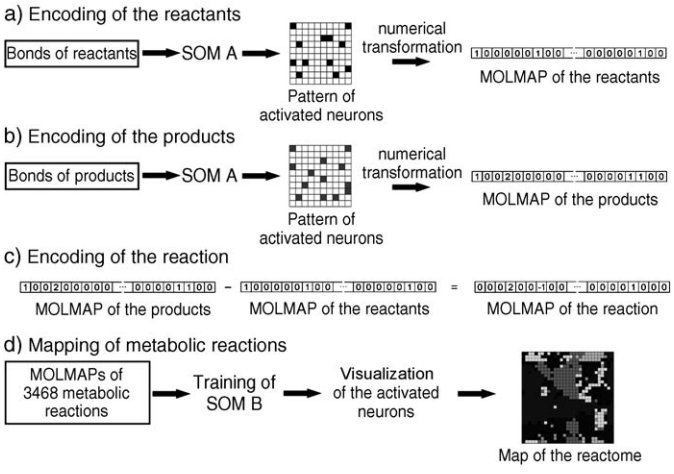

Scheme 1. Simplified illustration of the procedure used to encode a reaction (a–c), and to classify metabolic reactions (d).

(Scheme 1 a,b). To focus on functional groups, only bonds that involve a heteroatom, or an atom of a π system, were considered.

The difference between the MOLMAP of the products and the MOLMAP of the reactants is a descriptor of the reaction and represents the structural changes operated by the reaction. It can be interpreted as a fingerprint of the reaction[19] and was used in this work as a numerical code of the reaction (Scheme 1 c). The procedure for the generation of the MOLMAP reaction descriptors, and for reaction classification, is fully described in reference [19].

A dataset of 3468 reactions was extracted from the KEGG LIGAND database of enzymatic reactions (release of July 2005),[29–32] which consists of the reactions catalyzed by 1105 oxidoreductases, 1098 transferases, 622 hydrolases, 335 lyases, 172 isomerases, and 136 ligases. The selected dataset excluded reactions listed with more than one EC number, an incomplete EC number, or no assigned EC number. Reactions involving a compound not accepted by PETRA, as well as unbalanced reactions, were also excluded.

The reaction descriptors (MOLMAPs of the reactions) were calculated for all the reactions, and the relationship between the descriptors and the EC numbers was investigated with a new SOM (SOM B in Scheme 1 d). It must be emphasized that this SOM is independent of the SOM defined for the generation of MOLMAPs (SOM A in Scheme 1). The objects presented to SOM A are bonds, whereas the objects presented to the new SOM B are reactions. After training SOM B with the 3468 reactions, the neurons were colored according to the classes of the reactions that activated them. The resulting map (Figure 1) shows a remarkable clustering of the reactions according to the EC classification, with the three most populated classes showing the best clustering: oxidoreductases, transferases, and hydrolases. Ligases also exhibited good clustering.

The zooms in Figure 1 illustrate how the reactions were clustered in terms of the first three digits. For most of the map, the majority of the reactions activating the same neuron shared the first three EC digits.[33] Neuron H,23 (Figure 1) was activated by a reaction catalyzed by uracilylalanine synthase, which was listed in the database as EC 4.2.99.16 (a lyase). However, the neighbors of that neuron were assigned either to the transferase or the oxidoreductase classes. Interestingly, the EC number of this enzyme was transferred in 2002 to EC 2.5.1.53 (a transferase),[34,35] and only the September 2005 release of KEGG incorporated this change in the reaction file. A different case is the reaction catalyzed by 17α-hydroxyprogesterone aldolase, listed as EC 4.1.2.30 but exciting neuron K,18 in the middle of an oxidoreductase region. Significantly, this reaction involves the oxidation of nicotinamide adenine dinucleotide phosphate (NADPH) to $NADP^+$. All the reactions mapped into adjacent neurons are catalyzed by oxidoreductases and involve $NADP^+$ and NADPH. In 405 reactions involving oxidation/reduction of NADPH/$NADP^+$, only 11 are not officially classified as oxidoreductases.

The examples illustrate a new way to analyze relationships between reactions in genome-scale databases of metabolic transformations, to detect similarities not revealed by EC

 © 2006 Wiley-VCH Verlag GmbH & Co. KGaA, Weinheim

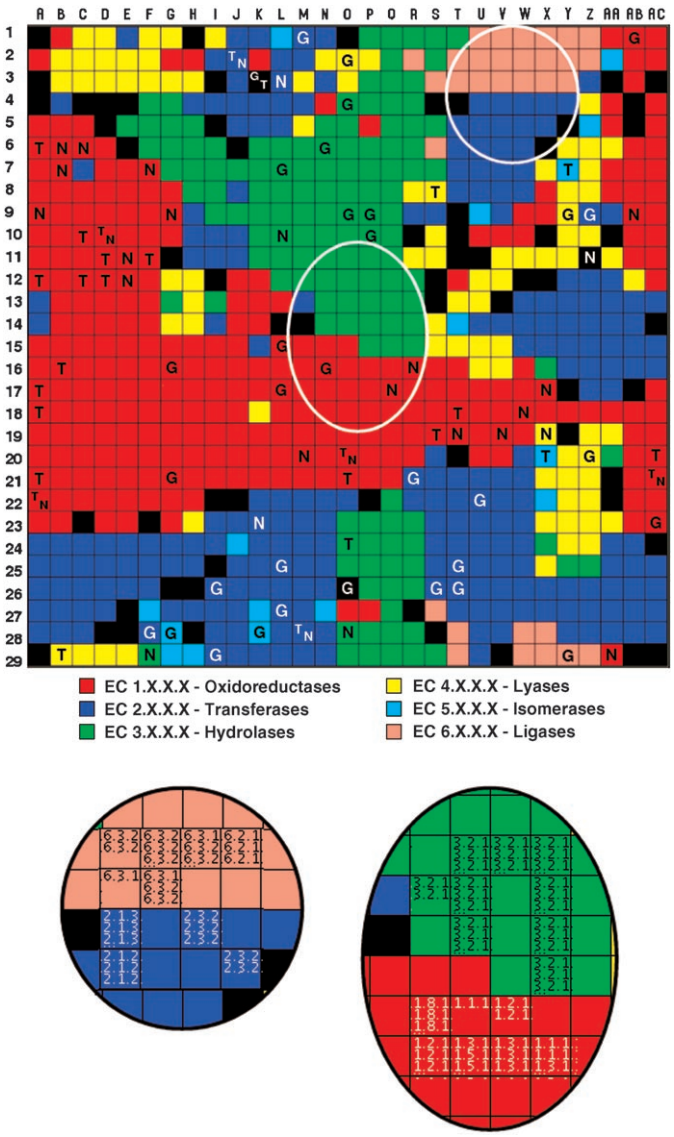

Figure 1. SOM of the reactome and its relationship with EC numbers. The ambiguous neurons were colored with black. The neurons activated by reactions of three different metabolic pathways are highlighted (G glycolysis/glyconeogenesis, N nitrobenzene degradation, T toluene and xylene degradation).

numbers, and to identify problematic classifications in terms of EC number.

With the wide range of biochemical reactions defined by the SOM of Figure 1, the analysis and comparison of metabolic pathways are also possible. This is demonstrated by mapping all the reactions from three different pathways—glycolysis/gluconeogenesis, nitrobenzene degradation, and toluene and xylene degradation—onto the same map (Figure 1). The pattern of neurons activated by glycolysis/gluconeogenesis reactions is significantly distinct from the other two, not only because different regions are involved, but also because different classes are preferred. For example, transferases and hydrolases are dominant in glycolysis/gluconeogenesis, whereas oxidoreductases are preferred by the two metabolic pathways of xenobiotics (which overlap considerably). This finding is in agreement with the well-known biological strategy of metabolizing aromatic compounds through oxidation. Neuron D,10 is an example of a neuron activated by reactions from the two pathways of xenobiotics: oxidation of 3-hydroxytoluene to 2,3-dihydroxytoluene and oxidation of phenol to catechol. Both are catalyzed by phenol 2-monooxygenase (EC 1.14.13.7).

To evaluate the ability of MOLMAPs to predict the entire EC number, experiments were performed with Random Forests.[36,37] A Random Forest is an ensemble of unpruned classification trees created by using random subsets (bootstrap samples) of the training data and random subsets of variables to define the best split at each node. It is a high-dimensional nonparametric method that works well on large numbers of variables. Prediction is made by majority vote of the individual trees. Performance is internally assessed with the prediction error for the objects left out in the bootstrap procedure. Herein, Random Forests were grown with the R program version 2.0.1[38] using the randomForest library.[39] Prediction of the EC number was obtained from the MOLMAPs of the reactions with accuracies of 94% for the first digit (six classes), 87% for the first two digits (53 subclasses), and 76% for the first three digits (140 subsubclasses) in the standard Random Forest cross-validation procedure. For the prediction of the entire EC number, a Random Forest was trained with reactions whose EC numbers were common to more than three cases (582 reactions with 110 different EC numbers). The full EC numbers were then correctly predicted for 82% of an independent test set with 110 reactions (one for each EC number present in the training set).

In conclusion, the results demonstrate the ability of MOLMAPs to classify metabolic reactions, and show a general compatibility between the new scheme and the EC classification. They open the way to a host of new investigations on the diversity analysis of metabolic reactions and comparison of metabolic pathways.

Received: October 31, 2005
Published online: February 24, 2006

Keywords: bioinformatics · chemoinformatics · computer chemistry · enzymes · metabolism

[1] K. Tipton, S. Boyce, *Bioinformatics* **2000**, *16*, 34–40.
[2] A. J. Barrett, C. R. Canter, C. Liebecq, G. P. Moss, W. Saenger, N. Sharon, K. F. Tipton, P. Vnetianer, V. F. G. Vliegenthart, *Enzyme Nomenclature*, Academic Press, San Diego, CA, **1992**.
[3] M. Kotera, Y. Okuno, M. Hattori, S. Goto, M. Kanehisa, *J. Am. Chem. Soc.* **2000**, *126*, 16487–16498.
[4] V. Hatzimanikatis, C. Li, J. A. Ionita, L. J. Broadbelt, *Curr. Opin. Struct. Biol.* **2004**, *14*, 300–306.
[5] W. Tian, J. Skolnick, *J. Mol. Biol.* **2003**, *333*, 863–892.
[6] L. Chen in *Handbook of Chemoinformatics, Vol. 1* (Eds.: J. Gasteiger, T. Engel), Wiley-VCH, Weinheim, **2003**, pp. 348–388.
[7] J. R. Rose, J. Gasteiger, *J. Chem. Inf. Comput. Sci.* **1994**, *34*, 74–90.
[8] L. Chen, J. Gasteiger, *J. Am. Chem. Soc.* **1997**, *119*, 4033–4042.

 © 2006 Wiley-VCH Verlag GmbH & Co. KGaA, Weinheim

[9] H. Satoh, O. Sacher, T. Nakata, L. Chen, J. Gasteiger, K. Funatsu, *J. Chem. Inf. Comput. Sci.* **1998**, *38*, 210 – 219.
[10] T. E. Moock, D. L. Grier, W. D. Hounshell, G. Grethe, K. Cronin, J. G. Nourse, J. Theodosiau, *Tetrahedron Comput. Methodol.* **1988**, *1*, 117 – 128.
[11] S. Fujita, *J. Chem. Inf. Comput. Sci.* **1986**, *26*, 205 – 212.
[12] S. S. Tratch, N. S. Zefirov, *J. Chem. Inf. Comput. Sci.* **1998**, *38*, 349 – 366.
[13] For Classify—The InfoChem Classification Program V. 2.5, see http://www.infochem.de/eng/downloads/Classify.pdf.
[14] J. B. Hendrickson, *J. Chem. Inf. Comput. Sci.* **1997**, *37*, 852 – 860.
[15] L. Chen, J. Gasteiger, *Angew. Chem.* **1996**, *108*, 844 – 846; *Angew. Chem. Int. Ed. Engl.* **1996**, *35*, 763 – 765.
[16] J. Gasteiger, M. Reitz, O. Sacher, *Proceedings of the Beilstein Institut Symposium "The Chemical Theatre of Biological Systems"*, Bozen, Italy, **2004**.
[17] T. Kohonen, *Self-Organization and Associative Memory*, Springer, Berlin, **1988**.
[18] J. Zupan, J. Gasteiger, *Neural Networks in Chemistry and Drug Design*, Wiley-VCH, Weinheim, **1999**.
[19] Q.-Y. Zhang, J. Aires-de-Sousa, *J. Chem. Inf. Model.* **2005**, *45*, 1775 – 1783.
[20] V. Simon, J. Gasteiger, J. Zupan, *J. Am. Chem. Soc.* **1993**, *115*, 9148 – 9159.
[21] J. Gasteiger, *Mini Rev. Med. Chem.* **2003**, *3*, 789 – 796.
[22] J. Gasteiger, M. Marsili, M. G. Hutchings, H. Saller, P. Low, K. Rafeiner, *J. Chem. Inf. Comput. Sci.* **1990**, *30*, 467 – 476.
[23] J. Gasteiger, M. Marsili, *Tetrahedron* **1980**, *36*, 3219 – 3228.
[24] H. Saller, J. Gasteiger, *Angew. Chem.* **1985**, *97*, 699 – 701; *Angew. Chem. Int. Ed. Engl.* **1985**, *24*, 687 – 689.
[25] H. G. Hutchings, J. Gasteiger, *Tetrahedron Lett.* **1983**, *24*, 2541 – 2544.
[26] H. G. Hutchings, J. Gasteiger, *J. Chem. Soc. Perkin Trans. 2* **1984**, 559 – 564.
[27] J. Gasteiger, *Tetrahedron* **1979**, *35*, 1419 – 1426.
[28] The program PETRA can be tested on the website http://www2.chemie.uni-erlangen.de/software/petra and is developed by Molecular Networks GmbH, http:www.mol-net.de.
[29] M. Kanehisa, *Trends Genet.* **1997**, *13*, 375 – 376.
[30] M. Kanehisa, S. Goto, S. Kawashima, Y. Okuno, M. Hatori, *Nucleic Acids Res.* **2004**, *32*, D277 – D280.
[31] S. Goto, T. Nishioka, M. Kanehisa, *Bioinformatics* **1998**, *14*, 591 – 599.
[32] M. Kanehisa, S. Goto, *Nucleic Acids Res.* **2000**, *28*, 27 – 30.
[33] The method exhibited robustness in relation to the selected physicochemical bond properties. For example, an experiment using the above-mentioned properties, except bond dissociation energy and resonance stabilization of charges generated by heterolysis, yielded essentially the same results.
[34] http://www.chem.qmul.ac.uk/iubmb/enzyme/EC4/2/99/16.html.
[35] http://www.chem.qmul.ac.uk/iubmb/enzyme/EC2/5/1/53.html.
[36] L. Breiman, *Mach. Learn.* **2001**, *45*, 5 – 32.
[37] V. Svetnik, A. Liaw, C. Tong, J. C. Culberson, R. P. Sheridan, B. P. Feuston, *J. Chem. Inf. Comput. Sci.* **2003**, *43*, 1947 – 1958.
[38] R Development Core Team, *R: A Language and Environment for Statistical Computing*, R Foundation for Statistical Computing, Vienna, **2004**. ISBN 3-900051-07-0, http://www.R-project.org.
[39] Fortran original by L. Breiman and A. Cutler; R port by A. Liaw and M. Wiener, **2004**. http://www.stat.berkeley.edu/users/breiman/.

 © 2006 Wiley-VCH Verlag GmbH & Co. KGaA, Weinheim

Computational Chemistry

DOI: 10.1002/anie.200504039

Effects of Intramolecular Hydrogen Bonding on the Ionization Energies of Proline**

Shan Xi Tian and Jinlong Yang*

Understanding the nature of inter- and intramolecular H-bonding is the focus of extensive research in the fields of chemistry and biochemistry because the thermodynamics and kinetics of many chemical and biochemical systems are determined to a large degree by H-bonding.[1] Structural information regarding the intermolecular H-bonding in complexes can be obtained from various spectroscopic experiments,[1] and the energetics can be predicted within a supermolecular, high-level ab initio approach. Although the nature of the intramolecular H-bonding is the same as for the intermolecular H-bonding, the evaluation of the intramolecular H-bonding energy has been challenging both experimentally and theoretically because intramolecular H-bonding is an intrinsic feature of the molecule involved.[1,2] Ionization energies (IEs) are important data for understanding the charge transfer, electrophilicity, and for modification of the diverse reactivity patterns of biological molecules.[1] Experimental studies indicate that the IE of a lone-pair orbital (n) of the H-bonding molecule is usually higher than that of the molecule without (or with very weak) intramolecular H-bonds,[3] and the excitation transition energy of the lone-pair orbital for the solvated molecule frequently differs from that for the free molecule in the gas-phase.[4] The effects of intramolecular H-bonding on the IEs are difficult to determine by ultraviolet photoelectron spectroscopy (UPS) because of the coexistence of several conformers.[5,6] For amino acids, both intramolecular H-bonding and intermolecular interactions play a role in protein folding and peptide assembly.[1] The IE values of isolated amino acids and their derivatives have been obtained by gas-phase UPS experiments.[5] Herein, we provide the first assignment of the UP spectrum of proline[5] based on ab initio electron-propagator theory[7] combined with natural bond orbital (NBO)[8] analyses and show that intramolecular H-bonding has a strong

[*] Prof. Dr. S. X. Tian, Prof. Dr. J. Yang
Hefei National Laboratory for Physical Sciences at Microscale
Department of Chemical Physics
University of Science and Technology of China
Hefei, Anhui 230026 (China)
Fax: (+86) 551-360-2969
E-mail: sxtian@ustc.edu.cn

[**] This work was partially supported by the NSFC (20503026, 20533030, and 50121202), the Virtual Laboratory for Computational Chemistry of CNIC, and the Supercomputing Center of CNIC, Chinese Academy of Sciences. We thank Prof. J. V. Ortiz at Kansas State University for helpful discussions.

Supporting information for this article is available on the WWW under http://www.angewandte.org or from the author.

© 2006 Wiley-VCH Verlag GmbH & Co. KGaA, Weinheim

influence on the electronic structure, and therefore the IEs, of proline.

Proline usually forms a kink as the β- or γ-turn in the peptides,[9] and it is a favorite organocatalyst for asymmetric synthesis.[10] These features depend strongly on the properties of the isolated species. Theoretical studies showed that four proline conformers (due to the carboxy *cis* and *trans* orientations and pyrrolidine ring puckering, labeled **Ia**, **Ib**, **IIa**, and **IIb** in Figure 1) have notable populations at low and moderate temperatures;[11] this result was supported by rovibrational spectroscopy experiments.[12] Conformers of types **I** and **II** have populations around 63 and 37%, respectively, according to the high-level calculations[11,12b] and supposing Boltzmann distributions at 430 K (see Supporting Information). The low-resolution He II UP spectrum of proline[5] has not been theoretically analyzed until now. In particular, it is unclear whether the two peaks in the first band[5] correspond to two cationic states of the most stable conformer or arise from pyrrolidine ring puckering or the variance in the intramolecular H-bonding strengths of *cis* and *trans* conformers.

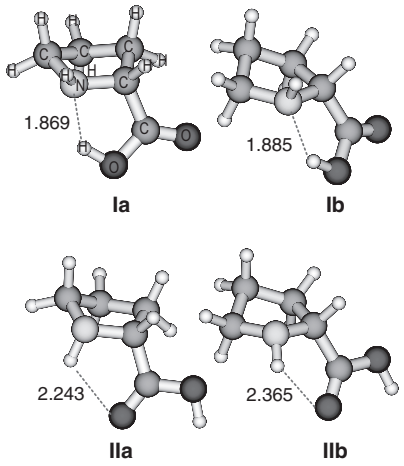

Figure 1. Proline conformers with their intramolecular H-bond lengths [Å].

While the density functional method does not provide reliable values for the relative energies of proline conformers, it can be used to predict structures and infrared vibrational frequencies that are in good agreement with the experimental observations.[12b] We optimized the geometrical parameters of **Ia**, **Ib**, **IIa**, and **IIb** by the hybrid density functional B3LYP method[13] using Dunning's aug-cc-pVDZ basis set.[14] The vertical IE values were calculated according to electron-propagator theory in the partial third-order (P3) approximation,[7] where a Dyson orbital (an integral of the wave functions between the neutral and cationic states) is proportional to a canonical Hartree–Fock orbital.[7] This method gives an average absolute error of less than 0.2 eV for the IEs below 20 eV.[7,15]

Table 1 shows the excellent agreement between the calculated IE values and the energies of the peak positions observed in the UP spectrum.[5] The small calculated IE difference (ca. 0.1 eV) for the HOMOs of **Ia** and **Ib** (or **IIa** and **IIb**) demonstrates that pyrrolidine ring puckering cannot lead to the peak split (0.5 eV) of the first band in the UP spectrum.[5] It is somewhat surprising that for conformers of types **I** and **II** distinctly different IE_{HOMO} values are calculated. According to the Dyson orbital plots with contour values of ± 0.03 shown in Figure 2a, two HOMOs are characterized as the lone-pair orbitals of N atoms (n_N). Thus, two peaks with a splitting of 0.5 eV[5] can be ascribed to the different energy levels of HOMOs (n_N) of the respective conformers, which means that the peak observed at IE = 9.0 eV is mainly due to the HOMOs of conformers **IIa** and **IIb**, while the next peak at IE = 9.5 eV is due to those of conformers **Ia** and **Ib**. The calculated IE_{HOMO} for **Ia** (or **Ib**) is 0.58 eV (or 0.81 eV) higher than that for **IIa** (or **IIb**), in agreement with the experimental peak split (0.5 eV).

Table 1: Calculated vertical IEs [eV] in comparison with experimental data.

	Ia	Ib	IIa	IIb	Exptl[a]
n_N			8.83	8.71	9.0
	9.41	9.52			9.5
n_O	10.51	10.45	10.67	10.62	10.6
π_{CO}	11.15	11.17	11.86	11.95	11.6
σ_{CC}	12.25	12.34	12.04	11.97	12.0

[a] Taken from the He II UP spectrum in reference [5].

The vertical IE_{HOMO} can be evaluated as the difference between the total energies of the neutral and cationic species at the neutral equilibrium structure. Intramolecular H-bonding will enhance the stabilities of both the neutral and cationic species, perhaps leading to more negative total energies. To elucidate the distinctly different IE_{HOMO} values for these two types of conformers, the intramolecular H-bonding strengths were compared in detail. The NBO analysis transforms the delocalized MOs into localized ones that are closely tied to chemical-bond concepts.[8] The H-bonding interaction can be treated by the second-perturbation energy, $E(2) = -n_\sigma F_{ij}^2/\delta\varepsilon$,[8,16] where F_{ij} is the Fock matrix between the unperturbed occupied lone pair (n) and unoccupied antibonding OH or NH natural orbitals (σ*) of proline, n_σ is the lone-pair orbital population, and $\delta\varepsilon$ is the energy difference between the unperturbed n and σ* orbitals.

The NBO analyses for the neutral conformers (**Ia**, **Ib**, **IIa**, and **IIb**) and their vertical ionized cations ($\mathbf{Ia}^+$, $\mathbf{Ib}^+$, $\mathbf{IIa}^+$, and $\mathbf{IIb}^+$) are given in Table 2. In NBO theory, the energy level of the n orbital involved in the H-bonding is lowered and its electron distribution becomes delocalized due to the perturbation of the n→σ* interaction. For example, as shown in Figure 2a, the energy level of the unperturbed n_O orbital is slightly lowered by 0.08 eV to form the next HOMO (HOMO−1, the perturbed n_O orbital) of **IIa** because of the weak N−H···O bond; the energy-level of the unperturbed n_N orbital is significantly lowered by 0.78 eV to form the HOMO (perturbed n_N orbital) of **Ia** because of the strong O−H···N bond. The H-bond distances of O−H···N are 1.869 and 1.885 Å (Figure 1), while the N−H···O distances are much longer. It is known for neutral proline that the O−H···N bonds are much stronger than the N−H···O bonds, as derived from

 © 2006 Wiley-VCH Verlag GmbH & Co. KGaA, Weinheim

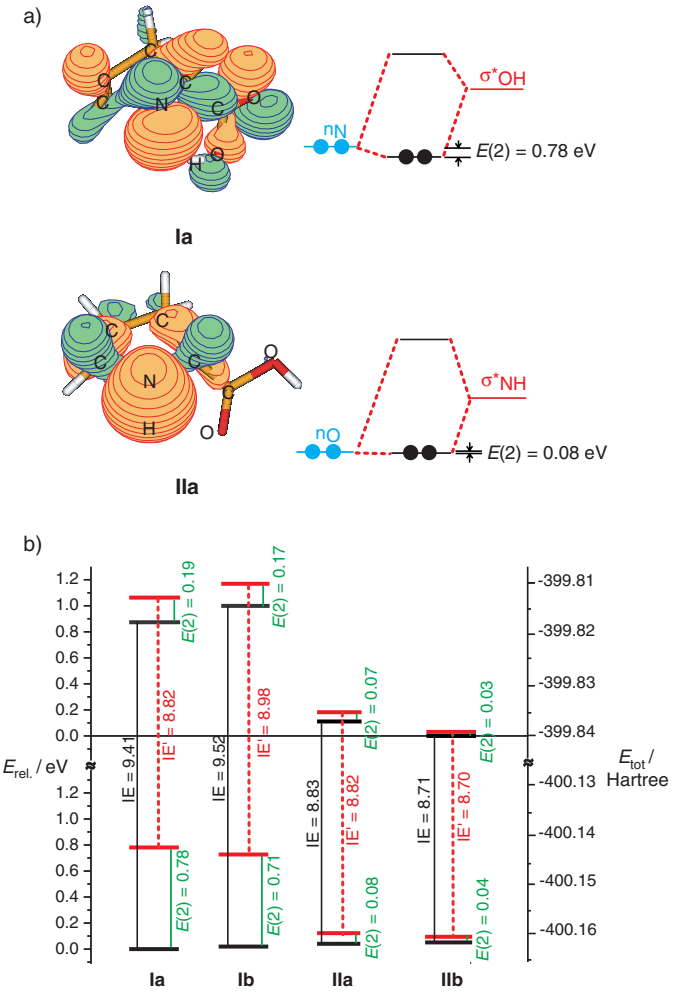

Figure 2. a) Dyson orbital plots of the HOMOs of **Ia** and **IIa**, and $E(2)$ values for their intramolecular H-bonding interactions. The unperturbed energy levels are shown in blue and red, the perturbed (real) levels are shown in black. b) The relationship among the IE_{HOMO}, IE'_{HOMO}, and $E(2)$ values (top row: cations, bottom row: neutral species). The perturbed energy levels are shown in black, the unperturbed levels in red; $IE_{HOMO} = IE'_{HOMO} + \Delta E(2)$; $\Delta E(2) = E(2)$-(neutral) $- E(2)$ (cation).

Table 2: NBO analyses of the intramolecular H-bonds in the neutral and cationic species.[a]

	$E(2)$ [kcal mol^{-1}]	$\delta\varepsilon$ [au]	F_{ij} [au]
Ia: $n_N \rightarrow \sigma^*_{OH}$	18.01	1.14	0.130
Ib: $n_N \rightarrow \sigma^*_{OH}$	16.31	1.16	0.124
IIa: $n_O \rightarrow \sigma^*_{NH}$	1.88	1.16	0.043
IIb: $n_O \rightarrow \sigma^*_{NH}$	1.01	1.16	0.041
Ia$^+$: $n_N \rightarrow \sigma^*_{OH}$	4.37	1.39	0.099
Ib$^+$: $n_N \rightarrow \sigma^*_{OH}$	3.92	1.41	0.094
IIa$^+$: $n_O \rightarrow \sigma^*_{NH}$	1.64	1.30	0.037
IIb$^+$: $n_O \rightarrow \sigma^*_{NH}$	0.72	1.05	0.035

[a] With the neutral equilibrium structures.

analysis of the electron densities, ρ, at the H-bond critical points.[11b] In Table 2, the intramolecular O–H···N bonds in **Ia**$^+$ and **Ib**$^+$ are found to be stronger than those in **IIa**$^+$ and **IIb**$^+$. Moreover, the O–H···N bond strength in the neutral species ($E(2) = 0.78$ eV for **Ia** and 0.71 eV for **Ib**) decreases dramatically after ionization ($E(2) = 0.19$ eV for **Ia**$^+$ and 0.17 eV for **Ib**$^+$), while the N–H···O bond strengths are similar for the neutral and cationic type-**II** conformers. The natural atomic charge analyses in the Supporting Information are in line with the above scenario.

If the $E(2)$ values are approximated to be the contributions of H-bonding stabilization to the total energies of the species, the relationship between the calculated IE_{HOMO}, IE'_{HOMO} (the ionization energies excluding the H-bonding stabilizations), and $E(2)$ values (both of the neutral and cationic species) can be determined (Figure 2b). The IE'_{HOMO} values are estimated to be 8.82, 8.98, 8.82, and 8.70 eV for **Ia**, **Ib**, **IIa**, and **IIb**, respectively. Without the effects of the O–H···N or N–H···O interactions, the IE'_{HOMO} values are appealingly close to the $IE_{HOMO(n_N)}$ (ca. 8.8 eV) of pyrrolidine.[17] The $E(2)$ changes ($\Delta E(2)$) from the neutral species to the cations are 0.59, 0.54, 0.01, and 0.01 eV for **Ia**, **Ib**, **IIa**, and **IIb**, respectively. The $\Delta E(2)$ differences between **Ia** and **IIa**, and between **Ib** and **IIb**, are 0.58 and 0.53 eV, respectively. The calculated IE_{HOMO} differences—0.58 eV between **Ia** and **IIa** and 0.81 eV between **Ib** and **IIb**—can be explained from the above $\Delta E(2)$ differences. If the small $E(2)$ values of the cations are omitted in the above calculations, the calculated IE_{HOMO} differences are approximately the $E(2)$ differences for the neutral species, that is, 0.70 eV between **Ia** and **IIa** and 0.67 eV between **Ib** and **IIb**.

The effect of intramolecular H-bonding on the IE_{HOMO} of **Ia** was further examined with P3 calculations by scanning the value for the H-O-C-N dihedral angle of **Ia** while keeping the residual geometrical parameters fixed. It can be seen from Figure 3 that $IE(n_N)$ decreases while $IE(n_O)$ remains almost constant when the H atom in the carboxy group leaves the H-O-C-N plane. The strong O–H···N bond disappears completely at a H-O-C-N dihedral angle around 95°, which gives an energy of about 0.75 eV for this intramolecular H-bond.

In general, strong intramolecular H-bonds lead to higher IEs for related MOs (e.g., the lone-pair orbitals), as was explained by the NBO analyses. The present theoretical approach could elucidate the effects of both inter- and intramolecular H-bonding on the electronic structures and

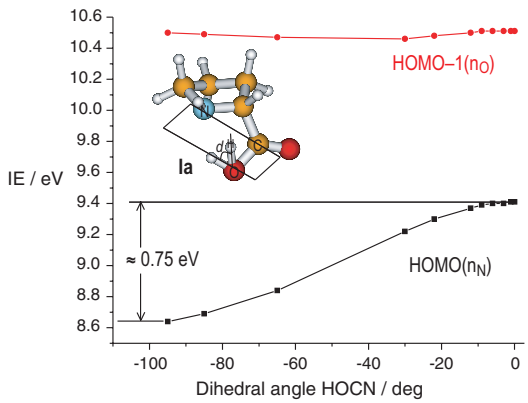

Figure 3. Variation of IE values when scanning the H-O-C-N dihedral angle in **Ia**.

© 2006 Wiley-VCH Verlag GmbH & Co. KGaA, Weinheim

related properties of other species. Furthermore, the different IE_{HOMO} values tuned by the strong H-bonding interactions profoundly affect charge transfer in biological systems since the IE_{HOMO} is closely related to the molecular chemical potential and the electrophilicity index.[18]

Received: November 14, 2005
Published online: February 22, 2006

Keywords: ab initio calculations · amino acids · hydrogen bonds · ionization potentials · photoelectron spectroscopy

[1] G. A. Jeffrey, *An Introduction to Hydrogen Bonding*, Oxford University Press, New York, **1997**.
[2] M. Davies, D. M. L. Griffiths, *J. Chem. Soc.* **1955**, 132.
[3] S. X. Tian, *J. Chem. Phys.* **2005**, *123*, 244310.
[4] C. E. Crespo-Hernandez, B. Cohen, P. M. Hare, B. Kohler, *Chem. Rev.* **2004**, *104*, 1977.
[5] P. H. Cannington, N. S. Ham, *J. Electron Spectrosc. Relat. Phenom.* **1983**, *32*, 139.
[6] Y. Zheng, J. J. Neville, C. E. Brion, *Science* **1995**, *270*, 786.
[7] J. V. Ortiz, *J. Chem. Phys.* **1996**, *104*, 7599.
[8] A. E. Reed, L. A. Curtiss, F. Weinhold, *Chem. Rev.* **1988**, *88*, 899.
[9] J. S. Richardson, D. C. Richardson, *Science* **1988**, *240*, 1648.
[10] C. Pidathala, L. L. Hoang, N. Vignola, B. List, *Angew. Chem.* **2003**, *115*, 2891; *Angew. Chem. Int. Ed.* **2003**, *42*, 2785.
[11] a) E. Czinki, A. G. Császár, *Chem. Eur. J.* **2003**, *9*, 1008; b) W. D. Allen, E. Czinki, A. G. Császár, *Chem. Eur. J.* **2004**, *10*, 4512.
[12] a) A. Lesarri, S. Mata, E. J. Cocinero, S. Blanco, J. C. Lopez, J. L. Alonso, *Angew. Chem.* **2002**, *114*, 4867; *Angew. Chem. Int. Ed.* **2002**, *41*, 4673; b) S. G. Stepanian, I. D. Reva, E. D. Radchenko, L. Adamowicz, *J. Phys. Chem. A* **2001**, *105*, 10664.
[13] a) C. Lee, W. Yang, R. G. Parr, *Phys. Rev. B* **1988**, *37*, 785; b) A. D. Becke, *J. Chem. Phys.* **1993**, *98*, 5648.
[14] T. H. Dunning, Jr., *J. Chem. Phys.* **1989**, *90*, 1007.
[15] Ab initio calculations were performed with Gaussian 98: Gaussian 98, Revision A.10, M. J. Frisch, et al. Gaussian, Inc., Pittsburgh PA, **2001**.
[16] E. D. Glendening, A. E. Reed, J. E. Carpenter, F. Weinhold, *NBO, Version 3.1.*.
[17] D. H. Aue, H. M. Webb, M. T. Bowers, *J. Am. Chem. Soc.* **1976**, *98*, 311.
[18] R. G. Parr, L. v. Szentpály, S. Liu, *J. Am. Chem. Soc.* **1999**, *121*, 1922.

 © 2006 Wiley-VCH Verlag GmbH & Co. KGaA, Weinheim

Self-Assembly

DOI: 10.1002/anie.200504192

A Selectivity-Driven Supramolecular Polymerization of an AB Monomer**

Oren A. Scherman, G. B. W. L. Ligthart, Rint P. Sijbesma, and E. W. Meijer**

In memory of Wallace H. Carothers

Since Carothers published his influential review on polymerization 75 years ago,[1] the formation of condensation polymers from AA, BB, and AB functionalized monomers has stood as a pillar of polymer science. The ability to achieve high-molecular-weight polymers through this route, however, is linked to reaction conversion, monomer purity, and, hence, reaction stoichiometry.[2] Condensation polymers formed in this manner are static, nonreversible materials. Over the last decade, however, there has been a growing interest in producing dynamic, reversible materials through self-assembly. The use of multiple hydrogen-bonded units[3,4] has been exploited in the self-assembly of supramolecular polymers as the association constant and dynamics between the subunits can be tuned.[5–7]

Supramolecular chemistry has produced several dynamic materials from AA + BB ditopic molecules with complementary hydrogen-bonding functionalities.[4,8] The close analogy with condensation polymerization implies also here that purity, stoichiometry, and conversion (determined by the association constant between A and B groups) strongly limit the degree of polymerization (DP). In the past, we have addressed two of those limitations (conversion and balancing stoichiometry) by using self complementarity and a very strong quadruple hydrogen-bonding motif based on 2-ureido-4-[1*H*]-pyrimidinone (UPy; $K_{dim} = 6 \times 10^7\,\text{M}^{-1}$ in $CHCl_3$).[3,9] These features allow simple AA monomers to produce supramolecular homopolymers with DPs controlled by concentration and temperature.[4] Recently, it was also found that the UPy unit is able to selectively form strong heterodimers in one of its tautomeric forms through a hydrogen-bonding

[*] Dr. O. A. Scherman, G. B. W. L. Ligthart, Dr. R. P. Sijbesma, Prof. Dr. E. W. Meijer
Laboratory of Macromolecular and Organic Chemistry
Eindhoven University of Technology
P.O. Box 513, 5600 MB Eindhoven (The Netherlands)
Fax: (+31) 40-245-1036
E-mail: r.p.sijbesma@tue.nl
e.w.meijer@tue.nl

[**] We thank the NSF (MPS-DRF Award CHE-0401407 for O.A.S.) and NWO (G.B.W.L.L.) for financial support and especially Haruki Ohkawa and Joost van Dongen for extensive efforts in recycling gel-permeation chromatography. This communication is dedicated to the 75th anniversary of the review by Wallace H. Carothers on polymerization.

Supporting information for this article is available on the WWW under http://www.angewandte.org or from the author.

© 2006 Wiley-VCH Verlag GmbH & Co. KGaA, Weinheim

acceptor-donor-donor-acceptor (ADDA) array with a complementary DAAD array of 2,7-diamido-1,8-naphthyridines[10,11] (Napys; Scheme 1a). The dual complexation modes of UPy result in *concentration-dependent selectivity* favoring UPy–Napy heterocomplexation over UPy homodimerization by a factor of $>20{:}1$ above 0.1 M ($K_a = 5 \times 10^6\ M^{-1}$ in $CHCl_3$).[12] Hence, well-defined supramolecular block copolymers from AA and BB type monomers were obtained. Nevertheless, the limitation of stoichiometric imbalance persists.

An alternative way to address this limitation is to use AB-type monomers that also introduce directionality into the main chain. For application in molecular devices, such monomers would be important as they allow for the directional growth of supramolecular polymers from solid surfaces.[13,14] For a variety of reasons, few reports have focused on the supramolecular polymerization properties, including low binding constants[8,15–17] and/or low solubilities,[18,19] of AB monomers that have limited DPs to less than 10. To be exploited as materials based on supramolecular polymers possessing higher DPs, strong hydrogen bonding between the A and B units is a prerequisite. Therefore, the UPy–Napy system seems eminently suitable to explore the directional growth of supramolecular AB polymers. Herein, we introduce the synthesis of a UPy–Napy monomer through selective olefin cross metathesis and evaluate its dynamics as a function of concentration in a selectivity driven ring-opening polymerization.

Synthesis of the AB material was designed to be both modular and based on linking chemistry that would not interfere with hydrogen bonding. Therefore, a convergent coupling approach using selective olefin-metathesis chemistry was chosen (Scheme 1b).[20] The linker unit was designed to ensure a transition from cyclic to linear species at a practical critical polymerization concentration (CPC),[21] which is determined by chain length and the presence of ring strain.[22,23] For a flexible linker of 20 atoms, a CPC of <100 mM is predicted. UPy acrylate **1** and Napy olefin **2**[24] were synthesized on a multigram scale and purified by column chromatography. When **1** was used in excess (1.25–2 equiv) of **2** in combination with the functional-group tolerant second-generation Grubbs catalyst, product **3** was obtained exclusively. The formation of any Napy–Napy or UPy–UPy homocoupled product was completely suppressed.

Yields varied from 50 to 97% and were highly dependent on the reaction conditions. Conventional heating in benzene or CH_2Cl_2 over a 24-h period led to conversions that were as high as 80%. Unexpectedly, the use of microwave heating[25–27] allowed for a simultaneous decrease in the amount of **1** necessary as well as increased conversion in considerably less time, subsequently leading to conversions that were as high as 97% in as little as 60 minutes (Table 1). Purification of product **3** was critical as any remaining monofunctional **1** or **2**

Table 1: Selective cross metathesis of **1** and **2** under varied reaction conditions.

Entry	Concentration [mM]	Catalyst [mol%]	[**1**]/[**2**]	*t*	Yield [%]
1[a]	50	9.5	2.1	24 h	55
2[b]	60	5	1.8	24 h	80
3[c]	60	3	1.3	30 min	68
4[c]	60	13	1.3	30 min	91
5[c]	83	6	1.3	45 min	91
6[c]	96	6	1.3	60 min	97

[a] Conventional heating, CH_2Cl_2, reflux in oil bath. [b] Conventional heating, C_6D_6, 50 °C. [c] Microwave heating, CH_2Cl_2, 55 °C.

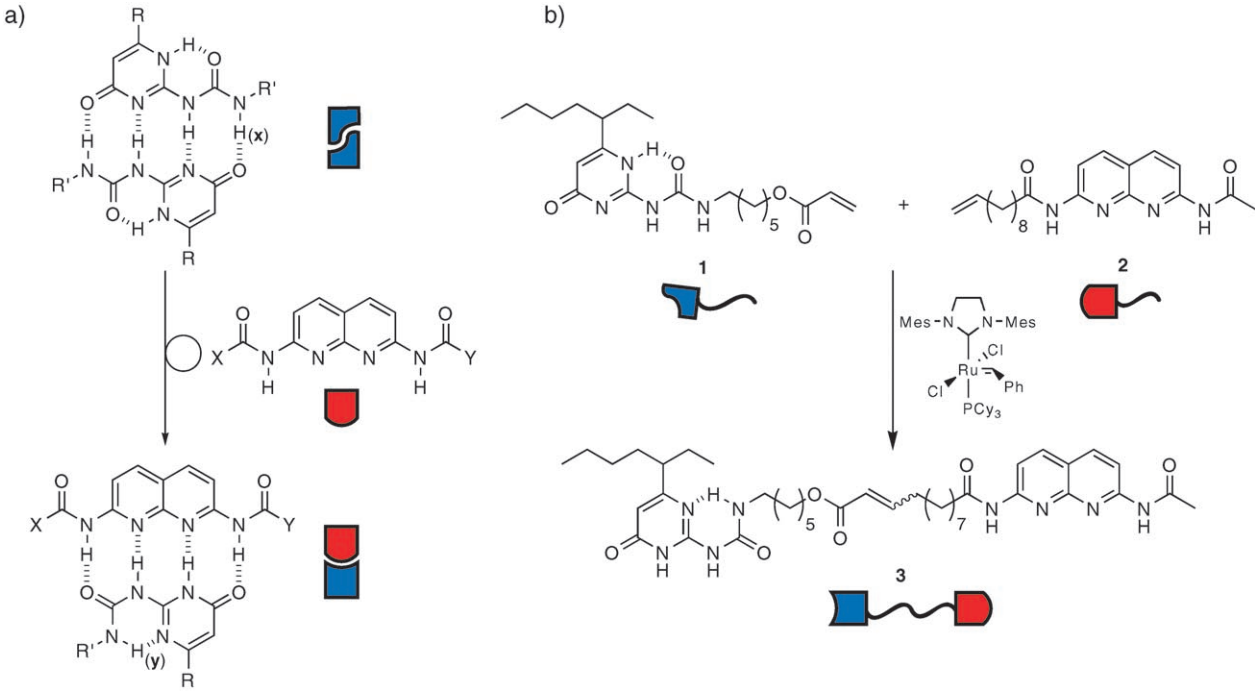

Scheme 1. a) Schematic representation of the dimerization equilibria of UPy and Napy. b) Synthesis of the AB molecule by selective cross metathesis.

 © 2006 Wiley-VCH Verlag GmbH & Co. KGaA, Weinheim

would certainly act as a chain stopper and/or initiator and severely limit the DP.[3,8] Isolation by both conventional column chromatography on silica gel and preparative HPLC was not possible due to the decomposition of **3**.[28] Therefore, purification was accomplished by preparative size-exclusion chromatography (SEC) in recycling mode. After several iterative purification runs, **3** was obtained in >99.5% purity.[29]

The ^{1}H NMR spectrum clearly shows that the acrylate resonances of **1** and the terminal olefin peaks of **2** do not appear in the spectrum of purified **3** (Figure 1a). The

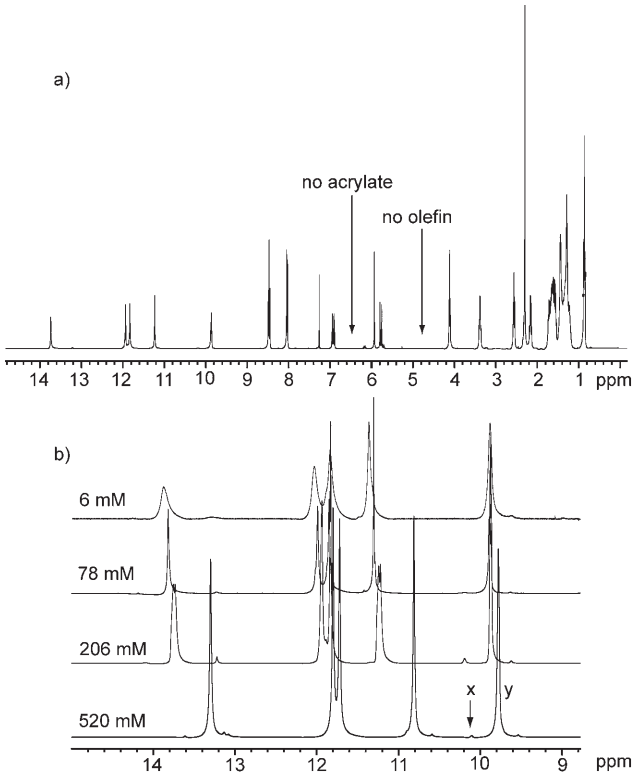

Figure 1. a) ^{1}H NMR spectrum of AB monomer **3**; b) NH region of the ^{1}H NMR spectra of AB monomer **3**, upfield shifts are likely due to an increase in the concentration.

downfield regions of the ^{1}H NMR spectra of **3** at various concentrations show the presence of five hydrogen-bond resonances indicative of the UPy–Napy heterodimer (Figure 1b). Additionally, smaller peaks that correspond to the self-complementary UPy–UPy dimer are observed at intermediate concentrations (e.g., resonance x; Figure 1b). The ureido NH proton next to the methylene moiety in UPy can be distinctly observed at $\delta = 10.2$ and 9.8 ppm (x and y, respectively) by ^{1}H NMR spectroscopic analysis. These shifts correspond to either the 4[1*H*]-pyrimidinone tautomer displaying an AADD array (UPy–UPy dimer) and the 6[1*H*]-pyrimidinone tautomer ADDA motif observed for the UPy–Napy heterodimer, respectively (see Scheme 1a for labels).

Remarkably, UPy homodimers are not present at low concentrations (<30 mM), and their fraction decreases after reaching a maximum relative intensity at approximately 150 mM, as can be seen qualitatively in Figure 1b. To gain insight into the supramolecular association processes, the ratio of UPy–UPy homodimer (x) to UPy–Napy heterodimer (y) was monitored as a function of concentration (Figure 2).

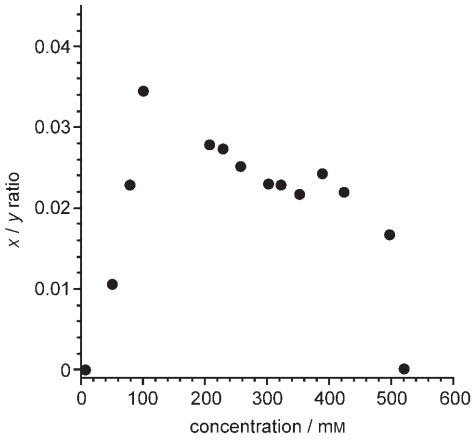

Figure 2. Ratio of UPy–UPy homodimer to UPy–Napy heterodimer as a function of concentration of AB monomer **3**.

A maximum value followed by a steady decrease in the plot of x/y is anticipated for a system which is simultaneously influenced by a ring-chain equilibrium[8] and by the concentration-dependent selectivity of UPy–UPy versus UPy–Napy complexation.[12] In such a system, complexation is expected to be exclusively *intra*molecular at low concentrations and selectively *inter*molecular at high concentrations. In between these two concentration limits, a complex and dynamic competition exists between inter- and intramolecular complexation. The dual-binding ability of UPy in combination with an entropically favored ring formation greatly complicates a full understanding of such a dynamic system.

Nevertheless, we suggest a simplified model for the dynamic system, as illustrated in Figure 3. The NMR data at

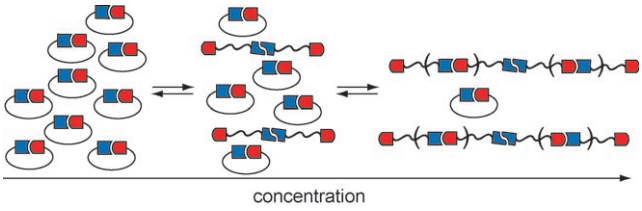

Figure 3. The proposed ring-opening polymerization of **3** as a function of concentration.

low concentrations taken in combination with the long, flexible linker (20 atoms) that span the UPy and Napy motifs suggests that AB monomer **3** exists exclusively as rings of different sizes, which are predominantly monomeric. When the concentration is increased to 100–300 mM, however, the NMR data shows that both the UPy–UPy and UPy–Napy couples exist. The presence of UPy–UPy dimers implies that uncomplexed Napy end groups *must* exist in solution. This behavior can be explained by a slight dip in selectivity between complementary units, as previously observed,[12] in combination with standard ring/chain equilibrium theories,

 © 2006 Wiley-VCH Verlag GmbH & Co. KGaA, Weinheim

which predict the formation of linear chains in addition to rings. At concentrations that exceed 500 mM, a high selectivity for intermolecular heterodimer formation results in a decreased net fraction of UPy homodimers with a commensurate increase in DP (≥ 40).

Overall, the model implies that nearly all chains accommodate a single UPy homodimer and two Napy end groups. Therefore, the DP of the linear fraction of **3** is predicted to be lower and increases at a slower rate (as a function of concentration[30]) than for either the UPy-based (AA) self-complementary supramolecular polymers or AA and BB copolymers, as reported previously by our group.[3,12] The system can be best described as a concentration-induced supramolecular ring-opening polymerization that arises from the concentration-dependent selectivity with the linear Napy–UPy/UPy–Napy assembly as the initiating species (Figure 3). Whether chain growth occurs solely at the Napy end groups (as in covalent ring-opening polymerization) or that exchange within the chain takes place as well, is part of our ongoing research on the dynamics of this system.

To test the validity of this model, Ubbelohde viscosity measurements were carried out at 25 °C in $CHCl_3$ and compared with data on bis(UPy) polymers **4**[3] and **5**,[31] which were previously reported to have CPC values of <10 and $\approx 90\ g\,L^{-1}$, respectively.

A double-logarithmic plot of specific viscosity (η_{sp}) versus concentration yields a linear relationship well above the CPC as seen over the entire concentration range of **4** (Figure 4).

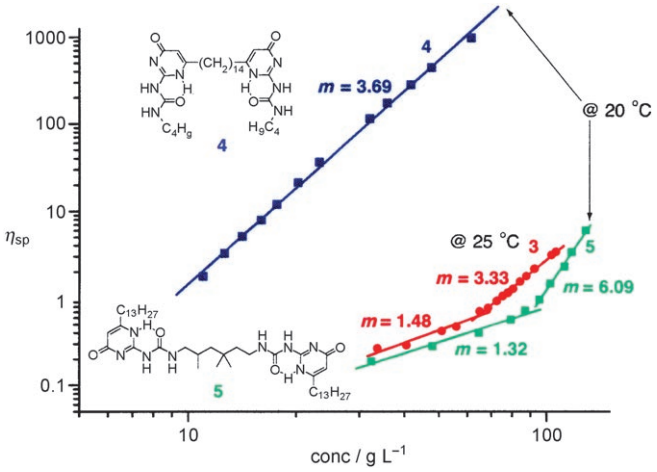

Figure 4. Solution viscosities of Upy–Napy monomer **3** (99.5% purity),[32] bis(UPy) **4**, and bis(UPy) **5**.

However, similar to the transition of **5**, a clear change in slope for **3** at approximately $60\ g\,L^{-1}$ indicates a transition from cycles to linear chains—a ring-opening supramolecular polymerization.[8,31] This change in slope results in a value of η_{sp} for **3**, which is approximately 2000 times lower than that of **4**. In addition, the slope for **3** above the CPC is lower than that of **4** and **5** because of the slower increase of DP with concentration. This behavior can be attributed to the presence of Napy "end groups" on every chain and is analogous to controlling DPs in condensation polymerization. Furthermore, when all solvent is removed, pure **3** is obtained as a free-standing elastic film; to the best of our knowledge, this polymeric material is the first based on the supramolecular self-assembly of an AB monomer.

In conclusion, we have prepared a new AB-type monomer containing both UPy and Napy quadruple hydrogen-bonding moieties which addresses the issue of stoichiometric imbalance in AA + BB-type supramolecular polymer self-assembly. Monomer **3** likely exists as a cycle at low concentrations and undergoes a selectivity driven ring-opening polymerization as the concentration increases, thus illustrating directional growth of a supramolecular polymer. Contrary to previously reported supramolecular polymerizations of bifunctional UPy monomers, this system likely undergoes ring-opening polymerization from a linear "initiating species" formed on account of concentration-dependent selectivity. Herein, we have shown that both stoichiometry and directional growth can be addressed by use of a heteroditopic monomer bearing strong, complementary hydrogen-bonding arrays. Such a system should have dramatic implications for surface-initiated supramolecular polymerization as well as bottom-up strategies towards nanoscale-device construction.

Experimental Section

3 (conventional): A 10-mL Schlenk tube containing a stirring bar was charged with **1** (79.6 mg, 0.20 mmol) and **2** (39.2 mg, 0.11 mmol) and purged with argon. Freshly distilled CH_2Cl_2 (1.8 mL) was added, and the reaction mixture was stirred at room temperature under argon to fully dissolve all solids. The second generation Grubbs ruthenium catalyst (5.4 mg, 6.4×10^{-3} mmol) was added to the reaction mixture as a solid, a reflux condenser was attached, and the reaction vessel was placed in an oil bath preheated to 45 °C. The reaction mixture was stirred at reflux for 24 h and then cooled to room temperature, the stirring bar was removed, and the reaction mixture was then concentrated in vacuo. The crude product was then analyzed by ^{1}H NMR spectroscopic analysis before purification by preparative recycling gel-permeation chromatography (rGPC).

3 (microwave heating): A 12-mL microwave-reactor tube containing a 2-cm microwave absorbing bar and stirring bar was charged with **1** (100.0 mg, 0.25 mmol), **2** (70.9 mg, 0.19 mmol), and the second generation Grubbs ruthenium catalyst (10.1 mg, 1.2×10^{-2} mmol) and was purged with argon. Freshly distilled CH_2Cl_2 (2.0 mL) was added by syringe, and the reaction vessel was placed into the microwave reactor. The temperature heating profile for the reaction mixture was as follows: RT → 55 °C over a 2-min period (200-W maximum power), the reaction mixture was held at 55 °C (isothermal, 200-W maximum power) for a set amount of time (30–60 min). The crude reaction mixture was concentrated and analyzed by ^{1}H NMR spectroscopic analysis before purification by preparative rGPC. ^{1}H NMR (400 MHz, $CDCl_3$): $\delta = 13.74$ (1H, s), 11.93 (1H, s), 11.83 (1H, s), 11.23 (1H, s), 9.87 (1H, t, $J = 5.2$ Hz), 8.47 (2H, t, $J = 8.0$ Hz), 8.04 (2H, d, $J = 8.4$ Hz), 6.92 (*trans*) (1H, dt, $J = 15.6$ Hz, $J = 7.2$ Hz), 6.17 (*cis*) (1H, dt, $J = 11.6$ Hz, $J = 6.0$ Hz), 5.93 (1H, s), 5.77 (*trans*) (1H, d, $J = 15.6$), 5.71 (*cis*) (1H, d, $J = 11.6$ Hz), 4.11 (2H, t, $J = 6.4$ Hz), 3.38 (2H, q, $J = 6.0$ Hz), 2.56 (2H, t, $J = 7.2$ Hz), 2.35–2.25 (4H, m), 2.16 (2H, q, $J = 7.2$ Hz), 1.75–1.20 (28H, m), 0.86 ppm (6H, m); ^{13}C NMR (100 MHz, $CDCl_3$): $\delta = 174.4$, 171.3, 171.1, 166.8, 165.2, 155.9, 155.7, 155.5, 153.8, 150.8, 149.7, 139.4, 139.2, 121.3, 119.9, 117.8, 115.1, 114.9, 106.3, 77.4, 64.2, 48.9, 40.1, 37.3, 37.2, 33.9, 32.2, 29.8, 29.7, 29.6, 29.4, 29.3, 29.1, 28.7, 28.1, 27.4, 26.9, 26.0, 25.5, 24.6, 14.1, 12.1 ppm; FTIR: 3178, 3001, 2929, 2856, 1699, 1676, 1619, 1536, 1507, 1460, 1414, 1379, 1321, 1307, 1282, 1234, 1215, 1173, 1141, 1052, 1004, 978, 925, 851, 836,

 © 2006 Wiley-VCH Verlag GmbH & Co. KGaA, Weinheim

798, 751, 706, 665 cm^{-1}; MS (MALDI-TOF): 747.43 $[M+H]^+$, 769.40 $[M+Na]^+$, 785.38 $[M+K]^+$.

Received: November 24, 2005
Published online: February 27, 2006

Keywords: directionality · hydrogen bonds · metathesis · ring-opening polymerization · supramolecular polymers

[1] W. H. Carothers, *Chem. Rev.* **1931**, *8*, 353.
[2] G. Odian, *Principles of Polymerization*, Wiley, New York, **1991**.
[3] R. P. Sijbesma, F. H. Beijer, L. Brunsveld, B. J. B. Folmer, J. H. K. K. Hirschberg, R. F. M. Lange, J. K. L. Lowe, E. W. Meijer, *Science* **1997**, *278*, 1601.
[4] L. Brunsveld, B. J. B. Folmer, E. W. Meijer, R. P. Sijbesma, *Chem. Rev.* **2001**, *101*, 4071.
[5] A. Ciferri, *Supramolecular Polymers, 2nd ed.*, CRC, Boca Raton, **2005**.
[6] J.-M. Lehn, *Supramolecular Chemistry*, Wiley-VCH, **1995**.
[7] R. P. Sijbesma, E. W. Meijer, *Chem. Commun.* **2003**, 5.
[8] A. T. ten Cate, R. P. Sijbesma, *Macromol. Rapid Commun.* **2002**, *23*, 1094.
[9] S. H. M. Söntjens, R. P. Sijbesma, M. H. P. van Genderen, E. W. Meijer, *J. Am. Chem. Soc.* **2000**, *122*, 7487.
[10] P. S. Corbin, S. C. Zimmerman, *J. Am. Chem. Soc.* **1998**, *120*, 9710.
[11] X.-Z. Wang, X.-Q. Li, X.-B. Shao, X. Zhao, P. Deng, X.-K. Jiang, Z.-T. Li, Y.-Q. Chen, *Chem. Eur. J.* **2003**, *9*, 2904.
[12] G. B. W. L. Ligthart, H. Ohkawa, R. P. Sijbesma, E. W. Meijer, *J. Am. Chem. Soc.* **2005**, *127*, 810.
[13] J. van der Gucht, N. A. M. Besseling, M. A. Cohen Stuart, *J. Am. Chem. Soc.* **2002**, *124*, 6202.
[14] Theoretical work by van der Gucht and co-workers has suggested that interactions between particles sheathed with supramolecular polymers based on either symmetric or asymmetric monomers have properties which are quite different; see ref. [13].
[15] N. Yamaguchi, D. S. Nagvekar, H. W. Gibson, *Angew. Chem. Int. Ed.* **1998**, *37*, 2361.
[16] M. Miyauchi, Y. Takashima, H. Yamaguchi, A. Harada, *J. Am. Chem. Soc.* **2005**, *127*, 2984.
[17] S. J. Cantrill, G. J. Youn, J. F. Stoddart, D. J. Williams, *J. Org. Chem.* **2001**, *66*, 6857.
[18] R. K. Castellano, J. Rebek, Jr., *J. Am. Chem. Soc.* **1998**, *120*, 3657.
[19] K. Kim, D. Kim, J. W. Lee, Y. H. Ko, K. Kim, *Chem. Commun.* **2004**, 848.
[20] T.-L. Choi, C. W. Lee, A. K. Chatterjee, R. H. Grubbs, *J. Am. Chem. Soc.* **2001**, *123*, 10417.
[21] G. Ercolani, L. Mandolini, P. Mencarelli, S. Roelens, *J. Am. Chem. Soc.* **1993**, *115*, 3901.
[22] C. Galli, L. Mandolini, *Eur. J. Org. Chem.* **2000**, 3117.
[23] S. H. M. Söntjens, R. P. Sijbesma, M. H. P. van Genderen, E. W. Meijer, *Macromolecules* **2001**, *34*, 3815.
[24] G. B. W. L. Ligthart, H. Ohkawa, R. P. Sijbesma, E. W. Meijer, *J. Org. Chem.* **2006**, in press.
[25] E. Comer, M. G. Organ, *J. Am. Chem. Soc.* **2005**, *127*, 8160.
[26] S. Garbacia, B. Desai, O. Lavastre, C. O. Kappe, *J. Org. Chem.* **2003**, *68*, 9136.
[27] F. C. Bargiggia, W. V. Murray, *J. Org. Chem.* **2005**, *70*, 9636.
[28] 2,7-Diamido-1,8-naphthyridines are quite prone to acidic or basic hydrolysis because of the electron-poor character of the naphthyridine core, which makes the carbon atom in the amide carbonyl group more electrophilic; a full study will be reported elsewhere.
[29] SEC with THF with an analytical single-pore-size column and a UV/Vis detector was used to determine the purity of monomer **3**.
[30] An increase in selectivity predicts an increase of DP from 7 to 60, at which point the concentration of monomers in chains increases from 0.001 to 1M.
[31] B. J. B. Folmer, R. P. Sijbesma, E. W. Meijer, *J. Am. Chem. Soc.* **2001**, *123*, 2093.
[32] When the purity of **3** is 95%, the slope is <2.

 © 2006 Wiley-VCH Verlag GmbH & Co. KGaA, Weinheim

Natural Products

DOI: 10.1002/anie.200504466

Stereocontrolled Synthesis of Model Core Systems of Lomaiviticins A and B**

K. C. Nicolaou, Ross M. Denton, Achim Lenzen, David J. Edmonds, Ang Li, Robert R. Milburn, and Scott T. Harrison*

Dedicated to Professor K. Peter C. Vollhardt on the occasion of his 60th birthday

Lomaiviticins A (**1**) and B (**2**, Figure 1) were isolated in 2001 from the fermentation broth of a species of the actinomycete genus *Micromonospora*.[1] Both natural products were shown to be highly active DNA-damaging agents. The more abundant compound, lomaiviticin A, exhibited extremely potent cytotoxicity against a broad range of cancer cell lines in vitro, with IC_{50} values ranging from 98 to 0.01 ng mL^{-1}. The cytotoxicity profile of the lomaiviticins differs significantly from that of other DNA-damaging agents, such as mitomicin C and adriamycin, hinting at a possible new mode of action for the former compounds. Furthermore, lomaiviticins A and B displayed powerful antibiotic activity against the pathogenic Gram-positive bacteria *Enterococcus faecium* and *Staphylococcus aureus*. Two studies investigating the mecha-

[*] Prof. Dr. K. C. Nicolaou, Dr. R. M. Denton, Dr. A. Lenzen, Dr. D. J. Edmonds, A. Li, Dr. R. R. Milburn, S. T. Harrison
Department of Chemistry and
The Skaggs Institute for Chemical Biology
The Scripps Research Institute
10550 North Torrey Pines Road, La Jolla, CA 92037 (USA)
Fax: (+1) 858-784-2469
E-mail: kcn@scripps.edu
and
Department of Chemistry and Biochemistry
University of California, San Diego
9500 Gilman Drive, La Jolla, CA 92093 (USA)

[**] We thank Dr. D. H. Huang, Dr. G. Siuzdak, and Dr. R. K. Chadha for NMR spectroscopic, mass spectrometric, and X-ray crystallographic assistance, respectively. Financial support for this work was provided by grants from the National Institutes of Health (USA), the Skaggs Institute for Chemical Biology, and American Biosciences, and postdoctoral fellowships from the Alexander von Humboldt Foundation (to A.L.) and European Merck (to D.J.E.).

WILEY InterScience DISCOVER SOMETHING GREAT
© 2006 Wiley-VCH Verlag GmbH & Co. KGaA, Weinheim

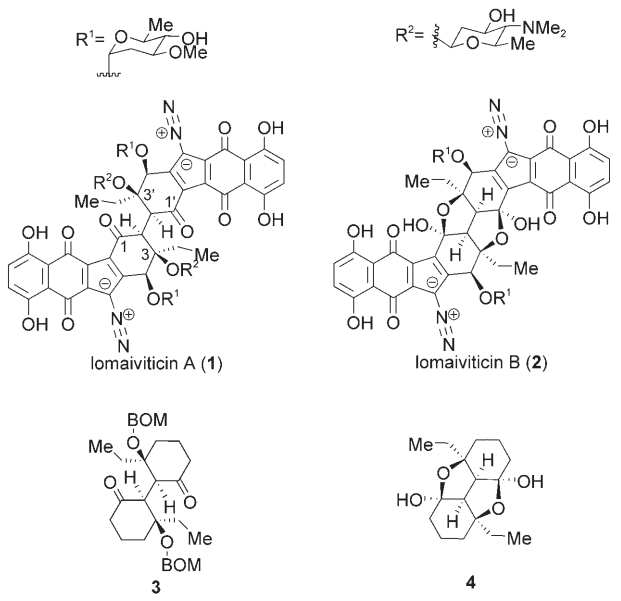

Figure 1. Structures of lomaiviticins A (**1**) and B (**2**) and model systems **3** and **4** (BOM = benzyloxymethyl).

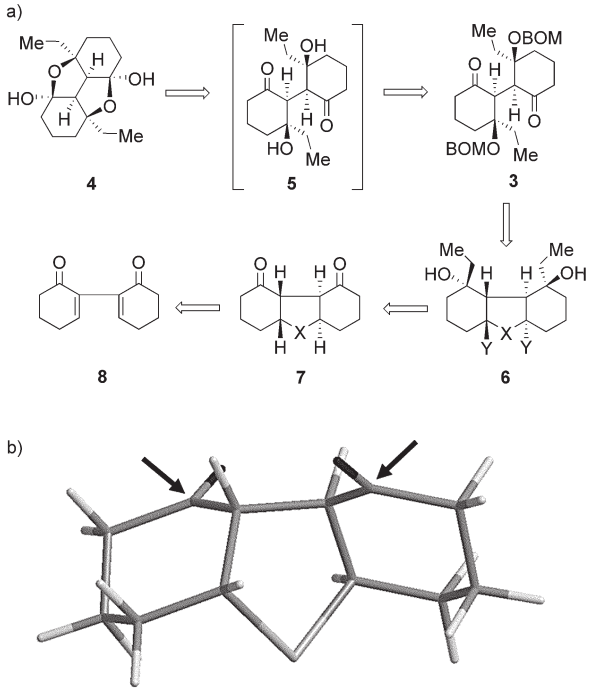

Scheme 1. a) The bridged tricyclic scaffold strategy to the core structures **3** and **4** of the lomaiviticins shown retrosynthetically. b) Energy-minimized model of tricyclic system **7** showing the expected trajectory of nucleophilic addition to the tethered carbonyl groups (X = S, C; Y = OR).

nism of DNA interaction of related compounds have been reported;[2] both studies indicate that the diazo group plays a key role in the biological activity of these molecules. Structural elucidation revealed striking and complex molecular architectures for the lomaiviticins. Conspicuous features of these intriguing molecules include the diazobenzofluorene structure of the monomeric units, reminiscent of the simpler kinamycin antibiotics,[3] the *N*,*N*-dimethyl derivative of the rare amino sugar pyrrolosamine attached to the core through a β-glycosidic bond, the tertiary glycosides of lomaiviticin A, the two hydroxyfuran moieties of lomaiviticin B, and, of course, the central linkage. In combination, these unusual structural motifs constitute a formidable challenge to chemical synthesis. We felt that the central core of these target molecules posed perhaps the most significant challenge to any total synthesis of the lomaiviticins and therefore sought to prepare **3** and **4** (Figure 1) as models for lomaiviticins A and B, respectively. The problems to be addressed include the construction of the hindered central carbon–carbon bond and the stereocontrolled formation of the sensitive tertiary β-hydroxy ketone units. Herein, we report the synthesis of model systems **3** and **4**, which represent the central structural motifs of lomaiviticins A and B.

Our answer to the challenge posed by model systems **3** and **4** is shown retrosynthetically in Scheme 1. We planned to introduce the tertiary alcohol groups through organometallic addition to a dimeric ketone, such as **7**. The tethering group X was introduced to provide a conformationally locked framework to control the stereochemistry of the double addition, as shown in Scheme 1 (bottom), while serving as latent functionality for the installation of the carbonyl groups needed in the final products, **3** and **4**. We planned to introduce the tethering group through a double Michael addition of a suitable nucleophile to dimeric enone **8**, itself formed by reductive coupling of the monomeric iodoenone.[4]

Initially, we investigated the possible use of tricyclic sulfide **9** (Scheme 2). It was envisaged that the sulfide could be converted into the required diketone by iterative Pummerer rearrangements and hydrolysis of the resulting cyclic double hemithioacetal. Treatment of bis-enone **8**[4] with sodium hydrosulfide under mildly basic conditions ($NaHCO_3$) gave the anticipated tricyclic sulfide **9** as a single C_2-symmetric diastereoisomer in 77% yield. Attempts to introduce the ethyl substituent by treatment of **9** with EtMgBr or EtLi were unsuccessful; however, the use of the ethyl cerium reagent,[5] formed by premixing EtMgBr with anhydrous $CeCl_3$, gave the desired product **10** in excellent yield (96%). Protection of the tertiary alcohols (TBSOTf, Et_3N, 83%) gave the corresponding TBS ether **11**, which underwent clean oxidation to give sulfoxide **12** (H_2O_2, HFIP, 98%).[6] Disappointingly, despite screening a number of conditions, the Pummerer rearrangement of sulfoxide **12** could not be realized. Compound **12** was unreactive under most common Pummerer conditions,[7] but exposure to trifluoroacetic anhydride and pyridine resulted in formation of the trifluoromethyl enone **15** in moderate yield (54%). This reaction presumably proceeds via the generation of the desired sulfonium ion **13**, however deprotonation to give the vinyl sulfide **14** is favored over addition of trifluoroacetate to give the Pummerer rearrangement product. Apparently, C-acylation of **14** and loss of a second proton gives **15**. Single-crystal X-ray analysis[8] of **15** (structure not shown) served to confirm the stereochemistry of the tricyclic system as well as the

 © 2006 Wiley-VCH Verlag GmbH & Co. KGaA, Weinheim

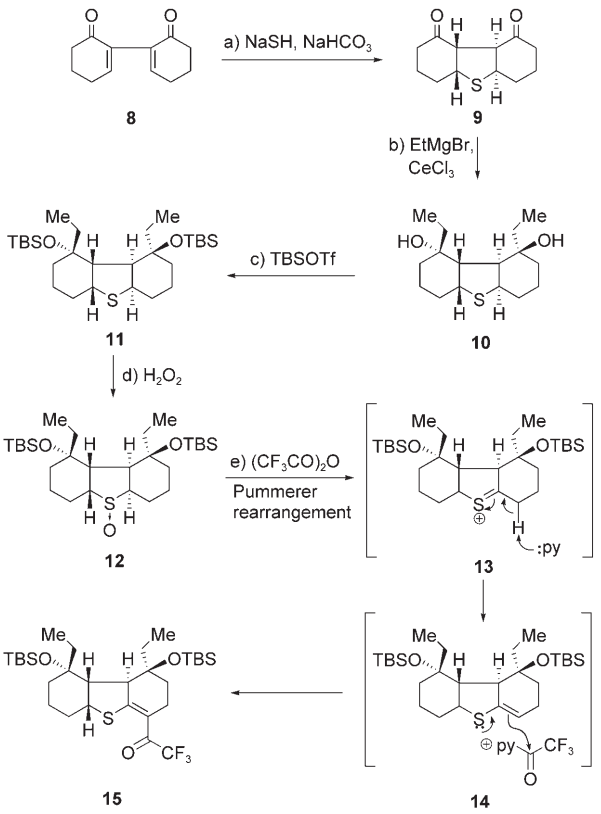

Scheme 2. The tetrahydrothiophene approach to the lomaiviticin core structure. Reagents and conditions: a) NaSH (0.9 equiv), H_2O/MeOH (1:1), 25 °C, 1 h, 77%; b) EtMgBr (8.0 equiv), $CeCl_3$ (12 equiv), THF, −40 °C, 35 min, 96%; c) TBSOTf (2.1 equiv), Et_3N (10.0 equiv), CH_2Cl_2, 25 °C, 2 h, 83%; d) 35% aq. H_2O_2 (4.0 equiv), HFIP/CH_2Cl_2 (2:1), 25 °C, 1 h, 98%; e) TFAA (6.0 equiv), py (10 equiv), CH_2Cl_2, 25 °C, 23 h, 54%. THF = tetrahydrofuran; TBSOTf = *tert*-butyldimethylsilyl trifluoromethanesulfonate; HFIP = 1,1,1,3,3,3-hexafluoropropan-2-ol; TFAA = trifluoroacetic anhydride; py = pyridine.

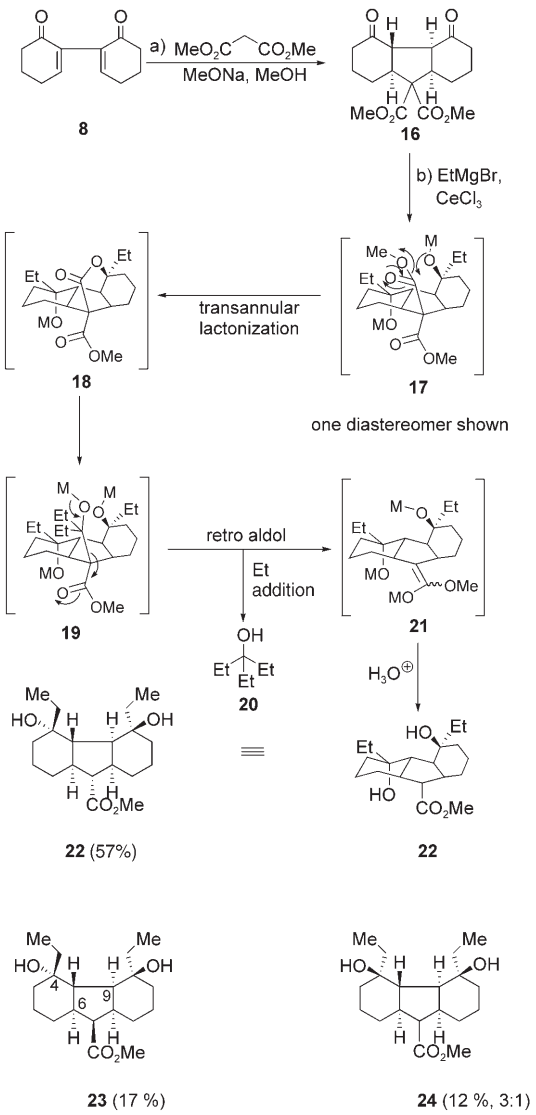

Scheme 3. Carbon-tethering of bis-enone **8** and stereoselective introduction of the ethyl groups. Reagents and conditions: a) dimethyl malonate (1.0 equiv), MeONa (1.1 equiv), MeOH, 70 °C, 1 h, 85%; b) EtMgBr (8.0 equiv), $CeCl_3$ (12 equiv), THF, 25 °C, 10 min, **22** (57%), **23** (17%), **24** (12%; 3:1 mixture of diastereoisomers).

identity of this unexpected product. Vinyl sulfide **14** could be isolated in low yield (ca. 15%) from this reaction, however, the acylation step was competitive with its formation and could not be averted to a significant degree. All attempts to hydrolyze the vinyl sulfide were unsuccessful. Similarly, attempts to effect Pummerer rearrangement of the sulfoxide derived from dihydroxy sulfide **10** were unsuccessful, leading only to decomposition. Faced with this roadblock, we sought an alternative bridging group and a new series of intermediates to reach **3** and **4**.

The anion of dimethyl malonate was found to add to bis-enone **8** in good yield (NaOMe, 85%), again yielding the product as a single diastereoisomer **16** (Scheme 3). Interestingly, in contrast to the sulfide described above, the malonate adduct was not C_2-symmetric, however, the stereochemistry adjacent to the ketone groups was correct (see below). Treatment of diketone **16** with the ethyl cerium reagent resulted in rapid double addition with concomitant loss of one of the ester groups of the malonate unit. A possible mechanism for this intriguing cascade transformation is shown in Scheme 3. Following nucleophilic addition to the ketone groups of **16**, a proximity-induced lactonization within product **17** provides δ-lactone **18**. Addition of two equivalents of the ethyl cerium reagent to the lactone[5] moiety of **18** gives a new tertiary alkoxide **19**, which can undergo a retroaldol reaction, leading to the formation of trianion **21** with concomitant expulsion of 3-pentanone. Further organometallic addition leads to tertiary alcohol **20**, a by-product that was detected in the ^{1}H NMR spectrum of the crude reaction mixture. Finally, protonation of trianion **21** on workup leads to the observed products. In contrast to the case of the cyclic sulfide (see above), the unsymmetrical nature of substrate **16** resulted in a mixture of products upon reaction with the cerium reagent. At −40 °C, four products were formed in 91% total yield. The mixture comprised two diol stereoisomers, each consisting of an approximately 3:1 mixture of

 © 2006 Wiley-VCH Verlag GmbH & Co. KGaA, Weinheim

epimers at the third newly formed stereocenter. X-ray crystallographic analysis[8] (see ORTEP drawing, Figure 2) revealed that the major epimer of the less polar diastereoisomer was diol **22**, which has the correct stereochemistry for

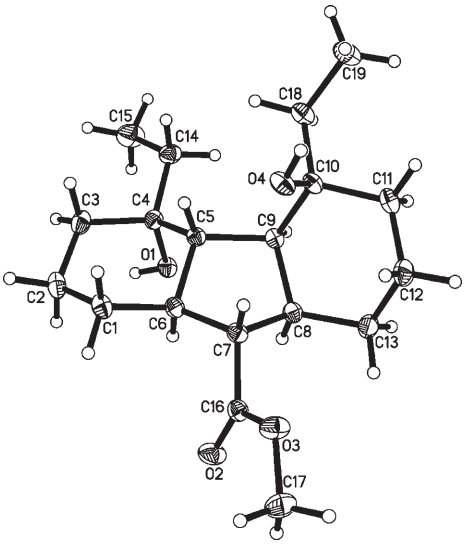

Figure 2. ORTEP drawing of compound **22** derived from X-ray crystallographic analysis (non-hydrogen atoms are shown as 30% ellipsoids).

the lomaiviticins. Optimization of the reaction temperature allowed the formation of **22** in 57% yield, together with its epimer **23** in 17% yield, and the undesired diol stereoisomer **24** (12% yield), the latter as a roughly 3:1 mixture of epimers at the ester-carrying center. It is thought that the diminished diastereoselectivity of this reaction, as compared to the same reaction of C_2-symmetric sulfide **9**, is specifically due to the *trans*-fused ring junction of diketone **16**.

With the four stereocenters of the targeted model core systems secured, we began to investigate the conversion of the now-redundant malonate-derived tether into the desired diketone functionality. Protection of the tertiary alcohols proved rather problematic, with only MOMCl or BOMCl reacting in the presence of Hünig's base to give doubly protected products **25a** (95%) and **25b** (ca. 95%), respectively (Scheme 4). We initially envisaged oxidative removal of the ester carbon through ozonolysis of the silyl ketene acetal of **25a**. Alternatively, oxidation of the ester enolate followed by reduction of the ester and cleavage of the resulting 1,2-diol would provide the same ketone. However, attempts to generate the enolates of **22** or **25a** were uniformly unsuccessful, as indicated by the absence of deuterium incorporation. Similarly, the use of amine bases and silyl triflates failed to provide any silyl ketene acetal products, and, rather, led only to decomposition. Inspection of the X-ray crystal structure of **22** (see Figure 2) revealed that the C6-C7-C8 bond angle is an unusually acute 99.07°, as compared to the optimal 109.5°. The apparent reluctance of the ester to undergo enolization may well be due to this distortion. This problem was circumvented by employing a stepwise removal of the ester carbon atom. Thus, ester **25b** (Scheme 4) was reduced (LAH, 89% from **22**) and the resulting primary alcohol was

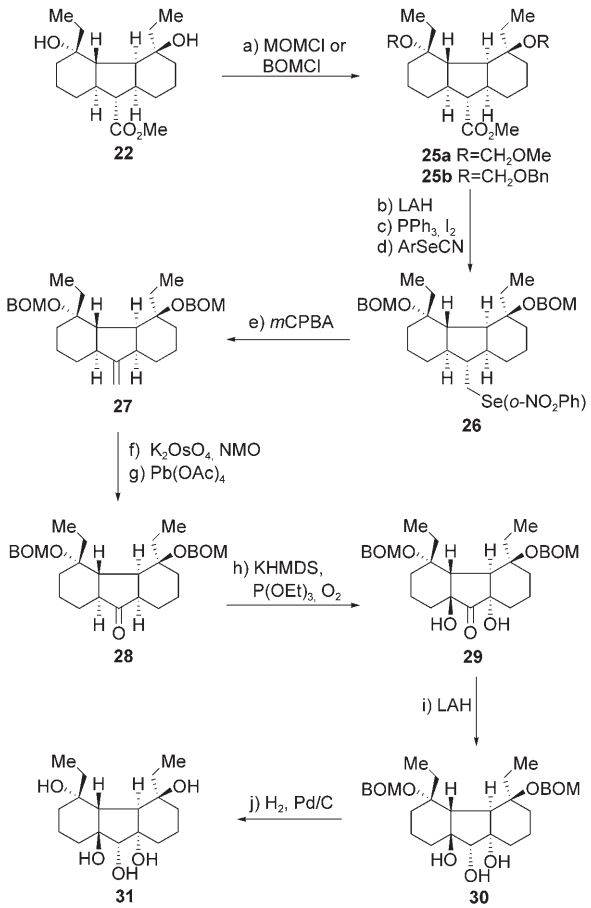

Scheme 4. Adjustment of the oxidation state of the carbon bridge of the tricyclic scaffold. Reagents and conditions: a) MOMCl or BOMCl (20 equiv), iPr$_2$NEt/CH$_2$Cl$_2$ (1:1), 25°C, 16 h, **25a** (95%), **25b** (ca. 95%); b) LAH (4.5 equiv), THF, 0→25°C, 2.5 h, 89% for two steps; c) I_2 (2.0 equiv), PPh_3 (2.0 equiv), imidazole (4.0 equiv), Et_2O/MeCN (3:1), 25°C, 30 min, 98%; d) *o*-nitrophenylselenocyanate (1.6 equiv), $NaBH_4$ (1.6 equiv), DMF, 0→25°C, 1 h, 97%; e) *m*CPBA (1.1 equiv), THF, 0→65°C, 1 h, 91%; f) K_2OsO_4 (5.0 mol%), NMO (2.0 equiv), acetone/water (4:1), 25°C, 72 h, 91%; g) Pb(OAc)$_4$ (1.0 equiv), CH_2Cl_2, 25°C, 10 min, 97%; h) KHMDS (8.0 equiv), P(OEt)$_3$, (10.0 equiv), THF, −78°C, 2 h, 86%; i) LAH (3.0 equiv), THF, 0→25°C, 50 min, 93%; j) H_2 (1 atm), 10% Pd/C (50 mol%), THF, 25°C, 3 h, 100%. MOM = methoxymethyl; LAH = lithium aluminum hydride; DMF = dimethylformamide; *m*CPBA = 3-chloroperbenzoic acid; NMO = *N*-methylmorpholine-*N*-oxide; HMDS = hexamethyldisilazane.

converted into *o*-nitrophenylselenide **26** (*o*-$NO_2C_6H_4SeCN$, $NaBH_4$, 97%) via the corresponding iodide, which was formed by reaction of the alcohol with PPh_3/I_2/imidazole (98% yield). Oxidation of selenide **26** with dry *m*CPBA gave the corresponding selenoxide, which underwent elimination upon heating in THF to give olefin **27** (91% yield from **26**); the high temperature required again indicates the difficulty in forming an sp^2 center within the five-membered ring of these compounds. Two-step oxidative cleavage of **27** was cleaner and more efficient than ozonolysis and gave the desired ketone **28** in high overall yield (K_2OsO_4, NMO; Pb(OAc)$_4$, 91%). Ketone **28** underwent facile double oxygenation in a single operation to give dihydroxy ketone **29** (KHMDS, P(OEt)$_3$, O_2, 86%). The stereochemistry of **29**, which was

 © 2006 Wiley-VCH Verlag GmbH & Co. KGaA, Weinheim

formed as a single C_2-symmetric diastereoisomer, was thought to result from oxidation occurring from the less-hindered face of the enolate in each case to give the *cis–cis* product. Reduction of ketone **29** with LAH gave triol **30** (93%). At this point the routes to models **3** and **4** diverge, with the former being generated from **30** and the latter generated from **31**, the pentahydroxy derivative obtained by hydrogenolysis of **30** (H_2, Pd/C, 100% yield; Scheme 4).

Treatment of triol **30** with $Pb(OAc)_4$ led to the tetracyclic acetal **32** (Scheme 5). Unfortunately, complete cleavage to furnish diketone **3** could not be realized using excess $Pb(OAc)_4$ or by treament of **30** with $NaIO_4$. Acetal **32** could be reduced with $LiBH_4$ to give two triol diastereoisomers, as an inseparable 3:1 mixture, which underwent oxidative cleavage with $Pb(OAc)_4$ to give **33** in 66% yield over two steps, now as a separable 3:1 mixture of diastereoisomers. Attempted oxidation of this mixture was unsuccessful using a number of oxidants, however, the use of stoichiometric TPAP led to the slow oxidation of the major diastereoisomer of this mixture **33** to give the desired model core compound **3** of lomaiviticin A (see Table 1). Oxidation of the pure major diastereoisomer of **33** under the same conditions gave diketone **3** in 55% yield. The minor hemiacetal could not be oxidized, even after prolonged exposure to the reaction conditions. The success of this sequence was dependent on the conditions employed in the reduction of **32**. The use of a very large excess (60 equiv) of $LiBH_4$ was essential to the selective formation of the oxidizable diastereoisomer of hemiacetal **33**.

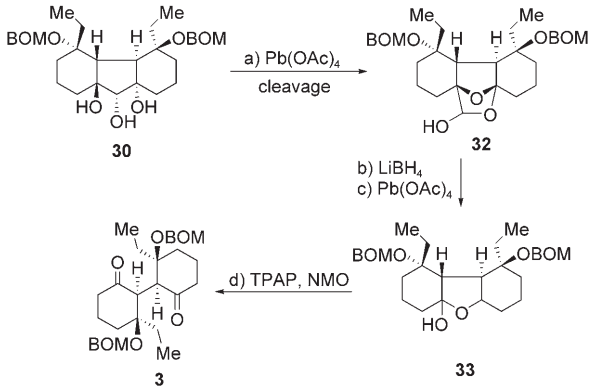

Scheme 5. Synthesis of the core model system **3** of lomaiviticin A. Reagents and conditions: a) $Pb(OAc)_4$ (1.4 equiv), CH_2Cl_2, 25 °C, 10 min, 90%; b) $LiBH_4$ (60 equiv), THF, 25 °C, 16 h; c) $Pb(OAc)_4$ (1.4 equiv), 25 °C, 10 min, 66% for two steps (ca. 3:1 d.r.); d) TPAP (1.0 equiv), NMO (2.0 equiv), CH_2Cl_2, 25 °C, 55%. TPAP = tetra-*n*-propylammonium perruthenate.

Alternatively, treatment of **31** with $Pb(OAc)_4$ led to monoformate **36** (Scheme 6), presumably through cleavage of the *cis*-1,2-diol moiety to give an intermediate keto-aldehyde **34**, followed by further oxidative cleavage of hemiacetal **35**. Interestingly, the ^{13}C NMR spectrum of the crude formate (in C_6D_6) suggests an "open" structure, with two ketone resonances and no hemiacetal resonance evident. Hydrolysis of the formate ester of this highly sensitive intermediate was best effected using half-saturated methanolic ammonia,[9] followed by quenching with pH 7 buffer, which allowed isolation of the desired dimeric hydroxyfuran model compound **4** in 40%

Table 1: Selected physical properties for compounds **3**, **4**, **15**, **22**, and **29**.

3: R_f=0.40 (silica gel, EtOAc/hexane 1:1); IR ν_{max} (film): 2936, 1696, 1454, 1030, 735, 670 cm^{-1}; ^1H NMR (500 MHz, $CDCl_3$): δ = 7.36–7.27 (m, 10H, 2×Ph), 4.86 (d, J = 7.5 Hz, 2H, 2×C*H*HO_2), 4.72 (d, J = 7.5 Hz, 2H, 2×CH*H*O_2), 4.68 (d, J = 11.6 Hz, 2H, 2×C*H*HPh), 4.55 (d, J = 11.6 Hz, 2H, 2×CH*H*Ph), 3.29 (s, 2H, 2×C*H*), 2.57 (2H, ddd, J = 14.0, 9.3, 7.0 Hz, 2×C*H*HC=O), 2.32 (td, J = 14.0, 5.6 Hz, 2H, 2×CH*H*C=O), 2.24 (ddd, J = 13.3, 10.2, 4.4 Hz, 2H, 2×C*H*HCEt), 1.99–1.92 (m, 2H, 2×C*H*H$(CH_2)_2$), 1.91–1.86 (m, 2H, 2×C*H*HCEt), 1.80 (qd, J = 14.8, 7.4 Hz, 2H, 2×C*H*HCH_3), 1.71–1.57 (m, 4H, 2×C*H*H$(CH_2)_2$ and 2×C*H*HCH_3), 0.92 ppm (t, J = 7.3 Hz, 6H, 2×CH_3); ^{13}C NMR (125 MHz, $CDCl_3$): δ = 212.9 (2×C=O), 137.9 (2×ArC), 128.4 (4×ArCH), 127.8 (4×ArCH), 127.6 (2×ArCH), 88.7 (2×CH_2O_2), 83.1 (2×CEt), 70.0 (2×CH_2Ph), 56.0 (2×CH), 40.7 (2×CH_2C=O), 30.6 (2×CH_2CEt), 28.4 (2×CH_2CH_3), 20.6 (2×$CH_2(CH_2)_2$), 7.7 ppm (2×CH_3); HRMS (ESI-TOF): m/z calcd for $C_{32}H_{42}O_6Na$ [M+Na]$^+$: 545.2873; found: 545.2871.

4: R_f=0.49 (silica gel, EtOAc/hexane 1:1); IR ν_{max} (film): 3412, 2932, 1460, 1132, 1100, 1064, 986 cm^{-1}; ^1H NMR (500 MHz, C_6D_6): δ = 2.87 (s, 2H, 2×C*H*), 2.18 (dq, J = 13.6, 7.4 Hz, 2H, 2×C*H*HCH$_3$), 2.04–2.00 (m, 2H, 2×C*H*HCEt), 1.97–1.93 (m, 2H, 2×C*H*HCOH), 1.80–1.71 (m, 2H, 2×C*H*H$(CH_2)_2$), 1.61 (br s, 2H, 2×O*H*), 1.41 (dq, J = 13.6, 7.3, 2H, 2×C*H*HCH$_3$), 1.27–1.22 (m, 2H, 2×C*H*H$(CH_2)_2$), 1.21 (td, J = 13.5, 3.4 Hz, 2H, 2×C*H*HCOH), 0.96 (td, J = 13.7, 3.3 Hz, 2H, 2×C*H*HCEt), 0.91 ppm (t, J = 7.4 Hz, 6H, 2×CH_3); ^{13}C NMR (150 MHz, C_6D_6): δ = 104.7 (2×COH), 85.1 (2×CEt), 60.4 (2×CH), 38.5 (2×CH_2COH), 37.3 (2×CH_2CH_3), 33.6 (2×CH_2CEt), 18.3 (2×$CH_2(CH_2)_2$), 8.5 ppm (2×CH_3); HRMS (ESI-TOF): m/z calcd for $C_{16}H_{26}O_4$ [M+H−H_2O]$^+$: 265.1798; found: 265.1797.

22: R_f=0.27 (silica gel, EtOAc/hexane 1:3); IR ν_{max} (film): 3386, 2937, 1718, 1455, 1168, 974 cm^{-1}; ^1H NMR (600 MHz, $CDCl_3$): δ = 3.69 (s, 3H, CH_3O), 2.39 (dd, J = 10.6, 7.6 Hz, 1H, C*H*CO_2Me), 2.27–2.24 (m, 1H, C*H*CHCO_2Me), 2.16 (qd, J = 11.7, 3.9 Hz, 1H, C*H*CHCO_2Me), 1.98 (t, J = 7.6 Hz, 1H, C*H*C(OH)Et), 1.94–1.85 (m, 2H, C*H*HCH_3 and C*H*HCHCHCO_2Me), 1.75 (dd, J = 11.7, 7.8 Hz, 1H, C*H*C(OH)Et), 1.70–1.37 (m, 13H, C*H*HCH_3, CH_2CH_3, and 5×CH_2), 1.23–1.16 (m, 1H, C*H*HCHCHCO_2Me), 0.92 (t, J = 7.4 Hz, 3H, CH_3), 0.88 ppm (t, J = 7.4 Hz, 3H, CH_3); ^{13}C NMR (150 MHz, $CDCl_3$): δ = 176.3 (C=O), 73.7 (COH), 73.1 (COH), 52.0 (*C*HCO_2Me), 51.8 (*C*HCOH), 51.5 (CH_3O), 45.7 (*C*HCOH), 44.7 (*C*HCHCO_2Me), 43.3 (CH*C*HCO_2Me), 34.8 (CH_2), 34.1 (CH_2CH_3), 34.0 (CH_2CH_3), 33.9 (CH_2), 29.3 (CH_2), 27.6 (CH_2), 21.5 (CH_2), 19.6 (CH_2), 7.5 (CH_3), 7.3 ppm (CH_3); HRMS (ESI-TOF): m/z calcd for $C_{19}H_{32}O_4Na$ [M+Na]$^+$: 347.2193; found: 347.2204.

29: R_f=0.80 (silica gel, EtOAc/hexane 1:1); IR ν_{max} (film): 3530, 3329, 2937, 2872, 1754, 1454, 1383, 1086, 1011 cm^{-1}; ^1H NMR (500 MHz, $CDCl_3$): δ = 7.33–7.28 (m, 10H, 2×Ph), 4.88 (d, J = 7.0 Hz, 2H, 2×C*H*HO_2), 4.78 (d, J = 7.0 Hz, 2H, 2×C*H*HO_2), 4.69 (s, 2H, 2×O*H*), 4.68 (d, J = 11.5 Hz, 2H, 2×C*H*HPh), 4.55 (d, J = 11.5 Hz, 2H, 2×CH*H*Ph), 2.29–2.25 (m, 4H, 2×C*H* and 2×C*H*H), 2.24–1.84 (m, 4H, 2×C*H*HCH_3 and 2×C*H*H), 1.79–1.72 (m, 2H, 2×C*H*H), 1.68–1.53 (m, 6H, 2×C*H*HCH_3 and 4×C*H*H), 1.51–1.44 (m, 2H, 2×C*H*H), 0.94 ppm (t, J = 7.5 Hz, 6H, 2×CH_3); ^{13}C NMR (125 MHz, $CDCl_3$): δ = 215.1 (C=O), 137.3 (2×ArC), 128.5 (4×ArCH), 127.9 (6×ArCH), 88.5 (2×CH_2O_2), 81.6 (2×COH), 76.2 (2×CEt), 71.0 (2×CH_2Ph), 49.7 (2×CH), 29.3 (2×CH_2), 28.7 (2×CH_2CH_3), 27.2 (2×CH_2), 15.6 (2×CH_2), 9.7 ppm (2×CH_3); HRMS (ESI-TOF): m/z calcd for $C_{33}H_{44}O_7Na$ [M+Na]$^+$: 575.2979; found: 575.2983.

 © 2006 Wiley-VCH Verlag GmbH & Co. KGaA, Weinheim

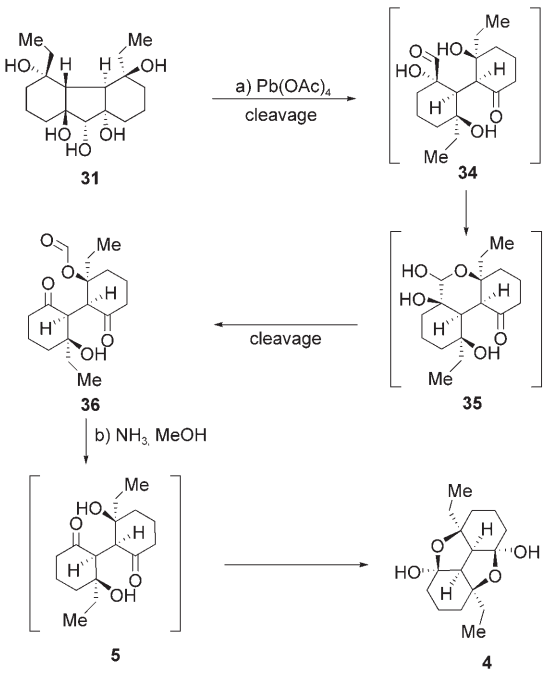

Scheme 6. Synthesis of the core structure **4** of lomaiviticin B. Reagents and conditions: a) $Pb(OAc)_4$ (2 equiv), CH_2Cl_2, 25 °C, 10 min, 95 %; b) NH_3, MeOH, 25 °C, 40 min, 40 % for two steps.

overall yield from **31**. The elegant C_2-symmetric structure of model system **4** is depicted in two views in Figure 3.

In conclusion, we have demonstrated the feasibility of a bridged carbocycle approach to the core dimeric structure of the lomaiviticin natural products. This strategy allows the controlled formation of four contiguous stereocenters and the preparation of systems representing either lomaiviticin A or B. Work is currently underway to apply this strategy to the total synthesis of these fascinating natural products.

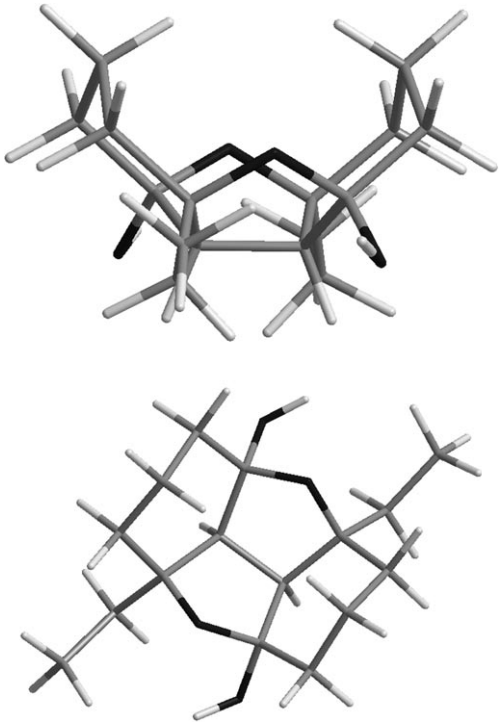

Figure 3. Two perspective views of a possible conformation of the cage structure of model compound **4**. O black; C dark gray; H pale gray.

Received: December 15, 2005
Revised: January 5, 2006
Published online: February 22, 2006

Keywords: antitumor agents · Michael addition · natural products · total synthesis

[1] H. He, W.-D. Ding, V. S. Bernan, A. D. Richardson, C. M. Ireland, M. Greenstein, G. A. Ellestad, G. T. Carter, *J. Am. Chem. Soc.* **2001**, *123*, 5362 – 5363.
[2] a) R. S. Laufer, G. I. Dmitrienko, *J. Am. Chem. Soc.* **2002**, *124*, 1854 – 1855; b) K. S. Feldman, K. J. Eastman, *J. Am. Chem. Soc.* **2005**, *127*, 15344 – 15345.
[3] a) S. J. Gould, N. Tamayo, C. R. Melville, M. C. Cone, *J. Am. Chem. Soc.* **1994**, *116*, 2207 – 2208; b) S. Mithani, G. Weeratunga, N. J. Taylor, G. I. Dmitrienko, *J. Am. Chem. Soc.* **1994**, *116*, 2209 – 2210.
[4] G. Lin, R. Hong, *J. Org. Chem.* **2001**, *66*, 2877 – 2880.
[5] a) T. Imamoto, N. Takiyama, K. Nakamura, T. Hatajima, Y. Kamiya, *J. Am. Chem. Soc.* **1989**, *111*, 4392 – 4398; b) H.-J. Liu, K.-S. Shia, X. Shang, B.-Y. Zhu, *Tetrahedron* **1999**, *55*, 3803 – 3830.
[6] K. S. Ravikumar, Y. M. Zhang, J.-P. Bégué, D. Bonnet-Delpon, *Eur. J. Org. Chem.* **1998**, 2937 – 2940.
[7] a) A. Padwa, D. E. Gunn, Jr., M. H. Osterhout, *Synthesis* **1997**, 1353 – 1377; b) S. K. Bur, A. Padwa, *Chem. Rev.* **2004**, *104*, 2401 – 2432.
[8] CCDC 292940 (**22**) and 292941 (**15**) contain the supplementary crystallographic data for this paper. These data can be obtained free of charge from The Cambridge Crystallographic Data Centre via www.ccdc.cam.ac.uk/data_request/cif.
[9] F. E. Ziegler, A. Kneisley, *Tetrahedron Lett.* **1987**, *28*, 1725 – 1728.

 © 2006 Wiley-VCH Verlag GmbH & Co. KGaA, Weinheim

Antimalarial Drugs

DOI: 10.1002/anie.200503071

Artemisone—A Highly Active Antimalarial Drug of the Artemisinin Class**

Richard K. Haynes, Burkhard Fugmann, Jörg Stetter, Karl Rieckmann, Hans-Dietrich Heilmann, Ho-Wai Chan, Man-Ki Cheung, Wai-Lun Lam, Ho-Ning Wong, Simon L. Croft, Livia Vivas, Lauren Rattray, Lindsay Stewart, Wallace Peters, Brian L. Robinson, Michael D. Edstein, Barbara Kotecka, Dennis E. Kyle, Bernhard Beckermann, Michael Gerisch, Martin Radtke, Gabriele Schmuck, Wolfram Steinke, Ute Wollborn, Karl Schmeer,* and *Axel Römer*

[*] Prof. Dr. R. K. Haynes, Dr. H.-W. Chan, Dr. M.-K. Cheung, Dr. W.-L. Lam, Dr. H.-N. Wong
Department of Chemistry
Open Laboratory of Chemical Biology
Institute of Molecular Technology for Drug Discovery and Synthesis
The Hong Kong University of Science and Technology
Clear Water Bay, Kowloon, Hong Kong (P.R. China)
Fax: (+852) 2358-1594
E-mail: haynes@ust.hk

Dr. B. Fugmann
Bayer Innovation GmbH (Germany)

Prof. Dr. J. Stetter
Bayer AG Central Research (Germany)

Prof. Dr. K. Rieckmann, Dr. M. D. Edstein, Dr. B. Kotecka, Dr. D. E. Kyle[+]
Army Malaria Institute (AMI)
Enoggera, Queensland 4052 (Australia)

Prof. Dr. H.-D. Heilmann, Dr. B. Beckermann, Dr. M. Gerisch, Dr. M. Radtke, Dr. G. Schmuck, Dr. W. Steinke
Bayer HealthCare (Germany)

Dr. S. L. Croft, Dr. L. Vivas, Dr. L. Rattray, Dr. L. Stewart
London School of Hygiene and Tropical Medicine (UK)

Prof. Dr. W. Peters, B. L. Robinson
Northwick Park Institute for Medical Research, Harrow (UK)

Dr. U. Wollborn
Bayer MaterialScience AG (Germany)

Dr. K. Schmeer
Bayer CropScience AG (Germany)

Dr. A. Römer
Analytik und Metabolismusforschung Service GmbH (Germany)

[+] Current affiliation:
Walter Reed Army Institute of Research (USA)

[**] Work at the HKUST was funded by Bayer AG Central Research, Leverkusen, the Institute of Molecular Technology for Drug Discovery and Synthesis through the HKSAR University Grants Committee Areas of Excellence Fund, and the HKSAR Research Grants Council through the Competitive Earmarked Research Grants Scheme. The Medicines for Malaria Venture (MMV), Geneva, also provided financial support of the work at Bayer, and through Bayer at HKUST and other centers. Dr. W. Collins (Centers for Disease Control, Atlanta) supplied *P. falciparum* FVO strain used for the primate studies.

Supporting information for this article is available on the WWW under http://www.angewandte.org or from the author.

The artemisinins are the most potent and rapidly acting antimalarial drugs. In response to the global threat of multidrug-resistant malaria, they are now widely used in combination therapies with drugs that have a longer half life.[1] The parent, artemisinin (**1**), is converted by reduction

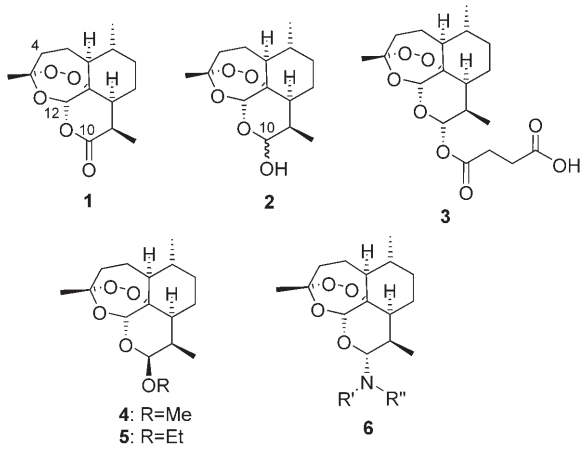

into dihydroartemisinin (DHA, **2**)[2] and then into the hemiester artesunate (ATS, **3**; 65% yield from DHA).[3] Artemether (**4**)[4] and arteether (**5**)[5] are obtained from DHA, methanol, and an acid catalyst in about 60% yield after fractional crystallization to remove the α-epimers. Therefore, the most accessible derivative is ATS (**3**). Although artemisinins display variable pharmacokinetics and low bioavailability,[6] such properties are countered by selective uptake into parasitized erythrocytes.[7] Their induction of phase I enzymes, primarily CYP3A4 and CYP2B6, leads to a time-dependent decrease in efficacy.[8] Additionally, metabolism of artesunate and the ethers to DHA (**2**) is facile.[8,9] The artemisinins, especially DHA, are neurotoxic according to in vivo assays with animal models[10] and in vitro studies with neuronal cell cultures.[11–13] Although neurotoxicity is dependent upon the route of administration in animal screens,[14] it has not yet been definitively established to be a problem in humans.[15] From a regulatory viewpoint, however, it is a contentious issue, and the development of new artemisinin therapies must be conducted with this in mind.

Despite an immense effort, no new artemisinin derivative has reached development status. 10-Alkylaminoartemisinins **6** ($R' = H$, alkyl; $R'' =$ alkyl; $R', R'' =$ cycloalkyl) are an artemisinin class whose preparation entails chemistry distinct to that leading to other derivatives and which extends the efficacy limit beyond those of the known artemisinins.[16,17] For any such compound to be developed into a new drug, the production cost must be comparable to that of ATS (**3**),[18] unless a greater efficacy is obtained when a commensurate increase in cost is permitted. As the interaction of artemisinins with their likely target, the PfATP6 Ca^{2+} pump, is still unclear,[19,20] a "rational design" approach is not possible and emphasis must be placed on improving systemic behavior. Whilst this depends upon a number of factors,[21] an enhancement of aqueous solubility to a limiting value and attenuation of lipophilicity as assessed through the $\log P$ parameter (P is

InterScience
© 2006 Wiley-VCH Verlag GmbH & Co. KGaA, Weinheim

the octanol–water partition coefficient) are beneficial.[22,23] One report in the artemisinin area addresses the lipophilicity issue, wherein enzymatic hydroxylation of the lipophilic arteether ($\log P$ = 3.89–3.99) provides products with $\log P$ values of 2.6–2.7, considered to be in an optimal range for systemic activity.[24] However, the corollary that lipophilic artemisinins are neurotoxic[25,26] adds substantial impetus to the drive to attenuate lipophilicity. As neurotoxicity is likely to be associated with a specific target,[11,27] a linear correlation between neurotoxicity and lipophilicity for a compound series is unlikely.[25] However, it is clear that in order to depress neurotoxicity, $\log P$ must be reduced and, at the same time, phase I metabolism to DHA must be blocked. As the alkylaminoartemisinins **6** will not undergo such metabolism, polar groups inert to phase I and phase II metabolism[26] are best incorporated into the 10-alkylamino substituent itself. However, the use of hydroxy, carboxy, or primary amino groups capable of forming phase II conjugates is proscribed.

The amines **9**–**11**[16,28,29] and **12**–**16**[30] (40–60%) were obtained from DHA α-trimethylsilyl ether **7** and trimethylsilyl bromide (TMSBr), followed by treatment of the intermediate bromide **8** formed in situ with the amine nucleophile (Scheme 1, route a). Oxidation of the sulfide **12** also provided sulfoxide **13** or sulfone **14**. A more straightforward route involved treatment of DHA first with a mixture of NaBr and TMSCl in toluene and then with the amine (Scheme 1, route b). Under these condition, DHA is converted by the TMSBr formed in situ into the TMS ether **7**, and then into the bromide **8**, whose presence was detected by ^{1}H NMR spectroscopy.[28] For most compounds, products from multigram- or multikilogram-scale reactions (compounds **12** and **14**) were isolated by crystallization of the crude product mixtures. Thus, the candidate compounds are relatively accessible and are produced as isomerically pure, air-stable substances.

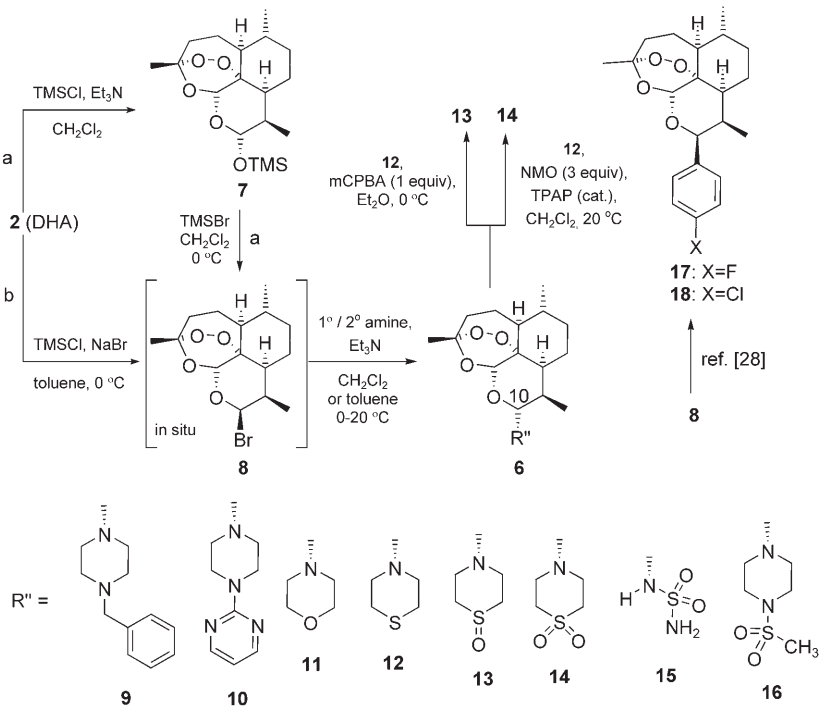

Scheme 1. Preparation of 10-alkylamino derivatives **9**–**16**; compound **13** is obtained by oxidation of **12**; compound **14** is obtained by either treatment of **8** with thiomorpholine-*S*,*S*-dioxide or oxidation of **12**, which itself is obtained from **8** and thiomorpholine.[16,29,30] Compounds **17** and **18** were prepared according to published procedures.[28] mCPBA = *m*-chloroperbenzoic acid; NMO = *N*-methylmorpholine-*N*-oxide; TPAP = tetra-*n*-propylammonium perruthenate.

Assessment of physicochemical properties, neurotoxicity, and efficacy against malaria was next carried out. For comparative purposes, the lipophilic 4-fluorophenyl and 4-chlorophenyl derivatives **17** and **18** were also studied.[16,28] Measured and calculated[31] $\log P$ values (Table 1) reveal that artemether **4** is relatively lipophilic. Because DHA (**2**) exists as two epimers in solution, $\log P$ appears as two values, 2.35 and 2.73; the solubility of **2** could not be measured because of decomposition. Compounds **9**, **10**, and **12**, and especially **17** and **18**, are lipophilic with high $\log P$ values and very low aqueous solubility. Compound **14**, which is highly crystalline and easily purified, displays aqueous solubility that exceeds the limiting requirements for a drug.[22] Compounds **13** and **15** are more soluble but are more costly to prepare than **14**. Although compound **16** has a low calculated $\log P$ value, it also has a low aqueous solubility.

Neurotoxicity was assessed with the in vitro model developed for screening compounds required for medicinal and other purposes.[32] As artemisinins exert their neurotoxicity by acting selectively on brain stem cells,[11–13,27,33] primary neuronal brain stem cell cultures from fetal rats, with endpoints of cytotoxicity and neurofilament integrity, were used. Intracellular ATP levels, which are a sensitive and early marker of cytotoxicity,[27,33] were also measured (Table 2). With a "no observable effect concentration" (NOEC) on neurofilaments of less than 0.001 $\mu g\,mL^{-1}$, DHA displayed the greatest neurotoxicity. The neurotoxicity of **9**–**11** contrasts with the nontoxicity of **14**. NOEC and IC_{50} values for cytotoxicity with cortical neurons were generally

Table 1: Aqueous solubility and octanol–water partition coefficients.

	1	**3**	**4**	**9**	**10**	**11**	**12**	**13**	**14**	**15**	**16**	**17**	**18**
Solubility [$mg\,L^{-1}$][a]	63	565	117	8	< 2	28.4	< 2	1251	89	294	10	< 1	< 1
log *P*[b]	2.94	2.77	3.98	5.62	4.78	3.05	4.97	2.63	2.49	3.36	[c]	5.59	6.15
log *P* (calcd)[d]	3.15	3.04	3.51	5.15	4.07	3.26	3.98	2.03	2.08	2.29	2.30	5.18	5.58

[a] Aqueous solubility at pH 7.2. [b] Octanol–water partition coefficient for the neutral compound determined at pH 7.4, except that for artesunate (**3**) which was determined at pH 2 by HPLC. [c] Not determined. [d] Calculated log *P* value.[31]

 © 2006 Wiley-VCH Verlag GmbH & Co. KGaA, Weinheim

Table 2: Effects of the test compounds on viability and neurofilaments in rat primary neuronal brain stem cell cultures.[a]

Compound	Viability [$\mu g\,mL^{-1}$][b]		ATP [$\mu g\,mL^{-1}$][c]		Neurofilaments [$\mu g\,mL^{-1}$][d]	
	NOEC[e]	IC_{50}	NOEC[e]	IC_{50}	NOEC[e]	IC_{50}
1	1.0	>10	0.01	0.08	0.001	0.05
2	0.1	5.0	0.01	0.08	<0.001	0.01
3	0.1	>10	–	–	0.1	5.0
4	1.0	>10	–	–	0.01	0.1
9	0.1	>10	–	–	10	>10
10	0.01	10	–	–	0.1	3
11	0.1	4.5	<0.001	<0.001	0.001	0.04
12	1.0	>10	1.0	8.5	0.001	>10
14	>10	>10	>10	>10	>10	>10
15	10	>10	1	6.3	0.001	>10
17	1.0	>10	1	6.3	0.001	>10
18	1.0	>10	0.01	0.08	0.001	0.05

[a] Determined on fetal rat brain stem cells (E18–E19) cultured to generate a permanent neuronal network during days 1–8; compounds in dimethyl sulfoxide (DMSO) were applied at 0.001, 0.01, 0.1, 1, and 10 $\mu g\,mL^{-1}$ for 7 days starting on day 9. [b] Cytotoxicity was measured by viability based on the activity of neuron-specific enolases. [c] ATP (adenosine triphosphate) levels measured at 1 day after initial administration.[27,33,35] [d] Neurotoxicity was assessed by the effect on the cytoskeleton on day 7. [e] No observable effect concentration.

between in vivo and in vitro neurotoxicity has already been noted with artemisinins **1**–**4**.[11,13,27,33]

Antimalarial IC_{50} values from in vitro screens of the 10-alkylamino compounds **9**–**18** against *Plasmodium falciparum* chloroquine (CQ)-sensitive D6 or 3D7 and CQ-resistant W2 or K1 strains generally were substantially lower (to over 20-fold for compounds **9** and **10**) than those of ATS (**3**). The compounds also display superior activities in in vivo screens in the four-day Peters' model[36] against CQ-sensitive *P. berghei* and CQ-resistant *P. yoelii* in mice (Table 3). Compounds **9**–**12** were exceedingly active but are excluded from further consideration because of toxicity, and unfavorable physicochemical properties. Overall, compound **14** (artemisone) emerges as the development candidate.

Table 3: In vivo screens against CQ-sensitive *P. berghei* N strain and CQ-resistant *P. yoelii* NS strain.[a]

Compound	*P. berghei* ED_{90} [$mg\,kg^{-1}$]		*P. berghei* artesunate index[b]		*P. yoelii* ED_{90} [$mg\,kg^{-1}$]		*P. yoelii* artesunate index[b]
	sc	po	sc	po	sc	po	sc
3	7.2	7.1	1.0	1.0	22.0	–	1.0
9	0.8	3.5	9.0	2.0	0.85	3.0	25.9
10	0.6	2.8	12	2.5	0.52	2.0	42.3
14	1.5	3.1	4.8	2.3	3.9	5.0	5.6
17	1.16	5.0	6.2	1.4	1.08	–	20.4
18	3.8	4.6	1.9	1.7	3.0	–	7.3
3	4.6	9.3	1.0	1.0	42.0	–	1.0
11	0.18	1.3	25.6	7.15	1.25	1.84	33.6
12	0.51	1.9	9.0	4.9	0.61	2.0	81.0
3	12.0	–	1.0	–	50.0	–	1.0
13	9.0	–	1.3	–	10.0	–	5.0

[a] Peters' four-day test[36] with mice treated daily subcutaneously (sc) or orally (po) from the day of infection (day 0) through to day 3; results (ED_{90} values) are evaluated from parasite counts in peripheral blood on day 4. [b] ED_{90}(artesunate)/ED_{90}(compound).

greater than 10 $\mu g\,mL^{-1}$, even for the highly neurotoxic **11**. However, DHA is also cytotoxic towards cortical neurons (NOEC(DHA) = 1 $\mu g\,mL^{-1}$, NOEC(artemisinin) > 50 $\mu g\,mL^{-1}$) and non-neuronal cell lines (NOEC(liver HEP-G2, epithelium liver IAR, kidney LLC-PK1) = 0.1 $\mu g\,mL^{-1}$, NOEC(artemisinin) > 10 $\mu g\,mL^{-1}$).[27,32,33] In general, the lipophilic compounds are neurotoxic. Neurotoxicity of the polar ATS (**3**) is likely due to facile hydrolysis in situ to DHA. As the relatively polar DHA and artemisinin may undergo ring-opening under aqueous conditions to provide rather different structures,[7,34] the actual nature of the neurotoxic agent is uncertain. Compound **11** is anomalous in that it also elicits acute systemic toxicity in an in vivo screen. The outcome of pilot tolerability studies in animal models, which employ standard indicators of neurotoxic effects,[35] reflects the results of the in vitro studies. Oral administration via gavage in corn or sesame oil of ATS (**3**) at 10 and 50 $mg\,kg^{-1}\,day^{-1}$ for 14 days to female rats induces uncoordinated gait and vocalization from days 7–11 at the higher dose. Compounds **10** at the higher dose and **11** at the lower dose are fatally toxic from days 2–4, generating prior symptoms of acute systemic toxicity. At 50 $mg\,kg^{-1}\,day^{-1}$, substantial body-weight loss, coupled with reduced motility, uncoordinated gait, and piloerection are observed with compounds **9**, **12**, **17**, and **18**. Compound **16** induces uncoordinated gait from day 1, with a slight decrease in body weight. In contrast, no effects are detectable with compounds **13**–**15**; the weight gains are no different to controls. The parallel

Even though it is not the most active candidate, its lack of toxicity couples well with its accessibility and tractable physicochemical properties. It was therefore subjected to more-detailed screening in conjunction with the comparator drug, ATS (**3**), the most accessible of the current artemisinins.[1,9]

In comparative screens in vitro against a panel of multidrug-resistant isolates of *P. falciparum*, artemisone (**14**) is significantly more active than ATS, CQ, and pyrimethamine, irrespective of the resistance profile (Figure 1). Ex vivo bioassay represents an effective method for assessing both comparative bioavailability and efficacy of an orally administered drug.[38] Oral administration of a 30 $mg\,kg^{-1}$ single dose of artemisone (**14**) or ATS (**3**) to healthy Saimiri monkeys and assay of plasma amples drawn from the monkeys against *P. falciparum* K1 strikingly reveal that

 © 2006 Wiley-VCH Verlag GmbH & Co. KGaA, Weinheim

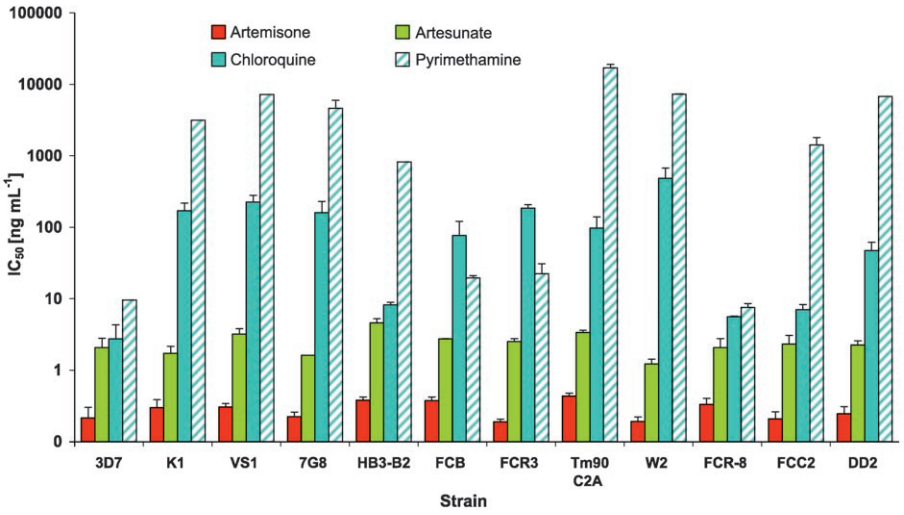

Figure 1. In vitro antimalarial activities for artemisone, artesunate, chloroquine (CQ), and pyrimethamine (PYR) against both drug-sensitive (3D7) *P. falciparum* and to isolates that are variously resistant (R) to CQ, PYR, and mefloquine (MFQ), assayed by administration of the compounds in DMSO to parasites incubated with ^{3}H-hypoxanthine. Inhibition of the uptake of hypoxanthine is expressed as the concentration at 50% inhibition (IC_{50}) in ng mL^{-1}.[37] 3D7 (clone of NF54 isolate, Netherlands); K1 (Thailand) CQ-R, PYR-R; VS1 (Vietnam) CQ-R, PYR-R; 7G8 (Brazil) CQ-R, PYR-R; HB3-B2 (Honduras) PYR-R; FCB (Colombia) CQ-R; FCR3 (Gambia) CQ-R, PYR-R; Tm90 C2A (Thailand) CQ-R, PYR-R, MFQ-R; W2 (Indochina) CQ-R, PYR-R; FCR-8 (Gambia); FCC2 (Hainan); DD2 (clone from W2) CQ-R, PYR-R. Error bars represent the standard deviation about the arithmetic mean.

artemisone has a greatly enhanced bioavailability, as reflected in the greater and significantly more sustained activity in plasma compared to ATS (Figure 2). Next, aotus monkeys infected with *P. falciparum* FVO isolate, which is resistant to CQ and antifolates, were treated with each of ATS and artemisone at 10 mg kg^{-1} day^{-1} for 3 days. The artemisone-treated group cleared parasites within 24 h after commencement of treatment, whereas parasites were still present 48 h after treatment with ATS (Table 4). One monkey (no. 7, Table 4) in the artemisone group was cured, and the others tended to have later recrudescences than monkeys in the ATS group. Complete cure was achieved in infected monkeys receiving a single oral dose of artemisone (10 mg kg^{-1}) plus mefloquine (MFQ, 5 mg kg^{-1}), although recrudescence occurred with a lower MFQ dose (2.5 mg kg^{-1}). Cure was also achieved with oral artemisone (10 mg kg^{-1} day^{-1}) plus amodiaquine (AQ, 20 mg kg^{-1} d^{-1}) given for 3 days. Therefore, in vivo efficacy is fully demonstrated. As the problem of recrudescence is common to all artemisinins, artemisone will best be used in conjunction with a longer half-life drug such as MFQ or AQ; this will additionally protect each drug partner against the emergence of resistance.[1,9,18]

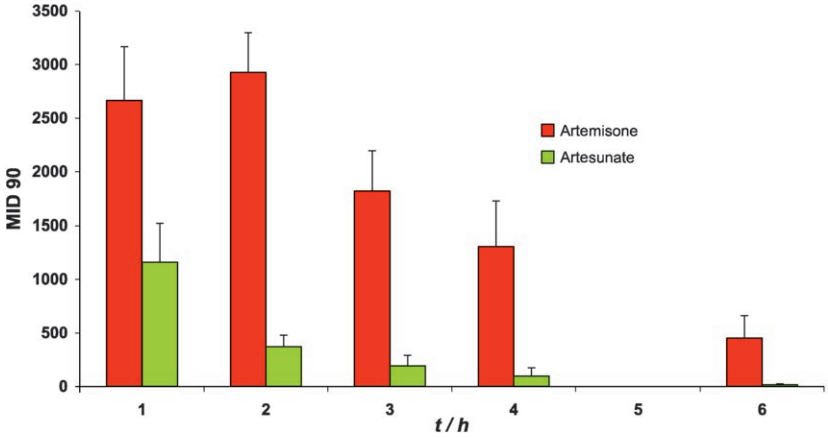

Figure 2. Ex vivo maximum inhibitory dilutions (MID) of plasma samples obtained from healthy Saimiri monkeys at 1–4 and 6 h after a single oral dose of artemisone (**14**) or artesunate (**3**; 10 mg kg^{-1} each) required to inhibit maturation of ≥90% *P. falciparum* K1 from rings to schizonts. Error bars represent the standard error of the mean of MID data obtained for four monkeys with each drug.

To demonstrate the lack of metabolism to DHA and to identify metabolites formed in vitro and in vivo, labeled artemisone **14*** incorporating either ^{14}C or ^{2}H in the metabolically inert 15-methyl group was required. The exocyclic methylidene was cleaved from artemisitene (**19**)[39] to give the known[40] dicarbonyl compound **16**, treatment of which with ^{2}H- or ^{14}C-methylidene triphenylphosphorane provided labeled artemisitene **19***, as shown in Scheme 2 for the deuteriated reagents. As attempted reduction of the exocyclic methylidene with conjugate hydride donors failed, the carbonyl group in **19*** was first reduced and the resulting allylic alcohol **21*** was reduced with either Et_3SiH for the ^{14}C-labeled compound or $Et_3Si^{2}H$ for the ^{2}H-labeled compound to give glycal **22***. The latter was converted into **12*** by stereoselective addition of HCl and treatment of the intermediate 10β-chloride with thiomorpholine to give labeled **12***; oxidation provided labeled artemisone **14***. This is the first semisynthesis of an artemisinin bearing a labeled group at a metabolically inert region of the artemisinin skeleton, for which total, albeit elegant, syntheses were previously used.[41]

In vitro incubation of **14*** with human liver microsomes gave after 30 min metabolites **M1** (≈34% of total radioactivity (TRA)), **M2** (≈19% of TRA), **M3** (≈16% of TRA), and smaller amounts of **M4** and **M5** (each <6% TRA) at approximately 77% conversion of **14*** (Scheme 2). Each metabolite was isolated and identified unambiguously by the use of 1D and 2D NMR spectroscopic analyses coupled with high-resolu-

 © 2006 Wiley-VCH Verlag GmbH & Co. KGaA, Weinheim

Table 4: In vivo activities of artesunate **3** and artemisone **14** against *P. falciparum* FVO in aotus monkeys.[a]

Monkey	Initial parasitaemia [$\times 10^3$ μL^{-1}]	Compound [10 mg kg^{-1} day^{-1}] days 0–2	Parasitaemia [$\times 10^3$ μL^{-1}] on day n[b] day 1	day 2	day 3	Time to recrudescence [days]
1	145	**3**	2.1	0.2	0	9
2	515	**3**	15	0.6	0	20
3	340	**3**	40	0.4	0	18
4	490	**14**	0	0	0	20
5	10	**14**	0	0	0	20
6	150	**14**	0	0	0	29
7	85	**14**	0	0	0	–

[a] Two aotus monkeys were infected with blood containing aotus-adapted *P. falciparum* FVO isolate resistant to CQ and antifolates. Blood was drawn from the infected monkeys and used to infect five malaria-naïve monkeys. 6–9 Days after inoculation, ATS (**3**) and artemisone (**14**) were administered orally for 3 days at 10 mg kg^{-1} day^{-1} (total 30 mg kg^{-1}). Thick blood films were examined microscopically twice a week; these were considered to be negative when no parasites were detected after examination of 100 microscopic fields ($\approx$0.1 mL blood). [b] Parasitaemia on days after the initial treatment on day 0.

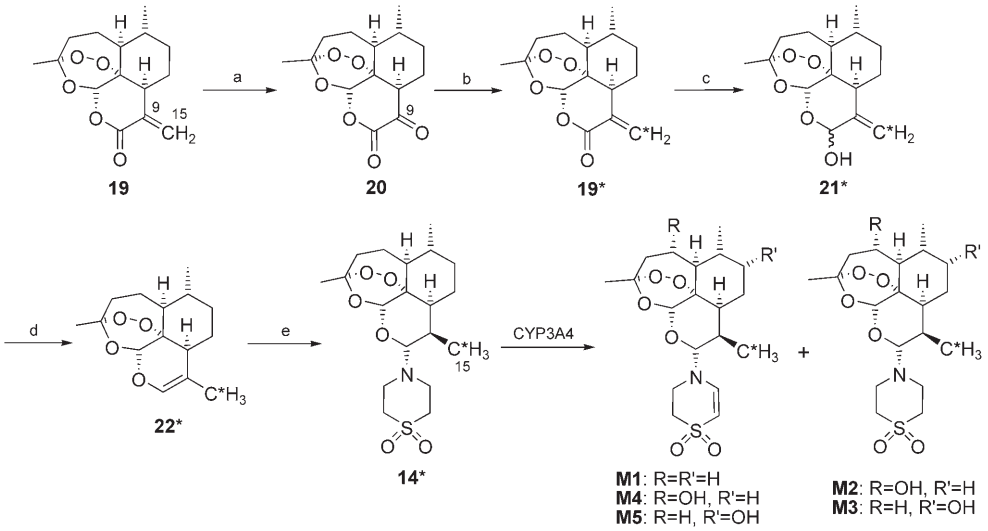

Scheme 2. Preparation of labeled artemisone **14*** ($C^*H_3 = {}^{14}CH_3$ or C^2H_3) and CYP3A4-mediated formation of metabolites **M1**–**M5** ($Ph_3P={}^{14}CH_2$, Et_3SiH for ^{14}C label; $Ph_3P=C^2H_2$, Et_3Si^2H for ^2H label; yields quoted for isolated deuteriated compounds). Reagents and conditions: a) $NaIO_4/RuCl_3$, CCl_4, MeCN, 20 °C, 54 %; b) $C^2H_3PPh_3Br$, *n*-C_4H_9Li, N_2, THF, −78 °C; then **20**, −78–20 °C, 20 h, 48 %; c) *i*Bu_2AlH, CH_2Cl_2, −78 °C, 2 h, >98 %; d) Et_3SiH or Et_3Si^2H, TFA, −78 °C, 4 h, 40 %; e) HCl, CH_2Cl_2, 0 °C; then thiomorpholine, Et_3N, 0 °C, 45 min; 50 % to **12***; then mCPBA, K_2CO_3, Et_2O, 0 °C, to **14***, 72 %. TFA = trifluoroacetic acid.

tion mass spectrometry. The identity of **M1** was also verified by independent preparation of unlabeled **M1** from artemisone and ozone, according to a method used to desaturate tertiary amines.[42] Rat and dog microsomes produce **M1** with larger amounts of **M2** and **M3**, and a large amount of **M1** with a small amount of **M3**, respectively. Incubation with human, dog, and rat hepatocytes largely reflect the metabolism with the microsomes. DHA could not be detected in any of the systems. Plasma from rats administered orally with artemisone contains **M2** and **M3** and minor amounts of **M1**, **M4**, and **M5**. As the in vivo plasma profile of metabolites of rats resembles the in vitro profiles from rat liver microsomes and hepatocytes, the metabolism of artemisone in humans will likely reflect formation of **M1**–**M5** in human microsomes and hepatocytes. Incubation of ^{14}C-labeled artemisone with human liver microsomes and 14 recombinant CYP isoforms together with selective inhibitors indicated that only recombinant CYP3A4 metabolizes artemisone in significant amounts, with troleandomycin, azamulin, and ketoconazole being efficient inhibitors. Treatment of human hepatocytes with 4–10000 ng L^{-1} of artemisone had a borderline inductive effect on CYP2B6 and CYP3A4 at the highest concentration, with no induction of CYP1A2 and CYP2C19. Incubation of artemisone and standard substrates with CYP1A2, -2A6, -2C9, -2C19, -2D6, -2E1, and -3A4 has no effect on substrate metabolism. Therefore, induction of CYP3A4 or CYP2B6 with artemisone, in contrast to the current artemisinins, will likely not be a problem in clinical use.[43]

All aspects of preclinical screening, including the results of pharmacokinetic studies and a detailed toxicological assessment, allow artemisone to be carried forward into clinical trials. We have shown that artemisinins which are structurally distinct to but significantly more active than current artemisinins can be prepared through embedding metabolically inert polar groups within the alkylamino substituents attached directly to C10 of the artemisinin nucleus. The development candidate chosen from within this class, artemisone, has a different metabolic profile to the current artemisinins and displays favorable physicochemical properties and negligible neuro- and cytotoxicities. Notably, in key with the enhanced antimalarial activity of artemisone, inhibition of the likely target, the parasite Ca^{2+} pump PfATP6,[19] is much greater for artemisone than artemisinin: K_i values for artemisinin and artemisone are 169 ± 31 and 1.7 ± 0.6 nM, respectively, and for the *P. vivax* orthologue, the K_i values are 7.7 ± 4.9 and 0.072 ± 0.012 nM, respectively.[20] The cost of artemisone, which is obtained in 2–3 steps from artemisinin, is compatible with the requirement for an antimalarial drug, and its enhanced activity over the current artemisinins will permit the use of lower clinical dose regimens, thereby augmenting the supply of artemisinin. Ironically, the current supply shortfall[44] is largely due to the demand for the fixed combination drug artemether–lumifantrine, of which that amount of drug containing half a gram of artemether is required to cure a malaria patient.[45] In 2005, the estimated global demand was for 120 million adult treatment courses.[46] Thus, approximately 114 tons of artemisinin is required, given that the overall chemical yield of

 © 2006 Wiley-VCH Verlag GmbH & Co. KGaA, Weinheim

artemether from artemisinin is 53%. The time to move on to new, more-active artemisinins is at hand.

Received: August 29, 2005
Revised: November 4, 2005
Published online: January 30, 2006

Keywords: antimalarial agents · artemisinins · medicinal chemistry · metabolism · neurotoxicity

[1] P. L. Olliaro, W. R. Taylor, *J. Postgrad. Med.* **2004**, *50*, 40–44.
[2] J.-M. Liu, M.-Y. Ni, J.-F. Fan, Y.-Y. Tu, Z.-H. Wu, Y.-L. Wu, W.-S. Zhou, *Acta Chim. Sin.* **1979**, *37*, 129–141.
[3] X. Liu, *Yao Xue Tong Bao* **1980**, *15*, 183; X. Liu, CN 85100781A, **1986** [*Chem. Abstr.* **1987**, *107*, 78111j]; Y. Li, P.-L. Yu, Y.-X. Chen, R.-Y. Ji, *Acta Chim. Sin.* **1982**, *40*, 557–561.
[4] Y. Li, P.-L. Yu, Y.-X. Chen, L.-Q. Li, Y.-Z. Gai, D.-S. Wang, Y.-P. Zheng, *Acta Chim. Sin.* **1981**, *16*, 429–439.
[5] A. Brossi, B. Venugopalan, L. Dominguez Gerpe, H. J. C. Yeh, J. L. Flippen-Anderson, P. Buchs, X.-D. Luo, W. Milhous, W. Peters, *J. Med. Chem.* **1988**, *31*, 645–650.
[6] Q.-G. Li, J. O. Peggins, L. L. Fleckenstein, K. Masonic, M. H. Heiffer, T. G. Brewer, *J. Pharm. Pharmacol.* **1998**, *50*, 173–182; V. Navaratnam, S. M. Mansor, N. W. Sit, J. Grace, Q.-G. Li, P. Olliaro, *Clin. Pharmacokinet.* **2000**, *39*, 255–270.
[7] N. Vyas, B. A. Avery, M. A. Avery, C. M. Wyandt, *Antimicrob. Agents Chemother.* **2002**, *46*, 105–109.
[8] J. M. Grace, A. J. Aguilar, K. M. Trotman, T. G. Brewer, *Drug Metab. Dispos.* **1998**, *26*, 313–317; M. A. van Agtmael, V. Gupta, T. H. van der Wösten, J.-P. B. Rutten, C. J. van Boxtel, *Eur. J. Clin. Pharmacol.* **1999**, *55*, 405–410; T. Gordi, R. Xie, N. V. Huong, D. X. Huong, M. O. Karlsson, M. Ashton, *Br. J. Clin. Pharmacol.* **2005**, *59*, 189–198.
[9] C. J. Woodrow, R. K. Haynes, S. Krishna, *Postgrad. Med. J.* **2005**, *81*, 71–78.
[10] T. G. Brewer, S. J. Grate, J. O. Peggins, P. J. Weina, J. M. Petras, B. S. Levine, M. H. Heiffer, B. G. Schuster, *Am. J. Trop. Med. Hyg.* **1994**, *51*, 251–259; S. Kamchonwongpaisan, P. McKeever, P. Hossler, H. Ziffer, S. R. Meshnick, *Am. J. Trop. Med. Hyg.* **1997**, *56*, 7–12; A. Nontprasert, M. Nosten-Bertrand, S. Pukrittayakamee, S. Vanijanonta, B. J. Angus, N. J. White, *Am. J. Trop. Med. Hyg.* **1998**, *59*, 519–522.
[11] D. L. Wesche, M. A. DeCoster, F. C. Tortella, T. G. Brewer, *Antimicrob. Agents Chemother.* **1994**, *38*, 1813–1819.
[12] J. Fishwick, W. G. McLean, G. Edwards, S. A. Ward, *Chem.-Biol. Interact.* **1995**, *96*, 263–271.
[13] W. G. McLean, S. A. Ward, *Med. Trop.* **1998**, *58*(Suppl. 3), 28–31.
[14] T. Gordi, E.-I. Lepist, *Toxicol. Lett.* **2004**, *147*, 99–107.
[15] R. Johann-Liang, R. Albrecht, *Clin. Infect. Dis.* **2003**, *36*, 1626–1627.
[16] R. K. Haynes, W.-Y. Ho, H.-W. Chan, B. Fugmann, J. Stetter, S. L. Croft, L. Vivas, W. Peters, B. L. Robinson, *Angew. Chem.* **2004**, *116*, 1405–1409; *Angew. Chem. Int. Ed.* **2004**, *43*, 1381–1385; R. K. Haynes, *Angew. Chem.* **2005**, *117*, 2100–2101; *Angew. Chem. Int. Ed.* **2005**, *44*, 2064–2065.
[17] R. K. Haynes, H.-W. Chan, W.-Y. Ho, C. K. F. Ko, L. Gerena, D. E. Kyle, W. Peters, B. L. Robinson, *ChemBioChem* **2005**, *6*, 659–667.
[18] Malaria Control Department & Essential Drugs and Medicines Policy Department, World Health Organization, Geneva, Access to Antimalarial Medicines: Improving the Affordability and Financing of Artemisinin-Based Combination Therapies, WHO/CDS/MAL/2003.1095, p. 30.
[19] U. Eckstein-Ludwig, R. J. Webb, I. D. A. van Goethem, J. M. East, A. G. Lee, M. Kimura, P. M. O'Neill, P. G. Bray, S. A. Ward, S. Krishna, *Nature* **2003**, *424*, 957–961.
[20] A.-C. Uhlemann, A. Cameron, U. Eckstein-Ludwig, G. Fischbarg, P. Iserovich, F. A. Zuniga, M. East, A. Lee, L. Brady, R. K. Haynes, S. Krishna, *Nat. Struct. Mol. Biol.* **2005**, *12*, 628–629.
[21] G. L. Patrick, *An Introduction to Medicinal Chemistry*, 2nd ed., Oxford University Press, Oxford, **2001**, chap. 10, pp. 223–224; G. L. Patrick, *An Introduction to Medicinal Chemistry*, 2nd ed., Oxford University Press, Oxford, **2001**, chap. 11, pp. 260–266.
[22] C. A. Lipinski, F. Lombardo, B. W. Dominy, P. J. Feeney, *Adv. Drug Delivery Rev.* **2001**, *46*, 3–26.
[23] R. Manhold, R. F. Bekker, K. Dross, G. Bijloo, G. de Vries, *Quant. Struct.-Act. Relat.* **1998**, *17*, 517–536.
[24] K. Ramu, J. K. Baker, *J. Med. Chem.* **1995**, *38*, 1911–1921.
[25] A. K. Bhattacharjee, J. M. Karle, *Chem. Res. Toxicol.* **1999**, *12*, 422–428.
[26] R. K. Haynes, *Curr. Opin. Infect. Dis.* **2001**, *14*, 719–772.
[27] G. Schmuck, E. Roehrdanz, R. K. Haynes, R. Kahl, *Antimicrob. Agents Chemother.* **2002**, *46*, 821–827.
[28] R. K. Haynes, H. W. Chan, M.-K. Cheung, S.-K. Chung, W.-L. Lam, H.-W. Tsang, A. Voerste, I. D. Williams, *Eur. J. Org. Chem.* **2003**, 2098–2114.
[29] R. K. Haynes, W. L. Lam, H. W. Chan, M. K. Cheung, H. W. Tsang, Synthesis and Antiparasitic Activity of Artemisinin Derivatives (Endoperoxides), International patent WO 2000004024A1, **2000** [*Chem. Abs.* **2000**, *132*, 122783].
[30] R. K. Haynes, Antiparasitic Artemisinin Derivatives, International patent WO 03/076446A1, **2002** [*Chem. Abs.* **2003**, *139*, 261439].
[31] A. K. Ghose, G. M. Crippen, *J. Chem. Inf. Comput. Sci.* **1987**, *27*, 21–35.
[32] G. Schmuck, H. J. Ahr, G. Schlüter, *In Vitro Mol. Toxicol.* **2000**, *13*, 37–49.
[33] G. Schmuck, R. K. Haynes, *Neurotoxic. Res.* **2000**, *2*, 37–49.
[34] J. K. Baker, J. D. McChesney, H.-T. Chi, *Pharm. Res.* **1993**, *10*, 662–666; B. Yagen, Y. M. Pu, H. J. Yeh, H. Ziffer, *J. Chem. Soc. Perkin Trans. 1* **1994**, 843–846; D. S. Torok, H. Ziffer, *Tetrahedron Lett.* **1995**, *36*, 829–832; R. K. Haynes, H.-O. Pai, A. Voerste, *Tetrahedron Lett.* **1999**, *40*, 4715–4718.
[35] G. Schmuck, M. Temerowski, R. K. Haynes, B. Fugmann, *Recent Res. Dev. Antimicrob. Agents Chemother.* **2003**, *3*, 35–47.
[36] W. Peters, B. L. Robinson in *Handbook of Animal Models of Infection* (Eds.: O. Zak, M. Sande), Academic Press, London, **1999**, Section VI, Parasitic Infection Models, chap. 92, pp. 756–771.
[37] R. E. Desjardins, C. J. Canfield, J. D. Haynes, J. D. Chulay, *Antimicrob. Agents Chemother.* **1979**, *16*, 710–718.
[38] B. M. Kotecka, K. H. Rieckmann, *Am. J. Trop. Med. Hyg.* **1993**, *49*, 460–464.
[39] L. Zhang, W.-S. Zhou, *Youji Huaxue* **1988**, *8*, 329–330 [*Chem. Abs.* **1989**, *111*, 78408]; L. Zhang, W.-S. Zhou, *Huaxue Xuebao* **1989**, *47*, 1117–1119 [*Chem. Abs.* **1990**, *112*, 217297]; S. Paitayatat, B. Tarnchompoo, Y. Thebtaranonth, Y. Yuthavong, *J. Med. Chem.* **1997**, *40*, 633–638; S. Ekthawatchai, J. Lertvorachon, P. Meepowpan, T. Thongpanchang, Y. Thebtaranonth, Y. Yuthavong, *Synth. Commun.* **2003**, *33*, 1855–1860.
[40] N. Acton, J. M. Karle, R. E. Miller, *J. Med. Chem.* **1993**, *36*, 2552–2557.
[41] M. A. Avery, J. D. Bonk, S. Mehrotra, *J. Labelled Compd. Radiopharm.* **1996**, *38*, 249–254; M. A. Avery, J. D. Bonk, J. Bupp, *J. Labelled Compd. Radiopharm.* **1996**, *38*, 263–267.
[42] P. S. Bailey, D. A. Mitchard, A.-I. Y. Khashab, *J. Org. Chem.* **1968**, *33*, 2675–2680.
[43] HPLC fractions (solutions in DMSO) of the metabolites isolated at Bayer Pharma (Germany) were submitted to preliminary screens at the Australian Army Malaria Institute against

 © 2006 Wiley-VCH Verlag GmbH & Co. KGaA, Weinheim

P. falciparum K1 in vitro. Metabolite **M1** ($IC_{50} = 1.7\ ng\,mL^{-1}$) and **M3** ($IC_{50} = 2.3\ ng\,mL^{-1}$) reveal similar activities to that of artemisone ($IC_{50} = 0.8\ ng\,mL^{-1}$), but **M2** is less active ($IC_{50} = 25.7\ ng\,mL^{-1}$).

[44] M. Enserink, *Science* **2005**, *307*, 33.

[45] M. van Vugt, S. Looareesuwan, P. Wilairatana, R. McGready, L. Villegas, I. Gathmann, R. Mull, A. Brockman, N. J. White, F. Nosten, *Trans. R. Soc. Trop. Med. Hyg.* **2000**, *94*, 545 – 548.

[46] from http://rbm.who.int/wmr2005/htm: Roll Back Malaria World Malaria Report 2005: Section III Global Financing, Commodities And Service Delivery; II. Commodities And Service Delivery, Roll Back Malaria Partnership, World Health Organization, Geneva.

 © 2006 Wiley-VCH Verlag GmbH & Co. KGaA, Weinheim

Mesoporous Materials

DOI: 10.1002/anie.200504191

Chiral Mesostructured Silica Nanofibers of MCM-41**

*Bo Wang, Cheng Chi, Wei Shan, Yahong Zhang, Nan Ren, Wuli Yang, and Yi Tang**

Mesostructured silica MCM-41 has been one of the most extensively studied mesostructured materials since its first synthesis by Mobil scientists in 1992.[1] Many important applications[2] of mesostructured silica MCM-41 in catalysis, separation, and nanoengineering are closely correlated to its ordered two-dimensional (2D) hexagonal mesostructure/mesopore. Besides the usual straight 2D hexagonal mesostructure,[3] various curved mesostructures of MCM-41 have also been reported by several research groups in the last decade,[4] which has aroused great academic interest in their enigmatic morphogenesis. Recently our research group has investigated the topological transformation of a series of vesicular MCM-41 compounds with different mesostructures in an alkaline synthesis system[5] that was initialy developed by Rathouský and co-workers.[6] The self-assembly of sodium silicate (SS) and cetyltrimethylammonium bromide (CTAB) into a hexagonal mesostructure in such a method is driven by the hydrolysis of ethyl acetate (EA). Herein we report that chiral mesostructured silica nanofibers of MCM-41 can be fabricated in this SS/CTAB/EA/H_2O system by simply lowering the SS and CTAB concentrations below 0.5 mol per 1000 mol H_2O. It is remarkable that two types of chiral mesostructures with different symmetries were synthesized from the usual achiral materials in this study. Moreover, a relationship between the chiral and ordinary achiral mesostructures of MCM-41 was revealed through a systematic investigation of the synthesis system.

The first type of chiral nanofibers of MCM-41 (Figure 1a, b) has a single twist axis. The XRD pattern of such a single-axis nanofiber (Figure 1c) reveals a highly ordered 2D hexagonal mesostructure with a lattice constant of 4.5 nm. The N_2 sorption isotherms of the calcined product show a steep capillary condensation at a P/P_0 ratio of 0.2:1–0.3:1, which corresponds to a BJH pore size of 2.4 nm (Figure 1d). The BET surface area and mesopore volume of the single-axis nanofiber are 960 $m^2 g^{-1}$ and 0.63 $cm^3 g^{-1}$, respectively. Analysis of the chiral mesostructure of the single-axis nanofibers by electron microscopy showed: 1) The twisted crystal facets could be distinguished from their field-emission SEM images (see Supporting Information); 2) periodic fringes along the axis of the nanofiber in the TEM image (Figure 1b); and 3) the observed fringes moved along the axis when the

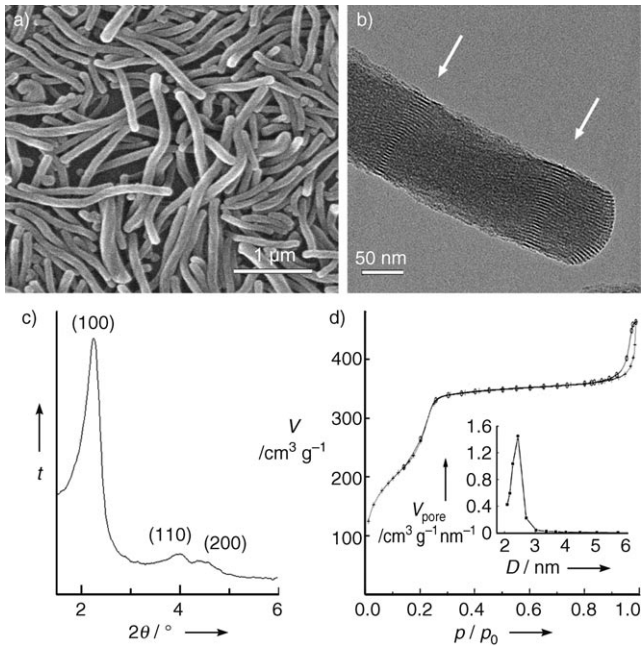

Figure 1. a) SEM image, b) TEM image, c) XRD pattern, and d) N_2 sorption isotherms of single-axis chiral nanofibers (SS/CTAB/EA/H_2O, molar ratio 0.19:0.16:2.7:1000).

[*] B. Wang,[+] C. Chi,[+] W. Shan, Dr. Y. H. Zhang, N. Ren, Prof. Y. Tang
Department of Chemistry and
Shanghai Key Laboratory of Molecular Catalysis and Innovative Materials
Fudan University
Shanghai 200433 (P.R. China)
Fax: (+86) 21-6564-1740
E-mail: yitang@fudan.edu.cn
Dr. W. L. Yang
Department of Macromolecular Science and
Key Laboratory of Molecular Engineering of Polymers
Ministry of Education
Fudan University
Shanghai 200433 (P.R. China)
[+] These authors contributed equally.

[**] We thank Prof. D. Y. Zhao for his very helpful discussions. This work was supported by the NSFC (20233030, 20325313, 20303003, 20421303, 20473022), the STCSM (05QMX1403, 05XD14002), and the Major State Basic Research Development Program (2003CB615807).

Supporting Information for this article is available on the WWW under http://www.angewandte.org or from the author.

InterScience
© 2006 Wiley-VCH Verlag GmbH & Co. KGaA, Weinheim

nanofiber was rotated around its twist axis, while the fringes appeared to be curved when the nanofiber was tilted vertically against its original direction (see Supporting Information). The above observations indicate that such a nanofiber is composed of chiral nanochannels with a single twist axis.[7b] Notably, the nanochannels at the end of some nanofibers become straight, which results in an additional set of fringes (Figure 1b). It was found by counting more than 400 single-axis nanofibers that the number of left-handed nanofibers is almost equal to the number of right-handed ones, thus demonstrating that the product is a racemic mixture.

The dimensions of the single-axis nanofibers vary significantly with the concentrations of the reactants in the SS/CTAB/EA/H_2O system: The length of the nanofibers increases with the concentration of CTAB (see Supporting Information) and varies from tens of nanometers to tens of micrometers, and the diameter of the nanofibers increases as the concentration of silicate increases (Figure 2). Interestingly, nanofibers with a large diameter have a large twist period. The coexistence of a large diameter and a small twist period would result in nanochannels with high curvatures, which is not preferred from an energy viewpoint. The twist period of the fibers synthesized at higher silicate concentrations becomes so large that the fibers are almost straight and chirality is no longer evident (Figure 2d). If the reactant concentrations are further increased, the obtained product becomes ordinary MCM-41 fibers (namely tubules[5]) with straight hexagonal mesostructures. On the basis of these results, the ordinary straight MCM-41 mesostructure can be regarded as a special case of a chiral mesostructure with a twist period of infinite length.

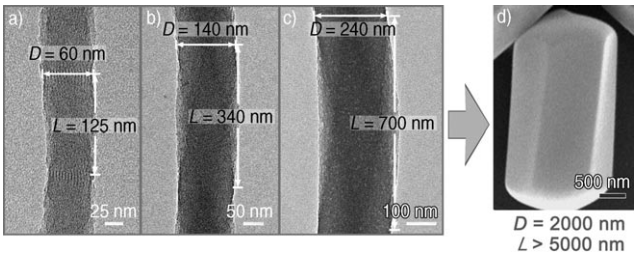

Figure 2. Electron micrographs of single-axis nanofiber samples obtained at different silicate concentrations (SS/CTAB/EA/H_2O, molar ratio x:0.16:2.7:1000), where a) $x = 0.17$, b) $x = 0.20$, c) $x = 0.23$, and d) $x = 0.50$. Both the diameter (D) and twist period ($6L$) of the nanofibers increase with the concentration of silicate. The chirality of the fiber obtained at a high silicate concentration becomes unobservable, and its mesostructure is close to the ordinary straight hexagonal mesostructure.

Another type of chiral nanofibers appeared in the MCM-41 products when the EA concentration was decreased in the synthesis system (Figure 3a). The nanofibers have two twist axes: one lies outside the nanofiber, and the other one lies in the center of the nanofiber. Some of these dual-axis nanofibers do not wind very regularly around their primary twist axes. The well-crystallized mesostructure of the dual-axis nanofiber enabled us to discover some distinct features. It was found that the primary and secondary twist not only share the same chirality but they also have the same period (Figure 4a).

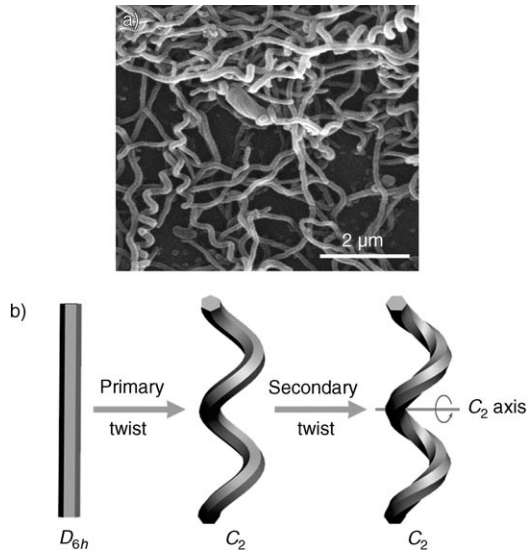

Figure 3. a) SEM image of dual-axis chiral nanofibers (SS/CTAB/EA/H_2O, molar ratio 0.19:0.16:0.50:1000). b) Transformation from a straight hexagonal fiber to a dual-axis fiber through two twist operations which is accompanied by a degradation of symmetry.

Surprisingly, every period of the dual-axis nanofiber has two instead of six[7c] sets of (100) fringes in the TEM image (see arrows in Figure 4c). This observation can be ascribed to the primary twist operation that degrades the symmetry of the nanofiber from the D_{6h} to the C_2 point group (Figure 3b). A three-dimensional model was built by performing two twist operations on a straight hexagonal mesostructure, and it is in excellent agreement with the SEM and TEM images of the dual-axis nanofiber (Figure 4).

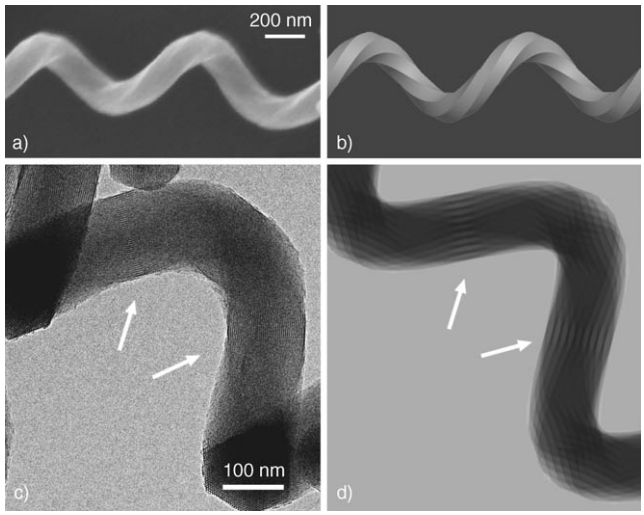

Figure 4. a) SEM image, b) simulated 3D model, c) TEM image, and d) simulated TEM image of a dual-axis nanofiber.

Two factors are critical for the synthesis of chiral MCM-41 nanofibers. One is the concentration ratio of CTAB to SS. No solid product could be obtained if the concentration ratio of CTAB/SS was above a certain value (approximately 3:1–4:1 at 25 °C). This result might be attributed to a shortage of the

 © 2006 Wiley-VCH Verlag GmbH & Co. KGaA, Weinheim

silicate source, that is, the amount of the silicates in solution is not sufficient for the cross-linking of silicate–CTA species into an aggregated form. Another factor is the synthesis temperature. The length of the nanofibers gradually decreases as the temperature increases, and is accompanied by a loss of the ordered mesostructure. No precipitate could be obtained from the synthesis solution when the temperature exceeded about 50 °C, thus suggesting that the aggregation of the silicate–CTA complexes was greatly hampered under such conditions. The recommended temperature for the synthesis of chiral MCM-41 nanofibers is between 18 and 25 °C.

In contrast to previous studies in which chiral surfactants were used to fabricate chiral mesostructures,[7–9] our synthesis of chiral MCM-41 was carried out without any chiral additives. Both the CTA^+ and silicon-oxygen tetrahedron have highly symmetric structures, thus the chirality of the MCM-41 nanofibers must originate from a chiral aggregation of these symmetric building blocks. Such chirality is analogous to that of many organic molecules which originates from an asymmetric combination of carbon, oxygen, and hydrogen atoms. Notably, the study by Che et al. showed that the use of a chiral surfactant (namely, sodium *N*-acyl-L-alanine) led to more left-handed fibers than right-handed ones,[7b] thus suggesting that the chiral surfactant may play a role in the breaking of the racemization of the obtained mesostructured silica. Another important question arising from our work is how the same chirality is maintained during the formation of every single MCM-41 nanofiber. We presume that two possible assembly routes may lead to this result. One possibility is that some chiral silicate–CTA intermediate species are formed during the assembly process and that species with the same chirality tend to assemble with each other, thus forming nanofibers with specific chiralities. Another possibility is that nuclei with different chiralities are formed at the beginning of the reaction, and then they induce the silicate and CTA^+ species to assemble into aggregates with the same chirality on the seed surface. As mentioned above, the chirality of the nanofibers becomes more prominent as its diameter decreases (Figure 2), which may suggest that the chiral mesostructure is more thermodynamically stable than the achiral one at small dimensions. The recent study of Stucky and co-workers[10] has shown that the physical confinement of mesostructured silica could also lead to the formation of chiral architectures. Thus, the dimensions may possibly play an important role in the symmetry breaking of the mesostructured silica.

In conclusion, two types of chiral MCM-41 nanofibers were synthesized from achiral surfactant and silicate reactants, and their chiral architectures were carefully characterized. A transformation from a chiral mesostructure to a straight achiral mesostructure was observed, thus demonstrating an interesting relationship between these two seemingly different structures. Furthermore, the self-assembly of nanosized chiral mesostructure in a diluted SS/CTAB/EA/H_2O system is an important supplement to the formation of micrometer-sized vesicles observed at higher reactant concentrations.[5] We expect that these results will contribute to the understanding of the formation of mesostructured silica MCM-41.[1,4d,11]

Experimental Section

In a typical synthesis of MCM-41 single-axis nanofibers, sodium silicate ($Na_2SiO_3 \cdot 9H_2O$, 0.45 g) and CTAB (0.5 g) were dissolved in H_2O (150 g) at 23 °C. Ethyl acetate (2.0 g) was added to the above solution under vigorous stirring. After stirring the mixture for about 30 s, the solution was left to stand in a water bath at 23 °C overnight. The product was isolated by centrifugation and then washed repeatedly with deionized water. The dried samples were calcined in air at 600 °C for 6 h to remove the surfactants. The reaction compositions for the synthesis of single-axis and dual-axis nanofibers were SS/CTAB/EA/H_2O 0.15–0.50:0.12–0.33:1.4–3.0:1000, and 0.15–0.30:0.16–0.50:0.3–0.5:1000 (in molar ratio), respectively.

Transmission electron microscopy (TEM) and scanning electron microscopy (SEM) images were obtained on JEOL JEM-2010 and Philips XL 30 instruments, respectively. The X-ray diffraction (XRD) patterns were taken on a Rigaku D/MAX-IIA diffractometer with $Cu_{K\alpha}$ radiation at 30 kV and 20 mA. Nitrogen sorption isotherms were measured on a Micromeritics TriStar 3000 system. The samples were degassed at 200 °C for about 3 h before the sorption measurement.

Received: November 24, 2005
Published online: February 24, 2006

Keywords: chirality · mesoporous materials · nanostructures · silica

[1] C. T. Kresge, M. E. Leonowicz, W. J. Roth, J. C. Vartuli, J. S. Beck, *Nature* **1992**, *359*, 710.
[2] A. Corma, *Chem. Rev.* **1997**, *97*, 2373; M. E. Davis, *Nature* **2002**, *417*, 813.
[3] H. P. Lin, C. Y. Mou, *Science* **1996**, *273*, 765.
[4] a) H. Yang, N. Coombs, G. A. Ozin, *Nature* **1997**, *386*, 692; b) H. P. Lin, Y. R. Cheng, C. Y. Mou, *Chem. Mater.* **1998**, *10*, 3772; c) S. M. Yang, W. J. Kim, *Adv. Mater.* **2001**, *13*, 1191; d) S. Sadasivan, C. E. Fowler, D. Khushalani, S. Mann, *Angew. Chem.* **2002**, *114*, 2255; *Angew. Chem. Int. Ed.* **2002**, *41*, 2151; e) J. Wang, J. Zhang, B. Y. Asoo, G. D. Stucky, *J. Am. Chem. Soc.* **2003**, *125*, 13966; f) J. Wang, C. Tsung, R. C. Hayward, Y. Wu, G. D. Stucky, *Angew. Chem.* **2005**, *117*, 336; *Angew. Chem. Int. Ed.* **2005**, *44*, 332.
[5] B. Wang, W. Shan, Y. H. Zhang, J. C. Xia, W. L. Yang, Z. Gao, Y. Tang, *Adv. Mater.* **2005**, *17*, 578.
[6] G. Schulz-Ekloff, J. Rathouský, A. Zukal, *Int. J. Inorg. Mater.* **1999**, *1*, 97.
[7] a) S. Che, A. E. Garcia-Bennett, T. Yokoi, K. Sakamoto, H. Kunieda, O. Terasaki, T. Tatsumi, *Nat. Mater.* **2003**, *2*, 801; b) S. Che, Z. Liu, T. Ohsuna, K. Sakamoto, O. Terasaki, T. Tatsumi, *Nature* **2004**, *429*, 281; c) T. Ohsuna, Z. Liu, S. Che, O. Terasaki, *Small* **2005**, *1*, 233.
[8] a) Y. Yang, M. Suzuki, S. Owa, H. Shirai, K. Hanabusa, *Chem. Commun.* **2005**, 4462; b) Y. Yang, M. Suzuki, H. Shirai, A. Kurose, K. Hanabusa, *Chem. Commun.* **2005**, 2032.
[9] A. M. Seddon, H. M. Patel, S. L. Burkett, S. Mann, *Angew. Chem.* **2002**, *114*, 3114; *Angew. Chem. Int. Ed.* **2002**, *41*, 2988.
[10] Y. Wu, G. Cheng, K. Katsov, S. W. Sides, J. Wang, J. Tang, G. H. Fredrickson, M. Moskovits, G. D. Stucky, *Nat. Mater.* **2004**, *3*, 816.
[11] a) A. Firouzi, D. Kumar, L. M. Bull, T. Besier, P. Sieger, Q. Huo, S. A. Walker, J. A. Zasadzinski, C. Glinka, J. Nicol, D. Margolese, G. D. Stucky, B. F. Chmelka, *Science* **1995**, *267*, 1138; b) A. Monnier, F. Schuth, Q. Huo, D. Kumar, D. Margolese, R. S. Maxwell, G. D. Stucky, M. Krishnamurty, P. Petroff, A. Firouzi, M. Janicke, B. F. Chmelka, *Science* **1993**, *261*, 1299.

 © 2006 Wiley-VCH Verlag GmbH & Co. KGaA, Weinheim

Cyclization Sequence

DOI: 10.1002/anie.200503874

Gold- or Platinum-Catalyzed Tandem Cycloisomerization/Prins-Type Cyclization Reactions**

José Barluenga, Alejandro Diéguez, Amadeo Fernández, Félix Rodríguez, and Francisco J. Fañanás*

Tandem (domino) reactions have emerged as powerful tools to meet the demands of modern organic chemistry (efficiency, compatibility with the environment, low production costs, etc.).[1] Moreover, gold and platinum complexes have been widely used in recent years as catalysts for the cyclization of enynes,[2] and interesting cyclic compounds have also been obtained from ω-alkynols by metal-catalyzed cycloisomerizations.[3] In this context, we have recently developed a tandem tungsten-catalyzed cycloisomerization/cyclopropanation reaction of 4-pentyn-1-ol derivatives for the synthesis of eight-membered carbocycles.[4,5] Encouraged by these results, we investigated similar tandem reactions by using different metal catalysts, and we describe herein a novel tandem 6-*exo* cycloisomerization/Prins-type cyclization of allyl-substituted 5-hexyn-1-ol derivatives catalyzed by gold and platinum complexes.

Initial studies in this field demonstrated that several metal complexes (W, Ru, Rh, Pt, Au) catalyze the *exo*-cycloisomerization of ω-alkynols to give acetal derivatives (Scheme 1).[6] We envisioned that such acetals with an allyl moiety in their structures could participate in a subsequent Prins-type cyclization,[7] in the presence of an appropriate nucleophile, to finally give interesting bicyclic compounds in a catalytic tandem process.

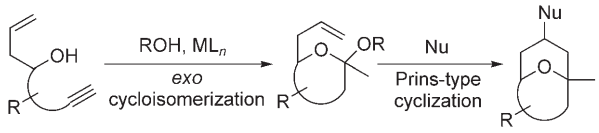

Scheme 1. Proposed tandem catalytic *exo* cycloisomerization/Prins-type cyclization reaction.

[*] Prof. Dr. J. Barluenga, Dr. A. Diéguez, A. Fernández, Dr. F. Rodríguez, Dr. F. J. Fañanás
Instituto Universitario de Química Organometálica "Enrique Moles"
Unidad Asociada al CSIC
Universidad de Oviedo
Julián Clavería, 8, 33006 Oviedo (Spain)
Fax: (+34) 98-510-3450
E-mail: barluenga@uniovi.es

[**] We gratefully acknowledge financial support from the DGICYT (BQU-2001-3853), FICYT (grant to A.D.), and MCYT ("Ramón y Cajal" contract to F.R.).

Supporting information for this article is available on the WWW under http://www.angewandte.org or from the author.

Initial attempts to promote the tandem sequence described above were performed with the model diallyl-substituted alkynol **1a** as starting material. Thus, we treated **1a** with 2 mol% of several gold and platinum complexes in methanol as solvent (Table 1).[8] The reaction with [$PtCl_2$-(cod)] as catalyst did not proceed at room temperature (Table 1, entry 1; cod = cycloocta-1,5-diene); **1a** was recovered quantitatively after 24 h. However, performing the reaction at 65 °C for 12 h produced the eight-membered carbocycle **2a** as a single diastereomer in 95% yield (Table 1, entry 2).[9] Interestingly, the Pt^{IV} complex $PtCl_4$ also catalyzes this transformation. The reaction proceeds very slowly at room temperature and after three hours **2a** was isolated in only 66% yield (Table 1, entry 3). However, at 65 °C the reaction was complete after only one hour and gave **2a** in 96% yield (Table 1, entry 4).

Table 1: Cycloisomerization reactions of the alkynol **1a** with several platinum and gold catalysts ML_n.

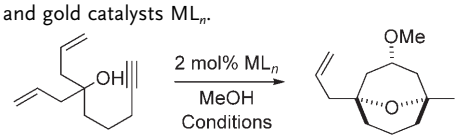

1a **2a**

Entry	ML_n	Conditions	Yield [%][a]
1	[$PtCl_2$(cod)]	RT, 24 h	0
2	[$PtCl_2$(cod)]	65 °C, 12 h	95
3	$PtCl_4$	RT, 3 h	66
4	$PtCl_4$	65 °C, 0.5 h	96
5	[AuCl(PPh_3)]	65 °C, 24 h	0
6	AuCl	65 °C, 12 h	55[b]
7	$AuCl_3$	RT, 1 h	94

[a] Yield of isolated product based on alkynol **1a**. [b] 42% of **1a** was recovered.

We then turned our attention to gold complexes (Au^I and Au^{III}). We did not observe any transformation with [AuCl-(PPh_3)], and compound **1a** was recovered quantitatively after 24 h at 65 °C (Table 1, entry 5). When AuCl was used as catalyst, however, compound **2a** was formed, although, after 12 h at 65 °C, the yield of isolated **2a** was only 55%, and 42% of **1a** was also recovered (Table 1, entry 6). The higher valent gold complex $AuCl_3$ gave excellent results. Thus, treatment of **1a** with 2 mol% $AuCl_3$ in methanol at room temperature for one hour furnished **2a** in 94% yield (Table 1, entry 7). Pt^{II}, Pt^{IV}, and Au^{III} complexes are therefore appropriate catalysts for the synthesis of eight-membered carbocycles such as **2a**.

Encouraged by these results, and aiming to obtain a variety of eight-membered carbocycles from simple starting materials, we next examined the scope of this catalytic process. As shown in Table 2, different substituents on the alkyne derivative **1** are tolerated. The reaction can also be performed with alkynol derivatives containing a heteroatom (Table 2, entries 11–13). Additionally, a number of alcohols proved to be effective nucleophiles. All three catalysts—[$PtCl_2$(cod)], $PtCl_4$, and $AuCl_3$—give the corresponding bicyclic compounds **2** in essentially the same yield. It is also important to note that in all cases only one diastereomer of

 © 2006 Wiley-VCH Verlag GmbH & Co. KGaA, Weinheim

Table 2: Cycloisomerization reactions of the alkynol derivatives **1a–g** in the presence of different alcohols.

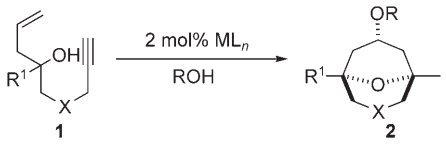

Entry	Alkynol	R^1	X	ML_n[a]	Product	R	Yield [%][b]
1	**1a**	allyl	CH_2	$[PtCl_2(cod)]$	**2b**	Et	92
2	**1a**	allyl	CH_2	$AuCl_3$	**2c**	Pr	94
3	**1b**	Me	CH_2	$[PtCl_2(cod)]$	**2d**	Me	94
4	**1b**	Me	CH_2	$AuCl_3$	**2e**	Et	96
5	**1c**	Bu	CH_2	$[PtCl_2(cod)]$	**2f**	Me	92
6	**1d**	*i*Pr	CH_2	$[PtCl_2(cod)]$	**2g**	Me	92
7	**1d**	*i*Pr	CH_2	$AuCl_3$	**2h**	Et	88
8	**1e**	*t*Bu	CH_2	$[PtCl_2(cod)]$	**2i**	Me	90
9	**1e**	*t*Bu	CH_2	$AuCl_3$	**2j**	Et	91
10	**1f**	H	CH_2	$PtCl_4$	**2k**	Me	88
11	**1g**	allyl	O	$PtCl_4$	**2l**	*i*Pr	93
12	**1g**	allyl	O	$PtCl_4$	**2m**	Me	95
13	**1g**	allyl	O	$AuCl_3$	**2n**	Pr	91

[a] When $[PtCl_2(cod)]$ was used as catalyst in MeOH the reaction was performed at 65 °C for 12 h; for all other alcohols the reaction was carried out at 80 °C for 12 h. When $PtCl_4$ and MeOH were used, the reaction was performed at 65 °C for 1 h; for all other alcohols the reaction was carried out at 80 °C for 1 h. All reactions with $AuCl_3$ were left at room temperature for 1 h. [b] Yield of isolated product based on alkynol **1**.

product **2** was formed. Structural assignment was based on a series of NMR studies, including COSY, NOESY, HMQC, and HMBC experiments.

To gain some insight into the mechanism of the reaction, we performed labeling studies with deuterated starting materials or solvents. Thus, the reaction of **1a** in CD_3OD in the presence of 2 mol% of $[PtCl_2(cod)]$ at 65 °C for 12 h cleanly afforded the heptadeuterated compound $[D_7]$-**2a** in 93% yield. Moreover, reaction of the deuterated alkyne $[D_1]$-**1a** in CH_3OH under the same conditions led to the formation of $[D_1]$-**2a** in 92% yield (Scheme 2).

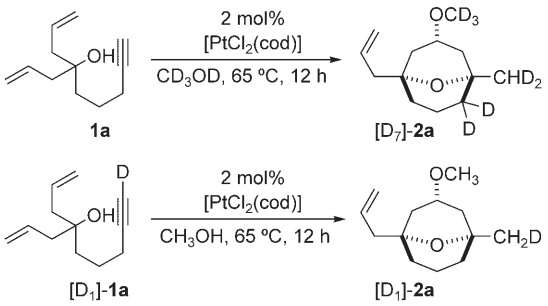

Scheme 2. Labeling experiments for the catalytic transformation of **1a** and $[D_1]$-**1a**.

All our experiments support a mechanism for the formation of compounds **2** based on a tandem sequence involving an initial 6-*exo* cycloisomerization followed by a Prins-type cyclization (Scheme 3). The reaction is initiated by coordination of the platinum or gold complex to the triple bond of the starting alkynol **1** to form intermediate **3**

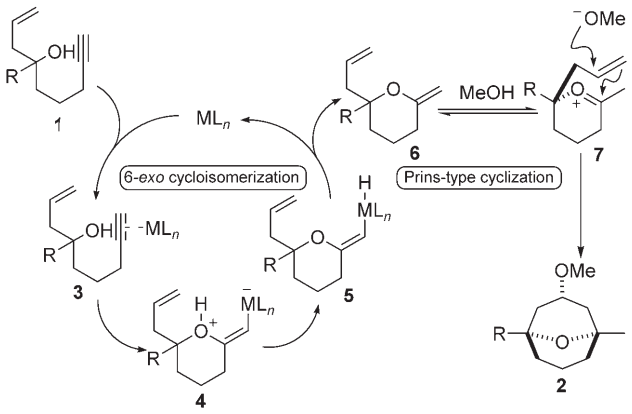

Scheme 3. Proposed mechanism for the formation of eight-membered carbocycles **2** from alkynols **1**.

according to the Dewar–Chatt–Duncanson model.[10] Intramolecular addition of the hydroxy group to the internal carbon atom of the triple bond generates **4**. Migration of the hydrogen atom from the oxygen to the metal atom then leads to the formation of hydride complex **5**, which, after reductive elimination, produces the exocyclic enol ether **6** and regenerates the catalytic species.[11] At this point the second part of the tandem sequence—the Prins-type cyclization—is initiated. In the alcohol solvent an equilibrium between intermediate **6** and oxocarbenium ion **7** is likely to occur. This oxocarbenium ion may exist as an ion-pair with the counterion, which also serves as the nucleophile. The cyclization step is believed to proceed through a chair-like transition state, thereby favoring nucleophilic trapping from an equatorial trajectory. This is consistent with the configuration of the stereogenic centers observed in the final products **2**. More support for this mechanistic proposal can be found in the previously discussed labeling experiments (Scheme 2). Formation of deuterated compounds $[D_1]$-**2a** and $[D_7]$-**2a** clearly supports a Lewis acid-type activation of the starting alkyne and rules out any possible mechanism initiated by an insertion of the metal species into the terminal C–H (or C–D) bond of the triple bond. Also, formation of $[D_7]$-**2a** is in good agreement with the participation of an oxocarbenium ion such as **7** as intermediate because the acidic hydrogen atoms in the α-positions to the oxocarbenium group are deuterated by CD_3OD prior to the cyclization step.

Additional experiments to further extend the synthetic possibilities of this tandem sequence are shown in Scheme 4. For example, when the catalytic reaction is performed with a

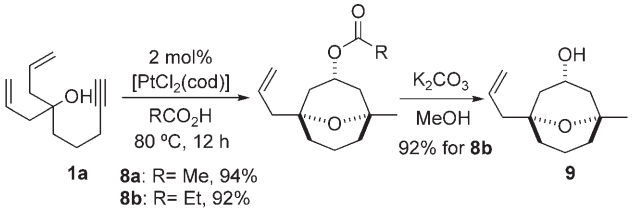

Scheme 4. Catalytic synthesis of ester derivatives **8a,b** and subsequent transformation of **8b** into alcohol **9**.

 © 2006 Wiley-VCH Verlag GmbH & Co. KGaA, Weinheim

carboxylic acid as solvent, the corresponding ester derivatives **8a**,**b** are formed in high yield and as single diastereoisomers. The hydroxy-substituted eight-membered carbocycle **9** could be easily obtained in 92% yield from the propionic acid derivative **8b** by treatment with potassium carbonate in methanol.

In summary, we have developed a highly efficient and general method for the diastereoselective synthesis of eight-membered carbocycles based on a new tandem platinum- or gold-catalyzed cycloisomerization/Prins-type cyclization reaction. The tandem sequence described here allows the straightforward and efficient synthesis of complex products, where several carbon–carbon and carbon–heteroatom bonds have been formed, from very simple starting materials. Moreover, as this chemical transformation does not produce any by-product, and only low amounts of the catalyst are needed, the process can be regarded as a modern, environmentally benign, and efficient reaction.

Received: November 2, 2005
Published online: February 24, 2006

Keywords: carbocycles · domino reactions · gold · homogeneous catalysis · platinum

[1] a) L. F. Tietze, F. Hautner in *Stimulating Concepts in Chemistry* (Eds.: F. Vögtle, J. F. Stoddart, M. Shibasaki), Wiley-VCH, Weinheim, **2000**, p. 38; b) K. C. Nicolaou, E. W. Yue, T. Oshima in *The New Chemistry* (Ed.: N. Hall), Cambridge University Press, Cambridge, **2001**, p. 168; c) L. F. Tietze, *Chem. Rev.* **1996**, *96*, 115; d) L. F. Tietze, U. Beifuss, *Angew. Chem.* **1993**, *105*, 103; *Angew. Chem. Int. Ed. Engl.* **1993**, *32*, 131.

[2] For some recent reviews, see: a) C. Bruneau, *Angew. Chem.* **2005**, *117*, 2380; *Angew. Chem. Int. Ed.* **2005**, *44*, 2328; b) L. Añorbe, G. Domínguez, J. Pérez-Castells, *Chem. Eur. J.* **2004**, *10*, 4938; c) S. T. Diver, A. J. Giessert, *Chem. Rev.* **2004**, *104*, 1317; d) A. Echavarren, C. Nevado, *Chem. Soc. Rev.* **2004**, *33*, 431.

[3] For a review, see: a) F. Alonso, I. P. Beletskaya, M. Yus, *Chem. Rev.* **2004**, *104*, 3079; b) B. Weyershausen, K. H. Dötz, *Eur. J. Inorg. Chem.* **1999**, 1057; c) F. E. McDonald, *Chem. Eur. J.* **1999**, *5*, 3103.

[4] a) J. Barluenga, A. Diéguez, F. Rodríguez, F. J. Fañanás, T. Sordo, P. Campomanes, *Chem. Eur. J.* **2005**, *11*, 5735; b) J. Barluenga, A. Diéguez, F. Rodríguez, F. J. Fañanás, *Angew. Chem.* **2005**, *117*, 128; *Angew. Chem. Int. Ed.* **2005**, *44*, 126.

[5] For some theoretical studies, see: T. Sordo, P. Campomanes, A. Diéguez, F. Rodríguez, F. J. Fañanás, *J. Am. Chem. Soc.* **2005**, *127*, 944, and ref. [4a].

[6] Detailed studies on this issue will be published in due course. For a recent paper on the *exo*-cycloisomerization reaction of ω-alkynols catalyzed by iridium complexes, see: E. Genin, S. Antoniotti, V. Michelet, J.-P. Genêt, *Angew. Chem.* **2005**, *117*, 5029; *Angew. Chem. Int. Ed.* **2005**, *44*, 4949.

[7] For some recent interesting papers on the Prins reaction (and related reactions) see the following and references therein: a) R. Jasti, C. D. Anderson, S. C. Rychnovsky, *J. Am. Chem. Soc.* **2005**, *127*, 9939; b) L. E. Overman, L. D. Pennington, *J. Org. Chem.* **2003**, *68*, 7143; c) C. S. J. Barry, S. R. Crosby, J. R. Harding, R. A. Hughes, C. D. King, G. D. Parker, C. L. Willis, *Org. Lett.* **2003**, *5*, 2429.

[8] The reactions with other metal complexes (Ru, Ir, Ni, In) were unsuccessful. However, promising preliminary results were obtained using silver and copper salts as catalysts.

[9] It is worth pointing out that cyclizations analogous to those observed for 1-en-6-ynes without hydroxy groups have not been observed: M. P. Muñoz, M. Méndez, C. Nevado, D. J. Cárdenas, A. M. Echavarren, *Synthesis* **2003**, 2898.

[10] For some references on alkynol activation by gold or platinum complexes, see: a) Y. Liu, F. Song, Z. Song, M. Liu, B. Yan, *Org. Lett.* **2005**, *7*, 5409; b) J. H. Teles, S. Brode, M. Chabanas, *Angew. Chem.* **1998**, *110*, 1475; *Angew. Chem. Int. Ed.* **1998**, *37*, 1415.

[11] A simple hydrolysis of the carbon–metal bond could also be considered. See ref. [5] for computational studies on the cycloisomerization of ω-alkynols.

 © 2006 Wiley-VCH Verlag GmbH & Co. KGaA, Weinheim

Gas-Phase studies

DOI: 10.1002/anie.200503235

Electrophilicity–Nucleophilicity Scale Also in the Gas Phase

Chagit Denekamp and Yana Sandlers*

Quantification of the known characteristics of organic substances is an ongoing objective for organic chemists. One of the important properties of organic cations is their electrophilicity. This property, which defines the reactivity of cationic intermediates towards nucleophiles is not easy to access. In fact, it is primarily necessary to establish whether or not electrophilicity can be defined without taking into account the counterpart nucleophile, the solvent, temperature, or any other experimental factor. There have been several attempts to quantify electrophilicity and nucleophilicity and recently it has been demonstrated that the rates of reactions of carbocations with uncharged nucleophiles obey a linear free-energy relationship ($\log k = s(E+N)$, where E and N denote electrophilicity and nucleophilicity parameters, respectively, and s is a nucleophile-specific slope factor).[1–10] Subsequently it has been unambiguously shown that the relative rate constants for electrophile–nucleophile coupling reactions follow linear free-energy relationships and that an electrophilicity parameter can be defined and measured regardless of the nucleophile and with some solvent effect. Good correlation is found between the experimental electrophilicity scale and a theoretical electrophilicity index, developed by Pérez and co-workers for a series of benzhydryl cations.[11,12]

[*] Dr. C. Denekamp, Y. Sandlers
Department of Chemistry
Technion—Israel Institute of Technology
Haifa 32000 (Israel)
Fax: (+972) 4829-3736
E-mail: chchagit@tx.technion.ac.il

Supporting information for this article is available on the WWW under http://www.angewandte.org or from the author.

© 2006 Wiley-VCH Verlag GmbH & Co. KGaA, Weinheim

Mass spectrometry is a powerful tool for studying the kinetics and mechanisms of organic reactions in the gas phase[13–16] and in particular of ion–molecule reactions.[17] Data from such studies deepened the understanding of the reaction chemistry of a wide range of reactive organic ions. Ion chemistry in the condensed phase is often dominated by ion pairing and solvation interactions which can mask the intrinsic reactivity of the reaction partners. In the absence of solvation and counter ions, gas-phase studies can reveal the details of reaction mechanisms and clearly characterize the intrinsic reactivity of ionic and neutral species. The purpose of this work was to study the reactivity of electrophilic intermediates in a solvent-free environment and compare these gas-phase results with the corresponding reactions in solution. Ion–molecule reactions were carried out with the aid of an FT-ICR mass spectrometer.

A schematic description of the experimental setup is presented in Figure 1: benzhydryl cations are generated from

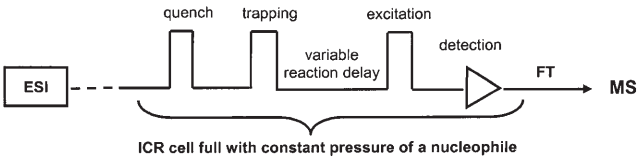

Figure 1. Sequence of events for an ion–molecule reaction in the FT-ICR mass spectrometer. ESI: electrospray ionization; FT: Fourier transformation; ICR: ion cyclotron resonance.

corresponding alcohols in the electrospray ion source. These ions are transferred and trapped in an ICR cell that is previously evacuated of any ions and flooded with a constant pressure of a neutral nucleophile. Any ionic impurities that are present with the desired ions are selectively ejected out of the cell. The ions react with the neutral gas during a variable reaction time after which all ions are detected. The decrease in relative intensity of the reacting cation with time is recorded and, assuming a pseudo-first-order reaction with respect to this cation and that the pressure of the neutral gas is unchanged, rate constants are derived.

To reduce errors, relative reaction rates were measured. The chosen reference cation is 4-methylbenzhydryl cation **5**.

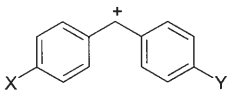

1: X=H; Y=CO_2CH_3 **4**: X=Y=F **7**: X=H; Y=OCH_3
2: X=H; Y=CF_3 **5**: X=H; Y=CH_3 **8**: X=OCH_3; Y=CH_3
3: X=Y=H **6**: X=Y=CH_3 **9**: X=Y=OCH_3

In the example shown in Figure 2, benzhydryl cations **3** and **5** reacted with pyrrolidine, forming products of *m*/*z* 238 and 252, respectively. The reactions were repeated at various reaction delays *t* and thus reaction rates could be derived from slopes of the curves representing the logarithm of the relative intensity of the cation peak as a function of time (Figure 3).

Table 1 lists the reaction rates that were measured for benzhydryl cations **1**–**9** in the presence of various amine

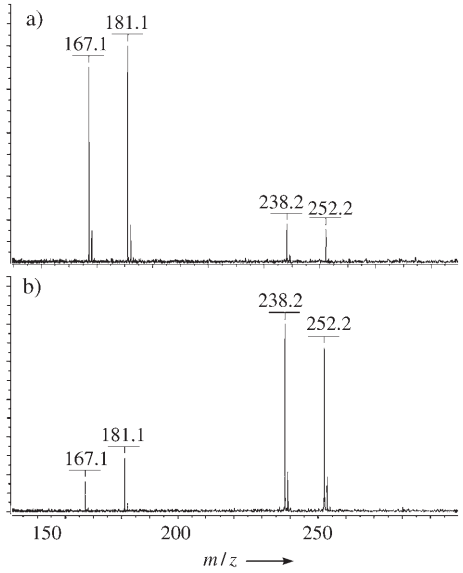

Figure 2. Products of the reaction of cations **3** (*m*/*z* 167) and **5** (*m*/*z* 181) with pyrrolidine after 1 (a) and 5 s (b).

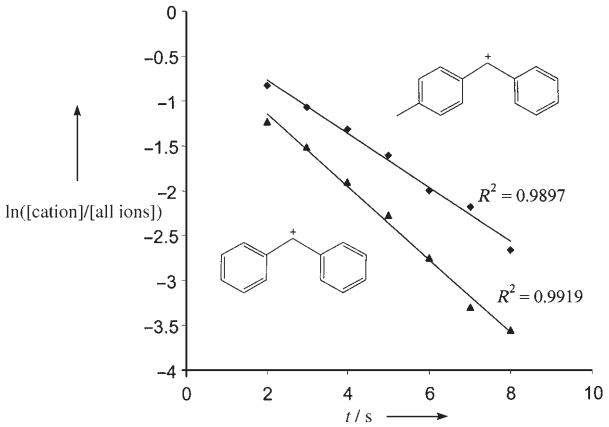

Figure 3. Pseudo-first-order disappearance of ions **3** and **5** in the presence of pyrrolidine.

nucleophiles. The experimental results support the assumption of pseudo-first-order reactions and linear regressions with $R^2 > 0.985$ were found for all the experiments. When it was not possible to use cation **5** as reference due to a large difference in reactivity, experimental results were normalized according to the rate constant of a mediator. Compound **1** was used as a mediator for **2**, and compound **8** as a mediator for **5**.

To compare the gas-phase rate constants with those obtained in solution and assess the relation between electrophilicity, nucleophilicity, and reaction rate ($\log k = s(E+N)$), cation **5** was chosen as reference a electrophile for which $E = 0$ and piperidine was chosen as reference nucleophile for which $N = 0$. These are not the references chosen by Mayr and co-workers, however, since the experimental limitations in our work are different from theirs is was necessary to choose different anchor points. All reaction rates were plotted against the rates of the chosen reference resulting in a series of curves from which electrophilicity and nucleophilicity parameters could be derived (Figure 4).

 © 2006 Wiley-VCH Verlag GmbH & Co. KGaA, Weinheim

Table 1: Relative reaction rates of ion–molecule reactions between cations **1**–**9** and neutral nucleophiles.

Nucleophile	Cation 1	2	3	4	5[a]	6	7	8	9
cyclohexylamine	0.69	0.93	0.40	0.35	0.26	0.15	–	–	–
propylamine	0.98	–	0.50	0.37	0.32	0.23	–	–	–
diisopropylamine	0.77	0.97	0.25	0.23	0.089	0.046	–	–	–
morpholine	1.8	2.2	0.75	0.65	0.46	0.24	–	–	–
pyridine	3.0	3.5	0.93	1.0	0.59	0.41	0.14	0.099	–
piperidine[a]	2.2	2.0	1.25	1.20	1.0	0.69	0.36	0.31	0.080
pyrrolidine	3.0	5.2	1.8	1.5	1.2	0.79	0.47	0.34	0.076

[a] Cation **5** is the reference electrophile and piperidine the reference nucleophile.

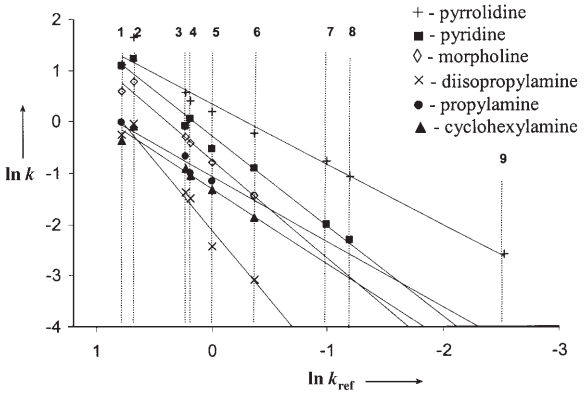

Figure 4. Free-energy correlations for the reactions of **1**–**9** (k) and the reference cation **5** (k_{ref}) with different nucleophiles.

Table 2 summarizes the experimental results, where E_{gas} values are electrophilicity parameters in the gas phase and N_{gas} are nucleophilicity values accordingly. Considering our

Table 2: E_{gas} and N_{gas} values that are derived from the experimental data presented herein.

Electrophile	E_{gas}	Nucleophile	N_{gas}
1	0.79	cyclohexylamine	−0.87
2	0.69	propylamine	−0.83
3	0.22	diisopropylamine	−0.78
4	0.18	morpholine	−0.39
5	0	pyridine	−0.15
6	−0.37	piperidine	0
7	−1.0	pyrrolidine	0.23
8	−1.2		
9	−2.5		

experimental error (that we estimate as 12%), a good agreement with Mayr's equation is observed. It is noteworthy that cross reactions that were performed between different ions indicate an error of 13%.

According to the work of Mayr and co-workers, an electrophilicity parameter can be defined as long as a reference reaction is chosen. These E values are valid regardless of the reaction type and solvent. On the other hand, nucleophilicity can be affected by the solvent. This effect can also be quantified and subsequently the Mayr equation is valid with a corrected nucleophilicity parameter.

The correlation between the nucleophilicities and pK_a values of carbanions is quite poor[9] much like the correlation between the N_{gas} values in Table 2 and gas-phase basicities. However, the correlation between Mayr's E values and the E_{gas} values in Table 2 is reasonable for most of the electrophiles (Figure 5, $R^2 = 0.978$). An exception is 4,4′-dimethoxy-

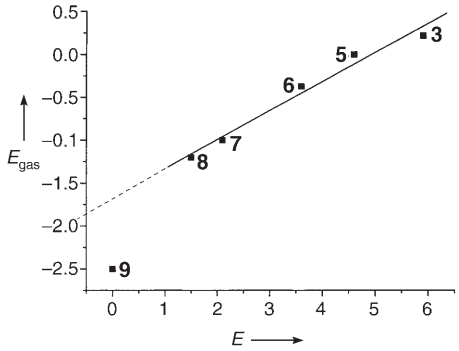

Figure 5. Correlation between Mayr's electrophilicity parameter E and our E_{gas} values.

benzhydryl cation **9** that appears too unreactive in the gas phase when compared with solution and other cations. As mentioned above, for extreme points it was not possible to use cation **5** as a reference owing to large differences in reaction rates and experimental results were normalized according to the rate constant of a mediator and this may be a source for considerable error.

As only three of the amines used herein were also used by Mayr and co-workers, it is currently impossible to examine the correlation between N and N_{gas} parameters.

In conclusion, we found that the kinetics of electrophile–nucleophile gas-phase reactions correlate well with values known for solution although the actual electrophilicity parameters are considerably smaller in the gas phase. The differences in reactivity of the cations under study may be surprising if one assumes that the association between them and the neutral amines occurs without barrier and should be controlled by the collision rate. There could be several explanations to the apparent results and calculations are now undertaken in order to gain better insight into this process. We are aware that association reactions may be controlled by the infrared emission rate, however, in such a case the substituent effect should not necessarily correlate with the

 © 2006 Wiley-VCH Verlag GmbH & Co. KGaA, Weinheim

substituent effect in solution. Preliminary calculations indicate that the formation of several ion–molecule complexes may interfere with the formation of stable adducts and affect the kinetic behavior of the system under study.

Experimental Section

Benzhydryl alcohol was purchased from Fluka (Sigma-Aldrich Co., Israel). Other alcohols were synthesized from the corresponding commercial benzophenones (**2**, **4**, **6**, and **9**) or aldehydes (**5**, **7**, and **8**) according to known procedures[18–20] (see the Supporting Information for further experimental details).

Ion–molecule reactions were carried out with a Bruker BioAPEX III 47e FT-ICR mass spectrometer (Bruker Analytical Systems, Inc., Billerica, MA) equipped with a 4.7-T superconducting magnet, an external source (Apollo ESI Source), and an infinity analyzer cell. Samples were dissolved in CH_3OH (0.01 mg mL^{-1}) and introduced into the ESI source at a flow rate of 0.3 μL min^{-1}. Ions were detected using the broadband detection mode covering a mass range from m/z 50 to 1000. Typically, eight individual transients were accumulated to improve the signal-to-noise ratio. Precursor ions were isolated using a series of "shot" frequency ejection pulses of 1000 μs duration to eject all other ions and avoid activation of precursor ions. Neutral amines were introduced into the ICR cell through a leak valve maintaining a constant pressure of ca. 4.2×10^{-9} mbar (indicated). Spectra were recorded after various reaction times with intervals depending on the reactivity.

Received: September 12, 2005
Revised: December 8, 2005
Published online: February 22, 2006

Keywords: electrophilicity · ion–molecule reactions · kinetics · linear free-energy relationships · mass spectrometry

[1] H. Mayr, M. Patz, *Angew. Chem.* **1994**, *106*, 938; *Angew. Chem. Int. Ed. Engl.* **1994**, *33*, 990.
[2] M. Roth, H. Mayr, *Angew. Chem.* **1995**, *107*, 2428; *Angew. Chem. Int. Ed. Engl.* **1995**, *34*, 2250.
[3] H. Mayr, T. Bug, M. F. Gotta, N. Hering, B. Irrgang, B. Janker, B. Kempf, R. Loos, A. Ofial, G. Remennikov, H. Schimmel, *J. Am. Chem. Soc.* **2001**, *123*, 9500.
[4] R. Lucius, R. Loos, H. Mayr, *Angew. Chem.* **2002**, *114*, 97; *Angew. Chem. Int. Ed.* **2002**, *41*, 92.
[5] S. Minegishi, H. Mayr, *J. Am. Chem. Soc.* **2003**, *125*, 286.
[6] H. Mayr, *Angew. Chem.* **1990**, *102*, 1415; *Angew. Chem. Int. Ed. Engl.* **1990**, *29*, 1371.
[7] H. Mayr, K.-H. Müller, D. Rau, *Angew. Chem.* **1993**, *105*, 1732; *Angew. Chem. Int. Ed. Engl.* **1993**, *32*, 1630.
[8] M. Patz, H. Mayr, J. Maruta, A. Fukuzumi, *Angew. Chem.* **1995**, *107*, 1351; *Angew. Chem. Int. Ed. Engl.* **1995**, *34*, 1225.
[9] R. Lucius, H. Mayr, *Angew. Chem.* **2000**, *112*, 2086; *Angew. Chem. Int. Ed.* **2000**, *39*, 1995.
[10] H. Mayr, O. Khun, M. F. Gotta, M. Patz, *J. Phys. Org. Chem.* **1998**, *11*, 642.
[11] L. R. Domingo, M. Arnó, R. Contreras, P. Pérez, *J. Phys. Chem. A* **2002**, *106*, 952.
[12] P. J. Pérez, A. Toro-Labbé, A. Aizman, R. Contreras, *J. Org. Chem.* **2002**, *67*, 4747.
[13] C. Denekamp, A. Mandelbaum, *J. Mass Spectrom.* **2001**, *36*, 422.
[14] C. Denekamp, A. Stanger, *Chem. Commun.* **2002**, 236.
[15] C. Denekamp, E. Tenetov, Y. Horev, *J. Am. Soc. Mass Spectrom.* **2003**, *14*, 790.
[16] C. Denekamp, Y. Sandlers, *J. Mass Spectrom.* **2005**, *40*, 1055.
[17] S. Gronert, *Chem. Rev.* **2001**, *101*, 329.
[18] Y. Senda, N. Kikuchi, A. Inu, H. Itoh, *Bull. Chem. Soc. Jpn.* **2000**, *73*, 237.
[19] *Vogel's Textbook of Practical Organic Chemistry* (Eds.: B. S. Furniss, A. J. Hannaford, P. W. G. Smith, A. R. Tathchell), 5th ed., Longman, **1989**.
[20] P. Knochel, W. Dohle, N. Gommermann, F. F. Kneisel, F. Kopp, T. Korn, I. Sapountzis, V. A. Vu, *Angew. Chem.* **2003**, *115*, 4438; *Angew. Chem. Int. Ed.* **2003**, *42*, 4302.

 © 2006 Wiley-VCH Verlag GmbH & Co. KGaA, Weinheim

Asymmetric Synthesis

DOI: 10.1002/anie.200503852

Enantioselective Synthesis of Cyclic Ethers through a Vanadium-Catalyzed Resolution/ Oxidative Cyclization**

*Aurélien Blanc and F. Dean Toste**

Over the past 25 years, transition-metal-catalyzed oxidative cyclization of bishomoallylic alcohols has been successfully applied to the formation of substituted tetrahydrofurans (THFs), and both *trans*- and *cis*-substituted rings are now accessible depending on the olefin substitution and metal used.[1,2] In this area, catalysts based on vanadium(v) have proven to be the most useful in this transformation. Indeed, the reagent combination of catalytic vanadyl acetylacetonate and *tert*-butylhydroperoxide (TBHP) as the primary oxidant can be employed for the selective conversion of bishomoallylic alcohols into functionalized *cis*-THFs by catalytic olefin epoxidation followed by epoxide ring opening [Eq. (1)].[1,2]

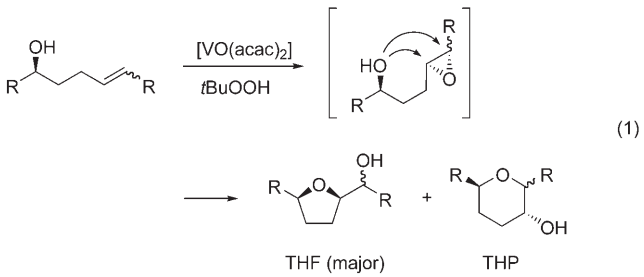

(1)

[*] Dr. A. Blanc, Prof. Dr. F. D. Toste
Department of Chemistry
University of California
Berkeley, CA 94720 (USA)
Fax: (+1) 510-643-9480
E-mail: fdtoste@berkeley.edu

[**] We gratefully acknowledge the University of California (Berkeley), Merck Research Laboratories, Bristol-Myers Squibb, Amgen Inc., DuPont, GlaxoSmithKline, Eli Lilly & Co., Abbott, and Pfizer for financial support. A.B. thanks the Swiss National Science Foundation for a postdoctoral fellowship.

Supporting information for this article is available on the WWW under http://www.angewandte.org or from the author.

WILEY InterScience DISCOVER SOMETHING GREAT
© 2006 Wiley-VCH Verlag GmbH & Co. KGaA, Weinheim

Recently, Hartung and co-workers[3] reported the oxidative cyclization of racemic bishomoallylic alcohols using vanadium(v)–oxo complexes with chiral, tridentate Schiff base ligands to induce high regio- and diastereoselectivities. In spite of the chiral ligand employed, the epoxidation/ring-opening reaction gave racemic 2,5-*cis*-THF rings as the major product. In accord with this report, our own attempts to introduce enantioselectivity in this reaction by resolution of bishomoallylic alcohols by catalytic epoxidation[4] resulted in very low stereoselectivity factors.[5] In sharp contrast, we recently described an efficient kinetic resolution of α-hydroxyesters catalyzed by a chiral vanadyl complex using molecular oxygen as the stoichiometric oxidant.[6] Notably, both allylic and homoallylic substrates showed good stereoselectivity in the resolution event and excellent chemoselectivity for alcohol oxidation over olefin epoxidation. The failure of the cyclization to provide enantioenriched cyclic ethers, prompted us consider an alternative one-pot strategy wherein the absolute stereochemistry is set using an asymmetric aerobic oxidation of unsaturated α-hydroxyesters followed by an epoxidation/cyclization reaction using the same vanadyl complex as a catalyst for both transformations.

The absence of vanadium-catalyzed olefin epoxidation under aerobic conditions led us to examine TBHP as an alternative oxidant for the epoxidation/cyclization reaction. Our preliminary results[7] showed that the best solvent for the asymmetric oxidative resolution of bishomoallylic alcohols was acetone (the best reaction rate and enantioselectivity was obtained for **1**, together with a stereoselectivity factor (*s*) of 35). Indeed, our initial attempts to obtain cyclic products from **1** in acetone, the solvent used for the kinetic resolution, resulted in chemoselective oxidation of the secondary alcohol even when TBHP was used as the stoichiometric oxidant (Table 1, entry 1). Fortunately, a pronounced solvent effect on the chemoselectivity of the oxidation reaction was observed. The vanadium-catalyzed oxidation of **1**, using $CHCl_3$ as the solvent and **L1** (Table 1, entry 2) or **L2** (Table 1, entry 4) as the ligand, cleanly afforded 2,5-*trans*-THP **2** (THP = tetrahydropyran; d.r. = > 95:5) with excellent diastereoselectivity accompanied by only minor amounts of THF **2a** (d.r. = 1:1) and α-ketoester **2b** (Table 1, entry 2).[8] In sharp contrast, classical conditions using $[VO(acac)_2]$/TBHP (acac = acetylacetone) gave poor selectivity for the formation of the THP and substantial amounts of alcohol oxidation (Table 1, entry 3). Based on these observations, the optimal procedure for the resolution/cyclization reaction simply requires a change of solvent and oxidant: acetone/O_2 used for the resolution is readily removed and replaced with $CHCl_3$/TBHP for oxidative cyclization.

Under these conditions ($[VO(OiPr)_3]$ (10 mol%), **L1** (11 mol%), O_2/acetone; then TBHP (0.55 equiv), $CHCl_3$), racemic unsaturated α-hydroxyester **1** was engaged in a tandem resolution/oxidative cyclization to give 2,5-*trans*-THP **2** in good yield (30%)[9] with excellent diastereo- and enantioselectivities (Scheme 1). The absolute stereochemistry of the chiral center bearing the ester was assigned the *R* configuration by analogy to the kinetic resolution of α-hydroxyesters.[6] We then examined the scope of different substrates with *E*- and *Z*-trisubstituted alkenes. As expected, compounds **3** and **5** gave 2,5-*trans*-substituted THPs **4** and **6** (in yields of 35 and 26%), respectively, with high diastereo- and enantioselectivities; furthermore, control of the C6 stereogenic center depended on the configuration of the olefin. Unsaturated α-hydroxyester **7**, with two double bonds, provided the possibility of carrying out a double cyclization. Unfortunately, the dioxacyclic compound was obtained as a mixture of two diastereoisomers (44% yield, d.r. = 1:1; $CHCl_3$, TBHP (2.2 equiv), 40 °C, 48 h), but tandem reaction conditions using 1.1 equivalents of TBHP gave **8** with high diastereoselectivity (d.r. = > 95:5) and in moderate yield (20%), as the double cyclization can not be completely prevented. While THP/THF ratios vary according to the substrate and remain on average at 4:1, in each case high diastereo- and enantioselectivities (d.r. = > 88:12, > 95% *ee*) were measured. The ketone resulting from the asymmetric oxidation was also recovered in good-to-moderate yield[7] and could be reused after reduction with sodium cyanoborohydride.

Enantiopure THF rings can also be synthesized as the exclusive regioisomer by using homoallylic alcohols in the tandem resolution/cyclization reaction. After resolution, alcohol **9** was efficiently converted into 2,4-*cis*-substituted THF product **10** (38% yield, d.r. = 95:5)

Table 1: Vanadium-catalyzed oxidative cyclization.[a]

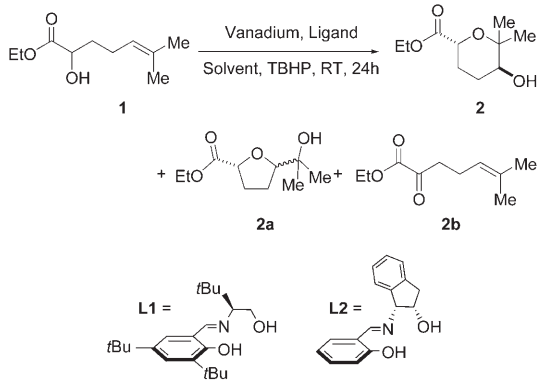

Entry	Vanadium/ligand[b]	Solvent	Yield of **2** [%] (*cis*/*trans*)[c]	**2a** [%][c]	**2b** [%][c]
1	$[VO(OiPr)_3]$/**L1**	acetone	–	–	75
2	$[VO(OiPr)_3]$/**L1**	$CHCl_3$	78 (> 95:5)	22	trace
3	$[VO(acac)_2]$	CH_2Cl_2	36 (> 95:5)	18	46
4	$[VO(OiPr)_3]$/**L2**	$CHCl_3$	83 (> 95:5)	17	–

[a] No kinetic resolution took place under these conditions [b] Vanadyl complex (10 mol%) and TBHP (1.5 equiv) were used. [c] Ratio of products and the d.r. were determined by ^{1}H NMR spectroscopic analysis.

 © 2006 Wiley-VCH Verlag GmbH & Co. KGaA, Weinheim

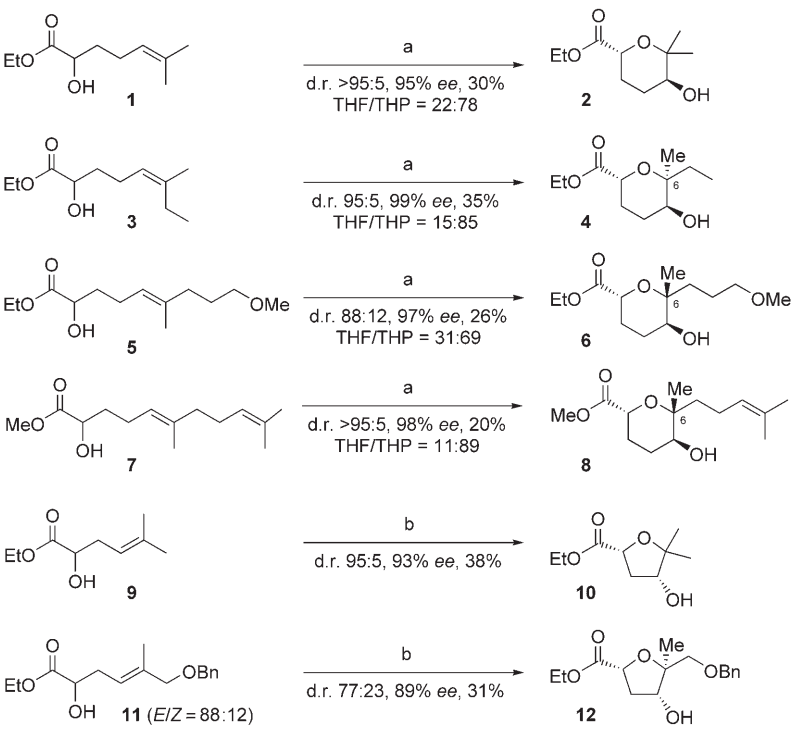

Scheme 1. Vanadium-catalyzed resolution/oxidative cyclization. Reagents and conditions: a) $[VO(OiPr)_3]$ (10 mol%), **L1** (11 mol%), O_2, acetone, 30°C, 30–48 h (≈50% conversion); then TBHP (0.55 equiv), $CHCl_3$, RT, 24–72 h; b) $[VO(OiPr)_3]$ (10 mol%), **L1** (11 mol%), O_2, acetone, 30°C, 30–48 h; TBHP (0.55 equiv), $CHCl_3$, RT, 3 h; then CSA (5 mol%), RT, 16 h.

by epoxidation and subsequent addition of camphor sulfonic acid (CSA; 5 mol%) to complete the cyclization. Homoallylic alcohol **11** also furnished 2,4-*cis*-substituted THF ring **12** as the major product in good yield (31%) with high enantiomeric excess (89% *ee*) and only a slight decrease in the diastereoselectivity.

The formation of 2,5-*trans*-substituted THP rings from bishomoallylic alcohols and 2,4-*cis*-substituted THFs from homoallylic alcohols suggests a reverse in the diastereoselectivity during the epoxidation step. Indeed, the chairlike transition-state model proposed for the epoxidation of homoallylic alcohols rationalizes the *syn* diastereoselectivity through a transition state that requires that the sterically more demanding substituent (here the ethyl ester) occupies a pseudoequatorial position to minimize steric interactions;[10] however, in the case of α-hydroxyesters we observed the formation of a 2,4-*cis*-THF ring which requires the epoxidation to proceed with *anti* selectivity. On the basis of the epoxidation mechanism[11] and the fact that vanadium(v)–oxo complexes may form complexes with coordination numbers of up to seven,[12] we hypothesize that the reversed selectivity can be accounted for by considering a transition state in which coordination of the ester carbonyl group to the Lewis acidic vanadium center places the ester in a pseudoaxial position (Scheme 2). Our stereochemical model can also be applied to the oxidative cyclization of bishomoallylic alcohols and explains the formation of 2,5-*trans*-THPs as major products instead of THF rings.[3b] Finally, we also observed a reverse selectivity in the oxidative cyclization of bishomoallylic α-hydroxyamide using 50 mol% rhenium(VII) oxide [Eq. (2)], presumably due a similar chelation of the amide carbonyl group to the rhenium center.[13,14]

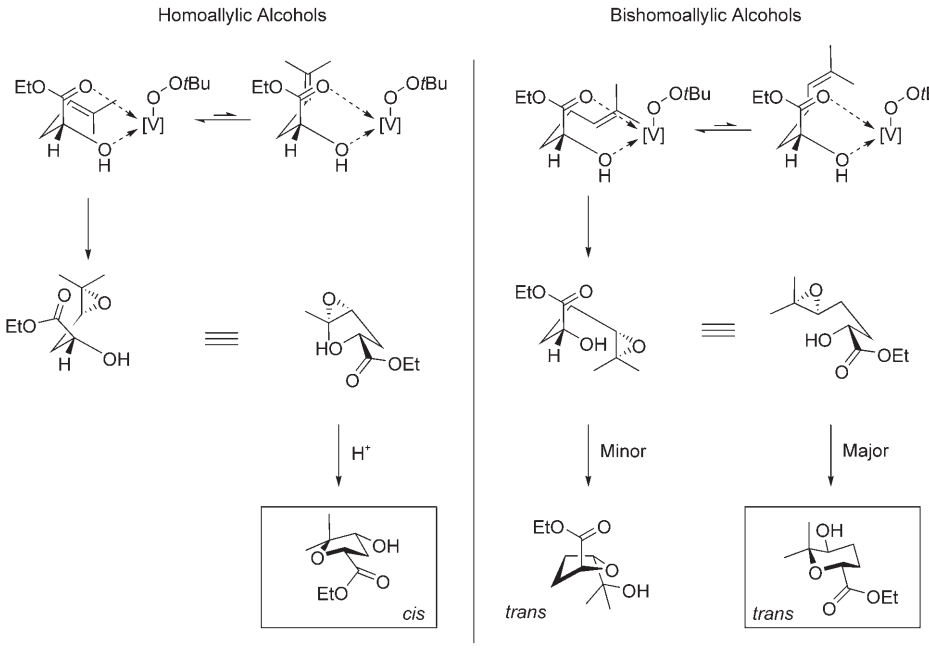

Scheme 2. Stereochemical model for the chelation-controlled vanadium-catalyzed epoxidation.

The enantioselective total synthesis of pantofuranoid E, isolated from *pantoneura plocamioides* (a red Antarctic alga),[15] highlights the application of the vanadium-catalyzed tandem sequence for the enantioselective construction of cyclic ethers (Scheme 3). The synthesis begins with 2,4-*cis*-THF **10**, available in 93% *ee* from our vanadium-catalyzed resolution/cyclization reaction. After protection of alcohol **10** with *tert*-butyldimethylsilyl (TBS; 95% yield), the ester group was directly converted into methyl ketone **15** by in situ formation of the Weinreb amide followed by addition of an excess of MeMgBr (76% yield).[16] Propargylic alcohol **16** was obtained in 60% yield (after desilylation) by addition of lithium trimethylsilylacetylide to **15** in the presence of anhydrous $CeCl_3$ (organocerium reagent), with d.r. = 4:1 in favor of the chelation-controlled product.[17] The

 © 2006 Wiley-VCH Verlag GmbH & Co. KGaA, Weinheim

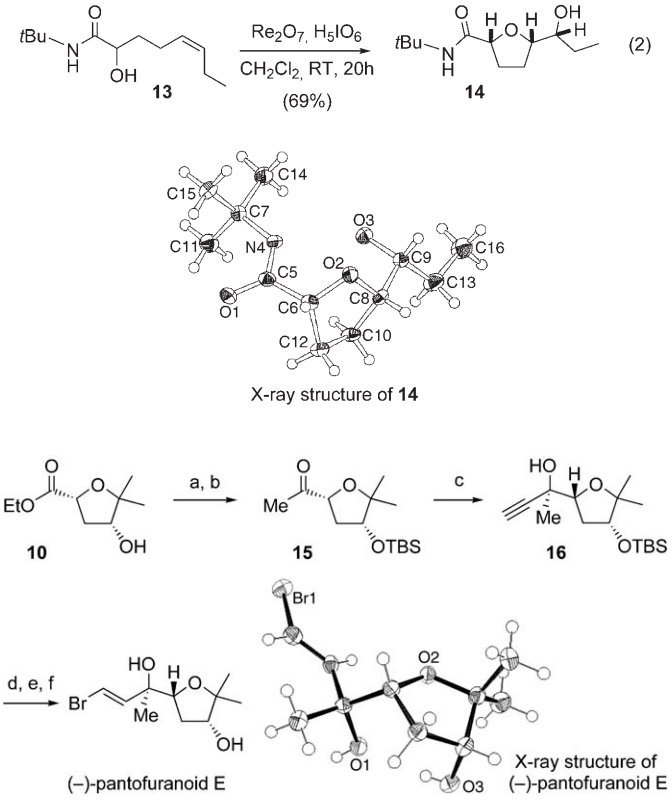

Scheme 3. Synthesis of (−)-pantofuranoid E. Reagents and conditions: a) TBSOTf, 2,6-lutidine, CH_2Cl_2, 0 °C, 30 min (95 %); b) Me-(MeO)NH·HCl, MeMgBr (2 equiv); then MeMgBr excess, THF, −78 °C, 2 h (76 %); c) lithium trimethylsilylacetylide, $CeCl_3$, Et_2O/Et_3N (1:1), −78 °C, 4 h; then K_2CO_3, MeOH, RT, 1 h (60 %, d.r. = 4:1); d) nBu_3SnH, $[PdCl_2(PPh_3)_2]$, CH_2Cl_2, 0 °C→RT, 30 min (82 %); e) NBS, CH_2Cl_2, 0 °C, 1 h (87 %); f) TBAF, THF, RT, 1 h (94 %). Tf = triflate.

installation of vinyl bromide was achieved in two steps from **16**: first palladium-catalyzed hydrostannation[18] of the alkyne was carried out (82 % yield) followed by tin/bromide exchange with *N*-bromosuccinimide (NBS; 87 % yield). Deprotection of the TBS group with tetrabutylammonium fluoride (TBAF) gave (−)-pantofuranoid E in 94 % yield. Notably, this total synthesis and X-ray structural studies allowed the assignment of the absolute configuration of pantofuranoid E.

In conclusion, we have developed a highly diastereo- and enantioselective synthesis of 2,5-*trans*-THPs and 2,4-*cis*-THFs using sequential resolution/oxidative cyclization of racemic bis- and homoallylic α-hydroxyesters. Both steps in the reaction sequence are catalyzed by a vanadium(v)–oxo complex with a readily available tridentate Schiff base ligand. Additionally, the reversed diastereoselectivity observed in the formation of 2,5-*trans*-THPs and 2,4-*cis*-THFs is attributed to chelation of the ester carbonyl group to the Lewis acidic vanadium catalyst during the epoxidation event. This synthetic method provides an efficient asymmetric synthesis of cyclic ethers, as demonstrated by an expeditious enantioselective synthesis of (−)-pantofuranoid E.

Received: October 31, 2005
Published online: February 27, 2006

Keywords: kinetic resolution · natural products · oxidation · tetrahydrofurans · tetrahydropyrans

[1] J. Hartung, M. Greb, *J. Organomet. Chem.* **2002**, *661*, 67–84.
[2] M. M. Faul, B. E. Huff, *Chem. Rev.* **2000**, *100*, 2407–2473.
[3] a) J. Hartung, P. Schmidt, *Synlett* **2000**, 367–370; b) J. Hartung, S. Drees, M. Greb, P. Schmidt, I. Svoboda, H. Fuess, A. Murso, D. Stalke, *Eur. J. Org. Chem.* **2003**, 2388–2408; c) J. Hartung, *Pure. Appl. Chem.* **2005**, *77*, 1559–1576.
[4] W. Zhang, A. Basak, Y. Kosugi, Y. Hoshino, H. Yamamoto, *Angew. Chem.* **2005**, *117*, 4363–4365; *Angew. Chem. Int. Ed.* **2005**, *44*, 4389–4391.
[5] The reaction of racemic bishomoallylic alcohol **1** was carried out under the conditions of Hartung ($[VO(OiPr)_3]$, $CHCl_3$, TBHP (1.1 equiv), RT, ligand **L1** (10 mol %)), and $s = 1.3$ was measured: $s = k_{rel(fast/slow)} = \ln[(1-c)(1-ee)]/\ln[(1-c)(1+ee)]$: "Kinetic Resolution": H. B. Kagan, J. C. Fiaud in *Topics in Stereochemistry*, *Vol. 18* (Eds.: E. L. Eliel, S. H. Wilen), Wiley, **1988**, pp. 249–330.
[6] A. T. Radosevich, C. Musich, F. D. Toste, *J. Am. Chem. Soc.* **2005**, *127*, 1090–1091.
[7] See the Supporting Information.
[8] Only trisubstituted olefins gave promising results under these conditions; substrates containing disubstituted alkenes gave only minor amounts of cyclic products, and only alcohol oxidation was observed even using $CHCl_3$/TBHP.
[9] Reported yields were calculated for racemic alcohols before the resolution (i.e., highest theoretical yield = 50 %).
[10] E. D. Mihelich, K. Daniels, D. J. Eickhoff, *J. Am. Chem. Soc.* **1981**, *103*, 7690–7692.
[11] H. Mimoun, M. Mignard, P. Brechot, L. Saussine, *J. Am. Chem. Soc.* **1986**, *108*, 3711–3718.
[12] D. Rehder, *Coord. Chem. Rev.* **1999**, *182*, 297–322.
[13] Kennedy oxidative cyclizations generally provide *trans*-substituted THFs: a) S. Tang, R. M. Kennedy, *Tetrahedron Lett.* **1992**, *33*, 5303–5306; for exceptions, see: b) S. C. Sinha, A. Sinha, S. C. Sinha, E. Keinan, *J. Am. Chem. Soc.* **1997**, *119*, 12014–12015; c) Y. Morimoto, T. Iwai, *J. Am. Chem. Soc.* **1998**, *120*, 1633–1634.
[14] Reversal in selectivity has also been observed for the titanium-catalyzed epoxidation of homoallylic α-amino alcohols, see: A. Krasiński, J. Jurczak, *Tetrahedron: Asymmetry* **2002**, *13*, 2075–2078.
[15] M. Cueto, J. Darias, *Tetrahedron* **1996**, *52*, 5899–5906.
[16] J. M. Williams, R. B. Jobson, N. Yasuda, G. Marchesini, U.-H. Dolling, E. J. J. Grabowski, *Tetrahedron Lett.* **1995**, *36*, 5461–5464.
[17] a) M. E. Jung, J. Pontillo, *J. Org. Chem.* **2002**, *67*, 6848–6851; b) E. M. Carreira, J. Du Bois, *Tetrahedron Lett.* **1995**, *36*, 1209–1212.
[18] B. M. Trost, Z. T. Ball, *Synthesis* **2005**, 853–887.

 © 2006 Wiley-VCH Verlag GmbH & Co. KGaA, Weinheim

Chirality

DOI: 10.1002/anie.200503423

Conglomerate-to-True-Racemate Reversible Solid-State Transition in Crystals of an Organic Disulfide-Based Iodoplumbate

Nicolas Mercier, Anne-Lise Barres, Michel Giffard, Ileana Rau, François Kajzar, and Bouchta Sahraoui*

In the solid state, crystalline racemates belong mainly to two classes. When both enantiomers are present in equal quantities in a well-defined arrangement within the crystal lattice, the compound is called a racemic compound or a true racemate (the most common type). In the second case, a mechanical mixture of crystals of the two pure enantiomers form a conglomerate (case of spontaneous resolution).[1] While a homochiral assemblage of molecules never crystallizes in a non-enantiomorphous crystal system, achiral molecules can crystallize in enantiomorphous systems. This case is observed especially when molecules that do not reveal configuration-arising chirality nevertheless adopt chiral conformations in the crystal.[2]

Disulfide functions are an important feature of proteins and biologically active polypeptides, in particular because of their inherent chirality, which may transmit stereochemical information, as suggested, for example, in prion proteins.[3] Disulfides (RSSR′) are in fact well known to show skewed, and thus chiral, conformations.[4] Obtaining a conglomerate from chiral conformers is quite scarce, but many of the known cases belong to the RXXR (X = O, S) series.[2a,5] However, let us note that the chirality of many "chiral disulfides" often comes from configurationally chiral ligands linked to chalcogenide atoms.[6] Anyway, racemization occurs in solution (if there is no chiral substituent) owing to the relatively low barrier of rotation of S–S bonds between both enantiomeric conformers.[7]

In the course of our investigations on perovskite-like compounds, we obtained crystals of $[\{H_3N(CH_2)_2SS(CH_2)_2NH_3\}PbI_5]\cdot H_3O$. For this compound, which contains neutralized cystamine molecules, a spontaneous resolution occurs. Remarkably, a change in the conformation of half of the disulfide molecules in the crystal state appears at 75 °C, thus leading to a true racemate. We also show that this remarkable solid-state transition of a conglomerate to a true racemate is reversible and that this compound may find applications as a reversible second harmonic generation (SHG) switchable material.

Compound $[\{H_3N(CH_2)_2SS(CH_2)_2NH_3\}PbI_5]\cdot H_3O$ was prepared under solvo-thermal conditions in a teflon-lined PARR autoclave (internal volume = 25 mL). The experimental conditions are as follows: equimolecular quantities of PbI_2 and $H_2N(CH_2)_2SS(CH_2)_2NH_2\cdot 2HCl$ (0.4 mmol), acetonitrile (4 mL), and concentrated HI (1 mL) were heated at 80 °C for 2 h and cooled down to room temperature with a ramp of 1 °C h^{-1}. This procedure led to the formation of yellow needle crystals of $[\{H_3N(CH_2)_2SS(CH_2)_2NH_3\}PbI_5]\cdot H_3O$ with crystal sizes of up to $2\times 0.8\times 0.5$ mm^3. The crystals were then filtered and washed with cold ethyl acetate. X-ray powder diffraction studies indicated a single-phase sample (see the Supporting Information). Differential scanning calorimetric (DSC) measurements and thermogravimetric (TG) analysis were performed in the ranges 20–350 and 20–950 °C, respectively. The compound melts at 250 °C, just before decomposition, which takes place in two steps up to 600 °C. Before the melting peak, two other endothermic peaks occur in the DSC curve at 75 and 200 °C, respectively (see the Supporting Information).

Compound α-$[\{H_3N(CH_2)_2SS(CH_2)_2NH_3\}PbI_5]\cdot H_3O$ crystallizes in the $P2_1$ chiral space group.[8] Its crystal structure is built up from zigzag chains of corner-sharing octahedra of lead iodide that run along the *b* axis separated by hydronium and $^+H_3N(CH_2)_2SS(CH_2)_2NH_3^+$ ions (Figure 1 a). Contrary to linear alkyl primary diammonium cations, which react in most cases with iodoplumbate anions to form 2D hybrid perovskites $(H_3N\text{-}R\text{-}NH_3)PbI_4$,[9] neutralized cystamine molecules preclude the formation of perovskite layers, certainly because of the steric and/or electronic effects of disulfide bridges. As a result, hydronium cations are finally incorporated into the structure and 1D PbI_5 chains of corner-sharing octahedra are formed. Such an inorganic network has been already described for other salts,[10] and Pb–I lengths in the range

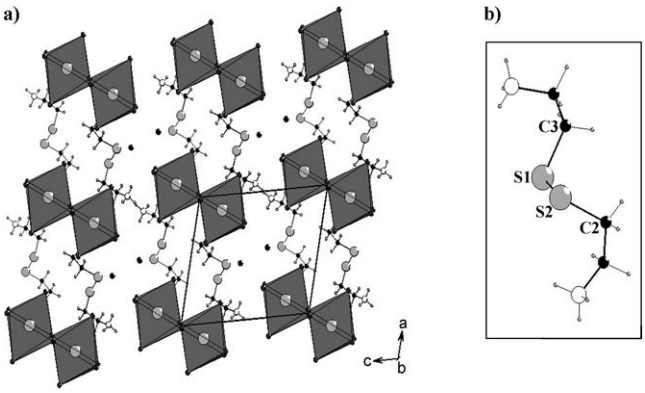

Figure 1. α-$[\{H_3N(CH_2)_2SS(CH_2)_2NH_3\}PbI_5]\cdot H_3O$: a) structure viewed along the *b* axis; b) disulfide molecule with the *M*-helical form (S1–C3 lies behind the plane of the page).

[*] Dr. N. Mercier, A.-L. Barres, Dr. M. Giffard
Laboratoire de Chimie
Ingénierie Moléculaire et Matériaux d'Angers
UMR-CNRS 6200, Université d'Angers
2 Boulevard Lavoisier, 49045 Angers (France)
Fax: (+33) 241-735-405
E-mail: nicolas.mercier@univ-angers.fr
Prof. B. Sahraoui
Laboratoire de Propriétés Optiques des Matériaux et Applications
UMR-CNRS 6136, Université d'Angers
2 Boulevard Lavoisier, 49045 Angers (France)
I. Rau, Dr. F. Kajzar
CEA-DRT/LITEN/GENEC/L2C—CEA Saclay
91191 Gif sur Yvette (France)

Supporting information for this article is available on the WWW under http://www.angewandte.org or from the author.

WILEY InterScience DISCOVER SOMETHING GREAT
© 2006 Wiley-VCH Verlag GmbH & Co. KGaA, Weinheim

3.115(1)–3.262(1) Å are in good agreement with those reported previously.[10] Hydronium cations, whose hydrogen atoms could not be located from the X-ray study, are roughly positioned in between the PbI_5 chains. Five O···I distances in the range 3.48(1)–3.71(1) Å are found, thus indicating quite strong interactions between the hydronium cation and iodine atoms of three neighboring inorganic chains. There is no direct interaction between the hydronium cation and sulfur atoms in the disulfide molecules (shortest O···S distance: 4.02(1) Å). Organic molecules also interact through hydrogen bonds with the iodoplumbate network, with one ammonium head being located in one PbI_5 chain, whereas the second is directed towards the interchain space (Figure 1a).

The main feature of α-[{$H_3N(CH_2)_2SS(CH_2)_2NH_3$}$PbI_5$]·$H_3O$ is the presence of only one enantiomeric form of disulfides. As known for many years, acyclic disulfides exist as an equilibrium mixture of two skewed enantiomeric conformers.[4] These conformers with idealized dihedral angles (C-S-S-C) of 90° correspond to global energetic minima, the barrier of rotation between both forms being relatively low (typically 6 kcal mol^{-1}).[6] In the solid state, acyclic disulfides also adopt a skewed geometry with a dihedral angle close to 90°. In our case, spontaneous resolution occurs during the crystallization process, with the molecules of the studied crystal (Flack absolute structure of 0.007(4)) displaying a *M* helicity (left-handed helical form) and a dihedral angle of −84° (Figure 1b). It must be also noted that an X-ray study of several other crystals chosen randomly showed that absolute structures are based either on molecules with *P* or *M* helicity, which confirms the obtention of a conglomerate.

Compound α-[{$H_3N(CH_2)_2SS(CH_2)_2NH_3$}$PbI_5$]·$H_3O$ exhibits a phase transition at 75 °C, which was first characterized from DSC analysis. The crystal cell of the high-temperature β phase, found from a powder X-ray pattern collected at 80 °C, was confirmed by single-crystal X-ray analysis. In fact, the phase transition does not affect the crystalline quality, which allowed us to perform the complete single-crystal X-ray study at 80 °C. The structure of β-[{$H_3N(CH_2)_2SS(CH_2)_2NH_3$}$PbI_5$]·$H_3O$ is described in the $P2_1/n$ space group.[11] The unit-cell transformation from the α to the β phase results in a change of parameters in the *a*–*c* plane, with the following relationships: $\vec{a}_\beta = (\vec{a}_\alpha + \vec{c}_\alpha)$, $\vec{b}_\beta = -\vec{b}_\alpha$, and $\vec{c}_\beta = (\vec{a}_\alpha - \vec{c}_\alpha)$ (Figure 2; the volume of the high-temperature phase is approximately twice the volume of the room-temperature phase). Although the view of the overall structure displayed in Figure 2 very much looks like the room-temperature phase (Figure 1), an important change concerns the organic molecules. The symmetry center in the structure of β-[{$H_3N(CH_2)_2SS(CH_2)_2NH_3$}$PbI_5$]·$H_3O$ implies that both disulfide conformers coexist, which means that half of the molecules undergo a conformational change during the phase transition (Figure 3).

Therefore, β-[{$H_3N(CH_2)_2SS(CH_2)_2NH_3$}$PbI_5$]·$H_3O$ is a racemic compound (also called a true racemate). Considering the four molecules contained in the unit cell of the high-temperature phase, we conclude that only molecules **3** and **4** (see Figure 2 for the numbering scheme) underwent a conformational change. Thus, molecules **1** and **2** on one hand and **3** and **4** on the other hand are always (as in α-[{$H_3N(CH_2)_2SS(CH_2)_2NH_3$}$PbI_5$]·$H_3O$) related to one another by a 2_1 axis located between the two neighboring hydronium cations (Figure 2). On the contrary, **1** and **4** are now, as are **2** and **3**, related by a symmetry center. Finally, **1** and **2** are *M*-helical disulfides and **3** and **4** are *P*-helical disulfides (Figure 3). To our knowledge, the heating-induced transformation of a conglomerate into a racemic compound, or the inverse, of a racemic compound into a conglomerate, in the solid state is a very uncommon phenomenon, and it has been described for enantiomerically stable molecules (either configurational enantiomers or atropisomers, i.e., rigid conformers) at a temperature close to the melting point;[2a,12a] in the case of 1,1′-binaphtyl, an enantiomer conversion (rotation about the interannular bond) in the solid state occurs during the heating of the quasi racemic binaphtyl to give only one enantiomer.[12b,c]

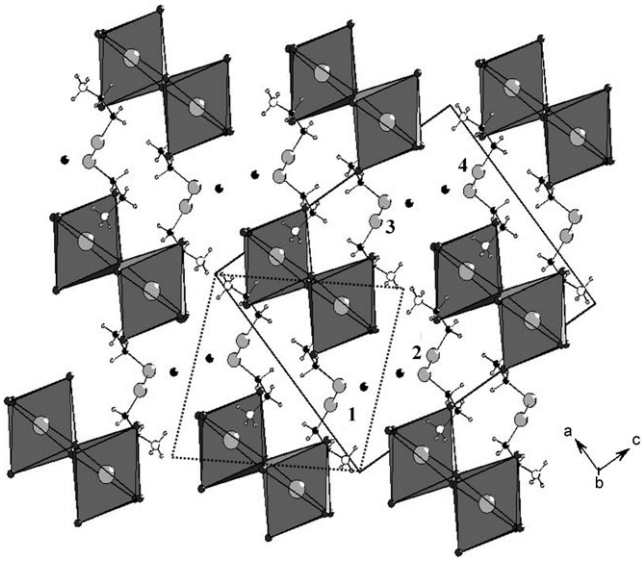

Figure 2. View along the *b* axis of the structure of β-[{$H_3N(CH_2)_2SS(CH_2)_2NH_3$}$PbI_5$]·$H_3O$. Molecules in the unit cell within the bold lines are numbered **1**–**4**. The unit cell of α-[{$H_3N(CH_2)_2SS(CH_2)_2NH_3$}$PbI_5$]·$H_3O$ (shifted $00^1/_2$ related to the α-phase cell drawn in Figure 1) appears within the dotted lines.

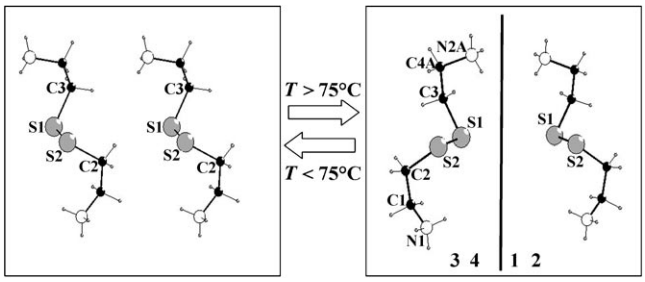

Figure 3. Schematic representation of the conformational change of molecules during the conglomerate-to-true-racemate transition at 75 °C. Molecules **1**–**4** correspond to those indicated in Figure 2. Only C4A and N2A atoms of the disordered C–N part of β-phase molecules are shown (S1–C3 lies behind the figure).

 © 2006 Wiley-VCH Verlag GmbH & Co. KGaA, Weinheim

Of course, one immediately wonders about the reversibility of the transition: will the crystal return to the homochiral structure after cooling? And if so, will it retain a memory of its initial chirality? Using the same crystal, a new X-ray study was performed at room temperature and showed first of all that the unit cell corresponded well to that previously observed for the α-[{$H_3N(CH_2)_2SS(CH_2)_2NH_3$}$PbI_5$]·$H_3O$ phase. Then, the structure of α-[{$H_3N(CH_2)_2SS(CH_2)_2NH_3$}$PbI_5$]·$H_3O$ was correctly refined after data collection with a Flack parameter of 0.49, thus indicating that the studied individual crystal could now be considered to be twinned conglomerate crystals (an equal mixture of homochiral lattice fragments of both stereochemistries), and thus that there is no memory of the initial chirality (a summary of the X-ray data is given in the Supporting Information).

Considering the β-[{$H_3N(CH_2)_2SS(CH_2)_2NH_3$}$PbI_5$]·$H_3O$ racemic compound, we wanted to discover the driving force that governs the exceptional transition to a conglomerate with the associated conformational change of half of the molecules when cooling down. The prediction of a given structure, or rather the explanation of a structural change, remains an elusive challenge in the case of molecular compounds owing to many repulsive or attractive (weak) interactions of equal force. Nevertheless, an accurate examination of both structures allows us to speculate that hydrogen bonding at the organic–inorganic interface seems to play a major role in this transformation. While hydrogen bonding of the hydronium cations[13] and the $N(2)H_3^+$ ammonium heads located in the PbI_5 chains remains roughly unchanged in both structures, an important change concerns the $N(1)H_3^+$ ammonium heads which interact with two inorganic chains (Table 1, Figure 4). Interactions of $N(1)H_3^+\cdots I$ in the α phase appear much stronger than in the β phase, as indicated by the H···I distances (α: 2.71–2.86; β: 2.96–3.02 Å) or the N(1)···I distances (α: 3.58(1)–3.65(1); β: 3.64(1)–3.83(1) Å) and can not be only explained by a contraction effect. By comparison, the strength of the $N(2)H_3^+\cdots I$ interactions, which on the contrary appear a little weaker in the α phase, do not change by the same proportion (e.g., the N···I distances vary from 3.66(1)–3.71(1) Å (average: 3.68 Å (α)) to 3.57(2)–3.84(2) Å (average: 3.72 Å (β)). Focusing on the $N(1)H_3^+\cdots I$ hydrogen bonding, Figure 4 clearly shows the influence of these interactions on the presence or loss of a symmetry center and on the molecular conformation in both structures. In summary, it seems that the key point is the stabilization of the α-phase structure (below 75 °C) by fairly strong hydrogen bonds when iodine atoms of a given PbI_6 octahedron interact with two $N(1)H_3^+$ ammonium heads, thus implying one molecular conformation only (Figure 4).

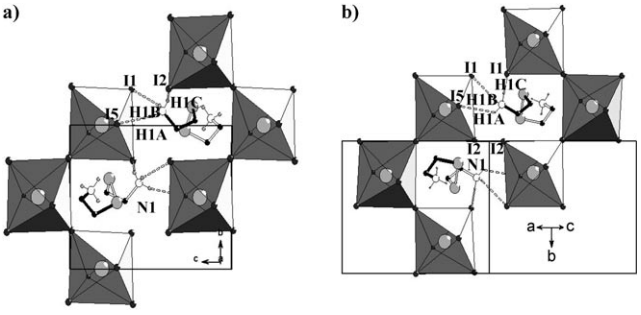

Figure 4. Hydrogen bonding at the interface between the $N(1)H_3^+$ ammonium heads and iodine atoms in a) α-[{$H_3N(CH_2)_2SS(CH_2)_2NH_3$}$PbI_5$]·$H_3O$ and b) β-[{$H_3N(CH_2)_2SS(CH_2)_2NH_3$}$PbI_5$]·$H_3O$. The S–C, C–C, and N–N bonds that lie in front of the plane of the paper (in the projections) appear in bold line. (C4B and N2B atoms of the disordered C–N part of the β-phase molecules not shown).

Interestingly, second-order nonlinear optical (NLO) properties, which are only observable in non-centrosymmetric materials, are evidenced in α-[{$H_3N(CH_2)_2SS(CH_2)_2NH_3$}$PbI_5$]·$H_3O$. The SHG measurements were performed by the powder Perry and Kurtz method[14] (1064-nm beam of a Nd/YAG pulsed laser) both on the yellow polycrystalline sample of the title compound and the reference powder 3-methyl-4-nitropyridine-1-oxide (POM). The effective $\chi^{(2)}_{eff}(-2\omega,\omega,\omega)$ susceptibility of α-[{$H_3N(CH_2)_2SS(CH_2)_2NH_3$}$PbI_5$]·$H_3O$ is 0.1 $\chi^{(2)}_{eff}(-2\omega,\omega,\omega)$ of POM. Good SHG properties have been already reported for some iodometallate salts,[15] which is explained in part by the presence of the highly polarizable iodine atoms. A study of SHG signals as a function of temperature shows that after unmodified behavior up to 75 °C, an abrupt decrease is observed at this temperature, at which the SHG intensity decreases to zero (see the Supporting Information). After cooling, a SHG green signal could be observed again, which confirms the reversible phase transition observed by the X-ray studies. Thus, the material works as a SHG switch driven by temperature, and the SHG intensity is not affected after 20 temperature cycles. In the large field of research into NLO compounds, molecular materials have been extensively studied over the past decade to achieve switchable NLO systems[16] through the possible modification of "push/pull" molecules, notably by using photochemical reactions.[17] In the solid state, this approach can lead to a modulation of the SHG intensity.[16a,17a,b] Herein, the on/off switchable NLO hybrid compound combines the useful properties of both the organic (molecular flexibility (switch)) and inorganic (polarizable iodometallate network) components. This transition can be also expected to be driven by other external stimuli, such as pressure, as we noticed that the volume of the high-temperature phase is unusually lower than the volume of the low-temperature phase (α: $2V = 2102$ Å^3; β: $V = 2084$ Å^3).

In conclusion, we have shown that a remarkable solid-state transition from a conglomerate to a true racemate occurs at 75 °C in the hybrid compound [{$H_3N(CH_2)_2SS(CH_2)_2NH_3$}$PbI_5$]·$H_3O$ and that this transformation is correlated to a change in the conformation of the disulfide components of this material, certainly driven by a change in the hydrogen bonding at the organic–inorganic interface. We also demonstrated that [{$H_3N(CH_2)_2SS(CH_2)_2NH_3$}$PbI_5$]·$H_3O$ can be considered as a switchable SHG material; therefore, further quantitative measurements of NLO properties should be performed on polycrystalline samples and single crystals.[18]

Received: September 28, 2005
Published online: February 15, 2006

 © 2006 Wiley-VCH Verlag GmbH & Co. KGaA, Weinheim

Keywords: chirality · conformers · disulfides · iodoplumbates · second harmonic generation · solid-state structures

[1] "IUPAC Tentative Rules for the Nomenclature of Organic Chemistry, Section E, Fundamental Stereochemistry": *J. Org. Chem.* **1970**, *35*, 2849 – 2857.

[2] a) J. Jacques, A. Collet, S. H. Wilen, *Enantiomers, Racemates and Resolutions*, Krieger, Malabar, FL, **1994**; b) E. Pidcock, *Chem. Commun.* **2005**, *27*, 3457 – 3459.

[3] M. Carmack, *J. Chem. Inf. Comput. Sci.* **2004**, *44*, 286 – 288.

[4] a) Review: R. Steudel, *Angew. Chem.* **1975**, *87*, 683 – 692; *Angew. Chem. Int. Ed. Engl.* **1975**, *14*, 655 – 664; b) J. Webb, R. W. Stickland, F. S. Richardson, *J. Am. Chem. Soc.* **1973**, *95*, 4775 – 4783; c) G. Gottarelli, B. Samori in *The Chemistry of Ethers, Crown Ethers, Hydroxyl Groups, and their Sulfur Analogues* (Ed.: A. Patai) Wiley, New York, **1980**, pp. 279 – 298; d) R. Steudel, Y. Drizdova, K. Miaskiewick, R. H. Hertwig, W. Koch, *J. Am. Chem. Soc.* **1997**, *119*, 1990 – 1996.

[5] Two of 32 corresponding molecular compounds found in the Cambridge Crystal Structure Database crystallize in a chiral space group when the search was restricted to acyclic molecules with the $\{N(CH_2)_2SS(CH_2)_2N\}$ fragment and no chiral ligand; see: a) I. Dediako-Amoa, R. Silerova, H. B. Kraatz, *Chem. Commun.* **2002**, 2430 – 2431; T. Ishida, M. Inoue, K. Kitamura, A. Wakahara, K. I. Tomita, M. Shinoda, *Acta Crystallogr. Sect. C* **1984**, *40*, 660 – 663.

[6] For example: a) L. A. Neubert, M. Carmack, *J. Am. Chem. Soc.* **1974**, *96*, 943 – 945; b) J. P. Casey, R. B. Martin, *J. Am. Chem. Soc.* **1972**, *94*, 6141 – 6151; D. L. Colman, E. R. Blout, *J. Am. Chem. Soc.* **1968**, *90*, 2405 – 2416; D. F. Mullica, M. L. Trawick, P. W. N. Wu, E. L. Sappenfield, *J. Chem. Crystallogr.* **1998**, *28*, 761 – 765; I. Dediako-Amoa, T. C. Sutherland, C. H. Li, R. Silerova, H. B. Kraatz, *J. Phys. Chem. B* **2004**, *108*, 704 – 714.

[7] R. R. Fraser, G. Boussard, J. K. Sanders, J. B. Lambert, C. Mixan, *J. Am. Chem. Soc.* **1971**, *93*, 3822 – 3823; I. de Sousa Moreira, J. B. de Lima, D. W. Franco, *Coord. Chem. Rev.* **2000**, *196*, 197 – 217.

[8] Single-crystal X-ray data for α-$[\{H_3N(CH_2)_2SS(CH_2)_2NH_3\}PbI_5]\cdot H_3O$: $C_4H_{17}I_5N_2OPbS_2$, $M_r = 1015.05$, monoclinic, $a = 10.4309(10)$, $b = 8.8823(8)$, $c = 11.721(2)$ Å, $\beta = 104.41(1)°$, $V = 1051.8(2)$ Å^3, space group $P2_1$, $Z = 2$, calculated density :3.205, crystal dimensions: $0.20 \times 0.10 \times 0.06$ mm^3, $T = 293$ K, Bruker Kappa CCD diffractometer, graphite monochromated $Mo_{K\alpha}$ radiation ($\lambda = 0.71073$ Å), $\mu = 15.54$ mm^{-1}, $2\theta_{max} = 60°$, 19090 measured reflections of which 5978 were unique ($R_{(int)} = 0.044$) and 5030 had $I/\sigma(I) > 2$; the intensities were corrected for Lorentz-polarization effects, as well as for absorption effect (SADABS). The structure was solved by direct methods, and refined by full-matrix least-squares routines against F^2 using the Shelxl97 package. The hydrogen atoms were treated with a riding model. The refinements of positions and anisotropic thermal motion parameters of the non-H atoms converge to $R(F) = 0.027$ (5030 reflections, 140 parameters), $wR2(F^2) = 0.060$ (all data), GOF on F^2 0.995, Flack absolute structure parameter 0.007(4), $\Delta\rho_{max} = 0.89$ e Å^{-3}, $\Delta\rho_{min} = -1.14$ e Å^{-3}. CCDC-284129 contains the supplementary crystallographic data for this paper. These data can be obtained free of charge from The Cambridge Crystallographic Data Centre via www.ccdc.cam.ac.uk/data_request/cif.

[9] D. B. Mitzi, *Prog. Inorg. Chem.* **1999**, *48*, 1 – 121.

[10] a) X. H. Zhu, N. Mercier, M. Allain, P. Frere, P. Blanchard, J. Roncali, A. Riou, *J. Solid State Chem.* **2004**, *177*, 1067 – 1071; b) G. C. Papavassiliou, G. A. Mousdis, C. P. Raptopoulou, A. Terzis, *Z. Naturforsch. B* **1999**, *54*, 1405 – 1409.

[11] Single-crystal X-ray data of β-$[\{H_3N(CH_2)_2SS(CH_2)_2NH_3\}PbI_5]\cdot H_3O$: $C_4H_{17}I_5N_2OPbS_2$, $M_r = 1015.05$, monoclinic, $a = 13.807(1)$, $b = 8.9915(8)$, $c = 16.931(1)$ Å, $\beta = 97.36(1)°$, $V = 1051.8(2)$ Å^3, space group $P2_1/n$, $Z = 4$, calculated density: 3.234, crystal dimensions: $0.20 \times 0.10 \times 0.06$ mm^3, $T = 360$ K, Bruker Kappa CCD diffractometer, graphite-monochromated $Mo_{K\alpha}$ radiation ($\lambda = 0.71073$ Å), $\mu = 15.68$ mm^{-1}, $2\theta_{max} = 60°$, 38438 measured reflections of which 6057 were unique ($R_{(int)} = 0.050$) and 4074 had $I/\sigma(I) > 2$; the intensities were corrected for Lorentz-polarization effects, as well as for absorption effect (SADABS); the structure was solved by direct methods and refined by full-matrix least-squares routines against F^2 using the Shelxl97 package; a statistical disorder affects the atoms of one CH_2–NH_3 part of molecules, each one being located on two positions. An identical occupation rate was first refined for atoms belonging to the same component, agitation parameters of each disordered atom being constrained to be equal and then fixed to 0.5. The H atoms were treated with a riding model. The refinements of positions and anisotropic thermal motion parameters of the non-H atoms converge to $R(F) = 0.035$ (4074 reflections, 154 parameters), $wR2(F^2) = 0.077$ (all data), GOF on $F^2 = 1.029$, $\Delta\rho_{max} = 1.07$ e Å^{-3}, $\Delta\rho_{min} = -1.14$ e Å^{-3}. CCDC-284130 contains the supplementary crystallographic data for this paper. These data can be obtained free of charge from The Cambridge Crystallographic Data Centre via www.ccdc.cam.ac.uk/data_request/cif.

[12] a) A. Collet, M. J. Brienne, J. Jacques, *Bull. Soc. Chim. Fr.* **1972**, 127 – 141; b) R. E. Pincock, K. R. Wilson, *J. Am. Chem. Soc.* **1971**, *93*, 1291 – 1292; c) K. R. Wilson, R. E. Pincock, *J. Am. Chem. Soc.* **1975**, *97*, 1474 – 1478.

[13] Five O···I distances are in the range 3.54–3.78 Å; these values can be compared to those found in α-$[\{H_3N(CH_2)_2SS(CH_2)_2NH_3\}PbI_5]\cdot H_3O$ (see text). The shorter O···S(molecules) distance observed in the β phase (3.78 Å compared to 4.02 Å in the α phase) nevertheless does not correspond to a significant interaction, notably compared to the hydronium/iodide interactions.

[14] S. K. Kurtz, T. T. Perry, *J. Appl. Phys.* **1968**, *39*, 3798 – 3813.

[15] a) E. Cariati, R. Ugo, F. Cariati, D. Roberto, N. Masciocchi, S. Galli, A. Sironi, *Adv. Mater.* **2001**, *13*, 1665 – 1668; b) A. M. Guloy, Z. Tang, B. Mirana, V. I. Srdanov, *Adv. Mater.* **2001**, *13*, 833 – 837.

[16] B. J. Coe, *Chem. Eur. J.* **1999**, *5*, 2464 – 2471; I. Asselberghs, K. Clays, A. Persoons, M. D. Ward, J. McCleverty, *J. Mater. Chem.* **2004**, *14*, 2831 – 2839.

[17] a) M. Sliwa, S. Letard, I. Malfrant, M. Nierlich, P. G. Lacroix, T. Asahi, H. Masuhara, P. Yu, K. Nakatami, *Chem. Mater.* **2005**, *17*, 4727 – 4735; b) R. Loucif-Saibi, J. Nakatani, J. Delaire, M. Dumont, Z. Sekkat, *Chem. Mater.* **1993**, *5*, 229 – 236; c) S. L. Gilat, S. H. Kawai, J. M. Lehn, *Chem. Eur. J.* **1995**, *1*, 275; d) S. Houbrechts, K. Clays, A. Persoons, Z. Pikramenou, J. M. Lehn, *Chem. Phys. Lett.* **1996**, *258*, 485 – 489.

[18] The following are given in the Supporting Information: full single-crystal X-ray data and complete tables of bond distances for α-$[\{H_3N(CH_2)_2SS(CH_2)_2NH_3\}PbI_5]\cdot H_3O$ and β-$[\{H_3N(CH_2)_2SS(CH_2)_2NH_3\}PbI_5]\cdot H_3O$; powder X-ray diffraction patterns of both room-temperature α and high-temperature β phases together with calculated patterns; TGA and DSC curves; a description of the SHG experiments.

 © 2006 Wiley-VCH Verlag GmbH & Co. KGaA, Weinheim

Template Synthesis

DOI: 10.1002/anie.200503625

Phosphorus-Containing [2]Catenanes as an Example of Interlocking Chiral Structures

Agnès Theil, Caroline Mauve, Marie-Thérèse Adeline, Angela Marinetti, and Jean-Pierre Sauvage*

In recent years, several synthetic strategies to [2]catenanes have been designed[1] which allow introduction of various functionalities in their backbone or at their periphery so as to generate targeted physical and chemical properties. For example, suitable functionalities such as coordinating sites and porphyrinic, disulfide, hydroxyl, and halide moieties have allowed the generation of photoinduced electron-transfer processes,[2] the adsorption of catenanes onto gold surfaces,[3] the building of light-driven machine prototypes,[4] and the development of polymerization processes.[5] In the increasingly active search for new structural motifs it is surprising that phosphorus functionalities have been neglected so far. To the best of our knowledge, no catenanes functionalized with phosphorus groups have been described to date. The only reported phosphorus-containing catenanes have phosphine–gold complexes as constitutive elements of the catenane framework itself,[6] and they have been mostly prepared and characterized as solid-state species.

In the present work we envisioned that the synthesis of [2]catenanes bearing phosphine oxide functions would afford potential binding sites for transition metals and, like the corresponding trivalent phosphines, they would open up new ways toward the application of catenanes in coordination chemistry and organometallic catalysis. Described herein is a potentially general, flexible, and modular synthetic approach for the preparation of the first [2]catenanes functionalized with phosphorus groups.

The synthetic approach is based on the strategy established many years ago, which takes advantage of the temporary, three-dimensional template effect of copper(I)/phenanthroline complexes to create the core of the interlocking rings.[7] The key step is a macrocyclization reaction between the phenanthroline diphenol **2**[8] and a suitable biselectrophile. As a new application of the method, the macrocyclization reaction has been performed here by using the phosphorus-containing biselectrophile (*S*,*S*)-**1**. The individual steps leading to catenane **6** are shown in Scheme 1.

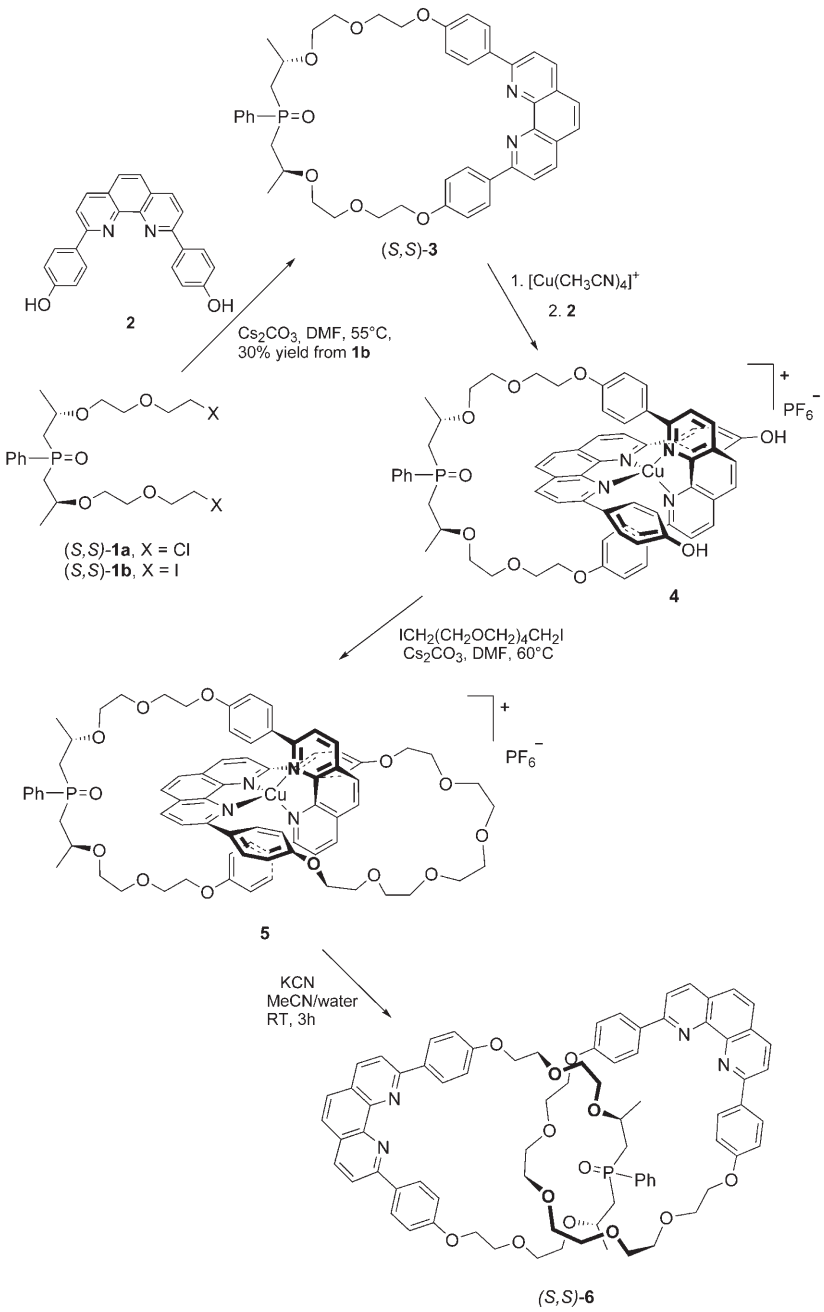

Scheme 1. Synthesis of the [2]catenane **6** bearing a phosphine oxide function.

The dichloride **1a** had been designed in previous work as a readily available starting material for building chiral macro-

[*] A. Theil, C. Mauve, M.-T. Adeline, Dr. A. Marinetti
Institut de Chimie des Substances Naturelles—CNRS UPR 2301
1, avenue de la Terrasse, 91198 Gif-sur-Yvette (France)
Fax: (+33) 1-6907-7247
E-mail: angela.marinetti@icsn.cnrs-gif.fr
Dr. J.-P. Sauvage
Laboratoire de Chimie Organo-Minérale—CNRS UMR 7513
Université Louis Pasteur
4, rue Blaise Pascal, 67070 Strasbourg (France)

Supporting information for this article (full synthetic details and characterization of new compounds) is available on the WWW under http://www.angewandte.org or from the author.

InterScience
© 2006 Wiley-VCH Verlag GmbH & Co. KGaA, Weinheim

cyclic phosphines in an optically pure form.[9] It was prepared from commercially available phenylphosphine and (*S*)-propylene oxide in a two-step synthesis. Unfortunately, **1a** proved to be insufficiently reactive for the purposes of the present work (incomplete conversion in its reaction with **2**) and so it was converted into the corresponding diiodide (*S*,*S*)-**1b**, whose reaction with the phenanthroline diphenol **2**[8] in DMF in the presence of cesium carbonate under high-dilution conditions led to the expected macrocycle (*S*,*S*)-**3** in 30% yield.

As mentioned above, the tetrahedral cores of catenanes can be formed by combining Cu^{I} salts with two suitable phenanthroline units. One of them can be part of a preformed macrocyclic structure such as **3**. Thus, addition of $[Cu(MeCN)_4]PF_6$ to a solution of **3** in dichloromethane, followed by addition of one equivalent of the phenanthroline diphenol **2** afforded the precatenane **4**, which was treated in situ with 1,14-diiodo-3,6,9,12-tetraoxatetradecane, a usual building block for catenanes, to form the copper catenate **5** containing two different, interlocking macrocycles. After preliminary purification by column chromatography, the copper was removed by means of a ligand-exchange reaction involving treatment of **5** with aqueous KCN under literature conditions.[8]

Not only does (*S*,*S*)-**6** represent the first known catenane bearing a phosphine oxide function, it is a chiral, enantiomerically pure species. The chirality of **6** relies, in a most classical way, on the incorporation of stereogenic carbon centers in the macrocyclic structure. Another interesting case would be that of topologically chiral catenane frameworks. In the case of mechanically interlocking macrocycles, chirality may result from one of two different structural arrangements: on one hand, topological chirality is foreseen for catenanes having oriented segments in their macrocyclic chains. Several examples of topologically chiral [2]catenanes of this family have been reported during the last few years which have generally been resolved by chromatography on chiral stationary phases.[10] On the other hand, enantiomers are expected when both macrocyclic moieties contain prochiral centers, for example, prochiral carbon atoms or phosphorus functions.[11] In this case (Figure 1) both rings are oriented as a consequence of the fact that the prochiral group makes the two faces of the macrocycle different from one another. In other words, each ring has a top face and a bottom face (the P=O and the P–Ph faces, respectively). This arrangement is sufficient to orient the other ring. (Note: strictly speaking, the two objects of Figure 1 are nevertheless not topological enantiomers since they can be interconverted by continuous deformation of bonds at the prochiral phosphorus centers in three-dimensional space.)

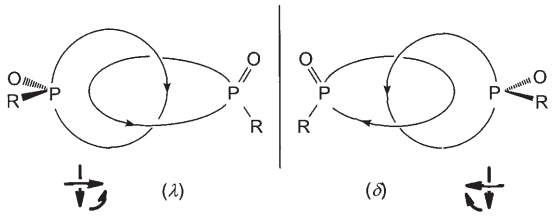

Figure 1. Schematic representation of enantiomeric [2]catenanes with stereogenic phosphorus centers. Assignment of the absolute configuration is made according to the oriented skew-lines convention.[12]

As far as we know, enantiomerically pure [2]catenane derivatives of this type have not been reported to date. In the current study, chiral [2]catenanes bearing prochiral phosphorus centers have been prepared in enantiomerically pure form.

The interlocking rings are obtained by addition of the phosphorus-containing diodide (*S*,*S*)-**1b** to the precatenane generated in situ from (*S*,*S*)-**3**, copper(I) hexafluorophosphate, and the phenanthroline diphenol **2** in the presence of cesium carbonate (Scheme 2). After purification of the reaction mixture by column chromatography, the cationic catenate **7** was characterized by mass spectrometry as well as by ^{1}H and ^{31}P NMR spectroscopy. The most representative ^{1}H NMR signals come from the phenyl groups attached to the phenantroline moiety: in analogous tetrahedral copper/bis(phenanthroline) complexes, the *meta*-phenyl protons are known to lie in the shielding field of the second phenanthroline moiety, which accounts for their high-field shifts at about $\delta = 6$ ppm.[13] The corresponding signals for **7** appear at $\delta =$ 6.03 (d, $J = 9.0$ Hz, 2H, H^{m}), 6.04 (d, $J = 9.0$ Hz, 2H, $H^{m'}$), 6.13 (d, $J = 8.5$ Hz, 2H, H^{m}), and 6.15 ppm (d, $J = 9.0$ Hz, 2H, $H^{m'}$).

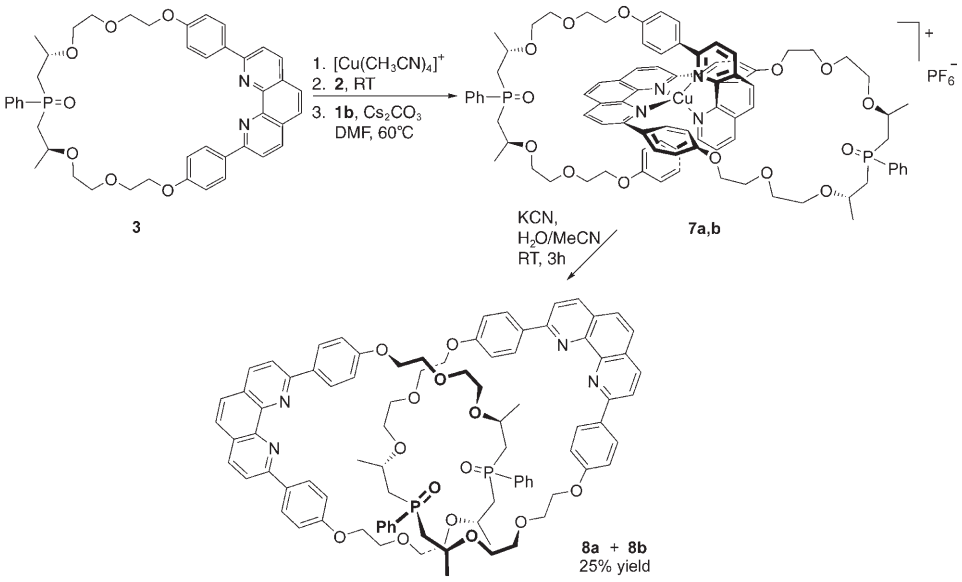

Scheme 2. Synthesis of the [2]catenane **8** bearing phosphine oxide functions.

 © 2006 Wiley-VCH Verlag GmbH & Co. KGaA, Weinheim

Complete characterization of **7** was prevented by the presence of the two expected diastereoisomers.

After removal of the copper, the two diastereoisomers of the free catenane **8** could be separated by preparative HPLC and fully characterized. Figure 2 shows the HPLC chromatogram as well as the 500 MHz ^{1}H NMR spectra in the aromatic region for the two isomers of **8**. It can be noticed that, in both isomers, the chiral environment markedly differentiates the two halves of the phenanthroline moiety, thus giving well-separated doublets for H^3 and H^8, as well as for H^4 and H^7. The corresponding signals of the parent macrocycle **3** merge into one another in the NMR spectrum despite the presence of stereogenic carbon atoms in the molecule ($\delta = 8.07$ (d, $J =$ 9.0 Hz, 2H, $H^{3,8}$), 8.26 ppm (d, $J = 8.0$ Hz, 2H, $H^{4,7}$)). Thus, it seems that the presence of the interlocking rings results in a more pronounced magnetic differentiation of the two sides of the whole molecule, including the phenanthroline nucleus.

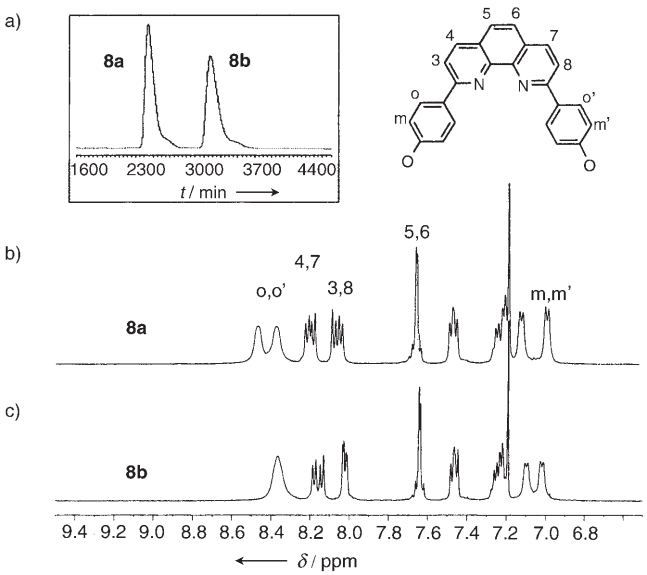

Figure 2. a) HPLC chromatogram of a mixture of **8a** and **8b**. b) Partial ^{1}H NMR spectra of solutions of **8a** and c) **8b** in $CDCl_3$. Assignments have been made by analogy to previously reported data (see ref. [13]).

Phosphine oxides **8** represent an unprecedented class of chiral phosphorus derivatives, that is, phosphorus-containing chiral [2]catenanes, whose properties in coordination chemistry and catalysis will be investigated in the near future.

This exploratory study has established that catenanes containing phosphine oxide functions can be generated by using the template effect of copper/phenanthroline complexes and suitable phosphorus-containing synthons. Stereogenic carbon atoms may be introduced into the above structures so as to produce chiral derivatives. In addition, chiral catenanes are generated as enantiomerically pure diastereomers when both of the interlocking rings bear phosphorus functions.

Experimental Section

8a,b: A degassed solution of $[Cu(MeCN)_4]PF_6$ (130 mg, 0.35 mmol) in MeCN (9 mL) was transferred to a solution of (*S*,*S*)-**3** (240 mg, 0.33 mmol) in CH_2Cl_2 (16 mL) by the double-ended-needle transfer technique. After stirring the mixture at room temperature for 0.5 h, a solution of **2** (120 mg, 0.33 mmol) in DMF (17 mL) was added, which resulted in the generation of a red-brown color corresponding to the formation of **4**. After stirring the mixture at room temperature for 1 h, the solvent was partially removed in vacuo, and then a solution of (*S*,*S*)-**1b** (0.35 mmol) in DMF (20 mL) was added. The mixture was added dropwise, within 8 h, to a suspension of Cs_2CO_3 (0.32 g, 1 mmol) in DMF (50 mL) kept at 55–60 °C. After the end of the addition, the heating was maintained for about 50 h. The DMF was then removed under vacuum and the residue dissolved in H_2O/CH_2Cl_2. The organic layer was washed with brine and water, concentrated to a volume of 20 mL, then stirred overnight with a saturated aqueous solution of KPF_6 to effect anion exchange. The organic layer was washed with brine and water, dried with $MgSO_4$, and the solvent was evaporated to dryness. The crude product was filtered through a column of silica gel using a CH_2Cl_2/MeOH gradient (from 95:5 to 75:15) as the eluent. Complex **7** (150 mg, 0.07 mmol, 29% yield) was obtained as a red-brown oil as a mixture of two diastereoisomers.

Demetalation of **7** (120 mg) was performed by vigorous stirring of a solution of the copper complex in MeCN (4 mL) with an excess of KCN (20 mg, 5 equiv) in water (1 mL) at room temperature for 3 h. The initial reddish-brown color disappeared. The organic layer was separated, dried over $MgSO_4$, and the solvents evaporated to dryness. The crude product was purified by column chromatography on silica gel with an AcOEt/MeOH gradient (from 100:0 to 70:30) as the eluent. Compound **8** was obtained as a mixture of two diastereoisomers in 85% yield (98 mg). ^{31}P NMR ($CDCl_3$): $\delta = 34.0$ ppm; HRMS (ESI): calcd for $C_{88}H_{95}N_4O_{14}P_2$: 1493.6320; found: 1493.6294.

The components of a sample of **8a**+**8b** (60 mg) were separated by preparative HPLC on a Waters SunFire C18 column with a mixture of H_2O/TFA/MeCN (66:0.1:34) as the eluent. The retention times of **8a** and **8b** were 23 and 30 min, respectively. After evaporation of the solvents, the residues were filtered through a short column of silica gel by eluting successively with chloroform and a mixture of AcOEt/MeOH (70:30) to remove the residual inorganic salts.

8a: ^{1}H NMR (500 MHz, $CDCl_3$): $\delta = 1.08$ (d, $J = 5.5$ Hz, 6H, Me), 1.28 (d, $J = 5.5$ Hz, 6H, Me), 1.91 (m, 2H, CH_2P), 2.10–2.20 (m, 4H, CH_2P), 2.40 (m, 2H, CH_2P), 3.27 (m, 4H), 3.38 (m, 2H), 3.51 (m, 2H), 3.60–3.70 (m, 10H), 3.82 (m, 4H), 3.90 (m, 6H), 4.20–4.30 (m, 8H), 7.10 (d, $J = 8.0$ Hz, 4H, H^m), 7.22 (d, $J = 6.5$ Hz, 4H, $H^{m'}$), 7.30 (m, 6H, PhH), 7.55 (m, 4H, PhH), 7.74 (m, 4H, $H^{5,6}$), 8.10 (d, $J = 8.5$ Hz, 2H, H^3/H^8), 8.14 (d, $J = 8.0$ Hz, 2H, H^3/H^8), 8.24 (d, $J = 9.0$ Hz, 2H, H^4/H^7), 8.27 (d, $J = 7.5$ Hz, 2H, H^4/H^7), 8.42 (brs, 4H, H^o), 8.51 ppm (brs, 4H, $H^{o'}$).

8b: ^{1}H NMR (500 MHz, $CDCl_3$): $\delta = 0.98$ (d, $J = 6.0$ Hz, 6H, Me), 1.27 (d, $J = 5.5$ Hz, 6H, Me), 1.90 (m, 2H, CH_2P), 2.10–2.20 (m, 4H, CH_2P), 2.35 (m, 2H, CH_2P), 3.18 (m, 2H), 3.24 (m, 2H), 3.31 (m, 2H), 3.40, (m, 2H), 3.5–3.7 (m, 12H), 3.70–3.90 (m, 8H), 4.15 (m, 4H), 4.23 (m, 4H), 7.01 (d, $J = 7.5$ Hz, 4H, H^m), 7.10 (d, $J = 7.5$ Hz, 4H, $H^{m'}$), 7.20 (m, 6H, PhH), 7.45 (m, 4H, PhH), 7.64 (m, 2H, $H^{5,6}$), 8.01 (d, $J = 8.5$ Hz, 2H, H^3/H^8), 8.02 (d, $J = 8.5$ Hz, 2H, H^3/H^8), 8.14 (d, $J = 8.5$ Hz, 2H, H^4/H^7), 8.18 (d, $J = 8.5$ Hz, 2H, H^4/H^7), 8.37 ppm (brs, 8H, $H^{o,o'}$).

Received: October 13, 2005
Published online: February 27, 2006

Keywords: catenanes · chirality · copper · phosphine oxide · template synthesis

[1] For reviews see: a) *Molecular Catenanes, Rotaxanes and Knots* (Eds.: J.-P. Sauvage, C. O. Dietrich-Buchecker), Wiley-VCH, Weinheim, **1999**; b) F. M. Raymo, F. Stoddart, *Chem. Rev.* **1999**,

 © 2006 Wiley-VCH Verlag GmbH & Co. KGaA, Weinheim

99, 1643 – 1663; c) J.-C. Chambron, J.-P. Collin, V. Heitz, D. Jouvenot, J.-M. Kern, P. Mobian, D. Pomeranc, J.-P. Sauvage, *Eur. J. Org. Chem.* **2004**, 1627 – 1638, and references therein.
[2] L. Flamigni, A. M. Talarico, J.-C. Chambron, V. Heitz, M. Linke, N. Fujita, J.-P. Sauvage, *Chem. Eur. J.* **2004**, *10*, 2689 – 2699.
[3] L. Raehm, J.-M. Kern, J.-P. Sauvage, C. Hamann, S. Palacin, J.-P. Bourgoin, *Chem. Eur. J.* **2002**, *8*, 2153 – 2162.
[4] P. Mobian, J.-M. Kern, J.-P. Sauvage, *Angew. Chem.* **2004**, *116*, 2446 – 2449; *Angew. Chem. Int. Ed.* **2004**, *43*, 2392 – 2395; J.-P. Sauvage, *Chem. Commun.* **2005**, 1507 – 1510.
[5] a) S. Menzer, A. J. P. White, D. J. Williams, M. Belohradsky, C. Hamers, F. M. Raymo, A. N. Shipway, J. F. Stoddart, *Macromolecules* **1998**, *31*, 295 – 307; b) D. Muscat, W. Köhler, H. J. Räder, K. Martin, S. Mullins, B. Müller, K. Müllen, Y. Geerts, *Macromolecules* **1999**, *32*, 1737 – 1745.
[6] C. P. McArdle, M. J. Irwin, M. C. Jennings, R. J. Puddephatt, *Angew. Chem.* **1999**, *111*, 3571 – 3573; *Angew. Chem. Int. Ed.* **1999**, *38*, 3376 – 3378.
[7] a) C. O. Dietrich-Buchecker, J.-P. Sauvage, J.-P. Kintzinger, *Tetrahedron Lett.* **1983**, *24*, 5095 – 5098; b) C. O. Dietrich-Buchecker, J.-P. Sauvage, J.-M. Kern, *J. Am. Chem. Soc.* **1984**, *106*, 3043 – 3045.
[8] C. Dietrich-Buchecker, J.-P. Sauvage, *Tetrahedron* **1990**, *46*, 503 – 512.
[9] A. Theil, J. Hitce, P. Retailleau, A. Marinetti, *Eur. J. Org. Chem.* **2006**, 154 – 161.
[10] a) D. K. Mitchell, J.-P. Sauvage, *Angew. Chem.* **1988**, *100*, 985 – 986; *Angew. Chem. Int. Ed. Engl.* **1988**, *27*, 930 – 931; b) J.-C. Chambron, D. K. Mitchell, J.-P. Sauvage, *J. Am. Chem. Soc.* **1992**, *114*, 4625 – 4631; c) C. Yamamoto, Y. Okamoto, T. Schmidt, R. Jäger, F. Vögtle, *J. Am. Chem. Soc.* **1997**, *119*, 10547 – 10548; d) C. Reuter, A. Mohry, A. Sobanski, F. Vögtle, *Chem. Eur. J.* **2000**, *6*, 1674 – 1682.
[11] a) C. P. NcArdle, S. Van, M. C. Jennings, R. J. Puddephatt, *J. Am. Chem. Soc.* **2002**, *124*, 3959 – 3965; b) A. Hori, T. Sawada, K. Yamashita, M. Fujita, *Angew. Chem.* **2005**, *117*, 4974 – 4977; *Angew. Chem. Int. Ed.* **2005**, *44*, 4896 – 4899.
[12] D. M. Walba, *Tetrahedron* **1985**, *41*, 3161 – 3212.
[13] C. O. Dietrich-Buchecker, P. A. Marnot, J.-P. Sauvage, J.-P. Kintzinger, P. Maltese, *Nouv. J. Chim.* **1984**, *8*, 573 – 582.

 © 2006 Wiley-VCH Verlag GmbH & Co. KGaA, Weinheim

Fullerenes

DOI: 10.1002/anie.200503705

Isolation and Characterization of $Sc_2C_2@C_{68}$: A Metal-Carbide Endofullerene with a Non-IPR Carbon Cage**

Zhi-Qiang Shi, Xin Wu, Chun-Ru Wang, Xin Lu,* and Hisanori Shinohara**

The geometries of pure-carbon fullerenes synthesized thus far follow exclusively the isolated-pentagon rule (IPR), which states that the pentagons in the most stable fullerenes are isolated from each other by hexagons.[1,2] Due to enhanced steric strain (steric effect) and resonance destabilization pertaining to the pentalene-type 8π-electron system (electronic effect), pure-carbon non-IPR fullerenes with abutted pentagons are always unstable and synthetically unattainable.[3] However, it appears that non-IPR fullerenes can be stabilized by either endohedral inclusion of electron-donating metal atoms/clusters[4,5] or exohedral derivatization,[6] as exemplified by such non-IPR fullerene derivatives as the endofullerenes $Sc_2@C_{66}$,[4b] $La_2@C_{72}$,[4c] and $Sc_3N@C_{68}$[5] as well as the exohedral derivative $C_{50}Cl_{10}$.[6] On the other hand, many metal-carbide endofullerenes, for example, $Sc_2C_2@C_{84}$,[7] $Ti_2C_2@C_{78}$,[8] $Y_2C_2@C_{82}$,[9] and $Sc_3C_2@C_{80}$,[10] have been synthesized and characterized exclusively with IPR-satisfying fullerene cages. Herein we report the isolation and characterization of $Sc_2C_2@C_{68}$, which is, to the best of our knowledge, the first metal-carbide endofullerene having a non-IPR cage.

[*] Dr. Z.-Q. Shi, Prof. Dr. C.-R. Wang
Institute of Chemistry
Chinese Academy of Sciences
Beijing 100080 (China)
Fax: (+86) 10-6265-2120
E-mail: crwang@iccas.ac.cn

X. Wu, Prof. Dr. X. Lu
State Key Laboratory of Physical Chemistry of Solid Surface &
Center for Theoretical Chemistry
Departmental of Chemistry
Xiamen University
Xiamen 361005 (China)
Fax: (+86) 592-218-3047
E-mail: xinlu@xmu.edu.cn

Prof. Dr. H. Shinohara
Department of Chemistry
Nagoya University
Nagoya, 464-8602 (Japan)
Fax: (+81) 52-789-2962
E-mail: noris@cc.nagoya-u.ac.jp

[**] C.-R.W. thanks NSFC (No. 50225206, 90206045, 20121301), National Key Project on Basic Research (Grant 2006CB30040, 2003CB716900), and National Center for Nanoscience and Technology of China. X.L. thanks NSFC (No. 20021002, 20425312, 20203013, 20423002, 90206038). H.S. thanks the JSPS for Future Program on New Carbon Nano-Materials for Financial support.

Supporting information for this article is available on the WWW under http://www.angewandte.org or from the author.

 © 2006 Wiley-VCH Verlag GmbH & Co. KGaA, Weinheim

The synthesis and isolation of Sc_2C_{70} are essentially analogous to those of other scandium metallofullerenes such as $Sc_2@C_{66}$ and $Sc_2C_2@C_{84}$ reported before.[4b,7] Briefly, soot containing Sc_2C_{70} and other metallofullerenes were generated by arc discharge of scandium/graphite carbide composite rods (Tokyo Tanso Co. Ltd., $12 \times 12 \times 300$ mm, 1.6 atom % Sc) in direct-current mode (350 A, 21 V) under a 17 L min^{-1} flow of helium at 50–100 Torr. The soot was Soxhlet-extracted with carbon disulfide for 12 h, and the soot extracts were redissolved in toluene. Sc_2C_{70} was isolated by multistage HPLC with two complementary types of column (5PYE and Buckyclutcher columns). The retention time of Sc_2C_{70} on the 5PYE column is very close to that of C_{76}; thus, stage 1 was HPLC on the 5PYE column to roughly separate Sc_2C_{70} and C_{76} from C_{60}, C_{70}, and higher fullerenes and metallofullerenes. In stage 2, recycling HPLC on the 5PYE column was performed to separate Sc_2C_{70} from C_{76}. After 8–10 cycles, separation into two subfractions was completed, whereby the first subfraction (pink) was Sc_2C_{70} with some minor impurities and the second subfraction (yellow) was C_{76}. In stage 3, recycling HPLC on the Buckyclutcher column was performed to further purify the Sc_2C_{70}. The purity (up to 99 %) of isolated Sc_2C_{70} was confirmed by laser-desorption time-of-flight (LD-TOF) mass spectrometry (Figure 1 a).

The relative yield of Sc_2C_{70} is roughly 0.1 % of that of C_{70}. We isolated about 3 mg of Sc_2C_{70} (black powder) for spectroscopic study and structural characterization. Solutions of Sc_2C_{70} in carbon disulfide or toluene are pink. The UV/Vis/NIR spectrum of Sc_2C_{70} in carbon disulfide solution shows absorption peaks at 570, 841, and 1126 nm (Figure 1 b), and it differs remarkably from that of empty C_{70} (absorptions at 472, 550, and 640 nm). The remote absorption onset of Sc_2C_{70} at about 1800 nm (≈ 0.69 eV) as compared to that of C_{70} at about 680 nm identifies it as a metallofullerene with a small band gap.

The ^{13}C NMR spectrum of Sc_2C_{70} in CS_2 solution is shown in Figure 1 c. Between $\delta = 135$ and 158 ppm, the spectrum consists of a series of 21 distinct lines that indicate at least 21 unique C atoms in as-prepared Sc_2C_{70}. Except for an impurity peak at 137.5 ppm (Figure 1 c), a wider range spectrum (not shown) shows no further resonances attributable to impurities.

With respect to the structure of Sc_2C_{70}, two models were considered: simple endohedral $Sc_2@C_{70}$ structure **1** and metal-carbide $Sc_2C_2@C_{68}$ structure **2**. For the simple endohedral $Sc_2@C_{70}$ structure, both the IPR-satisfying D_{5h}-symmetric C_{70} fullerene and all non-IPR C_{70} isomers that have 21 unique C atoms (i.e., #62, #3783, #4912, #6108, #7032, #7114, #8143 following the spiral algorithm[2]) were considered (Supporting Information). To attain a stable closed-shell electronic configuration,[8a,11,12] it is likely that a total of six valence electrons of the two encased Sc atoms would be donated to the carbon cage[13] to give a valence state of $(Sc^{3+})_2@C_{70}^{6-}$. Hence, we computed the structures of the hexaanions of the aforementioned C_{70} isomers at the semiempirical PM3[14] level of theory. In addition, the tetraanions and dianions of these C_{70} isomers were considered. The energies of the non-IPR C_{70}^{q-} ($q = 2$, 4, 6) isomers are much higher than that of the IPR-satisfying D_{5h}-symmetric C_{70}^{q-} (q = 2, 4, 6) predicted by the B3LYP[15]/6-31G//PM3 calculations[16] (Supporting Information). Hence, the $Sc_2@C_{70}$ structure **1** would preferentially adopt the IPR-satisfying D_{5h}-symmetric C_{70} cage, rather than any of the C_{2v}-symmetric non-IPR C_{70} cages. Though the D_{5h}-C_{70} cage has only five unique C atoms, encapsulation of Sc_2 in the D_{5h}-C_{70} cage can result in C_{2v}-symmetric geometries for $Sc_2@C_{70}$, which would give rise to 21 lines in the ^{13}C NMR spectrum. However, such a simple endohedral model is not supported by our quantum chemical calculations. The most stable C_{2v}-symmetric structure of $Sc_2@C_{70}$ (**1**) with D_{5h}-symmetic C_{70} cage, optimized at the GGA-PBE/DNP level of theory,[17,18] is shown in Figure 2; each Sc atom is bonded to a 5–6 ring fusion pertaining to the polar pentagon. The valence state of **1** is $(Sc^{2+})_2@(C_{70})^{4-}$; its HOMO consists predominantly of the d orbitals of the encased Sc^{2+} atoms (Supporting Information). Interestingly, a small barrier of only 1.6 kcal mol^{-1} (at transition state **1_TS**) is predicted for rotation of the Sc_2 unit around the C_5 axis of C_{70} at room

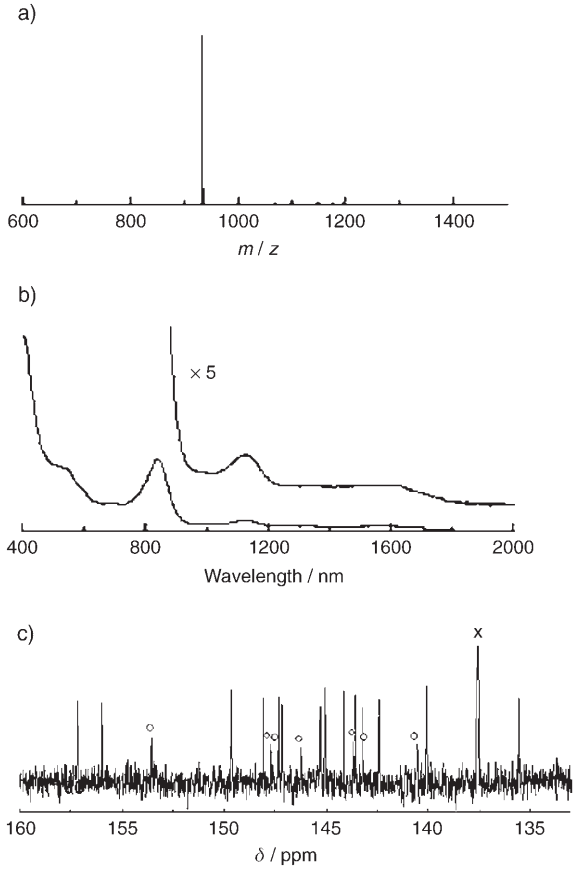

Figure 1. a) Time-of-flight mass spectrum of Sc_2C_{70} anions. b) UV/Vis/NIR absorption spectrum of Sc_2C_{70} in CS_2 solution. c) 125 MHz ^{13}C NMR spectrum of Sc_2C_{70} in CS_2 solution (27 °C, 100000 scans (5 d) on a Varian Inova-600 spectrometer; chromium(III) acetylacetonate was added as relaxation agent). The 21 distinct ^{13}C NMR lines are located at 135.57 (7.4), 140.09 (8.5), 140.53 (3.3), 142.38 (7.3), 143.17 (3.7), 143.22 (7.0), 143.57 (7.7), 143.65 (4.1), 144.14 (8.0), 145.05 (8.3), 145.26 (6.7), 146.23 (3.0), 147.16 (6.8), 147.3 (7.5), 147.35 (3.1), 147.74 (3.2), 148.09 (7.4), 149.62 (8.1), 153.54 (3.8), 155.95 (7.0), and 157.18 ppm (7.1), where the data in parentheses refer to relative intensity. The line marked with × is assigned to impurities on account of its unusual line width and unreasonably high intensity.

 © 2006 Wiley-VCH Verlag GmbH & Co. KGaA, Weinheim

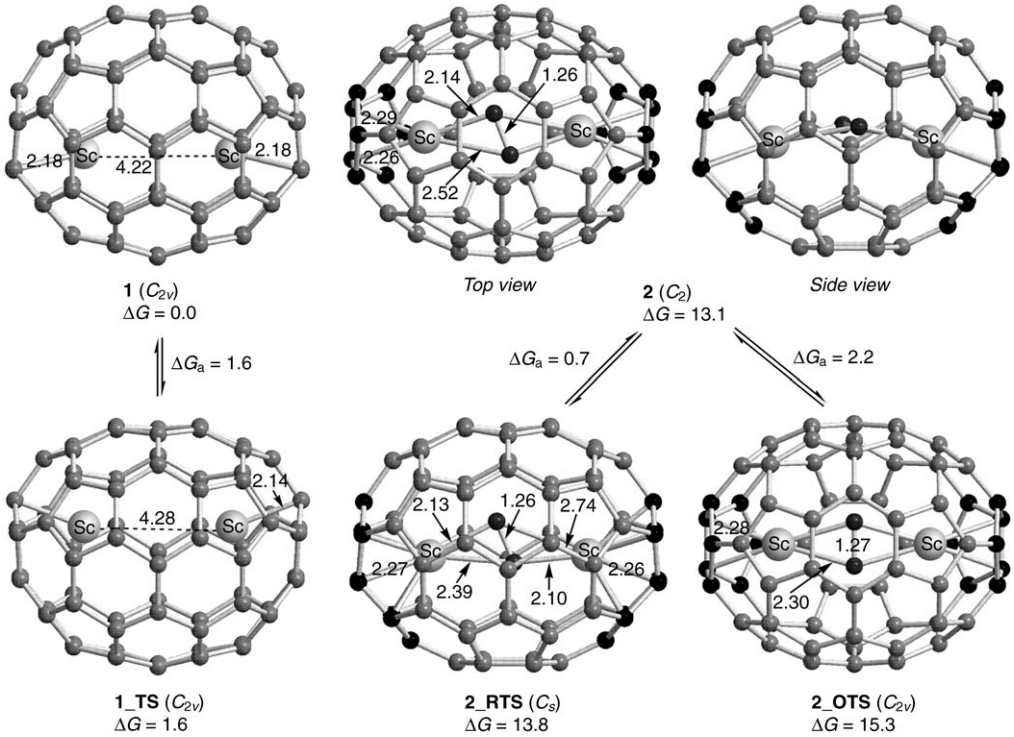

Figure 2. GGA-PBE/DNP predicted geometries (bond lengths [Å]), symmetries, and relative Gibbs free energies ΔG [kcal mol^{-1}] of Sc_2C_{70} isomers at $T = 298.15$ K. **1** is the optimized geometry of $Sc_2@C_{70}$; **1_TS** is the transition state for rotation of the Sc_2 unit around the C_5 axis of the D_{5h}-C_{70} cage. **2** is the optimized geometry of $Sc_2C_2@C_{68}$ with the non-IPR C_{68} (#6073) cage; **2_RTS** and **2_OTS** are the transition states for rotation and oscillation of the carbide moiety within **2**. These stationary points were confirmed to be local minima or transition states by harmonic vibrational analyses. ΔG_a [kcal mol^{-1}] is the free energy of activation for intramolecular rotation or oscillation.

temperature. Hence, rotation of the Sc_2 unit should be quite fast, and the C_{70} cage in **1** should maintain D_{5h} symmetry over a long timescale. As a result, $Sc_2@C_{70}$ (**1**) should display only five ^{13}C NMR lines at room temperature, in obvious disagreement with the measured spectrum shown in Figure 1 c. Hence, the synthesized Sc_2C_{70} does not exist in the $Sc_2@C_{70}$ form.

An alternative structural model for Sc_2C_{70} is $Sc_2C_2@C_{68}$ (**2**). According to the spiral algorithm,[2] C_{68} has no IPR-satisfying isomer but 6332 non-IPR isomers, of which only four C_{2v}-symmetric non-IPR isomers (i.e., #494, #465, #647, and #6073[2]) can produce 21 distinct lines in the ^{13}C NMR spectrum (Supporting Information). Among all 6332 non-IPR C_{68} isomers, C_{68} (#6073) has the smallest number (two) of pentagon–pentagon fusions. On the other hand, previous DFT computations on the metal-carbide endofullerene $Sc_2C_2@C_{84}$ revealed that the encased Sc_2C_2 cluster adopts the charge state $[Sc_2C_2]^{4+}$.[7b] Similarly, $Sc_2C_2@C_{68}$ (**2**) may have a charge state of $[Sc_2C_2]^{4+}@C_{68}^{4-}$ by donation of four electrons from the encased Sc_2C_2 cluster to the C_{68} cage. We computed structures and energies for the tetraanions of the four C_{2v}-symmetric non-IPR C_{68} isomers at the PM3 level of theory[14] and found that the C_{68}^{4-}(#6073) isomer is far more stable than the other three C_{68}^{4-} isomers (Supporting Information). Hence $Sc_2C_2@C_{68}$ (**2**) would preferentially adopt the C_{2v}-symmetric C_{68} (#6073) cage. For Sc_2C_2 encased in the C_{68}(#6073) cage, the most stable structure **2** predicted at the GGA-PBE/DNP level is C_2-symmetric (Figure 2). Although the computed free energy of **2** is 13.1 kcal mol^{-1} higher than that of **1**, the much larger predicted HOMO–LUMO gap of **2** (0.68 eV) relative to **1** (0.33 eV) suggests that **2** is kinetically more stable than **1**. More importantly, **2** has a normal valence state $(Sc^{3+})_2(C_2)^{2-}@C_{68}^{4-}$ that fulfills the rule of closed-shell electronic configuration,[8a,11,12] whereas $Sc_2@C_{70}$ (**1**) has the valence state $(Sc^{2+})_2@(C_{70})^{4-}$, which contains unusual Sc^{2+} cations.[13,19] Hence, $Sc_2C_2@C_{68}$ (**2**) is chemically more rational than $Sc_2@C_{70}$ (**1**). As shown in Figure 3, the two highest occupied molecular orbitals (HOMO and HOMO−1) and two lowest unoccupied molecular orbitals (LUMO and LUMO+1) of **2** are derived mainly from the orbitals of the C_{68}^{4-} cage with minor contribution from the encased cluster. These frontier orbitals should control the redox properties of **2**, for example, electrochemical redox potentials.

Furthermore, two transition states, **2_RTS** and **2_OTS**, were located for rotation of the encased acetylide (C_2^{2-}) group around the Sc–Sc axis and oscillation of the carbide moiety between the two Sc atoms, respectively (Figure 2). At room temperature, the rotational barrier (at **2_RTS**) is only 0.7 kcal mol^{-1}, whereas the barrier for the oscillation is 2.2 kcal mol^{-1} (at **2_OTS**). Due to the small barriers, rotation and oscillation of the encased carbide moiety within **2** should be rather fast at room temperature. Its C_{68} cage appears to be C_{2v}-symmetric by averaging over all rotating and oscillating structures on a long timescale, and this accounts for the observed 21 lines in the ^{13}C NMR spectrum. Accordingly, the synthesized Sc_2C_{70} can be reasonably assigned as $Sc_2C_2@C_{68}$ (**2**).

 © 2006 Wiley-VCH Verlag GmbH & Co. KGaA, Weinheim

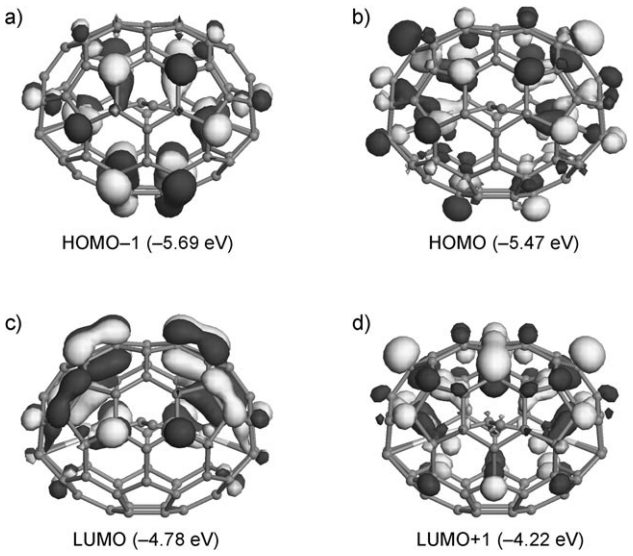

Figure 3. a, b) The two highest occupied molecular orbitals (HOMO and HOMO−1), and c, d) the two lowest unoccupied molecular orbitals (LUMO and LUMO+1) of $Sc_2C_2@C_{68}$ (**2**).

On account of the fascinating intramolecular dynamics of **2**, an accurate theoretical simulation of its ^{13}C NMR spectrum is nontrivial and requires molecular dynamics (MD) simulation followed by elaborate ^{13}C NMR computations on a large number of individual snapshots selected from the MD trajectory. Such a computational technique, though rather time-consuming, proved to be powerful in reproducing the experimental NMR spectrum of $Sc_3N@C_n$ ($n = 68$, 80).[20] Unfortunately, we cannot afford such a simulation due to hardware limitations. Nevertheless, we computed the ^{13}C NMR chemical shifts of **2** at the GIAO[21]-B3LYP/6-31G* level of theory using the B3LYP/6-31G* optimized geometries.[22] By averaging the chemical shifts of equivalent sites in the C_{68} cage, a total of 21 ^{13}C NMR chemical shifts ranging from 133.5 to 159.9 ppm were predicted for $Sc_2C_2@C_{68}$ (Supporting Information), in reasonable agreement with the experimental data, which range from 135.6 to 157.2 ppm. On the contrary, the computed ^{13}C NMR chemical shifts for static C_{2v}-symmetric $Sc_2@C_{70}$ (**1**) (Supporting Information) range from 130.1 to 159.4 ppm with an interval ($\Delta\delta = 29.3$ ppm) much larger than the experimental one ($\Delta\delta = 21.6$ ppm). So far as its intramolecular dynamic behavior is considered, **1** would display only five ^{13}C NMR signals ranging from 137.6 to 145.2 ppm (Supporting Information), inconsistent with the experimental spectrum (Figure 1c). These data further justify the $Sc_2C_2@C_{68}$ (**2**) structure for the synthesized Sc_2C_{70}. In addition, the predicted ^{13}C NMR chemical shift for the encapsulated acetylide group in $Sc_2C_2@C_{68}$ (**2**) is about 234.7 ppm, which is not observed in the NMR experiment, probably due to spin–rotation interaction[9] at room temperature.

Finally, it is noteworthy that the C_{68} cage of $Sc_2C_2@C_{68}$ (**2**) is different from that of the previously synthesized $Sc_3N@C_{68}$ (**3**).[5] Endofullerene **2** has the valence state $(Sc^{3+})_2(C_2)^{2-}@C_{68}^{4-}$, in which the C_{2v}-symmetric C_{68} (#6073) cage has two pentagon–pentagon pairs accommodating two Sc^{3+} ions. $Sc_3N@C_{68}$ (**3**) is in a valence state $(Sc^{3+})_3N^{3-}@C_{68}^{6-}$; its D_3-symmetric C_{68} (#6140) cage has three pentagon–pentagon pairs, each coordinated to an Sc^{3+} ion.[5,23] Accordingly, our synthesis of $Sc_2C_2@C_{68}$, in combination with the previous work on $Sc_3N@C_{68}$, clearly evidences that endohedral clusters such as Sc_2C_2 and Sc_3N function as templates for the synthesis of different non-IPR C_{68} cages.

Received: October 19, 2005
Revised: December 20, 2005
Published online: February 24, 2006

Keywords: density functional calculations · fullerenes · host–guest systems · scandium · structure elucidation

[1] H. W. Kroto, *Nature* **1987**, *329*, 529.
[2] P. W. Fowler, D. E. Manoloupoulos, *An Atlas of Fullerenes*, Oxford University Press, Oxford, **1995**.
[3] X. Lu, Z. Chen, *Chem. Rev.* **2005**, *105*, 3643.
[4] a) K. Kobayashi, S. Nagase, M. Yoshida, E. Osawa, *J. Am. Chem. Soc.* **1997**, *119*, 12693; b) C.-R. Wang, T. Kai, T. Tomiyama, T. Yoshida, Y. Kobayashi, E. Nishibori, M. Takata, M. Sakata, H. Shinohara, *Nature* **2000**, *408*, 426; c) H. Kato, A. Taninaka, T. Sugai, H. Shinohara, *J. Am. Chem. Soc.* **2003**, *125*, 7782.
[5] S. Stevenson, P. W. Fowler, T. Heine, J. C. Duchamp, G. Rice, T. Glass, K. Harich, E. Hajdu, R. Bible, H. C. Dorn, *Nature* **2000**, *408*, 428.
[6] a) S. Y. Xie, F. Gao, X. Lu, R. B. Huang, C.-R. Wang, X. Zhang, M. L. Liu, S. L. Deng, L. S. Zheng, *Science* **2004**, *304*, 699; b) X. Lu, Z. Chen, W. Thiel, P. v. R. Schleyer, R. B. Huang, L. S. Zheng, *J. Am. Chem. Soc.* **2004**, *126*, 14871; c) Z. Chen, *Angew. Chem.* **2004**, *116*, 4794; *Angew. Chem. Int. Ed.* **2004**, *43*, 4690.
[7] a) C.-R. Wang, T. Kai, T. Tomiyama, T. Yoshida, Y. Kobayashi, E. Nishibori, M. Takata, M. Sakata, H. Shinohara, *Angew. Chem.* **2001**, *113*, 411; *Angew. Chem. Int. Ed.* **2001**, *40*, 397; b) M. Krause, M. Hulman, H. Kuzmany, O. Dubay, G. Kresse, G. Seifert, C.-R. Wang, H. Shinohara, *Phys. Rev. Lett.* **2004**, *93*, 137403.
[8] a) K. Tan, X. Lu, *Chem. Commun.* **2005**, 4444; b) B. Cao, M. Hasegawa, K. Okada, T. Tomiyama, T. Okazaki, K. Suenaga, H. Shinohara, *J. Am. Chem. Soc.* **2001**, *123*, 9679; c) T. Yumura, Y. Sato, K. Suenaga, S. Iijima, *J. Phys. Chem. B* **2005**, *109*, 20251.
[9] a) T. Inone, T. Tomiyama, T. Sugai, H. Shinohara, *Chem. Phys. Lett.* **2003**, *382*, 226; b) T. Inone, T. Tomiyama, T. Sugai, T. Okazaki, T. Suematsu, N. Fujii, H. Utsumi, K. Nojima, H. Shinohara, *J. Phys. Chem. B* **2004**, *108*, 7573.
[10] Y. Iiduka, T. Wakahara, T. Nakahodo, T. Tsuchiya, A. Sakuraba, Y. Maeda, T. Akasaka, K. Yoza, E. Horn, T. Kato, M. T. H. Liu, N. Mizorogi, T. Kobayashi, S. Nagase, *J. Am. Chem. Soc.* **2005**, *127*, 12500.
[11] D. M. P. Mingos, T. Slee, Z. Lin, *Chem. Rev.* **1990**, *90*, 383, and references therein.
[12] a) H. W. Kroto, *Nature* **1987**, *329*, 529; b) P. W. Fowler, *J. Phys. Chem. Solids* **1993**, *54*, 1825; c) M.-F. Fan, Z. Lin, S. Yang, *J. Mol. Struct.* **1995**, *373*, 231; d) P. W. Fowler, F. Zerbetto, *Chem. Phys. Lett.* **1995**, *243*, 36.
[13] Sc^{2+} was long supposed in $Sc@C_{82}$ and $Sc_2@C_{84}$, but recent theoretical and experimental investigations revealed it is Sc^{3+} in either endofullerene: a) J. Lu, X. W. Zhang, X. G. Zhao, S. Nagase, K. Kobayashi, *Chem. Phys. Lett.* **2000**, *332*, 219; b) T. Pichler, Z. Hu, C. Grazioli, S. Legner, M. Knupfer, M. S. Golden, J. Fink, F. M. F. de Groot, M. R. C. Hunt, P. Rudolf, R. Follath, C. Jung, L. Kjeldgaard, P. Bruhwiler, M. Inakuma, H. Shinohara, *Phys. Rev. B* **2000**, *62*, 13196, and references therein.
[14] J. J. P. Stewart, *J. Comput. Chem.* **1989**, *10*, 209.

 © 2006 Wiley-VCH Verlag GmbH & Co. KGaA, Weinheim

[15] For the hybrid density functional B3LYP method, see a) A. D. Becke, *J. Chem. Phys.* **1993**, *98*, 5648; b) C. Lee, W. Yang, R. G. Parr, *Phys. Rev. B* **1988**, *37*, 785.

[16] For each anion, the total energy was computed at the B3LYP/6-31G level with use of its PM3 optimized geometry. The calculations were performed with the Gaussian 98 suite of programs: Gaussian 98 (Revision A.7), M. J. Frisch, G. W. Trucks, H. B. Schlegel, G. E. Scuseria, M. A. Robb, J. R. Cheeseman, V. G. Zakrzewski, J. A. Montgomery, R. E. Stratmann, J. C. Burant, S. Dapprich, J. M. Millam, A. D. Daniels, K. N. Kudin, M. C. Strain, O. Farkas, J. Tomasi, V. Barone, M. Cossi, R. Cammi, B. Mennucci, C. Pomelli, C. Adamo, S. Clifford, J. Ochterski, G. A. Petersson, P. Y. Ayala, Q. Cui, K. Morokuma, D. K. Malick, A. D. Rabuck, K. Raghavachari, J. B. Foresman, J. Cioslowski, J. V. Ortiz, B. B. Stefanov, G. Liu, A. Liashenko, P. Piskorz, I. Komaromi, R. Gomperts, R. L. Martin, D. J. Fox, T. Keith, M. A. Al-Laham, C. Y. Peng, A. Nanayakkara, C. Gonzalez, M. Challacombe, P. M. W. Gill, B. G. Johnson, W. Chen, M. W. Wong, J. L. Andres, M. Head-Gordon, E. S. Replogle, J. A. Pople, Gaussian, Inc., Pittsburgh, PA, **1998**..

[17] For GGA-PBE density functional theory, see J. P. Perdew, K. Burke, M. Ernzerhof, *Phys. Rev. Lett.* **1996**, *77*, 3865.

[18] DNP refers to double numerical basis sets plus polarization. The GGA-PBE/DNP calculations were performed with the Dmol^3 code implemented in Material Studio, Accelrys Inc.: a) B. Delley, *J. Chem. Phys.* **1990**, *92*, 508; b) B. Delley, *J. Chem. Phys.* **2000**, *113*, 7756.

[19] F. A. Cotton, G. C. Wilkinson, A. Murillo, M. Bochmann, *Advanced Inorganic Chemistry*, 6th ed., Wiley-Interscience, New York, **1999**, p. 221.

[20] a) J. U. Reveles, T. Heine, A. M. Köster, *J. Phys. Chem. A* **2005**, *109*, 7068; b) T. Heine, K. Vietze, G. Seifert, *Magn. Reson. Chem.* **2004**, *42*, 199; c) "Fullerenes": T. Heine in *Calculation of NMR and EPR Parameters: Theory and Applications* (Eds.: M. Kaupp, V. G. Malkin, M. Bühl), Wiley-VCH, Weinheim, **2004**.

[21] K. Wolinski, J. F. Hilton, P. J. Pulay, *J. Am. Chem. Soc.* **1990**, *112*, 8251, and references therein.

[22] The GIAO-B3LYP/6-31G* theory proved to be sufficiently accurate in reproducing ^{13}C NMR chemical shifts of fullerenes (e.g., C_{60}, C_{70}, C_{76}, and C_{78}) and the endofullerene $Sc_3N@C_{80}$ (II): a) G. Sun, M. Kertesz, *J. Phys. Chem. A* **2000**, *104*, 7398; b) J. C. Duchamp, A. Demortier, K. R. Fletcher, D. Dorn, E. B. Iezzi, T. Glass, H. C. Dorn, *Chem. Phys. Lett.* **2003**, *375*, 655.

[23] J. M. Campanera, C. Bo, J. M. Poblet, *Angew. Chem.* **2005**, *117*, 7396; *Angew. Chem. Int. Ed.* **2005**, *44*, 7230.

 © 2006 Wiley-VCH Verlag GmbH & Co. KGaA, Weinheim

Lipid Bilayers

DOI: 10.1002/anie.200504035

Antibiotic Action and Peptidoglycan Formation on Tethered Lipid Bilayer Membranes**

*Michael J. Spencelayh, Yaling Cheng, Richard J. Bushby, Timothy D. H. Bugg, Jian-jun Li, Peter J. F. Henderson, John O'Reilly, and Stephen D. Evans**

The inner-bilayer membranes of Gram-positive bacteria are surrounded by a layer of peptidoglycan, in the form of a polymer net, which serves to provide mechanical support against lysis due to osmotic stress. Prevention of peptidoglycan formation makes bacterial cells prone to lysis and represents one of the three main mechanisms of antibiotic action; the others being inhibition of protein synthesis and the inhibition of RNA/DNA synthesis.[1] Vancomycin has been a mainstay of the glycopeptide antibiotics and is active against a wide range of Gram-positive bacteria. However, the emergence of widespread resistance amongst pathogenic bacteria has highlighted the need for new and effective antibacterial compounds, and consequently there has been a significant effort devoted to understanding the mechanisms of antibiotic action and resistance.[2a–e]

Most studies performed, to date, on understanding the structure–function relationship involved in antibiotic interaction with peptidoglycan precursors have focused on the use of micelles, vesicles, and soluble precursors. Although important information has been gained from such studies, there are drawbacks in that either they do not represent a close mimic of the in vivo situation or, in the case of vesicles, they are not amenable to study by using the array of surface-science techniques currently available. In 1997, Williams et al. formed

[*] Prof. S. D. Evans
School of Physics and Astronomy
University of Leeds
Leeds, LS2 9JT (United Kingdom)
Fax: (+44) 113-343-1884
E-mail: s.d.evans@leeds.ac.uk

Prof. P. J. F. Henderson, Dr. J. O'Reilly
Astbury Centre for Structural Molecular Biology
University of Leeds
Leeds, LS2 9JT (UK)

Dr. M. J. Spencelayh, Dr. Y. Cheng, Prof. R. J. Bushby
Centre for Self-Organising Molecular systems
University of Leeds
Leeds, LS2 9JT (UK)

Prof. T. D. H. Bugg, Dr. J.-j. Li
Department of Chemistry
University of Warwick
Coventry, CV4 7AL (UK)

[**] The authors would like to thank GlaxoSmithKline (PA, USA) for funding this work. Ramoplanin was provided by Dr. S. Donadio (Vicuron Pharmaceuticals).

Supporting information for this article is available on the WWW under http://www.angewandte.org or from the author.

© 2006 Wiley-VCH Verlag GmbH & Co. KGaA, Weinheim

a "hybrid" bilayer that consisted of a lipid monolayer adsorbed onto a hydrophobic self-assembled monolayer (SAM).[3a] The lipid monolayer was decorated with *N*-α-Docosanoyl-ε-acetyl–Lys–D-Ala–D-Ala (Doc-KAA) and was shown to bind vancomycin and other glycopeptide antibiotics. The dissociation constant for vancomycin was determined to be ≈0.7 μM. In a subsequent study in which the terminal D-Ala residue was replaced by a D-lactate residue, the degree of binding was reduced significantly, yielding a K_d value of ≈1000 μM.[3b]

Solid-supported bilayer lipid membranes (sBLMs) and tethered-bilayer lipid membranes (tBLMs) have been used widely in recent years for the investigation of ion-channel proteins and the development of biosensors.[4a–f] These bilayers are fluid and represent a reasonable mimic, for many purposes, of the cell membrane.[4e,f]

Herein, we show that tBLMs can provide a suitable platform for addressing questions related to antibiotic resistance. We started by introducing two precursors to peptidoglycan formation—namely, the full-length "native" versions of lipid I and lipid II. The incorporation of functional lipid I or lipid II is demonstrated by specific binding of vancomycin and ramoplanin. In a further step, we showed that native *E. coli* membranes can be used to form tBLMs (and sBLMs) and that these contain the necessary functional proteins for the in vitro synthesis of the peptidoglycan cell wall. This system possibly represents the closest mimic of the in vivo situation yet.

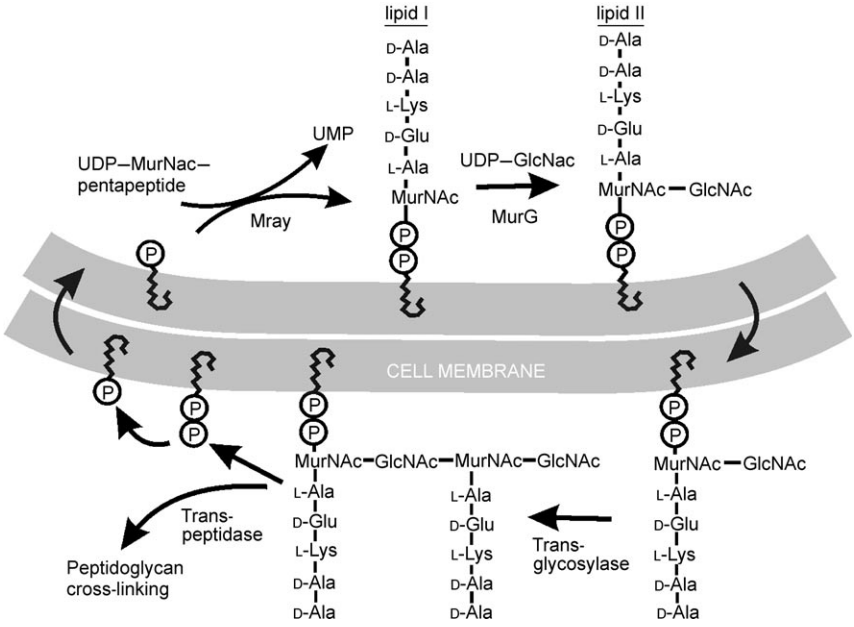

Figure 1. Schematic diagram showing the principal stages involved in in vivo cell-wall biosynthesis. UMP = uridine-5′monophosphate.

Figure 1 shows the major steps involved in in vivo cell-wall biosynthesis. Soluble UDP–MurNAc–pentapeptide (UDP = undecaprenyl phosphate, MurNAc = *N*-acetylmuramic acid) is localized at the membrane surface by the MraY enzyme and attached to the lipid carrier UDP. The resulting "lipid I" molecule is modified by the enzyme MurG, with the addition of UDP–GlcNAc (GlcNAc = *N*-acetylglucosamine), forming the "lipid II" molecule. Lipid II "flips" from the cytoplasm to the outside of the cell, where it is cross-linked, by the transglycosylase and transpeptidase enzymes, to form the peptidoglycan cell wall. The undecaprenyl lipid carrier is then recycled.[5,6a,b,7] The glycopeptide antibiotic, vancomycin, and the lipodepsipeptide antibiotic, ramoplanin, are believed to inhibit peptidoglycan biosynthesis by complexation with the peptidoglycan precursor (lipid II).[2a,5,6a,b,8] Vancomycin prevents transglycosylation by binding to the C-terminal D-Ala–D-Ala groups. The emergence of vancomycin resistance, due to mutation of the terminal D-Ala–D-Ala group to D-Ala–D-lactate has highlighted a need for alternative antibiotics.[1] Ramoplanin is a potential candidate, as it has been shown to inhibit the transglycosylasation step by binding to the MurNAc–L-Ala portion of lipid II, that is, close to the membrane interface.[9a–f]

The tethered lipid bilayers (Figure 2 A) were formed by immersing a "mixed", cholesteryl containing, self-assembled-

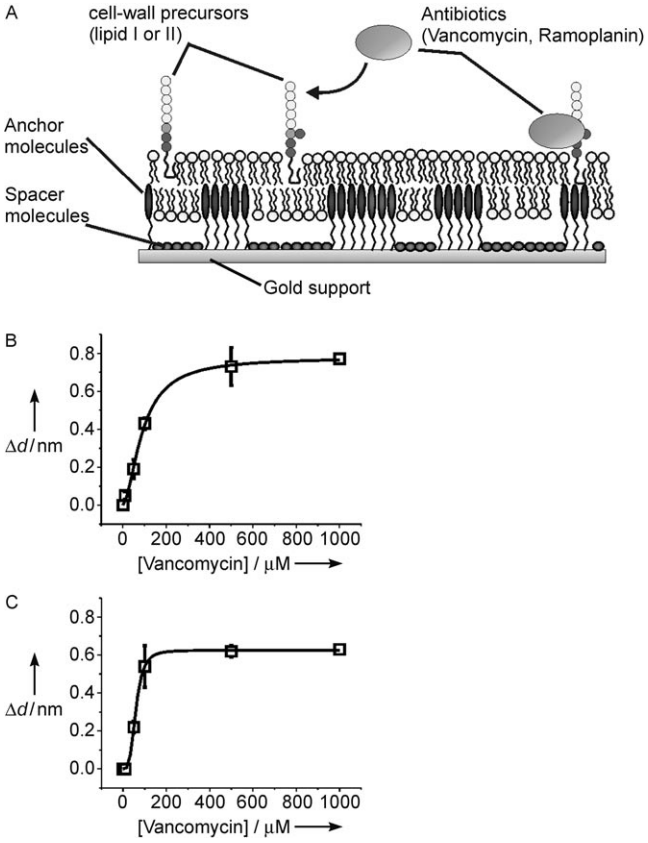

Figure 2. A) Schematic diagram showing the binding of glycopeptide antibiotics to cell-wall precursors in a tethered bilayer containing lipids I or II. B) Vancomycin binding to tethered bilayers containing lipid I. The Figure shows the increase in adsorbed-layer thickness, Δ*d*, as a function of antibiotic concentration, determined using SPR. C) Vancomycin binding to tethered bilayers containing lipid II. Error bars indicate the deviation observed between multiple experiments.

 © 2006 Wiley-VCH Verlag GmbH & Co. KGaA, Weinheim

monolayer (SAM) modified support into a solution containing egg-phosphatidylcholine (PC) vesicles.[4b] The vesicles contained lipid I or lipid II (20% by weight). Bilayer formation was traced by using surface plasmon resonance (SPR) and impedance spectroscopy. The fully formed bilayers gave capacitance values of 0.69 $\mu F\,cm^{-2}$, which is consistent with the determined thickness (from SPR) and indicates the formation of continuous bilayers with few defects.

The binding of vancomycin to lipid I (and lipid II) was measured through the incubation of the bilayers with solutions containing increasing concentrations of antibiotic. The amount of adsorbed material was determined by using SPR and plotted against the vancomycin concentration (Figure 2B, C). The data presented were corrected for nonspecific binding by subtraction of the change in thickness observed in the control experiments from that of pure egg-PC bilayers, that is, with no lipid I (or II) present, and tested over the same range of antibiotic concentrations. In all cases, the degree of nonspecific binding was less than 20% of that observed in the presence of lipid I (or II). The data were fitted by using the Hill equation to obtain estimates of the Hill coefficient, n_H, and the dissociation constant K_d (Table 1). The

Table 1: Equilibrium dissociation constants and Hill coefficients obtained from fits to the binding data in Figures 2 and 3.

Bilayer/Antibiotic	n_H[a]	K_d [μM][b]
lipid I/vancomycin	1.7 ± 0.3	91 ± 8
lipid II/vancomycin	3.5 ± 0.1	59 ± 0.5
lipid I/ramoplanin	1.3 ± 0.1	7.8 ± 0.4
lipid II/ramoplanin	2.1 ± 0.5	1.6 ± 0.2

[a] n_H = Hill coefficient [b] K_d = dissociation constant.

Hill coefficient relates to the degree of cooperativity in the binding event, with $n_H < 1$ indicating negative cooperativity and $n_H > 1$ indicating positive cooperativity. In both cases, we found that $n_H > 1$ (for lipid I and lipid II), suggesting that the binding of vancomycin to lipid II (or I) lowers the energy barrier for the binding of a subsequent vancomycin molecule (or dimer). Our results also indicate that vancomycin binding to lipid II is stronger (lower K_d) and has a greater degree of cooperativity (higher n_H) than to lipid I. The difference in K_d values (for lipid I and lipid II) implies that interactions between the precursor and sugar groups, attached to the peptide backbone of vancomycin, may also influence the nature of the interaction.[10a,b] It should be noted, however, that the K_d values for vancomycin are approximately an order of magnitude larger than those for the surface-bound peptide (KAA) analogues.[3a–d] To our knowledge, there has only been one study of vancomycin binding to lipid II, by Vollmerhaus and co-workers, in which a water soluble lipid II analogue was compared to the more widely studied KAA model peptide.[3e] The dissociation constant for the lipid II analogue was less than half that for the model peptide and similair to those reported by Williams, Whitesides, and co-workers.[3a–d] Although the absolute values determined from our systems do differ, the observed trends are similar despite that our systems are different (using native precursors embedded in a lipid bilayer).

Figure 3A shows a real-time SPR trace that tracks the binding of ramoplanin to a bilayer, incorporating lipid I, over a range of antibiotic concentrations. Figure 3B and C show the change in adsorbed layer thickness, as a function of

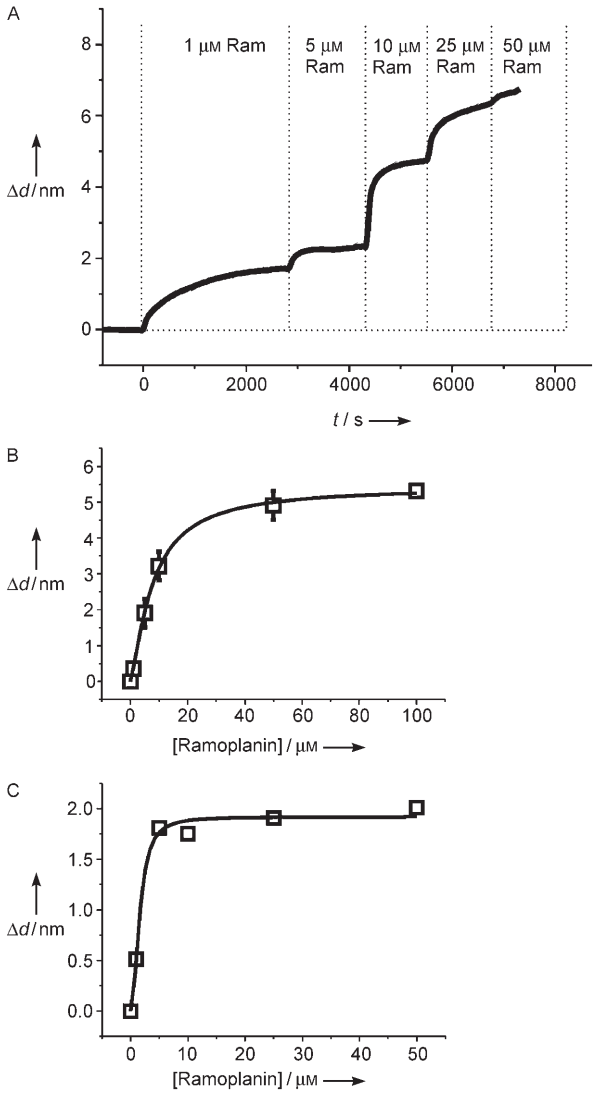

Figure 3. A) SPR measurements showing ramoplanin binding (change in thickness; Δd) to a tethered bilayer containing lipid I as a function of time. The vertical dashed lines indicate points at which the concentration of the antibiotic was increased. B) Change in thickness, Δd, of the adsorbed layer on a bilayer containing lipid I as a function of ramoplanin concentration. C) Change in thickness, Δd, of the adsorbed layer on a bilayer containing lipid II as a function of ramoplanin concentration. Error bars indicate the standard deviation observed between multiple experiments; note that experiments on lipid II containing bilayers were not repeated due to limited stocks of ramoplanin. Ram = ramoplanin.

ramoplanin concentration, upon incubation with bilayers that contain lipid I and lipid II, respectively. These data fits give Hill coefficients greater than one, suggesting the presence of a cooperative phenomenon. Further, the value of n_H for binding to lipid II is nearly twice that of lipid I, whereas the dissociation constant is approximately four-times smaller

 © 2006 Wiley-VCH Verlag GmbH & Co. KGaA, Weinheim

(Table 1). Walker, McCafferty, and co-workers have independently shown that ramoplanin undergoes aggregation resulting in formation of insoluble fibrils in the presence of the soluble analogues of lipid I and II.[9a–f] The detailed ^{1}H NMR spectroscopy studies performed by Walker, McCafferty, and co-workers provided a major advance in the identification of the binding interface and provided estimates of the dissociation constants for the soluble precursors citronellyl–lipid I ($K_d < 100$ μM)[9d] and citronellyl–lipid II ($K_d \approx 50$ nM).[9c] More recently, Walker and co-workers have reported that ramoplanin binds to analogues of lipid II between five and ten-times more strongly than to analogues of lipid I.[9g] As ramoplanin binding involves the MurNAc–GlcNAc moiety of lipid II, which resides close to the membrane interface, one might expect steric effects to affect the magnitude of the K_d values observed in our studies (compared to those found by using the water-soluble analogues cited above). Notwithstanding this, it is clear that our membrane consists of "native" peptidoglycan precursors that behave in a qualitatively similar manner to those reported by Walker and co-workers, and supports the notion that lipid II is the primary target (and that inhibition of the transglycosylase step is the primary mode of antibacterial action).[9g]

The native *E. coli* inner membrane contains the full range of intrinsic and extrinsic proteins necessary for bacterial cell-wall formation. Vesicles of this membrane, created by using the French-press technique, were used to form sBLMs and tBLMs of the native inner membrane. Figure 4 shows the kinetics of bilayer formation, as determined from SPR, and indicates that the bilayers are formed within 20 min and are stable to rinsing with buffer solution (see Experimental Section). The average thickness of the adsorbed lipid film was 3.8 ± 0.2 nm (obtained from fitting the "before" and "after" curves shown in the inset). If one takes into account the insertion of anchor groups into the lower leaflet of the membrane, we would expect a thickness change of 3.6 nm (taking the *E. coli* membrane thickness to be 4.5 nm),[11] that is, close to that found experimentally.

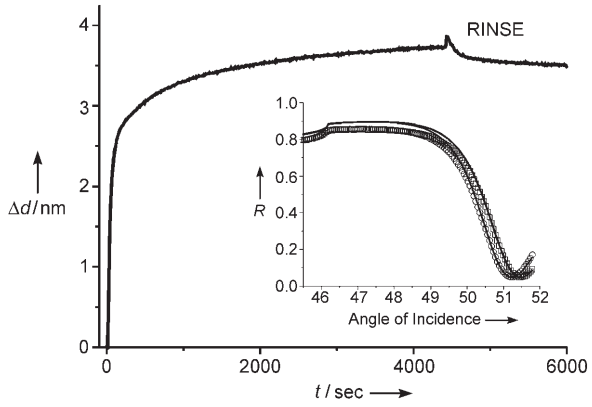

Figure 4. SPR trace showing the kinetics of adsorption (change in thickness, Δd, versus time). Insert: SPR curves showing the angular shift in the reflectance, R, minimum following adsorption of a 3.5-nm tethered proteolipid layer on a mixed SAM.

Figure 5 A shows an SPR trace showing the change in average thickness during peptidoglycan biosynthesis onto a preformed *E. coli* tBLM. At $t = 0$, the soluble precursors UDP–MurNAc–pentapeptide and UDP–GlcNAc (each at a concentration of 0.05 mg mL^{-1}) were introduced to the bathing solution. The resulting increase in thickness can be attributed to the attachment, modification, and cross-linking of the pentapeptide to form a peptidoglycan cell wall.[6b,7] In vivo, the first steps of peptidoglycan formation occur on the inner leaflet of the membrane before "flipping" to the outer leaflet for the later stages. It is likely that the in vivo bacterial inner-membrane proteins are arranged asymmetrically in the bilayer. The French-press method of vesicle preparation used herein forms both the inside-out and right-side-out vesicles. As a result, the "flipping" stage is not required for peptidoglycan synthesis on a tethered-membrane bilayer. The average thickness of the cell wall was 1.6 ± 0.2 nm. After a rinsing with clean buffer solution to remove any adventitiously bound material, this value fell to 1.1 ± 0.1 nm. The thickness of a fully formed *E. coli* cell wall in vivo is typically close to 3 nm, thus our data correspond to about 35% of a full peptidoglycan layer.[11] This compares favorably to previously reported values of in vitro cell-wall biosyntheses (measured in vesicles by the incorporation of radiolabeled precursors), which achieved 2% of the in vivo level.[6b] Traces 5 B–E show a number of control experiments that were designed to test the hypothesis outlined above. Trace 5 B shows the same experiment as that of trace 5 A, but in the absence of adenosinetriphosphate (ATP) and $MgCl_2$. ATP is required for the recycling of UDP molecules and Mg^{2+}

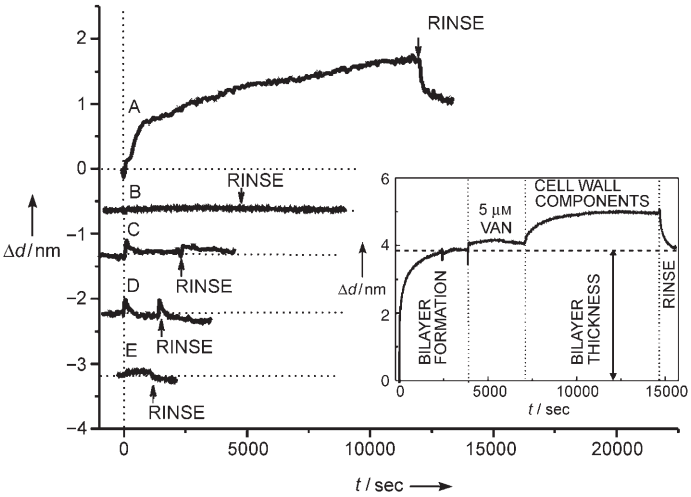

Figure 5. SPR kinetics traces showing changes in adsorbed film thickness, Δd, as a function of time. Trace A shows the formation of a peptidoglycan layer on a tethered *E. coli* membrane. Traces B–E show the results obtained in a number of control experiments (offset for clarity). Trace B shows the absence of ATP/Mg^{2+}, and Trace C shows the absence of UDP–GlcNAc. Trace D shows the absence of both UDP–GlcNAc and UDP–MurNAc–pentapeptide; and in trace E, the conditions are as for trace A except that the bilayer is formed from pure egg-PC vesicles. Inset: shows bilayer formation, followed by an attempt at peptidoglycan biosynthesis after the introduction of Vancomycin (VAN; 5 μM).

 © 2006 Wiley-VCH Verlag GmbH & Co. KGaA, Weinheim

ions that are cofactors for the proteins of cell-wall biosynthesis. In this experiment, no increase in thickness was observed, indicating the necessity for recycling of UDP to create sufficient quantities of lipid I in the bilayer. In the case of trace 5C, the UDP–GlcNAc molecule is missing from the experiment, and as a result, cell-wall biosynthesis can only proceed as far as the attachment of UDP–MurNAc–pentapeptide to the surface. Although lipid I to lipid II modification cannot occur as there is no substrate for the enzyme, a small change in thickness is observed ≈ 0.1 nm. This is possibly attributable to the localization of unmodified pentapeptide at the surface and is within the uncertainty of our measurements. The fourth trace, 5D, shows an experiment wherein both UDP–-MurNAc–pentapeptide and UDP–GlcNAc were omitted. The bilayer was rinsed with buffer solution containing only ATP and $MgCl_2$, and resulted in no increase in the thickness of the lipid layer. Trace 5E was obtained under the same conditions as trace 5A except that a pure egg-PC bilayer was used rather than the *E. coli* inner membrane. Once again, there was no evidence of any cell-wall biosynthesis. Finally, cell-wall biosynthesis was attempted in the presence of 5 mM Vancomycin, a glycopeptide antibiotic that disrupts cell walls by binding to lipid-linked precursors prior to transglycosylation.[2a–e] The resulting adsorbed film (see the inset in Figure 5) was readily removed by a single rinse with clean buffer solution, suggesting (at best) the formation of a weakened cell wall in the presence of the antibiotic.

These controls demonstrate that the increase in thickness observed requires; 1) the presence of both soluble cell-wall precursors (lipid I and II), 2) the presence of ATP and Mg^{2+}, 3) the use *E. coli* inner membranes, and 4) that it can be disrupted by glycopeptide antibiotics. These data strongly suggest that protein-mediated peptidoglycan cell-wall biosynthesis is occurring at the membrane surface, demonstrating that the proteins involved in bacterial cell-wall synthesis have been maintained in a functional form.

Herein we describe the first demonstration of a tethered bacterial membrane that is capable of the biosynthesis of a peptidoglycan cell wall. This system readily lends itself to a range of applications including the search for novel antibiotics and fundamental studies of cell-wall formation, for example, it is not known whether ramoplanin–lipid II complexes polymerize in the membrane as they do in solution. The planar nature of the tBLMs not only allows investigation with a wide range of analytical techniques, but also is compatible with array formation for high-throughput screening of novel bactericidal agents.

Experimental Section

The mixed SAMs were comprised of "anchor" molecules (HS-$(CH_2CH_2O)_5$ $CH_2CH_2NHCHO_2$-Cholesteryl) that were 50% by mole fraction on the surface and were designed to tether the lipid bilayer to the solid support. "Spacer" molecules ($HS(CH_2)_2OH$) were used to promote a hydrophilic region beneath the lipid bilayer. These SAMs were fully characterised by using X-ray photoelectron spectroscopy (XPS), wetting, and Ellipsometry.

The synthesis of lipids I and II was carried out according to the method of Brandish et al. with the exception that they were extracted by using 1-butanol.[12] *E. coli* strain JM1100 (pPER3) was grown, and the membranes were prepared by using a French press to make the inner-membrane vesicles (outer membrane not formed with this method).[13] All bilayers and cell walls were formed and rinsed in a buffer solution that contained Tris chloride (20 mM; pH 7.5; Tris = tris(hydroxymethyl)aminomethane), ATP (1 mM), and $MgCl_2$ (1 mM). Soluble UDP–MurNAc–pentapeptide was isolated from the *Bacillus subtilis* strain W23, HCINB 11824 (*17-18*). UDP–GlcNAc was obtained from Sigma (UK).

SPR experiments were performed in the Kretschmann configuration.[4b] A 50-nm layer of gold was thermally evaporated onto a high-refractive-index glass prism, $n = 1.847$. Resonance curves were obtained by recording the reflected intensity, R, that was normalized with respect to the incident intensity, R_o, as a function of the angle of incidence. Resonance curves were fitted by using a Levenberg–Marquardt algorithm, assuming each layer to be optically isotropic. With abrupt interfaces, a scattering-matrix method was used. The aqueous ambient was assumed to have a refractive index of $n = 1.333$, whereas that of the lipid, antibiotics, and peptidoglycan were assumed to be 1.5.

Received: November 14, 2005
Revised: January 9, 2006
Published online: February 24, 2006

Keywords: antibiotics · bacterial cell wall · lipids · ramoplanin · vancomycin

[1] S. B. Levy, B. Marshall, *Nat. Med.* **2004**, *10*, S122 – S129.
[2] a) T. D. H. Bugg, G. D. Wright, S. Dutkamalen, M. Arthur, P. Courvalin, C. T. Walsh, *Biochemistry* **1991**, *30*, 10408 – 10415; b) C. T. Walsh, *Science* **1993**, *262*, 164 – 164; c) A. El Zoeiby, F. Sanschagrin, R. C. Levesque, *Mol. Microbiol.* **2003**, *47*, 1 – 12; d) K. Kimura, T. D. H. Bugg, *Nat. Prod. Rep.* **2003**, *20*, 252 – 273; e) C. T. Walsh, G Wright, *Chem. Rev.* **2005**, *105*, 391 – 393.
[3] a) M. A. Cooper, D. H. Williams, Y. R. Cho, *Chem. Commun.* **1997**, 1625 – 1626; b) M. A. Cooper, D. H. Williams, *Chem. Biol.* **1999**, *6*, 891 – 899; c) J. H. Rao, L. Yan, J. Lahiri, G. M. Whitesides, R. M. Weis, H. S. Warren, *Chem. Biol.* **1999**, *6*, 353 – 359; d) J. H. Rao, L. Yan, B. Xu, G. M. Whitesides, *J. Am. Chem. Soc.* **1999**, *121*, 2629 – 2630; e) P. J. Vollmerhaus, E. Breukink, A. J. Heck, *Chem. Eur. J.* ***2003***, *9*, 1556 – 1565; f) D. Kahne, C. Lelmkuhler, W. Lu, C. T. Walsh, *Chem. Rev.* **2005**, *105*, 425 – 448.
[4] a) B. A. Cornell, V. L. B. BraachMaksvytis, L. G. King, P. D. J. Osman, B. Raguse, L. Wieczorek, R. J. Pace, *Nature* **1997**, *387*, 580 – 583; b) L. M. Williams, S. D. Evans, T. M. Flynn, A. Marsh, P. F. Knowles, R. J. Bushby, N. Boden, *Langmuir* **1997**, *13*, 751 – 757; c) S. Heyse, O. P. Ernst, Z. Dienes, K. P. Hofmann, H. Vogel, *Biochemistry* **1998**, *37*, 507 – 522; d) Z. Salamon, Y. Wang, J. L. Soulages, M. F. Brown, G. Tollin, *Biophys. J.* **1996**, *71*, 283 – 294; e) J. T. Groves, N. Ulman, S. G. Boxer, *Science* **1997**, *275*, 651 – 653; f) Y. L. Cheng, N. Boden, R. J. Bushby, S. Clarkson, S. D. Evans, P. F. Knowles, A. Marsh, R. E. Miles, *Langmuir* **1998**, *14*, 839 – 844.
[5] T. D. H. Bugg, *Comprehensive Natural Products Chemistry, Vol. 3* (Ed.: M. Pinto), Elsevier, Amsterdam, **1999**, p. 241 – 294.
[6] a) J. van Heijenoort, *Nat. Prod. Rep.* **2001**, *18*, 503 – 519; b) J. van Heijenoort, *Glycobiology* **2001**, *11*, 25R-36R.
[7] K. Lazar, S. Walker, *Curr. Opin. Chem. Biol.* **2002**, *6*, 786 – 793.
[8] D. G. McCafferty, P. Cudic, B. A. Frankel, S. Barkallah, R. G. Kruger, W. K. Li, *Biopolymers* **2002**, *66*, 261 – 284.
[9] a) M. C. Lo, H. Men, A. Branstrom, J. Helm, N. Yao, R. Goldman, S. Walker, *J. Am. Chem. Soc.* **2000**, *122*, 3540 – 3541; b) J. S. Helm, L. Chen, S. Walker, *J. Am. Chem. Soc.* **2002**, *124*, 13970 – 13971; c) Y. N. Hu, J. S. Helm, L. Chen, X. Y. Ye, S. Walker, *J. Am. Chem. Soc.* **2003**, *125*, 8736 – 8737; d) P. Cudic,

 © 2006 Wiley-VCH Verlag GmbH & Co. KGaA, Weinheim

J. K. Kranz, D. C. Behenna, R. G. Kruger, H. Tadesse, A. J. Wand, Y. I. Veklich, J. W. Weisel, D. G. McCafferty, *Proc. Natl. Acad. Sci. USA* **2002**, *99*, 7384 – 7389; e) P. Cudic, D. C. Behenna, J. K. Kranz, R. G. Kruger, A. J. Wand, Y. I. Veklich, J. W. Weisel, D. G. McCafferty, *Chem. Biol.* **2002**, *9*, 897 – 906; f) S. Walker, L. Chen, Y. Hu, Y. Rew, D. Shin, D. L. Boger, *Chem. Rev.* **2005**, *105*, 449 – 475; g) X. Fang, K. Tiyanont, Y. Zhang, J. Wanner, D. Boger, S. Walker, *Mol. Biosyst.* **2006**, *2*, 69 – 76.

[10] a) D. H. Williams, B. Bardsley, *Angew. Chem.* **1999**, *111*, 1264 – 1286; *Angew. Chem. Int. Ed.* **1999**, *38*, 1172 – 1193; b) G. J. Sharman, A. C. Try, R. J. Dancer, Y. R. Cho, T. Staroske, B. Bardsley, A. J. Maguire, M. A. Cooper, D. P. O'Brien, D. H. Williams, *J. Am. Chem. Soc.* **1997**, *119*, 12041 – 12047; c) W. G. Prowse, A. D. Kline, M. A. Skelton, R. J. Loncharich, *Biochemistry* **1995**, *34*, 9632 – 9644.

[11] D. Voet, J. G. Voet, C. W. Pratt, *Fundamentals of Biochemistry*, Wiley, New York, **1999**.

[12] P. E. Brandish, M. K. Burnham, J. T. Lonsdale, R. Southgate, M. Inukai, T. D. H. Bugg, *J. Biol. Chem.* **1996**, *271*, 7609 – 7614.

[13] *Membrane Transport—a Practical Approach* (Ed.: S. Baldwin), Oxford University Press, Oxford, **2000**.

 © 2006 Wiley-VCH Verlag GmbH & Co. KGaA, Weinheim

Organocatalysis

DOI: 10.1002/anie.200504301

Organocatalytic Sigmatropic Reactions: Development of a [2,3] Wittig Rearrangement through Secondary Amine Catalysis**

*Andrew McNally, Brian Evans, and Matthew J. Gaunt**

Sigmatropic rearrangements represent a fundamental method for the installation of molecular complexity in organic molecules.[1] Both the [2,3] and [3,3] variations have found widespread use in the chemical synthesis of natural products and medicinal agents. Because of the importance of these reactions, the development of asymmetric methods for sigmatropic rearrangements has attracted significant interest from the synthetic community.[1,2] Over recent years, there has been a number of new advances in catalytic and enantioselective [3,3] Claisen type transformations;[3] however, there are few general catalytic methods for the corresponding [2,3] Wittig rearrangement.[4] Our efforts towards the development of novel organocatalytic reactions that exploit catalyst-induced new reactivity in bifunctional α-substituted carbonyl compounds [Eqs. (1)–(3)][5] led us to envision that

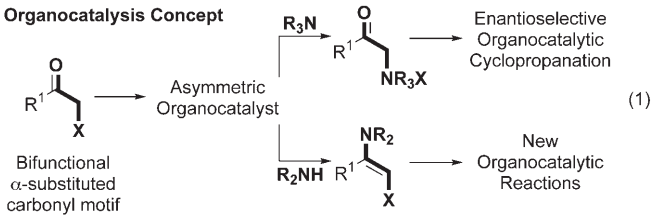

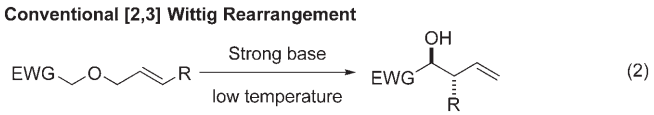

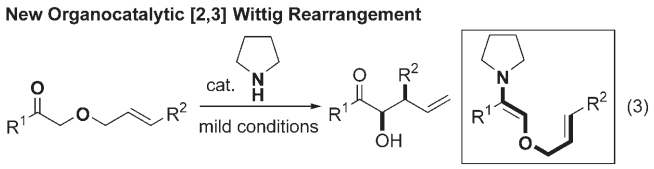

sigmatropic rearrangements could be developed through such a strategy. Herein, we describe a new organocatalytic [2,3] Wittig rearrangement by secondary amine catalysis through the intermediacy of an enamine [Eqs. (2) and (3)]. The new process operates under ambient and operationally simple conditions and also precludes the use of strong bases often required in conventional [2,3] Wittig rearrangements. Furthermore, this organocatalytic transformation provides an important platform for the development of a catalytic enantioselective [2,3] rearrangement.[6,7]

At the outset of this study, the catalytic rearrangement strategy was tested on ketone **1a** using 20 mol% pyrrolidine (**2a**) as the catalyst. We found that the rearrangement was effected in a range of solvents, although these reactions resulted in varying conversions as an equal mixture of *syn* and *anti* diastereomers (Table 1, entries 1–9). The reaction in methanol, however, showed complete conversion after 30 minutes and favored the formation of the *syn* isomer **3a** (d.r. = 3:1; Table 1, entry 10).[8a] This is notable as it displayed the opposite selectivity to reactions in all solvents tested, and the formation of the *syn* isomer is contrary to the conventional [2,3] Wittig rearrangement in which *E* alkenes generally form the *anti* isomer [Eq. (2)].[8b]

The influence of temperature was investigated next, and higher diastereoselectivities were achieved at lower temperatures (Table 1, entries 10–14). Complete conversion was observed at −5 °C, with a d.r. of 6.5:1 (**3a**/**4a**); however, the selectivity can be increased to 10:1 at −25 °C though the reaction was slower but still reached complete conversion after reaction for 90 h. The concentration of the reaction did

[*] A. McNally, Dr. M. J. Gaunt
Department of Chemistry
University of Cambridge
Lensfield Road, Cambridge, CB21EW (UK)
Fax: (+44) 122-333-6362
E-mail: mjg32@cam.ac.uk
Dr. B. Evans
GSK Medicines Research Centre
Gunnels Wood Road
Stevenage, Herts, SG1 2NY (UK)

[**] We gratefully acknowledge GSK and EPSRC for studentships (A.M.) and the Royal Society for a University Research Fellowship (M.J.G.). We also thank Professor Willie Motherwell for useful discussions and Professor Steven Ley for support and useful discussions.

Supporting information for this article is available on the WWW under http://www.angewandte.org or from the author.

InterScience
© 2006 Wiley-VCH Verlag GmbH & Co. KGaA, Weinheim

Table 1: Effect of solvent and temperature on the reaction.

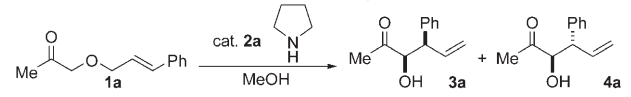

Entry	Solvent	Catalyst loading	Conc. [M]	T [°C]	Conv. [%][a]	t [h]	d.r. (**3a**:**4a**)
1	PhMe	20	0.5	23	40	24	1:1.5
2	Et_2O	20	0.5	23	90	24	1:1
3	MeCN	20	0.5	23	60	24	1:1
4	THF	20	0.5	23	75	24	1:1.5
5	EtOAc	20	0.5	23	50	24	1:1.5
6	$CHCl_3$	20	0.5	23	90	24	1:1
7	DMSO	20	0.5	23	30	24	1:1
8	DMF	20	0.5	23	50	24	1:1
9	MeOH	20	0.5	23	100	0.5	3:1
10	MeOH	20	0.5	5	100	12	4:1
11	MeOH	20	0.5	−5	100	24	6.5:1
12	MeOH	20	0.5	−10	90	24	7:1
13	MeOH	20	0.5	−25	70[b]	24	10:1
14	MeOH	20	0.125	−5	100	24	6.5:1
15	MeOH	5	0.5	−5	100	96	8:1
16	MeOH	0	0.5	23	0	96	nr

[a] Determined by ^{1}H NMR spectroscopic analysis. [b] Conversion = 100% at 90 h. nr = no reaction. DMF = dimethylformamide, DMSO = dimethyl sulfoxide.

not significantly affect the rearrangement (Table 1, entry 14). However, the catalyst loading could be decreased, and with 5 mol% of **2a** the reaction reached completion in 96 h with a slightly improved d.r. of 8:1 at −5 °C (Table 1, entry 7).[9,10] No reaction is observed in the absence of **2a** (Table 1, entry 16). The ^{1}H NMR spectra of the crude reaction mixtures showed only the rearranged product, and in contrast to many other [2,3] sigmatropic reactions there was no sign of the competing [1,2] rearrangement product.[1b] These results demonstrate that the new organocatalytic [2,3] rearrangement was readily effected under mild and operationally simple conditions, and we believe this represents the first example of such a process.

A proposed mechanism for the reaction is shown in Scheme 1. Formation of an iminium ion is followed by tautomerization to the corresponding enamine, and the rearrangement possibly proceeds via the *syn* transition state (*syn* TS) to form **3a** after hydrolytic release of the catalyst.[11] The requirement of methanol as the solvent to attain good diastereoselectivity suggests that the protic solvent influences the rearrangement through a hydrogen-bonding interaction with the ether oxygen atom, thus stabilizing the developing negative charge and thereby accelerating the rearrangement. Interestingly, however, the reaction seems to have a narrow tolerance to the acidity of the solvent. In the presence of trifluoroethanol or using the HCl salt of **2a**, the reaction is severely retarded or nonexistent in the respective cases. The assistance of Brønsted acids as additives in catalytic reactions has been well documented,[12] and they have recently been successfully employed as cocatalysts in organocatalytic processes.[9] We are currently investigating whether such additives can further influence the rearrangement.

The scope of the organocatalytic [2,3] Wittig rearrangement was evaluated first by studying the effect of the substituent at the ketone carbonyl group in **1**. Table 2 shows the results of reactions that were optimized to reach completion within 24 hours at the given temperature. The diastereoselectivity of the rearrangement can be improved at lower temperatures, although with increased reaction times. The new reaction worked for a range of simple ketones and gave rearranged products in excellent yields of the isolated products and good diastereoselectivity (Table 2, entries 1–6). The alkene substituents were also varied (Table 2, entries 7–14), and electron-rich or -deficient aromatic groups could be used to good effect (Table 2, entries 7–9). Substrates containing trisubstituted alkenes, 1,3-dienes, and enynes readily reacted to form rearranged products in good yield (Table 2, entries 10–12). Products with a quaternary center were also formed in good diastereoselectivity from the corresponding trisubstituted alkene, thus expanding the scope and utility of the organocatalytic [2,3] rearrangement strategy (Table 2, entry 13). Finally, as a surrogate to the crotyl group, an allylsilane substrate (Table 2, entry 14) rearranged smoothly, and the resulting product could be readily converted into the desired propionate motif through desilylation.[13] In all cases, the *syn* isomer **3** was observed as the major product and the assignment was based on analogy to the proven stereochemistry of **3a**.[8a]

With an effective diastereoselective catalytic reaction in hand, we investigated a chirality transfer process in the organocatalytic [2,3] rearrangement. Methyl ketone **1m** (94% *ee*)[14] rearranged to **3m** and maintained the enantiomeric excess of the starting ketone [Eq. (4)]. This result

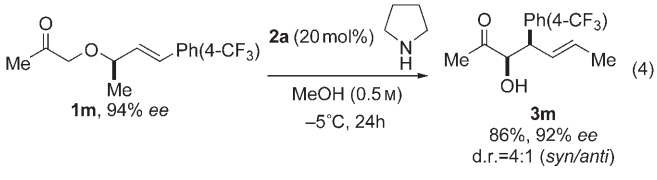

(4)

strongly suggests that the rearrangement proceeds through the conventional concerted mechanism as opposed to a stepwise ionic pathway. Moreover, an effective chirality transfer process represents an useful extension to this new catalytic methodology.

To investigate the potential of a catalytic asymmetric process, we tested the reaction with a chiral secondary amine

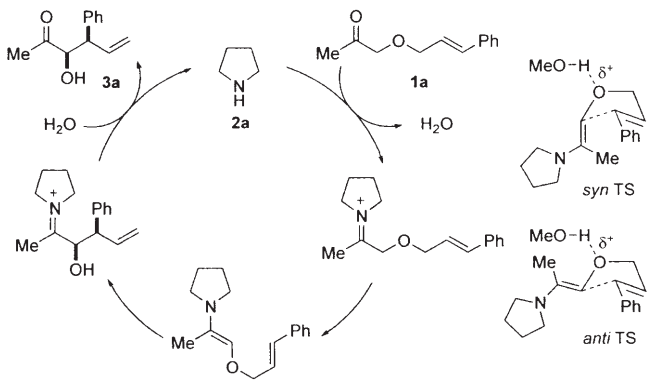

Scheme 1. Proposed mechanism of the rearrangement.

 © 2006 Wiley-VCH Verlag GmbH & Co. KGaA, Weinheim

Table 2: Scope of the organocatalytic [2,3] Wittig rearrangement.[c]

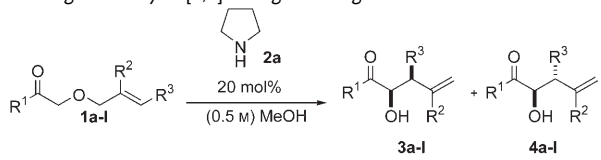

Entry	R^1	R^3	Product		t [h]	T [°C]	Yield [%][b]	d.r. (**3**:**4**)
1	Me	Ph	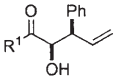	**3a**	24	−5	84	6.5:1
2	Me	Ph		**3a**	24	−8	96	4:1
3	Et	Ph		**3b**	72	−15	92	6:1
4	$-(CH_2)_2Ph$	Ph		**3c**	24	−10	86	3:1
5	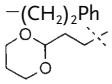	Ph		**3d**	24	−8	90	4:1
6	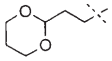	Ph		**3d**	72	−15	86	5:1
7	Et	4-OMePh		**3e**	24	−8	91	7:1
8	Me	4-OMePh	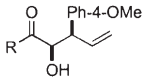	**3f**	24	−8	88	5:1
9	Me	4-CF_3Ph	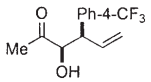	**3g**	24	−12	90	4.5:1
10	Me	R^2 = Ph	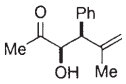	**3h**	24	−8	73	2:1
11	Me		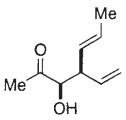	**3i**	24	5	82	3.5:1
12	Me		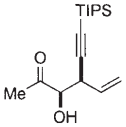	**3j**	24	23	84	1:1
13	Me	Me, Ph	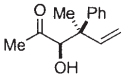	**3k**	72	23	55	4:1
14	$-(CH_2)_2Ph$	$-CH_2SiMe_3$	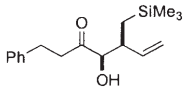	**3l**	24	23	85	4:1

[a] R^2 = H for all entries, except entry 10, in which R^2 = Me. [b] Yield of the isolated product after chromatography.

catalyst. Diamine **2b** catalyzed the reaction and afforded the rearranged product **3** in 60% *ee* for the *syn* isomer **3g** [Eq. (5)].[15] To the best of our knowledge, this reaction is the first organocatalytic enantioselective [2,3] Wittig rearrangement and represents an exciting lead towards the development of a catalytic enantioselective process. Towards this end, we are currently designing catalysts that will control both the enantio- and diastereoselectivity of this reaction.

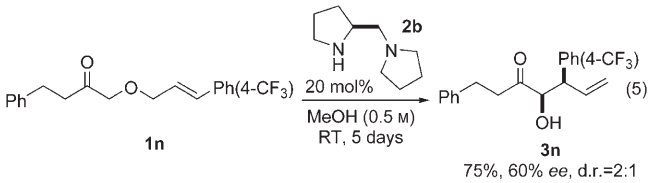

In summary, we have developed a new organocatalytic [2,3] Wittig rearrangement through secondary amine catalysis. This process displays a broad substrate scope and proceeds with good diastereoselectivity. The reaction conditions are remarkably mild, and the transformation is operationally simple to perform. We have also identified that allylic transposition of chirality can be achieved with an existing chiral centre and most importantly that a chiral pyrrolidine effects an organocatalytic enantioselective sigmatropic rearrangement. This process provides a platform for the further development of this reaction and related catalytic enantioselective rearrangement processes; these studies will be reported in due course.

Experimental Section

General Procedure: A precooled solution of pyrrolidine (20 mol%) in methanol (2 mL) was added to **1** (1 mmol), and the reaction mixture was stirred at the described temperature for the time stated. The reaction was quenched after completion with aqueous solution of hydrochloric acid (0.1M, 2 mL), and the aqueous layer was extracted with diethyl ether (3 × 10 mL). The combined organic extracts were washed with an aqueous saturated solution of sodium bicarbonate (10 mL), an aqueous saturated solution of brine (10 mL), dried over $MgSO_4$, and filtered. The resulting filtrate was concentrated in vacuo, and the crude product was purified by flash column chromatography on silica gel.

Received: December 3, 2005
Published online: February 22, 2006

Keywords: asymmetric synthesis · enantioselectivity · organocatalysis · sigmatropic rearrangements

[1] For the [3,3] rearrangement, see: a) A. M. Martin Castro, *Chem. Rev.* **2004**, *104*, 2939; [2,3] rearrangement: b) T. Nakai, K. Mikami, *Org. React.* **1994**, *46*, 105; c) "Rearrangements of Organolithium Compounds": K. Tomooka in *The Chemistry of Organolithium Compounds* (Eds.: Z. Rappaport, I. Marek), Wiley, New York, **2004**.

[2] For a review of asymmetric methods for [3,3] Claisen type rearrangements, see: H. Ito, T. Taguchi, *Chem. Soc. Rev.* **1999**, *28*, 43; see also ref. [1a].

[3] a) T. P. Yoon, D. W. C. MacMillan, *J. Am. Chem. Soc.* **2001**, *123*, 2911; b) L. Abraham, R. Czerwonka, M. Hiersemann, *Angew. Chem.* **2001**, *113*, 4835; *Angew. Chem. Int. Ed.* **2001**, *40*, 4700; c) L. Abraham, M. Körner, P. Schwab, M. Hiersemann, *Adv. Synth. Catal.* **2004**, *346*, 1281.

[4] For catalytic [2,3] rearrangements, see: a) D. M. Hodgson, F. Y. T. M. Pierard, P. A. Stupple, *Chem. Soc. Rev.* **2001**, *30*, 50, and references therein; for a catalytic enantioselective [2,3] propargylic rearrangement, see: b) G. A. Moniz, J. L.

 © 2006 Wiley-VCH Verlag GmbH & Co. KGaA, Weinheim

Wood, *J. Am. Chem. Soc.* **2001**, *123*, 5095; for an auxiliary controlled asymmetric example of the aza-Wittig rearrangement, see: c) J. A. Workman, N. P. Garrido, J. Sancon, E. Roberts, H. P. Wessel, J. B. Sweeney, *J. Am. Chem. Soc.* **2005**, *127*, 1066; and for a reagent-controlled asymmetric example, see: d) J. Blid, O. Panknin, P. Somfai, *J. Am. Chem. Soc.* **2005**, *127*, 9352.

[5] a) C. D. Papageorgiou, M. A. Cubillos de Dios, S. V. Ley, M. J. Gaunt, *Angew. Chem.* **2004**, *116*, 4741; *Angew. Chem. Int. Ed.* **2004**, *43*, 4641; b) N. Bremyer, S. C. Smith, S. V. Ley, M. J. Gaunt, *Angew. Chem.* **2004**, *116*, 2735; *Angew. Chem. Int. Ed.* **2004**, *43*, 2681.

[6] For organocatalysis reviews, see: a) P. Dalko, L. Moisan, *Angew. Chem.* **2004**, *116*, 5248; *Angew. Chem. Int. Ed.* **2004**, *43*, 5138; b) J. Seayad, B. List, *Org. Biomol. Chem.* **2005**, *3*, 719.

[7] For examples of secondary amine catalysis via enamines, see: a) A. B. Northrup, D. W. C. MacMillan, *Science* **2004**, *305*, 1752, and references therein; b) B. List *Acc. Chem. Res.* **2004**, *37*, 548; c) W. Notz, F. Tanaka, C. A. Barbas III, *Acc. Chem. Res.* **2004**, *37*, 580; d) K. Juhl, K. A. Jørgensen *J. Am. Chem. Soc.* **2002**, *124*, 2420; e) A. Cordova, H. Sunden, M. Engqvist, I. Ibrahem, J. J. Casas, *Am. Chem. Soc.* **2004**, *126*, 8914; f) T. Ishii, S. Fujioka, Y. Sekiguchi, H. Kotsuki, *J. Am. Chem. Soc.* **2004**, *126*, 9558; g) Y. Yamamoto, N. Momiyama, H. Yamamoto, *J. Am. Chem. Soc.* **2004**, *126*, 5962.

[8] a) The major diastereoisomer was confirmed to be the *syn* isomer by conversion into a six-membered cyclic derivative and analysis of NOE interaction enhancements (see the Supporting Information for details); b) an exception to this finding is: D. Enders, D. Backhaus, J. Runsink, *Tetrahedron* **1996**, *52*, 1503.

[9] Interestingly, we see a slightly improved diastereoselectivity in the rearrangements with a lower catalyst loading, and we also observed slight changes in diastereoselectivity as the reactions approached completion. We propose that as the reaction approaches completion with higher catalyst loadings partial epimerization takes place at the α-position because of increased change of reformation of the iminium adduct of **3**. This behavior has been observed in enamine-based conjugate-addition processes; see: T. J. Peelan, Y. Chi, S. H. Gellman, *J. Am. Chem. Soc.* **2005**, *127*, 11598.

[10] There was no reaction: in the absence of catalyst **2a**; when the homologous secondary amine piperidine was used as the catalyst; when one equivalent of triethylamine was used in place of pyrrolidine (**2a**), thus suggesting that the process was not base mediated.

[11] For a recent discussion on iminium ion geometry and enamine formation, see: I. K. Mannigan, A. B. Northrup, D. W. C. MacMillan, *Angew. Chem.* **2004**, *116*, 6890; *Angew. Chem. Int. Ed.* **2004**, *43*, 6722.

[12] For an account of Brønsted acid catalysis, see: P. M. Pihko, *Angew. Chem.* **2004**, *116*, 2110; *Angew. Chem. Int. Ed.* **2004**, *43*, 2062.

[13] B. M. Trost, L. T. Phan, *Tetrahedron Lett.* **1993**, *34*, 4735.

[14] The chiral center was installed by reduction of the corresponding enone with *N*-cyclohexyl-2-benzothiazolesulfenamide (CBS), see: E. J. Corey, C. J. Helal, *Angew. Chem.* **1998**, *110*, 2092; *Angew. Chem. Int. Ed.* **1998**, *37*, 1986.

[15] The isomer of **3n** shown was chosen arbitrarily; we do not know the absolute configuration of the product at this stage.

 © 2006 Wiley-VCH Verlag GmbH & Co. KGaA, Weinheim

Metallaboranes

DOI: 10.1002/anie.200504242

Molybdenum-Mediated Alkyne Incorporation into an Iridaborane Framework—Release of the Iridacarborane from the Molybdenum Coordination Sphere through a Dissociative Equilibrium**

*Frédéric de Montigny, Ramón Macias, Bruce C. Noll, and Thomas P. Fehlner**

Metals were used to facilitate synthesis long before the development of metal-coordination chemistry, but only then was the role of metal complexes in, for example, protecting and activating organic functional groups, understood.[1,2] Three steps constitute the essence of a metal-facilitated process: coordination of the metal to the substrate, chemical transformation of the substrate in a process not possible under the same conditions without metal coordination, and release of the product.

Compared to organometallic chemistry, less information is known about the role of metals in borane chemistry,[3] albeit that which is known, for example, Suzuki coupling,[4] functionalization of hydrocarbyl groups[5,6] and boranes,[7] and oxidative coupling of carboranes,[8] is important. Herein, we show that an iridaborane[9] that does not react with alkynes directly can be converted into an iridacarborane by the action of a coordinated Mo center. This transformation follows the classic pattern: addition to a Mo fragment, sequential addition and insertion of two alkynes at the Mo center, and loss of the Mo fragment as a result of decreased binding affinity of the Mo atom after alkyne incorporation.

We have already described the first step, that is, the addition of $[Mo(CO)_3(thf)_3]$ to $[(Cp^*IrH)B_4H_9]$[9] ($Cp^* = \eta^5$-C_5Me_5) to form *nido*-$[Cp^*Ir(B_4H_8)\{Mo(CO)_3(thf)\}]$ (**1**; Scheme 1).[10] The beauty of **1** lies in the fact that, although the THF ligand on Mo is easily lost, unimolecular closure of the cluster to give a less reactive *closo* form is prevented by the four edge-bridging hydrogen atoms. Thus, derivatives are easily prepared by displacement of THF by, for example, PR_3 without competition from closure of the cluster.

Although rhoda- and ruthenaboranes readily react with alkynes under mild conditions,[11,12] $[(Cp^*IrH)B_4H_9]$ does not. Suspecting that the absence of a facile pathway for alkyne coordination is the cause, we investigated the reaction of **1** with alkynes. Smooth reaction of **1** with an excess of 2-butyne generates $[Cp^*Ir(B_3H_3C_4Me_4)]$ (**2**) in modest yield after work

[*] F. de Montigny, R. Macias, B. C. Noll, Prof. T. P. Fehlner
Department of Chemistry & Biochemistry
University of Notre Dame
Notre Dame, IN 46556 (USA)
Fax (+1) 504-631-6652
E-mail: fehlner.1@nd.edu

[**] This work was supported by the National Science Foundation (CHE-0304008 and CHE-0443233).

© 2006 Wiley-VCH Verlag GmbH & Co. KGaA, Weinheim

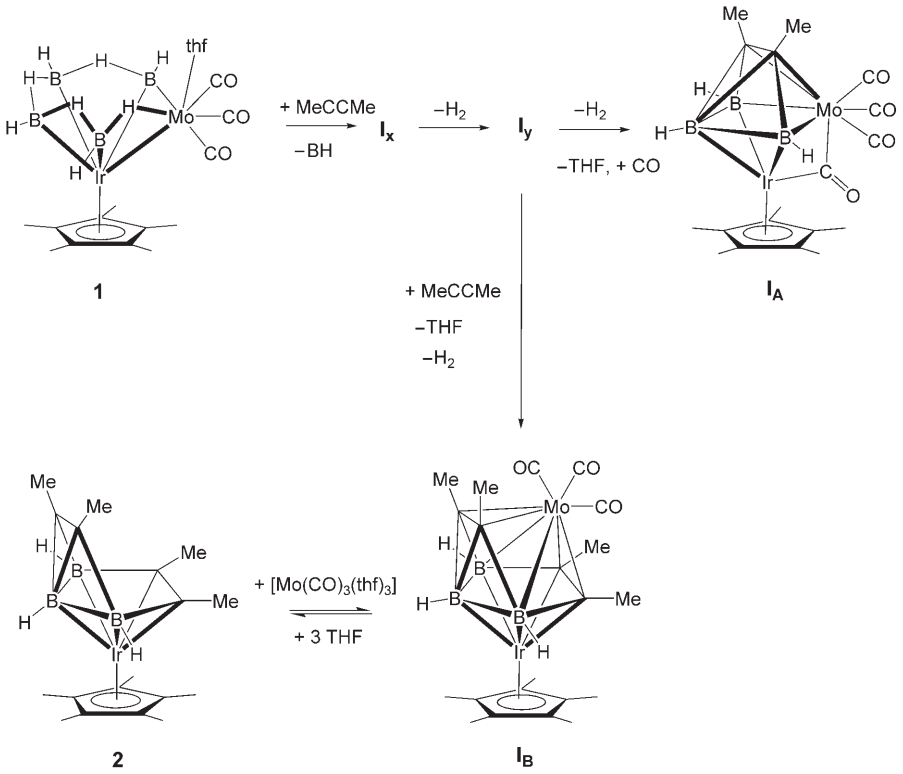

Scheme 1. Reaction of **1** with 2-butyne.

up. The structure of **2** comprises a 10 skeletal electron pair (sep) *nido*-tetracarbon metallacarborane (Figure 1[13] and Scheme 1). This structure has novel composition but is of a known structural type, which has been discussed in the literature.[14–16]

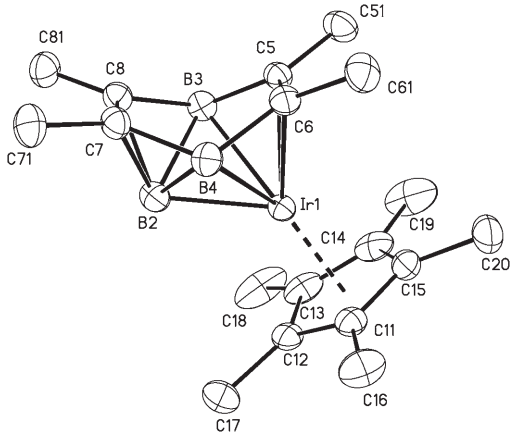

Figure 1. Molecular structure of **2**. Thermal ellipsoids are shown at 50% probability. Selected bond lengths [Å]: Ir1-B2 2.089(2), Ir1-B3 2.305(2), Ir1-B4 2.289(2), Ir1-C5 2.1619(19), Ir1-C6 2.1643(19), B2-B3 1.953(3), B2-B4 1.943(3), C5-B3 1.572(3), C8-B3 1.603(3), C7-B4 1.600(3), C6-B4 1.577(3), C5-C6 1.414(3), C7-C8 1.384(3).

The functional unsaturation at the Mo center in the cluster framework mediates the addition and insertion of two alkyne molecules, and time-dependent NMR studies reveal the manner of alkyne addition and release of the Mo fragment.

Addition of greater than two equivalents of 2-butyne to **1** generates an intermediate $\mathbf{I_x}$, which is rapidly converted into a second intermediate $\mathbf{I_y}$. In turn, $\mathbf{I_y}$ is converted into **2** and intermediate $\mathbf{I_B}$ in a mixture with a composition that is invariant with time. The spectroscopic data suggest that $\mathbf{I_B}$ is the adduct of **2**, that is, $[Cp^*Ir(B_3H_3C_4Me_4)\{Mo(CO)_3\}]$. Proof for the assignment comes from the addition of $[Mo(arene)(CO)_3]$ to **2** in THF to generate an equilibrium mixture of $\mathbf{I_B}$ and **2**. If a large excess of the Mo reagent is used, the amount of **2** decreases until only $\mathbf{I_B}$ is observed. Alternatively, addition of toluene, PPh_3, or MeCN increases the concentration of **2** at the expense of $\mathbf{I_B}$. These observations are consistent with the equilibrium shown in Equation (1).

$$\mathbf{2} + [Mo(CO)_3(thf)_3] \rightleftharpoons \mathbf{I_B} + 3\,THF \quad K_{eq} \quad (1)$$

Unambiguous confirmation of both the structure of $\mathbf{I_B}$ and the equilibrium stoichiometry resulted from the determination of the solid-state structure of $\mathbf{I_B}$ (Figure 2).[13] Complex $\mathbf{I_B}$ is a 10-sep *closo* cluster, but it does not exhibit a deltahedral tricapped trigonal-prismatic structure. The observed structure can be generated from a tricapped trigonal prism with the $\{Mo(CO)_3\}$ fragment in a capping position by two diamond–square–diamond rearrangements, thereby generating a six-connect vertex, which is occupied by the Mo fragment.

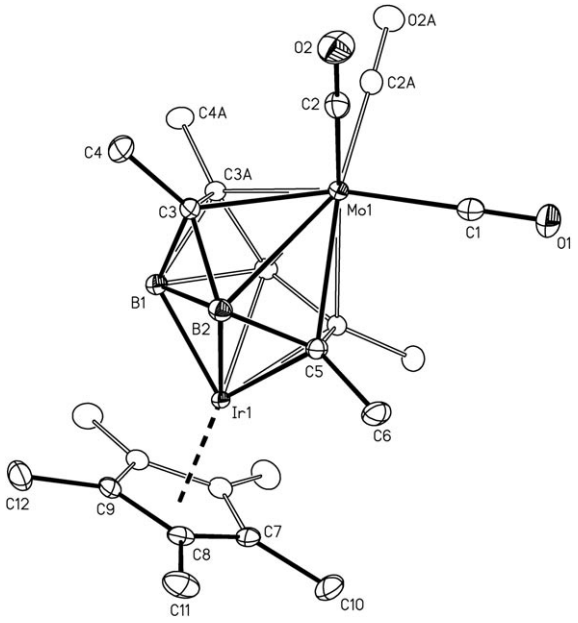

Figure 2. Molecular structure of $\mathbf{I_B}$. Thermal ellipsoids are shown at 50% probability. Selected bond lengths [Å]: Ir1-B1 2.053(2), Ir1-C5 2.1433(13), Ir1-B2 2.3077(16), Mo1-C3 2.2355(13), Mo1-C5 2.3884(13), Mo1-B2 2.5716(16).

 © 2006 Wiley-VCH Verlag GmbH & Co. KGaA, Weinheim

Alternatively, $\mathbf{I_B}$ is a complex of a $\{Mo(CO)_3\}$ fragment and an iridacarborane ligand, which implies a functional analogy between the six-atom open face of **2** and the π system of an arene.

The observed equilibrium [Eq. (1)] between $\mathbf{I_B}$ and **2** at room temperature suggests weak iridacarborane–Mo binding. Measurements of K_{eq} [Eq. (1)] with variable temperature yield the thermodynamic parameters $\Delta H° = 8$ kcal mol^{-1} and $\Delta S° = 38$ eu. Hence, displacement of THF from $[Mo(CO)_3(thf)_3]$ by **2** is a slightly endothermic process, which is driven by the large entropy associated with the displacement of three thf ligands. The increasing carbon content probably facilitates the release of the insertion product, and this point is established by the characterization of a second intermediate.

By limiting the alkyne concentrations, $[Cp^*Ir(B_3H_3C_2Me_2)\{Mo(CO)_3\}(\mu\text{-}CO)]$ ($\mathbf{I_A}$) is isolated from the reaction in low yield. Its structure (Figure 3 and Scheme 1) is that of an eight-sep *closo* cluster.[13] The fact that $\mathbf{I_A}$ is a *closo* cluster, is formed in low yield, and contains four CO ligands suggests that it is derived from, but is not, an intermediate on the reaction pathway. Indeed, addition of 2-butyne to $\mathbf{I_A}$ under the reaction conditions does not lead to **2**. Addition of PPh_3 does not generate a phosphine derivative of $\mathbf{I_A}$, thus suggesting $\mathbf{I_A}$ is derived from an active *nido* intermediate as a result of unimolecular loss of H_2 and subsequent displacement of thf by CO (Scheme 1).

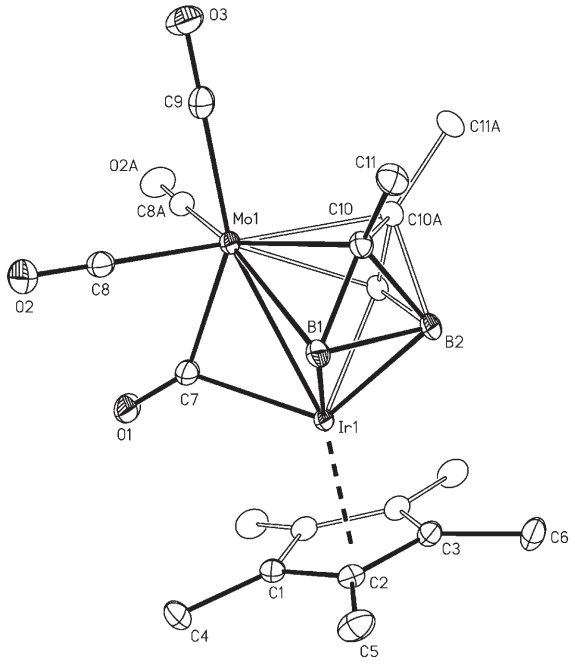

Figure 3. Molecular structure of $\mathbf{I_A}$. Thermal ellipsoids are shown at 50% probability. Selected bond lengths [Å]: Ir1-C7 2.138(3), Ir1-B1 2.146(2), Ir1-B2 2.214(3), Ir1-Mo1 2.8751(6), Mo1-C7 2.152(3), Mo1-C10 2.3185(17), Mo1-B1 2.461(2), O1-C7 1.183(3).

The existence of $\mathbf{I_A}$ is consistent with sequential addition of alkyne and also suggests that loss of a {BH} fragment occurs early in the reaction process. The stability of $\mathbf{I_A}$ relative to $\mathbf{I_B}$ corroborates the hypothesis that it is the increasing carbon content that leads to the ultimate release of the Mo fragment. Finally, partial spectroscopic data on $\mathbf{I_x}$ and $\mathbf{I_y}$ are consistent with species that lie between **1** and $\mathbf{I_A}$ and $\mathbf{I_B}$, as shown in Scheme 1. A full discussion of their properties will be published elsewhere.

The stoichiometric reaction sequence in Scheme 1, in combination with the previously described reaction cycle involving Lewis bases,[17] illustrates once again the ability to generate varied reactivity by choice of transition metals which are placed within the cluster framework. These effects parallel those found in organometallic chemistry but also display unique properties associated with the metal–boron interactions.

Experimental Section

A mixture of *arachno*-$[(Cp^*IrH)B_4H_9]$ (100 mg, 0.26 mmol) and $[Mo(CO)_3(tol)]$ (100 mg, 0.37 mmol; tol = toluene) in freshly distilled THF (5 mL) was stirred at 50 °C for 10 minutes. A large excess of 2-butyne (0.1 mL, 1.28 mmol) was added, and the reaction was stirred for 2 h. The mixture was purified by TLC (silica, hexane) to afford **2** (24 mg, 20%) and a trace of $\mathbf{I_A}$. Yellow crystals of **2** were obtained from hexane. Improved yields of $\mathbf{I_A}$ (4 mg, 2%) were obtained by using less than one equivalent of 2-butyne (0.02 mL, 0.25 mmol). A mixture of **2** (10 mg, 0.02 mmol) and $[Mo(CO)_3(tol)]$ (10 mg, 0.04 mmol) in dry $[D_8]$THF (0.5 mL) was heated at 50 °C for 3 h, at which point the ^{11}B NMR spectrum showed **2** had been converted predominantly into $\mathbf{I_B}$. Although some **2** was present, a few brown crystals of $\mathbf{I_B}$ were obtained from this solution at −20 °C. To obtain K_{eq} (1) as a function of temperature, a mixture of **2** (31 mg, 0.066 mmol) and $[Mo(CO)_3(tol)]$ (15 mg, 0.055 mmol) in $[D_8]$THF was heated at 50 °C for 3 h in an NMR tube and then equilibrated at the temperature of choice. The mole fraction of $\mathbf{I_B}$ was determined by ^{11}B NMR spectroscopy to be: 0.39 (−20 °C), 0.64 (0 °C), 0.68 (20 °C), 0.77 (50 °C), thus yielding $\ln K_{eq} = -3925\,(1/T) + 18.8$ ($R^2 = 0.96$).

2: ^{11}B NMR (128 MHz, $[D_6]$benzene, 22 °C): $\delta = 11.6$ (d, ^1J(H,B) = 157 Hz, 1B, BH), −10.4 ppm (d, ^1J(H,B) = 128 Hz, 2B, BH); ^{1}H{^{11}B} NMR (400 MHz, $[D_6]$benzene, 22 °C): $\delta = 5.16$ (s, 1H, BH_t), 2.30 (s, 2H, BH_t), 2.19 (s, 6H, CH_3), 1.88 (s, 6H, CH_3), 1.68 ppm (s, 15H, Cp*); ^{13}C{^{1}H} NMR (100 MHz, $[D_6]$benzene, 22 °C): $\delta = 133.5$ (CCH_3), 133.4 (CCH_3), 92.9 ($C_5(CH_3)_5$), 22.7 (CH_3), 19.0 (CH_3), 9.3 ppm ($C_5(CH_3)_5$); IR (KBr): $\tilde{\nu} = 2956$ (s), 2924 (s), 2855 (s), 2453 (s, BH), 2019 (w), 1950 (w), 1929 (w), 1460 (m), 1379 (m), 1262 (m), 1091 (m), 1029 (m), 951 (w), 798 cm^{-1} (s); LRMS (FAB): *m/z*: 471 $[M]^+$ (isotope envelope; 3B, 1Ir atoms, calcd for weighted average of isotopomers ($C_{18}H_{30}B_3Ir$) within the instrument resolution: 472.2256; found: 472.2258). Elemental analysis (%) calcd for $C_{18}H_{30}B_3Ir$: C 45.89, H 6.42; found: C 45.70, H 6.60.

$\mathbf{I_A}$: ^{11}B NMR (128 MHz, $[D_6]$benzene, 22 °C): $\delta = 33.4$ (d, ^1J(H,B) = 138 Hz, 2B, BH), 1.9 ppm (d, ^1J(H,B) = 168 Hz, 1B, BH); ^{1}H{^{11}B} NMR (400 MHz, $[D_6]$benzene, 22 °C): $\delta = 5.48$ (s, 2H, BH_t), 2.77 (s, 1H, BH_t), 2.24 (s, 6H, CH_3), 1.54 ppm (s, 15H, Cp*); IR (hexane): $\tilde{\nu} = 2518$ (w, BH), 2137 (w, CO), 2022 (s, CO), 1997 (s, CO), 1925 (s, CO), 1936 (s, CO), 1820 (m, μ-CO), 1271 (m), 1102 (m), 1011 cm^{-1} (m); LRMS (FAB): *m/z* (%): 626 (19) $[M]^+$, 598 (18) $[M-CO]^+$, 569 (65) $[M-(CO)_2]^+$, 513 (100) $[M-CH_3C_2CH_3-(CO)_2]^+$ (isotope envelopes).

$\mathbf{I_B}$: ^{11}B NMR (128 MHz, $[D_8]$THF, 22 °C): $\delta = 33.1$ (d, ^1J(H,B) = 160 Hz, 1B, BH), −10.6 ppm (d, ^1J(H,B) = 137 Hz, 2B, BH); ^{1}H-{^{11}B} NMR (400 MHz, $[D_8]$THF, 22 °C): $\delta = 5.36$ (s, 1H, BH_t), 2.44 (s, 6H, CH_3), 2.10 (s, 6H, CH_3), 1.92 (s, 15H, Cp*), 1.54 ppm (s, 2H, BH_t); ^{13}C{^{1}H} NMR (100 MHz, $[D_8]$THF, 22 °C): $\delta = 202.1$ (CO), 129.6 (CCH_3), 129.5 (CCH_3), 92.9 ($C_5(CH_3)_5$), 21.5 (CH_3), 18.5 (CH_3), 9.3 ppm ($C_5(CH_3)_5$); IR ($[D_8]$THF): $\tilde{\nu} = 2495$ (s, BH), 1980 (w, CO), 1941 (w, CO), 1893 (m, CO), 1854 cm^{-1} (m, CO). LRMS (FAB): *m/z*:

 © 2006 Wiley-VCH Verlag GmbH & Co. KGaA, Weinheim

471 $[M-Mo(CO)_3]^+$ (isotope envelope, 3 B, 1 Ir atoms corresponding to the fragment ion $[Cp^*IrC_4(CH_3)_4B_3H_3]^+$).

Received: November 29, 2005
Revised: January 11, 2006
Published online: February 27, 2006

Keywords: alkynes · carboranes · insertion · iridium · molybdenum

[1] C. Elschenbroich, A. Salzer, *Organometallics*, VCH, New York, **1989**.
[2] G. O. Spessard, G. L. Miessler, *Organometallic Chemistry*, Prentice Hall, Upper Saddle River, **1997**.
[3] R. N. Grimes in *Inorganometallic Chemistry* (Ed.: T. P. Fehlner), Plenum, New York, **1992**, p. 253.
[4] A. Suzuki, *Organoboranes in Organic Syntheses*, Hokkaido Univ., Sapporo, **2004**.
[5] H. Chen, S. Schlecht, T. C. Semple, J. F. Hartwig, *Science* **2000**, *287*, 1995.
[6] Z. Duan, M. J. Hampden-Smith, A. P. Sylwester, *Chem. Mater.* **1992**, *4*, 1146.
[7] L. G. Sneddon, M. J. Pender, K. M. Forsthoefel, U. Kusari, X. Wei, *J. Eur. Ceram. Soc.* **2005**, *25*, 91.
[8] R. N. Grimes in *Current Topics in the Chemistry of Boron* (Ed.: G. W. Kabalka), Royal Society of Chemistry, Cambridge, UK, **1994**, p. 269.
[9] X. Lei, M. Shang, T. P. Fehlner, *Chem. Eur. J.* **2000**, *6*, 2653.
[10] R. Macías, T. P. Fehlner, A. M. Beatty, B. Noll, *Organometallics* **2004**, *23*, 5994.
[11] H. Yan, A. M. Beatty, T. P. Fehlner, *Organometallics* **2002**, *21*, 5029.
[12] H. Yan, B. C. Noll, T. P. Fehlner, *J. Am. Chem. Soc.* **2005**, *127*, 4831.
[13] CCDC-252822 (**2**), CCDC-290040 ($\mathbf{I_A}$), and CCDC-290041 ($\mathbf{I_B}$) contain the supplementary crystallographic information for this paper. These data can be obtained free of charge from The Cambridge Crystallographic Data Centre via www.ccdc.cam.ac.uk/data_request/cif.
[14] R. P. Micciche, J. J. Briguglio, L. G. Sneddon, *Organometallics* **1984**, *3*, 1396.
[15] G. J. Zimmerman, L. G. Sneddon, *Inorg. Chem.* **1980**, *19*, 3650.
[16] B. Wrackmeyer, H.-J. Schanz, M. Hofmann, P. von R. Schleyer, R. Boese, *Eur. J. Inorg. Chem.* **1999**, 533.
[17] R. Macías, T. P. Fehlner, A. M. Beatty, *Angew. Chem.* **2002**, *114*, 4016; *Angew. Chem. Int. Ed.* **2002**, *41*, 3860.

 © 2006 Wiley-VCH Verlag GmbH & Co. KGaA, Weinheim

Microporous Materials

DOI: 10.1002/anie.200502553

NMR Studies on the Diffusion of Hydrocarbons on the Metal-Organic Framework Material MOF-5**

Frank Stallmach, Stefan Gröger, Volker Künzel, Jörg Kärger, O. M. Yaghi, Michael Hesse, and Ulrich Müller**

The outstanding conceptual approach of so-called reticular design[1] for the generation of metal-organic frameworks (MOFs) or coordination polymers enables the tailoring of solids with regular porosity on the nanometer scale. Since the discovery of this new family of nanoporous materials, and especially stimulated by the work on MOF-5[2] as its most prominent representative, research efforts primarily focused on the synthesis and analysis of these compounds.[3,4] Research in this area is prompted by intriguing opportunities in the design of new materials by simply linking metals, which act as coordination centers, using a variety of polyatomic organic bridging ligands,[1–4] and the potential application of the resulting tailored nanoporous host materials in adsorption, separation, gas storage, and heterogeneous catalysis.[3–7] For example, the self-assembly of dicarboxylic acids of different molecular lengths as the organic linkers and octahedral basic zinc acetate clusters as the metal coordination centers leads to mechanically and thermally robust solids,[3,8,9] which may facilitate even large-scale applications of MOFs in these industrially important fields.

Industrial applications would require the removal of the organic solvent present during synthesis, which often might be difficult, as well as the introduction and diffusion of valuable (non-native) molecules in the pore space. While adsorption studies with inert gases are performed in the context of basic material characterization, similar investigations with more relevant molecules are less common. Moreover, no experimental data exist on diffusion of such molecules through the pore space of MOF materials. To our knowledge, only theoretical results on diffusion in MOF have been published so far from MD simulations of argon in MOF-2, MOF-3, MOF-5, and CuBTC,[10,11] and of other gases (H_2, N_2, CO_2) and alkanes (methane, *n*-pentane, *n*-hexane, cyclohexane, *n*-heptane) in MOF-5.[11,12] Here, we present the first experimental diffusion studies on nanoporous metal-organic framework materials. We used MOF-5 that had been prepared on a kilogram scale and studied the mobility of methane, ethane, *n*-hexane, and benzene by pulsed field gradient (PFG) NMR,[13,14] which is a well-established technique for intracrystalline self-diffusion studies in microporous solids.[14a,15–17]

The synthesis of MOF-5 by an optimized large-scale preparation, the removal of organic solvent, and sample characterization by wet chemical analysis, adsorption studies (including isotherms of argon, methane, and ethane), X-ray diffraction, and solid-state ^{1}H(MAS) NMR are described in the Supporting Information. The results show the characteristics expected for MOF-5,[1,4] and there is no evidence that the material decomposes during the experiments. Electron micrographs of the obtained MOF-5 material, which has a specific surface area of 3400 $m^2 g^{-1}$, show well-shaped, high-quality cubic crystals with crystal sizes between 50 to 200 μm (Figure 1). They are sufficiently large to measure intracrystalline self-diffusion by PFG NMR. For these diffusion studies, volumetrically determined amounts of the sorbate gases (vapors) were adsorbed at 77 K onto activated MOF-5 samples in NMR sample tubes (Table 1). The absorbed amounts correspond to about five (benzene, *n*-hexane) and six (methane, ethane) carbon atoms of the adsorbate molecule per cavity of the MOF-5.

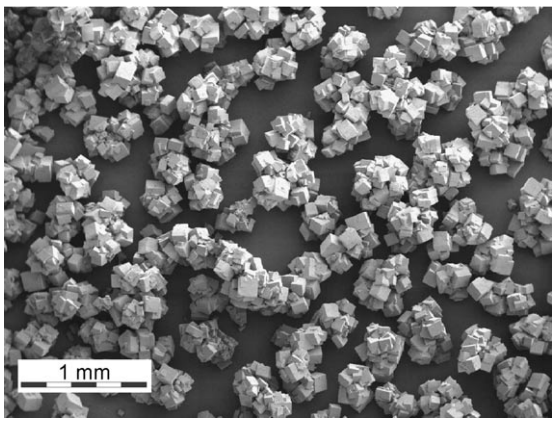

Figure 1. Scanning electron micrograph (SEM) of MOF-5 crystals obtained from the optimized large-scale preparation. The bar represents a length of 1 mm.

PFG NMR measurements were performed on the custom-built NMR spectrometer Fegris 400NT[18] using the 13-interval stimulated spin-echo pulse sequence with two pairs of alternating pulsed magnetic field gradients (amplitude g, width Δ) for diffusional encoding.[19] This technique is

[*] Dr. habil. F. Stallmach, S. Gröger, V. Künzel, Prof. J. Kärger
Fakultät für Physik und Geowissenschaften
Universität Leipzig
Linnèstrasse 5, 04103 Leipzig (Germany)
Fax: (+49) 341-973-2549
E-mail: stallmac@physik.uni-leipzig.de
Dr. M. Hesse, Dr. U. Müller
BASF Aktiengesellschaft
GCC/Z – M301, 67056 Ludwigshafen (Germany)
Fax: (+49) 621-605-6190
E-mail: ulrich.mueller@basf-ag.com
Prof. O. M. Yaghi
Department of Chemistry, University Michigan
930 North University Avenue
Ann Arbor, MI 48109-1055 (USA)

[**] This work was supported by the German Science Foundation (DFG) through the International Research Training Group "Diffusion in Porous Materials". We are grateful to two referees for their suggestions to include solid-state NMR data. We thank M. Wehring and W. Böhlmann (Leipzig) for acquiring these data.

Supporting information for this article is available on the WWW under http://www.angewandte.org or from the author.

 © 2006 Wiley-VCH Verlag GmbH & Co. KGaA, Weinheim

Table 1: Effective (D_{eff}) and intracrystalline self-diffusion coefficients (D_1, D_2) of hydrocarbons in MOF-5 for selected temperatures as measured by PFG NMR spectroscopy.[a]

Adsorbate	Loading [mg g^{-1}]	T [K]	Δ [ms]	D_{eff} [m^2 s^{-1}]	D_1 [m^2 s^{-1}]	D_2 [m^2 s^{-1}]	p_1 [%]	p_3 [%]
methane	120	298	5...40	$\approx 2.0\times10^{-6}$	$\approx 1.7\times10^{-7}$			
		173	5...80	1.9×10^{-7}	1.2×10^{-8}			
ethane	120	298	5...40	2.0×10^{-7}	2.1×10^{-8}			
		223	5...80	1.4×10^{-8}	1.9×10^{-8}	4.7×10^{-9}	60	1.2
n-hexane	100	298	10...20	1.8×10^{-9}	3.2×10^{-9}	4.0×10^{-10}	50	6.5
			40...80	2.6×10^{-9}	4.1×10^{-9}	4.5×10^{-10}	59	7.0
benzene	80	298	10...40	1.3×10^{-9}	1.8×10^{-9}	3.5×10^{-10}	72	1.5
			80	1.4×10^{-9}	2.0×10^{-9}	4.0×10^{-10}	60	2.5

[a] For ethane (at 223 K), *n*-hexane, and benzene, the intracrystalline diffusivities D_1 and D_2, and the percentages of fast-diffusing (p_1) and nondiffusing (p_3) fractions of the multiexponential fits displayed in Figure 2c, e, and f are given. For *n*-hexane and benzene for different observation times Δ slightly different fit parameters result.

primarily sensitive to the mean square displacement $\langle r^2(\Delta)\rangle$ of molecules during the time Δ between the pairs of pulsed field gradients, which is referred to as observation or diffusion time. For all adsorbates, the spin-echo intensity $M(b)$ was observed as a function of the parameter b, which is defined by $b=(\gamma g 2\delta)^2(\Delta-{}^1\!/_6\delta-{}^1\!/_2\tau)$.[19] Characteristic values of the experimentally varied gradient parameters (g, δ, Δ) and the radio-frequency pulse distance τ are summarized in the Experimental Section. Self-diffusion coefficients ($D=\langle r^2(\Delta)\rangle/(6\Delta)$) and information on diffusional exchange between gas and adsorbed phase during Δ were obtained by analyzing the slope and the shape of the plot of $\ln(M(b)/M_0)$ versus b, respectively.[13–17] To determine where the observed diffusion process takes place, the dependence of the spin-echo attenuation on observation time as well as on temperature was studied.

Figure 2 shows examples of such spin-echo attenuations in MOF-5. All plots of $\ln(M(b)/M_0)$ versus b deviate from linearity, which indicates a distribution of self-diffusion coefficients. Methane at all temperatures and ethane at the higher temperature show decreasing amounts of slowly decaying signal fractions with increasing diffusion time. Such behavior is well known from diffusion studies in zeolites,[16,17] where the different mobilities of the adsorbent molecules in intra- and intercrystalline space are detected by PFG NMR spectroscopy. This feature of PFG NMR spectroscopy is utilized by the fast NMR tracer exchange method to determine the fraction of molecules remaining during the diffusion time in the intracrystalline space, their self-diffusion coefficient D, and their mean intracrystalline lifetime τ_{intra}.[16,17] The curves in Figure 2a, b, and d are compatible with this fast tracer exchange method and were analyzed accordingly: The slope of the linear regression of the slowly decaying signal fraction yields the intracrystalline self-diffusion coefficient D. Its extrapolation to $b=0$ determines the relative amount $a(\Delta)$ of molecules remaining during the diffusion time only in the intracrystalline space. The regression lines and their interpolations are included in Figure 2a, b, and d.

In Figure 3 the temperature dependence of the intracrystalline self-diffusion coefficients for methane and ethane are shown and compared with corresponding values of self-diffusion in NaX zeolites.[20] Clearly, diffusion of methane and ethane in MOF-5 is faster than in NaX. This might be a consequence of the difference between the diameters of the large nanoporous cavities in MOF-5 (1.5 nm) and in NaX (1.2 nm).

The pronounced dependence of the spin-echo attenuation on the observation time (Figure 2a, b, and d) shows that methane and ethane exchange between intracrystalline and intercrystalline space already on the millisecond time scale of the PFG NMR experiment. Figure 4 plots the relative amounts $a(\Delta)$ of molecules diffusing only in the intracrystalline space as function of the diffusion time. These values decrease with increasing diffusion time, since more and more molecules reach

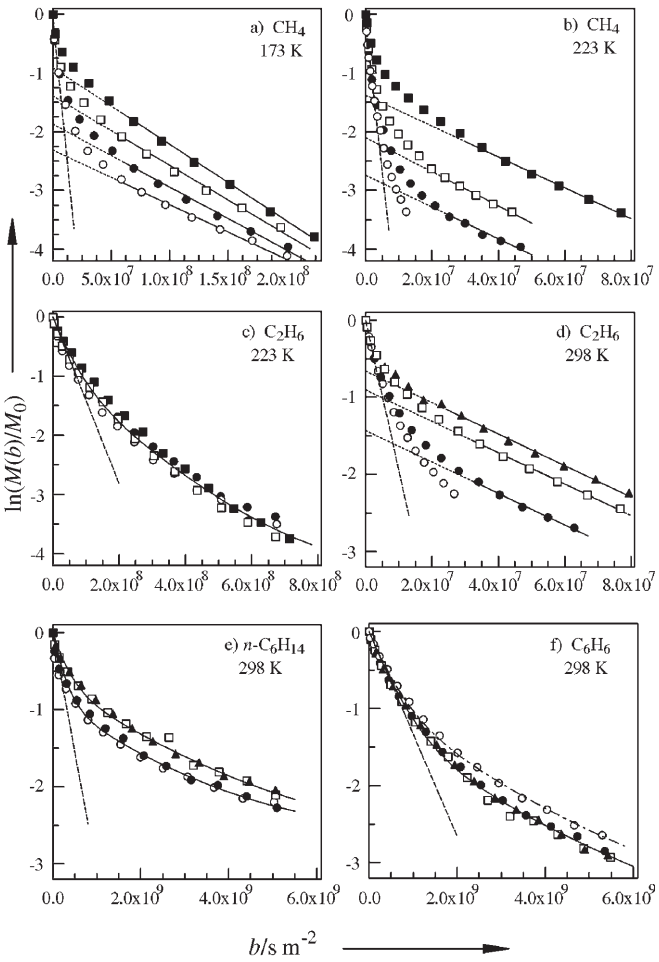

Figure 2. PFG NMR spin-echo attenuation ($\psi(b)$) and data analysis for: a,b) methane, c,d) ethane, e) *n*-hexane, and f) benzene in MOF-5 for observation times $\Delta=5$ ms (■), 10 ms (▲), 20 ms (□), 40 ms (●), and 80 ms (○), respectively. Dashed lines represent the initial decays yielding the effective self-diffusion coefficients. In the time-dependent decays of parts a, b, and d, solid and dotted lines represent linear regressions and their interpolations to $b=0$ in order to determine the intracrystalline self-diffusion coefficient D and lifetimes τ_{intra}. For attenuations observed in parts 2c, e, and f, fits using a multiexponential model are included.

 © 2006 Wiley-VCH Verlag GmbH & Co. KGaA, Weinheim

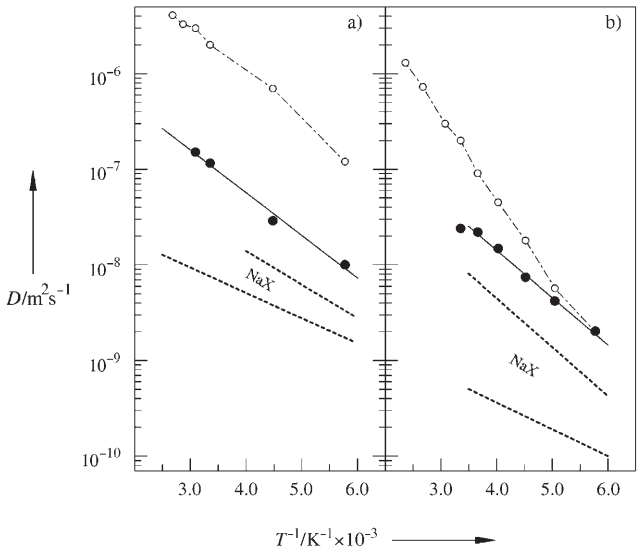

Figure 3. Arrhenius presentation of the intracrystalline (●) and effective (○) self-diffusion coefficients of: a) methane and b) ethane in MOF-5. The region between the dotted lines shows the range of intracrystalline self-diffusion coefficients in NaX zeolite for loadings from about 30–90 mg g^{-1} methane (part a) and 110 mg g^{-1} ethane (part b), respectively.[20] The solid lines correspond to activation energies of 8.5 kJ mol^{-1} (methane, part a) and 9.5 kJ mol^{-1} (ethane, part b) for adsorbate self-diffusion in MOF-5.

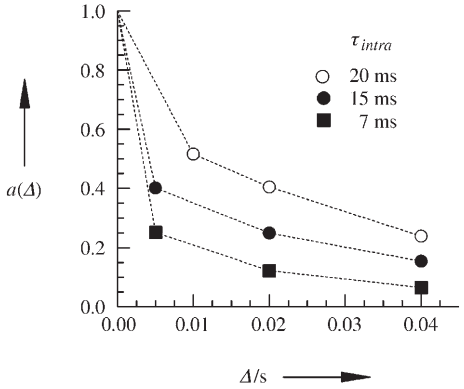

Figure 4. Relative amount $a(\Delta)$ of molecules that diffuse during the time interval Δ only in the intracrystalline space of MOF-5. Data are obtained for methane (● 173 K; ■ 223 K) and ethane (○, 289 K) from linear extrapolation of the PFG NMR spin-echo attenuations in Figure 2a, b, and d. They decrease with increasing Δ and, thus, give evidence for fast exchange between inter- and intracrystalline space. The dotted lines represent linear interpolations between the data points. Estimates for the mean intracrystalline lifetime τ_{intra} are included into the legend.

the crystal boundary and contribute to this exchange. The mean lifetime τ_{intra} of a diffusing molecule in the intracrystalline space is obtained by integrating over $a(\Delta)$.[16,17] The τ_{intra} values reported in Figure 4 were estimated by the area under the linear interpolation between the experimental data and are thus only rough estimates. Nevertheless, the results demonstrate that light hydrocarbons easily exchange between the intracrystalline phase in MOF-5 and the surrounding gas phase. Above room temperature this exchange is so fast that intracrystalline diffusion cannot be observed by PFG NMR spectroscopy. Therefore, for higher temperatures only the effective self-diffusion coefficients, which represent the long-range diffusion through the bed of MOF-5 crystals, are plotted in Figure 3.

Spin-echo attenuations for ethane at low temperatures as well as for *n*-hexane and benzene at room temperature (Figure 2c, e, and f) are qualitatively different from those discussed above. Within the experimental uncertainty, the observed decays do not depend on observation time Δ but are again nonlinear with b. This indicates a distribution of self-diffusion coefficients that is independent of observation time. Thus, regions with different adsorbate mobilities must exist within the MOF-5 sample, and the molecules do not exchange between these regions during the time scale of the NMR experiment. For quantitative analysis, the initial decay of the spin-echo attenuation was evaluated (see dashed lines in Figure 2). It yields the effective self-diffusion coefficient D_{eff}, which—regardless of the underlying distribution—coincides with the arithmetic mean diffusion coefficient. Additionally, the whole spin-echo attenuation curve is fitted by assuming a multiexponential decay yielding two diffusion coefficients ($D_i > 0$, $i = 1, 2$) with relative contributions p_i and a constant, nondiffusing ($D_3 = 0$) background contribution p_3. Solid lines in Figure 2c, e, and f represent the fits using this multi-exponential model. The effective self-diffusion coefficients and the results of the multiexponential model are given in Table 1.

The effective self-diffusion coefficients of *n*-hexane and benzene in the MOF-5 structure are only slightly smaller than their values in the neat liquids at the same temperature (C_6H_6: 2.21×10^{-9} m^{2}s^{-1}; C_6H_{14}: 4.26×10^{-9} m^{2}s^{-1}[21]). On the basis of the low loadings, visual inspection of the samples, and the absence of the typically long transverse relaxation time components of liquids, the presence of liquid droplets of *n*-hexane and benzene outside the MOF-5 crystals must be excluded. Thus, the presented effective diffusivities represent averaged intracrystalline mobilities. The multiexponential analysis shows that about 50–70% of the adsorbed molecules have liquidlike high mobilities. The residual fractions show significantly lower self-diffusion coefficients (see Table 1). The micropores in fractions of the MOF-5 crystals may be partially blocked by residual solvents or structural defects. Both effects reduce intracrystalline mobilities and may thus lead to a distribution of self-diffusion coefficients of adsorbed *n*-hexane, benzene, and even ethane (at low temperatures) as evidenced in the PFG NMR experiments.

The presence of about 0.2 molecules of the solvent diethylformamide (DEF) per cavity of the MOF-5 even after activation at 100 °C was observed by solid-state ^{1}H MAS NMR spectroscopy (see the Supporting Information). These residual DEF molecules are most likely the reason for the two signal fractions with reduced mobility, observed by PFG NMR spectroscopy owing to 1) their influence on a part of the adsorbed molecules and 2) their own contribution to the ^{1}H NMR signal observed.

With regard to point (1): The DEF molecules occupy pore space and may even block windows between MOF-5 cavities.

 © 2006 Wiley-VCH Verlag GmbH & Co. KGaA, Weinheim

This reduces adsorbate mobility and leads to the second component (D_2 in Table 1), in addition to the first component (D_1 in Table 1) represented by the adsorbate molecules in MOF-5 regions which are locally free of residual solvent molecules. The absence of diffusional exchange between the regions of different DEF content as evidenced in the *n*-hexane, benzene, and low-temperature ethane data suggests that these regions are macroscopically separated; that is, DEF molecules are not distributed homogeneously throughout the MOF-5 material. For example, since the applied washing procedures are more effective for the outer crystal regions, it could be that central regions of the large crystals contain a higher DEF concentration than the outer regions.

With regard to point (2): The ethyl groups of the residual DEF molecules contribute to the PFG NMR spin-echo signal, which is evidenced by the static ^{1}H NMR spectra of the activated samples presented in the Supporting Information. Since these DEF molecules are obviously strongly attached to the MOF-5 lattice, their signal is not attenuated in the PFG NMR experiment yielding the third, nondiffusing signal fraction (component p_3 in Table 1).

Regardless of their origins, both signal fractions with reduced mobilities do not influence significantly the overall fast effective diffusivities measured for the adsorbates in MOF-5. In the future, detailed investigations by solid-state NMR spectroscopy in combination with PFG NMR spectroscopy are desirable to quantify the effect of the solvent molecules on diffusion studies of guest molecules in nanoporous metal-organic framework materials.

For *n*-hexane, the fast component of intracrystalline diffusivity ($3.2–4.1\times10^{-9}\,m^2\,s^{-1}$, see Table 1) is in good agreement with the value of $2.2\times10^{-9}\,m^2\,s^{-1}$[12] predicted by MD simulation for a slightly higher loading. For methane, the intracrystalline self-diffusion coefficient measured by PFG NMR spectroscopy is about one order of magnitude higher than the value of $3.1\times10^{-8}\,m^2\,s^{-1}$[11,12] reported in MD simulations. This discrepancy might have its origin in the much lower loadings used in the MD simulations and/or in imperfections in the micropore structure which influence the experimental PFG NMR studies but which are not taken into account in the MD simulations. To our knowledge, there are no other diffusion data from metal-organic frameworks available for direct comparison between the two methods.

In conclusion, we have demonstrated for the first time the superior diffusional properties of organic gas molecules in the metal-organic framework compound MOF-5. The unique combination of high porosity with record number surface area and regular nanometer pores and the absence of nonpenetrable bulk matter might lead to interesting features for industrial gas processing and storage. The high gas molecule mobility in MOF-5 and its fast exchange with the surrounding gas atmosphere, in comparison to metal oxides, zeolites, carbons, resins, and numerous other materials, should result in much faster processing and lower energy consumption. In addition, the high surface area of MOF-5 of more than $3000\,m^2\,g^{-1}$ could lead to improved mass- and volume-specific gas-storage capacities thus giving lower investment costs for both stationary and mobile applications.

Experimental Section

Typical parameters for the ^{1}H PFG NMR diffusion studies with the 13-interval sequence at the Spectrometer Fegris 400NT[18] (400 MHz) were: 90°–180° radio-frequency distance $\tau = 500\,\mu s$, pulsed field gradient width $\delta = 150\,\mu s$, variable diffusion times $5\,ms \le \Delta \le 80\,ms$. Spin-echo attenuations were measured by increasing the pulsed field gradient intensity g from 0 up to a maximum value of $10\,T\,m^{-1}$. Sample temperature was controlled by a stream of air (above room temperature) or nitrogen (below room temperature) with an accuracy of $\pm$ 1 K.

Received: July 21, 2005
Revised: December 5, 2005
Published online: February 24, 2006

Keywords: alkanes · benzene · diffusion · microporous materials · NMR spectroscopy

[1] M. Eddaoudi, J. Kim, N. Rosi, D. Vodak, J. Wachter, M. O'Keeffe, O. M. Yaghi, *Science* **2002**, *295*, 469–472.
[2] H. Li, M. Eddaoudi, M. O'Keeffe, O. M. Yaghi, *Nature* **1999**, *402*, 276–289.
[3] J. L. C. Rowsell, O. M. Yaghi, *Microporous Mesoporous Mater.* **2004**, *73*, 3–14.
[4] S. Kaskel in *Handbook of Porous Solids* (Eds.: F. Schüth, K. S. W. Sing, J. Weitkamp), Wiley-VCH, Weinheim, **2002**, pp. 1190–1249.
[5] R. Q. Snurr, J. T. Hupp, S. T. Nguyen, *AIChE J.* **2004**, *50*, 1091–1095.
[6] X. Zhao, B. Xiao, A. J. Fletcher, K. M. Thomas, D. Bradshaw, M. J. Rosseinsky, *Science* **2004**, *306*, 1012–1015.
[7] O. R. Evans, H. L. Ngo, W. Lin, *J. Am. Chem. Soc.* **2001**, *123*, 10395–10396.
[8] U. Mueller, K. Harth, M. Hoelzle, M. Hesse, L. Lobree, W. Harder, O. M. Yaghi, (BASF AG), WO 03/064030, **2003**.
[9] O. M. Yaghi, M. Eddaoudi, H. Li, J. Kim, N. Rosi, (Univ. Michigan), WO 02/088148, **2002**.
[10] A. I. Skoulidas, *J. Am. Chem. Soc.* **2004**, *126*, 1356–1357.
[11] A. I. Skoulidas, D. S. Sholl, *J. Phys. Chem. B* **2005**, *109*, 15760–15768.
[12] L. Sarkisov, T. Düren, R. Q. Snurr, *Mol. Phys.* **2004**, *102*, 211–221.
[13] E. O. Stejskal, J. E. Tanner, *J. Chem. Phys.* **1965**, *42*, 288–299.
[14] a) J. Kärger, H. Pfeifer, W. Heink, *Adv. Magn. Reson.* **1988**, *12*, 1–88; b) Y. Cohen, L. Avram, L. Frish, *Angew. Chem.* **2005**, *117*, 524–560; *Angew. Chem. Int. Ed.* **2005**, *44*, 520–554.
[15] a) F. Stallmach, J. Kärger, *Adsorption* **1999**, *5*, 117–133; b) F. Stallmach, Habilitation thesis, Universität Leipzig (GE), **2004** [http://lips.informatik.uni-leipzig.de:80/pub/2004–19].
[16] J. Kärger, D. M. Ruthven, *Diffusion in Zeolites and Other Microporous Solids*, Wiley, New York, **1992**.
[17] O. Geier, R. Q. Snurr, F. Stallmach, J. Kärger, *J. Chem. Phys.* **2004**, *120*, 367–373.
[18] P. Galvosas, F. Stallmach, G. Seiffert J. Kärger, U. Kaess, G. Majer, *J. Magn. Reson.* **2001**, *151*, 260–268.
[19] R. M. Cotts, M. J. R. Hoch, T. Sun, J. T. Markert, *J. Magn. Reson.* **1989**, *83*, 252–266.
[20] J. Kärger, H. Pfeifer, M. Rauscher, A. Walter, *J. Chem. Soc. Faraday Trans. 1* **1980**, *76*, 717–737.
[21] M. Holz, H. Weingärtner, *J. Magn. Reson.* **1991**, *92*, 115–125.

 © 2006 Wiley-VCH Verlag GmbH & Co. KGaA, Weinheim

Switchable Biostructures

DOI: 10.1002/anie.200503820

Redox-Active Riboswitching: Allosteric Regulation of Ribozyme Activity by Ligand-Shape Control**

*Denise Strohbach, Nina Novak, and Sabine Müller**

Allosteric regulation is a fundamental principle in nature. Most enzymes working in metabolic pathways are regulated by interaction with other molecules acting as allosteric cofactors. Over the past decade, RNA conformation has been shown to respond to external stimuli. A number of ligand-specific molecular switches that are composed of aptamers attached to ribozyme structures have been developed.[1] Binding of a specific ligand to the aptamer domain either stabilizes or destabilizes the active conformation of the catalytic domain and results in an increase or decrease in catalytic activity. Riboswitches have also been discovered in nature; the mRNA conformation is changed upon interaction with a specific ligand and this results in inhibition/disruption of transcription or translation.[2] Although natural riboswitches can run through many cycles of switching, artificial riboswitches do not work in a reversible mode: the activity is either switched on or off in response to the addition of the allosteric cofactor. We set out to develop a system that has the potential to be regulated in a reversible manner. To this end, we have designed a hairpin ribozyme variant whose catalytic properties are dependent on flavine mononucleotide (FMN). Herein we show that ribozyme activity is switched on in the presence of FMN in the oxidized state, whereas under reducing conditions, FMN is released from its binding site and a clear decline in activity results.

To construct hairpin ribozyme variants that can be regulated in an allosteric way, we decided to replace helix 4 of the wild-type hairpin ribozyme[3] (Figure 1) with a specific sequence. This sequence acts as a communication module and connects the ribozyme moiety with the FMN-specific aptamer, which was previously identified by in vitro selection.[4] The 11-nucleotide bulge segment (nucleotides 8–13 and 24–28 in Figure 1b) has been used before for the construction of FMN-dependent hammerhead aptazymes[5] and for competitive regulation of modular allosteric aptazymes by a small molecule and an oligonucleotide effector.[6] Furthermore, a

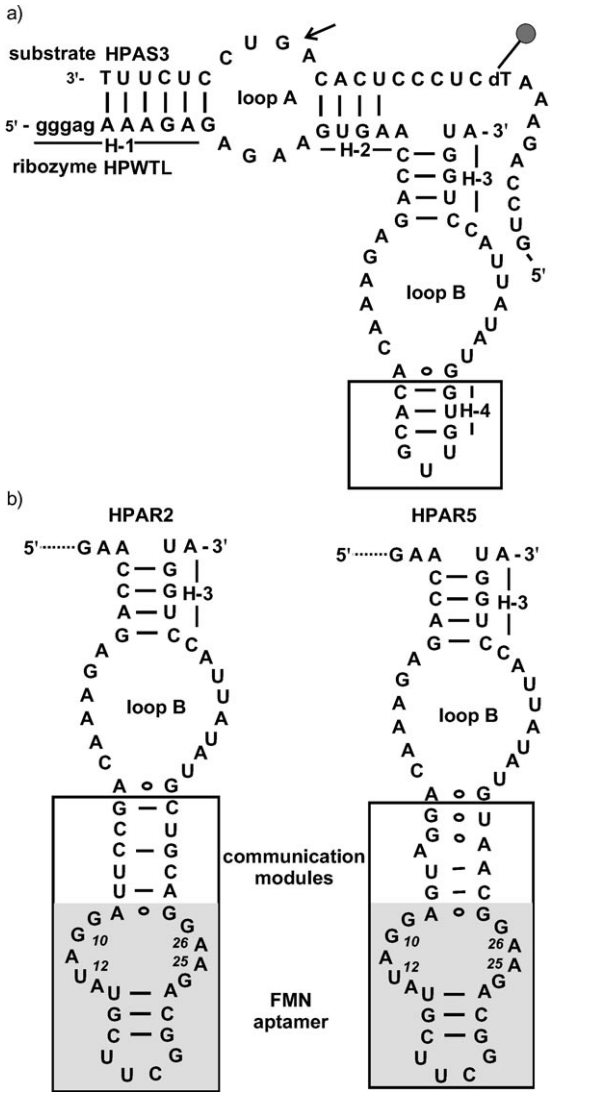

Figure 1. Secondary structure of the hairpin ribozyme and the engineered hairpin aptazymes. a) The structure of the wild-type hairpin ribozyme HPWTL in complex with the substrate HPAS3. The arrow marks the cleavage site, and the gray circle indicates a fluorescent moiety (Cy5) used for detection. Lower-case letters indicate vector nucleotides necessary for efficient transcription of the ribozyme. Helix 4 in the boxed area has been replaced with two different communication modules attached to the FMN aptamer leading to the aptazymes HPAR2 and HPAR5 as shown in part b). b) Secondary structure of hairpin aptazymes HPAR2 and HPAR5 (only loop B domain is shown) containing the FMN aptamer (gray box) adjoined to the ribozyme via communication modules (boxed).

natural RNA fold within mRNA has been discovered that specifically interacts with FMN to regulate the expression of bacterial genes involved in the biosynthesis and transport of riboflavin and FMN.[7] We have engineered two variants of hairpin aptazymes, HPAR2 and HPAR5 (Figure 1). In the absence of FMN, we expected the conformation of loop B to be less stable. Binding of FMN to the aptamer domain should trigger a conformational change within the bridge that in turn should cause a structural rearrangement of the adjoining ribozyme, thus dictating its activity. The communication module used in HPAR2 was developed by in vitro selection

[*] D. Strohbach, N. Novak, Prof. Dr. S. Müller
Ruhr-Universität Bochum
Fakultät Chemie
Universitätsstrasse 150, 44780 Bochum (Germany)
Fax: (+49) 234-321-4783
E-mail: sabine.w.mueller@rub.de

[**] This work was supported by the Volkswagenstiftung. We are grateful to Thomas Carell and Ulrich Hennecke for assistance with the FMN reduction protocol. We thank Wolfgang Schuhmann and Florin Turku for supporting us with the inert atmosphere reaction vessel.

Supporting information for this article is available on the WWW under http://www.angewandte.org or from the author.

 © 2006 Wiley-VCH Verlag GmbH & Co. KGaA, Weinheim

of FMN-dependent hammerhead ribozymes. A slip-structure mechanism has been suggested, whereby localized changes in base pairing occur and are dependent on the presence or absence of FMN.[5b] The second communication module used in HPAR5 comes from the selection of theophylline-dependent hepatitis-delta-virus ribozymes.[8]

In a first series of experiments, we studied the cleavage behavior of both aptazymes in the presence and absence of FMN. As can be seen from Figure 2a, HPAR2 readily cleaves

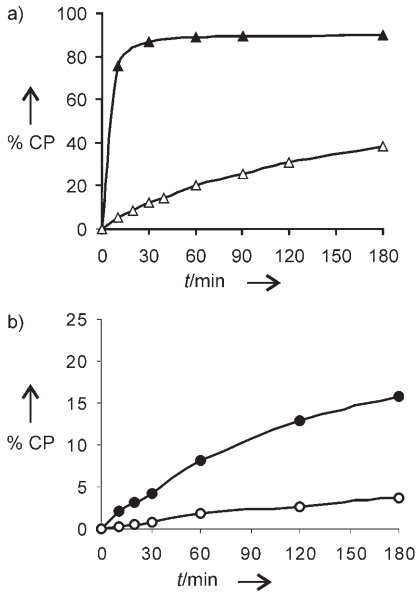

Figure 2. Time course of cleavage reactions of aptazyme HPAR2 (a) and HPAR5 (b) in the presence (▲ and ●, respectively) and absence (△ and ○, respectively) of FMN. CP = cleavage product.

the substrate HPAS3 (Figure 1) in the presence of FMN, whereas in the absence of the ligand, the activity is considerably reduced. HPAR5 (Figure 2b) shows rather poor activity in the presence of FMN and is virtually inactive in the absence of FMN. Nevertheless, allosteric activation is clearly observed in both cases: HPAR2 exhibits a 24-fold, and HPAR5 a 13-fold activity increase by FMN. The k_{obs} value of HPAR2, in the presence of FMN, approaches the k_{obs} value measured for awild-type hairpin ribozyme (Table 1). This demonstrates that the loss of activity caused by destabilization of loop B is fully restored by the addition of the allosteric ligand. Because of its high catalytic activity, HPAR2 was chosen for further kinetic studies. Next, we performed single-turnover experiments in increasing concentrations of FMN. The single-turnover reaction rates were found to be a function of FMN concentration, and the maximum cleavage rate was observed above 200 μM with a half value of around 37 μM (see the Supporting Information). This indicates that FMN saturates its binding site and that specific binding of FMN indeed leads to activation of the ribozyme. The half value of 37 μM represents an estimation of the K_D value of FMN. This value is within the range of K_D values that are reported in the literature ($\approx$500 nM for FMN with the original aptamer;[4] $\approx$130 μM for FMN with a hammerhead aptazyme[8]). The

Table 1: Constants determined for the cleavage reactions of aptazymes HPAR2 and HPAR5 in the absence and presence of FMN and of the wild-type hairpin ribozyme HPWTL.

		HPAR2	HPAR5	HPWTL
k_{obs}[a]	− FMN	0.007 ± 0.003	0.00012 ± 0.0001	0.22 ± 0.02
	+ FMN	0.17 ± 0.03	0.0016 ± 0.0002	0.23 ± 0.03
$K_{D,FMN}$[b]		36.8 ± 8.6	–	–
$k_{react,FMN}$[c]		0.25 ± 0.01	–	–
K_m(sto)[d]		502.9 ± 62.5	–	134 ± 40
k_{react}[e]		0.52 ± 0.03	–	0.54 ± 0.09

[a] k_{obs} [min^{-1}] describes the initial rate of cleavage reactions in the presence (200 μM) and absence of FMN. [b] $K_{D,FMN}$ [μM] is the disassociation constant of FMN in the aptazyme. [c] $k_{react,FMN}$ [min^{-1}] describes the maximum cleavage rate at saturating FMN concentrations in the presence of ribozyme (500 nM) and substrate (25 nM). [d] K_m(sto) [nM] is the single-turnover constant. [e] k_{react} [min^{-1}] describes the maximum cleavage rate at saturating concentrations of ribozyme in the presence of 25 nM substrate and 400-fold excess of FMN over ribozyme. For HPWTL, k_{react} remains unchanged in experiments with and without FMN.

first-order rate constant, $k_{react,FMN}$ (0.25 ± 0.01 min^{-1}, Table 1), should reflect FMN binding and the subsequent conformational rearrangement of loop B upon addition of the effector. Further kinetic analysis involved single-turnover experiments at saturating concentrations of FMN (400-fold excess over the ribozyme), and ribozyme excess over the substrate. With a rate constant (k_{react}) of 0.52 min^{-1}, and a single turnover constant K_m(sto) of 503 nM in the presence of FMN, aptazyme HPAR2 shows comparable cleavage activity with the corresponding nonallosteric wild-type hairpin ribozyme HPWTL (Table 1). To ensure that the observed increase of activity is indeed caused by binding of the effector molecule, control reactions (under identical conditions) were carried out with HPWTL. Cleavage activity remained the same in all of the experiments, independent of the presence or absence of FMN. This confirms the conclusion that FMN binds to the aptamer domain of HPAR2 in a specific way, and that the binding event dictates the catalytic activity of the aptazyme.

In nature, flavine mononucleotides play an important role as cofactors that mediate redox reactions when bound as prosthetic groups in flavoproteins. The isoalloxazin ring of FMN serves as a transient carrier of two hydrogen atoms that are removed from a substrate molecule upon oxidation. FMN, in its oxidized state, is a planar compound (owing to its conjugated aromatic-ring system), hydrogen transfer causes reduction of FMN, destroys the aromatic character, and induces a change in the molecular geometry: FMN is transformed from a planar structure to a rooflike bent shape[9] (Figure 3a). The structure of the FMN-aptamer complex in solution was characterized by ^{1}H NMR spectroscopy.[10] The analysis shows that complexation of FMN originates from hydrophobic stacking of the planar isoalloxazin ring involving G10, U12, and A25 (see Figure 1). The specificity is associated with an FMN–adenine base pair within the complex. Thus, binding of FMN is, to a large extent, stabilized by hydrophobic stacking of the aromatic isoalloxazin ring with the bases of the aptamer. This characteristic feature should allow FMN binding to be controlled by oxidation/reduction of the isoalloxazin ring. The change in the molecular shape of

 © 2006 Wiley-VCH Verlag GmbH & Co. KGaA, Weinheim

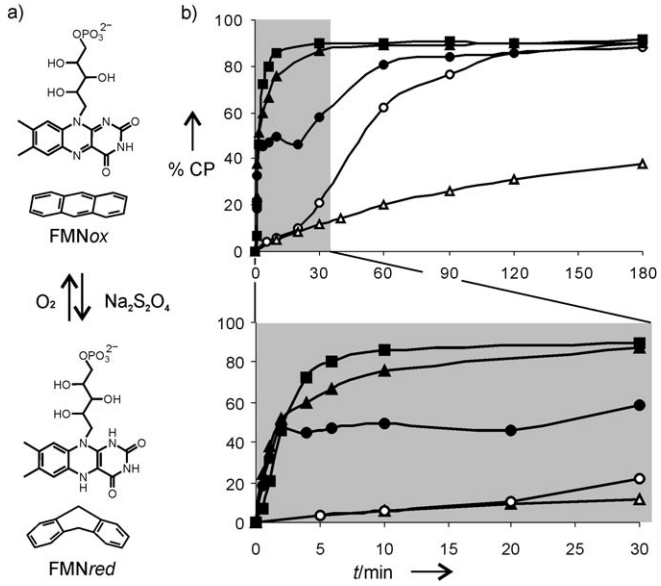

Figure 3. Regulation of ribozyme activity by control of the oxidation state of FMN. a) Change in the molecular shape of FMN upon reduction of the isoalloxazin unit. b) Time course of cleavage reactions of HPAR2 showing the dependence on FMN and dithionite. The gray area of the first diagram is magnified underneath. ■ = standard cleavage reaction of wild-type hairpin ribozyme HPWTL, used as a control; ▲ = reaction of HPAR2 in the presence of FMN; ● = reaction of HPAR2 in the presence of FMN and addition of dithionite 1.5 min after the reaction start; ○ = reaction of HPAR2 in the presence of FMN and dithionite from the reaction start; △ = reaction of HPAR2 in the absence of FMN. CP = cleavage product.

the ligand should significantly influence its binding ability and lead to activation/inactivation of the ribozyme.

Experimental proof of this suggestion involved the reduction of FMN with sodium dithionite. In an initial series of experiments, a 50-fold excess of $Na_2S_2O_4$ over FMN was added to the reaction mixture after 1.5 min. Disappearance of the pale-yellow color of the reaction mixture confirmed successful FMN reduction (the oxidized state of FMN is seen as a light-yellow color in solution owing to fluorescence of the FMN chromophore at 525 nm). Comparison of the time course of the reactions of HPAR2 in the presence of only FMN (Figure 3b, ▲) and in the presence of both FMN and dithionite (Figure 3b, ●) shows that the reaction is considerably slowed at the point of $Na_2S_2O_4$ addition (1.5 min). After 20 min the reaction rate increased again until the reaction reached saturation at 90% of substrate cleavage. This shows that, under the applied conditions, the reduced form of FMN is stable for approximately 20 min, and is then reoxidized by the oxygen present (the pale-yellow color reappeared, indicating regeneration of the chromophore). However, when the reaction was carried out in a specifically prepared reaction vessel that ensured a permanent argon atmosphere, the reduced form of FMN was stable for at least one hour (see the Supporting Information). In a second series of experiments, $Na_2S_2O_4$ was added prior to the reaction start; the curve profile is (Figure 3b; ○), in the initial phase, the same as that of the reaction performed in the complete absence of FMN (Figure 3b, △). As before, the activity rises after 20 min owing to reoxidation of FMN, and saturation is reached at 90% of substrate cleavage. Control reactions by using wild-type ribozyme HPWTL in the presence of only $Na_2S_2O_4$ and $Na_2S_2O_4$ in combination with FMN revealed no influence on cleavage activity (not shown).

The obtained results demonstrate that allosteric binding of FMN can be controlled by reduction/oxidation of the isoalloxazin ring resulting in a change of the molecular shape. To the best of our knowledge, this is the first demonstration of an aptazyme that can be regulated in response to the specific redox conditions in its surrounding medium and which has the potential to be reversibly switched on and off. Our results support the previously made suggestion that the binding mode of FMN is hydrophobic stacking of the aromatic ring with the nucleobases of the aptamer.[10] Furthermore, our results pave the way to engineered switchable molecular devices that implement reversible conversion between two different states with on/off functions. Moreover, in the context of the RNA-world theory, the designed allosteric system may be regarded as model for signaling cascades, which may have played functional roles in regulation of biological processes.

Received: October 28, 2005
Published online: February 27, 2006

Keywords: allosteric regulation · flavin mononucleotide (FMN) · redox chemistry · riboswitches · ribozymes

[1] a) M. Famulok, *Curr. Opin. Mol. Ther.* **2005**, *7*, 137–143; b) E. A. Davidson, A. D. Ellington, *Trends Biotechnol.* **2005**, *23*, 109–112; c) S. K. Silverman, *RNA* **2003**, *9*, 377–383.
[2] M. Mandal, R. R. Breaker, *Nat. Rev. Mol. Cell Biol.* **2004**, *5*, 451–463.
[3] a) P. A. Feldstein, J. M. Buzayan, G. Bruening, *Gene* **1989**, *82*, 53–61; b) A. Hampel, R. Tritz, *Biochemistry* **1989**, *28*, 4929–4933.
[4] P. Burgstaller, M. Famulok, *Angew. Chem.* **1994**, *106*, 1163–1166; *Angew. Chem. Int. Ed. Engl.* **1994**, *33*, 1084–1087.
[5] a) M. Araki, Y. Okuno, Y. Hara, Y. Sugiura, *Nucleic Acids Res.* **1998**, *26*, 3379–3384; b) G. A. Soukoup, R. R. Breaker, *Proc. Natl. Acad. Sci. USA* **1999**, *96*, 3584–3589.
[6] S. H. Najafi-Shoushtari, M. Famulok, *RNA* **2005**, *11*, 1514–1520.
[7] W. C. Winkler, S. Cohen-Chalamish, R. R. Breaker, *Proc. Natl. Acad. Sci. USA* **2002**, *99*, 15908–15913.
[8] A. Kertsburg, G. A. Soukoup, *Nucleic Acids Res.* **2002**, *30*, 4599–4606.
[9] a) C. Walsh, *Enzymatic Reaction Mechanisms*, Freeman, San Francisco, **1979**; b) C. T. W. Moonen, J. Vervoort, F. Müller, *Biochemistry* **1984**, *23*, 4859–4867; c) C. T. W. Moonen, J. Vervoort, F. Müller, *Biochemistry* **1984**, *23*, 4868–4872; d) P. Kierkegaard, R. Norrestam, P. E. Werner, I. Csöregh, M. von Glehn, R. Karlsson, M. Leijonmark, O. Rönnquist, B. Stensland, O. Tillberg, C. Torbjörnssen in *Flavins and Flavoproteins, Vol. 3* (Ed.: H. Kamin), University Park, Baltimore, **1971**, pp. 1–22.
[10] P. Fan, A. K. Suri, R. Fiala, D. Live, D. J. Patel, *J. Mol. Biol.* **1996**, *258*, 480–500.

 © 2006 Wiley-VCH Verlag GmbH & Co. KGaA, Weinheim

Asymmetric Polymerization

DOI: 10.1002/anie.200503496

Chiral Polyesters by Dynamic Kinetic Resolution Polymerization**

*Iris Hilker, Gouher Rabani, Gerard K. M. Verzijl, Anja R. A. Palmans, and Andreas Heise**

Chirality is one of the most intriguing features of natural compounds. It determines, for instance, whether a molecule has a beneficial biological function. Consequently, it is of paramount importance in drug discovery to master asymmetric synthesis. For this reason, a number of methods have been developed in modern organic chemistry to obtain enantiopure compounds from racemic mixtures, for example, chemoenzymatic dynamic kinetic resolution (DKR).[1] In this process, the enzymatic kinetic resolution of a racemic compound is combined with the in situ chemical racemization of the chiral center of the substrate. While the theoretical yield in a normal kinetic resolution process is limited to 50%, which corresponds to total conversion of the preferred enantiomer, in DKR quantitative substrate conversion and high optical purity (>99% *ee*) can be obtained.

Despite the numerous asymmetric methods in organic synthesis, concepts for making chiral synthetic polymers are still limited. One obvious reason is the need for optically pure monomers. Possible sources are naturally occurring optically pure monomers such as L-lactide, which, however, limits the range of available monomer building blocks.

An alternative is the direct resolution polymerization from synthetic racemic monomers.[2] While most chemical polymerization catalysts are nonstereoselective and therefore not suited for the direct resolution of racemic monomer mixtures, enzymes can be be employed successfully in kinetic resolution polymerizations. In the recent past we and others have shown this for the ring-opening polymerization (ROP) of chiral caprolactones.[2c–e] This process yields polymers with molecular weights of up to 5000 g mol^{-1} and with over 98% *ee*. However, due to the maximum conversion of 50% in kinetic resolutions it cannot be applied in the polycondensation of racemic diols and dicarboxylic acid derivatives. The reason is that in a typical polycondensation, significant molecular weights can be realized only at an almost quantitative monomer conversion. We anticipated that for chiral monomers this can be achieved by a process analogous to the DKR of small molecules.

Here we report on our investigation of a novel concept for the synthesis of chiral polyesters, a lipase-catalyzed dynamic kinetic resolution polymerization of racemic monomers. As shown in Scheme 1, a mixture of stereoisomers of a secondary

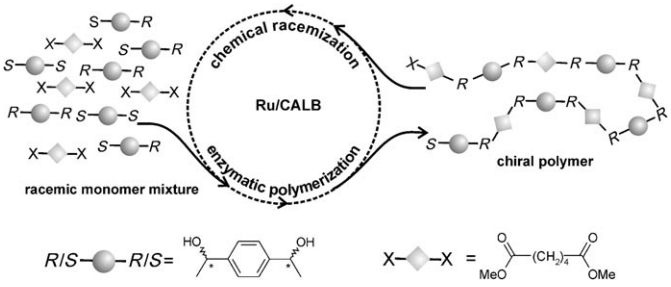

Scheme 1. Concept of dynamic kinetic resolution polymerization (DKRP) from a racemic diol and a dicarboxylic acid derivative. CALB = *Candida antarctica* lipase B.

diol is enzymatically polymerized with a difunctional acyl donor (dicarboxylic acid derivative). Because of its enantioselectivity the lipase converts only the hydroxy groups at the *R*-configured centers. In situ racemization of the hydroxy-substituted stereocenters from the *S* to the *R* configuration allows the polymerization to proceed to high conversion. We recently reported the combination of racemization and enzymatic ring opening of chiral lactones; the two reaction steps were conducted alternating in separate reaction vessels and low-molecular-weight oligomers were obtained (degree of polymerization 3–5).[3] In contrast, our goal here is the combination of DKR with a polymerization process in one pot, thereby building up polymers of significant molecular weight and with high optical purity.

The applied catalyst system consists of the Noyori-type ruthenium catalyst **3** and an immobilized *Candida antarctica* Lipase B (Novozym 435). This catalyst combination has been used successfully for the DKR of monofunctional compounds.[4] Since this combination tolerates a wide range of acyl donors, we expected that it would also be suitable with difunctional acyl donors for the formation of polycondensates. Based on the high enantioselectivity of CALB in the esterification of secondary benzylic alcohols (reactivity ratio $R/S \approx 1 \times 10^6$),[5] we chose the racemic α,α′-dimethyl-1,4-benzenedimethanol (**1**) as the diol component and dimethyl adipate (DMA, **2**) as the acyl donor (Scheme 2).

The selectivity of the catalyst combination with **2** as the acyl donor was confirmed in a DKR of racemic (monofunctional) 1-phenylethanol. The *R*-selective acylation proceeded smoothly within 18 h to provide the diester, and subsequent hydrolysis yielded pure *(R)*-1-phenylethanol with 99% *ee* (chiral GC). Subsequently, the DKR polymerization was conducted with **1** and **2** in a 1:1 molar ratio. In this process it is important that the acyl donor is present in stoichiometric

[*] Dr. I. Hilker, Dr. G. Rabani, G. K. M. Verzijl, Dr. A. Heise
DSM Research
P.O. Box 18, 6160 MD Geleen (The Netherlands)
Fax: (+31) 46-476-0508
E-mail: andreas.heise@dsm.com
Dr. A. R. A. Palmans
Laboratory of Macromolecular and Organic Chemistry
Technische Universiteit Eindhoven
P.O. Box 513, 5600 MB Eindhoven (The Netherlands)

[**] This work was supported in part by the Marie Curie Action RTN program "*Biocatalytic Approach to Material Design*" (BIOMADE; I.H. contract no. MRTN-CT-2004-505147) and by the NWO (grant to A.R.A.P.).

Supporting information for this article is available on the WWW under http://www.angewandte.org or from the author.

InterScience © 2006 Wiley-VCH Verlag GmbH & Co. KGaA, Weinheim

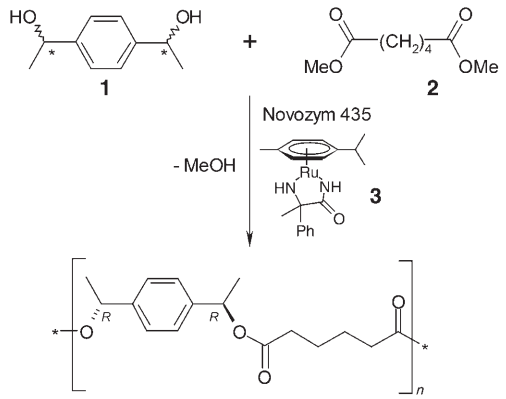

Scheme 2. Reaction sequence for the one-pot DKR polymerization.

amounts, whereas the use of an excess is common practice in conventional DKR. Control experiments proved that neither the ruthenium catalyst nor Novozym 435 alone led to polymer formation. As expected, with Novozym 435 only 50% conversion and thus low-molecular-weight oligomers were obtained since **1** consists of a statistical mixture of *R*,*R*, *S*,*S*, and *R*,*S* diastereoisomers (1:1:2). The extremely low reactivity of the hydroxy groups at the *S*-configured centers limits chain growth by acting as chain stoppers in the enzymatic (poly)esterification process. This proves that without transformation of hydroxy-substituted stereocenters, higher molecular weight products are not possible.

Polymers of higher molecular weight were obtained only when the immobilized lipase and the racemization catalyst were used in combination. The reaction was allowed to proceed over four days, during which time the molecular weight was seen to gradually increase to 3000–4000 g mol^{-1} according to size exclusion chromatography (SEC, polystyrene standards). Moreover, the optical rotation of the reaction mixture increased from −0.6° to 128° during the process, which further confirms the enrichment of *R*,*R* enantiomer in the reaction product. These results suggest that the enzymatic polymerization and the metal-catalyzed racemization work concurrently.

Further evidence for the in situ racemization was obtained by monitoring the change of the enantiomeric composition of **1** during the reaction by chiral GC (Figure 1). In order to assess both the diols present as unreacted monomers and incorporated in the polymer, the samples were hydrolyzed prior to chiral-GC analysis. Before the start of the reaction, the mixture shows the expected *S*,*S*/*R*,*R*/*R*,*S* diastereomer ratio (1:1:2) corresponding to a *R*/*S* group ratio of 1:1 (Figure 1). During the course of the reaction all hydroxy groups at *R*-configured centers are gradually incorporated into the polymerization product while re-equilibration by the racemization catalyst transforms free hydroxy-functionalized *S*-configured centers into the reactive *R* configuration. Consequently one expects the amount of *S*,*S*- and *R*,*S*-diol to decrease and the relative *R*/*S* group ratio to increase. Inspection of Figure 1 shows that after 30 h of reaction the *S*,*S* enantiomer has indeed almost completely disappeared while the ratio of *R*,*R* to *R*,*S* monomer is approximately 3:1 (*R*/*S* ≈ 7:1). After 70 h and 92% conversion of hydroxy groups, no further conversion was observed yielding a final *R*,*R*/*R*,*S* ratio of 16:1 (*R*/*S* ≈ 33:1). It is reasonable to assume that the racemization of the free diols as well as the esterification of the alcohols in *R* configuration occurs quickly. In comparison, long chains with a terminal hydroxy-substituted *S*-configured center would racemize much more slowly. This suggests that eventually all polycondensation products are end-capped with *S* stereocenters (chain stoppers). As a result, the racemization occurs at the end-groups of polymer chains of gradually increasing length.

An average degree of polymerization can be calculated from the final enantiomer composition if one assumes that all polymer chains are end-capped with an *R*,*S* diastereomer on both ends, in other words, each polymer chain contains two such units. For the detected *R*,*R*/*R*,*S* ratio of 16:1 this means an average degree of polymerization of 67 ($32 \times RR + 2 \times RS + 33 \times \mathbf{2}$), which corresponds to an maximum theoretical number average molecular weight of ca. 9300 g mol^{-1}. The average molecular weight obtained from SEC analysis is $M_w = 3400$ g mol^{-1} ($M_n = 2100$ g mol^{-1}) based on polystyrene standards (Figure 2). The discrepancy with the calculated molecular weight can be explained partly by the difference in the hydrodynamic volume between the SEC standards and the polyester. Furthermore, the calculation does not take further side reactions into account. ^{1}H NMR spectra indicate that approximately 3% of the hydroxy groups are oxidized to

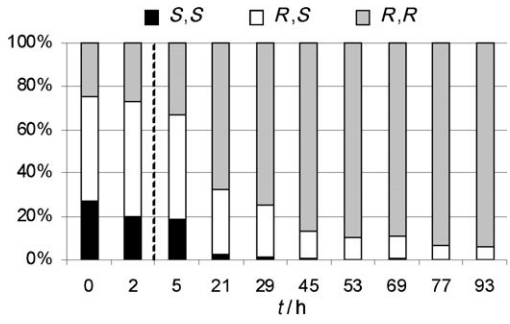

Figure 1. Change of overall stereoisomer composition of **1** during the course of DKR polymerization determined by chiral GC after polyester hydrolysis. Dashed line indicates the addition of **3**. Fresh lipase was added every 12 h.

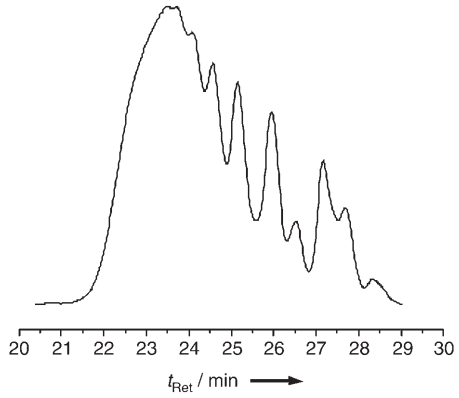

Figure 2. SEC plot of polymer obtained after DKR polymerization ($M_w = 3400$ g mol^{-1}; $M_n = 2100$ g mol^{-1}). t_{Ret} = retention time.

 © 2006 Wiley-VCH Verlag GmbH & Co. KGaA, Weinheim

the ketone, which creates monofunctional chain stoppers. This side reaction is caused by the racemization catalyst (hydrogen transfer) and consequently lowers the obtained molecular weight of the polymer. Minimizing all side reactions should eventually result in molecular weights close to the calculated one.

In conclusion we have shown that DKR can be combined with enzymatic polymerization for the synthesis of chiral polyesters from racemic secondary diols. This concept offers an efficient route for the one-pot synthesis of chiral polymers from nonnatural monomers. Further research will aim at understanding the mechanism and suppressing side reactions in order to increase the molecular weight of the polymeric product.[6]

Received: October 3, 2005
Published online: February 27, 2006

Keywords: chiral resolution · enzyme catalysis · polymerization

[1] a) A. L. E. Larsson, B. A. Persson, J.-E. Bäckvall, *Angew. Chem.* **1997**, *109*, 1256; *Angew. Chem. Int. Ed. Engl.* **1997**, *36*, 1211; b) O. Pamiès, J.-E. Bäckvall, *Chem. Rev.* **2003**, *103*, 3247; c) O. Pamiès, J.-E. Bäckvall, *TIBTECH* **2004**, *22*, 130; d) J. H. Choi, Y. K. Choi, Y. H. Kim, E. S. Park, E. J. Kim, M. J. Kim, J. W. Park, *J. Org. Chem.* **2004**, *69*, 1972; e) B. Martín-Matute, M. Edin, K. Bogár, J.-E. Bäckvall, *Angew. Chem.* **2004**, *116*, 6697; *Angew. Chem. Int. Ed.* **2004**, *43*, 6535; f) G. K. M. Verzijl, J. G. De Vries, Q. B. Broxterman, *Tetrahedron: Asymmetry* **2005**, *16*, 1603.

[2] a) S. Namekawa, S. Suda, H. Uyama, S. Kobayashi, *Int. J. Biol. Macromol.* **1999**, *25*, 145; b) H. Kikuchi, H. Uyama, S. Kobayashi, *Macromolecules* **2000**, *33*, 8971; c) T. F. Al-Azemi, L. Kondaveti, K. S. Bisht, *Macromolecules* **2002**, *35*, 3380; d) J. Peeters, M. Veld, F. Scheijen, A. Heise, A. R. A. Palmans, E. W. Meijer, *Biomacromolecules* **2004**, *5*, 1862; e) B. A. C. van As, P. Thomassen, B. Kalra, R. A. Gross, E. W. Meijer, A. R. A. Palmans, A. Heise, *Macromolecules* **2004**, *37*, 8973.

[3] B. A. C. van As, J. van Buijtenen, A. Heise, Q. B. Broxterman, G. K. M. Verzijl, A. R. A. Palmans, E. W. Meijer, *J. Am. Chem. Soc.* **2005**, *127*, 9964.

[4] G. K. M. Verzijl, J. G. De Vries, Q. B. Broxterman, PCT Int. Appl. WO 010396 A120011129, **2001**.

[5] A. O. Magnusson, M. Takwa, A. Hamburg, K. Hult, *Angew. Chem.* **2005**, *117*, 4658; *Angew. Chem. Int. Ed.* **2005**, *44*, 2.

[6] Supporting Information available: Experimental procedures, monomer conversion plot.

 © 2006 Wiley-VCH Verlag GmbH & Co. KGaA, Weinheim

Coordination Chemistry

DOI: 10.1002/anie.200504093

Borylene Transfer under Thermal Conditions: Synthesis and Structure of a Tetrarhodium Bisborylene Complex**

Holger Braunschweig, Melanie Forster, and Krzysztof Radacki*

Transition-metal borylene complexes have received considerable attention, owing to their close relationship to pivotal organometallic compounds, such as carbonyl and carbene complexes,[1–4] as well as their potential as sources of borylenes (that is, B–R) for organic reactions.[5] Despite recent successes in the realization of novel coordination modes in metalloborylene complexes[6,7] and heterodinuclear borylene complexes,[8,9] the scope of coordination modes encountered in borylene complexes is still very limited, as only combinations between a single borylene ligand and one or two metal centers are known. Given the parallels in the structural chemistry of borylene and carbonyl complexes, this fact is surprising, especially when the wealth of polynuclear carbonyl complexes is considered.[10] The main reason for this difference seems to be the ready availablity of the metastable CO, which reacts in various stoichiometries with metal precursors to yield polynuclear carbonyl compounds with complex structures. Similarly, the heavier congeners of borylenes, in particular Cp*Ga and Cp*In ($Cp^* = C_5Me_5$), are also available for the synthesis of mono- or polynuclear complexes.[11] As borylenes are extremely reactive species, they cannot be handled under standard conditions,[3] but must be generated within the coordination sphere of a transition metal. Salt-elimination reactions between anionic metal carbonylates and haloboranes have been used for the purpose, and the first bridged and terminal borylene complexes were thus obtained.[12,13] However, this method may have reached its limits, because it is restricted to a few specific combinations of transition metals and boranes.[14–16]

More recently, we were able to show that photochemically induced borylene transfer is a valuable method for the synthesis of borylene complexes that cannot be obtained by salt elimination.[17,18] Furthermore, this approach allows the transfer of the borylene unit to organic substrates.[5] The reactivity of borylene complexes toward transition-metal species under nonphotolytic (that is, thermal) conditions was previously restricted to the addition of the $\{Pd(PCy_3)\}$ fragment (Cy = cyclohexyl) to $[(OC)_5M{=}BN(SiMe_3)_2]$ (M = Cr, W), which resulted in the clean formation of the first

[*] Prof. H. Braunschweig, M. Forster, Dr. K. Radacki
Institut für Anorganische Chemie
Bayerische Julius-Maximilians-Universität Würzburg
Am Hubland, 97074 Würzburg (Germany)
Fax: (+49) 931-888-4623
E-mail: h.braunschweig@mail.uni-wuerzburg.de

[**] This work was supported by the Deutsche Forschungsgemeinschaft.

InterScience
© 2006 Wiley-VCH Verlag GmbH & Co. KGaA, Weinheim

complexes with semibridging borylene ligands.[9] Herein, we report the selective synthesis of a novel tetranuclear rhodium complex, which is the first example of a bisborylene complex. This compound is formed in high yield by an unprecedented metal–metal borylene transfer at ambient temperature.

The reaction of the terminal borylene complexes $[(OC)_5M{=}BN(SiMe_3)_2]$ (M = Cr, **1**; M = W, **2**) with $[\{RhCl(CO)_2\}_2]$ (**3**) in C_6D_6 yields, within minutes, the tetranuclear bisborylene complex $[Rh_4\{\mu\text{-}BN(SiMe_3)_2\}_2(\mu\text{-}Cl)_4(\mu\text{-}CO)(CO)_4]$ (**4**; Scheme 1). After recrystallization in hexane, **4** was isolated as air- and moisture-sensitive black crystals in 43% (M = Cr, **1**) or 41% (M = W, **2**) yield.

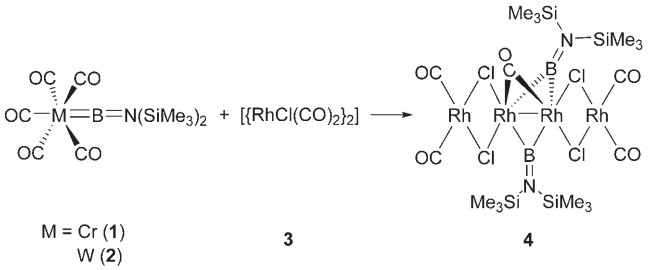

Scheme 1. Synthesis of the doubly borylene-bridged complex **4**.

The structure of **4** was unequivocally determined by single-crystal X-ray diffraction (Figure 1).[19] The core of the molecule is composed of a chain of four rhodium atoms, the internal metal centers are bridged by two borylene moieties and a CO ligand. The remarkably short Rh1–Rh2 distance between the two central rhodium atoms (2.5786(3) Å) is comparable to Rh–Rh distances of dinuclear complexes in which the rhodium atoms are bridged by three CO ligands, for example, 2.566(5) Å in $[Rh_2(\mu\text{-}CO)_3Cl_2(py)_4]$ (py = pyridine).[20] For both this compound and **4**, the presence of a Rh–Rh bond may be assumed, as the formal electron count of each rhodium center is odd. The distances between the central and terminal rhodium atoms, Rh1–Rh3 (3.0415(4) Å) and Rh2–Rh4 (3.0472(4) Å), are significantly longer than the Rh1–Rh2 distance. Both distances are, however, significantly shorter than the Rh–Rh bond in the starting compound **3** (3.31 Å).[21]

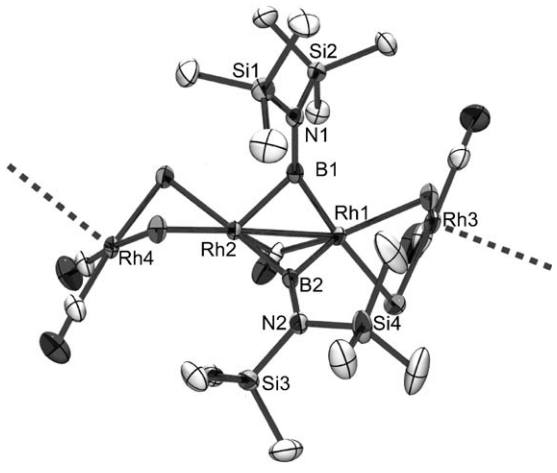

Figure 1. Molecular structure of **4** in the solid state. Bond lengths [Å] and angles [°]: Rh1–Rh2 2.5786(3), Rh1–Rh3 3.0415(4), Rh2–Rh4 3.0472(4), Rh3–Rh4 3.1833(4), B1–Rh1 2.004(3), B1–Rh2 2.051(3), B2–Rh1 2.076(3), B2–Rh2 2.003(3), B1–N1 and B2–N2 1.369(4); Si2-Si1-N1-B1 58.62(14), Si3-Si4-N2-B2 43.30(5). Thermal ellipsoids are set at 50% probability. Hydrogen atoms are omitted for clarity. Dashed lines indicate intermolecular Rh–Rh contacts.

The length of the B1–N1 and B2–N2 bonds (1.369(4) Å) is slightly shorter than that observed in the borylene-bridged manganese complex $[(\mu\text{-}BNMe_2)\{(\eta^5\text{-}C_5H_5)Mn(CO)_2\}_2]$ (1.390(1) Å),[12] indicating significant B–N double-bond character. The presence of the bulky $SiMe_3$ groups requires that the Si1-B1-Si2 and Si3-B2-Si4 planes twist by 58.6(14)° or 42.3(5)° out of the Rh1-B1-Rh2 and Rh1-B2-Rh2 planes, respectively, as previously described for similar structures.[22]

Interestingly, in the solid state, the individual tetramer units aggregate into neutral linear chains (Figure 2), featuring

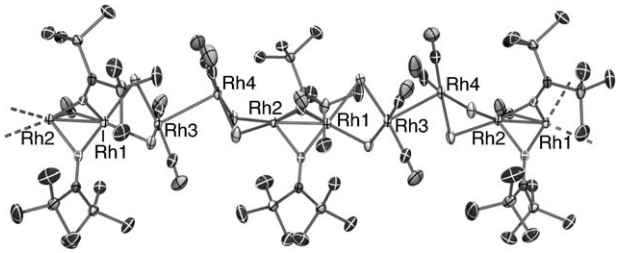

Figure 2. Linear chains of the tetranuclear complex **4** in the solid state. Thermal ellipsoids are set at 50% probability. Hydrogen atoms are omitted for clarity.

a relatively short intermolecular Rh3–Rh4 distance (3.1833(4) Å). This distance is longer than the Rh–Rh distances within the tetramers (2.5786(3)–3.0472(4) Å) and is approximately 0.3 Å longer than those in the mixed-valent polymer $[Rh(3,6\text{-}dbdiox\text{-}4,5\text{-}Cl_2)(CO)_2]_\infty$ (2.8629(2)–2.8984(3) Å; 3,6-dbdiox-4,5-Cl_2 = 3,6-di-*tert*-butyl-4,5-dichlorocatecholate),[23] but is similar to the Rh–Rh distances in the rhodium(I) complex $[Rh(3,6\text{-}dbsq)(CO)_2]_\infty$ (3.252(4) and 3.304(5) Å; 3,6-dbsq = 3,6-di-*tert*-butyl-1,2-benzosemiquinonate).[24]

Clearly, **4** is a product of a complicated reaction, in which $[M(CO)_6]$ (M = Cr, W) is also probably formed as a by-product. However, the $^{11}B\{^1H\}$ and ^1H NMR spectra of the reaction solutions reveal that they are surprisingly free from boron- or hydrogen-containing side products, with the exception of one equivalent of $Cl_2BN(SiMe_3)_2$ ($\delta(^{11}B)$ = 36 ppm; $\delta(^1H)$ = 0.21 ppm).[25] Since no loss of chloride ligands from the starting material **3** is required for the formation of **4**, it is likely that the side product $Cl_2BN(SiMe_3)_2$ is produced in an independent process. The $^{11}B\{^1H\}$ NMR spectrum of the new compound **4** features a broad singlet at δ = 74 ppm ($\omega_{1/2}$ = 1071 Hz), which is shifted upfield with respect to those of the starting materials (δ = 92 ppm, **1**; δ = 86 ppm, **2**).[16] Such an upfield shift is unusual, as borylene-bridged complexes usually exhibit downfield-shifted ^{11}B resonances between δ = 98 and 120 ppm.[2] The CO ligand remains in a bridging position in solution, as demonstrated by

 © 2006 Wiley-VCH Verlag GmbH & Co. KGaA, Weinheim

the presence of a band at $\tilde{\nu} = 1856\ cm^{-1}$ in the IR spectrum of **4** in toluene.

Herein, we have described the first transition-metal borylene complex featuring two bridging borylene ligands. The compound was obtained by an unprecedented thermal borylene-transfer reaction, and comprises a linear chain of four rhodium atoms, a relatively rare structural motif.

Experimental Section

All manipulations were conducted under an atmosphere of dry argon using either standard Schlenk techniques or a glove box.

4: Solid **3** (0.054 g, 0.138 mmol) was added to an orange solution of **1** (0.075 g, 0.207 mmol) in C_6D_6 (0.6 mL) at ambient temperature. The color of the solution changed immediately to dark brown. After 30 min, the solvent was removed in vacuo. The black solid obtained was dissolved in hexane (2 mL). After filtration, cooling the solution to −35 °C yielded black crystals of **4** (0.061 g, 43 %, based on rhodium). ^{1}H NMR (500 MHz, C_6D_6, 25 °C, TMS): $\delta = 0.45$ ppm (s, 36 H, $SiMe_3$); $^{13}C\{^1H\}$ NMR (126 MHz, C_6D_6, 25 °C): $\delta = 178.3$ (d, $^1J(C,Rh) = 76$ Hz, CO), 3.1 ppm (s, $SiMe_3$), a signal for the bridging CO was not observed; $^{11}B\{^1H\}$ NMR (64 MHz, C_6D_6, 25 °C): $\delta =$ 74 ppm (s, $\omega_{1/2} = 1071$ Hz). IR (toluene): $\tilde{\nu} = 2089$, 2032, 1944, 1856 cm^{-1} (C≡O). C,H,N analysis (%) calcd for $C_{17}H_{36}N_2B_2Cl_4O_5Si_4Rh_4$: C 19.71, H 3.50, N 2.70; found: C 20.07, H 3.18, N 2.30.

In an analogous manner, **4** was also obtained through the reaction of **2** (0.075 g, 0.152 mmol) and **3** (0.039 g, 0.101 mmol) in 41 % yield (based on rhodium, 0.040 g).

Received: November 17, 2005
Published online: February 24, 2006

Keywords: boron · borylene complexes · bridging ligands · rhodium

[1] H. Braunschweig, *Angew. Chem.* **1998**, *110*, 1882 – 1898; *Angew. Chem. Int. Ed.* **1998**, *37*, 1786 – 1801.
[2] H. Braunschweig, M. Colling, *Coord. Chem. Rev.* **2001**, *223*, 1 – 51.
[3] H. Braunschweig, *Adv. Organomet. Chem.* **2004**, *51*, 163 – 192.
[4] H. Braunschweig, M. Colling, *Eur. J. Inorg. Chem.* **2003**, 393 – 403.
[5] H. Braunschweig, T. Herbst, D. Rais, F. Seeler, *Angew. Chem.* **2005**, *117*, 7627 – 7629; *Angew. Chem. Int. Ed.* **2005**, *44*, 7461 – 7463.
[6] H. Braunschweig, K. Radacki, D. Scheschkewitz, G. R. Whittell, *Angew. Chem.* **2005**, *117*, 1685 – 1688; *Angew. Chem. Int. Ed.* **2005**, *44*, 1658 – 1661.
[7] H. Braunschweig, K. Radacki, D. Rais, F. Seeler, *Angew. Chem.* **2006**, *118*, 1087 – 1090; *Angew. Chem. Int. Ed.* **2006**, *45*, 1066 – 1067.
[8] H. Braunschweig, K. Radacki, D. Rais, F. Seeler, K. Uttinger, *J. Am. Chem. Soc.* **2005**, *127*, 1386 – 1801.
[9] H. Braunschweig, D. Rais, K. Uttinger, *Angew. Chem.* **2005**, *117*, 3829 – 3832; *Angew. Chem. Int. Ed.* **2005**, *44*, 3763 – 3766.
[10] F. A. Cotton, G. Wilkinson, *Advanced Inorganic Chemistry*, *5th ed.*, Wiley, New York, **1988**.
[11] C. Gemel, T. Steinke, M. Cokoja, A. Kempter, R. A. Fischer, *Eur. J. Inorg. Chem.* **2004**, 4161 – 4176.
[12] H. Braunschweig, T. Wagner, *Angew. Chem.* **1995**, *107*, 904 – 905; *Angew. Chem. Int. Ed. Engl.* **1995**, *34*, 825 – 826.
[13] H. Braunschweig, C. Kollann, U. Englert, *Angew. Chem.* **1998**, *110*, 3355 – 3357; *Angew. Chem. Int. Ed.* **1998**, *37*, 3179 – 3180.
[14] H. Braunschweig, C. Kollann, K. W. Klinkhammer, *Eur. J. Inorg. Chem.* **1999**, 1523 – 1529.
[15] H. Braunschweig, M. Colling, C. Kollann, K. Merz, K. Radacki, *Angew. Chem.* **2001**, *113*, 4327 – 4329; *Angew. Chem. Int. Ed.* **2001**, *40*, 4198 – 4200.
[16] D. L. Coombs, S. Aldridge, C. Jones, *Chem. Commun.* **2002**, 856 – 857.
[17] H. Braunschweig, M. Colling, C. Kollann, H.-G. Stammler, B. Neumann, *Angew. Chem.* **2001**, *113*, 2359 – 2361; *Angew. Chem. Int. Ed.* **2001**, *40*, 2298 – 2300.
[18] H. Braunschweig, M. Colling, C. Hu, K. Radacki, *Angew. Chem.* **2003**, *115*, 215 – 218; *Angew. Chem. Int. Ed.* **2003**, *42*, 205 – 208.
[19] Intensity data for **4** were collected on a Bruker APEX diffractometer with a CCD area detector and graphite-monochromated $Mo_{K\alpha}$ radiation. The structure was solved using direct methods, refined with the SHELX software package (G. Sheldrick, SHELX-97, Universität Göttingen, **1997**), and expanded using Fourier techniques. All non-hydrogen atoms were refined anisotropically. Hydrogen atoms were assigned idealized positions and were included in the structure-factor calculations. Crystal data for **4**: $C_{17}H_{36}B_2Cl_4N_2O_5Rh_4Si_4$, $M_r = 1035.90$, translucent black blocks, $0.24 \times 0.15 \times 0.08\ mm^3$, orthorhombic, *Pbca*, $a = 14.5097(12)$, $b = 21.4616(18)$, $c = 23.971(2)$ Å, $V = 7464.7(11)$ Å^3, $Z = 8$, $\rho_{calcd} = 1.844\ g\,cm^{-3}$, $\mu = 2.180\ cm^{-2}$, $F(000) = 4048$, $T = 153(2)$ K, $R_1 = 0.0335$, $wR_2 = 0.0767$, 7597 independent reflections ($2\theta = 52.72°$), 343 parameters. CCDC-293577 (**4**) contains the supplementary crystallographic data for this paper. These data can be obtained free of charge from The Cambridge Crystallographic Data Centre via www.ccdc.cam.ac.uk/data_request/cif.
[20] B. T. Heaton, C. Jacob, J. T. Sampanthar, *J. Chem. Soc. Dalton Trans.* **1998**, 1403 – 1410.
[21] L. F. Dahl, C. Martell, D. L. Wampler, *J. Am. Chem. Soc.* **1961**, *835*, 1761 – 1762.
[22] H. Braunschweig, C. Kollann, U. Englert, *Eur. J. Inorg. Chem.* **1998**, 465 – 468.
[23] M. Mitsumi, H. Goto, S. Umebayashi, Y. Ozawa, M. Kobayashi, T. Yokoyama, H. Tanaka, S. Kuroda, K. Toriumi, *Angew. Chem.* **2005**, *117*, 4236 – 4240; *Angew. Chem. Int. Ed.* **2005**, *44*, 4164 – 4168.
[24] C. W. Lange, M. Földeàki, V. I. Nevodchikov, V. K. Cherkasov, G. A. Abakumov, C. G. Pierpont, *J. Am. Chem. Soc.* **1992**, *114*, 4220 – 4222.
[25] A. J. Banister, N. N. Greenwood, B. P. Stranghan, J. Walker, *Z. Anorg. Allg. Chem.* **1976**, 421, 105 – 110.

 © 2006 Wiley-VCH Verlag GmbH & Co. KGaA, Weinheim

Photochemistry

DOI: 10.1002/anie.200504056

Efficient Photoionization of a Norrish II Diradical

Martin Goez and Valentin Zubarev*

The photochemistry of reactive intermediates in solution[1] is a fascinating subject because of its promise of new mechanisms and applications.[2] Photoionizations of excited singlet and triplet states are common; examples of photoionizations of radicals[3] and radical anions[4] are known. Here, we present the first report on the photoionization of a diradical and show that it is considerably more efficient than that of its precursor triplet.

We performed laser flash photolysis at very high light intensities, where mechanisms involving more than one photon reveal themselves much more clearly than under the usual conditions. Our setup[4c] allows two-flash two-color experiments (355 or 266 nm, pulse width 6 ns; 308 nm, pulse width 30 ns; freely adjustable interpulse delay) and homogeneously illuminates a well-defined reaction volume, thus permitting quantitative determinations of absolute concentrations of transients. As the primary observable, the concentration of the hydrated electron $e^{\bullet-}_{aq}$ directly at the end of a laser pulse was measured through its optical absorbance.[5]

Alkyl phenyl ketones M can be ionized with 308 nm light.[4d,6] The usual mechanism is a sequential two-photon process as displayed in Scheme 1. Absorption of the first

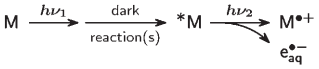

Scheme 1. Sequential two-photon ionization of a ketone, M.

photon leads to an intermediate *M, normally the triplet state, which is then ionized by the second photon. Even at our high light intensities, the rate of the first step is limited by the excitation of M because of the small extinction coefficient at 308 nm; the subsequent dark reactions to give *M, such as intersystem crossing, are much faster.

When the ketone bears a hydrogen atom in the γ position, its triplet is rapidly transformed into a 1,4-diradical by an intramolecular hydrogen abstraction (the Norrish II reaction).[7] We were interested in how this classic photoreaction influences the photoionization. Figure 1 compares the electron yields, as functions of the laser intensity in single-flash experiments at 308 nm, for two model compounds in degassed aqueous base (nominal concentration of KOH, 0.4 M), γ-methylvalerophenone as an efficient Norrish II substrate,[8]

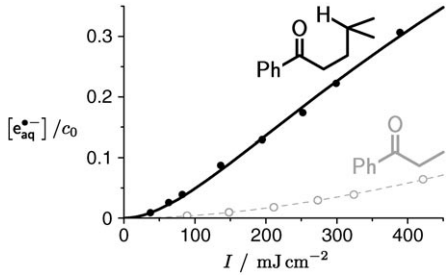

Figure 1. Electron concentrations relative to the substrate concentration c_0 as functions of the laser intensity I at 308 nm for propiophenone (open symbols and dashed line; $c_0 = 1.66\times10^{-4}$ M) and γ-methylvalerophenone (filled symbols and solid line; $c_0 = 7.15\times10^{-5}$ M) at pH 13.54. The formulas of the substrates are shown at the curves. The fit functions are given by Equation (1). Constant parameter $k_d\tau$: 0 (propiophenone) and 0.41 (γ-methylvalerophenone); best-fit parameters κ_{exc} and κ_{ion}: 1.02×10^{-3} cm² mJ^{-1} and 9.19×10^{-4} cm² mJ^{-1} (propiophenone); 1.21×10^{-3} cm² mJ^{-1} and 1.43×10^{-2} cm² mJ^{-1} (γ-methylvalerophenone). The ratio of the κ_{exc} was fixed at the ratio of the extinction coefficients of the two ketones at 308 nm (1.19).

and propiophenone as the longest-chain alkyl phenyl ketone that is not yet capable of undergoing this reaction. It is evident that the Norrish II substrate produces substantially more electrons.

The upward curvature of the intensity dependence bears out that the ionization of the Norrish II substrate is still biphotonic. With the mechanism of Scheme 1, the electron yield is determined by the (intensity-dependent) rates of both steps. As expected, the extinction coefficients of the two ground-state ketones, and thus the rates of production of *M for given laser intensity, are very similar. Hence, this step cannot explain the observed effect, and the different yields have to be ascribed to different properties of the photoionizable intermediate *M. It is natural to assume that they reflect the differences between the triplet (for propiophenone) and the Norrish II diradical (for γ-methylvalerophenone) because the latter is formed within less than 5 ns,[8] in other words, much faster than the duration of the laser pulse.

This is corroborated by the results of pH variation. As Figure 2 shows, the electron yield is independent of pH in the case of propiophenone, whereas a titration curve with a turning point at pH 11.5 is found in the case of γ-methyl-

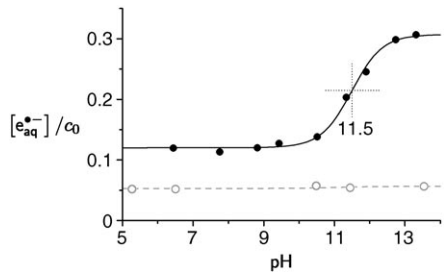

Figure 2. Dependence of the relative electron concentrations $[e^{\bullet-}_{aq}]/c_0$ on the pH (adjusted with KOH and phosphate buffers of variable composition) at 308 nm and constant excitation intensity (392 mJ cm^{-2}). Open symbols and dashed line: propiophenone, $c_0 \approx 2.7\times10^{-4}$ M; filled symbols and solid line: γ-methylvalerophenone, $c_0 \approx 7.9\times10^{-5}$ M. The exact pH and substrate concentration c_0 were determined before each experiment in the solution used.

[*] Prof. Dr. M. Goez, V. Zubarev
Fachbereich Chemie
Martin-Luther-Universität Halle-Wittenberg
Kurt-Mothes-Strasse 2, 06120 Halle/Saale (Germany)
Fax: (+49) 345-552-7657
E-mail: goez@chemie.uni-halle.de

© 2006 Wiley-VCH Verlag GmbH & Co. KGaA, Weinheim

valerophenone. Although in neutral solution the Norrish II substrate exhibits a reduced yield, it still produces more than twice the amount of electrons than the simpler ketone does.

The absorption spectrum of M is not influenced by the pH value. Nor can the extinction coefficient and photoionization quantum yield of the triplet change with pH, as the absence of an effect in the propiophenone experiment shows. The difference between the two substrates that persists in neutral solution finally excludes a transition from triplet ionization at low pH to diradical ionization at high pH as the origin of the pH dependence, which would also be difficult to reconcile with the short lifetime of the γ-methylvalerophenone triplet. Instead, a deprotonation of the diradical in basic medium provides a natural explanation.

Except for their intramolecular deactivation steps, Norrish II diradicals are describable as separate alkyl and ketyl radical moieties.[8] The alkyl radical moiety cannot be deprotonated, so it could only cause a pH-independent contribution to photoionization. Even that is thought very unlikely in our case because of insufficient absorption (the extinction coefficient of the *tert*-butyl radical at 308 nm is as low as $200\,\text{M}^{-1}\,\text{cm}^{-1}$).[9] In contrast, both the ketyl radical and its deprotonated form, the radical anion, have medium to strong absorptions at 308 nm, and their photoionization is much more favorable energetically than alkyl radical photoionization because the by-product is a closed-shell moiety, that is, the regenerated carbonyl group. Of importance for the electron yield is the red shift of the absorption band caused by the deprotonation,[10] which leads to a considerable increase of the extinction coefficient at 308 nm.

Definitive evidence that the Norrish II diradical is responsible for the difference in the electron yields was obtained by two-pulse experiments. They allow the separation of ground-state excitation and the actual photoionization, which provides a twofold advantage. First, the weak absorption of the ground-state ketone M at 308 nm can be overcome by the choice of a different wavelength, 266 nm, for the first pulse; when the second pulse is left at 308 nm, the small extinction coefficient of M is turned into an asset because that pulse now predominantly excites the intermediate. Second, the lifetime of the photoionizable intermediate can be determined by varying the interpulse delay.

With both ketones studied, the extinction coefficient of M is about 16 times higher at 266 nm than at 308 nm. However, this is not paralleled by a similar increase of the extinction coefficients of the photoionizable intermediates: at 266 nm, the electron yield is even slightly smaller than at 308 nm. With a suitably attenuated 266-nm pulse, about 30% of the substrate can be converted into *M with negligible electron generation. By the second pulse, at 308 nm, the respective intermediate is photoionized after a delay Δt.

In Figure 3 the electron yields relative to the maximum in each system have been plotted as functions of Δt, allowing a direct comparison of the lifetimes of the electron precursors. With propiophenone one observes a slow decrease on a timescale of a few microseconds, as expected for the photoionization of the triplet state. However, with γ-methylvalerophenone the decrease is much more rapid; a fit by a monoexponential decay curve gave a time constant of 74 ns.

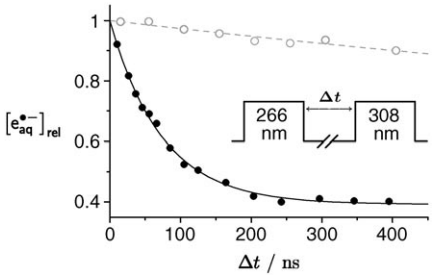

Figure 3. Two-pulse experiments with the pulse sequence represented in the inset; pulse intensities: 35 mJ cm^{-2} (266 nm) and 400 mJ cm^{-2} (308 nm). Shown are the electron yields scaled to maximum, $[e^-_{aq}]_{rel}$, as functions of the interpulse delay Δt for propiophenone (open symbols and dashed line; $c_0 = 1.66\times10^{-4}$ M) and γ-methylvalerophenone (filled symbols and solid line; $c_0 = 8.68\times10^{-5}$ M), both at pH 13.5.

It is well known[8] that Norrish II diradicals cleave on that timescale to give an alkene and an enol (or, in the case of a deprotonated diradical, an enolate). These diamagnetic products are not expected to be photoionized as efficiently as the diradical, if at all, so the two-pulse experiment monitors the diradical decay. For final confirmation, we omitted the second pulse and observed the decay of the diradical directly, using its characteristic absorption at 440 nm. The diradical lifetime obtained in this way (76 ns) and the decay time constant in the two-pulse experiment were identical within experimental error. A very similar lifetime (84 ns) was found in neutral solution.

We determined the pK_a of the γ-methylvalerophenone ketyl radical to be 9.7 by generating hydrated electrons from 8-amino-2-naphthalenesulfonic acid with 355-nm light at different pH values, scavenging them with our ketone, which does not absorb at that wavelength, and observing the ketyl radical or its anion at 308 nm. The obtained value agrees very well with that for the acetophenone ketyl radical (p$K_a = 10.0$).[10] The significantly higher turning point of the titration curve in Figure 2, at pH 11.5, presents a discrepancy that might seem to contradict the paradigm of independent ketyl and alkyl radical moieties in the Norrish II diradical.

An apparent pK_a in methanol/water of 11.8 was also reported for the diradical of γ-phenylbutyrophenone, a very close analogue to our diradical, and ascribed to a solvent effect.[11] In our experiments, however, an apparent pK_a that is shifted to a higher value is most likely due to a rate effect: Regardless of pH, direct formation of the diradical with the deprotonated ketyl moiety is impossible, because it is the product of an intramolecular hydrogen abstraction by the carbonyl group. At pH values higher than the true pK_a, the ketyl moiety will subsequently be deprotonated, resulting in a higher photoionization probability, but our experiment only responds to those deprotonated diradicals that are formed *within the duration of the laser pulse*. When the pH is increased, the concentration of proton acceptors rises, the deprotonation becomes faster, and the fraction of deprotonated diradicals available within the kinetic window increases. Experiments with different buffer concentrations might support this hypothesis, but the feasible range of variation is rather limited at that high pH.

 © 2006 Wiley-VCH Verlag GmbH & Co. KGaA, Weinheim

Scheme 2 summarizes the mechanism of the photoionization of γ-methylvalerophenone as inferred from these experiments. After excitation of the substrate by the first photon and intersystem crossing on a subnanosecond timescale,[6] the

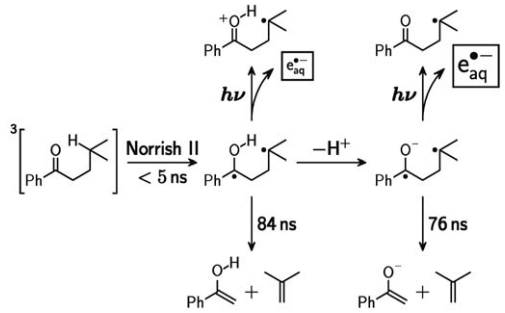

Scheme 2. Photoionization of γ-methylvalerophenone via its diradical.

first species potentially capable of absorbing the second photon is the triplet. However, the probability of its photoionization is low because it is converted into a Norrish II diradical within a few nanoseconds,[8] which is still fast compared to the duration of the ionizing laser pulse. In basic solution, the ketyl moiety of the diradical is deprotonated. Both the unmodified and the deprotonated ketyl moiety can be photoionized, the latter yielding more electrons, and this ionization competes with chemical deactivation of the diradical.

An approximate kinetic treatment is possible for the limiting cases of very high or very low pH, where the diradical is present exclusively in either of its two forms (see Figure 2). Photoionization of the short-lived precursor triplet and of the ketone formed by diradical cleavage are neglected, the latter because its concentration during the pulse is low and its structure precludes another Norrish II reaction, so its ionization must be less efficient than that of the parent compound. The mechanism is thus that of Scheme 1 enhanced by an additional light-independent deactivation pathway of *M (with rate constant k_d). With the assumption of a rectangular laser pulse of duration τ, diradical formation occurs with a rate constant $\kappa_{exc}I/\tau$ and photoionization with a rate constant $\kappa_{ion}I/\tau$, where each parameter κ is proportional to the product of the extinction coefficient of the species absorbing the photon and the quantum yield of the resulting process.[4e] The intensity dependence of the electron yield at the pulse end is given by Equation (1). When k_d is set to zero, Equation (1) can also be applied to the photoionization of propiophenone.

$$[e^{\bullet-}_{aq}]/c_0 = \frac{\kappa_{ion}I}{\kappa_{ion}I + k_d\tau}\left(1 - \frac{\kappa_{exc}I}{\kappa_{exc}I - (\kappa_{ion}I + k_d\tau)}\exp[-(\kappa_{ion}I + k_d\tau)] + \frac{\kappa_{ion}I + k_d\tau}{\kappa_{exc}I - (\kappa_{ion}I + k_d\tau)}\exp[-\kappa_{exc}I]\right) \quad (1)$$

Fitting Equation (1) to the data (see the legend of Figure 1) shows that for the deprotonated diradical the constant κ_{ion} is larger by a factor 15.6 compared to that of the triplet; in neutral solution, in other words, for the initially formed diradical, this factor is found to be only 2.1. The scavenging experiment described above gave extinction coefficients of the γ-methylvalerophenone ketyl radical and radical anion at 308 nm of 1900 and 15100 $M^{-1}cm^{-1}$, the ratio of which closely parallels the ratio of κ_{ion} in neutral and basic solution. Hence, we conclude that deprotonation of the ketyl moiety does not influence the photoionization quantum yield, and that the different electron yield (Figure 2) is solely due to the change of the extinction coefficient. The extinction coefficient of the γ-methylvalerophenone triplet should practically be identical to that of the propiophenone triplet, 4400 $M^{-1}cm^{-1}$ at 308 nm.[4d] The same comparison thus reveals that the quantum yield of photoionization of the diradical is almost five times higher than that of the triplet, which is in good agreement with the previously obtained[4d] ratio for the propiophenone triplet and radical anion.

Our results for other systems[4b–e] suggest that the conversion of a triplet state into the corresponding radical or radical anion, as can be achieved by the addition of a suitable quencher, is a general method to increase the photoionization quantum yield, presumably because this transformation suppresses reverse intersystem crossing of the upper excited state. The diradical studied here represents an intramolecular application of that principle.

Received: November 15, 2005
Published online: February 24, 2006

Keywords: diradicals · ketones · laser chemistry · photoionization · photolysis

[1] a) J. C. Scaiano in *Kinetics and Spectroscopy of Carbenes and Biradicals* (Ed.: M. S. Platz), Plenum, New York, **1990**, pp. 353–368; b) L. J. Johnston, *Chem. Rev.* **1993**, *93*, 251–266; c) W. G. McGimpsey in *Molecular and Supramolecular Photochemistry*, *Vol. 2* (Eds.: V. Ramamurthy, K. S. Schanze), Marcel Dekker, New York, **1998**, pp. 249–306; d) A. Natarajan, L. S. Kaanumalle, V. Ramamurthy in *CRC Handbook of Organic Photochemistry and Photobiology*, 2nd ed. (Eds.: W. Horspool, F. Lenci), CRC, Boca Raton, FL, **2004**, pp. 107/1–107/24.

[2] a) I. A. Shkrob, M. C. Sauer, Jr., A. D. Liu, R. A. Crowell, A. D. Trifunac, *J. Phys. Chem. A* **1998**, *102*, 4976–4989; b) C. R. Lambert, I. E. Kochevar, R. W. Redmond, *J. Phys. Chem. B* **1999**, *103*, 3737–3741; c) V. V. Jarikov, A. V. Nikolaitchik, D. C. Neckers, *J. Phys. Chem. A* **2000**, *104*, 5131–5140; d) M. Goez, V. Zubarev, *Angew. Chem.* **2001**, *113*, 2948–2951; *Angew. Chem. Int. Ed.* **2001**, *40*, 2867–2869; e) M. Goez, M. Schiewek, M. H. O. Musa, *Angew. Chem.* **2002**, *114*, 1606–1609; *Angew. Chem. Int. Ed.* **2002**, *41*, 1535–1538; f) M. Goez, B. H. M. Hussein, *Angew. Chem.* **2003**, *115*, 1697–1700; *Angew. Chem. Int. Ed.* **2003**, *42*, 1659–1661; g) M. Goez, D. von Ramin-Marro, M. H. O. Musa, M. Schiewek, *J. Phys. Chem. A* **2004**, *108*, 1090–1100; h) X. Cai, M. Sakamoto, M. Hara, S. Tojo, A. Ouchi, A. Sugimoto, K. Kawai, M. Endo, M. Fujitsuka, T. Majima, *J. Phys. Chem. A* **2005**, *109*, 3797–3802.

[3] a) R. W. Redmont, J. C. Scaiano, L. J. Johnston, *J. Am. Chem. Soc.* **1990**, *112*, 398–402; b) J. L. Faria, S. Steenken, *J. Am. Chem. Soc.* **1990**, *112*, 1277–1279; c) J. L. Faria, S. Steenken, *J. Phys. Chem.* **1993**, *97*, 1924–1930; d) J. L. Faria, S. Steenken, *J. Chem. Soc. Perkin Trans. 2* **1997**, 1153–1159.

[4] a) P. Natarajan, R. W. Fessenden, *J. Phys. Chem.* **1989**, *93*, 6095–6100; b) V. Zubarev, M. Goez, *Angew. Chem.* **1997**, *109*, 2779–2781; *Angew. Chem. Int. Ed. Engl.* **1997**, *36*, 2664–2666; c) M. Goez, V. Zubarev, G. Eckert, *J. Am. Chem. Soc.* **1998**, *120*, 5347–

 © 2006 Wiley-VCH Verlag GmbH & Co. KGaA, Weinheim

5348; d) M. Goez, V. Zubarev, *Chem. Phys.* **2004**, *307*, 15–26; e) M. Goez, B. H. M. Hussein, *Phys. Chem. Chem. Phys.* **2004**, *6*, 5490–5497.

[5] For better sensitivity, $e^{\cdot-}_{aq}$ was not observed at its absorption maximum (720 nm) but at 829 nm; see, Ref. [4d], footnote 9. By control experiments (saturation of the solutions with the electron scavenger N_2O) it was ascertained that no other species absorbs at 829 nm. The extinction coefficient of $e^{\cdot-}_{aq}$ at 829 nm, 13750 $M^{-1}cm^{-1}$, was determined by comparison with the maximum extinction coefficient at 720 nm.[4e]

[6] R. Boch, M. K. Whittlesey, J. C. Scaiano, *J. Phys. Chem.* **1994**, *98*, 7854–7857.

[7] P. J. Wagner, *Acc. Chem. Res.* **1971**, *4*, 168–177.

[8] J. C. Scaiano, *Acc. Chem. Res.* **1982**, *15*, 252–258, and references therein.

[9] C. Huggenberger, H. Fischer, *Helv. Chim. Acta* **1981**, *64*, 338–353.

[10] E. Hayon, T. Ibata, N. N. Lichtin, M. Simic, *J. Phys. Chem.* **1972**, *76*, 2072–2078.

[11] R. A. Caldwell, S. N. Dhawan, D. E. Moore, *J. Am. Chem. Soc.* **1985**, *107*, 5163–5166.

 © 2006 Wiley-VCH Verlag GmbH & Co. KGaA, Weinheim

Enzyme Inhibitors

DOI: 10.1002/anie.200504119

Starving the Malaria Parasite: Inhibitors Active against the Aspartic Proteases Plasmepsins I, II, and IV**

*Fraser Hof, Andri Schütz, Christoph Fäh, Solange Meyer, Daniel Bur, Jun Liu, Daniel E. Goldberg, and François Diederich**

The most dangerous of the malaria-causing parasites, *Plasmodium falciparum*, infects 300–660 million people each year.[1] The plasmepsins (PMs) are a family of *Plasmodium* aspartic proteases that digest human hemoglobin and deliver amino acids that are required for growth.[2,3] In the search for targets for new antimalarial therapies, the mutually redundant proteolytic activity of plasmepsins for hemoglobin[4,5] requires inhibitors that are broadly active against all hemoglobin-degrading plasmepsins (PM I, PM II, PM IV, and HAP)[6] while remaining inactive against the most closely related human aspartic proteases (cathepsins D and E; hCat D and E). Among the plasmepsins, only the structure of PM II has been extensively characterized.[2,7–9] As a result of the similar sequence identity among the plasmepsins, we hypothesized that the renin-like flap-open conformation (Figure 1a), observed in two[9,10] of the fourteen known structures of PM II, would be accessible by each of the other three members of the Plasmepsin family. On this basis, we initiated a structure-based design program to explore the activity and selectivity of Plasmepsin inhibitors that target the flap pocket.

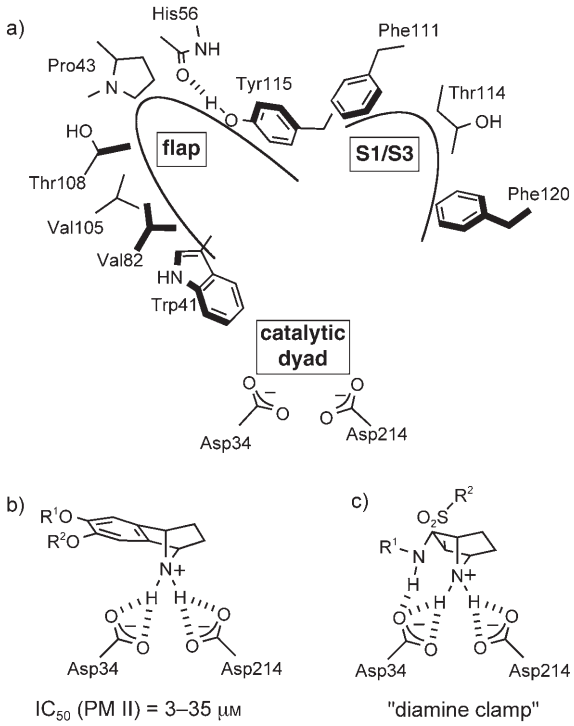

Figure 1. Plasmepsin II and the discussed inhibitors. a) Schematic diagram of the active site showing the catalytic dyad, the S1/S3 pocket, and the flap pocket. b) A bicyclic amine that engages the catalytic aspartate dyad of Plasmepsin II. c) A "diamine clamp" designed to provide extra hydrogen bonding to the catalytic residues.

Our earliest inhibitors (Figure 1b) displayed moderate activity (IC_{50} = 3000–35000 nM; IC_{50} = concentration of inhibitor at which 50% of the maximum initial rate is observed) for PM II.[11–13] Herein we report the creation and elaboration of a new core consisting of a bicyclic diamine that forms a hydrogen-bonded clamp around the catalytic aspartate residues (Figure 1c). The *exo* amino group additionally provides an attachment point for a pocket-directed binding substitu-

[*] A. Schütz, C. Fäh, Prof. Dr. F. Diederich
Laboratorium für Organische Chemie
ETH Zürich
Hönggerberg, HCI, 8093 Zürich (Switzerland)
Fax: (+41) 1-632-1109
E-mail: diederich@org.chem.ethz.ch
Dr. F. Hof
Department of Chemistry
University of Victoria
P.O. Box 3065, STN CSC, Victoria, BC, V8W 3V6 (Canada)
Dr. S. Meyer, Dr. D. Bur
Actelion Pharmaceuticals
Gewerbestrasse 16, 4123 Allschwil (Switzerland)
J. Liu, Prof. D. E. Goldberg
Howard Hughes Medical Institute
Departments of Medicine and Molecular Microbiology
Washington University
660 South Euclid Avenue, St. Louis, MO 63110-1093 (USA)

[**] F.H. thanks the Novartis Foundation and the Human Frontier Science Program for financial support. This research was supported by the ETH Research Council. We thank Anna Oksman for technical assistance.

Supporting information for this article is available on the WWW under http://www.angewandte.org or from the author.

InterScience DISCOVER SOMETHING GREAT
© 2006 Wiley-VCH Verlag GmbH & Co. KGaA, Weinheim

ent. The sulfone moiety in the β position serves to decrease the basicity of the amino groups that bind to the catalytic dyad, and can also be adorned as a second binding vector .

Our first generation of diamine-clamp inhibitors (e.g. (±)-**1**, Figure 2b) targeted the S1/S3 pocket with a sulfone-linked naphthyl substituent (for the synthesis, see the Supporting Information). Regardless of the identity of the *exo* amine substituent, the ability of these ligands to inhibit PM II was unexpectedly poor. IC_{50} values of 9500–60000 nM were observed and led us to re-evaluate our design. In particular, we were concerned that the aryl sulfone linkage might be too rigid to allow for the optimal orientation of the naphthalene binding element within the S1/S3 pocket (known to prefer aryl binding partners[3]). The density functional theory (DFT) dihedral-angle-driving calculation for the C1-S-C2-C3 dihedral angle (Figure 2a) continually varied between 0 and 180°. This revealed an unexpectedly strong preference for the orientation in which the π orbital of the *ipso* carbon atom bisects the two S=O bonds of the sulfone moiety. This conformational preference is also evident in a survey of aryl sulfone crystal structures in the Cambridge Structural Database (CSD).[14] The incorporation of this preference as an angle constraint within our molecular-mechanics-based modeling program[15] exposed the flaw in our original design; when the dihedral angle is properly set, the rigid aryl sulfone linkage directs the naphthyl substituent directly into Ile23 and Phe120, thus producing significantly unfavorable steric clashes (Figure 2b).

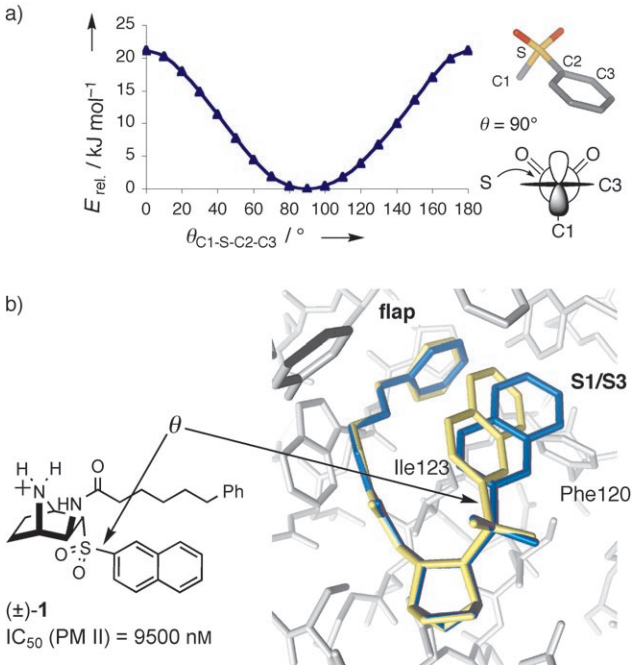

Figure 2. Conformational analysis of a first-generation diamine-clamp inhibitor. a) Relative energy while driving the dihedral angle $\theta_{C1\text{-}S\text{-}C2\text{-}C3}$ of an aryl sulfone from 0–180°. DFT-B3LYP calculations carried out using Spartan (6-31G* basis set, MP2 correlation).[19] A molecular model and a Newman projection of the optimal angle ($\theta_{C1\text{-}S\text{-}C2\text{-}C3} = 90°$) are shown at the right. b) MOLOC-generated models of inhibitor **1** within the active site of PM II. In the original, unconstrained model (blue), the naphthyl residue is allowed to comfortably fit within the S1/S3 binding pocket, but the model in which the conformational preference of the aryl sulfone is taken into account by fixing of the $\theta_{C1\text{-}S\text{-}C2\text{-}C3}$ at 90° (yellow) produces steric clashes with Ile123 and Phe120 of the enzyme. The enantiomer of the inhibitor that is predicted by modeling to bind into the active site is shown.

Subsequent modeling by using a properly fixed dihedral-angle constraint ($\theta_{C1\text{-}S\text{-}C2\text{-}C3} = 90°$) suggested a means by which we could exploit the rigid conformation of the aryl sulfone moiety. By using the enantiomer of the original aminosulfone core, but swapping the flap-binding element onto the *endo* sulfone vector and the S1/S3 binding element onto the more flexible *exo* amino vector, we arrived at a pseudo-enantiomeric family of structures that simultaneously engaged the catalytic dyad, flap pocket, and S1/S3 pocket with the appropriate binding elements (diamine clamp, hydrophobic chain, and aryl group, respectively; Figure 3).

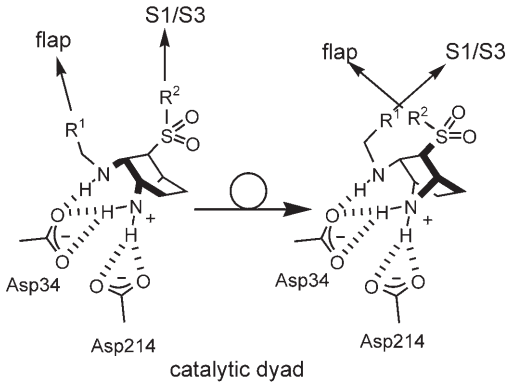

Figure 3. a) A pseudoenantiomeric second generation of inhibitors arising from the swap of flap and S1/S3 substituents between the amine and sulfone functionalities.

The target compounds were synthesized as shown in Scheme 1.[16] The key *exo* amino substituent is attached through a diastereoselective Michael-type addition of alkyl amines to the vinyl sulfones (±)-**2** and (±)-**3** to give the desired *exo*-amino/*endo*-sulfone isomers (±)-**4** and (±)-**5**, respectively. Subsequent functional group manipulation provided a second generation of diamine clamp inhibitors consisting of (±)-**6**, (±)-**7** (via (±)-**8**), (±)-**9**, (±)-**10** (via (±)-**11**), and (±)-**12**.

The in vitro activities of (±)-**7**, (±)-**9** and (±)-**10**, and (±)-**12** for PM II showed that the affinity of these ligands was significantly improved, with IC_{50} values ranging from 130 to 400 nM (Table 1, column 3[17]). The presence of the hexyl chain that, according to our modeling, occupies the flap pocket (compare compounds (±)-**6** and (±)-**7**), is responsible for the potency (>100-fold difference for PM II) as well as the selectivity ((±)-**7** shows IC_{50}(hCat D)/IC_{50}(PM II) > 15, whereas (±)-**6** shows essentially no discrimination). The aryl substituent directed into the S1/S3 pocket can be decreased in size (see compound (±)-**12**) without affecting activity (IC_{50}(PM II) = 210 nM) or selectivity (IC_{50}(hCat D)/IC_{50}(PM II) > 13). Furthermore, an increase in size, for example, through introduction of a biaryl substituent (as in

 © 2006 Wiley-VCH Verlag GmbH & Co. KGaA, Weinheim

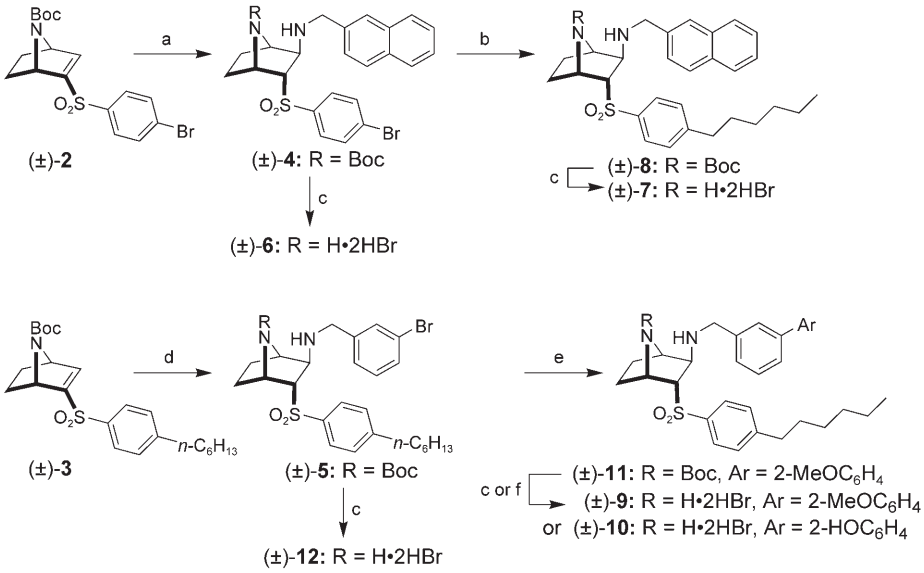

Scheme 1. Synthesis of second-generation diamine-clamp inhibitors from vinyl sulfone precursors (±)-**2** and (±)-**3**. a) 2-Naphthylmethylamine, 95 °C, 16 h; 81 %. b) *n*-$C_6H_{13}B(OH)_2$, $Pd(OAc)_2$, 2-(dicyclohexylphosphanyl)biphenyl, K_3PO_4, PhMe, 80 °C, 16 h; 65 %. c) BBr_3, CH_2Cl_2, −78 °C, 15 min; 85–100 %. d) 3-Bromobenzylamine, 70 °C, 1 h; 65 %. e) 2-Methoxyphenylboronic acid, $Pd(OAc)_2$, 2-(dicyclohexylphosphanyl)biphenyl, K_3PO_4, DMF, 90 °C, 16 h; 76 %. f) BBr_3, CH_2Cl_2, −78 °C. Ar = aryl group, Boc = *tert*-butyloxycarbonyl, DMF = *N*,*N*-dimethylformamide

Table 1: Inhibition of plasmepsins and human cathepsins by "diamine-clamp" inhibitors targeting the flap pocket.

Compound	PM I[a,b]	PM II[a,b]	PM II[a,c]	PM IV[a,c]	hCat D[a,c]	hCat E[a,c]	Culture[d]
(±)-**6**	n.d.	n.d.	14800	17300	18000	30500	n.d.
(±)-**7**	100	370	130	50	2030	7050	5500
(±)-**9**	210	2100	390	180	1410	5910	3700
(±)-**10**	290	930	400	110	1500	5400	2200
(±)-**12**	150	670	210	30	2800	5200	7100
(−)-**12**	n.d.	n.d.	45	10	n.d.	n.d.	n.d.
(+)-**12**	n.d.	n.d.	3260	33900	n.d.	n.d.	n.d.

[a] IC_{50} values (nM) are averages of two to three repetitions of a fluorogenic proteolysis assay (see the Supporting Information).[9,20] The estimated error for this assay is ±50 %. [b] Values determined at Washington University: [enzyme] = 1 nM, [substrate] = 1 μM, 100 mM acetate buffer, pH 5.1. [c] Values determined at Actelion Pharmaceuticals: [enzyme] = 1 nM, [substrate] = 1 μM, 50 mM acetate buffer, pH 5.0, 12.5 % glycerol, 10 % Me_2SO, 0.1 % BSA. [d] Culture IC_{50} values (nM) obtained by triplicate analysis of the dose-dependent ^{3}H-hypoxanthine uptake by cultured *Plasmodium falciparum* (3D7) parasite (see the Supporting Information).[21] Estimated errors are ±10 %. n.d. = not determined.

compounds (±)-**9** and (±)-**10**), leads to an insignificant dropoff in activity (IC_{50}(PM II) = 390 and 400 nM, respectively).

A selection of compounds was tested against a wide panel of plasmepsins (Table 1). Although these compounds were designed based upon a three-dimensional structure of PM II, all of the noncontrol compounds were found to be more-potent inhibitors of PM I and IV, than of PM II. These compounds retain little affinity for hCat D and E, which means that either there are significant differences in the structure of the flap pocket, or that it is missing altogether. The ligands with the biphenyl S1/S3 substituents ((±)-**9** and (±)-**10**) are the most active against the human enzymes, whereas that with the smaller S1/S3 substituent (bromoaryl compound (±)-**12**) displays the best overall selectivity (IC_{50}-(hCat D)/IC_{50}(PM IV) = 90 and IC_{50}-(hCat E)/IC_{50}(PM IV) = 173). Compound (±)-**6**, which lacks an appropriate flap substituent, is inactive in all assays. It can therefore be seen that the hexylphenyl substituent is responsible for the potent activity against PM I, II, and IV. This suggests that the flap-open conformation is likely to be accessible by each of these three enzymes, and that the binding energy provided by occupation of the mostly hydrophobic flap pockets of PM I, II, and IV is significant.

To further clarify the binding mode of these inhibitors, compound (±)-**5** was resolved into its enantiomers (+)-**5** and (−)-**5** by preparative chiral HPLC.[18] The enantiomers of **5** were then subsequently deprotected to give the optically pure inhibitors (+)-**12** and (−)-**12**. The IC_{50} values of (−)-**12** for PM II (45 nM) and PM IV (10 nM) are, within error, twofold better than those of the racemate, and (+)-**12** is practically inactive against PM II and IV (IC_{50} = 3260 and 33900 nM, respectively). Modeling of the two enantiomers show that the better-binding enantiomer ((−)-**12**) fits nicely within the active site and simultaneously engages the catalytic dyad, flap pocket, and the S1/S3 pocket. The other enantiomer, however, can be docked into the active site only in a less-preferred binding orientation (see the Supporting Information). On the basis of this information, the absolute configuration of the active enantiomer ((−)-**12**) was tentatively assigned as shown in Figure 4.

Finally, compounds (±)-**7**, (±)-**9**, (±)-**10**, and (±)-**12** were tested for parasite-growth inhibition in cultures of parasite-infected red blood cells (Table 1, column 7). The growth of the parasites is indicated

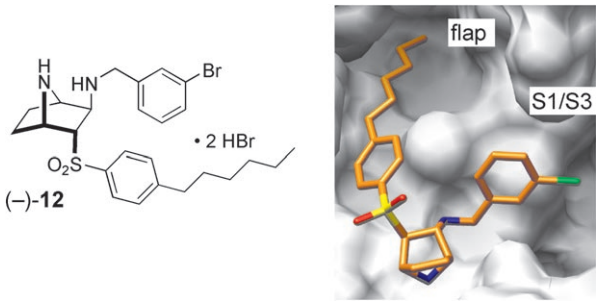

Figure 4. Absolute configuration of the active enantiomer (−)-**12** (left), proposed on the basis of molecular modeling within the active site of PM II (right). Several residues have been removed from the model to permit visualization of the flap pocket, occupied by the *n*-hexyl chain of the inhibitor. This image was prepared using MSMS and Chimera.[22,23]

 © 2006 Wiley-VCH Verlag GmbH & Co. KGaA, Weinheim

by uptake of ^{3}H-hypoxanthine, which is measured by scintillation counting on isolated cells after a period of incubation with the inhibitor (see the Supporting Information). The culture IC_{50} values range from 2200 to 7100 nM. Although the new diamine-clamp compounds are significantly less active in culture than in vitro, these results demonstrate that they are sufficiently active against the Plasmepsin family to shut down parasite growth.

Taken together, these results suggest that a conformation with a flap-open pocket is accessible for each member of the Plasmepsin family, and that engaging this pocket with a complementary hydrophobic substituent provides significant binding energy. These compounds all display high selectivity against the human cathepsins D and E, suggesting that this design principle holds promise for the production of useful broad-spectrum plasmepsin inhibitors that remain innocuous to the most closely related human enzymes. The bicyclic diamine clamp introduced in this work shows potent inhibition of targeted structures while allowing for significant discrimination between different classes of aspartic proteases. We are currently working to improve the in vivo biological activity in an effort to develop the diamine-clamp inhibitors as a new class of antimalarials.

Received: November 19, 2005
Published online: February 27, 2006

Keywords: aspartic proteases · drug design · inhibitors · malaria · medicinal chemistry

[1] R. W. Snow, C. A. Guerra, A. M. Noor, H. Y. Myint, S. I. Hay, *Nature* **2005**, *434*, 214 – 217.
[2] A. M. Silva, A. Y. Lee, S. V. Gulnik, P. Majer, J. Collins, T. N. Bhat, P. J. Collins, R. E. Cachau, K. E. Luker, I. Y. Gluzman, S. E. Francis, A. Oksman, D. E. Goldberg, J. W. Erickson, *Proc. Natl. Acad. Sci. USA* **1996**, *93*, 10034 – 10039.
[3] C. Boss, S. Richard-Bildstein, T. Weller, W. Fischli, S. Meyer, C. Binkert, *Curr. Med. Chem.* **2003**, *10*, 883 – 907.
[4] A. L. Omara-Opyene, P. A. Moura, C. R. Sulsona, J. A. Bonilla, C. A. Yowell, H. Fujioka, D. A. Fidock, J. B. Dame, *J. Biol. Chem.* **2004**, *279*, 54088 – 54096.
[5] J. Liu, I. Y. Gluzman, M. E. Drew, D. E. Goldberg, *J. Biol. Chem.* **2005**, *280*, 1432 – 1437.
[6] A. Nezami, T. Kimura, K. Hidaka, A. Kiso, J. Liu, Y. Kiso, D. E. Goldberg, E. Freire, *Biochemistry* **2003**, *42*, 8459 – 8464.
[7] a) O. A. Asojo, S. V. Gulnik, E. Afonina, B. Yu, J. A. Ellman, T. S. Haque, A. M. Silva, *J. Mol. Biol.* **2003**, *327*, 173 – 181; b) T. S. Haque, A. G. Skillman, C. E. Lee, H. Habashita, I. Y. Gluzman, T. J. A. Ewing, D. E. Goldberg, I. D. Kuntz, J. A. Ellman, *J. Med. Chem.* **1999**, *42*, 1428 – 1440.
[8] N. Khazanovich Bernstein, M. M. Cherney, C. A. Yowell, J. B. Dame, M. N. G. James, *J. Mol. Biol.* **2003**, *329*, 505 – 524.
[9] L. Prade, A. F. Jones, C. Boss, S. Richard-Bildstein, S. Meyer, C. Binkert, D. Bur, *J. Biol. Chem.* **2005**, *280*, 23837 – 23843.
[10] J. Yuvaniyama, A. D'Arcy, C. Öfner, H. Lötscher, D. Bur, G. E. Dale, H. P. Märki, F. K. Winkler, R. P. Moon, R. G. Ridley in Symposium on *"Parasite proteases as drug targets"*, University of Glasgow, UK, **2000**.
[11] D. A. Carcache, S. R. Hörtner, A. Bertogg, F. Diederich, A. Dorn, H. P. Märki, C. Binkert, D. Bur, *Helv. Chim. Acta* **2003**, *86*, 2192 – 2209.
[12] D. A. Carcache, S. R. Hörtner, P. Seiler, F. Diederich, A. Dorn, H. P. Märki, C. Binkert, D. Bur, *Helv. Chim. Acta* **2003**, *86*, 2173 – 2191.
[13] D. A. Carcache, S. R. Hörtner, A. Bertogg, C. Binkert, D. Bur, H. P. Märki, A. Dorn, F. Diederich, *ChemBioChem* **2002**, *3*, 1137 – 1141.
[14] The conformational restriction of aryl sulfones was first brought to our attention in the form of a CSD survey carried out by Dr. Klaus Müller and F. Hoffman-La Roche, which was presented during a seminar series at the ETH Zürich in 2004. See the Supporting Information.
[15] All enzyme–inhibitor complexes were modeled using the MAB force field as implemented in the program MOLOC: a) P. R. Gerber, K. Müller, *J. Comput.-Aided Mater. Des.* **1995**, *9*, 251 – 268; b) Gerber Molecular Design (http://www.moloc.ch).
[16] All new compounds were fully characterized by m.p., IR, ^{1}H and ^{13}C NMR, MS, and HRMS or elemental analysis.
[17] Inhibition studies for PM II were, as indicated in Table 1 and the Supporting Information, carried out in two different laboratories under different conditions, and as such, the slightly different values for PM II inhibition are not unexpected. The results in Table 1, column 3, which were obtained under conditions identical to those used for PM IV and both human cathepsins, are considered for the purposes of discussions in the text relating to selectivity.
[18] Baseline separation was achieved by using a semipreparative Chiralpak AD-H column and eluting with hexane/*i*PrOH/$HNMe_2$ (80:20:0.1). This separation was conducted at Chiral Technologies Europe, 67404 Illkirch, France.
[19] Spartan'04, Wavefunction, Inc., Irvine, USA, **2004**.
[20] K. E. Luker, S. E. Francis, I. Y. Gluzman, D. E. Goldberg, *Mol. Biochem. Parasitol.* **1996**, *79*, 71 – 78.
[21] I. Y. Gluzman, S. E. Francis, A. Oksman, C. E. Smith, K. L. Duffin, D. E. Goldberg, *J. Clin. Invest.* **1994**, *93*, 1602 – 1608.
[22] M. F. Sanner, A. J. Olson, J. C. Spehner, *Biopolymers* **1996**, *38*, 305 – 320.
[23] Molecular-graphics images were produced by using the Chimera package from the Computer Graphics Laboratory, University of California, San Francisco (supported by NIH P41 RR-01081): C. C. Huang, G. S. Couch, E. F. Pettersen, T. E. Ferrin, *Pac. Symp. Biocomput.* **1996**, *1*, 724; http://www.cgl.ucsf.edu/chimera.

 © 2006 Wiley-VCH Verlag GmbH & Co. KGaA, Weinheim

Cover Picture

Yossi Weizmann, Zoya Cheglakov, Valeri Pavlov, and Itamar Willner*

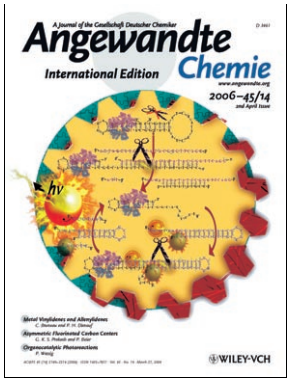

A catalytic cutter for the sensitive detection of a target DNA, a Tay–Sachs disorder mutant, is described by I. Willner and co-workers in their Communication on page 2238 ff. As the cover picture shows, a tailored nucleic acid hairpin probe (top) is opened upon hybridization with the analyte DNA, activating the formation of the DNA cutter (central structure), which initiates the autonomous scission of a fuel substrate that leads to the replication of the catalytic cutter and to the formation of a fluorescent product as an optical readout signal.

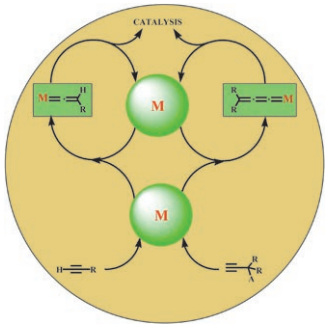

Organometallic Catalysis
Metal vinylidenes and allenylidenes are involved in numerous catalytic processes, such as alkene metathesis and coupling reactions. The state of the art in this field is summarized by C. Bruneau and P. H. Dixneuf in their Review on page 2176 ff.

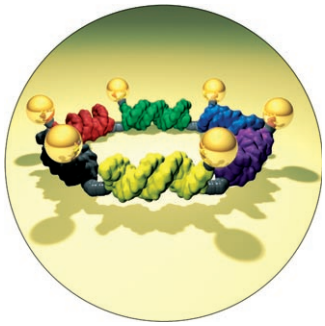

Nanoparticle Assemblies
In their Communication on page 2204 ff., H. F. Sleiman and F. A. Aldaye describe the use of DNA to mediate the organization of gold nanoparticles—an approach that can be generalized for the sequential and modular generation of a range of nanoparticle patterns.

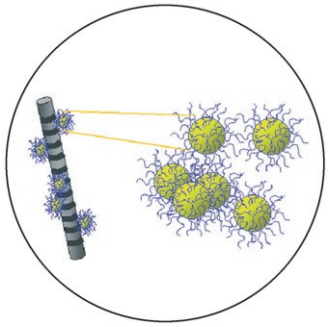

Nanobiotechnology
Collagen mimetic peptide functionalized nanoparticles form stable adducts with collagen fibers. In their Communication on page 2267 ff, S. M. Yu et al. describe the binding interactions between the peptide and type I collagen fibers.

Contents

VIP *The following Communications have been judged by at least two referees to be "very important papers" and will be published online at www.angewandte.org soon:*

*A. Kaminaga, V. Vanag, I. Epstein**
A Reaction-Diffusion Memory Device

*V. Stamenkovic, B. S. Moon, K. J. Mayrhofer, P. Ross, N. Markovic, J. Rossmeisl, J. Greeley, J. Nørskov**
Changing the Activity of Electrocatalysts for Oxygen Reduction by Tuning the Surface Electronic Structure

J. Blumberger, B. Ensing, M. Klein*
Formamide Hydrolysis in Alkaline Aqueous Solution: Insights from Ab Initio Metadynamics Calculations

G. Dolphin, P. Dumy, J. Garcia**
Control of Amyloid β-Peptide Protofibril Formation by a Designed Template Assembly

J. M. B. v. Colbe, W. Schmidt, M. Felderhoff, B. Bogdanovic, F. Schüth**
Hydrogen Isotope Scrambling on Doped Sodium Alanate

W. Zhao, Y. Gao, S. Kandadai, M. Brook, Y. Li**
DNA Polymerization on Gold Nanoparticles through Rolling Circle Amplification: Towards Scaffolds for Three-Dimensional Periodical Nanoassemblies

News

Chemoinformatics: Prize to J. Gasteiger ____ **2164**

Organometallic Chemistry: J. F. Hartwig Honored ____ **2164**

Biochemistry: P. G. Schultz Awarded ____ **2164**

Books

Handbook of C-H Transformations — Gerald Dyker — *reviewed by A. M. Echavarren* ____ **2165**

Organisilicon Chemistry VI — Norbert Auner, Johann Weis — *reviewed by G. Linti* ____ **2166**

Highlights

Photochemistry

P. Wessig* ____ **2168 – 2171**

Organocatalytic Enantioselective Photoreactions

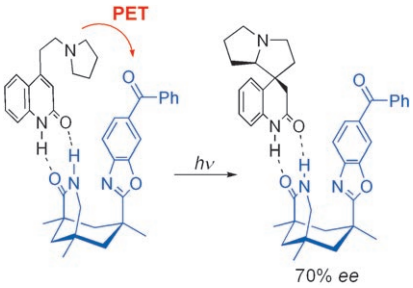

Light at the end of the tunnel. The reports on organocatalytic photoreactions that are also enantioselective are few and far between. Recently published work now highlights a breakthrough. When special catalysts derived from Kemp's triacid were used, selectivities of up to 70% *ee* were achieved (see scheme; PET = photo-induced electron transfer).

Asymmetric Synthesis

G. K. S. Prakash,* P. Beier ____ **2172 – 2174**

Construction of Asymmetric Fluorinated Carbon Centers

Various choices: Recent advances in the construction of asymmetric fluorinated carbon centers are discussed. Special attention is called to catalytic enantioselective reactions such as electrophilic fluorination (top) and decarboxylative allylation (bottom) of fluorinated substrates.

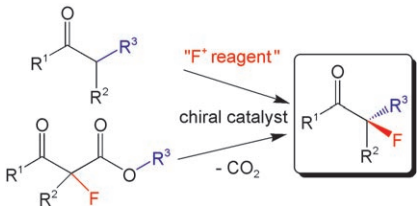

InterScience
© 2006 Wiley-VCH Verlag GmbH & Co. KGaA, Weinheim

Reviews

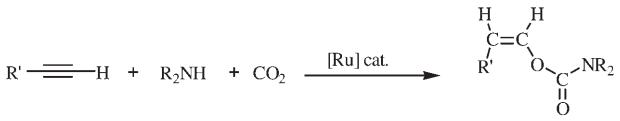

Versatile key intermediate metal vinylidenes and allenylidenes participate in numerous catalytic processes such as alkene metathesis, coupling reactions, and anti-Markovnikov additions to alkynes. The formation of a metal vinylidene intermediate in a catalytic reaction (see scheme) was first reported 20 years ago, and much development in the field has since taken place.

Organometallic Catalysis

C. Bruneau,* P. H. Dixneuf* **2176 – 2203**

Metal Vinylidenes and Allenylidenes in Catalysis: Applications in Anti-Markovnikov Additions to Terminal Alkynes and Alkene Metathesis

Communications

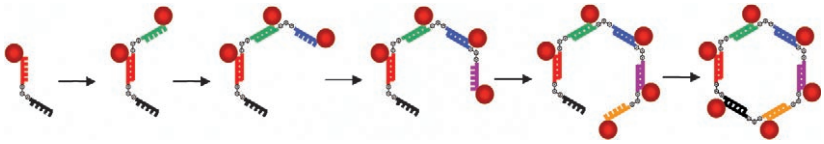

Six of one and half a dozen of the other: A cyclic hexamer of six gold nanoparticles was sequentially and selectively self-assembled by labeling each particle (red sphere) with a DNA-containing molecule (colored block), which serves to dictate its ultimate location within the final construct. This method may be used to construct any discrete well-defined pattern of nanoparticles.

Nanostructures

F. A. Aldaye, H. F. Sleiman* **2204 – 2209**

Sequential Self-Assembly of a DNA Hexagon as a Template for the Organization of Gold Nanoparticles

Controlled catalysis: The combination of magnetically and gravimetrically recoverable catalysts such as the nanoparticle-bound base (see picture; blue) and the resin-bound acid (green), respectively, allow the application of non-complementary catalysts to multistep, one-pot reaction cascades (e.g. **A**→**B**→**C**). The catalysts are recovered after reaction and reused in subsequent, unrelated reactions.

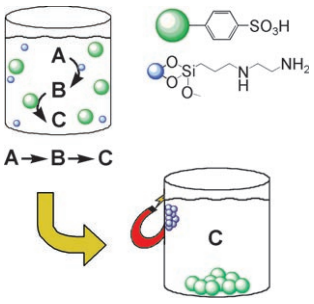

Heterogeneous Catalysis

N. T. S. Phan, C. S. Gill, J. V. Nguyen, Z. J. Zhang, C. W. Jones* **2209 – 2212**

Expanding the Utility of One-Pot Multistep Reaction Networks through Compartmentation and Recovery of the Catalyst

For the USA and Canada:
ANGEWANDTE CHEMIE International Edition (ISSN 1433-7851) is published weekly by Wiley-VCH PO Box 191161, D 69451 Weinheim, Germany. Air freight and mailing in the USA by Publications Expediting Inc. 200 Meacham Ave., Elmont, NY 11003. Periodicals postage paid at Jamaica NY 11431. US POSTMASTER: send address changes to *Angewandte Chemie*, Wiley-VCH, 111 River Street, Hoboken, NJ 07030. Annual subscription price for institutions: US$ 5685/5168 (valid for print and electronic / print or electronic delivery); for individuals who are personal members of a national chemical society prices are available on request. Postage and handling charges included. All prices are subject to local VAT/sales tax.

© 2006 Wiley-VCH Verlag GmbH & Co. KGaA, Weinheim

The best in chemistry –

for more than a hundred years

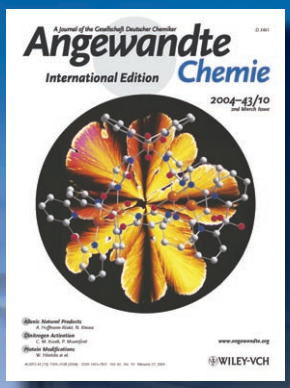

A Journal of the Gesellschaft Deutscher Chemiker

Angewandte
International Edition **Chemie**

www.angewandte.org

1888: ***The beginning of a success story***

Constant Innovations

1962: *First issue of the International Edition*
1976: *Graphical abstracts*
1979: *Cover pictures*
1988: *Centenary of Angewandte*
1989: *Routine use of color*
1991: *New section: Highlights*
1992: *Computerized editorial tracking system*
1995: *Internet service for readers*
1998: *Regular press service; full-text online*
2000: *New section: Essays; EarlyView: Communications available online ahead of the printed version*
2001: *New section: Minireviews*
2002: *Online submission of manuscripts*
2003: *Weekly publication; new section: News; new layout*
2004: *Backfiles (1962-1997); ManuscriptXpress: Online system for authors and referees*

Angewandte's advisors...

Jean-Marie Lehn
Université Strasbourg
Collège de France

» ***Angewandte Chemie*** *provides timely reviews of great depth and wide interest together with short reports of top quality frontier research. Creative work remains creative wherever it is published! However,* ***Angewandte Chemie*** *brings high visibility while keeping restrain and rigor. Finally, it is also supranational, as science is.* «

Angewandte Chemie International Edition *is a journal of the German Chemical Society (GDCh)*

GDCh

WILEY InterScience® DISCOVER SOMETHING GREAT

WILEY-VCH

1851404_gu

Do not touch! The surface of a living cell is soft and responsive and therefore high-resolution imaging of the cell membrane has not been possible to date. Now noncontact imaging of protein complexes in the plasma membrane of living cells has been demonstrated (see picture) and has been used to follow the cells' structural reorganization. This breakthrough opens up a wealth of new experiments in membrane and cell biology.

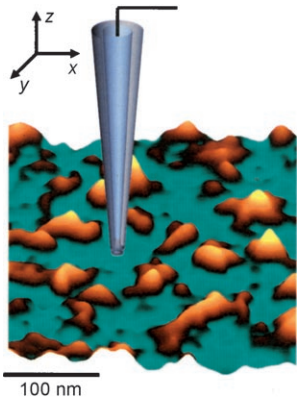

Membrane Protein Imaging

A. I. Shevchuk, G. I. Frolenkov, D. Sánchez, P. S. James, N. Freedman, M. J. Lab, R. Jones, D. Klenerman,* Y. E. Korchev* _____ **2212 – 2216**

Imaging Proteins in Membranes of Living Cells by High-Resolution Scanning Ion Conductance Microscopy

Sheer magnetism: The phase transitions and magnetic behavior of included oxygen in a single crystal were studied at low temperature. The system exhibits three correlated structural and magnetic phases. The distinct middle-temperature phase shows a one-dimensional-chain arrangement of oxygen trimers with an anomalous magnetization response to external magnetic fields.

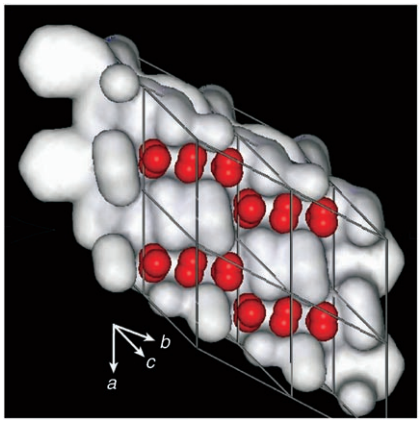

Host–Guest Systems

S. Takamizawa,* E. Nakata, T. Akatsuka _____ **2216 – 2221**

Magnetic Behavior of a 1D Molecular-Oxygen System Included within a Transformable Single-Crystal Adsorbent

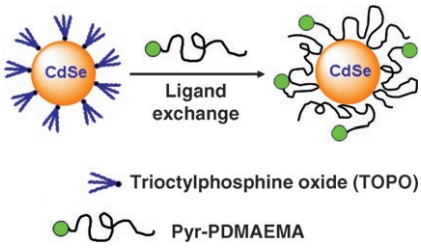

Hold on tight: Pyrene-labeled poly(dimethylaminoethyl methacrylate) (Pyr-PDMAEMA) was synthesized as a multidentate ligand for CdSe nanocrystals (NCs, see picture). The mean number of polymers that bind to each NC can be determined by a quantitative analytical method based on size-exclusion chromatography. Spectroscopic characterization of the eluted particles shows that Pyr-PDMAEMA binds tightly to these NCs.

Nanocrystals

M. Wang, T. E. Dykstra, X. Lou, M. R. Salvador, G. D. Scholes,* M. A. Winnik* _____ **2221 – 2224**

Colloidal CdSe Nanocrystals Passivated by a Dye-Labeled Multidentate Polymer: Quantitative Analysis by Size-Exclusion Chromatography

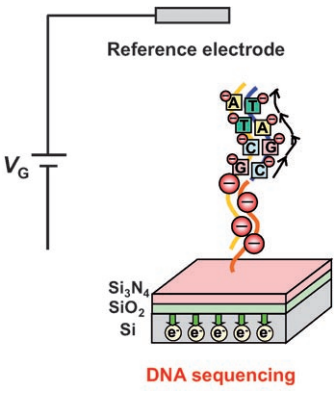

In charge: Label-free DNA sequencing can be performed by using a field-effect transistor to detect the intrinsic molecular charges (see picture). Oligonucleotide probes are immobilized on the Si_3N_4 gate surface, and complementary target DNA is hybridized with them. The change in charge density on the Si_3N_4/SiO_2 gate caused by each single-base extension can be measured as a shift in the threshold voltage. V_G = gate voltage.

DNA Sequencing

T. Sakata, Y. Miyahara* _____ **2225 – 2228**

DNA Sequencing Based on Intrinsic Molecular Charges

© 2006 Wiley-VCH Verlag GmbH & Co. KGaA, Weinheim

Contents

Gene Function

S. B. Cambridge,* D. Geissler, S. Keller, B. Cürten ——— **2229 – 2231**

A Caged Doxycycline Analogue for Photoactivated Gene Expression

High potential: High-resolution transgene expression in two biological applications demonstrates the potential of a photoactivated gene-expression technique. Irradiation of one half of a transgenic tobacco leaf produced a sharp boundary of reporter gene expression between photoactivated tissue and nonirradiated tissue (see picture). This method was established by synthesis of a photosensitive doxycycline analogue.

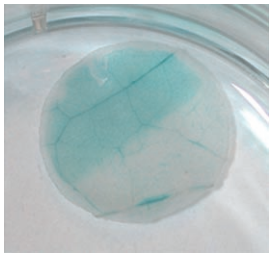

Block Copolymers

L. Yu, H. Zhang, J. Ding* ——— **2232 – 2235**

A Subtle End-Group Effect on Macroscopic Physical Gelation of Triblock Copolymer Aqueous Solutions

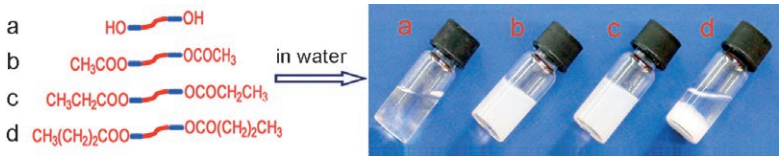

In the end: Alkyl end groups can induce a thermoreversible sol–gel transition in an otherwise sol-like suspension by affecting the macroscopic self-assembly behavior. The picture shows PLGA-PEG-PLGA triblock copolymer/water mixtures in the sol (polymer a), gel (polymers b and c), and precipitation states (polymer d). PLGA = poly(lactic acid-*co*-glycolic acid), PEG = poly(ethylene glycol).

Asymmetric Rearrangement

A. Nakazaki, T. Nakai, K. Tomooka* ——— **2235 – 2238**

Asymmetric Retro-[1,4] Brook Rearrangement and Its Stereochemical Course at Silicon

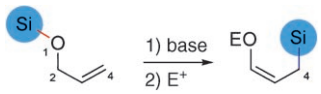

Taking the silyl group a step further: An unprecedented rearrangement in an anion derived from an allyloxysilane occurs by a [1,4] shift of the silyl group (see scheme). The asymmetric synthesis of enantiomerically enriched γ-functionalized allylsilanes with Si stereocenters can be accomplished with this retro-[1,4] Brook rearrangement. E = electrophile.

DNA Detection

Y. Weizmann, Z. Cheglakov, V. Pavlov, I. Willner* ——— **2238 – 2242**

Autonomous Fueled Mechanical Replication of Nucleic Acid Templates for the Amplified Optical Detection of DNA

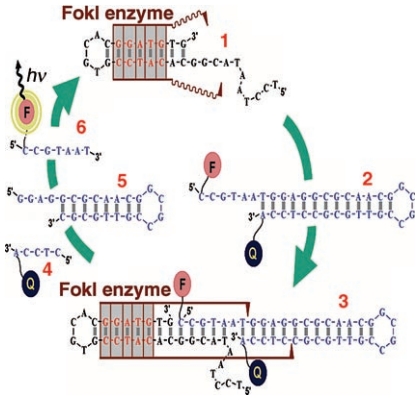

Fuel for a DNA machine: A FokI enzyme/DNA scission machine is triggered by the hybridization of its DNA hairpin structure with a target nucleic acid. The machine is fueled by a secondary fluorophore (F)- and quencher (Q)-functionalized nucleic acid **2**. Scission of **3** leads to replication of the machinery cutter **1** and yields a fluorescent product **6**, which provides an optical output for the machine (see scheme).

© 2006 Wiley-VCH Verlag GmbH & Co. KGaA, Weinheim

Homolytic aromatic substitution reactions are used for the efficient regioselective synthesis of helicenes, phenanthrenes, and azahelicenes. The use of halo and alkoxy substituents to control the stereochemical outcome of this approach and X-ray studies of the resulting helicenes are described (see structure; red O, gray C).

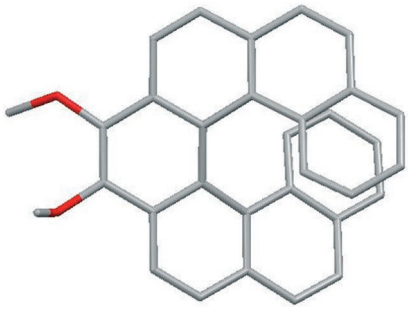

Polyaromatic Compounds

D. C. Harrowven,* I. L. Guy, L. Nanson ——— **2242 – 2245**

Efficient Phenanthrene, Helicene, and Azahelicene Syntheses

Aluminum siding: Reduction of $Ar'AlI_2$ ($Ar' = 2,6\text{-}Dipp_2C_6H_3$, $Dipp = 2,6\text{-}iPr_2C_6H_3$) in the presence of $Me_3SiCCSiMe_3$ afforded $(Ar'Al)_2(CSiMe_3)_2$ (see picture), a dialuminum-substituted cyclobutene analogue. The central four-membered Al_2C_2 ring adopts a folded geometry and is isoelectronic with aromatic cyclobutadiene dications.

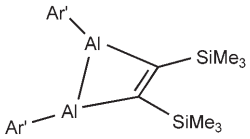

Four-Membered Rings

C. Cui,* X. Li, C. Wang, J. Zhang, J. Cheng, X. Zhu ——— **2245 – 2247**

Isolation of a 1,2-Dialuminacyclobutene

How low can you go? Polybenzoxazines can display surface free energies which are even lower than that of pure poly(tetrafluoroethylene). The contact angles and surface free energies were monitored during the polymerizations (see graph for an example). These materials are cheaper to prepare and easier to process than fluoropolymers.

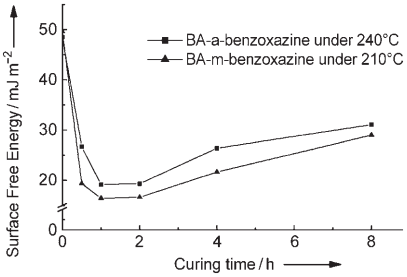

Wettability

C.-F. Wang, Y.-C. Su, S.-W. Kuo, C.-F. Huang, Y.-C. Sheen, F.-C. Chang* ——— **2248 – 2251**

Low-Surface-Free-Energy Materials Based on Polybenzoxazines

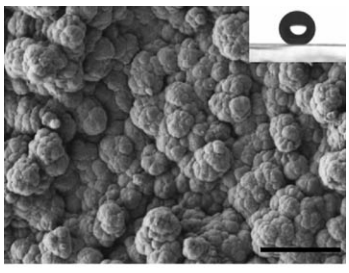

A cauliflowerlike surface (see picture, scale bar: 8 μm) and perfluorocarbon chains on the polymer backbone result in super water and oil repellency of a film of the fluorinated polythiophene shown that was electrochemically deposited on an indium tin oxide surface. The inset shows a camera image of a water droplet on the surface (contact angle > 150°).

Polymer Films

M. Nicolas, F. Guittard, S. Géribaldi* ——— **2251 – 2254**

Synthesis of Stable Super Water- and Oil-Repellent Polythiophene Films

© 2006 Wiley-VCH Verlag GmbH & Co. KGaA, Weinheim

Contents

Asymmetric Synthesis

M. Terada,* K. Machioka, K. Sorimachi ——— **2254 – 2257**

High Substrate/Catalyst Organocatalysis by a Chiral Brønsted Acid for an Enantioselective Aza-Ene-Type Reaction

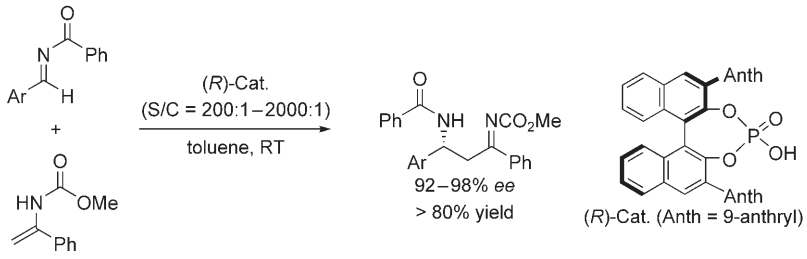

Lowering the load: A very small amount of a binaphthol-derived monophosphoric acid organocatalyst accelerates an aza-ene-type reaction of *N*-benzoylimines with enecarbamates to provide β-aminoimines with high enantiomeric purity. This catalysis with a high substrate/catalyst (S/C) ratio provides a practical route to 1,3-diamine derivatives of synthetic and biological importance.

High-Spin Systems

K. Sugisaki, K. Toyota,* K. Sato, D. Shiomi, T. Takui* ——— **2257 – 2260**

Ab Initio MO Analysis of the Excited Electronic States of High-Spin Quintet 2-Methylphenylene-1,3-dinitrene

The concept of orbital correlations between the benzene skeleton and the nitrene moieties of 2-methylphenylene-1,3-dinitrene was used to interpret the energy levels and characters of the excited electronic states of this typical high-spin quintet molecule by high-level ab initio MO calculations. Thus, the UV/Vis absorption spectrum of this dinitrene was assigned theoretically for the first time (see stick spectrum in the picture).

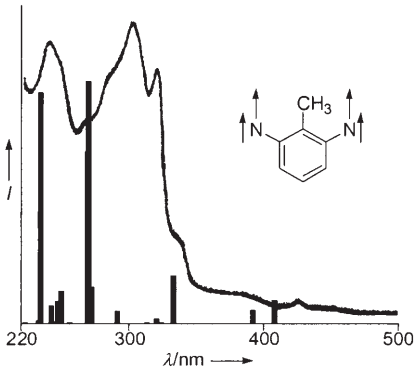

Asymmetric Hydrogenation

S.-M. Lu, Y.-Q. Wang, X.-W. Han, Y.-G. Zhou* ——— **2260 – 2263**

Asymmetric Hydrogenation of Quinolines and Isoquinolines Activated by Chloroformates

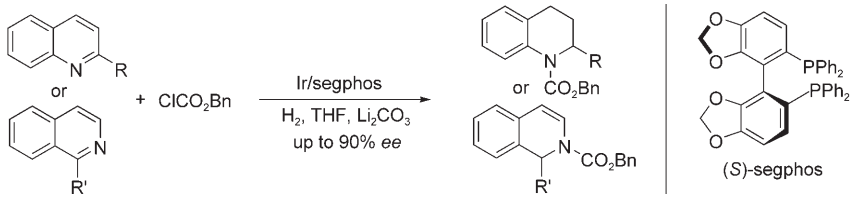

Active ingredient: Optically active tetrahydroquinolines and tetrahydroisoquinolines can be obtained by the asymmetric hydrogenation of quinolines and isoquinolines with chloroformates as the activating reagent (e.g., $ClCO_2Bn$, see scheme). The method has been applied to the asymmetric synthesis of several naturally occurring alkaloids. Bn = benzyl.

Polymerization

H. Li, A. Debuigne, R. Jérome,* P. Lecomte ——— **2264 – 2267**

Synthesis of Macrocyclic Poly(ε-caprolactone) by Intramolecular Cross-Linking of Unsaturated End Groups of Chains Precyclic by the Initiation

Biodegradable cyclic polyesters are synthesized by using an ε-caprolactone polymerization initiated by a cyclic tin alkoxide, followed by the addition and sequential polymerization of a few units of α-(1-acryloxyethyl)-ε-caprolactone. Tadpole-shaped polyesters with two tails of controllable length are readily prepared by this procedure (see picture).

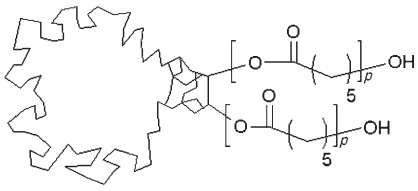

© 2006 Wiley-VCH Verlag GmbH & Co. KGaA, Weinheim

Collagen treatment: Gold nanoparticles conjugated with collagen mimetic peptide (CMP) form stable adducts with collagen fibers (see picture) that are visible by transmission electron microscopy, thereby allowing the study of binding interactions between CMPs and type I collagen fibers. This labeling technique may potentially be used to identify structural abnormalities in collagen fibers that are related to diseases.

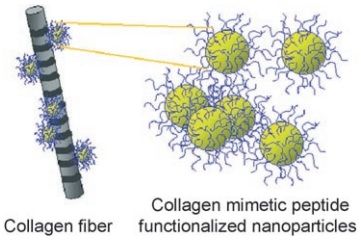

Nanobiotechnology

X. Mo, Y. An, C.-S. Yun, S. M. Yu* ——— 2267 – 2270

Nanoparticle-Assisted Visualization of Binding Interactions between Collagen Mimetic Peptide and Collagen Fibers

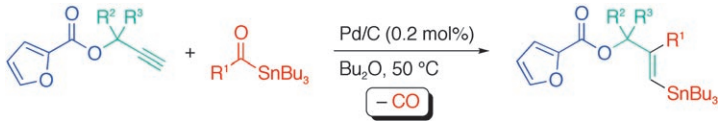

Out with the CO: The highly regio- and stereoselective aryl-, alkenyl-, and alkylstannylation of alkynes was achieved by the decarbonylative carbostannylation of propargyl 2-furoates in the presence of Pd/C. Various functionalized alkenylstannanes were obtained that contain nucleophilic alkenylstannane and electrophilic allyl furoate moieties, which can be transformed by coupling reactions.

C–C Coupling

Y. Nakao, J. Satoh, E. Shirakawa,* T. Hiyama* ——— 2271 – 2274

Regio- and Stereoselective Decarbonylative Carbostannylation of Alkynes Catalyzed by Pd/C

An efficient and convenient approach to the synthesis of spirocyclic oxindoles from iodoindoles involves a sequential intramolecular C–O Ullmann coupling reaction and Claisen rearrangement (see scheme). The one-pot procedure affords 3-spiro-2-oxindoles in good yield with excellent diastereoselectivities.

Domino Reactions

H. Miyamoto, Y. Okawa, A. Nakazaki, S. Kobayashi* ——— 2274 – 2277

Highly Diastereoselective One-Pot Synthesis of Spirocyclic Oxindoles through Intramolecular Ullmann Coupling and Claisen Rearrangement

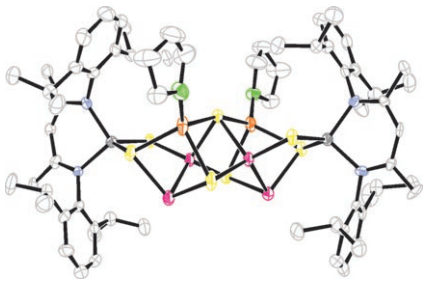

Donations accepted: The reaction of $[\{LAl[(SLi)_2(thf)_2]\}_2]$ ($L = HC(CMeNAr)_2$, $Ar = 2,6\text{-}iPr_2C_6H_3$) with $GeCl_2$·dioxane yields the novel $Ge^{II} \rightarrow Ge^{II}$-containing hetero-trimetallic $[L_2Al_2Ge_4Li_2S_7]$ cluster, which has a crablike structure (Al gray, Ge magenta, Li orange, S yellow, O green, N blue, C light gray). This cluster is the first aluminum-containing hetero-trimetallic sulfide.

Cluster Compounds

Z. Yang, X. Ma, R. B. Oswald, H. W. Roesky,* C. Cui, H.-G. Schmidt, M. Noltemeyer ——— 2277 – 2280

An Unprecedented Example of a Hetero-trimetallic Main-Group $[L_2Al_2Ge_4Li_2S_7]$ Cluster Containing a Ge^{II}–Ge^{II} Donor–Acceptor Bond

© 2006 Wiley-VCH Verlag GmbH & Co. KGaA, Weinheim

Contents

Immunoassays

J. D. Uram, K. Ke, A. J. Hunt, M. Mayer* ——— 2281 – 2285

Label-Free Affinity Assays by Rapid Detection of Immune Complexes in Submicrometer Pores

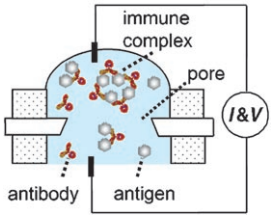

Resistance movement: A submicrometer conical pore was used for the single-aggregate detection and characterization of immune complexes consisting of proteins such as staphylococcal enterotoxin B and antibodies. The developed assay is rapid, label-free, requires no immobilization or modification of the antibody or antigen, and can be performed with antibodies or proteins in serum.

Heterogeneous Catalysis

W. Deng, M. Flytzani-Stephanopoulos* ——— 2285 – 2289

On the Issue of the Deactivation of Au–Ceria and Pt–Ceria Water–Gas Shift Catalysts in Practical Fuel-Cell Applications

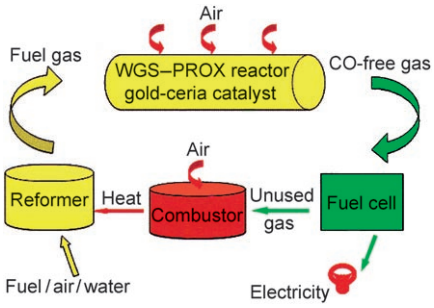

A small amount of gaseous oxygen (air) added to the feed gas stabilizes nanostructured Au–ceria and Pt–ceria catalysts for the water–gas shift (WGS) reaction in H_2-rich gases and start/stop operation. Au–ceria materials emerge as practical alternatives to expensive Pt-based catalysts for total CO removal from reformate gas mixtures for fuel-cell use. PROX = preferential oxidation of CO.

Synthetic Methods

C.-G. Dong, Q.-S. Hu* ——— 2289 – 2292

Annulative Tandem Reactions Based on Pd^0/tBu$_3$P-Catalyzed Cross-Coupling and C(sp^3)–H Bond Activation

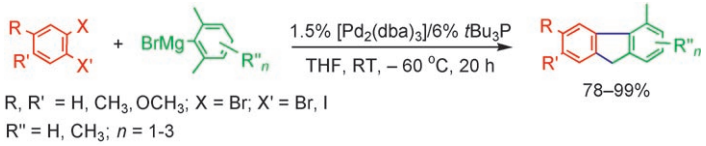

All together now: Pd^0/tBu$_3$P-catalyzed annulative tandem reactions of 1,2-dihalobenzenes were carried out with hindered Grignard reagents. This new type of tandem reaction is believed to occur through cross-coupling followed by cyclization with C(sp^3)–H bond activation as the key step and allows one-step access to potentially useful substituted fluorenes in high yield from readily available 1,2-dibromobenzenes and 1-bromo-2-iodobenzene.

Si=P Species

M. Driess,* S. Block, M. Brym, M. T. Gamer ——— 2293 – 2296

Synthesis of a "Half"-Parent Phosphasilene $R_2Si{=}PH$ and Its Metalation to the Corresponding *P*-Zinciophosphasilene [$R_2Si{=}PM$]

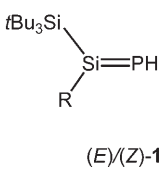

(*E*)/(*Z*)-**1**

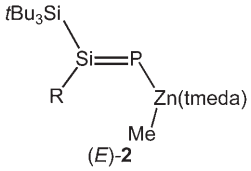

(*E*)-**2**

Remarkably stable—even with a hydrogen atom at the low-coordinate phosphorus center! A straightforward synthesis provides the thermally robust phosphasilenes (*E*)/(*Z*)-**1**, which have a terminal PH group. These compounds can be cleanly metalated with dimethylzinc in the presence of tmeda (tetramethylethylenediamine) to afford exclusively the *P*-zincio-substituted phosphasilene **2** with *E* configuration. R = 2,4,6-triisopropylphenyl.

© 2006 Wiley-VCH Verlag GmbH & Co. KGaA, Weinheim

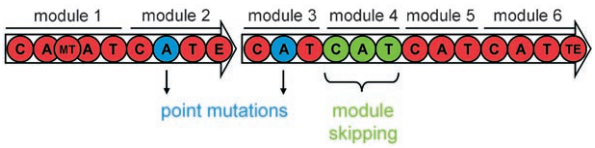

Big effects from small changes: In a comparative analysis of the nonribosomal peptide synthetases (NRPSs) from the biosynthetic pathways of two highly related myxobacterial lipopeptides, module skipping and point mutations are directly correlated to structural variations in these natural products. The skipping process during myxochromide S biosynthesis was characterized biochemically and represents the first example of a module skipping in NRPS systems.

Biosynthesis

S. C. Wenzel, P. Meiser, T. M. Binz, T. Mahmud, R. Müller* ____ **2296 – 2301**

Nonribosomal Peptide Biosynthesis: Point Mutations and Module Skipping Lead to Chemical Diversity

---

A 16-membered ring consisting of eight aluminum or gallium atoms and eight phosphorus atoms is the central structural motif in the polycyclic compounds formed through the reaction of the diphosphanyldisiloxane $O(SiiPr_2PH_2)_2$ with MEt_3 (M = Al, Ga; see the heteroatom framework of the gallium compound).

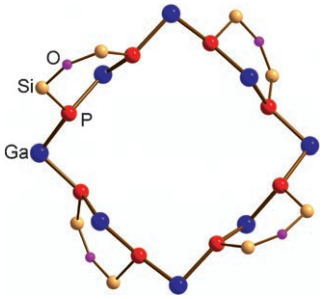

Main Group Element Compounds

C. von Hänisch,* S. Stahl ____ **2302 – 2305**

Synthesis of Macrocyclic Aluminum–Phosphorus and Gallium–Phosphorus Compounds

---

Just two oxidation states are involved in the homogeneous reduction of azo compounds at a single palladium catalyst site. The reaction proceeds through an intermediate state in which the catalyst displays a novel palladadiaziridine structure, and ethanol or related alcohols can be employed as the terminal reducing agent (see scheme).

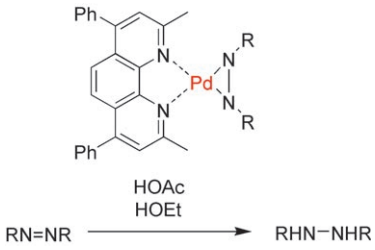

Homogeneous Catalysis

K. Muñiz,* M. Nieger ____ **2305 – 2308**

Catalytic Activation of N–N Multiple Bonds: A Homogeneous Palladium Catalyst for Mechanistically Unprecedented Reduction of Azo Compounds

---

Sources

Product and Company Directory

You can start the entry for your company in "Sources" in any issue of *Angewandte Chemie*.

If you would like more information, please do not hesitate to contact us.

Wiley-VCH Verlag – Advertising Department
Tel.: 0 62 01 - 60 65 65
Fax: 0 62 01 - 60 65 50
E-Mail: MSchulz@wiley-vch.de

Service

Keywords ____ *2310*

Authors ____ *2311*

Preview ____ *2313*

© 2006 Wiley-VCH Verlag GmbH & Co. KGaA, Weinheim

Corrigenda

Reaction Progress Kinetic Analysis: A Powerful Methodology for Mechanistic Studies of Complex Catalytic Reactions

D. G. Blackmond* _____ **4302–4320**

Angew. Chem. Int. Ed. **2005**, *44*

DOI 10.1002/anie.200462544

Reference [29] should read as listed below. The author apologizes for this oversight.

[29] T. Schultz, PhD Thesis, Universität Basel (Switzerland), **2004**.

Diagnostics of Single Base-Mismatch DNA Hybridization on Gold Nanoparticles by Using the Hyper-Rayleigh Scattering Technique

P. C. Ray* _____ **1151–1154**

Angew. Chem. Int. Ed. **2006**, *45*

DOI 10.1002/anie.200503114

The TEM image in Figure 4 showing aggregated gold nanoparticles after the addition of target DNA into the probe DNA was not the data recorded in the study but instead an image reported by Sato et al. (see Reference [1m]) which was used for comparative purposes. The correct image of the sample from the study is shown below (Figure 4). The author apologizes for this oversight and emphasizes that the error does not affect the discussion of the results in the Communication.

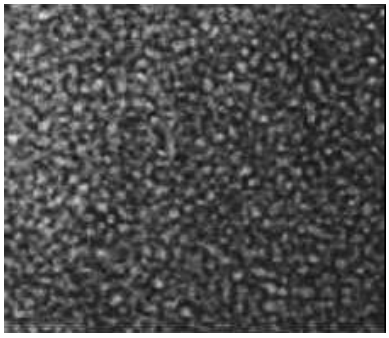

Figure 4. TEM image of aggregated gold nanoparticles after the addition of target DNA into the probe DNA.

[1] m) K. Sato, K. Hosokawa, M. Maeda, *J. Am. Chem. Soc.* **2003**, *125*, 8102.

For more information on ChemMedChem see www.chemmedchem.org

 © 2006 Wiley-VCH Verlag GmbH & Co. KGaA, Weinheim

Awarded...

ACS Awards to J. Gasteiger...

Johann Gasteiger (University of Erlangen-Nürnberg) receives the American Chemical Society (ACS) Award for Computers in Chemical & Pharmaceutical Research. He is recognized for his achievements in the field of chemoinformatics, including the development of databases such as Beilstein, simulation of chemical reactions and synthesis design, modeling of physicochemical effects, drug design, and simulation and analysis of spectra. He coauthored a book entitled *Neural Networks in Chemistry and Drug Design*[1a] and edited the *Handbook of Chemoinformatics*.[1b]

J. Gasteiger

Gasteiger is head of the Chemistry–Information–Computers division of the Gesellschaft Deutscher Chemiker (GDCh, German Chemical Society).

Gasteiger completed his PhD in 1971 at the Ludwig-Maximilians-Universität in Munich under the guidance of R. Huisgen on mechanistic studies of the reactions of cyclooctatetraene. He then joined A. Streitwieser at the University of California in Berkeley as a postdoctoral fellow, carrying out ab initio calculations on carbanions. He then joined the Technical University of Munich as a scientific assistant and later completed his habilitation in 1979 on models and algorithms for chemical reactions and reactivity. In 1994 he moved to Erlangen as professor, where he co-founded the Computer Chemistry Center with T. Clark und P. von R. Schleyer.

... and J. F. Hartwig ...

The ACS Award in Organometallic Chemistry for 2006 is presented to John F. Hartwig (Yale University, New Haven, CT, USA). Hartwig studied chemistry at Princeton and completed his PhD at the University of California in Berkeley working with R. G. Bergman and R. A. Andersen. He then worked as an American Cancer Society postdoctoral fellow with S. J. Lippard at the Massachusetts Institute of Technology. In 1992 he joined Yale University, where he is now a professor. His research focuses on the development of new transition-metal-catalyzed reactions and the elucidation of their mechanisms. He recently reported in *Angewandte Chemie* on highly reactive, general, and long-lived catalysts for coupling heteroaryl and aryl chlorides with primary nitrogen nucleophiles,[2a] as well as the regiospecific side-chain functionalization of linear low-density polyethylene with polar groups.[2b]

J. F. Hartwig

... and P. G. Schultz

Peter G. Schultz (Scripps Research Institute, La Jolla, CA) is the recipient of the Arthur C. Cope Award for his work on catalytic antibodies.[3a] Schultz completed his PhD in 1984 at the California Institute of Technology under the guidance of P. Dervan on synthetic molecules that cleave DNA, and then carried out postdoctoral research with C. Walsh at the Massachusetts Institute of Technology. In 1985 he joined the University of California in Berkeley as an assistant professor and was appointed full professor in 1989. During his time at Berkeley he also held positions as a project leader at the Lawrence Berkeley National Laboratory and an investigator at the Howard Hughes Medical Institute. He joined the Scripps Research Institute in 1999. Schultz has founded several biotechnology companies and serves on the editorial boards of *ChemMedChem* and *ChemBioChem*, among others. He recently reported in *Angewandte Chemie* on a synthetic small molecule that induces neuronal differentiation of adult hippocampal neural progenitor cells.[3b]

P. G. Schultz

[1] a) J. Zupan, J. Gasteiger, *Neural Networks in Chemistry and Drug Design*, Wiley-VCH, Weinheim, **1999**; b) *Handbook of Chemoinformatics* (Ed.: J. Gasteiger), Wiley-VCH, Weinheim, **2003**.

[2] a) Q. Shen, S. Shekhar, J. P. Stambuli, J. F. Hartwig, *Angew. Chem.* **2005**, *117*, 1395; *Angew. Chem. Int. Ed.* **2005**, *44*, 1371; b) C. Bae, J. F. Hartwig, H. Chung, N. K. Harris, K. A. Switek, M. A. Hillmyer, *Angew. Chem.* **2005**, *117*, 6568; *Angew. Chem. Int. Ed.* **2005**, *44*, 6410.

[3] a) P. G. Schultz, J. Y. Lin, R. A. Lerner, *Angew. Chem.* **2002**, *114*, 4607; *Angew. Chem. Int. Ed.* **2002**, *41*, 4427; b) M. Warashina, K. Hoon Min, T. Kuwabara, A. Huynh, F. H. Gage, P. G. Schultz, S. Ding; *Angew. Chem.* **2006**, *118*, 605; *Angew. Chem. Int. Ed.* **2006**, *45*, 591.

DOI: 10.1002/anie.200600728

WILEY InterScience DISCOVER SOMETHING GREAT
© 2006 Wiley-VCH Verlag GmbH & Co. KGaA, Weinheim

Photochemistry

DOI: 10.1002/anie.200503908

Organocatalytic Enantioselective Photoreactions

*Pablo Wessig**

Keywords:
asymmetric catalysis · enantioselectivity · photochemistry · photoinduced electron transfer · sensitizers

In the area of enantioselective reactions tremendous progress has been made in the last decades, mainly because of the development of efficient transition-metal catalysts.[1] These transition-metal-catalyzed, enantioselective reactions will certainly continue to play a central role in synthetic organic chemistry in the future. However, the last years have seen an increasing trend to the use of metal-free catalysts, so-called organocatalysts.[2] The reasons are the often high costs of transition metals and the problems that their residues, mainly in pharmaceutical products, can cause. The 35-year-old Hajos–Parrish–Eder–Sauer—Wiechert reaction,[3] an asymmetric Robinson anellation catalyzed by the natural amino acid proline, is a classic example of organocatalysis.

If one considers the extensive knowledge concerning enantioselective catalysis in thermal organochemical reactions,[4] it is astonishing that so little is known about catalytic enantioselective photochemical reactions. Upon closer look the possible reasons become clear. The reaction rate in the electronic ground state is determined by the activation barrier, the height of which can be controlled by catalysts. Photochemical reactions often proceed by extremely fast elementary steps in the excited state. The macroscopically observed rate is mostly controlled by the addition of the "reagent light", that is, by the proton flow, and by the degree of "non-productive" chemical and physical channels of deactivation, which are expressed in terms of the quantum yield. Thus, it could be considered hopeless to try to catalyze photochemical reactions in the conventional sense, to say nothing of enantioselective reactions. Recently significant success has been achieved in this area, which is highlighted here. A range of approaches should also be mentioned that have been published lately, for example photoreactions in zeolites doped with chiral-auxiliary reagents and photoreactions in crystals, but they are not the main subject of this article.[5]

The known organocatalytic enantioselective photoreactions (OCEP)[6] are based on two different approaches. In the first, the photochemical excitation and the enantioselective key step are decoupled (Scheme 1). The prerequisite

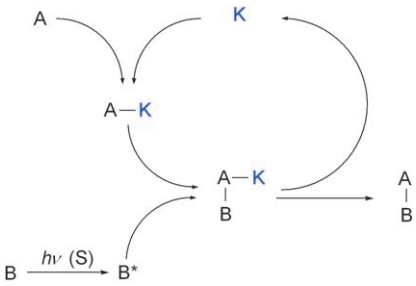

Scheme 1.

is that reactants **A** and **B** do not react with each other (or if they do, only very slowly) in either the ground state or in the excited state. One of the reactants (**B**) is, through sensitization (**S**) if necessary, converted into the excited state **B***, while the other reactant (**A**) forms a (not necessarily covalent) complex **A**–**K** with the chiral catalyst **K**. This complex now reacts with **B*** because of its changed electronic properties to give the complex **B**–**A**–**K**, which dissociates into the product **A**–**B**, releases **K**, and completes the catalytic cycle.

This concept is illustrated in research conducted by Cordóva et al. which is based on the fact that photochemically (sensitized) generated singlet oxygen (**B***) reacts with an enamine (**A**–**K**) but not with the carbonyl compound (**A**) from which it is formed. In the present case aldehydes[7a] and ketones[7b] were treated with singlet oxygen in the presence of a natural amino acid (Scheme 2). The carbonyl compound **1** and the amino acid **2** reversibly form enamine **3**, which reacts highly stereoselectively to give the hydroperoxides **4**. Subsequent hydrolysis (**4**→**5**) regenerates the organocatalyst, and the hydroperoxides **5** are transformed spontaneously into the α-hydroxycarbonyl compounds **6** (which in the case of an aldehyde are reduced to the corresponding 1,2-diols). Starting from the aldehydes an enantiomeric excess of up to 66% *ee* and from ketones even up to 72% *ee* could be achieved. Remarkably, the amino acid catalyst with the shortest side chain, alanine, provided the best selectivities. The relevance of this process in the prebiotic enantioselective formation of α-hydroxycarbonyl compounds was discussed but should be regarded critically. Furthermore, some mechanistic details of this reaction still remain vague: up to now the hydroperoxycarbonyl compounds **5** have not been detected but only postulated.

The second approach differs from the first mainly in the tight coupling of the energy transfer to the substrate and the enantioselective key step (Scheme 3). The central role is played

[*] Priv.-Doz. Dr. P. Wessig
Institut für Chemie
Humboldt-Universität zu Berlin
Brook-Taylor-Strasse 2
12489 Berlin (Germany)
Fax: (+49) 30-2093-7450
E-mail: pablo.wessig@chemie.hu-berlin.de

InterScience
© 2006 Wiley-VCH Verlag GmbH & Co. KGaA, Weinheim

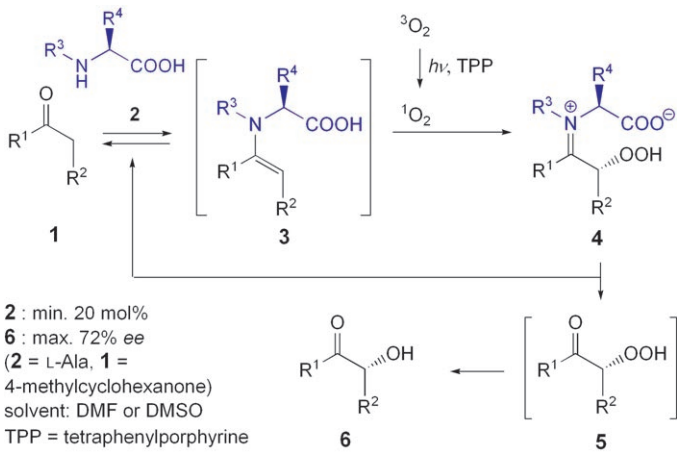

Scheme 2.

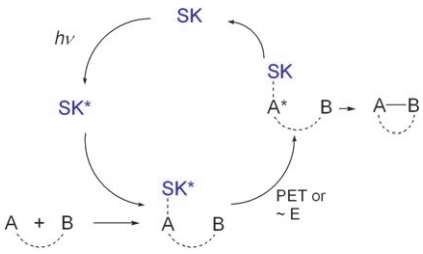

Scheme 3.

by a chiral complexing reagent **SK**, which at the same time acts as a sensitizer and transfers the energy to the substrate. The prerequisite is that **A** and **B** (which can be linked) are photochemically inactive or not very active. After the excitation of **SK**, a complex with **A** and **B** is formed, in which the excitation energy is transferred to the substrate; this can also be coupled with a photoinduced electron transfer (PET). The enantioselective key step then occurs, and **SK** is released again (Scheme 3, the excitation can alternatively proceed in the preformed complex).

The important points of this approach are high facial differentiation in the complex **SK**–**A**···**B** and the exclusion of intermolecular sensitization.[8] The complexation can be achieved by directed hydrogen bonds. In this context, Bach and his group have been examining an interesting class of complexing reagents for potential applications in enantioselective photoreactions. These reagents are derived from Kemp's triacid (**7**), which can be converted in a few steps into molecules with unique architecture.

The most impressive structural feature of compounds like **8** and **9** is the aryl moiety, which shields one face of the lactam ring like a rigid wall. If the substrate of a photochemical reaction also contains a lactam moiety, it can bind to a receptor like **8** through two hydrogen bonds and ideally can be attacked only from one side (Scheme 4).

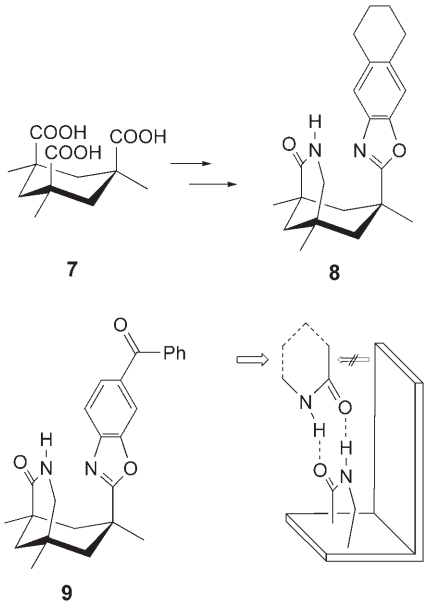

Scheme 4.

In the last years Bach et al. have applied this concept successfully to a range of photochemical reactions.[9–13] Despite impressive success, this approach had the disadvantage of requiring at least equimolar amounts of the complexing reagent; that is, it is not catalytic.

Most recently Bach and his co-workers achieved a breakthrough.[14] In contrast to the previously applied photochemically "passive" complexing reagents such as **8**, a reagent with an "integrated" photoelectron acceptor (**9**) is used. In the presence of only 0.3 equiv of **9** (pyrrolidinylethyl)quinolone **10** cyclizes to form the spiro compound **15** in 64% yield and with a selectivity of 70% *ee* (Scheme 5). The key step of this reaction probably is a photoinduced electron transfer (PET) in complex **11** from the nitrogen atom of the tertiary amine to the excited benzophenone chromophore in **9** with formation of the radical anion/radical cation pair **12**. This is followed by a proton transfer and formation of the radical pair **13**. A crucial point seems to be the existence of this radical pair in the triplet state,[15a] which prevents the radical centers from recombining through bond formation. An attack of the pyrrolidin-2-yl radical moiety on the C–C double bond of the quinolone proceeds preferably from the left side and the product complex **14** is formed by hydrogen back-transfer. The secret of success is probably the presence of a highly acidic OH group[15b] in complex **13**, which could stabilize **13** significantly relative to **11** and **14** by an additional hydrogen bond. The decrease in the enantiomeric excess at a lower catalyst concentration is ascribed to radical-chain processes[16] and insufficient complexation.

In the absence of face differentiation or complexation, the enantiomeric excess decreases, in keeping with the concept shown in Scheme 3, and no multiplication of chirality occurs. In one example, Krische et al.[17] employed receptor **16**, which contains a benzophenone moiety as a triplet sensitizer. Compound **16** is capable of binding quinolone **17** through hydrogen bonds with formation of complex **18** ($\lg K_a = 2.5 \pm 0.2$). After photochemical excitation the benzophenone moiety sensitizes the quinolone and the tricycle **20** is formed as a result of [2+2] cycloaddition. Receptor **16** can be applied in substoichiometric amounts (25 mol%), which proves a certain catalytic activity. However, the maximum achievable enantiomeric excess amounts to only 22% *ee* (with 1 equiv **16**, 19% *ee* with 0.25 equiv; Scheme 6). The yield of the

 © 2006 Wiley-VCH Verlag GmbH & Co. KGaA, Weinheim

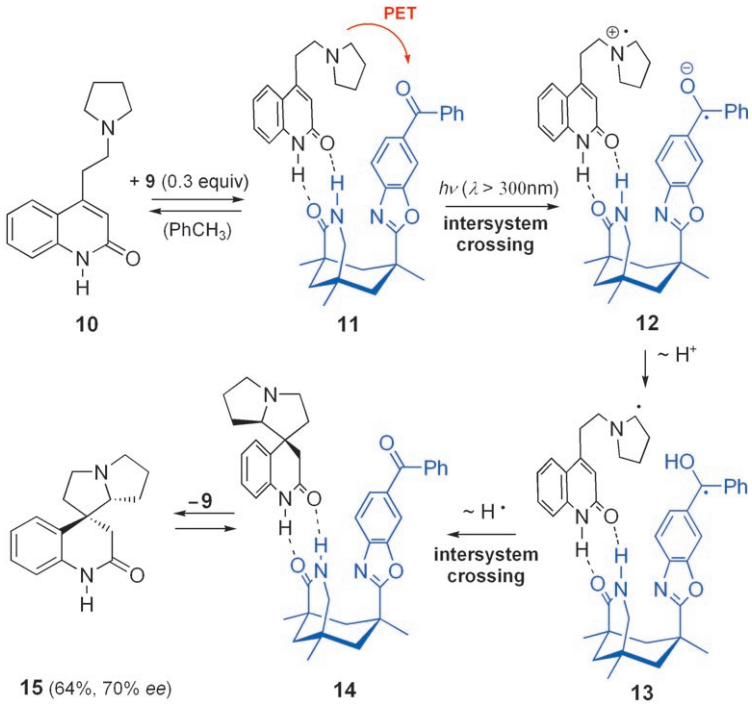

Scheme 5.

reaction was not noted, and the absolute configuration of the preferred enantiomer was not determined.

In summary, it can be stated that photochemical reactions can indeed be carried out enantioselectively, if suitable catalysts are used. Hopefully, based on the reported results, many more organocatalytic enantioselective photoreactions will be discovered in the next years.

Published online: February 24, 2006

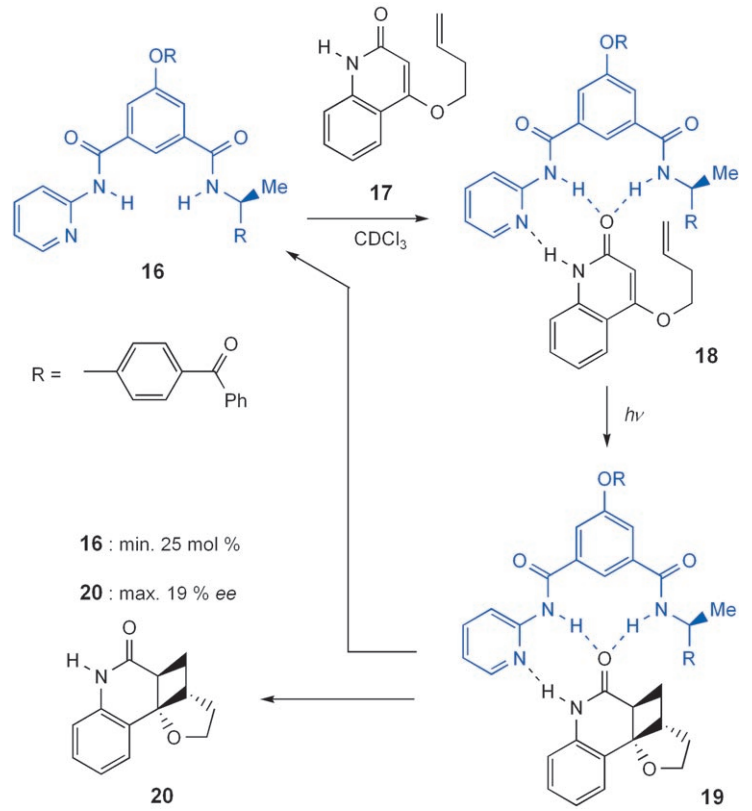

Scheme 6.

[1] Outstanding developments in this area have been honored with the Nobel Prize in Chemistry in 2001: a) R. Noyori, *Angew. Chem.* **2002**, *114*, 2108; *Angew. Chem. Int. Ed.* **2002**, *41*, 2008; b) W. S. Knowles, *Angew. Chem.* **2002**, *114*, 2096; *Angew. Chem. Int. Ed.* **2002**, *41*, 1998; c) K. B. Sharpless, *Angew. Chem.* **2002**, *114*, 2126; *Angew. Chem. Int. Ed.* **2002**, *41*, 2024.

[2] a) Special Issue "Asymmetric Organocatalysis", *Acc. Chem. Res.* **2004**, *37*(8); b) P. I. Dalko, L. Moisan, *Angew. Chem.* **2004**, *116*, 5248; *Angew. Chem. Int. Ed.* **2004**, *43*, 5138; c) S. Jayasree, B. List, *Org. Biomol. Chem.* **2005**, *3*, 719.

[3] a) Z. G. Hajos, D. R. Parrish, *J. Org. Chem.* **1974**, *39*, 1615; b) U. Eder, G. Sauer, R. Wiechert, *Angew. Chem.* **1971**, *83*, 492; *Angew. Chem. Int. Ed.* **1971**, *10*, 496.

[4] A CA search with the key word "catalytic enantioselective" yielded 124 hits for the year 2004.

[5] *Chiral Photochemistry. Molecular and Supramolecular Photochemistry, Vol. 11* (Eds.: Y. Inoue, V. Ramamurthy), Marcel Dekker, New York, **2004**.

[6] "Organocatalytic enantioselective" in this case means reactions in which the catalyst is an organic, metal-free substance bearing the stereochemical information.

[7] a) A. Córdova, H. Sundén, M. Engqvist, I. Ibrahem, J. Casas, *J. Am. Chem. Soc.* **2004**, *126*, 8914; b) H. Sundén, M. Engqvist, J. Casas, I. Ibrahem, A. Córdova, *Angew. Chem.* **2004**, *116*, 6694; *Angew. Chem. Int. Ed.* **2004**, *43*, 6532.

[8] Earlier reports by Kim and Schuster [a–c] and by Inoue et al. [d–f] about asymmetric cycloadditions with chiral sensitizers only gave very low yields and enantiomeric excesses: a) N. Akbulut, D. Hartsough, J. I. Kim, G. B. Schuster, *J. Org. Chem.* **1989**, *54*, 2549; b) J. I. Kim, G. B. Schuster, *J. Am. Chem. Soc.* **1990**, *112*, 9635; c) J. I. Kim, G. B. Schuster, *J. Am. Chem. Soc.* **1992**, *114*, 9309; d) Y. Inoue, T. Okano, N. Yamasaki, A. Tai, *J. Photochem. Photobiol. A* **1992**, *66*, 61; e) S. Asaoka, M. Ooi, P. Jiang, T. Wada, Y. Inoue *J. Chem. Soc. Perkin Trans. 2* **2000**, 77; f) Y. Inoue, N. Sugahara, T. Wada, *Pure Appl. Chem.* **2001**, *73*, 475.

 © 2006 Wiley-VCH Verlag GmbH & Co. KGaA, Weinheim

[9] [2+2] Cycloadditions: a) T. Bach, H. Bergmann, K. Harms, *J. Am. Chem. Soc.* **1999**, *121*, 10650; b) T. Bach, H. Bergmann, *J. Am. Chem. Soc.* **2000**, *122*, 11525; c) T. Bach, H. Bergmann, B. Grosch, K. Harms, *J. Am. Chem. Soc.* **2002**, *124*, 7982.
[10] [4+4] Cycloadditions: T. Bach, H. Bergmann, K. Harms, *Org. Lett.* **2001**, *3*, 601.
[11] Norrish—Yang reactions: a) T. Bach, T. Aechter, B. Neumüller, *Chem. Commun.* **2001**, 607; b) T. Bach, T. Aechter, B. Neumüller, *Chem. Eur. J.* **2002**, *8*, 2464.
[12] 6π Photocyclizations: T. Bach, B. Grosch, T. Strassner, E. Herdtweck, *J. Org. Chem.* **2003**, *68*, 1107.
[13] Diels—Alder reactions of photochemically generated dienols: a) B. Grosch, C. N. Orlebar, Y. Inoue, E. Herdtweck, W. Massa, T. Bach, *Angew. Chem.* **2003**, *115*, 3822; *Angew. Chem. Int. Ed.* **2003**, *42*, 3693; b) B. Grosch, C. N. Orlebar, E. Herdtweck, M. Kaneda, T. Wada, Y. Inoue, T. Bach, *Chem. Eur. J.* **2004**, *10*, 2179.
[14] A. Bauer, F. Westkämper, S. Grimme, T. Bach, *Nature* **2005**, *436*, 1139.
[15] a) After photochemical excitation benzophenone undergoes a very efficient intersystem crossing to the triplet state; b) the acidity of α-hydroxy-substituted radicals is comparable to that of carboxylic acids.
[16] S. Bertrand, N. Hoffmann, J.-P. Pete, *Eur. J. Org. Chem.* **2000**, 2227.
[17] D. F. Kauble, V. Lynch, M. J. Krische, *J. Org. Chem.* **2003**, *68*, 15.

WILEY InterScience®
DISCOVER SOMETHING GREAT
Access some of the finest full text journals, reference works, books, and databases from around the globe. It's just what you need to make some important discoveries of your own.
ABOUT US
VIEW DEMO
CONTACT US
HELP
Access your saved titles, articles, queries and alerts in My Profile.
USER NAME PASSWORD
Remember Me Go
Register Now | Athens Login
Forgot My Password

Manage your access easily with "MY PROFILE"

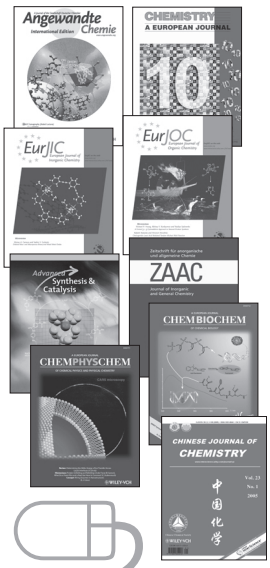

Simply register. Registration is fast and free to all internet users.

Easy Access
- Save Titles, Articles & Queries for quick access
- Set up roaming access to access content outside of your institutions network
- Get free online sample copies
- Get free online trial subscriptions
- View a complete list of your subscriptions and accessible products

Enhanced Tools
- Receive E-Mail Alerts when new content is available
- Purchase Article Select Tokens online
- Purchase individual articles online with Pay-Per-View

www.interscience.wiley.com

WILEY InterScience®
DISCOVER SOMETHING GREAT

17341502.vo

 © 2006 Wiley-VCH Verlag GmbH & Co. KGaA, Weinheim

Asymmetric Synthesis

DOI: 10.1002/anie.200503783

Construction of Asymmetric Fluorinated Carbon Centers

G. K. Surya Prakash and Petr Beier*

Keywords:
asymmetric catalysis · asymmetric synthesis · enantioselectivity · organofluorine compounds · palladium

Selectively fluorinated molecules are of central importance in the pharmaceutical and agrochemical industries as well as in the development of materials with novel properties. The fluorine atom endows unique properties to such molecules.[1] For example, in biologically active compounds the replacement of a hydrogen or hydroxy group with a fluorine atom often leads to improved characteristics including the resistance to metabolic transformations, increased stability, and enhanced lipophilicity.[2] The importance of chirality in medicinal chemistry is well documented,[3] and thus the methods for selective formation of carbon–fluorine bonds and in particular fluorinated stereogenic carbon centers are highly desirable.

Early methods for the preparation of stereogenic fluorinated carbon atoms relied on substrate-controlled diastereoselective fluorinations.[4] More recently reagent-controlled enantioselective fluorinations employing stochiometric amounts of electrophilic fluorinating agents have been reported. In these reactions chiral *N*-fluorosultams, -sulfonamides, or ammonium salts are used for the enantioselective fluorination of various enolizable substrates.[4a,5]

The first catalytic electrophilic fluorination was developed by Hintermann and Togni.[6] Using chiral titanium tadolate complexes such as **1** and **2** and nonchiral selectfluor **3**,[7] they achieved efficient fluorination of β-ketoesters **4** to give **5**, which contains a quarternary C–F stereogenic center, with up to 91% *ee* (Scheme 1).

Since then a number of other metal-based catalytic systems have appeared in the literature. Sodeoka and co-workers[8] developed dicationic palladium complexes **6** and **7** (Tf = trifluoromethanesulfonyl) for efficient fluorination of β-ketoesters (up to 94% *ee*), β-ketophosphonates (up to 98% *ee*), and oxindoles (up to 96% *ee*) using *N*-fluorobenzenesulfonimide (NFSI). Similar palladium species were used by Kim and Kim for the fluorination of α-cyanoacetates.[9]

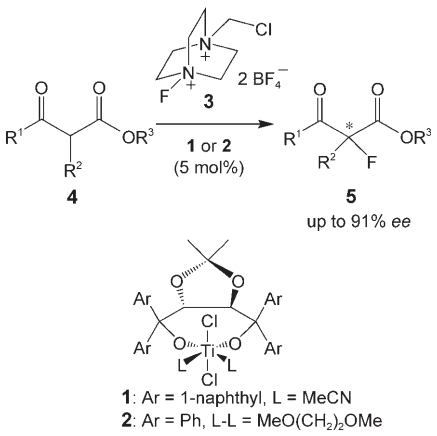

Scheme 1. The first catalytic electrophilic fluorination.

Various carbonyl compounds were enantioselectively fluorinated using *N*-fluorobenzenesulfonimide (NFSI) in the presence of catalytic amounts of Lewis acids like $Cu(OTf)_2$, $Ni(ClO_4)_2$, or $Zn(ClO_4)_2$ and chiral bisoxazoline ligands **8** or **9**.[10]

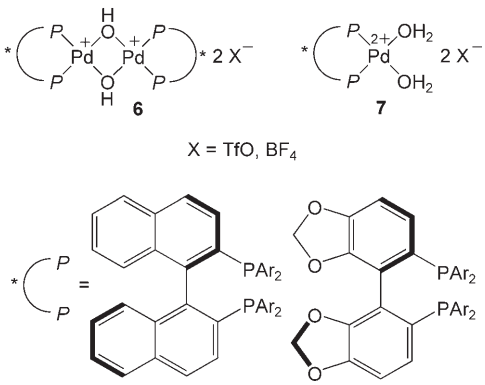

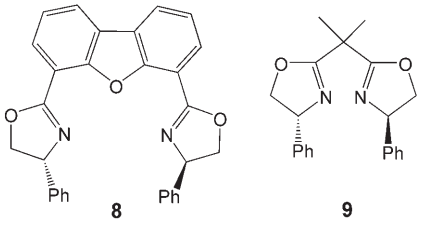

Kim and Park reported enantioselective fluorination of β-ketoesters with NFSI catalyzed by phase-transfer catalysts (cinchonine-derived quaternary ammonium salts).[11]

Very recently other direct organocatalytic enantioselective fluorinations of ketones and aldehydes were successfully realized. The first direct fluorination of aldehydes and ketones using selectfluor **3** catalyzed by (*S*)-proline and related compounds was reported by

[*] Prof. Dr. G. K. S. Prakash, Dr. P. Beier
Loker Hydrocarbon Research Institute and Department of Chemistry
University of Southern California
837 Bloom Walk
Los Angeles, CA 90034-1661 (USA)
Fax: (+1) 213-740-6270
E-mail: gprakash@usc.edu

InterScience
© 2006 Wiley-VCH Verlag GmbH & Co. KGaA, Weinheim

Enders and Hüttl.[12] However, the observed enantioselectivities were low. A much more efficient system was described by Jørgensen and co-workers.[13] The silylated prolinol derivative **10**, acting as a catalyst through an enamine mechanism, showed high activity and selectivity for the fluorination of enolizable aldehydes **11** (Scheme 2). The obtained α-fluoroaldehydes **12** were reduced to more stable and less volatile fluoroalcohols **13**. The bulky aryl groups in the catalyst **10** not only sterically shield one side of the enamine in the fluorination step but also prevent abstraction of the remaining proton to form a fluoroenamine. This explains the observed high *ee* values.

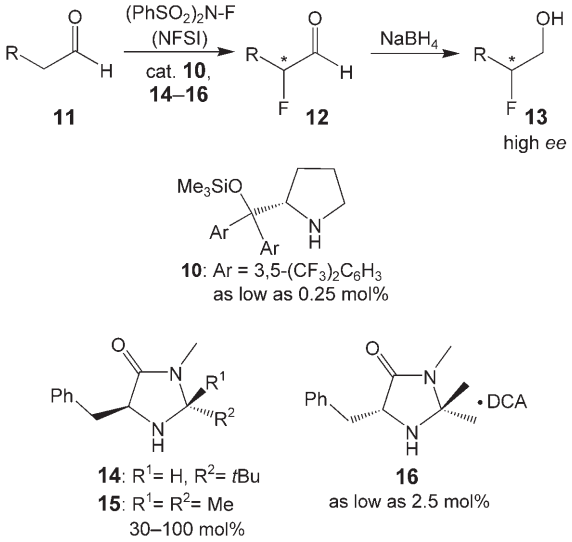

Scheme 2. Recent examples of organocatalytic enantioselective fluorination reactions. DCA = dichloroacetic acid.

In a study carried out by Barbas and coworkers,[14] imidazolidinones **14** and **15** were used as organocatalysts for the enantioselective fluorination of branched aldehydes with moderate enantioselectivities or as stoichiometric chiral promoters for the fluorination of straight-chain aldehydes **11** (up to 96% *ee*, Scheme 2). Beeson and MacMillan[15] exploited the imidazolidinone catalyst **16** in the electrophilic fluorination of a range of aldehydes (Scheme 2). In most cases alcohols **13** were obtained in excellent enantioselectivities (up to 99% *ee*). These mild organocatalytic fluorination methods[12–15] allow preparation of not only stable quaternary fluorinated carbon atoms in the form of α-fluoro, α-substituted carbonyl compounds but also much less stable α-fluoro aldehydes containing a tertiary C–F center.

In contrast, attempts to develop stoichiometric or catalytic enantioselective nucleophilic fluorination have not produced satisfactory yields and enantioselectivities so far.[4a,5a]

An alternative and elegant synthetic strategy based on enantioselective carbon–carbon bond reorganization rather than on enantioselective fluorination has been presented recently by Nakamura and co-workers.[16] Here racemic allylic α-fluoro-β-ketoesters **17** underwent a palladium-catalyzed enantioselective decarboxylation/allylation reaction in the presence of chiral phosphane-oxazoline ligand **18** to give an optically active α-fluoroketone **19** (Scheme 3).

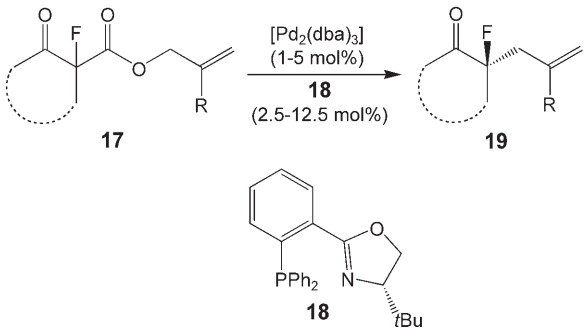

Scheme 3. Palladium-catalyzed enantioselective formation of α-fluoroketones **19** from racemic fluorinated β-ketoesters **17**. dba = dibenzylideneacetone.

In numerous cases, excellent yields and enantioselectivities have been achieved. The highest enantioselectivity was observed for cyclic ketones (up to 99% *ee* for **19a**), but the reaction was also applicable to acyclic substrates albeit with moderate enantioselectivities. Other types of chiral phosphine ligands including 2,2′-bis(diphenylphosphanyl)-1,1′-binaphthyl (binap) were not as selective as **18**, and the bulky *tert*-butyl group on the oxazoline ring was necessary to achieve good enantioselectivities. Furthermore, the reaction is also suitable for the construction of quaternary carbon centers with high enantioselectivities as exemplified in the product **19b**.

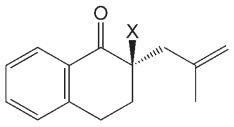

19a X = F, 99% *ee*
19b X = Me, 95% *ee*

Mechanistically the reaction resembles the Carroll rearrangement,[17] which proceeds either as a thermal or palladium-catalyzed process (Scheme 4). The enantioselectivity arises in the alkylation of the enolate by the cationic allylpalladium complex equipped with chiral phosphine ligands. It would be interesting to see whether the present methodology could be simplified to the intermolecular alkylation of fluorinated metal enolates or silyl enol ethers with suitable electrophiles (such as diallyl carbonate) in the presence of a metal catalyst.

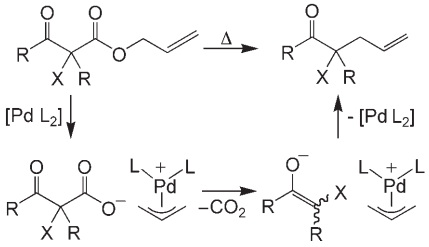

Scheme 4. Mechanism of palladium-catalyzed Carroll rearrangement.

The concept of the formation of stereogenic fluorinated carbon atoms from racemic or prochiral molecules is not entirely new. For instance, olefin hydrogenation has been applied successfully to fluorinated substrates (Scheme 5).[18]

 © 2006 Wiley-VCH Verlag GmbH & Co. KGaA, Weinheim

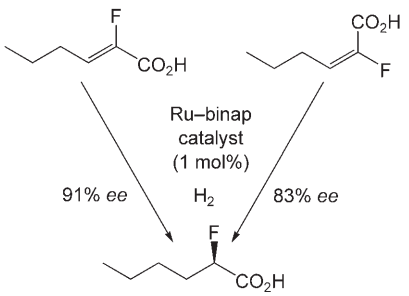

Scheme 5. Asymmetric hydrogenation of isomers of 2-fluoro-2-hexenoic acid.

Highly enantioselective catalytic Mukaiyama aldol reactions between fluorinated silyl acetals and various aldehydes have also been reported.[19] Shioiri and co-workers[20] also found that the asymmetric alkylation of racemic α-fluorotetralone (**20**) is catalyzed by phase-transfer organocatalyst **21** to give the chiral fluorinated ketone **22** (up to 91 % *ee*, Scheme 6).

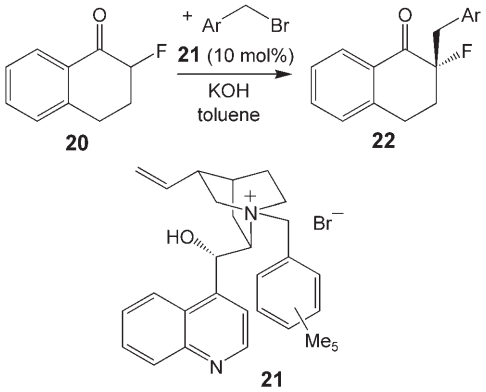

Scheme 6. Enantioselective catalytic alkylation of α-fluorotetralone (**20**).

It is not surprising that there has been considerable effort in the development of methods for the preparation of enantiomerically pure α-fluorocarbonyl compounds. They provide configurationally stable substitutes for molecules containing a tertiary chiral carbon atom next to a carbonyl group, an extremely important structural motif in medicinal chemistry. The recently discovered catalytic enantioselective alkylation[16] by Nakamura and co-workers represents a very efficient procedure for the construction of such structures. However, the mechanistic details and full scope of this transformation remain to be explored in more detail.

Published online: March 3, 2006

[1] a) P. Kirsch, *Modern Fluoroorganic Chemistry*, Wiley-VCH, Weinheim, **2004**; b) R. D. Chambers, *Fluorine in Organic Chemistry*, Blackwell, Oxford, **2004**.

[2] a) *Organofluorine Compounds in Medicinal Chemistry and Biomedical Applications* (Eds.: R. Filler, Y. Kobayashi, L. M. Yagupolskii), Elsevier Science, Amsterdam, **1993**; b) *Biomedical Frontiers of Fluorine Chemistry* (Eds.: I. Ojima, J. R. McCarthy, J. T. Welch), American Chemical Society, Washington, DC, **1996** (ACS Symposium Series 639); c) H.-J. Böhm, D. Banner, S. Bendels, M. Kansy, B. Kuhn, K. Müller, U. Obst-Sander, M. Stahl, *ChemBioChem* **2004**, *5*, 637 – 643.

[3] a) D. A. Williams, T. L. Lemke, *Foye's Principles of Medicinal Chemistry*, 5th ed., Lippincott Williams & Wilkins, Philadelphia, **2002**; b) G.-O. Lin, Y.-M. Li, A. S. C. Chan, *Principles and Applications of Asymmetric Synthesis*, Wiley-Interscience, New York, **2001**.

[4] a) J.-A. Ma, D. Cahard, *Chem. Rev.* **2004**, *104*, 6119 – 6146; b) V. A. Soloshonok, *Enantiocontrolled Synthesis of Fluoro-organic Compounds*, Wiley, Chichester, **1999**; c) *Asymmetric Fluoroorganic Chemistry* (Ed.: P. V. Ramachandran), American Chemical Society, Washington, DC, **2000** (ACS Symposium Series 746).

[5] a) H. Ibrahim, A. Togni, *Chem. Commun.* **2004**, 1147 – 1155; b) K. Muñiz, *Angew. Chem.* **2001**, *113*, 1701 – 1704; *Angew. Chem. Int. Ed.* **2001**, *40*, 1653 – 1656.

[6] a) L. Hintermann, A. Togni, *Angew. Chem.* **2000**, *112*, 4530 – 4533; *Angew. Chem. Int. Ed.* **2000**, *39*, 4359 – 4362; b) S. Piana, I. Devillers, A. Togni, U. Rothlisberger, *Angew. Chem.* **2002**, *114*, 1021 – 1024; *Angew. Chem. Int. Ed.* **2002**, *41*, 979 – 982.

[7] a) P. T. Nyffeler, S. G. Durón, M. D. Burkart, S. P. Vincent, C.-H. Wong, *Angew. Chem.* **2005**, *117*, 196 – 217; *Angew. Chem. Int. Ed.* **2005**, *44*, 192 – 212; b) R. E. Banks, *J. Fluorine Chem.* **1998**, *87*, 1 – 17; c) G. S. Lal, G. P. Pez, R. G. Syvret, *Chem. Rev.* **1996**, *96*, 1737 – 1756.

[8] a) Y. Hamashima, K. Yagi, H. Takano, L. Tamás, M. Sodeoka, *J. Am. Chem. Soc.* **2002**, *124*, 14530 – 14531; b) Y. Hamashima, T. Suzuki, Y. Shimura, T. Shimizu, N. Umebayashi, T. Tamura, N. Sasamoto, M. Sodeoka, *Tetrahedron Lett.* **2005**, *46*, 1447 – 1450; c) Y. Hamashima, T. Suzuki, H. Takano, Y. Shimura, M. Sodeoka, *J. Am. Chem. Soc.* **2005**, *127*, 10164 – 10165.

[9] H. R. Kim, D. Y. Kim, *Tetrahedron Lett.* **2005**, *46*, 3115 – 3117.

[10] a) J.-A. Ma, D. Cahard, *Tetrahedron: Asymmetry* **2004**, *15*, 1007 – 1011; b) N. Shibata, J. Kohno, K. Takai, T. Ishimaru, S. Nakamura, T. Toru, S. Kanemasa, *Angew. Chem.* **2005**, *117*, 4276 – 4279; *Angew. Chem. Int. Ed.* **2005**, *44*, 4204 – 4207; c) L. Bernardi, K. A. Jørgensen, *Chem. Commun.* **2005**, 1324 – 1326.

[11] D. Y. Kim, E. J. Park, *Org. Lett.* **2002**, *4*, 545 – 547.

[12] D. Enders, M. R. M. Hüttl, *Synlett* **2005**, 991 – 993.

[13] M. Marigo, D. Fielenbach, A. Braunton, A. Kjœrsgaard, K. A. Jørgensen, *Angew. Chem.* **2005**, *117*, 3769 – 3772; *Angew. Chem. Int. Ed.* **2005**, *44*, 3703 – 3706.

[14] D. D. Steiner, N. Mase, C. F. Barbas III, *Angew. Chem.* **2005**, *117*, 3772 – 3776; *Angew. Chem. Int. Ed.* **2005**, *44*, 3706 – 3710.

[15] T. D. Beeson, D. W. C. MacMillan, *J. Am. Chem. Soc.* **2005**, *127*, 8826 – 8828.

[16] M. Nakamura, A. Hajra, K. Endo, E. Nakamura, *Angew. Chem.* **2005**, *117*, 7414 – 7417; *Angew. Chem. Int. Ed.* **2005**, *44*, 7248 – 7251.

[17] R. Kuwano, N. Ishida, M. Murakami, *Chem. Commun.* **2005**, 3951 – 3952.

[18] M. Saburi, L. Shao, T. Sakurai, Y. Uchida, *Tetrahedron Lett.* **1992**, *33*, 7877 – 7880.

[19] K. Iseki, Y. Kuroki, Y. Kobayashi, *Tetrahedron Lett.* **1997**, *38*, 7209 – 7210.

[20] S. Arai, M. Oku, T. Ishida, T. Shioiri, *Tetrahedron Lett.* **1999**, *40*, 6785 – 6789.

 © 2006 Wiley-VCH Verlag GmbH & Co. KGaA, Weinheim

C. Bruneau and P. H. Dixneuf

DOI: 10.1002/anie.200501391

Organometallic Catalysis

Metal Vinylidenes and Allenylidenes in Catalysis: Applications in Anti-Markovnikov Additions to Terminal Alkynes and Alkene Metathesis

Christian Bruneau and Pierre H. Dixneuf**

Keywords:
alkene metathesis · allenylidenes · anti-Markovnikov addition · homogeneous catalysis · vinylidenes

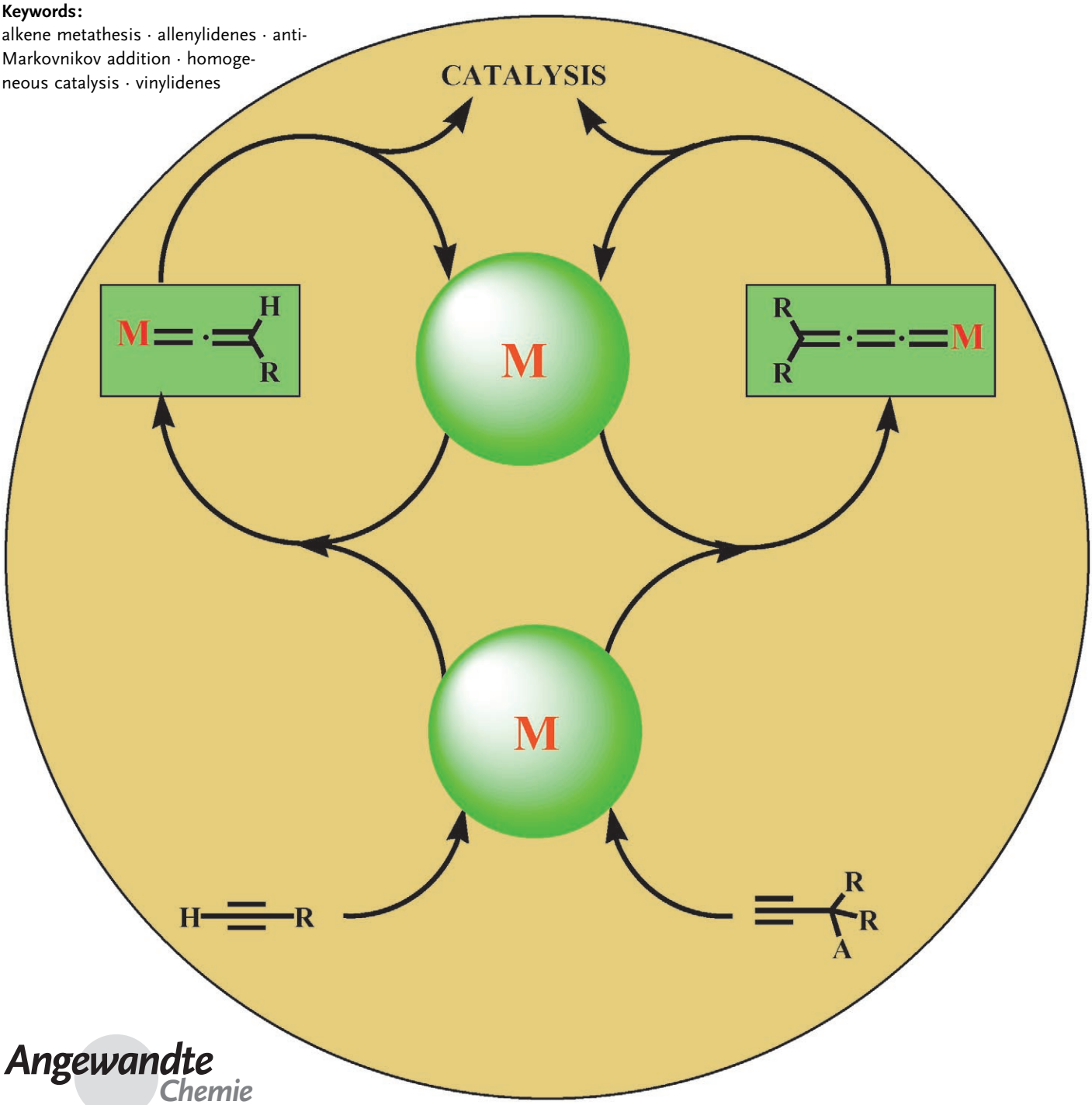

© 2006 Wiley-VCH Verlag GmbH & Co. KGaA, Weinheim

The involvement of a catalytic metal vinylidene species was proposed for the first time in 1986 to explain the regioselective formation of vinyl carbamates directly from terminal alkynes, carbon dioxide, and amines. Since this initial report, various metal vinylidenes and allenylidenes, which are key activation intermediates, have proved extremely useful for many alkyne transformations. They have contributed to the rational design of new catalytic reactions. This 20th anniversary is a suitable occasion to present the advancement of organometallic vinylidenes and allenylidenes in catalysis.

From the Contents

1. Introduction 2177
2. Catalytic Synthesis of Alkenyl Carbamates and Ureas: The Early Days 2178
3. Anti-Markovnikov Additions to Terminal Alkynes: Carbon–Heteroatom Coupling 2179
4. Metal Vinylidenes in Catalytic C–C Bond Formation 2185
5. Metal Vinylidenes in Alkene and Enyne Metathesis 2189
6. Metal Allenylidenes in Catalysis 2192
7. Ruthenium Allenylidenes as Catalyst Precursors in Alkene Metathesis 2195
8. Conclusions and Outlook 2199

1. Introduction

The stabilization of vinylidenes or allenylidenes upon coordination to a metal center is now a common feature encountered with many transition metals. The synthesis and stoichiometric reactivity of these unsaturated ligands have been broadly developed but are still under active investigation, and several aspects have already led to reviews.[1–14] Since the first mononuclear vinylidene complexes reported in 1972,[15] the most straightforward routes to vinylidene and allenylidene complexes is the direct activation of terminal alkynes and propargylic alcohols, respectively, thus allowing the involvement of these species in catalytic reactions from accessible acetylenic substrates.

The initial activation of alkynes into vinylidenes proceeds by η^2-coordination of the triple bond followed by 1,2-H migration,[16–19] or oxidative addition of the alkyne C(sp)–H bond to give an alkynyl metal intermediate, which rearranges through 1,3-H migration or by protonation.[2,20–22] To rationalize the alternative pathways, several theoretical studies have been carried out,[23–26] and recent experimental and theoretical studies have demonstrated that a bimolecular mode for the η^2-alkyne–η^1-vinylidene isomerization process was also possible.[27,28] Vinylidenes can also be produced from ruthenium hydride complexes by insertion of the triple bond to form a vinyl ruthenium species followed by α-H migration.[29,30] Internal alkynes bearing a labile substituent are also prone to form vinylidene derivatives. Trialkylsilyl,[31–37] alkylthiol,[38] triphenylstannane,[39] and iodide[40,41] are able to migrate and generate functionalized vinylidene metal complexes, and some of them have been involved in catalytic reactions.

The activation of propargylic alcohols to give allenylidene metal complexes M=C=C=CR_2 involves dehydration. This process mostly occurs via vinylidene intermediates, which have been observed or isolated as electron-rich metal complexes.

Vinylidenes and allenylidenes behave as electron-withdrawing ligands, thus both are subject to electrophilic additions and can be stabilized by electron-rich metal fragments.[1,8] To involve metal vinylidene and allenylidene intermediates in catalytic processes, the metal moiety must be chosen to allow a good compromise between ligand electrophilicity and metal–ligand bond stability.

The vinylidene ligand usually contains an electrophilic, coordinated carbon atom in the M=C=CHR moiety, as in any heteroallene, but also exhibits metal carbene M=C character. Thus, the three most-favored chemical processes leading to catalytic reactions are: 1) addition of nucleophiles at the coordinated Cα, 2) alkyl, alkenyl, or alkynyl migration from the metal center to Cα, 3) [2+2] cycloaddition of M=C with C=C or C≡C bonds with formation of metallacyclobutane and metallacyclobutene intermediates.

The coordinated allenylidenes are electrophilic and lead to nucleophilic additions at Cα, when the metal moiety does not sterically disfavor this addition, and at Cγ, whereas protonation and electrophilic additions preferentially take place at Cβ.[6–8,32]

The importance of metal vinylidene intermediates in catalysis has been pointed out in recent years,[7,9,42] and especially the specific aspects of ruthenium vinylidenes.[43] This Review presents the various aspects of metal vinylidene and allenylidene species in catalysis, with a special focus on the contribution of our own group. We wish to update our previous review on this topic[44] by showing recent advances in the field.

The formation of metal vinylidenes has been used to rationalize the anti-Markovnikov additions to alkynes. How-

[*] Dr. C. Bruneau, Prof. P. H. Dixneuf
Institut de Chimie, UMR 6509, CNRS-Université de Rennes 1
Organométalliques et Catalyse:
Chimie et Electrochimie Moléculaires
Campus de Beaulieu, 35042 Rennes Cedex (France)
Fax: (+33) 2-2323-6939
E-mail: christian.bruneau@univ-rennes1.fr
pierre.dixneuf@univ-rennes1.fr

 © 2006 Wiley-VCH Verlag GmbH & Co. KGaA, Weinheim

ever, evidence for vinylidene intermediates has not always been demonstrated; nevertheless, these anti-Markovnikov additions to terminal alkynes, when they are selective, will be presented as well.

Metal allenylidene intermediates in catalysis are part of an emerging field. Their formation has led to the development of direct propargylation reactions. They can also explain some unexpected catalytic reactions, although they have not been fully characterized. In other examples, metal allenylidenes have definitely been proved to be the precursors of catalytic species. The following aspects are discussed:

Metal vinylidenes in catalysis
- Formation of carbon–heteroatom bonds and anti-Markovnikov addition to alkynes;
- Carbon–carbon bond-forming reactions;
- Alkene metathesis.

Metal allenylidenes in catalysis
- Application as propargylation intermediates;
- Application as precursors of alkene metathesis catalysts.

2. Catalytic Synthesis of Alkenyl Carbamates and Ureas: The Early Days

The first catalytic synthesis of alkenyl carbamates by the combination of three substrates (alkyne, carbon dioxide, secondary amine) involved $[Ru_3(CO)_{12}]$ as catalyst precursor (1986).[45] It was the first anti-Markovnikov catalytic addition to alkynes with C–O bond formation. It was soon found that this reaction was better promoted by well-defined mononuclear ruthenium catalysts such as $[RuCl_2(pyridine)_2(norbornadiene)]$ and $[RuCl_2(PMe_3)(arene)]$ in acetonitrile under CO_2 (50 atm) (Scheme 1).[46]

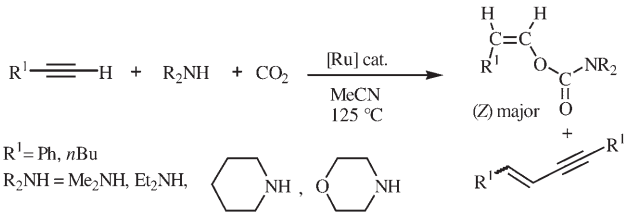

Scheme 1. Ruthenium-catalyzed synthesis of vinylic carbamates.

With these catalysts, the reaction was shown to be specific to terminal alkynes, afforded only the anti-Markovnikov product (by addition of the carbamate to the terminal carbon atom of the alkyne), and was accompanied by the formation of a small amount of the alkyne head-to-head dimerization product. To explain all these observations, the formation of a metal vinylidene intermediate in catalysis was suggested for the first time,[46] and the following cycle was proposed (Scheme 2). Only the direct protonation of the ruthenium atom is still in question now, as the ruthenium–carbon bond can be directly protonated.

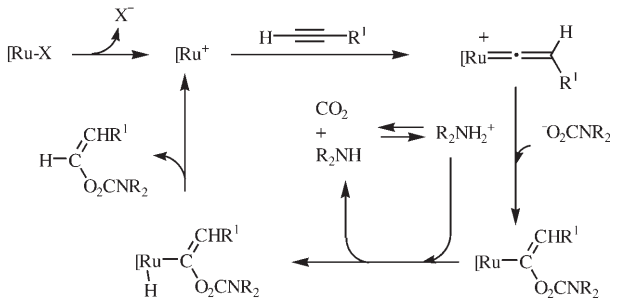

Scheme 2. Proposed catalytic cycle for the catalytic synthesis of vinylic carbamates.[46]

A tungsten vinylidene $[(CO)_4W{=}C{=}CHR]$ intermediate had been previously proposed as an initiator, thus not a catalytic species, in the photochemically assisted polymerization of terminal alkynes by $[W(CO)_6]$.[47]

It was already known that metal vinylidenes readily form upon the interaction of terminal alkynes with 16-electron metal intermediates through the now well-known η^2-alkyne → η^1-vinylidene rearrangement and that the vinylidene carbon atom linked to the metal center was an electrophilic site on the basis of several stoichiometric nucleophile additions.[1] The ruthenium vinylidene intermediate could not be observed in the catalytic synthesis of vinyl carbamates in an autoclave. Model studies on one of the best catalytic precursors, $[RuCl_2(PMe_3)(C_6Me_6)]$, showed that it smoothly reacted with terminal alkynes to generate a ruthenium vinylidene species, which readily added alcohol to form stable alkoxycarbene ruthenium complexes and thus tending

Christian Bruneau graduated in chemistry from the Institut National Supérieur de Chimie Industrielle de Rouen (France, 1974) and obtained his PhD at the University of Rennes (1979). He obtained a CNRS position in 1980, and from 1986 worked in the field of molecular catalysis with P. H. Dixneuf. He is now mainly involved in Ru-catalyzed selective transformations (metathesis, cycloisomerization, asymmetric catalysis). Since 2000, he has headed the CNRS Univ. of Rennes research group "Organometallics and Catalysis" (UMR 6509).

Pierre H. Dixneuf studied in Rennes (France) and obtained his PhD with R. Dabard, followed by postdoctoral work on heterocyclic carbene complexes with M. F. Lappert in Brighton (UK, 1972). He was appointed Professor in Rennes (1978). His interests include the design of carbon-rich organometallic reagents and molecular catalysts, especially Ru catalysts, the discovery and characterization of new catalytic pathways, the activation of alkynes via vinylidene and allenylidene intermediates or unusual oxidative couplings, and the selective catalytic formation of C–C and C=C bonds.

 © 2006 Wiley-VCH Verlag GmbH & Co. KGaA, Weinheim

to add nucleophiles at Cα (Scheme 3).[48,49] Notably, such unstable ruthenium vinylidene were characterized only recently with the bulky phosphine PR_3=PCy_3.[50]

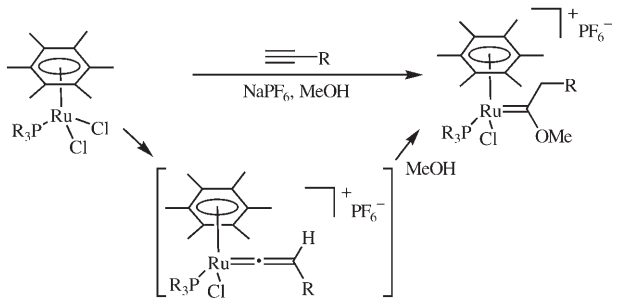

Scheme 3. Stoichiometric formation of ruthenium alkoxycarbenes via ruthenium vinylidenes.[49]

The catalytic addition of carbamates was then applied to specific alkynes and shown to be general.[51] The simple vinyl carbamates were obtained by the reaction of acetylene with an excess of secondary amine in the presence of either $RuCl_3{\cdot}x\,H_2O$[52] or [{$RuCl_2$(norbornadiene)}$_n$][53] as catalyst precursors (Scheme 4). *O*-1-(1,3-Dienyl) carbamates, with the

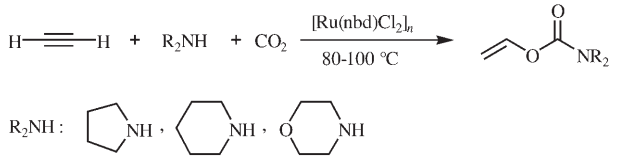

Scheme 4. Catalytic formation of vinyl carbamates from acetylene (nbd = norbornadiene).

Z isomer as the major product, were more efficiently obtained from 2-methyl-1-buten-3-yne, carbon dioxide, and a secondary amine in the presence of [Ru(methallyl)$_2$(diphenylphosphanylethane)] as catalyst precursor (Scheme 5).[54] This carbamate synthesis avoids the use of phosgene derivatives and thus presents advantages over the classical route based on a carbamoyl chloride and an aldehyde enolate.

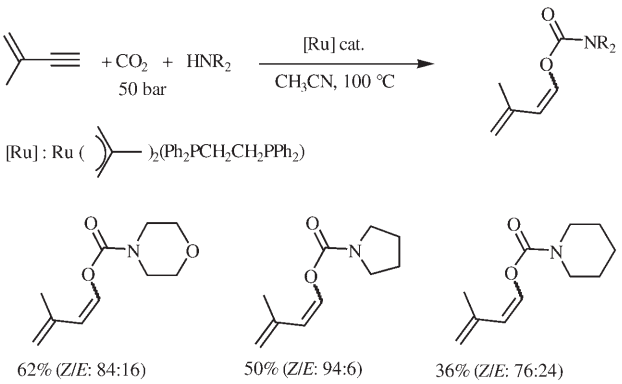

Scheme 5. Preparation of dienyl carbamates from 1,3-enynes.

The formation of vinyl or dienyl carbamates was not possible from primary amines and CO_2. Cyclohexylamine and acetylene under CO_2 (50 bar) in the presence of $RuCl_3{\cdot}x\,H_2O$ and PBu_3 in toluene provided dicyclohexylurea.[55,56] The reaction was improved by using propargyl alcohol instead of

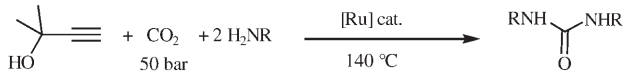

Scheme 6. Formation of symmetrical ureas from primary amines.

acetylene, without additional solvent, and [$RuCl_2(PR_3)$(arene)] complexes as catalyst precursors (Scheme 6).[55] This reaction likely resulted from addition of the primary amine to a transient ruthenium vinylidene, followed by nucleophilic addition of a second molecule of the amine at the carbonyl carbon atom to generate the symmetrical urea.

Since this first catalytic application, many metal vinylidenes, especially ruthenium vinylidenes, were suggested or proved to be key catalyst species in anti-Markovnikov additions of heteroatom or carbon nucleophiles to terminal alkynes. Some examples are presented in this Review.

3. Anti-Markovnikov Additions to Terminal Alkynes: Carbon–Heteroatom Coupling

The formation of metal vinylidene intermediates creates an electron deficiency at the coordinated carbon atom and thus favors the anti-Markovnikov addition of nucleophiles to terminal alkynes. Labeling experiments that indicate the 1,2-migration of the terminal acetylenic proton also corroborate this mechanism. Metal vinylidene intermediates have not been observed in some anti-Markovnikov additions. Nevertheless, the usefulness of the transformations justifies a brief discussion.

3.1. Catalytic Addition of Carboxylic Acids to Alkynes: A Convenient Synthesis of 1-Alkenyl Esters

Carboxylic acids add to terminal alkynes in the presence of a variety of ruthenium precursors that favor the Markovnikov addition to produce enol esters, which lead to geminal esters.[57–60] The first generation of active catalysts included [$Ru_3(CO)_{12}$],[61] [$Ru(cod)_2$]/PR_3[62] (cod = cycloocta-1,5-dienyl), [$RuCl_2(PR_3)$(arene)],[63–65] and [{$Ru(O_2CH)(CO)_2(PR_3)$}$_2$],[66] which allowed the preparation of enol esters from functionalized alkynes and acids. Carboxylic acids react with propargylic alcohols in the presence of these catalytic systems, but lead to β-ketoesters rather than to hydroxy enol esters.[62,67,68] Recently, the catalytic addition of carboxylic acids to alkynes was revisited with other ruthenium catalyst systems, including [{$RuCl_2$(*p*-cymene)}$_2$]/P(furyl)$_3$/base,[69] [$RuCl_2(PCy_3)_2$(=C=CH*t*Bu)], [$RuCl_2(PCy_3)_2$(bis(mesityl)imidazolylidene)(=C=CH*t*Bu)], [$RuCl(L)_2$(=C=

© 2006 Wiley-VCH Verlag GmbH & Co. KGaA, Weinheim

CH*t*Bu)]BF_4,[70] and salicylaldimine-containing ruthenium complexes.[71–73]

Attempts were made to reverse the addition regioselectivity of carboxylic acids to alkynes in order to produce 1-alkenyl esters, which are protected intermediates in the selective transformation of alkynes into aldehydes. As vinylidenes are electron-withdrawing ligands, efforts were made to introduce electron-rich ligands at the ruthenium center so as to stabilize the vinylidene intermediates formed from the alkyne. Ru(methallyl)$_2$(diphenylphosphanylalkane) proved to be successful and provided the first metal catalysts that favored the anti-Markovnikov addition of carboxylic acids to terminal alkynes to form *Z* and *E* enol esters with high regioselectivity (Scheme 7).[74]

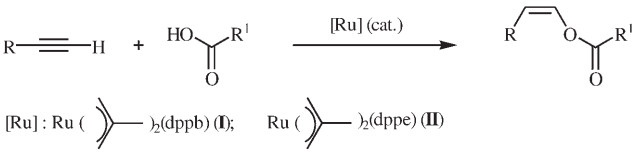

Scheme 7. Anti-Markovnikov addition of carboxylic acids to terminal alkynes. dppe = $Ph_2PCH_2CH_2PPh_2$, dppb = $Ph_2P(CH_2)_4PPh_2$.

The best catalyst precursors were [Ru(methallyl)$_2$(dppb)] (**I**; dppb = diphenylphosphanylbutane) and [Ru(methallyl)$_2$-(dppe)] (**II**; dppe = diphenylphosphanylethane), which also led to a remarkable stereoselectivity in favor of the *Z* isomer; the overall reaction thus corresponds to a formal *trans* addition of RC(O)O-H to the triple bond. The formation of a vinylidene intermediate according to a mechanism proposed by Wakatsuki by initial protonation of the ruthenium center[75] cannot be excluded.

The choice of the appropriate catalyst precursor **I** or **II** depends on the steric demand of both the alkyne and the carboxylic acid. In the presence of catalytic amounts of **I**, whose Ru(dppb) moiety is more sterically demanding than the Ru(dppe) group of **II**, a variety of carboxylic acids add with high regioselectivity to nonhindered substrates such as phenylacetylene, 1-hexyne,[76] and diynes.[77] Aliphatic carboxylic acids, substituted aromatic acids, and N-protected amino acids react under mild conditions and provide *Z* enol esters with high regioselectivity and without racemization of the stereogenic centers of optically pure amino acid derivatives. The reaction temperature, which allows complete conversion with good regioselectivity, can be decreased from 80 to 0 °C, when the acidity of the carboxylic acid increases in the pK_a range from 5 to 1.5. The milder conditions lead to the highest regioselectivity (*Z*) of the addition (Table 1).[76] Functionalized *Z* enol esters can be prepared in nonpolar solvents such as toluene or pentane; conjugated enynes selectively produce dienyl esters (Scheme 8, Table 1).[78]

With more bulky alkynes such as trimethylsilylacetylene or propargylic ethers, [Ru(methallyl)$_2$(dppe)] (**II**), in which the ruthenium site is less sterically hindered than that of **I**, is a more suitable catalyst precursor. For instance, the addition of benzoic acid to $Me_3SiC{\equiv}CH$ takes place at 60 °C in toluene in the presence of 1 mol % of both catalysts **I** and **II**; however, **II** gives the (*Z*)-2-trimethylsilylethenyl benzoate in 88 % yield after 3 h, whereas **I** leads to only 34 % yield after 24 h. Similarly, the transformation of bulky propargylic ethers is faster with **II** than with **I**. In both cases, very good regioselectivity is obtained.[79]

Notably, the stereoselective formal *trans* addition of the RCO_2 and H fragments to the triple bond has never been explained.

From catalyst **I**, we have shown that the first step of the catalytic reaction is the formation of [Ru(O_2CR)$_2$(dppb)] complexes with elimination of the allylic ligands upon

Table 1: Regioselective anti-Markovnikov addition of carboxylic acids to alkynes.

Cat.[a]	Acid[b]	Alkyne	*T* [°C]	Yield [%]	*Z* sel.[c]	Ref.
I	$PhCO_2H$	$C_4H_9C{\equiv}CH$	65	95	98	[76]
	$PhCO_2H$	$PhC{\equiv}CH$	100	97	96	
	CH_3CO_2H	$PhC{\equiv}CH$	45	90	99	
	$CHCl_2CO_2H$	$PhC{\equiv}CH$	20	78	100	
	CF_3CO_2H	$PhC{\equiv}CH$	0	61	100	
	Ph_2CHCO_2H	$C_4H_9C{\equiv}CH$	65	97	100	
	2,6-$F_2C_6H_3CO_2H$	$C_4H_9C{\equiv}CH$	65	94	96	
	L-Boc-PheOH	$C_4H_9C{\equiv}CH$	65	97	100	
	L-Boc-AlaOH	$C_4H_9C{\equiv}CH$	65	71	94	
	L-Cbz-AlaOH	$PhC{\equiv}CH$	65	98	100	
	$CH_2{=}CHCO_2H$	$PhC{\equiv}CH$	45	65	99	
	$MeOCH_2CO_2H$	$PhC{\equiv}CH$	65	96	97	
	2-$HOC_6H_4CO_2H$	$PhC{\equiv}CH$	80	94	100	
	2-$AcOC_6H_4CO_2H$	$PhC{\equiv}CH$	80	98	100	
	$MeOCH_2CO_2H$	(*Z*)-$MeOCH{=}CHC{\equiv}CH$	65	69	99	[78]
	n-$C_4H_9CO_2H$	(*Z*)-$MeOCH{=}CHC{\equiv}CH$	65	75	98	
	$CH_2{=}C(Me)CO_2H$	(*Z*)-$MeOCH{=}CHC{\equiv}CH$	65	60	97	
	$PhCO_2H$	(*Z*)-$MeOCH{=}CHC{\equiv}CH$	65	81	98	
	p-$ClC_6H_4CO_2H$	(*Z*)-$MeOCH{=}CHC{\equiv}CH$	65	68	99	
	$PhCO_2H$	$CH_2{=}C(Me)C{\equiv}CH$	65	92	99	
	n-$C_4H_9CO_2H$	$CH_2{=}C(Me)C{\equiv}CH$	45	77	100	
II	$PhCO_2H$	$Me_3SiC{\equiv}CH$	60	88	100	[76]
	$CH_2{=}C(Me)CO_2H$	$Me_3SiC{\equiv}CH$	50	76	100	
	L-Boc-AlaOH	$Me_3SiC{\equiv}CH$	50	75	100	
	$PhCO_2H$	$MeOC(Me)_2C{\equiv}CH$	80	86	94	[79]
	$PhCO_2H$	$MeOC(Me)(Et)C{\equiv}CH$	80	73	99	
	$PhCO_2H$	$MeOC(nC_5H_{11})HC{\equiv}CH$	80	98	95	
	$PhCO_2H$	$C_3H_5OC(nC_5H_{11})HC{\equiv}CH$	80	96	99	
	$PhCO_2H$	$MeOC(Me)(iBu)C{\equiv}CH$	80	74	98	
	$PhCO_2H$	$MeOC(Me)(Ph)C{\equiv}CH$	80	95	98	

[a] **I**: [Ru(methallyl)$_2$(dppb)]; **II**: [Ru(methallyl)$_2$(dppe)]. [b] Boc = *tert*-butoxycarbonyl, Cbz = benzyloxycarbonyl. [c] *Z* selectivity: 100 *Z*/*Z* + *E*.

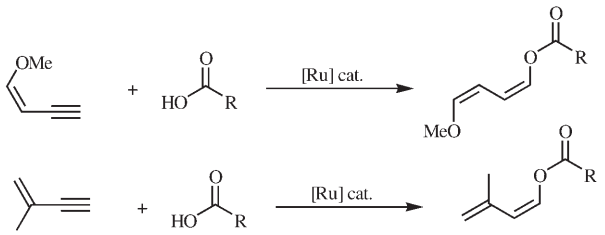

Scheme 8. Ruthenium-catalyzed synthesis of dienyl esters.

 © 2006 Wiley-VCH Verlag GmbH & Co. KGaA, Weinheim

protonation by RCO_2H. We have shown that these complexes are also efficient catalysts for the anti-Markovnikov addition and that the reaction does not proceed through insertion of the triple bond into a Ru–carboxylate bond. As the O_2CR ligand binds reversibly in the η^2 and η^1 modes, a vacant site is temporarily liberated at the metal center. The involvement of a vinylidene intermediate resulting from coordination of the alkyne was suggested.[76] Some ruthenium complexes containing the tris(pyrazolyl)borate (Tp) ligand, such as [RuCl(Tp)(pyridine)$_2$], [RuCl(Tp)(cod)], and [RuCl(Tp)(tmeda)] (tmeda = *N*,*N*,*N*′,*N*′-tetramethylenediamine), have been applied in the addition of benzoic acid to phenylacetylene to produce selectively *Z* and *E* enol benzoates.[80]

The enynyl ruthenium complex [Ru(Tp)(PhC=C(Ph)C≡CPh)(PMe*i*Pr$_2$)] is remarkably active in the production of unsaturated lactones by endocyclization of α,ω-alkynoic acids (Scheme 9).[81] In this reaction the presence of the basic phosphine favors the alkyne to vinylidene tautomerism and allows the formation of macrocyclic enol lactones.

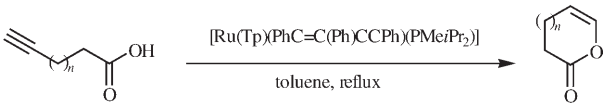

n = 1 (97%), 2 (95%), 7 (84%)

Scheme 9. Ruthenium-catalyzed formation of lactones through regioselective intramolecular addition.

More recently, new (arene)ruthenium catalysts that promote anti-Markovnikov addition of carboxylic acids to terminal alkynes have been developed, for example, [RuCl$_n$(*p*-cymene)(triazol-5-ylidene)] (*n* = 1, 2). The reaction produces *Z* and *E* enol esters, depending on both the catalyst and the substrate.[82] The association of [{RuCl$_2$(*p*-cymene)}$_2$] with P(*p*-ClC$_6$H$_4$)$_3$ and dimethylaminopyridine at 60 °C in toluene also affords the *Z* vinyl esters with very high regio- and stereoselectivity.[69]

The anti-Markovnikov addition of benzoic acid to propargylic alcohols in the presence of the catalyst **II** at 50 °C in toluene affords bifunctionalized 3-hydroxy-1-propen-1-yl benzoates with a stereoselectivity in favor of the *Z* isomer, depending on the starting propargylic alcohol (Scheme 10).[83,84] These compounds, which are, in fact, protected aldehydes, can be transformed upon thermal or acidic treatment into conjugated enals, resulting from the formal isomerization of propargylic alcohol.[83,84]

3.2. Intermolecular Addition of Alcohols

The intermolecular addition of alcohols to alkynes is a difficult reaction. To date, only allylic alcohols have undergone addition to phenylacetylene in the presence of [RuCl(Tp)(pyridine)$_2$] catalyst. The reaction produces allyl β-styryl ether and 2-phenylpent-4-enal through a Claisen rearrangement of the ether. This is a rare example of the direct formation of a C–O ether bond.[80]

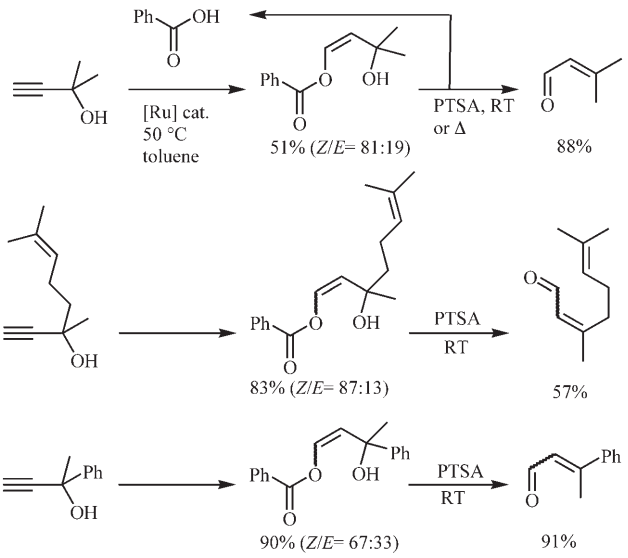

Scheme 10. Regioselective formation of functionalized hydroxylated 1-alkenyl esters. PTSA = *para*-toluenesulfonic acid.

Whereas [RuCl(Cp*)(cod)] (Cp* = C$_5$Me$_5$) promotes the oxidative coupling of allyl alcohol with alkynes and alkynols to form γ,δ-unsaturated aldehydes[85,86] and 5-methylenetetrahydropyrans,[87,88] respectively, the reaction catalyzed by [RuCl(Cp)(PPh$_3$)$_2$]/NH$_4$PF$_6$ promotes the formation of ruthenium vinylidene species and follows a completely different pathway. The expected addition of the hydroxy group to the vinylidene ligand takes place but is followed by a skeleton rearrangement leading to unsaturated ketones.[89–91] The mechanism of this reconstitutive condensation involves the formation of an allyl acyl metal intermediate, which releases the unsaturated ketone by C–C bond formation (Scheme 11).[92]

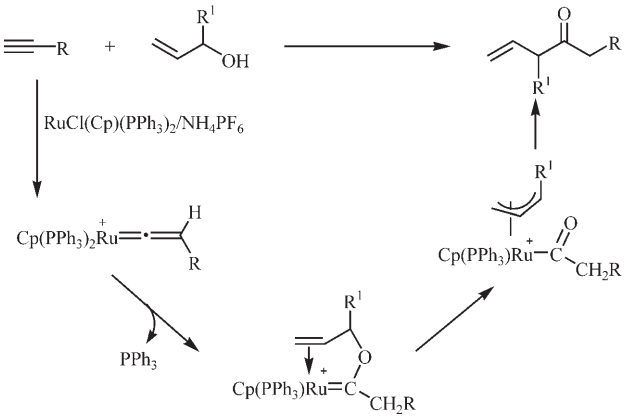

Scheme 11. Catalytic cycle for the [RuCl(Cp)(PPh$_3$)$_2$]/NH$_4$PF$_6$-catalyzed addition of allylic alcohols to alkynes.

3.3. Intramolecular Addition of O-Nucleophiles: Cyclization of ω-Acetylene Alcohols, Epoxides, and Ketones

The stoichiometric metal-assisted cycloisomerization of alkynols to oxacycloalkylidene complexes via hydroxylated

 © 2006 Wiley-VCH Verlag GmbH & Co. KGaA, Weinheim

vinylidene metal intermediates is well documented for Group 6–10 transition metals.[93] The catalytic version, illustrated by the *endo* cyclization of 3- and 4-alkyn-1-ols to give cyclic five- and six-membered enol ethers has been extensively studied, especially with molybdenum[94] and tungsten[95,96] carbonyl promoters (Scheme 12).[97,98] $[Mo(CO)_6]$, $[W(CO)_6]$, $[W(CO)_5(thf)]$, and $[W(CO)_5(Et_3N)]$ are the most commonly used catalyst precursors, and photochemical activation is often used to generate the active promoters. These catalytic systems usually do not exhibit high turnover numbers, but are compatible with a variety of functional groups such as ethers, esters, amides, and carbamates, and thus have been used in sugar, aminosugar, and polyol chemistry.[99–103] $[Mo(CO)_5(Et_3N)]$ (10 mol%) also allowed the azacyclization of 2-ethynylaniline into indole in 79% yield.[104]

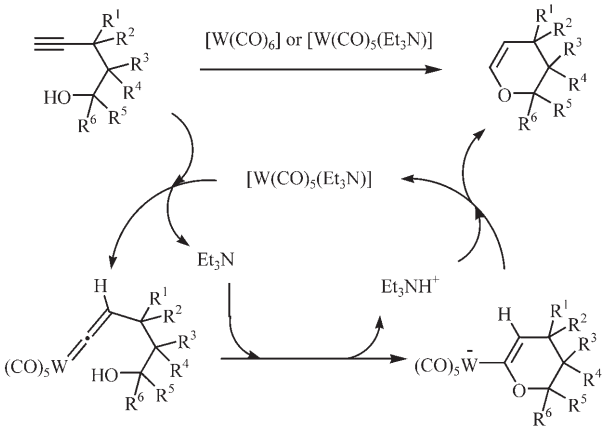

Scheme 12. Cyclization of acetylenic alcohols via metal vinylidene intermediates.

Similar cycloisomerizations of homo- and bis-homopropargylic alcohols into five- and six-membered oxygen-containing heterocycles have been performed with Rh^I catalyst precursors such as $[\{Rh(cod)Cl\}_2]$, in the presence of an excess of an electron-poor phosphine such as a tris(monofluoro- or difluorophenyl)phosphine, or $[RhCl(PAr_3)_3]$ without any further additive.[105] The electron-poor tris(*p*-fluorophenyl)phosphine (in the complex $[RuCl(Cp)\{(p\text{-}FC_6H_4)_3P)\}_2]$) in the presence of Bu_4NPF_6 and *N*-hydroxysuccinimide sodium salt selectively provided dihydropyrans from pent-4-yn-1-ols.[106] Transient metal oxacarbenes can be converted into cyclic esters by selective oxidation by adding *N*-hydroxysuccinimide as a mild oxidant to a catalytic system based on [RuCl(Cp)(cod)], trisfurylphosphine in the presence of Bu_4NBr, or Bu_4NPF_6 in a DMF/water mixture. The preparation of a variety of γ-butyrolactones from functionalized homopropargylic alcohols was thus possible.[107] δ-Lactones were selectively obtained in satisfactory yields from pent-4-yn-1-ols in the presence of $[RuCl(Cp)\{(p\text{-}MeOC_6H_4)_3P\}_2]$ associated to excess electron-rich phosphine $(p\text{-}MeOC_6H_4)_3P$, Bu_4NPF_6, and $NaHCO_3$.[106]

Ethynyloxiranes are also prone to generate metal vinylidene complexes, which can rearrange through oxirane opening and nucleophilic addition of the oxygen atom at the vinylidene Cα position to provide furan derivatives according to the general catalytic cycle described in Scheme 13. $[Mo(CO)_5(Et_3N)]$[108] (at room temperature) and $[RuCl(Tp)(PPh_3)(CH_3CN)]$[109] are efficient catalysts for the preparation of these substituted furans from ethynyloxiranes, as they tolerate a variety of functional groups such as alcohols, ethers, esters, nitriles, and tosylamides.

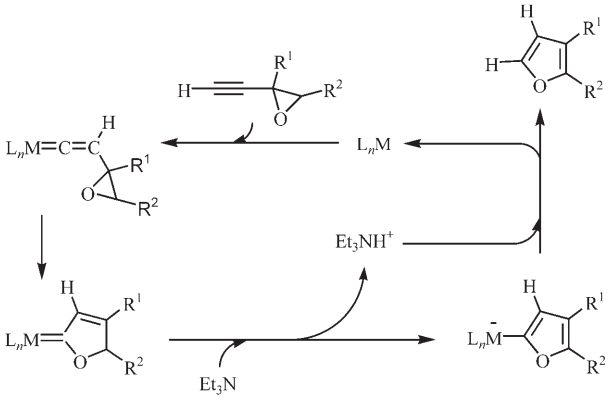

Scheme 13. Catalytic formation of furans from ethynyloxiranes via metal vinylidene intermediates.

When the starting oxirane is an (*o*-ethynyl)phenyl epoxide, the reaction catalyzed by $[Ru(Tp)(PPh_3)(MeCN)_2]PF_6$, proceeds through oxygen transfer from the epoxide to the terminal alkyne carbon atom and generates a reactive ketene, leading to naphthol, alkylideneindanone, or ester derivatives, depending on the nature of the substrate and the solvent (Scheme 14).[110] In the presence of the same catalyst, 1-iodo-2-naphthol and 2-iodobenzo[*d*]oxepin can be selectively obtained from iodoalkynes in DMF and benzene, respectively.[111]

Tungsten– and chromium–carbonyl complexes activate the terminal triple bond of 1-acyl-2-ethynylcyclopropanes to generate metal vinylidene species, which undergo cyclopropane ring opening and cyclization into a seven-membered oxacycloheptadienylidene by attack of the oxygen atom at the electrophilic vinylidene carbon center. The formation of the aromatic phenol is then favored (Scheme 15).[112,113]

3.4. Addition of Water to Terminal Alkynes: Transformation of Alkynes into Aldehydes

The hydration of terminal alkynes to form aldehydes through anti-Markovnikov addition of water to a triple bond was performed for the first time in the presence of arene ruthenium catalysts such as $[RuCl_2(C_6H_6)(PPh_2C_6F_5)]$ (10 mol%) in the presence of $PPh_2(C_6F_5)$ (30 mol%) or $[\{RuCl_2(C_6H_6)\}_2]$ associated to an excess of the water-soluble ligand $(3\text{-}NaO_3SC_6H_4)_3P$ in alcohol (Scheme 16).[114] These catalytic systems involved large amounts of metal catalyst and additive, and the selectivity remained unsatisfactory. Cyclopentadienyl–ruthenium complexes bearing appropriate

 © 2006 Wiley-VCH Verlag GmbH & Co. KGaA, Weinheim

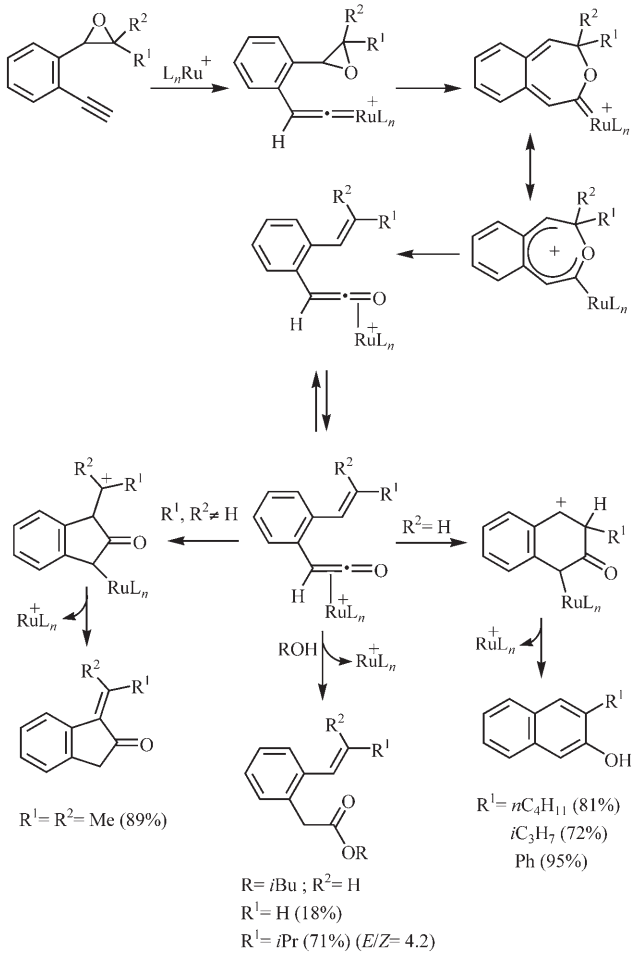

Scheme 14. Ruthenium-catalyzed cyclization of (*o*-ethynyl)phenyl epoxides.

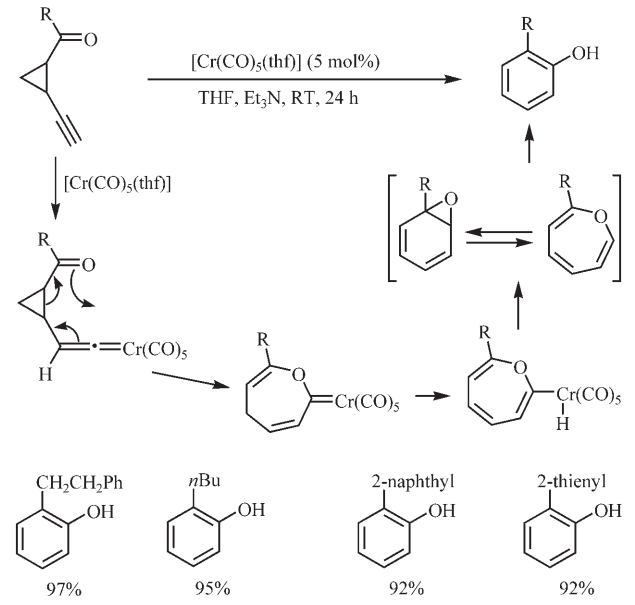

Scheme 15. Tungsten- and chromium-catalyzed formation of phenols from 1-acyl-2-ethynylcyclopropanes.

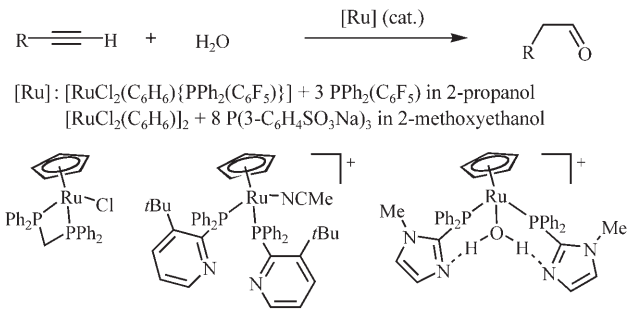

Scheme 16. Ruthenium-catalyzed hydration of terminal alkynes.

bidentate or monodentate phosphine ligands led to a dramatic improvement of both the activity and regioselectivity of the reaction. For instance, [RuCl(Cp)(dppm)] is an efficient catalyst and provides high selectivity and tolerates a variety of functional groups at 100 °C.[115] The substitution of classical phosphine or diphosphine by a phosphanylimidazole[116] or a phosphanylpyridine[117] ligand has led to new catalyst precursors that are very active and regioselective in water and allow the reaction to proceed at room temperature (Scheme 16).

Remarkably, the indenyl complex $[RuCl(indenyl)(PPh_3)_2]$ is also efficient for the anti-Markovnikov hydration of terminal alkynes in aqueous media and micellar solutions.[118] This system can be applied to the hydration of propargylic alcohols to produce β-hydroxyaldehydes selectively, in contrast to $[RuCl(Cp)(PMe_3)_2]$ in 2-propanol, which leads to enals through dehydration of the alcohol and hydration of the triple bond.[119] On the basis of the isolation of intermediate by-products, deuterium-labeling experiments, and DFT calculations, the mechanism is proposed to involve first protonation of a η^2-alkyne–ruthenium(II) species to give a ruthenium(IV) vinylidene intermediate via a Ru^{IV} vinyl species, rather than the direct protonation of the vinylidene.[75] Addition of water to the α-carbon atom of the ruthenium(IV) vinylidene is then followed by reductive elimination and releases the aldehyde (Scheme 17).

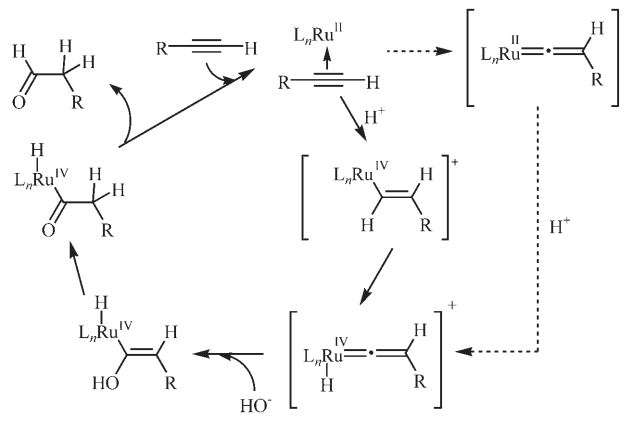

Scheme 17. Mechanism for ruthenium vinylidene formation and catalytic hydration of terminal alkynes.

 © 2006 Wiley-VCH Verlag GmbH & Co. KGaA, Weinheim

A new ruthenium-catalyzed tandem formation of C–O and C–C bonds to produce cyclopentanones from terminal 1,5-enynes and water was recently reported.[120] It first involves the addition of water to a ruthenium vinylidene intermediate to form an acyl ruthenium moiety, and then the formal insertion of an electron-deficient double bond into the acyl–ruthenium bond. The most active precursor for this transformation was found to be the trinuclear complex $[Ru_3Cl_5(dppm)_3]PF_6$ (2 mol%, 120°C, dioxane), and satisfactory yields (23–81%) were obtained for this hydrative cyclization.

3.5. Addition of Diphenylphosphine

The addition of secondary phosphines HPR_2 to prop-2-ynols in the presence of $[RuCl(C_5Me_5)(cod)]$ or $[RuCl(C_5Me_5)(PPh_3)_2]$ provides the first regio- and stereoselective direct hydrophosphination of propargylic alcohols and leads to bifunctionalized *Z* olefins (Scheme 18).[121] It was shown

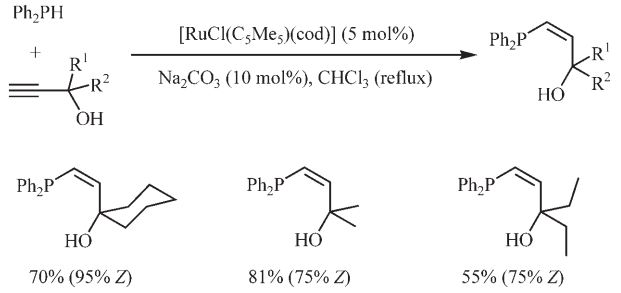

Scheme 18. Anti-Markovnikov addition of a secondary phosphine to propargylic alcohols.

that $[Ru(PR_3)_2C_5Me_5]X$ activate propargylic alcohols to give the vinylidene complexes $[Ru{=}C{=}CHCR_2OH(PR_3)_2C_5Me_5]X$ rather than the expected ruthenium allenylidenes $[Ru{=}C{=}C{=}CR_2(PR_3)_2C_5Me_5]X$.[122] Thus, this intermediate is subject to nucleophilic addition at the coordinated carbon atom. Indeed, the reaction of propargylic alcohols with diphenylphosphine in the presence of $[Ru(PPh_3)_2C_5Me_5]PF_6$ as catalyst affords the anti-Markovnikov addition product (Scheme 18). However, the same transformation proceeds more readily in the presence of $[RuCl(C_5Me_5)(cod)]$, which in the presence of PPh_2H and $NaPF_6$ (2 equiv) gives $[Ru(C_5Me_5)(PPh_2H)_2]PF_6$. Thus, the reaction of tertiary propargylic alcohols with diphenylphosphine in the presence of Na_2CO_3 in refluxing $CHCl_3$ led to 3-diphenylphosphanylprop-2-enols in good yields with high stereoselectivity in favor of the *Z* isomer (75:25–95:5). The kinetic product is always the *Z* derivative, but simple silica gel chromatography transforms it completely into the *E* isomer.

As $[Ru(C_5Me_5)(L)_2]^+$ catalyzes the reaction, and as the 3-hydroxy vinylidene intermediate $[Ru{=}C{=}CHCH_2OH(C_5Me_5)(PMe_2Ph)_2]PF_6$ was isolated upon reaction of $[RuCl(C_5Me_5)(PMe_2Ph)_2]$, $NaPF_6$, and $HC{\equiv}CCH_2OH$,[122] the mechanism shown in Scheme 19 is plausible.

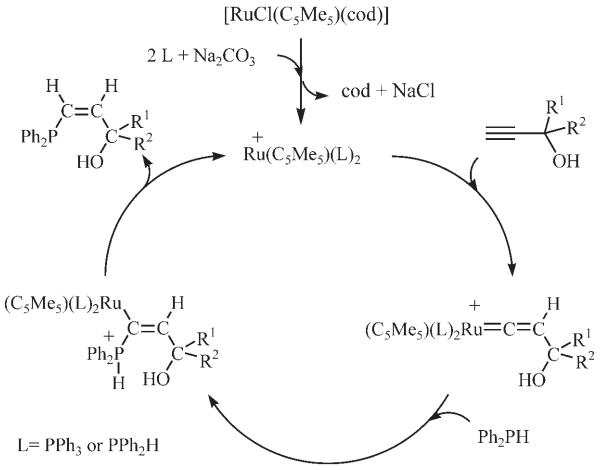

Scheme 19. Mechanism for the addition of phosphines to propargylic alcohols.

3.6. Catalytic Addition of N-Nucleophiles to Alkynes: Direct Transformation of Alkynes into Nitriles and Enamide Derivatives

A ruthenium vinylidene species is also proposed as the key intermediate in the regioselective addition of 1,1-dimethylhydrazine to terminal alkynes in the presence of $[RuCl(Tp)(PPh_3)_2]$ as catalyst precursor to give nitriles (Scheme 20).[123] The addition of hydrazine to the vinylidene ligand generates a hydrazino carbene, which loses dimethylamine and provides nitriles from aromatic and aliphatic alkynes (Scheme 20).[123]

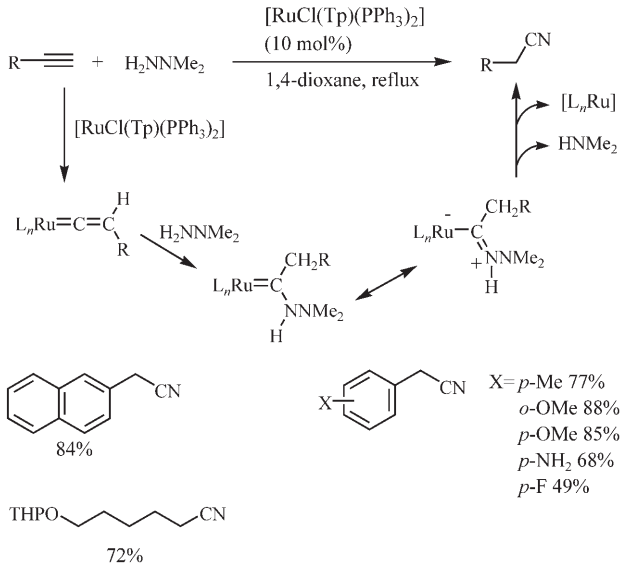

Scheme 20. Ruthenium-catalyzed addition of dimethylhydrazine to alkynes. THP = tetrahydropyranyl.

The direct addition of secondary amides to terminal alkynes in the presence of $[Ru_3(CO)_{12}]$ associated to PCy_3 at 180°C to form *E* and *Z* enamides was reported in 1995.[124] Insertion of a triple bond into a Ru–H bond resulting from

 © 2006 Wiley-VCH Verlag GmbH & Co. KGaA, Weinheim

N–H activation was proposed as the preferred mechanism. More recently, *E* enamides were formed regio- and stereoselectively in the presence of a catalytic system based on [Ru(methallyl)$_2$(cod)], tributylphosphine, and dimethylaminopyridine (DMAP) in toluene at 100 °C (Scheme 21).[125]

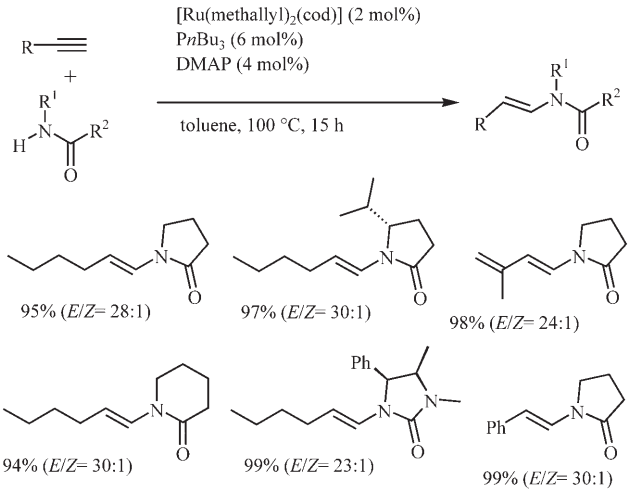

Scheme 21. Ruthenium-catalyzed addition of secondary amido derivatives to alkynes.

This catalytic system is closely related to our system, which allows the addition of carboxylic acids to terminal alkynes (see Section 3.1) and the addition of a variety of N-nucleophiles such as amides, lactams, anilides, ureas, and carbamates. Under similar conditions,[125] but in the presence of $Cy_2PCH_2PCy_2$ and water as additives, instead of P*n*Bu$_3$ and DMAP, the catalytic anti-Markovnikov addition selectively provides the *Z* isomers.

4. Metal Vinylidenes in Catalytic C–C Bond Formation

The formation of metal vinylidene intermediates has been used to promote new carbon–carbon bond-forming reactions by the addition of carbon centers to the electrophilic vinylidene carbon atom. These reactions include dimerization of terminal alkynes, cycloisomerization of conjugated dienynes and unconjugated enynes, and mixed coupling of terminal alkynes and olefins through [2+2] cycloaddition.

4.1. Dimerization of Terminal Alkynes

The head-to-head dimerization of terminal alkynes into enynes requires the coordination of two molecules of alkyne at the metal center. The characterization of ruthenium enynyl intermediates [Ru-C(=CHR)-C≡CR] (Scheme 22) during the formation of enynes has revealed that the reaction does not proceed through insertion of the triple bond into a metal–alkynyl bond, as observed with palladium catalysts, but rather involves the migration of an alkynyl ligand onto the Cα atom

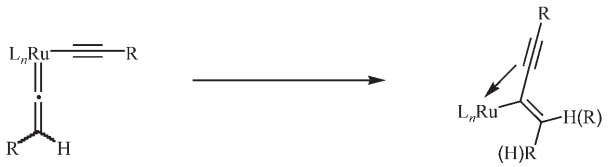

Scheme 22. Formation of ruthenium enynyl intermediates.

of a ruthenium vinylidene intermediate. Upon protonation of this enynyl species by the acidic proton of the terminal alkyne, enynes are selectively produced (Scheme 23).[126,127] Depending on the ancillary ligands, the enynyl ruthenium can rearrange into a cumulenyl ruthenium species, and protonolysis gives butatriene compounds (Scheme 23).[128–130] In both cases, the products result from selective head-to-head dimerization of the starting terminal alkyne.

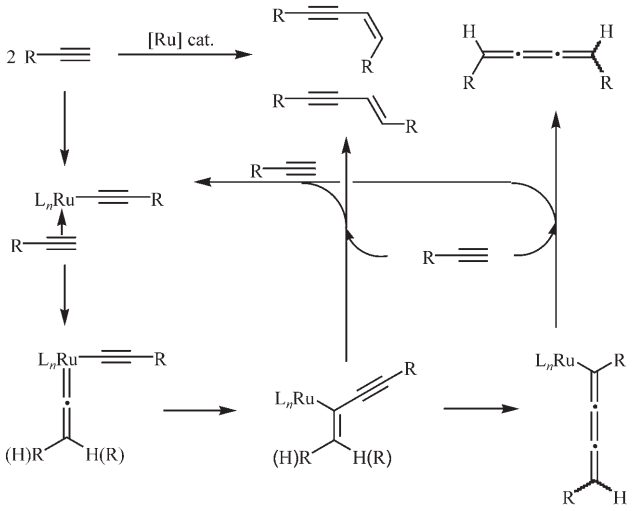

Scheme 23. Dimerization of terminal alkynes via ruthenium vinylidene intermediates.

A variety of ruthenium complexes containing trispyrazolyl,[131–134] P(CH$_2$CH$_2$PR$_2$)$_3$,[126,127] N(CH$_2$CH$_2$PR$_2$)$_3$,[135] pentamethylcyclopentadienyl,[136] indenyl,[137,138] and maltolato ligands,[139] the metathesis catalysts [RuCl$_2$(PCy$_3$)$_2$(=CHPh)][140] and [RuCl$_2$(P*i*Pr$_3$)$_2$(=C=CHPh)],[141,142] as well as a dinuclear (C$_5$H$_5$)$_2$Ru$_2$ complex[143] promote the formation of *Z* and *E* enynes. Polyaddition of 2,7-diethynyl-9,9-dioctylfluorene with [RuCl$_2$(P*i*Pr$_3$)$_2$(=C=CHPh)] in the presence of *N*-methylpyrrolidine produces polymers containing the enynyl fragment with high *Z* selectivity.[141]

On the other hand, the formation of butatrienes is favored with bulky alkynes, for example, *tert*-butylacetylene or benzylacetylene, in the presence of catalytic precursors such as [RuH$_2$(CO)(PPh$_3$)$_2$],[128] [Ru(cod)(cot)] (cot = cyclooctatriene),[128,129] or [RuH$_3$(C$_5$H$_5$)(PCy$_3$)].[136,144] The hydrative dimerization of terminal alkynes catalyzed by [RhCl(PPh$_3$)$_3$] in the presence of a stoichiometric amount of 2-amino-3-picoline and benzoic acid (5 mol%) at 110 °C in toluene was recently reported.[145] The proposed mechanism involves the

 © 2006 Wiley-VCH Verlag GmbH & Co. KGaA, Weinheim

nucleophilic addition of the amino group of 2-amino-3-picoline to a transient rhodium vinylidene species followed by formation of an heterometallacycle, which upon reductive elimination and hydrolysis provides conjugated enones (Scheme 24).

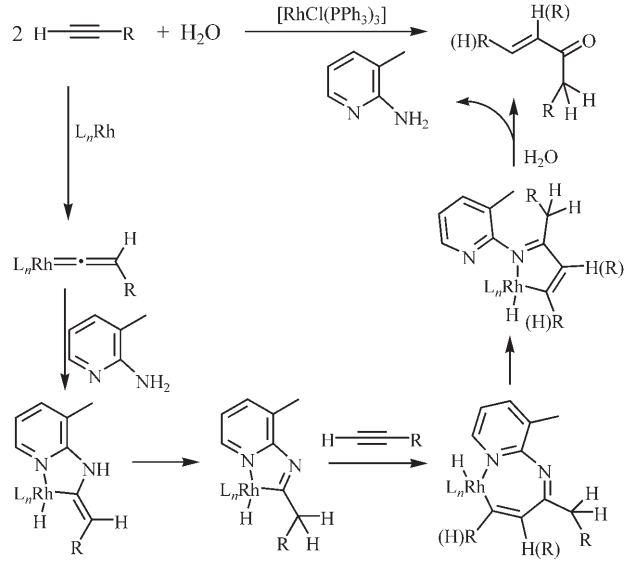

Scheme 24. Rhodium-catalyzed hydrative dimerization of terminal alkynes.

Aryl acetylenes dimerize to 1-aryl naphthalenes at 180 °C in the presence of ruthenium and rhodium porphyrin complexes. The formation of a porphyrin metal vinylidene, which undergoes a Diels–Alder reaction with the triple bond of the same terminal alkyne or another internal alkyne and then H migration and aromatization, has been postulated to explain this unprecedented type of cyclodimerization (Scheme 25).[146]

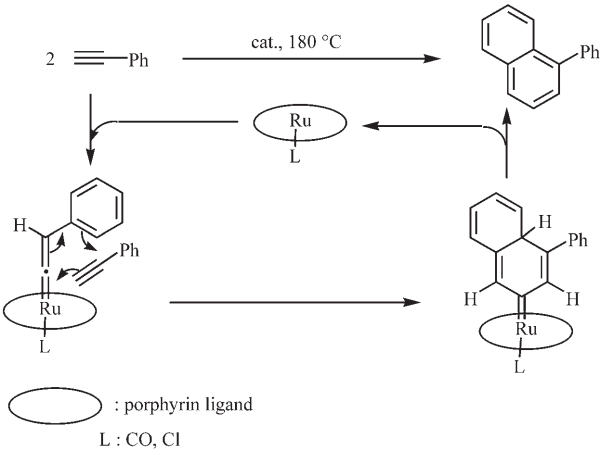

Scheme 25. Ruthenium–porphyrin catalysts for unusual dimerization of terminal alkynes into naphthalene derivatives.

4.2. Cycloisomerization of Conjugated Dienynes: Synthesis of Polycyclic Compounds

We define conjugated dienynes as substrates that contain a triple bond and two double bonds in conjugated positions, one or two of them being part of an aromatic motif, even though this type of carbon–carbon bond cannot be regarded as an olefinic double bond. These structures allow the elaboration of polycyclic systems via metal vinylidene intermediates. The addition of nucleophilic C=C bonds to electrophilic vinylidene carbon atoms has been attempted with a variety of metal precursors.[147] The cycloisomerization of conjugated 1,3-dien-5-ynes in the presence of a ruthenium catalyst is expected to involve as key steps 1) the formation of a ruthenium vinylidene intermediate, and 2) the electrocyclization of the dienyl vinylidene species with aromatization. This reaction has been carried out with $[RuCl_2(p\text{-cymene})(PPh_3)]$ as catalyst precursor in the presence of NH_4PF_6 as chloride abstractor, and polycyclic and heterocyclic aromatic compounds have been obtained in good yields (Scheme 26).[148] Labeling experiments have shown the 1,2-migration of the terminal acetylenic hydrogen atom, which strongly supports the formation of the ruthenium vinylidene intermediate.[149]

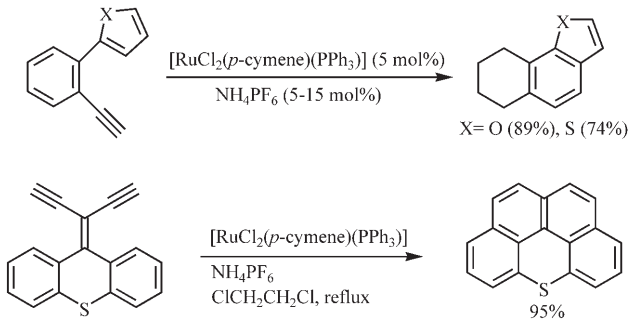

Scheme 26. Ruthenium-catalyzed cycloisomerization of dienynes.

$[RuTp(PPh_3)(MeCN)_2]PF_6$ also promotes these cycloaromatization reactions with substrates containing a more substituted terminal double bond. When the external double bond of the 1,3-dien-5-yne structure is substituted by a halogen atom (mainly I), halogen migration takes place during the cyclization.[150] When the same double bond is substituted by a *p*-tolyl or a *p*-anisyl group, not only the expected compounds are obtained but also those resulting from a skeleton rearrangement arising from 5-*endo*-dig cyclization and 1,2-aryl shift.[150] Finally, the presence of two substituents at the terminal olefin leads to the formation of the vinylidene ruthenium intermediate followed by 6-*endo*-dig cyclization and alkyl migration to form a naphthalene derivative, and 5-*endo*-dig cyclization to produce an alkenyl indene (Scheme 27).[151] All these possibilities are illustrated in Scheme 28.[150,151]

Trialkylsilyl alkynes can be activated by metal complexes to generate metal vinylidene derivatives. As illustrated in Scheme 29, rhodium complexes $[\{RhCl(CO)_2\}_2]$[152] and

 © 2006 Wiley-VCH Verlag GmbH & Co. KGaA, Weinheim

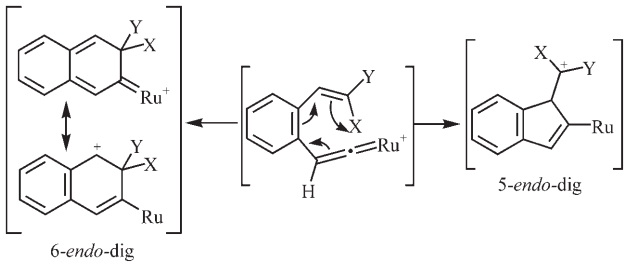

Scheme 27. The 6-*endo*-dig and 5-*endo*-dig cyclization of dienynes.

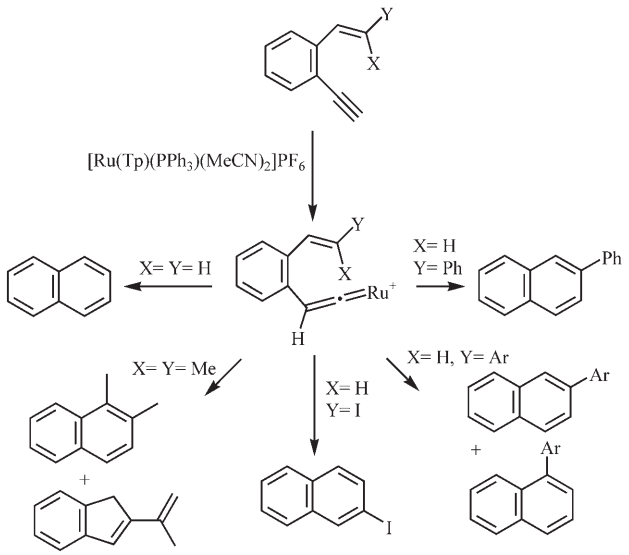

Scheme 28. Various possibilities for the cyclization/rearrangement of dienynes via ruthenium vinylidene intermediates.

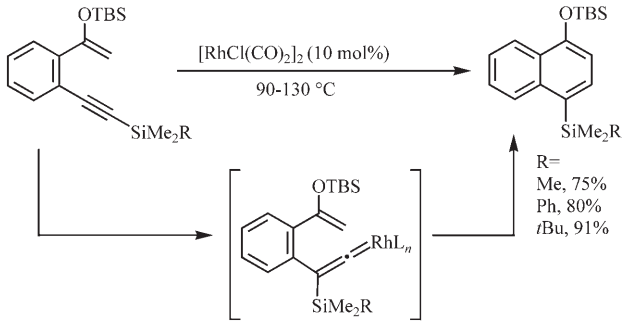

Scheme 29. Rhodium-catalyzed cyclization of silylated dienynes.

$[\{RhCl(P\mathit{i}Pr_3)_2\}_2]$[41] allow the aromatization of a dienyne containing a trimethylsilyl-substituted triple bond. In this process, the formation of the silylvinylidene rhodium species results from 1,2-migration of the trimethylsilyl group.

Activation of a terminal aromatic 3-ene-1,5-diyne by $[RuCl(Cp)(PMe_3)_2]$ allowed the isolation of a ruthenium vinylidene, which subsequently underwent stoichiometric thermal cycloaromatization.[153] On the basis of the experiment, it was suggested the cycloaromatization was a radical process involving a metal fragment. A series of rhodium-catalyzed radical cycloaromatizations were then described, for example, that of acyclic enediyne at 50–80 °C with catalytic $[RhCl(\mathit{i}Pr_3P)_2]$ (5 mol %) in the presence of Et_3N.[154,155]

Under milder conditions, the electrocyclization of aromatic enynes was successfully performed in the presence of $[W(CO)_5(thf)]$ catalyst precursor (Scheme 30).[156] Substituted

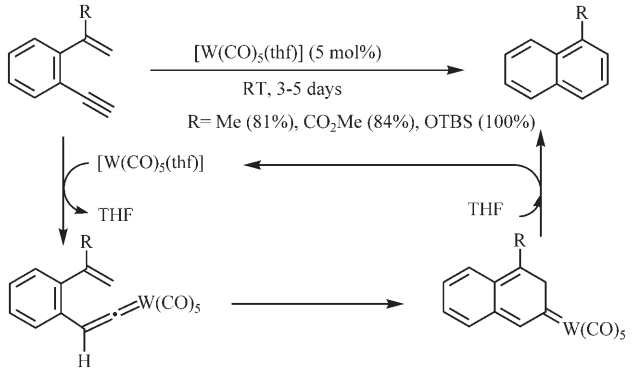

Scheme 30. Tungsten-catalyzed aromatization of dienynes. TBS = *tert*-butyldimethylsilyl.

naphthalene derivatives were produced in excellent yields at room temperature via neutral vinylidene tungsten(carbonyl) species. Indirect evidence for tungsten vinylidene intermediates was given by the isolation of metal pyranylidene complexes from β-ethynyl α,β-unsaturated esters.[157] Aromatic alkynyl imines react in a similar manner in refluxing THF in the presence of $[W(CO)_5(thf)]$ (20 mol %) to give 2-arylated quinolines (Scheme 31).[158]

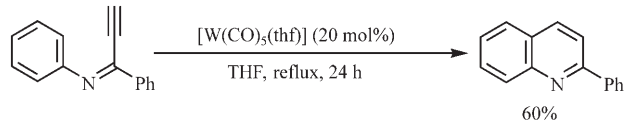

Scheme 31. Tungsten-catalyzed cyclization of alkynyl imines.

Carbocycles are also efficiently constructed from ω-acetylene silyl enol ethers at room temperature in the presence of $[W(CO)_5(thf)]$ (10 mol %) as precatalyst (Scheme 32).[159–161] The reaction involves the *endo*-dig cyclization of an intermediate ene-vinylidene tungsten moiety, followed by formation of a ketone through elimination of silanol, which is favored by the addition of 2 equivalents of water in the reaction medium.

The possibility of generating iodovinylidene complexes through activation of iodoalkyne by $[W(CO)_5(thf)]$ opens a new route to produce iodo-substituted aromatic derivatives through catalytic electrocyclization of 6-iodo-1,3-dien-5-ynes (Scheme 33).[162] This reaction produces useful substrates for further coupling reactions, but is restricted to iodo derivatives. The cyclization of ω-iodoacetylenic silyl enol ethers to produce cyclic iodoalkenes also proceeds in the presence of $[W(CO)_5(thf)]$, but requires a stoichiometric amount of tungsten complex.[41,162]

 © 2006 Wiley-VCH Verlag GmbH & Co. KGaA, Weinheim

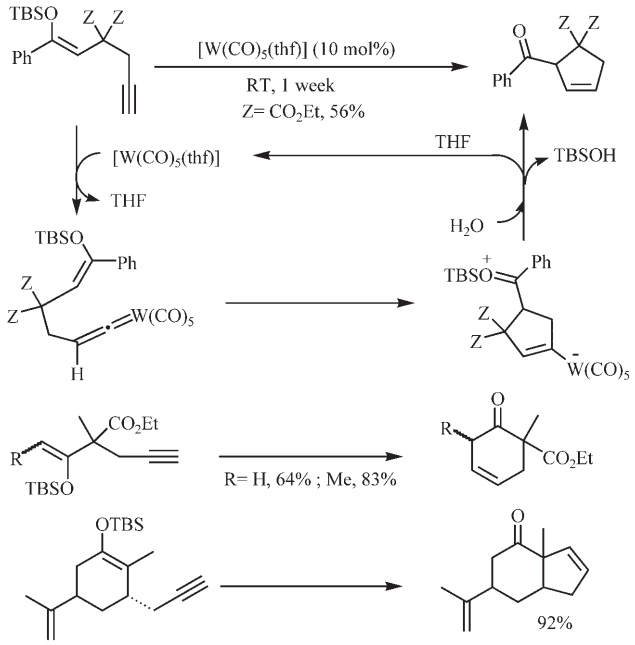

Scheme 32. Cyclization of acetylene silyl enol ethers.

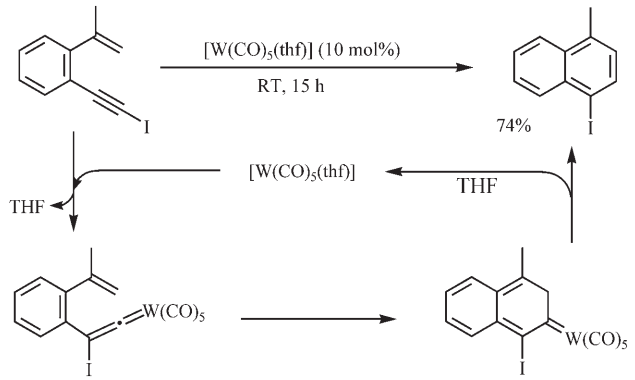

Scheme 33. Tungsten-catalyzed cycloisomerization of an iodoalkyne.

The preparation of 9-halophenanthrenes by cycloisomerization of 2-haloethynylbiphenyl substrates and 1,2-halide migration in the presence of catalytic amounts of AuCl seems to be the first example of gold vinylidene in catalysis.[163]

4.3. Coupling of Terminal Alkynes and Olefins

4.3.1. Intermolecular Coupling of Terminal Alkynes and Olefins through [2+2] Cycloaddition

Several stoichiometric reactions have shown that an olefin and a metal vinylidene moiety can undergo [2+2] cycloaddition. Thus, the vinylidene M=Cα bond reacts with a bidentate olefinic ligand (cod or (buta-1,3-dienyl)diphenylphosphine) to generate η^3-allyl ligands,[164,165] whereas the Cα=Cβ double bond interacts with an allyldiphenylphosphine ligand to give a cyclobutylidene ring through [2+2] cycloaddition (Scheme 34).[166,167]

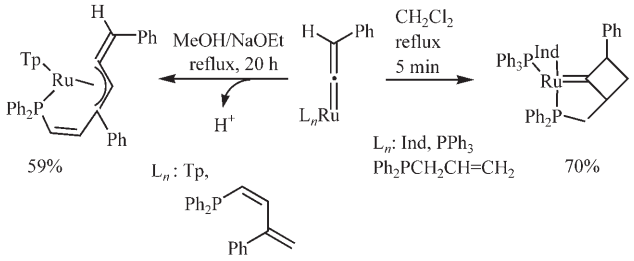

Scheme 34. Stoichiometric [2+2] cycloaddition reactions involving the vinylidene C=C and M=C double bonds.

The first type of reaction has been extended to catalytic reactions for the coupling of alkynes with olefins to produce conjugated dienes, with favored head-to-head coupling, in the presence of $[RuClCp(PPh_3)_2]/NaPF_6$ as catalyst precursor (Schemes 35 and 36).[168]

When the reaction is carried out with conjugated enynes such as cycloalkenylacetylene or the corresponding trime-

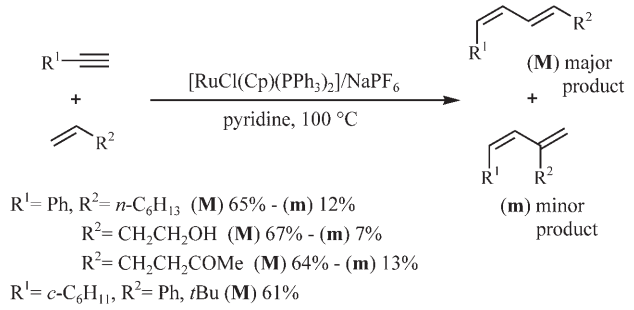

Scheme 35. Ruthenium-catalyzed coupling of alkynes with olefins.

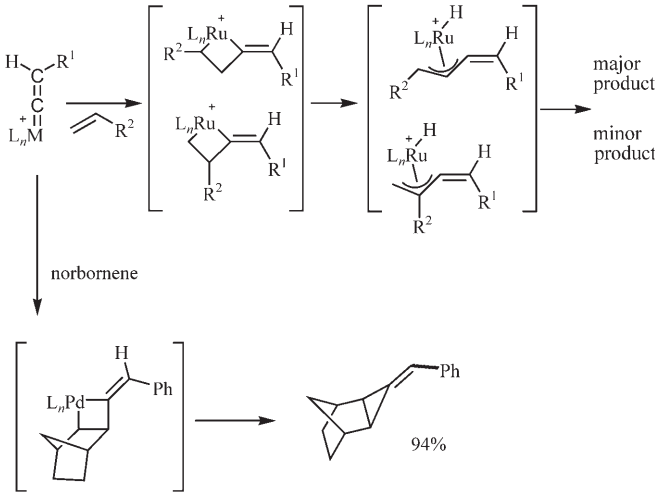

Scheme 36. Postulated catalytic cycle for the ruthenium- and palladium-catalyzed coupling of alkynes with olefins.

 © 2006 Wiley-VCH Verlag GmbH & Co. KGaA, Weinheim

thylsilyl-protected alkyne, the ruthenium-catalyzed reaction directly leads to bicyclic dienes through selective head-to-head coupling followed by thermal elecrocyclization.[169] Notably, the same final products can be obtained from a propargylic alcohol substrate such as 1-ethynylcyclohexanol, which is known to generate a ruthenium vinylvinylidene intermediate upon dehydration (Scheme 37).

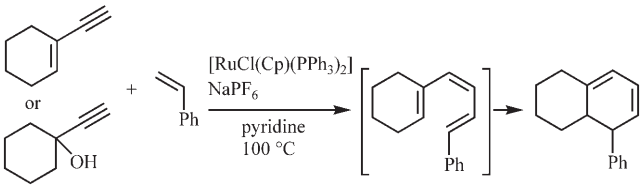

Scheme 37. Ruthenium-catalyzed coupling of propargylic alcohols or conjugated enynes with styrene.

If the formation of an allylic intermediate is not favored (Scheme 36), cyclopropane formation takes place. The formation of benzylidenecyclopropane is thus observed when phenylacetylene is treated with strained cycloolefins in the presence of a palladium precursor bearing phosphinous acid ligands.[170] Vinylidenecyclopropanes are formed from propargylic acetates and result from the [2+2] cycloaddition of the olefinic bond with a metal allenylidene intermediate.[170] To our knowledge, these are the first examples of palladium vinylidene and allenylidene intermediates in catalysis.

The alkenylation of pyridine derivatives with trimethylsilylacetylenes, which is performed at 150 °C with $[RuCl(Cp)(PPh_3)_2]/NaPF_6$, is also assumed to involve a ruthenium vinylidene intermediate and a [2+2] cycloaddition with the coordinated pyridine group (Scheme 38).[171]

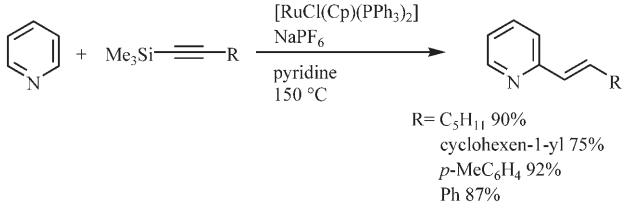

Scheme 38. Alkenylation of pyridine with alkynes.

4.3.2. *Intramolecular C–C Bond Formation from Enynes*

The $[RuTp(PPh_3)(MeCN)_2]PF_6$ precursor (10 mol%) promotes the intramolecular formation of cyclopentadienes from (*Z*)-3-en-1-ynes bearing a hydrogen atom at C5 in very good yields (71–89%) at 80 °C through a 1,5-sigmatropic hydrogen shift within the ruthenium vinylidene intermediates (Scheme 39).[172] The formation of cyclopentadiene (and related isomers) derivatives is also possible from propargylic alcohols able to release *Z* enynes upon dehydration catalyzed by the same ruthenium precursor.

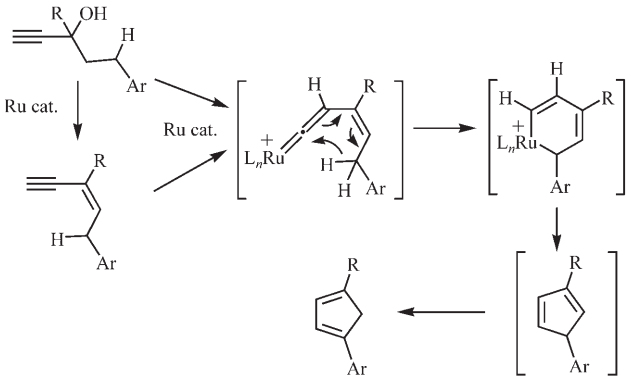

Scheme 39. Formation of cyclopentadienes from *Z* enynes.

5. Metal Vinylidenes in Alkene and Enyne Metathesis

5.1. Alkyne Polymerization and Ring-Opening Olefin Metathesis with Metal Vinylidene Initiators

The first example of metal vinylidene as a polymerization initiator was in the polymerization of phenylacetylene through the generation of $[(CO)_4W{=}C{=}CHPh]$ in situ upon photochemical activation of $[W(CO)_6]$.[47] This reaction was further developed with other transition metals,[173,174] and used to produce block copolymers from norbornene and alkynes.[175]

The discovery of well-defined ruthenium alkylidene catalysts of the type $[RuX_2(=CHR)(PR_3)_2]$ for alkene metathesis[176–181] has motivated the preparation of homologous vinylidene complexes such as $[RuCl_2(=C=CHR')(PR_3)_2]$ and their evaluation in ring-opening olefin-metathesis polymerization (ROMP).[182,183] Their catalytic activity for ROMP was first disclosed for $[RuCl_2(=C=CH_2)(PCy_3)_2]$,[184] and then extended to analogous precursors containing other phosphines (such as PPh_3 and $PiPr_3$) and a vinylidene ligand generated from various alkynes (such as *tert*-butylacetylene, phenylacetylene, ferrocenylacetylene, and *p*-methoxyphenylacetylene).[185,186] The precatalysts $[RuCl_2(=C=CHR)(L)_2]$ have been used successfully for the ROMP of a variety of functionalized norbornene derivatives including esters, ethers,[187] and carboximides.[188] The molecular weight was controlled by addition of vinyl ether and vinyl thioether as chain-transfer reagents.[187,189] ROMP of norbornene can be initiated with the precursors $[RuCl(C_5Me_5)(=C=CHPh)(PPh_3)]$ and $[RuCl(Tp)(=C=CHPh)(PPh_3)]$, and their activity is enhanced by addition of Lewis acids such as $BF_3{\cdot}Et_2O$ or $[PdCl_2(MeCN)_2]$.[190]

5.2. Alkene Metathesis with Vinylidenes Generated In Situ

Ruthenium vinylidene complexes that are active in ROMP have also been shown to perform well in olefin-ring-closing and cross-metathesis reactions, which are now well developed in fine chemistry for access to cyclic or macrocyclic compounds and functionalized internal double bonds. As an

 © 2006 Wiley-VCH Verlag GmbH & Co. KGaA, Weinheim

example, $[RuCl_2(=C=CHFc)(PCy_3)_2]$ (Fc = ferrocenyl) (2 mol%) catalyze the ring-closing metathesis of 1,6- and 1,7-dienes to produce five- and six-membered rings in more than 90% yield in $CDCl_3$ at 60°C, whereas enynes and dienynes were also cyclized into alkenyl cycloalkenes according to a metathesis mechanism.[187]

Ruthenium carbene complexes bearing 1,3-imidazol-2-ylidene or 1,3-imidazolin-2-ylidene instead of bulky basic phosphine ligands[191] were shown to be more efficient catalysts for both olefin and enyne metathesis.[191–201] Attempts to produce more-active ruthenium vinylidene catalysts by introduction of such heterocyclic diaminocarbene ligands proved to be less successful, and the idea of catalytic species generated in situ emerged. The first example of such a catalytic system was based on $[\{RuCl_2(p\text{-cymene})\}_2]$, 1,3-bis(mesityl)imidazolium chloride, sodium *tert*-butylate, and *tert*-butylacetylene.[202] The system allowed the ring-closing metathesis of a variety of dienyl malonates at 80°C to afford five-, six-, and seven-membered rings, the metathesis cyclization of enynes, the cross-metathesis of propenylbenzene, and the ring-opening metathesis of cod. At the same time, we reported that a catalytic system generated in situ from $[\{RuCl_2(p\text{-cymene})\}_2]$, 1,3-bis(mesityl)imidazolium chloride, and cesium carbonate (1:2:4) promoted the cyclization of enynes to form the conjugated alkenyl cycloalkene compounds at 80°C in toluene.[203] With a similar approach, but using the saturated 1,3-bis(mesityl)imidazolinium chloride as diaminocarbene precursor, attempts were made to generate coordinatively unsaturated species **III** and then **IV**[204] in situ (Scheme 40).

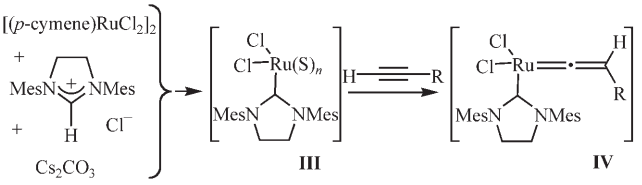

Scheme 40. Generation of NHC ruthenium vinylidene species in situ. Mes = mesityl.

This approach was based on our previous observation that the same precursor $[\{RuCl_2(p\text{-cymene})\}_2]$ and Cs_2CO_3 transform a benzimidazolium salt into a ruthenium carbene complex and that the *p*-cymene ligand was labile (Scheme 41).[205] Thus, with the catalytic species generated in situ expected to be of type **III**, cyclic siloxanes[204,206] as well as terpenoid derivatives[207,208] presenting enyne structures were selectively produced in good yields (Scheme 42). Notably, the species **III** generated in situ is more active than $[RuCl_2(NHC)(p\text{-cymene})]$ (NHC = N-heterocyclic carbene) precatalysts.[203]

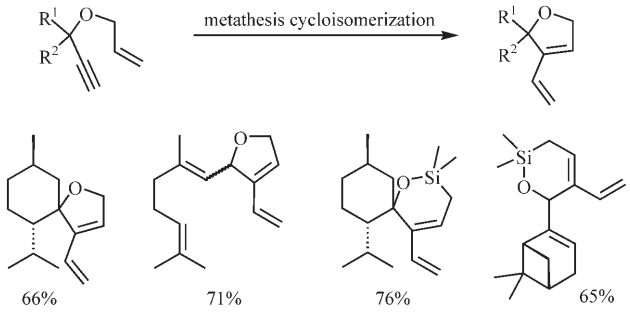

Scheme 42. Rearrangement of enynes derived from terpenoids in the presence of a three-component catalytic system.

However, the catalysts generated in situ did not promote the ring-closing metathesis of 1,6-dienes expected in the absence of an initiating carbene, but provided cycloisomerization compounds at 80°C in very good yields (Scheme 43).[209] As an attempt to produce a ruthenium vinylidene species of type **IV**, a catalyst was generated in situ as previously, but in the presence of a terminal alkyne (Scheme 40). This catalyst does, indeed, promote the RCM of the same dienes. Especially in the presence of acetylene (1 bar), an active alkene metathesis catalyst is at play (Scheme 44).[209,210] No cycloisomerization was observed

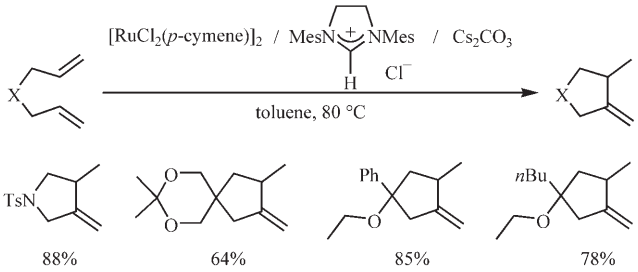

Scheme 43. Ruthenium-catalyzed cycloisomerization of dienes.

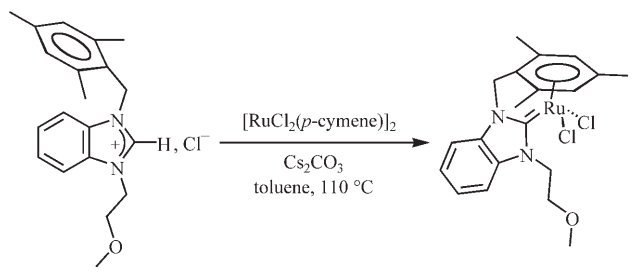

Scheme 41. Stoichiometric formation of a diaminocarbene–ruthenium complex.

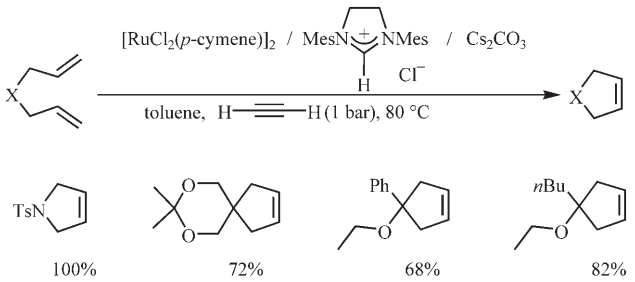

Scheme 44. Generation of an olefin-metathesis catalyst in the presence of a terminal alkyne.

 © 2006 Wiley-VCH Verlag GmbH & Co. KGaA, Weinheim

under these conditions, although this reaction is faster than RCM. Thus, in the presence of the ruthenium species **III**, the alkyne (RC≡CH; R = Ph, *n*Bu, H) rapidly generates another catalytic species **IV** that inhibits the cycloisomerization reaction in favor of the metathesis reaction. To rationalize these reactivities, it was proposed that the first step is the deprotonation of the imidazolinium salt to generate a NHC carbene, which is trapped by the ruthenium center with removal of the arene ligand and gives rise to a coordinatively unsaturated ruthenium species **III** that catalyzes the metathesis or cycloisomerization of enynes and dienes. In the presence of a terminal alkyne, a metal vinylidene intermediate **IV** is readily formed and provides an olefin-metathesis catalyst (Scheme 45).[202,209,210]

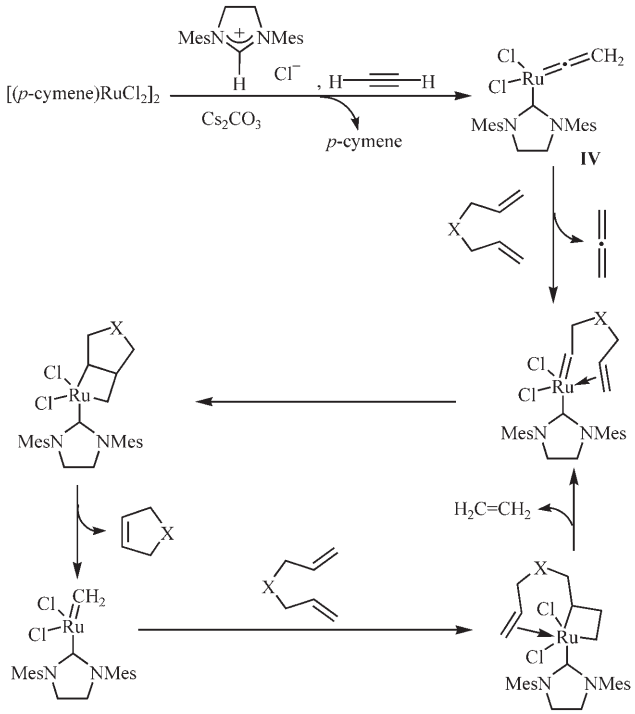

Scheme 45. Catalytic cycle for the four-component catalytic system active in RCM.

5.3. Vinylidene Ruthenium Intermediates Generated In Situ as Precursors of Alkenyl Carbene Metal Catalysts

Owing to the lack of initiating carbene, the 16-electron complex [RuCl(PCy$_3$)(*p*-cymene)]OTf does not transform diallyl tosylamide into its ring-closing-metathesis product. In contrast, it was surprising that the same precursor transformed mixed allyl propargyl ethers into their RCM products,[50] the alkenyl cycloalkenes usually resulting from the action of an alkene-metathesis catalyst (Scheme 46).[178,211,212]

This catalytic reaction suggested that the complex [RuCl(*p*-cymene)(PCy$_3$)]TfO (**Va**) activates the allyl propargyl ether and generates a carbene-metathesis catalyst. First, it was thought that a ruthenium vinylidene complex might be formed from the ruthenium precursor and the terminal alkynes as illustrated in Scheme 47. However, these vinylidene complexes (R = Ph, CH_2Ph) did not catalyze the RCM of dienes, and previously generated allenylidene ruthenium complexes[213–216] appeared to be less effective enyne-RCM catalysts than those arising from **Va** and enynes. To elucidate the nature of the catalytic species, the precursor **Vb**, which contains the stabilizing counteranion $B(Ar^F)_4^-$, was treated with a stoichiometric amount of an enyne at −30 °C, and the new alkenyl carbene complex **VII** was formed together with acrolein. The formation of **VII** was explained as occurring via the ruthenium vinylidene **VI** followed by a pericyclic retro-ene rearrangement (Scheme 48).[50] This hypothesis was

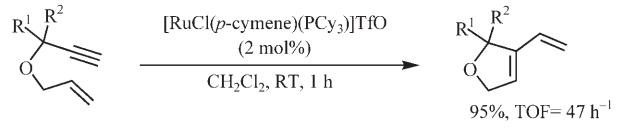

Scheme 46. Transformation of enynes in the presence of [RuCl(*p*-cymene)(PCy$_3$)]OTf.

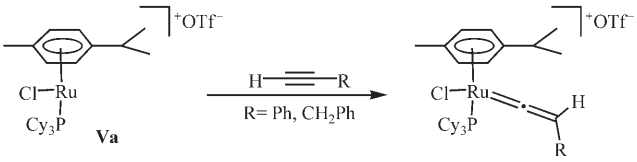

Scheme 47. Formation of ruthenium vinylidene complexes from **Va**.

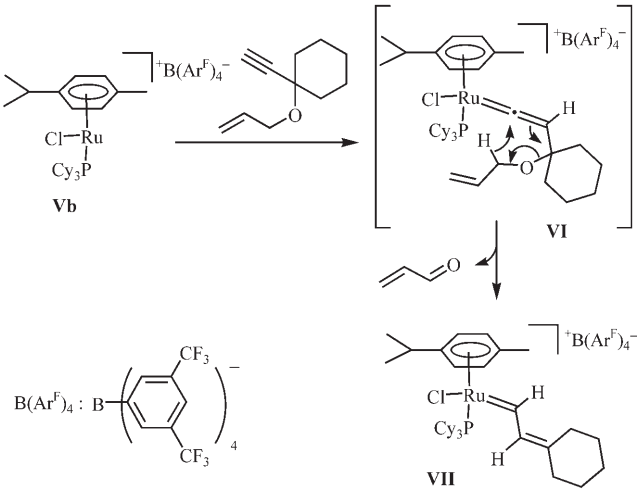

Scheme 48. Formation of a ruthenium alkenylcarbene from a propargylic enyne.

strengthened by the activation of propargyl propyl ether by **Va** to give propanal and the corresponding alkenyl carbene ruthenium complex **VIII** (Scheme 49).

Although the alkenyl carbene ruthenium complex **VII**, which contains the $B(Ar^F)_4^-$ anion, is not an efficient RCM catalyst, complex **VIII** and the accompanying TfO^- anion proved to be an efficient catalyst for the RCM of enynes with activity analogous to that in the transformation of enynes in the presence of **Va**. This confirms that intermediates **VIII**,

 © 2006 Wiley-VCH Verlag GmbH & Co. KGaA, Weinheim

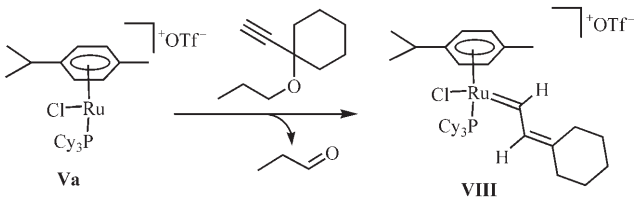

Scheme 49. Formation of a ruthenium alkenylcarbene through activation of a propyl propargyl ether.

which arise from vinylidene intermediates of type **VI**, are active species in this reaction. More importantly, the complex **VIII** was revealed as an excellent catalyst for the RCM reaction of a variety of dienes under mild conditions (Table 2).

Table 2: Diene RCM reactions with complex **VIII** (2 mol%) at room temperature.

Entry	Substrate	Product	*t*	Conv. [%]	TOF [h^{-1}]
1	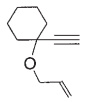	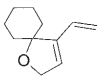	1 h	99	49
2	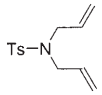		15 min	95	190
3	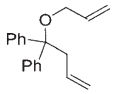		4 h	99	12
4	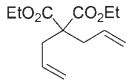	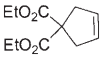	2 h	99	25
5	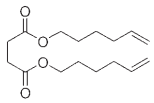	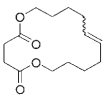	1 h	99	49

This study shows several innovative aspects arising from the vinylidene intermediate **VI**, the key activation species of enynes with 16-electron complex **V**. It leads to a new method to generate alkenyl carbene metal complexes from a propargyl ether and an allyl or an alkyl group. It is thus in contrast to the previous methods to generate alkenyl carbene ruthenium by initial formation of allenylidene,[217] by activation of a cyclopropene derivative[218] or propargyl chloride,[219] or by stoichiometric metathesis of butadiene.[220] This reaction readily generates new RCM catalysts for enynes and dienes. It also offers a remarkable example of a molecule, the enyne, that creates its own catalyst, the alkenyl carbene ruthenium, to initiate its own catalytic transformation into an alkenyl cycloalkene.

5.4. Molybdenum Vinylidene for Allenyne Metathesis

We have just shown that ruthenium vinylidenes either isolated or generated in situ can generate active ruthenium carbene species for olefin metathesis. The reverse process was recently reported by Murakami et al., who proposed the formation of a molybdenum vinylidene from a molybdenum carbene, which appears to be a key catalytic intermediate for the metathesis rearrangement of allenynes (Scheme 50).[221]

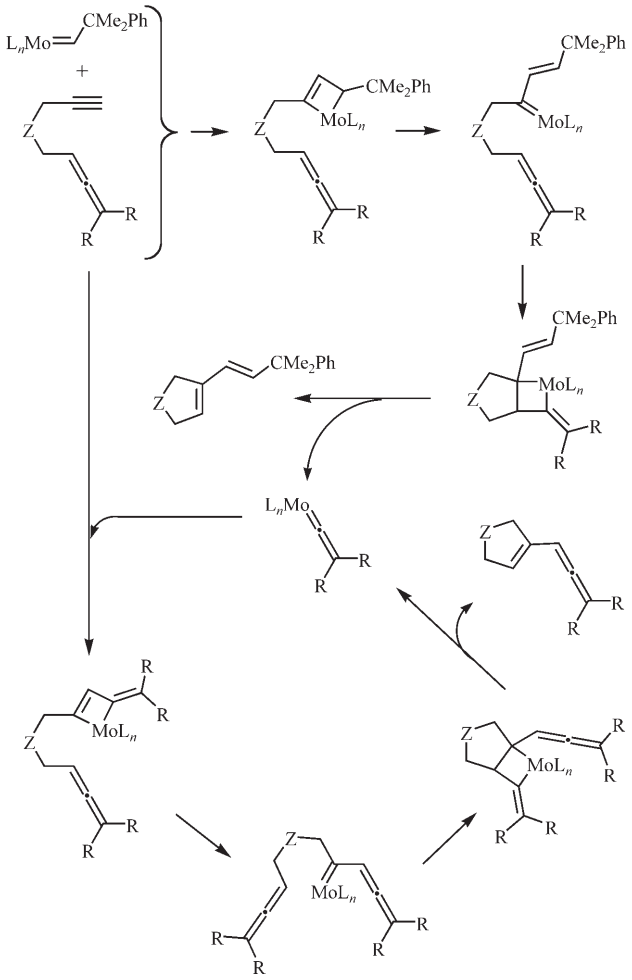

Scheme 50. Molybdenum-catalyzed allenyne metathesis.

The reaction takes place at room temperature and provides conjugated vinyl allenes in good yields (71–84%) which can be used as 1,3-dienes for Diels–Alder reactions. The reaction works well when Z = TsN, $(MeO_2C)C$, BnN, but no reaction occurs with terminal allenes, internal triple bonds, and ethers; attempts to form six-membered rings were unsuccessful.

6. Metal Allenylidenes in Catalysis

The discovery by Selegue[222] that a 16-electron ruthenium intermediate promotes the activation/dehydration of propargyl alcohols (which led to the generation of the first ruthenium allenylidene complex) lay the path to a large variety of metal allenylidene complexes from readily accessible propargyl alcohols. Several reviews summarize the synthetic approaches and stoichiometric reactions.[5,6,8,9,223,224] These reactions revealed the electrophilic properties of the

 © 2006 Wiley-VCH Verlag GmbH & Co. KGaA, Weinheim

Cα and Cγ carbon atoms of the M=C=C=CR$_2$ moiety in the addition of alcohols and amines at Cα and that of phosphines or hydride at Cγ.[217,225–227] In contrast, Cβ is nucleophilic and is readily protonated to give alkenyl carbyne metal complexes.[228,229]

Only recently have metal allenylidene complexes or metal allenylidene intermediates, generated in situ by activation of propargyl alcohol derivatives, emerged as catalyst precursors or catalyst intermediates.[43] Significant advances were recently made in the direct propargylation of a variety of substrates by propargyl alcohols[230–233] and in alkene metathesis promoted by ruthenium allenylidene complexes.[234] Among the metal allenylidene species, mainly ruthenium moieties were involved as catalytic intermediates and catalyst precursors. The first example was reported in 1992 by Trost and Flygare, who showed that [RuCl(Cp)(PPh$_3$)$_2$]/NH$_4$PF$_6$ was an efficient catalyst for coupling hydroxylated propargylic alcohols with allylic alcohol according to Scheme 51.[235]

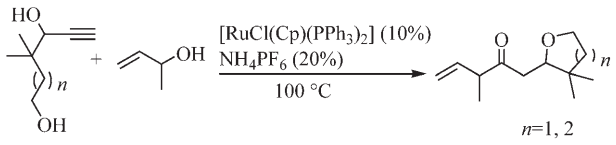

Scheme 51. Ruthenium-catalyzed coupling of propargylic and allylic alcohols via ruthenium allenylidene intermediates.

This reaction is initiated by the formation of a ruthenium allenylidene moiety, which undergoes an intramolecular reaction with the hydroxy group at Cγ to generate a ruthenium vinylidene intermediate (Scheme 52). Then, upon

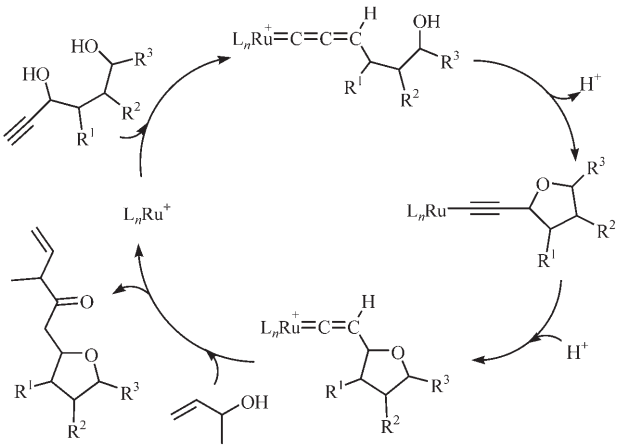

Scheme 52. Catalytic cycle for the ruthenium-catalyzed coupling of propargylic and allylic alcohols via a ruthenium allenylidene intermediate.

intermolecular addition of the allylic alcohol and skeleton rearrangement, the tetrahydrofuran compound bearing an unsaturated ketone branch is formed (see Section 2.2)

At about the same time, we found that [RuCl$_2$(PPh$_3$)(*p*-cymene)] promotes the formation of allyl propargyl ether from allyl alcohol and 2-phenylbut-3-yn-2-ol at 60 °C (Scheme 53). This reaction corresponds to the formal substitution of the hydroxy group by an allyloxy group with elimination of water and was thought to proceed through nucleophilic addition of the alcohol to Cγ of a ruthenium allenylidene intermediate.[236]

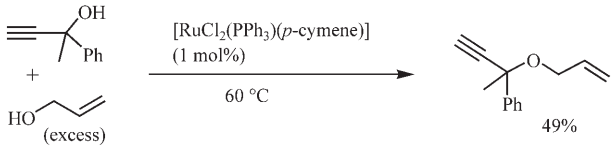

Scheme 53. Ruthenium-catalyzed formation of allyl propargyl ethers.

The more-efficient cationic 16-electron complex [Ru(methallyl)(CO)(dppf)]SbF$_6$ (dppf = diphenylphosphanylferrocene), generated upon chloride abstraction from [RuCl(methallyl)(CO)(dppf)] with AgSbF$_6$, produced a variety of propargylic ethers from 1,1-diphenylprop-2-yn-1-ol and aliphatic alcohols (Scheme 54).[231] In the absence of any other

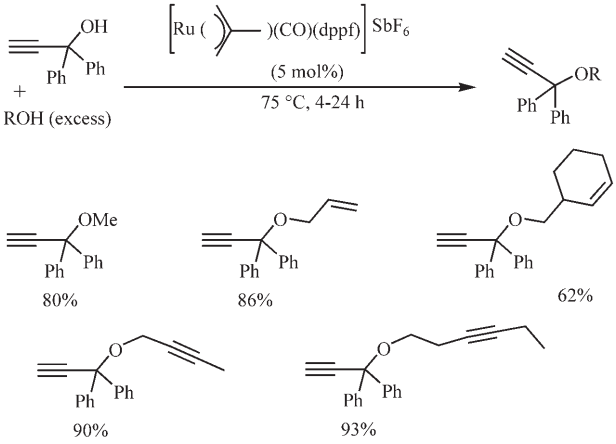

Scheme 54. Formation of propargylic ethers with [Ru(methallyl)(CO)(dppf)]SbF$_6$ as catalyst precursor.

alcohol, the starting propargylic alcohol isomerized quantitatively into 3,3-diphenylprop-2-enal. Both compounds probably arise from the alkynol-activation process, which leads first to a 3-hydroxyalkenylidene and then to an allenylidene ruthenium intermediate, which reacts either with the freed water at Cα to give the enal or with the nucleophilic alcohol at Cγ to form propargylic ethers.

We also recently reported the first propargylation of furans catalyzed by the mononuclear ruthenium complexes [RuCl(PR$_3$)(*p*-cymene)]OTf (R = Ph, Cy) (Scheme 55).[232] A study of the catalytic precursor, but with the B(Ar^F)$_4^-$ anion, showed that the two primary products, the ruthenium allenylidene complex and water, which arises from dehydration of the propargylic alcohol, react by addition at Cα to form a stable vinylic hydroxycarbene ruthenium intermediate, which upon heating at above 50 °C evolves into the carbonyl cationic species [RuCl(PCy$_3$)(CO)(*p*-cymene)]$^+$.[232] This complex exhibits good catalytic activity for the prop-

 © 2006 Wiley-VCH Verlag GmbH & Co. KGaA, Weinheim

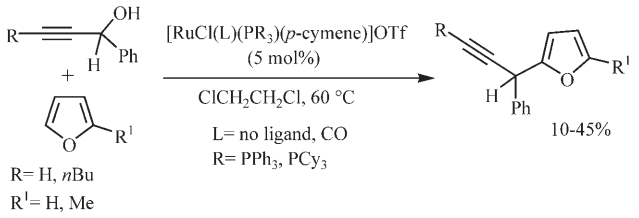

Scheme 55. Ruthenium-catalyzed propargylation of furans.

argylation of furans and is likely a catalytic species (Scheme 56). However, a propargylic alcohol such as *n*BuC≡CCH(Ph)OH also reacted with 2-methylfuran to

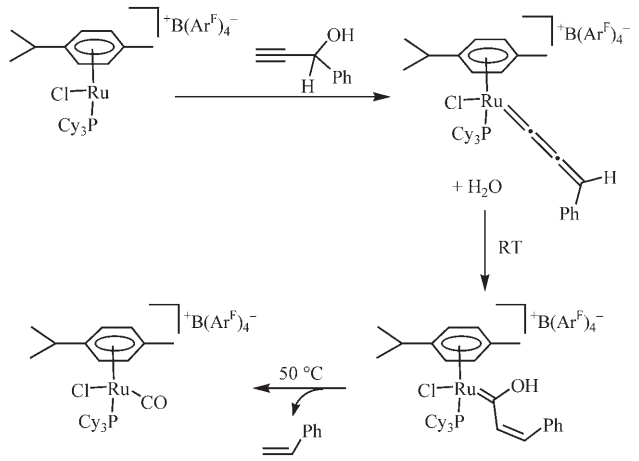

Scheme 56. Transformation of [RuCl(PCy3)(CO)(*p*-cymene)][B(ArF)4] in the presence of propargyl alcohol and water.

form the corresponding 5-methylfuran-2-yl propargylic compound. This indicates that the formation of a metal allenylidene intermediate is not an essential condition in this catalytic reaction. Dicationic [Ru(MeCN)(*p*-cymene)(bisoxazoline)]$(BF_4)_2$ complexes were also used for the propargylation of furan and arene derivatives.[233]

The most general results in the direct propargylation with propargylic alcohols were obtained in the presence of thiolate-bridged binuclear ruthenium precatalysts in the series [(Cp*)RuCl(μ^2-SR)$_2$RuCl(Cp*)] by Nishibayashi et al.[230] This ruthenium-catalyzed substitution of propargylic alcohols proceeded successfully with a variety of oxygen, nitrogen, phosphorus, sulfur, and carbon nucleophiles, including aliphatic alcohols,[230,237,238] phenols,[230,239] aromatic amines,[237,238] amides,[237,238] phosphine oxides,[237] thiols,[237,240] ketones,[238,241–245] aromatic heterocycles,[238,246] and olefins[247] (Scheme 57). This catalyst also effects the dehydration of propargylic alcohols.[230]

It has been shown that in most cases, the first step is the addition of a nucleophile at the Cγ atom of the allenylidene that results from activation of the propargylic alcohol. The second step is the ligand exchange between the vinylidene formed at one of the ruthenium sites and another propargylic alcohol, a determining step that is assumed to be facilitated by the presence of the other ruthenium center, which is not directly involved in the allenylidene formation (Scheme 58).

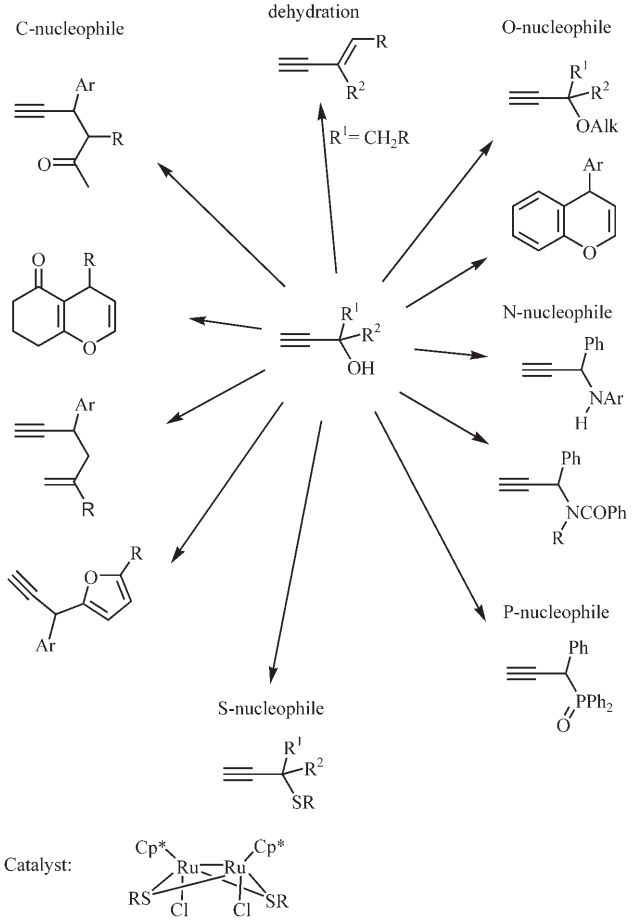

Scheme 57. Examples of propargylation of various nucleophiles.

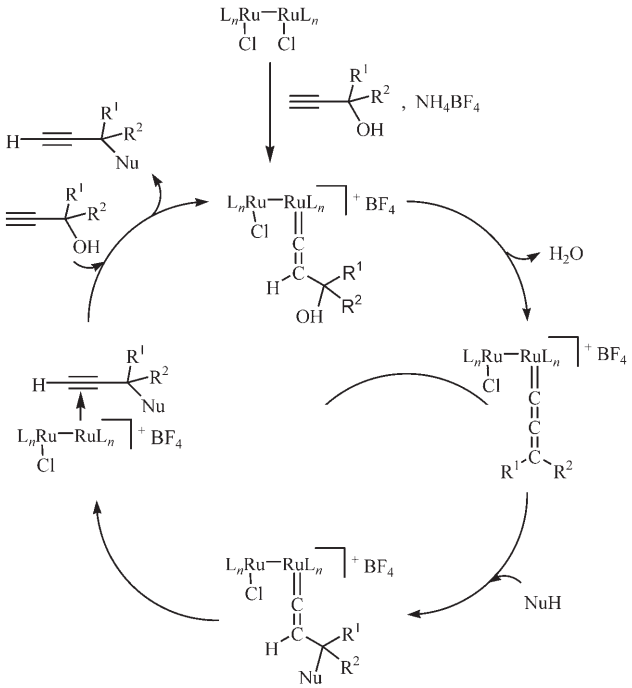

Scheme 58. General scheme for the propargylation of nucleophiles catalyzed by diruthenium complexes.

 © 2006 Wiley-VCH Verlag GmbH & Co. KGaA, Weinheim

Several examples involving nucleophilic addition at the coordinated allenylidene carbon atom have also been reported. Thus, the addition of water to propargylic alcohols in 2-propanol/water at 100 °C in the presence of catalytic amounts of $[RuCl(Cp)(PMe_3)_2]$ leads to conjugated enals with *E* stereoselectivity (see Section 2.4).[119]

The activation of propargylic alcohols in the presence of $[RuTp(PPh_3)(MeCN)_2]PF_6$ provides a terminal olefin with cleavage of the triple bond and elimination of carbon monoxide (Scheme 59).[248] The reaction proceeds via a

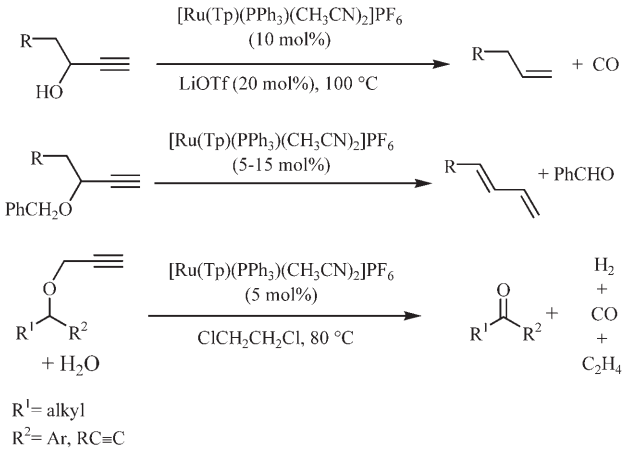

Scheme 59. Catalytic transformations of propargylic alcohols and ethers in the presence of $[RuTp(PPh_3)(CH_3CN)_2]PF_6$.

ruthenium allenylidene intermediate, which traps the formed water molecule at Cα to generate an acyl ligand that decomposes through decarbonylation. The reaction proceeds in toluene at 110 °C in the presence of LiOTf (20 mol %) and produces a variety of 4-aryl prop-1-enes in good yields from 5-aryl pent-1-yn-3-ols.

The same catalyst $[RuTp(PPh_3)(MeCN)_2]PF_6$ promotes the conversion of 3-benzyl but-1-ynyl ethers into 1,3-dienes and benzaldehyde (Scheme 59).[249,250] When applied to cyclic propargyl ethers, this transformation allows the formation of dienes with a tethered aldehyde functionality. Another application of this catalyst precursor led to the formation of aryl and alkynyl ketones from aryl and alkynyl propargyl ethers, respectively, in the presence of water through cleavage of the carbon–carbon triple bond (Scheme 59).[251] These transformations are based on the formation of a ruthenium allenylidene intermediate with cleavage of the ether bond followed by nucleophilic attack of the freed alcohol at the allenylidene Cα atom and hydrogen transfer. Some of these reactions can also be explained as occurring through vinylidene formation and retro-ene reaction of the benzyl group.[50]

7. Ruthenium Allenylidenes as Catalyst Precursors in Alkene Metathesis

Ruthenium allenylidene complexes have, to date, found very few applications in catalysis. Besides the dimerization of tin hydrides, in which the $[RuCp(=C=C=CPhAr)(PPh_3)_2]PF_6$ complex is transformed into a ruthenium alkynyl species,[252] and the transetherification of tethered vinyl ethers,[253] the main application of metal allenylidenes is in alkene metathesis.

7.1. The First Reaction Steps

Well-defined ruthenium alkylidenes of the type $[RuCl_2(PCy_3)_2(=CHR)]$ (R = Ph, $CH=CR_2$) were revealed as efficient alkene metathesis and as functional-group-tolerant catalysts.[180,218,254] They have initiated efforts for the search of new neutral 16-electron ruthenium catalysts that contain an initiating (:CHR) carbene ligand. The first metal allenylidene complexes as alkene-metathesis precursors $[RuCl(=C=C=CR_2)(PR_3)(p\text{-cymene})]X$ were reported in 1998.[255] These ionic, 18-electron, well-defined precursors contain the $:C=C=CR_2$ moiety as an "initiator" and introduced a new orientation in the search for catalysts. They raised questions about their behavior in alkene metathesis. Applications of ruthenium allenylidenes in various aspects of alkene metathesis of dienes and enynes were first developed before the mechanism of the reaction was solved.

The arene ruthenium allenylidene metathesis-catalyst precursors were simply made from $[RuCl_2(PR_3)(arene)]$ complexes containing a bulky electron-releasing phosphine after displacement of a chloride (Scheme 60). Their large-

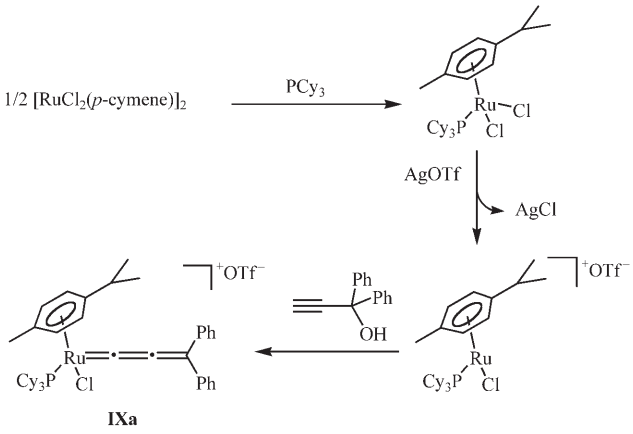

Scheme 60. Straightforward preparation of the ruthenium allenylidene catalyst precursor **IXa**.

scale preparation from commercially available $[\{RuCl_2(p\text{-cymene})\}_2]$ can be carried out in one pot. The activity of the catalysts, which is evaluated from the product yields and reaction times (turnover frequency (TOF)) of the RCM reaction of the diene to form the cyclic alkene (Scheme 61), increases with the electron richness of phosphine ligand in the order $PPh_3 \ll PiPr_3 < PCy_3$.[255] The counteranion of these ionic precursors has a dramatic influence on the catalytic activity, which increases with the sequence $BF_4^- \ll BPh_4^- \approx PF_6^- \ll TfO^-$.[216,256]

$[RuCl(=C=C=CR_2)(PCy_3)(p\text{-cymene})]PF_6$ **IXb** was evaluated for the ring-closing metathesis of dienes and the formation of macrocycles and showed an activity and func-

 © 2006 Wiley-VCH Verlag GmbH & Co. KGaA, Weinheim

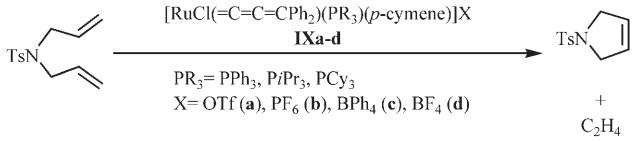

Scheme 61. RCM reaction with ruthenium allenylidene catalyst precursors **IX**.

tional-group tolerance similar to those of $[RuCl_2(PCy_3)_2(=CHPh)]$ (Scheme 62).[216] Complex **IXa** also promotes the RCM reaction of a family of α-aminophosphonates (Scheme 63).[257] It is now well accepted that the transformation of enynes into alkenyl cycloalkenes is promoted by alkene-metathesis catalysts.[178,211] This cycloisomerization reaction is also promoted by ruthenium allenylidene precursors, for example, the skeleton rearrangement of propargyl allyl ethers into alkenylcycloalkenes in the presence of **IXb** (Scheme 64). However, the activity increase significantly upon preliminary photochemical activation as an attempt to displace the arene from the metal.[258] Ruthenium allenylidenes also give access to functionalized fluorinated bicyclic amino esters through an initial enyne-RCM step (Scheme 65).[259]

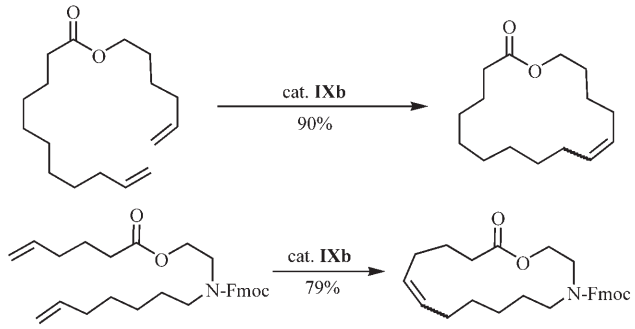

Scheme 62. Macrocycle formation catalyzed by ruthenium allenylidene catalyst **IXb**. Fmoc = 9-fluorenylmethoxycarbonyl.

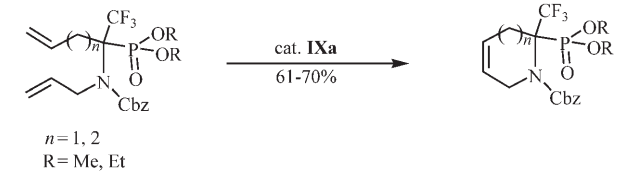

Scheme 63. Synthesis of fluorine-containing cyclic aminophosphonates through diene RCM.

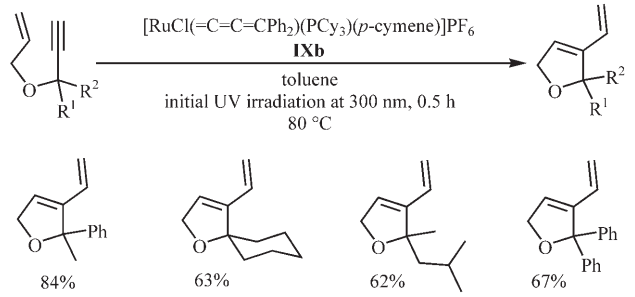

Scheme 64. Enyne metathesis catalyzed by the ruthenium allenylidene precursor **IXb**.

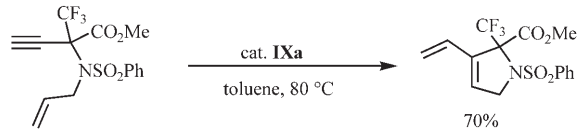

Scheme 65. Preparation of fluorinated cyclic amino acid derivatives involving enyne metathesis.

7.2. Ruthenium Allenylidenes in the Polymerization of Cyclic Olefins

ROMP of cyclic olefins provides macromolecules with evenly distributed functional groups and C=C bonds that can be hydrogenated[260] or functionalized.[261] The complex **IXa** readily initiates the ROMP of norbornene at room temperature and that of cyclooctene at 80 °C (Table 3).[262]

Preactivation of the catalyst before addition of the cyclic olefin, either thermally or photochemically in order to favor arene displacement and/or allenylidene rearrangement (see Section 7.1), allows the ROMP of cyclooctene at room temperature with rather good polydispersity. As the loss of the arene ligand was suggested as a first step of initiation, arene-free neutral and ionic ruthenium allenylidene complexes containing the dimethyl sulfoxide (dmso) ligand were prepared. Although they constitute a new family of ruthenium allenylidenes, they are not more efficient for ROMP than arene complexes, likely as a result of the strong dmso–ruthenium bond (Scheme 66).[263]

Table 3: ROMP of cycloalkenes with ruthenium allenylidene catalysts.

Monomer	Catalyst	Ratio[a]	Conditions	Yield [%]	M_0[b] ($\times 10^{-3}$)	PDI[c]	*cis*[d] [%]
norbornene	$[RuCl(=C=C=CPh_2)(PCy_3)(p\text{-cymene})]OTf$	1000:1	5 min, 22 °C	90	198	1.8	25
cyclooctene	$[RuCl(=C=C=CPh_2)(PCy_3)(p\text{-cymene})]OTf$	1000:1	5 min, 80 °C	90	267	1.4	22
cyclooctene	$[RuCl(=C=C=CPh_2)(PCy_3)(p\text{-cymene})]OTf$	150:1	UV, 2 h, 22 °C	99	143	1.8	–
norbornene	$RuCl_2(=C=C=CPh_2)(PCy_3)_2(dmso)$	300:1	4 h, 60 °C	56	16	4.1	–
norbornene	$[RuCl(=C=C=CPh_2)(PCy_3)(dmso)_2]OTf$	300:1	4 h, 60 °C	70	37	3.9	15

[a] Monomer/catalyst molar ratio. [b] M_n: molecular weight (number average) [g mol^{-1}]. [c] Polydispersity of the polymer. [d] Percentage of *cis* double bonds in the polymer.

 © 2006 Wiley-VCH Verlag GmbH & Co. KGaA, Weinheim

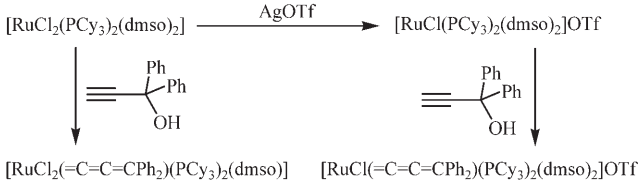

Scheme 66. Preparation of ruthenium–dmso allenylidene precursors.

7.3. Allenylidene Metal Complexes in Alkene Metathesis

The discovery of the alkene-metathesis activity of ruthenium allenylidene complexes $[RuCl(=C=C=CR_2)(PCy_3)(arene)]^+X^-$ led several groups to design new allenylidene metal complexes and evaluate them in this reaction. The first targets were the neutral analogues of the Grubbs catalysts $[RuCl_2(=C=C=CR_2)(PCy_3)(L)]$ ($L = PCy_3$, NHC). Nolan and co-workers prepared neutral ruthenium allenylidene complexes such as **X**,[264] but their catalytic activity remained moderate (Scheme 67). The ionic complex **XI** (analogous to **IX b** but containing an NHC ligand) was also prepared, but its activity did not reach that of **IX**.[265]

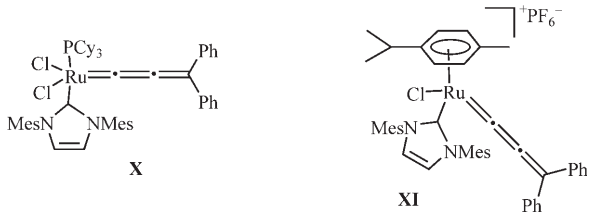

Scheme 67. Examples of ruthenium allenylidene complexes.

The attempts to produce neutral allenylidene complexes containing the poorer-electron-releasing ligand PPh_3 failed, and the indenylidene complex **XII** was obtained instead (Scheme 68)[264,266] This reaction suggested that the ruthenium allenylidene was first generated, followed by intramolecular rearrangement by electrophilic substitution of the aryl group as observed for higher cumulenylidene ruthenium complexes.[267] Fürstner and co-workers showed that the related indenylidene ruthenium complexes containing PCy_3 (**XIII**) or NHC as ligands were actually very efficient catalysts for the ring-closing metathesis of a variety of functionalized dienes to

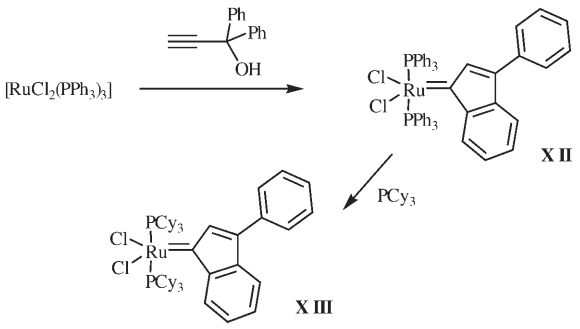

Scheme 68. Formation of ruthenium indenylidene complexes.

produce small rings and macrocycles.[264,266,268–277] Precursor **XIII** presumably affords the same catalytic species as the Grubbs catalyst after the first reaction step with an alkene.

In contrast, Werner and co-workers produced an 18-electron allenylidene ruthenium complex **XIV** containing a hemilabile phosphine; however, the O–Ru bond was probably too stable to be readily displaced by an alkene in olefin metathesis[278] (Scheme 69). Moise and Le Gendre introduced a titanium(IV)-containing phosphine and produced complex **XV**, which is analogous to precursor **IX b** and exhibits similar activity[279] (Scheme 69).

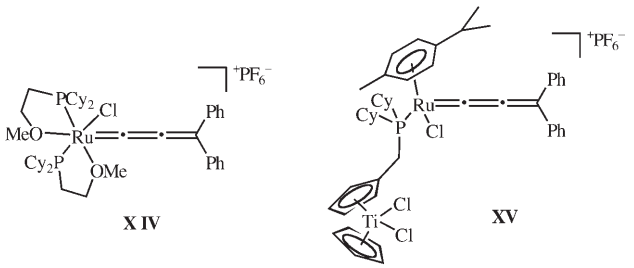

Scheme 69. Examples of ruthenium allenylidenes, potential metathesis catalysts.

Our group undertook the preparation of arene ruthenium allenylidene complexes with a chelating arene NHC ligand (Scheme 70).[205] The neutral precursors **XVI** lead to unstable

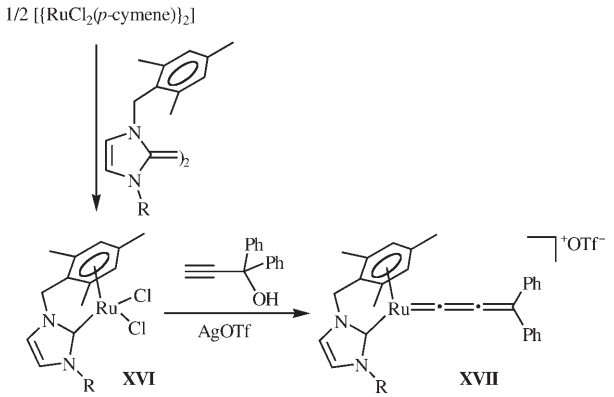

Scheme 70. Ruthenium allenylidene complexes with chelating NHC ligands.

ruthenium allenylidenes **XVII.** However, the resulting catalysts transform dienes either through alkene metathesis or cycloisomerization. The nature of the substrate and the solvent influence both activity and selectivity, but the activity is always lower than that with nonchelating arene complexes.

However, the allenylidene complexes generated in situ from benzimidazole–ruthenium(II) precursors and propargylic alcohol in the presence of AgOTf selectively lead to cycloisomerization of 1,6-dienes (Scheme 71);[280] formation of the α-methylene pyrrolidine or the pyrroline derivative is very strongly dependent on the nature of the benzimidazole ligand. Thus, complexes **XVIII a,b** selectively afford the

 © 2006 Wiley-VCH Verlag GmbH & Co. KGaA, Weinheim

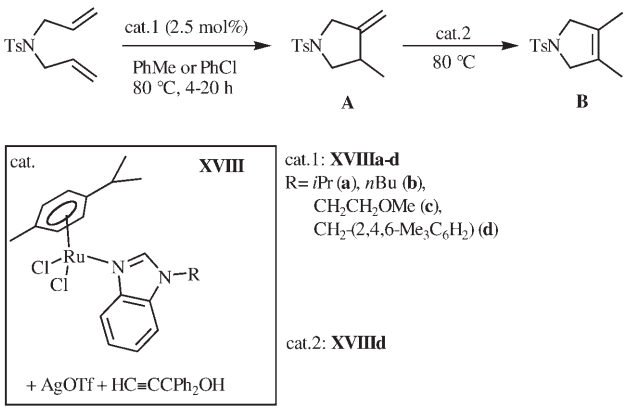

Scheme 71. Ruthenium benzimidazole precursors for diene cycloisomerization.

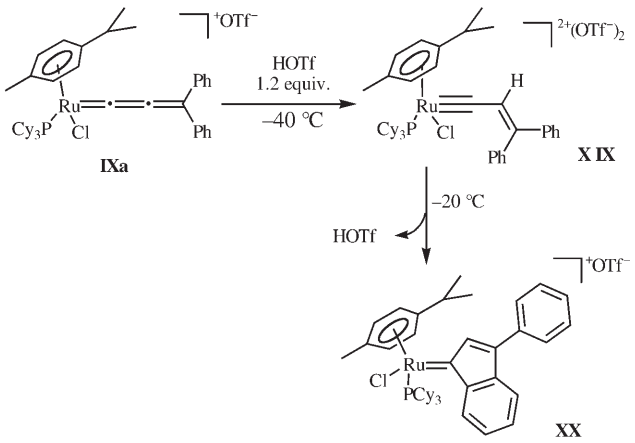

Scheme 72. Formation of an indenylidene ruthenium complex from ruthenium allenylidene.

classic isomerization product **A**, whereas **XVIIId** more readily leads further to the tetrasubstituted cyclic olefin **B** (Table 4). However, no proof can be given that the allenylidene or rearranged indenylidene product is the catalyst for such a reaction.

Table 4: Cycloisomerization of diallyl tosylamide at 80 °C with ruthenium precursors **XVIII a–d**.

Catalyst	Solvent	*t* [h]	Conversion [%]	**A** [%]	**B** [%]
XVIIIa	PhCl	18	100	100	
XVIIIb	PhCl	10	100	100	
XVIIId	PhMe	4	100	100	
XVIIId	PhMe	10	100		100
XVIIId	PhCl	6	98	60	38
XVIIId	PhCl	10	100		100

7.4. Alkene-Metathesis Catalysts from Ruthenium Allenylidenes

Kinetic studies of the ring-closing metathesis of diallyl tosylamide in the presence of **IXa,b** by NMR and UV/Vis spectroscopy revealed that they actually generate a new cationic species.[281] The nature of this catalytic species was established in another observation. It was noticed that protonation of **IXa** with HBF_4 led to a significant increase in the catalyst activity in the RCM of diallyl tosylamide.[216,256] The addition of trifluoromethanesulfonic acid (TfOH) to **IXa** in the polymerization of cyclooctene was even more dramatic: for a cyclooctene/**IXa** ratio of 1000:1, the TOF for ROMP at room temperature was 63 h^{-1} and when TfOH (5 equiv relative to **IXa**) was added, the TOF reached 57200 h^{-1}. ^1H, ^{13}C NMR spectroscopy showed that the addition of 1.2 equivalents of TfOH (relative to **IXa**) at −40 °C first transforms the allenylidene complex into an unstable dicationic alkenylcarbyne complex **XIX.** At −20 °C, this intermediate **XIX** quantitatively rearranges into the new indenylidene complex **XX** with release of TfOH (Scheme 72).[228] This was the first directly observed rearrangement of an allenylidene complex into an indenylidene complex. This observation confirmed the very reasonable hypothesis that indenylidene is formed from an allenylidene metal complex (Scheme 68). Thus, this rearrangement is favored by weakly electron releasing ligands (PPh_3) or by protonation when an electron-rich ligand such as PCy_3 is present. The addition of acid to generate a dicationic species actually favors electrophilic substitution. In thermally initiated catalytic reactions, allenylidene complexes **IXa,b** are progressively transformed into the indenylidene active species, whereas the addition of acid quantitatively generates species **XX**.

This catalyst **XX** proved to be very active in alkene metathesis when the reaction takes place at 0 °C or at room temperature. Thus, the catalyst **XX** generated in situ catalyzes the RCM of dienes at 0 °C in high yield and short reaction time (Scheme 73).[228] Very high turnover numbers, up to 10^6 h^{-1}, have also been attained in the ROMP of cyclooctene (Table 5).

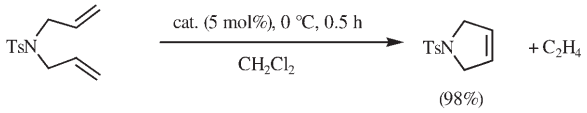

Scheme 73. RCM of dienes promoted by catalyst **XX**.

Table 5: Cyclooctene polymerization with catalysts **XX** at room temperature.[a]

Cyclooctene/Ru	TfOH[b]	*t*	Yield	TOF[c]
1000:1	–	15 h	95	63
1000:1	5	1 min	95	57200
10000:1	5	5 min	97	116400
100000:1	100	5 min	88	1096000

[a] Cyclooctene: 4.5×10^{-3} mol. [b] TfOH (equiv relative to Ru (**IXa**)). [c] Turnover frequency [h^{-1}].

Cyclopentene is a cyclic olefin that is difficult to polymerize. Polymerization occurs under [W(=CH*t*Bu)(O*t*Bu)$_2$(NAr)] catalysis at −40 °C (monomer/W = 200:1).[282,283] Cyclopentene was polymerized with **XX** (generated in situ from **IXa**) and TfOH (5 equiv) at −40 °C to give the polymer in 91 % yield (cyclooctene/Ru = 1000:1; TOF = 44000 h^{-1}).[228] The ADMET polymerization of decadiene

 © 2006 Wiley-VCH Verlag GmbH & Co. KGaA, Weinheim

was also performed with **IXa** and TfOH (5 equiv) at 0 °C in 12 h to give the polymer in 94% yield (Scheme 74).[228]

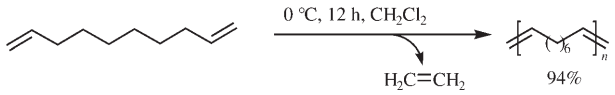

Scheme 74. ADMET polymerization of 1,9-decadiene in the presence of **IXa** and TfOH (5 equiv).

For practical aspects, the active ionic (arene)ruthenium indenylidene catalyst precursors are readily prepared from [{$RuCl_2$(*p*-cymene)}$_2$]. The complex **IXa** is first obtained in a three-step one-pot sequence; protonation affords **XX** quantitatively which can be isolated or used as is. It can be expected that the arene interacts more strongly with the indenylidene ligand in **XX** than with the allenylidene in **IXa**; arene release is thus favored and the active species **XXI** is generated faster (Scheme 75).

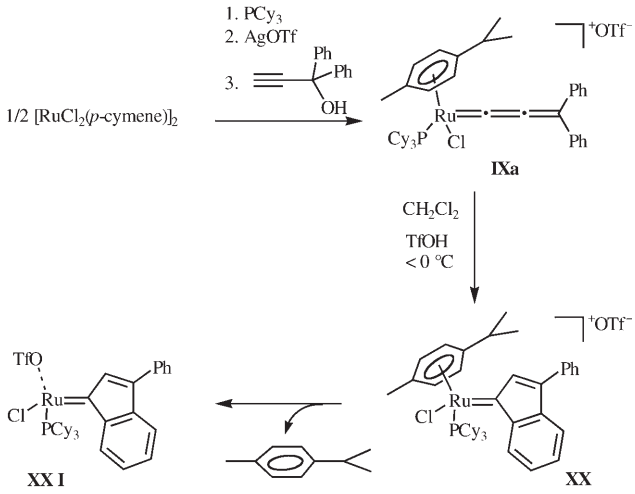

Scheme 75. Generation of active catalytic species **XXI**.

The generation of catalyst **XX** in the presence of acid might explain the results obtained by Picquet et al. in the alkene metathesis with **IXa** in a protonated ionic liquid (imidazole). The ionic liquid protonated **IXa** and accelerated the formation of the active species **XX** and **XXI** in situ.[284]

7.5. Recyclable Ruthenium Allenylidenes

The weakness of any type of ruthenium alkene-metathesis catalyst is connected to its low stability, which requires high activity or high loading for compensation. There have, however, been attempts to recover catalysts generated from ruthenium allenylidene complexes. Peruzzini et al. prepared a water-soluble ionic allenylidene complex [{RuCl(μ-Cl)(=C=C=CPh_2)($Ph_2PC_6H_4SO_3^-$)$_2$}$_2$]Na_4 that allows the ring opening/cross-coupling of cyclopentene with methyl acrylate in water (Scheme 76).[285] Despite the moderate yields, it was shown that allenylidene ruthenium catalysts can tolerate water.

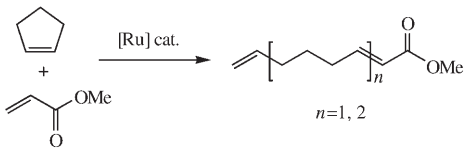

Scheme 76. Ring opening and cross-metathesis catalyzed by a water-soluble ruthenium allenylidene complex.

Akiyama and Kobayashi immobilized [$RuCl_2(PR_3)$] moieties by coordination to arene rings of polystyrene; the coordination polymer obtained was further transformed into polystyrene–[{RuCl(=C=C=CR_2)(PR_3)}$_x$] complexes. Good activity in alkene metathesis was still observed after the third recycling step. However, the conditions for catalyst regeneration are rather drastic (20 mol% catalyst, 12 h, *i*PrOH/hexane, reflux) and the allenylidene or indenylidene moieties are probably not retained.[286]

Ionic liquids constitute an elegant solution for the recycling of catalysts as they are nonvolatile, reusable, and insoluble in many organic solvents, thus offering biphasic catalytic systems.[287–289] The ionic nature of the well-defined allenylidene ruthenium complexes makes them very soluble in imidazolium salts. They promote RCM of dienes in imidazolium salts containing triflate TfO^- or PF_6^- anions at 80 °C.[290] However, the activity in this medium is lower than in a homogeneous phase (toluene), but the catalyst can be recycled twice owing to its moderate stability. A ROMP was carried out in an ionic liquid for the first time with allenylidene ruthenium complex **IXa** in C1-methylated methylbutylimidazolium salts. The catalyst can be recycled four times without loss of activity.[291]

8. Conclusions and Outlook

The formation of vinylidene and allenylidene metal complexes through activation of terminal alkynes and propargylic alcohols, respectively, has led to a variety of novel catalytic organic transformations. This type of addition is now possible for the formation of a large variety of carbon–heteroatom bonds. Carbon–carbon bond-forming reactions have been made possible by nucleophilic addition but also through the involvement of the carbene M=C bond and the Cβ=Cγ double bond, which have led to cycloaromatization, cycloisomerization, and unusual [2+2] addition reactions.

The facile formation of allenylidene metal intermediates provides an efficient route for the direct propargylation of a variety of O-, N-, P-, S-, and C-nucleophiles by substitution at Cγ of propargylic alcohols. Addition at Cα is mainly observed in the case of small nucleophiles such as water.

Vinylidene and allenylidene ruthenium complexes as well as intermediates generated in situ have revealed efficient catalytic activities in alkene and enyne metathesis. Studies of these catalytic reactions at the metal center revealed subtle transformations of these catalyst precursors, which allowed new catalytic species such as metal carbenes and alkenyl carbenes.

 © 2006 Wiley-VCH Verlag GmbH & Co. KGaA, Weinheim

Further developments in the field of metal vinylidenes and allenylidenes in catalysis can be foreseen, such as cascade sequences involving several types of the elementary reactions described herein.

Received: April 22, 2005
Published online: March 7, 2006

[1] M. I. Bruce, A. G. Swincer, *Adv. Organomet. Chem.* **1983**, *22*, 59.
[2] A. B. Antonova, A. A. Ioganson, *Russ. Chem. Rev.* **1989**, *58*, 1197.
[3] M. I. Bruce, *Chem. Rev.* **1991**, *91*, 197.
[4] H. Werner, *J. Organomet. Chem.* **1994**, *475*, 45.
[5] H. Werner, *Chem. Commun.* **1997**, 903.
[6] M. I. Bruce, *Chem. Rev.* **1998**, *98*, 2797.
[7] M. C. Puerta, P. Valerga, *Coord. Chem. Rev.* **1999**, *193–195*, 977.
[8] S. Rigaut, D. Touchard, P. H. Dixneuf, *Coord. Chem. Rev.* **2004**, *248*, 1585.
[9] V. Cadierno, M. P. Gamasa, J. Gimeno, *Coord. Chem. Rev.* **2004**, *248*, 1627.
[10] H. Werner, *Coord. Chem. Rev.* **2004**, *248*, 1693.
[11] D. A. Valyaev, O. V. Semeikin, N. A. Ustynyuk, *Coord. Chem. Rev.* **2004**, *248*, 1679.
[12] J. P. Selegue, *Coord. Chem. Rev.* **2004**, *248*, 1543.
[13] M. I. Bruce, *Coord. Chem. Rev.* **2004**, *248*, 1603.
[14] J. W. Herndon, *Coord. Chem. Rev.* **2004**, *248*, 3.
[15] R. B. King, M. S. Saran, *J. Chem. Soc. Chem. Commun.* **1972**, 1053.
[16] J. Silvestre, R. Hoffmann, *Helv. Chim. Acta* **1985**, *68*, 1461.
[17] Y. Wakatsuki, N. Koga, H. Yamazaki, K. Morokuma, *J. Am. Chem. Soc.* **1994**, *116*, 8105.
[18] M. A. Jimenez Tenorio, M. Jimenez Tenorio, M. C. Puerta, P. Valerga, *Organometallics* **1997**, *16*, 5528.
[19] D. Touchard, P. Haquette, N. Pirio, L. Toupet, P. H. Dixneuf, *Organometallics* **1993**, *12*, 3132.
[20] I. de los Rios, M. Jimenez Tenorio, M. C. Puerta, P. Valerga, *J. Am. Chem. Soc.* **1997**, *119*, 6529.
[21] Y. Wakatsuki, *J. Organomet. Chem.* **2004**, *689*, 4092.
[22] E. Bustelo, J. J. Carbo, A. Lledos, K. Mereiter, M. C. Puerta, P. Valerga, *J. Am. Chem. Soc.* **2003**, *125*, 3311.
[23] J. Ipaktschi, J. Mohseni-Ala, S. Uhlig, *Eur. J. Inorg. Chem.* **2003**, 4313.
[24] R. Stegmann, G. Frenking, *Organometallics* **1998**, *17*, 2089.
[25] A. Marrone, C. Coletti, N. Re, *Organometallics* **2004**, *23*, 4952.
[26] F. De Angelis, A. Sgamellotti, N. Re, *Organometallics* **2002**, *21*, 5944.
[27] E. Bustelo, M. Jimenez-Tenorio, M. C. Puerta, P. Valerga, *Eur. J. Inorg. Chem.* **2001**, 2391.
[28] M. Baya, P. Crochet, M. A. Esteruelas, A. M. Lopez, J. Modrego, E. Onate, *Organometallics* **2001**, *20*, 4291.
[29] M. Olivan, O. Eisenstein, K. G. Caulton, *Organometallics* **1997**, *16*, 2227.
[30] M. Olivan, E. Clot, O. Eisenstein, K. G. Caulton, *Organometallics* **1998**, *17*, 3091.
[31] H. Sakurai, T. Fujii, K. Sakamoto, *Chem. Lett.* **1992**, 339.
[32] N. G. Connelly, A. G. Orpen, A. L. Rieger, P. H. Rieger, *J. Chem. Soc. Chem. Commun.* **1992**, 1293.
[33] H. Werner, M. Baum, D. Schneider, B. Windmüller, *Organometallics* **1994**, *13*, 1089.
[34] D. Peron, A. Romero, P. H. Dixneuf, *Gazz. Chim. Ital.* **1994**, *124*, 497.
[35] D. Schneider, H. Werner, *Angew. Chem.* **1991**, *103*, 710; *Angew. Chem. Int. Ed. Engl.* **1991**, *30*, 700.
[36] J. Foerstner, A. Kakoschke, R. Goddard, J. Rust, R. Wartchow, H. Butenschön, *J. Organomet. Chem.* **2001**, *617–618*, 412.
[37] H. Katayama, K. Onitsuka, F. Ozawa, *Organometallics* **1996**, *15*, 4642.
[38] D. C. Miller, R. J. Angelici, *Organometallics* **1991**, *10*, 79.
[39] M. Baum, N. Mahr, H. Werner, *Chem. Ber.* **1994**, *127*, 1877.
[40] C. Löwe, H.-U. Hund, H. Berke, *J. Organomet. Chem.* **1989**, *371*, 311.
[41] T. Miura, H. Murata, K. Kiyota, H. Kusama, N. Iwasawa, *J. Mol. Catal. A* **2004**, *213*, 59.
[42] F. Alonso, I. P. Beletskaya, M. Yus, *Chem. Rev.* **2004**, *104*, 3079.
[43] C. Bruneau, *Top. Organomet. Chem.* **2004**, *11*, 125.
[44] C. Bruneau, P. H. Dixneuf, *Acc. Chem. Res.* **1999**, *32*, 311.
[45] Y. Sasaki, P. H. Dixneuf, *J. Chem. Soc. Chem. Commun.* **1986**, 790.
[46] R. Mahé, P. H. Dixneuf, S. Lécolier, *Tetrahedron Lett.* **1986**, *27*, 6333.
[47] S. J. Landon, P. M. Shulman, G. L. Geoffroy, *J. Am. Chem. Soc.* **1985**, *107*, 6739.
[48] K. Ouzzine, H. Le Bozec, P. H. Dixneuf, *J. Organomet. Chem.* **1986**, *317*, C25.
[49] H. Le Bozec, K. Ouzzine, P. H. Dixneuf, *Organometallics* **1991**, *10*, 2768.
[50] R. Castarlenas, M. Eckert, P. H. Dixneuf, *Angew. Chem.* **2005**, *117*, 2632; *Angew. Chem. Int. Ed.* **2005**, *44*, 2576.
[51] R. Mahé, Y. Sasaki, C. Bruneau, P. H. Dixneuf, *J. Org. Chem.* **1989**, *54*, 1518.
[52] Y. Sasaki, P. H. Dixneuf, *J. Org. Chem.* **1987**, *52*, 314.
[53] C. Bruneau, P. H. Dixneuf, S. Lécolier, *J. Mol. Catal.* **1988**, *44*, 175.
[54] J. Höfer, H. Doucet, C. Bruneau, P. H. Dixneuf, *Tetrahedron Lett.* **1991**, *32*, 7409.
[55] J. Fournier, C. Bruneau, P. H. Dixneuf, S. Lécolier, *J. Org. Chem.* **1991**, *56*, 4456.
[56] C. Bruneau, P. H. Dixneuf, *J. Mol. Catal.* **1992**, *74*, 97.
[57] C. Fischmeister, C. Bruneau, P. H. Dixneuf, *Ruthenium in Organic Synthesis* (Ed.: S.-I. Murahashi), Wiley-VCH, Weinheim, **2004**, p. 189.
[58] C. Bruneau, M. Neveux, Z. Kabouche, C. Ruppin, P. H. Dixneuf, *Synlett* **1991**, 755.
[59] C. Bruneau, P. H. Dixneuf, *Chem. Commun.* **1997**, 507.
[60] P. H. Dixneuf, C. Bruneau, *Transition Metal Catalysed Reactions* (Eds.: S.-I. Murahashi, S. G. Davis), Blackwell, Oxford, **1991**, p. 391.
[61] M. Rotem, Y. Shvo, *Organometallics* **1983**, *2*, 1689.
[62] T. Mitsudo, Y. Hori, Y. Yamakawa, Y. Watanabe, *J. Org. Chem.* **1987**, *52*, 2230.
[63] C. Ruppin, P. H. Dixneuf, *Tetrahedron Lett.* **1986**, *27*, 6323.
[64] C. Ruppin, P. H. Dixneuf, S. Lécolier, *Tetrahedron Lett.* **1988**, *29*, 5365.
[65] K. Philippot, D. Devanne, P. H. Dixneuf, *J. Chem. Soc. Chem. Commun.* **1990**, 1199.
[66] M. Neveux, B. Seiller, F. Hagedorn, C. Bruneau, P. H. Dixneuf, *J. Organomet. Chem.* **1993**, *451*, 133.
[67] D. Devanne, C. Ruppin, P. H. Dixneuf, *J. Org. Chem.* **1988**, *53*, 925.
[68] C. Bruneau, Z. Kabouche, M. Neveux, B. Seiller, P. H. Dixneuf, *Inorg. Chim. Acta* **1994**, *222*, 154.
[69] L. J. Goossen, J. Paetzold, D. Koley, *Chem. Commun.* **2003**, 706.
[70] T. Opstal, F. Verpoort, *Tetrahedron Lett.* **2002**, *43*, 9259.
[71] T. Opstal, F. Verpoort, *Synlett* **2002**, 935.
[72] B. De Clercq, F. Verpoort, *J. Organomet. Chem.* **2003**, *672*, 11.
[73] K. Melis, D. De Vos, P. Jacobs, F. Verpoort, *J. Organomet. Chem.* **2003**, *671*, 131.
[74] H. Doucet, J. Höfer, C. Bruneau, P. H. Dixneuf, *J. Chem. Soc. Chem. Commun.* **1993**, 850.

 © 2006 Wiley-VCH Verlag GmbH & Co. KGaA, Weinheim

[75] M. Tokunaga, T. Suzuki, N. Koga, T. Fukushima, A. Horiuchi, Y. Wakatsuki, *J. Am. Chem. Soc.* **2001**, *123*, 11917.
[76] H. Doucet, B. Martin-Vaca, C. Bruneau, P. H. Dixneuf, *J. Org. Chem.* **1995**, *60*, 7247.
[77] A. Kabouche, Z. Kabouche, C. Bruneau, P. H. Dixneuf, *J. Chem. Res. Miniprint* **1999**, 1247.
[78] H. Doucet, J. Höfer, N. Derrien, C. Bruneau, P. H. Dixneuf, *Bull. Soc. Chim. Fr.* **1996**, *133*, 939.
[79] H. Doucet, N. Derrien, Z. Kabouche, C. Bruneau, P. H. Dixneuf, *J. Organomet. Chem.* **1997**, *551*, 151.
[80] C. Gemel, G. Trimmel, C. Slugovc, S. Kremel, K. Mereiter, R. Schmid, K. Kirchner, *Organometallics* **1996**, *15*, 3998.
[81] M. Jimenez Tenorio, M. C. Puerta, P. Valerga, F. J. Moreno-Dorado, F. M. Guerra, G. M. Massanet, *Chem. Commun.* **2001**, 2324.
[82] K. Melis, P. Samulkiewiecz, J. Rynkowski, F. Verpoort, *Tetrahedron Lett.* **2002**, *43*, 2713.
[83] M. Picquet, C. Bruneau, P. H. Dixneuf, *Chem. Commun.* **1997**, 1201.
[84] M. Picquet, A. Fernandez, C. Bruneau, P. H. Dixneuf, *Eur. J. Org. Chem.* **2000**, 2361.
[85] S. Dérien, P. H. Dixneuf, *J. Chem. Soc. Chem. Commun.* **1994**, 2551.
[86] S. Dérien, D. Jan, P. H. Dixneuf, *Tetrahedron* **1996**, *52*, 5511.
[87] S. Dérien, B. Gomez Vicente, P. H. Dixneuf, *Chem. Commun.* **1997**, 1405.
[88] S. Dérien, P. H. Dixneuf, *J. Organomet. Chem.* **2004**, *689*, 1382.
[89] B. M. Trost, G. Dyker, R. J. Kulawiec, *J. Am. Chem. Soc.* **1990**, *112*, 7809.
[90] B. M. Trost, R. J. Kulawiec, A. Hammes, *Tetrahedron Lett.* **1993**, *34*, 587.
[91] B. M. Trost, J. A. Flygare, *J. Org. Chem.* **1994**, *59*, 1078.
[92] B. M. Trost, R. J. Kulawiec, *J. Am. Chem. Soc.* **1992**, *114*, 5579.
[93] B. Weyershausen, K. H. Dötz, *Eur. J. Inorg. Chem.* **1999**, 1057.
[94] F. E. McDonald, C. B. Connolly, M. M. Gleason, T. B. Towne, K. D. Treiber, *J. Org. Chem.* **1993**, *58*, 6952.
[95] F. E. McDonald, K. S. Reddy, Y. Diaz, *J. Am. Chem. Soc.* **2000**, *122*, 4304.
[96] Y. Sheng, D. Musaev, K. S. Reddy, F. E. McDonald, K. Morokuma, *J. Am. Chem. Soc.* **2002**, *124*, 4149.
[97] F. E. McDonald, *Chem. Eur. J.* **1999**, *5*, 3103.
[98] T. Nowroozi-Isfahani, D. G. Musaev, F. E. McDonald, K. Morokuma, *Organometallics* **2005**, *24*, 2921.
[99] F. E. McDonald, M. M. Gleason, *Angew. Chem.* **1995**, *107*, 356; *Angew. Chem. Int. Ed. Engl.* **1995**, *34*, 350.
[100] F. E. McDonald, M. M. Gleason, *J. Am. Chem. Soc.* **1996**, *118*, 6648.
[101] P. Wipf, T. H. Graham, *J. Org. Chem.* **2003**, *68*, 8798.
[102] W. W. Cutchins, F. E. McDonald, *Org. Lett.* **2002**, *4*, 749.
[103] M. H. Davidson, F. E. McDonald, *Org. Lett.* **2004**, *6*, 1601.
[104] F. E. McDonald, A. K. Chatterjee, *Tetrahedron Lett.* **1997**, *38*, 7687.
[105] B. M. Trost, Y. H. Rhee, *J. Am. Chem. Soc.* **2003**, *125*, 7482.
[106] B. M. Trost, Y. H. Rhee, *J. Am. Chem. Soc.* **2002**, *124*, 2528.
[107] B. M. Trost, Y. H. Rhee, *J. Am. Chem. Soc.* **1999**, *121*, 11680.
[108] F. E. McDonald, C. C. Schultz, *J. Am. Chem. Soc.* **1994**, *116*, 9363.
[109] C.-Y. Lo, H. Guo, J.-J. Lian, F.-M. Shen, R.-S. Liu, *J. Org. Chem.* **2002**, *67*, 3930.
[110] R. J. Madhushaw, M.-Y. Lin, S. M. Abu Sohel, R.-S. Liu, *J. Am. Chem. Soc.* **2004**, *126*, 6895.
[111] M.-Y. Lin, S. J. Maddirala, R.-S. Liu, *Org. Lett.* **2005**, *7*, 1745.
[112] K. Ohe, T. Yokoi, F. Nishino, S. Uemura, *J. Am. Chem. Soc.* **2002**, *124*, 526.
[113] K. Miki, S. Uemura, K. Ohe, *Chem. Lett.* **2005**, *34*, 1068.
[114] M. Tokunaga, Y. Wakatsuki, *Angew. Chem.* **1998**, *110*, 3024; *Angew. Chem. Int. Ed.* **1998**, *37*, 2867.
[115] T. Suzuki, M. Tokunaga, Y. Wakatsuki, *Org. Lett.* **2001**, *3*, 735.
[116] D. B. Grotjahn, C. D. Incarvito, A. L. Rheingold, *Angew. Chem.* **2001**, *113*, 4002; *Angew. Chem. Int. Ed.* **2001**, *40*, 3884.
[117] D. B. Grotjahn, D. A. Lev, *J. Am. Chem. Soc.* **2004**, *126*, 12232.
[118] P. Alvarez, M. Bassetti, J. Gimeno, G. Mancini, *Tetrahedron Lett.* **2001**, *42*, 8467.
[119] T. Suzuki, M. Tokunaga, Y. Wakatsuki, *Tetrahedron Lett.* **2002**, *43*, 7531.
[120] Y. Chen, D. M. Ho, C. Lee, *J. Am. Chem. Soc.* **2005**, *127*, 12184.
[121] F. Jérôme, F. Monnier, H. Lawicka, S. Dérien, P. H. Dixneuf, *Chem. Commun.* **2003**, 696.
[122] R. Le Lagadec, E. Roman, L. Toupet, U. Müller, P. H. Dixneuf, *Organometallics* **1994**, *13*, 5030.
[123] Y. Fukumoto, T. Dohi, H. Masaoka, N. Chatani, S. Murai, *Organometallics* **2002**, *21*, 3845.
[124] T. Kondo, A. Tanaka, S. Kotachi, Y. Watanabe, *J. Chem. Soc. Chem. Commun.* **1995**, 413.
[125] L. J. Goossen, J. E. Rauhaus, G. Deng, *Angew. Chem.* **2005**, *117*, 4110; *Angew. Chem. Int. Ed.* **2005**, *44*, 4042.
[126] C. Bianchini, M. Peruzzini, F. Zanobini, P. Frediani, A. Albinati, *J. Am. Chem. Soc.* **1991**, *113*, 5453.
[127] C. Bianchini, P. Frediani, D. Masi, M. Peruzzini, F. Zanobini, *Organometallics* **1994**, *13*, 4616.
[128] H. Yamazaki, *J. Chem. Soc. Chem. Commun.* **1976**, 841.
[129] Y. Wakatsuki, H. Yamazaki, N. Kumegawa, T. Satoh, J. Y. Satoh, *J. Am. Chem. Soc.* **1991**, *113*, 9604.
[130] Y. Wakatsuki, H. Yamazaki, *J. Organomet. Chem.* **1995**, *500*, 349.
[131] C. Slugovc, K. Mereiter, E. Zobetz, R. Schmid, K. Kirchner, *Organometallics* **1996**, *15*, 5275.
[132] C. Slugovc, D. Doberer, C. Gemel, R. Schmid, K. Kirchner, B. Winkler, F. Stelzer, *Monatsh. Chem.* **1998**, *129*, 221.
[133] S. Pavlik, C. Gemel, C. Slugovc, K. Mereiter, R. Schmid, K. Kirchner, *J. Organomet. Chem.* **2001**, *617–618*, 301.
[134] M. A. Jimenez Tenorio, M. Jimenez Tenorio, M. C. Puerta, P. Valerga, *Organometallics* **2000**, *19*, 1333.
[135] X. Chen, P. Xue, H. H. Y. Sung, I. D. Williams, M. Peruzzini, C. Bianchini, G. Jia, *Organometallics* **2005**, *24*, 4330.
[136] C. S. Yi, N. Liu, *Organometallics* **1996**, *15*, 3968.
[137] M. Bassetti, S. Marini, F. Tortorella, V. Cadierno, J. Diez, M. Pilar Gamasa, J. Gimeno, *J. Organomet. Chem.* **2000**, *593–594*, 292.
[138] M. Bassetti, S. Marini, J. Diaz, M. P. Gamasa, J. Gimeno, Y. Rodriguez-Alvarez, S. Garcia-Grande, *Organometallics* **2002**, *21*, 4815.
[139] M. D. Fryzuk, M. J. Jonker, S. J. Rettig, *Chem. Commun.* **1997**, 377.
[140] K. Melis, D. De Vos, P. Jacobs, F. Verpoort, *J. Organomet. Chem.* **2002**, *659*, 159.
[141] H. Katayama, M. Nakayama, T. Nakano, C. Wada, K. Akamatsu, F. Ozawa, *Macromolecules* **2004**, *37*, 13.
[142] H. Katayama, H. Yari, M. Tanaka, F. Ozawa, *Chem. Commun.* **2005**, 4336.
[143] H. Matsuzaka, Y. Takagi, Y. Ishii, M. Nishio, M. Hidai, *Organometallics* **1995**, *14*, 2153.
[144] C. S. Yi, N. Liu, *Synlett* **1999**, 281.
[145] Y. J. Park, B.-I. Kwon, J.-A. Ahn, H. Lee, C.-H. Jun, *J. Am. Chem. Soc.* **2004**, *126*, 13892.
[146] E. Elakkari, B. Floris, P. Galloni, P. Tagliatesta, *Eur. J. Org. Chem.* **2005**, 889.
[147] C. Nevado, A. M. Echavarren, *Synthesis* **2005**, 167.
[148] P. M. Donovan, L. T. Scott, *J. Am. Chem. Soc.* **2004**, *126*, 3108.
[149] C. A. Merlic, M. E. Pauly, *J. Am. Chem. Soc.* **1996**, *118*, 11319.
[150] H.-C. Shen, S. Pal, J.-J. Lian, R.-S. Liu, *J. Am. Chem. Soc.* **2003**, *125*, 15762.

 © 2006 Wiley-VCH Verlag GmbH & Co. KGaA, Weinheim

[151] R. J. Madhushaw, C.-Y. Lo, C.-W. Hwang, M.-D. Su, H.-C. Shen, S. Pal, I. R. Shaikh, R.-S. Liu, *J. Am. Chem. Soc.* **2004**, *126*, 15560.
[152] J. W. Dankwardt, *Tetrahedron Lett.* **2001**, *42*, 5809.
[153] Y. Wang, M. G. Finn, *J. Am. Chem. Soc.* **1995**, *117*, 8045.
[154] K. Ohe, M. Kojima, K. Yonehara, S. Uemura, *Angew. Chem.* **1996**, *108*, 1823; *Angew. Chem. Int. Ed. Engl.* **1996**, *35*, 1823.
[155] T. Manabe, S. Yanagi, K. Ohe, S. Uemura, *Organometallics* **1998**, *17*, 2942.
[156] K. Maeyama, N. Iwasawa, *J. Org. Chem.* **1999**, *64*, 1344.
[157] K. Ohe, K. Miki, T. Yokoi, F. Nishino, S. Uemura, *Organometallics* **2000**, *19*, 5525.
[158] K. Sangu, K. Fuchibe, T. Akiyama, *Org. Lett.* **2004**, *6*, 353.
[159] K. Maeyama, N. Iwasawa, *J. Am. Chem. Soc.* **1998**, *120*, 1928.
[160] N. Iwasawa, T. Miura, K. Kiyota, H. Kusama, K. Lee, P. H. Lee, *Org. Lett.* **2002**, *4*, 4463.
[161] H. Kusama, H. Yamabe, N. Iwasawa, *Org. Lett.* **2002**, *4*, 2569.
[162] T. Miura, N. Iwasawa, *J. Am. Chem. Soc.* **2002**, *124*, 518.
[163] V. Mamane, P. Hannen, A. Fürstner, *Chem. Eur. J.* **2004**, *10*, 4556.
[164] C. Slugovc, K. Mereiter, R. Schmid, K. Kirchner, *J. Am. Chem. Soc.* **1998**, *120*, 6175.
[165] C. Slugovc, K. Mereiter, R. Schmid, K. Kirchner, *Organometallics* **1999**, *18*, 1011.
[166] P. Alvarez, E. Lastra, J. Gimeno, M. Bassetti, L. R. Falvello, *J. Am. Chem. Soc.* **2003**, *125*, 2386.
[167] M. Bassetti, P. Alvarez, J. Gimeno, E. Lastra, *Organometallics* **2004**, *23*, 5127.
[168] M. Murakami, M. Ubukata, Y. Ito, *Tetrahedron Lett.* **1998**, *39*, 7361.
[169] M. Murakami, M. Ubukara, Y. Ito, *Chem. Lett.* **2002**, 294.
[170] J. Bigeault, L. Giordano, G. Buono, *Angew. Chem.* **2005**, *117*, 4831; *Angew. Chem. Int. Ed.* **2005**, *44*, 4753.
[171] M. Murakami, S. Hori, *J. Am. Chem. Soc.* **2003**, *125*, 4720.
[172] S. Datta, A. Odedra, R.-S. Liu, *J. Am. Chem. Soc.* **2005**, *127*, 11606.
[173] T. A. Vijayaraj, G. Sundararajan, *J. Mol. Catal. A* **1995**, *99*, 47.
[174] T. Szymanska-Buzar, *J. Mol. Catal.* **1994**, *93*, 137.
[175] B. Gita, G. Sundararajan, *Tetrahedron Lett.* **1993**, *34*, 6123.
[176] A. Fürstner, *Top. Organomet. Chem.* **1998**, *1*, 37.
[177] R. H. Grubbs, S. Chang, *Tetrahedron* **1998**, *54*, 4413.
[178] M. Mori, *Top. Organomet. Chem.* **1998**, *1*, 133.
[179] A. Fürstner, *Angew. Chem.* **2000**, *112*, 3140; *Angew. Chem. Int. Ed.* **2000**, *39*, 3012.
[180] T. M. Trnka, R. H. Grubbs, *Acc. Chem. Res.* **2001**, *34*, 18.
[181] R. H. Grubbs, *Handbook of metathesis*, Wiley-VCH, Weinheim, **2003**.
[182] H. Katayama, F. Ozawa, *Coord. Chem. Rev.* **2004**, *248*, 1703.
[183] V. Dragutan, I. Dragutan, *Platinum Met. Rev.* **2004**, *48*, 148.
[184] P. Schwab, R. H. Grubbs, J. W. Ziller, *J. Am. Chem. Soc.* **1996**, *118*, 100.
[185] H. Katayama, F. Ozawa, *Chem. Lett.* **1998**, 67.
[186] H. Katayama, F. Ozawa, *Organometallics* **1998**, *17*, 5190.
[187] H. Katayama, H. Urushima, F. Ozawa, *J. Organomet. Chem.* **2000**, *606*, 16.
[188] A. Pineda Contreras, A. Masiel Cerda, M. A. Tlenkopatchev, *Macromol. Chem. Phys.* **2002**, *203*, 1811.
[189] H. Katayama, F. Yonezawa, M. Nagao, F. Ozawa, *Macromolecules* **2002**, *35*, 1133.
[190] H. Katayama, T. Yoshida, F. Ozawa, *J. Organomet. Chem.* **1998**, *562*, 203.
[191] T. Weskamp, W. C. Schattenmann, M. Spiegler, W. A. Herrmann, *Angew. Chem.* **1998**, *110*, 2631; *Angew. Chem. Int. Ed.* **1998**, *37*, 2490.
[192] L. Ackermann, A. Fürstner, T. Weskamp, F. J. Kohl, W. A. Herrmann, *Tetrahedron Lett.* **1999**, *40*, 4787.
[193] A. K. Chatterjee, R. H. Grubbs, *Org. Lett.* **1999**, *1*, 1751.
[194] L. Jafarpour, J. Huang, E. D. Stevens, S. P. Nolan, *Organometallics* **1999**, *18*, 3760.
[195] M. Scholl, S. Ding, C. W. Lee, R. H. Grubbs, *Org. Lett.* **1999**, *1*, 953.
[196] T. Weskamp, F. J. Kohl, W. Hieringer, D. Gleich, W. A. Herrmann, *Angew. Chem.* **1999**, *111*, 2573; *Angew. Chem. Int. Ed.* **1999**, *38*, 2416.
[197] A. K. Chatterjee, J. P. Morgan, M. Scholl, R. H. Grubbs, *J. Am. Chem. Soc.* **2000**, *122*, 3783.
[198] C. W. Lee, R. H. Grubbs, *Org. Lett.* **2000**, *2*, 2145.
[199] J. P. Morgan, R. H. Grubbs, *Org. Lett.* **2000**, *2*, 3153.
[200] J. A. Smulik, S. T. Diver, *Org. Lett.* **2000**, *2*, 2271.
[201] D. L. Wright, J. P. Schulte II, M. A. Page, *Org. Lett.* **2000**, *2*, 1847.
[202] J. Louie, R. H. Grubbs, *Angew. Chem.* **2001**, *113*, 253; *Angew. Chem. Int. Ed.* **2001**, *40*, 247.
[203] L. Ackermann, C. Bruneau, P. H. Dixneuf, *Synlett* **2001**, 397.
[204] D. Sémeril, M. Cléran, C. Bruneau, P. H. Dixneuf, *Adv. Synth. Catal.* **2001**, *343*, 184.
[205] B. Cetinkaya, S. Demir, I. Özdemir, L. Toupet, D. Sémeril, C. Bruneau, P. H. Dixneuf, *Chem. Eur. J.* **2003**, *9*, 2323.
[206] D. Sémeril, M. Cléran, A. Jimenez Perez, C. Bruneau, P. H. Dixneuf, *J. Mol. Catal. A* **2002**, *190*, 9.
[207] J. Le Nôtre, C. Bruneau, P. H. Dixneuf, *Eur. J. Org. Chem.* **2002**, 3816.
[208] J. Le Nôtre, A. Acosta Martinez, P. H. Dixneuf, C. Bruneau, *Tetrahedron* **2003**, *59*, 9425.
[209] D. Sémeril, C. Bruneau, P. H. Dixneuf, *Helv. Chim. Acta* **2001**, *84*, 3335.
[210] D. Sémeril, C. Bruneau, P. H. Dixneuf, *Adv. Synth. Catal.* **2002**, *344*, 585.
[211] M. Mori, *J. Mol. Catal. A* **2004**, *213*, 73.
[212] S. T. Diver, A. J. Giessert, *Chem. Rev.* **2004**, *104*, 1317.
[213] A. Fürstner, M. Liebl, C. W. Lehmann, M. Picquet, R. Kunz, C. Bruneau, D. Touchard, P. H. Dixneuf, *Chem. Eur. J.* **2000**, *6*, 1847.
[214] A. Fürstner, M. Picquet, C. Bruneau, P. H. Dixneuf, *Chem. Commun.* **1998**, 1315.
[215] M. Picquet, D. Touchard, C. Bruneau, P. H. Dixneuf, *New J. Chem.* **1999**, *23*, 141.
[216] A. Fürstner, M. Liebl, C. W. Lehmann, M. Picquet, R. Kunz, C. Bruneau, D. Touchard, P. H. Dixneuf, *Chem. Eur. J.* **2000**, *6*, 1847.
[217] D. Pilette, K. Ouzzine, H. Le Bozec, P. H. Dixneuf, C. E. F. Rickard, W. R. Roper, *Organometallics* **1992**, *11*, 809.
[218] S. T. Nguyen, L. K. Johnson, R. H. Grubbs, J. W. Ziller, *J. Am. Chem. Soc.* **1992**, *114*, 3974.
[219] T. E. Wilhelm, T. R. Belderrain, S. N. Brown, R. H. Grubbs, *Organometallics* **1997**, *16*, 3867.
[220] P. Schwab, R. H. Grubbs, J. W. Ziller, *J. Am. Chem. Soc.* **1996**, *118*, 100.
[221] M. Murakami, S. Kadowaki, T. Matsuda, *Org. Lett.* **2005**, *7*, 3953.
[222] J. P. Selegue, *Organometallics* **1982**, *1*, 217.
[223] D. Touchard, P. H. Dixneuf, *Coord. Chem. Rev.* **1998**, *178–180*, 409.
[224] V. Cadierno, M. P. Gamasa, J. Gimeno, *Eur. J. Inorg. Chem.* **2001**, 571.
[225] M. A. Esteruelas, A. V. Gomez, A. M. Lopez, J. Modrego, E. Onate, *Organometallics* **1997**, *16*, 5826.
[226] S. Rigault, F. Monnier, F. Mousset, D. Touchard, P. H. Dixneuf, *Organometallics* **2002**, *21*, 2654.
[227] V. Cadierno, S. Conejero, M. P. Gamasa, J. Gimeno, L. R. Falvello, R. M. Llusar, *Organometallics* **2002**, *21*, 3716.
[228] R. Castarlenas, P. H. Dixneuf, *Angew. Chem.* **2003**, *115*, 4662; *Angew. Chem. Int. Ed.* **2003**, *42*, 4524.

 © 2006 Wiley-VCH Verlag GmbH & Co. KGaA, Weinheim

[229] S. Rigault, D. Touchard, P. H. Dixneuf, *Organometallics* **2003**, *22*, 3980.
[230] Y. Nishibayashi, M. D. Milton, Y. Inada, M. Yoshikawa, I. Wakiji, M. Hidai, S. Uemura, *Chem. Eur. J.* **2005**, *11*, 1433.
[231] V. Cadierno, J. Diez, S. E. Garcia-Garrido, J. Gimeno, *Chem. Commun.* **2004**, 2716.
[232] E. Bustelo, P. H. Dixneuf, *Adv. Synth. Catal.* **2005**, *347*, 393.
[233] C. Fischmeister, L. Toupet, P. H. Dixneuf, *New J. Chem.* **2005**, *29*, 765.
[234] R. Castarlenas, C. Fischmeister, C. Bruneau, P. H. Dixneuf, *J. Mol. Catal. A* **2004**, *213*, 31.
[235] B. M. Trost, J. A. Flygare, *J. Am. Chem. Soc.* **1992**, *114*, 5476.
[236] B. Seiller, DEA report, University of Rennes **1992**.
[237] Y. Nishibayashi, I. Wakiji, M. Hidai, *J. Am. Chem. Soc.* **2000**, *122*, 11019.
[238] Y. Nishibayashi, H. Imajima, G. Onodera, M. Hidai, S. Uemura, *Organometallics* **2004**, *23*, 26.
[239] Y. Nishibayashi, Y. Inada, M. Hidai, S. Uemura, *J. Am. Chem. Soc.* **2002**, *124*, 7900.
[240] Y. Inada, Y. Nishibayashi, M. Hidai, S. Uemura, *J. Am. Chem. Soc.* **2002**, *124*, 15172.
[241] Y. Nishibayashi, I. Wakiji, Y. Ishii, S. Uemura, M. Hidai, *J. Am. Chem. Soc.* **2001**, *123*, 3393.
[242] Y. Nishibayashi, G. Onodera, Y. Inada, M. Hidai, S. Uemura, *Organometallics* **2003**, *22*, 873.
[243] Y. Nishibayashi, M. Yoshikawa, Y. Inada, M. D. Milton, M. Hidai, S. Uemura, *Angew. Chem.* **2003**, *115*, 2785; *Angew. Chem. Int. Ed.* **2003**, *42*, 2681.
[244] Y. Nishibayashi, M. Yoshikawa, Y. Inada, M. Hidai, S. Uemura, *J. Org. Chem.* **2004**, *69*, 3408.
[245] Y. Nishibayashi, H. Imajima, G. Onodera, Y. Inada, M. Hidai, S. Uemura, *Organometallics* **2004**, *23*, 5100.
[246] Y. Nishibayashi, M. Yoshikawa, Y. Inada, M. Hidai, S. Uemura, *J. Am. Chem. Soc.* **2002**, *124*, 11846.
[247] Y. Nishibayashi, Y. Inada, M. Hidai, S. Uemura, *J. Am. Chem. Soc.* **2003**, *125*, 6060.
[248] S. Datta, C.-L. Chang, K.-L. Yeh, R.-S. Liu, *J. Am. Chem. Soc.* **2003**, *125*, 9294.
[249] K.-L. Yeh, B. Liu, Y.-T. Lai, C.-W. Li, R.-S. Liu, *J. Org. Chem.* **2004**, *69*, 4692.
[250] K.-L. Yeh, B. Liu, C.-Y. Lo, H.-L. Huang, R.-S. Liu, *J. Am. Chem. Soc.* **2002**, *124*, 6510.
[251] H.-C. Shen, H.-L. Su, Y.-C. Hsueh, R.-S. Liu, *Organometallics* **2004**, *23*, 4332.
[252] S. M. Maddock, M. G. Finn, *Angew. Chem.* **2001**, *113*, 2196; *Angew. Chem. Int. Ed.* **2001**, *40*, 2138.
[253] M. Saoud, A. Romerosa, S. Manas Carpio, L. Gonsalvi, M. Peruzzini, *Eur. J. Inorg. Chem.* **2003**, 1614.
[254] S. T. Nguyen, R. H. Grubbs, *J. Am. Chem. Soc.* **1993**, *115*, 9858.
[255] A. Fürstner, M. Picquet, C. Bruneau, P. H. Dixneuf, *Chem. Commun.* **1998**, 1315.
[256] M. Picquet, D. Touchard, C. Bruneau, P. H. Dixneuf, *New J. Chem.* **1999**, *23*, 141.
[257] S. N. Osipov, O. I. Artyushin, A. F. Kolomiets, C. Bruneau, M. Picquet, P. H. Dixneuf, *Eur. J. Org. Chem.* **2001**, 3891.
[258] M. Picquet, C. Bruneau, P. H. Dixneuf, *Chem. Commun.* **1998**, 2249.
[259] D. Sémeril, J. Le Nôtre, C. Bruneau, P. H. Dixneuf, A. F. Kolomiets, S. N. Osipov, *New J. Chem.* **2001**, *25*, 16.
[260] S. D. Drouin, F. Zamanian, D. E. Fogg, *Organometallics* **2001**, *20*, 5495.
[261] C. W. Bielawski, J. Louie, R. H. Grubbs, *J. Am. Chem. Soc.* **2000**, *122*, 12872.
[262] R. Castarlenas, D. Sémeril, A. F. Noels, A. Demonceau, P. H. Dixneuf, *J. Organomet. Chem.* **2002**, *663*, 235.
[263] I. Alaoui Abdallaoui, D. Sémeril, P. H. Dixneuf, *J. Mol. Catal. A* **2002**, *182–183*, 577.
[264] H.-J. Schanz, L. Jafarpour, E. D. Stevens, S. P. Nolan, *Organometallics* **1999**, *18*, 5187.
[265] L. Jafarpour, J. Huang, E. D. Stevens, S. P. Nolan, *Organometallics* **1999**, *18*, 3760.
[266] A. Fürstner, O. Guth, A. Duffels, G. Seidel, M. Liebl, B. Gabor, R. Mynott, *Chem. Eur. J.* **2001**, *7*, 4811.
[267] D. Touchard, P. Haquette, A. Daridor, L. Toupet, P. H. Dixneuf, *J. Am. Chem. Soc.* **1994**, *116*, 11157.
[268] A. Fürstner, O. R. Thiel, L. Ackermann, H.-J. Schanz, S. P. Nolan, *J. Org. Chem.* **2000**, *65*, 2204.
[269] A. Fürstner, F. Jeanjean, P. Razon, *Angew. Chem.* **2002**, *114*, 2203; *Angew. Chem. Int. Ed.* **2002**, *41*, 2097.
[270] A. Fürstner, W. Leitner, *Angew. Chem.* **2003**, *115*, 320; *Angew. Chem. Int. Ed.* **2003**, *42*, 308.
[271] A. Fürstner, O. R. Thiel, *J. Org. Chem.* **2000**, *65*, 1738.
[272] A. Fürstner, T. Müller, *J. Am. Chem. Soc.* **1999**, *121*, 7814.
[273] A. Fürstner, K. Radkowski, C. Wirtz, R. Goddard, C. W. Lehmann, R. Mynott, *J. Am. Chem. Soc.* **2002**, *124*, 7061.
[274] B. Scheiper, F. Glorius, A. Leitner, A. Fürstner, *Proc. Natl. Acad. Sci. USA* **2004**, *101*, 11960.
[275] P. Davoli, A. Spaggiari, L. Castagnetti, F. Prati, *Org. Biomol. Chem.* **2004**, *2*, 38.
[276] E. Diez, D. J. Dixon, S. V. Ley, A. Polara, F. Rodriguez, *Helv. Chim. Acta* **2003**, *86*, 3717.
[277] E. P. Kündig, A. Bellido, K. P. Kaliappan, A. R. Pape, S. Radix, *Synlett* **2003**, 2407.
[278] S. Jung, C. D. Brandt, H. Werner, *New J. Chem.* **2001**, *25*, 1101.
[279] P. Le Gendre, M. Picquet, P. Richard, C. Moise, *J. Organomet. Chem.* **2002**, *643–644*, 231.
[280] I. Özdemir, E. Cetinkaya, B. Cetinkaya, M. Cicek, D. Sémeril, C. Bruneau, P. H. Dixneuf, *Eur. J. Inorg. Chem.* **2004**, 418.
[281] M. Bassetti, F. Centola, D. Sémeril, C. Bruneau, P. H. Dixneuf, *Organometallics* **2003**, *22*, 4459.
[282] P. Dounis, W. J. Feast, A. M. Kenwright, *Polymer* **1995**, *36*, 2787.
[283] R. R. Schrock, K. B. Yap, D. C. Yang, H. Sitzmann, L. R. Sita, G. C. Bazan, *Macromolecules* **1989**, *22*, 3191.
[284] M. Picquet, I. Tkatchenko, I. Tommasi, P. Wasserscheid, J. Zimmermann, *Adv. Synth. Catal.* **2003**, *345*, 959.
[285] M. Saoud, A. Romerosa, M. Peruzzini, *Organometallics* **2000**, *19*, 4005.
[286] R. Akiyama, S. Kobayashi, *Angew. Chem.* **2002**, *114*, 2714; *Angew. Chem. Int. Ed.* **2002**, *41*, 2602.
[287] P. Wasserscheid, W. Keim, *Angew. Chem.* **2000**, *112*, 3926; *Angew. Chem. Int. Ed.* **2000**, *39*, 3772.
[288] H. Olivier-Bourbigou, L. Magna, *J. Mol. Catal. A* **2002**, *182*/183, 419.
[289] T. Welton, *Coord. Chem. Rev.* **2004**, *248*, 2459.
[290] D. Sémeril, H. Olivier-Bourbigou, C. Bruneau, P. H. Dixneuf, *Chem. Commun.* **2002**, 146.
[291] S. Csihony, C. Fischmeister, C. Bruneau, I. T. Horvath, P. H. Dixneuf, *New J. Chem.* **2002**, *26*, 1667.

 © 2006 Wiley-VCH Verlag GmbH & Co. KGaA, Weinheim

Communications

DOI: 10.1002/anie.200502481

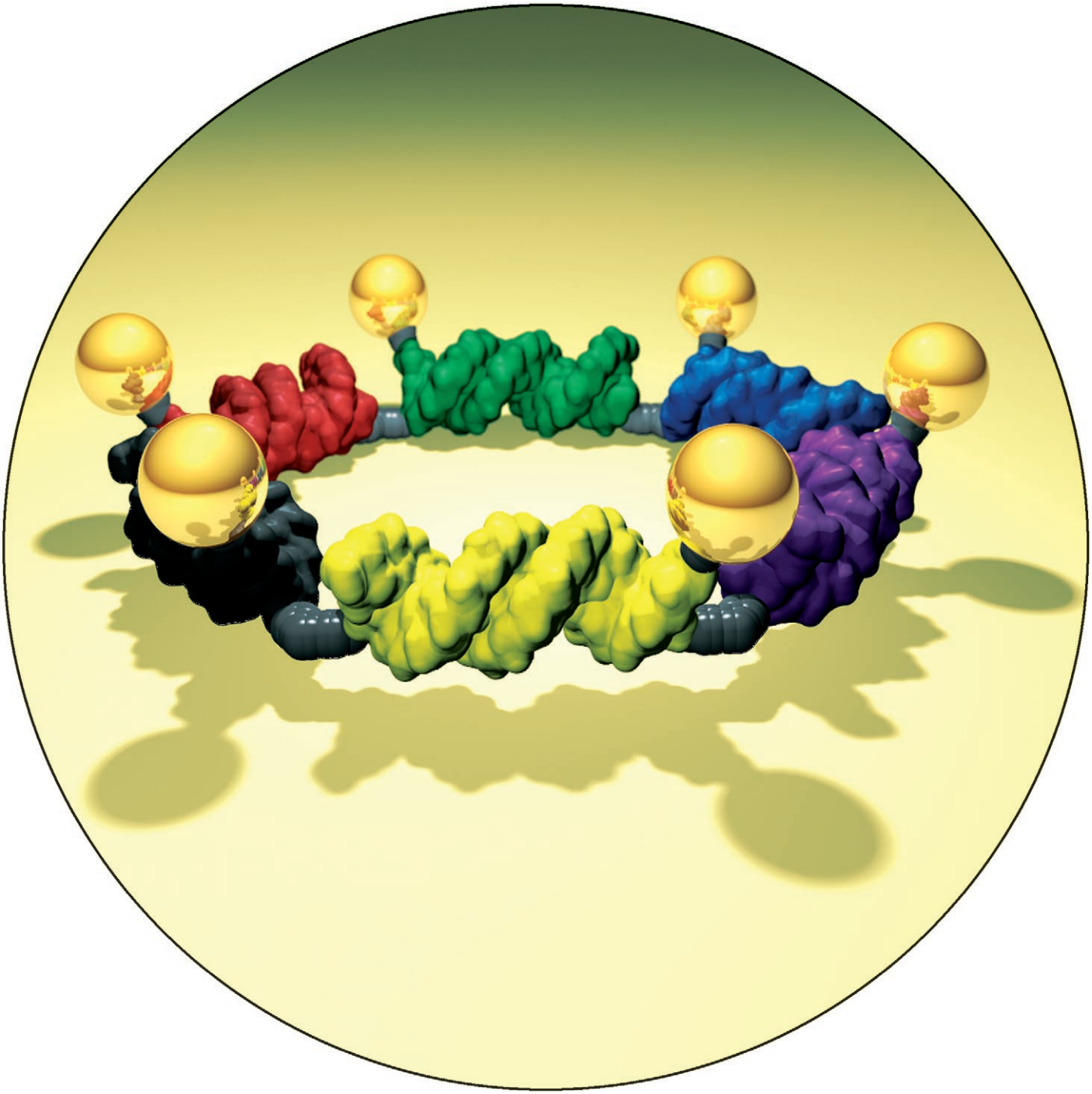

DNA molecules with rigid organic vertices can provide gold nanoparticles with an exact "address" that dictates their final location in a well-defined assembly. For more information on the DNA-mediated organization of six gold nanoparticles into a cyclic hexameric structure, see the Communication by F. A. Aldaye and H. F. Sleiman on the following pages.

WILEY InterScience DISCOVER SOMETHING GREAT
© 2006 Wiley-VCH Verlag GmbH & Co. KGaA, Weinheim

Nanostructures

DOI: 10.1002/anie.200502481

Sequential Self-Assembly of a DNA Hexagon as a Template for the Organization of Gold Nanoparticles**

*Faisal A. Aldaye and Hanadi F. Sleiman**

In memory of Henry Taube

There has been significant interest in the organization of colloidal nanocrystals, such as metal, semiconductor, and magnetic nanoparticles into higher-order aggregates.[1] To date, almost all reported systems have been two- and three-dimensional extended periodic arrays of particles.[1–3] On the other hand, the ability to organize nanoparticles according to a deliberately designed pattern, and to modify this design at will, remains a central challenge in nanoscience. As a result of the novel electron and optical transport properties of these nanoparticle assemblies,[1,2] this organization of nanoparticles into patterns will contribute to the bottom-up design of nanoscale circuitry, which can accomplish complex functions. DNA holds great promise as a building block towards this goal because of its sequence programmability, selective molecular recognition ability, and the relative rigidity of its double-helical form.[4] A particularly attractive approach would be to label each nanoparticle with a DNA-containing molecule, which can provide it with an exact "address" to dictate its final position within the assembly. Herein, we report the synthesis of six DNA molecules, each containing two different DNA arms held together by a rigid organic vertex. Sequential self-assembly of these building blocks results in the selective formation of a discrete, hexagonal DNA nanostructure that contains a cyclic arrangement of six DNA duplexes and six rigid vertices. By labeling six gold nanoparticles with these DNA molecules, we then demonstrate the organization of the first example of a discrete, small cyclic assembly of gold nanoparticles in a sequential and specific manner. Overall, this sequence provides what is to our knowledge a unique approach for the modular and programmable assembly of colloidal nanoparticles into novel, well-defined structures.

In the design of the building blocks for this assembly, a rigid 120° synthetic vertex **1** and short DNA strands were used in order to ensure that the final construct is geometrically well-defined. A cyclic rather than linear structure for the nanoparticle assembly was selected because of its potential to lead to unique nanoelectronic properties and also because its restricted conformational mobility compared to its linear counterpart can result in significant spatial control over the positions of these particles. Six DNA building blocks **2a**–**2f**, in which the organic linker **1** is conjugated to two 17-mer DNA arms, were synthesized (Scheme 1). The DNA sequences

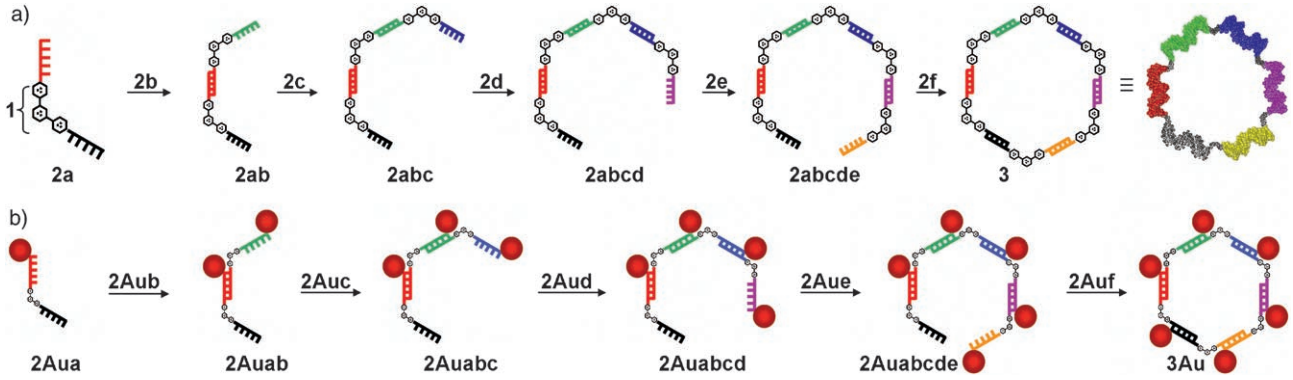

Scheme 1. Sequential self-assembly of a) **2a**–**2f** and b) **2Aua**–**2Auf** to give the hexagonal assemblies **3** and **3Au**, respectively (red spheres represent Au nanoparticles). An energy-minimized structure of **3** (AMBER force-field method) is also shown.[17]

[*] F. A. Aldaye, Prof. H. F. Sleiman
Department of Chemistry
McGill University
801 Sherbrooke Street W.
Montreal, Quebec H3A 2K6 (Canada)
Fax: (1+) 514-398-3797
E-mail: hanadi.sleiman@mcgill.ca.

[**] This work was supported by the NSERC, the Canada Foundation for Innovation, Nanoquebec, Research Corporation, the Center for Self-Assembled Chemical Structures, and the NSERC Strategic Grant Program. We thank Antisar R. Hlil for MALDI-TOF MS measurements. H.F.S. is a Cottrell Scholar of the Research Corporation.

Supporting information for this article is available on the WWW under http://www.angewandte.org or from the author.

were designed such that each building block contains only one arm that is complementary to one arm of the next building block, with the remaining arms of building blocks **2a** and **2f** being complementary to one another. This would be expected to result in selective and sequential access to a cyclic and hexameric DNA architecture **3**, containing linker molecule **1** at its corners (Scheme 1). The building blocks were terminated with an amine unit for subsequent conjugation to a gold nanoparticle. Solid-phase automated synthesis of **2a**–**2f** was performed by construction of the first DNA arm, followed by the addition of the vertex **1** as its phosphoramidite derivative, subsequent synthesis of the second arm, and finally termination using an amino amidite derivative.[17]

© 2006 Wiley-VCH Verlag GmbH & Co. KGaA, Weinheim

We then examined the ability of the building blocks **2a**–**2f** to undergo sequential self-assembly into the desired DNA hexagonal structure **3**. Figure 1 shows a native polyacrylamide gel of this study. Molecule **2a** alone showed a band of

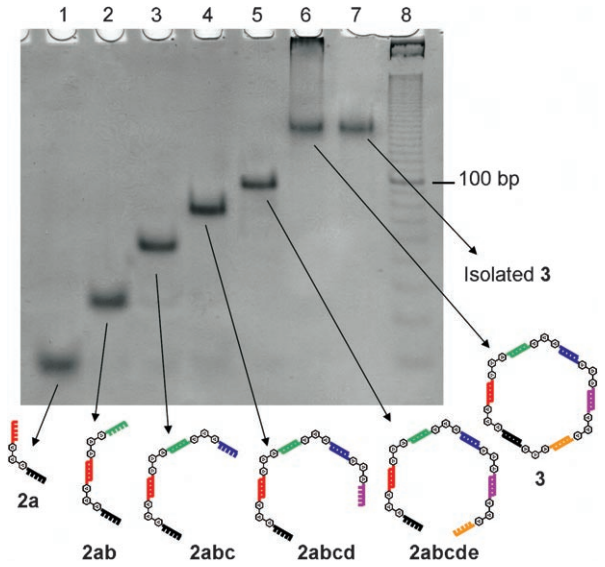

Figure 1. Native polyacrylamide gel of the sequential addition of **2a**–**2f** to form **2ab**, **2abc**, **2abcd**, **2abcde**, and **3** (lanes 2–6, respectively), and of isolated **3** (lane 7). A molecular-weight marker with 10-bp increments from 10 to 330 bp was used, with the most intense band corresponding to 100 bp (lane 8; bp = base pairs).

relatively high mobility. The assemblies of two (**2ab**), three (**2abc**), four (**2abcd**), and five (**2abcde**) building blocks showed well-defined, single bands of steadily decreasing mobility. This behavior is consistent with the clean and quantitative formation of discrete duplex assemblies containing the desired number of building blocks in each case. These assignments also correlate well with the 10-base-pair linear DNA ladder in lane 8 of Figure 1. The addition of the sixth building block **2f** to **2abcde** is expected to result in both duplex formation and subsequent cyclization (lane 6 in Figure 1). A single band of reduced mobility relative to that of **2abcde** was observed and assigned to the hexameric DNA assembly **3**. In addition, a second band of low mobility was detected, suggesting the concomitant formation of higher-order oligomeric species. Although **3** is calculated to contain 102 base pairs, it was found to move as a 200-mer when compared to the molecular-weight marker. This difference is consistent with the fact that cyclic structures tend to travel anomalously in gel electrophoresis as compared to their linear counterparts.[5] The yield of hexamer **3** relative to that of the oligomeric species was optimized as a function of hybridization temperature and time.[6,17] Note that subjecting the mixture of **3** and oligomers to repeated heating and cooling cycles (90 °C to 20 °C) resulted in a marked increase in the ratio of hexamer **3** to the oligomers. This observation is consistent with the significant stability of **3** and suggests that the higher-order oligomers are kinetic products. Isolation of DNA hexamer **3** in pure form was then performed directly from the gel using electroelution (Figure 1, lane 7).[6,17]

Supramolecular self-assembled structures have been traditionally generated by the one-pot assembly of identical sets of building blocks.[7] The sequential nature of the approach described here, however, allows for the use of different building blocks in each step and can thus potentially result in the modular synthesis of a large set of nanostructures, with precise spatial positioning of these different building blocks.

The cyclic nature of **3** was essential for its use as an effective template. To establish that this hexamer is indeed cyclic, we first performed studies on **3** using the enzyme mung bean nuclease (MBN), which has been demonstrated to cleave single-stranded DNA preferentially over the double-stranded form.[8] MBN is thus expected to degrade linear open structures containing single-stranded DNA, but it is not expected to degrade cyclic closed structures that contain only double-stranded DNA. When purified **3** was treated with MBN under conditions that have been optimized for the digestion of single-stranded DNA,[17] no change in band mobility was observed (Figure 2a) which indicates that **3** is cyclic. In a second experiment, we deliberately synthesized a linear hexamer **2abcdef′**, which is structurally similar to hexamer **3** but is derived from non-complementary sequences

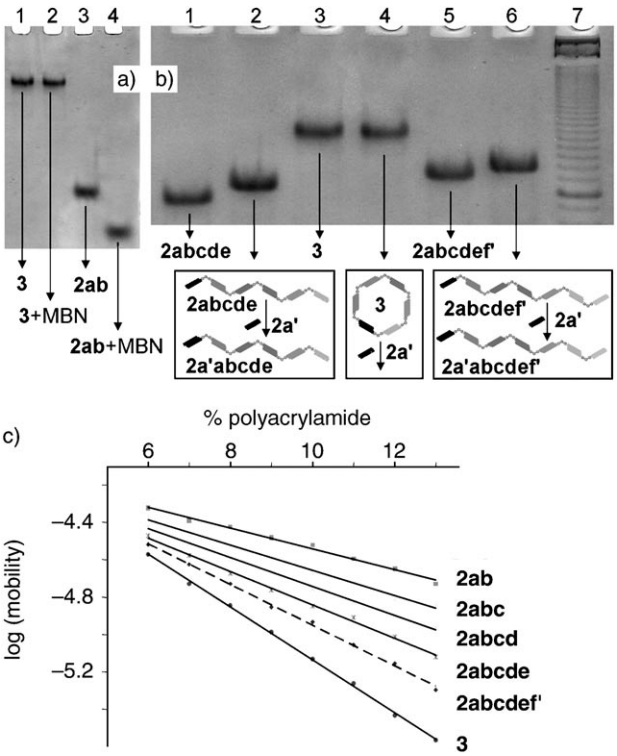

Figure 2. a) Polyacrylamide gel of the enzymatic digestion of **3** by mung bean nuclease (MBN). Lane 1: hexamer **3**; lane 2: hexamer **3** and MBN; lane 3: **2ab** containing double- and single-stranded DNA (control); lane 4: **2ab** and MBN. b) Lane 1: linear pentamer **2abcde**; lane 2: **2abcde** and single-arm complement **2a′**, showing a reduction in mobility due to hybridization; lane 3: DNA hexamer **3**; lane 4: DNA hexamer **3** and **2a′**, showing no change in band mobility; lane 5: deliberately synthesized linear hexamer **2abcdef′**; lane 6: linear hexamer **2abcdef′** and **2a′**, showing a reduction in band mobility due to hybridization; lane 7: 10-bp DNA marker with the intense band representing 100 bp. c) Ferguson plot analysis of **2ab**, **2abc**, **2abcd**, **2abcde**, **2abcdef′**, and **3**.

© 2006 Wiley-VCH Verlag GmbH & Co. KGaA, Weinheim

a and **f′** and thus cannot cyclize (Figure 2b). Interestingly, the mobility of this linear hexamer (lane 5, Figure 2b) is very different from that of hexamer **3** (lane 3, Figure 2b) and now correlates well with the linear 10-base-pair DNA marker (lane 7, Figure 2b). This observation is again consistent with the cyclic nature of **3**. In a third experiment, we synthesized **2a′**, which contains a single DNA arm complementary to **2a**. Addition of **2a′** to the linear pentameric and hexameric assemblies (**2abcde** and **2abcdef′**) resulted in bands of reduced mobility, consistent with their hybridization with the available single-stranded **2a** (lanes 2 and 6, respectively, in Figure 2b). However, no observable shift in band mobility was detected from the addition of **2a′** to **3**, in which all arms are double stranded, consistent with its cyclic nature (lane 4, Figure 2b). Finally, Ferguson plot analysis on linear structures **2ab**, **2abc**, **2abcd**, **2abcde**, and **2abcdef′** revealed a steadily increasing gel retardation coefficient, while hexamer **3** had an anomalously higher retardation coefficient compared to the trend of its linear counterparts (Figure 2c).[17] All these experiments establish **3** as a hexameric cyclic DNA structure containing six double-stranded DNA arms and six rigid organic vertices. Higher-order DNA structures containing branched oligonucleotides,[4,9] and to a lesser extent, flexible organic[10] and inorganic[11] molecules as their corner units, have been previously generated. In this respect, molecule **3** is the first example of a DNA nanostructure with fully rigid organic vertices,[10] and as such, it constitutes a promising approach for the organization of nanoparticles.

To demonstrate the potential of this method for the sequential organization of nanoparticles, we labeled six gold nanoparticles with each of molecules **2a**–**2f**. Covalent attachment to the amino end of **2a**–**2f** was carried out by incubating these molecules with 1.4-nm particles monofunctionalized with a succinimidyl ester moiety.[12,17] The resulting gold-labeled building blocks **2Aua**–**2Auf** were purified by agarose gel electrophoresis. We established that each building block was indeed attached to a gold nanoparticle by UV/Vis spectroscopy, which showed the presence of both DNA ($\lambda_{max} = 260$ nm) and gold ($\lambda = 260$ and 420 nm), and by agarose electrophoresis gels stained with ethidium bromide to visualize the DNA and with silver enhancement[13] to visualize the gold particles. The ratio of DNA to gold nanoparticles in these building blocks was confirmed as 1:1 by both UV/Vis spectroscopy and titration experiments.[14,17]

We then performed the sequential assembly of the gold-labeled building blocks **2Aua**–**2Auf**. Figure 3a and b show the analysis of this assembly with native agarose gel electrophoresis. Again, the sequential assemblies of the first five Au-labeled building blocks show single bands of steadily decreasing mobility. These bands correspond to discrete groupings containing one, two, three, four, and five gold nanoparticles, with even spacing consisting of a 17-mer DNA duplex and the rigid organic spacer (approximately 6 nm). The addition of the sixth building block **2Auf** to the pentamer **2Auabcde** gave a band of reduced mobility relative to this pentamer, as well as oligomeric species of lower electrophoretic mobility. Visualization using ethidium bromide and silver enhancement staining confirmed that the species represented by this band does in fact contain both DNA and gold nanoparticles. This

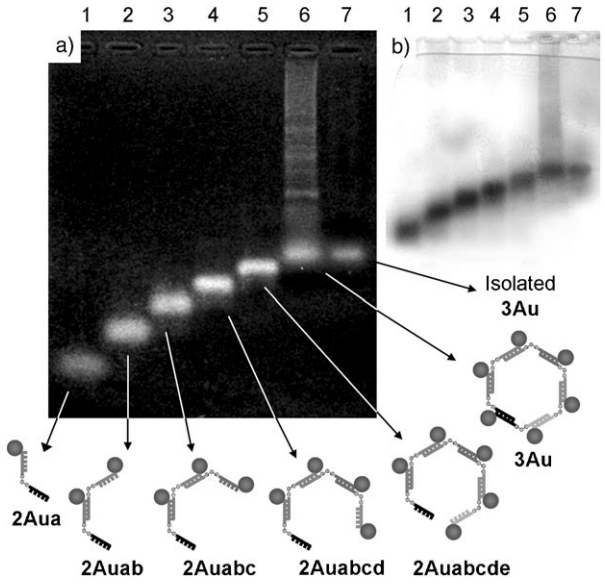

Figure 3. Agarose gels of the sequential assembly of gold-conjugated building blocks **2Aua**–**2Auf** (lanes 1–6) and the isolation of **3Au** (lane 7), as visualized by a) ethidium bromide and b) silver enhancement staining.

band was accordingly assigned to the discrete hexamer of gold nanoparticles **3Au** and was subsequently purified by electroelution (lane 7 in Figure 3a and b). Note that the sequential nature of this assembly provides internal markers for every step of this process and strongly establishes the self-assembly of the gold nanoparticle hexamer. Thus, during each step of this process, a pure gold–DNA building block containing a 1:1 ratio of gold nanoparticles to DNA strand is added. The observation of a single band of steadily reduced mobility after each addition establishes the clean and quantitative incorporation of this building block into the assembly. Thus, the gel in Figure 3 represents the assembly of groupings of steadily increasing numbers of gold nanoparticles. In a similar experiment to the unlabeled building blocks, we constructed a linear assembly of six gold nanoparticles **2Auabcdef′**, which is structurally similar to **3Au** but does not have the correct sequence for cyclization. When the linear assembly **2Auabcdef′** was compared to hexamer **3Au**, it was found to display noticeably faster electrophoretic mobility, consistent with the cyclic nature of **3Au**. Similarly, when a gold-conjugated structural analogue of **2a′** (**2Aua′**) was added to the preformed linear pentameric and hexameric assemblies **2Auabcde** and **2Auabcdef′**, as well as to **3Au**, only the linear, single-strand-containing structures **2Auabcde** and **2Auabcdef′** resulted in an observable retardation in band mobility (Figure 4). This data is consistent with the assignment of **3Au** as a discrete, cyclic hexamer of gold nanoparticles.

DNA has been used to mediate the assembly of extended arrays[2] and linear groupings of gold nanoparticles.[3a–c] In addition, two recent examples of discrete and flexible two-dimensional assemblies of Au particles using branched DNA and biotin–avidin interactions have been reported.[3d–e] The self-assembly of discrete particle assemblies such as **3Au**

 © 2006 Wiley-VCH Verlag GmbH & Co. KGaA, Weinheim

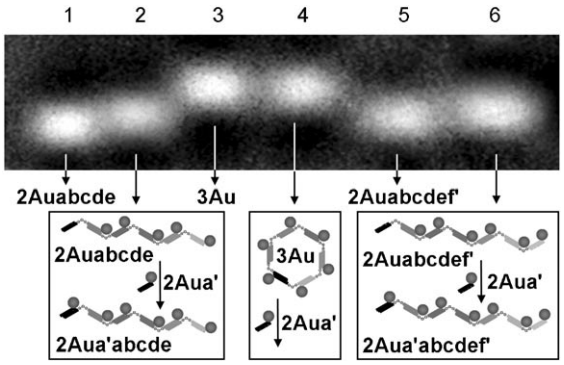

Figure 4. Agarose gel analysis: Lane 1: linear pentamer of gold nanoparticles **2Au abcde**; lane 2: **2Au abcde** and gold-labeled single-arm complement **2Au a′**, showing a reduction in band mobility; lane 3: DNA-templated gold hexamer **3Au**; lane 4: **3Au** and **2Au a′**, showing no change in band mobility; lane 5: deliberately synthesized linear hexamer of gold nanoparticles **2Au abcdef**; lane 6: **2Au abcdef** and **2Au a′**, showing a reduction in band mobility due to hybridization.

allows for the use of new variables to tune the ensemble properties of nanoparticles, namely the assembly size and geometry, as well as the number and identity of constituent particles. Many applications can be anticipated for these controlled assemblies, such as modular biodetection tools,[2d] model systems for the study of individual charge transport within groupings of nanoparticles ("single electronics"),[15] and for optical waveguides below the diffraction limit of light ("nanoscale optics").[16] Interestingly, although the linear groupings of gold particles generated in this work represent a useful method to organize any number of different nanoparticles, with the distance between them being dictated by the length of the DNA arms used, the final assemblies are in fact expected to be conformationally mobile. The use of a cyclic rigid template for **3Au**, on the other hand, conformationally locks the system and is expected to provide a higher level of spatial control over the discrete nanoparticle assembly.

In summary, we have demonstrated the organization of six gold nanoparticles into a discrete, well-defined, two-dimensional hexamer using a cyclic scaffold that contains both rigid organic vertices and double-stranded DNA arms. Our approach may be generalized for the construction of any discrete assembly of nanoparticles in which it is a requirement to spatially position the particles in a well-defined organized pattern. Because of the sequential nature of this method, different types of nanoparticles can be appended on each of the building blocks, thus potentially resulting in heteroassemblies of precisely positioned nanoparticles. By varying the length of the DNA arms and the type of vertices, one can envisage the construction of a plethora of scaffolds of different sizes on which nanoparticles may be organized (i.e. triangles, squares, pentagons, etc). Finally, the use of vertices that contain three or more DNA arms can extend this organizational control into the third dimension.

Received: July 15, 2005
Revised: December 13, 2005
Published online: February 27, 2006

Keywords: DNA · gold · nanostructures · self-assembly · supramolecular chemistry

[1] a) M. P. Pileni, *J. Phys. Chem. B* **2001**, *105*, 3358–3371; b) C. P. Collier, T. Vossmeyer, J. R. Heath, *Annu. Rev. Phys. Chem.* **1998**, *49*, 371–404; c) K. Beomseok, C. A. Marcelo, S. L. Tripp, A. Wei, *Langmuir* **2004**, *20*, 9360–9365, and references therein.

[2] Examples of extended gold–DNA assemblies: a) C. A. Mirkin, R. L. Letsinger, R. C. Mucic, J. J. Storhoff, *Nature* **1996**, *382*, 607–609; b) H. Li, S. H. Park, J. H. Reif, T. H. LaBean, H. Yan, *J. Am. Chem. Soc.* **2004**, *126*, 418–419; c) J. D. Le, Y. Pinto, N. C. Seeman, K. Musier-Forsyth, T. A. Taton, R. A. Kiehl, *Nano Lett.* **2004**, *4*, 2343–2347; d) N. L. Rosi, C. A. Mirkin, *Chem. Rev.* **2005**, *105*, 1547–1562.

[3] Discrete gold nanoparticle assemblies: a) C. J. Loweth, B. W. Caldwell, X. Peng, P. A. Alivisatos, P. G. Schultz, *Angew. Chem.* **1999**, *111*, 1925–1929; *Angew. Chem. Int. Ed.* **1999**, *38*, 808–1812; b) A. P. Alivisatos, K. P. Johnsson, X. Peng, T. E. Wilson, C. J. Loweth, M. P. Bruchez, P. G. Schultz, *Nature* **1996**, *382*, 609–611; c) C. M. Niemeyer, *Angew. Chem.* **2001**, *113*, 4254–4287; *Angew. Chem. Int. Ed.* **2001**, *40*, 4128–4158, and references therein; d) S. A. Claridge, S. L. Goh, J. M. J. Frechet, S. C. Williams, C. M. Micheel, P. A. Alivisatos, *Chem. Mater.* **2005**, *17*, 1628–1635; e) A. Fu, C. M. Micheel, J. Cha, H. Chang, H. Yang, P. A. Alivisatos, *J. Am. Chem. Soc.* **2004**, *126*, 10832–10833.

[4] a) N. C. Seeman, *Biochemistry* **2003**, *42*, 7259–7269; b) N. C. Seeman, *Annu. Rev. Biophys. Biomol. Struct.* **1998**, *27*, 225–248; c) J. J. Storhoff, C. A. Mirkin, *Chem. Rev.* **1999**, *99*, 1849–1862; d) C. M. Niemeyer, *Curr. Opin. Chem. Biol.* **2000**, *4*, 609–618.

[5] D. M. Heuer, S. Saha, L. A. Archer, *Biopolymers* **2003**, *70*, 471–481, and references therein.

[6] The self-assembly of the linear constructs is essentially quantitative. Also, the self-assembly of the DNA hexagon is quite efficient. The isolated yield of the hexagon is 60%, whereas the amount of hexagon in the crude mixture is 75% (evaluated from UV/Vis spectroscopy). Scale-up of this synthesis is expected to produce more oligomers if the concentration of DNA is increased. However, the yield of the DNA hexagon should not be affected if volumes are increased but similar concentrations of DNA are used.

[7] J. W. Steed, J. L. Atwood, *Supramolecular Chemistry*, Wiley, New York, **2000**.

[8] a) W. D. Kroeker, D. Kowalski, M. Laskowski, Sr. , *Biochemistry* **1976**, *15*, 4463–4467; b) P. H. Johnson, M. Laskowski, Sr., *J. Biol. Chem.* **1970**, *245*, 891–898.

[9] a) W. M. Shih, J. D. Quispe, G. F. Joyce, *Nature* **2004**, *427*, 618–621; b) D. Liu, M. Wang, Z. Deng, R. Walulu, C. Mao, *J. Am. Chem. Soc.* **2004**, *126*, 2324–2325.

[10] a) J. Shi, D. E. Bergstrom, *Angew. Chem.* **1997**, *109*, 70–72; *Angew. Chem. Int. Ed. Engl.* **1997**, *36*, 111–113; b) M. S. Shchepinov, K. U. Mir, J. K. Elder, M. D. Frank-Kamenetskii, E. Southern, *Nucleic Acids Res.* **1999**, *27*, 3035–3041; c) M. Scheffler, A. Dorenbeck, S. Jordan, M. Wustefeld, G. von Kiedrowski, *Angew. Chem.* **1999**, *111*, 3514–3518; *Angew. Chem. Int. Ed.* **1999**, *38*, 3312–3315.

[11] a) D. Mitra, N. Di-Cesare, H. F. Sleiman, *Angew. Chem.* **2004**, *116*, 5928–5932; *Angew. Chem. Int. Ed.* **2004**, *43*, 5804–5808; b) I. Vargas-Baca, D. Mitra, H. J. Zulyniak, J. Banerjee, H. F. Sleiman, *Angew. Chem.* **2001**, *113*, 4765–4768; *Angew. Chem. Int. Ed.* **2001**, *40*, 4629–4632; c) K. V. Gothelf, A. Thomsen, M. Nielsen, E. Clo, R. S. Brown, *J. Am. Chem. Soc.* **2004**, *126*, 1044–1046; d) S. M. Waybright, C. P. Singleton, K. Wachter, C. J. Murphy, U. H. F. Bunz, *J. Am. Chem. Soc.* **2001**, *123*, 1828–1833; e) J. L. Czlapinkski, T. L. Sheppard, *J. Am. Chem. Soc.* **2001**, *123*, 8618–8619; f) K. M. Stewart, J. Rojo, L. W. McLaughlin, *Angew. Chem.* **2004**, *116*, 5932–5932; *Angew. Chem. Int. Ed.* **2004**, *43*,

 © 2006 Wiley-VCH Verlag GmbH & Co. KGaA, Weinheim

5808 – 5811; g) A. Arafat, K. Schroen, L. C. P. M. de Smet, E. J. R. Sudholter, Z. Han, *J. Am. Chem. Soc.* **2004**, *126*, 8600 – 8601.
[12] a) J. F. Hainfeld, R. D. Powell, *Cell Division* **1997**, *4*, 308 – 324; b) F. R. Furuya, J. F. Hainfeld, *J. Histochem. Cytochem.* **1992**, *40*, 177.
[13] J. E. Beesley in *Colloidal Gold: Principles, Methods, and Applications, Vol. 1* (Ed.: M. A. Hayat), Academic Press, New York, **1989**, pp. 421 – 425. Experiments were conducted to demonstrate that silver enhancement does not stain bands containing just DNA (see Supporting Information).
[14] The 1:1 ratio of DNA to gold was verified by 1) UV/Vis quantification of a band solely due to the gold particles versus a band due to DNA; 2) titration experiments of the gold–DNA constructs with their complementary partners which showed that a single hybridized product is only obtained at a 1:1 ratio; 3) silver enhancement staining of the bands under conditions where DNA alone does not stain; and 4) significantly reduced band mobility on native agarose gels compared to DNA alone.
[15] For a comprehensive discussion of single electronics and for further references, see: U. Simon, in *Nanoparticles: From Theory to Application*, G. Schmid, Wiley-VCH, Weinheim, **2004**.
[16] a) S. A. Maier, M. L. Brongersma, P. G. Kik, S. Meltzer, A. A. G. Requicha, H. A. Atwater, *Adv. Mater.* **2001**, *13*, 1501 – 1505; b) S. A. Maier, M. L. Brongersma, P. G. Kik, S. Meltzer, A. A. Requicha, B. E. Koel, H. A. Atwater, *Adv. Mater.* **2003**, *15*, 562.
[17] See Supporting Information. Please also note that molecules **2** and **2Au** shown in Scheme 1 are expected to be conformationally mobile and are only shown as schematic representations.

 © 2006 Wiley-VCH Verlag GmbH & Co. KGaA, Weinheim

Heterogeneous Catalysis

DOI: 10.1002/anie.200503445

Expanding the Utility of One-Pot Multistep Reaction Networks through Compartmentation and Recovery of the Catalyst**

*Nam T. S. Phan, Christopher S. Gill, Joseph V. Nguyen, Z. John Zhang, and Christopher W. Jones**

Living systems combine the use of highly specific catalysts coupled with compartmentation in different regions of the cell to control multistep reaction networks, which are used to synthesize the complex organic molecules that cells need to survive.[1] Although there has been significant progress in mimicking nature's reaction cascade strategy over the past decades, the manipulation of sequential reactions using multiple catalysts in a single vessel is still relatively rare. Over the years, non-natural systems based on single- or multi-enzyme-mediated reaction sequences have been demonstrated, mimicking some aspects of nature's synthetic strategy.[2] Nonetheless, the vast majority of chemical syntheses are still conducted using the traditional paradigm of single catalytic reactions with homogeneous or heterogeneous chemical catalysts, followed by costly catalyst and/or product purification steps.[3] A primary reason is that controlling one-pot, multistep reactions using traditional homogeneous catalysts is rather difficult as, unlike for biocatalysts, interactions between soluble catalysts can cause deactivation. Many examples of complex reaction sequences or cascades do not use multiple catalysts, whereas in other cases combinations of homogeneous, heterogeneous, or enzyme catalysts in one pot were used to direct sequential reactions.[2,4,5] These cases represent carefully constructed systems that were optimized for one specific sequence. In such cases, standard workup procedures after the reaction most likely result in the used catalysts simply becoming a component of the reaction waste.[5] A critical aspect of living systems that thus far has not been effectively applied is the use of multiple combinations of catalysts sequentially.[6] An approach to achieve this within the chemical catalysis paradigm is to develop the ability to separate the multiple catalysts used in one-pot, multireaction cascades in essentially pure form, allowing reuse of the recovered catalysts in numerous other catalytic reactions, potentially in a combinatorial manner. Herein, we demonstrate this approach using a combination of catalysts recovered by magnetic,[7] gravimetric,[8] and membrane methods,[9–10] allowing excellent control of multistep reactions with recovery of each individual catalyst. In particular, the use of magnetically separable catalysts allows the creation of a variety of versatile catalysts that can be easily recovered without the need for specialized equipment. Furthermore, the recovered catalysts can be reused in different, subsequent multistep one-pot reactions. This is an unprecedented level of control over multistep, one-pot catalytic reactions.

This concept was demonstrated by combining base catalysts that are magnetically recoverable with acid catalysts that are recovered gravimetrically. Superparamagnetic spinel ferrite nanoparticles were prepared according to published procedures[11] and functionalized through silane chemistry with *N*-[3-(trimethoxysilyl)propyl]ethylenediamine to create surface base sites.[12] The basic nanoparticle solids were then used in conjunction with a sulfonic acid polymer resin in the tandem deacetalization–Knoevenagel reaction (see Supporting Information for experimental details and characterization of the catalyst). Both catalysts and all the reagents were added to a reaction vessel at time zero, and the contents were stirred for a prescribed period of time while the course of the reaction was monitored by GC. Complete conversion of **1** into **2** and **2** into **3** (Figure 1, blue box) was observed in just 30 minutes, with average turnover frequencies (TOF) of 3 h^{-1}

[*] Dr. N. T. S. Phan, C. S. Gill, Dr. J. V. Nguyen, Prof. C. W. Jones
School of Chemical & Biomolecular Engineering
Georgia Institute of Technology
Atlanta, GA 30332 (USA)
Fax: (+1) 404-894-2866
E-mail: cjones@chbe.gatech.edu
Prof. Z. J. Zhang
School of Chemistry and Biochemistry
Georgia Institute of Technology
Atlanta, GA 30332 (USA)

[**] The US DOE Office of Basic Energy Sciences is acknowledged for financial support through Catalysis Science Contract No. DE-FG02-03ER15459. DuPont is also thanked for a Young Professor Award. C.W.J. acknowledges support from ChBE at GT through the J. Carl & Sheila Pirkle Faculty Fellowship.

Supporting information for this article is available on the WWW under http://www.angewandte.org or from the author.

 © 2006 Wiley-VCH Verlag GmbH & Co. KGaA, Weinheim

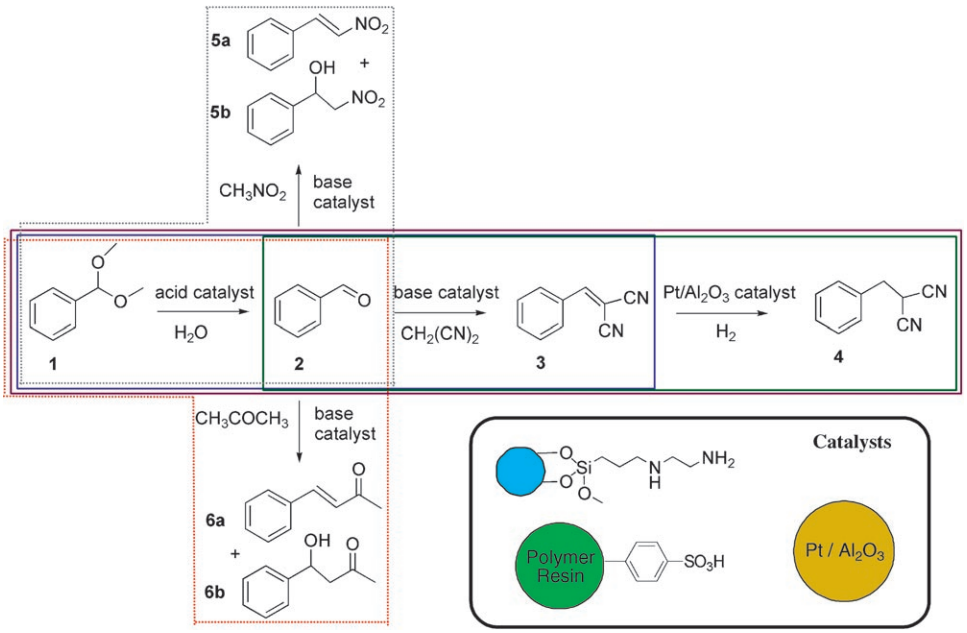

Figure 1. Multistep reaction networks controlled by the combination of different solid catalysts in a single vessel. See text for details.

for the acid resin catalyst and 75 h^{-1} for the basic magnetic catalyst. After reaction, the catalysts were separated by sonicating the reaction vessel and affixing a small permanent magnet externally to one wall of the vessel. The nonmagnetic resin catalyst was removed from the reaction vessel by decantation while the magnetic nanoparticle base catalyst was held stationary in the vessel by the magnet. Each catalyst was recovered in essentially pure form, as indicated by elemental analysis of the recovered catalysts. The amount of sulfur, an elemental tag for the resin catalyst, detected in the magnetic nanoparticle catalyst before and after reaction was essentially identical (0.07 % S in the magnetic base catalysts before reaction and 0.05 % S after reaction). The same is true of the amount of iron, an elemental tag for the magnetic catalyst, in the resin catalyst before and after reaction (0.01 % Fe in the acid resin catalyst before reaction and 0.03 % Fe after reaction). Reuse of the separated catalysts in the same reaction gave the same results with the same kinetic profile, indicating that no noticeable deactivation of the catalyst occurred upon combination of the two opposing catalysts (Figure 2).[13] Note also that each catalyst on its own was unable to promote the conversion of **1** into **3**, indicating that the tandem action of two catalysts was required to complete the sequence, as is often seen in biological systems (Table 1). These data, when combined with the results of elemental analysis, show that the catalysts can be recovered in pure form and that they can be subsequently reused without loss of performance. This is the first example of a multistep, one-pot reaction in which the catalysts can be recovered in pure form and used in later manipulations (see below).

To show the versatility of this method, the recovered magnetic nanoparticle catalyst was then effectively used in a second multistep, one-pot reaction (Figure 1, green box) in conjunction with a new solid catalyst, Pt/Al_2O_3. This tandem Knoevenagel–hydrogenation reaction was carried out in one pot with all reagents and catalysts added at time zero. The reaction was started at atmospheric pressure, and after a period of time the pressure of the reaction was increased to 1000 psig (pounds per square inch gauge) H_2 to facilitate completion of the second reaction. In this case, **2** was converted into **3** using the basic catalyst and **3** was hydrogenated to **4** by the supported platinum, with both reactions going to completion. Similar results were also obtained when the one-pot reaction was pressurized to 1000 psig H_2 at time zero and maintained at this pressure throughout the course of the reaction (Table 1). As before, the individual catalysts were recovered through the magnetic separation process described above. The reaction sequence was then extended to three steps, again with catalyst recovery, with conversion of **1**

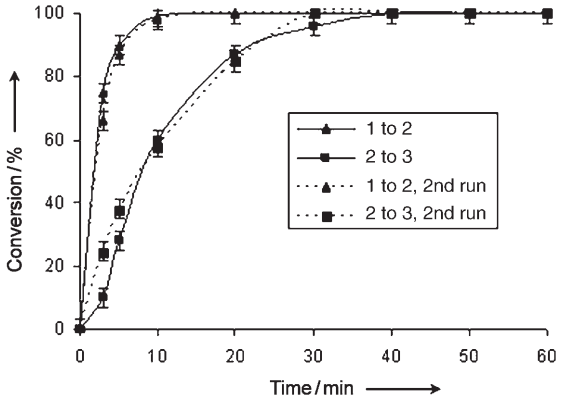

Figure 2. One-pot sequential reactions with acidic polymer resin and basic magnetic nanoparticle catalysts. Triangles and squares represent kinetic data for the reactions of **1**→**2** and **2**→**3**, respectively.[13] Broken lines show kinetic data for reactions with recycled catalysts.

into **4** (Figure 1, violet box) by adding the base catalysts supported on magnetic nanoparticles and the polymeric acid catalyst into the vessel along with the platinum catalyst enclosed in a membrane. In this case, all components were added to the reactor at time zero and the reaction was started at 1 atm total pressure. After 60 minutes, the hydrogen pressure was increased to 1000 psig to carry out the final step of the reaction. The overall yield of the final product **4** was 78 % (Table 1); 100 % yield of **4** was obtained in the absence of a membrane. This result indicated that some transport effects were slowing the final reaction when the membrane was used.

Stepwise control over the reaction sequence and the ability to continually reuse the original catalysts in multiple

 © 2006 Wiley-VCH Verlag GmbH & Co. KGaA, Weinheim

Table 1: Results (% conversion) of catalytic reaction sequences carried out in one pot with multiple opposing catalysts.

Catalyst	Conv. [%]	Conv. [%]
Blue Sequence **1**→**2**→**3**[a]	**1**→**2**	**2**→**3**
solid acid and solid base	100	100
solid acid	100	0
solid base	0	0
solid acid and homogeneous base	0	0
solid base and homogeneous acid	0	0
homogeneous acid and base	0	0
Green Sequence **2**→**3**→**4**[a]	**2**→**3**	**3**→**4**
solid base and Pt/Al_2O_3	100	100
Violet Sequence **1**→**2**→**3**→**4**[a]	**1**→**3**	**3**→**4**
solid acid, solid base, and Pt/Al_2O_3	100	78 (100[b])
Gray Sequence **1**→**2**→**5a**+**5b**[a]	**1**→**2**	**2**→**5a**+**5b**
solid acid and solid base	100	100 (4:1 **5a**/**5b**)
Red Sequence **1**→**2**→**6a**+**6b**[a]	**1**→**2**	**2**→**6a**+**6b**
solid acid and solid base	100	82 (26:1 **6a**/**6b**)

[a] See Figure 1 for reaction sequences. [b] In the absence of a membrane. In this case, the Pt/Al_2O_3 and the polymer resin were obtained after the reaction as a mixture, although the magnetic catalyst could be isolated.

reactions was demonstrated by the conversion of **1** to **2** to **5a** and **5b** (Figure 1, gray box) using the same acid and base catalysts. By adding the magnetic nanoparticles used in the first two reaction sequences (**1**→**2**→**3** and **2**→**3**→**4**) and the acidic resin used in the first reaction sequence (**1**→**2**→**3**) to new reagents in a single vessel, the synthesis of **5a** and **5b** was achieved with complete conversion of **1** into **5a** and **5b**. Note that this sequence represents the third use of a single sample of magnetic catalyst and the second use of a single sample of the acid catalyst. Similarly, products **6a** and **6b** were prepared in another one-pot reaction (Figure 1, red box) with excellent results.[14]

In summary, we have shown that excellent control of a reaction sequence using chemical catalysts can be achieved by 1) using combinations of a few versatile catalysts that can be used in a variety of reactions, with recovery of the catalyst in pure form after the reaction; 2) compartmentation of catalytic sites to allow for use of catalysts that would self-quench in homogeneous media;[5] and 3) regulation of the reaction pathway by manipulating the reaction conditions, including control of the catalysts and reagents that are present. The combination of magnetically and gravimetrically recoverable catalysts allowed the first successful application of opposing catalysts to multistep, one-pot catalytic reactions including the ability to steer the direction of the reaction at each step, all with recovery of each individual catalyst after use. The successful use of the recovered catalysts in combination with other catalysts in subsequent, unrelated reactions showed the versatility of this approach.[15] A library of magnetically and gravimetrically recoverable catalysts could thus be generated and used in a variety of one-pot multistep catalytic reactions, and this methodology may be further expanded almost without limit through other means of catalyst separation, such as membrane encapsulation.[16]

Received: September 29, 2005
Revised: November 9, 2005
Published online: March 10, 2006

Keywords: acidity · heterogeneous catalysis · magnetic properties · nanostructures · synthetic methods

[1] J. Ovádi, P. A. Srere, *Int. Rev. Cytol.* **2000**, *192*, 255.
[2] a) A. Bruggink, R. Schoevaart, T. Kieboom, *Org. Process Res. Dev.* **2003**, *7*, 622; b) R. Schoevaart, F. van Rantwijk, R. A. Sheldon, *J. Org. Chem.* **2000**, *65*, 6940; c) P. A. Srere, B. Mattiass, K. Mosbach, *Proc. Natl. Acad. Sci. USA* **1973**, *70*, 2534; d) S. F. Mayer, W. Kroutil, K. Faber, *Chem. Soc. Rev.* **2001**, *30*, 332; e) R. Schoevaart, F. van Rantwijk, R. A. Sheldon, *Chem. Commun.* **1999**, 2465; f) N. Nakajima, K. Tanizawa, H. Tanaka, K. Soda, *J. Biotechnol.* **1988**, *8*, 243.
[3] Simplified workup of the reaction and purification of the product in sequences of reactions can be achieved by following the example of Ley and co-workers, who have used a variety of polymer-supported catalysts, reagents, and scavengers in complex reaction sequences. For example, see: a) I. R. Baxendale, S. V. Ley, C. Piutti, *Angew. Chem.* **2002**, *114*, 2298; *Angew. Chem. Int. Ed.* **2002**, *41*, 2194; b) R. I. Storer, T. Takemoto, P. S. Jackson, S. V. Ley, *Angew. Chem.* **2003**, *115*, 2625; *Angew. Chem. Int. Ed.* **2003**, *42*, 2521; c) S. V. Ley, I. R. Baxendale, G. Brusotti, M. Caldarelli, A. Massi, M. Nesi, *Farmaco* **2002**, *57*, 321.
[4] a) J. C. Wasilke, S. J. Obrey, R. T. Baker, G. C. Bazan, *Chem. Rev.* **2005**, *105*, 1001, 2005; b) L. F. Tietze, U. Beifuss, *Angew. Chem.* **1993**, *105*, 137; *Angew. Chem. Int. Ed. Engl.* **1993**, *32*, 131; c) L. F. Tietze, M. E. Lieb, *Curr. Opin. Chem. Biol.* **1998**, *2*, 363; d) L. F. Tietze, *Chem. Rev.* **1996**, *96*, 115; e) A. J. McCarroll, J. C. Walton, *J. Chem. Soc. Perkin Trans. 1* **2001**, 3215; f) P. J. Parsons, C. S. Penkett, A. J. Shell, *Chem. Rev.* **1996**, *96*, 195; g) K. C. Nicolau, T. Montagnon, S. A. Snyder, *Chem. Commun.* **2003**, 551; h) E. V. Gorobets, M. S. Miftakhov, F. A. Valeev, *Russ. Chem. Rev.* **2000**, *69*, 1001; i) J. M. Lee, Y. Na, H. Han, S. Chang, *Chem. Soc. Rev.* **2004**, *33*, 302; j) M. Burk, J. R. Lee, J. P. Martinez, *J. Am. Chem. Soc.* **1994**, *116*, 10847; k) S. E. Denmark, A. Thorarensen, *Chem. Rev.* **1996**, *96*, 137; l) M. Makkee, A. P. G. Kieboom, H. Van Bekkum, *J. Chem. Soc. Chem. Commun.* **1980**, 930; m) R. Schoevaart, T. Kieboom, *Top. Catal.* **2004**, *27*, 3; n) R. Schoevaart, T. Kieboom, *Tetrahedron Lett.* **2002**, *43*, 3399; o) M. Makkee, A. P. G. Kieboom, H. Van Bekkum, *Carbohydr. Res.* **1985**, *138*, 237; p) G. H. Posner, *Chem. Rev.* **1986**, *86*, 831; q) A. L. E. Larsson, B. A. Persson, J. E. Bäckvall, *Angew. Chem.* **1997**, *109*, 1256; *Angew. Chem. Int. Ed. Engl.* **1997**, *36*, 1211; r) B. A. Persson, A. L. E. Larsson, M. Le Ray, J. E. Bäckvall, *J. Am. Chem. Soc.* **1999**, *121*, 1645.
[5] Using solid catalysts, a catalyst mixture may be recovered although its separation into pure components is generally not possible using published methodologies. a) F. Gelman, J. Blum, D. Avnir, *J. Am. Chem. Soc.* **2000**, *122*, 11999; b) F. Gelman, J. Blum, D. Avnir, *Angew. Chem.* **2001**, *113*, 3759; *Angew. Chem. Int. Ed.* **2001**, *40*, 3647; c) F. Gelman, J. Blum, D. Avnir, *J. Am. Chem. Soc.* **2002**, *124*, 14460; d) F. Gelman, J. Blum, H. Schuman, D. Avnir, *J. Sol-Gel Sci. Technol.* **2003**, *26*, 43; e) F. Gelman, J. Blum, D. Avnir, *New J. Chem.* **2003**, *27*, 205; f) K. Motokura, N. Fujita, K. Mori, T. Mizugaki, K. Ebitani, K. Kaneda, *J. Am. Chem. Soc.* **2005**, *127*, 9674; g) B. Helms, S. J. Guillaudeau, Y. Xie, M. McUrdo, C. J. Hawker, J. M. J. Fréchet,

 © 2006 Wiley-VCH Verlag GmbH & Co. KGaA, Weinheim

Angew. Chem. **2005**, *117*, 6542; *Angew. Chem. Int. Ed.* **2005**, *44*, 6384.

[6] As noted in reference [3], Ley and co-workers have demonstrated that complex, multistep organic syntheses can be carried out with simplified workup procedures by using polymer supported reagents, catalysts, and scavengers. However, the recovery and reuse of pure catalysts from a mixture of catalysts used in a multistep, one-pot reaction has not been demonstrated.

[7] Magnetic catalysts have been reported for a number of years. For example, see: a) W. Teunissen, A. A. Bol, J. W. Geus, *Catal. Today* **1999**, *48*, 329; b) G. M. Whitesides, R. J. Kazlauskas, L. Josephson, *Trends Biotechnol.* **1983**, *1*, 144; c) C. L. Hill, A. Lamotte, W. Althoff, J. C. Brunie, G. M. Whitesides, *J. Catal.* **1976**, *43*, 53; d) X. Gao, K. M. K. Yu, K. Y. Tam, S. K. Tsang, *Chem. Commun.* **2003**, *24*, 2998; e) T.-J. Yoon, W. Lee, Y.-S. Oh, J.-K. Lee, *New J. Chem.* **2003**, *27*, 227; f) X. Q. Liu, J. M. Xing, Y. P. Guan, G. B. Shan, H. Z. Liu, *Colloids Surf. A* **2004**, *238*, 127; g) A. H. Lu, W. C. Li, A. Kiefer, W. Schmidt, N. Matoussevitch, H. Bonnemann, B. Spliethoff, B. Tesche, E. Bill, A. Kiefer, F. Schuth, *J. Am. Chem. Soc.* **2004**, *126*, 8618; h) W. Schmidt, E. Bill, G. Fink, F. Schuth, *Angew. Chem.* **2004**, *116*, 4403; *Angew. Chem. Int. Ed.* **2004**, *43*, 4303; i) A. Hu, G. T. Yee, W. Lin, *J. Am. Chem. Soc.* **2005**, *127*, 12486.

[8] Gravimetric separation implies the recovery of solid catalysts from liquid media by means of filtration or settling.

[9] Membranes are increasingly used for recycling homogeneous catalysts. For example, see: H. P. Dijkstra, G. P. M. Van Klink, G. Van Koten, *Acc. Chem. Res.* **2002**, *35*, 798.

[10] Membranes have been effectively used for enzyme manipulation, and membrane reactors currently represent the state-of-the-art in the commercial practice of biocatalytic reactions. For an early example, see: a) M. D. Bednarski, H. K. Chenault, E. S. Simon, G. M. Whitesides, *J. Am. Chem. Soc.* **1987**, *109*, 1283; for a review, see: b) J. Wötinger, A. S. Bommarius, K. Drauz, C. Wandrey, *Org. Process Res. Dev.* **2001**, *5*, 241; c) J. Wötinger, A. S. Bommarius, K. Drauz, *Appl. Catal. A* **2001**, *221*, 171.

[11] A. J. Rondinone, A. C. S. Samia, Z. J. Zhang, *J. Phys. Chem. B* **1999**, *103*, 6876.

[12] X. C. Shen, X. Z. Fang, Y. H. Zhou, H. Liang, *Chem. Lett.* **2004**, *33*, 1468.

[13] The data in Figure 2 for the first and second runs for the conversion of **1**→**2**→**3** match each other quite well, except for what appears to be a slight incubation period in the conversion of **2** into **3** in the first run. As this reaction was run in a two-step, one-pot sequence, there is some delay in the conversion of **2** into **3** because the former is formed in situ. In contrast, the second set of data for the conversion of **2** into **3** come from the one-pot reaction of **2**→**3**→**4**. In this case, **2** is present at the outset and there is therefore no delay in its conversion. The second set of data for the conversion of **1** into **2** come from the single reaction **1**→**2** using the acid resin catalyst recovered from the one-pot reaction of **1**→**2**→**3**.

[14] No kinetic data were collected for the conversion of **1** into **5a** and **5b** or into **6a** and **6b**. Consequently, no reliable TOF values were obtained.

[15] Recently, Leitner and co-workers demonstrated that polymer-supported Rh complexes can be effectively recovered and reused in a sequence of different reactions through the clever use of miscibility manipulation using supercritical CO_2. They coined the term "cartridge catalysis" for this methodology: M. Solinas, J. Jiang, O. Stelzer, W. Leitner, *Angew. Chem.* **2005**, *117*, 1370; *Angew. Chem. Int. Ed.* **2005**, *44*, 2291.

[16] For production purposes, high-throughput approaches to multistep catalytic reactions based on a) membranes or b) fixed beds are also promising: a) B. B. Lakshmi, C. R. Martin, *Nature* **1997**, *388*, 758; b) A. M. Hafez, A. E. Taggi, T. Dudding, T. Lectka, *J. Am. Chem. Soc.* **2001**, *123*, 10853.

 © 2006 Wiley-VCH Verlag GmbH & Co. KGaA, Weinheim

Membrane Protein Imaging

DOI: 10.1002/anie.200503915

Imaging Proteins in Membranes of Living Cells by High-Resolution Scanning Ion Conductance Microscopy**

Andrew I. Shevchuk, Gregory I. Frolenkov, Daniel Sánchez, Peter S. James, Noah Freedman, Max J. Lab, Roy Jones, David Klenerman, and Yuri E. Korchev**

Advances in imaging and microscopy have driven many discoveries in biology over the past century. Electron-microscopy-based techniques (for example, freeze-fracture, freeze-etching, and/or immunogold labeling[1]) have provided a wealth of evidence that cell plasma membranes are organized into structural and functional microdomains.[2] However, these techniques are only applicable to fixed or frozen cells, thereby precluding live imaging of functionally important membrane structures in living cells. Lower-resolution optical methods such as fluorescent-molecule video imaging[3] and single-particle tracking of gold-conjugated ligands[4] have been used successfully to follow the dynamics of specific molecules in the plasma membrane of living cells. The disadvantage of these tracking methods is that they require labeling and hence do not image the relative position of the

[*] Dr. D. Klenerman
Department of Chemistry, Cambridge University
Cambridge, CB2 1EW (UK)
Fax: (+44) 1223-336-362
E-mail: dk10012@cam.ac.uk

Dr. A. I. Shevchuk, Dr. D. Sánchez, Prof. Dr. M. J. Lab, Prof. Dr. Y. E. Korchev
Division of Medicine, Imperial College London
MRC Clinical Sciences Centre
London W12 0NN (UK)
Fax: (+44) 208-383-8306
E-mail: y.korchev@ic.ac.uk

Dr. G. I. Frolenkov
Department of Physiology, University of Kentucky
MS-508, Chandler Medical Center
800 Rose Street, Lexington, KY 40536-0298 (USA)

P. S. James, Dr. R. Jones
Laboratory of Molecular Signalling
The Babraham Institute
Cambridge, CB2 4AT (UK)

N. Freedman
Ionscope Limited
The London BioScience Innovation Centre
2 Royal College Street, London NW1 0NH (UK)

[**] This work was funded by the Biotechnology and Biological Sciences Research Council (UK). The development of the high-resolution scanning ion conductance microscopy instrument was performed in collaboration with Ionscope Limited (UK).

Supporting information for this article is available on the WWW under http://www.angewandte.org or from the author.

WILEY InterScience DISCOVER SOMETHING GREAT
© 2006 Wiley-VCH Verlag GmbH & Co. KGaA, Weinheim

tagged reporter with respect to the surrounding proteins and other membrane structures.

In contrast to the techniques above, scanning probe microscopy (SPM) does not require extensive specimen preparation and potentially could be used for high-resolution imaging in living cells. The most developed version of these techniques, atomic force microscopy (AFM), can image proteins on hard substrates and has also been successfully applied for imaging living cells,[5,6] but so far it has not been possible to achieve molecular resolution on the surface of living cells. This is due to difficulties in controlling the probe–sample separation over the soft and responsive cell surface. However, a special form of SPM, scanning ion conductance microscopy (SICM), originally developed by Hansma and co-workers,[7] has been successfully adapted by us for living-cell imaging.[8]

SICM is based on a scanned nanopipette and uses the ion current that flows between an electrode in the pipette and a bath electrode for feedback control of the pipette–sample distance. This distance is maintained at the pipette inner radius during the scan, thereby allowing noncontact imaging of the cell surface in physiological buffer with a resolution determined by the pipette inner radius.[9,10] Essentially there is a hemisphere, with the same radius as the pipette inner radius, centered at the pipette tip that senses the surface by reduction in the flow of ion current. Unlike the situation in AFM, this means that the sensing is both vertically under the pipette and also laterally, thereby helping to prevent the pipette walls from touching the cell surface.

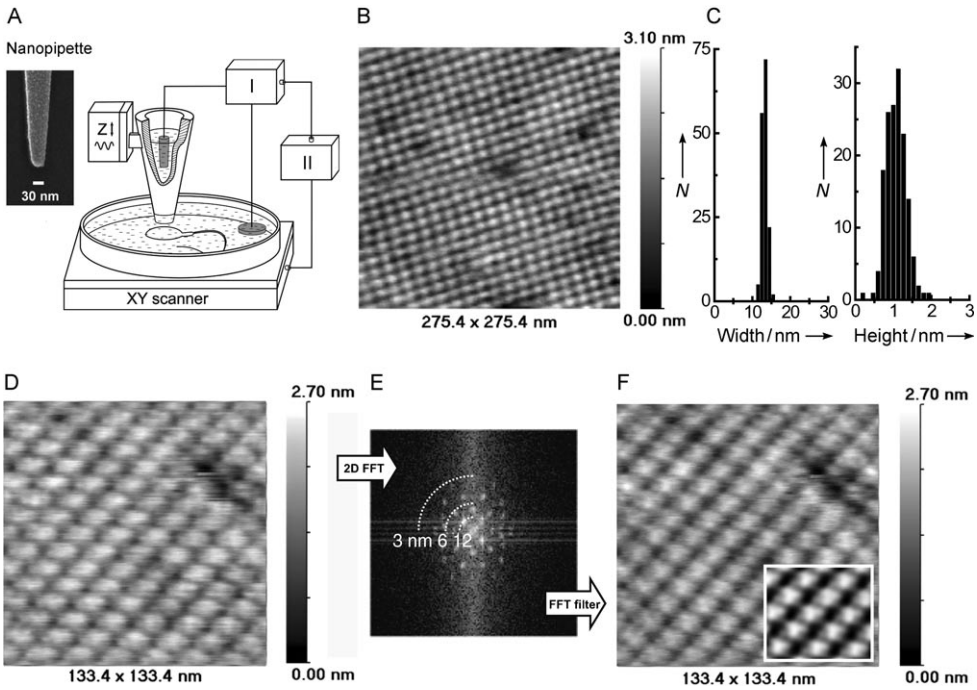

Figure 1. Verification of the SICM resolution by direct imaging of single proteins. A) Schematic diagram of the high-resolution SICM experimental setup (I: ion-current amplifier; II: scanner control). For details see text. The inset shows an SEM image of the tip of a typical nanopipette used for SICM imaging. B) A typical raw SICM image of the S-layer protein of *Bacillus sphaericus* on a mica surface. C) S-layer protein width and height distributions based on SICM measurements. D) Smaller-range SICM scan of the S-layer protein. E) 2D FFT of the image in (D). F) FFT-filtered image produced from (D) by selecting nine pairs of spots in the power spectrum in (E). The inset shows the correlation-averaged image of S-layer proteins calculated from the FFT-filtered data.

Herein, we describe scanning that utilizes very narrow quartz pipettes with an inner diameter of the tip of about 13 nm. The extremely small diameter of the pipettes, custom-designed software, and enhanced mechanical stability of the system have allowed us to improve the resolution of SICM[8] by an order of magnitude. We demonstrate this by imaging individual proteins crystallized on a flat surface or protruding at the external surface of the plasma membrane of a living cell (spermatozoon), whilst maintaining the noncontact advantage of SICM. These advances have made it possible to directly image protein complexes in the membrane of a living cell.

Figure 1 A shows a schematic diagram of the experimental setup. The scanning nanopipette is mounted on a computer-controlled piezo device that provides motion in the vertical direction. The position of the pipette relative to the sample strongly influences the ion current flowing through the pipette; this is then measured by a current amplifier. The pipette's vertical position is then readjusted by the computer to maintain constant nanopipette tip–sample separation, at approximately one pipette radius from the surface, by using the amplified ion current as the feedback signal. The topographical image is generated by measuring the movements of the pipette in the z direction, as the sample is raster-scanned under the pipette in the x and y directions. A quantitative analysis shows that the opening of an ion channel underneath the pipette has a negligible effect on the topography measured (see the Supporting Information).The apparent outer diameter of the tip of the typical quartz nanopipette used for SICM imaging was about 30 nm (including a 2.5-nm platinum coating), as observed by scanning electron microscopy (SEM; Figure 1 A, inset). Assuming that the inner/outer diameter ratio of the capillary template is preserved during the pulling process, we estimate the inner diameter of the quartz pipette tip to be about 12.5 nm.

The SICM resolution was determined by imaging a monolayer of S-layer (cell surface layer) proteins from *Bacillus sphaericus* CCM 2177 on a mica surface (Figure 1 B). The monolayer consists of identical 120-kDa protein subunits, 13.1 nm apart, arranged in a square lattice. Individual protein molecules are clearly identifiable in the unprocessed SICM image and we could also detect the occasional protein missing from the array. Repeated scans of the sample gave identical images, a result indicating that the nanopipette is not

 © 2006 Wiley-VCH Verlag GmbH & Co. KGaA, Weinheim

disrupting the protein layer. A statistical analysis of the width and height of the proteins showed a narrow distribution of widths centered at (13.19 ± 0.04) nm (Figure 1C). This is in good agreement with previous measurements of 13.1 nm for the S-layer protein lattice spacing.[11,12] The pipette is too wide to enter the holes in the lattice and hence it can only record the tops of the protein subunits, thereby measuring a height change of (1.058 ± 0.013) nm.[11]

A higher-resolution unprocessed SICM image is shown in Figure 1D and a computed two-dimensional fast Fourier transform (FFT) of this image is shown in Figure 1E. The dashed-line quarter circles mark spatial frequencies corresponding to 12, 6, and 3 nm resolution, respectively. The spatial frequency at which it is still possible to see distinct features can be used to estimate the SICM resolution. Since there are discrete spots between the 3 and 6 nm rings this indicates that the lateral resolution is 3–6 nm. After FFT filtering (Figure 1F) and correlation averaging (Figure 1F, inset), it is possible to also identify some structural features of individual S-layer proteins. Similar triangular structures have been observed in processed AFM images by Wetzer et al.[13]

Having established that the technique has sufficient resolution to image individual protein molecules, we then applied it to the plasma membrane of a living specialized cell, a boar spermatozoon. Spermatozoa were chosen as an example of a highly polarized cell whose plasma membrane is compartmentalized into functionally and topographically different domains, known as the anterior acrosome, equatorial segment, equatorial subsegment, postacrosome, midpiece, and principal piece.[14] In order to first characterize the specimen by a proven technique, an SEM image of the equatorial segment of a boar spermatozoon, after a spontaneous acrosome reaction in physiological buffer, was taken, along with a high-resolution image of the subsegment (see the Supporting Information).

Figure 2A shows an SICM image of the head and anterior midpiece of a living boar spermatozoon that has initiated a spontaneous acrosome reaction in physiological buffer. The boxed area in Figure 2A, shown at higher resolution in Figure 2B, corresponds to the equatorial segment and its contained subsegment. SICM images at this resolution are similar to SEM and AFM images and reveal protrusions of similar size. The topographical features shown were not observed in non-acrosome-reacted spermatozoa (Figure 2C), a result that is in good agreement with the fact that the equatorial segment only becomes fusogenic after the acrosome reaction when new antigenic epitopes appear as a result of membrane reorganization.[15,16] At higher resolution, however, on the acrosome-reacted sperm, these protrusions appear as small projecting particles (Figure 2D). There are stable regions that are clearly identifiable in the two scans taken 10 min apart (Figure 2D, examples highlighted with dashed lines).

Analysis of the distribution of the width (Figure 2E) and height (Figure 2F) of the particles revealed two populations. The diameter of the small particles was ≈ 14 nm and of the large particles was ≈ 30 nm (Figure 2E). The heterogeneous nature of the particles is reflected in the frequency distribution of their heights (Figure 2F). The densities of the small and large complexes were 380 and 220 per μm^2, respectively.

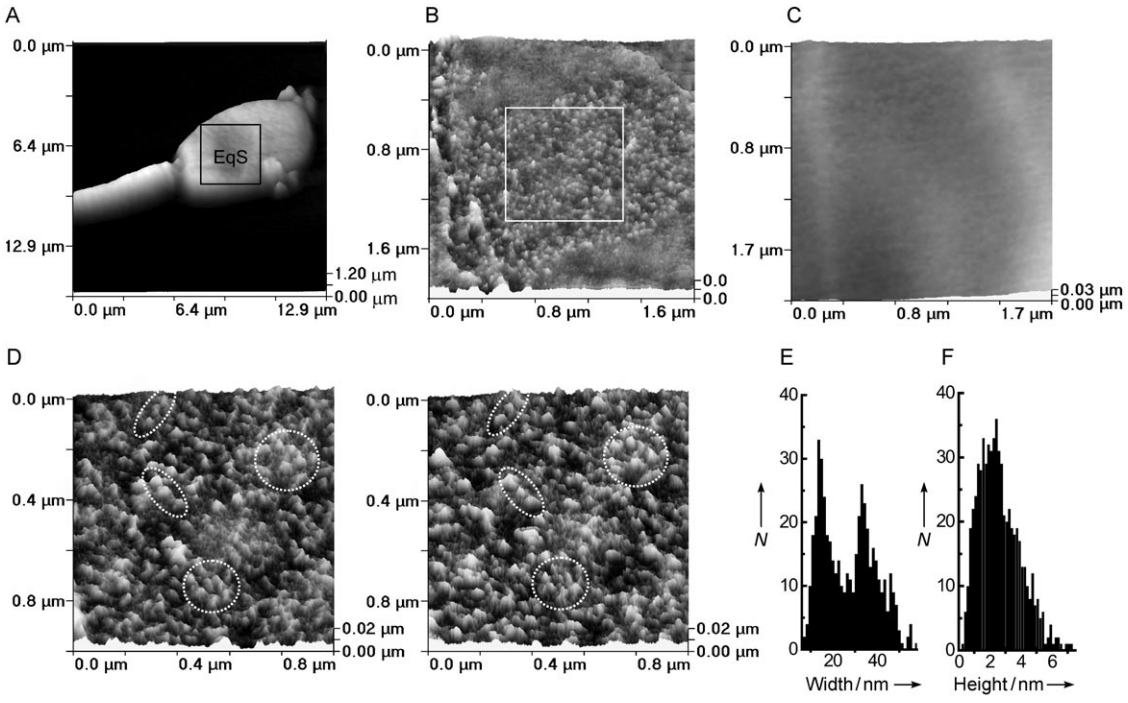

Figure 2. Changes in the organization of protein complexes on the surface of living spermatazoa imaged by SICM. A) Low-resolution SICM image of a boar spermatozoon undergoing a spontaneous acrosome reaction. B) A higher-resolution image of the equatorial segment (EqS) region of the sperm marked in (A) reveals flat and more convoluted areas (subsegments) of the membrane. C) A low-resolution SICM image of a boar spermatozoon prior to the spontaneous acrosome reaction reveals a featureless surface. D) Two consecutive images of the area boxed in (B) recorded 10 min apart. The distribution of E) the widths and F) the heights of individual proteins calculated from various SICM topographical images.

 © 2006 Wiley-VCH Verlag GmbH & Co. KGaA, Weinheim

The particles that we have imaged here are reminiscent of the intramembranous particles (IMPs) described in freeze-fracture studies of boar sperm plasma membranes.[17,18] Two types of IMPs, ≈ 8 nm and > 10 nm in diameter, were present on both the protoplasmic (P) and external (E) faces of the bilayer and were most numerous over the anterior acrosomal and equatorial segment domains. The densities of the smaller and larger IMPs were 670 and 270 per μm^2, respectively, values that are close to the coverage of the proteins estimated by our SICM measurements. IMPs are generally thought to represent transmembrane proteins or protein complexes.[19] Many have been identified as ion channels (for example, the band 3 anion transporter in erythrocytes[20]) or multisubunit receptors (for example, acetylcholine receptors[21]) and found to interact with the cytoskeleton. In this respect, it may be significant that voltage-dependent Ca^{2+} ion channels and actin have been localized to the equatorial segment of boar and human sperm.[22,23] On the basis of their size, density, and distribution, it is likely that most of the features shown in Figure 2D are the topographical images of the external portions of proteins or protein complexes. The differences in size of the IMPs detected by freeze-fracture studies[17] and the proteins seen in the SICM images may reflect the effects of fixation or instrumentation, or both, while the differences in density could be due to the fact that some IMPs do not extend a sufficient distance beyond the outer leaflet of the bilayer to be detectable in the SICM image.

Figure 3A presents topographical images, taken 10 min apart, of an area of membrane where the vast majority of proteins are stable and only two small areas exhibit aggregation (marked with dashed lines). To facilitate visualization of these changes, artificial color was applied to both images, the early one in red and the later image in green. In the overlay image (Figure 3B), yellow color appears in those places where the position and shape of the proteins did not change. Figure 3C and D show areas with fewer stable proteins and provide examples of what appear to be structural (large circle) and orientational (small circle) changes. In Figure 3E and F, lateral shift of a relatively large horseshoe-shaped protein complex (top left, uncircled) is apparent, along with evidence for disassembly (top-right circle) and appearance de novo of other components or fast diffusion (central circle). Note that the majority of proteins remained largely unchanged (yellow color in the overlay images), a result indicating that the illustrated dynamics are not a measurement artifact. Also, in control experiments in which spermatozoa were fixed in 4% formaldehyde, no structural changes or rearrangements were observed over a similar timeframe (data not shown).

Thus, by imaging a living spermatozoon at different time intervals, we have found that some proteins are remarkably stable in position, possibly because they are anchored to the cytoskeleton which permits only reorientation and structural changes. Other proteins disappear from or appear on the

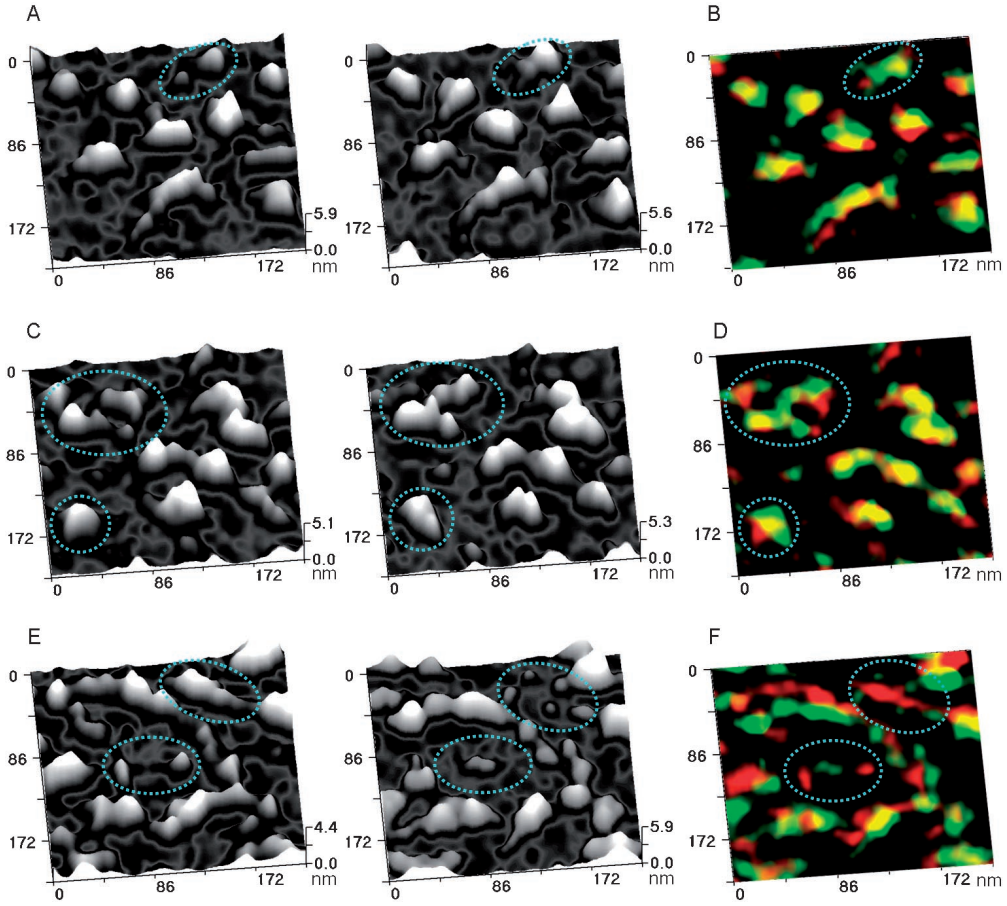

Figure 3. Direct imaging by SICM of the dynamics of single proteins and protein complexes in the membrane overlying the equatorial subsegment (representative zoomed images from Figure 2D). For details of what is shown in A–F, see text.

 © 2006 Wiley-VCH Verlag GmbH & Co. KGaA, Weinheim

external surface of the membrane, thereby suggesting removal, insertion, or very fast diffusion[24] that is beyond the current temporal resolution of SICM. Immobile membrane proteins have been postulated as diffusion barriers on cell surfaces.[4] Our measurements provide evidence for these immobile proteins. These experiments demonstrate that SICM can follow changes in the structure of the surface of living cells at the resolution of individual protein complexes. There is a trade-off between scan speed and image quality in these experiments; hence, imaging of smaller regions and improvements such as modulation at higher frequency should allow faster events to be imaged.

In summary, we have shown that SICM can be performed at a sufficient resolution on living cells to image fixed or slowly diffusing individual protein complexes in the plasma membrane and to follow their reorganization over time. In general such proteins are likely to be present on highly structured cells where specific functions are associated with particular specialized regions or domains. The capability to image living cells at a resolution sufficient for the identification of protein complexes, directly and without labeling, opens up a wealth of new possibilities in membrane biology, such as the spatial mapping of slowly diffusing proteins (for example, ion channels) and the direct imaging of the organization of microdomains or diffusion barriers.

Received: November 4, 2005
Published online: February 28, 2006

Keywords: cells · imaging · membrane proteins · membranes · scanning probe microscopy

[1] P. Rock, M. Allietta, W. W. Young, Jr., T. E. Thompson, T. W. Tillack, *Biochemistry* **1990**, *29*, 8484 – 8490.
[2] K. Simons, E. Ikonen, *Nature* **1997**, *387*, 569 – 572.
[3] G. J. Schutz, M. Sonnleitner, P. Hinterdorfer, H. Schindler, *Mol. Membr. Biol.* **2000**, *17*, 17 – 29.
[4] K. Murase, T. Fujiwara, Y. Umemura, K. Suzuki, R. Iino, H. Yamashita, M. Saito, H. Murakoshi, K. Ritchie, A. Kusumi, *Biophys. J.* **2004**, *86*, 4075 – 4093.
[5] A. Sharma, K. I. Anderson, D. J. Muller, *FEBS Lett.* **2005**, *579*, 2001 – 2008.
[6] M. K. Tsilimbaris, E. Lesniewska, S. Lydataki, C. Le Grimellec, J. P. Goudonnet, I. G. Pallikaris, *Invest. Ophthalmol. Visual Sci.* **2000**, *41*, 680 – 686.
[7] P. K. Hansma, B. Drake, O. Marti, S. A. Gould, C. B. Prater, *Science* **1989**, *243*, 641 – 643.
[8] Y. E. Korchev, C. L. Bashford, M. Milovanovic, I. Vodyanoy, M. J. Lab, *Biophys. J.* **1997**, *73*, 653 – 658.
[9] Y. E. Korchev, M. Milovanovic, C. L. Bashford, D. C. Bennett, E. V. Sviderskaya, I. Vodyanoy, M. J. Lab, *J. Microsc.* **1997**, *188*, 17 – 23.
[10] J. Gorelik, A. I. Shevchuk, G. I. Frolenkov, I. A. Diakonov, M. J. Lab, C. J. Kros, G. P. Richardson, I. Vodyanoy, C. R. Edwards, D. Klenerman, Y. E. Korchev, *Proc. Natl. Acad. Sci. USA* **2003**, *100*, 5819 – 5822.
[11] E. S. Gyorvary, O. Stein, D. Pum, U. B. Sleytr, *J. Microsc.* **2003**, *212*, 300 – 306.
[12] N. Ilk, C. Vollenkle, E. M. Egelseer, A. Breitwieser, U. B. Sleytr, M. Sara, *Appl. Environ. Microbiol.* **2002**, *68*, 3251 – 3260.
[13] B. Wetzer, D. Pum, U. B. Sleytr, *J. Struct. Biol.* **1997**, *119*, 123 – 128.
[14] D. J. Ellis, S. Shadan, P. S. James, R. M. Henderson, J. M. Michael Edwardson, A. Hutchings, R. Jones, *J. Struct. Biol.* **2002**, *138*, 187 – 198.
[15] H. Takano, R. Yanagimachi, U. A. Urch, *Zygote* **1993**, *1*, 79 – 91.
[16] C. A. Allen, D. P. Green, *J. Cell Sci.* **1995**, *108*, 767 – 777.
[17] F. Suzuki-Toyota, Y. Itoh, K. Naito, *Dev. Growth Differ.* **2000**, *42*, 265 – 273.
[18] F. W. Kan, D. S. Pinto, *J. Histochem. Cytochem.* **1987**, *35*, 1069 – 1078.
[19] D. S. Friend, L. Orci, A. Perrelet, R. Yanagimachi, *J. Cell Biol.* **1977**, *74*, 561 – 577.
[20] T. Inoue, A. Kanzaki, A. Yawata, A. Tsuji, K. Ata, N. Okamoto, H. Wada, I. Higo, T. Sugihara, O. Yamada, *Int. J. Hematol.* **1994**, *59*, 157 – 175.
[21] A. G. Yee, G. D. Fischbach, M. J. Karnovsky, *Proc. Natl. Acad. Sci. USA* **1978**, *75*, 3004 – 3008.
[22] S. Benoff, *Hum. Fertil.* **1999**, *2*, 42 – 55.
[23] M. Camatini, A. Casale, *Gamete Res.* **1987**, *17*, 97 – 105.
[24] A. E. Cowan, D. E. Koppel, L. A. Vargas, G. R. Hunnicutt, *Dev. Biol.* **2001**, *236*, 502 – 509.

 © 2006 Wiley-VCH Verlag GmbH & Co. KGaA, Weinheim

Host–Guest Systems

DOI: 10.1002/anie.200501639

Magnetic Behavior of a 1D Molecular-Oxygen System Included within a Transformable Single-Crystal Adsorbent**

Satoshi Takamizawa, Ei-ichi Nakata, and Takamasa Akatsuka*

Paramagnetic gas molecules with a $^3\Sigma_g^-$ ground state, of which oxygen is the simplest and most stable, exhibit interesting magnetic properties when incorporated into clathrate compounds.[1] The unusual paramagnetic behavior of included oxygen in a 1D channel of a metal–organic gas adsorbent was reported by Mori et al. in 1997,[2] and caught the attention of theoreticians[3] owing to the interest in oxygen-based Haldane systems.[4] The report, together with the worldwide growth of synthetic studies of gas-adsorbing crystalline microporous metal-complex systems,[5] inspired an analogous experiment by Kitaura et al. in 2002,[6] in which a microporous copper coordination polymer was used as host. In contrast, we

[*] Dr. S. Takamizawa, E. Nakata, T. Akatsuka
International Graduate School of Arts and Sciences
Yokohama City University
Kanazawa-ku, Yokohama, Kanagawa 236-0027 (Japan)
Fax: (+81) 45-787-2187
E-mail: staka@yokohama-cu.ac.jp

[**] This work was financially supported by the Ministry of Education, Culture, Sports, Science and Technology, Japan (Nos. 16750051 and 17036056) and a grant for the 2005 Strategic Research Project (No. K17025) of Yokohama City University.

Supporting information for this article is available on the WWW under http://www.angewandte.org or from the author.

WILEY InterScience DISCOVER SOMETHING GREAT
© 2006 Wiley-VCH Verlag GmbH & Co. KGaA, Weinheim

recently reported the possible effective use of a single-crystal host to observe the exact structure and low-dimensional physical properties of included light-gas guests through the control of gas pressure and temperature.[7] Although we successfully determined the exact oxygen-inclusion crystal structure for the single-crystal adsorbent $[\{M_2(bza)_4(pyz)\}_n]$ (**1**) (bza = benzoate; pyz = pyrazine; M = Rh^{II}, Cu^{II}), the adsorbed oxygen molecules could not be observed by crystallographic analysis at temperatures exceeding 90 K.[7,8] This difficulty is probably caused by the easy diffusion of adsorbed oxygen within the host crystal at higher temperatures. Thus, substitution at the channel surface that can hinder the thermal motion of the adsorbed guests would be advantageous in the observation of guest alignment and physical properties over a wide temperature range.

To modify the channel surface, we synthesized the methyl-substituted pyrazine analogue $[\{Rh^{II}_2(bza)_4(2\text{-mpyz})\}_n]$ (**2**) (2-mpyz=2-methylpyrazine) with the same method used to prepare **1**.[9,10] The single crystals obtained consisted of infinite 1D coordination-polymer skeletons formed by 2-mpyz links in the axial direction of the dinuclear rhodium benzoate core. Oxygen-inclusion crystals of **2** were generated by the forcible gas-adsorption method under about 1.0 MPa pressure at room temperature. X-ray crystallographic measurements were performed over a wide temperature range (10–298 K).[11–14] Surprisingly, the adsorbed oxygen molecules could be observed even at room temperature (see Supporting Information). On cooling to 190 K, these molecules appeared as a saturated inclusion state with the chemical composition **2**·3 O_2, which is very similar to that of **1** without guests at room

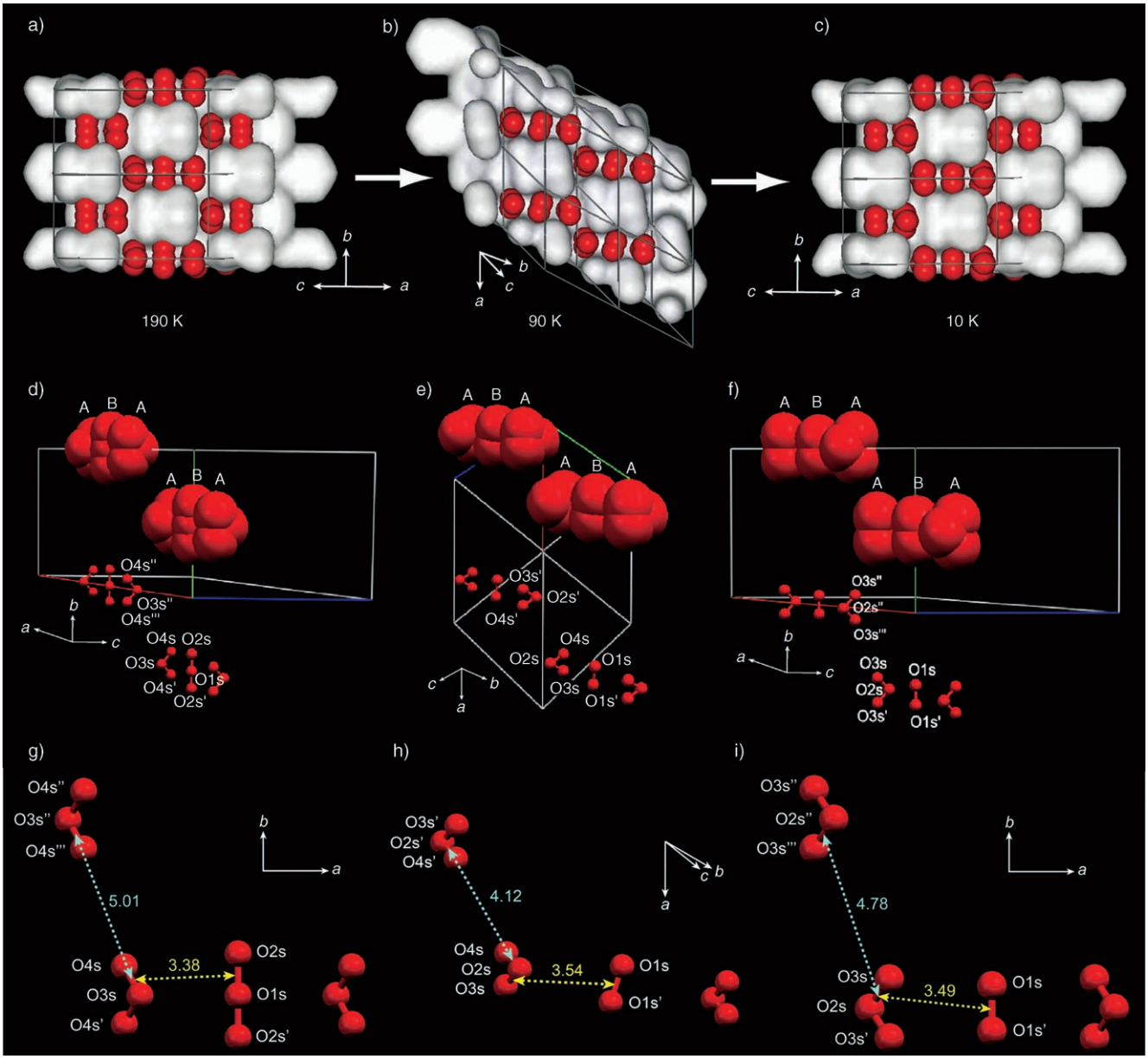

Figure 1. Temperature-induced phase transitions of inclusion crystal **2**·3 O_2 ($C2/m$ at 190 K, $P\bar{1}$ at 90 K, and $C2/m$ at 10 K): a)–c) Crystal intersection views; d)–f) oxygen arrangement; g)–i) magnified units with shortest intermolecular distances (Å) extracted from (a)–(c). a),d),g) 190 K; b),e),h) 90 K; c),f),i) 10 K.)

 © 2006 Wiley-VCH Verlag GmbH & Co. KGaA, Weinheim

temperature.[15] These results demonstrate that substitution on the channel surface is beneficial for the observation of light guests with crystallography, probably because of contact between the methyl moieties on the pyrazine rings and the oxygen molecules at position A (Figure 1).

As the temperature was decreased, X-ray crystallographic analysis clearly showed crystal-phase transitions. The crystal structures determined were classified into three temperature phases based on the symmetry of the host lattice: high, $C2/m$ (298 K, 190 K); middle, $P\bar{1}$ (90 K); and low, $C2/m$ (10 K). The middle phase with the triclinic $P\bar{1}$ space group is formed abruptly, sandwiched by the phases with the monoclinic $C2/m$ space group (Figure 1). As the high- and low-temperature phases are similar, the middle $P\bar{1}$ phase can be regarded as a wedged-crystal phase, in which the structures of the inner space are transformed from isolated cages to connected 1D channels. This suggests that the host transformation could be caused by the transformation of the guest aggregate.

From the point of view of the guest-oxygen arrangement, the structure of the inclusion compound is changed significantly by the transformation of the inner space (Figure 1 and Table 1). In all three phases, the oxygen molecules construct an $O_2(A)\cdots O_2(B)\cdots O_2(A)$ periodic trimer unit with the molecular axis perpendicular to the long axis of the inner spaces and located at the position of the "twist" among the neighbors.[16] The intratrimer distance $O_2(A)\cdots O_2(B)$ was found to increase with decreasing temperature; the shortest interatomic (intermolecular) distances were 3.40 (3.38), 3.42 (3.54), and 3.50 (3.49) Å at 190 K, 90 K, and 10 K, respectively. In contrast, intertrimer distances $O_2(A)\cdots O_2(A')$ were 4.71 (5.01), 4.00 (4.12), and 4.07 (4.78) Å at 190 K, 90 K, and 10 K, respectively, which means that the intertrimer distances go through a minimum at about 90 K (Table 1 and Figure 3). The structural difference demonstrates that the oxygen alignment in the middle $P\bar{1}$ crystal phase is more one-dimensional than the discrete trimers of the other two phases.

As for the temperature dependence of the magnetic susceptibility of the included oxygen in **2**, an almost continuous curve was observed at a magnetic field of 1×10^4 Oe (lowest trace in Figure 2a). This magnetic behavior is completely different from that of bulk solid oxygen. $M(O_2)T$ plateaus with a maximum value of 0.84 emu mol^{-1} Oe K ($\mu_{eff}=2.6$ BM) between 50 and 140 K, which is less than the 1.00 emu mol^{-1} Oe K ($\mu_{eff}=2.83$ BM) expected for the free $S=1$ spin state, thus indicating a weak antiferromagnetic interaction among the included oxygen molecules; $M(O_2)T$ then gradually decreases at temperatures below 50 K (Figure 2a, inset, lowest trace). The estimated Weiss constants θ for the $\chi_M(O_2)^{-1}$ versus T curve are -16.85 K (12–52 K) and -8.64 K (54–104 K) (see Supporting Information). It seems natural to consider $z=4/3$ in accord with the trimer structure observed by X-ray crystallographic analysis, which gave an exchange constant J/k_B of -11.2 K (12–52 K) and -5.6 K (54–104 K), respectively.[17] The decrease in the MT versus T curve above 140 K was probably caused by the desorption of the included oxygen.

As the applied field was increased, a different magnetic state grew in the middle temperature region (54–104 K), whereas the outer temperature regions were only slightly influenced by the magnitude of the magnetic field (Figure 2a). This temperature region displays nonlinearity in the relationship between the magnetization and the applied magnetic field, which can be clearly observed in the M versus T and MT versus T curves at various fields (Figure 2a). Because the boundary temperature is independent of the magnetic field and corresponds to the crystal phase transition,

Table 1: Pertinent interatomic distances among neighboring oxygen molecules.

T [K]	190		90		10	
Space group	$C2/m$		$P\bar{1}$		$C2/m$	
V/Z [Å^3]	891		868.7		845.0	
O–O [Å]	O(1s)–O(2s)*[a]	1.149(7)	O(1s)–O(1s′)$^{\#1}$	1.145(4)	O(1s)–O(1s′)$^{\#1}$	1.143(9)
	O(3s)–O(4s)*	1.143(9)	O(2s)–O(3s)*	1.148(17)	O(2s)–O(3s)*	1.142(9)
			O(2s)–O(4s)*	1.147(9)		
Intratrimer $O_2(A)\cdots O_2(B)$ [Å]	O(1s)–O(3s)	3.40(4)	O(1s)–O(2s)	3.74(4)	O(1s)–O(2s)	3.55(2)
	O(1s)–O(4s)*	3.50(5)	O(1s)–O(3s)*	3.77(3)	O(1s)–O(3s)*	3.50(4)
	O(1s)–O(4s′)*$^{\#1}$	3.50(5)	O(1s)–O(4s)*	3.72(4)	O(1s)–O(3s′)*$^{\#2}$	3.73(3)
	O(2s)*–O(3s)	3.59(4)	O(1s′)$^{\#1}$–O(2s)	3.58(4)		
	O(2s)*–O(4s)*	3.43(5)	O(1s′)$^{\#1}$–O(3s)*	3.42(3)		
	O(2s)*–O(4s′)*$^{\#1}$	3.92(5)	O(1s′)$^{\#1}$–O(4s)*	3.67(4)		
Intertrimer $O_2(A)\cdots O_2(A')$ [Å]	O(3s)–O(3s″)$^{\#2}$	5.52(4)	O(2s)–O(2s′)$^{\#2}$	4.55(8)	O(2s)–O(2s″)$^{\#3}$	5.64(2)
	O(3s)–O(4s″)*$^{\#2}$	5.00(5)	O(2s)–O(3s′)*$^{\#2}$	4.97(4)	O(2s)–O(3s″)*$^{\#3}$	4.78(3)
	O(3s)–O(4s‴)*$^{\#3}$	6.35(5)	O(2s)–O(4s′)*$^{\#2}$	4.13(5)	O(2s)–O(3s‴)*$^{\#4}$	6.09(3)
	O(4s)*–O(4s″)*$^{\#2}$	4.71(11)	O(3s)*–O(3s′)*$^{\#2}$	5.59(4)	O(3s)*–O(3s″)*$^{\#3}$	4.07(7)
	O(4s)*–O(3s″)*$^{\#2}$	5.00(5)	O(3s)*–O(4s′)*$^{\#2}$	4.76(5)	O(3s)*–O(3s‴)*$^{\#4}$	5.34(3)
	O(4s′)* $^{\#1}$–O(4s‴)*$^{\#3}$	7.26(9)	O(4s)*–O(4s′)*$^{\#2}$	4.00(9)	O(3s′)*$^{\#2}$–O(3s‴)*$^{\#4}$	6.71(7)

[a] *50% occupancy atom. The atomic labels correspond to those in Figure 1. Symmetry codes for 190 K: #1(x, 1−y, z), #2(1.5−x, 0.5−y, 2−z), #3(1.5−x, 1.5+y, 2−z); for 90 K: #1(1−x, 1−y, 2−z), #2(1−x, −y, 2−z); for 10 K: #1(1−x, −y, 2−z), #2(x, −y, z), #3(0.5−x, −0.5−y, 2−z), #4(0.5−x, −0.5+y, 2−z).

 © 2006 Wiley-VCH Verlag GmbH & Co. KGaA, Weinheim

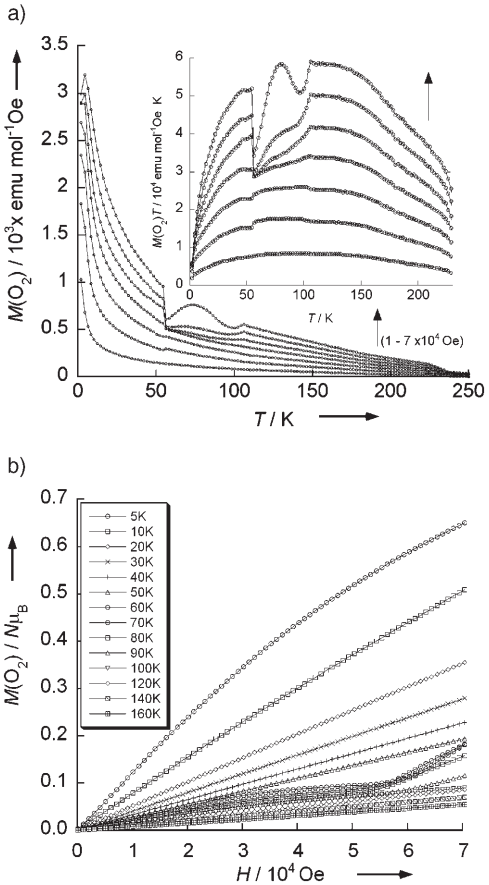

Figure 2. Temperature dependence of magnetic behavior of included O_2 in **2**: a) M versus T and MT versus T (inset) curves under various magnetic fields (1–7×10^4 Oe at 1×10^4-Oe intervals); b) magnetization curves. The temperatures for (b) are 5 K, 10–100 K at 10-K intervals, and 100–160 K at 20-K intervals. Calculation of the molar magnetization $M(O_2)$ was based on the mass of crystal **2** with the saturated formula of **2**·3 O_2.

the three observed temperature regions in the magnetic behavior correlate with the temperature-induced phase transitions of the included oxygen aggregates. The spin correlation of included oxygen is depicted in Figure 3 with both observed and calculated J/k_B values. The calculations were made by correlating the experimental decay with the increase in intermolecular distance R, which is applicable for bulk solid oxygen.[18] The values of J_{calcd}/k_B are in good agreement with J_{obs}/k_B, which demonstrates the validity of

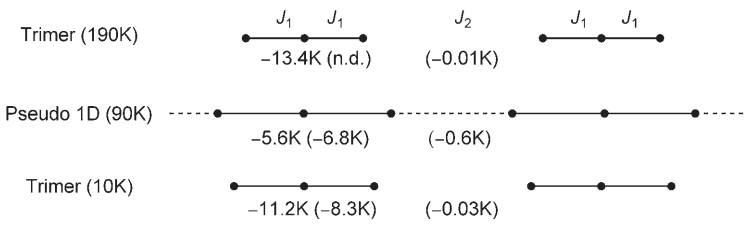

Figure 3. Magnetic exchange correlation for the three temperature phases of the oxygen-inclusion system. The depicted values denote J_{obs}/k_B (J_{calcd}/k_B). The experimental J_{obs}/k_B was obtained from the Weiss constant and the calculated J_{calcd}/k_B was estimated by using the empirical correlation with intermolecular distance in crystallography (see main text).

estimating J values by using intermolecular distances. The intertrimer J_{calcd}/k_B values indicate that the magnetic structure is an isolated trimer in the high- and low-temperature $C2/m$ phases, whereas in the middle $P\bar{1}$ phase it can be treated as a pseudo-1D chain in connecting neighboring trimers with weak antiferromagnetic couplings of ≈1 K.[19] Although the description of the relationship between the arrangement of the oxygen molecules and the magnetic interaction for the three temperature phases is valid, the magnetic dependency on the magnetic field could not be explained. The M versus H curves in Figure 2b show the bend in the magnetization curves at about 6×10^4 Oe in the middle-temperature region. Given the weak exchange interaction and the low energy scale of ≈8 K at the point of inflection, the temperatures in this region are too high to allow the observed abnormal behavior. There is thus a need to consider other factors.

In the M versus H curves, hysteresis loops, which close at zero magnetic field, were only observed in the middle phase (Figure 4). As the reversing point changed at 60 K, the hysteresis began to appear after the inflection point was

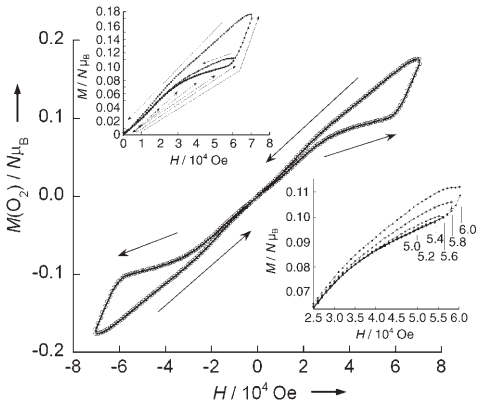

Figure 4. Magnetization curves of included O_2 in **2** at 60 K. Insets: The returning magnitude of H increases in 1×10^4-Oe steps from 1×10^4 to 7×10^4 Oe (upper) and in 0.2×10^4-Oe steps from 5×10^4 to 6×10^4 Oe (bottom). Hysteresis loops were observed at fields greater than 5.4×10^4 Oe.

passed, indicating a critical magnetic field of 5.6×10^4 Oe (Figure 4 inset). The three magnetic regions correspond to the three temperature phases of the included-oxygen system. In comparing the boundary temperatures of **2**·3 O_2 of 54 K ($T_{low–middle}$) and 104 K ($T_{middle–high}$) with the phase-transition temperatures of bulk oxygen of 54.8 K (T_{mp}) and 90.2 K (T_{bp}), the state of the included oxygen can be understood in terms of the gas, liquid, and solid states of bulk oxygen. This raises the likelihood that the structural phase transitions of the included-oxygen system are temperature-induced, and the middle-temperature phase is a mesophase, between solid and fluid states. The boundary temperatures indicate gas-adsorption saturation at $T_{middle–high}$ by reaching the saturated vapor pressure of the surrounding oxygen gas, and solidification at $T_{low–middle}$ through 3D ordering by intermolecular interactions through the separating host walls. Thus, the

 © 2006 Wiley-VCH Verlag GmbH & Co. KGaA, Weinheim

state of the included-oxygen aggregates can be categorized into three phases: 1) a high-temperature phase that has a gas adsorption equilibrium state with diffusion under unsaturated conditions; 2) a middle-temperature phase that has a saturated condition with high flexibility, which can have an "inclusion plastic crystal" nature;[20] 3) a low-temperature phase that has a 3D ordered cocrystal state. Consequently, the abnormal magnetic behavior of the middle-temperature phase could be explained by the fluctuation of its "soft" arrangement to reach the most stable configuration in the presence of an external magnetic field. The critical magnetization point may induce the relatively large motion of the guest oxygen, which is consistent with the observed closed hysteresis loop at the origin caused by slow relaxation of the structural rearrangement process once the critical magnetic field is passed. The observed bent magnetization curve probably indicates that the configuration changes to enhance antiferromagnetic interaction by the increase of the magnetic field up to the critical point and its rapid weakening after passing the point. There is also the possibility of a slight change in the magnetic correlation in the middle phase caused by a change in temperature.

In summary, this is the first successful attempt at capturing both the crystal structures and the magnetic behavior of included oxygen over a wide temperature range, which showed the temperature-induced phase transition of included oxygen from a trimer to a pseudo-1D chain system inside the crystal channels of **2**. Furthermore, the middle-temperature phase displays an abnormal sensitivity to external magnetic fields that is probably the result of the structural flexibility of the paramagnetic molecular-oxygen chain. This method has the potential for advancing the experimental study of low-dimensional physicochemical properties in generating real low-dimensional molecular/atomic aggregates/clusters with various degrees of structural freedom under the control of arrangement dimensionality. This would improve the observation of specific quantum effects by signal enhancement to perceptible bulk levels.

Experimental Section

All single-crystal X-ray analyses were performed on a Bruker Smart APEX CCD area diffractometer with a helium-flow temperature controller (Japan Thermal Eng. TC-10 KCP) and graphite-monochromated $Mo_{K\alpha}$ radiation ($\lambda = 0.71073$ Å). A single crystal of **2** was sealed in a glass capillary containing liquid oxygen in a liquid-nitrogen bath. The inner pressure at room temperature was estimated by the ratio of the volumes of liquid oxygen and inner space, giving 1.0 MPa at room temperature. Empirical absorption corrections were applied by using the SADABS program. The structures were solved by direct methods (SHELXS-97) and refined by full-matrix least-squares calculations on F^2 (SHELXL-97) with the SHELX-TL program package. Non-hydrogen atoms were refined anisotropically; hydrogen atoms were fixed at calculated positions and refined with a riding model. CCDC-271313–271316 contain the supplementary crystallographic data for this paper. These data can be obtained free of charge from The Cambridge Crystallographic Data Centre via www.ccdc.cam.ac.uk/data_request/cif.

Magnetic measurements were performed on a SQUID magnetometer (Quantum Design MPMS-XL). Crystals of **2** were packed in a glass tube with pressurized oxygen gas at room temperature (2.0 MPa). The glass cell has a mechanism that can separate the condensed excess oxygen from the crystals of **2**. Calculation of the molar magnetization and susceptibility of included oxygen was based on the mass of **2** with the chemical composition of $\mathbf{2}\cdot 3O_2$ after deducting the trace background values of cell and host crystal **2**.

Received: May 12, 2005
Revised: December 12, 2005
Published online: March 2, 2006

Keywords: host–guest systems · magnetic properties · phase transitions · solid-state structures · X-ray diffraction

[1] a) D. F. Evans, R. E. Richards, *Nature* **1952**, *169*, 246; b) A. H. Cooke, H. Meyer, W. P. Wolf, *Proc. R. Soc. London Ser. A* **1957**, *225*, 112.
[2] a) W. Mori, T. C. Kobayashi, J. Kurobe, K. Amaya, Y. Narumi, T. Kumada, K. Kindo, H. A. Katori, T. Goto, N. Miura, S. Takamizawa, H. Nakayama, K. Yamaguchi, *Mol. Cryst. Liq. Cryst.* **1997**, *306*, 1; b) W. Mori, S. Takamizawa in *Organometallic Conjugation* (Eds.: A. Nakamura, N. Ueyama, K. Yamaguchi), Kodansha Springer, Tokyo, **2002**, chap. 6, pp. 179–213.
[3] a) M. Okumura, S. Yamanaka, W. Mori, K. Yamaguchi, *THEOCHEM* **1994**, *116*, 177; b) M. Otani, H. Miyagi, N. Suzuki, *Phys. B* **1999**, *265*, 60; c) T. Kawakami, S. Takamizawa, Y. Kitagawa, T. Maruta, W. Mori, K. Yamaguchi, *Polyhedron* **2001**, *20*, 1197.
[4] F. D. M. Haldane, *Phys. Lett. A* **1983**, *93*, 464.
[5] a) M. Fujiwara, K. Seki, W. Mori, S. Takamizawa, Patent No. JP 09132580, **1995**, M. Fujiwara, K. Seki, W. Mori, S. Takamizawa, Patent No. EP 0727608, **1996**; b) W. Mori, F. Inoue, K. Yoshida, H. Nakayama, S. Takamizawa, M. Kishita, *Chem. Lett.* **1997**, 1219; c) M. Kondo, T. Yoshitomi, K. Seki, H. Matsuzaka, S. Kitagawa, *Angew. Chem.* **1997**, *109*, 1844; *Angew. Chem. Int. Ed. Engl.* **1997**, *36*, 1725; d) H. Li, M. Eddaoudi, T. L. Groy, O. M. Yaghi, *J. Am. Chem. Soc.* **1998**, *120*, 8571.
[6] R. Kitaura, S. Kitagawa, Y. Kubota, T. C. Kobayashi, K. Kindo, Y. Mita, A. Matsuo, M. Kobayashi, H.-C. Chang, T. Ozawa, M. Suzuki, M. Sakata, M. Takata, *Science* **2002**, *298*, 2358.
[7] S. Takamizawa, E. Nakata, T. Saito, *Angew. Chem.* **2004**, *116*, 1392; *Angew. Chem. Int. Ed.* **2004**, *43*, 1368.
[8] S. Takamizawa, E. Nakata, T. Saito, T. Akatsuka, K. Kojima, *Cryst. Eng. Comm.* **2004**, *6*, 197.
[9] S. Takamizawa, T. Hiroki, E. Nakata, K. Mochizuki, W. Mori, *Chem. Lett.* **2002**, 1208.
[10] $[\{Rh_2(bza)_4(2\text{-mpyz})\}_n]$ (**2**) was obtained as red plates in 60.7% yield; elemental analysis: calcd (%): C 50.53, H 3.34, N 3.62; found: C 49.99, H 3.31, N 3.62.
[11] Crystal data for $\mathbf{2}\cdot 3O_2$ at 10 K: 880.35 g mol^{-1}, monoclinic, $C2/m$, $a = 18.768(5)$, $b = 9.563(3)$, $c = 12.483(3)$ Å, $\beta = 131.032(4)°$, $V = 1690.0(8)$ Å^3, $Z = 2$, $\rho_{calcd} = 1.729$ Mg m^{-3}, $R_1 = 0.0975(0.1533)$, $wR_2 = 0.2370(0.2679)$ for 836 reflections with $I > 2\sigma(I)$ (for 1243 reflections (3347 total measured)), goodness-of-fit on $F^2 = 1.177$, largest diff. peak (hole) = 1.299(−1.688) e Å^{-3}.
[12] Crystal data for $\mathbf{2}\cdot 3O_2$ at 90 K: 880.35 g mol^{-1}, triclinic, $P\bar{1}$, $a = 9.621(3)$, $b = 10.560(3)$, $c = 10.739(3)$ Å, $\alpha = 71.830(6)$, $\beta = 64.110(5)$, $\gamma = 63.428(5)°$, $V = 868.7(4)$ Å^3, $Z = 1$, $\rho_{calcd} = 1.682$ Mg m^{-3}, $R_1 = 0.0892(0.1935)$, $wR_2 = 0.1483(0.1932)$ for 1363 reflections with $I > 2\sigma(I)$ (for 2831 reflections (3934 total measured)), goodness-of-fit on $F^2 = 0.926$, largest diff. peak (hole) = 1.111(−1.578) e Å^{-3}.
[13] Crystal data for $\mathbf{2}\cdot 3O_2$ at 190 K: 880.35 g mol^{-1}, monoclinic, $C2/m$, $a = 18.96(3)$, $b = 9.673(15)$, $c = 12.49(2)$ Å, $\beta = 128.92(3)°$, $V = 1782(5)$ Å^3, $Z = 2$, $\rho_{calcd} = 1.640$ Mg m^{-3}, $R_1 = 0.0733(0.1501)$, wR (0.2392) for 699 reflections with $I > 2\sigma(I)$ (for 1368 reflec-

 © 2006 Wiley-VCH Verlag GmbH & Co. KGaA, Weinheim

tions (3175 total measured)), goodness-of-fit on $F^2 = 0.984$, largest diff. peak (hole) = 0.918(−1.505) e Å^{-3}.

[14] Crystal data for **2**·2 O_2 at 298 K: 848.35 g mol^{-1}, monoclinic, $C2/m$, $a = 18.921(8)$, $b = 9.708(4)$, $c = 12.432(5)$ Å, $\beta = 128.173(8)°$, $V = 1795.1(13)$ Å^3, $Z = 2$, $\rho_{calcd} = 1.569$ Mg m^{-3}, $R_1 = 0.1307$ (0.2453), $wR_2 = 0.2784(0.3521)$ for 406 reflections with $I > 2\sigma(I)$ (for 942 reflections (1909 total measured)), goodness-of-fit on $F^2 = 0.969$, largest diff. peak (hole) = 1.542(−1.364) e Å^{-3}.

[15] S. Takamizawa, E. Nakata, H. Yokoyama, K. Mochizuki, W. Mori, *Angew. Chem.* **2003**, *115*, 4467; *Angew. Chem. Int. Ed.* **2003**, *42*, 4331.

[16] O_2(A) shows disordered structure in all phases, whereas O_2(B) is only disordered in that at 190 K, which may be reflected from thermal motion (see Supporting Information).

[17] Molecular field approximation: $J/k = 3\theta/(2zS(S+1))$; z = number of nearest neighbors. The exchange constant J is defined by the Hamiltonian constraint $H = -2J\boldsymbol{S}_i\boldsymbol{S}_j$.

[18] C. Uyeda, K. Sugiyama, M. Date, *J. Phys. Soc. Jpn.* **1984**, *54*, 1107. This describes the correlation for solid oxygen between antiferromagnetic exchange coupling J and intermolecular distance R: $J = J_0 \exp\{-\alpha(R-R_0)\}$ ($J_0/k_B = -30$ K, $\alpha = 4.3$ Å^{-1}, $R_0 = 3.2$ Å).

[19] To understand the magnetic interaction, the configuration of and distance between the oxygen molecules should be considered. The configuration is critical for the sign and magnitude of the magnetic exchange interaction described in reference [3a].

[20] S. Takamizawa, E. Nakata, T. Saito, T. Akatsuka, *Inorg. Chem.* **2005**, *44*, 1362.

 © 2006 Wiley-VCH Verlag GmbH & Co. KGaA, Weinheim

Nanocrystals

DOI: 10.1002/anie.200502538

Colloidal CdSe Nanocrystals Passivated by a Dye-Labeled Multidentate Polymer: Quantitative Analysis by Size-Exclusion Chromatography**

Mingfeng Wang, Tieneke E. Dykstra, Xudong Lou, Mayrose R. Salvador, Gregory D. Scholes, and Mitchell A. Winnik**

Quantum dots are a class of colloidal semiconductor nanocrystals (NCs) that show unique size-dependent optical properties.[1] These materials are of great interest for applications in light-emitting diodes,[2] photovoltaic devices,[3] and biological labels.[4] High-quality NCs of II–VI semiconductor materials such as CdSe and CdTe can be obtained with controlled sizes and shapes through an organometallic approach.[5] These as-prepared NCs, which are chemically passivated by a layer of organic ligands such as tri-*n*-octylphosphine oxide (TOPO), are dispersible only in nonpolar organic solvents and are typically unstable in solution in the absence of excess free ligands.[1b,6] These factors limit their use for biological and material applications. As a consequence, ligand-based functionalization of the NC surface is an essential step to control their physical properties as well as to provide the necessary chemical accessibility and biological functionality.

For this purpose, various polymeric substances such as organic dendrons,[7] linear[8–9] or hyperbranched[10] polymers, chemically-modified proteins,[11] and amphiphilic polymers[12] have been employed to manipulate the surface properties of NCs through a ligand-exchange or micellar encapsulation process. Analytical methods such as dynamic light scattering,[9c,10] gel electrophoresis,[7,9b,12c] fluorescence resonance energy transfer,[9e,11] thermogravimetric analysis,[12b] and atomic force microscopy[13] have been used to characterize the polymer binding on NCs. However, the quantitative analysis of polymeric ligands on NCs still remains a considerable challenge. There are two distinct problems that need to be solved. First, one needs a methodology to separate the NC from free polymer. The polymer is normally added in excess to ensure that the NC surfaces are saturated or encapsulated, and this excess polymer is very difficult to remove from the sample. This problem can in principle be solved by centrifugation or dialysis,[12d] but then one encounters the second problem. One needs analytical methods to determine if any free polymer remains in the solution and to quantify the amount of polymer bound to the NC. This paper presents a quantitative analytical method based upon size-exclusion chromatography (SEC) that addresses this need.

To facilitate the detection of polymeric ligands on NCs by spectroscopic methods, we synthesized a low-molecular-weight sample of poly(dimethylaminoethyl methacrylate) labeled at one end with pyrene as a fluorescent tracer (Pyr-PDMAEMA, $M_n = 6700$) by atom-transfer radical polymerization (ATRP; for details of the synthesis and characterization, see the Supporting Information). Pyr-PDMAEMA can bind to CdSe NCs as a multidentate ligand, as there is a dimethylamino function on each pendant group (Scheme 1). The CdSe NCs were prepared by an established organometallic synthesis with TOPO as ligands.[5] Two samples were used in this study. The first ($CdSe_{520\,nm}$) had a diameter of 3.4 ± 0.3 nm as determined by transmission electron microscopy (TEM) and an emission maximum at $\lambda_{em} = 520$ nm. The particle diameter of the second sample ($CdSe_{550\,nm}$) was 4.0 ± 0.4 nm and the emission maximum was at $\lambda_{em} = 550$ nm. Both samples were purified by precipitation in methanol and dispersed in tetrahydrofuran (THF) before use. The mixture of CdSe–TOPO NCs and Pyr-PDMAEMA was stirred in THF overnight at room temperature, and a homogenous transparent solution was obtained.

[*] M. Wang, T. E. Dykstra, X. Lou, M. R. Salvador, G. D. Scholes, M. A. Winnik
Department of Chemistry
University of Toronto
80 St. George Street, Toronto, M5S 3H6 Ontario (Canada)
Fax: (+1) 416-978-0541
E-mail: gscholes@chem.utoronto.ca
mwinnik@chem.utoronto.ca

[**] The authors thank NSERC Canada for their support of this research. G.D.S. acknowledges the A. P. Sloan Foundation. We thank Dr. M. A. Hines for the kind gift of ZnSe samples. We acknowledge helpful discussions with Dr. X.-S. Wang and Dr. Z. Yin, as well as the help of Mr. Y. Wang, Dr. N. Coombs, and Dr. M. Mamak for the TEM measurements.

Supporting information for this article is available on the WWW under http://www.angewandte.org or from the author.

 © 2006 Wiley-VCH Verlag GmbH & Co. KGaA, Weinheim

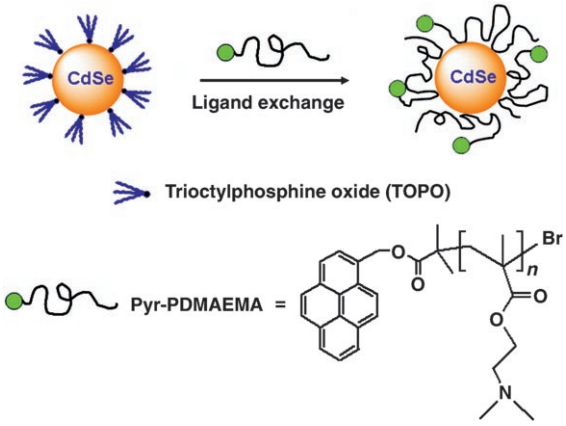

Scheme 1. Ligand exchange between TOPO-capped CdSe NCs and the multidentate homopolymer (Pyr-PDMAEMA) terminated by a pyrene group.

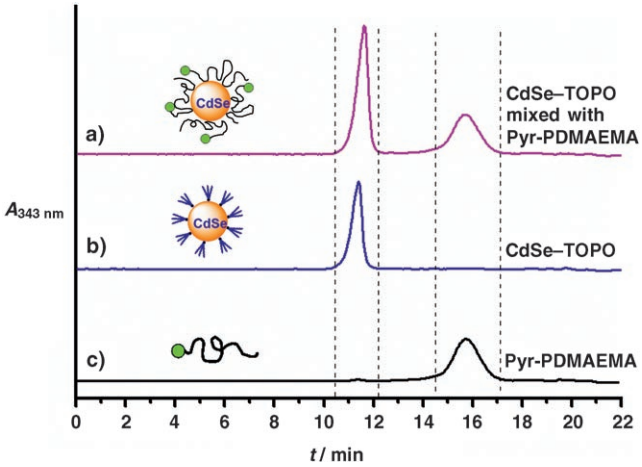

Figure 1. SEC traces of signal intensity versus elution time of TOPO-capped $CdSe_{520\,nm}$ NCs (c), Pyr-PDMAEMA (b), and a mixture of both components (a). The first elution peak in (a) at 11.5 min is attributed to CdSe NCs, while the peak at 15.7 min is derived from the excess free polymer in the mixture. Eluant: NMP; flow rate: 0.6 mL min^{-1}.

SEC is a commonly used method to determine the molecular weight and size distribution of organic polymers, but its application to inorganic colloidal particles is rare.[14] When a CdSe NC sample mixed with excess Pyr-PDMAEMA was injected into the SEC column, two peaks were observed. The first peak (at 11.5 min, Figure 1a) is attributed to the $CdSe_{520\,nm}$ NCs and the second peak (at 15.7 min) is due to the excess free polymer in the mixture. At 343 nm, the UV/Vis detector monitors both the $S_0 \rightarrow S_2$ absorption of pyrene as well as the continuum absorption below 510 nm of the $CdSe_{520\,nm}$ NCs. It is evident from the SEC traces of $CdSe_{520\,nm}$ itself (Figure 1b) and of pure Pyr-PDMAEMA (Figure 1c) that the NCs elute much faster than the free polymer. The low molecular weight and relatively low polydispersity (PDI) of the polymer facilitates the separation of the components. Our results are consistent with those reported by Wilcoxon et al.,[14d] who found that dense Au colloids in water eluted at the size cutoff of their aqueous SEC column, thus giving a sharper peak than with linear, commercial polymer standards such as polyethylene glycol.

Although the chromatogram in Figure 1a indicates clear separation of the NCs and free polymer, it provides no information about the nature of the surface groups on the CdSe particles. To obtain this vital information, we collected the material corresponding to the band at $t = 10$ to 12 min in Figure 1a and analyzed the sample by UV/Vis and fluorescence spectroscopy. Figure 2a shows that a new band at 346 nm, attributed to pyrene absorption, is evident in the absorption spectrum of the NCs separated by the SEC column. More-striking evidence for the presence of pyrene is seen in the photoluminescence (PL) spectrum presented in Figure 2b, in which the characteristic emission band of the pyrene chromophore from 370 to 430 nm is well resolved

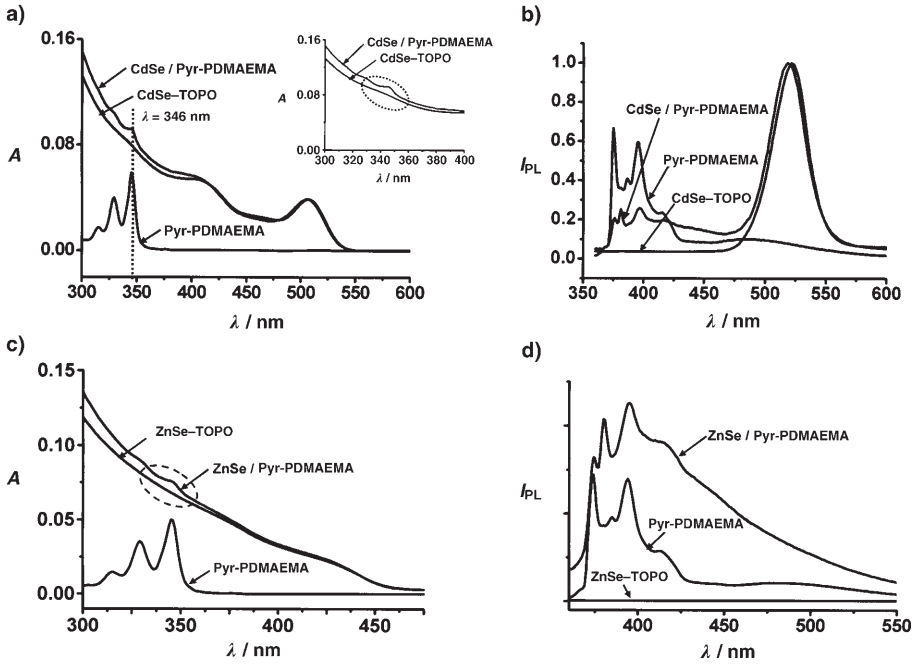

Figure 2. Absorption (a, c) and emission (b, d) spectra of $CdSe_{520\,nm}$/Pyr-PDMAEMA (a, b) and ZnSe/Pyr-PDMAEMA (c, d) complexes after separation by the SEC column. For comparison, the absorbance and photoluminescence spectra of TOPO-capped CdSe and ZnSe NCs as well as Pyr-PDMAEMA are also shown. The inset in (a) highlights the absorption difference around 346 nm between CdSe–TOPO and CdSe/Pyr-PDMAEMA. The pyrene groups on the ZnSe/Pyr-PDMAEMA complex show both monomer emission (370 to 420 nm) and a longer-wavelength emission that may be due to an excimer, but which needs further investigation. ZnSe–TOPO, as shown in (d), is nonfluorescent.

 © 2006 Wiley-VCH Verlag GmbH & Co. KGaA, Weinheim

from the quantum-dot emission. The strong emission at longer wavelength indicates that the photoluminescence of CdSe NCs is preserved after ligand exchange with the polymer and passage through the SEC column.

As polymers with many functional binding sites bind to surfaces cooperatively, desorption of the polymer from the surface is anticipated to be very slow. We tested the reversibility of the adsorption by re-injecting into the SEC column samples of the CdSe/Pyr-PDMAEMA NCs that had been collected from the column. Reanalysis by SEC of the samples that were allowed to stand in *N*-methyl-2-pyrrolidinone solution for up to one week showed only the NC peak at 12 min and no detectable trace of free Pyr-PDMAEMA (an example is provided in the Supporting Information). This result suggests that the binding of the polymer on the NCs is strong, and no dissociation can be detected.

To test the scope of our methodology, we repeated these experiments with a sample of TOPO-stabilized ZnSe NCs (synthesized according to the method of Hines[15]). The results (see Figure 2c,d and Supporting Information) demonstrate that Pyr-PDMAEMA binds to the ZnSe surface without dissociation. This result, coupled with our earlier finding that PDMAEMA homopolymer adsorbs strongly to the surface of ZnS-overcoated CdSe NCs, suggests that this polymer is an effective multidentate ligand for a wide variety of NCs.

The dye at the end of the polymer chain makes it possible to determine the mean number of polymers bound to each NC particle. This information could in principle be obtained from Figure 2a,c by assuming additivity of the absorbance of the dye and NC at 346 nm. This analysis is complicated not only by the background contribution of the NC itself,[11] but also by band broadening and possible dipole-strength redistribution of the pyrene in the vicinity of the NC. Evidence for these effects is seen in Figure 2 as enhanced absorbance at wavelengths at which the expected contribution of free pyrene groups is small and as the long wavelength tail in the pyrene emission for dyes bound to the NC.[16] The origin of this effect is not understood, but points to an interaction of some of the pyrene groups with the NC surface.

As a consequence, we developed a different approach based upon monitoring the amount of free polymer removed from a calibrated polymer solution by the addition of TOPO-covered NCs. Two samples with the same concentration of Pyr-PDMAEMA but different concentrations of $CdSe_{520\,nm}$ were prepared and examined by SEC. Figure 3 shows that, for injections of identical volume, the intensity of the peak corresponding to excess polymer in the chromatogram of $CdSe_{520\,nm}$/Pyr-PDMAEMA decreases with the increase in NC concentration. This experiment can be calibrated by injecting identical volumes (50 μL) of a series of solutions with varying polymer concentration (Figure 4). As an example, a sample was prepared by mixing 0.5 mL of 1.68×10^{-5} M TOPO-capped $CdSe_{550\,nm}$ NCs with 0.5 mL of a 3.3 mg mL^{-1} (4.93×10^{-4} M) solution of Pyr-PDMAEMA. From the SEC results for this mixture, we deduce that the concentration of free polymer chains in the solution decreased from 2.47×10^{-4} to $1.42(\pm0.16)\times10^{-4}$ M. From three separate measurements, we calculate that on average 12.5 ± 1.9 polymer molecules were bound to each $CdSe_{550\,nm}$ particle. Analogous experiments with the smaller $CdSe_{520\,nm}$ NC led to the conclusion that on average 4.6 ± 0.6 polymers were bound to each particle.

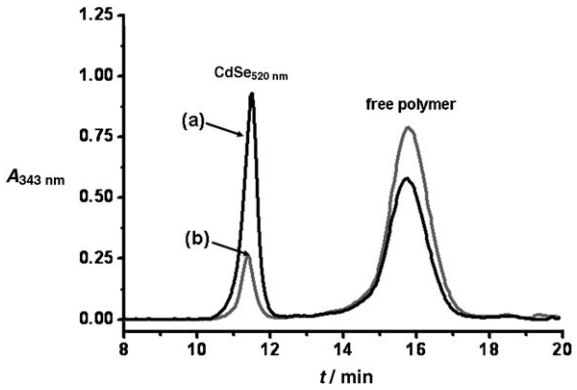

Figure 3. SEC traces of Pyr-PDMAEMA mixed with different concentrations of TOPO-capped $CdSe_{520\,nm}$ NCs: a) 1.2×10^{-5} M CdSe–TOPO and 2.5×10^{-2} M Pyr-PDMAEMA; b) 2.4×10^{-6} M CdSe–TOPO and 2.5×10^{-2} M Pyr-PDMAEMA. Injection volume: 50 μL ; eluant: NMP; flow rate: 0.6 mL min^{-1}.

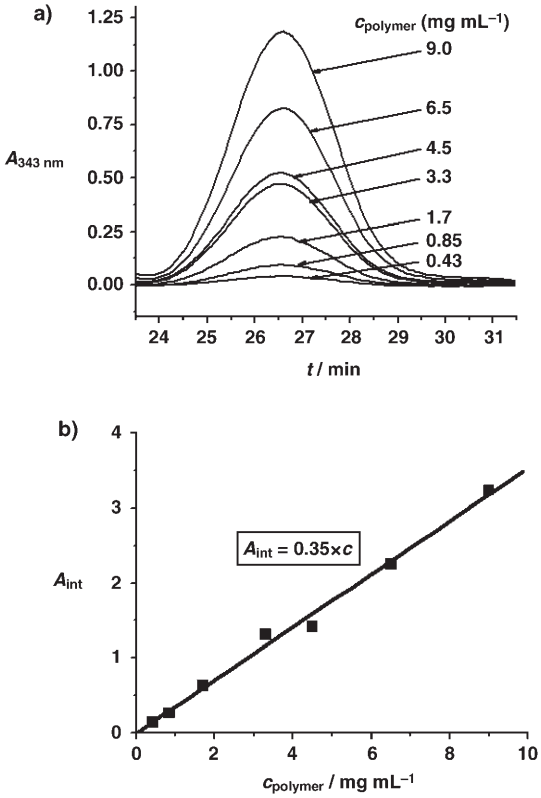

Figure 4. a) SEC traces of Pyr-PDMAEMA for a series of solutions of varying concentration in THF. The injection volume (50 μL) was identical for all samples. b) A calibration curve showing that the integrated areas (A_{int}) of the peaks corresponding to the polymer in the SEC chromatograms in (a) increase linearly with polymer concentration. Eluant: NMP; flow rate: 0.5 mL min^{-1}.

In summary, SEC analysis combined with spectroscopic characterization has provided unambiguous evidence that the pyrene-labeled polymer Pyr-PDMAEMA becomes tightly

 © 2006 Wiley-VCH Verlag GmbH & Co. KGaA, Weinheim

bound to CdSe NCs. The NCs are eluted much faster through the chromatographic column than the pure polymer. As a result, the excess free polymer is separated effectively from the polymer-bound NCs by the SEC column. Moreover, the number of the polymeric ligands bound to each NC was quantified from the SEC chromatogram by comparing the amount of the polymer chains in solution before and after addition of CdSe–TOPO NCs. This approach can be applied to any system in which one can synthesize a derivative of a multidentate ligand bearing a single dye substituent, and is thus expected to be of great utility for the characterization of other NC systems in which a protein, dendron, or polymer is bound to the surface.

Experimental Section

The SEC measurements were performed by using an AM Gel Linear/5 exclusion column (American Polymer Standards Corporation) and a Viscotek VE-1121 GPC solvent pump. The flow rate was 0.6 mL min^{-1} and the injected volume was 50 μL unless indicated specifically. *N*-Methyl-2-pyrrolidinone (NMP; HPLC grade) was used as the mobile phase. Two detectors were used: a Viscotek VE-3210 UV/Vis detector ($\lambda = 343$ nm) and a Waters 410 differential refractometer (RI).

The extinction coefficient of the CdSe NCs was determined by the empirical equation $\varepsilon = 5857 \times (d)^{2.65}$ (d is the diameter of the CdSe NCs, as determined by TEM).[17] From the absorbance (A) of first peak around 510 nm, the concentration (c) of NCs in THF was calculated through the Beer–Lambert law ($c = A/(\varepsilon l)$). Optical absorption spectra were collected at room temperature on a Perkin–Elmer Lambda 25 spectrometer using 1.00-cm quartz cuvettes. Photoluminescence spectra were measured with a SPEX Fluorolog-3 spectrofluorometer (Jobin Yvon/SPEX, Edison, New Jersey).

Received: July 20, 2005
Revised: December 21, 2005
Published online: March 3, 2006

Keywords: cadmium selenide · nanocrystals · polymers · quantum dots · size-exclusion chromatography

[1] a) H. Weller, *Angew. Chem.* **1993**, *105*, 43; *Angew. Chem. Int. Ed. Engl.* **1993**, *32*, 41; b) A. P. Alivisatos, *J. Phys. Chem.* **1996**, *100*, 13226.
[2] a) J. Lee, V. C. Sundar, J. R. Heine, M. G. Bawendi, K. F. Jensen, *Adv. Mater.* **2000**, *12*, 1102; b) S. Coe, W. K. Woo, M. Bawendi, V. Bulovic, *Nature* **2002**, *420*, 800; c) N. Tessler, V. Medvedev, M. Kazes, S. Kan, U. Banin, *Science* **2002**, *295*, 1506.
[3] W. U. Huynh, J. J. Dittmer, A. P. Alivisatos, *Science* **2002**, *295*, 2425.
[4] a) M. P. Bruchez, M. Moronne, P. Gin, S. Weiss, A. P. Alivisatos, *Science* **1998**, *281*, 2013; b) W. C. W. Chan, S. Nie, *Science* **1998**, *281*, 2016; c) X. Michalet, F. F. Pinaud, L. A. Bentolila, J. M. Tsay, S. Doose, J. J. Li, G. Sundaresan, A. M. Wu, S. S. Gambhir, S. Weiss, *Science* **2005**, *307*, 538.
[5] a) C. B. Murray, D. J. Norris, M. G. Bawendi, *J. Am. Chem. Soc.* **1993**, *115*, 8706; b) L. Manna, E. C. Scher, A. P. Alivisatos, *J. Am. Chem. Soc.* **2000**, *122*, 12700.
[6] a) J. E. Bowen Katari, V. L. Colvin, A. P. Alivisatos, *J. Phys. Chem.* **1994**, *98*, 4109; b) J. Aldana, Y. A. Wang, X. Peng, *J. Am. Chem. Soc.* **2001**, *123*, 8844.
[7] Y. A. Wang, J. J. Li, H. Chen, X. Peng, *J. Am. Chem. Soc.* **2002**, *124*, 2293.
[8] H. Skaff, T. Emrick, *Angew. Chem.* **2004**, *116*, 5497; *Angew. Chem. Int. Ed.* **2004**, *43*, 5383.
[9] a) D. E. Fogg, L. H. Radzilowski, R. Blanski, R. R. Schrock, E. L. Thomas, *Macromolecules* **1997**, *30*, 417; b) S. Kim, M. G. Bawendi, *J. Am. Chem. Soc.* **2003**, *125*, 14652; c) X.-S. Wang, T. E. Dykstra, M. R. Salvador, I. Manners, G. D. Scholes, M. A. Winnik, *J. Am. Chem. Soc.* **2004**, *126*, 7784; d) H. T. Uyeda, I. L. Medintz, J. K. Jaiswal, S. M. Simon, H. Mattoussi, *J. Am. Chem. Soc.* **2005**, *127*, 3870; e) I. Potapova, R. Mruk, C. Hübner, R. Zentel, T. Basché, A. Mews, *Angew. Chem.* **2005**, *117*, 2490; *Angew. Chem. Int. Ed.* **2005**, *44*, 2437.
[10] T. Nann, *Chem. Commun.* **2005**, 1735.
[11] A. R. Clapp, I. L. Medintz, J. M. Mauro, B. R. Fisher, M. G. Bawendi, H. Mattoussi, *J. Am. Chem. Soc.* **2004**, *126*, 301.
[12] a) B. Dubertret, P. Skourides, D. J. Norris, V. Noireaux, A. H. Brivanlou, A. Libchaber, *Science* **2002**, *298*, 1759; b) I. Potapova, R. Mruk, S. Prehl, R. Zentel, T. Basché, A. Mews, *J. Am. Chem. Soc.* **2003**, *125*, 320; c) T. Pellegrino, L. Manna, S. Kudera, T. Liedl, D. Koktysh, A. L. Rogach, S. Keller, J. Rädler, G. Natile, W. J. Parak, *Nano Lett.* **2004**, *4*, 703; d) X. Gao, Y. Cui, R. M. Levenson, L. W. K. Chung, S. Nie, *Nat. Biotechnol.* **2004**, *22*, 969; e) Y. Nagasaki, T. Ishii, Y. Sunaga, A. Watanabe, H. Otsuka, K. Kataoka, *Langmuir* **2004**, *20*, 6396.
[13] T. Hashimoto, A. Okumura, D. Tanabe, *Macromolecules* **2003**, *36*, 7324.
[14] a) M. L. Steigerwald, A. P. Alivisatos, J. M. Gibson, T. D. Harris, R. Kortan, A. J. Muller, A. M. Thayer, T. M. Duncan, D. C. Douglass, L. E. Brus, *J. Am. Chem. Soc.* **1988**, *110*, 3046; b) Ch.-H. Fischer, H. Weller, L. Katsikas, A. Henglein, *Langmuir* **1989**, *5*, 429; c) K. A. Littau, P. J. Szajowski, A. J. Muller, A. R. Kortan, L. E. Brus, *J. Phys. Chem.* **1993**, *97*, 1224; d) J. P. Wilcoxon, J. E. Martin, F. Parsapour, B. Wiedenman, D. F. Kelley, *J. Chem. Phys.* **1998**, *108*, 9137.
[15] M. A. Hines, P. Guyot-Sionnest, *J. Phys. Chem. B* **1998**, *102*, 3655. The sample was non-emissive as prepared.
[16] This does not seem to be a problem for dyes that absorb at longer wavelengths than the NC and are located at a distance from the NC surface.[9e,11]
[17] W. W. Yu, L. Qu, W. Guo, X. Peng, *Chem. Mater.* **2003**, *15*, 2854.

 © 2006 Wiley-VCH Verlag GmbH & Co. KGaA, Weinheim

DNA Sequencing

DOI: 10.1002/anie.200503154

DNA Sequencing Based on Intrinsic Molecular Charges**

*Toshiya Sakata and Yuji Miyahara**

Gene functional analyses have proceeded remarkably in the fields of molecular biology, pharmacogenomics, and clinical research, on the basis of completion of the decoding of the human genome. The analysis of nucleotide variation has become increasingly important for the assembly of a high-resolution map of disease-related loci and for clinical diagnostics. The most common form of genomic variation is single-nucleotide polymorphism (SNP), which is an important marker in personalized medicine that affects disease susceptibility and resistance. Although a number of methods for SNP analysis have been developed,[1–7] DNA sequencing techniques still need to be improved in terms of cost, simplicity, and throughput to analyze not only SNPs but also genomic variations, such as insertion/deletion and short tandem repeats.

We have been investigating a new approach to the direct, simple, and highly sensitive detection of nonlabeled molecular recognition events on a miniaturized and arrayed solid-state device.[8] Recently, several types of field-effect devices have been used for the electrochemical detection of hybridization events on a solid surface.[9] As DNA molecules are negatively charged in an aqueous solution, the number of negative charges at the gate surface of field-effect devices increases as a result of hybridization and extension reactions. The charge-density change is directly transduced into an electrical signal by the field effect. Based on this principle, point-mutation analysis was carried out by using the PCR products amplified with allele-specific primers.[9e] In this case, the overall specificity was determined from that of the allele-specific PCR. A single-base mismatch could also be distinguished by hybridization with complementary and mismatched DNA probes immobilized on the capacitor-type field-effect devices.[9b]

We propose a new method for DNA sequencing of known as well as unknown sequence variants, which is based on detection of the intrinsic charges of DNA molecules by using the field effect. Herein, we report the direct transduction of single-base extension at the gate surface into an electrical signal, and the possibility of label-free DNA sequencing based on the intrinsic charges of DNA molecules.

Oligonucleotide probes are immobilized on the Si_3N_4 gate surface, and the complementary target DNA is hybridized with these probes. The hybridization events are followed by the introduction of DNA polymerase and one of each deoxynucleotide (dCTP, dATP, dGTP, or dTTP). DNA polymerase extends the immobilized oligonucleotide probes in a template-dependent manner (Figure 1). As a result of the extension reaction, the number of negative charges increases at the gate surface of the field-effect transistor (FET) because of the intrinsic negative charges of the incorporated molecules. This change in charge density can be detected as a shift in the threshold voltage (V_T) of the FET. Thus, iterative addition of each deoxynucleotide and measurement of the threshold voltage allow direct, simple, and label-free DNA sequencing.

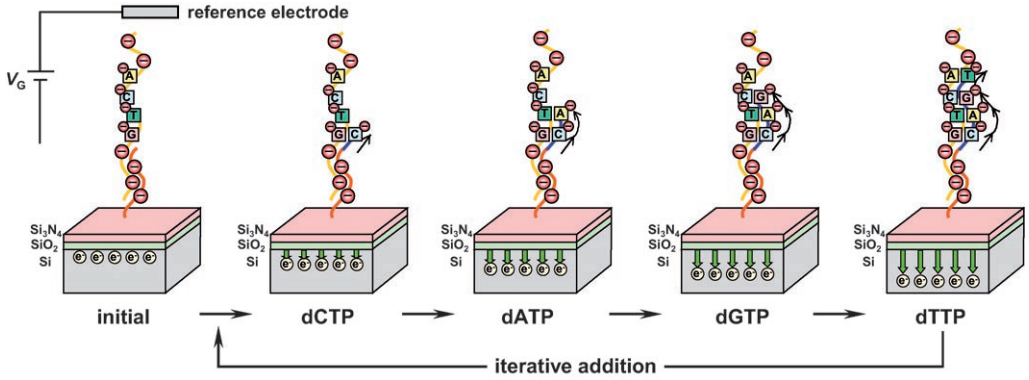

Figure 1. DNA sequencing based on FETs in combination with an extension reaction. Each deoxynucleotide is incorporated into the probe–target duplex on the FET in the following order: dCTP, dATP, dGTP, and dTTP.

The FET chip (Figure 2A) is immersed in a measurement solution together with an Ag/AgCl reference electrode with saturated KCl solution. The potential of the measurement solution is controlled and fixed by the gate voltage (V_G) through the reference electrode (Figure 2B). The base sequences of the factor VII gene, which include two SNP sites, and of the hereditary hemochromatosis gene

[*] Dr. T. Sakata, Dr. Y. Miyahara
Biomaterials Center
National Institute for Materials Science
1-1 Namiki, Tsukuba, Ibaraki 305-0044 (Japan)
Fax: (+81) 29-860-4714
E-mail: miyahara.yuji@nims.go.jp

[**] We thank Dr. Y. Horiike, Dr. J. Tanaka, Dr. H. Otsuka, and A. Ueda of the National Institute for Materials Science, Japan, Y. Nakajima of Ryokusei M.E.S. Co., Ltd., Japan, M. Kamahori of Hitachi Ltd., Japan, and Dr. P. Fortina of Thomas Jefferson University, USA, for their help and useful discussions.

© 2006 Wiley-VCH Verlag GmbH & Co. KGaA, Weinheim

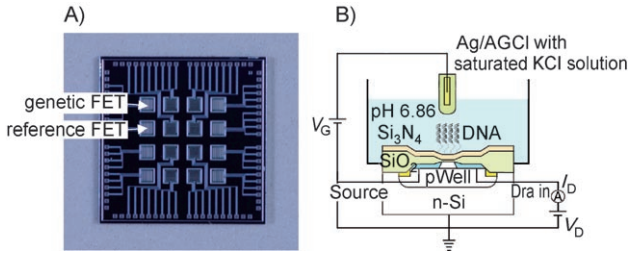

Figure 2. A) Photograph of the fabricated FET chip. Sixteen FETs and a temperature sensor are integrated in a 5×5-mm^2 chip. The FETs are of the n-channel depletion type with Si_3N_4/SiO_2 as a gate insulator. Two FETs were used for DNA sequencing: one FET with immobilized oligonucleotide probes and the other as a reference FET without oligonucleotide probes. B) Schematic diagram showing measurements of the electrical characteristics of a FET. The shift of the threshold voltage (V_T) was determined from the gate voltage–drain current (V_G–I_D) characteristics in a phosphate buffer solution (0.025 M Na_2HPO_4/0.025 M KH_2PO_4, pH 6.86). An Ag/AgCl electrode with saturated KCl solution was used as reference electrode.

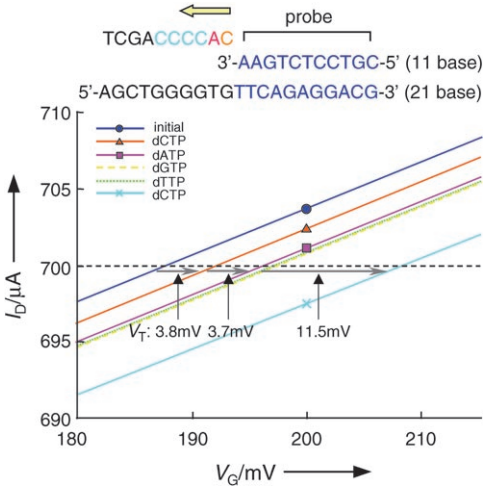

Figure 3. V_T shifts after a single-base extension reaction at the gate surface. The threshold voltages were shifted in the positive direction because of the intrinsic negative charges of deoxynucleotides. The amount of the V_T shift was determined at a constant drain current of 700 μA.

(Table 1[10]) were used to demonstrate the principle of DNA sequencing based on the FET. We paid special attention to the buffer concentration to be used for measuring the change in charge density at the gate surface. The change in potential induced by adsorption of proteins at the gate surface was reported to be dependent on the electrolyte concentration.[11] It is therefore important to optimize the Debye length at the gate insulator/solution interface. Herein, a 0.025 M phosphate buffer solution was used for measuring the change in charge density at the gate surface, whereas a conventional reaction mixture was used for the single-base extension reaction.

Table 1: Base sequences for oligonucleotide probes and targets for the −122 and R353Q regions of factor VII gene and the C282Y regions of hereditary hemochromatosis gene.[10]

Locus	Function	Sequence
R353Q	R353Q wild-type	
	probe	5′-amino group-CCACTACCG-3′ (9mer)
	target	5′-ACGTGCCCCGGTAGTGG-3′ (17mer)
−122	−122 wild-type	
	probe	5′-amino group-CGTCCTCTGAA-3′ (11mer)
	target	5′-AGCTGGGGTGTTCAGAGGACG-3′ (21mer)
C282Y	C282Y wild-type	
	probe	5′-amino group-AGATATACGTG-3′ (11mer)
	target	5′-CTCCACCTGGCACGTATATCT-3′ (21mer)

The 11-base oligonucleotide probes were immobilized on the gate surface and hybridized with the 21-base target DNA for the base sequence of −122 (Table 1[10]). The shifts of the V_G–I_D characteristics, that is, the V_T shifts, were measured after incorporation of deoxynucleotides (Figure 3). When the FET was soaked in a DNA polymerase buffer solution containing dCTP, the V_T shifted in the positive direction by 3.8 mV after single-base extension. Next, the FET was soaked in a DNA polymerase buffer solution containing dATP, and the V_T value shifted further in the positive direction by 3.7 mV, because dATP was incorporated into the probe–target duplex on the FET. When the measurements of the V_T shifts after the single-base extension reaction were performed 15 times, the average V_T shift was 3.2 mV with a standard deviation of 1.1 mV.

When the FET was introduced into a buffer solution containing dGTP and dTTP, the V_T value remained nearly constant because the deoxynucleotides were not incorporated into the noncomplementary base sequence. In this case, the average V_T shift was 0.03 mV with a standard deviation of 0.67 mV. Thus, the V_T shifts based on single-base extension were large enough to be detected and had a sufficient signal-to-noise ratio. Moreover, the V_T value shifted in the positive direction by 11.5 mV when the FET was soaked again in the buffer solution containing dCTP. This is because four dCTP molecules with negative charges were incorporated into the probe–target duplex on the gate surface.

To evaluate the FETs in combination with single-base extension for DNA sequencing, we prepared four kinds of buffer solutions containing both DNA polymerase and either dCTP, dATP, dGTP, or dTTP. The FETs hybridized with target DNA were immersed in these buffer solutions for the single-base extension reaction, and the shift of the V_T value was measured in a phosphate buffer solution (0.025 M) after washing the FETs. The cycle of single-base extension and measurement of the V_T was repeated iteratively to determine the base sequence of the target DNA. When the base sequence of the R353Q region of the factor VII gene was used as target DNA, the V_T shifted in the positive direction only after single-base extension with the specific deoxynucleotides that were complementary to the base sequence of the target DNA (Figure 4 A). The change in V_T for three-base extension, GGG, was 6.9 mV, which was larger than that for one-base extension but was not three times that expected

 © 2006 Wiley-VCH Verlag GmbH & Co. KGaA, Weinheim

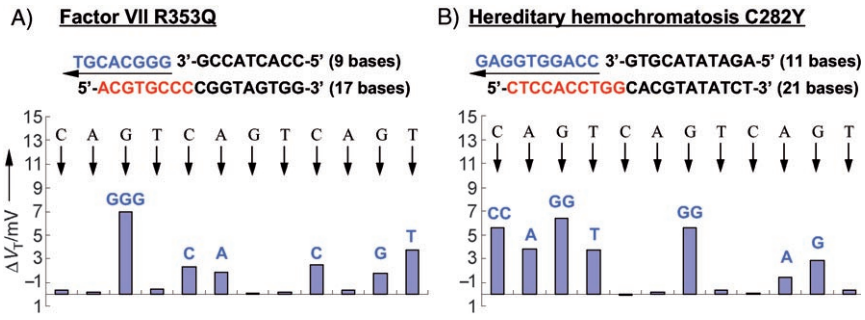

Figure 4. DNA sequencing by the method presented herein. DNA polymerase extends the immobilized oligonucleotide probes with each deoxynucleotide in a template-dependent manner. The base sequences of the R353Q region of the factor VII gene (A) and the C282Y region of the hereditary hemochromatosis gene (B) were successfully determined.

from the number of intrinsic charges. Although the linear relationship between the base length synthesized by the extension reaction and the V_T shift was obtained in the range from 0 to 30 bases,[12] it is important to detect single-base extension quantitatively to reduce the base-call error, especially for continuous sequences of the same base. The density and orientation of the immobilized oligonucleotide probes have to be controlled during a series of extension reactions at 72 °C. Further improvement of the precision of the base call is also expected by automation of the extension reaction and V_T measurements.

The C282Y region of the hereditary hemochromatosis gene was used as another example of DNA sequencing with FETs and single-base extension (Figure 4B). The positive V_T shifts could be detected in accordance with the base sequence of the target DNA. In this case, the average V_T shift for two-base incorporation was 5.8 mV with a standard deviation of 0.4 mV, whereas the average V_T shift for single-base extension was 3.2 mV, as described previously. The V_T shift for two-base extension was approximately twice as big as that for single-base extension. Thus, the results of the iterative extension reaction and detection of the threshold voltage indicated the ability of a direct, simple, and potentially precise DNA sequencing analysis by using the FETs.

The number of bases that can be analyzed by the proposed method is about ten at present. The V_T shift for single-base extension became gradually smaller as the number of bases increased by more than ten bases. One of the reasons for this limitation is the Debye length at the gate insulator/solution interface. Any change in charge density induced outside the Debye length cannot be detected with a FET. The lateral extension reaction in which DNA probes are extended in parallel with the gate surface would be effective for DNA sequencing with long base length. Another reason for the limitation would be the peeling off of the immobilized oligonucleotide probes from the surface of the gate insulator as the temperature stress of the extension reaction at 72 °C is applied repeatedly. A stronger immobilization method for oligonucleotide probes on the Si_3N_4 surface has to be adopted to analyze longer base sequences. The density of the immobilized oligonucleotide probes was calculated by the Graham equation.[9b] As the measured V_T shift was 3.2 mV on average for single-base extensions, the resulting probe density at the gate surface was 7.3×10^{11} cm^{-2}. This value is similar to the reported values for field-effect devices.[13]

The above results demonstrate that single-base extension with any deoxynucleotide can be directly transduced into an electrical signal by the FETs, and that DNA sequencing can be achieved based on the intrinsic charges of DNA molecules without any labeling material. It is possible to integrate multiple FETs and signal-processing circuits in a single chip by using advanced semiconductor technology. Simultaneous analyses of various base sequences that include SNPs can be realized with the FETs. As the output of the FET is an electrical signal, it is easy to standardize the results obtained with the FETs as compared to analyses based on fluorescence detection. Therefore, the platform based on FETs is suitable for a miniaturized and arrayed system for SNP genotyping, as well as DNA sequencing in clinical research and diagnostics.

Experimental Section

Insulated-gate FETs were fabricated by standard integrated-circuit technology except for deposition of the gate electrode. The gate structure and the fabrication process for the FETs are described in detail elsewhere.[14] A temperature sensor and 16 FETs were integrated in a 5×5-mm^2 chip (Figure 2A). We used an n-channel depletion-mode FET with a double layer of Si_3N_4/SiO_2 as the gate insulator on which oligonucleotide probes were immobilized. The thicknesses of the Si_3N_4 and SiO_2 layers were 140 and 35 nm, respectively. The channel width W and the channel length L were designed to be 2400 and 5 μm, respectively, and as a result, the ratio W/L was 480:1. The fabricated FET chip was mounted on a flexible polyimide film with patterned copper electrodes and wire-bonded. The FET chip was encapsulated with an epoxy resin (ZC-203, Nippon Pelnox) except for the gate areas. The typical drifts of these FET devices were about 0.1 mV h^{-1}. Herein, both the fabricated FETs and commercial ion-selective FETs (ISFETs, BAS Inc.) were used. The FETs were immersed in a phosphate buffer solution (0.025 M Na_2HPO_4/0.025 M KH_2PO_4, pH 6.86, Wako) with an Ag/AgCl reference electrode with saturated KCl solution (Figure 2B). The electrical characteristics of the FETs, such as the V_G–I_D characteristics, were measured in a phosphate buffer solution of pH 6.86 at room temperature by using a semiconductor parameter analyzer (4155C, Agilent). The V_T shift was determined after each single-base extension reaction. It was defined as the difference in the V_G–I_D characteristics at a constant drain current of 700 μA.

Oligonucleotides were synthesized by the phosphoramidite method and purified by HPLC (Espec). The 5′-end of the synthesized oligonucleotide probe was modified with an amino group for attachment to the Si_3N_4 surface. The base sequences of the factor VII gene, which include two SNP sites, −122 (21 bases) and R353Q (17 bases), and those of the hereditary hemochromatosis gene, which include C282Y (21 bases) (Table 1[10]), were used as model samples. The base lengths of the oligonucleotide probes were 9 or 11 bases.

The surface of the Si_3N_4 layer was cleaned with 1 M NaOH for 1 h at room temperature and silanized in toluene (Sigma-Aldrich) containing (3-aminopropyl)triethoxysilane (2 wt%, Sigma-Aldrich).

 © 2006 Wiley-VCH Verlag GmbH & Co. KGaA, Weinheim

The aminosilanized Si_3N_4 surface was rinsed in toluene and dried in vacuo at 110 °C for 0.5 h. Reactive amino groups were then introduced at the Si_3N_4 surface.

Oligonucleotide probes were immobilized on the modified Si_3N_4 surface by using glutaraldehyde as a bifunctional cross-linking agent. The aminosilanized Si_3N_4 surface was soaked in a glutaric dialdehyde (25 wt %, Sigma-Aldrich) solution with sodium cyanoborohydride (0.5 g per 50 mL, Sigma-Aldrich) for 4 h at room temperature, followed by rinsing in deionized water and drying in vacuo at room temperature for 1 h. Oligonucleotide probes were dissolved in Tris-Cl/EDTA (TE) buffer (pH 8.0, Nippon Gene) at a concentration of 100 μM. To couple the amino-modified oligonucleotides with the glutaraldehyde-treated Si_3N_4 surface, the FET chip was kept at 50 °C in the oligonucleotide solution with sodium cyanoborohydride (0.5 g per 50 mL) overnight to complete the coupling reaction. The FET chip was then soaked in a phosphate buffer solution (0.04 M Na_2HPO_4/0.03 M KH_2PO_4, pH 7.0, Wako) with glycine (1M, Wako) at 50 °C for 1 h to block any remaining glutaraldehyde groups. The FET chip was washed with phosphate buffer solution (pH 7.0) and deionized water, and dried in vacuo at room temperature for 1 h. The oligonucleotide probes were confirmed to be immobilized at the surface of Si_3N_4 by time-of-flight secondary-ion mass spectrometric (TOF-SIMS) analysis.[8b] The surface-modified FET chip was then ready for use in DNA sequencing studies.

The oligonucleotide probes immobilized on the FET chip were hybridized with target DNA. This DNA was prepared by dissolving target oligonucleotides in a hybridization buffer solution, which was composed of 4 × SSC + 0.1 % SDS (Invitrogen, SSC = sodium chloride/sodium citrate), at a concentration of 100 μM. The FET with the oligonucleotide probe was kept in the hybridization buffer solution containing the target oligonucleotide for 12 h at room temperature. After hybridization, the FET was washed with 1 × SSC + 0.03 % SDS, 0.2 × SSC, 0.05 × SSC, and deionized water at room temperature to remove nonhybridized oligonucleotides.

A thermostable DNA polymerase was used for DNA sequencing based on the single-base extension reaction. The reaction mixture contained KCl (50 mM), Tris-HCl (20 mM, pH 8.4), $MgCl_2$ (3 mM), *Taq* DNA polymerase (0.1 U μL^{-1}, Invitrogen), and deoxynucleotide (5 mM of either dCTP, dATP, dGTP, or dTTP; Invitrogen). After hybridization with the target oligonucleotide, the DNA polymerase-assisted synthesis with all four deoxynucleotides was carried out at the gate surface of the FET at 72 °C for 10 min. After incorporation of each deoxynucleotide, the FET was washed with deionized water and dried in vacuo at room temperature.

Received: September 6, 2005
Revised: January 6, 2006
Published online: February 28, 2006

Keywords: DNA · molecular electronics · polymorphism · semiconductors · sequence determination

[1] a) H. S. Rye, M. A. Quesada, K. Peck, R. A. Mathies, A. N. Glazer, *Nucleic Acids Res.* **1991**, *19*, 327 – 333; b) N. J. Dovichi, *Electrophoresis* **1997**, *18*, 2393 – 2399; c) N. J. Dovichi, J. Z. Zhang, *Angew. Chem.* **2000**, *112*, 4635 – 4640; *Angew. Chem. Int. Ed.* **2000**, *39*, 4463 – 4468.

[2] a) R. A. Mathies, X. C. Huang, *Nature* **1992**, *359*, 167 – 169; b) T. Anazawa, S. Takahashi, H. Kambara, *Anal. Chem.* **1996**, *68*, 2699 – 2704; c) J. Zhang, M. Yang, X. Puyang, Y. Fang, L. M. Cook, N. J. Dovichi, *Anal. Chem.* **2001**, *73*, 1234 – 1239.

[3] a) D. J. Fu, K. Tang, A. Braun, D. Reuter, B. Darnhofer-Demar, D. P. Little, M. J. O'Donnell, C. R. Cantor, H. Koster, *Nat. Biotechnol.* **1998**, *16*, 381 – 384; b) M. T. Roskey, P. Juhasz, I. P. Smirnov, E. J. Takach, S. A. Martin, L. A. Haff, *Proc. Natl. Acad. Sci. USA* **1996**, *93*, 4724 – 4729; c) J. R. Edwards, Y. Itagaki, J. Ju, *Nucleic Acids Res.* **2001**, *29*, e104.

[4] M. Ronaghi, M. Uhlen, P. Nyren, *Science* **1998**, *281*, 363 – 365.

[5] S. Drmanac, D. Kita, I. Labat, B. Hauser, C. Schmidt, J. D. Burczak, R. Drmanac, *Nat. Biotechnol.* **1998**, *16*, 54 – 58.

[6] S. Brenner, M. Johnson, J. Bridgham, G. Golda, D. H. Lloyd, D. Johnson, S. Luo, S. McCurdy, M. Foy, M. Ewan, R. Roth, D. George, S. Eletr, G. Albrecht, E. Vermaas, S. R. Williams, K. Moon, T. Burcham, M. Pallas, R. B. DuBridge, J. Kirchner, K. Fearon, J. Mao, K. Corcoran, *Nat. Biotechnol.* **2000**, *18*, 630 – 634.

[7] a) M. Ronaghi, *Genome Res.* **2001**, *11*, 3 – 11; b) T. Nordstrom, B. Gharizadeh, N. Pourmand, P. Nyren, M. Ronaghi, *Anal. Biochem.* **2001**, *292*, 266 – 271.

[8] a) T. Sakata, H. Otsuka, Y. Miyahara, *MRS Proceedings* **2003**, *782*, 393 – 398; b) T. Sakata, M. Kamahori, Y. Miyahara, *Mater. Sci. Eng. C* **2004**, *24*, 827 – 832; c) T. Sakata, Y. Miyahara, *ChemBioChem* **2005**, *6*, 703 – 710.

[9] a) E. Souteyrand, J. P. Cloarec, J. R. Martin, C. Wilson, I. Lawrence, S. Mikkelsen, M. F. Lawrence, *J. Phys. Chem. B* **1997**, *101*, 2980 – 2985; b) J. Fritz, E. B. Cooper, S. Gaudet, P. K. Sorger, S. R. Manails, *Proc. Natl. Acad. Sci. USA* **2002**, *99*, 14142 – 14146; c) F. Uslu, S. Ingebrandt, D. Mayer, S. Böcker-Meffert, M. Odenthal, A. Offenhäusser, *Biosens. Bioelectron.* **2004**, *19*, 1723 – 1731; d) D.-S. Kim, Y.-T. Jeong, H.-J. Park, J.-K. Shin, P. Choi, J.-H. Lee, G. Lim, *Biosens. Bioelectron.* **2004**, *20*, 69 – 74; e) F. Pouthas, C. Gentil, D. Cote, U. Bockelmann, *Appl. Phys. Lett.* **2004**, *84*, 1594 – 1596; f) D.-S. Kim, Y.-T. Jeong, H.-K. Lyu, H.-J. Park, H. S. Kim, J.-K. Shin, P. Choi, J.-H. Lee, G. Lim, M. Ishida, *Jpn. J. Appl. Phys.* **2003**, *42*, 4111 – 4115.

[10] T. Kajiyama, Y. Miyahara, L. J. Kricka, P. Wilding, D. J. Graves, S. Surrey, P. Fortina, *Genome Res.* **2003**, *13*, 467 – 475.

[11] H. Nakajima, M. Esashi, T. Matsuo, *Nippon Kagaku Kaishi* **1980**, *10*, 1499 – 1508.

[12] T. Sakata, Y. Miyahara, *Asia-Pacific Conference of Transducers and Micro–Nano Technology* (APCOT MNT 2004), Sapporo, **2004**, *3–1*, 189 – 193.

[13] A. Poghossian, A. Cherstvy, S. Ingebrandt, A. Offenhäusser, M. J. Schöning, *Sens. Actuators B* **2005**, *111–112*, 470 – 480.

[14] T. Sakata, M. Kamahori, Y. Miyahara, *Jpn. J. Appl. Phys.* **2005**, *44*, 2854 – 2859.

 © 2006 Wiley-VCH Verlag GmbH & Co. KGaA, Weinheim

Gene Function

DOI: 10.1002/anie.200503339

A Caged Doxycycline Analogue for Photoactivated Gene Expression**

Sidney B. Cambridge, Daniel Geissler, Sandro Keller, and Beate Cürten*

Conditional gene-expression paradigms are crucial tools for the study of genes and gene functions. However, none of the currently available paradigms permits transgene expression with high spatial and temporal resolution; rather, they usually rely on specific expression patterns enabled by endogenous promoters. To improve the resolution of transgene expression, we synthesized a photosensitive ("caged") doxycycline analogue for precise light-controlled activation of genes based on the "Tet-on" (Tet = tetracycline) system.[1] Because of the ease and precision with which light can be manipulated, this approach should make it possible to target subsets of cells for transgene expression which can range from single cells and tissue patches to whole organs.[2]

To implement a photoactivated gene-expression system that is generally applicable in any organism at any stage, we based our approach on a conditional gene-expression paradigm that uses a small, membrane-permeant molecule for induction. The most prominent inducible system by far is the Tet system, which is commonly used for the induction of transgenes in cell culture, tissues, and whole organisms.[1] The most potent analogue for the Tet system is doxycycline, which can bind to a modified and mutated version of the Tet repressor fused to a transcriptional activation domain (rtTA) and induce transgenes under the control of the Tet promoter.[3] Because doxycycline (Scheme 1) has several functional groups that may be derivatized, it was necessary to specifically target a group that is essential for transcriptional activity and block this activity by "caging" with a photosensitive protecting group. It was previously shown that the phenolic β-diketone system (highlighted in red, Scheme 1) is important for the formation of the doxycycline–magnesium complex, which binds to the rtTA protein with high affinity.[4] We therefore attempted to generate a 1-(4,5-dimethoxy-2-nitrophenyl)ethyl (DMNPE) ether of doxycycline (DMNPE-caged doxycycline) from the commercially available doxycycline hyclate (hydrochloride hemiethanolate hemihydrate) with the DMNPE moiety attached at the phenolic β-diketone system.

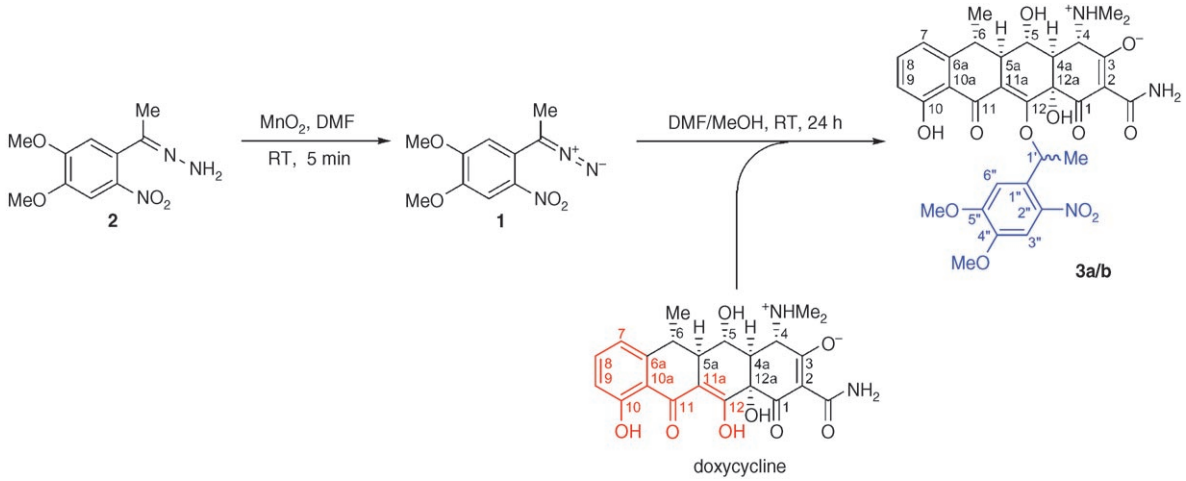

Scheme 1. Synthesis and structure of caged doxycyclines **3a** and **3b**. The phenolic β-diketone system (ketone enol form) is highlighted in red in doxycycline, and the caging group in blue in **3a**/**3b**. DMF = *N*,*N*-dimethylformamide.

Doxycycline hydrochloride was neutralized with KOH and then treated with an approximate fivefold excess of freshly prepared 1-(4,5-dimethoxy-2-nitrophenyl)diazoethane (**1**) obtained from 4,5-dimethoxy-2-nitroacetophenone hydrazone (**2**) by oxidation with MnO_2. The alkylation

[*] Dr. S. B. Cambridge, D. Geissler
Max-Planck-Institut für Neurobiologie
Am Klopferspitz 18, 82152 München-Planegg (Germany)
Fax: (+49) 89-899-50043
E-mail: sidney@neuro.mpg.de
S. Keller
Leibniz Institute of Molecular Pharmacology (FMP)
Robert-Rössle-Strasse 10
13125 Berlin (Germany)
Dr. B. Cürten
CarboGen AG
Neulandweg 5
5502 Hunzenschwil (Switzerland)

[**] We thank T. Bonhoeffer for continued support of this project; P. Schmieder (FMP) and E. Krause (FMP) for the NMR spectroscopic and mass-spectrometric analysis, respectively; R. Scholz for help with the photoactivation of the tobacco leafs (in the laboratory of C. Gatz); B. Schwappach for providing the Chinese hamster ovary cells; and T. Bonhoeffer, V. Hagen, and V. Stein for critical reading of the manuscript. This study was supported by the Max-Planck society; a DFG fellowship (B.C.); a Volkswagen-Stiftung grant, a Minorities in Neuroscience Fellowship Program, and a Schloessmann Fellowship (S.B.C.); and the European Commission (grant no. QLK3-CT-2002-01989; S.K.).

Supporting information for this article is available on the WWW under http://www.angewandte.org or from the author.

© 2006 Wiley-VCH Verlag GmbH & Co. KGaA, Weinheim

of doxycycline with **1** resulted in two stable diastereomers of DMNPE-caged doxycycline (**3a** and **3b**) as main products and a few unstable caged side products. Because the unstable by-products complicated the separation of the stable isomers, they were selectively hydrolyzed by brief treatment of the reaction mixture with diluted trifluoroacetic acid (TFA) at 40 °C prior to preparative HPLC separation. The stable diastereomers **3a** and **3b** were then isolated by reversed-phase C-18 HPLC, whereby the yield of each isomer was about 8 %.

The structures of **3a** and **3b** were clarified by comprehensive NMR spectroscopic analysis (see Supporting Information). Heteronuclear multiple-bond correlation (HMBC) spectra of **3a** and **3b** showed cross-correlation between H1′ and C12 in both cases, and also between the three protons of the methyl group at C1′ and C12 in the case of **3a**. Consequently, the DMNPE-caging group must have been conjugated with C12, which is part of the phenolic β-diketone system. This analysis strongly suggests that **3a** and **3b** are two diastereomers which only differ in their configuration of the asymmetric C1′ center of the DMNPE moiety. In addition, the etherification of the C12 hydroxy group of doxycycline is substantiated by a strong shift in the signals of C12 in the ^{13}C NMR spectra of **3a** and **3b** by $\Delta\delta = 15$ and 18 ppm, respectively, to higher fields relative to the chemical shift of C12 in doxycycline (see Supporting Information for the ^{1}H and ^{13}C NMR data of doxycycline).

Both diastereomers are characterized by a notable long-wavelength absorption maximum at around 345 nm (see Table 1 and Supporting Information), which is caused by the overlap of the long-wavelength absorption bands of the phenolic β-diketone system in doxycycline and the DMNPE chromophore. Irradiation of **3a** and **3b** between 300 and 400 nm in aqueous buffer solution led to the photorelease of doxycycline, as confirmed by HPLC analysis (data not shown), and the 4,5-dimethoxy-2-nitrosoacetophenone by-product of the caging group, which did not show any harmful effect in the biological experiments. Furthermore, **3a** and **3b** displayed acceptable photochemical quantum yields (Table 1).

Table 1: Properties of **3a** and **3b**.

Caged doxycycline	Absorbance maximum[a] λ_{max} [nm]	Extinction coefficient[a] ε_{max} [$M^{-1}cm^{-1}$]	Photolysis quantum yield ϕ[b]	Solubility[a] c_{sat} [μM]
3a	≈347	10500	0.013	380
3b	345.5	11400	0.075	770

[a] In HEPES buffer solution, pH 7.2. [b] In HEPES buffer solution (pH 7.2)/acetonitrile (80:20, v/v).

Compounds **3a** and **3b** were relatively soluble in aqueous 2-[4-(2-hydroxyethyl)-1-piperazinyl]ethanesulfonic acid (HEPES) buffer solution at pH 7.2 (Table 1). This solubility is essential for applications of caged doxycycline in sensitive tissues, such as the nervous system, which do not tolerate alcohols or other organic solvents as vehicles.[5] Thus, concentrated stock solutions can be readily prepared and maintained in water. In addition, **3a** and **3b** were tested for their hydrolytic stability in aqueous buffers. Incubation for 2 days at 37 °C did not lead to release of doxycycline, as determined by HPLC analysis (data not shown). Pilot experiments to assess the suitability of **3a** and **3b** for photoactivated gene expression showed that **3a** had only little background activity, whereas **3b** produced significant transgene expression even in the absence of irradiation. We currently do not understand the reason for this difference especially as both molecules are stable isomers. However, given that both isomers displayed surprisingly different physicochemical properties, differences in their biological properties were therefore not unexpected. Consequently, **3a** was used for all further experiments.

Caged doxycycline should ideally be membrane permeant so that photoactivated gene expression is able to control transgene expression in single cells. Although in many applications doxycycline may be photoreleased extracellularly to subsequently diffuse into the cytoplasm for transgene induction, this scenario will probably not permit single-cell resolution. The membrane permeability of **3a** was therefore assessed by isothermal titration calorimetry (ITC).[6,7] A comparison of ITC uptake and release protocols demonstrated that **3a** can quickly cross the membranes of large unilamellar vesicles (LUVs) composed of the zwitterionic phospholipid 1-palmitoyl-3-oleoyl-*sn*-glycero-2-phosphocholine (POPC).

Figure 1 a shows a good simultaneous fit (red lines) to the heats of the reaction Q obtained in uptake (diamonds) and release (circles) experiments. This fit was based on the assumptions of ideal mixing and full lipid accessibility of the caged compound, that is, complete transbilayer equilibration within the time needed for a single injection. In contrast, based on the assumption that **3a** cannot traverse membranes, the fit in Figure 1 b failed to describe the experimental data, as there were significant deviations at low injection numbers n (see Supporting Information for the ITC experimental data). Repetition of the experiment again with **3a** and once with a mixture of **3a**/**3b** produced almost identical results (data not shown). The validity of using ITC to test for membrane permeability was demonstrated in another set of experiments

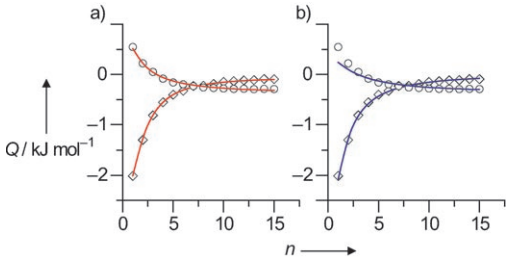

Figure 1. ITC analysis of translocation of **3a** across POPC membranes. The heats of the reaction of water–membrane partitioning Q obtained in uptake (diamonds) and release (circles) experiments are plotted versus the injection number n. a) The fit (red lines) matches the experimental data well (based on the assumption of complete membrane permeation). b) A poor fit (blue lines) is obtained particularly for the critical early injections (assuming no detectable membrane permeation on the experimental timescale).

 © 2006 Wiley-VCH Verlag GmbH & Co. KGaA, Weinheim

which showed the differential temperature-dependent membrane partitioning of sodium dodecyl sulfate (SDS; see Supporting Information).[7] Taken together, the data strongly suggest that the chemically modified doxycycline retained the ability to passively cross membranes, which in turn should aid the photoactivation of single cells.

To determine if caged doxycycline could be used for photoactivated gene expression, two different expression paradigms were tested. First, as a proof-of-principle experiment, we employed stably transfected Chinese hamster ovary (CHO) cells which express M2-rtTA[8] and contain a tetracycline-dependent enhanced green fluorescent protein (EGFP) construct. Incubation of these cells with unmodified doxycycline led to widespread green-fluorescent-protein (GFP) fluorescence (Figure 2a). Conversely, incubation with **3a** did not produce any fluorescence, thus indicating that its transcriptional activity was inhibited (Figure 2b). However, irradiation of cells in the same dish with long-wavelength UV light induced significant EGFP expression similar to EGFP levels seen with unmodified doxycycline. These data demonstrated that caged doxycycline can be used for photoactivated gene expression as a tool for localized transgene expression.

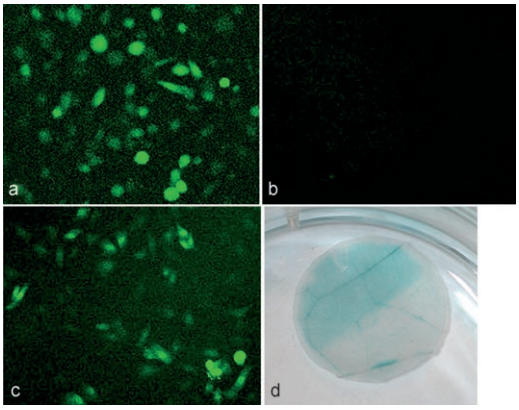

Figure 2. Spatially restricted photoactivated gene expression. a) CHO cells (M2-rtTA: tetEGFP) incubated with unmodified doxycycline. b) CHO cells incubated with **3a**, no irradiation. c) Same dish as in Figure 2b; irradiation-induced, widespread EGFP fluorescence. d) A sharp boundary between irradiated and non-irradiated areas was revealed by photoactivation of a GUS reporter gene in one half of transgenic tobacco tissue.

To test photoactivation in a three-dimensional tissue, a second paradigm was employed using transgenic tobacco leafs which harbored a quasi Tet-on system based on de-repression of a constitutive cauliflower mosaic virus (CaMV) 35S promoter which drives a β-glucuronidase (GUS) reporter gene.[9] Thus, in the absence of doxycycline, the Tet repressor prevents transcription from a modified CaMV promoter that contains three repressor binding sites. Incubation of leaf tissue with **3a** followed by irradiation produced a sharp boundary of GUS expression between the irradiated and non-irradiated areas (Figure 2d). To our knowledge, this method is the first that uses photoactivation based on an inducible gene expression paradigm to direct transgene expression with high precision in compact tissue as opposed to dispersed cells in culture.

In conclusion, we demonstrated that transgene expression can be accurately manipulated by simple irradiation with UV light. The doses of UV light needed for induction were not harmful, as no signs of cell damage were apparent (see Supporting Information). Previously, small-molecule-based photoactivated gene expression was demonstrated in cell culture with caged tamoxifen by global irradiation of the entire cell-culture medium.[10] Although this approach did not yield any spatial resolution, a different approach by Lawrence and co-workers in which caged ecdysone was applied followed by local photoactivation indeed induced transgene expression only in irradiated 293T cells.[11] The photoactivated gene-expression system described herein is based on the popular Tet system, which provides a rich infrastructure of Tet-dependent transgenes in various organisms that range from yeast to plants and mice. Thus, we have established a paradigm for the photoactivation of genes with single-cell resolution. We predict that this approach will be a tremendously powerful tool for various research areas, including single-cell lineage tracing during the development or implementation of a better cancer model by induction of oncogenes in single cells surrounded by a wild-type background.

Received: September 20, 2005
Revised: January 2, 2006
Published online: February 28, 2006

Keywords: caged compounds · gene expression · membranes · photolysis

[1] M. Gossen, A. L. Bonin, S. Freundlieb, H. Bujard, *Curr. Opin. Biotechnol.* **1994**, *5*, 516–520.
[2] S. B. Cambridge, R. L. Davis, J. S. Minden, *Science* **1997**, *277*, 825–828.
[3] M. Gossen, S. Freundlieb, G. Bender, G. Muller, W. Hillen, H. Bujard, *Science* **1995**, *268*, 1766–1769.
[4] W. Hinrichs, C. Kisker, M. Duvel, A. Muller, K. Tovar, W. Hillen, W. Saenger, *Science* **1994**, *264*, 418–420.
[5] G. Lindner, G. Grosse, *Z. Mikrosk.-Anat. Forsch.* **1976**, *90*, 557–564.
[6] H. H. Heerklotz, H. Binder, R. M. Epand, *Biophys. J.* **1999**, *76*, 2606–2613.
[7] S. Keller, H. H. Heerklotz, A. Blume, *J. Am. Chem. Soc.* **2005**, *128*, 1279–1286.
[8] S. Urlinger, U. Baron, M. Thellmann, M. T. Hasan, H. Bujard, W. Hillen, *Proc. Natl. Acad. Sci. USA* **2000**, *97*, 7963–7968.
[9] C. Gatz, C. Frohberg, R. Wendenburg, *Plant J.* **1992**, *2*, 397–404.
[10] Y. H. Shi, J. T. Koh, *ChemBioChem* **2004**, *5*, 788–796.
[11] W. Lin, C. Albanese, R. G. Pestell, D. S. Lawrence, *Chem. Biol.* **2002**, *9*, 1347–1353.

 © 2006 Wiley-VCH Verlag GmbH & Co. KGaA, Weinheim

Block Copolymers

DOI: 10.1002/anie.200503575

A Subtle End-Group Effect on Macroscopic Physical Gelation of Triblock Copolymer Aqueous Solutions**

*Lin Yu, Huan Zhang, and Jiandong Ding**

During the last few decades, many researchers have investigated the self-assembly behavior of amphiphilic block copolymers. Most of these studies concerned nanostructures that resulted from self-assembly. In contrast, we have studied the end-group effect on the macroscopic self-assembly, which leads to formation of a biocompatible hydrogel. Although fruitful phenomena related to the end-group effect on microscopic molecular conformation and nanoscale aggregates have been observed in various organic molecules in selective solvents,[1–4] reports of the end-group effect on the condensed-state behavior of self-assembled soft matter are rather limited.

As a biomimetic wet material, polymeric hydrogel is a very important type of soft matter. Hydrogels capable of responding to external influences, such as temperature,[5–8] pH,[9] light,[10,11] counterion changes,[12] biological molecules,[13] and multiple factors,[14,15] have been extensively investigated, as they have great potential value in drug-delivery systems and tissue engineering,[16–19] sensors and valves,[20,21] surface patterning,[22,23] and tunable optics.[24] Some biodegradable/bioabsorbable hydrogels can form a gel in situ, and therefore are especially attractive as injectable biomaterials.[16,25–27] Amorphous and biodegradable polymers with thermoinduced shape memory are also promising for use in minimally invasive surgery.[28–30] Most hydrogels are formed by irreversible chemical cross-linking, but reversible physical gelation is another interesting topic in both fundamental research and potential applications. Recently, a few stimuli-responsive biodegradable physical gels have been reported in some multicomponent polymers, for instance, poly(ethylene glycol)–poly(α-hydroxy acid),[16,31] poly(ethylene glycol)–polycaprolactone,[6,7] chitosan–glycerol phosphate,[32] and copolypeptides.[33,34]

[*] L. Yu, H. Zhang, Prof. Dr. J. Ding
Key Laboratory of Molecular Engineering of Polymers
Department of Macromolecular Science
Fudan University
Shanghai 200433 (China)
Fax: (+86) 21-6564-0293
E-mail: jdding1@fudan.edu.cn

[**] We are grateful for the financial support from the NSF of China (20374015, 50533010, and 20574013), the Key Grant of the Chinese Ministry of Education (305004), 973 Project and 863 Project (2005CB522700) from the Chinese Ministry of Science and Technology, and the Science and Technology Developing Foundation of Shanghai (04JC14019 and 055207082).

Supporting information for this article is available on the WWW under http://www.angewandte.org or from the author.

Herein, we report the discovery that an alkyl end group can induce a thermoreversible physical gelation in an otherwise sol-like suspension. It is well-known that an end group with an opposite lyophilicity can lead to the formation of nanoparticles through self-assembly.[35] Nevertheless, the alkyl end-group effect leading to macroscopic gelation reported herein is rather unique. Such a subtle effect for biodegradable synthetic molecules in water is very interesting and meaningful for biomaterials and other applications.

A series of barbell-like ABA-type triblock copolymers of poly(ethylene glycol) (PEG) and poly(lactic acid-*co*-glycolic acid) (PLGA), that is, PLGA-PEG-PLGA with different end caps, were synthesized and characterized. PEG is hydrophilic, whereas PLGA is hydrophobic and biodegradable by the hydrolysis of ester bonds.[19,30,36,37] Both PEG and PLGA are biocompatible and have been clinically used as implant biomaterials. The block copolymer composed of PLGA and PEG with the composition described is, by itself, not transformed into gels by changing the temperature, but we found that some of its derivatives exhibited a reversible sol–gel transition as a function of temperature. A very subtle end-group effect on the macroscopic self-assembly of soft matter has thus been revealed. The mechanism of the underlying sol–gel transition is also discussed.

The symmetric PLGA-PEG-PLGA copolymer with two hydroxy end groups (sample A) was synthesized by the ring-opening polymerization of DL-lactide and glycolide in the presence of PEG. Its derivatives with other end-capping groups (samples B–D) were prepared through the alcoholysis of acyl chloride (see Supporting Information). Formation of the PLGA-PEG-PLGA triblock copolymer and its derivatives was confirmed by ^{1}H NMR spectroscopy in $CDCl_3$. The extent of esterification was higher than 90% for all derivatives.

Gel-permeation chromatography (GPC) was used to determine the molecular weight of the polymers and its distribution. All of the GPC traces of the triblock copolymer and its derivatives were unimodal with a polydispersity of less than 1.2. Data for the four samples are listed in Table 1.

The original PLGA-PEG-PLGA block copolymer is quite hydrophilic, and thus sample A was soluble in water (Figure 1a). However, a physical gel was observed at room temperature when the hydroxy end groups were replaced with acetate groups (Figure 1b). The sample with propionate end groups also formed a gel (Figure 1c). The end-group effect is

 InterScience © 2006 Wiley-VCH Verlag GmbH & Co. KGaA, Weinheim

Table 1: Characteristics of the four samples A–D.

Sample	M_n[a]	LA/GA [mol/mol][b]	M_n[c]	(M_w/M_n)[c]	CMC [wt%][d]	CGC [wt%][e]
A	900-1000-900	1.6	3172	1.14	0.047 ± 0.005	–
B	943-1000-943	1.6	3240	1.13	0.034 ± 0.003	16
C	957-1000-957	1.6	3389	1.15	0.027 ± 0.002	14
D	971-1000-971	1.6	3484	1.11	–	–

[a] The number-average molecular weight (M_n) of the central block PEG was provided by Aldrich. [b] The molar ratio of lactide/glycolide (LA/GA) and thus the M_n of each PLGA block was calculated from ^{1}H NMR experiments. [c] The M_n of the copolymers and their polydispersity indexes (M_w/M_n) were measured by GPC. [d] The critical micelle concentration (CMC) was measured by the method of hydrophobic probe solubilization at 25 °C. [e] The critical gel concentration (CGC) was obtained from the phase diagram in Figure 2.

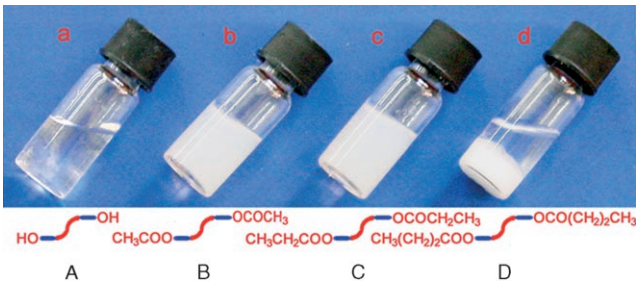

Figure 1. a–d) Images of the triblock copolymer/water mixtures showing the sol, gel, gel, and precipitation states for samples A–D, respectively. Concentration: 25 wt%; temperature: 25 °C.

so subtle that the butyrate end groups led to precipitation in the whole temperature region (from 0 to 50 °C, Figure 1 d).

The condensed states of samples B and C were highly dependent on temperature. The phase diagrams of the PLGA-PEG-PLGA derivatives with acetate and propionate end groups are shown in Figure 2. The sol–gel transition was determined by the test-tube inversion method.[31] The sample was regarded as a gel if no flow was observed 30 s after the vial was inverted. Both the upper critical solution temperature (UCST) and lower critical solution temperature (LCST) were established. The polymer–water mixtures had three

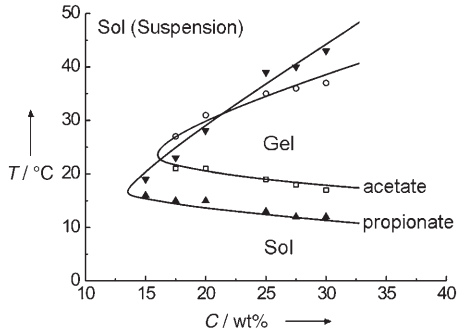

Figure 2. Phase diagrams of PLGA-PEG-PLGA block copolymers B and C in water at various temperatures T and concentrations C. The symbols ▲ and ▼ indicate the boundaries of sol–gel and gel–sol (suspension) for sample B, while □ and ○ indicate these boundaries for sample C.

physical states at 0 to 50 °C: solution, gel, and re-solution again (the re-solution was actually a flowable suspension that eventually led to precipitation). The degradation time was on the order of weeks (data not shown), whereas the measurement of a phase diagram lasted for 8–10 h. Material degradation during the measurement should be insignificant, and therefore the approach to determining the phase diagrams is valid even for such a biodegradable material.

Figure 2 also indicates that the critical gel concentration (CGC) drops from 16–14 wt% on changing the end group from the acetate to the propionate group. The increase of hydrophobicity of the end group strengthens the hydrophobic interaction between chains, which is responsible for the decrease of the CGC and also of the sol–gel phase-transition temperature.

Rheological measurement or dynamic mechanical analysis was used to obtain the storage modulus G' and viscosity η (associated with dissipative modulus G''). G' and η are measures of the load-bearing capacity and dissipated energy, respectively, when a material undergoes a cyclic deformation. An abrupt increase of both G' and η was found with an increase in temperature. The rheological measurements demonstrated that even the original PLGA-PEG-PLGA block copolymer could exhibit significant thermosensitivity. (The highest viscosity was not large enough to allow the aqueous solution to act like a "gel", and thus the thermoinduced transition of the virgin polymer was hidden in the test-tube inversion experiment.) The data from different samples were similar at low temperatures, but were very different at high temperatures. The results at low and high temperatures (Figure 3) indicate that the thermosensitivity of the derivative capped with alkyl groups was much more significant than that of the virgin polymer with the hydroxy end groups, as the mechanical quantities spanned more than four orders of magnitude for samples B and C but just two orders of magnitude for sample A. Figure 3 also reveals that the transition temperature was lowered with an increase in hydrophobicity of the end groups, which was consistent with the measurements from the test-tube inversion experiments (Figure 2).

Our rheological measurements confirm that despite hysteresis, the sol–gel transition is basically thermoreversible. Recovery to the sol state on cooling sample C occurred rather slowly because of the more hydrophobic propionate end groups, and thus a very striking hysteresis was observed during the first heating and cooling cycle. Nevertheless, after further cooling for a sufficiently long time, the second heating process resulted in a good consistency with the first heating cycle (Figure 3). Hence, the sol–gel transition in our samples is thermodynamically reversible.

A question now arises: do the amphiphilic molecules form a gel straightforwardly or through a hierarchical mechanism, namely, first forming micelles and then forming a gel by further aggregation of percolated micelles? A comparison of the critical micelle concentration (CMC) and CGC should thus be performed. The CMC was determined by the hydrophobic dye solubilization method with 1,6-diphenyl-1,3,5-hexatriene (DPH) as the probe,[38] and the CGC was obtained from the phase diagrams in Figure 2 by the test-tube inversion

 © 2006 Wiley-VCH Verlag GmbH & Co. KGaA, Weinheim

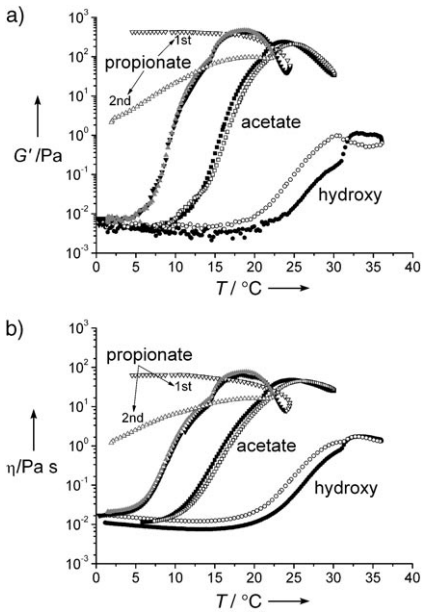

Figure 3. a) Storage modulus G' and b) viscosity η of the block copolymers PLGA-PEG-PLGA with hydroxy, acetate, and propionate end groups in aqueous solution (20 wt%) as a function of temperature T in dynamic rheological measurements. Heating and cooling rates: 0.5 K min^{-1}; oscillatory frequency: 10 rad s^{-1}. The filled and empty symbols represent the data resulting from heating and cooling, respectively. After the first heating and cooling cycle, sample C and the coaxial Couette cylinder were placed in a refrigerator at 4 °C for 12 h; then a second heating and cooling cycle was recorded.

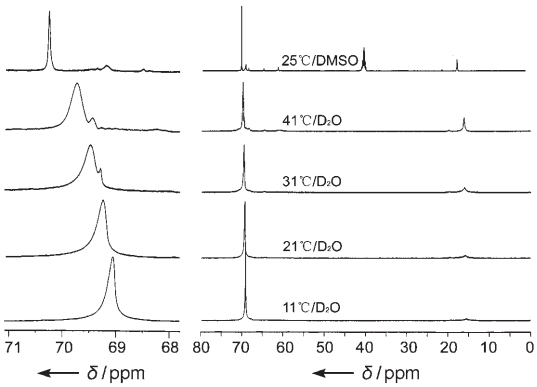

Figure 4. ^{13}C NMR spectra of PLGA-PEG-PLGA copolymer with acetate end groups (sample B) in D_2O (25 wt%) at the indicated temperatures. The solution was equilibrated for 20 min at the setting temperature before measurement. The spectrum in [D_6]DMSO is shown as control.

method. Table 1 summarizes the data for the PLGA-PEG-PLGA triblock copolymer and its derivatives. According to these results, the CGC is much higher than the CMC for all of the available samples. Therefore, micelles must have been formed before gelation.

Dynamic light scattering showed that the micelles from samples A–C had average hydrodynamic radii of 11.3, 18.6, and 22.2 nm, respectively, measured at 14 °C at a low concentration (0.5 wt%). Micellar aggregates were also detected with an increase of temperature or concentration. Strong evidence for the integrality of micelles in aggregation came from NMR experiments. To interpret the molecular mechanism of the sol–gel phase transition, the ^{13}C NMR spectra[31] of the polymers were measured in both water and dimethyl sulfoxide (DMSO; Figure 4). DMSO is a good solvent for all of the copolymer blocks, so both the methyl group of PLGA and the ethylene group of PEG are shown as sharp peaks in [D_6]DMSO. Water is a good solvent for PEG but a poor solvent for PLGA. Therefore in water, the methyl group (15–16 ppm) of PLGA appears as a broadened and collapsed peak in the sol state (11 °C), whereas the ethylene group (69–70 ppm) of PEG appears as a sharp peak. During the sol–gel transition (21 °C), these characteristics in the NMR spectra remained unchanged, thus indicating no considerable change in the core–corona micellar structure during physical gelation. On increasing the temperature to 31 °C (the gel state), the PEG peak split into two separate subpeaks, with a strong subpeak at $\delta = 69.5$ ppm and a weak one at $\delta =$ 69.3 ppm, and the height of the peak from the methyl group of PLGA was slightly enhanced. This behavior might have been caused by an increase in the thermal motion of the hydrophobic chain and the disturbance of the micellar structure. At a higher temperature (41 °C) the PEG peak split further, whereas the height of the peak from the methyl group of PLGA increased significantly. This finding suggests that the core–corona structure of the micelles in the aqueous environment was broken and the hydrophobic blocks were exposed to water, which led to a re-sol state at 41 °C as shown in the phase diagram (Figure 2).

Combination of the data in Figures 1 to 4 confirms the hierarchical mechanism for the physical gelation studied herein: the amphiphilic block copolymers are first assembled into micelles; then the micelles are further aggregated to form a macroscopic gel, and an intact micellar structure is kept during the sol–gel transition. Although the quantitative theoretical prediction of the phase-transition point is still open, the LCST behavior implies that both micellization and gelation are driven by an entropy effect that results from the hydrophobic interaction. The alkyl group is rather hydrophobic and the gelation is very sensitive to the end groups. The sol–gel transition cannot happen unless the hydrophobic interaction is strong enough to induce the large-scale self-assembly of micelles. Gelation also cannot occur when the micellar structure is broken at higher temperatures, or when the block copolymer derivative is over-hydrophobic and leads to macroscopic phase separation between polymer and water. Therefore, the end-group effect is especially significant when an amphiphilic block copolymer has a moderate lyophilicity with a subtle balance between hydrophilicity and hydrophobicity.

In summary, PLGA-PEG-PLGA and its derivatives were synthesized, and a surprising end-group effect on the macroscopic self-assembly behavior was found. The aqueous solution of the PLGA-PEG-PLGA triblock copolymer exhibited a sol state in the temperature range examined. In contrast, the polymer derivatives end-capped with acetate or propionate groups underwent a reversible sol–gel transition as a function of temperature, whereas the block copolymer capped with the butyrate group precipitated in water. The

 © 2006 Wiley-VCH Verlag GmbH & Co. KGaA, Weinheim

mechanism of the sol–gel transition of the thermogelling derivatives was further discussed. Our study also reveals that a small end group in a moderately lyophilic polymer can adjust not only the microscopic self-assembled nanostructures, but also the macroscopic condensed-state behavior of the underlying soft matter as a result of large-scale self-assembly. Thus, this research gives some new insights into the relationship between physical gelation and chemical composition, and affords a molecule-design approach to preparing novel injectable biomedical materials and intelligent wet devices.

Received: October 8, 2005
Revised: December 18, 2005
Published online: March 3, 2006

Keywords: block copolymers · gels · phase transitions · self-assembly · sol–gel processes

[1] C. H. Tung, Y. M. Wang, *J. Am. Chem. Soc.* **1990**, *112*, 6322.
[2] A. C. Smith, D. H. Macartney, *J. Org. Chem.* **1998**, *63*, 9243.
[3] S. Y. Liu, T. J. Hu, H. J. Liang, M. Jiang, C. Wu, *Macromolecules* **2000**, *33*, 8640.
[4] X. B. Shao, X. K. Jiang, S. Z. Zhu, Z. T. Li, *Tetrahedron* **2004**, *60*, 9155.
[5] E. Wischerhoff, T. Zacher, A. Laschewsky, E. Rekai, *Angew. Chem.* **2000**, *112*, 4771; *Angew. Chem. Int. Ed.* **2000**, *39*, 4602.
[6] M. J. Hwang, J. M. Suh, Y. H. Bae, S. W. Kim, B. Jeong, *Biomacromolecules* **2005**, *6*, 885.
[7] S. J. Bae, J. M. Suh, Y. S. Sohn, Y. H. Bae, S. W. Kim, B. Jeong, *Macromolecules* **2005**, *38*, 5260.
[8] H. Yan, H. Fujiwara, K. Sasaki, K. Tsujii, *Angew. Chem.* **2005**, *117*, 1987; *Angew. Chem. Int. Ed.* **2005**, *44*, 1951.
[9] S. C. Ji, J. D. Ding, *Polym. J.* **2001**, *33*, 701.
[10] S. Nayak, L. A. Lyon, *Chem. Mater.* **2004**, *16*, 2623.
[11] J. J. D. de Jong, P. R. Hania, A. Pagzlys, L. N. Lucas, M. de Loos, R. M. Kellogg, B. L. Feringa, K. Duppen, J. H. van Esch, *Angew. Chem.* **2005**, *117*, 2425; *Angew. Chem. Int. Ed.* **2005**, *44*, 2373.
[12] H.-J. Kim, J.-H. Lee, M. Lee, *Angew. Chem.* **2005**, *117*, 5960; *Angew. Chem. Int. Ed.* **2005**, *44*, 5810.
[13] J. T. Suri, D. B. Cordes, F. E. Cappuccio, R. A. Wessling, B. Singaram, *Angew. Chem.* **2003**, *115*, 6037; *Angew. Chem. Int. Ed.* **2003**, *42*, 5857.
[14] S. F. Peng, C. Wu, *Macromolecules* **2001**, *34*, 568.
[15] K. J. C. van Bommel, C. van der Pol, I. Muizebelt, A. Friggeri, A. Heeres, A. Meetsma, B. L. Feringa, J. van Esch, *Angew. Chem.* **2004**, *116*, 1695; *Angew. Chem. Int. Ed.* **2004**, *43*, 1663.
[16] B. Jeong, Y. H. Bae, D. S. Lee, S. W. Kim, *Nature* **1997**, *388*, 860.
[17] G. M. Zentner, R. Rathi, C. Shih, J. C. McRea, M. H. Seo, H. Oh, B. G. Rhee, J. Mestecky, Z. Moldoveanu, M. Morgan, S. Weitman, *J. Controlled Release* **2001**, *72*, 203.
[18] J. C. Tiller, *Angew. Chem.* **2003**, *115*, 3180; *Angew. Chem. Int. Ed.* **2003**, *42*, 3072.
[19] Y. Zhang, W. Zhu, B. B. Wang, J. D. Ding, *J. Controlled Release* **2005**, *105*, 260.
[20] J. H. Holtz, S. A. Asher, *Nature* **1997**, *389*, 829.
[21] D. J. Beebe, J. S. Moore, J. M. Bauer, Q. Yu, R. H. Liu, C. Devadoss, B. H. Jo, *Nature* **2000**, *404*, 588.
[22] Z. B. Hu, Y. Y. Chen, C. J. Wang, Y. D. Zheng, Y. Li, *Nature* **1998**, *393*, 149.
[23] K. Y. Suh, R. Langer, J. Lahann, *Adv. Mater.* **2004**, *16*, 1401.
[24] J. Kim, M. J. Serpe, L. A. Lyon, *Angew. Chem.* **2005**, *117*, 1357; *Angew. Chem. Int. Ed.* **2005**, *44*, 1333.
[25] Y. L. Cao, A. Rodriguez, M. Vacanti, C. Ibarra, C. Arevalo, C. A. Vacanti, *J. Biomater. Sci. Polym. Ed.* **1998**, *9*, 475.
[26] X. Q. Jia, J. A. Burdick, J. Kobler, R. J. Clifton, J. J. Rosowski, S. M. Zeitels, R. Langer, *Macromolecules* **2004**, *37*, 3239.
[27] X. Q. Jia, G. Colombo, R. Padera, R. Langer, D. S. Kohane, *Biomaterials* **2004**, *25*, 4797.
[28] A. Lendlein, S. Kelch, *Angew. Chem.* **2002**, *114*, 2138; *Angew. Chem. Int. Ed.* **2002**, *41*, 2034.
[29] A. Lendlein, R. Langer, *Science* **2002**, *296*, 1673.
[30] A. Alteheld, Y. K. Feng, S. Kelch, A. Lendlein, *Angew. Chem.* **2005**, *117*, 1212; *Angew. Chem. Int. Ed.* **2005**, *44*, 1188.
[31] B. Jeong, Y. H. Bae, S. W. Kim, *Macromolecules* **1999**, *32*, 7064.
[32] A. Chenite, C. Chaput, D. Wang, C. Combes, M. D. Buschmann, C. D. Hoemann, J. C. Leroux, B. L. Atkinson, F. Binette, A. Selmani, *Biomaterials* **2000**, *21*, 2155.
[33] A. P. Nowak, V. Breedveld, L. Pakstis, B. Ozbas, D. J. Pine, D. Pochan, T. J. Deming, *Nature* **2002**, *417*, 424.
[34] A. Aggeli, M. Bell, N. Boden, L. M. Carrick, A. E. Strong, *Angew. Chem.* **2003**, *115*, 5761; *Angew. Chem. Int. Ed.* **2003**, *42*, 5603.
[35] K. Ito, K. Tanaka, H. Tanaka, G. Imai, S. Kawaguchi, S. Itsuno, *Macromolecules* **1991**, *24*, 2348.
[36] L. B. Wu, J. D. Ding, *Biomaterials* **2004**, *25*, 5821.
[37] L. B. Wu, H. Zhang, J. C. Zhang, J. D. Ding, *Tissue Eng.* **2005**, *11*, 1105.
[38] P. Alexandridis, J. F. Holzwarth, T. A. Hatton, *Macromolecules* **1994**, *27*, 2414.

 © 2006 Wiley-VCH Verlag GmbH & Co. KGaA, Weinheim

Asymmetric Rearrangement

DOI: 10.1002/anie.200503734

Asymmetric Retro-[1,4] Brook Rearrangement and Its Stereochemical Course at Silicon**

*Atsuo Nakazaki, Takeshi Nakai, and Katsuhiko Tomooka**

The trialkylsilyl group shift from the oxygen atom of a silyl ether to a carbanion terminus—the retro-Brook rearrangement—is useful for the preparation of functionalized organo-

[*] Dr. A. Nakazaki, Prof. Dr. T. Nakai, Prof. Dr. K. Tomooka
Department of Applied Chemistry
Graduate School of Science and Engineering
Tokyo Institute of Technology
Meguro-ku, Tokyo 152-8552 (Japan)
Fax: (+81) 3-5734-3931
E-mail: ktomooka@apc.titech.ac.jp

[**] This research was supported by a Grant-in-Aid for Scientific Research on Priority Areas (A) "Creation of Biologically Functional Molecules", Basic Area (B) No. 14350473, Exploratory Research No. 17655038, and the 21st Century COE Program "Creation of Molecular Diversity and Development of Functionalities" from the Ministry of Education, Culture, Sports, Science, and Technology, Japan. The authors thank Dr. Kazunobu Igawa and Tomohiro Shimono for helpful discussions and technical assistance.

Supporting information for this article is available on the WWW under http://www.angewandte.org or from the author.

© 2006 Wiley-VCH Verlag GmbH & Co. KGaA, Weinheim

silanes.[1] Among numerous variants, the rearrangement of an allyloxysilane system is one of the most attractive because of the great synthetic potential of the resultant allylsilanes.[2] In addition to the normal [1,2] shift, a [1,4] shift is possible in this particular system [Eq. (1)]. To the best of our knowledge, however, the [1,4] rearrangement leading to a γ-alkoxyallylsilane system has remained elusive.[3]

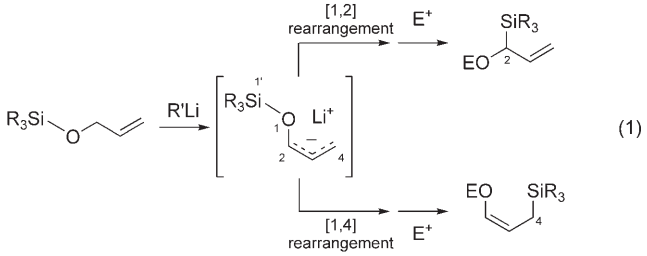

(1)

Herein, we report the retro-[1,4] Brook rearrangement of a simple allyloxysilane, in which the judicious choice of electrophile (E), solvent system, and migrating silyl group (R_3Si) enables this unprecedented [1,4] periselectivity. Of particular note is the stereospecificity of this process, which has been unequivocally determined by using an enantiomerically pure allyloxysilane with a silicon stereocenter [Eq. (2)]. Asymmetric synthesis of γ-functionalized allylsilanes with a stereogenic Si-center is accomplished with this retro-[1,4] Brook rearrangement.

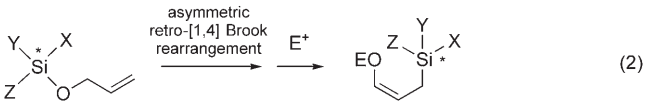

(2)

Initial experiments focused on the retro-[1,4] Brook rearrangement of the simple allyloxysilane **1a** with *t*BuLi in THF. When the reaction was quenched with chlorotrimethylsilane as an electrophile, the [1,2] product **2a** (E = Me_3Si) was obtained exclusively; this result is consistent with the claim of Chan and Lau that no [1,4] product **3a** (E = Me_3Si) was formed (Table 1, entry 1).[3c] In sharp contrast, with *tert*-butyldimethylsilyl trifluoromethanesulfonate (*t*$BuMe_2SiOTf$) as an electrophile, the [1,4] rearrangement product **3b**[4] (E = *t*$BuMe_2Si$) was formed in 25% yield with excellent *Z* selectivity, along with the [1,2] product **2b** (E = *t*$BuMe_2Si$) in 45% yield (Table 1, entry 2). Furthermore, addition of hexamethylphosphoramide (HMPA) as a cosolvent improves the [1,4] selectivity and suppresses the formation of the usual [1,2] product completely (Table 1, entry 3).[5]

This highly electrophile- and solvent-dependent periselectivity suggested that the rearrangement would be reversible, and that its product distribution might be determined at the stage of enolate trapping, although the exact origin of the product changeover is not clear at present.[6] Notably, a reaction in THF/HMPA quenched with iodomethane provides (*Z*)-$Et_3SiOCH{=}CHCH_2Me$ exclusively, and none of the retro-Brook rearrangement products was formed; this finding is consistent with the results of Still and Macdonald.[3a] Under the optimized conditions using HMPA and *t*$BuMe_2SiOTf$, allyloxysilanes with bulkier silyl groups undergo selective retro-[1,4] rearrangement to give **3** in high yields. For example, the reaction of *t*$BuPh_2Si$ ether **1b** or Ph*t*Bu(OMe)Si ether **1c** gave the [1,4] products (*Z*)-**3c** and (*Z*)-**3d** as the sole products in 95 and 72% yields, respectively. At this stage, we became aware that the effect of an electrophile on the periselectivity becomes negligible as long as *t*$BuPh_2Si$ or Ph*t*Bu(OMe)Si is used as the migrating group. For example, not only *t*$BuMe_2SiOTf$ but also Et_3SiCl, MeOCOCl, and *i*Pr_2NCOCl gave the retro-[1,4] Brook rearrangement products **3e–h** in moderate to high yields (Table 1, entries 6–9). Moreover, Ph*t*Bu(OMe)Si ethers **4** with various substitution patterns in the allyl moiety were smoothly converted into the corresponding retro-[1,4] Brook rearrangement products **5** (Table 2). It is particularly noticeable that the resulting double bonds are formed with high stereoselectivity (Table 2, entries 1–4).

Furthermore, moderate to good diastereoselectivities were observed in the case of a γ-substituted system ($R^3 \neq H$) (Table 2, entries 3 and 4).[7] Although the stereoselectivity did not reach a practically useful level, these reactions are rare examples of asymmetric induction from Si* to C*.[8–10]

Our attention was next directed toward the stereochemical course at the migrating silicon center, which has been a fundamental but unsettled problem of the retro-Brook rearrangement.[11–13] To gain a definitive answer to the question, we chose the enantiomerically defined chiral allyloxysilane (*S*)-**1c** as substrate, which was readily available from our previously developed [1,4]-aryl migration reaction.[14,15] Rearrangement product **3d** derived from (*S*)-**1c** (>95% *ee*) obtained with >95% *ee* by chiral HPLC analysis, which clearly shows that the rearrangement proceeds in a stereospecific manner at the migrating silicon center (Scheme 1).[16]

To determine whether this reaction proceeds with retention or inversion with respect to the configuration of the silicon

Table 1: Rearrangement of allyloxysilane **1**.

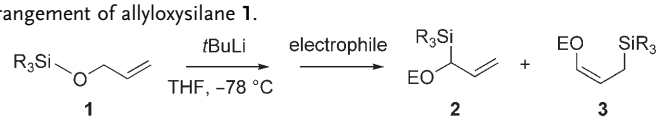

1 **2** **3**

Entry	Substrate	R_3Si	E	**2**	Yield [%][a]	**3**	Yield [%][a]
1	**1a**	Et_3Si	Me_3Si[d]	**2a**	85	**3a**	n.d.
2	**1a**	Et_3Si	*t*$BuMe_2Si$[e]	**2b**	45	**3b**	25
3[b]	**1a**	Et_3Si	*t*$BuMe_2Si$[e]	**2b**	n.d.	**3b**	56
4[b]	**1b**	*t*$BuPh_2Si$	*t*$BuMe_2Si$[e]	**2c**	n.d.	**3c**	95
5[b]	**1c**	Ph*t*Bu(OMe)Si	*t*$BuMe_2Si$[e]	**2d**	n.d.	**3d**	72
6[b,c]	**1b**	*t*$BuPh_2Si$	Et_3Si[d]	**2e**	n.d.	**3e**	98
7[b,c]	**1c**	Ph*t*Bu(OMe)Si	Et_3Si[d]	**2f**	n.d.	**3f**	81
8[b]	**1c**	Ph*t*Bu(OMe)Si	MeOCO[d]	**2g**	n.d.	**3g**	96
9[b,c]	**1c**	Ph*t*Bu(OMe)Si	*i*Pr_2NCO[d]	**2h**	n.d.	**3h**	50 [d]

[a] Yields of isolated products; n.d. = not detected by ^1H NMR spectroscopy or TLC analyses. [b] Reaction performed with 4.5 equiv of HMPA. [c] Reaction performed at −78→0°C. [d] β-Silylpropanal (from hydrolysis of **3h**) was obtained as a by-product in 11% yield. [e] Reacted as the chloride salt. [f] Reacted as the triflate salt.

 © 2006 Wiley-VCH Verlag GmbH & Co. KGaA, Weinheim

Table 2: Rearrangement of allyloxysilane **4**.

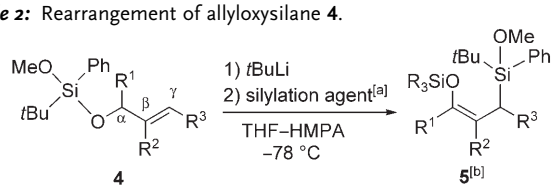

Entry	Substrate	R^1	R^2	R^3	R_3Si	Yield [%][c]	d.r.[d]
1	**4a**	Me	H	H	$tBuMe_2Si$	69	–
2	**4b**	H	Me	H	Et_3Si	80	–
3	**4c**	H	H	Me	$tBuMe_2Si$	10	83:17
4	**4d**	H	H	Me_3Si	$tBuMe_2Si$	72	66:34

[a] $tBuMe_2SiOTf$ or Et_3SiCl. [b] Geometrical purities are >98%. [c] Yields of isolated products. [d] Stereoisomers over the silicon stereocenter and the adjacent stereogenic carbon center in **5**. d.r. = diastereomeric ratio.

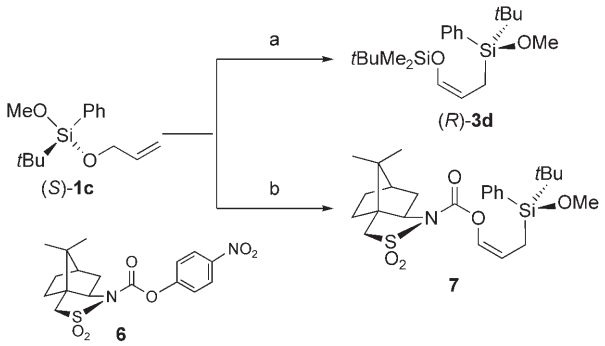

Scheme 1. Rearrangement of allyloxysilane (*S*)-**1c**. a) *t*BuLi, THF, HMPA, −78 °C; then $tBuMe_2SiOTf$, −78→0 °C, 72% (>95% *Z*, >95% *ee*); b) *t*BuLi, THF, HMPA, −78 °C; then **6**, −78→0 °C, 66% (d.r. = >95:<5). Tf = trifluoromethanesulfonyl.

center, we prepared **7** by trapping the lithium enolate with an enantiomerically pure sultam derivative **6**,[17] and a single-crystal X-ray diffraction study of **7** was performed.[18] As shown in Figure 1, the absolute configuration of the silicon center has been determined as the *R* configuration on the

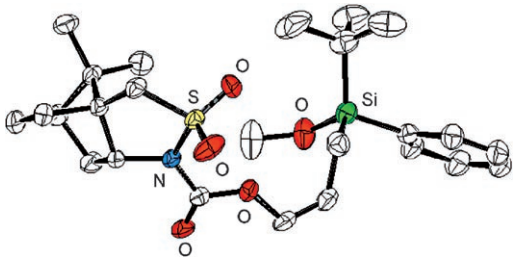

Figure 1. Molecular structure of **7** in the solid state. Hydrogen atoms have been omitted for clarity. The thermal ellipsoid probabilities are shown at 50%.

basis of the known chirality of sultam, which indicates that this novel retro-[1,4] Brook rearrangement proceeds via retention of configuration at the silicon center.

A plausible mechanism of this rearrangement is shown in Equation (3). Deprotonation of the allyloxysilane in α-position by *t*BuLi gives allyloxy anion **I** in cisoid form owing to the Li–O coordination,[19] and the γ carbon attacks the

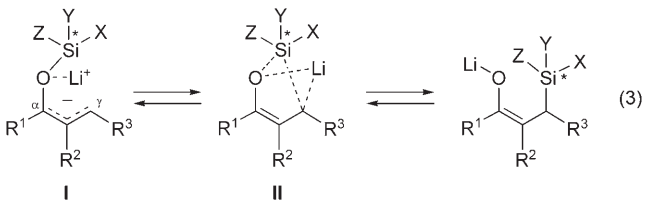

silicon atom. The silyl group then eliminates the oxygen through a five-membered transition state or intermediate **II**[20,21] with the least motion; thus, the configuration of the silicon center was retained without racemization.

In summary, we have described an unprecedented example of retro-[1,4] Brook rearrangement in an allyloxysilane system, the stereochemical course of which was clarified for the first time. The reaction provides not only synthetically attractive allylsilanes, but it also serves as a stereospecific approach to multifunctionalized chiral silanes. A detailed mechanistic study of the rearrangement and asymmetric synthesis using Si stereocenters is in progress.

Received: October 21, 2005
Revised: December 16, 2005
Published online: March 3, 2006

Keywords: asymmetric synthesis · chirality · rearrangement · silanes

[1] For reviews, see: a) R. West in *Advances in Organometallic Chemistry*, *Vol. 16* (Eds.: F. G. A. Stone, R. West), Academic Press, New York, **1977**, pp. 1–31; b) A. G. Brook, A. R. Bassindale in *Rearrangements in Ground and Excited States*, *Vol. 2* (Ed.: P. de Mayo), Academic Press, New York, **1980**, pp. 149–227; c) K. Tomooka in *The Chemistry of Organolithium Compounds*, *Vol. 2* (Eds.: Z. Rappoport, I. Marek), Wiley, Chichester, **2004**, pp. 749–828.
[2] For reviews, see: a) I. Fleming, A. Barbero, W. Walter, *Chem. Rev.* **1997**, *97*, 2063–2192; b) A. Hosomi, K. Miura, *Bull. Chem. Soc. Jpn.* **2004**, *77*, 835–851; c) L. Chabaud, P. James, Y. Landais, *Eur. J. Org. Chem.* **2004**, 3173–3199.
[3] For representative studies on retro-[1,2] Brook rearrangement, see: a) W. C. Still, T. L. Macdonald, *J. Am. Chem. Soc.* **1974**, *96*, 5561–5563; b) A. Hosomi, H. Hashimoto, H. Sakurai, *J. Org. Chem.* **1978**, *43*, 2551–2552; c) P. W. K. Lau, T. H. Chan, *J. Organomet. Chem.* **1979**, *179*, C24–C28.
[4] The structure of **3b** was confirmed by conversion to the corresponding β-silyl propinaldehyde by acidic hydrolysis. The details are given in the Supporting Information.
[5] A large excess of HMPA is important for high [1,4] selectivity. Indeed, a reaction with 1 equiv of HMPA provides [1,4] product **3b** in 38% yield, along with [1,2] product **2b** in 8% yield.
[6] Coordination of an electrophile or solvent to the lithium ion might affect the reactivity of the allylic anion. Further work, including NMR and IR analyses of the intermediate, is under way to elucidate the reaction mechanism.
[7] The relative configuration has not been determined.
[8] For reviews of asymmetric synthesis based on silicon stereocenters, see: a) T. H. Chan, D. Wang, *Chem. Rev.* **1992**, *92*, 995–1006; b) S. Bienz, *Chimia* **1997**, *51*, 133–139; c) M. Oestreich, *Chem. Eur. J.* **2006**, *12*, 30–37.
[9] For representative studies on chirality transfer from silicon to carbon, see: intramolecular version: a) D. R. Schmidt, S. J. O'Malley, J. L. Leighton, *J. Am. Chem. Soc.* **2003**, *125*, 1190–

 © 2006 Wiley-VCH Verlag GmbH & Co. KGaA, Weinheim

1191; intermolecular version: b) M. Oestreich, S. Rendler, *Angew. Chem.* **2005**, *117*, 1688–1691; *Angew. Chem. Int. Ed.* **2005**, *44*, 1661–1664, and references therein.

[10] We also attempted to form a C–C bond by the reaction of the lithium enolate with a carbon electrophile. Thus, silane **4a** was treated successively with *t*BuLi and iodomethane to afford the expected product **8** in 65% yield (d.r. = 66:34) [Eq. (4)].

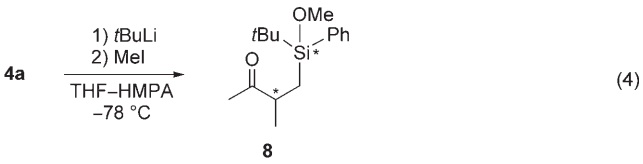

(4)

[11] The stereochemical course of the nucleophilic substitution on the silicon center has been investigated in various systems; it strongly depends on the leaving groups. a) L. H. Sommer in *Stereochemistry, Mechanism and Silicon*, McGraw-Hill, New York, **1965**; b) L. H. Sommer, *Intra-Sci. Chem. Rep.* **1973**, *7*, 1–44.

[12] The stereochemical course of the retro-[1,2] Brook rearrangement at a lithiated carbanion center has been investigated. For inversion of configuration at the benzylic anion, see: a) A. Wright, R. West, *J. Am. Chem. Soc.* **1974**, *96*, 3227–3232; for retention of configuration at the aliphatic anion, see: b) R. J. Linderman, A. Ghannam, *J. Am. Chem. Soc.* **1990**, *112*, 2392–2398.

[13] Ab initio calculations have shown that the configuration at the silicon center is retained in retro-[1,2] Brook rearrangements. Y. Wang, M. Dolg, *Tetrahedron* **1999**, *55*, 12751–12756.

[14] K. Tomooka, A. Nakazaki, T. Nakai, *J. Am. Chem. Soc.* **2000**, *122*, 408–409.

[15] Allyloxysilane (*S*)-**1c** was prepared from (*S*)-3-hydroxypyrrolidin-2-one in six steps. Details are given in the Supporting Information.

[16] The enantiomeric excess of (*R*)-**3d** was determined by chiral HPLC analysis of its derivative **9**: Chiralcel OD (4.6 × 250 mm), hexane/2-propanol (10:1), 0.5 mL min^{-1}, UV/Vis detection at λ = 254 nm, room temperature; t_R = 11.8 min for *R*-isomer, 14.2 min for *S*-isomer. DIBAL = diisobutyl aluminium hydride [Eq. (5)].

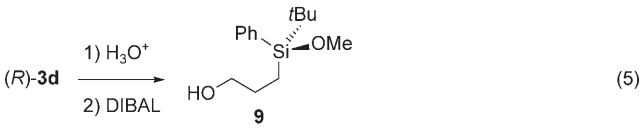

(5)

[17] Newly developed sultam derivative **6** was prepared from *S*-(−)-sultam, *p*-nitrobenzoyl chloride, and Et_3N in 78% yield.

[18] CCDC-277991 contains the supplementary crystallographic data for this paper. These data can be obtained free of charge from The Cambridge Crystallographic Data Centre via www.ccdc.cam.ac.uk/data_request/cif.

[19] For the formation of *Z*-vinyl ether from allyl ether via the cisoid allylic anion, see: a) M. Schlosser, S. Strunk, *Tetrahedron* **1989**, *45*, 2649–2664; b) A. R. Katritzky, M. Piffl, H. Lang, E. Anders, *Chem. Rev.* **1999**, *99*, 665–722, and reference [3a].

[20] Wright and West have proposed pentacoordinated silicon as a reasonable intermediate for the retro-[1,2] Brook rearrangement. See reference [12a].

[21] Recently, a pentaorganosilicate has been reported: E. P. A. Couzijn, M. Schakel, F. J. J. de Kanter, A. W. Ehlers, M. Lutz, A. L. Spek, K. Lammertsma, *Angew. Chem.* **2004**, *116*, 3522–3524; *Angew. Chem. Int. Ed.* **2004**, *43*, 3440–3442.

 © 2006 Wiley-VCH Verlag GmbH & Co. KGaA, Weinheim

DNA Detection

DOI: 10.1002/anie.200503810

Autonomous Fueled Mechanical Replication of Nucleic Acid Templates for the Amplified Optical Detection of DNA**

*Yossi Weizmann, Zoya Cheglakov, Valeri Pavlov, and Itamar Willner**

The self-replication of molecular or macromolecular units has attracted substantial research efforts over the past fifteen years, and the relevance of these systems to prebiotic chemical evolution and optimal synthetic machines has been discussed.[1] The different replication systems that have been developed include nucleotide-based oligomers,[2–6] peptides,[7–10] molecular conjugates,[11,12] micelles,[13] and vesicles.[14] The application of self-replicating systems is scarce, and only chemical amplification in synthesis[15,16] or the preparation of nanoparticles in self-reproducing micelles[17] were demonstrated. Amplification is a central aspect in bioanalytical science, and enzyme conjugates,[18] DNAzymes,[19] and, more recently, nanoparticles[20] have been widely used as amplifying labels for biorecognition events. The polymerase chain reaction (PCR) is the standard method for the chemical amplification of nucleic acids.

The information encoded in DNA sequences and structures has also been employed to develop nanomachines[21,22] such as unidirectional walkers[23] and gears.[24] Herein, we report on the development of an enzyme/DNA scission machine that is triggered by the hybridization of a pretailored DNA hairpin structure with a target nucleic acid. The machine is fueled by a secondary dye/quencher-functionalized nucleic acid, and upon operation, it replicates the machinery cutter. The scission of the fuel yields a fluorescent waste product that provides the optical readout signal for the replicating machine. Herein, we describe the analysis of one of the Tay–Sachs genetic disorder mutants. The method reveals a new concept that could substitute PCR amplification and highlights the use of self-replication in amplified DNA sensing.

The operation of the replication machine is discussed with regards to, first, the formation of the scission machine and its operation in the presence of the dye/quencher nucleic acid fuel (Figure 1) and, second, the triggering of the DNA scission

[*] Y. Weizmann, Z. Cheglakov, Dr. V. Pavlov, Prof. I. Willner
Institute of Chemistry
The Farkas Center for Light-Induced Processes
The Hebrew University of Jerusalem
Jerusalem 91904 (Israel)
Fax: (+972) 2-6527-715
E-mail: willnea@vms.huji.ac.il

[**] This research was supported by the Israel Ministry of Science as an Infrastructure Project.

Supporting information for this article is available on the WWW under http://www.angewandte.org or from the author.

© 2006 Wiley-VCH Verlag GmbH & Co. KGaA, Weinheim

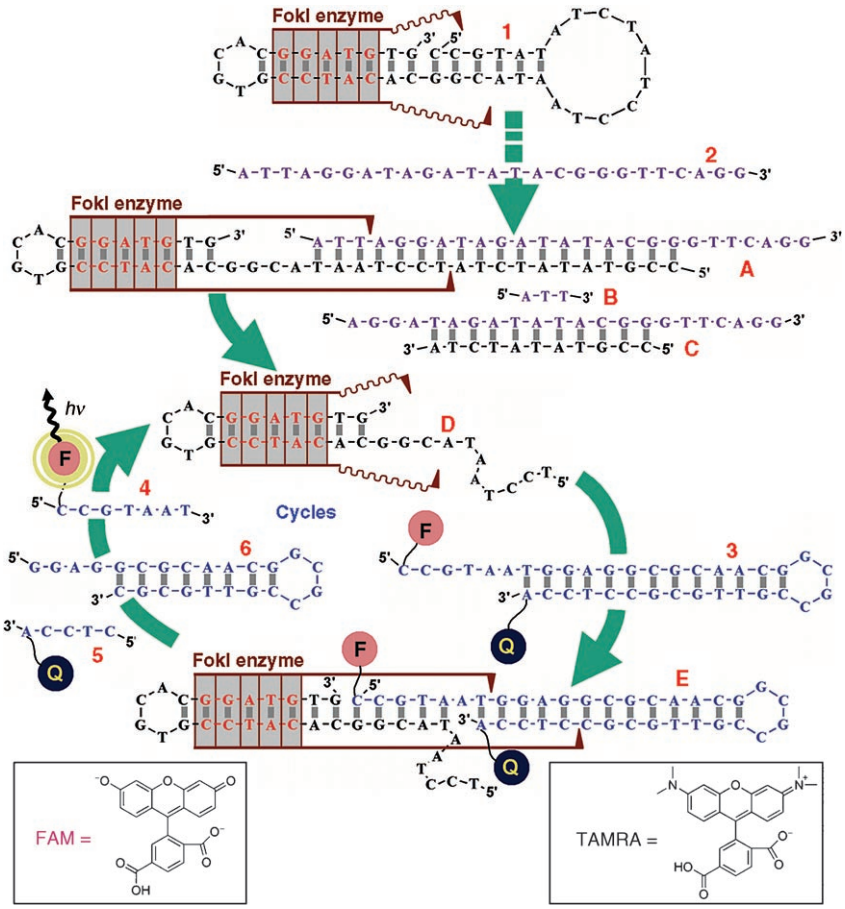

Figure 1. Scheme of the amplified detection of DNA using FokI/DNA as a biocatalytic template for the scission of a fluorophore (F; FAM)/quencher (Q; TAMRA) fuel substrate to yield a fluorescent waste product.

machine by the analyte DNA and the fueled operation of the machine.

The DNA hairpin structure **1** is predesigned to analyze the DNA mutant **2**, which is one of the mutants characteristic of the Tay–Sachs genetic disorder. The disorder leading to Tay–Sachs disease is caused by a deficiency of the enzyme hexosaminidase, which degrades GM_2 ganglioside to GM_3.[25] The disease is fatal in early childhood, and a recent survey reported that one in 30 Ashkenazi Jews is a carrier of the defective gene.[26] The hairpin structure **1** includes the built-in sequence for the association of the endonuclease FokI. The larger loop of **1** and part of the double-stranded stem include the encoded base sequence that is complementary to the analyzed nucleic acid. The hybridization of **1** with the mutant **2** opens the loop structure and yields the double-stranded complex **A**.[27] The latter complex includes the specific base sequence that is cleaved by FokI to yield the products **B**, **C**, and **D** (see Figure 1, the scission region is marked with arrows). The product **D** consists of a FokI/DNA template that acts as the catalytic cutting machine. The interaction of **D** with the FAM/TAMRA fluorophore/quencher-functionalized nucleic acid structure **3**, which acts as the fuel, results in the formation of the double-stranded complex **E**. The latter complex includes the base sequence that is cleaved by FokI, and the scission process leads to the fluorescent product **4**, the TAMRA-tethered nucleic acid **5**, the hairpin structure **6**, and the regeneration of the catalytic FokI/DNA cutter, **D**. Thus, the primary triggering of the FokI/DNA biocatalytic machine by the opening of the analyzing hairpin **1** by **2** allows the amplified detection of **2** through the cyclic catalytic cleavage of the fuel to give the fluorescent product **4**.

Figure 2A shows the evolution of the fluorescence in the system at various time intervals of operation of the FokI/DNA machine upon analyzing **2** at a concentration of 1×10^{-6} M. The fluorescence increases with time, implying that the catalytic scission of **3** proceeds. Figure 2B shows the evolution of the fluorescence intensities in the system upon analyzing different concentrations of **2** ($\lambda_{ex}=$ 495 nm, fluorescence monitored at $\lambda=$ 520 nm). Figure 2B, curve d shows that no fluorescence is generated in the system when a foreign DNA that is non-complementary to **1** is included in the system. Under these conditions, the hairpin structure **1** remains in its closed state, and the scission machine is not activated towards the cutting of the fuel product **3**. Figure 2B, curve e depicts the results of a further control experiment, in which the normal gene **2a** is used to trigger the scission machine. As the normal gene is only partially complementary to **1**, the opening of the hairpin structure **1** to form **A** and the triggering of the machine that cleaves the fuel are inefficient.

Note that the mutant **2** at a concentration of 1×10^{-10} M leads to a fluorescence that is approximately fourfold higher than that generated by the normal gene **2a** at a concentration of 1×10^{-6} M. Thus, the FokI/DNA template scission catalyst, **D**, allows the specific analysis of **2** with a sensitivity limit of 1×10^{-10} M. The increase in the fluorescence intensities upon analyzing the different concentrations of **2** reveals, however, a tendency to deviate from linearity and to reach a saturation value. This result is consistent with the fact that the product **4** may form, by hybridization, a complex with the catalytic cutter **D**. This complex inhibits the catalytic scission of the fuel substrate **3**. This product inhibition is pronounced as the reaction proceeds, and thus **4** is accumulated in the system (see Supporting Information for the simulation of the experimental data by a kinetic scheme that includes the different complexes in the system).

Figure 3 outlines the development of a self-replicating system of the FokI/DNA template scission machine for the amplified analysis of the mutant **2**. The hairpin structure **1** is used as the sensing matrix for **2** and yields, as before, the catalytic FokI/DNA template cutter **D** after scission of the double-stranded complex **A**. The fuel substrate in this system

 © 2006 Wiley-VCH Verlag GmbH & Co. KGaA, Weinheim

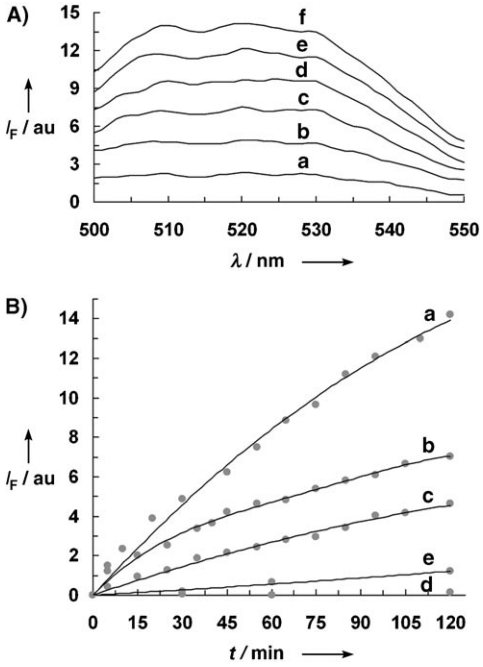

Figure 2. A) Time-dependent fluorescence spectra of a system analyzing the Tay–Sachs genetic disorder mutant **2** (1×10^{-6} M) according to Figure 1 at a) 20, b) 40, c) 60, d) 85, e) 105, and f) 120 min (I_F = fluorescence intensity). B) Time-dependent changes in fluorescence (λ_{em} = 520 nm) upon analyzing different concentrations of the mutant **2**: a) 1×10^{-6} M, b) 1×10^{-9} M, and c) 1×10^{-10} M; d) fluorescence changes upon analyzing a foreign DNA (5′-CTCCCGTCTAATGCGCTTCCCTGTTTT-3′, 1×10^{-6} M); e) fluorescence changes upon analyzing the normal gene **2a** (5′-GGGCCATAGGATATACGGTTCAGG-3′, 1×10^{-6} M). All systems include the probe DNA **1** (1×10^{-6} M), FokI (0.08 units μL^{-1}), and the fuel substrate **3** (1×10^{-6} M). λ_{ex} = 495 nm. Gray dots correspond to experimental data, while the solid curves correspond to the simulated fits (see Supporting Information).

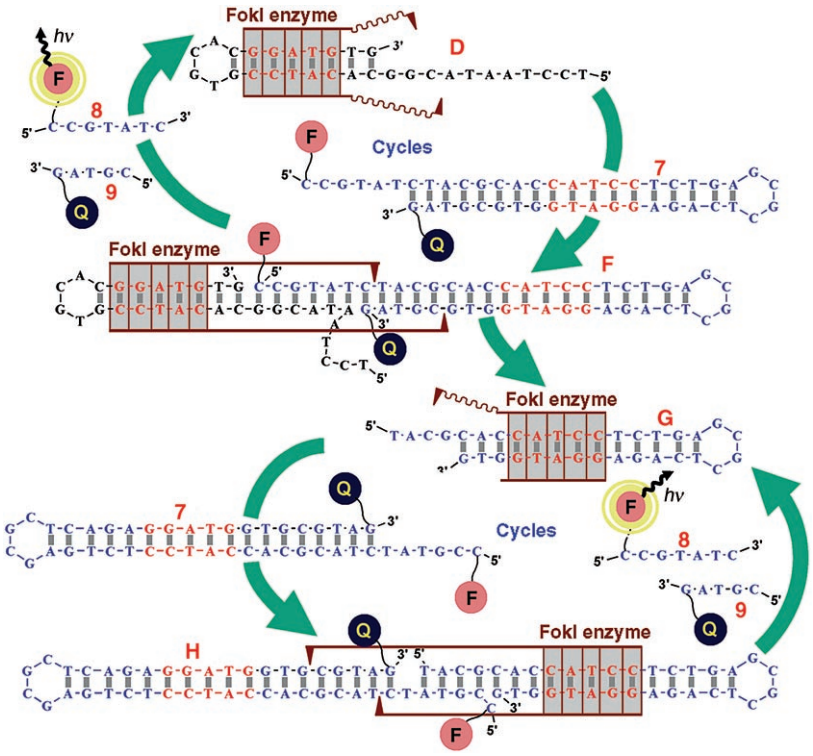

Figure 3. Scheme of the amplified detection of DNA using FokI/DNA as a biocatalytic template that cuts the fluorophore/quencher-labeled fuel substrate into a self-replicating FokI/DNA biocatalyst and fluorescent waste product.

is the beacon structure **7**, which includes the FAM/TAMRA dye/quencher labels, a base sequence that is complementary to the catalytic machine, and a double-stranded nucleic acid sequence that binds the FokI enzyme. The hybridization of **7** with the catalytic cutter **D** yields the double-stranded complex **F**. The scission of the sequence-specific double-stranded complex leads to the separation of the fluorophore-labeled nucleic acid **8** and the quencher-labeled nucleic acid **9**, and to the formation of a new FokI/DNA template catalytic machine **G**. The FokI/DNA machine **G** recognizes the fuel substrate **7**, the same fuel substrate that lead to the fluorescent waste product **8**.

After the formation of the double-stranded assembly **H**, the FokI unit cleaves the DNA and yields a new FokI/DNA cutter of structure **G**, while generating the fluorescent waste product **8**. Thus, the system depicted in Figure 3 drives the continuous regeneration of the catalytic FokI/DNA entity **D** and leads to the formation of the self-replicating FokI/DNA catalyst **G**. Both catalysts **D** and **G** are recycled in the replication process.

Figure 4A shows the evolution of the fluorescence intensities in the system upon analyzing **2** at a concentration of 1×10^{-11} M, using the replication of the biocatalytic machine **D** and **G** as the amplifying unit. At this concentration of the analyte, the nonreplicated biocatalytic machine **D**, shown in Figure 1, does not show any noticeable fluorescence at this time interval of analysis. Figure 4B depicts the time-dependent increase in the fluorescence intensities upon analyzing different concentrations of the mutant **2** by the self-replicating biocatalytic cutter.

The system allows the analysis of **2** with a sensitivity limit of 1×10^{-14} M. Analysis of the normal gene **2a**, which includes nine base-mismatches as compared to the mutant **2**, at a concentration of 1×10^{-6} M reveals a twofold lower fluorescence intensity. Also, the system that includes a foreign DNA yields only a weak background fluorescence (Figure 4B, curve f). The results clearly indicate that the replication of the FokI/DNA template biocatalytic cutters allows the ultrasensitive analysis of the mutant **2**. Nonetheless, we observe relatively small differences in the evolved fluorescence intensities upon changing the concentration of **2** by orders of magnitude. We also observe a tendency to reach saturation of the evolved fluorescence. The non-exponential growth of the fluorescence intensities and the saturation effects are attributed to several origins: 1) The biocatalytic cutter **D** hybridizes with **8** and thus blocks the hybridization of the fuel substrate **7**. 2) The biocatalytic cutter **G** is hybridized with the fluorescent product **8**, thus inhibiting the hybridization and scission of **7** by **D** and **G**. (see Supporting Information for the detailed kinetic scheme and a simulation of the experimental data).

 © 2006 Wiley-VCH Verlag GmbH & Co. KGaA, Weinheim

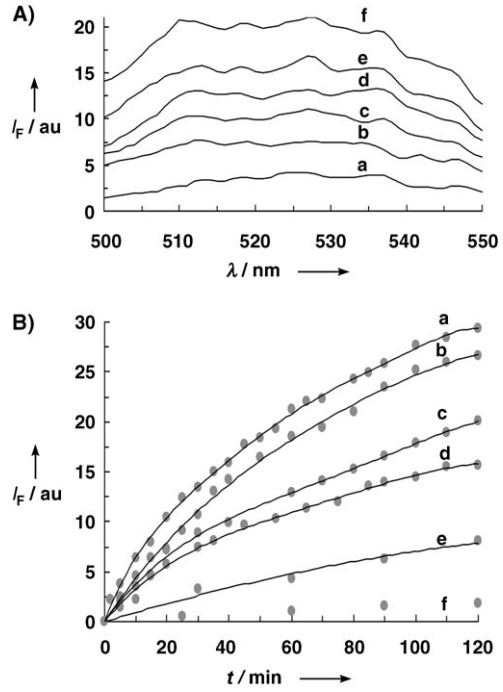

Figure 4. A) Time-dependent fluorescence spectra of a system analyzing the Tay–Sachs genetic disorder mutant **2** (1×10^{-11} M) according to Figure 3 at a) 10, b) 20, c) 40, d) 60, e) 90, and f) 120 min. B) Time-dependent changes in fluorescence ($\lambda_{em}=520$ nm) upon analyzing different concentrations of the mutant **2**: a) 1×10^{-6} M, b) 1×10^{-9} M, c) 1×10^{-11} M, and d) 1×10^{-14} M; e) analysis of the normal gene **2a** (5′-GGGCCATAGGATATACGGTTCAGG-3′, 1×10^{-6} M); f) analysis of a foreign DNA (5′-CTCCCGTCTAATGCGCTTCCCTGTTTT-3′, 1×10^{-6} M). All systems include the probe DNA **1** (1×10^{-6} M), FokI (0.08 units μL^{-1}), and the fuel substrate **3** (1×10^{-6} M). $\lambda_{ex}=495$ nm. Gray dots correspond to experimental data, while the solid curves correspond to the simulated fits (see Supporting Information).

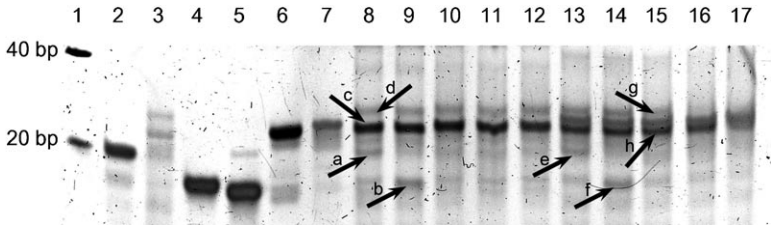

Figure 5. Non-denaturating PAGE analysis of the mutant **2** by the hairpin sensing nucleic acid **1** by the FokI-induced mechanical scission of the fuel **3** or **7.** Lane 1: 20- and 40-base-pair (bp) nucleic acid markers. Lane 2: the foreign nucleic acid (5′-CTCCCGTCTAATGCGCTTCCCTGTTTT-3′). Lane 3: hairpin **1**. Lane 4: mutant **2**. Lane 5: normal gene **2a** (5′-GGGCCATAGGATATACGGTTCAGG-3′). Lane 6: fuel **3**. Lane 7: fuel **7**. (The concentration of all components in lanes 1–7 is 1×10^{-6} M). Lanes 8 and 9: analysis of the foreign DNA and normal gene (5×10^{-8} M), respectively, for 1 h, according to Figure 1. Lanes 10–12: analysis of mutant **2** (5×10^{-8} M) at $t=0$, 30, and 60 min, respectively. (For all systems, the concentration of **1** and **3** is 1×10^{-6} M.) Lanes 13 and 14: analysis of the foreign DNA or the normal gene **2a**, respectively, according to Figure 3. Lanes 15–17: analysis of **2** (5×10^{-8} M) at $t=0$, 30, and 60 min, respectively. (For all systems, the concentration of **1** and **7** is 1×10^{-6} M.) See text for details of bands a–h.

Further support for the autonomous FokI-induced scission of the fuel **3** by the cutter **D**, according to Figure 1, and for the autonomous replication of the cutter **G** upon the scission of the fuel **7**, according to Figure 3, were obtained by polyacrylamide gel electrophoresis (PAGE) experiments (Figure 5). Lane 1 consists of two markers that exhibit 20 and 40 base-pairs, respectively. Lanes 2–7 include the respective control runs of the separate components involved in the two systems. Lanes 8 and 9 correspond to control experiments in which the foreign DNA or the normal gene **2a**, respectively, is analyzed in the presence of the sensing nucleic acid **1**, according to Figure 1. After 1 h of interaction the bands characteristic of the foreign nucleic acid and the normal gene **2a**, (bands a and b, respectively) remain intact, and similarly the intensities of the bands that correspond to the analyzing hairpin **1** and the fuel **3** (bands c and d) are unchanged. These results confirm that the foreign nucleic acid or the normal gene **2a** do not activate the scission process. Lanes 10, 11, and 12 show the analysis of the mutant **2** according to Figure 1 at $t=0$, 30, and 60 min of reaction, respectively. The band corresponding to **2** is not visible already at $t=0$, owing to hybridization of **2** with the analyzing hairpin **1**. The intensities of the bands characteristic of the fuel **3**, however, gradually decrease as the reaction proceeds, consistent with the scission of the fuel substrate. Similarly, lanes 13 and 14 correspond to the analysis of the foreign DNA (band e) or the normal gene **2a** (band f), respectively, according to Figure 3. The bands of the foreign DNA or the normal gene **2a** and the bands of the hairpin **1** and the fuel substrate **7** are unaffected after 1 h of reaction, implying that no scission takes place. Lanes 15, 16, and 17 show the analysis of the mutant **2** according to Figure 3 at $t=0$, 30, and 60 min of reaction, respectively. The bands g and h, which correspond to the hairpin **1** and the fuel **7**, are depleted, implying that scission occurs. Note that the time-dependent disappearance of the bands corresponding to the hairpin **1** and the fuel **7** in the latter system is substantially faster than the depletion of the intensities of the bands of **1** and **3** in the former system. This is consistent with the fact that in the latter system replication of the cutter occurs, leading to the enhanced scission of the fuel substrate.

In summary, the present study has introduced a new approach for the amplified detection of DNA using a replicating FokI/DNA template as a biocatalytic machine. The concept involves two parts: 1) The primary design of a probe hairpin nucleic acid structure that is complementary to the target DNA and yields, upon opening, the sequence domain for scission by FokI and the formation of the catalytic cutter. 2) The design of the fuel substrate that leads to the replication of the biocatalyst and to the formation of the fluorescent product. The highly sensitive detection of DNA has thus been demonstrated. In principle, this method could enable the detection of a single DNA copy.

Experimental Section

Materials: FokI restriction endonuclease was purchased from New England Biolabs, Ltd. All other materials were purchased from Sigma.

Assay: DNA replication was performed in a solution consisting of **1** (0.92 μM), or **3** or **7** (0.6 nM). Different concentrations of the analyte **2** and the FokI restriction enzyme (0.08 U μL^{-1}) in a buffer solution of 50 mM potassium acetate, 20 mM Tris acetate, and 10 mM Mg acetate at pH 7.2 at 37 °C was used as the reaction medium. Time-dependent

 © 2006 Wiley-VCH Verlag GmbH & Co. KGaA, Weinheim

changes in the fluorescence emission were measured at $\lambda_{ex} = 495$ nm, $\lambda_{em} = 520$ nm.

Received: October 27, 2005
Revised: December 25, 2005
Published online: March 2, 2006

Keywords: DNA · enzymes · fluorescence · self-replication

[1] A. Robertson, A. J. Sinclair, D. Philp, *Chem. Soc. Rev.* **2000**, *29*, 141 – 152.
[2] W. O. Zielinskio, L. E. Orgel, *Nature* **1987**, *327*, 346 – 347.
[3] T. Li, K. C. Nicolaou, *Nature* **1994**, *369*, 218 – 221.
[4] G. Von Kiedrowski, *Angew. Chem.* **1986**, *98*, 932 – 935; *Angew. Chem. Int. Ed. Engl.* **1986**, *25*, 932 – 935.
[5] D. Sievers, G. Von Kiedrowski, *Nature* **1994**, *369*, 221 – 224.
[6] N. Paul, G. F. Joyce, *Proc. Natl. Acad. Sci. USA* **2002**, *99*, 12733 – 12740.
[7] D. H. Lee, J. R. Granja, J. A. Martinez, K. Severin, M. R. Ghadiri, *Nature* **1996**, *382*, 525 – 528.
[8] S. Yao, I. Ghosh, R. Zutshi, J. Chmielewski, *Nature* **1998**, *396*, 447 – 450.
[9] S. Yao, I. Ghosh, R. Zutshi, J. Chmielewski, *Angew. Chem.* **1998**, *110*, 489 – 492; *Angew. Chem. Int. Ed.* **1998**, *37*, 478 – 481.
[10] S. Yao, I. Ghosh, R. Zutshi, J. Chmielewski, *J. Am. Chem. Soc.* **1997**, *119*, 10559 – 10560.
[11] J. S. Nowick, Q. Feng, T. Tjivikua, P. Ballester, J. Rebek, Jr., *J. Am. Chem. Soc.* **1991**, *113*, 8831 – 8839.
[12] E. A. Wintner, M. M. Conn, J. Rebek, Jr., *J. Am. Chem. Soc.* **1994**, *116*, 8877 – 8884.
[13] P. A. Bachmann, P. L. Luisi, J. Lang, *Nature* **1992**, *357*, 57 – 59.
[14] T. Oberholzer, R. Wick, P. L. Luisi, C. K. Biebricher, *Biochem. Biophys. Res. Commun.* **1995**, *207*, 250 – 257.
[15] A. Luther, R. Brandsch, G. Von Kiedrowski, *Nature* **1998**, *396*, 245 – 248.
[16] J. Chen, S. Körner, S. L. Craig, S. Lin, D. M. Rudkevich, J. Rebek, Jr., *Proc. Natl. Acad. Sci. USA* **2002**, *99*, 2593 – 2596.
[17] P. Dutta, J. H. Fendler, *J. Colloid Interface Sci.* **2002**, *247*, 47 – 53.
[18] F. Patolsky, A. Lichtenstein, I. Willner, *Nat. Biotechnol.* **2001**, *19*, 253 – 257.
[19] T. Niazov, V. Pavlov, Y. Xiao, R. Gill, I. Willner, *Nano Lett.* **2004**, *4*, 1683 – 1687.
[20] J. Wang, G. Liu, A. Merkoci, *J. Am. Chem. Soc.* **2003**, *125*, 3214 – 3215.
[21] F. C. Simmel, W. U. Dittmer, *Small* **2005**, *1*, 284 – 299.
[22] B. Samori, G. Zuccheri, *Angew. Chem.* **2005**, *117*, 1190 – 1206; *Angew. Chem. Int. Ed.* **2005**, *44*, 1166 – 1181.
[23] J. S. Shin, N. A. Pierce, *J. Am. Chem. Soc.* **2004**, *126*, 10834 – 10835.
[24] Y. Tian, C. D. Mao, *J. Am. Chem. Soc.* **2004**, *126*, 11410 – 11411.
[25] R. A. Gravel, J. T. R. Clarke, M. M. Kaback, D. Mahuran, K. Sandhoff, K. Suzuki in *The Metabolic and Molecular Bases of Inherited Diseases*, *Vol. 2*, (Eds.: C. R. Scriver, A. L. Beaudet, W. S. Sly, D. Valle), McGraw-Hill, New York, **1995**, pp. 2839 – 2879.
[26] R. Myerowitz, F. C. Costigan, *J. Biol. Chem.* **1988**, *263*, 18587 – 18589.
[27] S. Tyagi, F. R. Kramer, *Nat. Biotechnol.* **1996**, *14*, 303 – 308.

 © 2006 Wiley-VCH Verlag GmbH & Co. KGaA, Weinheim

Polyaromatic Compounds

DOI: 10.1002/anie.200504287

Efficient Phenanthrene, Helicene, and Azahelicene Syntheses**

David C. Harrowven, Ian L. Guy, and Lana Nanson*

For many years, helicenes were regarded as little more than an academic curiosity. More recently, their extraordinary optical,[1] electronic,[2] and chelating[3] properties have rekindled an interest in these nonplanar condensed aromatic compounds in fields as diverse as liquid crystals,[4] sensors,[5] dyes,[5] asymmetric synthesis,[3,6,7] molecular recognition,[3,6,7] polymer synthesis,[8] and materials science.[8] Helicenes have classically been prepared by the oxidative photocyclization of bis(stilbene)s.[9,10] Though useful, complex product mixtures often arise as a result of poor regiocontrol in the photocyclization step or competitive side reactions, such as photoinduced dimerization or benzo[*ghi*]perylene formation.[10] The challenge of developing efficient routes to helicenes that are amenable to scale-up has inspired many imaginative approaches,[11,12] including strategies based on Diels–Alder cycloadditions,[13] carbenoid insertions,[14] radical cyclizations, and metal-mediated cycloisomerizations.[15,16] Herein, we report a short and efficient entry to helicenes, azahelicenes, and phenanthrenes in which the use of halo and alkoxy substituents to control both the stereochemical course of Wittig reactions and the regiochemical course of homolytic aromatic substitution reactions is a key feature.

The strategy developed is exemplified by the synthesis of 5-aza[5]helicene (**4**) outlined in Scheme 1.[17] This synthesis relies on the use of cooperative *ortho* effects to control the stereochemical course of a Wittig reaction[18] and the counterintuitive use of a halide atom as a protecting group in a homolytic aromatic substitution reaction. Thus, phosphonium salt **2** and 2-chloroquinoline-3-carboxaldehyde were first condensed under standard Wittig conditions to give azastilbene **3** in near quantitative yield as a 16:1 mixture of *Z* and *E* isomers (as determined by ^{1}H NMR spectroscopic integration[18a]). Isomer (*Z*)-**3** was then exposed to 2.4 equivalents of tributyltin hydride and 0.4 equivalents of VAZO to induce selective homolysis of the carbon–iodine bond.[19] Homolytic substitution at C4 of the quinoline moiety followed to give 5-aza[5]helicene **4** in 75% yield.[20] Notably, no products arising from the addition of the aryl radical intermediate to C2 of the

[*] Prof. D. C. Harrowven, I. L. Guy, L. Nanson
School of Chemistry
University of Southampton
Highfield, Southampton, SO17 1BJ (UK)
Fax: (+44) 238-059-6805
E-mail: dch2@soton.ac.uk

[**] Financial support from the EPSRC through the Doctoral Training Account is gratefully acknowledged.

Supporting information for this article is available on the WWW under http://www.angewandte.org or from the author.

WILEY InterScience DISCOVER SOMETHING GREAT
© 2006 Wiley-VCH Verlag GmbH & Co. KGaA, Weinheim

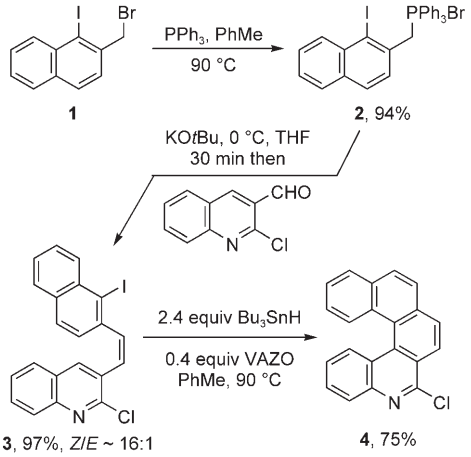

Scheme 1. Synthesis of 6-chloro-5-aza[5]helicene. VAZO = 1,1′-azobis-(cyclohexanecarbonitrile).

quinoline moiety were observed,[20] as the attached chlorine atom arrested that *ortho*-cyclization mode.

This method provides a powerful means of preparing all kinds of condensed polyaromatic compounds with predictable regiocontrol. For example, 1-chloro- and 1-bromophenanthrene were readily prepared from phosphonium salts **5** and **6**, respectively, by condensation with 2-iodobenzaldehyde and treatment of the resulting stilbenes **7** and **8** with 2.4 equivalents of tributyltin hydride and 0.4 equivalents of azoisobutyronitrile (AIBN; Scheme 2).[21,22] In each case, the carbon–

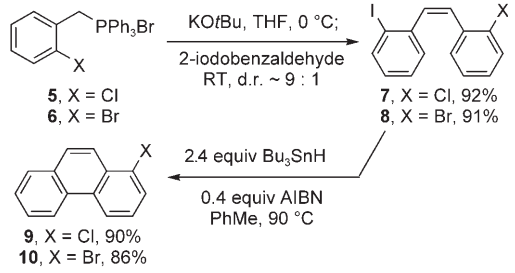

Scheme 2. 1-Halophenanthres from 2-iodo-2′-halostilbenes.

iodine bond was homolyzed selectively to generate an aryl radical donor,[19] thus leaving the second halide atom to serve as a protecting group for the attached *ortho*-carbon atom in the radical acceptor. The same two-step sequence was effective over a broad range of substrates, as evidenced by the examples outlined in Scheme 3 and the Supporting Information.

The impressive degree of *Z* selectivity achieved in the Wittig reaction when both the ylide and aldehyde contained an *ortho*-halo or *ortho*-alkoxy substituent,[18] meant that the method could be usefully employed in a bidirectional sense for the synthesis of helicenes (Scheme 4). To that end, a double Wittig reaction between bis(aldehyde) **16** and (*ortho*-iodoaryl)triphenylphosphonium salt **15a** gave the expected bis(stilbene) **17a** in near quantitative yield as an inseparable 4:1 mixture of *Z*,*Z* and *E*,*Z* isomers. Treatment with 4.4 equivalents of tributyltin hydride and 0.4 equivalents of

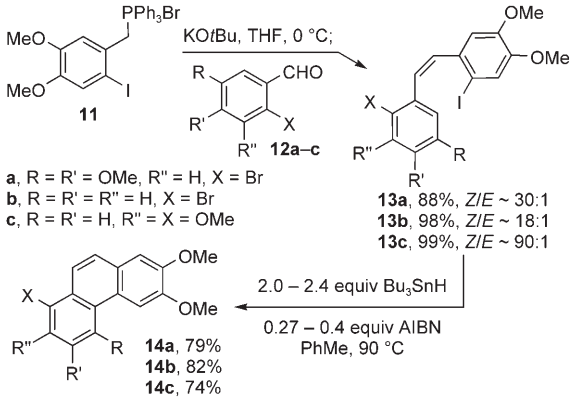

Scheme 3. Highly stereoselective syntheses of *Z* stilbenes and regioselective syntheses of phenanthrenes.

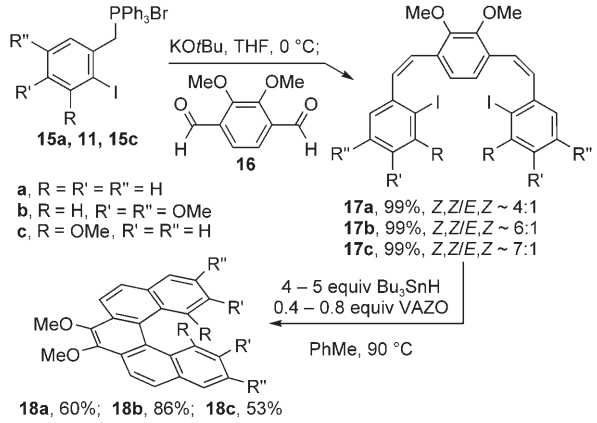

Scheme 4. [5]Helicenes by tandem radical cyclization.

VAZO then gave 7,8-dimethoxy[5]helicene (**18a**) in 60% yield (thus representing a 75% yield based on (*Z*,*Z*)-**17a**). The related syntheses of 2,3,7,8,12,13-hexamethoxy[5]helicene (**18b**) and 1,7,8,14-tetramethoxy[5]helicene (**18c**) were achieved in the same fashion in 73 and 46% overall yield, respectively, from the respective phosphonium salts **11** and **15c**.

The method was next extended to [7]helicenes by conjoining bis(aldehyde) **16**[23] with 2 equivalents of phosphonium salt **2**. The resulting 3:1 mixture of *Z*,*Z* and *E*,*Z* bis-(stilbene)s **19** was separated by column chromatography, and (*Z*,*Z*)-**19** was treated with 5 equivalents of tributyltin hydride and 0.4 equivalents of VAZO in toluene at 90 °C to give 9,10-dimethoxy[7]helicene (**20**) as large yellow needles in 75% yield (Scheme 5).

Further points of interest were noted following X-ray crystallographic analysis of helicenes **18b**, **18c**, and **20** (see Table 1 and the Supporting Information). Whereas crystallization of **18b** (from toluene/pentane) and **20** (from EtOAc) led to racemic crystal forms, *rac*-**18c** (from EtOAc/hexane) spontaneously formed enantiomorphous single crystals. This phenomenon is extremely rare within the [5]helicene series,[24] having been observed just once before with the condensed [5]helicene 7:8,9:10-dibenzo-1,2,3,4-tetrafluorotriphenylene.[25] In addition, there appear to be two distinct helicene

 © 2006 Wiley-VCH Verlag GmbH & Co. KGaA, Weinheim

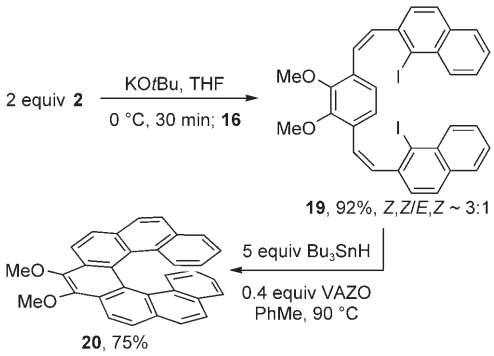

Scheme 5. Synthesis of 9,10-dimethoxy[7]helicene.

Table 1: X-ray crystal structures of **18b**, **18c**, and **20** which show face and side elevations (hydrogen atoms are omitted for clarity; red O).

18b	**18c**	**20**
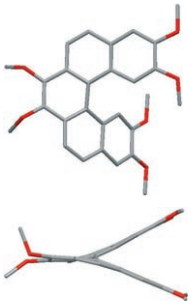	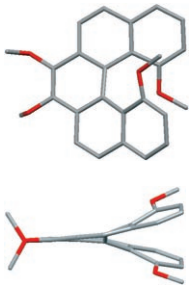	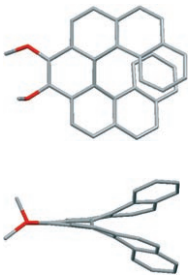

forms—type I in which the burden of torsional strain is mainly accommodated by the central arene (exemplified by **18b**), and type II in which each of the internal arenes is distorted to a similar extent (exemplified by **18c** and **20**).

In summary, concise and efficient routes to phenanthrenes, helicenes, and azahelicenes have been achieved by using homolytic aromatic substitution reactions. Points of interest from a synthetic perspective are the use of halo and alkoxy substituents to control the stereochemical course of Wittig reactions which lead to stilbene and bis(stilbene) precursors[18] and their subsequent role as protecting groups in homolytic aromatic substitution reactions. Notable from a structural perspective is the recognition of two distinct helicene types and the spontaneous formation of enantiomorphous single crystals on recrystallization of *rac*-**18c** from ethyl acetate/hexane.

Received: December 2, 2005
Published online: February 28, 2006

Keywords: helicenes · homolytic aromatic substitution · polyaromatic compounds · protecting groups · radical cyclization

[1] a) T. J. Wigglesworth, D. Sud, T. B. Norsten, V. S. Lekhi, N. R. Branda, *J. Am. Chem. Soc.* **2005**, *127*, 7272–7273; b) E. Botek, B. Champagne, M. Turki, J.-M. André, *J. Chem. Phys.* **2004**, *120*, 2042–2048; c) C. Nuckolls, T. J. Katz, T. Verbiest, S. Van Elshocht, H.-G. Kuball, S. Kiesewalter, A. J. Lovinger, A. Persoons, *J. Am. Chem. Soc.* **1998**, *120*, 8656–8660.

[2] a) F. Furche, R. Ahlrichs, C. Wachsmann, E. Weber, A. Sobanski, F. Vögtle, S. Grimme, *J. Am. Chem. Soc.* **2000**, *122*, 1717–1724; b) G. Treboux, P. Lapstun, Z. Wu, K. Silverbrook, *Chem. Phys. Lett.* **1999**, *301*, 493–497; c) D. Beljonne, Z. Shuai, J. L. Brédas, M. Kauranen, T. Verbiest, A. Persoons, *J. Chem. Phys.* **1998**, *108*, 1301–1304.

[3] a) Y. Xu, Y. X. Zhang, H. Sugiyama, T. Umano, H. Osuga, K. Tanaka, *J. Am. Chem. Soc.* **2004**, *126*, 6566–6567; b) I. Sato, R. Yamashima, K. Kadowaki, J. Yamamoto, T. Shibata, K. Soai, *Angew. Chem.* **2001**, *113*, 1130–1132; *Angew. Chem. Int. Ed.* **2001**, *40*, 1096–1098.

[4] C. Nuckolls, R. Shao, W.-G. Jang, N. A. Clark, D. M. Walba, T. J. Katz, *Chem. Mater.* **2002**, *14*, 773–776.

[5] a) B. Laleu, P. Mobian, C. Herse, B. W. Laursen, G. Hopfgartner, G. Bernardinelli, J. Lacour, *Angew. Chem.* **2005**, *117*, 1913–1917; *Angew. Chem. Int. Ed.* **2005**, *44*, 1879–1883; b) M. T. Reetz, S. Sostmann, *Tetrahedron* **2001**, *57*, 2515–2520.

[6] a) S. D. Dreher, T. J. Katz, K.-C. Lam, A. L. Rheingold, *J. Org. Chem.* **2000**, *65*, 815–822; b) M. T. Reetz, S. Sostmann, *J. Organomet. Chem.* **2000**, *603*, 105–109; c) M. T. Reetz, E. W. Beuttenmüller, R. Goddard, *Tetrahedron Lett.* **1997**, *38*, 3211–3214.

[7] a) H. Sugiura, Y. Takahira, M. Yamaguchi, *J. Org. Chem.* **2005**, *70*, 5698–5708; b) O. Ermer, J. Neudoerfl, *Helv. Chim. Acta* **2001**, *84*, 1268–1313; c) E. Murguly, R. McDonald, N. R. Branda, *Org. Lett.* **2000**, *2*, 3169–3172; d) K. Deshayes, R. D. Broene, I. Chao, C. B. Knobler, F. Diederich, *J. Org. Chem.* **1991**, *56*, 6787–6795; e) L. Owens, C. Thilgen, F. Diederich, C. B. Knobler, *Helv. Chim. Acta* **1993**, *76*, 2757–2774.

[8] a) A. J. Lovinger, C. Nuckolls, T. J. Katz, *J. Am. Chem. Soc.* **1998**, *120*, 264–268; b) T. P. Bender, Y. Qi, J. P. Gao, Z. Y. Wang, *Macromolecules* **1997**, *30*, 6001–6006; c) Y. J. Dai, T. J. Katz, *J. Org. Chem.* **1997**, *62*, 1274–1285; d) J. M. Fox, D. Lin, Y. Itagaki, T. Fujita, *J. Org. Chem.* **1998**, *63*, 2031–2038.

[9] See for example: a) R. El Abed, B. B. Hassine, J.-P. Genêt, M. Gorsane, A. Marinetti, *Eur. J. Org. Chem.* **2004**, 1517–1522; b) H. Meier, M. Schwertel, D. Schollmeyer, *Angew. Chem.* **1998**, *110*, 2224–2226; *Angew. Chem. Int. Ed.* **1998**, *37*, 2110–2113; c) A. M. Gilbert, T. J. Katz, W. E. Geiger, M. P. Robben, A. L. Rheingold, *J. Am. Chem. Soc.* **1993**, *115*, 3199–3211; d) C. A. Liberko, L. L. Miller, T. J. Katz, L. Liu, *J. Am. Chem. Soc.* **1993**, *115*, 2478–2482; e) B. Yang, L. Liu, T. J. Katz, C. A. Liberko, L. L. Miller, *J. Am. Chem. Soc.* **1991**, *113*, 8993–8994; f) L. Liu, B. Yang, T. J. Katz, M. K. Poindexter, *J. Org. Chem.* **1991**, *56*, 3769–3775.

[10] a) K. Yano, M. Osatani, K. Tani, T. Adachi, K. Yamamoto, H. Matsubara, *Bull. Chem. Soc. Jpn.* **2000**, *73*, 185–189; b) C. Stammel, R. Froehlich, C. Wolff, H. Wenck, A. de Meijere, J. Mattay, *Eur. J. Org. Chem.* **1999**, 1709–1718; c) A. Terfort, H. Goerls, H. Brunner, *Synthesis* **1997**, 79–86; d) L. Liu, T. J. Katz, *Tetrahedron Lett.* **1991**, *32*, 6831–6834; e) W. H. Laarhoven, W. J. C. Prinsen, *Top. Curr. Chem.* **1984**, *125*, 63–130.

[11] a) A. Urbano, *Angew. Chem.* **2003**, *115*, 4116–4119; *Angew. Chem. Int. Ed.* **2003**, *42*, 3986–3989; b) R. H. Martin, *Angew. Chem.* **1974**, *86*, 727–738; *Angew. Chem. Int. Ed. Engl.* **1974**, *13*, 649–660.

[12] a) K. Nakano, Y. Hidehira, K. Takahashi, T. Hiyama, K. Nozaki, *Angew. Chem.* **2005**, *117*, 7298–7300; *Angew. Chem. Int. Ed.* **2005**, *44*, 7136–7138: ; b) Y. Ogawa, M. Toyama, M. Karikomi, K. Seki, K. Haga, T. Uyehara, *Tetrahedron Lett.* **2003**, *44*, 2167–2170; c) D. Peña, A. Cobas, D. Pérez, E. Guitián, L. Castedo, *Org. Lett.* **2003**, *5*, 1863–1866; d) Y. Ogawa, T. Ueno, M. Karikomi, K. Seki, K. Haga, T. Uyehara, *Tetrahedron Lett.* **2002**,

 © 2006 Wiley-VCH Verlag GmbH & Co. KGaA, Weinheim

43, 7827 – 7829; e) C. A. Beaumont, J. B. Jones, D. S. Brown, A. G. Massey, J. Watkin, *J. Organomet. Chem.* **1988**, *344*, 1 – 8.
[13] a) M. C. Carreno, M. Gonzalez-Lopez, A. Urbano, *Chem. Commun.* **2005**, 611 – 613; b) M. C. Carreno, S. Garcia-Cerrada, A. Urbano, *Chem. Eur. J.* **2003**, *9*, 4118 – 4131; c) M. del Mar Real, J. P. Sestelo, L. A. Sarandeses, *Tetrahedron Lett.* **2002**, *43*, 9111 – 9114; d) M. C. Carreno, S. Garcia-Cerrada, A. Urbano, *J. Am. Chem. Soc.* **2001**, *123*, 7929 – 7930; e) K. Paruch, T. J. Katz, C. Incarvito, K.-C. Lam, B. Rhatigan, A. L. Rheingold, *J. Org. Chem.* **2000**, *65*, 7602 – 7608; f) T. J. Katz, *Angew. Chem.* **2000**, *112*, 1997 – 1999; *Angew. Chem. Int. Ed.* **2000**, *39*, 1921 – 1923.
[14] F. Dubois, M. Gingras, *Tetrahedron Lett.* **1998**, *39*, 5039 – 5040.
[15] a) D. C. Harrowven, M. I. T. Nunn, D. R. Fenwick, *Tetrahedron Lett.* **2002**, *43*, 7345 – 7347; b) D. C. Harrowven, M. I. T. Nunn, D. R. Fenwick, *Tetrahedron Lett.* **2002**, *43*, 3189 – 3191.
[16] a) I. G. Stara, I. Stary, A. Kollarovic, F. Teply, D. Saman, P. Fiedler, *Collect. Czech. Chem. Commun.* **2003**, *68*, 917 – 930; b) F. Teply, I. G. Stará, I. Stary, A. Kollárovic, D. Saman, L. Rulísek, P. Fiedler, *J. Am. Chem. Soc.* **2002**, *124*, 9175 – 9180; c) I. G. Stará, Z. Alexandrová, F. Teply, P. Sehnal, I. Stary, D. Saman, M. Budesínsky, J. Cvacka, *Org. Lett.* **2005**, *7*, 2547 – 2550.
[17] a) S. Abbate, C. Bazzini, T. Caronna, F. Fontana, C. Gambarotti, F. Gangemi, G. Longhi, A. Mele, I. N. Sora, W. Panzeri, *Tetrahedron* **2006**, *62*, 139 – 148; b) C. Bazzini, S. Brovelli, T. Caronna, C. Gambarotti, M. Giannone, P. Macchi, F. Meinardi, A. Mele, W. Panzeri, F. Recupero, A. Sironi, R. Tubino, *Eur. J. Org. Chem.* **2005**, 1247 – 1257; c) K. Sato, A. Arai in *Cyclophane Chemistry for the 21st Century* (Ed.: H. Takemura), Research Signpost, Kerena, India, **2002**, pp. 173 – 197; d) H. A. Staab, M. A. Zirnstein, C. Krieger, *Angew. Chem.* **1989**, *101*, 73 – 75; *Angew. Chem. Int. Ed. Engl.* **1989**, *28*, 86 – 88.
[18] a) E. C. Dunne, É. J. Coyne, P. B. Crowley, D. G. Gilheany, *Tetrahedron Lett.* **2002**, *43*, 2449 – 2453; see also: b) J.-J. Hwang, R.-L. Lin, R.-L. Shieh, J.-J. Jwo, *J. Mol. Catal. A* **1999**, *142*, 125 – 139.
[19] a) H. Togo, *Advanced Free Radical Reactions for Organic Synthesis*, Elsevier, Oxford, UK, **2004**; b) C. Chatgilialoglu, *Organosilanes in Radical Chemistry*, Wiley, Chichester, UK, **2003**.
[20] a) D. C. Harrowven, B. J. Sutton, *Prog. Heterocycl. Chem.* **2004**, *16*, 27 – 53; b) D. C. Harrowven, B. J. Sutton, S. Coulton, *Tetrahedron* **2002**, *58*, 3387 – 3400; c) D. C. Harrowven, B. J. Sutton, S. Coulton, *Tetrahedron Lett.* **2001**, *42*, 2907 – 2910.
[21] A. Studer, M. Bossart, *Tetrahedron* **2001**, *57*, 9649 – 9667.
[22] a) D. C. Harrowven, M. I. T. Nunn, D. R. Fenwick, *Tetrahedron Lett.* **2002**, *43*, 3185 – 3188; b) I. S. Aidhen, N. S. Narasimhan, *Indian J. Chem. Sect. B* **1993**, *32*, 211 – 221.
[23] N. Kuhnert, G. M. Rossignolo, A. Lopez-Periago, *Org. Biomol. Chem.* **2003**, *1*, 1157 – 1170.
[24] a) C. Stammel, R. Fröhlich, C. Wolff, H. Wenck, A. de Meijere, J. Mattay, *Eur. J. Org. Chem.* **1999**, 1709 – 1718; b) A. Terfort, H. Görls, H. Brunner, *Synthesis* **1997**, 79 – 86; c) A. A. Frimer, J. D. Kinder, W. J. Youngs, M. B. Meador, *J. Org. Chem.* **1995**, *60*, 1658 – 1664; d) R. Kuroda, *J. Chem. Soc. Perkin Trans. 2* **1982**, 789 – 794.
[25] D. J. Morrison, T. K. Trefz, W. E. Piers, R. McDonald, M. Parvez, *J. Org. Chem.* **2005**, *70*, 5309 – 5312.

 © 2006 Wiley-VCH Verlag GmbH & Co. KGaA, Weinheim

Four-Membered Rings

DOI: 10.1002/anie.200504329

Isolation of a 1,2-Dialuminacyclobutene**

Chunming Cui, Xiaofei Li, Chunhua Wang, Jianying Zhang, Jinpei Cheng, and Xiaoqing Zhu*

Dedicated to Professor Herbert W. Roesky

In recent years, small-ring systems that incorporate heavier main-group elements have drawn intense attention because of their unique structural features and high reactivity.[1,2,3] Among such rings, those which contain three-coordinate Group 13 elements and olefinic-carbon units (cyclopropene and cyclobutene analogues) are particularly attractive since they are isoelectronic with the smallest members of the Hückel aromatic series, that is, the cyclopropenium ion and the cyclobutadiene dication, respectively. The carboranes $(CH)_2(BH)_n$ ($n = 1,2$) and their derivatives have been intensively investigated both experimentally and theoretically.[2] Thus, theoretical studies of $(CH)_2(BH)_2$ revealed that the stable 1,3-diboretene isomer preferentially adopted a nonplanar, puckered geometry similar to that predicted for $(CH)_4^{2+}$, which was subsequently verified experimentally.[2] Accordingly, the synthesis and characterization of the heavier congeners of the formally 2π MC_2 and M_2C_2 rings (M = Al, Ga, In, Tl) are of fundamental interest as a result of their potential aromaticity. Surprisingly, such ring systems are rare in the literature. The recently reported AlC_2 rings of cyclopropene derivatives with bulky ligands are the only known examples in this series, in which the aluminum atoms are all four-coordinate.[3] Stable metallacyclobutene M_2C_2 rings which contain M–M bonds have remained unknown until now. Herein, we report the synthesis and single-crystal X-ray structure of the 1,2-dialuminacyclobutene $(Ar'Al)_2(CSiMe_3)_2$ (**2**; $Ar' = 2,6\text{-}Dipp_2C_6H_3$, $Dipp = 2,6\text{-}i\text{Pr}_2C_6H_3$).

The bulky terphenyl ligand Ar′, which was originally prepared by Power and co-workers, has proved effective for the stabilization of monovalent heavier Group 13 elements.[4] However, the "dialuminene" Ar′AlAlAr′ has not been isolated and was postulated as an intermediate in the formation of a bicyclic Al_2C_6 ring through a [2+4] cycloaddition upon crystallization from toluene.[5] Our interest in this system stems from the recent findings that aluminum

[*] Prof. Dr. C. Cui, X. Li, C. Wang, J. Zhang, Prof. Dr. J. Cheng, Prof. Dr. X. Zhu
State Key Laboratory of Elemento-Organic Chemistry
Nankai University
Tianjin, 300071, P.R. China
Fax: (+86) 22-2350-3461
E-mail: cmcui@nankai.edu.cn

[**] This work was supported by the National Natural Science Foundation of China (20421202) and the NCET.

Supporting information for this article is available on the WWW under http://www.angewandte.org or from the author.

© 2006 Wiley-VCH Verlag GmbH & Co. KGaA, Weinheim

cyclopropene analogues could be generated by facile reductive coupling reactions of aluminum diiodide precursors in the presence of alkynes. Thus, reduction of $Ar'AlI_2$ (**1**)[5] with two equivalents of KC_8 in the presence of $Me_3SiCCSiMe_3$ in toluene at room temperature afforded **2** (Scheme 1) as

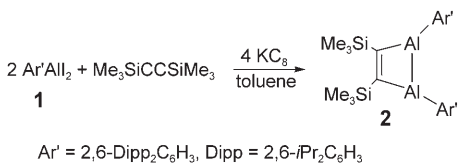

Scheme 1. Synthesis of **2**.

orange-red crystals in good yield, along with a small amount of the known compound Ar′(I)AlAl(I)Ar′ (**3**).[5] The similar reaction with only one equivalent of KC_8 leads to the formation of **3** as the major product, as indicated by spectroscopic and single-crystal X-ray analyses. Compound **2** could also be obtained by the reduction of **3** in the presence of the acetylene. The mechanism for the formation of **2** is not clear at this stage. It is possible that $K^+[Me_3SiCCSiMe_3]^{\bullet-}$ promotes the reduction process,[3a] which is followed by KI elimination as proposed previously,[3a] since in the absence of the acetylene, the reduction did not proceed under similar conditions. Compound **2** is soluble in aromatic solvents and decomposed in [D$_8$]toluene at 100 °C within 20 minutes to form a complicated mixture, but is stable in the solid state at this temperature for several hours. Compound **2** was fully characterized by ^{1}H, ^{13}C, and ^{29}Si NMR spectroscopy, UV/Vis spectroscopy, and single-crystal X-ray analysis.[6]

The ^{29}Si NMR spectrum of **2** contains one singlet ($\delta = -13.2$ ppm), which indicates the existence of the $Me_3SiCCSiMe_3$ olefinic carbon atoms.[3a] The low-field resonance ($\delta = 235.0$ ppm) in the ^{13}C NMR spectrum also supports the presence of this structural unit. The ^{1}H NMR spectrum shows the 1:1 ratio of the Ar′ ligands to the $SiMe_3$ groups. The structure of **2** was finally confirmed by a single-crystal X-ray analysis.

Single crystals of **2** suitable for X-ray analysis were obtained from toluene at room temperature. The most prominent feature of the structure (Figure 1) is the four-membered Al_2C_2 ring, which is folded (dihedral angles: 24.6, 25.0°). The geometry around each carbon atom in the ring is almost planar, but the Si1-C64-C65-Si2 unit is twisted (torsion angle: 18.6°). The three-coordinate aluminum atoms are distorted from planarity (angular sum: 351.75° at Al1, 353.22° at Al2). The C64–C65 bond length (1.362(3) Å) is consistent with a C–C double bond, and the Al–C_{ring} bond lengths (2.006(2), 2.007(2) Å) indicate single bonding. The Al1–Al2 bond length (2.4946(9) Å) is shorter by about 0.1 to 0.26 Å than those for known divalent aluminum dimers[5,7] and only slightly longer than that found in the anionic radical $Trip_2AlAlTrip_2^{\bullet-}$ (2.470(2) Å; Trip = 2,4,6-iPr$_3$C$_6$H$_2$), in which an Al–Al π bond was proposed.[8]

Preliminary B3LYP/6-31G* calculations[9] were performed on the model compound $(PhAl)_2(CSiMe_3)_2$ (**4**), for which the Ar′ ligand was replaced by a phenyl group, and

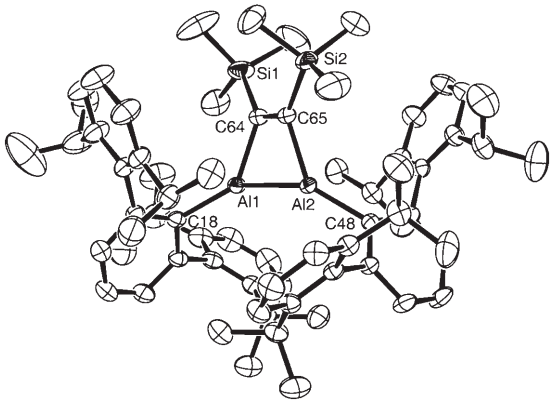

Figure 1. Thermal-ellipsoid drawing of **2** (30% probability). Hydrogen atoms are not shown. Selected bond lengths [Å] and angles [°]: Al1–Al2 2.4946(9), Al1–C64 2.006(2), Al2–C65 2.007(2), C64–C65 1.362(3), Al1–C18 1.979 (2), Al2–C48 1.978(2); C18-Al1-Al2 141.11(7), C18-Al1-C64 137.53, C64-Al1-Al2 73.11(7), C65-Al2-Al1 72.17(7), C48-Al2-Al1 143.16(6), C48-Al(2)-C65 137.97(9), C64-C65-Al2 105.48(15), C65-C64-Al1 103.82(15).

predict geometrical features that are quite similar to those found in the X-ray structure of **2**, except that the aluminum atoms adopt a planar geometry in **4**. The 1,2-dialuminacyclobutene structure of **4** is 67.9 kJ mol^{-1} more stable than the corresponding puckered 1,3 isomer. Similar calculations on the parent molecule $(HAl)_2(CH)_2$ (**5**) also show that the 1,2 isomer is energetically more favorable than its puckered 1,3 isomer, while the former is almost planar (dihedral angle: 0.03°). This finding is consistent with our experimental result that the isomerization of **2** to the 1,3-dialumina Al_2C_2 isomer was not observed in solution or in the solid state at high temperature (100–160 °C). In contrast, the experimental and theoretical studies for diboretenes revealed that puckered 1,3-B_2C_2 skeletons are more stable than the corresponding planar 1,2 isomers.[2] The folded Al_2C_2 framework of **2** and **4** versus the nearly planar geometry of **5** may be attributed to the sterically demanding $SiMe_3$ and Ar′ groups. Close H···H contacts were observed in **2** between the two $SiMe_3$ groups (2.086, 2.255 Å) and between the two Ar′ groups (2.293, 2.596 Å) and may also lead to the geometric distortion of the aluminum atoms in **2** from planarity.

The calculated HOMO and LUMO maps for the model compound **4** are shown in the Supporting Information. Most of the electron density in the HOMO is located at the orbitals of the olefinic carbon atoms in the ring. The LUMO has a significant contribution from the empty Al 3p orbitals. The calculated energy gap between the HOMO–LUMO orbitals is $\Delta E = 13.4$ kJ mol^{-1}. The small HOMO–LUMO gap indicates a non-aromatic ring.[10] The calculations also revealed that the π electrons are mostly localized in the C=C moiety. The structure of **2** also does not meet the classic criteria for aromaticity (ring planarity, cyclic bond equalization). The short Al–Al bond length in **2** might be related to the favored ring-atom geometries that are associated with the strained ring.

The UV/Vis spectrum of **2** in *n*-hexane showed two maxima at 381.0 and 297.0 nm, and the former maximum

 © 2006 Wiley-VCH Verlag GmbH & Co. KGaA, Weinheim

vanished immediately when the solution was exposed to air. This absorption might be a result of electronic transitions within the Al_2C_2 ring.

In summary, the reduction of $Ar'AlI_2$ in the presence of $Me_3SiCCSiMe_3$ afforded the 1,2-dialuminacyclobutene **2**, the first heavier Group 13 M_2C_2 ring system. Compound **2** features an unprecedented folded Al_2C_2 skeleton and a short Al–Al separation. The geometrical features of **2** and the calculations on the model compound **4** do not support the notion of aromaticity of the 2π Al_2C_2 ring system. The calculations predict that the folded 1,2-dialuminacyclobutene is energetically more favorable than its puckered 1,3 isomer. Investigation of the reaction chemistry of **2** is currently in progress.

Experimental Section

2: A solution of $Ar'AlI_2$ (**1**, 0.67 g, 1 mmol) and bis(trimethylsilyl) acetylene (0.17 g, 1 mmol) in toluene (35 mL) was added to a suspension of KC_8, which was freshly prepared from graphite and potassium (0.080 g, 2.02 mmol), in toluene (10 mL). The mixture was stirred at room temperature for 50 h and filtered, and the red filtrate was concentrated (ca. 15 mL). Storage at 5 °C overnight afforded a small amount of yellow crystals of **3** (ca. 3 %). The mixture was filtered, and the filtrate was concentrated (ca. 5 mL) and stored at −30 °C overnight to give orange-red crystals of **2** (0.32 g, 62.0 %). M.p. 161 °C (decomp.); ^{1}H NMR (400 MHz, C_6D_6): $\delta = -0.002$ (s, 18 H, $SiMe_3$), 0.58 (d, $J = 6.40$ Hz, 12 H, $CHMe_2$), 0.93 (d, $J = 6.80$ Hz, 12 H, $CHMe_2$), 1.15 (d, $J = 6.40$ Hz, 12 H, $CHMe_2$), 1.34 (d, $J = 6.80$ Hz, 12 H, $CHMe_2$), 2.86 (sept, $J = 6.80$ Hz, 8 H, $CHMe_2$), 7.02 (d, $J = 7.20$ Hz, 4 H, ArH), 7.06 (br s, 4 H, ArH), 7.18–7.23 ppm (m, 10 H, ArH); ^{13}C NMR (125.8 MHz, C_6D_6): $\delta = 2.8$ ($SiMe_3$), 22.3 ($CHMe_2$), 23.2 ($CHMe_2$), 26.0 ($CHMe_2$), 27.0 ($CHMe_2$), 30.4 ($CHMe_2$), 31.2 ($CHMe_2$), 123.5 (*m*-Dipp), 127.0 (*p*-C_6H_3), 129.8 (*m*-C_6H_3), 142.4 (*p*-Dipp) 145.6 (*i*-Dipp), 147.0 (*o*-Dipp), 149.1 (*o*-C_6H_3), 150.6 (*i*-C_6H_3), 235.0 ppm ($CSiMe_3$); ^{27}Al NMR (104.24 MHz, [D_8]toluene): could not be observed; ^{29}Si NMR (79.48 MHz, [D_8]toluene): $\delta = -13.2$ ppm; UV/Vis (hexanes): λ_{max}[nm] (ε in $mol^{-1}\,L\,cm^{-1}$): 297 (8000), 381 (2100). Elemental analysis (%) calcd for $C_{68}H_{94}Al_2Si_2$ (1021.57): C 79.95, H 9.27; found: C 80.30, H 9.04.

Received: December 6, 2005
Revised: January 6, 2006
Published online: March 6, 2006

Keywords: aluminum · aromaticity · cyclobutenes · four-membered rings · pi interactions

[1] a) J. Escudié, C. Couret, H. Ranaivonjatovo, J. Satgé, *Coord. Chem. Rev.* **1994**, *130*, 427; b) A. Sekiguchi, V. Y. Lee, *Chem. Rev.* **2003**, *103*, 1429; c) C. Cui, M. M. Olmstead, P. P. Power, *J. Am. Chem. Soc.* **2004**, *126*, 5062; d) V. Y. Lee, K. Takanashi, T. Matsuno, M. Ichinohe, A. Sekiguchi, *J. Am. Chem. Soc.* **2004**, *126*, 4758.

[2] See, for example: a) K. Krogh-Jespersen, P. von R. Schleyer, J. A. Pople, D. Cremer, *J. Am. Chem. Soc.* **1978**, *100*, 4301; b) K. Krogh-Jespersen, D. Cremer, J. D. Dill, J. A. Pople, P. von R. Schleyer, *J. Am. Chem. Soc.* **1981**, *103*, 2589; c) P. H. M. Budzelaar, K. Krogh-Jespersen, T. Clark, P. von R. Schleyer, *J. Am. Chem. Soc.* **1985**, *107*, 2773; d) A. Maier, M. Hofmann, H. Pritzkow, W. Siebert, *Angew. Chem.* **2002**, *114*, 1600; *Angew. Chem. Int. Ed.* **2002**, *41*, 1529; e) R. Wehrmann, C. Puess, H. Klusik, A. Berndt, *Angew. Chem.* **1984**, *96*, 372; *Angew. Chem. Int. Ed. Engl.* **1984**, *23*, 372; f) D. E. Kaufmann, R. Boese, A. Scheer, *Chem. Ber.* **1994**, *127*, 2349; g) M. L. McKee, *Inorg. Chem.* **2000**, *39*, 4206.

[3] a) C. Cui, S. Köpke, R. Herbst-Irmer, H. W. Roesky, M. Noltemeyer, H.-G. Schmidt, B. Wrackmeyer, *J. Am. Chem. Soc.* **2001**, *123*, 9091; b) W. Uhl, T. Spies, R. Koch, W. Saak, *Organometallics* **1999**, *18*, 4598; c) H.-J. Himmel, *Organometallics* **2003**, *22*, 2679; d) H. W. Roesky, *Inorg. Chem.* **2004**, *43*, 7264; e) H. Zhou, J. Chai, Q. Ma, V. Jancik, H. W. Roesky, H. Fan, R. Herbst-Irmer, *J. Am. Chem. Soc.* **2004**, *126*, 9472; f) H. Zhu, J. Chai, H. Fan, H. W. Roesky, C. He, V. Jancik, H.-G. Schmidt, M. Noltemeyer, W. A. Merrill, P. P. Power, *Angew. Chem.* **2005**, *117*, 5220; *Angew. Chem. Int. Ed.* **2005**, *44*, 5090.

[4] a) N. J. Hardman, R. J. Wright, A. D. Phillips, P. P. Power, *Angew. Chem.* **2002**, *114*, 2966; *Angew. Chem. Int. Ed.* **2002**, *41*, 2842; b) R. J. Wright, A. D. Phillips, N. J. Hardman, P. P. Power, *J. Am. Chem. Soc.* **2002**, *124*, 8538.

[5] R. J. Wright, A. D. Phillips, P. P. Power, *J. Am. Chem. Soc.* **2003**, *125*, 10784.

[6] Crystallographic data for **2**·toluene: $Mo_{K\alpha}$ radiation ($\lambda = 0.71073$ Å) at 273(2) K, monoclinic, space group $P2_1/c$, $a = 16.8314(9)$, $b = 16.4648(9)$, $c = 25.4086(13)$ Å, $\beta = 98.8530(10)°$, $Z = 4$, $R_1 = 0.0498$, $wR_2 = 0.1341$ for 12276 reflections ($I > 2\sigma(I)$); $R1 = 0.0784$, $wR2 = 0.1551$ for all data. CCDC-291899 contains the supplementary crystallographic data for this paper. These data can be obtained free of charge from The Cambridge Crystallographic Data Centre via www.ccdc.cam.ac.uk/data_request/cif.

[7] a) C. Pluta, K.-R. Pörschke, C. Krüger, K. Hildenbrand, *Angew. Chem.* **1993**, *105*, 451; *Angew. Chem. Int. Ed. Engl.* **1993**, *32*, 388; b) W. Uhl, A. Vester, W. Kaim, J. Poppe, *J. Organomet. Chem.* **1993**, *454*, 9; c) W. Uhl, U. Schutz, W. Kaim, E. Waldhör, *J. Organomet. Chem.* **1995**, *501*, 79; d) K. Klimek, C. Cui, H. W. Roesky, H.-G. Schmidt, M. Noltemeyer, *Organometallics* **2000**, *19*, 3085.

[8] R. J. Wehmschulte, K. Ruhlandt-Senge, M. M. Olmstead, H. Hope, B. E. Sturgeon, P. P. Power, *Inorg. Chem.* **1993**, *32*, 2983.

[9] All calculations were performed with the Gaussian 98 package. The geometries of the model compound **4** were fully optimized by employing the B3LYP/6-31G* method, and the nature of the stationary points was characterized by analytical-frequency calculations. The natural-bond-orbital method was used to perform the charge-density analysis; Gaussian 98 (Revision A.7), M. J. Frisch, G. W. Trucks, H. B. Schlegel, G. E. Scuseria, M. A. Robb, J. R. Cheeseman, V. G. Zakrzewski, J. A. Montgomery, R. E. Stratmann, J. C. Burant, S. Dapprich, J. M. Millam, A. D. Daniels, K. N. Kudin, M. C. Strain, O. Farkas, J. Tomasi, V. Barone, M. Cossi, R. Cammi, B. Mennucci, C. Pomelli, C. Adamo, S. Clifford, J. Ochterski, G. A. Petersson, P. Y. Ayala, Q. Cui, K. Morokuma, D. K. Malick, A. D. Rabuck, K. Raghavachari, J. B. Foresman, J. Cioslowski, J. V. Ortiz, B. B. Stefanov, G. Liu, A. Liashenko, P. Piskorz, I. Komaromi, R. Gomperts, R. L. Martin, D. J. Fox, T. Keith, M. A. Al-Laham, C. Y. Peng, A. Nanayakkara, C. Gonzalez, M. Challacombe, P. M. W. Gill, B. G. Johnson, W. Chen, M. W. Wong, J. L. Andres, M. Head-Gordon, E. S. Replogle, J. A. Pople, Gaussian, Inc., Pittsburgh, PA, **1998**..

[10] F. D. Proft, P. Geerlings, *Chem. Rev.* **2001**, *101*, 1451.

 © 2006 Wiley-VCH Verlag GmbH & Co. KGaA, Weinheim

Wettability

DOI: 10.1002/anie.200503957

Low-Surface-Free-Energy Materials Based on Polybenzoxazines

*Chih-Feng Wang, Yi-Che Su, Shiao-Wie Kuo, Chih-Feng Huang, Yuung-Ching Sheen, and Feng-Chih Chang**

Hydrophobicity and oleophobicity are highly desirable properties for materials that are used in a wide range of applications.[1–11] In this context, poly(tetrafluoroethylene) (teflon) is considered to be the "benchmark" low-surface-free-energy material as it combines water repellence[12] with other desirable properties.[13] Unfortunately, the use of teflon comes with certain disadvantages, such as those resulting from its low oil repellence, high cost, and poor processability. Considerable research efforts have therefore been directed towards the development of nonwettable, low-surface-free-energy polymeric materials that exhibit good film-forming characteristics.[14,15]

Intra- and intermolecular interactions are important for the surface properties of polymers. Jiang et al.[16] have reported that at temperatures above the lower critical solution temperature (LCST), the compact, collapsed conformation of poly(*N*-isopropylacrylamide) (PNIPAAm) chains induced by intramolecular hydrogen bonding between the C=O and N–H groups in the main PNIPAAm chains leads to a low surface free energy and high contact angle for water. When the temperature is below the LCST, however, the predominantly intermolecular hydrogen bonding between the main PNIPAAm chains and water molecules leads to a higher surface free energy and lower water contact angle. In addition, Chung et al.[17] have reported that the presence of amide groups in a fluorinated-main-chain liquid-crystalline polymer system tends to induce strong intermolecular hydrogen bonding, which results in higher surface free energies and higher degrees of hydrophilicity. According to these previous studies, it appears that intramolecular hydrogen bonding tends to lower the surface free energy more than intermolecular hydrogen bonding between main polymer chains.

Polybenzoxazines have many unique properties, such as low water absorption, high moduli,[18] and high glass-transition temperatures.[19] It is generally believed that hydrogen bonding between polybenzoxazine polymer chains plays an important role in promoting these attractive properties.[18] We report here that these readily available polybenzoxazines display extremely low surface free energies, even lower than that of pure teflon.

We used two bifunctional benzoxazine monomers, namely 2,2-bis(3-phenyl-3,4-dihydro-2*H*-1,3-benzoxazinyl)propane (BA-a) and 2,2-bis(3-methyl-3,4-dihydro-2*H*-1,3-benzoxazinyl)propane (BA-m). By spin-coating, we produced films that were subsequently cured in an oven to obtain ultrathin films with a thickness of about 150 nm. Table 1 lists the surface roughness and advancing contact angles of BA-a and BA-m polybenzoxazines after various curing times. The advancing contact angle is relatively less sensitive to surface roughness and heterogeneity than the receding angle, therefore the advancing angle data are commonly used to calculate the components of surface and interfacial tension.[20,21] In the BA-a polybenzoxazine system at a curing temperature of 180 °C, the advancing contact angle of diiodomethane increases with increasing curing time (from 41° after 1 h to 71° after 22 h). In contrast, the advancing contact angles of both water and ethylene glycol increased only slightly. In the case of samples kept at a higher curing temperature (240 °C),

Table 1: Root-mean-square (rms) surface roughness and advancing contact angles for water, ethylene glycol (EG), and diiodomethane (DIM) on BA-a and BA-m polybenzoxazine film structures (standard deviations in the range 0.3–2.0).The corresponding surface-free-energies (γ) are also given.

T [°C]	*t* [h]	Roughness (rms) [nm]	Contact angle [°] H_2O	EG	DIM	γ [mJ m^{-2}]
		BA-a polybenzoxazines				
60	1	2.1	97.9	73.2	17.6	48.45
180	1	1.4	99.5	74.8	40.6	39.31
	2	1.1	98.6	78.5	49.2	34.72
	4	1.0	98.7	82.1	61.0	27.99
	8	1.5	103.0	83.5	69.8	22.98
	22	1.0	104.3	83.1	70.8	22.43
240	0.5	1.7	108.5	84.1	63.2	26.73
	1	1.0	111.5	88.6	76.8	19.21
	2	1.2	110.7	88.1	76.5	19.38
	4	1.8	92.3	71.4	63.8	27.11
	8	1.3	79.4	61.3	55.7	32.03
		BA-m polybenzoxazines				
60	1	0.8	75.3	67.6	12.6	49.58
180	1	1.0	101.8	77.5	52.4	32.93
	2	0.4	109.3	83.2	59.2	29.04
	4	0.5	113.7	89.7	72.5	21.49
	8	0.3	113.6	92.1	81.0	17.02
	22	0.6	112.9	92.4	80.8	17.10
210	0.5	0.4	105.2	80.4	76.4	19.37
	1	0.2	114.0	93.3	82.1	16.43
	2	0.5	112.5	90.3	81.7	16.63
	4	0.7	103.0	75.5	72.2	21.65
	8	0.2	80.4	56.8	59.3	28.98

[*] C.-F. Wang, Dr. S.-W. Kuo, Dr. C.-F. Huang, Prof. F.-C. Chang
Institute of Applied Chemistry
National Chiao Tung University
30050 Hsinchu (Taiwan)
Fax: (+886) 3-513-1512
E-mail: changfc@mail.nctu.edu.tw
Dr. Y.-C. Su, Y.-C. Sheen
Material and Chemical Research Laboratories
Industrial Technology Research Institute
30050 Hsinchu (Taiwan)

Supporting Information for this article is available on the WWW under http://www.angewandte.org or from the author.

InterScience
© 2006 Wiley-VCH Verlag GmbH & Co. KGaA, Weinheim

the contact angles of all three liquids increased initially during the first hour and then decreased steadily upon increasing the curing time. Curing at 240 °C for 1 h led to the highest contact angles for all three liquids (112° for water, 84° for ethylene glycol, and 77° for diiodomethane). For BA-m polybenzoxazine treated at a curing temperature of 180 °C, the advancing contact angles of all three liquids increased upon increasing the curing time, but tended to level off after 8 h. When cured at 210 °C, the contact angles of all three liquids followed similar trends to those observed for the BA-a polybenzoxazine cured at 240 °C, and curing at 210 °C for 1 h led to the highest contact angles (114° for water, 93° for ethylene glycol, and 82° for diiodomethane). The root-mean-square (rms) roughness of all polybenzoxazines is lower than 3 nm, therefore the influence of topography on the surface free energy is negligible.

We evaluated the surface free energies, γ, (Table 1) by using van Oss and Good's three-liquid method.[22,23] For BA-a polybenzoxazine held at a curing temperature of 180 °C, the total surface free energy decreased substantially from 39.3 to 23 mJ m^{-2} upon increasing the curing time from 1 to 8 h. Further increasing the curing time from 8 to 22 h did not result in any significant reduction in surface free energy. At a higher curing temperature (240 °C), however, the surface free energy decreased initially and then increased steadily upon increasing the curing time. The lowest value of the surface free energy was 19.2 mJ m^{-2} after curing at 240 °C for 1 h. For the BA-m polybenzoxazine cured at a relatively low temperature (180 °C), the surface free energy decreased from 32.9 to 17 mJ m^{-2} upon increasing the curing time from 1 h to 8 h and then remained nearly constant up to 22 h. After curing temperature at 210 °C, the surface free energy followed a similar trend to that of BA-a polybenzoxazine cured at 240 °C. In the BA-m polybenzoxazine system, curing at 210 °C for 1 h resulted in the lowest surface free energy (16.4 mJ m^{-2}). For comparison, the surface free energy of teflon (21 mJ m^{-2}) was also determined by using the same liquids.[24] To our surprise, the surface free energies of these fluorine- and silicone-free polybenzoxazines are significantly lower than that of pure teflon.

According to previous studies,[25,26] the surface free energy in an epoxy system increases upon increasing the curing time, whereas in this study we found that the surface free energies of the polybenzoxazine systems (at 180 °C) generally decrease upon increasing the curing time. We believe that these polybenzoxazines possess lower surface free energies than the epoxy systems due to the presence of strong intramolecular hydrogen bonding. Ishida et al. have reported that the network structure of polybenzoxazine is supported by strong hydrogen-bonding interactions between the polymer chains, which act as chemical cross-links.[18] The hydrogen bond network structures of BA-a and BA-m polybenzoxazines have been discussed widely.[27] To determine the degree of hydrogen bonding within these polybenzoxazines, we performed curve-resolving of their FTIR spectra with respect to the corresponding frequencies of each hydrogen-bonded species (Figure 1).

The distribution of hydrogen-bonded species in the polybenzoxazine is affected greatly by the amino groups in

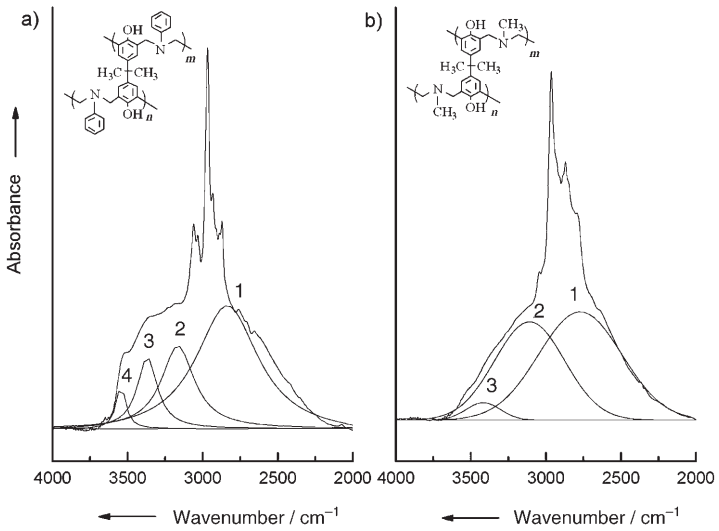

Figure 1. Curve fitting for the FTIR spectra of polybenzoxazines: a) BA-a polymer (curing temperature: 240 °C; curing time: 1 h) and b) BA-m polymer (210 °C, 1 h). 1) $O^-\cdots H^+N$ intramolecular hydrogen bonding; 2) OH···N intramolecular hydrogen bonding; 3) OH···O intermolecular hydrogen bonding; 4) OH···π intramolecular hydrogen bonding.

the Mannich bridges. For example, the network structure of the BA-m polybenzoxazine consists mainly of OH···N and $O^-\cdots H^+N$ intramolecular hydrogen bonds (proton-transfer equilibrium), whereas that of the BA-a polybenzoxazine possesses a relatively small number of such bonds. In the latter, however, some of the hydroxy groups form OH···O intermolecular hydrogen bonds. Consequently, the surface free energy of the BA-m polybenzoxazine is lower than that of the BA-a polybenzoxazine. This phenomenon can be explained by considering the fact that the strength of a hydrogen bond depends on the electronegativity of the group attached to the nitrogen atom: the electron density around the nitrogen atom attached to the benzene ring in the BA-a polybenzoxazine is lower than that in the BA-m polybenzoxazine because the electrons of the nitrogen atom of the former are more delocalized than those of the latter. Both BA-a and BA-m polybenzoxazines display strong intramolecular hydrogen bonding, which results in relatively low surface free energies. Higher curing temperatures tend to disrupt these hydrogen-bonding interactions and the resultant ratio of intra- and intermolecular hydrogen bonds may change after the sample is cooled to ambient temperature. Figure 2 displays the FTIR spectra of the BA-a and BA-m polybenzoxazine thin films as a function of the curing time (0 to 8 h) at 240 and 210 °C, respectively. The peak at 3417 cm^{-1} corresponds to the OH···O intermolecular hydrogen bonds of the BA-a polybenzoxazine, and it is clear that the fraction of these intermolecular hydrogen bonds increases upon increasing the curing time. In the FTIR spectra of the BA-m polybenzoxazine, the peak at 3397 cm^{-1} reflects the OH···O intermolecular hydrogen bonds.[27] After curing the BA-m benzoxazine at 210 °C for 1 h, a minor portion of the hydrogen-bonding interactions have been converted into OH···O intermolecular hydrogen bonds. The intensity of the signals corresponding to

 © 2006 Wiley-VCH Verlag GmbH & Co. KGaA, Weinheim

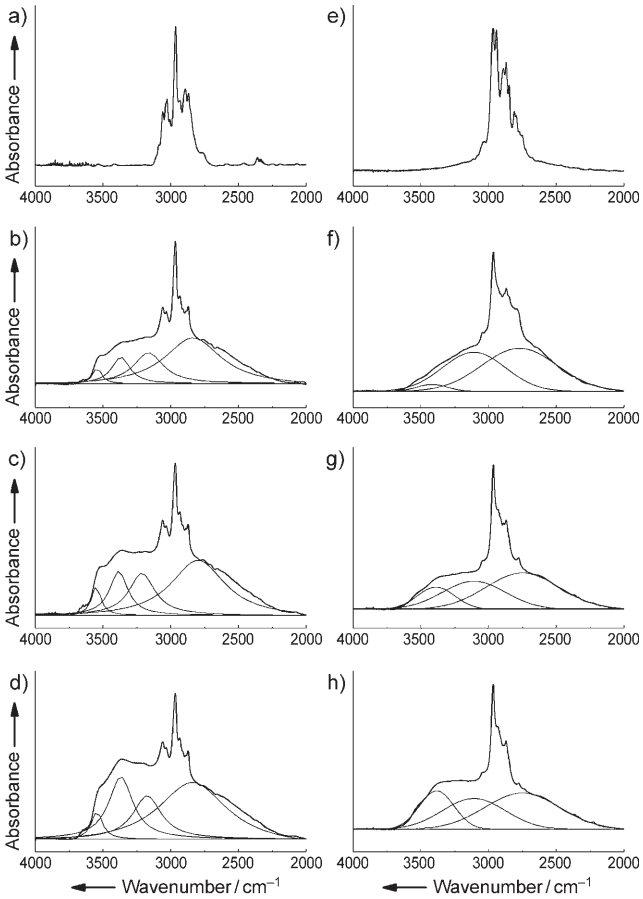

Figure 2. Curve fitting for the FTIR spectra of BA-a polybenzoxazines cured at 240 °C for a) 0, b) 1, c) 4, and d) 8 h, and BA-m polybenzoxazines cured at 210 °C for e) 0, f) 1, g) 4, and h) 8 h.

these hydrogen bonds increases upon increasing the curing time.

Combining our analyses of the FTIR spectra (Figure 3a), the variations in the water contact angles (Figure 3b), and the surface free energies (Figure 3c), it is clear that enhanced intramolecular hydrogen bonding leads to a decrease in the surface free energy and an increase in the water contact angle, whereas increasing the fraction of intermolecular hydrogen bonding leads to the opposite effect. These observations are in good agreement with the results of previous studies on surface-free-energy effects.[16,17]

In conclusion, from analyses of FTIR spectra and surface free energies we have found that strong intramolecular hydrogen bonding between the hydroxy groups of polybenzoxazines decreases their surface free energies, whereas intermolecular hydrogen bonding between the hydroxy groups of polybenzoxazines increases them. The lowest surface free energies that we observed for the BA-a and BA-m polybenzoxazine systems were 19.2 and 16.4 mJ m^{-2}, respectively. These values are lower than that of pure teflon (21 mJ m^{-2}). While polybenzoxazines and fluoropolymers both possess low surface free energies, the former are cheaper to prepare and easier to process, and therefore polybenzoxazines might replace fluoropolymers in biotechnological applications[28] and as low-surface-free-energy coatings.[29]

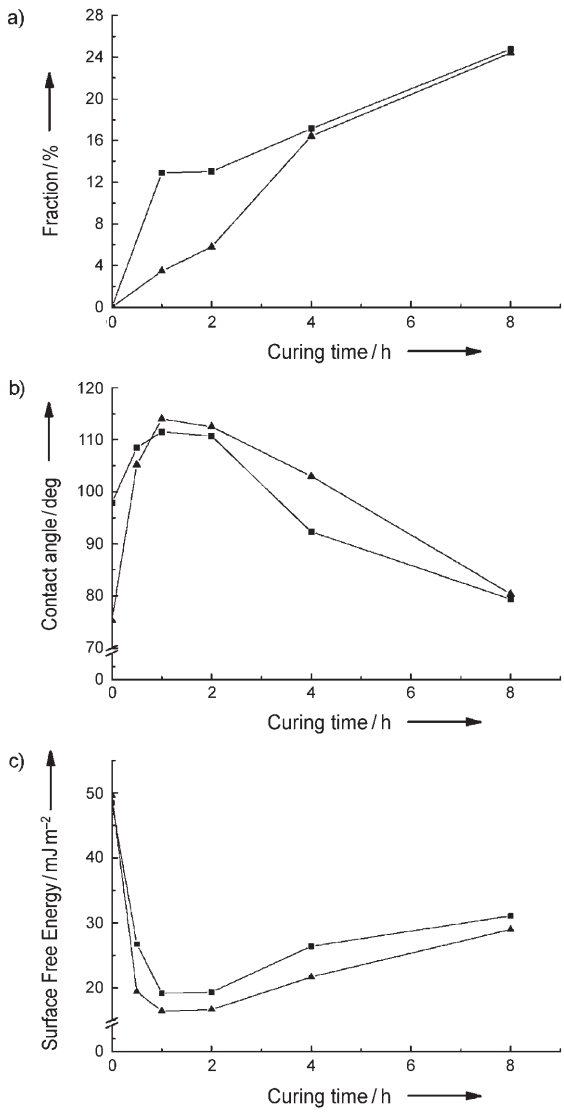

Figure 3. Variations of a) the fraction of intermolecular hydrogen bonding, b) the water contact angles, and c) the surface free energies of the BA-a (■, cured at 240 °C) and BA-m polybenzoxazines (▲, cured at 210 °C).

These BA-a and BA-m polybenzoxazines are examples of the first new class of low-surface-free-energy polymer materials since the discovery of the well-known fluoropolymers and silicones.

Experimental Section

A BA-a or BA-m benzoxazine (Shikoku Corp.) solution (30 mg mL^{-1} in tetrahydrofuran) was spin-coated onto a glass slide (100 × 100 × 1 mm^3) at 1500 rpm for 45 s. The sample was left to dry at 60 °C for 1 h before it was cured in an oven (Table 1). Infrared spectra were recorded with a Nicolet Avatar 320 FTIR spectrophotometer. The sample was prepared by casting the THF solution directly onto a potassium bromide plate and curing under conditions similar to those used in the bulk preparation. The advancing contact angle of the polymer sample was measured at 25 °C with a Kruss GH-100 goniometer interfaced with image-capture software by injecting a 5-μL liquid drop. Deionized water, ethylene glycol (≥ 99 %; Aldrich),

 © 2006 Wiley-VCH Verlag GmbH & Co. KGaA, Weinheim

and diiodomethane (99%; Aldrich) were used as standards to measure the surface free energies. Surface roughness profiles of film structures were acquired with a Digital Instruments DI5000 scanning probe microscope.

Received: November 8, 2005
Revised: January 2, 2006
Published online: February 28, 2006

Keywords: hydrogen bonds · materials science · polymers · solid-state structures · thin films

[1] H. Li, X. Wang, Y. Song, Y. Liu, Q. Li, L. Jiang, D. Zhu, *Angew. Chem.* **2001**, *113*, 1793; *Angew. Chem. Int. Ed.* **2001**, *40*, 1743.
[2] P. Aussillous, D. Quéré, *Nature* **2001**, *411*, 924.
[3] L. Feng, S. Li, Y. Li, H. Li, L. Zhang, J. Zhai, Y. Song, B. Liu, L. Jiang, D. Zhu, *Adv. Mater.* **2002**, *14*, 1857.
[4] S. Wang, L. Feng, H. Liu, T. Sun, X. Zhang, L. Jiang, D. Zhu, *ChemPhysChem* **2005**, *6*, 1475.
[5] N. J. Shirtcliffe, G. McHale, M. I. Newton, C. C. Perry, *Langmuir* **2005**, *21*, 937.
[6] B. Boutevin, Y. Pietrasanta, *Fluorinated Acrylates and Polyacrylates: Derivatives and Applications*, EREC, Paris, **1988**.
[7] L. Klinger, J. R. Griffith, C. J. N. Rall, *Org. Coat. Appl. Polym. Sci. Proc.* **1983**, *48*, 407.
[8] C. Bonardi, Eur. Pat Appl. EP 426530, **1991**.
[9] C. G. DeMarco, A. J. Macquade, S. J. Kennedy, *J. Mod. Text. Mag.* **1960**, *2*, 50.
[10] Y. Matsumoto, K. Yoshida, M. Ishida, *Sens. Actuators A* **1998**, *66*, 308.
[11] M. H. Anderson, C. S. Lyons, B. D. Wigness, U.S. Pat. 4536179, **1985** *Chem. Abstr.* **1981**, *95*, 209403.
[12] S. Wu, *Polymer Interface and Adhesion*, Marcel Dekker, New York, **1982**. p. 142.
[13] A. E. Feiring, J. F. Imbalzano, D. L. Kerbow, *Adv. Fluoroplast. Plast. Eng.* **1994**, 27.
[14] H. Kobayashi, M. J. Owen, *Trends Polym. Sci.* **1995**, *3*, 5.
[15] D. L. Schmidt, C. E. Coburn, B. M. DeKoven, G. E. Potter, G. F. Meyers, D. A. Fischer, *Nature* **1994**, *368*, 41.
[16] T. Sun, G. Wang, L. Feng, B. Liu, Y. Ma, L. Jiang, D. Zhu, *Angew. Chem.* **2004**, *116*, 361; *Angew. Chem. Int. Ed.* **2004**, *43*, 357.
[17] K. X. Ma, T. S. Chung, *J. Phys. Chem. B* **2001**, *105*, 4145.
[18] H. Ishida, D. J. Allen, *J. Polym. Sci., Part B* **1996**, *34*, 1019.
[19] H. Ishida, Y. Rodriguez, *Polymer* **1995**, *36*, 3151.
[20] R. J. Good, C. J. van Oss, *Modern Approaches to Wettability: Theory and Applications* (Eds.: M. E. Schrader, G. Loeb), Plenum, New York, **1992**, pp. 1–27.
[21] J. Drelich, J. D. Miller, R. J. Good, *J. Colloid Interface Sci.* **1996**, *179*, 37.
[22] C. J. van Oss, L. Ju, M. K. Chaudhury, R. J. Good, *J. Colloid Interface Sci.* **1989**, *128*, 313.
[23] C. J. van Oss, M. K. Chaudhury, R. J. Good, *Chem. Rev.* **1988**, *88*, 927.
[24] J. Tsibouklis, M. Stone, A. A. Thorpe, P. Graham, T. G. Nevell, R. J. Ewen, *Langmuir* **1999**, *15*, 7076.
[25] S. A. Page, R. Mezzenga, L. Boogh, J. C. Berg, J.-A. E. Manson, *J. Colloid Interface Sci.* **2000**, *222*, 55.
[26] R. Mezzenga, S. A. Page, J.-A. E. Manson, *J. Colloid Interface Sci.* **2002**, *250*, 121.
[27] H. D. Kim, H. Ishida, *J. Phys. Chem. A* **2002**, *106*, 3271.
[28] J. Tsibouklis, M. Stone, A. A. Thorpe, P. Graham, V. Peters, R. Heerlien, J. R. Smith, K. L. Green, T. G. Nevell, *Biomaterials* **1999**, *20*, 1229.
[29] A. F. Thunemann, A. Lieske, B. R. Paulke, *Adv. Mater.* **1999**, *11*, 321.

 © 2006 Wiley-VCH Verlag GmbH & Co. KGaA, Weinheim

Polymer Films

DOI: 10.1002/anie.200503892

Synthesis of Stable Super Water- and Oil-Repellent Polythiophene Films

*Mael Nicolas, Frédéric Guittard, and Serge Géribaldi**

Throughout the last few decades, since the discovery of electrical conductivity in doped polyacetylene,[1,2] there has been tremendous interest in conjugated-polymer technology,[3–5] and synthetic methods are well established.[6,7] Among conjugated polymers, polythiophenes exhibit some unique advantages for developing various applications.[8–12] Like a number of electric or electronic materials, polythiophene films are markedly influenced by environmental exposure, particularly to moisture, but only a few studies have been made on the role of water, in contrast to the effect of air.[13–15]

In general, the wettability of solid surfaces is governed by both the chemical composition and the geometrical microstructure of the surface.[16–26] The main chemical approach is the introduction of perfluorocarbon chains on the polymer backbone. However, though some work has been devoted to fluorinated polythiophenes, little specific attention was paid to their surface wettability.[8,9,27–34] Moreover, it is well known that fluorine-containing polymers are usually quite susceptible to rapid rearrangement when the polymer surface is contacted with water, particularly for short perfluorinated side chains (typically $n \leq 8$ in C_nF_{2n+1} groups), to minimize the interfacial free-energy response to the environmental media. Consequently, high contact angles that are observed on dry surfaces can quickly decrease in the wet state, in contradiction with the aim of creating low-surface-energy materials for long-term use in a polar environment.[35–38]

Thus, if the goal is to obtain stable water-repellent conductive polythiophene or other polymer films, it appears necessary to combine the chemical "fluorine" approach with a geometrical approach leading to the formation of fractal or rough surface structures. Ulgade et al. reported a SEM study on the growth of electrochemically generated polythiophene films in which the optimization of parameters of the electropolymerization process, particularly monomer and electrolyte concentrations, allows the structure and morphology of the obtained polymer to be controlled.[39] More recently, Tsujii et al. succeeded in the electrochemical synthesis of environmentally stable super water-repellent polyalkylpyrrole films by template-free growth of aligned needle-like structures.[40] The electrochemical method was recently used to prepare super-hydrophobic metal surfaces.[41–43]

[*] Dr. M. Nicolas, Prof. Dr. F. Guittard, Prof. Dr. S. Géribaldi
Laboratoire de Chimie des Matériaux Organiques et Métalliques (CMOM), EA 3155
Université de Nice-Sophia Antipolis
Parc Valrose, 06108 Nice Cedex 2 (France)
Fax: (+33) 4-92-07-61-56
E-mail: geribald@unice.fr

© 2006 Wiley-VCH Verlag GmbH & Co. KGaA, Weinheim

Herein, we report on the preparation of temporally stable super water-repellent polythiophene films (contact angle >150°) by simultaneously exploiting the two parameters governing the wettability of a solid surface, that is, the introduction of perfluorinated groups in the monomer molecule and the formation of rough surface structures. The fluorinated chain also leads to the films being oil-repellent (contact angle of 135° with hexadecane). The surface properties of the electrodeposited polythiophene film obtained from 2-(thiophen-3-yl)ethyl 4,4,5,5,6,6,7,7,8,8,9,9,10,10,11,11,11-heptadecafluoroundecanoate as a model fluorinated monomer are compared with those of a film formed by slow evaporation of a chloroform solution of the fluorinated polythiophene chemically obtained from the same monomer.

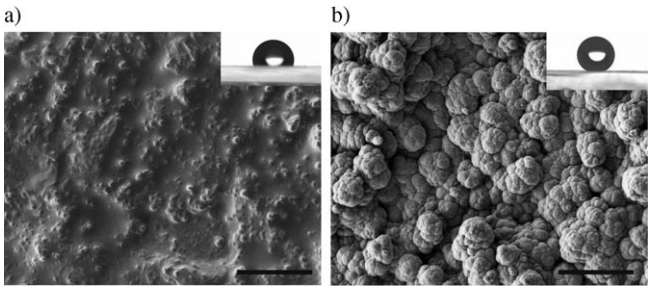

Figure 1. SEM images of the poly(fluorinated thiophene) films (scale bar: 8 μm). Insets: camera images of a water droplet on the film. a) Film formed by drop casting of a chloroform solution of polymer on a glass plate; b) electrodeposited film on ITO electrode.

The chosen fluorinated monomer was synthesized by adaptation of previously described procedures (Scheme 1 a). Electrochemical polymerization of the monomer was carried out in thoroughly dried acetonitrile containing Bu_4NPF_6 as supporting electrolyte, while chemical polymerization was performed by using $FeCl_3$ as oxidant in dry chloroform (Scheme 1 b and c). Figure 1 shows the chemically and electrochemically synthesized poly(fluorinated thiophene) films. The electrodeposited polythiophene exhibits a cauliflowerlike structure, as previously reported by Ulgade et al.[39] In comparison with the flat chemically formed polymer sample, the rough electrodeposited film shows not only super water repellency, with contact angles to water larger than 150°, but also oil repellency with contact angles to hexadecane 50° larger than those measured for the chemically formed polymer (Table 1). According to the literature,[17] this difference in oil wettability could appear unexpected if it originated only from the surface roughness. However, by modifying the latter, the surface energy is also changed because of different arrangements of trifluoromethyl groups at the top of the surface.[19,21] The surface energy of the electrodeposited film and its dispersive and polar components could not be evaluated by using the Owens–Wendt–Fowkes concept, whereas they were determined for the chemically deposited film (Table 1).[44,45]

Table 1: Contact angles [°] of both polymer films.

Film	$\theta_{water,\,static}$	$\theta_{water,\,advancing}$	$\theta_{water,\,receding}$	$\theta_{diiodomethane,\,static}$	$\theta_{hexadecane,\,static}$
chemically obtained[a]	108	105	32	96	78
electrodeposited[b]	153	151	145	137	135

[a] The surface energy γ (11.8 mN m^{-1}) and its dispersive and polar components γ^d (9.5) and γ^p (2.3), respectively, were obtained by using the Owens–Wendt–Fowkes concept.[44,45] [b] The surface energy of the electrodeposited film and its dispersive and polar components are too low to be evaluated by using the Owens–Wendt–Fowkes concept.

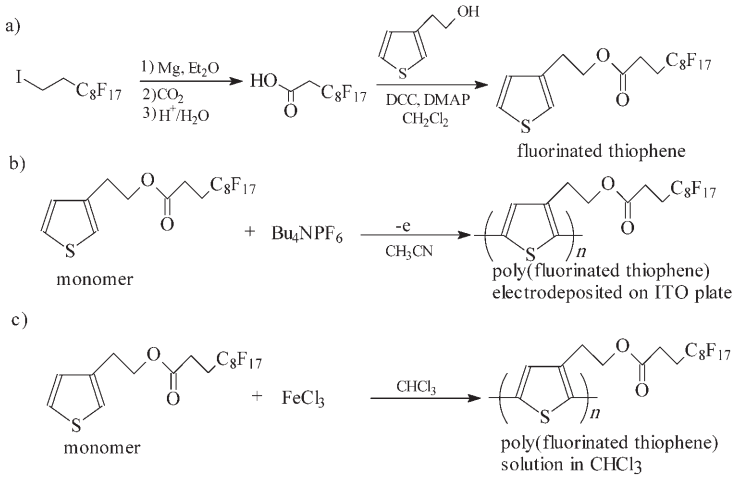

Scheme 1. a) Synthesis of the fluorinated model monomer (DCC: dicyclohexylcarbodiimid, DMAP: 4-dimethylaminopyridine); b) electrochemical polymerization; c) chemical polymerization.

Figure 2 shows the temporal stabilities of the films in terms of contact angle to water over a ten-minute period. The contact angle on the electrodeposited film remains constant, while the rapid decrease of that on the chemically deposited film is evidence for surface instability. To check this proposal and to describe more precisely the hydrophobicity of these surfaces, both advancing and receding contact angles for water must be considered. In particular, the difference between them (hysteresis) is essential for verifying ultrahydrophobic behavior.[46,47] Measurements on chemically

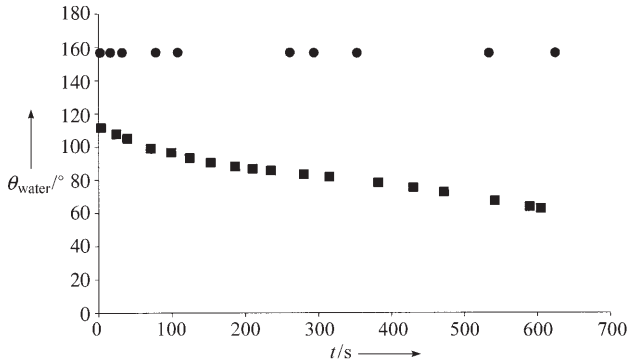

Figure 2. Short-term stabilities of the poly(fluorinated thiophene) films in terms of contact angle to water θ_{water} (● from electrodeposition; ■ deposited from chloroform solution).

 © 2006 Wiley-VCH Verlag GmbH & Co. KGaA, Weinheim

formed poly(fluorinated thiophene) surfaces showed a high hysteresis value (> 70°, see Table 1). In this case, constant receding values were not obtained, and an initial receding contact angle is given. The time-dependent receding angle and large hysteresis, as well as the short-term instability of the static angle, suggest that the surface is changed by interaction with water. The reasons for this phenomenon could be reorganization of the surface, penetration of the liquid, heterogeneity, and so on.[48,49] On the other hand, the electrodeposited poly(fluorinated thiophene) surfaces exhibit very small hysteresis of the contact angle (< 10°) with the result that water droplets roll easily. Thus, these surfaces can be defined as ultrahydrophobic, that is, they exhibit both large water contact angle and small hysteresis.[46,47]

Measurements performed every week over a long period (> 60 d) led to contact angles of (150 ± 3)° and (105 ± 4)° for electrochemically and chemically deposited films, respectively. This super water and oil repellency and the short- and long-term stabilities of the electrodeposited poly(fluorinated thiophene) film must be attributed not only to the incorporation of fluorocarbon chains on the polythiophene backbone, but also to the surface morphology.

In conclusion, we have shown that the combination of the two factors—that is, chemical composition and geometrical structure—that govern the wettability of a solid surface by a liquid leads to super water-repellent and oil-repellent electrodeposited solid polythiophene thin films. In our case, the simultaneous use of a perfluoralkyl group on the monomer core and electrochemical polymerization allows stable orientation of the fluorocarbon chains in a rough, cauliflowerlike surface that leads to exceptionally high contact angles with both water and oil. It is clear from these experiments that the type of deposition (electrodeposition vs classical coating) has a major effect on the morphology. Submicroscopic aggregates are observed only in electrodeposited films and must be correlated with the unexpectedly stable, highly hydrophobic and oleophobic films. Some parameters, such as the film thickness, the use of other electrode materials (Au, glassy carbon, etc.), and the modification of surface properties by oxidizing the polymer, must be studied for a better understanding of this phenomenon and in the hope of obtaining similar results with shorter fluorocarbon chains. Grafted conductive polymers could also be an unconventional tool to achieve strong bioactive surface properties, and work in this direction is currently underway.

Experimental Section

Synthesis of the fluorinated monomer: 4,4,5,5,6,6,7,7,8,8,9,9,10,10,11,11,11-Heptadecaundecanoic acid (5 mmol), synthesized as previously described,[50,51] DCC (5 mmol), and DMAP (0.5 mmol) were mixed under nitrogen with CH_2Cl_2 (25 mL). The reaction mixture was stirred for 3 h at room temperature, and then 2-(thiophen-3-yl)ethanol (5 mmol) was added and stirring was continued overnight. After filtration and evaporation of solvent, the crude product was purified by liquid chromatography (eluent: dichloromethane/hexane 1/1).

Preparation of poly(fluorinated thiophene) films: Chemical polymerization of the fluorinated monomer was performed in chloroform at room temperature. $FeCl_3$ (5 mmol) was added to a solution of the fluorinated monomer (1 mmol) in dry chloroform (20 mL). The reaction mixture was stirred overnight and methanol (100 mL) was added to precipitate the polymer. After filtration, the dark blue polymer was washed continuously with methanol in a soxhlet apparatus for 24 h, and the soluble fraction obtained by extraction with chloroform for a further 24 h. Then, the polythiophene film was coated onto glass by drop casting a solution of the polymer in chloroform (5 g L^{-1}).

Electrochemical polymerization was performed at room temperature in a three-electrode cell in thoroughly dried acetonitrile containing Bu_4NPF_6 (100 mmol) as supporting electrolyte and fluorinated thiophene (20 mmol). The film was potentiostatically electroformed with an anodic limit close to the irreversible oxidation peak potential of the monomer (e.g., 2.10 V) under the following conditions: ITO/glass working electrode, reaction time 300 s, electropolymerization charge 500 mC cm^{-2}. The film was washed with acetonitrile to eliminate reactants. Films were finally dried for a few days at room temperature under reduced pressure.

Measurements of static and dynamic contact angles, surface energy, and temporal stability of the contact angles of the films: Contact angles were measured by the sessile-drop method on a Krüss DSA10 contact-angle goniometer. They were recorded at (22 ± 1) °C with distilled water, diiodomethane, and hexadecane as wetting liquids. Water and hexadecane contact angles were taken as indexes of hydrophobicity and oleophobicity, respectively. Short-term stability of the film surfaces was evaluated by measuring the evolution of the contact angle of a water droplet placed on the surface for a period of 10 min. The advancing and receding contact angles for water were determined by sessile-drop experiments, which were analyzed by axisymmetric drope shape analysis-profile (ADSA-P).[52] Contact angles for water on both chemically and electrochemically deposited poly(fluorinated thiophene) films were also determined every week over a long period of time to take into account the long-term stability of the films. All the angles reported herein were the average of at least five measurements on various parts of each film.

SEM measurements: Scanning electron microscopy of the films was carried out with a JEOL 6700F microscope, after covering them with a thin layer of sputtered carbon obtained by thermal evaporation. The electrodeposited films on ITO plate were directly observed.

Received: November 3, 2005
Revised: December 13, 2005
Published online: February 28, 2006

Keywords: electrochemistry · hydrophobic effect · polymers · surface chemistry · thin films

[1] T. Ito, H. Shirakawa, S. Ikeda, *J. Polym. Sci. Polym. Chem. Ed.* **1974**, *12*, 11 – 20.
[2] D. Egbe, C. Bader, J. Nowotny, E. Klemm, *Proc. SPIE-Int. Soc. Opt. Eng.* **2004**, *5215*, 79.
[3] S. Asavapiriyanont, G. K. Chandler, G. A. Gunawardena, D. Pletcher, *J. Electroanal. Chem.* **1984**, *177*, 229 – 244.
[4] P. G. Pickup, R. A. Osteryoung, *J. Am. Chem. Soc.* **1984**, *106*, 2294 – 2299.
[5] R. E. Noftleand, D. Pletcher, *J. Electroanal. Chem.* **1987**, *227*, 229 – 235.
[6] M. Satoh, K. Kaneto, K. Yoshino, *Synth. Met.* **1986**, *14*, 289 – 296.
[7] *Handbook of Conjugated Polymers* (Eds.: T. A. Skotheim, R. L. Elsenbaumer, J. R. Reynolds), Marcel Dekker, New York, **1996**.
[8] J. Roncali, *Chem. Rev.* **1992**, *92*, 711 – 738.
[9] *Handbook of Oligo- and Polythiophenes* (Ed.: D. Fichou), Wiley-VCH, Weinheim, **1999**.

 © 2006 Wiley-VCH Verlag GmbH & Co. KGaA, Weinheim

[10] M. Andersson, O. Thomas, W. Mammo, M. Svensson, M. Theander, O. Onganas, *J. Mater. Chem.* **1999**, *9*, 1933 – 1940.
[11] J. D. Tovar, T. M. Swager, *J. Polym. Sci. Part A* **2003**, *41*, 3693 – 3702.
[12] F. Aubertin, Y. Zhao, *J. Polym. Sci. Part A* **2004**, *42*, 3445 – 3455.
[13] G. Horowitz, X. Peng, D. Fichou, F. Garnier, *J. Appl. Phys.* **1990**, *67*, 528 – 532.
[14] R. Turcu, O. Pana, I. Bratu, M. Bogdan, *J. Mol. Electron.* **1990**, *6*, 1 – 4.
[15] S. Hoshino, M. Yoshida, S. Uemura, T. Kodzasa, N. Takada, T. Kamata, K. Yase, *J. Appl. Phys.* **2004**, *95*, 5088 – 5092.
[16] T. Onda, S. Shibuichi, N. Satoh, K. Tsujii, *Langmuir* **1996**, *12*, 2125 – 2127.
[17] K. Tsujii, T. Yamamoto, T. Onda, S. Shibuichi, *Angew. Chem.* **1997**, *109*, 1042 – 1044; *Angew. Chem. Int. Ed. Engl.* **1997**, *36*, 1011 – 1012.
[18] K. Tsujii in *Surface Activity: Principles, Phenomena, and Applications* (Ed.: T. Tanaka), Academic Press, New York, **1998**, pp. 52 – 54.
[19] S. Shibuichi, T. Yamamoto, T. Onda, K. Tsujii, *J. Colloid Interface Sci.* **1998**, *208*, 287 – 294.
[20] H. Li, X. Wang, Y. Song, Y. Liu, Q. Li, L. Jiang, D. Zhu, *Angew. Chem.* **2001**, *113*, 1793 – 1796; *Angew. Chem. Int. Ed.* **2001**, *40*, 1743 – 1746.
[21] D.-H. Jung, I. J. Park, Y. K. Choi, S.-B. Lee, H. S. Park, J. Rühe, *Langmuir* **2002**, *18*, 6133 – 6139.
[22] L. Feng, S. Li, Y. Li, H. Li, J. Zhai, L. Zhang, Y. Song, L. Jiang, D. Zhu, *Angew. Chem.* **2002**, *114*, 1269 – 1271; *Angew. Chem. Int. Ed.* **2002**, *41*, 1221 – 1223.
[23] L. Feng, S. Li, Y. Li, H. Li, L. Zhang, J. Zhai, Y. Song, B. Liu, L. Jiang, D. Zhu, *Adv. Mater.* **2002**, *14*, 1857 – 1860.
[24] L. Feng, Z. Zhang, Z. Mai, Y. Ma, B. Liu, L. Jiang, D. Zhu, *Angew. Chem.* **2004**, *116*, 2046 – 2048; *Angew. Chem. Int. Ed.* **2004**, *43*, 2012 – 2014.
[25] T. Sun, G. Wang, L. Feng, B. Liu, Y. Ma, L. Jiang, D. Zhu, *Angew. Chem.* **2004**, *116*, 361 – 364; *Angew. Chem. Int. Ed.* **2004**, *43*, 357 – 360.
[26] C.-T. Hsieh, J.-M. Chen, R.-R. Kuo, T.-S. Lin, C.-F. Wu, *Appl. Surf. Sci.* **2005**, *240*, 318 – 326.
[27] W. Büchner, R. Gareau, J. Roncali, M. Lemaire, *J. Fluorine Chem.* **1992**, *59*, 301 – 309.
[28] S. K. Ritter, R. E. Noftle, A. E. Ward, *Chem. Mater.* **1993**, *5*, 752 – 754.
[29] L. Robitaille, M. Leclerc, *Macromolecules* **1994**, *27*, 1847 – 1851.
[30] J. S. Middlecoff, D. M. Collard, *Synth. Met.* **1997**, *84*, 221 – 222.
[31] A. Facchetti, Y. Deng, A. Wang, Y. Koide, H. Sirringhaus, T. J. Marks, R. H. Friend, *Angew. Chem.* **2000**, *112*, 4721 – 4725; *Angew. Chem. Int. Ed.* **2000**, *39*, 4547 – 4551.
[32] X. M. Hong, J. C. Tyson, J. S. Middlecoff, D. M. Collard, *Macromolecules* **1999**, *32*, 4232 – 4239.
[33] X. M. Hong, J. C. Tyson, D. M. Collard, *Macromolecules* **2000**, *33*, 3502 – 3504.
[34] S. Thomas, C. Zhang, S.-S. Sun, *J. Polym. Sci. Part A* **2005**, *43*, 4280 – 4287.
[35] T. Maekawa, S. Kamata, M. Matsuo, *J. Fluorine Chem.* **1991**, *54*, 84.
[36] S. Takahashi, T. Kasemura, K. Asano, *Polymer* **1997**, *38*, 2107 – 2111.
[37] M. Morita, H. Ogisu, M. Kubo, *J. Appl. Polym. Sci.* **1999**, *73*, 1741 – 1749.
[38] M. Xiang, X. Li, C. K. Ober, K. Char, J. Genzer, E. Sivaniah, E. J. Kramer, D. A. Fischer, *Macromolecules* **2000**, *33*, 6106 – 6119.
[39] L. Ulgade, J. C. Bernede, M. A. Del Valle, F. R. Diaz, P. Leray, *J. Appl. Polym. Sci.* **2002**, *84*, 1799 – 1809.
[40] H. Yan, K. Kurogi, H. Mayama, K. Tsujii, *Angew. Chem.* **2005**, *117*, 3519 – 3522; *Angew. Chem. Int. Ed.* **2005**, *44*, 3453 – 3456.
[41] X. Zhang, F. Shi, X. Yu, H. Liu, Z. Wang, L. Jiang, X. Li, *J. Am. Chem. Soc.* **2004**, *126*, 3064 – 3065.
[42] S. Wang, L. Feng, H. Liu, T. Sun, X. Zhang, L. Jiang, D. Zhu, *ChemPhysChem* **2005**, *6*, 1475 – 1478.
[43] N. J. Shirtcliffe, G. McHale, M. I. Newton, C. C. Perry, *Langmuir* **2005**, *21*, 937 – 943.
[44] D. K. Owens, R. C. Wendt, *J. Appl. Polym. Sci.* **1969**, *13*, 1741 – 1747.
[45] F. M. Fowkes, *J. Phys. Chem.* **1963**, *67*, 2538 – 2541.
[46] W. Chen, A. Y. Fadeev, M. C. Hsieh, D. Öner, J. Youngblood, T. J. MacCarthy, *Langmuir* **1999**, *15*, 3395 – 3399.
[47] R. M. Jisr, H. H. Rmaile, J. B. Schlenoff, *Angew. Chem.* **2005**, *117*, 792 – 795; *Angew. Chem. Int. Ed.* **2005**, *44*, 782 – 785.
[48] R. Bongiovanni, G. Malucelle, A. Priola, *J. Colloid Interface Sci.* **1995**, *171*, 283 – 287.
[49] S. Takahashi, T. Kasemura, K. Asano, *Polymer* **1997**, *38*, 2107 – 2111.
[50] E. T. McBee, R. D. Battershell, H. P. Braendlin, *J. Org. Chem.* **1963**, *28*, 1131 – 1133.
[51] K. von Werner, H. Blank, A. Gisser, A. Manhart, *J. Fluorine Chem.* **1980**, *16*, 193 – 197.
[52] D. Y. Kwok, T. Gietzelt, K. Grundke, H.-J. Jacobasch, A. W. Neumann, *Langmuir* **1997**, *13*, 2880 – 2894.

 © 2006 Wiley-VCH Verlag GmbH & Co. KGaA, Weinheim

Asymmetric Synthesis

DOI: 10.1002/anie.200503477

High Substrate/Catalyst Organocatalysis by a Chiral Brønsted Acid for an Enantioselective Aza-Ene-Type Reaction**

Masahiro Terada, Kyoko Machioka, and Keiichi Sorimachi*

The enantioselective catalysis of organic reactions that involve small organic molecules, known as organocatalysis, has become a rapidly growing area of research, as it offers operational simplicity together with mild reaction conditions and is environmentally benign.[1] Although organocatalysis has proven to be beneficial in many respects, one critical drawback inherent in the methodologies reported to date is the inadequate catalytic efficiency.[2] Most organocatalytic reactions are performed at substrate-to-catalyst (S/C) molar ratios of 10 or less to achieve sufficient yields and avoid loss of

[*] Prof. Dr. M. Terada, K. Machioka, K. Sorimachi
Department of Chemistry
Graduate School of Science
Tohoku University
Aramaki, Aoba-ku, Sendai 980-8578 (Japan)
Fax: (+81) 22-795-6602
E-mail: mterada@mail.tains.tohoku.ac.jp

[**] This work was partially supported by a Grant-in-Aid for Scientific Research from the Ministry of Education, Culture, Sports, Science and Technology, Japan, and The Tokuyama Science Foundation.

Supporting information for this article is available on the WWW under http://www.angewandte.org or from the author.

WILEY InterScience DISCOVER SOMETHING GREAT
© 2006 Wiley-VCH Verlag GmbH & Co. KGaA, Weinheim

enantioselectivity. One of the greatest challenges in practical organocatalysis is to decrease the catalyst loading to ensure a high efficiency. Akiyama and co-workers and our group have independently developed binaphthol-derived monophosphoric acids **1** as organocatalysts for enantioselective carbon–carbon bond-forming reactions.[3,4] Herein, we report high S/C organocatalysis with **1** as the chiral Brønsted acid[5,6] for enantioselective reactions of *N*-benzoylimines **2** with enamides or enecarbamates **3**. The reaction conditions allow imine/catalyst molar ratios of up to 2000 to afford the corresponding β-aminoimine adducts **4** in high yields without considerable loss of enantioselectivity [Eq. (1)].

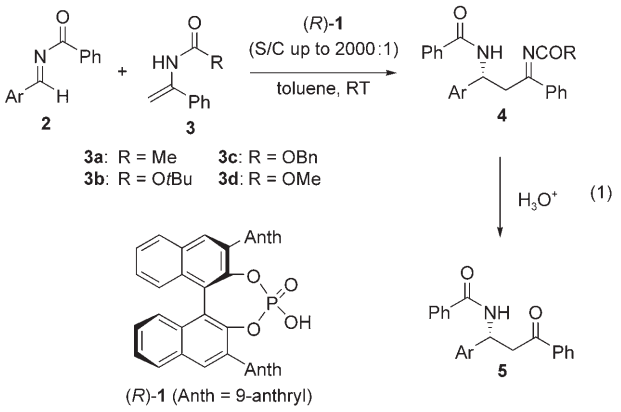

Recently Kobayashi and co-workers successfully demonstrated the first use of enamides and enecarbamates as nucleophiles in enantioselective reactions with either glyoxylates or glyoxylate-derived imines catalyzed by chiral copper complexes.[7] Their mechanistic proposal, in which the reaction proceeds by an aza-ene-type pathway, inspired us to develop a highly efficient organocatalytic reaction using a phosphoric acid catalyst **1** (Scheme 1). In our catalytic reaction, it is thought that **1** is assembled into the transient structure of the aza-ene-type reaction of **2** with **3** through a hydrogen-bonding network (Scheme 1a). Thus, the key aspect of catalysis is the dual function of the phosphoric acid moiety,[3c,4b] which electrophilically activates **2** through the proton (hollow circle) and accepts the NH proton (dashed circle) of **3** through the Lewis basic phosphoryl oxygen atom. Subsequent bond recombination, which leads to the aza-ene-type product and regeneration of the catalyst **1**, would ideally take place (Scheme 1b,c). On the basis of this mechanistic assumption, the dual function of **1** through these hydrogen-bonding interactions allows the reaction to operate under high S/C conditions.

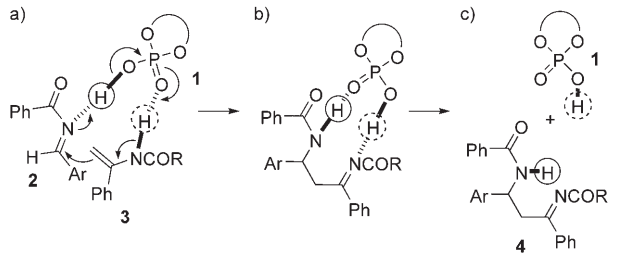

Scheme 1. Mechanistic assumption of the aza-ene-type reaction catalyzed by **1**; see text for details.

We first set the S/C ratio to 50:1 (2 mol%) using the binaphthol-derived monophosphoric acid **1** to ascertain the viability of the high S/C ratio in the aza-ene-type reaction. The catalytic efficiency was screened in the reaction of the benzaldehyde-derived *N*-benzoylimine (**2**; Ar = Ph) with an enamide **3a** in various solvents at room temperature. The yields and enantioselectivities were determined after the hydrolysis of imine adducts **4** to β-aminoketones **5** under acidic work-up conditions (concentrated HBr in MeOH).[8] Representative results are given in Table 1. Among the solvents tested, toluene was the best with respect to both yield and enantiomeric excess (Table 1, entries 1–3 versus 4), though the reaction also tolerated common organic solvents. In addition to the enamide **3a**, we examined enecarbamates **3b–d** (Table 1, entries 5–7). The steric bulk of the alkoxy moiety of the enecarbamates exhibited a dramatic effect on the enantioselectivity. That is, the enantioselectivity increased with the decrease in the steric demand of the alkoxy moiety, thus following the order *t*BuO **3b** < BnO **3c** < MeO **3d** and reaching 95% *ee* in the reaction with the less hindered methyl carbamate **3d** (Table 1, entry 7). Lowering the reaction temperature to 0°C led to a slight increase in the enantiomeric excess, although with some loss of catalytic efficiency (Table 1, entry 8). With successful results for the catalytic efficiency in the initial screening, we decreased the catalyst loading and set the S/C ratio to more than 1000:1 (0.1 mol%; Table 1, entries 9–11). The decrease in catalyst loading was clearly still effective, although a prolonged reaction time was required to achieve a comparable level of product formation (Table 1, entries 9 and 10); the enantioselectivity and the yield were maintained at an equally high level. It should be emphasized that the reaction can be performed without considerable loss of enantioselectivity, even when the S/C

Table 1: Chiral Brønsted acid-catalyzed reaction of imine **2** (Ar = Ph) with an enamide **3a** and enecarbamates **3b–d**.[a]

Entry	3	S/C[b] (mol%)	Solvent	*t* [h]	Yield [%][c]	*ee* [%][d]
1	**3a**	50:1 (2)	CH_2Cl_2	0.5	77	69
2	**3a**	50:1 (2)	$(CH_2Cl)_2$	0.5	61	70
3	**3a**	50:1 (2)	Et_2O	0.5	71	80
4	**3a**	50:1 (2)	toluene	0.5	90	86
5	**3b**	50:1 (2)	toluene	1	94	60
6	**3c**	50:1 (2)	toluene	1	55	83
7	**3d**	50:1 (2)	toluene	1	85	95
8[e]	**3d**	50:1 (2)	toluene	1	76	96
9	**3d**	1000:1 (0.1)	toluene	2	64	95
10	**3d**	1000:1 (0.1)	toluene	5	82	95
11	**3d**	2000:1 (0.05)	toluene	5	85	93

[a] Unless otherwise noted, all reactions were carried out with 0.10 mmol of **2** (Ar = Ph) and 0.12 mmol of **3** in a 0.1 M solution at room temperature. [b] Molar ratio of imine **2**/catalyst **1**. [c] Yield of the isolated product of **5** after hydrolysis of **4**. [d] Enantiomeric excess was determined by chiral HPLC analysis (see the Supporting Information). [e] Reaction performed at 0°C.

 © 2006 Wiley-VCH Verlag GmbH & Co. KGaA, Weinheim

ratio was increased to as much as 2000:1 (0.05 mol%; Table 1, entry 11).

The applicability of the present high S/C organocatalysis to a series of *N*-benzoylimines **2** was investigated.[9] We set the S/C ratio to 1000:1 (0.1 mol%) to ensure the catalytic efficiency of **1**. Table 2 shows *para*- and *meta* substitution or

Table 2: Enantioselective aza-ene-type reaction of an enecarbamate **3d** with various *N*-benzoylimines **2** catalyzed by (*R*)-**1** with a S/C ratio of 1000:1 [0.1 mol%; Eq. (1)][a]

Entry	Ar	Yield [%][b]	*ee* [%][c]
1	*p*-Me-C_6H_4–	90	95
2	*m*-Me-C_6H_4–	83	93
3	*o*-Me-C_6H_4–	61	93
4[d]	*o*-Me-C_6H_4–	84	93
5	*p*-MeO-C_6H_4–	82	92
6	*p*-Br-C_6H_4–	89	96
7	*m*-Br-C_6H_4–	85	95
8[e]	*o*-Br-C_6H_4–	53	95
9[d]	*o*-Br-C_6H_4–	82	96
10	*p*-F-C_6H_4–	89	95
11	*p*-Cl-C_6H_4–	84	95
12	*p*-NC-C_6H_4–	97	98
13	1-naphthyl–	88	95
14	2-naphthyl–	91	95
15	(*E*)-C_6H_5-CH=CH–	81	93

[a] Unless otherwise noted, all reactions were carried out using 0.1 mmol of imine **2** in 0.1 M toluene solution at room temperature for 5 h. The molar ratio of imine **2**/enecarbamate **3d**/catalyst **1** was 1000:1200:1 (S/C = 1000:1). [b] Yield of the isolated product of **5** after hydrolysis of **4**. [c] Enantiomeric excess was determined by chiral HPLC analysis (see the Supporting Information). [d] The molar ratio of imine **2**/enecarbamate **3d**/catalyst **1** was 200:240:1 (S/C = 200:1). [e] Reaction performed for 12 h.

connection with a fused-ring system resulted in excellent yields and enantioselectivities, irrespective of the electronic nature of the substituents. Although *ortho* substitution led to a decrease in the catalytic efficiency, thus giving the product in moderate yields (Table 2, entries 3 and 8), the yields were improved in these cases by lowering the S/C ratio to 200:1 (0.5 mol%; Table 2, entries 4 and 9). An imine derived from an α,β-unsaturated aldehyde was also applicable to the present high S/C organocatalysis, thus giving the product in good yield with high enantioselectivity (Table 2, entry 15).

The utility of the high S/C process was further evaluated by performing a large-scale experiment [Eq. (2)]. The reaction proceeded smoothly without any detrimental effect even on a gram scale. It is noteworthy that only an amount of 3.5 mg of **1** was sufficient to yield 1.7 g of the β-aminoimine product **4** (Ar = Ph) with high enantiomeric excess on completion of the reaction.

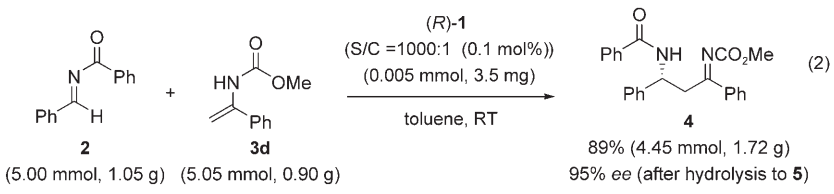

(2)

Finally, the synthetic utility of this transformation was demonstrated by derivatization of **4** to C_2-symmetric 1,3-diamine **7**, which is potentially useful as a chiral ligand of metal complexes and a building block in the synthesis of natural products and pharmaceutical compounds (Scheme 2).[10] The reduction of **4** (Ar = Ph, R = OMe)[11] by

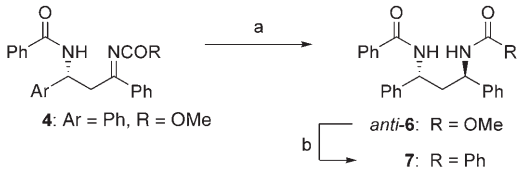

Scheme 2. Synthetic utility of β-aminoimine products **4**. Conditions: a) Red-Al, THF, −78→−60 °C, 24 h, 79% (*anti*/*syn* = 87:13); b) PhCOCl/NaI, CH_3CN, 60 °C, 12 h, 92%. Red-Al = sodium bis(2-methoxyethoxy)aluminum hydride.

Red-Al afforded *anti*-1,3-diamine **6** in predominantly good yield. A subsequent exchange reaction of the protecting groups[12] from a methoxycarbonyl to a benzoyl moiety led to C_2-symmetric (*R*,*R*)-**7** without any loss of enantiomeric excess during the course of the experiments.

In conclusion, we have successfully developed a highly efficient enantioselective aza-ene-type reaction of *N*-benzoylimines **2** with enecarbamates. The reaction can be performed at extremely low loading of the chiral Brønsted acid catalyst **1** without notable loss in enantioselectivity. The present method provides a practical route to synthetically useful β-aminoimine derivatives which can be readily transformed to 1,3-diamine derivatives of synthetic and biological importance. Further investigation of the reaction mechanisms and potential of the high S/C organocatalysis is in progress with the aim of developing practical organic transformations.

Experimental Section

A typical procedure for the enantioselective aza-ene-type reaction catalyzed by chiral Brønsted acid (*R*)-**1** (S/C = 1000:1): A dried test tube was charged with *N*-benzoylaldimine (**2**; Ar = Ph; 20.9 mg, 0.10 mmol) and the atmosphere replaced with nitrogen. After **2** (Ar = Ph) was dissolved in toluene (0.9 mL), a solution of chiral phosphoric acid (*R*)-**1** (0.1 mL, 0.0001 mmol) in toluene (0.001 M) and then enecarbamate **3d** (21.3 mg, 0.12 mmol) was added at room temperature.The reaction mixture was stirred for over 5 h at ambient temperature. The reaction was quenched by addition of saturated aqueous $NaHCO_3$, and the resulting solution was extracted with dichloromethane and dried over anhydrous Na_2SO_4. After the solvent was evaporated, the residue was dissolved in methanol (2.0 mL) and an aqueous solution of HBr (48%, 0.6 mL) was added. The reaction mixture was stirred at room temperature for 5 min, and then the reaction was quenched by addition of saturated aqueous $NaHCO_3$ at 0 °C. The resulting mixture was warmed up to room temperature and extracted with dichloromethane. The combined organic layers were dried over anhydrous Na_2SO_4. After the solvents were evaporated, the crude material was purified by chromatography (hexane/EtOAc, 8:1→1:1)

 © 2006 Wiley-VCH Verlag GmbH & Co. KGaA, Weinheim

to give β-aminoketone **5** (Ar = Ph) in 82% yield (95% *ee*) as a white solid.

Received: October 1, 2005
Published online: March 3, 2006

Keywords: asymmetric synthesis · Brønsted acids · ene reaction · organocatalysis · phosphoric acid

[1] a) P. I. Dalko, L. Moisan, *Angew. Chem.* **2004**, *116*, 5248 – 5286; *Angew. Chem. Int. Ed.* **2004**, *43*, 5138 – 5175; b) "Organic Catalysis": Special issue, *Adv. Synth. Catal.* **2004**, *346*; c) "Enantioselective Organocatalysis": Special issue, *Acc. Chem. Res.* **2004**, *37*; d) A. Berkessel, H. Gröger, *Asymmetric Organocatalysis—From Biomimetic Concepts to Powerful Methods for Asymmetric Synthesis*, Wiley-VCH, Weinheim, **2005**; e) J. Seayad, B. List, *Org. Biomol. Chem.* **2005**, *3*, 719 – 724; f) Y. Hayashi, *J. Synth. Org. Chem. Jpn.* **2005**, *63*, 464 – 477.

[2] For some excellent studies describing high S/C (greater than 200:1) organocatalysis, see: a) J. T. Su, P. Vachal, E. N. Jacobsen, *Adv. Synth. Catal.* **2001**, *343*, 197 – 200; b) P. Vachal, E. N. Jacobsen, *J. Am. Chem. Soc.* **2002**, *124*, 10012 – 10014; c) S. Saaby, M. Bella, A. K. Jørgensen, *J. Am. Chem. Soc.* **2004**, *126*, 8120 – 8121; d) S. Shirakawa, K. Yamamoto, M. Kitamura, T. Ooi, K. Maruoka, *Angew. Chem.* **2005**, *117*, 631 – 634; *Angew. Chem. Int. Ed.* **2005**, *44*, 625 – 628; e) M. Kitamura, S. Shirakawa, K. Maruoka, *Angew. Chem.* **2005**, *117*, 1573 – 1575; *Angew. Chem. Int. Ed.* **2005**, *44*, 1549 – 1551.

[3] a) D. Uraguchi, M. Terada, *J. Am. Chem. Soc.* **2004**, *126*, 5356 – 5357; b) D. Uraguchi, K. Sorimachi, M. Terada, *J. Am. Chem. Soc.* **2004**, *126*, 11804 – 11805; c) D. Uraguchi, K. Sorimachi, M. Terada, *J. Am. Chem. Soc.* **2005**, *127*, 9360 – 9361; d) M. Terada, K. Sorimachi, D. Uraguchi, *Synlett* **2006**, 133 – 136.

[4] Similar binaphthol-derived monophosphoric acids were independently developed, see: a) T. Akiyama, J. Itoh, K. Yokota, K. Fuchibe, *Angew. Chem.* **2004**, *116*, 1592 – 1594; *Angew. Chem. Int. Ed.* **2004**, *43*, 1566 – 1568; b) T. Akiyama, H. Morita, J. Itoh, K. Fuchibe, *Org. Lett.* **2005**, *7*, 2583 – 2585; c) T. Akiyama, Y. Saitoh, H. Morita, K. Fuchibe, *Adv. Synth. Catal.* **2005**, *347*, 1523 – 1526; d) T. Akiyama, Y. Tamura, J. Itoh, H. Morita, K. Fuchibe, *Synlett* **2006**, 141 – 143; also see: e) M. Rueping, E. Sugiono, C. Azap, T. Theissmann, M. Bolte, *Org. Lett.* **2005**, *7*, 3781 – 3783; f) G. B. Rowland, H. Zhang, E. B. Rowland, S. Chennamadhavuni, Y. Wang, J. C. Antilla, *J. Am. Chem. Soc.* **2005**, *127*, 15696 – 15697; g) S. Hoffmann, A. M. Seayad, B. List, *Angew. Chem.* **2005**, *117*, 7590 – 7593; *Angew. Chem. Int. Ed.* **2005**, *44*, 7424 – 7427; h) R. I. Storer, D. E. Carrera, Y. Ni, D. W. MacMillan, *J. Am. Chem. Soc.* **2006**, *128*, 84 – 86.

[5] For reviews, see: a) P. R. Schreiner, *Chem. Soc. Rev.* **2003**, *32*, 289 – 296; b) P. M. Pihko, *Angew. Chem.* **2004**, *116*, 2110 – 2113; *Angew. Chem. Int. Ed.* **2004**, *43*, 2062 – 2064.

[6] For recent selected examples of asymmetric Brønsted acid catalysis, see: a) Y. Huang, A. K. Unni, A. N. Thadani, V. H. Rawal, *Nature* **2003**, *424*, 146; b) G. D. Joly, E. N. Jacobsen, *J. Am. Chem. Soc.* **2004**, *126*, 4102 – 4103; c) A. N. Thadani, A. R. Stankovic, V. H. Rawal, *Proc. Natl. Acad. Sci. USA* **2004**, *101*, 5846 – 5850; d) H. Du, D. Zhao, K. Ding, *Chem. Eur. J.* **2004**, *10*, 5964 – 5970; e) M. S. Taylor, E. N. Jacobsen, *J. Am. Chem. Soc.* **2004**, *126*, 10558 – 10559; f) N. Momiyama, H. Yamamoto, *J. Am. Chem. Soc.* **2005**, *127*, 1080 – 1081; g) A. K. Unni, N. Takenaka, H. Yamamoto, V. H. Rawal, *J. Am. Chem. Soc.* **2005**, *127*, 1336 – 1337; h) W. Zhuang, R. G. Hazell, K. A. Jørgensen, *Org. Biomol. Chem.* **2005**, *3*, 2566 – 2571; i) W. Zhuang, T. B. Poulsen, K. A. Jørgensen, *Org. Biomol. Chem.* **2005**, *3*, 3284 – 3289; j) T. Tonoi, K. Mikami, *Tetrahedron Lett.* **2005**, *46*, 6355 – 6358; k) R. P. Herrera, V. Sgarzani, L. Bernardi, A. Ricci, *Angew. Chem.* **2005**, *117*, 6734 – 6737; *Angew. Chem. Int. Ed.* **2005**, *44*, 6576 – 6579; l) M. S. Taylor, N. Tokunaga, E. N. Jacobsen, *Angew. Chem.* **2005**, *117*, 6858 – 6862; *Angew. Chem. Int. Ed.* **2005**, *44*, 6700 – 6704; m) V. B. Gondi, M. Gravel, V. H. Rawal, *Org. Lett.* **2005**, *7*, 5657 – 5660.

[7] a) R. Matsubara, Y. Nakamura, S. Kobayashi, *Angew. Chem.* **2004**, *116*, 1711 – 1713; *Angew. Chem. Int. Ed.* **2004**, *43*, 1679 – 1681; b) R. Matsubara, Y. Nakamura, S. Kobayashi, *Angew. Chem.* **2004**, *116*, 3320 – 3322; *Angew. Chem. Int. Ed.* **2004**, *43*, 3258 – 3260; c) R. Matsubara, P. Vital, Y. Nakamura, H. Kiyohara, S. Kobayashi, *Tetrahedron* **2004**, *60*, 9769 – 9784.

[8] The absolute configuration of **5** (Ar = Ph) was determined to be *R* (see the Supporting Information).

[9] We employed the acetone-derived enecarbamate **8** instead of the acetophenone-derived enecarbamate **3d** to expand the substrate scope. The reaction of **8** with imine **2** (Ar = Ph) worked well under the high S/C conditions (0.1 mol% of **1**), and subsequent hydrolysis gave the corresponding product **9** in good yield (80%). Unfortunately, however, the enantiomeric excess was moderate (44% *ee*); further screening of the catalyst, reactants, and reaction conditions is required to improve the enantiomeric excess (see Supporting Information).

[10] For example, see: a) A. Kaiser, P. Bielmeier, W. Wiegrebe, *Monatsh. Chem.* **1997**, *128*, 1247 – 1254; b) G. H. P. Roos, A. R Donovan, *Tetrahedron: Asymmetry* **1999**, *10*, 991 – 1000; c) S. E. Denmark, J.-H. Kim, *Can. J. Chem.* **2000**, *78*, 673 – 688; see also Ref. [7a] and references therein.

[11] A single geometric isomer of **4** was obtained, but the configuration has not yet been determined.

[12] M. Ihara, A. Hirabayashi, N. Taniguchi, K. Fukumoto, *Heterocycles* **1992**, *33*, 851 – 858.

 © 2006 Wiley-VCH Verlag GmbH & Co. KGaA, Weinheim

High-Spin Systems

DOI: 10.1002/anie.200502695

Ab Initio MO Analysis of the Excited Electronic States of High-Spin Quintet 2-Methylphenylene-1,3-dinitrene**

Kenji Sugisaki, Kazuo Toyota, Kazunobu Sato, Daisuke Shiomi, and Takeji Takui**

Organic-molecule-based magnetism is the focus of current interest in chemistry and materials science.[1] Molecular entities as models for organic magnetism date back to pilot

[*] K. Sugisaki, K. Toyota, K. Sato, D. Shiomi, Prof. T. Takui
Departments of Chemistry and Materials Science
Graduate School of Science, Osaka City University
3-3-138, Sugimoto, Sumiyoshi-ku, Osaka 558-8585 (Japan)
Fax: (+81) 6-6605-3137
E-mail: toyota@sci.osaka-cu.ac.jp
takui@sci.osaka-cu.ac.jp

[**] This work has been supported by Grants-in-Aid for Scientific Research from the Ministry of Education, Sports, Culture, Science and Technology, Japan.

Supporting information for this article is available on the WWW under http://www.angewandte.org or from the author.

© 2006 Wiley-VCH Verlag GmbH & Co. KGaA, Weinheim

molecules such as quintet *m*-phenylenebis(phenylmethylene)[2] and quintet phenylene-1,3-dinitrene.[2] Topologically controlled robust spin polarization to realize molecular spins states higher than quartets in the molecular frame links chemistry to magnetism.[3] Since then, great attention has been paid to the electronic structures of high-spin nitrenes as heteroatomic molecules, both experimentally[4,5] and theoretically.[2c,d,6]

Quantitative ab initio MO calculations on the electronic states of such high-spin systems have been challenging due to the intrinsic complexity of such systems (e.g., quasidegeneracy and spin contamination). Most of the theoretical studies have been confined to the energy gaps between spin states.[2d,6–8] Excited electronic states of high-spin nitrenes and carbenes have been documented for only a few systems, and all of the theoretical studies deal with triplet-state mononitrenes[9,10] or monocarbenes.[11] Disclosing the nature of the excited electronic states of high-spin molecular entities seems an important issue from the viewpoint of materials science. For example, photoinduced spin alignment through π conjugation by mediating the excited triplet states of anthracene and pyrene was recently reported.[12]

Herein, we applied multiconfiguration quasidegenerate second-order perturbation theory (MCQDPT2)[13] in its single-state form, which is equivalent to the MRMP2 model of Hirao,[14] to the excited electronic states of a typical quintet ground-state dinitrene, namely, 2-methylphenylene-1,3-dinitrene (**1**), in an attempt to assign its UV/Vis spectrum and to analyze the relationship between oligo spin sites and electronic states for the first time.

The UV/Vis absorption spectrum of **1** was measured by Chapyshev and Tomioka,[5a] who reported that **1** has weak and moderately strong absorption bands around 400 and 300 nm, respectively. They also reported a broad peak at about 712 nm, but this peak is not assignable to the quintet states of **1**, as discussed below. To our knowledge, assignments of electronic transition spectra of quintet molecular systems by ab initio calculation have not been documented to date. For triplet analogues, Platz et al. calculated the electronic states of phenylnitrene (**2**) by the CASPT2 method,[9] and its UV/Vis absorption spectrum was successfully assigned to the electronic states described as linear combinations of π→SOMO and SOMO→π* excitations (denoted LC states). Similar assignments have also been reported for triplet phenylcarbene.[11]

The equilibrium geometry of **1** was optimized at the UB3LYP/6-311G** level of theory. In the CASSCF computation, we assigned 16 electrons and 12 orbitals to the active space (Figure 1). Chipman's DZP plus diffuse basis set[15] was adopted for the calculation of the electronic states. The Gaussian 03 program package[16] was used for DFT calculations, and GAMESS[17] for CASSCF and MCQDPT2 calculations. Absolute energies for the electronic states and the optimized geometry of **1** are provided as Supporting Information.

Quintet **1** has C_s symmetry with the mirror plane including the π-conjugated atoms, and the electronic ground state is the 1A′ state. The experimental and theoretical UV/Vis absorption spectra of **1** are illustrated in Figure 2, and the

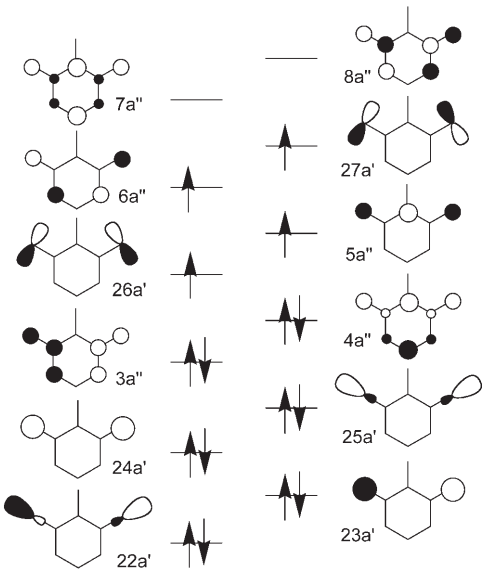

Figure 1. Active space for the CASSCF computation.

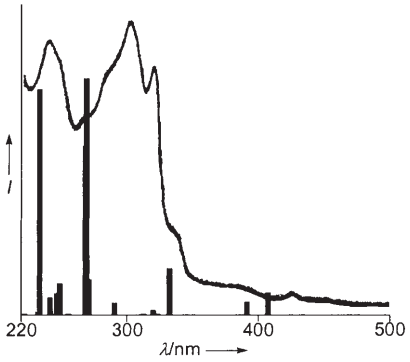

Figure 2. Experimental (line) and theoretical (bars) UV/Vis absorption spectra of **1**.

corresponding electronic states are listed in Table 1. Calculations of the oscillator strength for electronic transitions are based on the CASSCF wavefunctions. The LC states are responsible for most of the observed bands, and the excitations from the lone pairs of the nitrene nitrogen atoms to the SOMO have relatively large oscillator strengths, as shown for **2**.[9] It is impossible to assign a broad band observed around 712 nm to quintet **1** because there are no electronic states in the longer wavelength region ($\lambda > 450$ nm) of the calculated spectrum.

Our interest lies in the relationship between oligo spin sites and electronic states. This has been a long-standing issue in theoretical chemistry. Our discussion focuses on the LC states, which contribute mainly to the UV/Vis absorption spectrum, with emphasis on the orbital correlation approach (OCA) to explain the order of orbital energy levels. We consider the orbital correlation between the benzene skeleton and symmetry-adapted linear combination (SALC) MOs of the nitrene moieties. The energy levels of excited states of **1** can be understood in terms of orbital energies if we can approximate energies of configuration state functions (CSFs) by the orbital energy difference and ignore the difference in

 © 2006 Wiley-VCH Verlag GmbH & Co. KGaA, Weinheim

Table 1: Electronic states of **1**.

State	Nature	ΔE [eV]	λ [nm]	f [a]
$^5A'$	0.92 (ground-state configuration)			
$^5A'$	0.69 (4a″→6a″)−0.51 (6a″→7a″)	3.030	409.2	0.00855
$^5A'$	0.65 (4a″→5a″)−0.50 (5a″→7a″)	3.156	392.9	0.00476
$^5A'$	0.90 (22a′→26a′)	3.723	333.0	0.01813
$^5A'$	0.43 (3a″→6a″)−0.34 (6a″→8a″)	3.869	320.5	0.00154
$^5A'$	0.48 (4a″→5a″)+0.26 (5a″→7a″)	3.881	319.5	0.00024
$^5A'$	0.78 (25a′→27a′)	4.266	290.6	0.00446
$^5A'$	0.25 (4a″→6a″)+0.47 (6a″→7a″)	4.612	268.8	0.09294
$^5A'$	0.42 (5a″→8a″)	4.623	268.2	0.06605
$^5A'$	0.54 (3a″→26a′, 27a′→7a″)	5.042	245.9	0.00821
$^5A'$	0.47 (3a″→6a″)+0.57 (6a″→8a″)	5.326	232.8	0.08870
$^5A'$	0.59 (4a″→7a″)	5.357	231.4	0.00088
$^5A'$	0.39 (4a″→26a′, 27a′→8a″)	6.035	205.4	0.00066
$^5A'$	0.31 (3a″→5a″)+0.59 (5a″→8a″)	6.137	202.0	0.93072
$^5A''$	0.82 (4a″→26a′)	3.828	323.9	0.00002
$^5A''$	0.63 (4a″→26a′)	3.962	312.9	0.00000
$^5A''$	0.93 (22a′→6a″)	4.574	271.1	0.01380
$^5A''$	0.63 (3a″→26a′)	4.866	254.8	0.00002
$^5A''$	0.75 (25a′→5a″)	4.992	248.4	0.01216
$^5A''$	0.48 (27a′→7a″)−0.36 (3a″→27a′)	5.135	241.5	0.00018
$^5A''$	0.55 (27a′→7a″)+0.51 (25a′→5a″)	5.148	240.8	0.00651
$^5A''$	0.52 (27a′→7a″)−0.35 (3a″→27a′)	5.606	221.2	0.00002

[a] Oscillator strength.

strength of the configuration interaction and correlation effects considered by MCQDPT2.

We idealized the system as unsubstituted phenylene-1,3-dinitrene with C_{2v} symmetry. The p orbitals of the two nitrogen atoms can form a_2 and b_1 SALC MOs, which correlate to π orbitals with the same symmetry of the benzene skeleton, and this gives rise to splitting as depicted in Figure 3. The energy gaps among the b_1 orbitals (corresponding to 4a″ and 7a″) are smaller than those among the a_2 orbitals (3a″ and 8a″) because of the smaller coefficient of the p orbitals on the carbon atoms in the 1,3-positions, and therefore the (4a″→SOMO)±(SOMO→7a″) states are expected to have lower excitation energy than the (3a″→SOMO)±(SOMO→8a″)

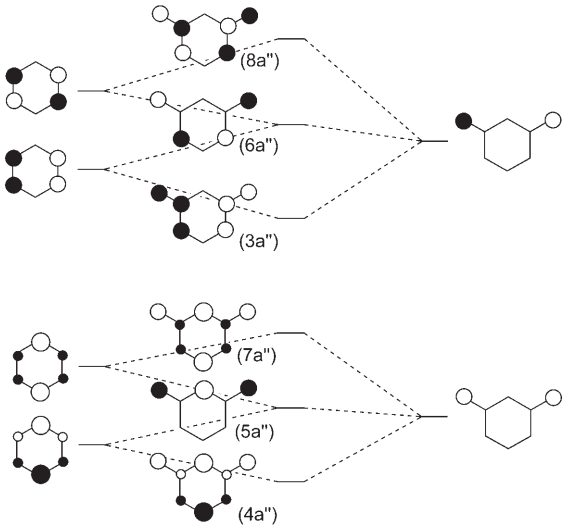

Figure 3. Orbital correlation scheme of species with a_2 (top) and b_1 symmetry (bottom).

states. The present analysis by OCA leads to the same conclusion as computationally demanding ab initio calculations with regard to the order of the orbitals and excited states of **1**.

The possibility to discuss substituent effects on the excited states of nitrenes and carbenes with a benzene scaffold in terms of OCA would be useful. Note that the OCA analysis is not applicable directly to an electronic structure that is modified drastically from a reference system. Zhang, Li, and Jiang reported that push–pull-type *m*-phenylene biradicals have nontypical nondisjoint SOMOs.[7] Winter, Falvey, and Cramer reported that strongly electron-donating substituents at the *m* positions result in a (π,π*)-type triplet ground state in phenylnitrenium ions.[8] Our preliminary calculations have shown that OCA predicts correct trends of the band shifts for derivatives of phenylnitrene (**2**) with electronically weak substituents, but the OCA-based model is broken when a robust substituent such as a nitro group is introduced, as will be reported in a forthcoming publication.

Received: August 1, 2005
Revised: December 25, 2005
Published online: March 6, 2006

Keywords: ab initio calculations · electronic structure · excited states · high-spin systems · nitrenes

[1] a) K. Itoh, M. Kinoshita, *Molecular Magnetism: New Magnetic Materials*, Gordon and Breach, Amsterdam, **2000**; b) P. M. Lahti, *Magnetic Properties of Organic Materials*, Marcel Dekker, New York, **1999**; c) K. Itoh, T. Takui, *Proc. Jpn. Acad. Ser. B* **2004**, *80*, 29–40.
[2] a) K. Itoh, *Chem. Phys. Lett.* **1967**, *1*, 235–238; b) E. Wasserman, R. W. Murray, W. A. Yager, A. M. Trozzolo, G. J. Smolinsky, *J. Am. Chem. Soc.* **1967**, *89*, 5076–5079; c) J. F. Orsen, *Spectrosc. Lett.* **1969**, *2*, 217–223; d) A. S. Ichimura, P. M. Lahti, *Mol. Cryst. Liq. Cryst. Sci. Technol. Sect. A* **1993**, *232*, 393–400.
[3] K. Itoh, *Pure Appl. Chem.* **1978**, *50*, 1251–1259.
[4] a) S. V. Chapyshev, R. Walton, J. A. Sanborn, P. M. Lahti, *J. Am. Chem. Soc.* **2000**, *122*, 1580–1588; b) R. S. Kalgutkar, P. M. Lahti, *Tetrahedron Lett.* **2003**, *44*, 2625–2628; c) S. V. Chapyshev, R. Walton, P. R. Serwinski, P. M. Lahti, *J. Phys. Chem. A* **2004**, *108*, 6643–6649.
[5] a) S. V. Chapyshev, H. Tomioka, *Bull. Chem. Soc. Jpn.* **2003**, *76*, 2075–2089; b) S. V. Chapyshev, *Mendeleev Commun.* **2002**, *12*, 168–170; c) T. Sato, A. Narazaki, Y. Kawaguchi, H. Niino, G. Bucher, D. Grote, J. J. Wolff, H. H. Wenk, W. Sander, *J. Am. Chem. Soc.* **2004**, *126*, 7846–7852.
[6] a) A. Nicolaides, T. Nakayama, K. Yamazaki, H. Tomioka, S. Koseki, L. L. Stracener, R. J. McMahon, *J. Am. Chem. Soc.* **1999**, *121*, 10563–10572; b) A. Nicolaides, T. Enyo, D. Miura, H. Tomioka, *J. Am. Chem. Soc.* **2001**, *123*, 2628–2636; c) T. Enyo, A. Nicolaides, H. Tomioka, *J. Org. Chem.* **2002**, *67*, 5578–5587.
[7] G. Zhang, S. Li, Y. Jiang, *J. Phys. Chem. A* **2003**, *107*, 5573–5582.
[8] A. H. Winter, D. E. Falvey, C. J. Cramer, *J. Am. Chem. Soc.* **2004**, *126*, 9661–9668.
[9] N. P. Gritsan, Z. Zhu, C. M. Hadad, M. S. Platz, *J. Am. Chem. Soc.* **1999**, *121*, 1202–1207.
[10] A. Maltsev, T. Bally, M.-L. Tsao, M. S. Platz, A. Kuhn, M. Vosswinkel, C. Wentrup, *J. Am. Chem. Soc.* **2004**, *126*, 237–249.
[11] S. Matzinger, T. Bally, *J. Phys. Chem. A* **2000**, *104*, 3544–3552.

 © 2006 Wiley-VCH Verlag GmbH & Co. KGaA, Weinheim

[12] a) Y. Teki, S. Miyamoto, M. Nakatsuji, Y. Miura, *J. Am. Chem. Soc.* **2001**, *123*, 294 – 305; b) Y. Teki, M. Kimura, S. Narimatsu, K. Ohara, K. Mukai, *Bull. Chem. Soc. Jpn.* **2004**, *77*, 95 – 99.
[13] H. Nakano, *J. Chem. Phys.* **1993**, *99*, 7983 – 7992.
[14] a) K. Hirao, *Chem. Phys. Lett.* **1992**, *190*, 374 – 380; b) K. Hirao, *Chem. Phys. Lett.* **1992**, *196*, 397 – 403; c) K. Hirao, *Chem. Phys. Lett.* **1993**, *201*, 59 – 66.
[15] D. M. Chipman, *Theor. Chim. Acta* **1989**, *76*, 73 – 84.
[16] Gaussian 03 (Revision B.01), M. J. Frisch, G. W. Trucks, H. B. Schlegel, G. E. Scuseria, M. A. Robb, J. R. Cheeseman, J. A. Montgomery, Jr., T. Vreven, K. N. Kudin, J. C. Burant, J. M. Millam, S. S. Iyengar, J. Tomasi, V. Barone, B. Mennucci, M. Cossi, G. Scalmani, N. Rega, G. A. Petersson, H. Nakatsuji, M. Hada, M. Ehara, K. Toyota, R. Fukuda, J. Hasegawa, M. Ishida, T. Nakajima, Y. Honda, O. Kitao, H. Nakai, M. Klene, X. Li, J. E. Knox, H. P. Hratchian, J. B. Cross, V. Bakken, C. Adamo, J. Jaramillo, R. Gomperts, R. E. Stratmann, O. Yazyev, A. J. Austin, R. Cammi, C. Pomelli, J. W. Ochterski, P. Y. Ayala, K. Morokuma, G. A. Voth, P. Salvador, J. J. Dannenberg, V. G. Zakrzewski, S. Dapprich, A. D. Daniels, M. C. Strain, O. Farkas, D. K. Malick, A. D. Rabuck, K. Raghavachari, J. B. Foresman, J. V. Ortiz, Q. Cui, A. G. Baboul, S. Clifford, J. Cioslowski, B. B. Stefanov, G. Liu, A. Liashenko, P. Piskorz, I. Komaromi, R. L. Martin, D. J. Fox, T. Keith, M. A. Al-Laham, C. Y. Peng, A. Nanayakkara, M. Challacombe, P. M. W. Gill, B. Johnson, W. Chen, M. W. Wong, C. Gonzalez, J. A. Pople, Gaussian, Inc., Wallingford, CT, **2004**.
[17] M. W. Schmidt, K. K. Baldridge, J. A. Boatz, S. T. Elbert, M. S. Gordon, J. H. Jensen, S. Koseki, N. Matsunaga, K. A. Nguyen, S. J. Su, T. L. Windus, M. Dupuis, J. A. Montgomery, *J. Comput. Chem.* **1993**, *14*, 1347 – 1363.

 © 2006 Wiley-VCH Verlag GmbH & Co. KGaA, Weinheim

Asymmetric Hydrogenation

DOI: 10.1002/anie.200503073

Asymmetric Hydrogenation of Quinolines and Isoquinolines Activated by Chloroformates**

*Sheng-Mei Lu, You-Qing Wang, Xiu-Wen Han, and Yong-Gui Zhou**

Despite significant progress in the area of asymmetric hydrogenation,[1] the enantioselective hydrogenation of aromatic and heteroaromatic compounds still remains a major challenge. Only a few examples with moderate enantioselectivity, which rely on unique catalyst systems and suffer from a limited scope of suitable substrates, have been described so far.[2] There are several reasons that might explain this situation. First, heteroaromatic compounds have a resonance stability that might impede enantioselective reduction with hydrogen.[3] Second, heteroaromatic compounds containing nitrogen and sulfur atoms may poison the catalyst. Third, little attention has been directed to these challenging substrates relative to alkenes, ketones, and imines. The low activity of aromatic compounds may be the main reason. In spite of these difficulties, the search for an effective asymmetric hydrogenation of heteroaromatic compounds continues because of the usefulness and importance of a method for the preparation of optically active heteroaromatic compounds.

Recently, we developed the first asymmetric hydrogenation of quinolines using [{IrCl(cod)}$_2$]/MeO-biphep/I$_2$ (cod = 1,5-cyclooctadiene; MeO-biphep = (2,2′-dimethoxybiphenyl-6,6′-diyl)bis(diphenylphosphine) as the catalyst system.[2f,g] It was found that the substrate scope was limited to quinoline derivatives and that the hydrogenation reaction cannot proceed for isoquinolines under standard conditions. As tetrahydroquinolines and tetrahydroisoquinolines are important structural units in naturally occurring alkaloids and biologically active compounds,[4] we are interested in exploring a general strategy for the asymmetric hydrogenation of aromatic compounds containing nitrogen. By analysis of the possible mechanism of the reported hydrogenation of aromatic compounds, we envisioned that the key factor for such reactions is to find a way to activate the substrate, and we selected chloroformates as the activating reagent[5] for the following reasons: 1) the aromaticity should be partially destroyed by the formation of quinolinium and isoquinolinium salts; 2) bonding of the activating reagent to the N atom may avoid poisoning of the catalyst; and 3) the attached CO_2R group is probably important for coordination between substrate and catalyst, and thus is beneficial to the control of enantioselectivity. Herein, we present our preliminary results on the asymmetric hydrogenation of quinolines and isoquinolines by this strategy (Scheme 1).

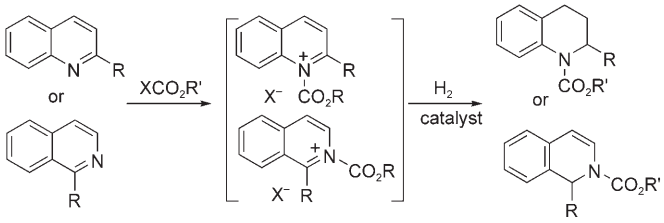

Scheme 1. Hydrogenation of quinolines and isoquinolines.

In our previous research work, iodine was necessary for full conversion and high enantioselectivity. Without iodine, the reaction only proceeded with very low conversion (< 5%).[2f] Herein, we tried to hydrogenate 2-methylquinoline (**1a**) in the absence of iodine using [{IrCl(cod)}$_2$]/*rac*-MeO-biphep as the catalyst and benzyl chloroformate as the activating reagent. When the reaction was performed in toluene under hydrogen (600 psi) at room temperature, only

[*] Dr. S.-M. Lu, Dr. Y.-Q. Wang, Prof. X.-W. Han, Prof. Y.-G. Zhou
State Key Laboratory of Catalysis
Dalian Institute of Chemical Physics
Chinese Academy of Sciences
457 Zhongshan Road, Dalian 116023 (P.R. China)
Fax: (+86) 411-8437-9220
E-mail: ygzhou@dicp.ac.cn

[**] We are grateful for the financial support from the National Science Foundation of China and Dalian Institute of Chemical Physics (K2004E03), Chinese Academy of Sciences.

Supporting information for this article is available on the WWW under http://www.angewandte.org or from the author.

InterScience © 2006 Wiley-VCH Verlag GmbH & Co. KGaA, Weinheim

moderate conversion (55%) into 2-methyl-3,4-dihydro-2*H*-quinolin-1-carboxylic acid benzyl ester (**2a**) was obtained. Analysis of the mechanism and the experimental result indicated that the hydrogen chloride produced might block the reaction by the formation of the hydrogen chloride salt of quinoline. Therefore, the addition of base to neutralize hydrogen chloride is necessary for full conversion. A survey of bases and solvents revealed that organic bases, such as Et_3N and iPr_2NEt, are ineffective because of their strong coordinative ability. When using Li_2CO_3 as a base, the reaction in THF could proceed completely to give the desired product **2a**.

The effects of various activating reagents on enantioselectivity and conversion were examined with (*R*)-MeO-biphep (1 mol%) as the chiral ligand. As shown in Table 1

Table 1: Optimization of the reaction conditions for hydrogenation of 2-methylquinoline **1a**.[a]

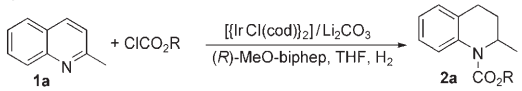

Entry	Activator	*T* [°C]	H_2 [psi]	Conversion [%][b]	*ee* [%][c] (configuration)
1	$ClCO_2Bn$	25	600	>95	82 (*R*)
2	$ClCO_2Me$	25	600	>95	83 (*R*)
3	$ClCO_2Et$	25	600	>95	83 (*R*)
4	$ClCO_2Ph$	25	600	>95	82 (*R*)
5	ClCOPh	25	600	<5	–
6	$BrCOCH_3$	25	600	<5	–
7	Ac_2O	25	600	<5	–
8[d]	$ClCO_2Bn$	25	600	17	−44 (*S*)
9	$ClCO_2Bn$	25	900	>95	82 (*R*)
10	$ClCO_2Bn$	25	300	69	82 (*R*)
11	$ClCO_2Bn$	3	600	47	83 (*R*)
12	$ClCO_2Bn$	50	600	>95	81 (*R*)

[a] See the Experimental Section for details. [b] Determined by ^1H NMR spectroscopic analysis. [c] Determined by HPLC with an AS-H column. [d] 4-Å molecular sieves (60 mg) were added.

(entries 1–4), the hydrogenation of **1a** activated by other chloroformates (R = Me, Et, Ph) proceeds smoothly to afford the corresponding products in high conversion with similar enantioselectivity. Other reagents, such as ClCOPh, $BrCOCH_3$, and Ac_2O, were ineffective (Table 1, entries 5–7). Considering the easy deprotection of Cbz-protected groups (Cbz = carbobenzyloxy), we chose benzyl chloroformate as the activating reagent throughout the following reactions. The effect of the water produced in the reaction was also investigated. Unexpectedly, by adding 4-Å molecular sieves, the conversion decreased greatly and the configuration of the product was reversed (Table 1, entry 8), which demonstrates that water might be important for the conversion and enantioselectivity. The reason is unclear and awaits further study. A change in hydrogenation pressure and reaction temperature had no clear effect on enantioselectivity, but conversion was decreased under lower pressure and temperature (Table 1, entries 9–12).

To further improve the reaction, the amounts of Li_2CO_3 and the substrate concentration were investigated. Concentrations of Li_2CO_3 of 0.6–3.0 equivalents gave products of similar conversion and enantioselectivity. The substrate concentration had almost no effect on the conversion and enantioselectivity.

Other commercially available chiral ligands were also tested under the optimal conditions. It was shown that bisphosphine ligands with a biphenyl motif gave a higher enantioselectivity than those with binaphthyl structures: (5,5′-dichloro-6,6′-dimethoxybiphenyl-2,2′-bis(diphenylphosphino)1,1′-biphenyl (90% *ee*), (4,4′-bi-1,3-benzodioxole-5,5′-diyl)bis(diphenylphosphine) (segphos, 90% *ee*), (2,3,2′,3′-tetrahydro-5,5′-bis(1,4-benzodioxin)-6,6′-diyl)bis(diphenylphosphine) (synphos, 83% *ee*), (2,2′-(1,6-dioxahexano)biphenyl-6,6′-diyl)bis(diphenylphosphine) (C4-tunaphos, 84% *ee*), 1,1′-binaphthalene-2,2′-diylbis(diphenylphosphine) (binap, 72% *ee*), 3,5-xylyl-binap (67% *ee*); other electron-rich bisphosphine ligands gave poor results (1,2-bis(2,5-dimethylphospholano)benzene (Me-duphos): <5% conversion; 2,3-*O*-isopropylidene-2,3-dihydroxy-l,4-bis(diphenylphosphanylbutane (diop): 15% conversion, 39% *ee*); monophosphine ligand 2-diphenylphosphanyl-2′-methoxy-1,1′-binaphthalene (mop) and N,P ligands gave less than 10% conversion. Thus, the best ligand for the reaction is segphos.

A variety of substituted quinoline derivatives were hydrogenated under the optimized conditions with the Ir/(*S*)-segphos/Li_2CO_3/$ClCO_2Bn$/THF catalyst system. Several 2-alkyl-substituted quinolines were hydrogenated with high enantioselectivities regardless of the length of the chain (Table 2, entries 1–5). The reaction is not very sensitive to the substituent at the 6-position (Table 2, entries 6–8). Lower conversion and enantioselectivity were obtained with 2-phenyl-substituted quinoline (Table 2, entry 9), which is probably attributable to the steric bulkiness of the phenyl

Table 2: Hydrogenation of quinolines **1** activated by $ClCO_2Bn$.[a]

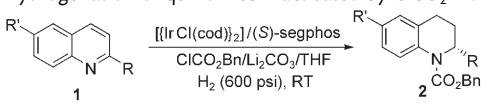

1 2

Entry	**1/2**	R′/R	Yield [%][b]	*ee* [%][c] (configuration)[d]
1	**a**	H/Me	90	90 (*S*)
2	**b**	H/Et	85	90 (*S*)
3	**c**	H/*n*Pr	80	90 (*S*)
4	**d**	H/*n*Bu	88	89 (*S*)
5	**e**	H/*n*-pentyl	91	89 (*S*)
6	**f**	Me/Me	90	89 (*S*)
7	**g**	F/Me	83	89 (*S*)
8	**h**	MeO/Me	92	90 (*S*)[e]
9	**i**	H/Ph	41	80 (*R*)
10	**j**	H/phenethyl	86	90 (*S*)
11	**k**	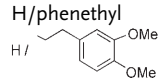	80	90 (*S*)
12	**l**	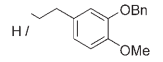	88	88 (*S*)

[a] See the Experimental Section for details. [b] Yields of the isolated products based on quinolines. [c] Determined by HPLC analysis with chiral column. [d] Determined by the described procedure; other products determined by analogy with **2a** or comparison with reported data. [e] Reaction at 50°C.

 © 2006 Wiley-VCH Verlag GmbH & Co. KGaA, Weinheim

group. 2-Arenethyl-substituted quinolines also gave good asymmetric induction (Table 2, entries 10–12).

The absolute configuration of the quinoline hydrogenation product was determined by the following chemical transformation. Compound (+)-**2a** was converted iinto the known (−)-**3a**[2f] with H_2/Pd/C in THF [Eq. (1)]. On the basis of the sign of optical rotation and absolute configuration (*S*) of (−)-**3a**, (+)-**2a** was assigned as *S*. The configurations of the other compounds are assumed by analogy with **2a**.

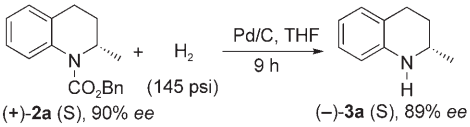

(1)

Gratifyingly, we found that the reaction worked well when the substrate was extended from quinolines to isoquinolines. In the case of 1-methylisoquinoline (**4a**), only the partially hydrogenated product dihydroisoquinoline (**5a′**) was obtained in 87% yield with 76% *ee* under the above conditions [Eq. (2)]. The reaction did not occur without benzyl chloroformate.

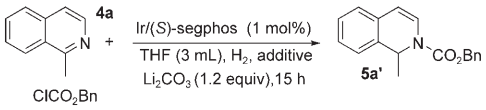

(2)

To improve the enantioselectivity, the effects of solvent, base, activating reagent, and chiral ligand were investigated. The results indicated that THF/Li_2CO_3/$ClCO_2Bn$/segphos is the best combination in our screened conditions. An equivalent amount of LiCl was produced during this reaction, and hence the effect of lithium salts with different counterions on the enantioselectivity was investigated.[6] Lithium salts influenced the reaction: when 1.0 equivalent of $LiSO_3CF_3$ or $LiBF_4$ was used, the *ee* increased from 76 to 83% (see the Supporting Information).

The results for the reaction of some isoquinolines under optimal conditions are summarized in Table 3. 1-Alkyl-substituted isoquinolines were hydrogenated with moderate to good enantioselectivities regardless of the length of the chain (Table 3, entries 1–4, 8, and 9). For 1-phenylisoquinoline, 82% *ee* (**5e**, $ClCO_2Me$ as the activating reagent) and 83% *ee* (**5e′**, $ClCO_2Bn$ as the activating reagent) can be obtained, but the conversions are moderate, which might be a result of the steric effect of the bulky phenyl group. A low enantioselectivity of 10% *ee* was obtained for 1-benzylisoquinoline (Table 3, entry 5); the reason is not yet clear. Notably, to the best of our knowledge, this is the first example of the asymmetric hydrogenation of isoquinoline derivatives.

The application of the present method to the enantioselective synthesis of several biologically active compounds proved its utility. For example, the reduction of **2c**, **2e**, and **2k** with $LiAlH_4$ in Et_2O gives the N-methylation[7] products in high yield (Scheme 2), which are the naturally occurring tetrahydroquinoline alkaloids **3c**,[8] angustureine (**3e**),[4c,8] and cuspareine (**3k**),[4e,8] respectively. Similarly, the naturally occurring tetrahydroisoquinoline alkaloids **7a**[4d,9] and carnegine (**7f**)[10] were also synthesized in three steps starting from isoquinolines.

Table 3: Asymmetric hydrogenation of activated isoquinolines **4**.[a]

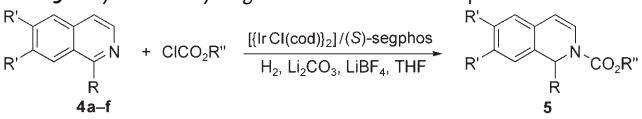

Entry	R′/R	R″	Product	Yield [%][b]	*ee* [%][c] (configuration)[d]
1	H/Me	Me	**5a**	85	80 (*S*)
2	H/Me	Bn	**5a′**	87	83 (*S*)
3	H/Et	Me	**5b**	85	62 (*S*)[e]
4	H/*n*Bu	Me	**5c**	87	60 (*S*)[e]
5	H/Bn	Me	**5d**	83	10 (*S*)[e]
6	H/Ph	Me	**5e**	57	82 (*S*)
7	H/Ph	Bn	**5e′**	49	83 (*S*)
8	MeO/Me	Me	**5f**	57	63 (*S*)
9	MeO/Me	Bn	**5f′**	46	65 (*S*)[f]

[a] See the Experimental Section for details. [b] Yields of the isolated products based on isoquinolines. [c] Determined by HPLC analysis with a chiral column. [d] Determined by comparison of rotation sign with reported data or by analogy. [e] Determined by conversion into tetrahydroisoquinoline; see the Supporting Information for details. [f] Without $LiBF_4$.

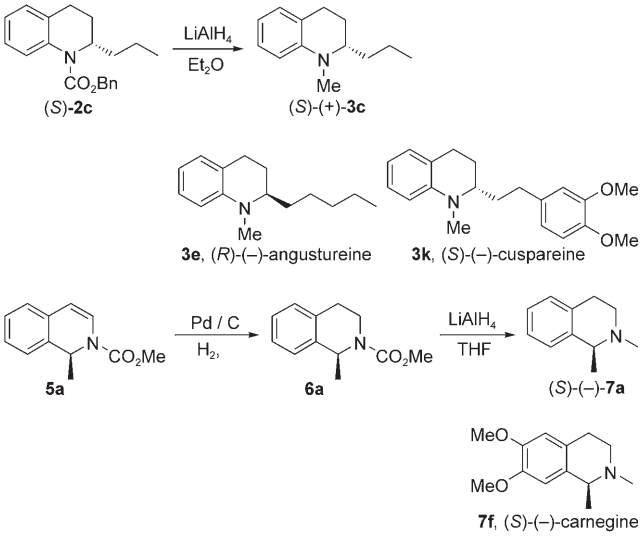

Scheme 2. Application of the enantioselective hydrogenation of quinolines and isoquinolines in the synthesis of naturally occuring alkaloids.

In conclusion, a new strategy for the asymmetric hydrogenation of quinolines and isoquinolines has been developed by using chloroformates as activating agents, thus providing a new avenue for the hydrogenation of heteroaromatic compounds. This method has been successfully applied to the asymmetric synthesis of several naturally occurring alkaloids. Further work will be directed toward the development of the hydrogenation of other heteroaromatic compounds.

 © 2006 Wiley-VCH Verlag GmbH & Co. KGaA, Weinheim

Experimental Section

In a glove box, THF (3 mL) was added to a mixture of [{IrCl(cod)}$_2$] (3.4 mg, 0.005 mmol) and (*S*)-segphos (6.8 mg, 0.011 mmol). Similarly, THF (2 mL) was added to a mixture of Li_2CO_3 (79 mg, 1.2 mmol) and substrate **1a** (1.0 mmol). Both mixtures were stirred at room temperature for 10 min, then benzyl chloroformate (1.1 mmol) was added to the solution of Li_2CO_3 and substrate. Next, the in situ prepared catalyst solution was added with a syringe. The hydrogenation was performed at room temperature under H_2 (600 psi) for 12–15 h. After carefully releasing the hydrogen, the reaction mixture was diluted with diethyl ether (20 mL), and saturated sodium carbonate aqueous solution (10 mL) was added. After stirring for 15 min, the aqueous layer was extracted with diethyl ether (3 × 15 mL), dried over sodium sulfate, and concentrated to afford the crude product **2a**. Clean up was performed on a column of silica gel eluted with hexane/EtOAc (10:1) to give the pure product. The enantiomeric excesses were determined by chiral HPLC with AS-H columns. Yield 90%, 90% *ee*, $[\alpha]_D^8 = +105.2$ ($c = 0.98$, $CHCl_3$). ^{1}H NMR (400 MHz, $CDCl_3$): $\delta = 1.18$ (d, $J = 6.4$ Hz, 3H), 1.52 (m, 1H), 2.22 (m, 1H), 2.66 (m, 2H), 4.65 (m, 1H), 5.16, 5.29 (AB system, $J = 12.6$ Hz, 2H), 7.02–7.15 (m, 3H), 7.31–7.37 (m, 5H), 7.56 ppm (d, $J = 8.0$ Hz, 1H); ^{13}C NMR (100 MHz, $CDCl_3$): $\delta = 20.2$, 25.8, 31.7, 50.3, 68.0, 125.0, 126.1, 126.7, 128.4, 128.5, 128.6, 129.2, 132.5, 137.2, 155.3 ppm; HRMS for $C_{18}H_{20}NO_2$ [*M*+1]: *m*/*z* calcd 282.1489, found 282.1476; HPLC (AS-H, eluent: hexane/*i*PrOH 95:5, detector: 254 nm, flow rate: 0.5 mL min^{-1}): (*S*) $t_1 = 5.5$ min, (*R*) $t_2 = 6.2$ min.

Received: August 29, 2005
Revised: November 21, 2005
Published online: March 3, 2006

Keywords: asymmetric synthesis · chloroformates · enantioselectivity · hydrogenation · quinolines

[1] For reviews, see: a) *Catalytic Asymmetric Synthesis* (Ed.: I. Ojima), Wiley-VCH, Weinheim, **1999**; b) *Asymmetric Catalysis in Organic Synthesis* (Ed.: R. Noyori), Wiley, New York, **1994**; c) *Comprehensive Asymmetric Catalysis*, *Vol. 1* (Eds.: E. N. Jacobsen, A. Pfaltz, H. Yamamoto), Springer, Berlin, **1999**.

[2] For some examples of asymmetric hydrogenation of heteroaromatic compounds, see: a) R. Kuwano, K. Sato, T. Kurokawa, D. Karube, Y. Ito, *J. Am. Chem. Soc.* **2000**, *122*, 7614–7615; b) C. Bianchini, P. Barbaro, G. Scapacci, *J. Organomet. Chem.* **2001**, *621*, 26–33; c) M. Studer, C. Wedemeyer-Exl, F. Spindler, H. U. Blaser, *Monatsh. Chem.* **2000**, *131*, 1335–1343; d) S. Murata, T. Sugimoto, S. Matsuura, *Heterocycles* **1987**, *26*, 763–766; e) J. P. Henschke, M. J. Burk, C. G. Malan, D. Herzberg, J. A. Peterson, A. J. Wildsmith, C. J. Cobley, G. Casy, *Adv. Synth. Catal.* **2003**, *345*, 300–307; f) W. B. Wang, S. M. Lu, P. Y. Yang, X. W. Han, Y. G. Zhou, *J. Am. Chem. Soc.* **2003**, *125*, 10536–10537; g) S. M. Lu, X. W. Han, Y. G. Zhou, *Adv. Synth. Catal.* **2004**, *346*, 909–912; h) R. Kuwano, K. Kaneda, T. Ito, K. Sato, T. Kurokawa, Y. Ito, *Org. Lett.* **2004**, *6*, 2213–2215; i) C. Bianchini, P. Barbaro, G. Scapacci, E. Farnetti, M. Graziani, *Organometallics* **1998**, *17*, 3308–3310; j) C. J. Cobley, J. P. Henschke, *Adv. Synth. Catal.* **2003**, *345*, 195–201; k) L. J. Xu, K. H. Lam, J. X. Ji, Q.-H. Fan, W.-H. Lo, A. S. C. Chan, *Chem. Commun.* **2005**, 1390–1393; l) S. A. Raynor, J. M. Thomas, R. Raja, B. F. G. Johnson, R. G. Belle, M. D. Mantle, *Chem. Commun.* **2002**, 1925–1926; m) H. U. Blaser, H. Hornig, M. Studer, C. Wedemeyer-Exl, *J. Mol. Catal. A* **1999**, *139*, 253–257; for efficient chiral-auxiliary-based hydrogenation reactions, see: n) F. Glorius, N. Spielkamp, S. Holle, R. Goddard, C. W. Lehmann. *Angew. Chem.* **2004**, *116*, 2910–2913; *Angew. Chem. Int. Ed.* **2004**, *43*, 2850–2852; o) B. Scheiper, F. Glorius, A. Leitner, A. Furster, *Proc. Natl. Acad. Sci. USA* **2004**, *101*, 11960–11965. During preparation of this manuscript, the Ir-catalyzed asymmetric hydrogenation of *N*-iminopyridinium ylides with high enantioselectivity was reported: p) C. Y. Legault, A. B. Charette, *J. Am. Chem. Soc.* **2005**, *127*, 8966–8967.

[3] C. W. Bird, *Tetrahedron* **1992**, *48*, 335–340.

[4] a) J. D. Keay in *Comprehensive Organic Synthesis*, *Vol. 8* (Eds.: B. M. Trost, I. Fleming), Pergamon, Oxford, **1991**, pp. 579–601; b) *Comprehensive Natural Products Chemistry*, *Vols. 1–9* (Eds.: D. H. R. Barton, K. Nakanishi, O. Meth-Cohn), Elsevier, Oxford, **1999**; c) I. Jacquemond-Collet, S. Hannedouche, N. Fabre, I. Fouraste, C. Moulis, *Phytochemistry* **1999**, *51*, 1167–1169; d) J. H. Rokotoson, N. Fabre, I. Jacquemond-Collet, S. Hannedouche, N. Fabre, I. Fouraste, C. Moulis, *Planta Med.* **1998**, *64*, 760–762; e) P. J. Houghton, T. Z. Woldemariam, Y. Watanabe, M. Yates, *Planta Med.* **1999**, *65*, 250–254; f) M. Chrzanowska, M. D. Rozwadowska, *Chem. Rev.* **2004**, *104*, 3341–3370.

[5] For some recent reactions based on activation by chloroformates, see: a) S. H. Lee, Y. S. Park, M. H. Nam, C. M. Yoon, *Org. Biomol. Chem.* **2004**, *2*, 2170–2172; b) C. Legault, A. B. Charette, *J. Am. Chem. Soc.* **2003**, *125*, 6360–6361; c) E. Ichikawa, M. Suzuki, K. Yabu, M. Albert, M. Kanai, M. Shibasaki, *J. Am. Chem. Soc.* **2004**, *126*, 11808–11809; d) F. Amiot, L. Cointeaux, E. J. Silve, A. Alexakis, *Tetrahedron* **2004**, *60*, 8221–8231, and references therein.

[6] For reviews on the additive effect, see: a) E. M. Vogl, H. Groger, M. Shibasaki, *Angew. Chem.* **1999**, *111*, 1672–1680; *Angew. Chem. Int. Ed.* **1999**, *38*, 1570–1577; b) K. Fagnou, M. Lautens, *Angew. Chem.* **2002**, *114*, 26–29; *Angew. Chem. Int. Ed.* **2002**, *41*, 26–47.

[7] a) A. Alexakis, F. Amiot, *Tetrahedron: Asymmetry* **2002**, *13*, 2117–2122; b) K. Soai, A. Ookawam, T. Kaba, K. Ogawa, *J. Am. Chem. Soc.* **1987**, *109*, 7111–7115; c) C. L. Gibson, *Tetrahedron: Asymmetry* **1999**, *10*, 1551–1561.

[8] I. Jacquemond-Collet, J. M. Bessiere, S. Hannedouche, C. Bertrand, I. Fouraste, C. Moulis, *Phytochem. Anal.* **2001**, *12*, 312–319.

[9] T. Shinohara, A. Takeda, J. Toda, T. Sano, *Chem. Pharm. Bull.* **1998**, *46*, 430–433.

[10] a) S. G. Pyne, P. Bloem, S. L. Chapman, C. E. Dixon, R. Griffith, *J. Org. Chem.* **1990**, *55*, 1086–1093; b) K. Ito, S. Akashi, B. Saito, T. Katsuki, *Synlett* **2003**, 1809–1812; c) T. S. Kaufman, *Tetrahedron: Asymmetry* **2004**, *15*, 1203–1237.

 © 2006 Wiley-VCH Verlag GmbH & Co. KGaA, Weinheim

Polymerization

DOI: 10.1002/anie.200503961

Synthesis of Macrocyclic Poly(ε-caprolactone) by Intramolecular Cross-Linking of Unsaturated End Groups of Chains Precyclic by the Initiation**

Haiying Li, Antoine Debuigne, Robert Jérome, and Philippe Lecomte*

Recent decades have witnessed steadily increasing progress in the area of so-called macromolecular engineering of the main families of synthetic polymers.[1] Ring-shaped copolymers show a unique topology as a result of the absence of any chain end and exhibit distinct properties to their linear counterparts, such as glass-transition temperatures, order–disorder transitions, reduced viscosities, and lower hydrodynamic volumes.[2] In the field of nanotechnology, macrocyclic polyesters are very promising for the production of heterophase materials with smaller size domains.[2] However, only a limited effort has been devoted to the purposeful synthesis of macrocycles and more complex architectures derived from them. The usual route towards macrocycles relies on the unimolecular coupling of the two identical chain ends (X) of linear chains by a difunctional agent, Y–Y.[2] The 1:1 molar ratio of the mutually reactive groups X and Y is of the utmost importance, as is the case for any coupling reaction. Under these conditions, the cyclization yield is expressed by Equation (1), where C_{equal} is the concentration at which the

$$\text{Cyclization yield} = C_{equal}/(C_{equal} + C) \quad (1)$$

probability for the intra- and intermolecular reactions to occur is the same [Eq. (2)].[2]

$$C_{equal} = [3/(2\pi < r^2 >)]^{3/2} M/N_A \quad (2)$$

In Equation (2), $< r^2 >$ is the mean-square end-to-end distance of the linear chains, C is the polymer concentration in $g\,mL^{-1}$, N_A is the Avogadro number, and M is the molecular weight.

According to the statistical Equation (1), the yield of intramolecular cyclization is as high as the polymer concentration is low ($C < 10^{-5}$ M). The large quantity of solvent that is accordingly needed is a severe limitation on the production of a reasonable amount of macrocycles. As a rule, the selective synthesis of high-molecular-weight cyclic polymers requires an even more diluted medium than the cyclization of oligomers. Even under optimized conditions, macrocycles are often contaminated by undesired polycondensates, whose the elimination by fractionation is very tedious.

The general route has been improved by Deffieux and co-workers who coupled the mutually reactive hetero end groups X and Y of linear precursors,[3] so that there is no need for coupling agents and the ideal stoichiometry is a substantial advantage. Alternatively, Tezuka et al. cyclized linear poly(tetrahydrofuran) chains capped by an olefin at both ends by ring-closing metathesis mediated by the Grubbs catalyst.[4] Nevertheless, high dilution remains a requirement in these two alternatives. Recently, Kricheldorf and Schwarz revised the classical theory of step-growth polycondensation and showed that macrocycles can be selectively prepared under kinetic control provided that no side reaction takes place and that conversion is close to 100 %.[5] Remarkably, high dilution is not required; however, molecular weight is more difficult to control compared with living/controlled processes. Recently, Grubbs and co-workers initiated the ring-opening metathesis polymerization of cyclooctene by a cyclic ruthenium carbene complex, thus leading to macrocyclic poly(cyclooctene).[6] Polymerization can be conducted at high concentration, even in bulk.

Herein, we report a novel route to the synthesis of biodegradable cyclic polyesters. The strategy is based on two previous contributions. Kricheldorf initiated the ring-opening polymerization of lactones and lactides by cyclic tin dialkoxides, for example, 2,2-dibutyl-2-stanna-1,3-dioxepane (DSDOP). The growing chains are closed by two endocyclic tin alkoxides, which are hydrolyzable (Scheme 1).[7] It was proposed the rings were clipped by reaction of the macrocycles with 1,3-dithian-2-one, so a less hydrolyzable carbonate group is therefore substituted for the endocyclic tin alkoxide.[8] Nevertheless, significant chain degradation could not be avoided, at least in our hands. Quite interestingly, Miller and co-workers reported the intramolecular cross-linking of poly(ε-caprolactone) (PCL) bearing randomly distributed acrylic unsaturated units at ultrahigh dilution so as to prepare nanoparticles of very small size.[9]

Herein, the ε-caprolactone (εCL) polymerization has been initiated by a cyclic tin alkoxide (DSDOP), followed by the addition and sequential polymerization of a few units of α-(1-acryloxyethyl)-ε-caprolactone (αAεCL).[10] The intramolecular cross-linking of the pendant acrylic unsaturated units is expected to result in macrocyclic polyesters free of any endocyclic tin alkoxide (Scheme 1), provided at least some of the double bonds in one end block of the PCL chains reacts with a double bond in the second end block. Therefore, the length of the poly(αAεCL) may not be extremely short, although undesirable intermolecular cross-linking could occur in case of blocks that are too long.

One advantage of the strategy proposed herein for the synthesis of macrocycles is that there is no linear intermediate at any stage of the process, so that macrocyclic polyesters that are free of any knot are prepared. Indeed, whenever macrocycles are synthesized from a linear precursor, chains of high

[*] H. Li, Dr. A. Debuigne, Prof. R. Jérome, Dr. P. Lecomte
Center of Education and Research on Macromolecules (CERM)
University of Liège
Sart-Tilman, B6, 4000 Liège (Belgium)
Fax: (+32) 4-366-3497
E-mail: rjerome@ulg.ac.be

[**] The authors are much indebted to the "Belgian Science Policy" for financial support and a fellowship to H.L. in the frame of the "Interuniversity Attraction Poles" Programme (PAI V/03): Supramolecular Chemistry and Supramolecular Catalysis. P.L. is research associate with the Belgian "Fonds National de la Rechecherche Scientifique".

InterScience
© 2006 Wiley-VCH Verlag GmbH & Co. KGaA, Weinheim

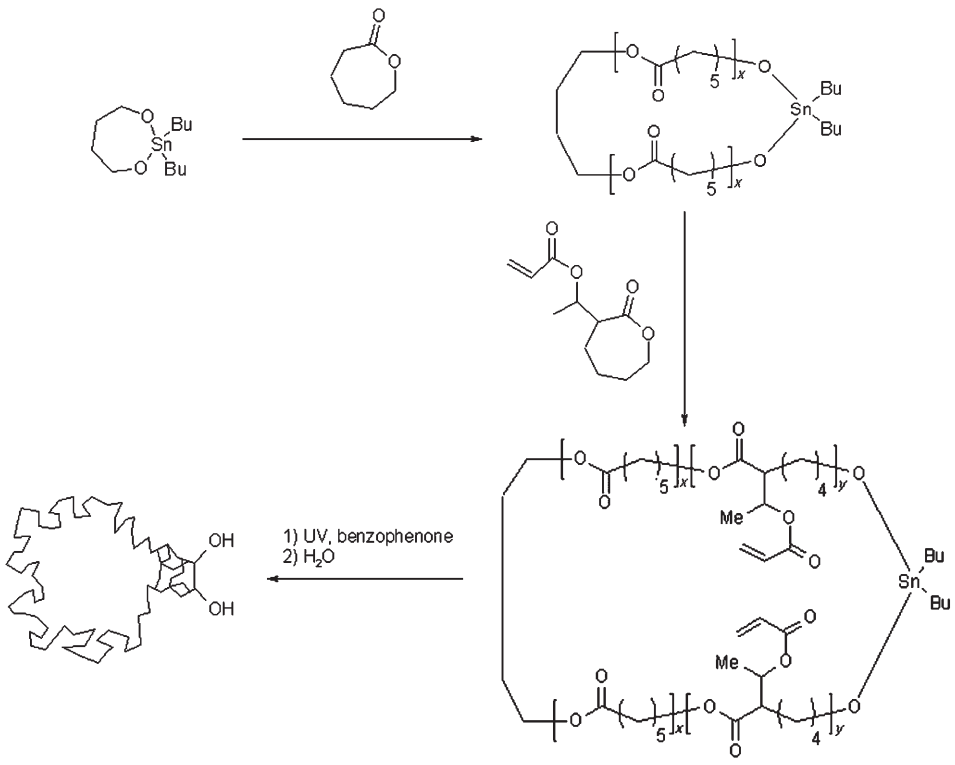

Scheme 1. Synthetic strategy for the synthesis of a macrocyclic polyester free from tin alkoxide.

enough molecular weight can become entangled, thus leading to physical cross-links or knots that impact the macroscopic properties of the macrocycles.[11]

Moreover, the statistics of the cyclization are favorably changed because the probability of an intra-reaction (P_{intra}) is higher when the precursor is cyclic rather than linear, as result of the permanent proximity of the end groups to be coupled. C_{equal} is then higher, which means that a high cyclization yield can be observed at higher concentration. Clearly, the new strategy is very well-suited to high-molecular-weight chains, whose macrocyclization from linear precursors is very challenging. The independence of P_{intra} on the chain molecular weight is the key feature that makes the cyclization depend mainly on the reactivity of the unsaturated units. In parallel, the probability for inter-reactions decreases upon increasing molecular weight, which accounts for C_{equal} increasing with the length of the chains to be cyclized.

In this preliminary study, only chains of a medium molecular weight ($M_{n,th.} = 26000$; th. = theoretical) have been considered in relation to feasible characterization by NMR spectroscopy. The quantitative polymerization of εCL was initiated in toluene by DSDOP according to the procedure reported by Kricheldorf ($[CL]_0/[DSDOP]_0 = 200{:}1$, $[Sn] = 3.2 \times 10^{-2}$ M, 40 °C, 2 h).[7] Then, a fresh feed of αAεCL was added to the polymerization medium ($[\alpha A\varepsilon CL]_0/[DSDOP]_0 = 15{:}1$). A sample was withdrawn after heating for 2 h at 40 °C and hydrolyzed into the parent linear copolyester for characterization. Measurement by linear PCL calibration gave a $M_{n,SEC}$ (SEC = size-exclusion chromatography) value of 24000. Although $M_{n,SEC}$ cannot strictly be compared to the theoretical value ($M_{n,th.} = 26000$), the agreement is good because of the low content of αAεCL in the copolyester. The SEC trace is symmetrical and the polydispersity index (1.45) is in line with values reported by Kricheldorf for the ring-opening polymerization of lactones.[7] Figure 1 shows the ^{1}H NMR spectrum of the copolymer, which confirms the incorporation of a few acrylic units. From the integration of the signals assigned to the acrylic double bonds ($\delta = 6.4$, 6.1, and 5.8 ppm for vinylic H) and to PCL ($\delta = 4.2$ ppm for CH_2–O), an average number of 14.3 αAεCL units has been calculated (7 units in each outer block), which is close to the theoretical value of 15 and indicates a quasi complete conversion in the second step of the process.

The copolymerization medium was diluted with toluene ($[Sn] = 2.8 \times 10^{-4}$ M) and irradiated by UV (350–420 nm, 1000 W) at room temperature

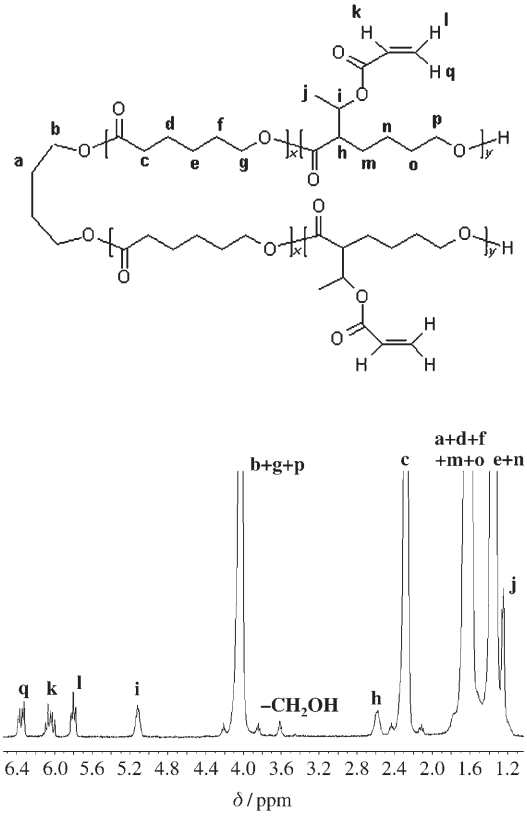

Figure 1. ^{1}H NMR spectrum for the triblock copolymer of εCL and αAεCL.

 © 2006 Wiley-VCH Verlag GmbH & Co. KGaA, Weinheim

for 120 min in the presence of 1 mol% of benzophenone with respect to the acrylic units. According to ^{1}H NMR spectroscopic analysis of the copolyester, the average number of the acrylic units has decreased from 14.3 to 6.5, which confirms the expected occurrence of the cross-linking reaction. The SEC trace of the copolyester in THF is symmetrical, and the polydispersity index ($M_w/M_n = 1.45$) remains unchanged. Figure 2 compares the SEC traces for the hydrolyzed sample before and after UV treatment. The apparent $M_{n,SEC}$ decreases from 24000 to 20800 upon cross-linking, which is consistent with the lower hydrodynamic volume that cyclic macromolecules exhibit with respect to the linear counterparts.[2] This observation confirms that the ring shape of the copolyester is maintained after hydrolysis of the endocyclic tin alkoxide. The ratio of the molecular weights at the maximum of the elution peaks ($M_{p,SEC(cyclic)}/M_{p,SEC(linear)}$) is 0.76:1, in agreement with data reported for other cyclic polymers.[2] Remarkably, the concentration of the chains (2.8×10^{-4} M or ≈ 0.78 wt%) at which the UV cyclization was carried out is at least one order of magnitude higher relative to the cyclization of linear precursors ($< 10^{-5}$ M). Nevertheless, the concentration at which intramolecular cross-linking is carried out and the average number of acrylic unsaturated units per chain are key parameters for the success of cyclization. Indeed, gelation occurs as result of intermolecular cross-linking when either the chain concentration (e.g., 5.0×10^{-3} M) or the number of acrylic units (e.g., 25) is too high. In contrast, whenever the average number of unsaturated units is too low (7), the apparent molecular weight measured by SEC remains unchanged, which indicates that intramolecular cross-linking does not take place and that no chain degradation is triggered by UV irradiation. Therefore, when the SEC chromatograms are shifted towards lower molecular weight, the reason is the cyclization and not degradation.

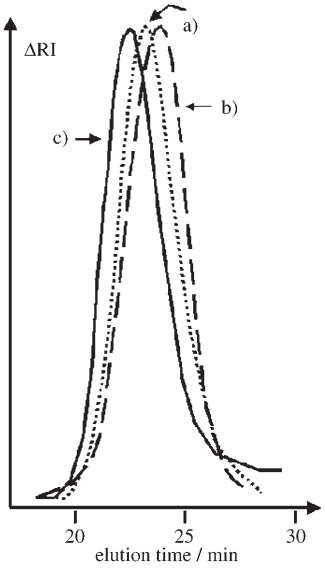

Figure 2. SEC traces of the a) linear precursor, b) cyclic PCL after UV treatment, and c) tadpole-shaped copolyester. RI = refractive index.

Additional evidence for successful cyclization is the ratio (g) of the intrinsic viscosity [η] of the copolyester after and before UV treatment. This ratio ($g = [\eta]_{cyclic}/[\eta]_{linear}$) in toluene at 25 °C is 0.69:1, which is again quite consistent with observations reported for other macrocyclic (co)polymers.[2]

Importantly, the tin alkoxide is preserved during the UV cross-linking, in sharp contrast to traditional cyclization techniques that consume the reactive end groups. Indeed, polymerization of εCL can be resumed after the UV treatment. For example, the copolyester was added with εCL ($[CL]_0/[Sn]_0 = 108:1$, $M_{n,th.} = 38000$) just after cyclization. The tin alkoxide was hydrolyzed after 2 h at 40 °C, and the polymer collected by precipitation into heptane. The SEC trace remained symmetrical, the polydispersity index unchanged ($M_w/M_n = 1.4$), and the apparent molecular weight increased significantly ($M_{n,SEC} = 30500$; Figure 2). It can, thus, be concluded that resumption of polymerization is effective and that tadpole-shaped polyesters with two tails of a controllable length can be readily prepared (Scheme 2).

A novel strategy has been successfully tested for the synthesis of cyclic polyesters. It relies on the intramolecular photochemical cross-linking of acrylic unsaturated units at both ends of chains synthesized by ring-opening polymerization initiated by a cyclic tin alkoxide. This process is very well suited to the synthesis of high-molecular-weight macrocycles. Quite interestingly, the propagating tin alkoxides remain active after cyclization and are available for further derivatization and macromolecular engineering. As a very straightforward example, εCL polymerization was resumed after cyclization to lead to tadpole-shaped chains, thus grafting two adjacent tails onto the macrocycles. Further investigations are now devoted to the synthesis of polyesters with novel architectures based on macrocyclic building blocks.

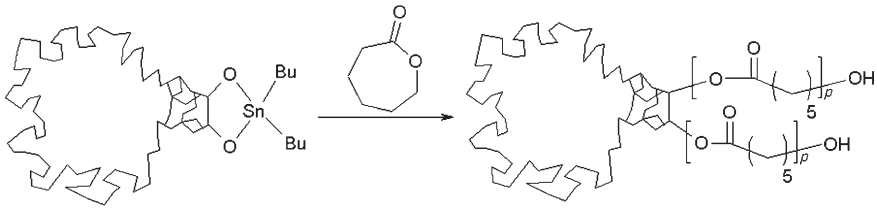

Scheme 2. Synthesis of a tadpole-shaped copolyester.

Received: November 8, 2005
Published online: March 3, 2006

Keywords: macrocycles · polyesters · polymers · ring-opening polymerization

[1] N. Hadjichristidis, M. Pitskalis, S. Pispas, H. Iatrou, *Chem. Rev.* **2001**, *101*, 3747–3792.
[2] J. Roovers in *Cyclic Polymers, 2nd ed.* (Ed.: J. A. Semlyen), Kluwer, Dordrecht, **2000**, 347–383.

 © 2006 Wiley-VCH Verlag GmbH & Co. KGaA, Weinheim

[3] L. Rique-Lurbet, M. Schappacher, A. Deffieux, *Macromolecules* **1994**, *27*, 6318 – 6324.
[4] Y. Tezuka, R. Komiya, M. Washizuka, *Macromolecules* **2003**, *36*, 12 – 17.
[5] H. R. Kricheldorf, G. Schwarz, *Macromol. Rapid Commun.* **2003**, *24*, 359 – 381.
[6] Ch. W. Bielawski, D. Benitez, R. H. Grubbs, *Science* **2002**, *297*, 2041 – 2044.
[7] H. R. Kricheldorf, *J. Polym. Sci. A* **2004**, *42*, 4723 – 4742.
[8] H. R. Kricheldorf, S.-R. Lee, N. Schittenhelm, *Macromol. Chem. Phys.* **1998**, *199*, 273 – 282.
[9] D. Mecerreyes, V. Lee, C. J. Hawker, J. L. Hedrick, A. Wursch, W. Volksen, T. Magbitang, E. Huang, R. D. Miller, *Adv. Mater.* **2001**, *13*, 204 – 208.
[10] Very briefly, αAεCL was synthesized by reaction of acryloyl chloride with α-(1-hydroxyethyl)-ε-caprolactone in the presence of triethylamine (the detailed experimental procedure will be reported in a forthcoming publication); α-(1-hydroxyethyl)-ε-caprolactone was synthesized according to J. Chrisoffers, H. Oertling, P. Fischer, W. Frey, *Tetrahedron* **2003**, *59*, 3769 – 3778.
[11] G. Hadziioannou, P. M. Cotts, G. ten Brinke, C. C. Han, P. Lutz, C. Strazielle, P. Rempp, A. Kovacs, *Macromolecules* **1987**, *20*, 493 – 497.

 © 2006 Wiley-VCH Verlag GmbH & Co. KGaA, Weinheim

Nanobiotechnology

DOI: 10.1002/anie.200504529

Nanoparticle-Assisted Visualization of Binding Interactions between Collagen Mimetic Peptide and Collagen Fibers**

*Xiao Mo, Yoojin An, Chang-Soo Yun, and Seungju M. Yu**

Collagen is the structural framework for a wide range of animal connective tissues. It is known to induce cell proliferation and differentiation by direct epitope binding and by serving as a reservoir for growth factors and signaling molecules.[1] In the past, collagen mimetic peptide (CMP), a synthetic peptide composed of a collagen-like repetitive amino acid sequence, has played a central role in elucidating the triple-helical structure and thermal stability of natural collagens.[2–7] Herein, we show for the first time that a biochemically inert but highly helicogenic CMP, $(Pro\text{-}Hyp\text{-}Gly)_7$ (Hyp = hydroxyproline), binds preferentially to the gap regions within the surface of intact type I collagen fibers. This binding behavior was demonstrated by synthesizing CMP-conjugated gold nanoparticles (NPs) that are colloidally stable under a wide range of aqueous conditions and by transmission electron microscopy (TEM) observation of their attraction to type I collagen fibers under physiological conditions. The results suggest that such binding affinity may exist in other natural proteins/peptides that contain collagen-like sequences.[8] The study also demonstrates the potential use of nanoparticle-labeling techniques in detecting structurally unstable domains in collagen fibers which are related to many debilitating human diseases.[9]

The collagen triple helix is composed of three poly-(proline)-II strands that are held together by interchain hydrogen bonds.[4,10] This structure is similar to the double-helical structure of DNA. Both collagen and DNA exhibit melting transitions that reflect the stability and strength of the multiplex assemblies. Strand invasion in DNA by short DNA strands or peptide nucleic acids is well documented.[11] Although collagens are known to incorporate thermally unstable domains where small segments of the triple helix are thought to be partially unraveled,[12] strand invasion by other collagen molecules or collagen analogues have not been reported to date.

We previously presented a method of collagen modification that uses CMP as a collagen-specific molecular "hitchhiker".[13] Our results suggested that the CMP, $(Pro\text{-}Hyp\text{-}Gly)_x$ binds to a film composed of type I collagen molecules (in nonfibrous form) through a process that involves both strand invasion and assembly of a triple helix. However, the binding location and physical state of the collagen molecules that interact with CMP have not been studied in detail.

In nature, type I collagen exists not as individual molecules but instead forms fibrous bundles of high tensile strength. Under TEM, collagen fibers exhibit characteristic banding patterns that indicate the structural integrity of the collagen molecules and the regularity of their assembly. The banding patterns also provide approximate position markers along the length of collagen molecules. As CMP is invisible under TEM, we prepared CMP-conjugated gold nanoparticles to use as an electron-dense TEM marker for the location of CMPs. We investigated binding between type I collagen fibers and CMP-conjugated gold nanoparticles to study the associative interactions and to determine if strand invasion occurs in collagen fibers without destroying native structures.

Biomolecule-functionalized nanoparticles are widely used as sensors and visualization tools.[14–18] Gold nanoparticles are one of the most popular type of nanoparticles for immunolabeling markers because their synthesis and conjugation with biomolecules are relatively easy to perform.[19,20] In the past,

[*] Prof. S. M. Yu
Department of Materials Science & Engineering and
Department of Chemistry
The Johns Hopkins University
3400 N. Charles Street, Baltimore, MD 21218 (USA)
Fax: (+1) 410-516-5293
E-mail: yu@jhu.edu
X. Mo, Y. An,[+] Dr. C.-S. Yun[++]
Department of Materials Science & Engineering
The Johns Hopkins University
3400 N. Charles Street, Baltimore, MD 21218 (USA)
[+] Present address: Department of Bioengineering
University of Pennsylvania
125 South 31st St., Philadelphia, PA 19104 (USA)
[++] Present address: Medicinal Science Division
Korea Research Institute of Chemical Technology
P.O. Box 107, Yuseong-gu, Daejeon 305-600 (Korea)
[**] This work was supported by the NSF (CTS-0210220) and the NIH (GM-74812).
Supporting information for this article is available on the WWW under http://www.angewandte.org or from the author.

 © 2006 Wiley-VCH Verlag GmbH & Co. KGaA, Weinheim

antibody-passivated gold nanoparticles were used successfully to identify specific types of collagen fibers in tissue samples.[21]

We synthesized a series of three CMPs, each with a single cysteine at the N terminus (Table 1, Cys-CMPs **1**–**3**) by using conventional Fmoc-mediated solid-phase peptide-coupling methods (Fmoc = 9-fluorenylmethoxycarbonyl). We also prepared a fourth peptide **4** with an amino acid sequence whose composition is identical to that of **3** but is scrambled such that it is unable to support a triple-helical structure. The melting transition temperatures (Table 1) of these compounds as determined by circular dichroism (CD) spectroscopy are consistent with those of other CMP analogues reported previously.[22,23] We used the citrate reduction method to prepare gold nanoparticles with a diameter of 13.2 ± 3.5 nm.[24] Incubation of the gold nanoparticles and the Cys-CMPs **1**–**4** at room temperature produced CMP-functionalized gold nanoparticles (Table 2; **NP-X** (**X** = **1**–**4**)). We were unable to determine the melting temperatures of CMPs bound to the surfaces of the gold nanoparticles because CD measurements were hampered by light scattering from the nanoparticles. Calorimetric analysis was unsuccessful as a result of the trace amount of CMPs present on the surfaces of the nanoparticles.[25]

Table 1: Melting transition temperatures of CMP derivatives as determined by CD spectroscopy.

Compound	Sequence	T_m [°C]
1	Cys-(Pro-Hyp-Gly)$_3$	–
2	Cys-(Pro-Hyp-Gly)$_5$	21
3	Cys-(Pro-Hyp-Gly)$_7$	39
4	Cys-(Pro$_7$Hyp$_7$Gly$_7$)[a]	–

[a] Cys-GPGP*PP*PPGPPP*GP*P*PP*GP*GG (Cys = cysteine, P = Pro = proline, P* = Hyp = hydroxyproline, G = Gly = glycine).

Table 2: Properties of CMP-functionalized Au nanoparticles.

Conjugate	Particle size [nm][a]	Peptide layer thickness [nm][b]	Number of peptides per nanoparticle
NP-1	17.2 ± 3.7	2.0 (2.8)	582 ± 32
NP-2	20.5 ± 3.3	3.65 (4.7)	444 ± 18
NP-3	26.9 ± 4.6	6.85 (6.6)	399 ± 21
NP-4	16.2 ± 3.1	1.5 (n.a.)	524 ± 59

[a] Determined by DLS studies. [b] Measured peptide layer thickness; the estimated length of the CMP in poly(proline)-II helical conformation is given in parentheses. n.a. = not applicable.

To use **NP-X** for collagen binding experiments, first, we had to ensure that the CMPs were structurally unimpaired on the surfaces of the gold nanoparticles. The CMP-functionalized gold nanoparticles were characterized by dynamic light scattering (DLS) studies, and the thicknesses of the peptide layers on the surfaces of the nanoparticles were determined by comparing hydrodynamic sizes of the nanoparticles before and after conjugation to CMP. The peptide layer thicknesses of **NP-1**, **NP-2**, and **NP-3** were 2.0, 3.65, and 6.85 nm, respectively (Table 2). These values are commensurate with the estimated lengths of the corresponding CMPs in helical conformations.[4] In contrast, the peptide layer thickness of **NP-4** was only 1.5 nm, indicating that this peptide is either a random coil or has a distinctively different secondary structure that tends to lie flat on the particle surface.

The average number of CMPs on the gold nanoparticles was determined by measuring the concentrations of free CMPs that remain in solution after the removal of the nanoparticles from a series of incubation mixtures with varying CMP/NP ratios.[26,27] The numbers of CMPs immobilized on the surfaces of the nanoparticles were 582, 444, and 399 for **NP-1**, **NP-2**, and **NP-3**, respectively (Table 2).[27] These values correspond to the effective footprint areas (per single chain) of 94, 123, and 137 Å^2, respectively, which are comparable to the cross-sectional area of the CMP triple helix (80 Å^2).[4] The peptide layer seems to be composed of laterally packed single-stranded CMPs. Anchoring the ends of the peptide chains to the surface of the nanoparticles appears to prohibit the staggered chain arrangement of the CMPs which is critical for the triple-helix structure.[28]

The data from DLS studies and the average number of peptides per nanoparticle are in agreement with the CMPs standing upright on the surfaces of the nanoparticles in an extended conformation that resembles the poly(proline)-II helix.[29] In negatively stained TEM micrographs, the peptides appear as a dense white layer that covers the surface of the gold nanoparticles.[27] During the preparation of the sample for TEM studies, all CMP-functionalized nanoparticles assembled into a pseudohexagonal lattice, indicating that the CMPs fully passivated the surfaces of the nanoparticles and prevented them from aggregating.[30] In contrast, unmodified nanoparticles formed aggregates without any order.[27]

We determined the colloidal stability of the **NP-X** samples in water because peptide-conjugated nanoparticles are prone to aggregation, which is not ideal for the labeling of biological samples. The CMP-conjugated gold nanoparticles were highly stable in aqueous solution. By UV/Vis spectroscopic analysis we were unable to detect any signs of aggregation in buffer solutions of up to 5 M NaCl or within a pH range from 0 to 14 (Figure 1 A–D). The red shift (5 nm) of the plasmon bands at 520 nm for the gold nanoparticles after their conjugation with CMP signifies a change in the local dielectric permittivity of the nanoparticles caused by the surface-passivating layer of CMP.[26] All the samples of **NP-X** can be freeze-dried, stored, and resuspended in water without aggregation of the particles.

Peptides usually make poor passivating layers for nanoparticles, and even peptides that are carefully designed to disperse nanoparticles did not protect them under such a wide range of conditions.[26] CMP triple helices consist of three parallel peptide chains; hence, the association of peptides with antiparallel alignment from two different nanoparticles is unlikely. We believe that the high content of hydroxyproline and the extended conformation of the peptides, as shown by DLS, cause the CMPs to mimic the behavior of poly(ethylene glycol) brushes on surfaces and prevent aggregation of the nanoparticles in aqueous solution.

Type I collagen fibers were prepared by adjusting the pH value and ionic strength of a solution of acid-soluble type I collagen.[31] To form a fiber, collagen molecules align head to

 © 2006 Wiley-VCH Verlag GmbH & Co. KGaA, Weinheim

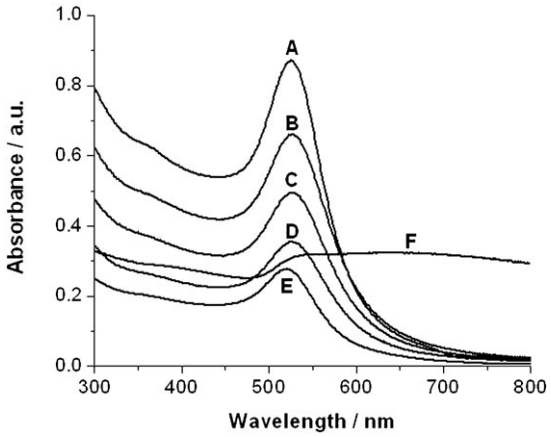

Figure 1. UV/Vis spectra of **NP-3** in water (A), in 5 M NaCl solution (B), in 100 mM NaCl solution at pH 0 (C), and in 100 mM NaCl solution at pH 14 (D), and of unmodified gold nanoparticles (passivated by citrate) in water (E) and in 100 mM NaCl solution at pH 7 (F). Functionalized nanoparticles **NP-3** remains dispersed even in solutions that are very acidic or basic and at high salt concentrations. Similar results were obtained for **NP-1** and **NP-2**. In contrast, unmodified nanoparticles form large aggregates at physiological ionic strength (100 mM NaCl) as revealed by a broad absorption between 600 and 800 nm (F).

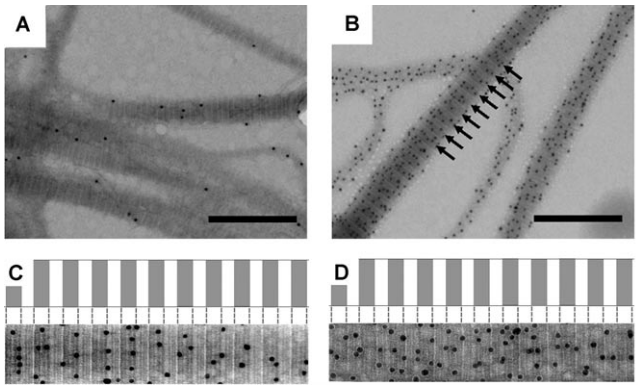

Figure 2. TEM micrographs of reconstituted type I collagen fibers after incubation with **NP-4** (A) and **NP-3** (B–D). Functionalized nanoparticles **NP-4** shows little affinity to collagen fibers. In contrast, **NP-3** shows strong affinity to collagen fibers. Binding occurred preferentially to the dark bands (arrows in (B) and gray boxes in (C)) of collagen fibers when the experiment was performed at 25 °C. There was no such preference when the collagen fibers and **NP-3** were incubated at 40 °C and cooled to room temperature (D). Scale bar: 400 nm.

tail in the direction of the long axis in overlapping rows, with a gap between the molecules within each row. Accumulation of staining agents (e.g. uranyl acetate) in these gap regions produces the dark bands that repeat every 67 nm along the length of the fiber. Compound **3** has the highest melting temperature among the three CMPs, suggesting that it may form the most stable adduct with the collagen fiber. Therefore, we focused our initial efforts on studying the binding of **NP-3** to collagen fibers.

When **NP-3** or **NP-4** were incubated with type I collagen fibers in phosphate buffer solution at 25 °C, TEM studies revealed drastically contrasting results. Functionalized nanoparticles **NP-4** exhibited little binding to the collagen fibers, whereas **NP-3** was highly attracted to the collagen fibers (Figure 2). Moreover, **NP-3** seemed to bind preferentially to the gap regions (dark bands) of the fiber (indicated by arrows in Figure 2B; see also Figure 2C). Owing to the large particle size and limitations of TEM resolution, we were unable to determine the exact locations of these binding sites within the gap regions. However, careful analysis of the nanoparticle distribution revealed twice as many **NP-3** particles per unit area in the collagen gap regions (dark bands) than on the overlap regions (light bands). This binding preference was diminished when **NP-3** and the collagen fibers were incubated at 40 °C and allowed to cool to room temperature (Figure 2D).

The results indicate that CMP-functionalized gold nanoparticles bind to the collagen fiber in its native state and preferentially to a few domains within the collagen molecules, and that the propensity of CMPs to form a triple helix is critical in the binding process. Collagen fibers exhibited clear banding morphology even after incubation with the nanoparticles, suggesting that they remain intact. This observation was not surprising as the incubation temperatures in our experiments were kept below the melting temperature of collagen fibers (65.1 °C).[32] Recent studies using calorimetry and isothermal CD spectroscopy demonstrated that type I collagen molecules are unstable at body temperature.[33] Miles and Bailey identified thermally unstable domains in collagen according to a deficiency of helix-stabilizing hydroxyproline.[12] Many small domains that lack hydroxyproline are scattered throughout the collagen molecule, but the three most unstable domains, with long stretches that are deficient in hydroxyproline, are all located within the gap region of the collagen fiber that exhibited high affinity to **NP-3**.

Hydroxyproline is a strong stabilizer of triple helices. The $(Pro\text{-}Hyp\text{-}Gly)_x$ peptide sequence conjugated to the nanoparticle has a stronger propensity to form triple helices than the thermally unstable domains of collagen which are composed largely of Hyp-deficient Pro-Pro-Gly repeat units. The melting temperature of the $[(Pro\text{-}Pro\text{-}Gly)_{10}]_3$ homotrimer is approximately 19 °C below that of the $[(Pro\text{-}Pro\text{-}Gly)_{10}\{(Pro\text{-}Hyp\text{-}Gly)_{10}\}_2]$ heterotrimer.[34] Collagen strands in the thermally unstable domains that are unable to form stable triple helices because they lack hydroxyproline in all three collagen strands may still be able to form a stable triple-helical complex with **NP-3**, because the CMP **3** provides the helix-stabilizing hydroxyproline unit. We believe that accumulation of **NP-3** in the gap region of collagen fiber indicates a preferential interaction of CMP with the thermally labile domains of collagen molecules. The occasional presence of nanoparticles at the overlap regions may arise from the binding of the gold nanoparticles to minor Hyp-deficient domains and/or their binding non-specifically to collagen. We speculate that at a higher incubation temperature (40 °C), other regions of the molecules became disentangled and susceptible to invasion by CMPs. Cooling of this incubation mixture resulted in a stable **NP-3**–collagen complex with no observable binding preference for the gap regions (Figure 2D).

 © 2006 Wiley-VCH Verlag GmbH & Co. KGaA, Weinheim

More studies are needed to elucidate the precise mechanisms underlying CMP–collagen interactions. However, our results indicate for the first time that CMP interacts with intact collagen fibers in a structure-dependent manner. The interaction occurs preferentially at the gap regions of the fiber that incorporate structurally labile domains. Within the collagen superfamily exists a class of collagen known as fibril-associated collagens with interrupted triple helices (FACITs).[8] FACITs do not form fibrous structure by themselves but are always found as individual collagen molecules that decorate the surface of collagen fibers. Strand invasion or similar forms of strand association by collagen and collagen derivatives may uncover the behavior of FACITs and other proteins that incorporate collagen-like sequences.[8,35] CMP-functionalized gold nanoparticles are easy to prepare, highly stable, and form stable adducts with collagen fibers that are visible by TEM. The described nanoparticle-labeling technique can potentially be used to identify structural abnormalities in collagen fibers that are related to debilitating human diseases.[9]

Experimental Section

Synthesis of gold nanoparticles: Trisodium citrate solution (25 mL, 38.8 mM) was quickly added to a refluxing aqueous solution of $HAuCl_4$ (250 mL, 1 mM) with vigorous stirring (the color of the solution changed from pale yellow to deep red after adding the citrate solution). The solution was heated at reflux for an additional 15 min, cooled, and filtered through a glass filter.

Surface functionalization of gold nanoparticles with **1**–**4**: Purified Cys-CMPs **1**–**4** (0.5 mL, 500 μM) were added to solutions of gold nanoparticles (5 mL, 17 nM), and the reaction mixtures were incubated at room temperature for 24 h. Excess CMPs were removed by repeated centrifugation and washing in deionized water.

TEM analysis of **NP-3**-decorated collagen fibers: A drop (8 μL) of a suspension of type I collagen fibers (0.3 mg mL^{-1} in PBS containing 1% BSA) was added to a holey carbon TEM grid (PBS = phosphate buffer solution; BSA = bovine serum albumin). A solution of **NP-3** (3 nM in PBS containing 1% BSA) was added to the grid, and the sample was incubated for 5 min at 25°C or at 40°C, followed by washing with deionized water (for the experiment at 40°C, the sample was allowed to cool to room temperature before washing with deionized water). The collagen fibers were stained with uranyl acetate (1% solution).

Received: December 21, 2005
Published online: March 2, 2006

Keywords: fibrous proteins · gold · helical structures · nanostructures · peptides

[1] M. E. Nimni, *Collagen*, CRC, Boca Raton, **1988**.
[2] Y. B. Feng, G. Melacini, J. P. Taulane, M. Goodman, *J. Am. Chem. Soc.* **1996**, *118*, 10351.
[3] M. Goodman, M. Bhumralkar, E. A. Jefferson, J. Kwak, E. Locardi, *Biopolymers* **1998**, *47*, 127.
[4] J. Bella, M. Eaton, B. Brodsky, H. M. Berman, *Science* **1994**, *266*, 75.
[5] A. V. Persikov, J. A. M. Ramshaw, B. Brodsky, *J. Biol. Chem.* **2005**, *280*, 19343.
[6] E. S. Eberhardt, N. Panasik, R. T. Raines, *J. Am. Chem. Soc.* **1996**, *118*, 12261.
[7] S. K. Holmgren, K. M. Taylor, L. E. Bretscher, R. T. Raines, *Nature* **1998**, *392*, 666.
[8] L. M. Shaw, B. R. Olsen, *Trends Biochem. Sci.* **1991**, *16*, 191.
[9] G. A. Di Lullo, S. M. Sweeney, J. Korkko, L. Ala-Kokko, J. D. San Antonio, *J. Biol. Chem.* **2002**, *277*, 4223.
[10] A. Rich, F. H. C. Crick, *J. Mol. Biol.* **1961**, *3*, 483.
[11] N. J. Peffer, J. C. Hanvey, J. E. Bisi, S. A. Thomson, C. F. Hassman, S. A. Noble, L. E. Babiss, *Proc. Natl. Acad. Sci. USA* **1993**, *90*, 10648.
[12] C. A. Miles, A. J. Bailey, *Micron* **2001**, *32*, 325.
[13] A. Y. Wang, X. Mo, C. S. Chen, S. M. Yu, *J. Am. Chem. Soc.* **2005**, *127*, 4130.
[14] C. A. Mirkin, R. L. Letsinger, R. C. Mucic, J. J. Storhoff, *Nature* **1996**, *382*, 607.
[15] M. G. Ryadnov, D. N. Woolfson, *J. Am. Chem. Soc.* **2004**, *126*, 7454.
[16] R. Chakrabarti, A. M. Klibanov, *J. Am. Chem. Soc.* **2003**, *125*, 12531.
[17] J. W. Liu, Y. Lu, *J. Am. Chem. Soc.* **2003**, *125*, 6642.
[18] A. G. Tkachenko, H. Xie, D. Coleman, W. Glomm, J. Ryan, M. F. Anderson, S. Franzen, D. L. Feldheim, *J. Am. Chem. Soc.* **2003**, *125*, 4700.
[19] M. A. Hayat, *Colloidal Gold*, Academic Press, San Diego, **1989**.
[20] E. Katz, I. Willner, *Angew. Chem.* **2004**, *116*, 6166; *Angew. Chem. Int. Ed.* **2004**, *43*, 6042.
[21] D. E. Birk, J. M. Fitch, J. P. Babiarz, T. F. Linsenmayer, *J. Cell Biol.* **1988**, *106*, 999.
[22] Y. B. Feng, G. Melacini, J. P. Taulane, M. Goodman, *Biopolymers* **1996**, *39*, 859.
[23] L. E. Bretscher, C. L. Jenkins, K. M. Taylor, M. L. DeRider, R. T. Raines, *J. Am. Chem. Soc.* **2001**, *123*, 777.
[24] K. C. Grabar, R. G. Freeman, M. B. Hommer, M. J. Natan, *Anal. Chem.* **1995**, *67*, 735.
[25] T. Gore, Y. Dori, Y. Talmon, M. Tirrell, H. Bianco-Peled, *Langmuir* **2001**, *17*, 5352.
[26] R. Levy, N. T. K. Thanh, R. C. Doty, I. Hussain, R. J. Nichols, D. J. Schiffrin, M. Brust, D. G. Fernig, *J. Am. Chem. Soc.* **2004**, *126*, 10076.
[27] See Supporting Information.
[28] J. Kwak, A. De Capua, E. Locardi, M. Goodman, *J. Am. Chem. Soc.* **2002**, *124*, 14085.
[29] A. A. Adzhubei, M. J. E. Sternberg, *J. Mol. Biol.* **1993**, *229*, 472.
[30] M. Schulz-Dobrick, K. V. Sarathy, M. Jansen, *J. Am. Chem. Soc.* **2005**, *127*, 12816.
[31] B. R. Williams, R. A. Gelman, D. C. Poppke, K. A. Piez, *J. Biol. Chem.* **1978**, *253*, 6578.
[32] C. A. Miles, M. Ghelashvili, *Biophys. J.* **1999**, *76*, 3243.
[33] E. Leikina, M. V. Mertts, N. Kuznetsova, S. Leikin, *Proc. Natl. Acad. Sci. USA* **2002**, *99*, 1314.
[34] D. A. Slatter, C. A. Miles, A. J. Bailey, *J. Mol. Biol.* **2003**, *329*, 175.
[35] M. Koch, J. E. Foley, R. Hahn, P. H. Zhou, R. E. Burgeson, D. R. Gerecke, M. K. Gordon, *J. Biol. Chem.* **2001**, *276*, 23120.

 © 2006 Wiley-VCH Verlag GmbH & Co. KGaA, Weinheim

C–C Coupling

DOI: 10.1002/anie.200504283

Regio- and Stereoselective Decarbonylative Carbostannylation of Alkynes Catalyzed by Pd/C**

Yoshiaki Nakao, Jun Satoh, Eiji Shirakawa, and Tamejiro Hiyama**

The carbometalation reaction of alkynes allows the simultaneous, stereoselective formation of both carbon–carbon and carbon–metal bonds and provides us with a highly powerful tool for the synthesis of novel organometallic reagents that contain multisubstituted ethenes.[1] In particular, the palladium- or nickel-catalyzed carbostannylation of alkynes affords highly functionalized alkenylstannanes, which undergo various chemoselective transformations, such as the Kosugi–Migita–Stille coupling reaction.[2,3] Alkynyl, allyl, and acylstannanes which reportedly undergo oxidative addition of a C–Sn bond to palladium(0) and nickel(0) complexes,[4] are successfully applied to the carbostannylation reaction, whereas aryl-, alkenyl-, and alkylstannanes are found to be sluggish probably because of their low potential for oxidative addition to low-valent transition-metal complexes.[5,6] Herein, we report the first examples of aryl-, alkenyl-, and alkylstannylations of alkynes through the decarbonylative addition of acylstannanes[7] catalyzed by Pd/C [Eq. (1)].[8]

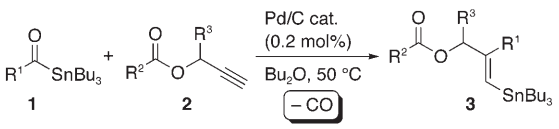

1 2 3 (1)

During our investigation of the acylstannylation of alkynes, we observed that the reaction of benzoyl(tributyl)stannane (**1a**) with propargyl acetate (**2a**; 2.0 equiv) using 2.5 mol% of $[Pd_2(dba)_3]$ (dba = dibenzylideneacetone) in Bu_2O[9] at 50 °C for 12 h gave (*E*)-2-phenyl-1-(tributylstannyl)propen-3-yl acetate (**3a**) in 29% yield, as estimated by ^{119}Sn NMR spectroscopic analysis (Table 1, entry 1). The yield increased to 44% with propargyl benzoate

Table 1: Palladium-catalyzed phenylstannylation of propargyl esters.[a]

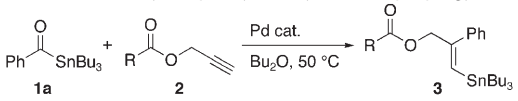

1a 2 3

2a: R = Me
2b: R = Ph
2c: R = 4-MeO–C_6H_4
2d: R = 4-CF_3–C_6H_4
2e: R = 2-furyl

Entry	Alkyne	Pd catalyst	*t* [h]	Yield of **3** [%][b]
1	**2a**	$[Pd_2(dba)_3]$ (2.5 mol%)	12	29 (**3a**)
2	**2b**	$[Pd_2(dba)_3]$ (2.5 mol%)	10	44 (**3b**)
3	**2c**	$[Pd_2(dba)_3]$ (2.5 mol%)	12	47 (**3c**)
4	**2d**	$[Pd_2(dba)_3]$ (2.5 mol%)	24	37 (**3d**)
5	**2e**	$[Pd_2(dba)_3]$ (2.5 mol%)	12	51 (**3e**)
6	**2e**	$[Pd_2(dba)_3]$ (0.1 mol%)	17	66 (**3e**)
7	**2e**	Pd/C (10 wt%; 0.2 mol% Pd)	42	77 (77)[c] (**3e**)

[a] The reaction was carried out in Bu_2O (0.15 mL) using **1a** (40 mg, 0.10 mmol) and an alkyne (0.20 mmol) in the presence of a palladium catalyst at 50 °C. [b] Estimated by ^{119}Sn NMR spectroscopic analysis with Bu_4Sn as the internal standard. [c] Yield of the isolated product based on **1a**.

(**2b**; Table 1, entry 2). The introduction of an electron-donating methoxy group at the 4-position of the phenyl ring of **2b** slightly improved the yield (Table 1, entry 3), whereas a lower yield was observed with an electron-withdrawing substituent (Table 1, entry 4). We thus surveyed various propargyl arenecarboxylates with an electron-rich aromatic group and finally found that heteroaromatic propargyl 2-furoate (**2e**) was the most effective (Table 1, entry 5). Surprisingly, use of a smaller amount (0.1 mol%) of $[Pd_2(dba)_3]$ gave a better result (Table 1, entry 6); inexpensive and readily separable Pd/C (0.2 mol% of Pd) was equally effective to give phenylstannylation product **3e** in 77% yield (Table 1, entry 7), though 42 hours was needed for completion. It is worth noting that no regio- and stereoisomers were observed, no benzoylstannylation product (non-decarbonylative addition, see below) was detected, and a small amount (< 5% as determined by ^{119}Sn NMR spectroscopy) of a bis-stannylation product was observed as a by-product in the crude reaction mixture. Nickel catalysts, such as $[Ni(cod)_2]$ (cod = cyclooctadiene), which catalyzed non-decarbonylative additions of acylstannanes across internal alkynes,[2b,f] were totally ineffective.

We next examined the substrate scope and found that a substituent such as a methoxy, chloro or *ortho*-methyl group in aroylstannanes (**1b–1e**) was tolerated (Table 2, entries 1–4), whereas 2-furoylstannane **1f** gave the corresponding furylstannylation product in a modest yield (Table 2, entry 5). The reaction of 3-methyl-2-butenoylstannane (**1g**) or propanoylstannane (**1h**) gave an alkenyl- or alkylstannylation product in 73 or 42% yield, respectively (Table 2, entries 6 and 7). Propargyl 2-furoates with a substituent such

[*] Prof. Dr. E. Shirakawa
Department of Chemistry
Graduate School of Science
Kyoto University, Kyoto 606-8502 (Japan)
Fax: (+81) 75-753-3988
E-mail: shirakawa@kuchem.kyoto-u.ac.jp
Dr. Y. Nakao, J. Satoh, Prof. Dr. T. Hiyama
Department of Material Chemistry
Graduate School of Engineering
Kyoto University, Kyoto 615-8510 (Japan)
Fax: (+81) 75-383-2445
E-mail: thiyama@npc05.kuic.kyoto-u.ac.jp

[**] This work was supported financially by Grant-in-Aids for Creative Scientific Research (No. 16GS0209) and COE Research on "Elements Science" and on a "United Approach to New Material Science" from MEXT.

Supporting information for this article is available on the WWW under http://www.angewandte.org or from the author.

 © 2006 Wiley-VCH Verlag GmbH & Co. KGaA, Weinheim

Table 2: Palladium-catalyzed decarbonylative carbostannylation of propargyl 2-furoates.[a]

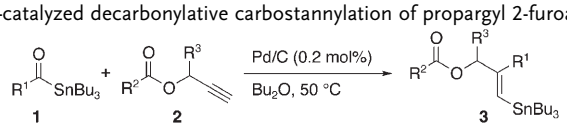

1 2 3

Entry	Acylstannane	Alkyne	*t* [h]	Product	Yield [%][b]
1	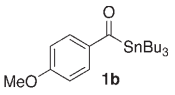 **1b**	**2e**	38	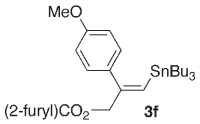 **3f**	65
2	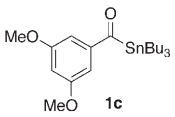 **1c**	**2e**	46	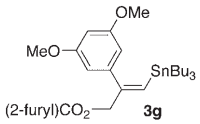 **3g**	61
3	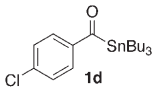 **1d**	**2e**	37	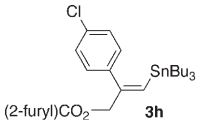 **3h**	58
4	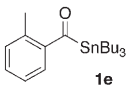 **1e**	**2e**	40	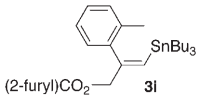 **3i**	82
5	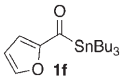 **1f**	**2e**	40	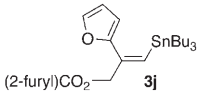 **3j**	45
6	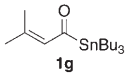 **1g**	**2e**	48	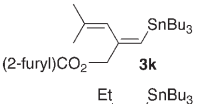 **3k**	73
7	**1h**	**2e**	40	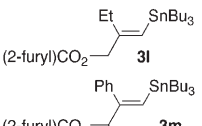 **3l**	42
8	**1a**	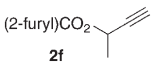 **2f**	38	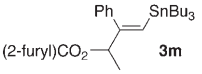 **3m**	35
9	**1a**	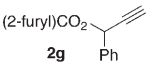 **2g**	40	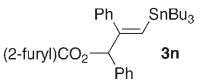 **3n**	65
10	**1a**	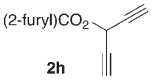 **2h**	42	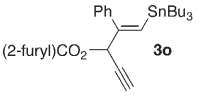 **3o**	46

[a] Unless otherwise noted, the reaction was carried out in Bu_2O (0.15 mL) with an acylstannane (0.10 mmol) and an alkyne (0.20 mmol) in the presence of Pd/C (10 wt%, 0.2 mg; 0.2 mol% Pd) at 50°C. [b] Yield of the isolated product based on the acylstannane.

as a methyl, phenyl or ethynyl group at the propargyl position (**2d**–**2f**) also underwent the reaction with **1a** (Table 2, entries 8–10). On the other hand, the reaction of **1a** with homopropargyl 2-furoate was sluggish (< 20% yield), and other alkynes, such as *N*-propargylsuccinimide, homopropargyl phenyl ether, ethyl propiolate, 2-butyn-4-yl 2-furoate and 1-octyne, were completely inert to the present reaction.

In view of the proposed mechanism of the previously reported palladium- or nickel-catalyzed carbostannylations of alkynes,[2] it is reasonable to consider that the catalytic cycle of the present reaction should consist of 1) oxidative addition of a C–Sn bond, 2) insertion of an alkyne, and 3) reductive elimination to give the decarbonylative carbostannylation product with decarbonylation after step (1) or (2). Treatment of **1a** with $[Pd_2(dba)_3]$ in the absence of an alkyne gave no decarbonylated product, tributyl(phenyl)stannane, but benzil and hexabutyldistannane [Eq. (2)]. The result shows that the decarbonylation is likely to take place after step (2), namely, not before insertion of an alkyne moiety.[10] Accordingly, the catalytic cycle may be described as shown in Scheme 1. Thus, after oxidative addition to an acyl–Sn bond, regioselective insertion of an alkyne into the Pd–Sn bond triggered by the coordination of the ester carbonyl group gave alkenyl palladium complex **5**.[11] Considering the high efficiencies of the arenecarboxylates with an electron-rich 2-furyl or 4-methoxyphenyl group (Table 1, entries 3 and 5), the high nucleophilicity of the carbonyl group in the arenecarboxylates is likely to be important in the promotion of this insertion step. Decarbonylation[12] from **5** followed by reductive elimination, which may be driven by the π-accepting character of the carbonyl ligand[13,14] in **6**, gives the decarbonylative carbostannylation product and regenerates the palladium(0) complex.

The carbostannylation products are unique reagents that possess both nucleophilic alkenylstannane and electrophilic allyl carboxylate moieties. The synthetic versatility of the tin reagents is demonstrated in Scheme 2. Reaction of **3e** with methyl 2-(bromomethyl)acrylate (**9**) under $[Pd_2(dba)_3]$ catalysis proceeded selectively at the alkenylstannane moiety to give **10**, whereas treatment of **3e** with sodium malonate in the presence of a Pd/PPh_3 catalyst transformed the furoate moiety to give **11** exclusively in 74% yield. These transformations were performed sequentially with bifunctional substrate **12** to afford cyclized product **14** via **13**.

In summary, we have demonstrated the decarbonylative addition of acylstannanes across propargyl 2-furoates to achieve the first aryl-, alkenyl-, and alkylstannylation reactions of alkynes. Both of the thus-obtained alkenylstannane and allyl furoate functionalities in the products have been shown to undergo the Kosugi–Migita–Stille cross-coupling and the Tsuji–Trost allylation, respectively. Our current efforts are directed to the expansion of the scope and elucidation of the detailed mechanism of the present chemistry.

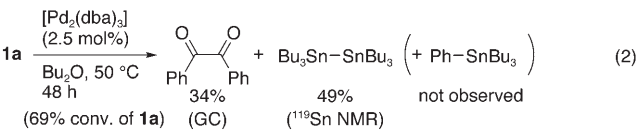

(2)

 © 2006 Wiley-VCH Verlag GmbH & Co. KGaA, Weinheim

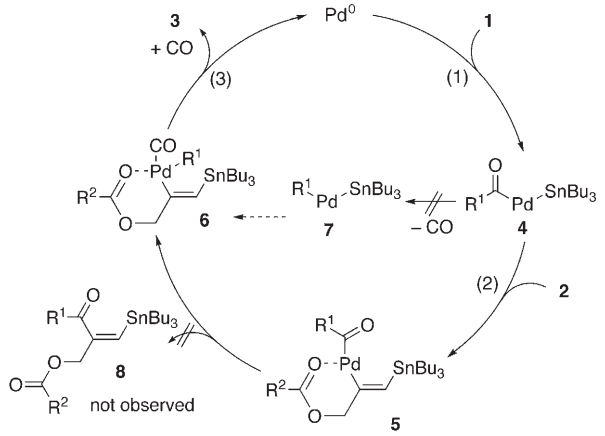

Scheme 1. A plausible catalytic cycle; see text for details.

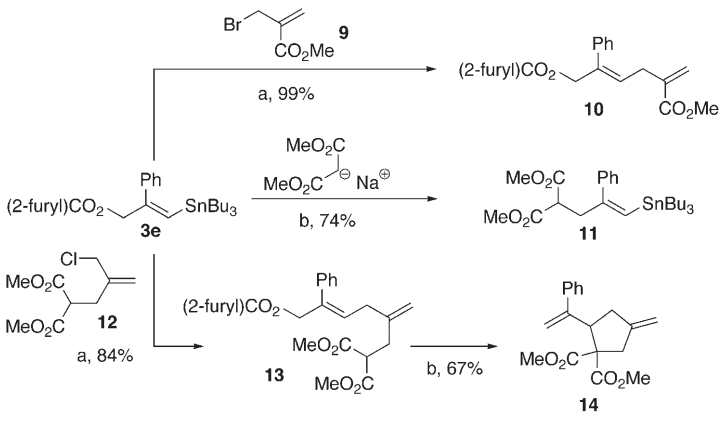

Scheme 2. Transformations of phenylstannylation product **3e**. a) $[Pd_2(dba)_3]$ (5 mol%), *N*-methylpyrrolidone, 50°C, 2–3 h; b) $[\{PdCl(\eta^3C_3H_5)\}_2]$ (2.5 mol%), PPh_3 (10 mol%), THF, room temperature, 3.5 h.

Experimental Section

General procedure for the decarbonylative carbostannylation of propargyl esters: Pd/C (10 wt%, 0.2 mg) was added to a solution of an acylstannane (0.10 mmol) and a propargyl ester (0.20 mmol) in dibutyl ether (0.15 mL), and the resulting reaction mixture was stirred at 50°C for the time specified in Tables 1 and 2. The reaction mixture was filtered through a Florisil pad, concentrated in vacuo, and purified by flash chromatography (hexane/ethyl acetate) on silica gel to give carbostannylation products.

Received: December 2, 2005
Published online: March 3, 2006

Keywords: C–C coupling · metalation · palladium · tin

[1] a) J. F. Normant, A. Alexakis, *Synthesis* **1981**, 841–870; b) P. Knochel in *Comprehensive Organic Synthesis, Vol. 4* (Eds.: B. M. Trost, I. Fleming, M. F. Semmelhack), Pergamon, New York, **1991**, pp. 865–911; c) I. Marek, J. F. Normant in *Metal-Catalyzed Cross-Coupling Reactions* (Eds.: F. Diederich, P. J. Stang), Wiley-VCH, Weinheim, **1998**, pp. 271–337; d) A. G. Fallis, P. Forgione, *Tetrahedron* **2001**, *57*, 5899–5913.

[2] a) E. Shirakawa, H. Yoshida, T. Kurahashi, Y. Nakao, T. Hiyama, *J. Am. Chem. Soc.* **1998**, *120*, 2975–2976; b) E. Shirakawa, K. Yamasaki, H. Yoshida, T. Hiyama, *J. Am. Chem. Soc.* **1999**, *121*, 10221–10222; c) E. Shirakawa, H. Yoshida, Y. Nakao, T. Hiyama, *Org. Lett.* **2000**, *2*, 2209–2211; d) H. Yoshida, E. Shirakawa, T. Kurahashi, Y. Nakao, T. Hiyama, *Organometallics* **2000**, *19*, 5671–5678; e) R. Hua, S. Onozawa, M. Tanaka, *Organometallics* **2000**, *19*, 3269–3271; f) E. Shirakawa, Y. Yamamoto, Y. Nakao, T. Tsuchimoto, T. Hiyama, *Chem. Commun.* **2001**, 1926–1927; g) B. Martín-Matute, E. Buñuel, M. Méndez, C. Nieto-Oberhuber, D. J. Cárdenas, A. M. Echavarren, *J. Organomet. Chem.* **2003**, *687*, 410–419; h) E. Shirakawa, Y. Yamamoto, Y. Nakao, S. Oda, T. Tsuchimoto, T. Hiyama, *Angew. Chem.* **2004**, *116*, 3530–3533; *Angew. Chem. Int. Ed.* **2004**, *43*, 3448–3451; for accounts, see: i) E. Shirakawa, T. Hiyama, *Bull. Chem. Soc. Jpn.* **2002**, *75*, 1435–1450; j) E. Shirakawa, T. Hiyama, *J. Organomet. Chem.* **2002**, *653*, 114–121.

[3] The allylstannylation of alkynes through the nucleophilic addition of allylstannanes across alkynes activated by a Lewis acid is known, see: a) N. Asao, Y. Matsukawa, Y. Yamamoto, *Chem. Commun.* **1996**, 1513–1514; b) Y. Matsukawa, N. Asao, H. Kitahara, Y. Yamamoto, *Tetrahedron* **1999**, *55*, 3779–3790; for the radical-mediated allylstannylation of alkynes, see: c) K. Miura, D. Itoh, T. Honda, H. Saito, H. Ito, A. Hosomi, *Tetrahedron Lett.* **1996**, *37*, 8539–8542.

[4] For alkynylstannanes, see: a) B. Cetinkaya, M. F. Lappert, J. McMeeking, D. E. Palmer, *J. Chem. Soc., Dalton Trans.* **1973**, 1202–1208; b) E. Shirakawa, H. Yoshida, T. Hiyama, *Tetrahedron Lett.* **1997**, *38*, 5177–5180; c) M. Herberhold, U. Steffl, W. Milius, B. Wrackmeyer, *Chem. Eur. J.* **1998**, *4*, 1027–1032; d) T. Matsubara, K. Hirao, *Organometallics* **2002**, *21*, 4482–4489; for allyl and acylstannanes, see references [2g] and [2e], respectively.

[5] Many reports on the oxidative addition of organostannanes to platinum(0) complexes are available, see: a) C. Eaborn, A. Pidcock, B. R. Steele, *J. Chem. Soc., Dalton Trans.* **1976**, 767–776; b) G. Butler, C. Eaborn, A. Pidcock, *J. Organomet. Chem.* **1978**, *144*, C23–C25; c) G. Butler, C. Eaborn, A. Pidcock, *J. Organomet. Chem.* **1979**, *181*, 47–59; d) C. Eaborn, K. Kundu, A. Pidcock, *J. Chem. Soc., Dalton Trans.* **1981**, 1223–1332.

[6] The palladium-catalyzed arylstannylation of norbornene using aryl(trichloro)stannanes has been proposed to proceed through the oxidative addition of an Ar–Sn bond to palladium(0) complexes, see: a) K. Fugami, Y. Mishiba, S. Hagiwara, D. Koyama, M. Kameyama, M. Kosugi, *Synlett* **2000**, 553–555; aryl- and alkenylstannanes undergo the palladium-catalyzed dimerization/carbostannylation of alkynes not through oxidative addition but through the reaction with palladacyclopentadienes; see: b) H. Yoshida, E. Shirakawa, Y. Nakao, Y. Honda, T. Hiyama, *Bull. Chem. Soc. Jpn.* **2001**, *74*, 637–647.

[7] Acyl(tributyl)stannanes are readily prepared by the reaction of aldehydes with tributylstannylmagnesium or -lithium reagents, see: a) M. Kosugi, H. Naka, T. Sano, T. Migita, *Bull. Chem. Soc. Jpn.* **1987**, *60*, 3462–3464; b) J. A. Marshall, A. W. Garofalo, K. W. Hinke, *Org. Synth.* **1999**, *77*, 98–106.

[8] For decarbonylative 1,4-carbosilylation of 1,3-dienes through three-component coupling, see: a) Y. Obora, Y. Tsuji, T. Kawamura, *J. Am. Chem. Soc.* **1995**, *117*, 9814–9821; b) Y. Obora, Y. Tsuji, T. Kawamura, *J. Am. Chem. Soc.* **1993**, *115*, 10414–10415.

[9] The use of other ethereal solvents, such as THF, 1,4-dioxane, 1,2-dimethoxyethane (DME), toluene, and dimethyl formamide (DMF), gave inferior results.

[10] In contrast, benzoyl(trimethyl)stannane is readily decarbonylated to give trimethyl(phenyl)stannane upon treatment with a catalytic amount of $[Ni(cod)_2]$ in the absence of an unsaturated

 © 2006 Wiley-VCH Verlag GmbH & Co. KGaA, Weinheim

compound, see: E. Shirakawa, Y. Nakao, H. Yoshida, T. Hiyama, *J. Am. Chem. Soc.* **2000**, *122*, 9030 – 9031.

[11] A similar regioselective insertion of propargyl pivalate into a H–Pt bond has been proposed, see: G. Stork, M. E. Jung, E. Colvin, Y. Noel, *J. Am. Chem. Soc.* **1974**, *96*, 3684 – 3686.

[12] Acyl–palladium intermediates are reluctant to undergo decarbonylation ($\approx$200 °C), as observed in the palladium-catalyzed decarbonylation of acyl halides or aldehydes, whereas the presence of an alkene and/or a base accelerates decarbonylation in the decarbonylative coupling reaction of acid chlorides with alkenes; see reference [8] and a) J. O. Hawthorne, M. H. Wilt, *J. Org. Chem.* **1960**, *25*, 2215 – 2216; b) J. Tsuji, K. Ohno, *J. Am. Chem. Soc.* **1968**, *90*, 94 – 98; c) J. W. Verbicky, Jr., B. A. Dellacoletta, L. Williams, *Tetrahedron Lett.* **1982**, *23*, 371 – 372; d) H.-U. Blaser, A. Spencer, *J. Organomet. Chem.* **1982**, *233*, 267 – 274.

[13] No side products, such as a hydrostannylation product derived from β-hydride elimination, were observed during the reaction of tributyl(propanoyl)stannane (Table 2, entry 7), thus implying rapid reductive elimination from **6**; for CO-induced reductive elimination, see: T. Yamamoto, J. Ishizu, T. Kohara, S. Komiya, A. Yamamoto, *J. Am. Chem. Soc.* **1980**, *102*, 3758 – 3764.

[14] The reaction under identical conditions to entry 4 in Table 2 but under a CO atmosphere (1 atm) gave adduct **3i** in less than 20% yield, and no trace amounts of a non-decarbonylative adduct, such as **8**, was observed.

 © 2006 Wiley-VCH Verlag GmbH & Co. KGaA, Weinheim

Domino Reactions

DOI: 10.1002/anie.200504247

Highly Diastereoselective One-Pot Synthesis of Spirocyclic Oxindoles through Intramolecular Ullmann Coupling and Claisen Rearrangement**

*Hiroshi Miyamoto, Yoichiro Okawa, Atsuo Nakazaki, and Susumu Kobayashi**

Oxindoles that incorporate a quaternary stereogenic center at C3 are attractive targets in organic synthesis because of their significant biological activities as well as wide-ranging utility as synthetic intermediates for alkaloids, drug candidates, and clinical pharmaceuticals.[1] Therefore, a number of synthetic methods have been developed in pursuit of this structure, including intermolecular alkylations,[2] palladium-catalyzed reactions,[1c,3] cycloadditions,[4] and sigmatropic rearrangements.[5] We recently developed the stereoselective synthesis of spiro[4.5]decane frameworks through a Claisen rearrangement of alkenyl bicyclic dihydropyrans.[6,7] On the basis of this result, we envisioned that a Claisen rearrangement of alkenyl pyranoindoles **2** would produce 3-spiro-2-oxindoles **3**, which are potential synthetic intermediates for indole alkaloids. Pyranoindoles **2** might, in turn, be prepared by an intramolecular Ullmann coupling (IUC) of haloindoles **1** bearing an allylic alcohol unit (Scheme 1).[8]

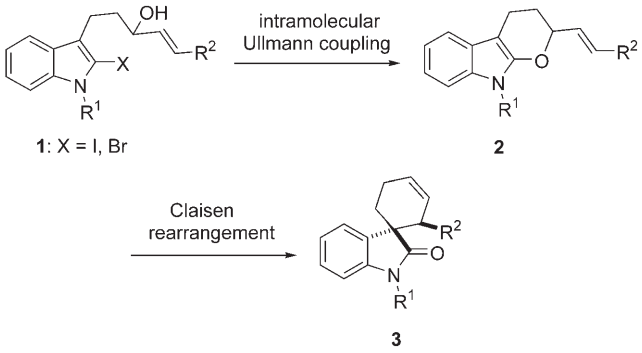

Scheme 1. General scheme for the construction of spirocyclic oxindoles **3**.

Herein we report an efficient and convenient method for the synthesis of spirocyclic oxindoles from haloindoles. The most striking feature of this approach is that it is a one-pot procedure in which the IUC of **1** and Claisen rearrangement of **2** proceed successively to provide 3-spiro-2-oxindoles **3** in good yields with high diastereoselectivities.[9]

To our knowledge, few general procedures are available for the preparation of **2**, and considering the reported properties of the unsubstituted pyranoindole, it was anticipated that **2** would be sensitive to acidic conditions.[10] Hence, we decided to examine the transition-metal-catalyzed intramolecular C–O coupling of **1** which is usually carried out under basic conditions. For C–O bond formation, the copper-mediated Ullmann-type reaction was chosen owing to its ease and lower cost.[11] Although several recent syntheses have involved IUC, these examples are much rarer than the intermolecular version.[12] As a preliminary survey, we compared several known procedures in which various 2-haloindoles **1** (R^1 = Me, SO_2Ph, R^2 = Me, *n*Bu) were employed. As a result, the Hauptman protocol (CuCl/2-aminopyridine, NaOMe)[13] was found to be effective and proceeds in moderate yield (up to 60%). However, direct application of the original Hauptman method to our indole substrates suffered from poor reproducibility. After many trials with **1a**, which can be readily prepared from commercially available *N*-methylindole by a three-step sequence,[14] we solved this problem with the following minor modifications: 1) Addition of a small amount of MeOH (≈2% *v*/*v*), and 2) more base (NaOMe). Under these optimized

[*] Y. Okawa, Dr. A. Nakazaki, Prof. Dr. S. Kobayashi
Faculty of Pharmaceutical Sciences
Tokyo University of Science
2641 Yamazaki, Noda-shi, Chiba 278-8510 (Japan)
Fax: (+81) 4-7121-3671
E-mail: kobayash@rs.noda.tus.ac.jp
H. Miyamoto
Process Development Laboratories
Sankyo Co. Ltd.
1-12-1 Shinomiya, Hiratsuka-shi, Kanagawa 254-8560 (Japan)

[**] We thank Professor Takao Ikariya and Professor Shigeki Kuwata (Tokyo Institute of Technology) for X-ray crystallographic analysis. We also thank Shin-Etsu Chemical Co. Ltd. for a gift of silicone oil.

Supporting information for this article is available on the WWW under http://www.angewandte.org or from the author.

InterScience
© 2006 Wiley-VCH Verlag GmbH & Co. KGaA, Weinheim

conditions, the yield of **2a** increased to 91% with good reproducibility (Scheme 2). The IUC of **1a** proceeded rapidly and was completed within 10 min. Interestingly, neither dehalogenated product **A** nor the product of cross-coupling

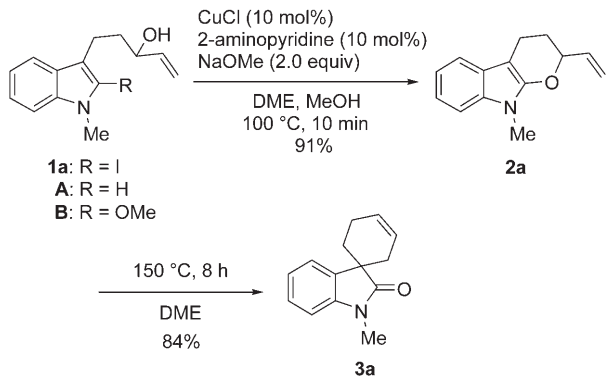

Scheme 2. Stepwise synthesis of oxindole **3a**. DME = 1,2-dimethoxyethane.

with NaOMe, **B**, was obtained. Finally, the isolated product **2a** underwent Claisen rearrangement, as expected, to afford the desired oxindole **3a** by heating in 1,2-dimethoxyethane (DME) at 150 °C.

As **2a** is relatively unstable, especially under acidic conditions, we next attempted a one-pot synthesis of **3a** (Table 1). When the reaction mixture was heated at 100 °C for 24 h, **3a** was obtained in 53% yield (Table 1, entry 1). On the other hand, when the reaction temperature was increased to 150 °C after complete formation of **2a** (100 °C, 10 min), the rearrangement of **2a** proceeded cleanly to afford **3a** in 84% yield (Table 1, entry 2). The IUC was completed with 5 mol% of CuCl and 2-aminopyridine, although a longer reaction time

Table 1: One-pot synthesis of oxindole **3a**.[a]

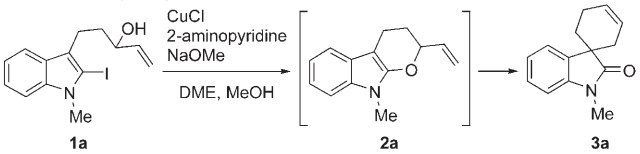

Entry	CuCl [mol%]	2-NH_2Py [mol%]	[**1a**] [mol L^{-1}]	Conditions	Yield of **3a** [%][b]
1	10	10	0.05	100 °C, 24 h	53[c]
2	10	10	0.05	100 °C, 10 min 150 °C, 12 h	84
3	5	5	0.05	100 °C, 3 h 150 °C, 12 h	80
4	10	10	0.10	100 °C, 10 min 150 °C, 12 h	72
5	0	0	0.05	100 °C, 24 h	6[d]

[a] Reaction conditions: indole **1a** (0.5 mmol), NaOMe/MeOH (25 wt%; 2.0 equiv), Ar, sealed tube. [b] Yield of isolated product. [c] **2a** was also obtained in 22% yield. [d] **1a** was recovered (74%) along with **2a** (10%).

was required (Table 1, entry 3). An increase in the concentration of **1a** from 0.05 to 0.10 mol L^{-1} resulted in a slightly lower yield owing to side reactions during the IUC step (Table 1, entry 4). In the absence of CuCl and 2-aminopyridine, the IUC was sluggish; the yield of **3a** dropped to 6%, and 74% of **1a** was recovered (Table 1, entry 5). This result clearly indicates that CuCl and 2-aminopyridine efficiently catalyze the IUC.

To study the effect of substituents on the Claisen rearrangement, compounds **1** with a variety of substituents on the allylic alcohol unit were explored next (Table 2). Notably, all the indoles with *trans*-oriented substituents on the allylic double bond afforded the corresponding oxindoles as a single isomer, irrespective of the substituents (Table 2, entries 1, 2, 6–11).[15] The relative configuration was assigned on the basis of an X-ray crystal structure of oxindole **3h** and NOE experiments.[14] The configuration of these products indicates that the Claisen rearrangement proceeds through a boatlike transition state, analogously to previous results.[16] In contrast, the reaction of the *cis* isomer **1c** did not give the desired product; instead decomposition of the initially formed **2c** was observed (Table 2, entry 3). This result can be rationalized by considering the unfavorable transition state as a result of the steric repulsion between the *cis*-oriented methyl group and the hydrogen atoms of the dihydropyran ring.

The rate of the Claisen rearrangement is strongly dependent on the presence of substituents on the allylic double bond. The reaction of substrates with an alkyl or aryl substituent on the allylic double bond is fast (Table 2, entries 1, 6, 8–10). In contrast, substrates with no substituent on the allylic double bond react slowly (Table 1, entry 2).[7a]

In the case of bromoindole **4**, although the reactivity in the IUC is apparently lower than that of iodide **1b**, the reaction proceeded to afford oxindole **3b** in 55% yield (Table 2, entry 2). Notably, sterically hindered substrates such as **1e** and **1g** gave the desired **3e** and **3g**, respectively, in good yields (Table 2, entries 5, 7). The slow reaction of **1g** could be accelerated without any side reactions by increasing the temperature. The fact that diol **1i** gave **3i** exclusively in 93% yield indicates that the allylic hydroxy group reacts selectively and that the IUC is tolerant of unprotected hydroxy groups (Table 2, entry 9). The low yield observed for **1k**, which bears a silyl group, is due to the formation of the desilylated products **3a** and its double-bond isomer (Table 2, entry 11).

The synthetic utility of N-methylated oxindoles is rather limited owing to the difficulty in the deprotection of the *N*-

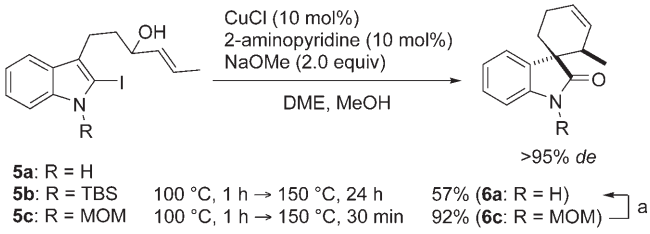

Scheme 3. Preparation of oxindole **6a**. Reagents and conditions: a) TMSCl, NaI, CH_3CN, 0 °C; then Et_3N, MeOH, 55 °C, 81%. MOM = methoxymethyl.

 © 2006 Wiley-VCH Verlag GmbH & Co. KGaA, Weinheim

Table 2: Synthesis of spirocyclic oxindoles.[a]

Entry	Substrate	Product[b]	Conditions	Yield [%][c]	*de* [%][d]
1	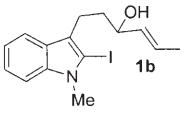 **1b**	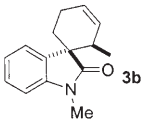 **3b**	100 °C, 30 min 150 °C, 1 h	89	> 95
2	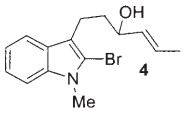 **4**	**3b**	100 °C, 24 h	55[e]	> 95
3	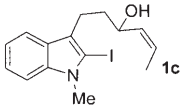 **1c**	Complex mixture	100 °C, 1.5 h 150 °C, 6 h	–	–
4	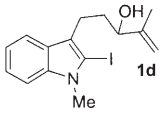 **1d**	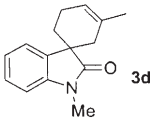 **3d**	100 °C, 4 h 150 °C, 1 h	80	–
5	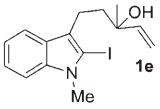 **1e**	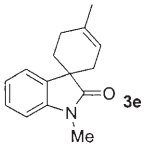 **3e**	130 °C, 21 h 150 °C, 1 h	84	–
6	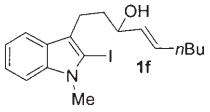 **1f**	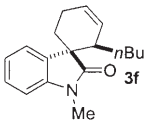 **3f**	100 °C, 1 h 150 °C, 1 h	92	> 95
7	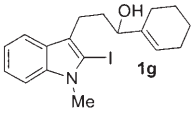 **1g**	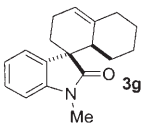 **3g**	100 °C, 22 h 120 °C, 11 h	89 90	> 95 > 95
8	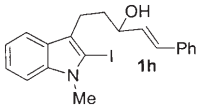 **1h**	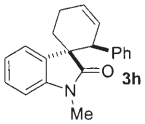 **3h**	100 °C, 1 h	84	> 95
9	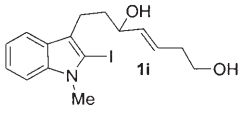 **1i**	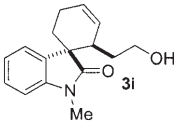 **3i**	100 °C, 30 min 150 °C, 1 h	93	> 95
10	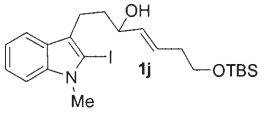 **1j**	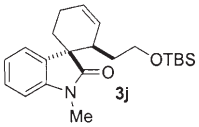 **3j**	100 °C, 1 h 150 °C, 40 min	66[f]	> 95
11	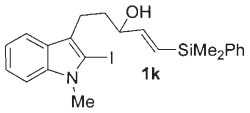 **1k**	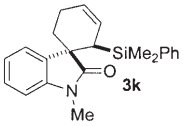 **3k**	100 °C, 5 h 150 °C, 2 h	20[g]	> 95

[a] Reaction conditions: substrate (0.5 mmol), CuCl (10 mol%), 2-aminopyridine (10 mol%), DME (10 mL), NaOMe/MeOH (25 wt%; 2.0 equiv), Ar, sealed tube. Reaction time and temperature were not optimized for each substrate. [b] For the determination of relative configuration, see the Supporting Information. [c] Yield of isolated product. [d] Determined by ^{1}H NMR spectroscopic analysis. [e] **4** was recovered (31%). [f] **3i** was isolated in 25% yield (> 95% *de*). [g] **3a** and its regioisomer were isolated in 47% yield (**3a**/isomer 2:1). TBS = *tert*-butyldimethylsilyl.

methyl group. Thus, we extended this method to the synthesis of free (NH) oxindoles. The unprotected iodoindole **5a** is not a suitable starting material for conversion into **6a**, as **5a** readily decomposes. Thus, several N-protected iodoindole substrates were prepared and exposed to similar conditions. *N*-TBS indole **5b** afforded the desired **6a** in 57% yield (Scheme 3). In this reaction, all of **5b** was converted into **5a** upon heating to 100 °C, as monitored by HPLC analysis. However, the subsequent IUC of **5a** was rather slow, and the reaction temperature had to be elevated to 150 °C to allow complete consumption of **5a**. In contrast, the methoxymethyl (MOM) group was found to be a suitable protecting group for the present transformation. The IUC of **5c** and Claisen rearrangement of the resultant pyranoindole proceeded smoothly to give **6c** in 92% yield as a single isomer. The MOM group was readily cleaved (81% yield) by the Fukuyama procedure.[17]

In summary, we have developed a convenient and efficient method for the preparation of spirocyclic oxindoles with vicinal stereogenic centers from the corresponding 2-haloindoles by a one-pot IUC and Claisen rearrangement. The IUC is a simple and low-cost method for the preparation of the rearrangement precursors, alkenyl pyranoindoles. The Claisen rearrangement of the pyranoindoles proceeds smoothly to give the desired oxindoles in good yields with high diastereoselectivities. The Claisen rearrangement is stereospecific in most cases; hence this method is also applicable to the enantioselective synthesis of spirocyclic oxindoles. Further applications of this reaction to chiral nonracemic substrates and the synthesis of natural products are underway.

Received: November 30, 2005
Published online: March 3, 2006

Keywords: cyclization · domino reactions · oxindoles · sigmatropic rearrangement · spiro compounds

[1] a) C. Marti, E. M. Carreira, *Eur. J. Org. Chem.* **2003**, 2209; b) M. Toyota, M. Ihara, *Nat. Prod. Rep.* **1998**, *15*, 327; c) A. B. Dounay, K. Hatanaka, J. J. Kodanko, M. Oestreich, L. E. Overman, L. A. Pfeifer, M. M. Weiss, *J. Am. Chem. Soc.* **2003**, *125*, 6261, and references therein.

[2] For recent examples, see: a) A. Huang, J. J. Kodanko, L. E. Overman, *J. Am. Chem. Soc.*

 © 2006 Wiley-VCH Verlag GmbH & Co. KGaA, Weinheim

2004, *126*, 14043; b) T. D. Bagul, G. Lakshmaiah, T. Kawabata, K. Fuji, *Org. Lett.* **2002**, *4*, 249.
[3] For a review on the intramolecular Heck reaction, see: a) A. B. Dounay, L. E. Overman, *Chem. Rev.* **2003**, *103*, 2945; for a recent example, see: b) B. M. Trost, M. U. Frederiksen, *Angew. Chem.* **2005**, *117*, 312; *Angew. Chem. Int. Ed.* **2005**, *44*, 308.
[4] For recent examples, see: a) S. R. Yong, M. C. Williams, S. G. Pyne, A. T. Ung, B. W. Skelton, A. H. White, P. Turner, *Tetrahedron* **2005**, *61*, 8120; b) E. M. Beccalli, F. Clerici, M. L. Gelmi, *Tetrahedron* **2003**, *59*, 4615.
[5] For recent examples, see: a) T. Kawasaki, A. Ogawa, R. Terashima, T. Saheki, N. Ban, H. Sekiguchi, K. Sakaguchi, M. Sakamoto, *J. Org. Chem.* **2005**, *70*, 2957; b) Z. Mao, S. W. Baldwin, *Org. Lett.* **2004**, *6*, 2425; c) K. I. Booker-Milburn, M. Fedouloff, S. J. Paknoham, J. B. Strachan, J. L. Melville, M. Voyle, *Tetrahedron Lett.* **2000**, *41*, 4657; d) M. Somei, F. Yamada, T. Izumi, M. Nakajou, *Heterocycles* **1997**, *45*, 2327.
[6] A. Nakazaki, H. Miyamoto, K. Henmi, S. Kobayashi, *Synlett* **2005**, *9*, 1417.
[7] For recent reviews on the Claisen rearrangement, see: a) A. M. M. Castro, *Chem. Rev.* **2004**, *104*, 2939; b) Y. Chai, S. Hong, H. A. Lindsay, C. McFarland, M. C. McIntosh, *Tetrahedron* **2002**, *58*, 2905.
[8] Excellent results have been reported in related examples of the Claisen rearrangement of 2-(allyloxy)indole systems.[5a]
[9] For an example of a domino copper-catalyzed C–O coupling and Claisen rearrangement in simple acyclic substrates, see: G. Nordmann, S. L. Buchwald, *J. Am. Chem. Soc.* **2003**, *125*, 4978.
[10] T. Hino, H. Miura, R. Murata, M. Nakagawa, *Chem. Pharm. Bull.* **1978**, *26*, 3695.
[11] For recent reviews on copper-catalyzed C–O bond formation, see: a) S. V. Ley, A. W. Thomas, *Angew. Chem.* **2003**, *115*, 5558; *Angew. Chem. Int. Ed.* **2003**, *42*, 5400; b) I. P. Beletskaya, A. V. Cheprakov, *Coord. Chem. Rev.* **2004**, *248*, 2337.
[12] For recent examples of applications of copper-catalyzed intramolecular C–O coupling in organic synthesis, see: a) C. Pan, Z. Ma, J. Yu, Z. Zhang, A. Hui, Z. Wang, *Synlett* **2005**, *12*, 1922; b) Y. Fang, C. Li, *Chem. Commun.* **2005**, 3574.
[13] P. J. Fagan, E. Hauptman, R. Shapiro, A. Casalnuovo, *J. Am. Chem. Soc.* **2000**, *122*, 5043.
[14] For details, see the Supporting information.
[15] In all successful cases in Table 2, the Claisen rearrangement also proceeded during the first heating step for the IUC.
[16] a) G. Büchi, J. E. Powell, Jr., *J. Am. Chem. Soc.* **1970**, *92*, 3126; b) H. Ko, E. Kim, J. E. Park, D. Kim, S. Kim, *J. Org. Chem.* **2004**, *69*, 112.
[17] T. Fukuyama, G. Liu, *J. Am. Chem. Soc.* **1996**, *118*, 7426.

 © 2006 Wiley-VCH Verlag GmbH & Co. KGaA, Weinheim

Cluster Compounds

DOI: 10.1002/anie.200503940

An Unprecedented Example of a Heterotrimetallic Main-Group $[L_2Al_2Ge_4Li_2S_7]$ Cluster Containing a Ge^{II}–Ge^{II} Donor–Acceptor Bond**

Zhi Yang, Xiaoli Ma, Rainer B. Oswald, Herbert W. Roesky, Chunming Cui, Hans-Georg Schmidt, and Mathias Noltemeyer*

Dedicated to Professor Hansgeorg Schnöckel on the occasion of his 65th birthday

Metal polysulfido complexes, especially of the hetero-multimetallic species, have attracted much interest because of their inherent fundamental chemistry as well as their potential applications.[1] In this field of research much has been focused on transition metals, whereas main-group-metal polysulfido complexes, particularly those bearing two or more different main-group metals, are very rare.[2] Although aluminum is the most abundant metal in the earth's crust, there are only a few aluminum-containing hetero-bimetallic sulfides known (Al-(μ-S)-Fe,[3] Al-(μ-S)-M (M = Zr, Ti)[4,5] because of the limitations in available synthetic methods. Furthermore, no aluminum-containing main-group hetero-trimetallic sulfides have been reported. Recently, $[\{LAl[(SLi)_2(thf)_2]\}_2]$ (**1**) was prepared by our research group and gives access to the preparation of aluminum-containing hetero-bimetallic sulfides.[4] Herein, we report a unique class of hetero-trimetallic main-group polysulfido $[L_2Al_2Ge_4Li_2S_7]$ cluster, in which the germanium(II) metal atoms act both as donors and acceptors in a single hetero-trimetallic species. To the best of our knowledge, such an example has never been demonstrated.

$[\{LAl(\mu\text{-}S)_2Ge_2\}_2(\mu\text{-}S)_3Li_2(thf)_2]$ (**2**) was synthesized by the reaction of **1** with $GeCl_2$·dioxane in a 7:16 molar ratio

[*] Z. Yang, X. Ma, Prof. Dr. H. W. Roesky, H.-G. Schmidt, M. Noltemeyer
Institut für Anorganische Chemie
Universität Göttingen
Tammannstrasse 4, 37077 Göttingen (Germany)
Fax: (+49) 551-39-3373
E-mail: hroesky@gwdg.de
Dr. R. B. Oswald
Institut für Physikalische Chemie
Universität Göttingen
Tammannstrasse 6, 37077 Göttingen (Germany)
Prof. Dr. C. Cui
Department of Chemistry
State Key Laboratory of Elemento-Organic Chemistry
Nankai University
Tianjin 300071 (P.R. China)

[**] This work was supported by the Fonds der Chemischen Industrie and the Göttinger Akademie der Wissenschaften. L = HC-(CMeNAr)$_2$, Ar = 2,6-*i*Pr$_2$C$_6$H$_3$.

Supporting information for this article is available on the WWW under http://www.angewandte.org or from the author.

© 2006 Wiley-VCH Verlag GmbH & Co. KGaA, Weinheim

(Scheme 1). $GeCl_2$·dioxane in THF was added to the solution of **1** in THF at −30 °C. Compound **1** is sparingly soluble in THF and thus formed a suspension in THF at low temperature. However, after adding $GeCl_2$·dioxane, the suspension became clear very quickly, which is an indication of the progress of the reaction. Subsequently, the solution was slowly warmed to room temperature. The solvent was removed in vacuo and the residue extracted with toluene. The resulting solution was kept at room temperature to enable isolation of **2** as light-yellow crystals. Corresponding reactions of **1** with $SnCl_2$ and $PbCl_2$ were tried. After adding $SnCl_2$ or $PbCl_2$ to **1** in THF, a dark-brown or black suspension appeared immediately. The dark isolated solids were not soluble in organic solvents and contained SnS and PbS, respectively.

Compound **2** was characterized by ^1H, ^{13}C, and ^7Li NMR spectroscopy in [D_6]benzene and by elemental analysis. Only one set of resonances for the ligand L is detected in the ^1H and ^{13}C NMR spectra of **2**, thus indicating that the two ligands are in the same chemical environment and are symmetrically arranged. Compound **2** is highly soluble both in benzene and toluene, but sparingly soluble in hexane.

Crystals of X-ray quality were obtained from a solution of **2** in toluene that was kept at room temperature for two days and crystallized in the monoclinic space group $P2_1/c$.[6] Its molecular structure is shown in Figure 1. It is interesting to note that the whole molecule has a crablike geometry, in which the core cluster is the crab's body, the two β-diketiminato ligands are its side claws, and the two {Li(thf)} units are its front pincers. The structure can also be viewed as a derivative of norbornane, if one omits the Li centers. The significant difference between the structure of **2** and those of [$LAl(\mu\text{-}S)_2MCp_2$] (M = Zr, Ti; Cp = C_5H_5),[4] which were prepared by the reaction of **1** with [Cp_2MCl_2], was a surprise. The structures of [$LAl(\mu\text{-}S)_2MCp_2$] (M = Zr, Ti) each contain an AlS_2M four-membered ring, whereas **2** consists of two AlS_2Ge_2 five-membered rings (Figure 2), which are connected by three sulfur bridges, thus forming the [$L_2Al_2Ge_4Li_2S_7$] cluster. Each AlS_2Ge_2 five-membered ring is in a gauche conformation. The two germanium atoms are connected by a Ge→Ge bond and are arranged opposite to the AlS_2 plane. The Ge→Ge bond length is 2.537 Å, which is longer than those reported for compounds containing a Ge=Ge double bond (2.213 to 2.347 Å).[7] Therefore, the Ge→Ge interaction in **2** should be considered a donor–acceptor bond. This kind of bonding has so far only been reported for [$(Me_3SiN{=}PPh_2)_2C{=}Ge{\rightarrow}Ge{=}C(Ph_2P{=}NSiMe_3)_2$],[8] however without support from experiment or theory. In this compound, the four-coordinate germanium atom behaves as a

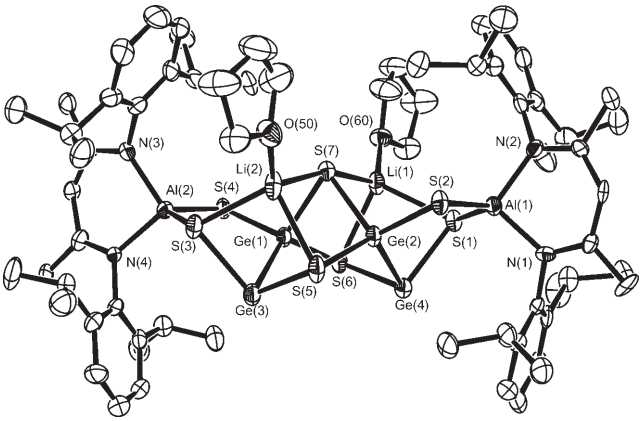

Figure 1. Molecular structure of **2**, thermal ellipsoids set at 50% probability. All hydrogen atoms and the toluene molecule are omitted for clarity. Selected bond lengths [Å] and angles [°]: Al(2)-S(4) 2.238(3), Al(2)-S(3) 2.221(4), Ge(1)-S(4) 2.233(3), Ge(3)-S(3) 2.408(2), Ge(1)-Ge(3) 2.532(1), Ge(1)-S(6) 2.246(2), Ge(1)-S(7) 2.345(2), Ge(3)-S(5) 2.395(3), Ge(4)-S(6) 2.386(3), Ge(2)-S(7) 2.332(3), Ge(2)-S(5) 2.256(2), Ge(2)-Ge(4) 2.537(1), Ge(4)-S(1) 2.387(2), Ge(2)-S(2) 2.239(3), Li(2)-S(3) 2.419(15), Li(2)-S(5) 2.455(15), Li(2)-S(7) 2.502(15); S(3)-Al(2)-S(4) 112.73(14), Al(2)-S(3)-Ge(3) 101.48(11), Al(2)-S(4)-Ge(1) 96.40(12), S(4)-Ge(1)-Ge(3) 111.03(7), S(3)-Ge(3)-Ge(1) 85.76(6), S(3)-Ge(3)-S(5) 94.22(9), S(4)-Ge(1)-S(6) 106.60(10), Ge(1)-S(6)-Ge(4) 99.97(10), Ge(1)-S(7)-Ge(2) 82.30(6), Ge(3)-S(5)-Ge(2) 99.94(10).

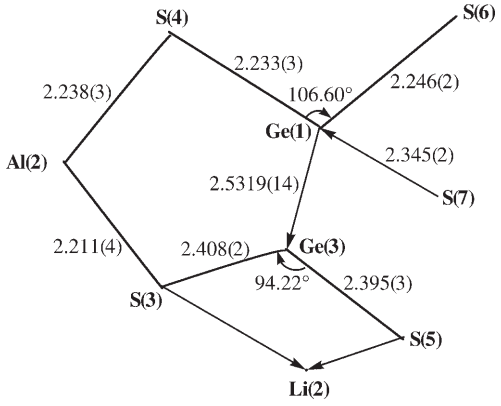

Figure 2. Comparison of the different coordination sites of the four-coordinate and the three-coordinate germanium atoms.

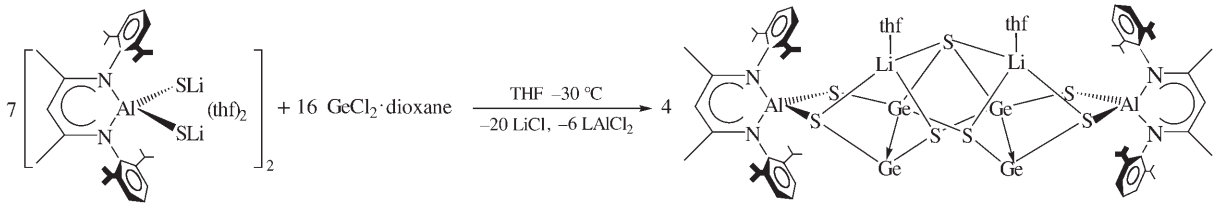

1 **2**

Scheme 1. Synthesis of **2**.

 © 2006 Wiley-VCH Verlag GmbH & Co. KGaA, Weinheim

donor, while the other, two-coordinate germanium atom behaves as an acceptor, and each germanium atom is coordinated both by carbon and nitrogen atoms. However, in compound **2**, two germanium atoms are four-coordinate and behave as donors, while the other two germanium atoms are three-coordinate and function as acceptors. Each germanium atom is surrounded by sulfur atoms. Each three-coordinate germanium atom has a lone pair of electrons, which is not included in the Ge→Ge bond. The two AlS_2Ge_2 five-membered rings are connected by three sulfur and two lithium atoms. Each of these sulfur atoms is coordinated to two germanium atoms, which are part of different five-membered rings. The germanium atoms with coordination number 3 have longer Ge–S bonds (av. 2.394 Å) than those with coordination number 4 (av. 2.244 Å). In the AlS_2Ge_2 five-membered ring, the $Ge–S_{(Al\text{-}S\text{-}Ge)}$ bond for the three-coordinate germanium atom (Ge(3)–S(3), 2.408(2) Å) is longer than that for the four-coordinate germanium atom (Ge(1)–S(4), 2.233(3) Å). The remaining Ge–S bond with three-coordinate germanium (Ge(3)–S(5), 2.395(3) Å) is also longer than the corresponding four-coordinate one (Ge(1)–S(6), 2.246(2) Å). The two $Ge_{(3\text{-coordinate})}$–S bond lengths are almost the same, and the two $Ge_{(4\text{-coordinate})}$–S bond lengths are nearly equal. This result could be explained by the fact that the $Ge_{(3\text{-coordinate})}$–S bonds (Ge(3)–S(3), Ge(3)–S(5)) are part of the Ge(3)–S(5)–Li(2)–S(3) four-membered ring. The strain of the ring makes the two $Ge_{(3\text{-coordinate})}$–S bonds longer than those in the noncyclic units. These Ge–S bond lengths are consistent with those of compounds previously reported (2.129–2.386 Å).[9] The S(3)-Ge(3)-S(5) angle (94.22°) is more acute than the S(4)-Ge(1)-S(6) (106.60°) angle, as a result of the strain of the GeS_2Li four-membered ring. The two lithium atoms are each coordinated to three sulfur atoms with the Li–S bond lengths (2.418 to 2.502 Å) comparable to those in the structure of the starting material **1** (2.478 to 2.424 Å).

According to the crystallographic data, there is a strong indication for the existence of a chemical bond between the germanium atoms. Thus, the molecule was investigated by means of quantum-chemical calculations. In a two-step approach, the molecule was first fully optimized with the DFT variant B3LYP,[10,11] as implemented in the Gaussian G03[12] program suite employing a 6-31G[13–15] basis set, and the resulting electronic structure was analyzed to get insight into the molecular orbitals.

As shown in Table 1, the resulting structure compares well with the data obtained by X-ray analysis and gives convincing support for the bond analysis. The NBO[16–18] results show that Ge(1) and Ge(2) each form one bond to their neighboring germanium atoms and three bonds to the sulfur atoms. The differences between the calculated and experimental bond lengths and angles result from the fact that Ge–Ge and Ge–S bonds are quite different when looking at the orbitals from which they are built. The valence orbitals (4s and 4p) of the germanium atoms Ge(1) and Ge(2) turn into p-rich hybrids of type $sp^{1.6}$, $sp^{3.37}$, $sp^{3.44}$, and $sp^{4.9}$ in the molecule, while the molecular orbitals of Ge(3) and Ge(4) can be described as pure p orbitals.

Table 1: Calculated bond lengths and angles for **2**.

Distance	Å	Angle	Deg
Ge(1)-Ge(3)	2.563	S(4)-Ge(1)-S(6)	110.91
Ge(1)-S(4)	2.308	Ge(1)-S(7)-Ge(2)	83.92
Ge(1)-S(6)	2.321	Al(2)-S(3)-Ge(3)	100.73
Ge(1)-S(7)	2.420	S(4)-Ge(1)-Ge(3)	112.65
Al(2)-S(4)	2.326	Al(2)-S(4)-Ge(1)	95.34
Li(2)-S(7)	2.544	Ge(1)-S(6)-Ge(4)	102.23
Ge(3)-S(3)	2.471	S(3)-Ge(3)-S(5)	92.70
Ge(3)-S(5)	2.513	S(3)-Ge(3)-Ge(1)	86.52
Al(2)-S(3)	2.281	Ge(3)-S(5)-Ge(2)	102.30

The orbitals and their contributions are summarized in Table 2 (for clarity reasons only the values for Ge(1) and Ge(3) are given). Looking at the contributions of the germanium atoms in the Ge–Ge bond, it is clear that the overlap of the hybrid orbital with the pure p orbitals is large enough to form a bond with a length of 2.53 Å. Additional stabilization of this bond arises from the donor–acceptor interaction with the unoccupied antibonding Ge–S orbitals. This two-electron stabilizing interaction amounts to nearly 20 kcal mol^{-1}.

Table 2: Selected calculated data for **2**.

Bond	Occ.[a]	MO 1	Contr.[b] [%]	Type (contr. [%])	MO 2	Contr. [%]	Type (contr. [%])
Ge(1)-Ge(3)	1.878	Ge(1)	67.4	s(38.1) $p^{1.62}$(61.9)	Ge(3)	32.6	s(5.1) $p^{18.55}$(94.9)
Ge(1)-S(4)	1.950	Ge(1)	32.0	s(22.9) $p^{3.37}$(77.1)	S(4)	68.0	s(17.9) $p^{4.60}$(82.1)
Ge(1)-S(6)	1.960	Ge(1)	32.6	s(22.5) $p^{3.44}$(77.5)	S(6)	67.4	s(16.4) $p^{5.10}$(83.6)
Ge(1)-S(7)	1.950	Ge(1)	28.3	s(16.8) $p^{4.95}$(83.2)	S(7)	71.7	s(12.6) $p^{6.94}$(87.4)
Ge(3)-S(3)	1.942	Ge(3)	21.2	s(3.7) $p^{25.95}$(96.3)	S(3)	78.8	s(17.6) $p^{4.70}$(82.4)
Ge(3)-S(5)	1.941	Ge(3)	21.7	s(3.6) $p^{26.58}$(96.4)	S(5)	78.3	s(13.7) $p^{6.33}$(86.3)

[a] Occupancy. [b] Contribution.

In summary, we have synthesized and characterized a hetero-trimetallic $[L_2Al_2Ge_4Li_2S_7]$ cluster, which is the first polyhedron that contains a $Ge^{II}→Ge^{II}$ donor–acceptor bond with four-coordinate germanium atoms behaving as donors and three-coordinate germanium atoms showing acceptor properties. Moreover, the claim of a $Ge^{II}→Ge^{II}$ donor–acceptor bond is supported by theoretical calculations. In the molecular structure, the AlS_2Ge_2 five-membered rings are unique, as such rings have not been reported before.

 © 2006 Wiley-VCH Verlag GmbH & Co. KGaA, Weinheim

Experimental Section

All manipulations were performed under a dry and oxygen-free atmosphere (N_2 or Ar) by using Schlenk-line and glovebox techniques.

2: A solution of $GeCl_2$·dioxane (0.23 g, 1 mmol) in THF (10 mL) was added dropwise to a solution of **1** (0.67 g, 0.5 mmol) in THF (20 mL) at −30 °C. After the addition was complete, the reaction mixture was allowed to warm to room temperature, and stirring of the mixture was continued for 12 h. Finally, the solvent was removed in vacuo and the crude product was extracted with toluene (10 mL). After keeping the solution at room temperature for 2 days, **2** was isolated as light-yellow crystals. Yield: 0.27 g (69 %). Decomposition without melting at 300 °C. ^{1}H NMR (500 MHz, C_6D_6, 25 °C, TMS): δ = 1.15 (d, ^3J(H,H) = 6.8 Hz, 24 H, CH(CH_3)$_2$), 1.20 (d, ^3J(H,H) = 6.8 Hz, 24 H, CH(CH_3)$_2$), 1.49 (m, 8 H, O(CH$_2$CH_2)$_2$), 2.10 (s, 12 H, CH_3), 3.30 (sept, ^3J(H,H) = 6.8 Hz, 8 H, CH(CH$_3$)$_2$), 3.63 (m, 8 H, O(CH_2CH$_2$)$_2$), 4.88 (s, 2 H, CH), 7.30–7.40 ppm (m, 12 H, *m*-, *p*-ArH); ^{13}C NMR (125.77 MHz, C_6D_6, 25 °C, TMS) δ = 21.39 (CH$_3$), 23.41 (CH(CH_3)$_2$), 24.47 (CH(CH_3)$_2$), 25.16 (O(CH$_2$CH_2)$_2$)), 28.63 (CH(CH$_3$)$_2$), 67.99 (O(CH_2CH$_2$)$_2$), 94.28 (γ-CH), 123.57, 128.02, 137.86, 142.78 (Ar), 161.51 ppm (CN); ^{7}Li NMR (116.64 MHz, C_6D_6, 25 °C, $LiNO_3$) δ = 0.43 ppm. Elemental analysis calcd (%) for $C_{66}H_{98}Al_2Ge_4Li_2N_4O_2S_7$ (1564.24): C 50.75, H 6.32, N 3.59; found: C 50.21, H 6.14, N 3.14.

Received: November 7, 2005
Revised: January 6, 2006
Published online: March 3, 2006

Keywords: aluminum · cluster compounds · germanium · N ligands · sulfur

[1] N. Takeda, N. Tokitoh, R. Okazaki, *Top. Curr. Chem.* **2003**, *231*, 153–202.
[2] a) M. R. Dubois, *Chem. Rev.* **1989**, *89*, 1–9; b) C. Copéret, M. Chabanas, R. P. Saint-Arroman, J.-M. Basset, *Angew. Chem.* **2003**, *115*, 164–191; *Angew. Chem. Int. Ed.* **2003**, *42*, 156–181; c) C. Sinonnet-Jégat, F. Sécheresse, *Chem. Rev.* **2001**, *101*, 2601–2611; d) M. Draganjac, T. B. Rauchfuss, *Angew. Chem.* **1985**, *97*, 745–760; *Angew. Chem. Int. Ed. Engl.* **1985**, *24*, 742–757; e) A. Müller, W. Jaegermann, J. H. Enemark, *Coord. Chem. Rev.* **1982**, *46*, 245–280; f) A. Müller, E. Diemann, R. Jostes, H. Bögge, *Angew. Chem.* **1981**, *93*, 957–977; *Angew. Chem. Int. Ed. Engl.* **1981**, *20*, 934–954; g) D. Coucouvanis, *Adv. Inorg. Chem.* **1998**, *45*, 1–73; h) J. W. Kolis, *Coord. Chem. Rev.* **1990**, *105*, 195–219; i) A. Müller, *Polyhedron* **1986**, *5*, 323–340; j) R. Okazaki, *Phosphorus Sulfur Silicon Relat. Elem.* **2001**, *168*, 41–50.
[3] J. J. Weers, D. P. Eyman, *J. Organomet. Chem.* **1985**, *286*, 47–54.
[4] V. Jancik, H. W. Roesky, D. Neculai, A. M. Neculai, R. Herbst-Irmer, *Angew. Chem.* **2004**, *116*, 6318–6322; *Angew. Chem. Int. Ed.* **2004**, *43*, 6192–6196.
[5] C. J. Harlan, A. R. Barron, *J. Cluster Sci.* **1996**, *7*, 455–467.
[6] Crystal data for **2**·toluene: $C_{73}H_{106}Al_2Ge_4Li_2N_4O_2S_7$, M_r = 1564.24, monoclinic, space group $P2_1/c$, a = 17.5307(14), b = 21.8268(11), c = 21.3419(14) Å, $\alpha = \gamma = 90°$, β = 100.785(6)°, V = 8022.0(9) Å^3, Z = 4, ρ_{calcd} = 1.370 g cm^{-3}, $F(000)$ = 3440, $1.67 \le \theta \le 24.66°$, R_1 = 0.0599, wR_2 = 0.0654 ($I > 2\sigma(I)$); residual electron density: 1.122/−0.387 e Å^{-3}. The structure was solved with SHELXS-90 [19] and refined with SHELXL-97. [20] All non-hydrogen atoms were refined anisotropically. All hydrogen atoms were included at geometrically calculated positions and refined using the riding model. CCDC-287829 contains the supplementary crystallographic data for this paper. These data can be obtained free of charge from The Cambridge Crystallographic Data Centre via www.ccdc.cam.ac.uk/data_request/cif.
[7] a) K. M. Baines, W. G. Stibbs, *Adv. Organomet. Chem.* **1996**, *39*, 275–324; b) L. Pu, A. D. Phillips, A. F. Richards, M. Stender, R. S. Simons, M. M. Olmstead, P. P. Power, *J. Am. Chem. Soc.* **2003**, *125*, 11626–11636; c) M. Stender, A. D. Phillips, R. J. Wright, P. P. Power, *Angew. Chem.* **2002**, *114*, 1863–1865; *Angew. Chem. Int. Ed.* **2002**, *41*, 1785–1787; d) H. Schäfer, W. Saak, M. Weidenbruch, *Angew. Chem.* **2000**, *112*, 3847–4849; *Angew. Chem. Int. Ed.* **2000**, *39*, 3703–3705.
[8] W.-P. Leung, Z. X. Wang, H.-W. Li, T. C. W. Mak, *Angew. Chem.* **2001**, *113*, 2569–2571; *Angew. Chem. Int. Ed.* **2001**, *40*, 2501–2503.
[9] a) Z. T. Cygan, J. W. Kampf, M. M. B. Holl, *Inorg. Chem.* **2004**, *43*, 2057–2063; b) Z. T. Cygan, J. W. Kampf, M. M. B. Holl, *Organometallics* **2004**, *23*, 2370–2375; c) Z. T. Cygan, J. W. Kampf, M. M. B. Holl, *Inorg. Chem.* **2003**, *42*, 7219–7226; d) I. V. Borisova, C. Eaborn, M. S. Hill, V. N. Khrustalev, M. G. Kuznetzova, J. D. Smith, Y. A. Ustynyuk, V. V. Lunin, N. N. Zemlyansky, *Organometallics* **2002**, *21*, 4005–4008; e) M. Unno, Y. Kawai, H. Shioyama, H. Matsumoto, *Organometallics* **1997**, *16*, 4428–4434; f) M.-S. Wang, W.-T. Chen, L.-Z. Cai, G.-W. Zhou, G.-G. Guo, J.-S. Huang, *J. Cluster Sci.* **2003**, *14*, 495–504.
[10] C. Lee, W. Yang, R. G. Parr, *Phys. Rev. B.* **1988**, *37*, 785–789.
[11] B. Miehlich, A. Savin, H. Stoll, H. Preuss, *Chem. Phys. Lett.* **1989**, *157*, 200–206.
[12] Gaussian 03, *Revision C.02*, M. J. Frisch et al., see Supporting Information.
[13] R. Ditchfield, W. J. Hehre, J. A. Pople, *J. Chem. Phys.* **1971**, *54*, 724–728.
[14] P. C. Hariharan, J. A. Pople, *Theor. Chim. Acta* **1973**, *28*, 213–218.
[15] V. A. Rassolov, M. A. Ratner, J. A. Pople, P. C. Redfern, L. A. Curtiss, *J. Comput. Chem.* **2001**, *22*, 976–984.
[16] J. P. Foster, F. Weinhold, *J. Am. Chem. Soc.* **1980**, *102*, 7211–7218.
[17] A. E. Reed, F. Weinhold, *J. Chem. Phys.* **1985**, *83*, 1736–1740.
[18] A. E. Reed, L. A. Curtiss, F. Weinhold, *Chem. Rev.* **1988**, *88*, 899–926.
[19] G. M. Sheldrick, *SHELXS-90*, Program for Structure Solution; *Acta Crystallogr. Sect. A* **1990**, *46*, 467–473.
[20] G. M. Sheldrick, *SHELXL-97*, Program for Crystal Structure Refinement; University of Göttingen, Germany, **1997**.

 © 2006 Wiley-VCH Verlag GmbH & Co. KGaA, Weinheim

Immunoassays

DOI: 10.1002/anie.200502862

Label-Free Affinity Assays by Rapid Detection of Immune Complexes in Submicrometer Pores**

*Jeffrey D. Uram, Kevin Ke, Alan J. Hunt, and Michael Mayer**

We present herein a method that uses a submicrometer pore to detect and characterize immune complexes consisting of proteins such as staphylococcal enterotoxin B (an agent with bioterrorism potential) and polyclonal antibodies. The assay is rapid, label free, requires no immobilization or modification of the antibody or antigen, and achieves single-aggregate sensitivity by monitoring changes in electrical resistance when immune complexes pass through the submicrometer pore. Adopting a recently developed nanofabrication technique based on a femtosecond-pulsed laser made it possible to fabricate pores with conical geometries and diameters as small as 575 nm. These pores allowed sensing of immune complexes that consisted of 610–17 300 proteins and detection of proteins at concentrations as low as 30 nM. Monitoring the passage of individual immune complexes enabled determination of the size distribution and the growth of these complexes. This method senses immune complexes (and potentially other molecules or nanoparticles that can be induced to form specific assemblies) in solution, and the antibody or antigen to be detected can be present in complex media such as serum. Owing to the small footprint and simple detection scheme, submicrometer pore-based sensing of specific complexes may enable portable or high-throughput immunoassays for diagnostics and biodefense.

Coulter counting, which monitors the transient change in resistance (resistive pulse) that occurs when a particle passes through a small pore filled with electrolyte, is a technique for detecting and analyzing micro-, and increasingly, nanoscale objects. As the sensitivity of a Coulter counter increases with decreasing pore diameter and length,[1] numerous techniques have been developed for the fabrication of single-nanopore[2–10] or nanotube membranes.[1,11–13] Pore-forming proteins in planar lipid bilayers (PLBs) have been elegantly used as versatile nanopore sensors;[14–20] fabricated structures, in comparison, can offer a high degree of robustness and withstand environmental stress such as vibration, pressure, extreme pH, and elevated temperatures. Fabricated nanopores and nanotubes have been used for resistive-pulse sensing to detect viruses,[21] the aggregation of colloids,[22] DNA,[4,7–11] nanoparticles,[1,13,23,24] and proteins.[12,25] The two reports of protein detection relied either on immobilized molecular-recognition agents on the walls of the nanopore[25] or on functionalized colloids.[12] We hypothesized that a specific protein could be detected rapidly, without the need for immobilization or labeling, by combining a submicrometer pore with Coulter counting to monitor the formation of immune complexes in solution.

We adopted and optimized a recently developed nanomachining technique that employs femtosecond-pulsed lasers[26–28] to fabricate submicrometer pore structures in borosilicate glass coverslides (see Figure 1 and the Supporting Information). This technique has the advantage that it does not require masks, etching, or high vacuum and that it can fabricate in glass. Glass is an excellent substrate material owing to its low-noise properties,[29] its chemical and mechanical robustness, and its amenability to surface functionalization. Furthermore, laser nanomachining is able to fabricate complicated 3D structures in optically transparent substrates.[30] This enabled us to generate pores with a conical geometry and diameters of 575, 650 (Figure 1b,c), and 900 nm (see the Supporting Information). The conical shape made it possible to produce low-resistance pores in thick (> 1 μm) membranes that have low electrical capacitance.[31]

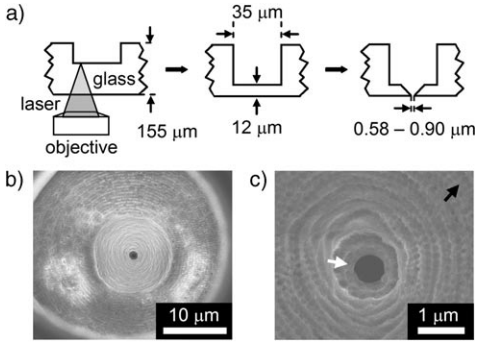

Figure 1. Laser-based fabrication of submicrometer pores with conical geometry. a) Femtosecond-pulsed lasers enabled nanomachining of conical pores in glass with diameters as small as 575 nm; b) Scanning electron microscope (SEM) image looking into the 35-μm cylinder of a pore (see a); c) SEM image focused on the narrowest part of the pore (diameter: 650 nm). The conical shape of the pores was confirmed by observing different focal planes with SEM (white arrow: in focus, black arrow: out of focus).

[*] Prof. M. Mayer
Departments of Biomedical Engineering and Chemical Engineering
University of Michigan
Engineering Research Building (ERB), Room 4107
2200 Bonisteel Blvd., Ann Arbor, MI 48109-2099 (USA)
Fax: (+1) 734-763-4371
E-mail: mimayer@umich.edu
J. D. Uram, K. Ke
Department of Biomedical Engineering
University of Michigan
Ann Arbor, MI 48109-2099 (USA)
Prof. A. J. Hunt
Department of Biomedical Engineering and Center for Ultrafast Optical Science
University of Michigan
Ann Arbor, MI 48109-2099 (USA)

[**] This work was supported by an NSF CAREER award (M.M.) and by a research grant from IMRA America and AISIN USA as well as seed funds from the College of Engineering, University of Michigan. The authors thank Daniel J. Estes, Amy P. Wong, Irina Gitlin, and Paul Bina for valuable discussions.

Supporting information for this article is available on the WWW under http://www.angewandte.org or from the author.

 © 2006 Wiley-VCH Verlag GmbH & Co. KGaA, Weinheim

Decreasing the resistance increases the amplitude of resistive pulses as well as the rate of transport through the pore for a given pore diameter.[7,24] Lowering the capacitance can reduce electrical-current noise,[31,32] which permits recording at high bandwidths[31] and increases the sensitivity of the Coulter counter.[13]

We mounted the glass slide with the pores onto a fluidic setup (Figure 2) made of poly(dimethylsiloxane) (PDMS) to

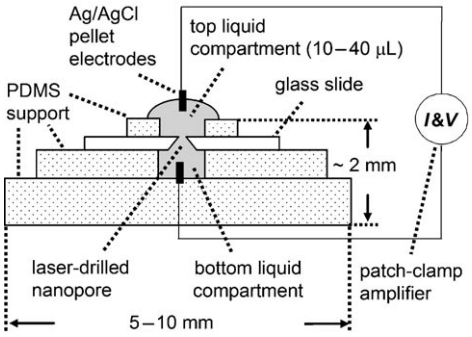

Figure 2. Side view of the experimental setup. A patch-clamp amplifier applies a constant voltage and detects small changes in current (pA-range) with fast time resolution (10–50 kHz). A poly(dimethylsiloxane) (PDMS) fluidic setup allows for replacement of solution on either side of the submicrometer pore.

characterize their electrical properties and to perform affinity assays. The composition of the recording buffer, the resulting electrical resistances, and noise values of the pores are listed in the Supporting Information. Before studying immune complexes, we characterized the response of the nano-Coulter counter by using synthetic nanoparticles. In a cylindrical pore, the resistive pulse from a spherical particle is proportional to the volume of the particle (as long as the particle diameter is less than ≈ 0.4 of the diameter of the pore).[1] When we passed particles with diameters of 100, 130, and 160 nm through a conical pore, we observed a linear relationship between the amplitude of the current peak and the particle volume (see the Supporting Information). This linear relationship, in conjunction with evidence that particles of the same volume but varying shape give rise to resistive pulses with similar amplitudes,[33] made it possible to estimate the volume of the immune complexes and consequently the number of proteins in a complex (see the Supporting Information).

To use the submicrometer pores to detect and characterize immune complexes, we monitored the resistive pulses that occurred when these complexes passed through the pore. The antibody–antigen model system investigated herein consisted of a goat anti-mouse antibody and a mouse monoclonal anti-baculovirus antibody as the antigen (see the Supporting Information). We examined three different equimolar concentrations (15, 30, and 151 nM) of the antigen and the anti-mouse antibody by using a pore with a diameter of 650 nm. The assay was able to detect immune complexes at a concentration of 151 nM and 30 nM as shown by the resistive pulses in Figure 3b,c; we did not detect any immune complexes at a concentration of 15 nM of antibody and antigen.

Figure 3b,c shows that the amplitudes of many resistive pulses, caused by the immune complexes formed at a concentration of 151 nM, were considerably larger than those formed at 30 nM. This result indicates that the immune complexes grew larger at 151 nM than they did at 30 nM, and may explain why no immune complexes could be detected at a concentration of 15 nM. Indeed, the immune complexes that formed at a concentration of 151 nM grew so large that they eventually blocked the pore (Figure 3b, the arrow indicates the onset of pore blockage; see the Supporting Information).

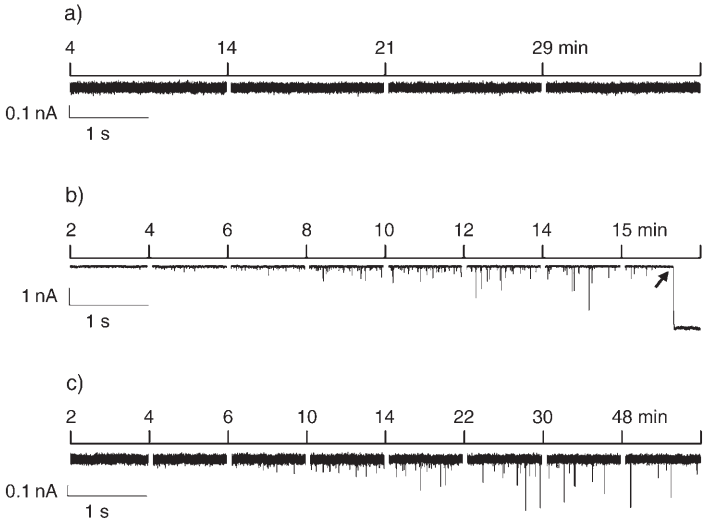

Figure 3. Time courses of the formation of immune complexes in solution. a) Control experiment with the antigen (mouse monoclonal anti-baculovirus antibody) and a nonspecific anti-rabbit antibody, both at a final concentration of 151 nM; b) At a final concentration of 151 nM of antigen and the specific anti-mouse antibody, detectable immune complexes formed rapidly and eventually blocked the pore (arrow). Note the *y*-scale of b) is ten times larger than the scale of the other traces owing to the large size of the immune complexes; c) At a lower antibody–antigen concentration (30 nM), detectable immune complexes formed but were smaller and did not block the pore. Each current trace is composed of multiple, short-duration recordings (length 1–2 s; see marked scale) that were taken from data files recorded during the course of the experiment; a small gap separates each of these short recordings. The time in minutes, after the addition of anti-mouse or anti-rabbit antibody to the recording buffer that contained the antigen, is indicated above the beginning of each short recording. These recordings therefore represent short "snapshots" of the current activity throughout the entire experiment of several minutes duration. A pore with a diameter of 650 nm (Figure 1b,c) was used for these experiments.

We performed a control experiment by using the same antigen and a nonspecific goat anti-rabbit antibody at a concentration of 151 nM. We did not detect any immune complexes or pore blockage in the presence of this control antibody (Figure 3a). Subsequent addition of the anti-mouse antibody at a concentration of 151 nM produced detectable

 © 2006 Wiley-VCH Verlag GmbH & Co. KGaA, Weinheim

immune complexes within 3 minutes, and blockage of the pore, owing to large immune complexes ("immunospecific" blockage), occurred after approximately 9 minutes. This blockage provided a dramatic response (significant and permanent change in the resistance of the submicrometer pore) that could be sensed by using simple electronics with low time resolution; it may potentially be useful for disposable, ultrasmall, and portable low-power sensors for the detection of biowarfare agents such as staphylococcal enterotoxin B (SEB) (see Figure 4), botolinum toxin, or ricin.[25]

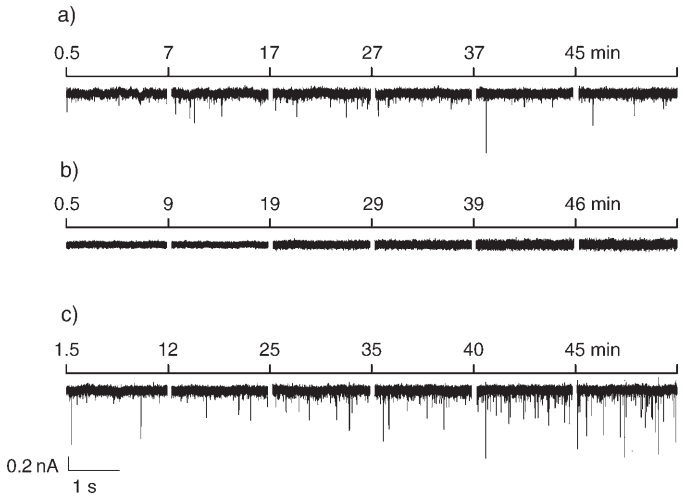

Figure 4. Detection of staphylococcal enterotoxin B (SEB) by sensing the formation of immune complexes in media containing a complex sample matrix. a) Current traces of anti-SEB serum only: one microliter of anti-SEB serum was added to 29 μL of recording buffer. The nonspecific events were caused by serum components that were not removed by a membrane filter with pores of 0.1 μm; b) Current traces of SEB only (final concentration: 200 nM); c) Current traces of SEB and anti-SEB serum: SEB at a final concentration of 200 nM and 1 μL of anti-SEB serum in a total volume of 32 μL. The addition of anti-SEB serum caused a significant increase in the number and size of events compared to a). Each current trace is composed of multiple, short-duration (length 2 s, see marked scale) recordings that were taken from data files recorded at different times during the experiment; a small gap separates each recording. The time in minutes after the addition of anti-SEB serum, or SEB, to the recording buffer is indicated above the beginning of each short recording.

To test the ability of the pore-based sensor to detect proteins on a relevant system in complex media, we detected staphylococcal enterotoxin B (SEB) by using sheep anti-SEB serum. SEB is a causative agent of food poisoning and has the potential for bioterrorism according to the National Institute of Allergy and Infectious Disease of the USA.[34] The addition of the anti-SEB serum to a solution containing SEB caused a large increase in the size and number of detectable aggregates when compared with the anti-SEB serum alone (Figure 4). We obtained similar results with a second system that employed rabbit antiserum to detect a monoclonal antibody (see the Supporting Information). These results demonstrate that submicrometer pore-based sensors can detect immune complexes in media that contain complex samples such as blood serum.

In addition to detecting immune complexes, and hence antigens or antibodies, submicrometer pore-based Coulter counting offers the possibility to evaluate specific properties of these complexes, such as their volume and growth rate. These properties are important as the size of an immune complex influences its physiological properties, for instance its clearance from circulation and its adherence to phagocytes.[35] Studying polydisperse immune complexes is difficult owing to their large heterogeneity. Light-scattering techniques have been used;[35,36] however, as they measure multiple particles at once, these techniques can be problematic for characterizing polydisperse samples.[37] In contrast, Coulter counting measures each particle individually and therefore can provide information on the volume, polydispersity, and growth of the immune complexes with single-aggregate sensitivity.

To demonstrate these capabilities, we monitored the increase in volume of immune complexes over time (Figure 5a,d). The general trend of the average peak amplitudes compares well with data obtained by light scattering.[36] The sigmoidal shape in Figure 5d may be a consequence of a thermodynamically stable size of the immune complexes.[38,39] Figure 5a,d shows that the standard deviation in the amplitude of the current peaks increased significantly during the growth of the immune complexes, therefore indicating a strong increase in the polydispersity of the complexes. Interestingly, the majority of the immune complexes sensed shortly after the addition of antibody (Figure 5b,e) had volumes that were comparable to complexes that were sensed after 8 (Figure 5c) and 40 min (Figure 5f). With increasing time, however, a fraction of the complexes reached volumes that were approximately two-times larger than that of the majority of the volumes (Figure 5f). This result suggests that the later stage of growth may have been caused by collisions between slowly diffusing complexes[36] and may explain the relatively rare formation of complexes that are significantly larger than the majority.

As a result of the linear relationship between the peak amplitude and volume of immune complexes, we were able to estimate the number of proteins in an aggregate by assuming a molecular volume of 347 nm^3 for an immunoglobulin G antibody.[40] The volumes of the immune complexes sensed by the pore with a diameter of 650 nm and an antibody antigen concentration of 151 nM ranged from 2.1×10^5–6.0×10^6 nm^3, which corresponds to aggregates of 610–17300 proteins.

Submicrometer pore-based detection of immune complexes offers a general, rapid, label-free, and solution-based method for the detection of any protein or particle that can be triggered to form a detectable assembly, while providing information on the volume, growth, and polydispersity of individual aggregates. The detection limit of 30 nM for antigens compares favorably to other label-free detection techniques such as affinity capillary electrophoresis (ACE), gel-based immunoprecipitation, and direct immunoaggregation assays based on light scattering, all of which have detection limits between 10 and 1000 nM depending on the technique.[41–43] In addition to its benefits for affinity assays with small footprints and reagent requirements, the technique presented herein may be particularly useful for in situ

 © 2006 Wiley-VCH Verlag GmbH & Co. KGaA, Weinheim

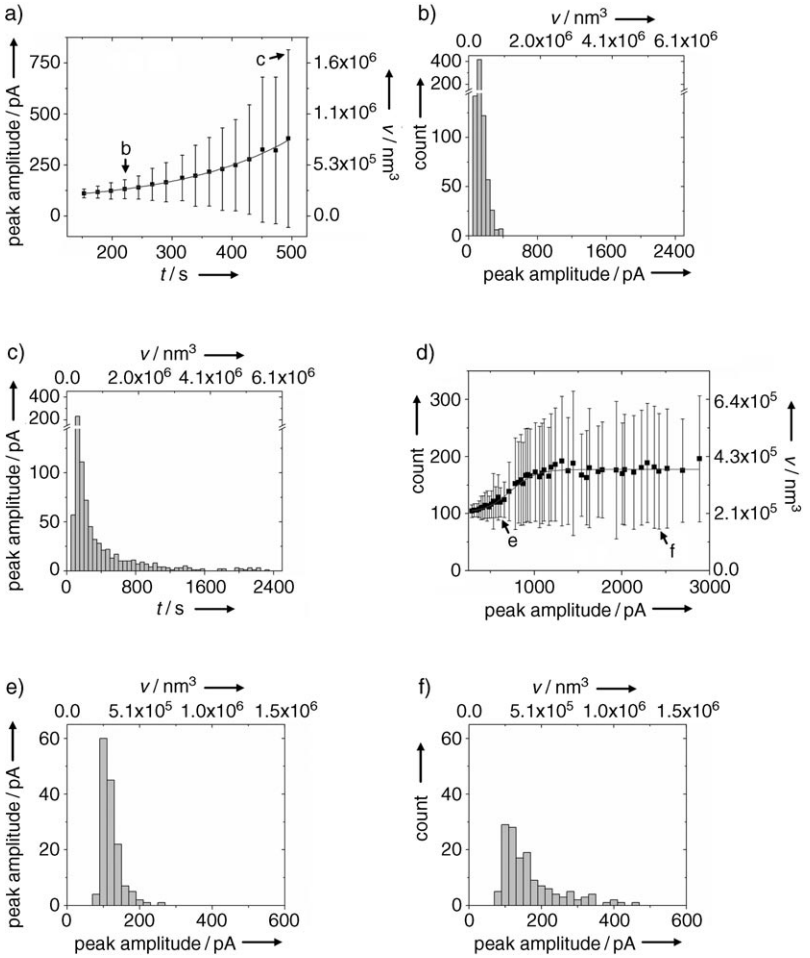

Figure 5. Time course of the current peak amplitudes and volumes of immune complexes. a) Growth of immune complexes at a concentration of 151 nM of both antigen (mouse monoclonal anti-baculovirus antibody) and anti-mouse antibody. A first-order exponential function was fitted to the data.[36] The small letters in graph a) corresponds to the time points from which the histograms shown in b) and c) were extracted; b) Peak amplitudes and volumes recorded at 240 s after the addition of anti-mouse antibody; c) Peak amplitudes and volumes recorded 490 s after addition of anti-mouse antibody. Note that 74% of the complexes maintained their volumes compared to b); however, a small fraction of complexes reached volumes that were up to ten times larger than in b); d) Growth of immune complexes at a concentration of 30 nM. A sigmoidal function was fitted to the data.[36] The small letters in graph d) correspond to the time points from which the histograms shown in e) and f) were estracted. e) Peak amplitudes and volumes recorded at 610 s after the addition of anti-mouse antibody; f) Peak amplitudes and volumes recorded 2400 s after the addition of anti-mouse antibody. Note the occurrence of peak amplitudes with approximately two, three, and four times the change in current (≈200, 300, 400 pA) of those shown in e). Each point in a), d) reflects the average amplitude and aggregate volume obtained from peaks over a period of 20 s.

monitoring of controlled assemblies of nanoparticles,[44–46] thereby addressing an urgent need in nanotechnology.[47]

Received: August 11, 2005
Revised: December 19, 2005
Published online: February 28, 2006

Keywords: Coulter counting · immunoassays · nanomachining · nanotechnology

[1] R. W. DeBlois, C. P. Bean, *Rev. Sci. Instrum.* **1970**, *41*, 909.
[2] N. Fertig, A. Tilke, R. H. Blick, J. P. Kotthaus, J. C. Behrends, G. ten Bruggencate, *Appl. Phys. Lett.* **2000**, *77*, 1218.
[3] P. Y. Apel, Y. E. Korchev, Z. Siwy, R. Spohr, M. Yoshida, *Nucl. Instrum. Methods Phys. Res. Sect. B* **2001**, *184*, 337.
[4] J. Li, D. Stein, C. McMullan, D. Branton, M. J. Aziz, J. A. Golovchenko, *Nature* **2001**, *412*, 166.
[5] C. C. Harrell, S. B. Lee, C. R. Martin, *Anal. Chem.* **2003**, *75*, 6861.
[6] A. J. Storm, J. H. Chen, X. S. Ling, H. W. Zandbergen, C. Dekker, *Nat. Mater.* **2003**, *2*, 537.
[7] P. Chen, T. Mitsui, D. B. Farmer, J. Golovchenko, R. G. Gordon, D. Branton, *Nano Lett.* **2004**, *4*, 1333.
[8] H. Chang, F. Kosari, G. Andreadakis, M. A. Alam, G. Vasmatzis, R. Bashir, *Nano Lett.* **2004**, *4*, 1551.
[9] J. B. Heng, C. Ho, T. Kim, R. Timp, A. Aksimentiev, Y. V. Grinkova, S. Sligar, K. Schulten, G. Timp, *Biophys. J.* **2004**, *87*, 2905.
[10] A. Mara, Z. Siwy, C. Trautmann, J. Wan, F. Kamme, *Nano Lett.* **2004**, *4*, 497.
[11] O. A. Saleh, L. L. Sohn, *Nano Lett.* **2003**, *3*, 37.
[12] O. A. Saleh, L. L. Sohn, *Proc. Natl. Acad. Sci. USA* **2003**, *100*, 820.
[13] T. Ito, L. Sun, R. M. Crooks, *Anal. Chem.* **2003**, *75*, 2399.
[14] J. J. Kasianowicz, E. Brandin, D. Branton, D. W. Deamer, *Proc. Natl. Acad. Sci. USA* **1996**, *93*, 13770.
[15] L. Gu, O. Braha, S. Conlan, S. Cheley, H. Bayley, *Nature* **1999**, *398*, 686.
[16] C. Schmidt, M. Mayer, H. Vogel, *Angew. Chem.* **2000**, *112*, 3267; *Angew. Chem. Int. Ed.* **2000**, *39*, 3137.
[17] A. F. Sauer-Budge, J. A. Nyamwanda, D. K. Lubensky, D. Branton, *Phys. Rev. Lett.* **2003**, *90*, 238101.
[18] S. Howorka, J. Nam, H. Bayley, D. Kahne, *Angew. Chem.* **2004**, *116*, 860; *Angew. Chem. Int. Ed.* **2004**, *43*, 842.
[19] E. Berkane, F. Orlik, A. Charbit, C. Danelon, D. Fournier, R. Benz, M. Winterhalter, *J. Nanobiotechnology* **2005**, *3:3*.
[20] J. Sánchez-Quesada, A. Saghatelian, S. Cheley, H. Bayley, M. R. Ghadiri, *Angew. Chem. Int. Ed.* **2004**, *43*, 3063.
[21] R. W. DeBlois, E. E. Uzgiris, D. H. Cluxton, H. M. Mazzone, *Anal. Biochem.* **1978**, *90*, 273.
[22] G. K. von Schulthess, G. B. Benedek, R. W. DeBlois, *Macromolecules* **1983**, *16*, 434.
[23] O. A. Saleh, L. L. Sohn, *Rev. Sci. Instrum.* **2001**, *72*, 4449.
[24] T. Ito, L. Sun, M. A. Bevan, R. M. Crooks, *Langmuir* **2004**, *20*, 6940.
[25] Z. Siwy, L. Trofin, P. Kohli, L. A. Baker, C. Trautmann, C. R. Martin, *J. Am. Chem. Soc.* **2005**, *127*, 5000.
[26] C. B. Schaffer, A. Brodeur, J. F. García, E. Mazur, *Opt. Lett.* **2001**, *26*, 93.
[27] A. P. Joglekar, H. Liu, G. J. Spooner, E. Meyhöfer, G. Mourou, A. J. Hunt, *Appl. Phys. B* **2003**, *77*, 25.
[28] A. P. Joglekar, H. Liu, E. Meyhöfer, G. Mourou, A. J. Hunt, *Proc. Natl. Acad. Sci. USA* **2004**, *101*, 5856.
[29] J. L. Rae, R. A. Levis, *Methods Enzymol.* **1992**, *207*, 66.
[30] K. Ke, E. Hasselbrink, A. J. Hunt, *Proc. SPIE-Int. Soc. Opt. Eng.* **2005**, *5714*, 53.
[31] M. Mayer, J. K. Kriebel, M. T. Tosteson, G. M. Whitesides, *Biophys. J.* **2003**, *85*, 2687.
[32] R. A. Levis, J. L. Rae, *Methods Enzymol.* **1998**, *293*, 218.
[33] R. K. Eckhoff, *J. Sci. Instrum.* **1967**, *44*, 648.
[34] http://www.niaid.nih.gov/dmid/eid/erd.htm.

 © 2006 Wiley-VCH Verlag GmbH & Co. KGaA, Weinheim

[35] R. M. Murphy, H. Slayter, P. Schurtenberger, R. A. Chamberlin, C. K. Colton, M. L. Yarmush, *Biophys. J.* **1988**, *54*, 45.
[36] N. N. Gorgani, S. B. Easterbrook-Smith, J. G. Altin, *Biochim. Biophys. Acta* **1996**, *1317*, 45.
[37] A. Bootz, V. Vogel, D. Schubert, J. Kreuter, *Eur. J. Pharm. Biopharm.* **2004**, *57*, 369.
[38] J. Liu, P. Lester, S. Builder, S. J. Shire, *Biochemistry* **1995**, *34*, 10474.
[39] L. C. Santora, Z. Kaymakcalan, P. Sakorafas, I. S. Krull, K. Grant, *Anal. Biochem.* **2001**, *299*, 119.
[40] S. W. Schneider, J. Lärmer, R. M. Henderson, H. Oberleithner, *Pflügers Arch.* **1998**, *435*, 362.
[41] R. M. Guijt-van Duijn, J. Frank, G. W. K. van Dedem, E. Baltussen, *Electrophoresis* **2000**, *21*, 3905.
[42] I. Roitt, J. Brostoff, D. Male, *Immunology*, 6th ed., Mosby, Edinburgh, UK, **2001**.
[43] C. P. Price, D. J. Newman, in *Principles and Practice of Immunoassay*, 2nd ed., Stockton Press, New York, NY, **1997**, *443*.
[44] P. Hazarika, B. Ceyhan, C. M. Niemeyer, *Angew. Chem.* **2004**, *116*, 66631; *Angew. Chem. Int. Ed.* **2004**, *43*, 6469.
[45] Z. Tang, N. A. Kotov, *Adv. Mater.* **2005**, *17*, 951.
[46] J. Yang, M. Mayer, J. K. Kriebel, P. Garstecki, G. M. Whitesides, *Angew. Chem.* **2004**, *116*, 1581; *Angew. Chem. Int. Ed.* **2004**, *43*, 1555.
[47] S. C. Glotzer, M. J. Solomon, N. A. Kotov, *AIChE J.* **2004**, *50*, 2978.

 © 2006 Wiley-VCH Verlag GmbH & Co. KGaA, Weinheim

Heterogeneous Catalysis

DOI: 10.1002/anie.200503220

On the Issue of the Deactivation of Au–Ceria and Pt–Ceria Water–Gas Shift Catalysts in Practical Fuel-Cell Applications**

*Weiling Deng and Maria Flytzani-Stephanopoulos**

In recent years, nanostructured Au catalysts have attracted a lot of attention as potential candidates for the removal of poisonous carbon monoxide from synthesis gas streams, thus upgrading hydrogen gas to be used as fuel at the anode of low-temperature fuel cells. The interest in Au nanoparticles has been motivated by the pioneering work of Haruta et al., who demonstrated the extremely high activity of finely dispersed Au on reducible oxide supports for CO oxidation.[1,2] Gold oxide systems have also been evaluated as potential catalysts for the water–gas shift (WGS) reaction[3–8] and the preferential oxidation of CO in H_2-rich fuel-gas streams.[9–16] Among these catalysts, the combination of Au with nanoscale cerium oxide (ceria) has been shown to be the most active low-temperature WGS catalyst[5,8] and one of the most selective preferential oxidation (PROX) catalysts[14–16] for application at 80–120 °C.

Nanocrystalline ceria has unique properties as an oxide support, as it increases the activity of Au toward CO oxidation[17] and the WGS reaction[4,5] by more than two orders of magnitude relative to microcrystalline ceria. Similar findings have been reported by Gorte and co-workers for Pt-group metals on nanoscale ceria.[18] Evidence in the literature has been mounting on the participation of the surface oxygen atoms of ceria in the catalysis of CO oxidation by dioxygen or water.[4,19,20]

Deactivation with time-on-stream and/or in shut-down/restart operation currently plagues all known WGS catalysts based on ceria[21–24] or copper oxide.[25] Kim and Thompson reported fast deactivation of their Au–ceria catalyst, which they attributed to the blockage of the active sites by carbonates and/or formates formed during the WGS reaction.[21] However, this fast extensive initial decline of activity of Au–ceria in the WGS reaction was not observed in a less H_2-rich gas composition.[5] In their report on the deactivation of Pt–ceria with time-on-stream, Zalc et al. claimed that over-reduction of ceria cannot be avoided, thus rendering ceria-supported catalysts impractical for the WGS reaction in fuel-cell systems.[22] Furthermore, in cyclic operation, including shut-down to room temperature and start-up of reactors, severe deactivation has been reported both for Pt–ceria[23] and Au–ceria[5] WGS catalysts. The activity of Pd–ceria and Pt–ceria for the WGS reaction can be partially recovered by reoxidation of the catalyst in oxygen at high temperatures (600 °C),[24] but this process is not practical in the continuous operation of a fuel-cell system. To the best of our knowledge, no in situ remedy of the deactivation problem has been reported. Herein, we present a new way to stabilize the activity of Au–ceria catalysts for the WGS and PROX reactions under realistic operating conditions.

We started from the observation that Au–ceria catalysts have excellent stability with time-on-stream under PROX conditions at 120 °C.[14] We further studied this type of catalyst in shut-down/start-up cycles of the PROX reactor under conditions that allowed water condensation on the catalyst. Interestingly, this did not affect the subsequent catalyst activity at 120 °C (Figure 1). After reaching steady state at 120 °C in the PROX reaction, the 0.28 $AuCe(Gd)O_x$ catalyst sample was cooled to room temperature and held under a continuous flow of the same gas mixture for 2 h before being reheated to 120 °C. Stable CO conversion was recovered. The sample was then cooled down to room temperature and held in the flowing full gas stream for 6 h; again, no drop of activity was found after reheating at 120 °C. Excellent performance in the shut-down/start-up cycling of the PROX reactor was also observed with another Au–ceria (La-doped) sample (0.57 $AuCe(La)O_x$; Figure 1). Remarkable stability was further found for the 0.28 $AuCe(Gd)O_x$ sample at higher conversions of CO when working with a higher O_2/CO ratio

[*] W. Deng, Dr. M. Flytzani-Stephanopoulos
Department of Chemical and Biological Engineering
Tufts University
Medford, MA 02155 (USA)
Fax: (+1) 617-627-3991
E-mail: mflytzan@tufts.edu

[**] This work was supported by the National Science Foundation, NIRT (Grant 0304515), and the Department of Energy, Basic Energy Sciences, Hydrogen Fuel Initiative (Grant DE-FG02-05ER15730).

Supporting information for this article is available on the WWW under http://www.angewandte.org or from the author.

 © 2006 Wiley-VCH Verlag GmbH & Co. KGaA, Weinheim

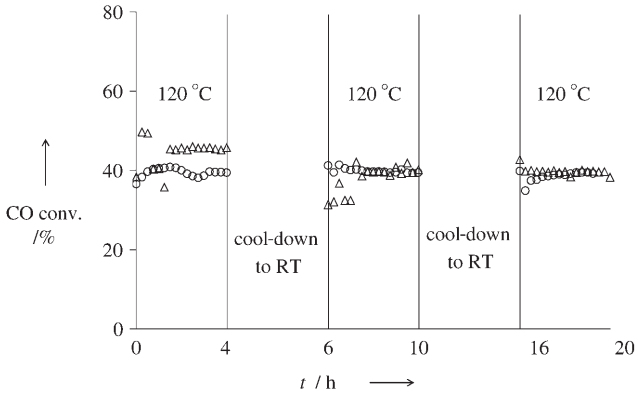

Figure 1. CO conversion versus time during a shut-down simulation of a PROX reactor using Au–ceria catalysts. Triangles: 0.28 AuCe(Gd)O_x; circles: 0.57 AuCe(La)O_x. Feed-gas mixture: 1:0.5:50:10:15:23.5 CO/O_2/H_2/H_2O/CO_2/He; W/F: 0.096 g s cm^{-3}. conv. = conversion. W/F = catalyst weight/gas flow rate.

(see the Supporting Information). Similarly, a Pt–ceria catalyst prepared by deposition–precipitation on nanocrystalline ceria also shows a stable performance in the shut-down/start-up operation, except that the CO conversion is only 10% because of the lower selectivity of this catalyst toward CO oxidation.

In stark contrast to the above, shut-down under WGS reaction conditions severely deactivates the Au–ceria[5] and Pt–ceria[23] catalysts. Formation of cerium(III) hydroxycarbonate was identified by X-ray diffraction (XRD; see the Supporting Information). To probe the reasons for the deactivation of Au–ceria in the WGS shut-down process further, we conducted temperature-programmed oxidation (TPO) of a used catalyst, 5.8 AuCe(La)O_x, which was retrieved after shut-down in the full gas mixture. Fresh 5.8 AuCe(La)O_x was also tested for comparison. As shown in Figure 2, adventitious carbonates were present on both the fresh and used catalysts, with a peak for CO_2 centered at around 160 °C and a corresponding peak for H_2O at the same temperature. However, in the used catalyst only, another CO_2 elution took place, with a peak centered at a higher temperature (approximately 320 °C). Water was also eluted over the same temperature range. We attribute the second set of peaks

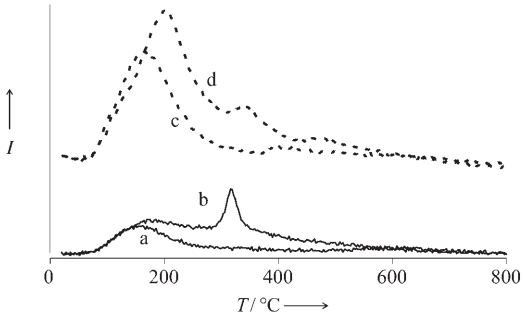

Figure 2. TPO profiles of 5.8 AuCe(La)O_x, as prepared and after a WGS shut-down operation. a) CO_2 from the fresh catalyst, b) CO_2 from the used catalyst, c) H_2O from the fresh catalyst, d) H_2O from the used catalyst.

to the oxidative decomposition of cerium(III) hydroxycarbonate. We believe that this species forms and causes the deactivation of Au–ceria catalysts during WGS shut-down, thus explaining why activity could not be recovered when the WGS reaction was reheated to 300 °C after the stop–start cycle. This reaction gas mixture, containing no oxygen, can not bring about the decomposition of cerium(III) hydroxycarbonate. To examine the recovery of activity when cerium(III) hydroxycarbonate is decomposed, reaction rates over three materials were measured in the 11:26:26:7:30 gas mixture of CO/H_2O/H_2/CO_2/He. All samples were first aged in this gas mixture at 300 °C for 5 h. The reaction rate for the fresh 5.8 AuCe(La)O_x catalyst was 3.6 μmol $CO_2\,g_{cat}^{-1}\,s^{-1}$ at 175 °C. After treatment in the WGS shut-down/start-up process, the deactivated catalyst shows a rate of only 0.9 μmol $CO_2\,g_{cat}^{-1}\,s^{-1}$. When the deactivated catalyst was oxidized at 375 °C in 10:90 O_2/He to complete the decomposition of cerium(III) hydroxycarbonate, the WGS reaction rate at 175 °C was 3.3 μmol $CO_2\,g_{cat}^{-1}\,s^{-1}$, a value close to the fresh material. However, this process is not a practical way to regenerate the catalyst in fuel-cell applications.

The TPO of the used Au–ceria catalysts retrieved from the start/stop operation under PROX conditions did not show the presence of cerium(III) hydroxycarbonate (see the Supporting Information). This discovery motivated us to consider the addition of gaseous oxygen as a potential stabilizer of the WGS activity of Au–ceria as oxygen is the main variant in the gas composition between the PROX and WGS reaction conditions.[26] Stability tests were carried out under the WGS reaction conditions with 0.5 mol% O_2 added into the feed-gas stream (see the Supporting Information). The long-term WGS stability of the 5.8 AuCe(La)O_x and 0.28 AuCe(Gd)O_x catalysts in the full reformate gas mixture (11:26:26:7:30 CO/H_2O/H_2/CO_2/He) with or without the addition of oxygen showed a clear trend of improved stability with the addition of 0.5 mol% O_2. The surface area of the used 0.28 AuCe(Gd)O_x catalyst when oxygen was added to the gas mixture was 123.6 $m^2\,g^{-1}$, which is higher than the surface area (103.7 $m^2\,g^{-1}$) of the used material after 50 hours on-stream without oxygen being present. It has been reported that the WGS gas composition controls the ratio of oxidized to neutral Au.[5] In the absence of in situ characterization, it is difficult to establish the effect of the two different gas mixtures on the oxidation state of the Ce and Au components; in particular, we do not know whether stabilization of oxidized Au suppresses the sintering of the ceria nanoparticles. However, XRD analysis of the two used materials is indicative of the structural difference between them: the size of the ceria particle (based on ⟨111⟩ diffraction) of 0.28 AuCe(Gd)O_x exposed to the oxygen-laden gas mixture remained the same as for the fresh material (5.4 nm), whereas the size of the ceria particle grew to 5.8 nm in the sample used in the O_2-free WGS gas composition.

We ruled out a potential thermal effect from the addition of oxygen in the WGS reaction gas mixture. Whereas oxidation of H_2 or CO by the added oxygen would increase the bed temperature, the catalyst runs almost isothermally at 300 °C under the conditions used. For the hypothetical case in which the reactor would run adiabatically with the gas

 © 2006 Wiley-VCH Verlag GmbH & Co. KGaA, Weinheim

composition used, we calculated an adiabatic temperature rise of 94 °C based on the combustion of 1 mol % CO with 0.5 mol % O_2 in the stream. Would operation at 400 °C therefore be the reason for the observed stability? Clearly, this is not the case as when the reaction was conducted at 400 °C in the full gas mixture without the addition of oxygen, the Au–ceria catalyst deactivated with time-on-stream (see the Supporting Information). The stabilization is not due to temperature rise. The maximum temperature increase in the gas film around the catalyst particles that results from the CO combustion reaction is < 0.1 °C, and the maximum temperature gradient within the particles is 23.6 °C (see the Supporting Information). We propose that even such a small amount of oxygen in the reacting gas mixture can change the dynamic surface equilibrium of the Au–ceria catalyst and modify the amount of oxidized Au/Ce species, which in turn controls the structural stability and activity of the surface in the WGS reaction mixture. Further work is warranted to examine this behavior in detail.

Another sequence of tests was conducted to investigate the effect of oxygen addition on the catalyst stability in the shut-down/start-up operation. The WGS reaction was carried out at 300 °C in the full 11:26:26:7:0.5:29.5 gas mixture of CO/H_2O/H_2/CO_2/O_2/He over 5.8 AuCe(La)O_x for 2 hours (Figure 3), and the CO conversion was over 65 %. When the heater was turned off, the same gas mixture, but without H_2O, was kept flowing through the reactor during the cooling transient (2 h), and the WGS reaction ceased. However, CO oxidation continued to occur at temperatures below 50 °C, thus accounting for the almost complete conversion of oxygen by CO oxidation. High CO conversion was recovered when the WGS reaction was restarted at 300 °C. The second cooling process was carried out in the full gas mixture (with 26 % H_2O present). Even in the presence of the gradually condensing water vapor, CO oxidation also took place at low temperature. Upon reheating, there was no decrease in the conversion of CO. Thus, shut-down/start-up in the full WGS gas mixture with the addition of 0.5 mol % oxygen does not affect the subsequent activity of the catalyst. Similar stabilization of the activity of the Au–ceria catalyst was observed in the shut-down (to room temperature)/start-up (at 150 °C) cyclic operation of the WGS reaction with 0.5 mol % O_2 present in the full WGS reaction gas mixture (see the Supporting Information). Both XRD and TPO analyses confirm that no cerium(III) hydroxycarbonate was formed during these cyclic tests.

How does oxygen prevent the deactivation of Au–ceria catalysts in the WGS reaction even during shut-down at room temperature? If oxygen stabilizes the activity, the oxygen concentration at the reactor outlet has to have a finite value. Otherwise, only a part of the catalyst bed can be under a higher oxygen potential, while the rest of the bed would deactivate as usual. The outlet oxygen concentration was estimated to be 930 ppm based on the rate of CO oxidation measured at 25 °C for this type of catalyst. The value measured experimentally was close at 726 ppm. Thus, oxygen is present throughout the catalyst bed and prevents the deactivation of ceria. From our findings, it appears that the oxygen potential of the gas, and not CO oxidation, is the critical factor for the observed stabilization, as clearly shown in Figure 4. Accordingly, in the shut-down process, CO was removed from the gas mixture during the cooling process to eliminate the effect of CO oxidation. Almost all of the oxygen added broke through at the exit of the reactor when the temperature was lower than 60 °C (hydrogen oxidation is also quenched at temperatures lower than 60 °C). When CO was added into the gas and the WGS reaction was restarted at 300 °C, full recovery of the activity was achieved. Evidently, the added oxygen oxidizes Ce^{III} to Ce^{IV}, thus preventing the formation of cerium(III) hydroxycarbonate. The TPO profile of the used 5 AuCe(La)O_x catalyst retrieved from this process is shown in Figure 5. CO_2 elution from the used catalyst is

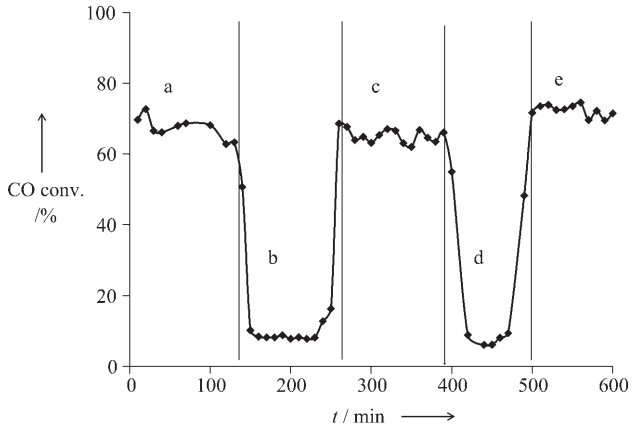

Figure 3. The effect of the addition of gaseous oxygen on 5.8 AuCe(La)O_x activity during a WGS shut-down/start-up operation. a) Reaction at 300 °C in feed gas; b) cool-down to room temperature in feed gas, except H_2O was preremoved; c) reaction at 300 °C in feed gas; d) cool-down to room temperature in feed gas; e) reaction at 300 °C in feed gas. Feed-gas mixture: 11:26:26:7:0.5:29.5 CO/H_2O/H_2/CO_2/O_2/He; S.V. = 30000 h^{-1}. S.V. = space velocity.

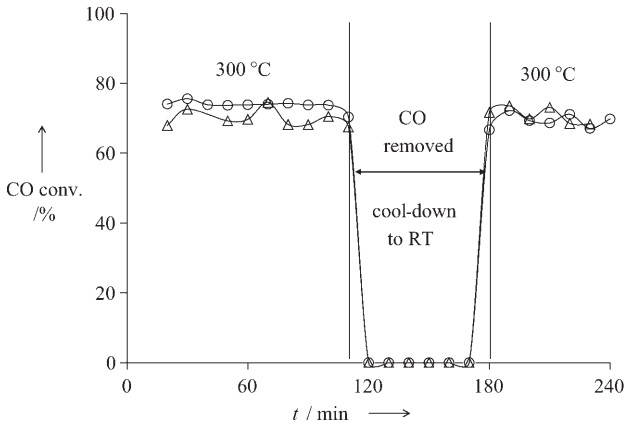

Figure 4. A stable WGS shut-down/start-up operation with 5 AuCe(La)O_x and 0.64 AuCe(Gd)O_x catalysts in the presence of added oxygen (CO was removed during the cooling process). Circles: 5 AuCe(La)O_x; triangles: 0.64 AuCe(Gd)O_x. Feed-gas mixture: 11:26:26:7:0.5:29.5 CO/H_2O/H_2/CO_2/O_2/He; S.V. = 30000 h^{-1}.

 © 2006 Wiley-VCH Verlag GmbH & Co. KGaA, Weinheim

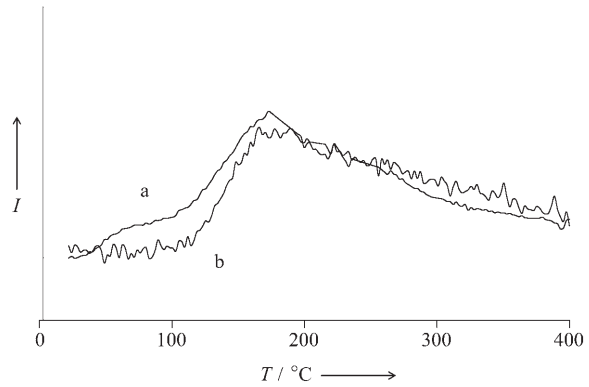

Figure 5. TPO profiles of fresh and used 5 AuCe(La)O_x catalyst after a WGS shut-down operation (CO was removed during the cooling process). a) Elution of CO_2 from used material, b) elution of CO_2 from fresh material. Test gas: 20:80 O_2/He (50 $cm^3 min^{-1}$ (NTP)); heating rate: 5 °C min^{-1}.

similar to the fresh material, thus proving that cerium(III) hydroxycarbonate did not form in the oxygen-laden WGS reaction gas mixture.

During the shut-down/start-up process, the addition of 0.5 mol% O_2 to a 10:10:60:7:13 gas mixture of CO/H_2O/H_2/CO_2/He did not stabilize the WGS activity of PtCe(La)O_x (see the Supporting Information). Pt-ceria has a much higher light-off temperature for CO oxidation than Au–ceria and does not sustain CO oxidation under shut-down conditions. It is possible that the oxygen potential in this particular gas mixture with very high H_2 content (60%) is not high enough to keep Pt–ceria free of carbonate. The oxygen potential was changed by varying the ratio of O_2/H_2 (Figure 6). We found that the addition of 1 mol% O_2 in the 11:26:26:7:30 gas mixture of CO/H_2O/H_2/CO_2/He was enough to stabilize this type of catalyst and prevent its deactivation. The higher concentration of oxygen gave better recovery than 0.5 mol% O_2, thus confirming that the oxygen potential is the key factor

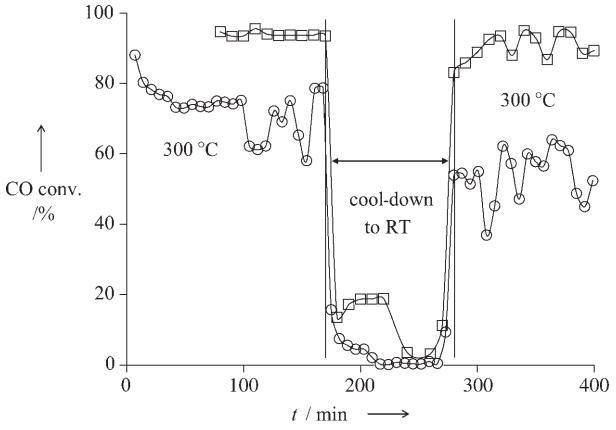

Figure 6. Oxygen potential effect on Pt–ceria WGS shut-down/start-up activity. Catalyst: 2.2 PtCe(La)O_x; squares: 1 mol% O_2 in feed gas; circles: 0.5 mol% O_2 in feed gas. Feed-gas mixture: 11:26:26:7:0.5:29.5 or 11:26:26:7:1:29 CO/H_2O/H_2/CO_2/O_2/He; S.V. = 50000 h^{-1}; catalyst was run at 300 °C for 3 h, then cooled to room temperature during shut-down with gas flowing for approximately 2 h, then reheated to 300 °C.

controlling the deactivation of ceria-based catalysts. Pt–ceria catalysts require a higher oxygen potential to stabilize their WGS activity relative to Au–ceria catalysts. This behavior may be attributed to over-reduction of ceria caused by Pt.[22] There was no improvement in the Pt–ceria stability by adding 0.5 mol% O_2 in the gas stream in a time-on-stream stability test at 300 °C, but the CO conversion was increased. Hence, the selectivity to CO oxidation was higher than hydrogen oxidation at 300 °C (see the Supporting Information).

In summary, we have reported herein that in the presence of a small amount of gaseous oxygen Au–ceria or Pt–ceria catalysts show remarkable stability in the WGS reaction in the full fuel-gas mixture both at low and high temperatures and, very importantly, in a cyclic shut-down/start-up operation. Therefore, nanostructured Au–ceria or Pt–ceria materials can be developed as active and stable catalysts for the WGS reaction. As Au–ceria catalysts are also very active for the PROX reaction, it is possible to combine the WGS and PROX reactors in one unit containing the Au–ceria catalyst. This approach has a clear advantage for application to fuel-gas clean-up for fuel-cell use under realistic operating conditions.

Experimental Section

High-content ($\approx$5 atom%) Au–ceria catalysts were prepared by deposition/precipitation of Au onto nanocrystalline ceria prepared separately (see the Supporting Information), whereas low-content (< 0.6 atom%) Au–ceria catalysts were prepared either by leaching weakly bound Au from the high-content Au–ceria samples with a solution of sodium cyanide[4] or by a one-pot gelation/coprecipitation (UGC) method using urea as the precipitation agent.[14] The catalysts are denoted as *a* AuCe(La)O_x or *a* AuCe(Gd)O_x, where *a* is the Au content in atomic percent, Ce(La)O_x is 10 atom% La-doped ceria, and Ce(Gd)O_x is 10 atom% Gd-doped ceria. The PtCe(La)O_x catalyst was prepared by incipient wetness impregnation (IMP) of the same nanocrystalline ceria. WGS reaction tests were conducted at atmospheric pressure in a heated quartz-tube microreactor containing the catalyst powder as a packed bed. The feed- and product-gas streams were analyzed by a HP-6890 gas chromatograph (GC) equipped with a thermal conductivity detector (TCD). The WGS gas mixture molar composition was 11:26:7:26:30 CO/H_2O/CO_2/H_2/He; whereas the molar composition of the gas mixture for the PROX reaction was: 1:0.5:10:15:50:23.5 CO/O_2/H_2O/CO_2/H_2/He. Characterization techniques used include Brunauer–Emmet–Teller (BET), XRD, and TPO analysis. TPO was used to investigate the carbon deposition or carbonate presence in the used catalysts. The catalysts in fine-powder form were oxidized at a heating rate of 5 °C min^{-1} from room temperature to 400 or 800 °C in 20:80 O_2/He (50 $cm^3 min^{-1}$ at normal temperature and pressure (NTP)). An on-line residual gas analyzer (MKS-model RS-1) was used to detect CO, CO_2, H_2O, and O_2.

Received: September 10, 2005
Revised: December 12, 2005
Published online: March 3, 2006

Keywords: cerium · fuel cells · gold · heterogeneous catalysis · platinum

[1] M. Haruta, N. Yamada, T. Kobayashi, S. Iijima, *J. Catal.* **1989**, *115*, 301 – 309.

 © 2006 Wiley-VCH Verlag GmbH & Co. KGaA, Weinheim

[2] M. Haruta, S. Tsubota, T. Kobayashi, H. Kageyama, M. J. Genet, B. Delmon, *J. Catal.* **1993**, *144*, 175 – 192.
[3] Q. Fu, A. Weber, M. Flytzani-Stephanopoulos, *Catal. Lett.* **2001**, *77*, 87 – 95.
[4] Q. Fu, H. Saltsburg, M. Flytzani-Stephanopoulos, *Science* **2003**, *301*, 935 – 938.
[5] Q. Fu, W. Deng, H. Saltsburg, M. Flytzani-Stephanopoulos, *Appl. Catal. B* **2005**, *56*, 57 – 68.
[6] D. Andreeva, V. Idakiev, T. Tabakova, A. Andreev, *J. Catal.* **1996**, *158*, 354 – 355.
[7] A. Venugopal, M. S. Scurrell, *Appl. Catal. A* **2004**, *258*, 241 – 249.
[8] H. Sakurai, T. Akita, S. Tsubota, M. Kiuchi, M. Haruta, *Appl. Catal. A* **2005**, *291*, 179 – 187.
[9] C. K. Costello, H. Y. Yang, Y. Wang, J.-N. Lin, L. D. Marks, M. C. Kung, H. H. Kung, *Appl. Catal. A* **2003**, *243*, 15 – 24.
[10] B. Schumacher, Y. Denkwitz, V. Plzak, M. Kinne, R. J. Behm, *J. Catal.* **2004**, *224*, 449 – 462.
[11] M. M. Schubert, V. Plzak, J. Garche, R. J. Behm, *Catal. Lett.* **2001**, *76*, 143 – 150.
[12] M. Manzoli, A. Chiorino, F. Boccuzzi, *Appl. Catal. B* **2004**, *52*, 259 – 266.
[13] O. Goerke, P. Pfeifer, K. Schubert, *Appl. Catal. A* **2004**, *263*, 11 – 18.
[14] W. Deng, J. De Jesus, H. Saltsburg, M. Flytzani-Stephanopoulos, *Appl. Catal. A* **2005**, *291*, 126 – 135.
[15] G. Panzera, V. Modafferi, S. Candamano, A. Donato, F. Frusteri, P. L. Antonucci, *J. Power Sources* **2004**, *135*, 177 – 183.
[16] A. Luengnaruemitchai, S. Osuwan, E. Gulari, *Int. J. Hydrogen Energy* **2004**, *29*, 429 – 435.
[17] S. Carrettin, P. Concepcion, A. Corma, J. M. Lopez Nieto, V. F. Puentes, *Angew. Chem.* **2004**, *116*, 2592 – 2594; *Angew. Chem. Int. Ed.* **2004**, *43*, 2538 – 2540.
[18] S. Hilaire, X. Wang, T. Luo, R. J. Gorte, J. Wagner, *Appl. Catal. A* **2001**, *215*, 271 – 278.
[19] J. Guzman, S. Carrettin, A. Corma, *J. Am. Chem. Soc.* **2005**, *127*, 3286 – 3287.
[20] G. Jacobs, A. Crawford, L. Williams, P. M. Patterson, B. H. Davis, *Appl. Catal. A* **2004**, *267*, 27 – 33.
[21] C. H. Kim, L. T. Thompson, *J. Catal.* **2005**, *230*, 66 – 74.
[22] J. M. Zalc, V. Sokolovskii, D. G. Loffler, *J. Catal.* **2002**, *206*, 169 – 171.
[23] X. Liu, W. Ruettinger, X. Xu, R. Farrauto, *Appl. Catal. B* **2005**, *56*, 69 – 75.
[24] X. Wang, R. J. Gorte, J. P. Wagner, *J. Catal.* **2002**, *212*, 225 – 230.
[25] W. Ruettinger, X. Liu, R. Farrauto, US patent 20020141938.
[26] Provisional patent application, Tufts University, Nov. 5, **2004**.

 © 2006 Wiley-VCH Verlag GmbH & Co. KGaA, Weinheim

Synthetic Methods

DOI: 10.1002/anie.200504310

Annulative Tandem Reactions Based on Pd^0/tBu_3P-Catalyzed Cross-Coupling and $C(sp^3)$–H Bond Activation**

*Cheng-Guo Dong and Qiao-Sheng Hu**

Over recent decades, transition-metal-catalyzed bond-forming reactions using the cross-coupling strategy have become extremely powerful tools for the synthesis of an array of small organic molecules and macromolecules.[1,2] More recently, transition-metal-catalyzed carbon–carbon bond-forming reactions by $C(sp^3)$–H bond activation have emerged as new efficient tools for synthetic organic chemistry.[3,4] Inspired by recent elegant examples of tandem/"domino" reactions,[5–7] we reasoned that these two types of powerful transition-metal-catalyzed reactions could be transformed into even more powerful tools if they could be arranged to occur in a tandem or "domino" fashion. We were particularly attracted by the possibility of having ring-forming tandem or "domino" reactions that combine transition-metal-catalyzed cross-couplings and an $C(sp^3)$–H bond-activation strategy, as such reactions could not only concomitantly generate multiple bonds with a rapid increase in molecular complexity but also allow us to access ring systems that are difficult to access by other methods. Herein, we report a new type of such annulative tandem reaction—Pd^0/tBu_3P-catalyzed tandem reactions of 1,2-dihalobenzenes with hindered Grignard reagents—which provides efficient access to substituted fluorenes.[8,9]

Our mechanistic consideration of the Pd-catalyzed tandem reaction of 1,2-dihalobenzenes is shown in Scheme 1. We envisioned that a Pd^0-catalyzed reaction of a 1,2-dihalobenzene with an organometallic reagent would generate the initial cross-coupling product **I** and recognized that its subsequent oxidative-addition product, the Pd^{II} complex **II**, could 1) couple with another equivalent of an organometallic reagent to yield the direct cross-coupling product and/or 2) undergo intramolecular $C(sp^3)$–H bond activation followed by cyclization (Scheme 1). As the cross-coupling of aryl halides with organometallic reagents is well

[*] C.-G. Dong, Prof. Dr. Q.-S. Hu
Department of Chemistry
College of Staten Island and
Graduate Center of the City University of New York
Staten Island, NY 10314 (USA)
Fax: (+1) 718-982-3910
E-mail: qiaohu@mail.csi.cuny.edu

[**] We thank the NIH (GM69704) for funding. Partial support from the PSC-CUNY Research Award Program is gratefully acknowledged. We thank Ms. Hui-Yu Liu and Ms. Anna P. Yeung for some experimental work, Prof. Shuiqin Zhou for helpful discussions, and Prof. Alec Greer for help with the GCMS analysis.

Supporting information for this article is available on the WWW under http://www.angewandte.org or from the author.

 © 2006 Wiley-VCH Verlag GmbH & Co. KGaA, Weinheim

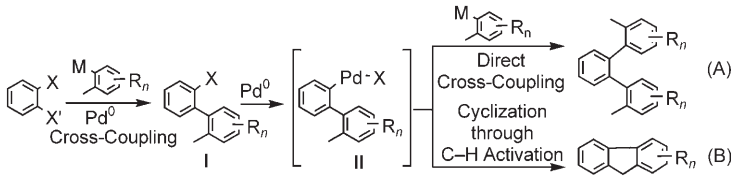

Scheme 1. Competition between direct cross-coupling (path A) and cyclization through C(sp^3)–H bond activation (path B).

established,[1] the challenge to realize a ring-forming tandem reaction through a C–H bond-activation reaction thus lies in how to achieve cyclization by intramolecular C–H bond activation (path B) over the intermolecular direct cross-coupling process (path A). Based on reports that sterically hindered substrates/reagents were more reluctant to undergo cross-coupling reactions,[10] we surmised that the cyclization pathway should be more favored with bulkier substrates and/or reagents. We thus began our study by examining the cyclization behavior of 2-bromo-2′-methylbiphenyls under cross-coupling reaction conditions (namely, in the presence of ArM)[11] and expected the products to be formed via complex **II**. With Pd^0/tBu_3P as the catalyst,[12] we found that although 2-bromo-2′-methylbiphenyl only yielded the direct cross-coupling product with *o*-tolylboronic acid (Table 1, entry 1), it indeed yielded more cyclization product with a bulkier Grignard reagent, which served as both a coupling reagent and base (Table 1, entries 2 and 3). The use of the bulkier 2-bromo-2′,4′,6′-trimethylbiphenyl as the substrate led to clean cyclization with 2-mesitylmagnesium bromide, thus suggesting the cyclization pathway through C–H activation could be efficiently controlled over the direct cross-coupling process by adjusting the bulkiness of the substrates/reagents.

With the feasibility of cyclization through C–H bond activation established, we turned our attention to test the annulative tandem reaction of 1,2-dibromobenzene with 2-mesitylmagnesium bromide, which was expected to proceed via complex **II** as the intermediate. We were pleased to find that the annulative tandem reaction took place as expected in excellent yield (Table 2, entry 1). This result encouraged us to examine a number of 1,2-dihalobenzenes for this new type of annulative tandem reaction (Table 2). We found good-to-excellent yields were observed for 1,2-dibromobenzenes (Table 2, entries 1–7) and 1-bromo-2-iodobenzene (Table 2, entries 8,9). 1,2-Dibromo-4,5-dimethylbenzene and 1,2-dibromo-4,5-dime-

Table 1: Pd-catalyzed cyclization of 2-bromo-2′-methylbiaryl compounds.[a]

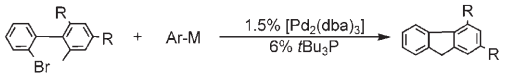

Entry	R	ArM	Base	*T*	Yield [%]
1	H	$B(OH)_2$	K_3PO_4	RT/reflux	0[b]
2	H	MgBr	MgBr	RT	< 2[c]
3	H	MgBr	MgBr	RT	19[d]
4	CH_3	MgBr	MgBr	RT	91[e]

[a] Reaction conditions: Aryl bromide (1.0 equiv) and either an arylboronic acid (1.5 equiv) and K_3PO_4 (3 equiv) or a Grignard reagent (2.5 equiv) in THF (2 mL). [b] 1,2-Diarylbenzene was obtained in 37% yield. [c] 1,2-Diarylbenzene was obtained in 68% yield. [d] 1,2-Diarylbenzene was obtained in 43% yield based on GCMS. [e] Yield of the isolated product.

Table 2: Pd-catalyzed tandem reactions of 1,2-dihalobenzenes with hindered Grignard reagents.[a]

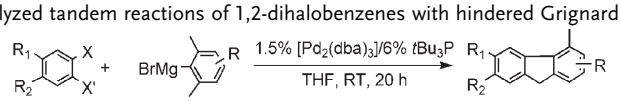

Entry	Aryl dihalide	BrMg–R	Substituted fluorene	Yield [%][b]
1		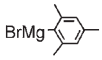		99
2		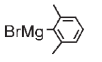		99
3		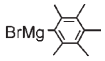		93
4		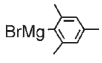	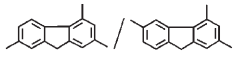	99 (44/56)[c]
5		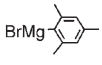	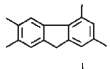	95[d]
6		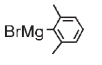	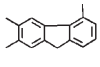	91[d]
7		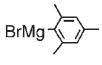	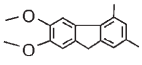	78[d]
8		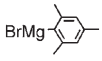		99
9		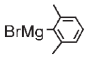		89
10		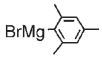		3[e] (94)[d,f]
11		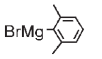		2[e] (97)[d,f]
12		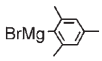		3[e] (96)[d,f]

[a] Reaction conditions (not optimized): aryl dihalide (1.0 equiv), Grignard reagent (2.5 equiv), Pd catalyst (3 mol%), THF (2 mL), room temperature. [b] Yields of the isolated products. [c] Ratio based on ^1H NMR spectroscopic analysis. [d] Reaction temperature: 60°C. [e] Based on ^1H NMR spectroscopic analysis. [f] In parenthesis: yields of the isolated product for 2-chlorobiaryl compounds **I**.

 © 2006 Wiley-VCH Verlag GmbH & Co. KGaA, Weinheim

thoxybenzene, which are more electron rich than 1,2-dibromobenzene, required heating to 60 °C for the reaction to go to completion. We also found that 1-chloro-2-halobenzenes only gave very low yields of fluorenes and excellent yields of 2-chlorobiphenyls (**I**, X = Cl) were obtained (Table 2, entries 10–12).[13]

We carried out preliminary studies on whether the first carbon–carbon bonding-forming step indeed proceeded through the envisioned cross-coupling strategy.[14–16] As the formation of **I** and the subsequent oxidative addition of **I** with Pd^0 are involved in such a cross-coupling process, we reasoned that it could be validated by the detection of the existence of this intermediate. Reactions with 1-chloro-2-halobenzenes as the substrates were apparently consistent with the formation of the first carbon–carbon bond through the cross-coupling strategy, with **I** (X = Cl) being obtained in excellent yields (Table 2, entries 10–12) because of its reluctance to undergo oxidative addition with Pd^0/tBu$_3$P under the new tandem reaction conditions (Scheme 2). Because **I** (X = Br) can

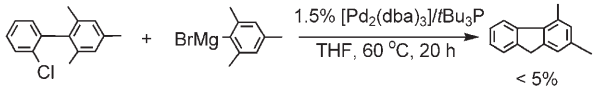

Scheme 2. Pd-catalyzed reactions of 2-chloro-2′,4′,6′-trimethylbiphenyls with 2-mesitylmagnesium bromide.

readily undergo oxidative addition with Pd^0/tBu$_3$P, the detection of the existence of **I** (X = Br) in Pd^0/tBu$_3$P-catalyzed tandem reactions of 1,2-dibromobenzenes would require the reactions to be stopped before completion by methods such as using a limited amount of Grignard reagent. We thus carried out the reaction of 1,2-dibromobenzene with 0.5 equivalents of 2-mesitylmagnesium bromide. Our results showed that **I** was observed in 7% yield (Table 3, entry 1). As the envisioned cross-coupling strategy also involves the oxidative addition of **I** with a regenerated Pd^0 species, substrates such as 1,2-dibromo-4-methylbenzene that yield less reactive **I**, or substrates such as 1-bromo-2-iodobenzene[15,16] that undergo oxidative addition faster than **I** (X = Br), should lead to the detection of greater amounts of **I** (X = Br); indeed, our study on these substrates showed that more of **I** was found (Table 3, entries 2,3). In combination with our recent observation of preferential oxidative addition with Pd^0/tBu$_3$P,[17] the detection of a significant amount of **I** strongly suggests that the cross-coupling strategy should be a main pathway, if not the only one,[18,19] for the first carbon–carbon bond-forming step of the reaction of 1,2-dibromobenzenes and 1-bromo-2-iodobenzene with hindered Grignard reagents.

We also extended the tandem reaction to 1,2,4,5-tetrabromobenzene as a substrate and found that the tandem reaction occurred as expected to give indenofluorenes in good yield (Scheme 3).[20]

In summary, we have demonstrated that cyclization through C(sp^3)–H bond activation in the Pd^0/tBu$_3$P-catalyzed reactions of 2-bromo-2′-methylbiphenyls could be efficiently achieved by employing hindered substrates/reagents. Furthermore, we have developed a new type of Pd-catalyzed annulative tandem reaction of 1,2-dibromobenzenes and 1-bromo-2-iodobenzene with hindered Grignard reagents based on a Pd-catalyzed cross-coupling reaction and C–H activation strategy. This new type of tandem reaction allows efficient access to potentially useful substituted fluorenes. Future work will focus on expansion of the reaction scope, elucidation of more detailed reaction mechanisms, and extension of the cyclization strategy for the preparation of other cyclic compounds and substituted oligofluorenes/polyfluorenes.

Table 3: Pd-catalyzed reactions of 1,2-dihalobenzenes with a limited amount of 2-mesitylmagnesium bromide.[a]

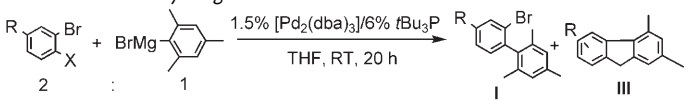

Entry	X	R	Conversion [%][b]	**I** [%]	**III** [%]
1	Br	H	48	7	93
2	Br	CH_3	45	12	88
3	I	H	34	19.5	80.5

[a] Reaction conditions: aryl dihalide (1.0 equiv), Grignard reagent (0.5 equiv), Pd catalyst (3 mol%), THF (2 mL), room temperature, 20 h. Ratio **I**/**III** was based on GCMS data. [b] Based on 1,2-dihalobenzene.

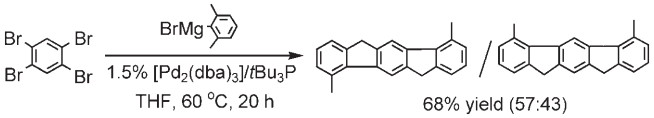

Scheme 3. Pd-catalyzed tandem reaction of 1,2,4,5-tetrabromobenzene with 2,6-dimethyphenylmagnesium bromide.

Experimental Section

General procedure for the palladium-catalyzed tandem reaction of 1,2-dihalobenzenes with hindered Grignard reagents: In a glove box with a N_2 atmosphere, [Pd_2(dba)$_3$] (13.7 mg, 0.015 mmol; dba = dibenzylideneacetone) and tBu$_3$P (12.1 mg, 0.06 mmol) were added to a mixture of dihalobenzenes (1.0 mmol) and THF (2.0 mL) in a Schlenk flask. After stirring the reaction mixture for 5–10 min, the Grignard reagent (2.5 mL, 1M in THF, 2.5 mmol) was added. The reaction mixture was allowed to stir in a N_2 atmosphere for 20 h, quenched with water, and extracted with ethyl acetate. The organic layer was washed with brine, and the solvent was evaporated under vacuum. Flash chromatography on silica gel (hexane/ethyl acetate, 100:0→90:10) gave the reaction products.

Received: December 4, 2005
Published online: March 3, 2006

Keywords: C–H activation · cross-coupling · palladium · phosphanes · tandem reactions

[1] a) *Transition-Metal-Catalyzed Cross-Coupling Reactions* (Eds.: F. Diederich, P. J. Stang), Wiley-VCH, New York, **1998**; b) M. Beller, C. Bolm, *Transition Metals for Organic Synthesis*, Wiley-VCH, Weinheim, **1998**; c) J. P. Collman, L. S. Hegedus, J. R. Norton, R. G. Finke, *Principles and Applications of Organotransition Metal Chemistry*, University Science Books, Mill

 © 2006 Wiley-VCH Verlag GmbH & Co. KGaA, Weinheim

Valley, CA, **1987**; d) H. Shinokubo, K. Oshima, *Eur. J. Org. Chem.* **2004**, 2081 – 2091.

[2] a) K. C. Nicolaou, P. G. Bulger, D. Sarlah, *Angew. Chem.* **2005**, *117*, 4516 – 4563; *Angew. Chem. Int. Ed.* **2005**, *44*, 4442 – 4489; b) Q.-S. Hu in *Synthetic Methods for Step-Growth Polymers* (Eds.: M. Rogers, T. Long), Wiley, New York, **2003**, pp. 467 – 526.

[3] Recent reviews of C–H activation: a) *Handbook of C–H Transformations: Application in Organic Synthesis*, *Vol. 2* (Ed.: G. Dyker), Wiley-VCH, Weinheim, **2005**; b) F. Kakiuchi, N. Chatani, *Adv. Synth. Catal.* **2003**, *345*, 1077 – 1101; c) V. Ritleng, C. Sirlin, M. Pfeffer, *Chem. Rev.* **2002**, *102*, 1731 – 1770; d) C. Jia, T. Kitamura, Y. Fujiwara, *Acc. Chem. Res.* **2001**, *34*, 633 – 639.

[4] For recent examples: a) Z. Li, C.-J. Li, *J. Am. Chem. Soc.* **2005**, *127*, 3672 – 3673; b) B. Sezen, D. Sames, *J. Am. Chem. Soc.* **2005**, *127*, 5284 – 5285; c) L. Shi, Y.-Q. Tu, M. Wang, F.-M. Zhang, C.-A. Fan, Y.-M. Zhao, W.-J. Xia, *J. Am. Chem. Soc.* **2005**, *127*, 10836 – 10837; d) D. Shabashov, O. Daugulis, *Org. Lett.* **2005**, *7*, 3657 – 3659; e) T. E. Barder, S. D. Walker, J. R. Martinelli, S. L. Buchwald, *J. Am. Chem. Soc.* **2005**, *127*, 4685 – 4696; f) B. DeBoef, S. J. Sames, D. Pastine, *J. Am. Chem. Soc.* **2004**, *126*, 6556 – 6557; g) L. V. Desai, K. L. Hull, M. S. Sanford, *J. Am. Chem. Soc.* **2004**, *126*, 9542 – 9543; h) B. Sezen, D. Sames, *J. Am. Chem. Soc.* **2004**, *126*, 13244 – 13246.

[5] For recent general reviews on tandem reactions, see: a) L. F. Tietze, N. Rackelmann, *Pure Appl. Chem.* **2004**, *76*, 1967 – 1983; b) K. C. Nicolaou, T. Montagnon, S. A. Snyder, *Chem. Commun.* **2003**, 551 – 564; c) P. J. Parsons, C. S. Penkett, A. J. Shell, *Chem. Rev.* **1996**, *96*, 195 – 206; d) L. F. Tietze, *Chem. Rev.* **1996**, *96*, 115 – 136.

[6] Recent examples of annulative tandem reactions based on transition-metal-catalyzed addition/cross-coupling strategies: a) J. E. Ney, J. P. Wolfe, *J. Am. Chem. Soc.* **2005**, *127*, 8644 – 8651; b) Q. Huang, A. Fazio, G. Dai, M. A. Campo, R. C. Larock, *J. Am. Chem. Soc.* **2004**, *126*, 7460 – 7461; c) J. P. Wolfe, M. A. Rossi, *J. Am. Chem. Soc.* **2004**, *126*, 1620 – 1621; d) R. Lira, J. P. Wolfe, *J. Am. Chem. Soc.* **2004**, *126*, 13906 – 13907; e) J. E. Ney, J. P. Wolfe, *Angew. Chem.* **2004**, *116*, 3689 – 3692; *Angew. Chem. Int. Ed.* **2004**, *43*, 3605 – 3608; f) X. Tong, D. Li, Z. Zhang, X. Zhang, *J. Am. Chem. Soc.* **2004**, *126*, 7601 – 7607; g) D. F. Cauble, J. D. Gipson, M. J. Krische, *J. Am. Chem. Soc.* **2003**, *125*, 1110 – 1111.

[7] For a report on Pd-catalyzed tandem cross-coupling cyclization by aromatic C–H bond activation, see: H. A. Wegner, L. T. Scott, A. de Meijere, *J. Org. Chem.* **2003**, *68*, 883 – 887.

[8] Fluorenes are typically prepared by more than one step, for example, see: a) I. A. Kashulin, I. E. Nifant'ev, *J. Org. Chem.* **2004**, *69*, 5476 – 5479; b) R. A. Abramovitch, T. Chellathurai, I. T. McMaster, T. Takaya, C. I. Azogu, D. P. Vanderpool, *J. Org. Chem.* **1977**, *42*, 2914 – 2919.

[9] Fluorene-based molecules, including polymers, have been established as promising sensors and light-emitting materials; for example, see: a) R. Rathore, V. J. Chebny, S. H. Abdelwahed, *J. Am. Chem. Soc.* **2005**, *127*, 8012 – 8013; b) D. Marsitzky, R. Vestberg, P. Blainey, B. T. Tang, C. J. Hawker, K. R. Carter, *J. Am. Chem. Soc.* **2001**, *123*, 6965 – 6972.

[10] For leading references, see: a) O. Navarro, R. A. Kelly III; S. P. Nolan, *J. Am. Chem. Soc.* **2003**, *125*, 16194 – 16195; b) J. Yin, M. P. Rainka, X.-X. Zhang, S. L. Buchwald, *J. Am. Chem. Soc.* **2002**, *124*, 1162 – 1163; c) N. Kataoka, Q. Shelby, J. P. Stambuli, J. F. Hartwig, *J. Org. Chem.* **2002**, *67*, 5553 – 5566; d) A. F. Littke, C. Dai, G. C. Fu, *J. Am. Chem. Soc.* **2000**, *122*, 4020 – 4028.

[11] Pd-catalyzed cyclizations by $C(sp^3)$–H activation are rare: a) O. Baudoin, A. Herrbach, F. Gueritte, *Angew. Chem.* **2003**, *115*, 5914 – 5918; *Angew. Chem. Int. Ed.* **2003**, *42*, 5736 – 5740; b) R. Suau, J. M. Lopez-Romero, R. D. Rico, *Tetrahedron Lett.* **1996**, *37*, 9357 – 9360; c) G. Dyker, *J. Org. Chem.* **1993**, *58*, 6426 – 6428; d) G. Dyker, *Angew. Chem.* **1994**, *106*, 117 – 119; *Angew. Chem. Int. Ed. Engl.* **1994**, *33*, 103 – 105; e) G. Dyker, *Angew. Chem.* **1992**, *104*, 1079 – 1081; *Angew. Chem. Int. Ed. Engl.* **1992**, *31*, 1023 – 1025.

[12] Pd^0/tBu$_3$P was chosen as our catalyst because of its ability to undergo oxidative addition with a $C(sp^2)$–Br bond at room temperature; see reference [10d].

[13] Attempts to try and improve the yields of the cyclization products, including raising the temperature to reflux in THF or THF/dioxane were made, but no significant improvement in yield was observed (less than 5%); for a recent review on Pd-catalyzed cross-coupling of aryl chlorides, see: A. F. Littke, G. C. Fu, *Angew. Chem.* **2002**, *114*, 4350 – 4386; *Angew. Chem. Int. Ed.* **2002**, *41*, 4176 – 4211.

[14] The direct formation of benzyne intermediates for 1-bromo-2-chlorobenzene and 1,2-dibromobenzenes was ruled out by the following experiments: 1) no reaction was observed when mixing 1-bromo-2-chlorobenzene or 1,2-dibromobenzene with 2-mesitylmagnesium bromide and 2) no Diels–Alder addition product was observed when the reaction was carried out in the presence of furan (see the Supporting Information).

[15] 1-Bromo-2-iodobenzenes have been reported to form benzyne upon treatment with Grignard reagents; for example, see: H. Hart, K. Harada, C.-J. F. Du, *J. Org. Chem.* **1985**, *50*, 3104 – 3110.

[16] Although trapping the benzyne intermediate with furan in the absence of a palladium source was successful for 1-bromo-2-iodobenzene, it was unsuccessful in the presence of a palladium source. This observation suggested that either the direct formation of the benzyne intermediate did not occur or that the formed benzyne intermediate interacted with the Pd source rather than having reacted with furan. As the palladium source was used in a catalytic amount relative to the excess of furan, the latter case was unlikely. The observation of a significant amount of **I** (X = Br) with a limited amount of 2-mestitylmagnesium bromide (Table 3, entry 3) suggested that the initial oxidative addition of Pd^0 with 1-bromo-2-iodobenzene with 2-mesitylmagnesium bromide took place much faster than their direct exchange benzyne-forming reaction.

[17] C.-G. Dong, Q.-S. Hu, *J. Am. Chem. Soc.* **2005**, *127*, 10006 – 10007.

[18] At present, we cannot completely rule out the possibility of the initial oxidative-addition products of 1,2-dihalobenzenes, which bears a leaving group at their *ortho* position, with Pd^0 to undergo elimination to form palladium-coordinated benzynes; for Pd-coordinated benzyne complexes formed from $[Pd^{II}XL_n\{o\text{-}Ph[B(OH)_2]\}]$, see: M. Retboll, A. J. Edwards, A. D. Rae, A. C. Willis, M. A. Bennett, E. Wenger, *J. Am. Chem. Soc.* **2002**, *124*, 8348 – 8360.

[19] For examples of the carbopalladation of benzynes, see: a) Z. Liu, X. Zhang, R. C. Larock, *J. Am. Chem. Soc.* **2005**, *127*, 15716 – 15717; b) T. T. Jayanth, M. Jeganmohan, C.-H. Cheng, *Org. Lett.* **2005**, *7*, 2921 – 2924; c) M. Jeganmohan, C.-H. Cheng, *Org. Lett.* **2004**, *6*, 2821 – 2824; d) T. Matsubara, *Organometallics* **2003**, *22*, 4297 – 4304; e) H. Yoshida, Y. Honda, E. Shirakawa, T. Hiyama, *Chem. Commun.* **2001**, 1880 – 1881; f) E. Yoshikawa, K. V. Radhkrishan, Y. Yamamoto, *J. Am. Chem. Soc.* **2000**, *122*, 7280 – 7286.

[20] For examples of photonic materials containing indenofluorene units, see: a) T. Hadizad, J. Zhang, Z. Y. Wang, T. C. Gorjanc, C. Py, *Org. Lett.* **2005**, *7*, 795 – 797; b) P. Sonar, J. Zhang, A. C. Grimsdale, K. Mullen, M. Surin, R. Lazzaroni, P. Leclere, S. Tierney, M. Heeney, I. McCulloch, *Macromolecules* **2004**, *37*, 709 – 715; c) S. Setayesh, D. Marsitzky, K. Mullen, *Macromolecules* **2000**, *33*, 2016 – 2020.

 © 2006 Wiley-VCH Verlag GmbH & Co. KGaA, Weinheim

Si=P Species

DOI: 10.1002/anie.200504145

Synthesis of a "Half"-Parent Phosphasilene $R_2Si{=}PH$ and Its Metalation to the Corresponding *P*-Zinciophosphasilene $[R_2Si{=}PM]$**

Matthias Driess, Stefan Block, Markus Brym, and Michael T. Gamer*

Dedicated to Professor Hansgeorg Schnöckel on the occasion of his 65th birthday

The isolation of compounds with low-coordinate silicon atoms,[1–3] in other words, silicon homologues of olefins, and more recently the synthesis of the first inert disilyne, an alkyne analogue with a silicon–silicon triple bond,[4] are major breakthroughs in contemporary silicon chemistry. Unsaturated silicon compounds with Si=X bonds (X = elements from Groups 14,[1] 15,[2] or 16 [3]) show an intriguing reactivity toward both electrophiles and nucleophiles, and are valuable building blocks for the synthesis of electronically unusual silicon compounds by means of addition reactions.

Another challenge is to use functional groups containing low-coordinate silicon atoms for the synthesis of novel conjugated heteroatom systems **A** and **B** by homo- and heterocoupling reactions of metal-substituted Si=X building blocks **C** (X = elements from Groups 14 or 15; Scheme 1). However, compounds of type **C** suitable as reagents for a nucleophilic transfer of intact Si=X moieties are still very rare. While lithium disilenylide derivatives of the type $R_2Si{=}SiR(Li)$, that is, disila analogues of vinyllithium, have been reported very recently,[5] related metal-substituted heterosilenes of the type $R_2Si{=}[X]M$ and $(M)RSi{=}[X]R$ are currently unknown, except for the *P*-ferrio-substituted phosphasilene $R_2Si{=}P[Fe(CO)_2(\eta^5\text{-}C_5H_5)]$ **D** (R = 2,4,6-iPr$_3$C$_6$H$_2$; Scheme 1).[6] Lithium disilenylides have been shown to undergo homocoupling to give the corresponding tetrasila-buta-1,3-dienes.[7]

P-metalated phosphasilenes of the type $R_2Si{=}PM$ should be easily accessible through metalation of "half"-parent phosphasilenes of the type $R_2Si{=}PH$; however, such a phosphasilene derivative is hitherto unknown. We report here the synthesis of the first isolable phosphasilene **1** with a PH group and its P-metalation with Me_2Zn in the presence of *N*,*N*,*N*′,*N*′-tetramethylethylenediamine (tmeda) to afford the crystalline *P*-zinciophosphasilene **2** in 87% yield (Scheme 2).

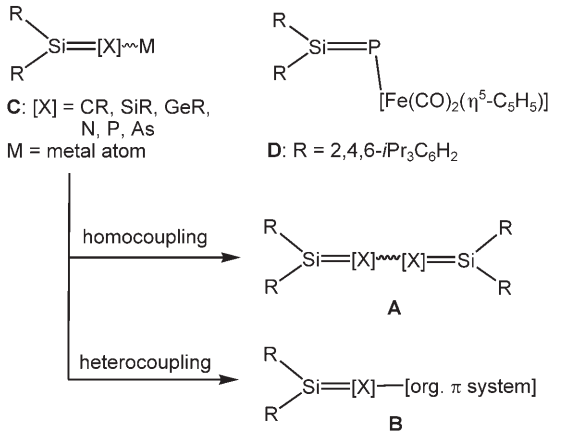

Scheme 1. The ferrio-substituted phosphasilene **D** and the conversion of X-metalated silenes **C** into **A** and **B**.

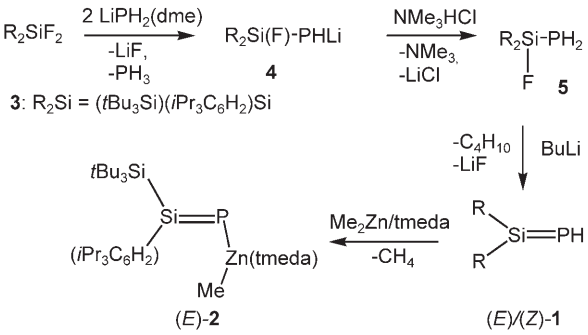

Scheme 2. Synthesis of **1** and **2** via the difluorosilane **3** and the (fluorosilyl)phosphanes **4** and **5**, respectively. dme = dimethoxyethane.

Phosphasilene **1** is easily accessible by a modified procedure analogous to the preparation of P-silyl-substituted phosphasilenes,[2f,g,i,k] starting from the bulky substituted difluorosilane (tBu$_3$Si)RSiF$_2$ **3** (R = 2,4,6-iPr$_3$C$_6$H$_2$) and $[LiPH_2(dme)]$ in the molar ratio of 1:2 (Scheme 2). The first step of this reaction leads solely to the corresponding lithium (fluorosilyl)phosphanide **4** (characterized by ^{31}P and ^{29}Si NMR spectroscopy, see the Supporting Information) along with PH_3 and LiF. Unexpectedly and in contrast to other lithium (fluorosilyl)phosphanides,[2l,8] solutions of **4** in THF already undergo LiF elimination above 30 °C, affording a mixture of the *Z* and *E* isomers of **1** in moderate yield (^{31}P NMR) besides several side-products, which could not be separated from **1**. However, compound **1** is surprisingly simple to prepare in quantitative yield by a modified procedure using LiF-free samples of **4** in hexane solutions at ambient temperature. This can be achieved by P-lithiation of purified (fluorosilyl)phosphane **5** with BuLi in hexane solution, and **5** is in turn easily accessible by mild protonation of **4** with NMe_3HCl (Scheme 2). Compound **5** can be isolated

[*] Prof. Dr. M. Driess, Dipl.-Chem. S. Block, Dr. M. Brym
Institut für Chemie
Metallorganik und Anorganische Materialien
Technische Universität Berlin
Strasse des 17. Juni 135, Sekr. C2, 10623 Berlin (Germany)
Fax: (+49) 30-314-22168
E-mail: matthias.driess@tu-berlin.de
Dr. M. T. Gamer
Institute of Chemistry
Freie Universität Berlin
Fabeckstrasse 34–36, 14195 Berlin (Germany)

[**] M = {Zn(tmeda)Me}; tmeda = *N*,*N*,*N*′,*N*′-tetramethylethylenediamine.

Supporting information for this article is available on the WWW under http://www.angewandte.org or from the author.

 © 2006 Wiley-VCH Verlag GmbH & Co. KGaA, Weinheim

in 91% yield in the form of colorless crystals, which have been characterized by NMR spectroscopy and elemental analysis (see the Supporting Information).

Phosphasilene **1** was isolated in the form of greenish yellow crystals in 88% yield, and its composition was confirmed by EIMS (*m*/*z* 462) and C,H analysis. The product consists of a 1:1.5 mixture of the *Z* and *E* isomers as proven by its ^{1}H, ^{31}P, and ^{29}Si NMR spectra. Thus, the ^{31}P NMR spectrum shows two doublet signals with ^{29}Si satellites at $\delta = 123.1$ ($^{1}J(P,H) = 123$, $^{1}J(^{31}P,^{29}Si) = 157$ Hz) and 134.2 ppm ($^{1}J(P,H) = 131$, $^{1}J(^{31}P,^{29}Si) = 130$ Hz). Accordingly, the ^{1}H NMR spectrum of the *E*/*Z* mixture exhibits two doublets for the protons of the PH groups at $\delta = 5.14$ ($^{1}J(^{31}P,^{1}H) = 131$ Hz) and 5.20 ppm ($^{1}J(^{31}P,^{1}H) = 123$ Hz), respectively. Based on selective NOE ^{1}H NMR experiments, one can assign the NMR resonances at $\delta = 5.14$ (^{1}H) and 123 ppm (^{31}P) to the *E* isomer (tBu$_3$Si,PH), while the signals at $\delta = 5.20$ (^{1}H) and 134.2 ppm (^{31}P) belong to the *Z* form.

Interestingly, the ^{1}J(P,H) coupling constants are approximately 80 Hz smaller than the characteristic values observed for secondary phosphanes R_2PH (R = alkyl, aryl, silyl) and significantly smaller than those of phosphaalkenes with a PH group ($^{1}J(^{31}P,^{1}H) = 140$–$208$ Hz).[9] This indicates that the phosphorus atom in **1** prefers more 3p character in the P–H bond. As expected, the ^{31}P nucleus in **1** is less shielded than those in P-silylated phosphasilenes of the type $R_2Si{=}PSiR_3$ ($\delta = -33$ to 28 ppm)[2k,i] but almost identical with the values reported for P-organo-substituted Si=P compounds ($\delta = 65$–136 ppm).[2k,i,o] The ^{29}Si resonance for the low-coordinate Si atom in **1** shows for each isomer a doublet at characteristically low field with a typical scalar ^{29}Si-^{31}P coupling constant. The signal at $\delta = 248.9$ ppm ($^{1}J(^{29}Si,^{31}P) = 130$ Hz) can be assigned to the *Z* isomer and that at $\delta = 249.8$ ppm ($^{1}J(^{29}Si,^{31}P) = 157$ Hz), to the *E* form.

A single-crystal X-ray diffraction analysis[10] confirms that the low-coordinate silicon atom adopts the trigonal-planar coordination geometry (Figure 1). The Si1–P1 distance of 209.4(5) pm is about 7% shorter than a Si–P single bond but only marginally longer (ca. 3 pm) than the respective value in P-silyl-substituted phosphasilenes.[2k,i] This indicates a shallow potential of the Si=P bond on the potential energy surface.[2n,o] The Si1–Si2 bond length of 239.8(5) pm is comparable to the values of other tBu$_3$Si-substituted silicon compounds.[11]

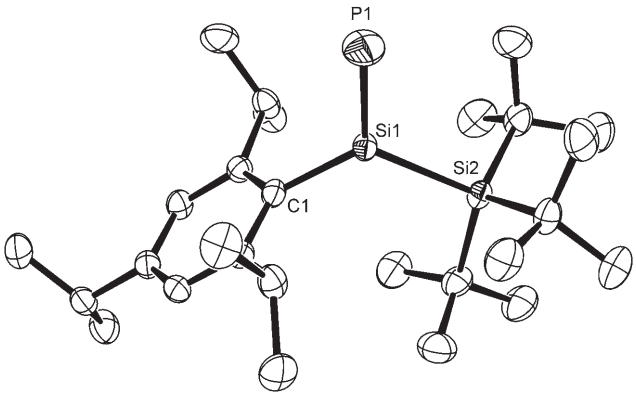

Figure 1. X-ray crystal structure of **1** (ellipsoids drawn at the 50% probability level; hydrogen atoms omitted for clarity). Selected distances [pm] and angles [°]: Si1–P1 209.4(5), Si1–Si2 239.8(5), Si1–C1 188.0(12); Si2-Si1-P1 121.5(2), C1-Si1-Si2 120.3(4), C1-Si1-P1 118.2(4); sum of the bond angles at Si1: 359.9°.

Although the substituents at the phosphorus atom are not very bulky, compound **1** survives heating in boiling toluene solution for several days. Since the Si=P bond appears to be sufficiently protected, we decided to use **1** as the starting material for the formation of an isolable, nucleophilic P-metal-subsituted phosphasilene. While lithiation of **1** with BuLi in nonpolar or polar donor solvents (ether, tmeda) at −78 °C did not lead to the desired P-lithiated phosphasilene as indicated by the ^{31}P NMR spectrum of the reaction mixture (no low-field resonances), its metalation with Me_2Zn in the presence of tmeda proceeded cleanly at −78 °C and furnished solely the desired *P*-zinciophosphasilene **2** (low-field $\delta(^{31}P)$ and $\delta(^{29}Si)$ signals). Alternatively, **2** was also accessible in high yield by a one-pot procedure, starting from **5** (see the Supporting Information).

P-zinciophosphasilene **2** was isolated in the form of orange crystals in 87% yield, and its composition and constitution was proven by EIMS (*m*/*z* 658), C,H analysis, and NMR spectroscopy. Because of the dominantly covalent character of the Zn–P bond, **2** does not dissociate in solutions in aromatic hydrocarbons and in ethers, as proven by cryoscopic measurements. Not only that, the steric demand of the {ZnMe(tmeda)} group at the phosphorus atom favors the *E* configuration as the lowest energy configuration; this was proven by variable-temperature (VT) ^{1}H, ^{31}P and ^{29}Si NMR spectroscopy. Thus, solutions of **2** in toluene exhibit in the temperature range from −80 to 80 °C only one singlet resonance signal in the ^{31}P NMR spectrum at unusual low field ($\delta = 227$ ppm). The extremely low-field resonance of the ^{31}P nucleus, which is roughly 100 ppm lower than that observed for (*Z*)- and (*E*)-**1** represents the least shielded chemical shift hitherto reported for a phosphasilene.[2j,k]

In contrast to the deshielding of the ^{31}P nucleus, the low-coordinate ^{29}Si atom in **2** ($\delta = 203$ ppm) is more shielded than that in (*Z*)/(*E*)-**1** ($\Delta\delta = 42$ ppm). This can be explained by stabilization of the n orbital at phosphorus through n(P)→σ*(Si–Si) hyperconjugation which, apparently, is more efficient in **2** than in **1** as a result of the higher negative partial charge at the phosphorus atom (Figure 2).[12] Similar shielding effects have been observed for related alkali-metal-substituted disilenylides ("disilavinyls") of the type [M(R_3Si)Si=Si(SiR_3)$_2$] (M = Li, Na, K),[5b,7b] which show extremely low-field signals for the metal-substituted silicon atoms. Accord-

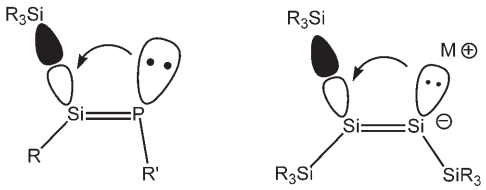

Figure 2. Proposed negative hyperconjugation n(P)→σ*(Si–Si) in **2** (left) and the analogous hyperconjugation σ(Si–M)→σ*(Si–Si) in isoelectronic silyl-substituted alkali-metal disilenylide compounds (right).[5b,7b]

 © 2006 Wiley-VCH Verlag GmbH & Co. KGaA, Weinheim

ingly, the resonance signal of the other low-coordinate ^{29}Si type is shifted to higher field as a result of σ(Si–M)→σ*(Si–Si) negative hyperconjugation (Figure 2).

The *E* configuration of **2** was confirmed by X-ray diffraction analysis.[10] This also proved that the Si1 atom has trigonal-planar geometry and that the Si1–P1 distance of 206.4(1) pm is significantly shorter than that in **1** (Figure 3).

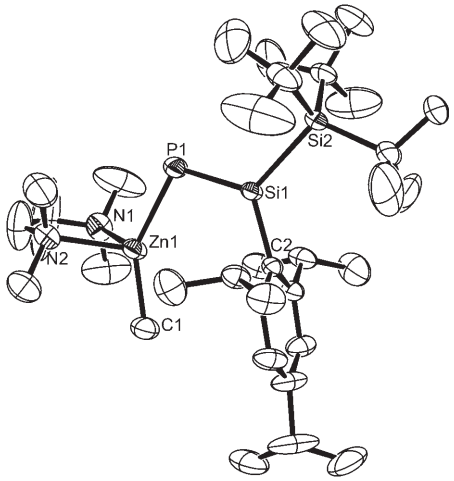

Figure 3. X-ray crystal structure of **2** (ellipsoids drawn at the 50% probability level; hydrogen atoms omitted for clarity). Selected distances [pm] and angles [°]: Si1–P1 206.4(1), Si1–Si2 240.2(1), Si1–C2 190.3(4), P1–Zn1 234.9(1), C1–Zn1 199.5(4); Si2-Si1-P1 118.10(6), Si2-Si1-C2 120.2(1), C2-Si1-P1 121.7(1), Si1-P1-Zn1 103.20(5); sum of the bond angles at Si1: 360°.

The shortening of the Si=P bond, the slight elongation of the Si1–Si2 bond, and the smaller P1-Si1-Si2 angle are consistent with the presence of hyperconjugative interactions as depicted in Figure 2. As expected, the Zn1 atom has tetrahedral coordination geometry and the value of the P1–Zn1 distance is typical for that of zincphosphanides.[13]

In summary, we have prepared the first phosphasilene derivatives with terminal hydrogen and zinc substituents at phosphorus by an unexpectedly simple procedure. These compounds represent a novel type of thermally robust building blocks in the chemistry of unsaturated silicon–phosphorus compounds. Investigations on the use of **1** and **2** for the synthesis of novel conjugated, electron-rich π systems of types **A** and **B** (see Scheme 1) by homo- or hetero-cross-coupling reactions are currently underway.

Received: November 21, 2005
Published online: March 3, 2006

Keywords: metalation · phosphanes · phosphasilenes · zinc

[1] Si=Si compounds: a) R. West, M. J. Fink, J. Michl, *Science* **1981**, *214*, 1343; b) S. Matsumoto, S. Tsutsui, E. Kwon, K. Sakamoto, *Angew. Chem.* **2004**, *116*, 4710; *Angew. Chem. Int. Ed.* **2004**, *43*, 4610. Reviews: c) R. West, *Angew. Chem.* **1987**, *99*, 1231; *Angew. Chem. Int. Ed. Engl.* **1987**, *26*, 1201; d) R. Okazaki, R. West, *Adv. Organomet. Chem.* **1995**, *39*, 231; e) R. West, *Polyhedron* **2002**, *21*, 467; f) A. Sekiguchi, V. Y. Lee, *Chem. Rev.* **2003**, *103*, 1429; g) N. Tokitoh, *Acc. Chem. Res.* **2004**, *37*, 86. Si=C compounds: h) A. G. Brook, S. C. Nyburg, F. Abdesaken, B. Gutekunst, G. Gutekunst, R. K. Kallury, Y. C. Poon, Y.-M. Chang, W. Wong-Ng, *J. Am. Chem. Soc.* **1982**, *104*, 5667; i) N. Wiberg, G. Wagner, G. Müller, **1985**, *97*, 220; *Angew. Chem. Int. Ed. Engl.* **1985**, *24*, 229; j) N. Wiberg, G. Wagner, *Chem. Ber.* **1986**, *119*, 1467; k) Reviews: A. G. Brook, K. M. Baines, *Adv. Organomet. Chem.* **1986**, *25*, 1; l) A. G. Brook, M. A. Brook, *Adv. Organomet. Chem.* **1996**, *39*, 71; m) "Silicon-Carbon and Silicon-Nitrogen Multiply Bonded Compounds": T. Müller, W. Ziche, N. Auner in *The Chemistry of Organic Silicon Compounds*, Vol. *2* (Eds.: Z. Rappoport, Y. Apeloig), Wiley, Chichester, **1998**, chap. 16, p. 857. Si=Ge and Si=Sn compounds: n) K. M. Baines, J. A. Cooke, *Organometallics* **1991**, *10*, 3419; o) K. M. Baines, J. A. Cooke, *Organometallics* **1992**, *11*, 3487; p) V. Y. Lee, M. Ichinohe, A. Sekiguchi, N. Takagi, S. Nagase, *J. Am. Chem. Soc.* **2000**, *122*, 9034; q) A. Sekiguchi, R. Izumi, V. Y. Lee, M. Ichinohe, *J. Am. Chem. Soc.* **2002**, *124*, 14822.

[2] Si=N compounds: a) N. Wiberg, K. Schurz, G. Reber, G. Müller, *J. Chem. Soc. Chem. Commun.* **1986**, 591; b) M. Hesse, U. Klingebiel, *Angew. Chem.* **1986**, *98*, 638; *Angew. Chem. Int. Ed. Engl.* **1986**, *25*, 649; Review: c) I. Hemme, U. Klingebiel, *Adv. Organomet. Chem.* **1996**, *39*, 159; see also reference [1m]. Si=P and Si=As compounds: d) C. N. Smit, F. Bickelhaupt, *Organometallics* **1987**, *6*, 1156; e) Y. van den Winkel, H. M. M. Bastiaans, F. Bickelhaupt, *J. Organomet. Chem.* **1991**, *405*, 183; f) M. Driess, H. Pritzkow, *Angew. Chem.* **1992**, *104*, 350; *Angew. Chem. Int. Ed. Engl.* **1992**, *31*, 316; g) M. Driess, S. Rell, H. Pritzkow, *J. Chem. Soc. Chem. Commun.* **1995**, 253; h) H. R. G. Bender, E. Niecke, M. Nieger, *J. Am. Chem. Soc.* **1993**, *115*, 3314; i) M. Driess, S. Rell, H. Pritzkow, R. Janoschek, *Angew. Chem.* **1997**, *109*, 1384; *Angew. Chem. Int. Ed. Engl.* **1997**, *36*, 1326; j) D. Lange, E. Klein, H. Bender, E. Niecke, M. Nieger, R. Pietschnig, W.W. Schoeller, H. Ranaivonjatovo, *Organometallics* **1998**, *17*, 2425; k) M. Driess, S. Rell, K. Merz, *Z. Anorg. Allg. Chem.* **1999**, *625*, 1119; Reviews: l) M. Driess, *Adv. Organomet. Chem.* **1996**, *39*, 193; m) M. Driess, *Coord. Chem. Rev.* **1995**, *145*, 1; n) see also: reference [1m], p. 1051; Theoretical aspects of Si=N, Si=P and Si=As compounds: o) K. J. Dykema, T. N. Truong, M. S. Gordon, *J. Am. Chem. Soc.* **1985**, *107*, 4535; p) M. Driess, R. Janoschek, *J. Mol. Struct.* **1994**, *323*, 129.

[3] a) H. Suzuki, N. Tokitoh, S. Nagase, R. Okazaki, *J. Am. Chem. Soc.* **1994**, *116*, 11578; b) N. Tokitoh, H. Suzuki, T. Matsumoto, Y. Matsuhashi, R. Okazaki, M. Goto, *J. Am. Chem. Soc.* **1991**, *113*, 7047; c) H. Suzuki, N. Tokitoh, R. Okazaki, S. Nagase, M. Goto, *J. Am. Chem. Soc.* **1998**, *120*, 11096; d) Review: "Chemistry of Compounds with Silicon–Sulfur, Silicon–Selenium and Silicon–Tellurium Bonds": D. A. Armitage in *The Chemistry of Organic Silicon Compounds*, Vol. *2* (Eds.: Z. Rappoport, Y. Apeloig), Wiley, Chichester, **1998**, chap. 31, p. 1869.

[4] a) N. Wiberg, W. Niedermayer, G. Fischer, H. Nöth, M. Suter, *Eur. J. Inorg. Chem.* **2002**, 1066; b) N. Wiberg, S. K. Vasisht, G. Fischer, P. Mayer, *Z. Anorg. Allg. Chem.* **2004**, *630*, 1823; c) A. Sekiguchi, R. Kinjo, M. Ichinohe, *Science* **2004**, *305*, 1755.

[5] a) D. Scheschkewitz, *Angew. Chem.* **2004**, *116*, 3025; *Angew. Chem. Int. Ed.* **2004**, *43*, 2965; b) S. Inoue, M. Ichinohe, A. Sekiguchi, *Chem. Lett.* **2005**, *34*, 1564.

[6] M. Driess, H. Pritzkow, U. Winkler, *J. Organomet. Chem.* **1997**, *529*, 313.

[7] a) M. Weidenbruch, S. Willms, W. Saak, G. Henkel, *Angew. Chem.* **1997**, *109*, 2612; *Angew. Chem. Int. Ed. Engl.* **1997**, *36*, 2503; b) M. Ichinohe, K. Sanuki, S. Inoue, A. Sekiguchi, *Organometallics* **2004**, *23*, 3088.

[8] a) M. Driess, U. Winkler, W. Imhof, L. Zsolnai, G. Huttner, *Chem. Ber.* **1994**, *127*, 1031; b) S. Ionkin, W. J. Marshall, *Organometallics* **2003**, *22*, 4136.

 © 2006 Wiley-VCH Verlag GmbH & Co. KGaA, Weinheim

[9] "Survey of ^{31}P NMR Data": K. Karaghiosoff in *Multiple Bonds and Low Coordination in Phosphorus Chemistry* (Eds.: O. Scherer, M. Regitz), Thieme, Stuttgart, **1990**, p. 467.

[10] **1**: Triclinic, space group $P\bar{1}$, $a = 8.488(2)$, $b = 9.388(2)$, $c = 18.944(4)$ Å, $\alpha = 78.627(17)$, $\beta = 84.363(18)$, $\gamma = 81.652(18)°$, $V = 1460.4(6)$ Å^3, $Z = 2$, $\rho_{calcd} = 1.053$ mg m^{-3}, $\mu(Mo_{K\alpha}) = 0.19$ mm^{-1}, 11516 collected reflections, 5122 crystallographically independent reflections [$R_{int} = 0.0359$], 5121 reflections with $I > 2\sigma(I)$, $\theta_{max} = 25.00°$, 271 refined parameters, $R(F_o) = 0.0459$ ($I > 2\sigma(I)$), $wR(F_o^2) = 0.1179$ (all data). **2**: Monoclinic, space group $P2_1/c$, $a = 14.6883(4)$, $b = 12.5931(3)$, $c = 24.4109(7)$ Å, $\beta = 101.7130(10)°$, $V = 4421.3(2)$ Å^3, $Z = 4$, $\rho_{calcd} = 1.076$ mg m^{-3}, $\mu(Mo_{K\alpha}) = 0.67$ mm^{-1}, 26671 collected reflections, 7772 crystallographically independent reflections [$R_{int} = 0.0448$], 5757 reflections with $I > 2\sigma(I)$, $\theta_{max} = 25.00°$,419 refined parameters, $R(F_o) = 0.0580$ ($I > 2\sigma(I)$), $wR(F_o^2) = 0.1476$ (all data). Each of the crystals were mounted on a glass capillary in perfluorinated oil and measured in a cold N_2 flow. The data of **1** were collected on a STOE IPDS 2T diffractometer with an area detector at 173 K ($Mo_{K\alpha}$ radiation, $\lambda = 0.71073$ Å) and those of **2** on a Bruker-AXS SMART CCD diffractometer at 173(2) K ($Mo_{K\alpha}$ radiation, $\lambda = 0.71073$ Å). The structures were solved by direct methods and were refined on F^2 with the SHELX-97[14] software package. The positions of the H atoms were calculated and considered isotropically according to a riding model. Absorption corrections were conducted using the SADABS program.[15] CCDC 289280 (**1**) and CCDC 289281 (**2**) contains the supplementary crystallographic data for this paper. These data can be obtained free of charge from The Cambridge Crystallographic Data Centre via www.ccdc.cam.ac.uk/data_request/cif.

[11] N. Wiberg, W. Niedermayer, H. Nöth, J. Knizek, W. Ponikwar, K. Polborn, *Z. Naturforsch. B* **2000**, *55*, 389, and references therein.

[12] T. Albright, J. K. Burdett, M.-H. Whangbo, *Orbital Interactions in Chemistry*, Wiley, Chichester, **1985**, p. 178.

[13] S. C. Goel, M. Y. Chiang, W. E. Buhro, *J. Am. Chem. Soc.* **1990**, *112*, 5636.

[14] G. M. Sheldrick, *SHELX-97 Program for Crystal Structure Determination*, Universität Göttingen (Germany), **1997**.

[15] G. M. Sheldrick, *SADABS Program for Empirical Absorption Correction of Area Detector Data*, Universität Göttingen (Germany), **1996**.

 © 2006 Wiley-VCH Verlag GmbH & Co. KGaA, Weinheim

Biosynthesis

DOI: 10.1002/anie.200503737

Nonribosomal Peptide Biosynthesis: Point Mutations and Module Skipping Lead to Chemical Diversity**

*Silke C. Wenzel, Peter Meiser, Tina M. Binz, Taifo Mahmud, and Rolf Müller**

Many pharmaceutically important peptides are nonribosomally biosynthesized by multifunctional protein complexes termed nonribosomal peptide synthetases (NRPSs).[1,2] NRPSs are the largest enzymes known in nature, they can exceed 1000 kilodaltons (kDa) in size, for example, the 1700-kDa cyclosporin synthetase. As NRPSs are not bound by the ribosome's rulebook, the structural diversity of their products is remarkably large. This is at least in part owing to their ability to synthesize and incorporate numerous unusual nonproteinogenic amino acids. To further increase chemical diversity, NRPSs can also interact with a second class of multimodular enzyme systems, the polyketide synthases (PKSs).[3,4] The resultant hybrid PKS/NRPS megasynthetase is capable of inserting short-chain carboxylic acids as monomers into the product, thereby further increasing the chemical diversity.[5] Since the mid-1980s, an increasing number of genes that encode NRPSs and PKSs of bacterial and fungal origin have been cloned, and subsequent biochemical and genetic studies have led to a (general) model of how these multimodular systems work.[1–4] The gained molecular understanding of multimodular megasynthetases has facilitated efforts to redesign NRPS and PKS systems to create new products with altered and/or increased activities.[6,7]

Herein, we focus on the biosynthesis of myxochromides, lipopeptides that are produced by a hybrid PKS/NRPS from several myxobacteria.[8] Recently, we described the structures

[*] Dipl.-Chem. S. C. Wenzel, Apotheker P. Meiser, Dipl.-Biol. T. M. Binz, Prof. Dr. R. Müller
Pharmaceutical Biotechnology, Saarland University
P.O. Box 151150, 66041 Saarbrücken (Germany)
Fax: (+49) 681-302-5473
E-mail: rom@mx.uni-saarland.de
Prof. Dr. T. Mahmud
College of Pharmacy, Oregon State University
Corvallis, OR 97331-3507 (USA)

[**] The authors would like to thank B. Arbogast and L. Barofsky (Mass Spectrometry Core of the Environmental Health Sciences Center, Oregon State University, NIH grant P30 ES00210) for the ESI/ICR and MALDI-TOF analysis and B. Hinkelmann and H. Schüler for performing a large-scale fermentation. We are also grateful to Prof. Dr. T. M. Zabriskie, Dr. H. B. Bode, and B. Lelarge for the critical review of this manuscript. This work was supported by grants from the BMB+F and the DFG. S.C.W. and R.M. would like to acknowledge a Kekulé fellowship of the Fonds der Chemischen Industrie and a DAAD fellowship.

Supporting information, including experimental data, for this article is available on the WWW under http://www.angewandte.org or from the author.

WILEY InterScience DISCOVER SOMETHING GREAT
© 2006 Wiley-VCH Verlag GmbH & Co. KGaA, Weinheim

and respective biosynthetic megasynthetase of myxochromides S_3 from *Stigmatella aurantiaca*.[9] A detailed analysis of the involved megasynthetase led to a model for myxochromide S biosynthesis that implied several striking deviations from standard PKS and NRPS biochemistry.[9,10] The PKS involved in the formation of the unsaturated myxochromide side chain was shown to be an iteratively acting enzyme with the intrinsic capacity to produce polyketide chains of varying length.[9,11] Iterative PKSs, capable of conducting multiple rounds of chain extension, were formerly thought to be employed exclusively by fungi and as such were falsely classified as "fungal PKS".[4,10,12]

These investigations led to the assumption that the (penta)peptide core of myxochromide S is formed through a unique module-skipping process during assembly by a hexamodular NRPS. Interestingly, myxochromides A, produced by *Myxococcus virescens*,[8] are structurally similar lipohexapeptides (Figure 1) that incorporate the same five amino acids (plus a proline) in a different sequence pattern. Intriguingly, the in silico analysis of the gene cluster for the biosynthesis of myxochromide S should theoretically coincide with that of the hexapeptide myxochromide A.[9]

To establish an evolutionary link between the biosyntheses of the two myxochromide compounds and to analyze the evolutionary connection to the NRPS system, we set out to identify the myxochromide A biosynthesis genes. As myxochromide A is known to be produced from several *Myxococcus* species,[8] we scanned the genome sequence of *M. xanthus* DK1622[28] for the presence of myxochromide biosynthetic genes. By using the sequence from the myxochromide S gene cluster (mch_S[9]) as a probe, we identified a very similar three-gene operon, which was later termed mch_A (see the Supporting Information). The encoded megasynthetase ($MchABC_A$) directs the biosynthesis of myxochromides A, as shown by gene-inactivation experiments (see the Supporting Information). To our knowledge, this finding correlates, for the first time, one of the approximately 18 gene clusters for secondary-metabolite biosynthesis found in the genome sequence of *M. xanthus* DK1622[13] to a specific product.

After isolation of myxochromides A from extracts of *M. xanthus* DK1050 (a derivative of DK1622 that is stable in the production of a yellow pigment[14]), structure elucidation was carried out with myxochromide A_3 (for the isolation procedure and structural data see the Supporting Information). Based on the NMR data, the original myxochromide A structure[8] was revised such that the α-carboxyl group of the glutamine formes an ester linkage with the threonine hydroxy group. This linkage was suggested in our previous work[9] based on theoretical biosynthetic assumptions. Determination of the absolute configuration of the amino acids correlates well with the results from Trowitzsch-Kienast and co-workers[8] and provides evidence that one of the two alanines has the D configuration. HPLC analysis of crude extracts from *M. xanthus* DK1050 indicates the presence of at least two further myxochromides (A_2 and A_4). HPLC/diode-array MS/MS analysis of an extract from a feeding experiment employing

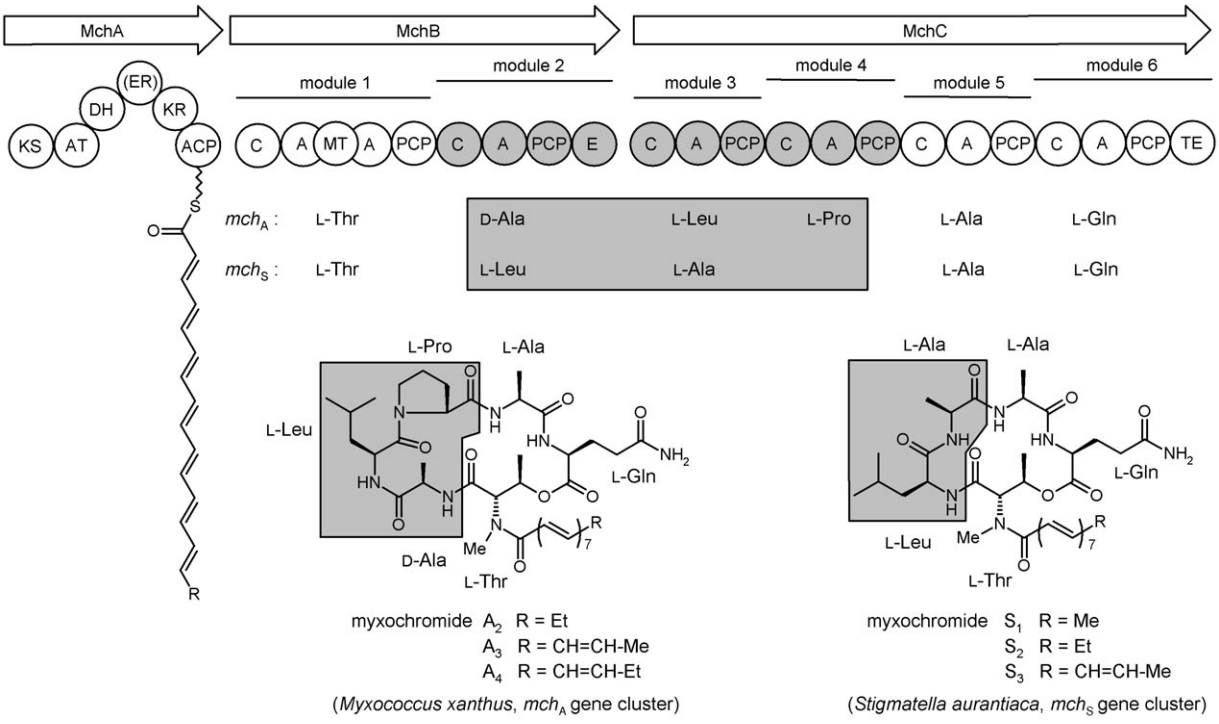

Figure 1. The myxochromide biosynthetic assembly line from *M. xanthus* DK1622 and *S. aurantiaca* DW4/3-1 with the corresponding products myxochromides A and myxochromides S. The amino acids incorporated into the mch_A and mch_S pathway are indicated below the corresponding NRPS modules. The structural differences in the peptide cores of myxochromides A and myxochromides S, caused by point mutations in modules 2–4, are highlighted in gray. KS = ketoacyl synthase, AT = acyl transferase, DH = β-hydroxyacyl dehydratase, ER = enoyl reductase, KR = β-ketoacyl reductase, ACP = acyl carrier protein, C = condensation domain, A = adenylation domain, PCP = peptidyl carrier protein, MT = methyl transferase, E = epimerization domain, TE = thioesterase.

 © 2006 Wiley-VCH Verlag GmbH & Co. KGaA, Weinheim

[U-$^{13}C_4$,$^{15}N_1$]threonine was performed and indicated that myxochromides A_{2-4} have the same peptide core but differ in the structures of their side chains (see the Supporting Information). In the MS/MS analysis, a specifically labeled threonine–polyketide side-chain fragment could be observed for each of the three types of myxochromide A, which is in agreement with the structures shown in Figure 1.

On first inspection, the previously identified myxochromide S biosynthetic proteins from *S. aurantiaca* and their counterparts from the myxochromide A pathway in *M. xanthus* DK1622 seem to be almost identical. Sequence analysis indicates a three-gene operon (*mch*ABC_S or *mch*ABC_A) encoding a bacterial type I PKS ($MchA_S$ and $MchA_A$) and two nonribosomal peptide synthetases ($MchBC_S$ and $MchBC_A$). In general, these megasynthetases are composed of numerous domains bundled together into functional modules that carry out biosynthetic steps involving monomer selection and activation, covalent binding as thioesters, and chain elongation and subsequent release.[1,3] Commonly, the order and the number of modules within a NRPS or PKS dictate the number and the sequence of amino acids (NRPSs) or carboxylic acids (PKSs) in the resultant product, which is why the enzymes have also been called "protein templates".[1,3] Comparison of the myxochromide S and A megasynthetases revealed an identical arrangement of modules and domains (Figure 1). However, there are intriguing and significant structural differences in the peptide cores of myxochromides S and A. In the myxochromide S structure, the sequence of two amino acids has changed from D-Ala/L-Leu to L-Leu/L-Ala, and the amino acid proline is absent in myxochromide S.

The myxochromide peptide backbones are synthesized by two NRPSs (MchBC) that employ adenylation (A) domains to recruit amino acids for the growing peptide chain. The specificity, order, and placement of the A domain within the megasynthetase provide the instructions for thiotemplated peptide biosynthesis.[1] Initially, we speculated that the structural differences in the peptide cores from the two types of myxochromides were caused by genetic exchange of the respective A domains or complete modules. Therefore, we expected to find a high degree of genetic similarity between modules or A domains specific for identical amino acids and more variation between the modules or domains that correspond, in terms of their arrangement, in the $MchBC_A$ and $MchBC_S$ megasynthetase. However, the amino acid and nucleotide identities between the corresponding domains and modules encoded in each gene cluster are much higher (approximately 70% nucleotide identity) than those between domains or modules that incorporate the same amino acids (approximately 58–59% nucleotide identity; see the Supporting Information).

As an alternative to the speculation above, a change in the nonribosomal code might be caused by point mutations in the gene cluster resulting in amino acid substitutions in the substrate-binding pocket of the A domains. To analyze this, the theoretical binding specificities of the A domain binding pocket were determined through the identification of the critical residues responsible for substrate recognition.[15,16] Next, these residues were compared with consensus sequences available in databases (Table 1 and Reference [29]). This shows that the observed point mutations in the A domains from module 2 and 3 of the *mch*$_S$ and *mch*$_A$ pathways lead to increased chemical diversity in myxochromide biosynthesis.

Table 1: Comparison of the putative specificity-conferring codes of the A domains from modules 2–4 from the *mch*$_A$ and *mch*$_S$ biosynthetic gene clusters with consensus sequences.[a]

Sequence	Activated residue	Residue according to GrsA Phe numbering[b]							
		235	236	239	278	299	301	322	330
consensus	alanine	D	V	W	V	I	A	A	V
module 2 *mch*$_A$	alanine	**D**	**V**	**W**	**V**	**I**	**A**	**A**	**V**
module 2 *mch*$_S$	leucine	**D**	**A**	**W**	**F**	**L**	**G**	**N**	**V**
consensus	leucine	D	A	W	F	L	G	N	V
module 3 *mch*$_A$	leucine	**D**	**A**	**W**	**F**	**L**	**G**	**N**	**V**
module 3 *mch*$_S$	alanine	**D**	**V**	M	F	**I**	G	I	**V**
consensus	proline	D	V	Q	F	I	A	H	V
module 4 *mch*$_A$	proline	**D**	**V**	**Q**	**F**	**I**	**A**	**H**	**V**
module 4 *mch*$_S$	proline	G	A	**Q**	**F**	**I**	**A**	Q	**V**

[a] Residues identical to the consensus sequences are shown in bold. [b] The numbering of the amino acids corresponds to the GrsA gramicidine synthetase. The GrsA phenylalanine substrate binding pocket has been crystallized,[27] which lead to the establishment of the nonribosomal code.[15,16]

Condensation (C) domains are thought to discriminate against elongation with "false" incoming aminoacyl-*S*-4′-phosphopantheine (Ppant) residues, and as a result, one would assume that the respective C domains in MchBC would disable further assembly of the intermediate.[7,17,18] However, in this case the C domains involved must inherit a promiscuous substrate specificity that allows for the production of novel compounds which might represent an evolutionary strategy to create chemical diversity. Although striking similarities could be observed between the C domains of modules 2 and 3 from both gene clusters (see the Supporting Information), further investigations are needed to clarify their role during myxochromide assembly.

Another interesting feature of the megasynthetase is that the L-leucine incorporated by module 2 into myxochromides S is not epimerized even though it contains an epimerization (E) domain. From sequence analysis, the respective E domain does not seem to be inactive but rather it seems likely that the epimerization domain is nonfunctional when the peptidyl carrier protein (PCP) domain from module 2 is charged with leucine instead of alanine, which is then epimerized to the D form in myxochromides A.

The myxochromide S NRPS, which is composed of six modules, does not match the five biosynthetic units incorporated into the peptide core, leading to the assumption that one module is skipped during the assembly process.[9] Structural comparison with the myxochromide A peptide core revealed that the fourth amino acid (L-proline) is not present in myxochromide S (Figure 1). Examination of the critical residues of module 4 from $MchC_S$ and $MchC_A$ reveals a high similarity to the proline-specific binding pockets (Table 1), which is in good agreement with the myxochromide A structure and also suggests that module 4 is skipped

 © 2006 Wiley-VCH Verlag GmbH & Co. KGaA, Weinheim

during myxochromide S assembly.[9] Module skipping has recently been described for an engineered PKS system[19] and is assumed to be responsible for the generation of minor by-products of PKS assembly lines.[10,12,20–22] To date, no such process has been described in the biochemistry of multimodular NRPSs.

Two different mechanisms can be considered (Figure 2). First, the complete module might be skipped as a result of direct transfer of the biosynthetic intermediate from module 3 to 5 (mechanism 1). Alternatively, a skipping process that involves PCP-to-PCP chain transfer (mechanism 2) requires that the PCP of the skipped module be posttranslationally activated but not primed with an extender aminoacyl moiety. In this case, the A domain in the skipped module must be inactive. Indeed, in the core regions of the A domain from module 4 of $MchC_S$, several variations from the normally conserved amino acids are conspicuous (see the Supporting Information). Nevertheless, variations could also be found in the PCP-domain core motif of this module. Most notably, the highly conserved serine residue (S), which is required for the posttranslational activation,[23] is not in the expected position (EDFFQMGGNPS compared to the core motif DxFFxLGGHSL; see the Supporting Information). In contrast to the A and PCP domains from module 4, inspection of the C domain core motifs does not indicate any specific deviations. We therefore set out to investigate the biochemical properties of the A and PCP domains of this module.

To answer the question if the A domain from module 4 is able to activate amino acids, the corresponding domains from the mch_S and mch_A gene clusters were expressed as glutathione-*S*-transferase (GST) fusion proteins in *Escherichia coli*. After affinity, purification, and cleavage of the GST fusion protein, an amino acid dependent ATP/PP_i exchange assay[24] showed that both domains are capable of specifically activating proline (Figure 3 a). It can thus be concluded that the specificity of the A domain of module 4 from $MchC_A$ coincides with the primary structure of myxochromides A. The finding that the A domain from module 4 of $MchC_S$ is active was unexpected because of mutations in highly conserved core motifs[2] (see the Supporting Information). For example, the exchange of the strictly conserved aspartate (D) for a glycine (G) residue in the core motif A4 (FDxS; shown to interact with the α-amino group of the substrate). Furthermore, the conserved asparagine (N) was exchanged for serine (S) as part of the core motif A5 (NxYGPTE), which interacts with the nucleotide ribose moiety.[2] Two additional

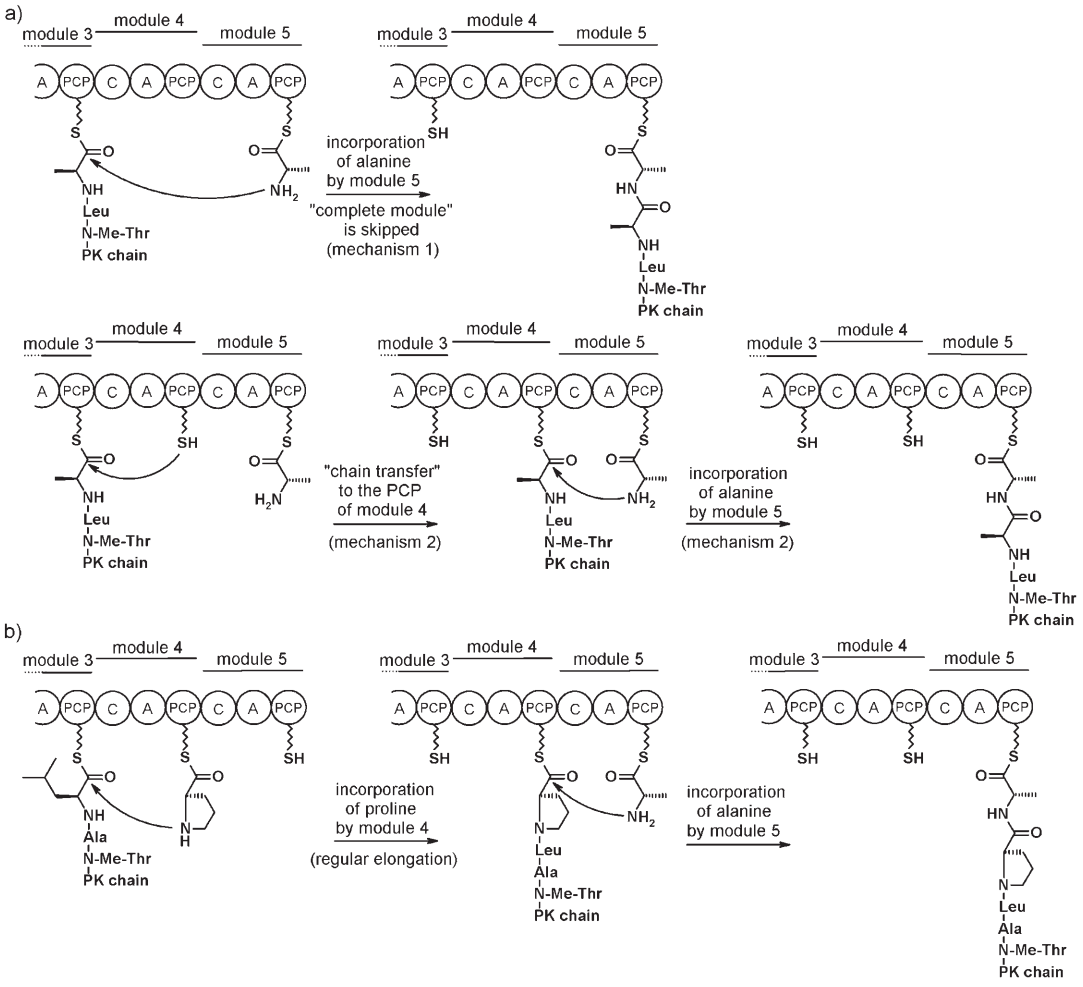

Figure 2. a) Alternative proposed mechanisms for module skipping during myxochromide S biosynthesis; b) Regular assembly of the myxochromide A peptide core.

 © 2006 Wiley-VCH Verlag GmbH & Co. KGaA, Weinheim

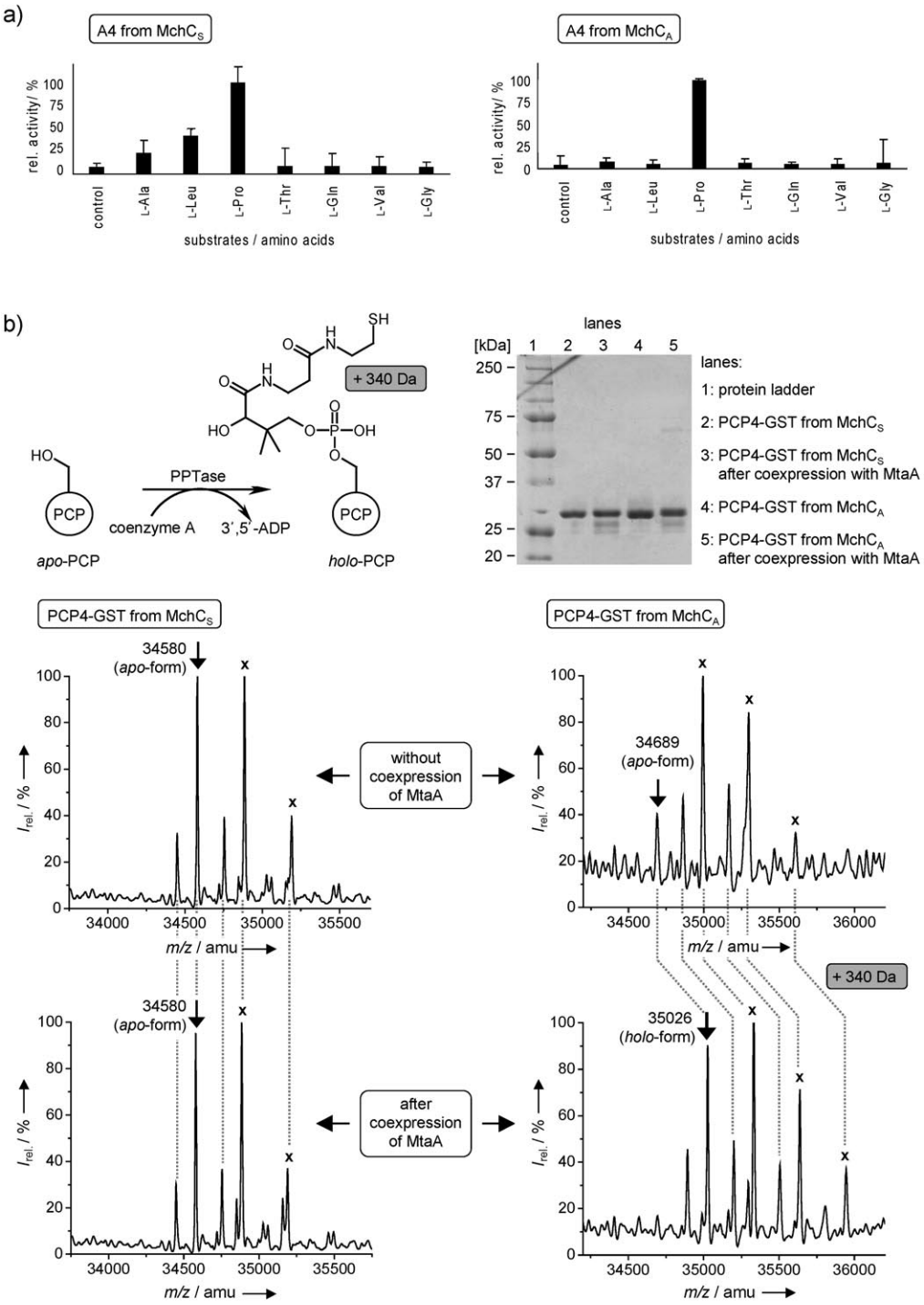

Figure 3. Biochemical investigations to elucidate the module-skipping process in myxochromide S biosynthesis. a) Relative substrate specificities of the adenylation domain of module 4 (A4) from MchC$_S$ and MchC$_A$ determined by ATP-PP$_i$ exchange reactions with different amino acids and a control without any amino acid. The highest activities were set at 100%. b) Activation of PCPs by the PPTase MtaA from the myxochromide producer *S. aurantiaca* DW4/3-1; SDS-PAGE of purified PCP-GST fusion proteins from module 4 (PCP4-GST) from MchCs and MchC$_A$ and subsequent mass analysis by HPLC-ESI/ICR. The PCPs were expressed with and without the PPTase MtaA.[26] The arrows indicate mass signals derived from GST fusions, whereas "×" marks signals occurring because of GST-fusion glutathione adducts. Expected masses for the PCP4-GST-fusion proteins: *apo*-PCP4-GST from MchC$_S$ = 34580 Da, *holo*-PCP4-GST from MchC$_S$ = 34920 Da, *apo*-PCP4-GST from MchC$_A$ = 34688 Da, *holo*-PCP4-GST from MchC$_A$ = 35028 Da.

mutations were also found in the core motif A7 (Y(RK)TGDL to FQTGDL), which is highly conserved in A domains and various ATPases (see the Supporting Information).

As the inactivity of the A domain is clearly not the reason for the module-skipping process, we next investigated whether the PCP from module 4 is posttranslationally activated. Posttranslational modification of carrier proteins

 © 2006 Wiley-VCH Verlag GmbH & Co. KGaA, Weinheim

implies the transfer of the 4′-Ppant moiety from coenzyme A to a highly conserved serine residue. 4′-Phosphopantetheinyl transferases (PPTases[25]) catalyze the conversion from the inactive *apo* form to the active *holo* form[23] of the enzyme (Figure 3b). The PPTase MtaA from the myxochromide S producer *S. aurantiaca* DW4/3-1 was previously identified and characterized.[26] Inactivation of *mtaA* in *S. aurantiaca* DW4/3-1 leads to a complete loss of natural product formation indicating that MtaA is responsible for the activation of all secondary-metabolite biosynthetic proteins in this strain including $MchABC_S$. Heterologous coexpression of MtaA with the PCP domain from the skipped module 4 from $MchC_S$ was performed in *E. coli* to investigate whether this domain can be activated. The PCP from module 4 of $MchC_A$ was included as a positive control. As negative controls, both domains were expressed in the absence of *mtaA*. After affinity purification of these proteins (as GST fusion proteins), their masses were measured by using Fourier transform ion cyclotron resonance mass spectrometry (FTICR-MS) (Figure 3b). This revealed a Ppant transfer to the PCP from $MchC_A$, whereas no mass shift could be observed when the PCP from module 4 of the mch_S pathway was analyzed. It can thus be concluded that this domain is not present in the active *holo* form and therefore module 4 is completely skipped during the biosynthetic process (see mechanism 1, Figure 2). To date, no such process has been described in the biochemistry of multimodular NRPSs, and of the skipping processes reported for polyketide biosynthesis,[10,12,19–21] only one has been analyzed biochemically.[19] For an engineered PKS system it was shown that the skipping process involves passage of the growing polyketide through the skipped module by direct ACP-to-ACP transfer.[19] In contrast, the module skipping during myxochromide S biosynthesis represents the first verified example that multimodular megasynthetases are able to skip a complete module, which requires structural flexibility within these giant assembly lines.

Recent biochemical investigations of NRPS- and PKS-catalyzed assembly processes clearly show that these multimodular enzymes do not always follow textbook biochemistry to generate natural products. This indicates that these biosynthetic systems are more flexible than originally thought.[10,12]

Herein, two highly similar myxochromide megasynthetases are compared revealing the genetic and biochemical basis for the generation of chemical diversity. A unique module-skipping process is caused by a "loss of function mutation" in the core motif of the respective PCP domain. Furthermore, it can be deduced that point mutations in the encoding DNA lead to amino acid substitutions in the specificity pocket of A domains resulting in different peptide core sequences. Therefore, the general assumption of a gatekeeper function for all C domains in NRPS has to be questioned. These findings are of significant importance for combinatorial approaches and should be taken into consideration in engineering NRPS and/or PKS biosynthetic pathways for generating novel "unnatural" natural products.

Received: October 21, 2005
Published online: February 28, 2006

Keywords: biosynthesis · module skipping · myxobacteria · natural products · peptides

[1] S. A. Sieber, M. A. Marahiel, *Chem. Rev.* **2005**, *105*, 715.
[2] M. A. Marahiel, T. Stachelhaus, H. D. Mootz, *Chem. Rev.* **1997**, *97*, 2651.
[3] J. Staunton, K. J. Weissman, *Nat. Prod. Rep.* **2001**, *18*, 380.
[4] D. Hopwood, *Chem. Rev.* **1997**, *97*, 2465.
[5] L. Du, B. Shen, *Curr. Opin. Drug Discovery Dev.* **2001**, *4*, 215.
[6] S. Donadio, M. Sosio, *Comb. Chem. High Throughput Screening* **2003**, *6*, 489.
[7] U. Keller, F. Schauwecker, *Comb. Chem. High Throughput Screening* **2003**, *6*, 527.
[8] W. Trowitzsch Kienast, K. Gerth, H. Reichenbach, G. Höfle, *Liebigs Ann. Chem.* **1993**, 1233.
[9] S. C. Wenzel, B. Kunze, G. Höfle, B. Silakowski, M. Scharfe, H. Blöcker, R. Müller, *ChemBioChem* **2005**, *6*, 375.
[10] S. C. Wenzel, R. Müller, *Curr. Opin. Chem. Biol.* **2005**, *9*, 447.
[11] S. C. Wenzel, F. Gross, Y. Zhang, J. Fu, F. A. Stewart, R. Müller, *Chem. Biol.* **2005**, *12*, 349.
[12] S. J. Moss, C. J. Martin, B. Wilkinson, *Nat. Prod. Rep.* **2004**, *21*, 575.
[13] H. B. Bode, R. Müller, *Angew. Chem.* **2005**, *117*, 6988; *Angew. Chem. Int. Ed.* **2005**, *44*, 6828.
[14] A. Martinezlaborda, M. Elias, R. Ruizvazquez, F. J. Murillo, *Mol. Gen. Genet.* **1986**, *205*, 107.
[15] G. L. Challis, J. Ravel, C. A. Townsend, *Chem. Biol.* **2000**, *7*, 211.
[16] T. Stachelhaus, H. D. Mootz, M. A. Marahiel, *Chem. Biol.* **1999**, *6*, 493.
[17] U. Linne, M. A. Marahiel, *Biochemistry* **2000**, *39*, 10439.
[18] P. J. Belshaw, C. T. Walsh, T. Stachelhaus, *Science* **1999**, *284*, 486.
[19] I. Thomas, C. J. Martin, C. J. Wilkinson, J. Staunton, P. F. Leadlay, *Chem. Biol.* **2002**, *9*, 781.
[20] I. H. Hardt, H. Steinmetz, K. Gerth, F. Sasse, H. Reichenbach, G. Höfle, *J. Nat. Prod.* **2001**, *64*, 847.
[21] B. Beck, Y. Yoon, K. Reynolds, D. Sherman, *Chem. Biol.* **2002**, *9*, 575.
[22] C. C. Aldrich, B. J. Beck, R. A. Fecik, D. H. Sherman, *J. Am. Chem. Soc.* **2005**, *127*, 8441.
[23] C. T. Walsh, A. M. Gehring, P. H. Weinreb, L. E. Quadri, R. S. Flugel, *Curr. Opin. Chem. Biol.* **1997**, *1*, 309.
[24] T. Stachelhaus, M. A. Marahiel, *J. Biol. Chem.* **1995**, *270*, 6163.
[25] R. H. Lambalot, A. M. Gehring, R. S. Flugel, P. Zuber, M. LaCelle, M. A. Marahiel, R. Reid, C. Khosla, C. T. Walsh, *Chem. Biol.* **1996**, *3*, 923.
[26] N. Gaitatzis, A. Hans, R. Müller, S. Beyer, *J. Biochem.* **2001**, *129*, 119.
[27] E. Conti, T. Stachelhaus, M. A. Marahiel, P. Brick, *EMBO J.* **1997**, *16*, 4174.
[28] The genome sequence is available at the Institute of Genomic Research, Rockville, MD, USA or from the website http://www.tigr.org.
[29] For databases of consensus sequences see, http://www.npbiogene.com/, http://jhunix.hcf.jhu.edu/≈ravel/nrps//

 © 2006 Wiley-VCH Verlag GmbH & Co. KGaA, Weinheim

Main Group Element Compounds

DOI: 10.1002/anie.200503531

Synthesis of Macrocyclic Aluminum–Phosphorus and Gallium–Phosphorus Compounds**

Carsten von Hänisch and Sven Stahl*

Compounds of the type $R_2Al{-}PR'_2$ and $R_2Ga{-}PR'_2$ show a strong tendency to form cyclic σ-donor–σ-acceptor species $[R_2M{-}PR'_2]_n$ (M = Al, Ga; $n = 2, 3$).[1,2] These compounds usually feature four- or six-membered rings (**I** or **II**). Monomeric compounds are only isolated when the substituents R and R′ are sterically very demanding.[3] Recently, we obtained the first evidence that larger cycles can also be synthesized. The reaction of the diphosphanylsilane $iPr_2Si(PH_2)_2$ with MEt_3 (M = Al, Ga, In) leads to the compounds $[iPr_2Si\{P(H)MEt_2\}_2]_2$.[4] The products feature an eight-membered M_4P_4 ring, in which the two pairs of opposing phosphorus atoms are bridged by iPr_2Si groups, resulting in an $M_4P_4Si_2$ adamantoid cage (**III**).

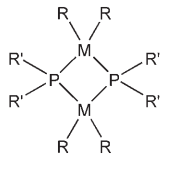

I

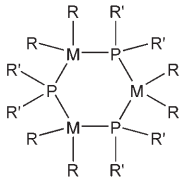

II

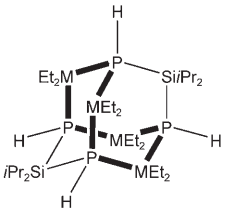

III

By varying the bridging units between the phosphorus atoms, it should be possible to obtain polycyclic compounds with new structural motifs. For this reason, we synthesized the diphosphanyldisiloxane $O(SiiPr_2PH_2)_2$ (**1**). The eight-membered ring compound $[O(SiiPr_2)_2PH]_2$ (**2**) was isolated as a byproduct. Both **1** and **2** were obtained from the reaction of the dichlorodisiloxane $O(SiiPr_2Cl)_2$ with two equivalents of $[LiPH_2(dme)]$ (dme = dimethoxyethane) in THF [Eq. (1)]. Compound **1** can be isolated in a pure form by distillation, and **2** can subsequently be obtained by recrystallization of the distillation residue.

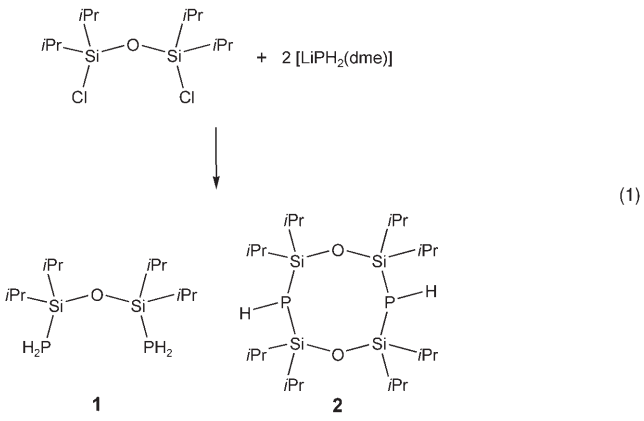

(1)

1 **2**

In the ^{31}P NMR spectrum of **1**, a triplet of higher order at $\delta = -261.8$ ppm represents the AA′ part of an $AA'X_2X'_2$ spin system. The ^1H NMR spectrum shows a doublet of higher order at $\delta = 1.32$ ppm, with a $^1J_{P,H}$ coupling constant of 185 Hz, that is assigned to the phosphanyl groups ($X_2X'_2$ part), as well as a multiplet at $\delta = 1.13$ ppm that is assigned to the isopropyl groups. In the $^{29}Si\{^1H\}$ NMR spectrum, the X part of an ABX spin system is observed, with $^1J_{Si,P}$ and $^3J_{Si,P}$ coupling constants of 24.3 and 0.12 Hz. Silicon satellites corresponding to the AB part of the spin system are detected in the $^{31}P\{^1H\}$ NMR spectrum. In the $^{13}C\{^1H\}$ NMR spectrum, a multiplet assigned to the tertiary carbon atoms, as well as two multiplets assigned to the diastereotopic methyl groups are observed. In the electron ionization (EI) mass spectrum of **1**, the molecular-ion ($[M]^+$) peak has a relative intensity of only 1.0%; however, strong signals are detected for the fragments $[M-PH_2]^+$, $[M-iPr]^+$, and $[M-PH_2-iPr]^+$.

The ^{31}P NMR spectrum of the cyclic compound **2** consists of a doublet at $\delta = -269$ ppm, with a $^1J_{P,H}$ coupling constant of 194 Hz. Colorless crystals of **2** were isolated from an *n*-pentane solution at −35 °C. The compound crystallizes in the tetragonal space group $P4_32_12$, with four molecules per unit cell (Figure 1).[5] In the crystal structure of **2**, the two phosphorus-bound hydrogen atoms are oriented *trans* to one another across the eight-membered ring. A twofold rotation axis passes through O(1) and O(2). The two Si–O–Si units of the ring are strongly twisted towards each other;

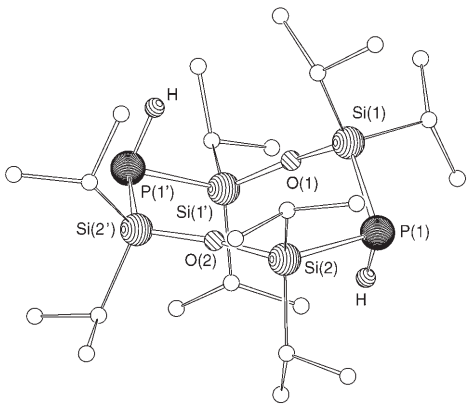

Figure 1. Molecular structure of **2**. Open circles are carbon atoms; the hydrogen atoms of the organic groups are omitted for clarity. Selected bond lengths [pm] and angles [°]: Si(1)–P(1) 226.3(1), Si(2)–P(1) 225.2(1), Si(1)–O(1) 163.1(1), Si(2)–O(2) 163.7(1); Si(1)-P(1)-Si(2) 105.74(2), O(1)-Si(1)-P(1) 112.81(4), O(2)-Si(2)-P(1) 113.47(5), Si(1)-O(1)-Si(1′) 163.75(11), Si(2)-O(2)-Si(2′) 168.14(10).

[*] Priv.-Doz. Dr. C. von Hänisch, S. Stahl
Institut für Nanotechnologie
Forschungszentrum Karlsruhe
Postfach 3640, 76021 Karlsruhe (Germany)
Fax: (+49) 7247-82-6368
E-mail: carsten.vonhaenisch@int.fzk.de

[**] The authors thank Dr. E. Matern for his help with the NMR experiments.

InterScience
© 2006 Wiley-VCH Verlag GmbH & Co. KGaA, Weinheim

therefore, the P(1)-Si(2)-Si(2′)-P(1′) torsion angle is only 9.59°, whereas P(1)-Si(1)-Si(1′)-P(1′) is −88.93°. This pronounced twist is due to the mutual repulsion of the sterically demanding isopropyl groups bound to the silicon atoms.

Compound **1** reacts with MEt_3 (M = Al, Ga) in benzene, with evolution of ethane [Eq. (2)]. Colorless crystals of the

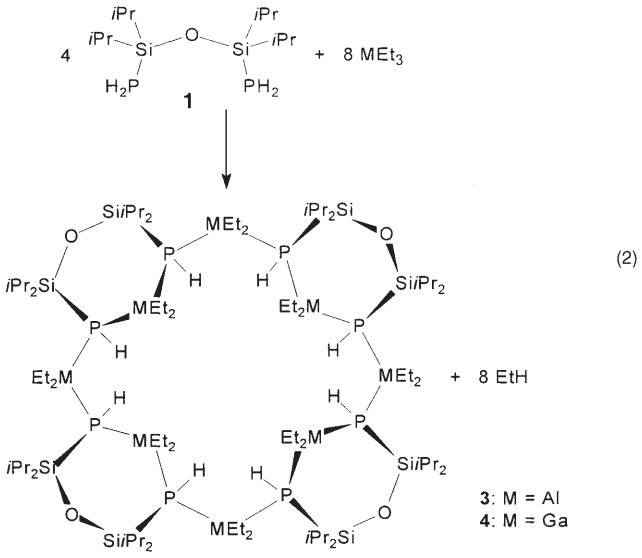

(2)

macrocyclic compounds **3** and **4** were isolated from the reaction mixtures. The macrocycles **3** and **4** crystallize isotypically in the tetragonal space group $P\bar{4}2_1c$ (Figure 2),

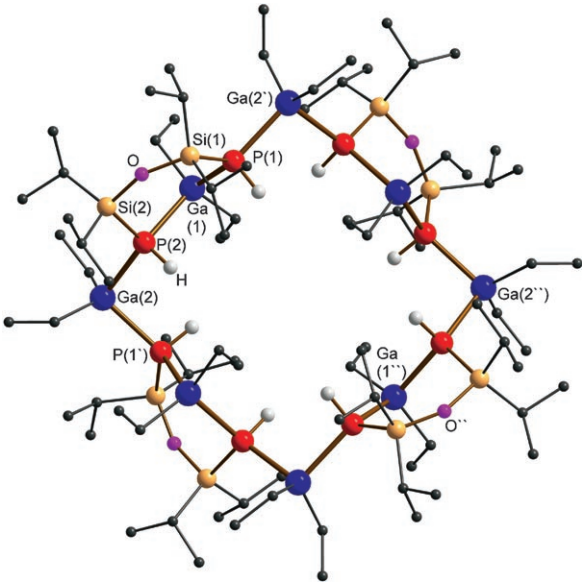

Figure 2. Molecular structure of **4**. Gray circles are carbon atoms; the hydrogen atoms of the organic groups are omitted for clarity. Selected bond lengths [pm] and angles [°]: Ga(1)–P(1) 245.5(2), Ga(1)–P(2) 244.8(2), Ga(2)–P(1′) 245.4(2), Ga(2)–P(2) 246.1(2), P(1)–Si(1) 227.9(2), P(2)–Si(2) 226.9(2), Si(1)–O 162.2(4), Si(2)–O 164.7(4); P(1)-Ga(1)-P(2) 102.32(5), P(1′)-Ga(2)-P(2) 97.69(5), Ga(1)-P(1)-Ga(2′) 122.19(6), Ga(1)-P(2)-Ga(2) 124.72(7), Si(1)-P(1)-Ga(1) 110.63(7), Si(1)-P(1)-Ga(2′) 114.56(7), Si(2)-P(2)-Ga(1) 105.77(7), Si(2)-P(2)-Ga(2) 115.63(7), Si(1)-O-Si(2) 155.5(3).

together with four benzene molecules per formula unit.[5] The macrocycles encircle the $\bar{4}$ axes in the unit cell (Figure 3). Four six-membered OSi_2P_2M rings are connected by MEt_2 fragments to form an inorganic pentacycle with a central 16-membered M_8P_8 ring. Pairs of phosphorus atoms in the central ring are bridged by Si–O–Si units. These Si–O–Si bridges are located alternately above and below the central macrocycle, which leads to a strong folding of the ring (Figure 3, bottom).

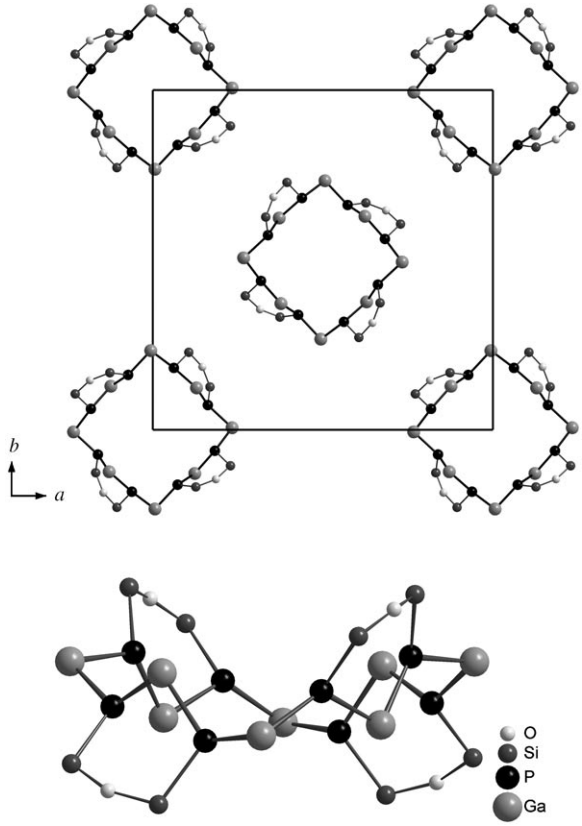

Figure 3. Top: packing of **4** in the unit cell, as viewed along the *c* axis. Bottom: side view of the heteroatom framework of **4**. Organic groups and hydrogen atoms are omitted for clarity.

Each phosphorus atom is also bonded to one hydrogen atom (located during the refinements of the crystal structures), which points into the central ring. In the IR spectra, bands at $\tilde{\nu} = 2300$ (**3**) and 2324 cm^{-1} (**4**), which are assigned to the P–H stretching vibrations, are observed. Moreover, the ^{31}P NMR spectra show doublets with $^1J_{PH}$ coupling constants of 256 (**3**) and 258 Hz (**4**) that are typical for four-coordinate phosphorus atoms. The aluminum or gallium atoms in **3** and **4** each bear two ethyl substituents and have tetrahedral coordination environments. The M–P bond lengths within and between the six-membered OSi_2P_2M rings are very similar, and range from 244.9–246.3 (**3**) or 244.8–246.1 pm (**4**). However, the P-M-P bond angles within and between the six-membered rings differ markedly: the P-M(1)-P angles are 102.77(7) (**3**) and 102.32(5)° (**4**), whereas the P-M(2)-P angles are 98.27(6) (**3**) and 97.69(5)° (**4**).

 © 2006 Wiley-VCH Verlag GmbH & Co. KGaA, Weinheim

The sizes of the inorganic macro(poly)cycles can be estimated from the following interatomic distances (Figure 2): **3**: Al(1)···Al(1″) 889.2(1), Al(2)···Al(2″) 1169.7(2), O···O″ 1176.0(1) pm; **4**: Ga(1)···Ga(1″) 891.6(1), Ga(2)···Ga(2″) 1167.2(2), O···O″ 1179.1(1) pm. A similar macrocycle is found in the compound $[\{P_4(C_2H_4)_2(AlMe_2)_2\}_4]\cdot 4\,AlMe_3$ recently described by Stephan and Hoskin.[6] However, this compound contains several P–P bonds in addition to Al–P bonds.

We are currently investigating whether other macrocyclic compounds can be synthesized when the organic substituents on the silicon and metal atoms are varied.

Experimental Section

1 and **2**: A solution of $O(Si\textit{i}Pr_2Cl)_2$[8] (5.0 g, 15.85 mmol) in THF (50 mL) was added dropwise to a solution of $[LiPH_2(dme)]$[7] (4.12 g, 31.71 mmol) in THF (100 mL) at 0 °C. The reaction mixture was subsequently warmed to 22 °C and stirred for 16 h, resulting in a clear solution. All volatile components were removed under vacuum, and the residue was dissolved in *n*-pentane (100 mL). After filtration and removal of the pentane under vacuum, the residue was distilled. Compound **1** is isolated at 80–85 °C and 1×10^{-3} mbar. Yield 2.42 g (49 %). ^{1}H NMR (C_6D_6, 25 °C, 400 MHz): $\delta = 1.13$ (m, $^3J_{H,H} = 7.5$ Hz, $^2J_{P,H} = 1.5$ Hz, *i*Pr, 28 H), 1.32 ppm (d, m, $^1J_{P,H} = 185$ Hz, $^5J_{P,H} = 0.45$ Hz, PH_2, 4 H); ^{13}C{^{1}H} NMR (C_6D_6, 25 °C, 100.6 MHz): $\delta = 17.38$ (m, $^2J_{P,C} = 8.3$ Hz, $^4J_{P,C} = -0.05$ Hz, $^4J_{P,P} = 6.8$ Hz, CH), 18.46 (m, $^3J_{P,C} = 2.0$ Hz, $^5J_{P,C} = 0.8$ Hz, CH_3), 18.50 ppm (m, $^3J_{P,C} = 2.3$ Hz, $^5J_{P,C} = 0.5$ Hz, CH_3); ^{29}Si{^{1}H} NMR (C_6D_6, 25 °C, 79.5 MHz): $\delta = 20.8$ ppm (m, $^1J_{P,Si} = 24.3$ Hz, $^3J_{P,Si} = 0.12$ Hz); ^{31}P NMR (C_6D_6, 25 °C, 161.9 MHz): $\delta = -261.8$ ppm (m, $^1J_{P,H} = 185$ Hz, $^5J_{P,H} = 0.45$ Hz); MS (EI, 70 eV): *m*/*z* (%): 310 (1.0) $[M]^+$, 277 (100) $[M-PH_2]^+$, 267 (4.0) $[M-i\text{Pr}]^+$, 233 (33) $[M-PH_2-i\text{Pr}]^+$ 105 (17) $[Si\textit{i}PrHPH_2]^+$, 43 (5) $[i\text{Pr}]^+$.

Recrystallization of the distillation residue from *n*-pentane (2 mL) at −35 °C yields **2** as large colorless crystals. Yield: 1.1 g (25 %). Elemental analysis (%) calcd for $C_{24}H_{58}O_2P_2Si_4$ (553.01): C 52.13, H 10.57; found: C 52.03, H 11.11. ^{1}H NMR (C_6D_6, 25 °C, 400 MHz): $\delta = 0.99$ (d, $^1J_{P,H} = 194$ Hz, PH, 2 H), 1.18 ppm (m, *i*Pr, 56 H); ^{13}C{^{1}H} NMR (C_6D_6, 25 °C, 100.6 MHz): $\delta = 18.8$ (d, $^2J_{P,C} = 13$ Hz, CH), 18.9 (d, $^2J_{P,C} = 3.7$ Hz, CH_3), 19.4 ppm (d, $^2J_{P,C} = 4.4$ Hz, CH_3); ^{29}Si{^{1}H} NMR (C_6D_6, 25 °C, 79.5 MHz): $\delta = 17.5$ ppm (dd, $^1J_{P,Si} = 40$ Hz, $^3J_{P,Si} = 0.55$ Hz); ^{31}P NMR (C_6D_6, 25 °C, 161.9 MHz): $\delta = -269$ ppm (d, $^1J_{P,H} = 194$ Hz); IR (KBr): $\tilde{\nu} = 2944$ (vs), 2890 (s), 2865 (vs), 2756 (w), 2723 (w), 2712 (w), 2304 (s), 2291 (s), 1462 (vs), 1387 (s), 1363 (m), 1239 (s), 1084 (vs), 1055 (vs), 1030 (vs), 999 (s), 985 (s), 918 (m), 881 (vs), 805 (w), 680 (s), 661 (s), 625 (w), 614 (m), 593 (s), 511 (w), 492 (m), 466 (s), 443 cm^{-1} (m); MS (EI, 70 eV): *m*/*z* (%): 552 (100) $[M]^+$, 509 (27.5) $[M-i\text{Pr}]^+$, 276 (3.6) $[M/2]^+$, 245 (98.7) $[OSi_2\textit{i}Pr_4H]^+$, 203 (22.9) $[OSi_2\textit{i}Pr_3H_2]^+$, 43 (6.6) $[i\text{Pr}]^+$.

3: $AlEt_3$ (0.15 g, 1.3 mmol) was added to a solution of **1** (0.2 g, 0.65 mmol) in benzene (10 mL). The reaction mixture was stirred for one minute and then kept without agitation for 20 h (stirring for the entire reaction time yields **3** as a microcrystalline precipitate). Subsequent cooling of the solution to 6 °C yields colorless needle-shaped crystals of $\mathbf{3}\cdot 4\,C_6H_6$. Yield: 0.15 g (48 %). Elemental analysis (%) calcd for $C_{80}H_{200}Al_8O_4P_8Si_8$ (1914.8): C 50.18, H 10.53; found: C 51.37, H 9.83. Thermal decomposition with gas formation at 170 °C. ^{31}P NMR ([D_8]toluene, 50 °C, 121.5 MHz): $\delta = -242$ ppm (d, $^1J_{P,H} = 256$ Hz); IR (KBr): $\tilde{\nu} = 2947$ (vs), 2894 (s), 2867 (vs), 2724 (w), 2300 (m), 1464 (vs), 1408 (m), 1386 (m), 1367 (m), 1226 (w), 1191 (w), 1161 (w), 1048 (vs), 990 (s), 951 (m), 919 (m), 883 (vs), 822 (w), 696 (m), 654 (s), 567 (s), 536 (w), 492 (w), 460 cm^{-1} (m).

4: $GaEt_3$ (0.20 g, 1.3 mmol) was added to a solution of **1** (0.2 g, 0.65 mmol) in benzene (10 mL). The reaction mixture was stirred for one minute and then kept without agitation for 20 h (stirring for the entire reaction time yields compound **4** as a microcrystalline precipitate). Subsequent cooling of the solution to 6 °C yields colorless needle-shaped crystals of $\mathbf{4}\cdot 4\,C_6H_6$. Yield: 0.24 g (65 %). Elemental analysis (%) calcd for $C_{80}H_{200}Ga_8O_4P_8Si_8$ (2256.7): C 42.58, H 8.93; found: C 41.44, H 8.80. Thermal decomposition with gas formation at 167 °C. ^{31}P NMR (C_6D_6, 50 °C, 121.5 MHz): $\delta = -229$ ppm (d, $^1J_{P,H} = 258$ Hz); IR (KBr): $\tilde{\nu} = 2947$ (vs), 2895 (s), 2867 (vs), 2725 (w), 2324 (m), 1464 (s), 1419 (m), 1385 (m), 1371 (w), 1231 (w), 1214 (w), 1189 (m), 1161 (w), 1071 (m), 1043 (vs), 992 (s), 959 (m), 932 (w), 920 (w), 882 (s), 815 (m), 694 (w), 655 (s), 610 (w), 568 (s), 538 (m), 498 (w), 460 cm^{-1} (m).

Received: October 5, 2005
Revised: December 14, 2005
Published online: February 28, 2006

Keywords: aluminum · gallium · macrocycles · phosphorus

[1] Reviews: a) A. H. Cowley, R. A. Jones, *Angew. Chem.* **1989**, *101*, 1235–1243; *Angew. Chem. Int. Ed. Engl.* **1989**, *28*, 1208–1216; b) S. Schulz, *Coord. Chem. Rev.* **2001**, *215*, 1–37; c) B. Neumüller, E. Iravani, *Coord. Chem. Rev.* **2004**, *248*, 817–834.

[2] a) J. F. Janik, E. N. Duesler, W. F. McNamara, M. Westerhausen, R. T. Paine, *Organometallics* **1989**, *8*, 506–514; b) R. L. Wells, M. F. Self, A. T. McPhail, S. R. Aubuchon, R. C. Woudenberg, J. P. Jasinski, *Organometallics* **1993**, *12*, 2832–2834; c) R. L. Wells, A. T. McPhail, M. F. Self, J. A. Laske, *Organometallics* **1993**, *12*, 3333–3339; d) L. K. Krannich, C. L. Watkins, S. J. Schauer, C. H. Lake, *Organometallics* **1996**, *15*, 3980–3984; e) J. F. Janik, R. L. Wells, V. G. Young, A. L. Rheingold, I. A. Guzei, *J. Am. Chem. Soc.* **1998**, *120*, 532–537; f) A. Schaller, H.-D. Hausen, J. Weidlein, P. Fischer, *Z. Anorg. Allg. Chem.* **2000**, *626*, 616–618.

[3] a) M. A. Petrie, K. Ruhlandt-Senge, P. P. Power, *Inorg. Chem.* **1992**, *31*, 4038–4039; b) M. A. Petrie, P. P. Power, *Inorg. Chem.* **1993**, *32*, 1309–1312; c) M. A. Petrie, P. P. Power, *J. Chem. Soc. Dalton Trans.* **1993**, 1737–1745; P. P. Power, *Chem. Rev.* **1999**, *99*, 3463–3503.

[4] C. von Hänisch, *Eur. J. Inorg. Chem.* **2003**, 2955–2958.

[5] STOE-IPDS2, $Mo_{K\alpha}$ radiation, graphite monochromator, $\lambda = 0.71073$ Å. The structures were solved by direct methods and refined by full-matrix least-squares techniques against F^2. **2**: tetragonal, $P4_32_12$, $Z = 4$, $a = 1335.3(2)$, $c = 1933.5(4)$ pm, $V = 3447.3(10)\times10^6$ pm^3, Flack parameter = 0.05(10), $\rho_{calcd} = 1.066$ g cm^{-3}, $\mu(Mo_{K\alpha}) = 0.283$ mm^{-1}, $T = 200$ K, $2\theta_{max} = 54°$, 27559 reflections measured, 3820 independent reflections, $R_{int} = 0.0686$, 3736 observed reflections ($F_o > 4\sigma(F_o)$), 150 parameters (P, Si, O, and C atoms were refined anisotropically; H atoms of the organic groups were calculated at ideal positions), $R1 = 0.0270$, $wR2 = 0.0751$ (all data), residual electron density = 0.168 e Å^{-3}. $\mathbf{3}\cdot 4\,C_6H_6$: tetragonal, $P\bar{4}2_1c$, $Z = 2$, $a = 2507.6(4)$, $c = 1131.0(2)$ pm, $V = 7112(2)\times10^6$ pm^3, refined as inversion twin, Flack parameter 0.12(19), $\rho_{calcd} = 1.031$ g cm^{-3}, $\mu(Mo_{K\alpha}) = 0.254$ mm^{-1}, $T = 200$ K, $2\theta_{max} = 50°$, 20078 reflections measured, 5866 independent reflections, $R_{int} = 0.0706$, 3972 observed reflections ($F_o > 4\sigma(F_o)$), 286 parameters (Al, P, Si, O, and C were refined anisotropically; H atoms of the organic groups were calculated at ideal positions. One ethyl group was refined with split positions; at these C atoms no H atoms were calculated), $R1 = 0.0528$, $wR2 = 0.1371$ (all data), residual electron density = 0.311 e Å^{-3}. $\mathbf{4}\cdot 4\,C_6H_6$: tetragonal, $P\bar{4}2_1c$, $Z = 2$, $a = 2503.3(4)$, $c = 1127.4(2)$ pm, $V = 7064(2)\times10^6$ pm^3, Flack parameter 0.005(16), $\rho_{calcd} = 1.208$ g cm^{-3}, $\mu(Mo_{K\alpha}) = 1.699$ mm^{-1}, $T = 200$ K, $2\theta_{max} = 52°$, 16100 reflections measured, 6144 independent reflections, $R_{int} = 0.0601$, 5087 observed reflections ($F_o > 4\sigma(F_o)$), 276 parameters (Ga, P, Si, O, and C were refined anisotropically; H atoms of the

 © 2006 Wiley-VCH Verlag GmbH & Co. KGaA, Weinheim

organic groups were calculated at ideal positions), $R1 = 0.0497$, $wR2 = 0.1449$ (all data), residual electron density = 0.901 e Å^{-3}. CCDC-285117 (**2**), CCDC-285118 (**3**), and CCDC-285119 (**4**) contain the supplementary crystallographic data for this paper. These data can be obtained free of charge from The Cambridge Crystallographic Data Centre via www.ccdc.cam.ac.uk/data_request/cif.

[6] A. J. Hoskin, D. W. Stephan, *Angew. Chem.* **2001**, *113*, 1917 – 1919; *Angew. Chem. Int. Ed.* **2001**, *40*, 1865 – 1867.

[7] H. Schäfer, G. Fritz, W. Hölderich, *Z. Anorg. Allg. Chem.* **1977**, *438*, 222 – 224.

[8] M. J. Robins, J. S. Wilson, F. Hansske, *J. Am. Chem. Soc.* **1983**, *105*, 4059 – 4065.

 © 2006 Wiley-VCH Verlag GmbH & Co. KGaA, Weinheim

Homogeneous Catalysis

DOI: 10.1002/anie.200503875

Catalytic Activation of N–N Multiple Bonds: A Homogeneous Palladium Catalyst for Mechanistically Unprecedented Reduction of Azo Compounds**

Kilian Muñiz and Martin Nieger*

Ready access to nitrogen compounds is of crucial importance, as these molecules are key substances for research in the life sciences. The catalytic reductive transformation of nitrogen–nitrogen multiple bonds at a metal complex constitutes a fundamental endeavor to this end. However, even a century after Haber's pioneering work on the heterogeneously catalyzed synthesis of ammonia from its elements,[1] only limited progress on the activation of N–N multiple bonds has been achieved. For the purpose of dinitrogen activation, nature employs nitrogenase metalloenzymes, which under physiological conditions transform dinitrogen into ammonia.[2] This fascinating process has stimulated interest in transition-metal complexes for dinitrogen reduction under nonbiological conditions.[3,4]

The coordination of dinitrogen to transition metals generates the conceptually simplest complexes with activated N–N multiple bonds. Despite all the progress in nitrogen fixation and in the design of suitable precursor transition-metal complexes,[5] almost all of these systems are limited to stoichiometric reactions. A noteworthy exception is the monomeric molybdenum complex bearing a tetradentate trisanilineamide ligand recently reported by Schrock[6] which was shown to be capable of coordinating dinitrogen and catalyzing consecutive cycles of ammonia formation. The mechanism of this process involves end-on binding of the N_2 molecule through preferential lone-pair coordination and follows the classical Chatt model.[7]

Electronic and structural constraints usually prevent the alternative, η^2-dinitrogen coordination mode **A**. However, these constraints do not necessarily apply to related nitrogen–nitrogen multiple-bond systems. In these cases, the side-on coordination in **B** should allow equal activation of the two nitrogen atoms involved and thus lead to simultaneous reduction. Moreover, the conversion of N–N multiple bonds other than dinitrogen is a promising source of alternative nitrogen-containing products for subsequent organic transformations.[8] In view of the manifold catalytic utility of palladium,[9] the lack of catalytic activation of N–N multiple bonds by this element is notable.[10] Thus, the synthesis and study of palladium compounds resulting from the complexation of N–N multiple bonds is an interesting task.[11]

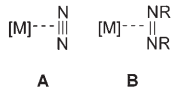

Herein, we present the synthesis of structurally defined palladium complexes of azo compounds, which originate from an initial η^2-coordination mode (**B**), and report the first catalytic reduction of an N–N double bond at a single palladium center under homogeneous conditions. Our investigation of the potential catalytic reactivity began with the synthesis of palladium complexes with azo ligands, which can be considered to be formal surrogates for the products of the first step in the reduction of dinitrogen. The known (bathocuproine)palladium(0) complex **1**[12] (bathocuproine = 2,9-dimethyl-4,7-diphenyl-1,10-phenanthroline) was treated with an equimolar amount of the azodiesters **2a–c** to form in an irreversible reaction the desired monomeric complexes **3a–c** as air- and moisture-stable yellow-to-orange solids (Scheme 1). The coordinated azo ligands in complexes **3a–c** do not dissociate on the NMR time scale, and the products

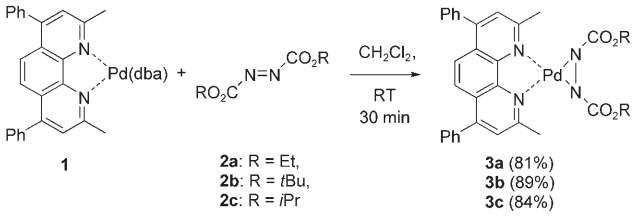

Scheme 1. Synthesis of palladadiaziridines **3a–c**. The yields of **3a–c** (given in parentheses) refer to isolated material. dba = *trans,trans*-dibenzylideneacetone.

[*] Prof. Dr. K. Muñiz
Faculté de Chimie, Institut Le Bel
Université Louis Pasteur
4, rue Blaise Pascal, 67070 Strasbourg Cedex (France)
Fax: (+33) 3-9024-1526
E-mail: muniz@chimie.u-strasbg.fr
Dr. M. Nieger
X-Ray Analysis
Institut für Anorganische Chemie
Universität Bonn
Gerhard-Domagk-Strasse 1, 53121 Bonn (Germany)

[**] This work was supported by the Université Louis Pasteur and by the Fonds der Chemischen Industrie. K.M. thanks Prof. J.-M. Lehn for providing temporary laboratory space at the Institut de Science et d'Ingénierie Supramoléculaires (ISIS).

Supporting information for this article is available on the WWW under http://www.angewandte.org or from the author.

 © 2006 Wiley-VCH Verlag GmbH & Co. KGaA, Weinheim

3a–c are inert towards subsequent exchange reactions with alkenes and other azo compounds.[13] For example, treatment of **3a** with an excess of **2b** led to no interconversion of the coordinated azodiester.

The product **3a** was crystallized from a solution in dichloromethane, and the structure obtained from the X-ray diffraction study of **3a**·CH_2Cl_2 is depicted in Figure 1. The expected C_2 symmetry of the complex is distorted as a result of unsymmetrical hydrogen bonding of the cocrystallized solvent molecule to the metal-coordinated azo group. Importantly, rather short Pd–N bond lengths in the range of 2.014–2.043 Å

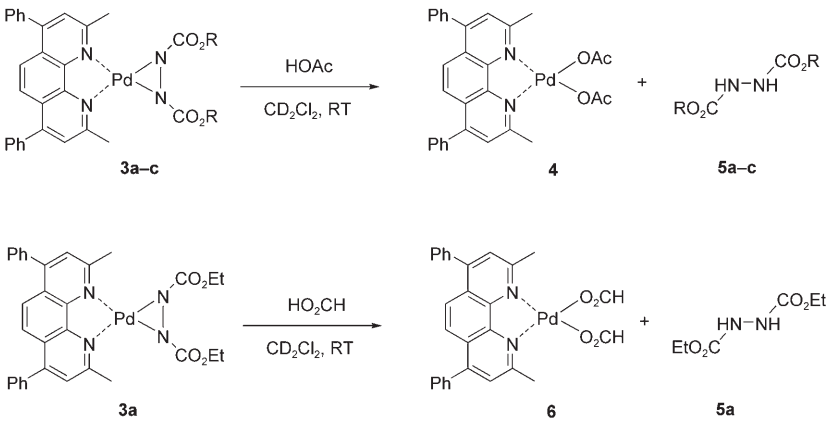

Scheme 2. Protonolysis of palladadiaziridines **3a–c**. R: see Scheme 1.

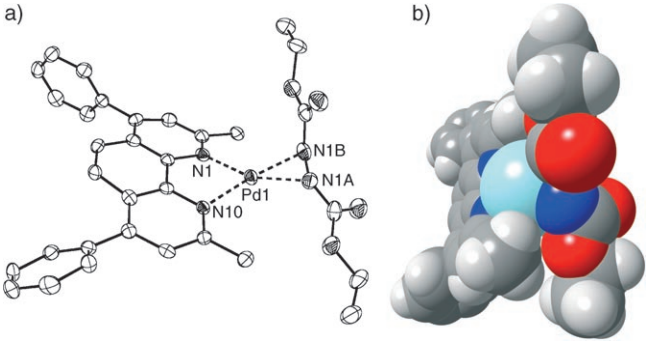

Figure 1. Solid-state structure of **3a**. a) ORTEP plot (thermal ellipsoids are drawn at 50% probability level). The cocrystallized dichloromethane molecule and all hydrogen atoms have been omitted for clarity. Selected bond lengths [Å] and angles [°]: N1A-N1B 1.404(5), Pd-N1A 2.043(3), Pd-N1B 2.014(4); N1B-Pd1-N1A 40.49(14), N1-Pd1-N10 78.93(14), N1B-N1A-Pd1 68.62(19), N1A-N1B-Pd1 70.9(2). b) Space-filling model of **3a**. Pd cyan, C gray, H white, N blue, O red.

are observed together with an N–N bond length of 1.404 Å, which establishes the single-bond character of the N–N bond and leads to the conclusion that a Pd-N-N three-membered ring is the dominating bonding situation. The overall structural composition is therefore best described as a palladadiaziridine. Thus, complexes **3a–c** represent a hitherto-unknown bonding situation within Pd complexes. In other words, the coordinative interaction of the azo compound with the initial Pd^0 center involves a formal redox process between the metal center and the incoming ligand and already entails the desired reduction of the N–N double bond. The space-filling model of **3a** (Figure 1b) illustrates that external electrophiles should be readily able to initiate reactions at the coordinated nitrogen atoms.

These conclusions were supported further by the observation that complexes **3a–c** readily undergo displacement of hydrazines upon protonolysis. For example, the addition of acetic acid to NMR sample solutions of **3a** and **3b** in CD_2Cl_2 led within seconds to clean formation of [(bathocuproine)Pd(OAc)$_2$] (**4**), as well as the *N*,*N*′-di(ethyloxycarbonyl)- and *N*,*N*′-di(*tert*-butyloxycarbonyl)-protected hydrazines **5a** and **5b**, respectively (Scheme 2). Complex **4** was identified on the basis of its NMR data by comparison with an authentic sample.[14] No reversible reaction between the formed palladium(II) complex and the hydrazine was observed, which suggests that hydrazine formation from protonation of complexes **3** represents the desired irreversible process. In an analogous reaction sequence, treatment of **3a** with formic acid led to quantitative production of the corresponding hydrazine **5a** and an unstable palladium formiate complex **6**, which decomposed over a period of two hours at room temperature to palladium black.[15]

The same reactivity of the preformed complexes **3a–c** was observed for reactions on a preparative (1-mmol) scale (Table 1). In this case, protonolysis with acetic acid (2.2 mmol) furnished the corresponding hydrazines **5a–c** in very good yields (88–94%). Also, protonolysis of **3d**, formed in situ by complexation of azobenzene, gave *N*,*N*′-diphenylhydrazine (**5d**) in 90% yield. This result confirms that this reaction is equally efficient for azo ligands with either electron-withdrawing or electron-donating substituents.

Table 1: Protonolysis of palladadiaziridines **3** under homogeneous conditions.[a]

Entry	Compound	Coordinated R_2N_2	Product $R_2(NH)_2$	Yield [%][b]
1	**3a**	R = CO_2Et	**5a**	92
2[c]	**3a**	R = CO_2Et	**5a**	93
3	**3b**	R = CO_2tBu	**5b**	94
4	**3c**	R = CO_2iPr	**5c**	88
5	**3d**[d]	R = Ph	**5d**	90

[a] Reaction conditions: 1 mmol **3** (c = 0.25 M solution in CH_2Cl_2, T = 25 °C), addition of 2.2 mmol acetic acid. [b] Yield of product after purification. [c] With formic acid. [d] Complex generated in situ.

In a subsequent experiment, the addition of ethanol to [(bathocuproine)Pd(OAc)$_2$] (**4**) led to facile reduction and regeneration of a formal palladium(0) complex. The reaction was complete within minutes at room temperature and produced a black precipitate. An NMR experiment in [D_6]benzene revealed that the product of the ethanol oxidation is acetaldehyde, which is in agreement with the earlier reports on bathocuproine-based palladium catalysts

 © 2006 Wiley-VCH Verlag GmbH & Co. KGaA, Weinheim

for efficient alcohol oxidation.[16] More importantly, when the same reaction was carried out in the presence of an excess of diethyl azodicarboxylate (dead, **2a**), quantitative formation of the initial azo complex **3a** was observed and the deposition of palladium black complex was thus prevented (Scheme 3).

Scheme 3. Reductive regeneration of palladadiaziridine **3a** from diacetate **4**.

On the basis of these three individual stoichiometric reactions, a catalytic cycle could be devised for the catalytic reduction of azo compound **2a** to give hydrazine **5a**. A solution (5 M) of **2a** in ethanol in the presence of palladium catalyst (2 mol%) and acetic acid (5 mol%) was reduced cleanly at 50 °C to yield hydrazine **5a** in excellent yield. Scheme 4 depicts the catalytic cycle. The palladadiaziridine is

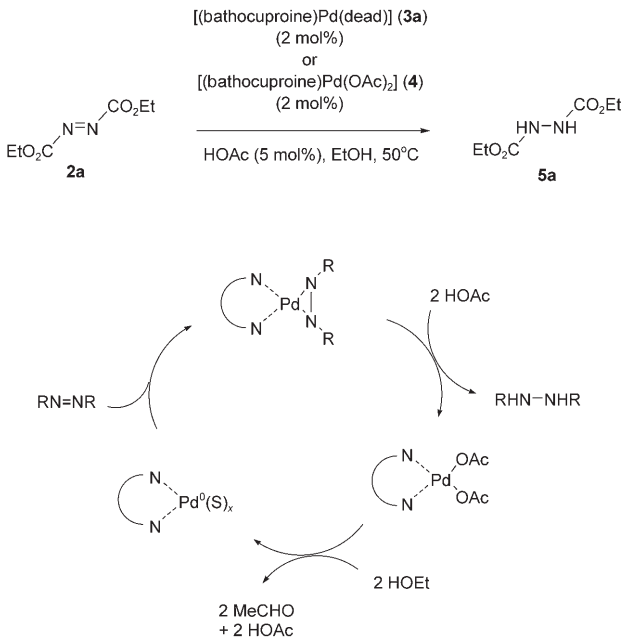

Scheme 4. Catalytic cycle for reduction of azo compounds to hydrazines with a bathocuproine–Pd catalyst. The bathocuproine ligand is represented schematically. S = solvent molecule.

protonated and releases the free hydrazine to form a palladium diacetate complex. Oxidation of ethanol to acetaldehyde concomitantly forms a palladium(0) complex and regenerates the catalytic amount of acetic acid. Coordination of the azo substrate to palladium(0) regenerates the palladadiaziridine and completes the catalytic cycle. This proposed overall catalytic cycle is supported by the fact that both the palladadiaziridine **3a** and the palladium diacetate **4** can be employed as the catalyst source with equal efficiency (91 and 89% yield, respectively). In one case, the catalyst loading of isolated **3a** could be further reduced to 0.5 mol% (substrate/catalyst ratio S/C = 200), and hydrazine **5a** was isolated after a reaction time of 36 h in 90% yield, which is equivalent to an average catalyst turnover number of 180. From a mechanistic point of view, the transition-metal catalysis cycles between the two Pd^0 and Pd^{II} oxidation states and involves only three defined catalyst states. Hence, any potential catalyst deactivation is largely avoided.

The observed process is universal. For example, the same reactivity at an S/C ratio of 50 was obtained for the reduction of azobenzene (**2d**) in ethanol (93% yield of hydrazine **5d**) and for **2c** in 2-propanol (87% yield of hydrazine **5c**). The latter catalysis required 3 days to reach completion because palladium reduction with 2-propanol to yield acetone is comparatively slow.[17]

The overall cycle from Scheme 4 is reminiscent of that discovered by EniChem for palladium-catalyzed production of hydrogen peroxide through dioxygen activation.[18] The corresponding (peroxo)palladium catalyst from this reaction was isolated by Stahl.[12] However, the azo activation reported herein has the advantage that it constitutes an irreversible process in which interaction between hydrazines and the palladium catalyst are absent, whereas the production of hydrogen peroxide requires biphasic conditions to prevent disproportionation.

In summary, we have discovered the first homogeneous transition-metal-catalyzed activation of azo compounds, which enables efficient reductive transformation of N–N multiple bonds at a single palladium catalyst site. The catalysis involves an intermediate state displaying a novel azo coordination mode to palladium(0), and the structure was established by independent isolation of a palladadiaziridine.[19] The present process constitutes a novel catalytic reaction and is important for the reduction of N–N multiple bonds.

Experimental Section

3a: A solution of [(bathocuproine)Pd(dba)] (802 mg, 1.14 mmol) in freshly distilled dichloromethane (2 mL) was treated with dead (**2a**, 200 μL, 1.27 mmol), and the resulting mixture was stirred at room temperature for 45 min. The solvent was removed under reduced pressure to a volume of approximately 0.5 mL, and the crude product was precipitated by addition of absolute diethyl ether (20 mL). The yellowish crude product was washed with further portions of diethyl ether, dried under reduced pressure, dissolved in dichloromethane (10 mL), and then filtered through a pad of celite. The remaining solution was evaporated to dryness under reduced pressure to leave the product as a yellow-to-orange solid (592 mg, 0.92 mmol, 81%). Crystals suitable for X-ray analysis were grown from a solution in dichloromethane at −20 °C.

Crystal structure of **3a**: $C_{32}H_{30}N_4O_4Pd \cdot CH_2Cl_2$: yellow crystals, crystal dimensions $0.25 \times 0.15 \times 0.10\ mm^3$; $M = 725.93$; monoclinic, space group $P2_1/c$ (No. 14), $a = 12.3133(4)$, $b = 15.1348(6)$, $c = 16.8231(7)$ Å, $\beta = 97.226(2)°$, $V = 3110.2(2)$ Å^3, $Z = 4$, $\mu(Mo_{K\alpha}) = 0.813\ mm^{-1}$, $T = 123(2)$ K, $F(000) = 1480$. 19374 reflections up to $2\theta_{max} = 50°$ were measured on a Nonius KappaCCD diffractometer with $Mo_{K\alpha}$ radiation, 5469 of which were independent and used for all calculations. The structure was solved by direct methods and refined to F^2 anisotropically; the positions of the H atoms were refined with a riding model. The final quality coefficient $wR2(F^2)$ for all data was

 © 2006 Wiley-VCH Verlag GmbH & Co. KGaA, Weinheim

0.0871, with a conventional $R(F) = 0.0425$ for 399 parameters. An empirical absorption correction was applied.

CCDC-288043 contains the supplementary crystallographic data for this paper. These data can be obtained free of charge from the Cambridge Crystallographic Data Centre via www.ccdc.cam.ac.uk/data_request/cif.

Received: November 2, 2005
Published online: March 3, 2006

Keywords: azo compounds · homogeneous catalysis · hydrazines · palladium · small rings

[1] a) F. Haber, G. Z. van Oordt, *Z. Anorg. Chem.* **1905**, *47*, 42; b) F. Haber, *Naturwissenschaften* **1922**, *10*, 133.
[2] a) O. Einsle, F. A. Tezcan, S. L. A. Andrade, B. Schmidt, M. Yoshida, J. B. Howard, D. C. Reed, *Science* **2002**, *297*, 1696; b) P. C. Dos Santos, R. Y. Igarashi, H.-I. Lee, B. M. Hoffman, L. C. Seefeldt, D. R. Dean, *Acc. Chem. Res.* **2005**, *38*, 208; c) B. K. Burgess, D. J. Lowe, *Chem. Rev.* **1996**, *96*, 2983; d) J. B. Howard, D. C. Rees, *Chem. Rev.* **1996**, *96*, 2965.
[3] a) C. E. Laplaza, C. C. Cummins, *Science* **1995**, *268*, 861; b) M. D. Fryzuk, J. B. Love, S. J. Rettig, V. G. Young, *Science* **1997**, *275*, 1445; c) Y. Nishibayashi, S. Iwai, M. Hidai, *Science* **1998**, *279*, 540; d) J. A. Pool, E. Lobkovsky, P. J. Cirik, *Nature* **2004**, *427*, 527; e) J. M. Smith, R. J. Lachicotte, K. A. Pittard, T. R. Cundari, G. Lukat-Rodgers, K. R. Rodgers, P. L. Holland, *J. Am. Chem. Soc.* **2001**, *123*, 9222.
[4] For recent reviews, see: a) B. A. MacKay, M. D. Fryzuk, *Chem. Rev.* **2004**, *104*, 385, and references therein; b) M. P. Shaver, M. D. Fryzuk, *Adv. Synth. Catal.* **2003**, *345*, 1061; c) see also: M. Reiher, B. Kirchner, J. Hutter, D. Sellmann, B. A. Hess, *Chem. Eur. J.* **2004**, *10*, 4443, and references therein.
[5] T. A. Bazhenova, A. E. Shilov, *Coord. Chem. Rev.* **1995**, *144*, 69.
[6] a) D. V. Yandulov, R. R. Schrock, *Science* **2003**, *301*, 76; b) R. R. Schrock, *Chem. Commun.* **2003**, 2389; c) R. R. Schrock, *Acc. Chem. Res.* **2005**, *39*, 955; for theoretical treatments, see: d) Z. Cao, Z. Zhou, H. Wan, Q. Zhang, *Int. J. Quantum Chem.* **2005**, *103*, 344; e) F. Studt, F. Tuczek, *Angew. Chem.* **2005**, *117*, 5783; *Angew. Chem. Int. Ed.* **2005**, *44*, 5639; f) B. Le Guennic, B. Kirchner, M. Reiher, *Chem. Eur. J.* **2005**, *11*, 7448; g) M. Reiher, B. Le Guennic, B. Kirchner, *Inorg. Chem.* **2005**, *44*, 9640.
[7] a) J. Chatt, A. J. Pearman, R. L. Richards, *Nature* **1975**, *253*, 39; b) J. Chatt, J. R. Dilworth, R. L. Richards, *Chem. Rev.* **1978**, *78*, 589.
[8] M. Hidai, Y. Mizobe, *Can. J. Chem.* **2005**, *83*, 358.
[9] J. Tsuji, *Palladium Reagents and Catalysts*, Wiley, New York, **2004**.
[10] For the use of palladium catalysts in conventional hydrogenation reactions of azo compounds, see: a) F. Figueras, B. Coq, *J. Mol. Catal. A* **2001**, *173*, 223; b) K. Abiraj, G. R. Srinivasa, D. C. Gowda, *Can. J. Chem.* **2005**, *83*, 517.
[11] For example, detection of palladium dinitrogen complexes has so far been limited to low-temperature matrix-isolation techniques: a) H. Huber, E. P. Kündig, M. Moskovits, G. A. Ozin, *J. Am. Chem. Soc.* **1973**, *95*, 332; b) for an early direct synthetic attempt, see: C. A. Tolman, D. H. Gerlach, J. P. Jesson, R. A. Schunn, *J. Organomet. Chem.* **1974**, *65*, C23.
[12] S. S. Stahl, J. L. Thorman, R. C. Nelson, M. A. Kozee, *J. Am. Chem. Soc.* **2001**, *123*, 7188.
[13] For reversible exchange of alkenes on bathocuproine-Pd-alkene complexes, see: S. S. Stahl, J. L. Thorman, N. de Silva, I. A. Guzei, R. W. Clark, *J. Am. Chem. Soc.* **2003**, *125*, 12.
[14] Treatment of bathocuproine with palladium(II) acetate in dichloromethane gives **4** as a yellow-to-ochre solid (96% yield after precipitation from diethyl ether). We find this procedure more convenient than those reported in the literature: R. Santi, A. M. Romano, R. Garrone, R. Millini, *J. Organomet. Chem.* **1998**, *566*, 37.
[15] Once the black palladium(0) species formed, it could not be treated with excess azo compound to regenerate complexes **3**. We thus rule out the involvement of heterogeneous reduction pathways.
[16] a) G.-J. ten Brink, I. W. C. E. Arends, R. A. Sheldon, *Science* **2000**, *287*, 1636; b) G.-J. ten Brink, I. W. C. E. Arends, M. Hoogenraad, G. Verspui, R. A. Sheldon, *Adv. Synth. Catal.* **2003**, *345*, 497.
[17] Monitoring the corresponding stoichiometric reduction by NMR spectroscopy revealed only incomplete reaction after 5 h at room temperature. This result suggests that palladium reduction is the rate-limiting step in the related catalytic reduction of **3c** to hydrazine **5c**, which is in agreement with the general behavior of **4** in alcohol oxidation reactions.[16]
[18] a) D. Bianchi, R. Bortolo, R. D'Aloisio, M. Ricci, *Angew. Chem.* **1999**, *111*, 734; *Angew. Chem. Int. Ed.* **1999**, *38*, 706; b) D. Bianchi, R. Bortolo, R. D'Aloisio, M. Ricci, *J. Mol. Catal. A* **1999**, *150*, 87; c) R. Bortolo, D. Bianchi, R. D'Aloisio, C. Querci, M. Ricci, *J. Mol. Catal. A* **2000**, *153*, 25.
[19] The catalytic behavior is not restricted to the bathocuproine ligand. Other 1,10-phenanthroline ligands induce comparable reactivity. Studies of the structural requirements of the ligand constitution are currently under way.

 © 2006 Wiley-VCH Verlag GmbH & Co. KGaA, Weinheim

Cover Picture

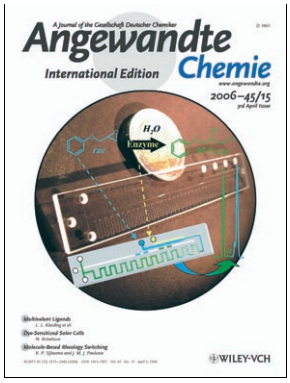

Detlev Belder,* Martin Ludwig, Li-Wen Wang, and Manfred T. Reetz*

Synthesis and analysis on a chip are possible with the microfluidic system shown (a two-Euro coin is shown for scale). D. Belder, M. T. Reetz et al. show in their Communication on page 2463 ff. how this chip is used to test enantioselective biocatalysts created by directed evolution. The model system used is the hydrolitic kinetic resolution of chiral glycidyl phenyl ether with different epoxide hydrolase mutants. Aided by integrated electrophoreses, chiral separation of the products is possible within 80 s.

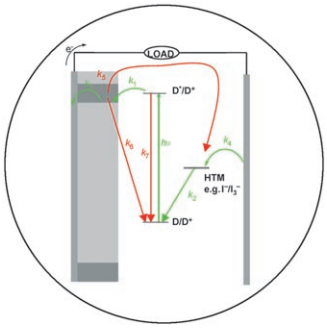

Solar Cells
In the Minireview on page 2338 ff., N. Robertson discusses the optimization of dye molecules for sensitized solar cells. Careful design of the dye can minimize energy-loss mechanisms and increase the efficiency of solar-to-electrical energy conversion.

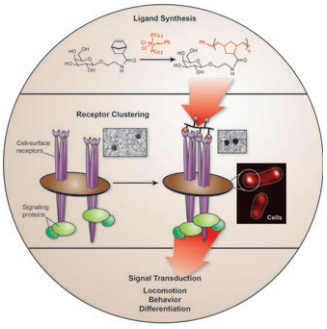

Bioorganic Chemistry
In their Review on page 2348 ff., L. L. Kiessling et al. describe the advantages of using synthetic multivalent ligands for studies on protein complexes.

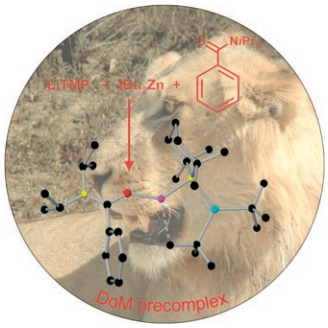

Directed ortho-Metalation
A precomplex formed from an aromatic amide, an alkali metal, and zinc that directs *ortho*-zincation is described by R. E. Mulvey et al. in their Communication on page 2370 ff.

Contents

VIP *The following Communications have been judged by at least two referees to be "very important papers" and will be published online at www.angewandte.org soon:*

*A. Kaminaga, V. Vanag, I. Epstein**
A Reaction-Diffusion Memory Device

*V. Stamenkovic, B. S. Moon, K. J. Mayrhofer, P. Ross, N. Markovic, J. Rossmeisl, J. Greeley, J. Nørskov**
Changing the Activity of Electrocatalysts for Oxygen Reduction by Tuning the Surface Electronic Structure

J. Blumberger, B. Ensing, M. Klein*
Formamide Hydrolysis in Alkaline Aqueous Solution: Insights from Ab Initio Metadynamics Calculations

G. Dolphin, P. Dumy, J. Garcia**
Control of Amyloid β-Peptide Protofibril Formation by a Designed Template Assembly

J. M. Bellosta von Colbe, W. Schmidt, M. Felderhoff, B. Bogdanovic, F. Schüth**
Hydrogen Isotope Scrambling on Doped Sodium Alanate

Meeting Reviews

Winter Workshop in Linz: Advances in Single-Molecule Research — J. Enderlein — **2330**

Books

Light is a Messenger — Graeme K. Hunter — *reviewed by B. Kahr* — **2332**

Highlights

Ultrasound-Induced Switching

J. M. J. Paulusse, R. P. Sijbesma* — **2334 – 2337**

Molecule-Based Rheology Switching

Sound-activated switching: The rheological behavior of fluids can be affected by external stimuli, as demonstrated by electrochemically and photochemically induced changes in viscosity and sol–gel transitions. Recently, ultrasound has emerged as a novel rheology switch for supramolecular polymers and networks.

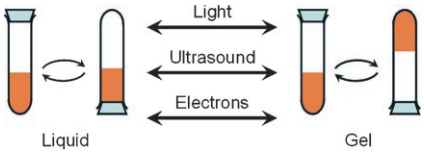

Minireviews

Dye-Sensitized Solar Cells

N. Robertson* — **2338 – 2345**

Optimizing Dyes for Dye-Sensitized Solar Cells

Soaking up the sun: Dye-sensitized solar cells have emerged as a cheap photovoltaic technology. Careful design of the dye is crucial to improve light harvesting and minimize energy loss. Dyes based on transition-metal complexes and organic molecules are discussed in the Minireview, as well as the influence of their properties on the efficiency of solar-to-electrical energy conversion.

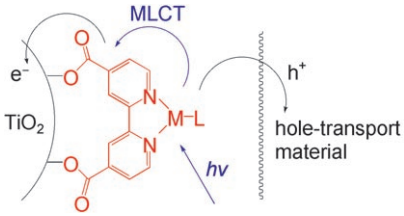

WILEY InterScience DISCOVER SOMETHING GREAT
© 2006 Wiley-VCH Verlag GmbH & Co. KGaA, Weinheim

Reviews

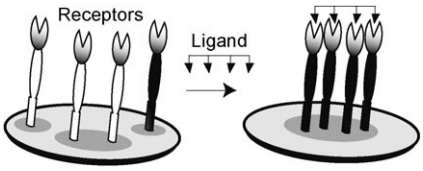

Receptors at the cell surface function within the context of highly organized multiprotein complexes. However, the mechanisms by which these receptors process, amplify, and integrate sensory information are unclear. Synthetic multivalent ligands with diverse structures can be used to reveal fundamental information for the elucidation of regulatory features in receptor systems.

Bioorganic Chemistry

L. L. Kiessling,* J. E. Gestwicki, L. E. Strong ——— **2348 – 2368**

Synthetic Multivalent Ligands as Probes of Signal Transduction

Communications

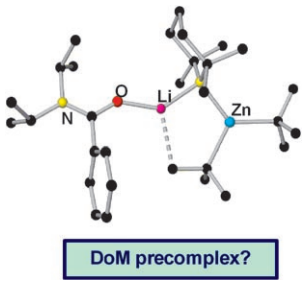

The predator meets its prey in the structure of [{(iPr)$_2$NC(Ph)(=O)}Li(μ-tmp)(μ-tBu)Zn(tBu)] which reveals an aromatic amide–alkali metal zincate "precomplex" for directed *ortho*-metalation (DoM) that exists prior to the devouring (*ortho*-zincation) of the amide by the zincate. tmp = 2,2,6,6-tetramethylpiperidide.

ortho-Metalation (1)

W. Clegg, S. H. Dale, E. Hevia, G. W. Honeyman, R. E. Mulvey* ——— **2370 – 2374**

Pre-Metalation Structural Insights into the Use of Alkali-Metal-Mediated Zincation for Directed *ortho*-Metalation of a Tertiary Aromatic Amide

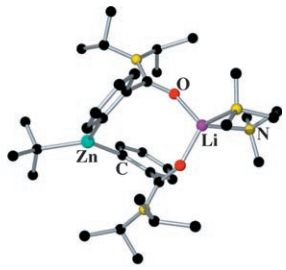

Catch me if you can: Invisible using standard electrophilic substitution detection methods, two distinct *ortho*-metalated "intermediates" generated by alkali-metal-mediated zincation of *N*,*N*-diisopropylbenzamide are structurally elucidated.

ortho-Metalation (2)

W. Clegg, S. H. Dale, R. W. Harrington, E. Hevia, G. W. Honeyman, R. E. Mulvey* ——— **2374 – 2377**

Post-Metalation Structural Insights into the Use of Alkali-Metal-Mediated Zincation for Directed *ortho*-Metalation of a Tertiary Aromatic Amide

For the USA and Canada:
ANGEWANDTE CHEMIE International Edition (ISSN 1433-7851) is published weekly by Wiley-VCH PO Box 191161, D 69451 Weinheim, Germany. Air freight and mailing in the USA by Publications Expediting Inc. 200 Meacham Ave., Elmont, NY 11003. Periodicals postage paid at Jamaica NY 11431. US POSTMASTER: send address changes to *Angewandte Chemie*, Wiley-VCH, 111 River Street, Hoboken, NJ 07030. Annual subscription price for institutions: US$ 5685/5168 (valid for print and electronic / print or electronic delivery); for individuals who are personal members of a national chemical society prices are available on request. Postage and handling charges included. All prices are subject to local VAT/sales tax.

© 2006 Wiley-VCH Verlag GmbH & Co. KGaA, Weinheim

The best in chemistry –

for more than a hundred years

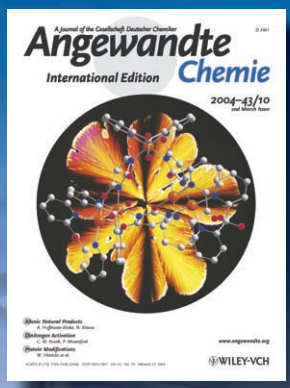

A Journal of the Gesellschaft Deutscher Chemiker

Angewandte
International Edition **Chemie**

www.angewandte.org

1888: ***The beginning of a success story***

Constant Innovations

1962: *First issue of the International Edition*
1976: *Graphical abstracts*
1979: *Cover pictures*
1988: *Centenary of Angewandte*
1989: *Routine use of color*
1991: *New section: Highlights*
1992: *Computerized editorial tracking system*
1995: *Internet service for readers*
1998: *Regular press service; full-text online*
2000: *New section: Essays; EarlyView: Communications available online ahead of the printed version*
2001: *New section: Minireviews*
2002: *Online submission of manuscripts*
2003: *Weekly publication; new section: News; new layout*
2004: *Backfiles (1962-1997); ManuscriptXpress: Online system for authors and referees*

Angewandte's advisors...

Martin Quack
Physical Chemistry,
ETH Zürich

»**Angewandte Chemie** *is my favourite journal covering all aspects of chemistry, from theoretical and physical chemistry to inorganic, organic, and biochemistry. It is by far the best journal worldwide for an overview of current research in chemistry as a whole. Beyond just publishing the best research in chemistry, it also helps us to fight the trend of too narrow specialization.*«

Angewandte Chemie International Edition *is a journal of the German Chemical Society (GDCh)*

GDCh

WILEY InterScience® DISCOVER SOMETHING GREAT

WILEY-VCH

1197/1404_gu

A complex pattern: Single-phase brookite, rutile, and rutile–anatase nanoparticles can be prepared from the new water-soluble titanium(IV) complex $(NH_4)_6[Ti_4(C_2H_2O_3)_4(C_2H_3O_3)_2(O_2)_4O_2]\cdot 4\,H_2O$. It appears that the structural similarity of the complex anion to the brookite architecture allows the directional synthesis of brookite nanopowders in a pure form (see scheme).

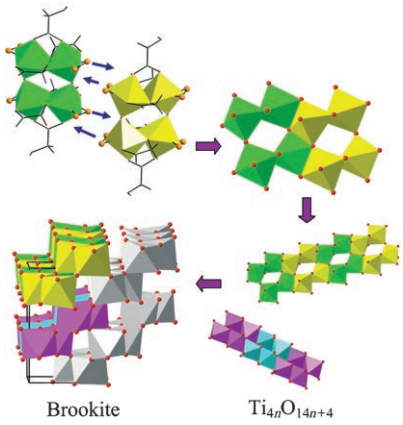

Nanostructures

K. Tomita, V. Petrykin, M. Kobayashi, M. Shiro, M. Yoshimura, M. Kakihana* ——— **2378 – 2381**

A Water-Soluble Titanium Complex for the Selective Synthesis of Nanocrystalline Brookite, Rutile, and Anatase by a Hydrothermal Method

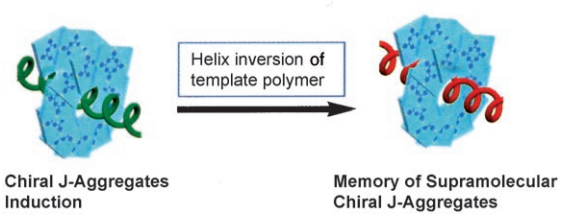

Helical Structures

H. Onouchi, T. Miyagawa, K. Morino, E. Yashima* ——— **2381 – 2384**

Assisted Formation of Chiral Porphyrin Homoaggregates by an Induced Helical Poly(phenylacetylene) Template and Their Chiral Memory

Long-term memory aid: A one-handed helical poly(phenylacetylene) with positively charged pendant groups can serve as the template for supramolecular helical arrays of achiral porphyrins with opposite charges in acidic water. The supramolecular chirality induced in the porphyrin aggregates can be memorized even after the template helical polymer loses its optical activity and inverts into the opposite helicity.

From solid to solid: Electrochemical conversion of solid terbium oxide into solid terbium metal was performed in molten $CaCl_2$ under the conditions for Ca deposition. Electron transfer to the solid oxide was more effective from the electrode than from the deposited Ca, and the process was controlled by mass transfer in the porous oxide electrode.

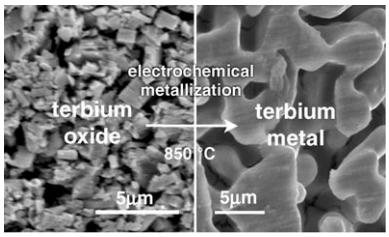

Electrochemistry

D. H. Wang, G. H. Qiu, X. B. Jin, X. H. Hu, G. Z. Chen* ——— **2384 – 2388**

Electrochemical Metallization of Solid Terbium Oxide

Completing a circle of reactions: Reaction of a U^V–imido complex (**2**) with a π acid (e.g., CH_3NC) affords a U^{IV}–heterocumulene complex (**3**), which reacts with an alkyl halide to yield the free carbodiimide and corresponding U^{IV}–halide complex (**4**). Reduction of complex **4** recovers **1**, thereby closing a cycle in which a nitrogen atom is transferred from a U^V–imido complex to a π acid by multiple-bond metathesis.

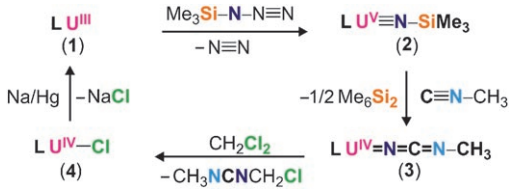

Nitrogen-Transfer Chemistry

I. Castro-Rodríguez, H. Nakai, K. Meyer* ——— **2389 – 2392**

Multiple-Bond Metathesis Mediated by Sterically Pressured Uranium Complexes

© 2006 Wiley-VCH Verlag GmbH & Co. KGaA, Weinheim

Contents

Protein Recognition

H. Nishino, C.-S. Huang, K. J. Shea* ——— **2392 – 2396**

Selective Protein Capture by Epitope Imprinting

Caught on film: A molecularly imprinted polymer (MIP) film imprinted with the peptide sequence from the C-terminus of cytochrome c (Cyt c) is able to selectively capture Cyt c from a solution of five different proteins. Such a method allows for the capture of target proteins based only on genomic information.

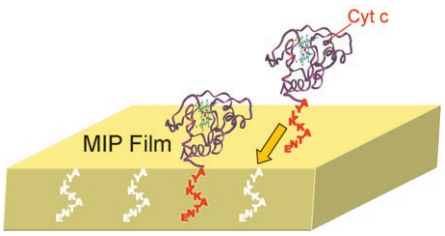

Nanomaterials

T. A. Martinek, A. Hetényi, L. Fülöp, I. M. Mándity, G. K. Tóth, I. Dékány, F. Fülöp* ——— **2396 – 2400**

Secondary Structure Dependent Self-Assembly of β-Peptides into Nanosized Fibrils and Membranes

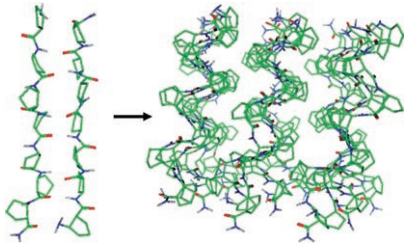

In control: The secondary structure dependent self-assembly of β-peptides in solution proves that natural biopolymers are not unique in their highly structured conformational behavior. Stereochemically controlled secondary structural units of β-peptide strands and helices intrinsically self-associate into pleated-sheet sandwiches (see picture) and helix-bundle membranes, respectively.

Living Polymerization

M. B. Harney, Y. Zhang, L. R. Sita* ——— **2400 – 2404**

Discrete, Multiblock Isotactic–Atactic Stereoblock Polypropene Microstructures of Differing Block Architectures through Programmable Stereomodulated Living Ziegler–Natta Polymerization

Tactics in polymerization: The molecular weight and the number, length, and placement of each stereoblock type in a polypropene were programmed to give discrete, multiblock, isotactic–atactic stereoblock microstructures. Several of these specifically designed stereoblock architectures give rise to thermoplastic elastomers (see picture; white and red blocks represent atactic and isotactic blocks, respectively).

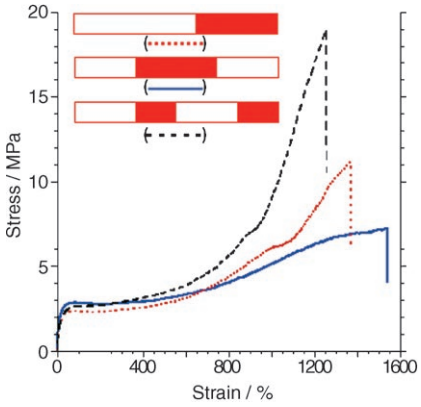

Dendrimers

K. Itami,* K. Tonogaki, T. Nokami, Y. Ohashi, J. Yoshida* ——— **2404 – 2409**

Palladium-Catalyzed Convergent Synthesis and Properties of Conjugated Dendrimers Based on Triarylethene Branching

Branching out: Pd-catalyzed iterative triarylations of vinylboronate afford conjugated dendrimers with triarylethene branches (see picture) in a flexible and convergent manner. These highly branched dendrimers reveal good solubility in common organic solvents and exhibit high quantum yields of fluorescence, with the color of the emission ranging from blue to red depending on the extent of branching and hence π conjugation.

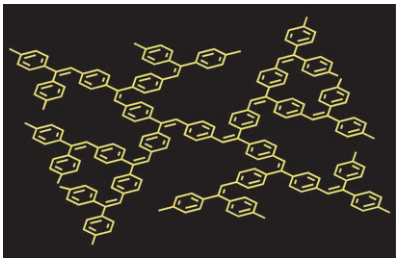

© 2006 Wiley-VCH Verlag GmbH & Co. KGaA, Weinheim

Ever-increasing through circles: Long single-stranded DNA molecules with repetitive sequence units were synthesized on gold nanoparticles through rolling circle amplification (RCA, see scheme). These special DNA–AuNP conjugates were then used as a scaffold for assembling periodic 3D nanostructures, which may find applications in nanocomputing devices, nanoelectronic circuits, and ultrasensitive biosensors.

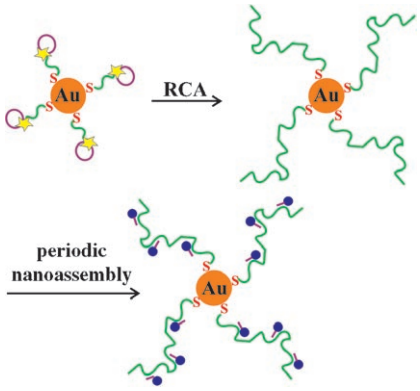

Nanobiotechnology

W. Zhao, Y. Gao, S. A. Kandadai, M. A. Brook,* Y. Li* ——— **2409 – 2413**

DNA Polymerization on Gold Nanoparticles through Rolling Circle Amplification: Towards Novel Scaffolds for Three-Dimensional Periodic Nanoassemblies

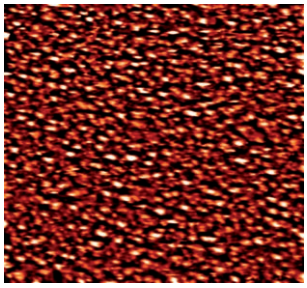

A change of behavior: Deposition of atomic oxygen on Au nanoparticles larger and smaller than about 0.7 nm (as determined by STM, see image) in height results in the formation of oxygen species that exhibit very different oxidation behaviors toward CO at room temperature. X-ray photoelectron spectroscopy has been used to explain these differences.

Nanostructures

D. C. Lim, I. Lopez-Salido, R. Dietsche, M. Bubek, Y. D. Kim* ——— **2413 – 2415**

Size-Selectivity in the Oxidation Behaviors of Au Nanoparticles

Chirality from blood: Serum albumins form strong complexes with Cu^{II}–phthalocyanines, leading to protein conjugates. These hybrid catalysts promote enantioselective Diels–Alder reactions, such as that of azachalcones **1** with cyclopentadiene (**2**) to give products **3** with 85–98% *ee*.

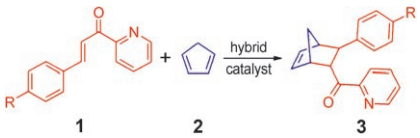

Asymmetric Catalysis

M. T. Reetz,* N. Jiao ——— **2416 – 2419**

Copper–Phthalocyanine Conjugates of Serum Albumins as Enantioselective Catalysts in Diels–Alder Reactions

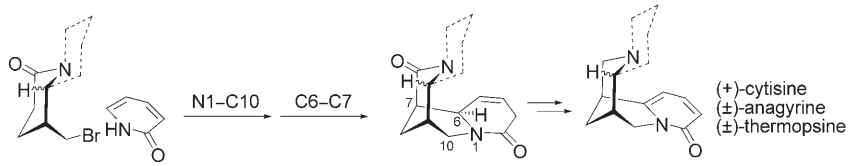

Looping the lupin: A general synthetic strategy for the construction of the lupin alkaloids has been defined and involves sequential formation of the N1—C10 and C6—C7 bonds, which are common to compounds of this class of natural products. The generality of the approach is exemplified by the syntheses of (+)-cytisine, (±)-anagyrine, and (±)-thermopsine (see scheme).

Natural Product Synthesis

D. Gray, T. Gallagher* ——— **2419 – 2423**

A Flexible Strategy for the Synthesis of Tri- and Tetracyclic Lupin Alkaloids: Synthesis of (+)-Cytisine, (±)-Anagyrine, and (±)-Thermopsine

© 2006 Wiley-VCH Verlag GmbH & Co. KGaA, Weinheim

Contents

Mixture Synthesis

D. P. Curran,* G. Moura-Letts, M. Pohlman ——— **2423 – 2426**

Solution-Phase Mixture Synthesis with Fluorous Tagging En Route: Total Synthesis of an Eight-Member Stereoisomer Library of Passifloricins

Double your pleasure: A new double-tagging approach is validated by making eight individual stereoisomers of passifloricin through the intermediacy of a pair of four-compound quasi-isomeric mixtures.

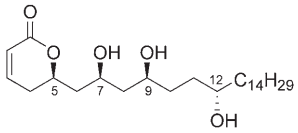

passifloricin A
(5*R*,7*S*,9*S*,12*S*)

Allylation

V. Rauniyar, D. G. Hall* ——— **2426 – 2428**

Catalytic Enantioselective and Catalyst-Controlled Diastereofacial-Selective Additions of Allyl- and Crotylboronates to Aldehydes Using Chiral Brønsted Acids

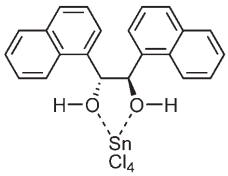

$[SnCl_4\{(R,R)\text{-}\mathbf{1}\}]$

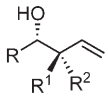

up to 80% *ee* and 98:2 d.r. with $[SnCl_4(\mathbf{1})]$ catalysis

Towards the ideal: A chiral diol–$SnCl_4$ complex is applied to the allylboration of aldehydes (see scheme). This approach highlights the use of chiral Brønsted acid catalysis in the development of an ideal method for the allylation of aldehydes which would display high diastereo- and enantioselectivity, wide substrate scope, and high practicality (ease of use, low cost, and low environmental impact).

Oligosaccharide Analysis

F. H. Cederkvist, A. D. Zamfir, S. Bahrke, V. G. H. Eijsink, M. Sørlie, J. Peter-Katalinić, M. G. Peter* ——— **2429 – 2434**

Identification of a High-Affinity-Binding Oligosaccharide by (+) Nanoelectrospray Quadrupole Time-of-Flight Tandem Mass Spectrometry of a Noncovalent Enzyme–Ligand Complex

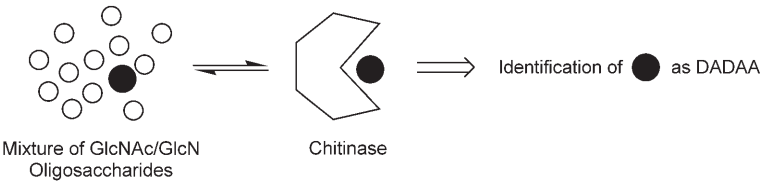

Mixture of GlcNAc/GlcN Oligosaccharides

Chitinase

Sugar fix: A noncovalent enzyme–ligand complex in a mixture of aminoglucan heterooligosaccharides and a chitinase is analyzed by nanoelectrospray ionization collision-induced dissociation tandem mass spectrometry. The enzyme selectively binds a pentasaccharide composed of three *N*-acetylglucosamine (GlcNAc, A) and two glucosamine (GlcN, D) units (see picture).

Monodispersed Materials

A. E. Garcia-Bennett,* K. Lund, O. Terasaki ——— **2434 – 2438**

Particle-Size Control and Surface Structure of the Cubic Mesocaged Material AMS-8

Monodispersed particles of the mesocaged material AMS-8 have been prepared by using nonionic polymeric cosurfactants to control the particle size. These particles are faceted, porous, and show surface structural characteristics that are typical of cubic AMS-8 (see picture), as well as an increased adsorption capacity as a result of the formation of intraparticle spaces.

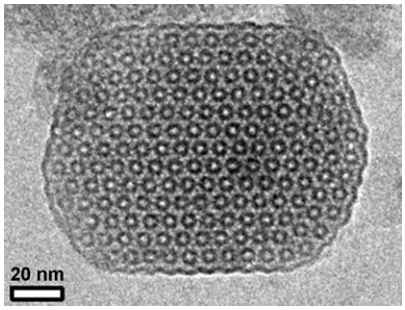

Intermolecular Bonding

W. Caminati,* S. Melandri, A. Maris, P. Ottaviani ——— **2438 – 2442**

Relative Strengths of the O—H···Cl and O—H···F Hydrogen Bonds

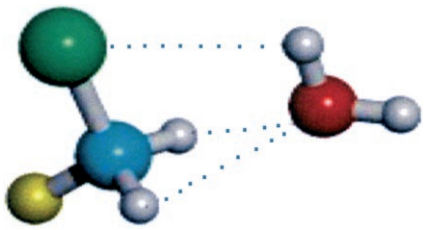

Which bond goes where? The observed conformer of $H_2O\cdots ClFCH_2$ displays one O—H···Cl and two weak C—H···O hydrogen-bonding interactions. The dissociation energy of this conformer is estimated to be 8.5 kJ mol^{-1} from the centrifugal distortion effects.

© 2006 Wiley-VCH Verlag GmbH & Co. KGaA, Weinheim

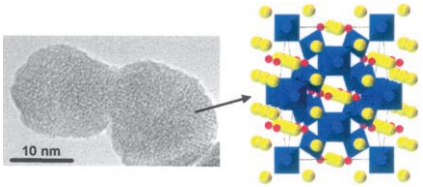

A 4-to-3 advantage: Hydrothermal synthesis provides access to $(Na_{1/3}Ce_{2/3})_2Ti_2O_7$, the first member of the pyrochlore family to contain solely Ce^{IV}, in nanoparticulate form (see picture; Na/Ce yellow, O red, $\{TiO_6\}$ octahedra blue). The new material undergoes facile and reversible reduction at temperatures as low as 150 °C, a property that is highly desirable for depollution catalysts.

Mixed-Metal Oxides

C. S. Wright, J. Fisher, D. Thompsett, R. I. Walton* ——— **2442 – 2446**

Hydrothermal Synthesis of a Cerium(IV) Pyrochlore with Low-Temperature Redox Properties

---

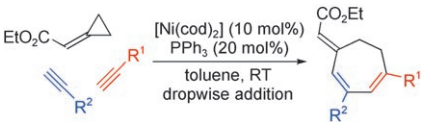

Ménage à trois: Seven-membered carbocycles are formed by the three-component [3+2+2] cycloaddition of ethyl cyclopropylideneacetate and two different alkynes in the presence of a Ni^0/PPh_3 catalyst (see scheme). In this one-pot reaction, a highly chemo- and regioselective coupling proceeds, and the cycloheptadiene derivatives are isolated as single isomers.

Synthetic Methods

S. Komagawa, S. Saito* ——— **2446 – 2449**

Nickel-Catalyzed Three-Component [3+2+2] Cocyclization of Ethyl Cyclopropylideneacetate and Alkynes—Selective Synthesis of Multisubstituted Cycloheptadienes

---

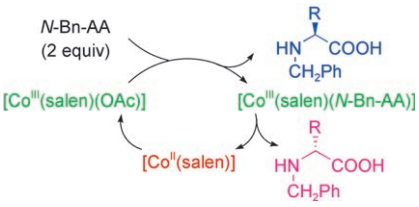

Liquidating the assets: Coordination of one enantiomer from a racemic mixture of *N*-benzyl α-amino acids (*N*-Bn-AA) to the lipophilic chiral $[Co^{III}(salen)(OAc)]$ complex results in its extraction into the organic phase. The enantiomer can then be released in excellent yield and high enantiomeric excess by reductive counterextraction. The cobalt(III) complex can be regenerated and re-used without loss of reactivity or selectivity.

Chiral Resolution

T. B. Reeve, J.-P. Cros, C. Gennari,* U. Piarulli,* J. G. de Vries ——— **2449 – 2453**

A Practical Approach to the Resolution of Racemic *N*-Benzyl α-Amino Acids by Liquid–Liquid Extraction with a Lipophilic Chiral Salen–Cobalt(III) Complex

---

An amicable separation: The reaction between the two aldehydes and amines shown gives initially a dynamic library of 11 imines, which collapses upon the addition of Fe^{II} and Cu^{I} ions to give only two complexes. The presence of both metals was found to be essential for this selectivity; in particular the thermodynamic stability of the low-spin Fe^{II} complex shown was found to play an important role.

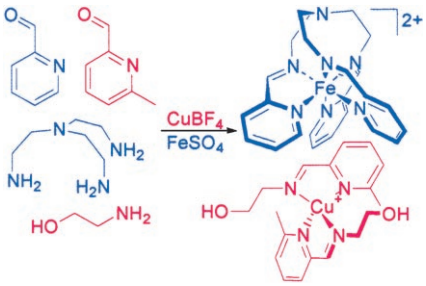

Self-Assembly

D. Schultz, J. R. Nitschke* ——— **2453 – 2456**

Choices of Iron and Copper: Cooperative Selection during Self-Assembly

© 2006 Wiley-VCH Verlag GmbH & Co. KGaA, Weinheim

Contents

VIP **Natural-Gas Hydrates**

J.-w. Lee, H. Lu, I. L. Moudrakovski, C. I. Ratcliffe, J. A. Ripmeester* _____ **2456 – 2459**

n-Pentane and *n*-Hexane as Coguests in Structure-H Hydrates in Mixtures of 2,2-Dimethylbutane and Methane

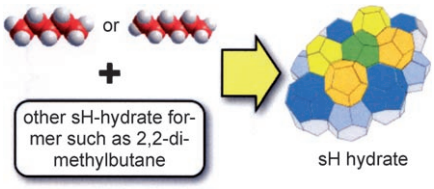

Room for two little ones? *n*-Pentane and *n*-hexane, previously regarded as non-hydrate forming, are found to form structure-H (sH) hydrates in mixtures with 2,2-dimethylbutane. Even though they are thought to be too large to fit into the largest cage of the sH hydrate, powder X-ray diffraction and NMR measurements show that they form gas hydrates in mixtures with other sH-hydrate formers.

Synthetic Methods

P. A. Wender,* M. P. Croatt, N. M. Deschamps _____ **2459 – 2462**

Metal-Catalyzed [2+2+1] Cycloadditions of 1,3-Dienes, Allenes, and CO

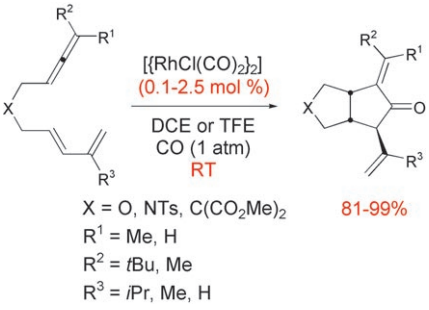

Closing the circle: Rh^{I}-catalyzed [2+2+1] cycloadditions are achieved under mild reaction conditions and in good to excellent yields with catalyst loading as low as 0.1 mol%. The diene–allenes react selectively with the proximal double bonds of the allene and diene units, thus allowing for a variety of substitutions. DCE = 1,2-dichloroethane, TFE = 2,2,2-trifluoroethanol, Ts = tosyl.

VIP **Chip Laboratories**

D. Belder,* M. Ludwig, L.-W. Wang, M. T. Reetz* _____ **2463 – 2466**

Enantioselective Catalysis and Analysis on a Chip

A chip off the old block: A prototype of a miniaturized catalysis laboratory is successfully applied for screening enantioselective biocatalysts created by directed evolution of enzymes. For this purpose an integrated microfluidic catalysis/analysis chip has been developed (see scheme SO: sample outlet, SI: alternative sample inlet, BI: buffer outlet).

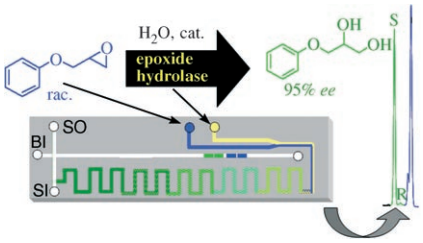

Synthetic Methods

M. Schelwies, P. Dübon, G. Helmchen* _____ **2466 – 2469**

Enantioselective Modular Synthesis of 2,4-Disubstituted Cyclopentenones by Iridium-Catalyzed Allylic Alkylation

Classy combo: Together, the asymmetric iridium-catalyzed allylic alkylation and ruthenium-catalyzed ring-closing metathesis lead to an efficient synthesis of chiral cyclopentenones (see scheme). One example is the synthesis of the antitumor agent *TEI-9826* with high enantiomeric purity.

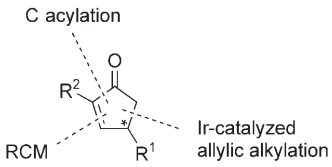

Enzyme Catalysis

R. Wombacher, S. Keiper, S. Suhm, A. Serganov, D. J. Patel, A. Jäschke* _____ **2469 – 2472**

Control of Stereoselectivity in an Enzymatic Reaction by Backdoor Access

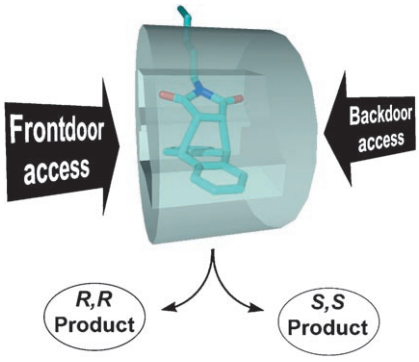

Sneaking in: The active site of a Diels–Alder ribozyme features two different "doors" through which the diene may enter. Depending on which door is used, either of the two enantiomeric Diels–Alder products is synthesized selectively. Enantioselectivity can be modulated by controlling access to the ribozyme's active site.

© 2006 Wiley-VCH Verlag GmbH & Co. KGaA, Weinheim

Magic ball: A spherical aggregate containing a core of 32 inorganic atoms (see structure) was prepared by coordination of a *cyclo*-P_4 tantalum complex to copper(I) chloride. The phosphorus/copper core exhibits an arrangement of alternating four- and six-membered rings, which are reminiscent of the hypothetical O_h-symmetric fullerene C_{32}.

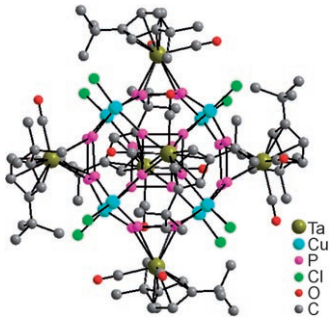

Fullerene-Like Molecules

B. P. Johnson, F. Dielmann, G. Balázs, M. Sierka, M. Scheer* ——— **2473 – 2475**

Spherical Cluster Comprising a Four- and Six-Membered-Ring Motif

Looking for outstanding employees?

Do you need another expert for your excellent team?
... Chemists, PhD Students, Managers, Professors, Sales Representatives...

Place an advert in the printed version and have it made available online for 1 month, free of charge!

Angewandte Chemie International Edition
Advertising Sales Department: Marion Schulz
Phone: 0 62 01 - 60 65 65
Fax: 0 62 01 - 60 65 50
E-Mail: MSchulz@wiley-vch.de

Service

Keywords ——— *2476*

Authors ——— *2477*

Preview ——— *2479*

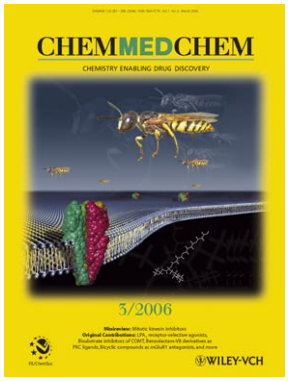

For more information on ChemMedChem see www.chemmedchem.org

© 2006 Wiley-VCH Verlag GmbH & Co. KGaA, Weinheim

Winter Workshop in Linz: Advances in Single-Molecule Research**

Jörg Enderlein

The Annual Linz Winter Workshop was held this year on February 3–6 and focused on advances in single-molecule research for biology and nanoscience, concentrating in particular on scanning probe microscopy as well as single-molecule fluorescence studies. A considerable number of presentations were concerned with methodological and technological aspects of scanning probe microscopy.

M. J. Miles (University of Bristol) reported on the development of a high-speed atomic force microscope (AFM) that can record up to 120 images per second[1] by operating the microscope under resonance conditions, which are usually avoided in conventional systems. The microscope allows the observation of fast processes with near-atomic resolution with amazingly low sample disturbance. R. Perez (University of Madrid) presented detailed ab initio model calculations on the interaction of an AFM probe with a molecular monolayer, showing the mechanical deformation of the layer by the probe. Such calculations play an increasingly important role in precise quantitative evaluation of AFM images and help to optimize experimental conditions for minimizing sample disturbance effects by the AFM.

T. Oosterkamp (University of Leiden) reported the latest progress of his group in employing carbon nanotubes as the tip material for AFM probes. The use of nanotubes promises better spatial resolution and the ability to scan surfaces with steep topographic profiles. However, reproducible manufacturing of these nanotube AFM probes is still extremely work-intensive and technically challenging. C. Kranz (Georgia Tech) reported on a remarkable combination of AFM with an electrochemical probe. By using thin-film chemical vapor deposition and focused ion-beam drilling, special AFM probes with integrated electrodes are produced that allow simultaneous recording of topographic as well as electrochemical data.[2] S. Lindsay (Arizona State University) focused on new types of AFM-coupled ligands used in so-called molecular recognition force microscopy. In this variant of AFM, the probe-coupled ligands are used to measure specific binding events between them and receptor molecules on a surface upon AFM scanning. This process allows a kind of chemical recognition of surface-adsorbed or bound molecules with nanometer resolution.

From the large number of presentations that dealt with applications of AFM in biological and chemical research, only a small number are mentioned here. G. J. Vancso (University of Twente) reported among other things on a molecular realization of a Carnot cycle. By repeated stretching and collapse of a redox–responsive molecule and switching the redox state of the molecule in the stretched and collapsed states, his group built a molecular heat engine. This result is an interesting step towards the construction of artificial molecular motors.[3]

Several remarkable talks were concerned with the structuring of surfaces on the molecular level. H. Yan (Arizona State University) reported on the assembly of modified DNA double strands for building large supramolecular structures in modular fashion by using the strands as building blocks.[4] G. Dietler (EPFL, Lausanne) discussed measuring scale exponents of the geometry of polymer chains by evaluating AFM images of surface-adsorbed DNA molecules. The values determined experimentally were in surprisingly good agreement with those from classical theoretical predictions. P. Williams (University of Nottingham) presented methodologically new simulations of AFM-based protein-folding experiments. The use of AFM for forced unfolding of individual proteins was a spectacular application of AFM during the last decade. A better theoretical understanding of the relevance of these experiments is welcome, in particular from the point of view of their relation to native folding/unfolding processes.

As every year, the workshop presented also outstanding work on fluorescence-based single-molecule spectroscopy. N. Dovichi (University of Washington) reported on his success in proteomics of single cells by combining gel electrophoresis with single-molecule sensitive detection of proteins that are tagged with green fluorescent proteins. With this technique, heterogeneous expression levels and heterogeneous post-translational protein modifications in different cells can be detected and statistically evaluated—a topic of great importance in current cell biology.

U. Kubitschek (University of Bonn) presented impressive in vivo video sequences with up to 340 frames per second of the diffusion of individual fluorescently tagged molecules within the cell nucleus. The talk by M. Garcia-Parajo (University of Barcelona) was concerned with near-field optical microscopy of fluorescently labeled cell membranes. The research of their group aims at studying the connection between clustering of transmembrane receptor proteins and so-called lipid rafts. The latter are thought to play an important role in the spatial organization of membrane proteins, an idea which was, however, not supported by the results presented therein.

[*] Dr. J. Enderlein
Institut für Biologische Informationsverarbeitung 1
Forschungszentrum Jülich
D-52425 Jülich (Germany)
E-mail: j.enderlein@fz-juelich.de

[**] VIII. Annual Linz Winter Workshop: Advances in Single-Molecule Research for Biology and Nanoscience, February 3–6, 2006, Linz (Austria).

InterScience
© 2006 Wiley-VCH Verlag GmbH & Co. KGaA, Weinheim

R. M. Berry (University of Oxford) reported on the structure and functioning of flagellar motors in *E. coli* bacteria.[5] By counting the number of individual molecules of green fluorescent proteins on the motor, his group could determine the number of subunits comprising a complete motor. Similarly impressive was the talk presented by M. Börsch (University of Stuttgart) on the functioning of the molecular motor ATPase, which was studied using Förster resonance energy transfer (FRET).

The contribution by B. Nilius (University of Leuven), although not on a single-molecule level but nonetheless scientifically excellent, was also concerned with the functioning of so-called transient receptor potential (TRP) ion channels, which play a pivotal role in thermal sensing.[6] Last but not least, the contribution by B. L. de Groot (Max Planck Institute, Göttingen) described molecular dynamics simulations of the permeation of water molecules through aquaporins, important water-transport systems within the cell membrane.[7]

In summary, the workshop presented exciting developments in the domains of scanning probe microscopy and fluorescence-based single-molecules studies, and we look forward with anticipation to next year's workshop.

[1] a) A. D. L. Humphris, J. K. Hobbs, M. J. Miles, *Appl. Phys. Lett.* **2003**, *83*, 6–8; b) A. D. L. Humphris, M. J. Miles, J. K. Hobbs, *Appl. Phys. Lett.* **2005**, *86*, 034106.

[2] A. Kueng, C. Kranz, A. Lugstein, E. Bertagnolli, B. Mizaikoff, *Angew. Chem.* **2005**, *117*, 3485–3488; *Angew. Chem. Int. Ed.* **2005**, *44*, 3419–3422.

[3] a) S. Zou, H. Schönherr, G. J. Vancso, *Angew. Chem.* **2005**, *117*, 978–981; *Angew. Chem. Int. Ed.* **2005**, *44*, 956–995; b) S. Zou, H. Schönherr, G. J. Vancso, *J. Am. Chem. Soc.* **2005**, *127*, 11230–11231.

[4] a) H. Yan, *Science* **2004**, *306*, 2048–2049; b) H. Yan, S. H. Park, G. Finkelstein, J. H. Reif, T. H. LaBean, *Science* **2003**, *301*, 1882–1884.

[5] a) W. S. Ryu, R. M. Berry, H. C. Berg, *Nature* **2000**, *403*, 444–447; b) Y. Sowa, A. D. Rowe, M. C. Leake, T. Yakushi. , M. Homma, A. Ishijima, R. M. Berry, *Nature* **2005**, *437*, 916–919.

[6] K. Talavera, K. Yasumatsu, T. Voets, G. Droogmans, N. Shigemura, Y. Ninomiya, R. F. Margolskee, B. Nilius, *Nature* **2005**, *438*, 1022–1025.

[7] B. L. de Groot, H. Grubmüller, *Science* **2001**, *294*, 2353–2357.

DOI: 10.1002/anie.200600875

GDCh

Gesellschaft Deutscher Chemiker

Call for Tenders Georg Manecke Scholarship

The Georg Manecke Foundation, managed and held in trust by the Gesellschaft Deutscher Chemiker (GDCh) supports younger scientists working in polymer science, including areas with biochemical and biotechnological applications.

In 2006 the foundation will award a Georg Manecke Scholarship of 8,000 EUR to a doctoral student/postdoctoral scientist, preferably from Central or Eastern Europe. The holder of the scholarship will work for at least six months in a German research institute of his/her choice. If required, the GDCh offers its assistance in selecting the host institution.

Applications with CV, university records/certificates, scientific interests, list of publications, and at least two references should be sent not later than **30 June 2006** to:

Gesellschaft Deutscher Chemiker, Kuratorium der "Georg-Manecke-Stiftung", Postfach 90 04 40, 60444 Frankfurt am Main,Germany.

For questions please contact Barbara Köhler, E-Mail: b.koehler@gdch.de, Tel. +49 (0)69 7917-323.

Contact

Gesellschaft
Deutscher Chemiker
Abt. Preise und Auszeichnungen
60444 Frankfurt a. M

E-Mail: b.koehler@gdch.de
Tel. 069/79 17-323
Fax: 069/7917-307

 © 2006 Wiley-VCH Verlag GmbH & Co. KGaA, Weinheim

Ultrasound-Induced Switching

DOI: 10.1002/anie.200503191

Molecule-Based Rheology Switching

*Jos M. J. Paulusse and Rint P. Sijbesma**

Keywords:
coordination chemistry · electrochemistry · gels · photochemistry · ultrasound

The control of rheological properties of fluids by external stimuli is a goal of longstanding fundamental and practical interest, with possible applications in clutches, brakes, vibration damping, seismic protection of structures, and other fields.[1–3] In order to achieve reversible switching of the viscosity of fluids, macroscopic physical phenomena as well as effects at the molecular level may be utilized. While applications of electrorheology[1–5] and magnetorheological materials[3,6] show the strength of macroscopic approaches, recent developments point out promising perspectives in molecule-based switching of rheological behavior. Chemists can contribute to this area by the design and development of molecules that are better able to transduce external stimuli into a reversible change in viscosity or even induce gelation. Some of the most successful molecular approaches in this field are the use of electrochemistry and photochemistry. More recently, the use of ultrasound was reported as an unexpected yet surprisingly effective stimulus for molecular switching of solvent viscosity.

Changes in rheological behavior in such systems have been studied with a wide range of techniques and with varying thoroughness. The methods range from mere visual inspection to establish the formation of gels (the "inverted test tube method"[7]) to detailed characterization with rheometry and transmission electron microscopy (TEM). As the level of characterization varies strongly in the reports discussed herein, it is sometimes difficult to establish whether true gels or simply very viscous solutions are described. Therefore, we indicate whenever there is ambiguity in the characterization.

Electric fields have been used for over 50 years[8] to switch the viscosity of solvents in electrorheological systems, but the use of electrochemistry based on molecular redox chemistry is more recent. Abe and co-workers[9] recently reported an iron-containing cationic surfactant **1** (Scheme 1), which forms wormlike micelles in water in the presence of sodium salicylate. Freeze fracture TEM studies showed that these micelles are up to several micrometers long and form an entangled network displaying remarkable viscoelasticity. Upon electrolytic oxidation of the system at a very low voltage, the ferrocenyl group was oxidized to a ferricinium cation. In this way, the ferrocene head group was switched from hydrophobic (reduced **1a**) to hydrophilic (oxidized **1b**). This oxidation breaks down the long wormlike micelles to elliptic micelles and single surfactant molecules. Whereas the mixture of **1** in water had a zero shear viscosity of 15 Pa s, the viscosity dropped to 2.5×10^{-3} Pa s upon oxidation. Although the reduction process takes a significant amount of time, the 6000-fold decrease in viscosity is nonetheless dramatic. The authors suggested applications in areas such as inkjet printing, although switching times should be improved significantly to achieve this.

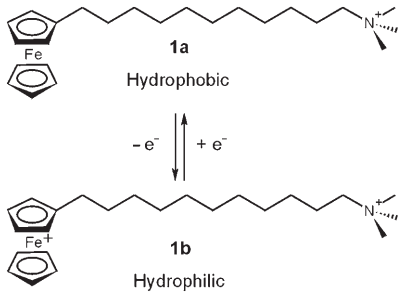

Scheme 1. Redox switching of head group affinity in (11-ferrocenylundecyl)trimethylammonium bromide **1**.

The conformational changes that can be brought about by irradiation with light have been used to switch between sol and gel states. Wolff et al. were among the first to recognize the potential of controlling rheological properties by light. Their studies concerned the selective production of the unstable head-to-head dimer of 9-methylanthracene by preorganization in micellar solutions of cetyltrimethylammonium bromide and subsequent irradiation with light (Scheme 2).[10] As a side effect the rheological properties of the solutions also changed when irradiated, which led the authors to investigate a range of anthracene derivatives.[11] The addition of 9-methylanthracene led to a

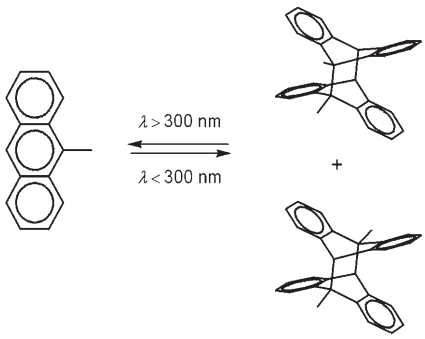

Scheme 2. Photodimerization of 9-methylanthracene leading to head-to-head and head-to-tail dimers.

[*] J. M. J. Paulusse, Dr. R. P. Sijbesma
Laboratory of Macromolecular and Organic Chemistry
Eindhoven University of Technology
P.O. Box 513
5600 MB Eindhoven (The Netherlands)
Fax: (+40) 247-2655
E-mail: R.P.Sijbesma@tue.nl

InterScience
© 2006 Wiley-VCH Verlag GmbH & Co. KGaA, Weinheim

strong enhancement of viscosity, as indicated by rheometric measurements. Upon photodimerization ($\lambda > 300$ nm), viscosity was reduced to approximately half the original value. Subsequent irradiation with light of shorter wavelength ($\lambda < 300$ nm) led to an increase in the viscosity.

The *cis–trans* isomerization in azo compounds[7,12,13] and stilbene[14,15] has been used for switching viscosity. The light-induced interconversion between the open and closed forms of molecules such as dithienylcyclopentene[16] has also been successfully employed.

Pioneering work in the area of photoresponsive organogelation was performed by Shinkai and co-workers,[7] who developed cholesterol-based gelators containing an azobenzene unit. Irradiation of the system at 330–380 nm led to isomerization of the azo linkage to its *cis* conformation and thereby disrupted gelation. Irradiation of the sol at wavelengths longer than 460 nm resulted in reversal of the isomerization and re-formation of the gel. The formation of the gel network was observed with scanning electron microscopy (SEM), and as this network consists of chiral stacks, circular dichroism spectroscopy was also used for characterization.

Pozzo and co-workers[17] employed the photochromic equilibrium of 3,3-diphenyl-3*H*-naphthopyran, which brings about a large conformational change in gelator **2** (Scheme 3). Two forms of the naphthopyran can be distinguished: a colored open form **2a** and a colorless closed form **2b**. When the naphthopyran unit is in its closed form, it does not influence the stacking process and the molecule acts as an efficient gelator. TEM measurements showed the formation of fibrous aggregates of **2** in dimethylformamide (DMF). Additional evidence for the formation of a gel was provided by frequency-sweep rheometric measurements, which showed that the elastic modulus G' and the loss modulus G'' were fairly independent of frequency over a wide range. Irradiation with UV light ($\lambda = 366$ nm) converted the naphthopyran unit into the open form and prevented the carbamate group from stacking. The isomerization was accompanied by a color change, and while the gel liquefied it became yellow. Heating converted the pyran unit back into the closed form, and upon cooling a colorless gel was again obtained.

Light has also been used to convert nongelating maleic acid amide **3** into gelating fumaric acid amide **4** (Scheme 4). A set of bis(amino acid) oxalamide gelators with excellent thermal stability were reported by Žinić and co-workers.[18] The same authors modified the original molecule with a carbon–carbon double bond, which permits control over gelation through light irradiation.[19] In the *cis* conformation maleic acid amide **3** is nonlinear, which caused the hydrogen-bonding motif to lose its self-complementarity. Upon irradiation with UV light, the double bond was isomerized to yield the fumaric acid amide **4**. This linear molecule closely resembles the bis(amino acid) oxalamide gelators, and upon isomerization the compound immediately led to gelation of the solvent. Long fibers were observed by TEM, and ^{1}H NMR analysis showed very broad signals caused by the long correlation times of the network. Heating to 80 °C caused the gel to liquefy, and the NMR spectrum corresponded to pure **4**.

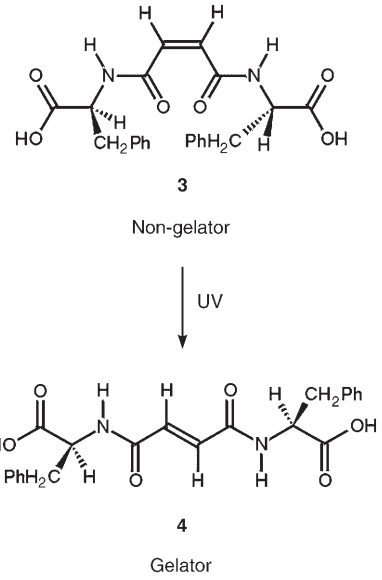

Scheme 4. *Cis–trans* isomerization of maleic acid amide **3** leading to fumaric acid amide **4**.

Very recently, the use of ultrasonic radiation has become a novel way to reversibly control aggregation by noncovalent interactions. The use of ultrasound to disrupt solid particles or biological tissue is well established,[20] and application of ultrasonic radiation for the breaking of covalent bonds in polymers has been the subject of numerous studies. However, in both applications the effect of ultrasound is irreversible. Two recent reports have introduced reversibility by making use of systems based on well-defined noncovalent interactions. Interestingly, these reports discuss opposite effects of ultrasound on chemically similar systems—both are palladium coordination complexes.

Whereas the work by us[21] reports the reversible breaking of noncovalent aggregates of **5**, the report of Naota and Koori[22] describes the aggregation of *anti*-**6** induced by short sonication, re-

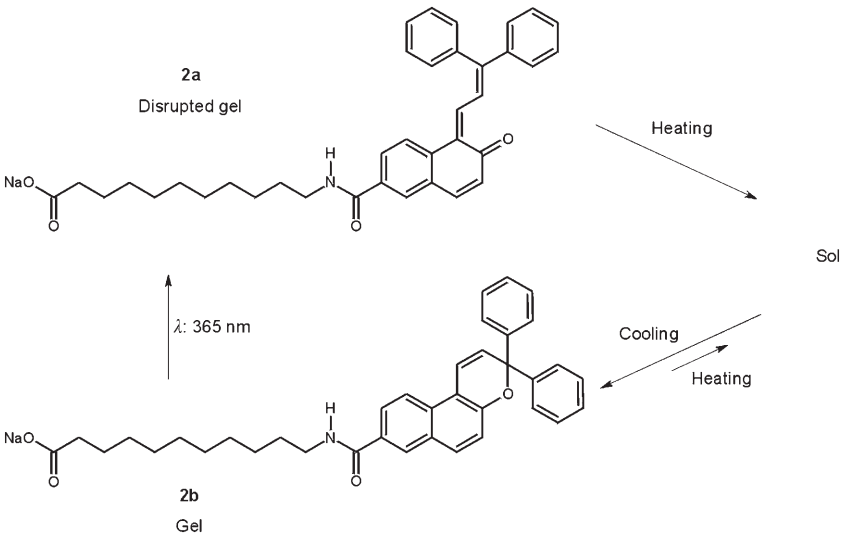

Scheme 3. Light-induced switching between open and closed structures of naphthopyran **2**.

 © 2006 Wiley-VCH Verlag GmbH & Co. KGaA, Weinheim

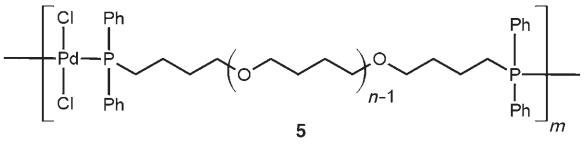

5

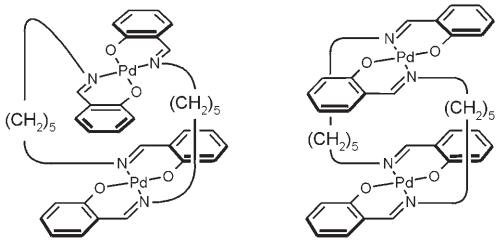

anti-**6** *syn*-**6**

sulting in instantaneous gelation of the solution.

In our study,[21] the ultrasonic scission of coordination polymer **5** was shown to be completely reversible. Sonication of a solution of **5** (10 g L^{-1}, 1.5 mM) in toluene resulted in decreases in the molecular weight from 180 to 90 kg mol^{-1} and in the specific viscosity from 5.4 to 1.5. Upon standing for 24 h, the original molecular weight was completely recovered, indicating that ultrasound selectively breaks the coordinative bonds between palladium and the phosphine groups and leaves the covalent bonds in the poly(tetrahydrofuran) part of the polymer untouched (Figure 1). The focus of this study was the potential of the method to create coordinatively unsaturated metal species with novel reactivity profiles, but it is clear that the ultrasound-induced changes in molecular weight are also of interest from the point of view of the reversible control of rheology.

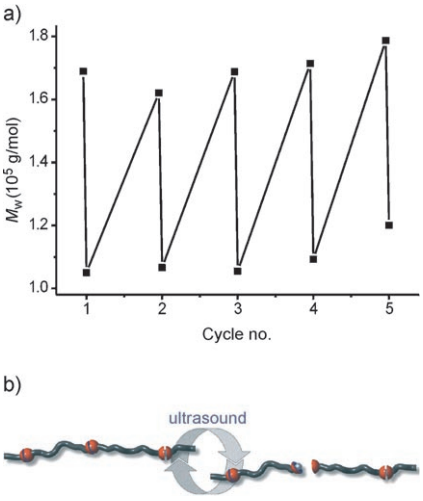

Figure 1. a) Weight-average molecular weight (M_w) of **5** during a reversibility test consisting of five cycles of sonication (1 h) followed by equilibration (23 h). b) Schematic representation of the ultrasonic scission process of **5**.

In a remarkable paper, Naota and Koori[22] described recently how dinuclear Pd complex *anti*-**6** was used to form solutions that gelate upon sonication. When solutions containing *anti*-**6** (≈10 mM) were sonicated for a short time (3 s to 3 min), an assembly process between the complex molecules was initiated that continued after sonication had ceased and eventually caused the solutions to gel. When the gels were heated above their gel temperatures and cooled to room temperature, stable liquids were recovered. The process is general in the sense that a wide range of organic solvents gave gels upon sonication. The phenomenon is especially insensitive to solvent polarity and is observed across the polarity spectrum from cyclohexane to dimethyl sulfoxide. Yet, gelation is highly solute-specific, as was exclusively observed for the complex *anti*-**6**. Salicylidene complexes with longer spacers were unable to gelate any organic solvent.[23] Even isomer *syn*-**6** did not form gels which indicates that the precise shape and conformation of the complex are essential for gelation. Most complexes other than *anti*-**6** responded to sonication. However, they did so by precipitating instead of giving a gel. This behavior suggests that similar assembly processes take place in each of the compounds, but that only *anti*-**6** is capable of capturing large amounts of solvent molecules in the process of aggregation.

Although rheological characterization of the gels was limited to visual inspection, detailed information on the composition of the gel was obtained in gelation experiments with nonracemic solutions of *anti*-**6**, which displays planar chirality. When enantiopure (−)-*anti*-**6** was used, no gelation was observed and the complex remained fully soluble after sonication. Enantioenriched solutions of *anti*-**6** did form gels, but remarkably the gel was fully racemic, while the excess of the (−) enantiomer remained in solution. These observations strongly suggest that aggregates with alternating (+) and (−) complexes are formed in the assembly process.

With regards to the mechanism of this unprecedented phenomenon, complex **6** is kinetically inert and maintains its structural integrity during the aggregation process, ruling out the formation of a coordination polymer as the cause of gelation. On the basis of NMR and UV spectral data, the authors concluded that "*gelation proceeds via the interpenetrative, consecutive stacking of planar monomer units*". This process in turn is caused by a conformational change from clothes-peg-like, as found in the crystal structure of *anti*-**6** (Figure 2a), to a more planar, stacked arrangement similar to that found in the crystal structure of *anti*-**7** (Figure 2b). The proposed process is shown schematically in Figure 3.

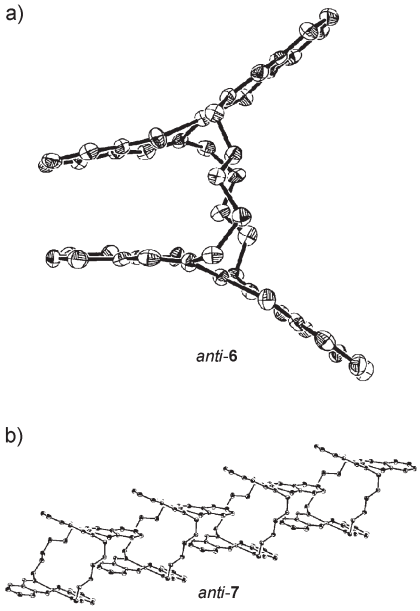

Figure 2. X-ray crystal structures of a) *anti*-**6** and b) stacked *anti*-**7** (Reprinted with permission from Reference [22]; copyright 2005 American Chemical Society).

Although this explanation must be considered unproven until more-detailed information on the structure of the gel is available (e.g. from diffraction experiments), it is adequate as a working hypothesis. Tentatively, the molecular details of the gelation process can therefore be summarized as follows: Upon triggering the system with an

 © 2006 Wiley-VCH Verlag GmbH & Co. KGaA, Weinheim

Figure 3. Proposed ultrasound-induced conformational change of *anti*-**6** leading to heterochiral aggregation.

external stimulus, an "infectious" conformation of the molecule is formed that induces the formation of fibrillar aggregates by propagation. These features display a surprising similarity to the process that is proposed to be responsible for prion diseases such as scrapie and BSE.[24–26] In these diseases, a so-called prion protein forms insoluble fibrils when a misfolded molecule induces identical conformational changes in other molecules, resulting in aggregation. Much research is devoted to elucidating the molecular details of prion diseases, but a synthetic analogue of fibril formation by initiation from a metastable state had not been reported so far.[27] Thus, the remarkable publication of Naota and Koori is interesting in two regards: It introduces ultrasound as a novel and unexpectedly effective external trigger to switch solvent viscosity, and it presents a purely synthetic analogue of prion proteins and their aggregation.

Further studies on the detailed mechanism of aggregation of **6**, including attempts to establish the generality and requirements of the process, are called for. For instance, considering the analogy with prions, it would be of interest to establish whether gels of **6** can be formed by seeding; in other words, whether they are "infectious". Without doubt, this original piece of research has the potential to be highly influential and should inspire many chemists to design and synthesize novel supramolecular systems that polymerize in a similar initiated fashion.

The work of Naota and Koori gives additional momentum to research on molecule-based rheology switching, an area that is already receiving intensive attention. Compared to switches based on physical phenomena, which have found numerous commercial applications, molecular rheology switches are in their infant stage. However, the unlimited possibilities for structural tuning provided by synthetic chemistry bode well for the future of the molecular approach.

Published online: February 27, 2006

[1] R. Stanway, J. L. Sproston, A. K. El-Wahed, *Smart Mater. Struct.* **1996**, *5*, 464.
[2] T. Hao, *Adv. Mater.* **2001**, *13*, 1847.
[3] J. D. Carlson, D. M. Catanzarite, K. A. St. Clair, *Int. J. Mod. Phys. B* **1996**, *10*, 2857.
[4] T. C. Halsey, *Science* **1992**, *258*, 761.
[5] W. J. Wen, X. X. Huang, S. H. Yang, K. Q. Lu, P. Sheng, *Nat. Mater.* **2003**, *2*, 727.
[6] S. Odenbach, *Int. J. Mod. Phys. B* **2000**, *14*, 1615.
[7] K. Murata, M. Aoki, T. Suzuki, T. Harada, H. Kawabata, T. Komori, F. Ohseto, K. Ueda, S. Shinkai, *J. Am. Chem. Soc.* **1994**, *116*, 6664.
[8] W. M. Winslow, US Patent 2417850, **1947**.
[9] K. Tsuchiya, Y. Orihara, Y. Kondo, N. Yoshino, T. Ohkubo, H. Sakai, M. Abe, *J. Am. Chem. Soc.* **2004**, *126*, 12282.
[10] T. Wolff, N. Müller, *J. Photochem.* **1983**, *23*, 131.
[11] N. Müller, T. Wolff, G. Von Buenau, *J. Photochem.* **1984**, *24*, 37.
[12] N. Koumura, M. Kudo, N. Tamaoki, *Langmuir* **2004**, *20*, 9897.
[13] C. T. Lee, K. A. Smith, T. A. Hatton, *Macromolecules* **2004**, *37*, 5397.
[14] J. Eastoe, M. Sanchez-Dominguez, P. Wyatt, R. K. Heenan, *Chem. Commun.* **2004**, 2608.
[15] S. Miljanic, L. Frkanec, Z. Meic, M. Žinić, *Langmuir* **2005**, *21*, 2754.
[16] J. J. D. de Jong, P. R. Hania, A. Pagzlys, L. N. Lucas, M. de Loos, R. M. Kellogg, B. L. Feringa, K. Duppen, J. H. van Esch, *Angew. Chem.* **2005**, *117*, 2425; *Angew. Chem. Int. Ed.* **2005**, *44*, 2373.
[17] S. A. Ahmed, X. Sallenave, F. Fages, G. Mieden-Gundert, W. M. Müller, U. Müller, F. Vögtle, J. L. Pozzo, *Langmuir* **2002**, *18*, 7096.
[18] J. Makarević, M. Jokić, L. Frkanec, D. Katalenic, M. Žinić, *Chem. Commun.* **2002**, 2238.
[19] L. Frkanec, M. Jokić, J. Makarević, K. Wolsperger, M. Žinić, *J. Am. Chem. Soc.* **2002**, *124*, 9716.
[20] J. Massey, K. N. Power, I. Manners, M. A. Winnik, *J. Am. Chem. Soc.* **1998**, *120*, 9533.
[21] J. M. J. Paulusse, R. P. Sijbesma, *Angew. Chem.* **2004**, *116*, 4560; *Angew. Chem. Int. Ed.* **2004**, *43*, 4460.
[22] T. Naota, H. Koori, *J. Am. Chem. Soc.* **2005**, *127*, 9324.
[23] When the salicylidene moieties are connected by a heptyl spacer, the complex is able to gelate benzene.
[24] F. E. Cohen, S. B. Prusiner, *Annu. Rev. Biochem.* **1998**, *67*, 793.
[25] J. W. Kelly, *Curr. Opin. Struct. Biol.* **1998**, *8*, 101.
[26] S. B. Prusiner, *Proc. Natl. Acad. Sci. USA* **1998**, *95*, 13363.
[27] For triggered formation of fibrils from stable peptide conformations, see: a) C. E. MacPhee, D. N. Woolfson, *Curr. Opin. Solid State Mater. Sci.* **2004**, *9*, 141; b) A. Banerjee, S. K. Maji, M. G. B. Drew, D. Haldar, A. K. Das, *Tetrahedron* **2004**, *60*, 5935.

© 2006 Wiley-VCH Verlag GmbH & Co. KGaA, Weinheim

Dye-Sensitized Solar Cells

DOI: 10.1002/anie.200503083

Optimizing Dyes for Dye-Sensitized Solar Cells

*Neil Robertson**

Keywords:
dyes/pigments · energy conversion · redox chemistry · semiconductors · sensitizers

Dye-sensitized solar cells (DSSCs) have emerged as an important cheap photovoltaic technology. Charge separation is initiated at the dye, bound at the interface of an inorganic semiconductor and a hole-transport material. Careful design of the dye can minimize loss mechanisms and improve light harvesting. Mass application of DSSCs is currently limited by manufacturing complexity and long-term stability associated with the liquid redox electrolyte used in the most-efficient cells. In this Minireview, dye design is discussed in the context of novel alternatives to the standard liquid electrolyte. Rapid progress is being made in improving the efficiencies of such solid and quasi-solid DSSCs which promises cheap, efficient, and robust photovoltaic systems.

1. Introduction

1.1. Design of Dye-Sensitized Solar Cells

Increasing energy demands and concerns over global warming have led to a greater focus on renewable energy sources in recent years. The conversion of solar energy is likely to play a key role as one of the technologies that can replace fossil fuels in the generation of mass energy. However, the current high cost of solar panels made from traditional inorganic semiconductors[1] imposes a restriction on their mass usage. Alternative cheaper solar energy technologies are therefore under intensive study, and in this context dye-sensitized solar cells (DSSCs) have emerged as an important class of photovoltaic device. DSSCs are currently undergoing rapid development in an effort to obtain robust, efficient, and cheap devices that are suitable for practical use.[2–4] An outline of the operation of a DSSC is illustrated in Figure 1. The system comprises a dye that is bound to the surface of an inorganic semiconductor. Typically nanocrystalline TiO_2 is used as it provides a large surface area to which the dye can adsorb, which is crucial for efficient light harvesting. The porous TiO_2 layer is interpenetrated by a hole-transport material (HTM), which may be a redox electrolyte in solution or a solid-state or quasi-solid-state (gel) material. Excitation of the dye leads to the injection of electrons from the excited dye to the conduction band of the TiO_2. The ground state of the dye is regenerated through reduction by the HTM to give the

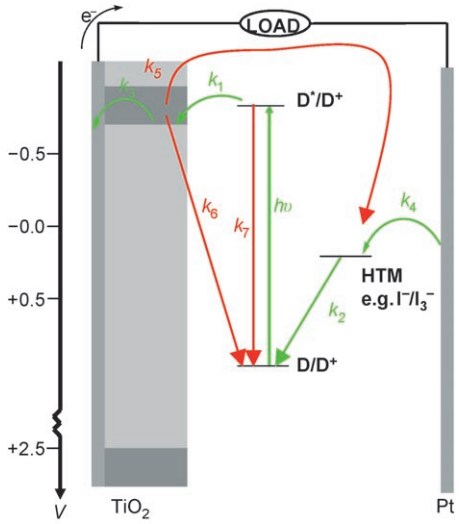

Figure 1. Outline of the operation of a DSSC (**D** = dye; *V* [V] vs standard calomel electrode (SCE)). The green arrows represent processes required for photovoltaic function: k_1 = charge injection, k_2 = dye regeneration, k_3 = charge collection at the conducting glass electrode, and k_4 = charge collection at the Pt electrode. The red arrows represent loss mechanisms: k_5 = charge recombination with the hole-transport material (HTM; dark current), k_6 = charge recombination with the oxidized dye (**D**$^+$), and k_7 = decay of the excited state of the dye (**D***).

[*] Dr. N. Robertson
School of Chemistry
University of Edinburgh
King's Buildings
West Mains Road
Edinburgh EH9 3JJ (UK)
Fax: (+44) 131-650-4743
E-mail: neil.robertson@ed.ac.uk

WILEY InterScience DISCOVER SOMETHING GREAT

© 2006 Wiley-VCH Verlag GmbH & Co. KGaA, Weinheim

required charge separation. Charges migrate and are collected at a transparent conducting electrode (electrons) and Pt electrode (holes). A number of parameters are used to characterize the detailed performance of a photovoltaic cell;[2] however, in this Minireview discussion is limited mainly to the overall efficiency of conversion of solar-to-electrical energy of the cell (η) and also to the incident photon to current efficiency (IPCE), which gives a measure of the efficiency as a function of wavelength of the incident light.

Following the initial development of this type of cell by O'Regan and Grätzel,[5] there has been further extensive study and optimization of the design, including modifications to the nanocrystalline semiconductor, the redox electrolyte, and the dye. Currently, the most efficient DSSCs show efficiencies of over 10%, which is sufficiently high to be of practical utility. The cells that display the highest efficiency, however, use an HTM comprising an I^-/I_3^- redox electrolyte solution that gives rise to poor long-term stability and manufacturing complexity.[6] The involvement of volatile I_2 and volatile solvent requires the cells to be sealed, and additionally, the I^-/I_3^- redox electrolyte can be corrosive towards the Pt electrode. Although some commercialization of DSSCs has begun, new aspects of cell design are being intensively explored to continue to address these limitations and open up DSSC technology to much wider exploitation. Thus, a number of alternative redox mediators and electrolyte systems have been explored, including I^-/I_3^- in either solid polymer,[7,8] gel,[6] ionic liquid,[9] or plastic crystal[10] systems; solid inorganic materials;[11] Co^{II}/Co^{III}[12] and $SeCN^-/(SeCN)_3^-$ redox couples;[9] and hole-conducting organic polymers[13] and small organic molecules.[14] However, a reduced efficiency has so far been achieved for such cells; for example, the maximum cell efficiencies observed for the gel-electrolyte systems, organic HTM systems, and ionic liquid systems are around 6, 4, and 8%, respectively. In each of these cases, the efficiencies are less than that for the optimized I^-/I_3^-/volatile solvent cell as a result of factors such as reduced hole mobility, poorer electron-transfer kinetics, and poorer contact at the dye–HTM interface. Much is now understood concerning loss mechanisms that arise within the system, and key processes are indicated in Figure 1.

Some recent overviews that discuss general aspects of DSSCs[1,2,4] have appeared along with a series of articles that give a detailed account of several specific topics within the field.[3] The aim of this Minireview is to provide a general overview of dye characteristics and illustrate the ways in which dye design has been used to enhance the efficiency of cells. The key challenge at present is to obtain efficiencies that are comparable to that for the optimized I^-/I_3^-/volatile solvent cell by using an HTM that is more suitable for mass production and long-term stability. The design of dyes will therefore be presented in this context in the quest for photovoltaic (PV) cells that are efficient, robust, and cheap to manufacture.

Neil Robertson studied chemistry at the University of Edinburgh and obtained his PhD there in 1992. He then carried out postdoctoral work at the Freie Universität Berlin and University of Wales, Bangor, where he first developed an interest in the electronic and magnetic properties of molecular materials. After a Royal Society of Edinburgh/BP Research Fellowship at Edinburgh (1996–1999) and a lectureship at Imperial College London, he took up his current position (2001) as a senior lecturer in chemistry at the University of Edinburgh.

1.2. General Design of Dyes

Progress in the optimization of the dye component of the cell has been made through systematic variation of the ligands, metal, and other substituent groups in candidate transition-metal complexes.[2,15,16,17] This systematic study has resulted in the development of mononuclear[2] and polynuclear[18] dyes based on metals such as Ru^{II},[19–21] Os^{II},[4,22,23] Pt^{II},[24,25] Re^{I},[26] Cu^{I},[27] and Fe^{II}.[28] Besides transition-metal complexes, a range of organic molecules have been explored, with recent examples including coumarin,[29] squaraine,[30] indoline,[31] hemicyanine,[32] and other conjugated donor–acceptor organic dyes,[33–36] and the best efficiency reported was 8% (see Figure 7a in Section 2.5).[31] Porphyrin dyes[37,38] and phthalocyanine dyes[39] have also been explored.

The dyes used in DSSC technology must conform to a number of essential design requirements in order to function. They must bind strongly to TiO_2 by means of an anchoring group, typically carboxylic or phosphonic acid groups, to ensure efficient electron injection into the TiO_2 conducting band and to prevent gradual leaching by the electrolyte. The LUMO of the dye must be sufficiently high in energy for efficient charge injection into the TiO_2, and the HOMO must be sufficiently low in energy for efficient regeneration of the oxidized dye by the HTM. The dye must absorb solar radiation strongly with absorption bands in the visible or near-IR region, preferably covering a broad range of wavelengths. Electron transfer from the dye to the TiO_2 must also be rapid in comparison with decay to the ground state of the dye. Dyes that show emission in the solution state at room temperature have typically been used, although this is not essential.[40]

The family of complexes $[\{(4,4'\text{-}CO_2H)_2(bipy)\}_2RuX_2]$ (bipy = 2,2′-bipyridyl; X = Cl, Br, I, CN, NCS) perform well;[19] for example, the dye $[\{(4,4'\text{-}CO_2H)_2bipy\}_2Ru(NCS)_2]$ (**N3**) and the doubly deprotonated analogue (**N719**, Figure 2) give a solar-to-electrical energy conversion efficiency of over 10%. Use of a terpyridyl ligand led to the so-called "black dye" (Figure 2), which gives a very high IPCE across the wavelength range 400–700 nm and a cell efficiency of over 10%.[21,41] Dyes are often referred to by codes (as indicated in the figures), which will be used in the remainder of the article.

2. Current Developments in Dye Design

As previously mentioned, the key limitations of DSSCs arise from the I^-/I_3^- liquid electrolyte and this has neces-

© 2006 Wiley-VCH Verlag GmbH & Co. KGaA, Weinheim

sitated the exploration of other cell designs that use an alternative HTM. Initial research into these modified cells with novel designs typically used dyes that were previously optimized for a cell with an I^-/I_3^- solution electrolyte as the HTM (e.g. **N3** or **N719**). As studies develop, however, it is apparent that innovation in transport materials should be carried out in conjunction with the development of new dyes to maximize the improvements in efficiency and stability. Thus, the exploration of new dye designs specifically for solid-state and quasi-solid-state cells is currently an area of high priority that has started to receive increased attention. Key approaches to this area of research are described in Section 2.1–2.5.

2.1. Enhanced Charge Separation in the Dye: Minimizing Charge Recombination

The complex **N3** (Figure 2) is a good illustration of the role that charge separation in the dye plays in controlling the kinetics of electron transfer. Absorption of the dye in the low-energy visible region involves an MLCT (metal-to-ligand charge transfer) transition that places the excited electron on the diimine, which is directly attached to the TiO_2. The result is ultrafast charge injection (see Section 2.2), however, the positive charge density that remains on the dye is distributed over the metal and also to some extent over the NCS ligands. The resulting spatial separation of the positive charge density on the dye and the injected electrons has the crucial effect of retarding the rate of charge recombination between the injected electrons and the dye cation, which is a key loss mechanism (Figure 1, k_6). Indeed, it has been shown that charge-recombination dynamics are closely dependent on this separation and, in contrast, show very little dependence on the thermodynamic driving force for the recombination, as determined by the reduction potential of the dye cation.[42]

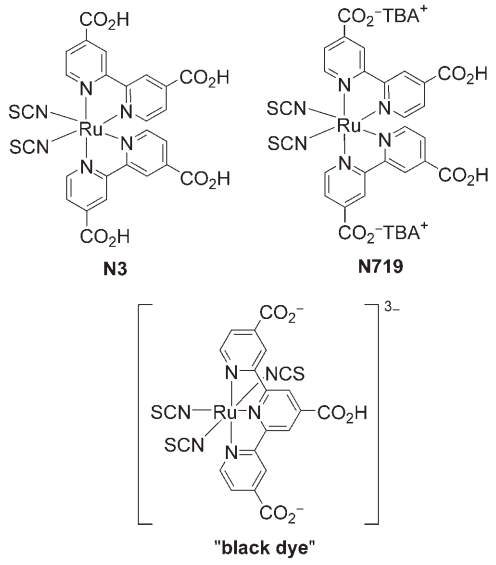

Figure 2. Examples of some Ru–polypyridyl dyes used in DSSCs that give cell efficiencies of over 10%. TBA = tetra-*n*-butylammonium.

Recent work has illustrated that this approach can be extended further and that dyes with attached electron-donor groups can locate the cationic charge at a greater distant from the TiO_2 surface.[43,44] For instance, the substituted porphyrin shown in Figure 3a attaches itself to the TiO_2 surface through

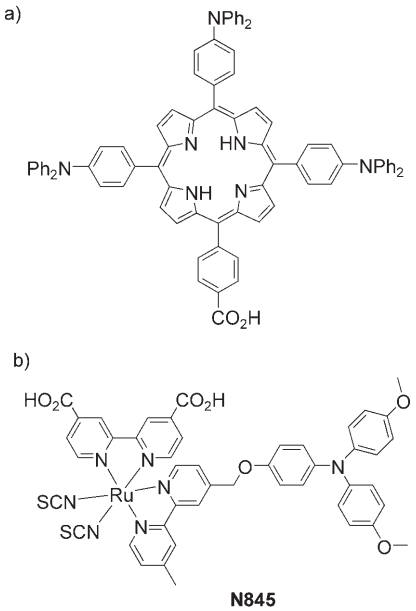

Figure 3. Examples of dyes with attached triarylamine electron-donor groups: a) a porphyrin dye[44] and b) Ru dye **N845**.[45]

its carboxylic acid group, and π–π* photoexcitation leads to charge injection.[44] It was found that recombination of the injected electron with the dye was an order of magnitude slower than for a comparable dye that lacked the electron-donor triphenylamine groups. This difference was attributed to the location of the cationic charge largely on the triphenylamine moieties of the dye and the consequently larger physical separation of the cationic charge from the TiO_2 surface. This approach was extended to the ruthenium dye **N845** (Figure 3b), which also contains an appended triarylamine moiety.[45] In this case, a 1000-fold retardation of the recombination dynamics was attributed to the 4 Å increase in distance between the cationic center of charge and the TiO_2 surface (as estimated from semi-empirical calculations) in comparison with **N719** (Figure 2).

2.2. Methods to Attach the Dye to TiO_2

The majority of dyes are linked to the TiO_2 semiconductor through acidic groups—mostly carboxylic acid or, less commonly, phosphonic acid linkers[46]—although a variety of other moieties also have been used.[47,48] Carboxylic acid groups can form ester linkages with the surface of the metal oxide to provide a strongly bound dye and good electronic communication between the two parts. However, the link can be hydrolyzed through the presence of water, an important factor in terms of the stability of the cell (see Section 2.3). The

© 2006 Wiley-VCH Verlag GmbH & Co. KGaA, Weinheim

dyes that have shown the highest cell efficiencies have used carboxylic acid linkers, although a recent study into phosphonic acid linkers reported the highest efficiency ($\geq 8\,\%$) for any dye with a non-carboxylic acid linker (**Z955**, Figure 4). In this case, modification of the linker from carboxylic to phosphonic acid groups resulted in an interrelated series of changes in the characteristics of the device; for example, a blue shift of the absorption maxima, good stability of the device, and slower charge-recombination kinetics for **Z955** relative to the analogous dye with carboxylic acid linkers (**Z907**, see Figure 5, Section 2.3). The increased number of protons on the phosphonic acid groups compared with carboxylic acid groups has been suggested as a factor in modifying the performance of the dye, as it has been observed that the efficiency of the solar cell can be influenced by changing the protonation of the acid groups. This is attributed to the effect of the bound dye on the energy of the TiO_2 conducting band, such that **N719**, which is deprotonated, gives a higher cell efficiency than the protonated analogue **N3** (Figure 2).[41]

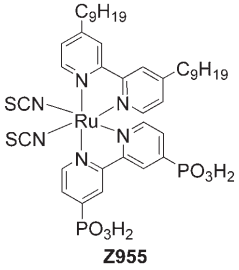

Z955

Figure 4. Ru–polypyridyl dye **Z955** with phosphonic acid linker groups.[46]

Besides the protonation state of the carboxylic acid group, the position of these linker groups on the bipyridyl moiety has been explored.[49,25] The large majority of studies involving bipyridyl groups employ 4,4′-substituted derivatives. The study of a Ru complex with carboxylic acid groups in the 3,3′-positions of the bipyridyl revealed a decreased efficiency of the cell,[49] whereas a study of Pt dyes showed the opposite effect with a slightly improved efficiency for the complex with 3,3′-substituted bipyridyl.[25] As substitution at the 3,3′-positions necessitates some twisting of the ligand, the consequences of the electronic alteration to the dye when bound to TiO_2 may be difficult to predict, however, it seems that further study of complexes with 3,3′-substituted bipyridyls is merited.

Charge injection from Ru–polypyridyl dyes linked through carboxylic acid groups is extremely rapid, and for dye-sensitized TiO_2 covered with an inert solvent it occurs on a femto- to picosecond timescale from the excited singlet and triplet states of the dye, respectively.[50] In a complete DSSC,[51,52] charge injection occurs on the picosecond timescale, with the composition of the redox electrolyte playing an important role in modifying the energetics of the TiO_2 conduction band and hence the charge-injection rate. This extremely rapid process leads to injection yields that approach 100 % for many dyes. However, as the excited-state lifetime of dyes such as **N3** can be as long as 50 ns, high injection yields may still be achieved with an injection rate that is several orders of magnitude slower than those observed. The unnecessarily rapid charge injection is referred to as "kinetic redundancy" and is important because the rates of charge injection (k_1) and the charge-recombination loss process (k_6) are correlated, as both are influenced by the strength of electronic communication of the dye with the TiO_2.[52] For an optimum device kinetic redundancy should be minimized, with charge injection only just fast enough to compete with excited-state decay such that loss through charge recombination is also minimized. Variation of the nature of the linker group between the dye and the TiO_2 can play a crucial role in this optimization and hence on the cell efficiencies achieved.

In an attempt to control these interfacial electron-transfer processes, Haque et al. studied an azobenzene dye encapsulated within a cyclodextrin molecule attached to TiO_2.[53] The cyclodextrin comprises a hydrophilic outer layer, which is suitable for adsorption onto the TiO_2 surface, and a hydrophobic inner surface. The spatial separation of the dye from the TiO_2 increased, however, the charge injection yield was comparable with a non-encapsulated dye analogue, in keeping with the kinetic redundancy argument. Importantly, the increased separation also led to a significantly slower rate for k_6, offering potential gains in cell efficiency. As well as these effects, the encapsulation approach has the possibility to enhance photochemical stability, redox reversibility, and electroluminescent efficiency.

These recent examples illustrate that much is now understood concerning the optimization of kinetic parameters for interfacial electron transfer. These studies, however, have typically involved use of the I^-/I_3^- solution redox electrolyte, and an important next step will involve the exploitation of these ideas in improving the lower efficiencies currently achieved in cells with alternative solid and quasi-solid hole-transport materials.

2.3. Hydrophobic Dyes

Dyes attached to TiO_2 through carboxylic acid groups are susceptible to desorption from the surface under the action of trace quantities of water and has serious consequences on the long-term stability of the resultant solar cells. It has been reported that dyes with attached hydrophobic chains (e.g. **Z907**, Figure 5) can display an enhanced stability towards desorption from TiO_2 induced by water in the liquid or gel electrolyte.[54,6] A cell based on **Z907** using a polymer gel I^-/I_3^- electrolyte was shown to combine a cell efficiency of 6.1 % with excellent stability to both prolonged thermal stress and light soaking that matched the criteria required for the outdoor use of solar cells.[6] Besides the role played by the gel electrolyte, the stability was attributed to the hydrophobic properties of the dye which enhanced stability towards water-induced desorption. This effect was illustrated with an analogous cell, which used **N719** in place of **Z907** as the dye, that displayed much poorer stability to thermal stress.

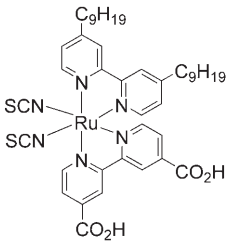

Z907

Figure 5. The amphiphilic dye **Z907**.

A significant loss mechanism involves recombination of electrons from the TiO_2 conduction band directly with the HTM, known as the dark current (k_5). In addition to the above considerations, it has also been suggested that dyes

 © 2006 Wiley-VCH Verlag GmbH & Co. KGaA, Weinheim

with attached hydrophobic groups can inhibit k_5 by forming a hydrophobic network that impedes the interaction between I_3^- and the TiO_2 surface and minimizes this loss. Evidence indicates that **N719** itself acts to suppress the dark current by forming a blocking layer on the TiO_2 surface,[55,25] and it may be that further addition of steric bulk to the dye might enhance this role.

Another benefit of amphiphilic dyes arises in cells where an organic HTM has been employed to replace the liquid electrolyte. In such cells, there is generally a poor interaction between the dye and the organic HTM[56] that leads to weaker electronic communication and slower regeneration kinetics (k_2) of the dye. Dyes with attached hydrophobic chains can enhance the wettability of the TiO_2 by the hole-conducting polymer enhancing interaction with the dye. Interfacial contact between the dye and the HTM is also important in the context of solid polymer electrolytes,[7] particularly for high-molecular-weight polymers that do not penetrate well into the nanopores of the TiO_2 semiconductor. It is also interesting to note in this context that the typically slower k_2 displayed with an organic HTM may lead to a requirement for dyes that have better long-term stability in their oxidized form.[23]

2.4. Extending the Spectral Coverage of Dyes

Currently, sensitizers such as **N3** and **N719** (Figure 2) show comparatively low IPCEs in the red and near-infrared (NIR) region of the electromagnetic spectrum. Control of the HOMO and LUMO levels of a dye is required to develop better red-absorbing dyes, as illustrated by the development of the "black dye" shown in Figure 2. Manipulation of the absorption spectrum of the dye also allows the possibility to develop solar cells that absorb in the NIR and are transparent to visible light, thus allowing their use as photovoltaic windows on buildings. To function as a DSSC, however, the LUMO must remain sufficiently higher than the edge of the conduction band of TiO_2 for efficient charge injection while the HOMO must remain sufficiently below the redox level of the HTM for efficient regeneration of the dye. The lower energy of longer-wavelength photons makes the development of appropriate red-absorbing dyes that adhere to these requirements a challenge, as the HOMO–LUMO gap is narrower. One manner in which this has been approached involves the study of Ru–polypyridyl dyes related to **N3** that are constrained to show *trans* geometry of the NCS ligands (for example, as shown in Figure 6a).[57] Such *trans*-Ru–polypyridyl complexes typically show lower-energy absorption in comparison with the *cis* analogues. The use of geometrically restrained ligands is required to prevent photoinduced isomerization of the *trans* form to the *cis* isomer. This approach has led to dyes that show absorption bands across the entire visible and NIR regions of the spectrum, and initial studies have suggested that these dyes may perform better than **N3** once their performance has been optimized.

It has been noted that in osmium complexes, spin-forbidden singlet–triplet MLCT excitation can show significant intensity at low energy as a result of the mixing of some

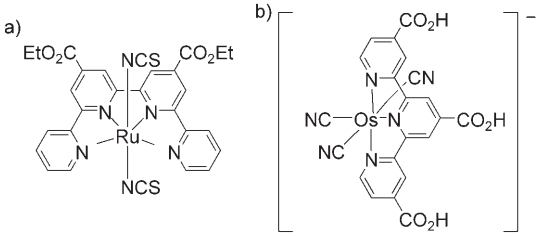

Figure 6. a) Ru complex with *trans* NCS ligands.[57] b) Example of an Os complex dye with a good incident photon to current efficiency at long wavelengths.[23]

singlet character through the larger spin–orbit coupling in heavier elements (heavy-atom effect).[23] For example, for the osmium complex shown in Figure 6b this has led to better IPCE values at longer wavelengths than for a comparable Ru complex dye, although over the whole spectral region the Ru complex performed better.

Another approach to long-wavelength sensitization involves the use of phthalocyanine dyes, which are known to display an intense absorption in the Q band at low energy as well as a higher energy Soret band. However, studies on phthalocyanines are hampered by poor solubility and also by their tendency to aggregate on the TiO_2 surface which leads to deactivation of the excited state of the dye. A recent example employed a titanium phthalocyanine dye with axial ligation to enable binding to TiO_2. Bulky terminal *tert*-butyl groups were also included to prevent aggregation of the dye and to improve solubility.[58] As expected for this class of molecule, an extremely intense Q band absorption ($\varepsilon = 135\,000\ cm^{-1}M^{-1}$) at $\lambda_{max} = 702$ nm was observed. Although in practice it was found that this particular dye was not able to efficiently inject electrons following excitation in the Q band, a key observation was the lack of aggregation of the dye when adsorbed onto TiO_2 which opens up the possibility to design other phthalocyanine sensitizers that exploit the intense absorption at low energy.

Similar considerations arise in the case of porphyrin dyes, which also display an intense, low-energy Q band absorption and show kinetics for charge-injection and charge-recombination processes that are comparable to those of the best Ru–polypyridyl dyes. Again a serious limitation arises from the tendency of the dye to aggregate, although poor electronic communication between the dye core and the carboxylate linker may also play a role. Recent reports of porphyrin dyes with a conjugated carboxylate linker revealed negligible evidence of aggregation and, thus, efficiencies of up to 5.6%, the highest known value for any porphyrin dye.[38] Significantly, these dyes show comparatively high molar extinction coefficients, for example, $\varepsilon = 18\,500\ cm^{-1}M^{-1}$ at $\lambda_{max} = 622$ nm, suggesting that further optimization of this family may be a fruitful source of novel long-wavelength-absorbing dyes.

The use of several dyes as cosensitizers has been explored to extend the spectral region of the sensitizing layer. In the case of organic dyes, this approach may also overcome the typically narrow absorption bands observed for these dyes. A difficulty of this approach involves the typical decrease in the sensitizing efficiency of the individual dyes upon mixing with

 © 2006 Wiley-VCH Verlag GmbH & Co. KGaA, Weinheim

another cosensitizer, as might be expected from simple considerations of the quantity of dye on the TiO_2 surface. A recent report[59] demonstrated that cosensitization using three organic dyes with complementary absorption spectra can lead to an overall efficiency of 6.5%. In this case, all three dyes in the mixture actually displayed higher IPCE values in their own spectral region than they did when used alone. Although this appears counterintuitive, it was attributed to two possible effects: 1) more complete packing of the three dyes on the semiconductor surface which blocks the dark current (k_5) and 2) an isolating effect that causes a decrease in the aggregation of each dye, thus minimizing loss through the associated deactivation of the excited state. This recent example thus demonstrates that a cosensitization approach can lead to enhanced spectral coverage and better enable the use of organic dyes, which typically display high extinction coefficients (see Section 2.5).

In an alternative approach to co-sensitization, both a Ru–polypyridyl dye and a Ru–phthalocyanine dye were used together, however, in this case a secondary layer of metal oxide was deposited onto the Ru–polypyridyl nanoparticles before attachment of the Ru–phthalocyanine layer.[60] This approach allowed near-monolayer coverage of both dyes, rather than a competition between the two for adsorption sites, and resulted in an electron-transfer cascade whereby the charge center of the dye cation was moved away from the TiO_2 surface by transfer between the two dye layers. The observation of efficient current generation through excitation of both dyes indicates that this is an important new approach in the development of panchromatic systems.

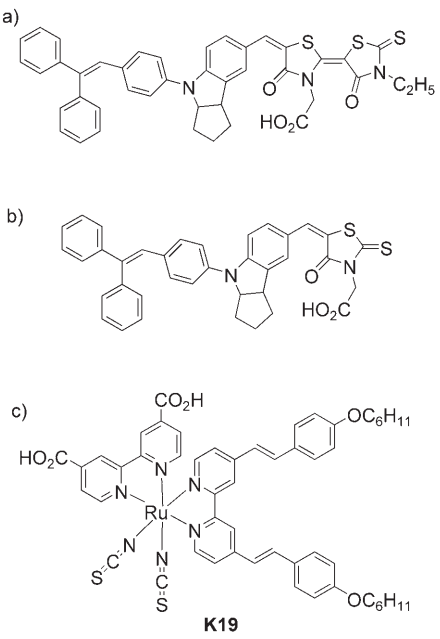

Figure 7. a, b) Organic dyes with high extinction coefficient that are used to a) give a high-efficiency DSSC[31] and b) make thin DSSCs with organic HTMs.[61] c) Ru dye **K19**, which was designed to give an increased extinction coefficient for the MLCT band.[62]

2.5. Enhancing Molar Extinction Coefficients

The use of dyes with a higher molar extinction coefficient clearly allows increased light harvesting of a given film thickness or, alternatively, thinner dye-sensitized films to be used which results in better efficiencies from decreased losses during charge transport through the nanocrystalline TiO_2. High extinction coefficients have been achieved by using organic dyes[34,29] rather than transition-metal complexes, however, the former typically suffer other disadvantages such as narrow absorption bands that limit the light-harvesting ability (see Section 2.4).[59] Enhancement of the extinction coefficient is particularly important in the context of cells that use organic materials as the HTM. For these devices the thickness of the film is crucial, as the limited charge-carrier mobility in the organic HTM leads to significant charge-carrier recombination (k_5) and a much lower efficiency. The use of a highly absorbing organic dye (Figure 7b) allowed a reduction in these losses through fabrication of a much thinner device, leading to the greatest efficiency recorded for an organic HTM cell of over 4%.[61]

Another recent approach involved the use of extended delocalized ligands for Ru complexes, for example, with the dye **K19** (Figure 7c).[62] This dye is related to the analogous amphiphilic dye **Z907** (Figure 5) but comprises additional stilbene units conjugated onto the hydrophobic ligand. Consequently, this dye retains the high stability to thermal stress and light soaking displayed by **Z907** that was attributed to the hydrophobic spectator ligand. In addition, however, **K19** shows a higher extinction coefficient for the low-energy band at $\lambda = 543$ nm of $\varepsilon = 18200\ cm^{-1}M^{-1}$ compared with $\varepsilon = 12200$ and $14000\ cm^{-1}M^{-1}$ for **Z907** and **N719** (Figure 2), respectively. A comparison of these three dyes demonstrates that under the same conditions **K19** reveals the highest efficiency of 7.0%, and interestingly this was achieved using a low-vapor-pressure electrolyte. A related approach also involved the use of 4,4′-bis(carboxyvinyl)-2,2′-bipyridyl ligands as extended delocalized units that increase the extinction coefficient of the dye. In this case, the extended bipy ligand was used to link to TiO_2 rather than as the spectator ligand.[63,64] As well as an increase in extinction coefficient, a red shift of the maxima of the MLCT band was observed and relates to extending the spectral coverage of the dye, as discussed in Section 2.4.

3. Summary and Outlook

Recently, much effort has been directed towards the optimization of all aspects of DSSCs, including the inorganic nanocrystalline semiconductor and the hole-transport material. Often, initial studies in this area have involved using the well-established dyes that worked best for previous DSSC designs. The well-known Ru complex dyes **N3**, **N719**, and the "black dye" (Figure 2) exhibit high efficiencies in the standard dye-sensitized solar cell with an I^-/I_3^- solution electrolyte, and it is questionable whether in these devices their performance will be significantly bettered. Dye-sensitized solar cells formed with alternative hole-transport

 © 2006 Wiley-VCH Verlag GmbH & Co. KGaA, Weinheim

materials, however, may offer different energy levels, different hydrophobicity/hydrophilicity properties, and different electron-transfer kinetics, and show a decrease in hole transport. A need has emerged to optimize the dye in conjunction with other design factors to best exploit and be fully compatible with other cell modifications that have taken place. For example: higher molar extinction coefficients may be crucial to allow thinner cells and the dominance of Ru–polypyridyl sensitizers may be challenged by organic, phthalocyanine, or porphyrin dyes in this type of device; the use of hydrophobic groups to enhance the stability of the device has become well established; near-IR dyes would allow photovoltaic windows to be developed; and cheaper dyes that do not contain expensive transition metals may also become more important in the context of commercialization. Dye-sensitized solar cells are beginning to be exploited as a commercial technology, and further developments in dye design will play a crucial part in the ongoing optimization of these devices.

The University of Edinburgh and the EPSRC (Supergen Project) are acknowledged for their recent support in this area.

Received: August 30, 2005
Published online: March 9, 2006

[1] M. Grätzel, *Nature* **2001**, *414*, 338.
[2] M. K. Nazeeruddin, M. Grätzel in *Comprehensive Coordination Chemistry II*, *Vol. 9* (Eds.: J. A. McCleverty, T. J. Meyer), Elsevier, Dordrecht, **2004**, chap. 16.
[3] Special issues on DSSC: *Coord. Chem. Rev.* **2004**, *248*, 1161–1530.
[4] M. Grätzel, *J. Photochem. Photobiol. C* **2003**, *4*, 145.
[5] B. O'Regan, M. Grätzel, *Nature* **1991**, *353*, 737.
[6] P. Wang, S. M. Zakeeruddin, J. E. Moser, M. K. Nazeeruddin, T. Sekiguchi, M. Grätzel, *Nat. Mater.* **2003**, *2*, 402.
[7] M.-S. Kang, J. H. Kim, Y. J. Kim, J. Won, N.-G. Park, Y. S. Kang, *Chem. Commun.* **2005**, 889.
[8] M.-S. Kang, Y. J. Kim, J. Won, Y. S. Kang, *Chem. Commun.* **2005**, 2686.
[9] P. Wang, S. M. Zakeeruddin, J. E. Moser, R. Humphrey-Baker, M. Grätzel, *J. Am. Chem. Soc.* **2004**, *126*, 7164.
[10] P. Wang, Q. Dai, S. M. Zakeeruddin, M. Forsyth, D. R. MacFarlane, M. Grätzel, *J. Am. Chem. Soc.* **2004**, *126*, 13590.
[11] Q.-B. Meng, K. Takahashi, X.-T. Zhang, I. Sutanto, T. N. Rao, O. Sato, A. Fujishima, *Langmuir* **2003**, *19*, 3572.
[12] H. Nusbaumer, S. M. Zakeeruddin, J.-E. Moser, M. Grätzel, *Chem. Eur. J.* **2003**, *9*, 3756.
[13] Y. Saito, T. Azechi, T. Kitamura, Y. Hasegawa, Y. Wada, S. Yanagida, *Coord. Chem. Rev.* **2004**, *248*, 1469.
[14] J. Krüger, R. Plass, L. Cevey, M. Piccirelli, M. Grätzel, U. Bach, *Appl. Phys. Lett.* **2001**, *79*, 2085.
[15] L. Spiccia, G. B. Deacon, C. M. Kepert, *Coord. Chem. Rev.* **2004**, *248*, 1329.
[16] R. Argazzi, N. Y. M. Iha, H. Zabri, F. Odobel, C. A. Bignozzi, *Coord. Chem. Rev.* **2004**, *248*, 1299.
[17] A. S. Polo, M. K. Itokazu, N. Y. M. Iha, *Coord. Chem. Rev.* **2004**, *248*, 1343.
[18] C. A. Bignozzi, R. Argazzi, C. J. Kleverlaan, *Chem. Soc. Rev.* **2000**, *29*, 87.
[19] M. K. Nazeeruddin, A. Kay, I. Rodicio, R. Humphry-Baker, E. Müller, P. Liska, N. Vlachopolous, M. Grätzel, *J. Am. Chem. Soc.* **1993**, *115*, 6382.
[20] A. Islam, H. Sugihara, K. Hara, L. P. Singh, R. Katoh, M. Yanagida, Y. Takahashi, S. Murata, H. Arakawa, *J. Photochem. Photobiol. A* **2001**, *145*, 135.
[21] M. K. Nazeeruddin, P. Pechy, M. Grätzel, *Chem. Commun.* **1997**, 1705.
[22] D. Kuciauskas, M. S. Freund, H. B. Gray, J. R. Winkler, N. S. Lewis, *J. Phys. Chem. B* **2001**, *105*, 392.
[23] R. Argazzi, G. Larramona, C. Contado, C. A. Bignozzi, *J. Photochem. Photobiol. A* **2004**, *164*, 15.
[24] A. Islam, H. Sugihara, K. Hara, L. P. Singh, R. Katoh, M. Yanagida, Y. Takahashi, S. Murata, H. Arakawa, *Inorg. Chem.* **2001**, *40*, 5371.
[25] E. A. M. Geary, L. J. Yellowlees, L. A. Jack, I. D. H. Oswald, S. Parsons, N. Hirata, J. R. Durrant, N. Robertson, *Inorg. Chem.* **2005**, *44*, 242.
[26] G. M. Hasselmann, G. J. Meyer, *Z. Phys. Chem.* **1999**, *212*, 39.
[27] N. Alonso-Vante, J.-F. Nierengarten, J.-P. Sauvage, *J. Chem. Soc. Dalton Trans.* **1994**, 1649.
[28] P. M. Jayaweera, S. S. Palayangoda, K. Tennakone, *J. Photochem. Photobiol. A* **2001**, *140*, 173.
[29] K. Hara, Z.-S. Wang, T. Sato, A. Furube, R. Katoh, H. Sugihara, Y. Dan-oh, C. Kasada, A. Shinpo, S. Suga, *J. Phys. Chem. B* **2005**, *109*, 15476.
[30] S. Alex, U. Santhosh, S. Das, *J. Photochem. Photobiol. A* **2005**, *172*, 63.
[31] T. Horiuchi, H. Miura, K. Sumioka, S. Uchida, *J. Am. Chem. Soc.* **2004**, *126*, 12218.
[32] Y.-S. Chen, C. Li, Z.-H. Zeng, W.-B. Wang, X.-S. Wang, B.-W. Zhang, *J. Mater. Chem.* **2005**, *15*, 1654.
[33] K. Hara, T. Sato, R. Katoh, A. Furube, T. Yoshihara, M. Murai, M. Kurashige, S. Ito, A. Shinpo, S. Suga, H. Arakawa, *Adv. Funct. Mater.* **2005**, *15*, 246.
[34] K. R. J. Thomas, J. T. Lin, Y.-C. Hsu, K.-C. Ho, *Chem. Commun.* **2005**, 4098.
[35] T. Kitamura, M. Ikeda, K. Shigaki, T. Inoue, N. A. Anderson, X. Ai, T. Lian, S. Yanagida, *Chem. Mater.* **2004**, *16*, 1806.
[36] K. Hara, M. Kurashige, S. Ito, A. Shinpo, S. Suga, K. Sayama, H. Arakawa, *Chem. Commun.* **2003**, 252.
[37] W. M. Campbell, A. K. Burrell, D. L. Officer, K. W. Jolley, *Coord. Chem. Rev.* **2004**, *248*, 1363.
[38] Q. Wang, W. M. Campbell, E. E. Bonfantani, K. W. Jolley, D. L. Officer, P. J. Walsh, K. Gordon, R. Humphrey-Baker, M. K. Nazeeruddin, M. Grätzel, *J. Phys. Chem. B* **2005**, *109*, 15397.
[39] T. Komori, Y. Amao, *J. Porphyrins Phthalocyanines* **2003**, *7*, 131.
[40] S. A. Haque, E. Palomares, B. M. Cho, A. N. M. Green, N. Hirata, D. R. Klug, J. R. Durrant, *J. Am. Chem. Soc.* **2005**, *127*, 3456.
[41] M. K. Nazeeruddin, S. M. Zakeeruddin, R. Humphrey-Baker, M. Jirousek, P. Liska, N. Vlachopoulos, V. Shklover, C.-H. Fischer, M. Grätzel, *Inorg. Chem.* **1999**, *38*, 6298.
[42] J. N. Clifford, E. Palomares, M. K. Nazeeruddin, M. Grätzel, J. Nelson, X. Li, N. J. Long, J. R. Durrant, *J. Am. Chem. Soc.* **2004**, *126*, 5225.
[43] R. Argazzi, C. A. Bignozzi, *J. Am. Chem. Soc.* **1995**, *117*, 11815.
[44] J. N. Clifford, G. Yahioglu, L. R. Milgrom, J. R. Durrant, *Chem. Commun.* **2002**, 1260.
[45] N. Hirata, J.-J. Lagref, E. J. Palomares, J. R. Durrant, M. K. Nazeeruddin, M. Grätzel, D. Di Censo, *Chem. Eur. J.* **2004**, *10*, 595.
[46] P. Wang, C. Klein, J. E. Moser, R. Humphrey-Baker, N.-L. Cevey-Ha, R. Charvet, P. Comte, S. M. Zakeeruddin, M. Grätzel, *J. Phys. Chem. B* **2004**, *108*, 17553.
[47] E. Galoppini, *Coord. Chem. Rev.* **2004**, *248*, 1283.
[48] S. Altobello, C. A. Bignozzi, S. Caramori, G. Larramona, S. Quici, G. Marzanni, L. R. Lakhmiri, *J. Photochem. Photobiol. A* **2004**, *166*, 91.

 © 2006 Wiley-VCH Verlag GmbH & Co. KGaA, Weinheim

[49] P.-H. Xie, Y.-J. Hou, T.-X. Wei, B.-W. Zhang, Y. Cao, C.-H. Huang, *Inorg. Chim. Acta* **2000**, *308*, 73.
[50] G. Benko, J. Kallioinen, J. E. I. Korppi-Tommola, A. P. Yartsev, V. Sundström, *J. Am. Chem. Soc.* **2002**, *124*, 489.
[51] Y. Tachibana, J. E. Moser, M. Grätzel, D. R. Klug, J. R. Durrant, *J. Phys. Chem.* **1996**, *100*, 20056.
[52] S. A. Haque, E. Palomares, B. M. Cho, A. N. M. Green, N. Hirata, D. R. Klug, J. R. Durrant, *J. Am. Chem. Soc.* **2005**, *127*, 3456.
[53] S. A. Haque, J. S. Park, M. Srinivasarao, J. R. Durrant, *Adv. Mater.* **2004**, *16*, 1177.
[54] S. M. Zakeeruddin, M. K. Nazeeruddin, R. Humphry-Baker, P. Pechy, P. Quagliotto, C. Barolo, G. Viscardi, M. Grätzel, *Langmuir* **2002**, *18*, 952.
[55] S. Ito, P. Liska, P. Comte, R. Charvet, P. Pechy, U. Bach, L. Schmidt-Mende, S. M. Zakeeruddin, A. Kay, M. K. Nazeeruddin, M. Grätzel, *Chem. Commun.* **2005**, 4351.
[56] Y. Saito, N. Fukuri, R. Senadeera, T. Kitamura, Y. Wada, S. Yanagida, *Electrochem. Commun.* **2004**, *6*, 71.
[57] T. Renouard, R.-A. Fallahpour, M. K. Nazeeruddin, R. Humphrey-Baker, S. I. Gorelsky, A. B. P. Lever, M. Grätzel, *Inorg. Chem.* **2002**, *41*, 367.
[58] E. Palomares, M. V. Marinez-Diaz, S. A. Haque, T. Torres, J. R. Durrant, *Chem. Commun.* **2004**, 2112.
[59] Y. Chen, Z. Zeng, C. Li, W. Wang, X. Wang, B. Zhang, *New J. Chem.* **2005**, *29*, 773.
[60] J. N. Clifford, E. Palomares, M. K. Nazeeruddin, R. Thampi, M. Grätzel, J. R. Durrant, *J. Am. Chem. Soc.* **2004**, *126*, 5670.
[61] L. Schmidt-Mende, U. Bach, R. Humphrey-Baker, T. Horiuchi, H. Miura, S. Ito, S. Uchida, M. Grätzel, *Adv. Mater.* **2005**, *17*, 813.
[62] P. Wang, C. Klein, R. Humphrey-Baker, S. M. Zakeeruddin, M. Grätzel, *J. Am. Chem. Soc.* **2005**, *127*, 808.
[63] M. K. Nazeeruddin, C. Klein, P. Liska, M. Grätzel, *Coord. Chem. Rev.* **2005**, *249*, 1460.
[64] C. Klein, M. K. Nazeeruddin, P. Liska, D. Di Censo, N. Hirata, E. Palomares, J. R. Durrant, M. Grätzel, *Inorg. Chem.* **2005**, *44*, 178.

 © 2006 Wiley-VCH Verlag GmbH & Co. KGaA, Weinheim

Bioorganic Chemistry

DOI: 10.1002/anie.200502794

Synthetic Multivalent Ligands as Probes of Signal Transduction

Laura L. Kiessling, Jason E. Gestwicki, and Laura E. Strong*

Keywords:
multivalent ligands · oligomerization · receptors · signal transduction · synapses

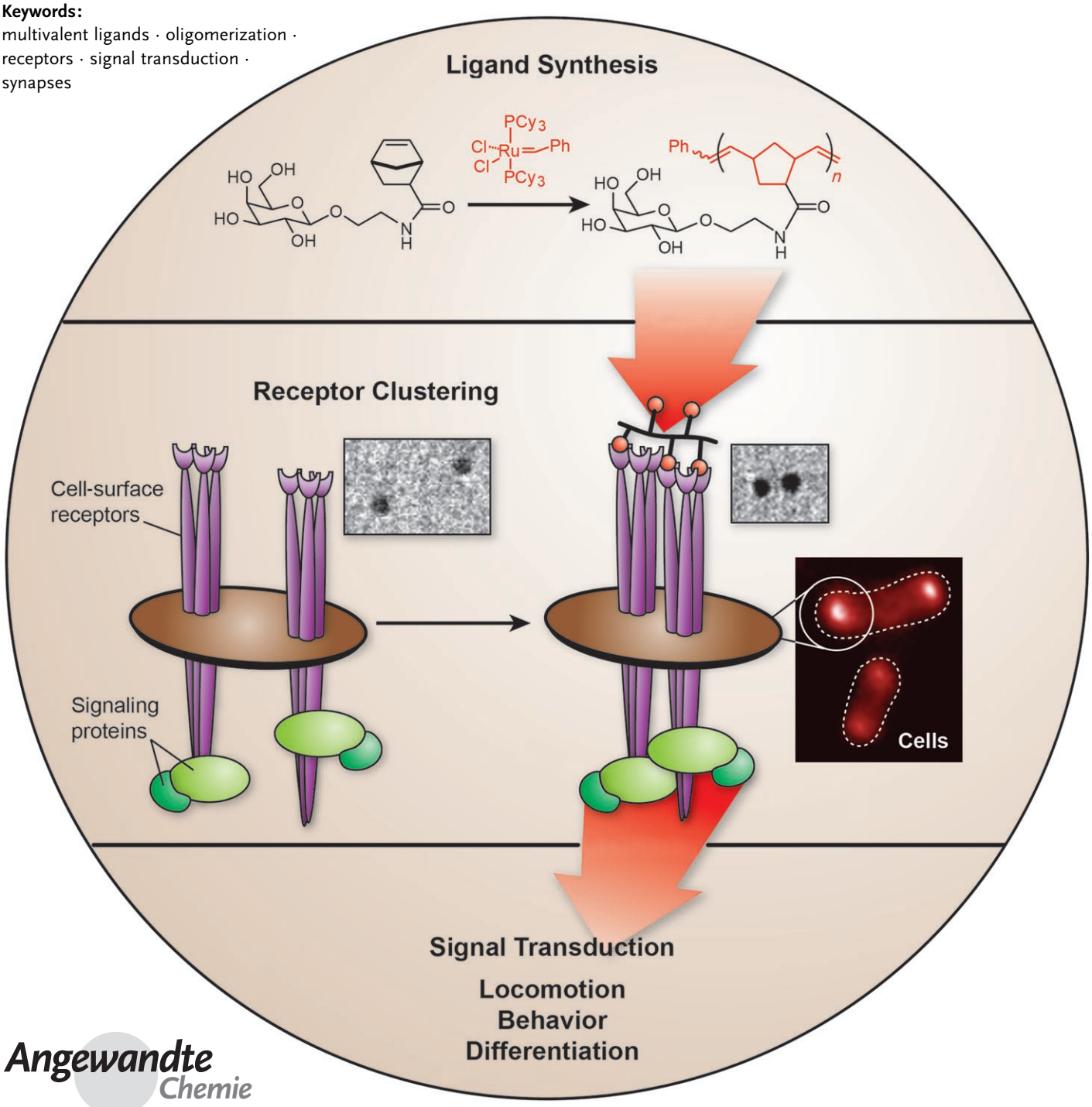

© 2006 Wiley-VCH Verlag GmbH & Co. KGaA, Weinheim

Cell-surface receptors acquire information from the extracellular environment and coordinate intracellular responses. Many receptors do not operate as individual entities, but rather as part of dimeric or oligomeric complexes. Coupling the functions of multiple receptors may endow signaling pathways with the sensitivity and malleability required to govern cellular responses. Moreover, multireceptor signaling complexes may provide a means of spatially segregating otherwise degenerate signaling cascades. Understanding the mechanisms, extent, and consequences of receptor co-localization and interreceptor communication is critical; chemical synthesis can provide compounds to address the role of receptor assembly in signal transduction. Multivalent ligands can be generated that possess a variety of sizes, shapes, valencies, orientations, and densities of binding elements. This Review focuses on the use of synthetic multivalent ligands to characterize receptor function.

From the Contents

1. Introduction—Receptor Function 2349

2. Direct and Indirect Interactions between Receptors 2349

3. Multivalent Ligands as Probes for Receptor–Receptor Interactions 2353

4. Using Multivalent Ligands to Gain Insight into Receptor Function 2357

5. Summary and Outlook 2364

1. Introduction—Receptor Function

To achieve success in the competition for favorable chemical and physical conditions, all organisms (from bacteria to worms to humans) must rapidly and accurately sense changes in their environments. Likewise, the complex orchestrations that govern developmental patterning or immunological responses rely on communication between cells and their environs. The task of monitoring extracellular conditions falls to the cell-surface receptors. These proteins coordinate the cell's internal machinery by collecting, compiling, and translating external information. The pressure for survival demands that responses to stimuli be sensitive and accurate; synergistic and competitive signals must be amplified and integrated. Thus, cells have developed sophisticated and elegant methods for achieving sensitive yet controllable receptor-mediated responses.

One important mechanism for efficient and sensitive signaling is to couple the functions of multiple cell-surface receptors,[1–9] most of which do not typically operate as individual entities, but function in concert. An emerging paradigm is that receptors within multireceptor signaling complexes communicate with each other.[7] Although evidence is mounting for communication between receptors, an understanding of the underlying mechanisms is elusive.

Chemical synthesis can provide a variety of compounds with which to address the role of receptor assembly in signal transduction. Multivalent ligands are well-suited to this task. They are capable of illuminating aspects of interreceptor processes that are not readily probed by using conventional approaches. We suggest that, as the focus shifts from investigations of the function of individual proteins toward the analysis of multireceptor signaling complexes, multivalent ligands will become even more valuable tools to probe sophisticated mechanistic questions. Moreover, multivalent ligands may provide new opportunities for manipulating receptor systems to dissect pathways and, ultimately, treat diseases. This Review focuses on the role of synthetic multivalent ligands as probes for the investigation of receptor collaboration.

2. Direct and Indirect Interactions between Receptors

2.1. Signaling Complexes

Receptors transmit information on extracellular signals to the internal machinery of the cell. Different receptors often share common cytoplasmic components, and therefore information transfer must be constrained to prevent unwanted exchange between disparate pathways.[7,10–12] To understand how signals are transmitted, it is necessary to unravel how cells can respond distinctly to different stimuli by using a set of common components.[7]

The subcellular localization of receptors into signaling complexes is proposed to be one mechanism by which cells achieve spatial and temporal regulation.[13–19] Multiprotein signaling complexes constitute the principle signaling units of neuronal synapses,[20,21] immune synapses,[13,22,23] focal adhesions,[24] and bacterial chemoreceptor arrays (Figure 1).[25,26]

[*] Prof. L. L. Kiessling, Dr. J. E. Gestwicki,[+] Dr. L. E. Strong[$]
Departments of Chemistry and Biochemistry
University of Wisconsin—Madison
1101 University Ave., Madison, WI 53706 (USA)
Fax: (+1) 608-265-0764
E-mail: kiessling@chem.wisc.edu

[+] Present address:
University of Michigan
210 Washtenaw Avenue, Ann Arbor, MI 48109 (USA)

[$] Present address:
Quintessence Biosciences
University Research Park
505 S. Rosa Rd., Madison, WI 53719 (USA)

© 2006 Wiley-VCH Verlag GmbH & Co. KGaA, Weinheim

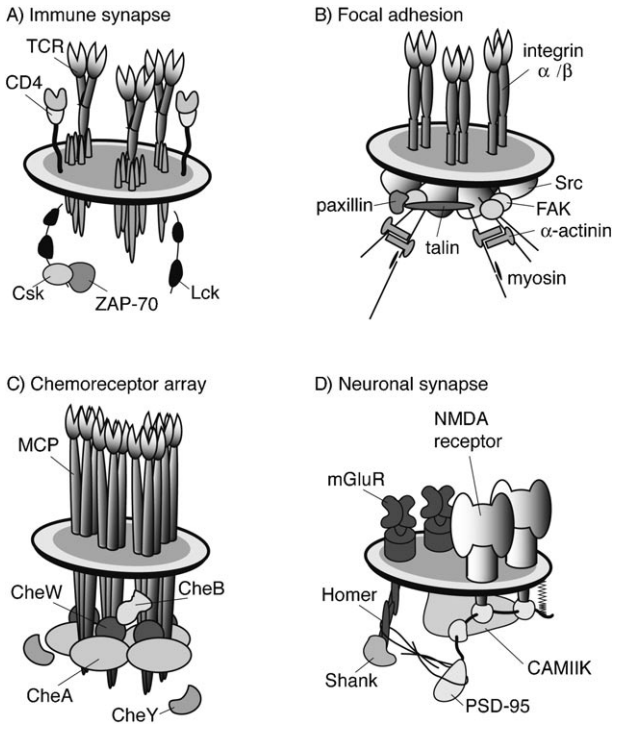

Figure 1. Examples of complexes involved in signal transduction: A) eukaryotic immune recognition; B) eukaryotic cell adhesion; C) prokaryotic chemotaxis; and D) neuronal signaling. These schematic depictions simplify the complexity of biological multiprotein signaling complexes.

These ensembles are composed of receptors, signaling proteins, adapter proteins, and cytoskeletal components.[27–29] Many signaling complexes in eukaryotic cells appear to be associated with detergent-insoluble lipid microdomains that provide unique physical environments for the concentration of signaling components.[30–35] Often it is not known whether cells use microdomains or other mechanisms to organize and assemble signaling components.

The formation of signaling complexes is not restricted to any particular receptor class. Data from microscopy, covalent cross-linking, and X-ray crystallography experiments have revealed that cell-surface receptors from many structural classes assemble into multireceptor complexes; these include some heptahelical G-protein-coupled receptors (GPCRs),[36–38] methyl-accepting chemotaxis proteins (MCPs),[39] gated ion channels,[40] receptor-protein tyrosine kinases (RPTKs),[41,42] and multichain immune recognition receptors (MIRRs).[22,33,35,43–45] The size of these ensembles varies: Some complexes are composed of two receptors while others contain thousands. Some receptors,[46–48] including the ryanodine receptor[40] and MCPs,[39] are so highly concentrated that they dominate certain cellular regions. Unfortunately, little is known about the structures of these assemblies, where they are localized within the cells, and how their localization influences signaling. Understanding these issues, however, could lead to new strategies to precisely control receptor function and therefore cellular responses. Although there remains a need to explore the role of receptor localization and assembly, the data acquired to date suggest some general basic principles for communication between the receptors.

Receptors can exchange information through direct protein–protein contacts or through intermediary proteins. Direct receptor contact typically involves interactions between specific protein regions.[49] For example, helix-mediated interactions are proposed to facilitate the dimerization and oligomerization of GPCRs (Figure 2).[38,50,51] Evidence for the functional importance of these interactions is suggested by engineering disrupting mutations in the proposed contact sites or by adding isolated transmembrane helices to GPCRs.[37,52,53] Although their effects on receptor oligomerization are not yet well-established, these manipulations modulate signaling; presumably, they disrupt receptor–receptor contacts. As mentioned above, an alternative strategy by which receptors exchange information is through intermediary proteins. These scaffolding proteins can organize multireceptor complexes, and thus act as frameworks for protein assembly. Examples of receptors localized by this mechanism include the MCPs and members of the tumor necrosis factor (TNF) receptors (Figure 2B, C).[54–56]

Ligand binding can transduce signals by directly stabilizing or destabilizing protein assemblies.[57–59] For example, data collected from diverse experiments suggest that binding of an attractant to a single MCP can elicit signaling from nearby MCP partners.[46,60–64] Similarly, cross-phosphorylation of some growth-factor receptors is facilitated by ligand-induced contacts.[65] In addition to homodimeric (or oligomeric)

Laura L. Kiessling gained her BS from the Massachusetts Institute of Technology, and completed her PhD in Chemistry at Yale working with Stuart Schreiber. After postdoctoral training at the California Institute of Technology with Peter Dervan, she began her independent career in 1991 at the University of Wisconsin-Madison, where she is currently a professor in both Chemistry and Biochemistry. Besides her long-standing interest in organic synthesis for investigating protein–carbohydrate interactions, she is also interested in multivalent binding events, biomolecular recognition, and signal transduction.

Jason E. Gestwicki gained a BS in Chemistry in 1997 from the State University of New York at Fredonia. In 2002, he completed his PhD in Biochemistry at the University of Wisconsin-Madison with Prof. Laura L. Kiessling. Most recently, he was a Helen Hay Whitney post-doctoral fellow at Stanford University with Prof. Gerald R. Crabtree, where he synthesized potent difunctional inhibitors of protein–protein interactions in neurodegenerative diseases. He joined the University of Michigan Medical School in 2005 as an Assistant Professor of Pathology and Research Assistant Professor in the Life Sciences Institute.

 © 2006 Wiley-VCH Verlag GmbH & Co. KGaA, Weinheim

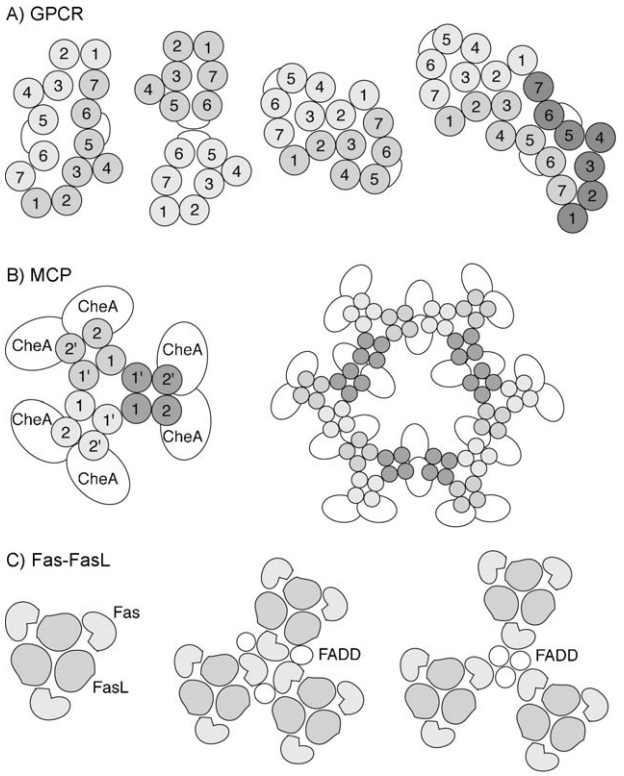

Figure 2. Proposed multireceptor assemblies for some receptors. A) Models of three heptahelical GPCR dimers and a trimer based on mutagenesis results and the structure of bacteriorhodopsin. Each numbered circle represents a transmembrane helix. A variety of 1–7, 5–6, and 2–3 dimers and multimers have been proposed. B) Bacterial chemoreceptors (methyl-accepting chemotaxis proteins, MCPs) are dimeric. These can assemble into a trimer-of-dimers, which can further interact with signaling proteins, such as the kinase CheA. Each MCP passes through the membrane twice (1 and 2) and coiled-coil interactions between these transmembrane domains (1 and 1′) mediate dimerization. A lattice model of MCP organization constructed of six of these trimers-of-dimers and 24 copies of CheA is shown. C) The Fas–FasL interaction has been modeled using protein interfaces suggested by mutagenesis and cross-linking studies. Both the receptor Fas and its corresponding ligand FasL are trimers. The corresponding trimeric complex may be employed as a unit in the lattice stabilized by the adapter protein FADD. Two models are shown with either Fas- or FADD-centered symmetries. See the text for details and literature references.

Laura E. Strong is the Vice President of Product Development at Quintessence Biosciences, Inc. She received her BS in chemistry at the University of Richmond, and earned a PhD in organic chemistry with Prof. Laura L. Kiessling at the University of Wisconsin–Madison (National Institutes of Health predoctoral fellow). While there, she was involved in developing the ring-opening metathesis polymerization to produce biologically active, multivalent ligands. She is co-author of twelve publications and co-inventor on three patent applications.

interactions, interactions between structurally dissimilar receptors have also been demonstrated.[66] The neuronal dopamine and GABA receptors, a gated ion channel, and a GPCR, have been shown to exchange information by direct contact.[67]

An alternative means by which ligands can induce information transfer and co-localization of receptors is by facilitating the recruitment of intermediary proteins to the target receptors; these intermediary proteins are called adapters or scaffolding proteins.[68–73] Specialized modules within intermediary proteins act as information conduits; examples include SH2, SH3, and PDZ domains. These domains participate in a series of protein–protein interactions that transfer information and localize receptors. The simplest adapters directly link one receptor to another. Additionally, many intermediary proteins contain multiple domains that facilitate communication between a receptor and a variety of membrane-associated and soluble signaling proteins.

2.2. Factors that Influence Communication between Receptors

An important first step in investigating and manipulating the function of a multireceptor signaling complex is defining the features. However, the potential diversity created by the presence of multiple receptors and modular adapters raises challenges for those that seek to understand them. The features of the immune synapse illustrate some of the issues relevant for elucidating the function of signaling complexes.

T lymphocytes are critical mediators of effective immune responses to invading pathogens. The contribution of T cells to the immune response is largely controlled by signaling through the T-cell receptor (TCR). Like many other important cell-surface receptors, the TCR can be assembled into a multireceptor complex. When a T cell contacts an antigen-presenting cell (namely, a dendritic or B cell), the cytoskeleton reorganizes, and adhesion receptors and the TCR undergo changes in localization at the interface. This interface has been referred to as the "immune synapse" (Figure 1 A).

The features of the immune synapse can vary. Its structure is influenced by the type of antigen-presenting cell (APC) involved, the type and activation state of the T cell, the duration of the T cell/APC interaction, and the local physiological environment in which it forms.[74] Powerful new imaging methods have been used to visualize immune synapses formed in vitro and in vivo; these studies reveal that dynamic changes in protein localization and organization can occur. At a molecular level, the role of protein organization within the synapse has not yet been established. It is not known whether the observed organization of the receptors on the T cell influences signaling.

It is clear that the TCR[75] and co-receptors, such as CD4,[76,77] are localized at the cell–cell interface. Some of these co-receptors (for example, CD4) augment the signal generated by the TCR; others attenuate it. The balance and orientation of these co-receptors can therefore tune the level of T-cell activation. This tuning is achieved by changes in the phosphorylation of intracellular protein domains and recep-

 © 2006 Wiley-VCH Verlag GmbH & Co. KGaA, Weinheim

tors; the immune synapse also contains kinases such as Lck and ZAP-70 that catalyze the phosphorylation of ligated receptors and other proteins.[77,78] Phosphorylation can have either a positive or negative impact on the subsequent recruitment or the enzymatic activity of various components of the signaling complex.

Evidence from microscopy and signaling experiments suggests that the immune synapse can be highly organized.[76] The cytoskeleton plays a critical role in organizing some cell-surface proteins, thus the findings that cytoskeletal components are critical for TCR signaling supports a role for receptor organization.[13,79,80] The positioning of proteins within the immune synapse is also highly dynamic. For example, when a T cell engages with a cell presenting an antigen, the negative regulator CD45 moves to the periphery of the synapse.[76,81–83] Under these circumstances, the TCR is recruited into the inner portion of the synapse. These changes in receptor positioning suggest that synapse organization affects signal transmission: These intricate, orchestrated[76] movements are believed to affect the transfer and propagation of the activating signal. The position of the TCR in relation to the various positive and negative regulators of its function appears to determine the signal intensity.

There are many parameters that can affect signal output, and dissecting the contribution of different factors to T-cell signaling is complicated. Factors that have been proposed to influence signal output[20] include the number of activated receptors, their identity, and stoichiometric ratio (Figure 3).[4,84,85] The stoichiometric composition of a signaling complex (that is, the number of activating versus dampening receptors) can influence the signal strength required to overcome thresholds. In addition to the identity and stoichiometric composition of receptors in the complex, signaling can also be influenced by the proximity and subcellular compartmentalization of receptors. Determining the relative contribution of all of the aforementioned variables remains a major challenge. To isolate and dissect such a complex signaling system a variety of biological and chemical methods are required. Multivalent ligands are valuable tools in the armamentarium.

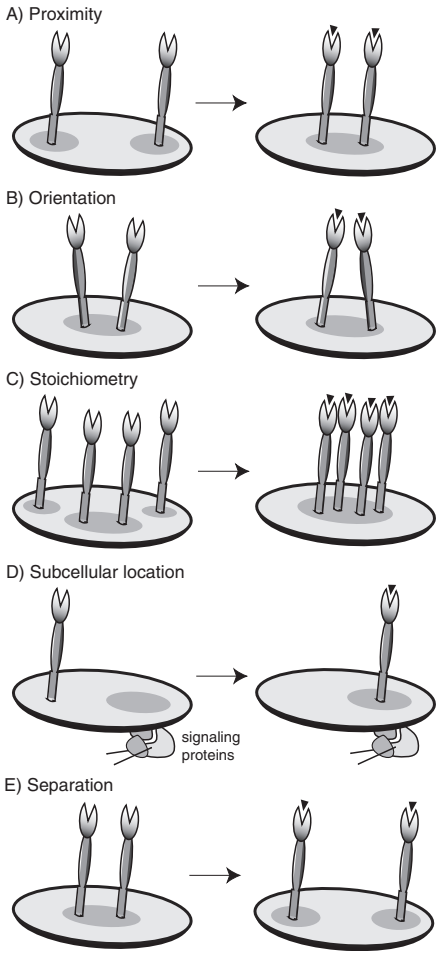

Figure 3. Possible methods for regulating interreceptor communication. A) The distance can influence the transfer of information between receptors or other proteins. B) The relative orientation of two receptors can influence the alignment of enzyme active sites and govern the rates of covalent modifications that result in signal generation. C) The number of receptors in a complex can influence the intensity of a signal. Additionally, the likelihood that receptors will come into contact increases when the numbers of localized receptors is greater. D) The subcellular location of a receptor controls the access of some intracellular signaling proteins to the receptor. Changes in position can govern the flow of information through a receptor or cluster of receptors. E) Ligand binding can lead to activation of receptors by separation when co-receptors act as negative regulators. This receptor mechanism is conceptually related to proximity-induced activation, but the underlying molecular interactions are quite different.

2.3. Challenges in Studying Receptor Function

Historically, cellular functions have been investigated by detailed examination of the structure and activity of a single protein component within a reaction pathway. Signal transduction involves the coordinated interactions of many different proteins. Thus, understanding cellular functions requires uncovering how heterogeneous collections of proteins interact at a supramolecular level. Advances in genomics, transgenic animal technologies, and chemical biology provide the means to identify components of a pathway. Elucidating the functional and structural relationships between these components remains a major challenge.[86–88] Even after evidence for physical association has been obtained, the order in which these interactions occur and their kinetics must be explored. Strategies that provide insight into complex cellular processes are needed.

Understanding multireceptor assemblies requires the use of methods that reveal both molecular and supramolecular detail. For example, immunoprecipitation, confocal microscopy, and Förster resonance energy transfer (FRET) experiments have been influential in exploring changes in subcellular protein distributions.[89,90] Moreover, fluorescent proteins and advanced imaging techniques have revolutionized the ability to follow proteins in live cells in real time.[91–93] Although these approaches provide insight into the operations of multiprotein complexes, the molecular details that underlie interreceptor processes often are obscure. This

 © 2006 Wiley-VCH Verlag GmbH & Co. KGaA, Weinheim

limited understanding arises from an old problem: the details revealed by an experiment are limited by the resolution of the investigative methods. For example, the optical resolution of light microscopy is approximately 200 nm. Fluorescence microscopy experiments, therefore, can be used to discern whether receptors are moving from one side of a cell to another, but information concerning the orientation of two adjacent receptors is more difficult to obtain.

Methods with superior resolution are required for investigating receptor–receptor interactions that occur over subnanometer distances. Although FRET can be used to investigate receptor assembly at this level, its application typically requires that cell lines be engineered to produce fluorescent proteins. Electron microscopy, which does not require transfected cell lines, has a limit of resolution of approximately 0.1 nm; thus, it reveals features that are 1000-fold smaller than those observed by optical microscopy. More recently, advances in single-particle methods have started to provide molecular detail for some signaling complexes.[45,92–94] These advances in experimental methodology provide a framework from which to develop reagents for studying the function of multireceptor complexes.

New methods for exploring receptor signaling also are emerging from synthetic organic chemistry and chemical biology. Chemical synthesis provides access to unique compounds that can be used to dissect the role of molecular interactions. These ligands, in concert with the new imaging techniques, can illuminate the roles of protein assemblies. This Review focuses on the application of synthetic multivalent ligands to the analysis of signaling complexes.[9,84]

3. Multivalent Ligands as Probes for Receptor–Receptor Interactions

3.1. Multivalent Ligand Structure and Function

Multivalent ligands present multiple copies of a recognition element (RE) from a central scaffold.[84,95–98] The REs of a multivalent ligand can be a carbohydrate, peptide, protein, or small molecule—any moiety that binds to a receptor. The scaffold determines the structural features of the multivalent ligand; it also dictates how easily they can be varied. These issues are relevant because the architecture of a multivalent ligand—its shape, orientation of the REs, flexibility, size, valency—can influence its biological activity and its mechanism of action.[99–101] For example, in systems that are activated by receptor clustering, the most potent ligands may be those with many, closely spaced REs. Ligands with defined features and tailored biological activities can be attained by chemical synthesis.

An important concept underlies the design of multivalent ligands that activate cellular signaling: many cell-surface receptors are modular. For example, some receptors possess intracellular catalytic domains, which are distinct from their extracellular binding domains; the RE-binding and signal-generating regions of receptors are therefore structurally and spatially distinct. Thus, multivalent binding to sites at the surface of the cell can be used to assemble and thereby influence interactions of distal intracellular (cytoplasmic) components. This situation is distinct from that encountered using typical catalysts for organic reactions, in which the formation of the catalyst–substrate complex results in a chemical transformation. Thus, substrate binding and catalytic activity are inextricably linked. Since binding and catalytic activity are separated for most cell-surface receptors, multivalent ligands can be used to manipulate the localization of intracellular catalytic domains. Ligand binding can promote changes in the receptor and therefore the catalyst environment which can enhance or restrict access of a substrate to the catalytic domain. In this way, a multivalent ligand can influence cellular responses.

As a result of the way in which they function, the nomenclature used to describe the activities of monovalent compounds can lead to confusion.[102] Bioactive and monovalent compounds are often referred to as agonists or antagonists: The former activates a response, while the latter inhibits it. There is often a mechanistic implication in the use of these terms—agonists are believed to induce a conformational change similar to that of the natural ligand, but antagonists induce an inactive conformation. It is these mechanistic implications that complicate the use of this nomenclature to describe multivalent ligands. An individual RE, for example, can be an agonist, partial agonist, or antagonist. Unlike a single RE, however, the ability of a multivalent ligand to activate or inhibit a biological response will be influenced not only by the RE itself but also by the architecture of the scaffold upon which it is displayed. A multivalent display of an RE that serves as a monovalent antagonist, for example, may lead to clustering of receptors; thus, the multivalent ligand could serve as an *agonist*.[103] Likewise, a multivalent ligand composed of REs that bind to a site remote from that of the physiological ligand can induce activation of some systems solely by decreasing the distances between the receptors.[104,105] Conversely, it has been proposed that multiple agonistic REs displayed in an orientation that holds receptors in unproductive arrangements for signaling can result in a multivalent *antagonist*.[106,107] Ligand-induced sequestering of key signaling proteins also can cause antagonist- or agonist-like effects.[108,109] Thus, instead of terming multivalent ligands agonists or antagonists, we refer to them as either multivalent effectors or inhibitors.[84] Inhibitors block receptor function and multivalent effectors activate cellular processes. This terminology does not imply any particular activity for an individual recognition element nor a specific binding mode; it is a function of *both* the RE identity and the architecture of the multivalent ligand.

3.2. Multivalent Ligand Architectures

A variety of natural, synthetic, and semisynthetic scaffolds have been used to probe receptor function (see Figure 4 for examples). These scaffolds vary in size, shape, and physical characteristics. Different scaffolds display REs differently (see Section 3.1); therefore, the structure of a scaffold can have a significant effect on its activity. For example, a globular

 © 2006 Wiley-VCH Verlag GmbH & Co. KGaA, Weinheim

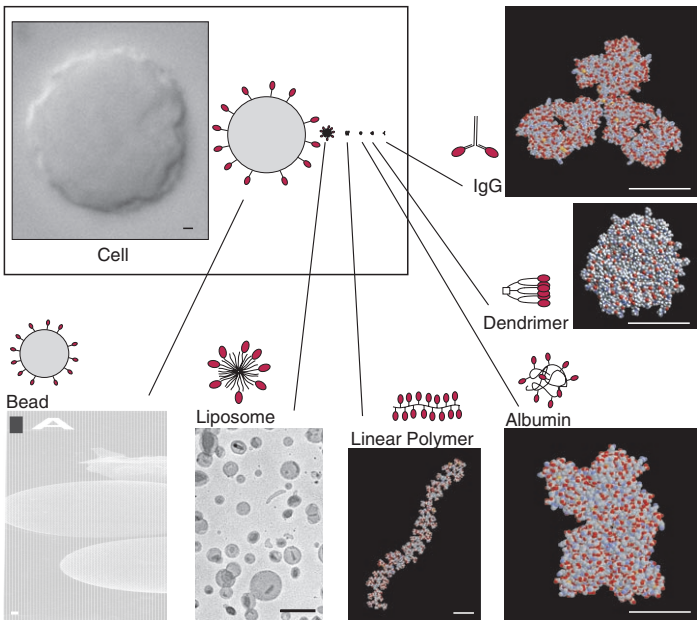

Figure 4. Scaled diagram of the scaffold structures of multivalent ligands. The boxes show a size comparison of the ligands to a mammalian lymphocyte. Size bars are as follows: cell and bead 1 μm; liposome and polymer 0.5 μm; antibody, dendrimer, and albumin 0.05 μm. The immunoglobulin structure is based on PDB 1IGT and the albumin is human serum albumin from PDB 1BM0. The beads are reproduced with permission from reference [262]. The liposomes are courtesy of A. Menon, the cell is a cultured Jurkat cell,[263] the dendrimer model was generated at the Caltech Molecular and Process Simulation Center, and the ROMP-derived polymer was designed by C. W. Cairo (unpublished results).

scaffold, such as a protein or dendrimer, may not be capable of spanning the large distances needed to cluster multiple proteins, but may effectively occupy multiple binding sites on an oligomeric receptor. Thus, the architecture of a ligand influences its ability to form different types of macromolecular receptor complexes.[84,100,110]

It is useful to examine the structural complexity of natural multivalent ligands to understand how to design synthetic multivalent ligands. The architectures of natural ligands are enormously diverse. For example, the TNF family member sTALL was found to be an ensemble of 60 monomer units that interact noncovalently to generate a symmetric "virus-like" complex.[94,111,112] It is hypothesized that the complex architecture of sTALL is required to organize multiple copies of its cell-surface receptor into an active signaling complex. Other natural ligands, such as lipopolysaccharides, mucins, and glycosaminoglycans, present a heterogeneous display of potential receptor binding sites, even within the same molecule.[113,114] A visual comparison between the architecture of sTALL and a typical glycosaminoglycan will reveal very few similarities in either size, shape, or RE density. However, despite their dramatic structural differences, both sTALL and glycosaminoglycans are involved in clustering cell-surface receptors. This simple observation can prompt hypotheses about how differences in the scaffold architecture might have an impact on the underlying signaling process. Often, however, it is difficult to determine which of the many possible ligand features influence activity. For example, naturally occurring polysaccharides vary in length, branching, and monosaccharide composition. Tracing the specific feature of a physiological multivalent ligand that is critical for activity can be arduous.

Synthetic organic chemistry can provide a wide range of defined multivalent ligand architectures. This diversity means that synthetic ligands can be used to dissect the features of physiological ligands that are responsible for their activity. For example, unlike natural ligands, the valency of a synthetic ligand can be systematically altered by varying the length or size of the scaffold. The effect of valency on the activity can be assessed by generating polymers of defined lengths. Similarly, the effect of dendrimer valency on activity can be explored by testing different generations. Examining the impact of these changes on the biological response illuminates the mechanisms underlying the function of natural receptor–ligand complexes to be illuminated. In the following sections we briefly introduce the synthesis and application of some structural classes of multivalent ligands. Finally, we discuss how synthetic multivalent ligands have been used to elucidate and exploit the mechanisms by which key receptors function.

3.3. Synthesis of Multivalent Ligands

The most versatile methods for synthesizing multivalent ligands involve adding REs to a preformed synthetic or naturally occurring scaffold. Scaffolds have been used from many structure classes: proteins, dendrimers, polymers, and solid supports.[115] With an appropriately functionalized scaffold (or RE), multiple copies of an RE can be appended. This approach provides straightforward access to ligands with variable valency and density of REs, since the mole fraction of functionalized RE used in the conjugation reaction can be readily controlled.[115] An alternative to this strategy is the approach typically used in creating polymer-based multivalent ligands: A single step can be used to assemble RE-bearing monomers into a multivalent product.

In most of the examples presented herein, the REs have been added to a preformed scaffold to generate the multivalent ligands. The examples that we discuss can guide the selection of scaffold; the corresponding literature references can be used to design the most efficient synthetic route.

3.3.1. Low-Molecular-Weight Ligands

We use the descriptor "low-molecular-weight ligands" to refer to compounds that present fewer than ten REs and are typically less than 1000 Da. The synthesis of such compounds can be quite challenging; however, some general strategies have been developed.[116–119] Although methods for the direct dimerization of individual REs are known,[119] low-molecular-weight multivalent ligands are typically generated by conjugation of REs to a core scaffold. An advantage of these ligands is that the core scaffold can be rigid to give rise to a specific orientation of the REs. Additionally, low-molecular-weight ligands can be generated by combinatorial approaches,[120,121] therefore allowing their shape, flexibility, and other structural features to be varied. Despite the

 © 2006 Wiley-VCH Verlag GmbH & Co. KGaA, Weinheim

opportunities to exert precise control over ligand features, most low-molecular-weight ligands are dimeric. Dimeric ligands can be more readily synthesized but can interact with only two cell-surface receptors; thus their utility for investigating the role of higher order receptor organization in signaling is limited.

3.3.2. Protein Conjugates

Semisynthetic routes to multivalent ligands often involve the incorporation of REs onto well-characterized carrier proteins such as streptavidin, bovine serum albumin (BSA), and keyhole limpet hemocyanin (KLH).[122,123] The size and shape of the scaffolds vary: the tetrameric streptavidin has a rectangular structure with dimensions of approximately 6 nm × 10 nm, while human serum albumin has a globular shape with a diameter of approximately 10 nm. The drawback of protein conjugates and other multivalent compounds generated by semisynthesis is their relative heterogeneity compared to scaffolds generated by chemical synthesis. Protein conjugation reactions typically depend on the presence and accessibility of specific endogenous amino acid side chains. Thus, the opportunities for controlling the orientation of the epitope are limited. Interestingly, this limitation has been partially overcome recently by introducing functionality to viral coat proteins. Viral particles bearing these modified proteins organize the functionality in defined patterns.[124–126] This is a promising strategy that is just beginning to be explored, and the scope of its application is not yet known.

3.3.3. Solid Supports

Receptor binding, activation, and endocytosis have been studied using functionalized beads and surfaces.[127–130] The beads employed in these investigations vary in composition: they can be derived from polystyrene, latex, polysaccharides, or other insoluble materials. The typical reactions used to conjugate binding epitopes to beads are straightforward and general, although rarely chemoselective or regioselective. A variety of small and large synthetic and natural REs have been incorporated. The number of potential sites that can be functionalized on the surface varies with the bead composition. Although beads are widely used, the orientation and availability of their binding sites has not been characterized; generally, the distribution of sites on the bead (and perhaps on the RE) is assumed to be random. Bead size is another variable that can influence bead activity. Indeed, the diameter of the beads can vary widely. For example, sepharose beads, which are used for size-exclusion chromatography, have diameters of 30 to 300 μm; latex beads, with diameters of 0.2 to 2 μm, are much smaller. The number of receptors that a functionalized bead can occupy will depend on many variables: the number of functional REs presented, the density of RE sites, and the size of the beads. The only variable that can be controlled readily is the size of the beads. As with protein scaffolds, a drawback of the beads is the lack of control they offer.

3.3.4. Liposomes

Liposomes are typically noncovalent assemblies that can be used to present multiple REs. It is the lipid–lipid interactions that give rise to the array;[131–133] thus, liposome composition can be controlled by varying the ratio of RE-bearing and unmodified lipids. Liposomes can be generated in a wide range of sizes. For example, liposomes generated by treatment with biobeads affords species with diameters of 0.05 to 0.5 μm.[134] Large liposomes (termed giant vesicles) with diameters of 5–200 μm can also be produced.[135] The size of the liposomes can be nearly homogeneous; however, the arrangement of REs within each liposome is difficult to regulate. Fluctuations in RE presentation within a liposome can be an advantage in generating RE displays that are highly active. The orientation and density of REs can change as the lipid components undergo two-dimensional diffusion; thus allowing the most active arrangement of REs to be found. This dynamic behavior is detrimental for mechanistic studies. Another potential drawback of liposomes is that individual components can partition into biological membranes; therefore, the use of liposomes can be problematic for mechanistic studies involving organisms or even cells.

3.3.5. Dendrimers

Dendrimers are often used as multivalent ligand scaffolds.[96,136–141] These ligands can be fairly homogeneous,[96] which can aid in relating ligand features to biological activity. Beads and carrier–protein conjugates often form heterogeneous populations of conjugates since the sites of RE conjugation are often unknown. In contrast, the architectural features of a dendrimeric ligand are defined by the choice of scaffold and the methods used for its synthesis. For example, starburst (PAMAM) dendrimers of generation 0 have diameters of 1.5 nm and valencies of four.[142] Each increase in generation increases the diameter by 0.7 to 1.6 nm while also doubling the maximum valency. Thus, as the size of the dendrimer increases, so does the RE density. Some of the REs of such highly functionalized dendrimers can be inaccessible to proteins.

3.3.6. Polymers

Modern polymer chemistry is providing new opportunities for the synthesis of tailored, biologically active polymeric (or oligomeric) ligands. The multivalent ligands derived from polymers are typically composed of a central backbone that presents multiple copies of an RE. Ligands of this type can be produced by using a variety of synthetic methods. Polymers are generally assembled in a single step by methods such as radical, ionic, or ring-opening metathesis polymerization of RE-bearing monomers.[101,143–149] Alternatively, REs can be appended to a preformed polymeric scaffold.[101,147] Certain polymerization reactions are more tolerant of biologically active functionality than others; thus, the type of epitopes to be incorporated will determine the most effective synthetic strategy.

© 2006 Wiley-VCH Verlag GmbH & Co. KGaA, Weinheim

Selective polymerization reactions enable the biologically active ligand to be synthesized with controlled valency.[84] Living polymerization reactions, in which the rates of chain termination are low, are powerful methods for generating well-defined multivalent ligands. Polymers of narrow polydispersity can be generated when the polymerizations have fast initiation and slow propagation rates.[150] Such polymerization reactions can be used to synthesize multivalent ligands with a variety of sizes. For example, linear polymers with molecular weights of approximately 3000 generated by ring-opening metathesis polymerization (ROMP) can span 100 nm.[151] Polymers displaying dendrimeric appendages can reach lengths of 10 to 100 nm.[152] In addition to allowing control over the degree of polymerization, living polymerization reactions can be used to synthesize block copolymers that display different REs (or simply different functionality) within each block.[153]

Polymers generated by ROMP have found increasing use as biologically active multivalent ligands.[101,149,154–158] Ruthenium–carbene catalysts for ROMP can be used to generate materials of distinct valency.[150,159–161] These ligands have been generated as inhibitors of saccharide–protein interactions,[151,162–164] as ligands for combating vancomycin-resistant bacteria,[156] and as effectors of biological responses.[46,165] Importantly, this polymerization method allows control over the display and density of REs.[166,167] The differences in activity between these compounds can, therefore, be attributed to specific aspects of ligand structure.

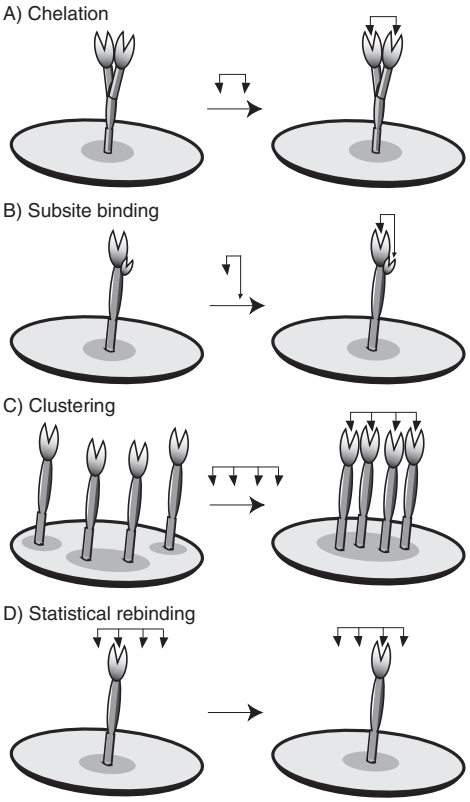

Figure 5. Receptor binding mechanisms that are unique to multivalent ligands.

3.3.7. Combinatorial Synthesis of Multivalent Ligands

Combinatorial methods offer a new approach to the synthesis of multivalent ligands. Combinatorial and diversity-oriented synthesis of monovalent molecules has facilitated the discovery of low-molecular-weight ligands that are optimally designed to bind to a target receptor.[168–173] Similarly, libraries of multivalent ligands might be expected to contain compounds that possess diverse activities.[119–121,166,167,174]

The technical hurdles to overcome in the synthesis of small-molecule libraries are different from those encountered with multivalent ligand libraries. For example, multivalent ligands bearing different REs can have different physical properties; therefore, they will require different purification methods. Combinatorial approaches to multivalent ligand synthesis are in their infancy, and only a few synthetic strategies for generating diverse multivalent ligands have been described.[119–121,153,166,167,174] Future advances in synthetic methods and purification technologies will be instrumental in providing multivalent materials with a broad range of architectural diversity.

3.4. Mechanisms of Multivalent Ligand Binding

Multivalent ligands can bind receptors in ways that are inaccessible to monovalent compounds (Figure 5).[100,115,175] For example, a ligand with multiple copies of an RE can bind to multiple binding sites on a single oligomeric receptor (examples of such receptors are immunoglobulins and some lectins). The cost for translational entropy is paid with the first receptor–ligand contact, and subsequent binding interactions proceed without additional penalties in translational entropy.[176] Excellent examples of this chelation binding mode are presented in recent studies directed at devising multivalent inhibitors of pentavalent toxins.[177–179] Similarly, certain receptors possess binding subsites in addition to their primary site of interaction. Unlike monovalent ligands, which can only access subsites adjacent to their primary binding pocket, multivalent ligands may gain binding energy from contacting more remote secondary sites.[180] Either an RE or another component of the scaffold can contact these subsites. In situations where the multivalent ligand occupies more than one binding site—whether it is a subsite or a primary site within an oligomeric receptor—the ligand typically will bind with a high functional affinity.[181] Another mechanism by which a multivalent ligand can act is through steric stabilization: The steric bulk of the multivalent ligand may preclude the engagement of a bound receptor with an opposing viral particle or cell.[182] This aspect of multivalent ligand activity is particularly relevant for inhibitors of binding interactions at the cellular or viral surface. All these binding modes together are unique to multivalent ligands and have led to numerous applications of these reagents as inhibitors of macromolecular interactions.

Multivalent ligands do not have to inhibit a process, they can act as *activators* of signal transduction. Multivalent ligands can bind avidly to multiple receptors on the cell surface, a process that is facilitated in the fluid lipid bilayer by

 © 2006 Wiley-VCH Verlag GmbH & Co. KGaA, Weinheim

the two-dimensional diffusion of receptors. The multivalent ligands can activate signaling pathways if they can cluster signaling receptors (Figure 5c). It is this mechanism, which is uniquely available to multivalent ligands, that is the focus of the remainder of this Review.

We have outlined the three major concepts that are critical for the application of multivalent ligands as probes of signal transduction: 1) signal transduction cascades are mediated by receptor–receptor interactions, and promoting receptor assembly is critical for signaling (Figure 3). 2) Multivalent ligands can interact with the target receptors through multiple binding modes (Figure 5). 3) The structure of a multivalent ligand will determine the favored binding modes (Figure 4). Thus, the structure of the ligand can be optimized to elicit the desired biological response.[84] In the next sections, we provide some examples that illustrate the utility of multivalent ligands as mechanistic probes.

4. Using Multivalent Ligands to Gain Insight into Receptor Function

The binding of a multivalent ligand to a cell surface can assemble a multiprotein complex with distinct features. The valency of the ligand, the orientation of REs, and the stability of the interaction can be used to control features of the complex: its stoichiometric composition, its size, the orientation of the receptors within it, and the lifetime of the complex. Thus, a multivalent ligand can have a marked influence on the output response of a signaling cascade. The following examples describe how specific multivalent ligands can be used to analyze signaling.

4.1. Receptor Proximity

The binding of multivalent ligands can result in clustering of the receptors in the membrane.[84] Here, we discuss some of the many examples in which the ability of multivalent ligands to promote clustering has been used to reveal aspects of receptor function.

4.1.1. Integrins

Integrins are cell-surface receptors that mediate cell adhesion; they also play a central role in the focal adhesion signaling complex.[24,183–185] Integrin function is important in multicellular organisms, and targeted deletion of integrin subunits can strongly impair tissue formation.[186] Given their fundamental physiological roles, it is not surpising that integrin-mediated adhesion and signaling events are carefully regulated.

A key feature of integrins is their ability to switch between low- and high-affinity binding modes.[187] These two modes are thought to allow rapid and reversible adjustments of the strength of the cell adhesion. This switch likely involves changes in the integrin conformation, proximity, or both.[188] Integrins are proposed to adopt at least two conformational states: a bent inactive state and an extended active state.[187] In addition, they can undergo changes in receptor proximity, which can be induced either by interaction with a ligand (an "outside-in" change) or by cellular activation (an "inside-out" change). Although there is evidence that both proximity and conformation influence signaling and adhesive strength, more specific and useful therapeutics may result from a deeper understanding of the relative contributions of these mechanisms. Insight into the influence of the receptor proximity in focal adhesion function is emerging from experiments with synthetic multivalent ligands.

One group of synthetic ligands used to probe integrin clustering are chemical inducers of dimerization (CIDs). CIDs are low-molecular-weight, cell-permeable, divalent ligands that can mediate the clustering of two receptors.[4,116,189–191] A key feature of CIDs is that they can oligomerize receptors fused to a specific ligand-binding protein (Figure 6). This strategy first utilized fusions to FKBP, a protein that binds to the immunosuppressant FK506.[189] FK506 is a low-molecular-weight drug that can be functionalized and converted into the dimer FK1012, which is capable of dimerizing FKBP. FKBP fusion proteins can be transfected or otherwise introduced into cells, thus permitting examination of the functional consequences of FK1012-mediated dimerization of the target fusion proteins. Ligand addition can induce formation of higher order assemblies if multiple copies of FKBP are fused to the target protein of interest.[192] Such strategies have been expanded to include heterodimerization and dimerization

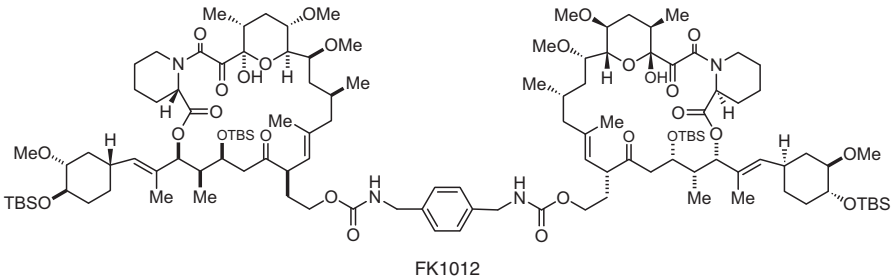

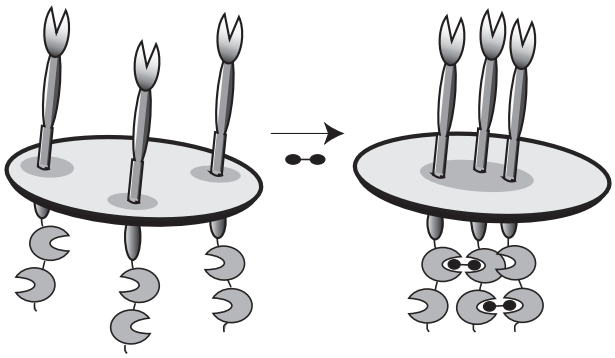

Figure 6. Depiction of the intracellular-mediated alteration of receptor proximity by CID. A receptor fused to a binding protein is expressed in a target cell. Addition of a small-molecule dimerization agent (FK1012) induces the clustering of the receptor. TBS = *tert*-butyldimethylsilyl.

© 2006 Wiley-VCH Verlag GmbH & Co. KGaA, Weinheim

agents that avoid endogenous proteins (for example, FKBP) and specifically target engineered fusion proteins.[192–194]

Both the proximity and conformation of the integrin contribute to the change in the binding affinity. A CID strategy was employed to dissect the role of conformational change from that of receptor proximity.[195] A gene encoding two copies of FKBP in tandem was fused to that encoding αIIb; the latter is a part of the integrin complex αIIb-β3. The addition of the dimerization agent AP1510 elicits integrin clustering in cells producing the fusion protein. If proximity alone is important for the switch between low and high affinity, one would expect that AP1510 would fully replace the need for a natural binding partner. As a measure of the switch to the high-affinity binding mode, an antibody (PAC1) was used that binds specifically to the high-affinity form of the integrin. Addition of the FKBP dimerization agent AP1510 to the cells resulted in a dose-dependent increase in the binding of PAC1. To investigate the role of the conformational change of the receptor, these authors used the monovalent antibody fragment LIBS that binds and potently activates integrins. The increase in binding observed in the presence of AP1510 was modest; the effect from LIBS treatment was more dramatic. These studies with CIDs indicate that, although there is a contribution from receptor proximity, other factors, such as adopting the high-affinity conformational state, contribute significantly to integrin-mediated cell adhesion.

Integrins are cell-surface proteins that are not only involved in adhesion but also in intracellular signaling. Signaling from integrins involves the activation of multiple pathways. As is the case for most complex signaling systems, efforts to deconvolute the contributions of each pathway are ongoing. The two kinases Syk and FAK are implicated in transducing signals through different pathways in integrin signaling. The formation of integrin clusters may favor information transfer through one of these pathways (Syk or FAK) over others. To test this hypothesis, the role of receptor proximity in signaling by Syk and FAK was explored with the dimeric ligand AP1510. When cells were treated with AP1510 alone to cluster the integrin αIIb-β3, an increase in tyrosine phosphorylation by Syk was observed. The requirements for activation of FAK, however, include both the receptor in the high-affinity state (treatment with LIBS) and oligomerization (treatment with AP1510). These results demonstrate the complex interplay between signaling, adhesion, and cellular response that can be achieved by changes in integrin occupancy, proximity, or both. These investigations illustrate the utility of the CID strategy for deconvoluting these contributions. One minor disadvantage of the CID approach, however, is that the cells need to be genetically engineered to express the fusion proteins.

Multivalent surfaces can be used to probe integrin function directly. Integrins can facilitate cell adhesion to extracellular matrix components as well as other cells.[185,196] The extracellular matrix, a naturally occurring multivalent display, may therefore also influence integrin activity.[197] In one study, surfaces were modified with monovalent fibrinogen or monovalent fibrin for use in cell-adhesion studies.[198] Lymphoblastoid B cells were allowed to adhere to the coated microtiter wells (Figure 7 A). The multivalent fibrin was able

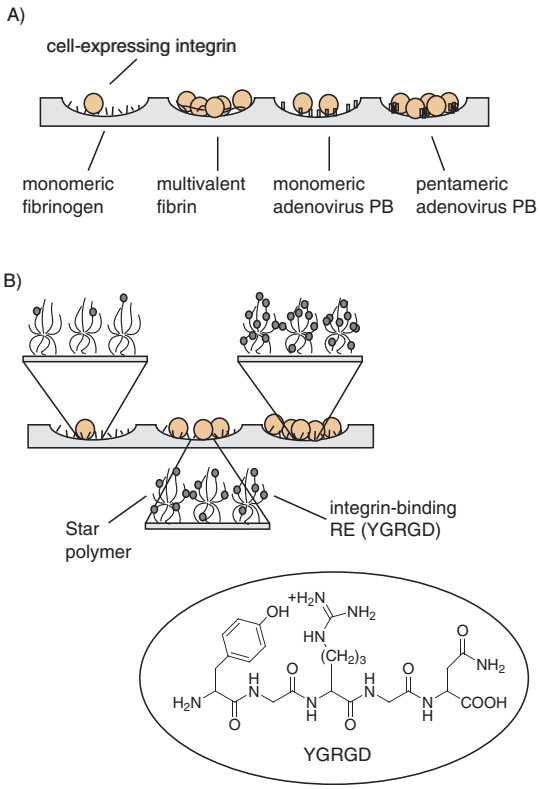

Figure 7. The density of REs presented influences the adhesion of cells to surfaces bearing integrin ligands. A) Surfaces coated with multivalent ligands have a greater functional affinity for B cells. B) Star polymers are depicted that display variable copies of the pentapeptide YGRGD (an integrin-binding RE). The relative potency of each surface is indicated by the number of cells bound.

to support cell adhesion but unactivated cells did not adhere to immobilized monovalent fibrinogen.

In a series of related experiments adenovirus PB, a ligand specific for the integrin $\alpha_v\beta_3$, was coated in wells in either its monomeric or pentameric form (Figure 7b). As in the fibrin experiment, the B cells attached selectively to the wells coated with multivalent ligand. To understand the mechanisms responsible for the differences in binding, the number of possible integrin binding sites in the wells displaying monomeric ($800\,\text{sites}\,\text{mm}^{-2}$) or pentameric ligand ($125\,\text{sites}\,\text{mm}^{-2}$) was determined by radioimmunoassay. Although it had sixfold fewer sites per mm^2, the surface displaying the pentameric integrin ligand was more adhesive. These results suggest that the local arrangement of binding sites, and not the overall number of sites, is critical for integrin-mediated adhesion.

These results are supported by additional data that indicate local RE density is important for the adhesion strength of integrin.[127] Maheshwari et al. used star polymers that display variable numbers of copies of the minimal integrin ligand YGRGD to investigate the impact of binding-site density on integrin-mediated cell migration and adhesion of $\alpha_v\beta_3$-bearing cells. The integrin $\alpha_v\beta_3$ binds RGD sequences, and surfaces with more YGRGD were more effective at interacting with cells (Figure 7B). Interestingly, however, when surfaces with equal numbers of REs but different local

 © 2006 Wiley-VCH Verlag GmbH & Co. KGaA, Weinheim

densities were compared, those with closely packed REs were more efficient at mediating cell migration and adhesion. These results suggest that clustering of the integrins improves their adhesive strength, probably through both enhanced functional affinity for the ligand and by activation of the signaling pathways.

These experiments with synthetic multivalent surfaces have highlighted a role for receptor proximity in integrin function. These studies also provide information about the most effective types of natural integrin ligands. Unfortunately, these multivalent surfaces cannot be used to explore integrin function in living organisms. Experiments utilizing soluble multivalent ligands could be used to investigate the consequences of integrin clustering in physiological settings.

4.1.2. G-Protein-Coupled Receptors

GPCRs are one of the largest families of mammalian cell-surface receptors. They participate in many important physiological processes. Their significance is underscored by their importance to medicine: over 50% of therapeutics on the market act through GPCRs.[199] Mounting evidence implicates GPCR homo- and heterodimerization in the regulation of signaling from these receptors.[117,200] Therefore, it would be valuable to elucidate the contribution of GPCR oligomerization to understand GPCR signaling and to exert control over it. The role of the ligand in modulating the clustering of GPCRs is unknown, but experiments using synthetic multivalent ligands are beginning to address this issue.

Low-molecular-weight divalent ligands have been used to assess the consequences of receptor dimerization.[103,117,186,201–207] An illustration of this approach is the use of the dimer of a GPCR ligand to activate neutrophil chemotaxis.[208] Neutrophils are attracted to sites of bacterial infection by by-products of bacterial protein synthesis, such as *N*-formylmethionine-containing peptide fragments. Perhaps the most widely studied neutrophil chemoeffector is *N*-formylmethionine-leucine-phenylalanine (fMLF), which is recognized by the formyl peptide receptor (FPR)—a GPCR. Dimers presenting two copies of fMLF were, therefore, employed to explore the role of receptor proximity in the regulation of FPR signaling.

Mono-, di-, and triethylene glycol-linked dimers of fMLF were generated by coupling a linker to the C terminus of the peptide. The monoethylene glycol dimer would not be expected to be capable of dimerizing the FPR; consequently, any enhanced chemotactic activity relative to fMLF is likely due to an increase in avidity. In contrast, the authors suggest that the triethylene glycol linked dimer may facilitate dimerization of the receptor, although the linker length required to simultaneously occupy two copies of the FPR is not known. The authors generated a series of divalent ligands, hoping that those with longer linkers might dimerize the FPR.

Two assays were used to explore FPR function: chemotaxis and superoxide production.[208] Neutrophils are recruited in vivo to the location of the invading pathogen through chemotaxis; the release of superoxide serves a killing role. These two cellular responses must occur with strict spatial and temporal control to minimize damage to healthy tissue. Specifically, chemotaxis towards a site of bacterial infection must precede superoxide formation or the neutrophils could prematurely release toxic oxygen species. Both of these responses can be elicited in response to ligand binding to FPR. It is important, therefore, to understand what factors influence the triggering of these distinct cellular responses.

The synthetic dimers were added to cells expressing FPR, and the chemotaxis and superoxide levels were monitored. The triethylene glycol linked dimer was the most active chemoattractant, while the monoethylene glycol dimer elicited the highest level of superoxide production. Although FPR dimerization was not tested directly, these results suggest that dimerization of the receptor may influence chemotactic responses. The increased ability of the monoethylene glycol dimer to elicit superoxide release was attributed to it having higher affinity for the FPR. Although the specific mechanisms of action of these divalent agents were not probed further, these initial results suggest that synthetic multivalent ligands will be useful in illuminating the role of receptor clustering in GPCR signaling in general, and chemotactic signaling in neutrophils in particular.

Receptor heterooligomerization can provide a means of integrating information from multiple pathways into a coherent cellular response. The consequences of GPCR heterodimer formation have been probed by creating heterodimeric ligands.[103] This approach was taken to study the effects of coclustering a GPCR that responds to enkephalin with one that is activated by neurotensin. Both natural ligands are important regulatory neuropeptides that function as synergistic activators of GPCR signaling.[209] The goal of the studies was to determine whether there might be a direct potentiation of signal through assembly of a heteroligomeric GPCR complex.

Cells expressing both receptors were treated with neurotensin, a mixture of neurotensin and enkephalin, or a difunctional neurotensin–enkephalin conjugate[209] The cytosolic cyclic GMP (cGMP) concentration was measured at a variety of ligand doses. Only a subtle increase in cGMP production was observed when both hormones were added separately. In contrast, the covalent heterodimer was a potent inducer. These data suggest that the forced proximity of the two receptors is the primary cause for the increased level of cGMP. As in the previous example, however, direct data in support of heterodimerization are lacking.

Further experimentation with ligands bearing higher valencies or more diverse architectures may afford more definitive insights into the effects of receptor proximity on GPCR-mediated signaling. It will be especially useful to couple signaling studies with those that address the influence of ligands on GPCR assembly. Since so many drugs target GPCRs, these investigations may facilitate the design of a new generation of therapeutics.[210]

4.1.3. T-Cell Receptors

T lymphocytes are key mediators of mammalian immunity.[13,22,78,211] These cells recognize foreign antigens through their T-cell receptors (TCRs). Binding at T-cell receptors can result in cellular activation, which can precipitate the killing

 © 2006 Wiley-VCH Verlag GmbH & Co. KGaA, Weinheim

of tumor cells, pathogens, and virally infected cells. As discussed in Section 1, when T cells encounter antigen-presenting cells, an immune synapse can form at the cell–cell interface. This immune synapse, which contains the TCR as well as other co-receptors and signaling components, possesses exquisite organization.[76]

There is evidence that changes in the organization of the TCR and other signaling components are important for T-cell activation; however, the contribution of various factors to TCR signaling remains unclear. Despite the large body of literature on TCR organization and signaling, questions remain concerning the molecular details of TCR function. For example, it is uncertain as to whether the dimerization of two TCRs is sufficient stimulus for T-cell activation or whether TCR oligomerization is required. The role of simple monovalent ligation of individual TCRs is also unknown.[212] The purpose of the synapse is unclear if individual or small groups of TCRs can activate signaling. Multivalent ligands will undoubtedly play prominent roles in addressing these fundamental issues.

One strategy for studying TCR function uses multivalent protein conjugates which are formed from the high-affinity interaction between biotin and the tetravalent protein streptavidin.[213] The four identical biotin-binding sites of streptavidin each bind with a dissociation constant of 10^{-15} M; therefore, biotinylated recognition elements can be readily displayed from a streptavidin scaffold. Since streptavidin is tetravalent, multivalent complexes can be generated that present 1, 2, 3, or 4 recognition epitopes per scaffold (Figure 8). Davis, McConnell, and co-workers developed streptavidin as a scaffold for the presentation of peptide-loaded major histocompatibility complexes (MHCs).[213] Since peptide-loaded MHCs can serve as ligands for the TCR, streptavidin-bound biotinylated MHC complexes can bind (in principle) up to four TCRs.

To generate these multivalent presentations, a peptide derived from moth cytochrome *c* (MCC) was added to the MHC. The resulting MCC–MHC complex was singly biotinylated and mixed with streptavidin; this procedure should yield a tetravalent complex that can bind the TCR (Figure 8). The amount of active MHC complex in the assembly reaction was varied to favor formation of mono-, di-, tri-, or tetrameric structures. Biotinylated MHC that lacks MCC was also produced, and these proteins, which cannot bind the TCR, were added to occupy the remaining streptavidin sites. A complex displaying four unloaded MHCs, which does not display foreign antigen, served as a control.

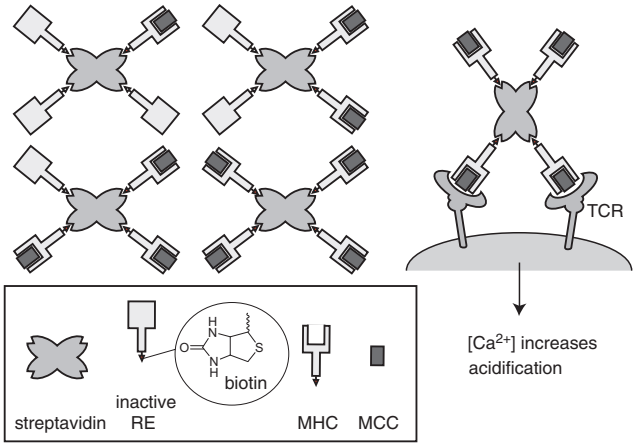

Figure 8. Schematic representation of streptavidin-MHC-MCC complexes. Left: Four complexes with one, two, three, or four biotinylated MHC-MCC moieties; right: a model for the activation of TCRs by multivalent engagement by the highest valency ligand.

To test the effects of the assemblies on T-cell activation, decreases in extracellular pH values and increases in the concentration of intracellular Ca^{2+} were measured. In both cases, the tetramer was the only ligand to elicit a significant increase in activity. Although effects arising from changes in binding kinetics cannot be ruled out, these experimental results suggest that changes in TCR proximity influence T-cell activation. Similar results were obtained using chemically defined peptide-based multivalent ligands, although a dimeric ligand was sufficient to activate TCR signaling.[214,215] These data taken together suggest that valency is an important feature of natural TCR ligands and that receptor proximity is important for the amplification of TCR-mediated signals.

Factors other than TCR ligation also contribute to activation and signal modulation. Indeed, numerous co-receptors serve to positively or negatively modulate the activation signal. One limitation of using streptavidin-based scaffolds is that it is difficult to incorporate multiple REs that can engage co-receptors and TCRs simultaneously. Thus, scaffolds that can be functionalized to present multiple types of REs have been employed.

A variety of beads and surfaces have been used as multivalent displays to explore T-cell signaling.[9,129,216–218] In this way, a study addressing the mechanism by which T-cell responses are enhanced by the co-receptor CD28 was undertaken.[87] Ligand binding to the TCR is necessary and sufficient for activation of T cells; however, co-stimulation of CD28 yields a more potent response. To determine the mechanism for enhanced signaling, beads were used to mimic the physical size of the surface of an antigen-presenting cell (APC), which presents ligands on its cell surface for the TCR and CD28.

Latex beads were modified to assess the consequences of simultaneous binding to receptors. Specifically, they were designed to cocluster the TCR and CD28: an antibody that recognizes the TCR and another that binds the co-receptor CD28 was attached. The beads were tested for their ability to induce cell proliferation, which occurs upon lymphocyte activation. If T-cell activation requires simultaneous binding of both the TCR and CD28, only the beads displaying REs for both receptors should activate the cells. Beads displaying only the TCR clustering element (anti-TCR) did not promote T-cell proliferation. In contrast, beads displaying both anti-TCR and anti-CD28 were potent activators of proliferation.

One explanation for the data is that simultaneous binding of CD28 and TCR promotes the co-localization of these receptors to a region of the membrane termed a lipid microdomain. It has been suggested that lipid microdomains concentrate signaling components and facilitate formation of mature signaling complexes. Support for a role for microdomains in enhancing signaling came from the concentration

 © 2006 Wiley-VCH Verlag GmbH & Co. KGaA, Weinheim

of a fluorescent marker of lipid rafts (fluorescein-labeled cholera toxin B subunit) into a dense fluorescent patch at the point of contact between the bead and the T cell. These results demonstrate that co-stimulation of the TCR and co-receptors can modify their distribution on the cell surface, which may modulate immune responses. An important caveat to these experiments, however, is that the REs on a bead-based multivalent ligand are immobilized. Thus, unlike cell-surface REs, the REs attached to the bead cannot undergo rearrangement. However, similar results were obtained when an antigen-presenting cell was used as a natural "ligand". This comparison suggests that the RE-decorated bead effectively mimics some aspects of an antigen-presenting cell.[219] Thus, a role for the CD28 co-receptor in regulating receptor proximity and immune function was implicated from studies using functionalized beads as multivalent ligands.

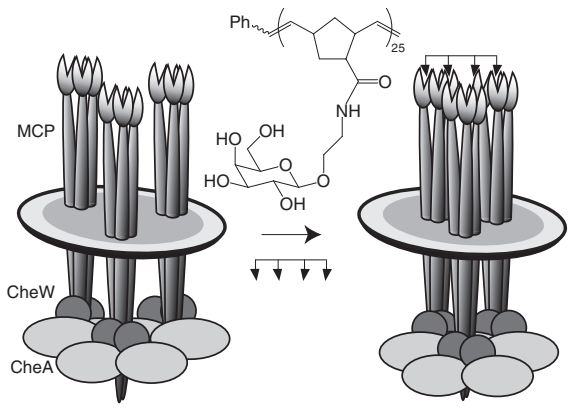

Figure 9. Investigation of receptor proximity effects in bacterial chemotaxis by using synthetic multivalent polymers. Addition of a multivalent ligand with sufficient valency can induce the reorganization of MCPs which potentiates signaling and activates bacterial locomotion.

4.1.4. ***Bacterial Chemoreceptors***

Bacteria must migrate towards nutrients and away from toxins to survive. Bacterial chemotaxis is driven by a well-characterized signaling pathway that is responsible for the detection of these nutrients and toxins.[220–222] Five types of membrane-bound chemoreceptors (MCPs) mediate chemotaxis in *Escherichia coli*. Each MCP type is responsible for detecting and mediating chemotaxis towards a subset of small molecules or other stimuli. Bacteria require integration of signals from multiple stimuli into a coherent response to initiate appropriate locomotion. Moreover, responses are mounted against stimuli at very low concentrations, which requires a significant level of signal amplification.[223–225]

The mechanism used by bacteria to amplify and integrate chemotactic signals has long been debated. One recent hypothesis is that signal amplification is achieved through interreceptor communication.[26,54,60,226,227] Interestingly, the MCPs are organized within the cell: They are concentrated at the poles of *Escherichia coli* and other bacterial species.[39,228] This organization of chemoreceptors into an array has been proposed to be important in signal transduction. Recent experiments using synthetic multivalent ligands and other approaches support such a view; they suggest that communication between homologous and heterologous MCPs within the chemoreceptor array is responsible for chemotactic responses.[46,54,60,62,229–231]

The first goal was to generate multivalent attractants that could cluster the chemoreceptors. ROMP was used to synthesize multivalent ligands that display chemotactic carbohydrate residues in sufficient valency (ca. 25 monomer units) to mediate MCP clustering, as shown by microscopy. This change in receptor proximity influenced signaling through the MCPs: ligands capable of clustering MCPs were also potent activators of chemotaxis (Figure 9). It was shown by using a fluorescent probe that galactose-bearing multivalent ligands cluster the galactose-sensing receptor Trg. Surprisingly, they also cluster the serine-sensing receptor Tsr. Tsr does not bind galactose; its presence in the cluster suggests that chemoreceptor–chemoreceptor interactions bring it into the cluster. These data indicate that there are interactions between different types of chemoreceptors.

Evidence in support of the functional significance of chemoreceptor–chemoreceptor interactions was obtained by examining the effects of receptor clustering on signal output. Specifically, a multivalent galactose derivative was introduced to cluster the chemoreceptors. When the bacteria had adapted to the multivalent attractant, the monovalent attractant serine was added. Under these conditions the chemotactic response to serine was potentiated by 100- to 1000-fold. This result indicates that heterologous MCPs communicate so as to amplify and integrate chemotactic signals. The proximity of multiple types of receptors is critical for signal amplification. Thus, a single receptor is not all that is needed to sense a particular compound—all chemoreceptor types contribute to proper sensing and signal amplification.

The application of multivalent chemoattractants to examine chemoreceptor proximity in chemotaxis illustrates their power: They can be used to explore signal transduction even when receptor dimerization is known to be required. Changes in receptor organization had not been implicated in chemotactic signal transduction: the role of receptor organization might have been overlooked because the known chemoattractants are monomeric, and the MCPs are dimeric in the absence of ligands. Nevertheless, studies indicate that changes in MCP proximity influence signal amplification, and evidence supporting such a model was obtained using multivalent ligands. Moreover, the use of these ligands did not require genetic manipulation of the bacteria; thus, the behavioral response elicited by the multivalent ligand could be directly analyzed under physiological conditions and in wild-type genetic backgrounds. These results underscore that soluble, structurally defined multivalent ligands are valuable probes.

4.2. Receptor Orientation

Many cell-surface receptors possess domains with intrinsic enzymatic activity, while some interact with proteins with catalytic domains. The substrates of these enzymatic activities are often other signaling proteins. The relative orientations of

 © 2006 Wiley-VCH Verlag GmbH & Co. KGaA, Weinheim

the active site of the receptor-associated enzyme as well as the substrate may influence the amount of product generated; this enzymatic efficiency, in turn, will influence signal transduction.[225,229,230,232] It is often unclear whether the activity of an assembled signaling complex is the result of a specific orientation of receptors within the complex or simply the localization of signaling components.[233] Since multivalent ligands can organize receptors into specific orientations, they have the potential to serve as tools for investigating the role of protein orientation in signaling.

4.2.1. G-Protein-Coupled Receptors (GPCRs)

One key feature of multivalent ligands is that they can occupy multiple binding sites on a single receptor and thereby exploit the chelate effect (Figure 5a).[176] Multivalent ligands that use this binding mode can interact with high functional affinities, and is an important determinant of agonist or antagonist potency. In a recent example, a low-molecular-weight dimer was constructed that can bind simultaneously to two sites on the corticotrophin-releasing factor receptor (CRFR-1). CRFR-1 is a GPCR that is a key regulator of adrenocorticotropic hormone (for example, testosterone) release during the stress response.[234]

A series of dimers was generated, in which different orientations of the REs were controlled by using helical and rigid linkers. The addition of these dimers to cells expressing CRFR-1 resulted in the release of testosterone. Potent activity was elicited by the dimers that maintained a *trans* orientation between the terminal REs. Ligands that did not maintain this orientation were tenfold less effective at causing testosterone release. The experiments conducted do not eliminate the possibility that the observed differences arise from ligand-induced changes in receptor oligomerization, but the results suggest that the orientation of REs can influence receptor activation.[117,235]

4.2.2. ZAP-70

Chemical synthesis can be used to create ligands to probe the role of protein orientation in assembled signaling complexes. In the previous example, the relative orientation of the binding moieties within a multivalent ligand influence its ability to elicit signaling through a target receptor. When a multivalent ligand acts by clustering receptors, however, the geometric constraints on the binding epitopes might be relaxed. In the few examples studied to date, the localization of receptors to a signaling complex is often more important than their specific orientation within the complex.[233,236] The ability of dimeric ligands to activate signaling by ZAP-70 is consistent with this view and highlights that different RE orientations often give rise to only subtle effects.[107]

ZAP-70 is a kinase whose function is required for the varied signaling functions of the T cell. If the orientation of ZAP-70 is important for its function, multivalent ligands that control its orientation should possess varying abilities to elicit T-cell activation. To this end, a series of small-molecule dimeric ligands was generated; each possessed conformationally restricted linkers between the two identical REs. The activity of this series was assessed by adding CIDs to cells encoding a membrane-docking protein (three copies of FKBP fused to a myristoylation domain of v-Src) and a ZAP-70–FKBP fusion protein (Figure 10). Presumably, these CIDs can

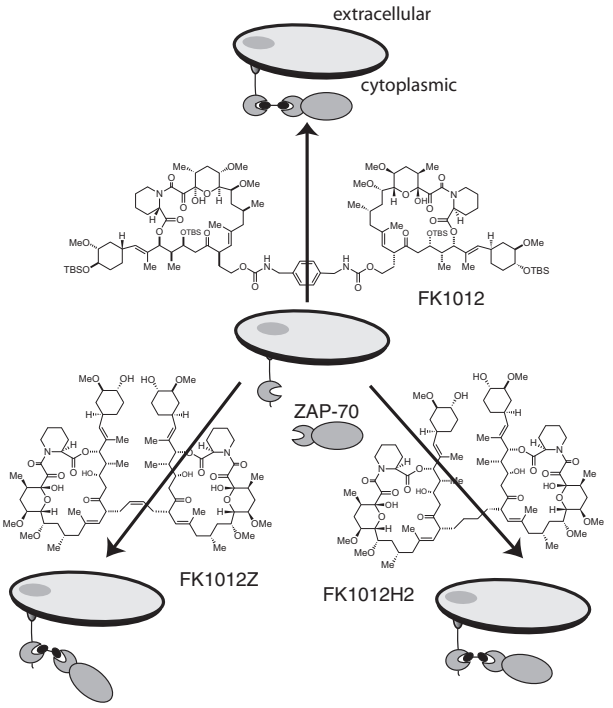

Figure 10. Investigation of the influence of the orientation of ZAP-70 on its kinase function by a CID strategy. The chemical structures of three dimerization agents FK1012, FK1012H2, and FK1012Z are shown. These dimers present REs in three distinct relative orientations, but their abilities to induce ZAP-70 activity were similar.

bind and cluster the fusion proteins, thereby recruiting ZAP-70 to the membrane. All of the synthetic CIDs mediated ZAP-70 recruitment and all activated signaling. While large changes in orientation may influence ZAP-70 signaling, the presumed changes in the orientation afforded by the CIDs had little effect.

The difference in the results of the CRFR-1 versus the ZAP-70 studies suggests a plasticity in the assembly of signaling complexes: For signal activation, the REs of dimeric ligands that occupy subsites within a receptor must be more carefully aligned than those that act by inducing changes in receptor proximity. Interestingly, these findings are consistent with studies in which fusion proteins have been used to test whether different assemblies of signaling domains influence output.[233,236] As with the ZAP-70 investigations, the orientation of different signaling domains was much less important than their recruitment to a signaling complex. It will be interesting to explore the generality of these findings further.

4.3. Composition of Receptor Clusters

The number of receptors in a complex can influence its biological activity. Cell adhesion is expected to be especially

 © 2006 Wiley-VCH Verlag GmbH & Co. KGaA, Weinheim

sensitive to the number of receptors in a complex; the functional affinity of the array is expected to be directly related to the number of receptor–ligand complexes formed.[100] Signal transduction processes also may be sensitive to the number of receptors in the complex; however, it can be difficult to determine the quantitative role of receptor composition in signaling. Multivalent ligands can be generated that vary in the density and valency of REs so as to investigate either cell adhesion or cell signaling. These ligands, therefore, may have the ability to generate specific clusters of receptors that vary in the number of proteins included. This strategy has been utilized to investigate the role of composition for receptor function.

4.3.1. *B-Cell-Antigen Receptor*

The B-cell-antigen receptor (BCR) is a complex comprised of proteins involved in the recognition of antigens and the generation of antibodies during acquired immune responses.[23,85,237] The activation of BCR-mediated functions must be strictly regulated, since inappropriate activation can cause autoimmune disease. Understanding the minimal requirements for BCR-mediated activity is therefore critical. Synthetic multivalent ligands have played key roles in investigating the importance of antigen stoichiometry in the activation of this system.

Pioneering work by Dintzis et al. and others in the field of BCR signaling in the 1970s and 1980s utilized synthetic multivalent ligands to explore the role of valency in B-cell responses.[238–242] The binding of a multivalent antigen to the B-cell receptors (BCRs) can activate B-cell signaling. A series of multivalent ligands were generated using polyacrylamide, dextran, carboxymethylcellulose, and polyvinyl alcohol as scaffolds to test how the valency of T-cell-independent antigens influences antibody production.[243] These ligands were injected into mice, and the efficiency of antibody production was measured. In every case, irrespective of the scaffold structure or the amount of polymer branching, the immunogenicity of the ligands strictly depended on the RE valency. From these data, the authors hypothesize that the number of BCRs included in a cluster is a principle determinant of function. Moreover, they propose that occupation of approximately 12 BCRs is required for B-cell activation. There are many steps in this complex system between B-cell activation and antibody production. These investigations highlight, however, the power of synthetic multivalent ligands for answering questions of fundamental biological importance.

4.3.2. *L-Selectin*

Leukocyte migration from the blood to lymphatic tissues is dependent on the function of L-selectin; L-selectin also mediates leukocyte recruitment to sites of inflammation.[244] L-selectin is displayed on the surface of leukocytes, and it typically localizes to patches at the tips of the cellular microvilli (Figure 11).[237,241–246] The natural ligands for L-selectin are glycoproteins displayed on the endothelium of the blood vessel.[247] The binding of L-selectin to these ligands slows the progress of cells through the blood vessels and allows tight adherence of the leukocyte to the endothelium. Physiological L-selectin ligands typically present multiple copies of derivatives of the sulfated sialyl Lewis x antigen (sLe^x); synthetic multivalent ligands that display these and related carbohydrate epitopes have been shown to be effective selectin ligands.[248–253] Multivalency, therefore, may be an important determinant of L-selectin function in vivo. Experiments using synthetic multivalent ligands have started to reveal the importance of multivalency and stoichiometry of selectin–ligand clusters for L-selectin recognition.

The role of the receptor composition in regulating the adhesion function of L-selectin was investigated using synthetic multivalent ligands derived from ROMP.[254] The polymers were specifically end-labeled with a single fluoro-

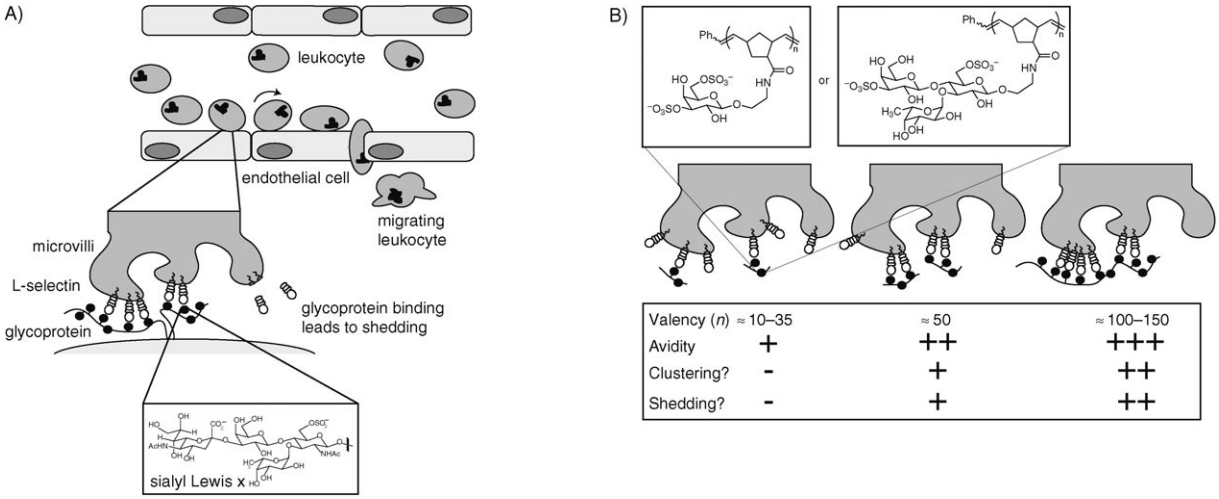

Figure 11. Multivalent ligands for L-selectin mimic cell-surface glycoproteins. A) L-selectin expressed on lymphocytes binds to glycoproteins on the endothelium. This interaction slows lymphocyte progression through the vessel and triggers proteolytic release of L-selectin. B) Multivalent polymers displaying sulfated carbohydrates also bind multiple copies of L-selectin, which leads to receptor clustering and proteolytic shedding. There is a direct relationship between the valency of the polymer, the number of L-selectin proteins bound, and the avidity of the interaction.

© 2006 Wiley-VCH Verlag GmbH & Co. KGaA, Weinheim

phore to visualize binding and to determine how many copies of a multivalent ligand bind L-selectin-positive cells.[255] It was found that the number of copies of L-selectin that bind to a multivalent sulfated carbohydrate derivative depends on its valency (Figure 11).[254] A related observation is that the functional affinity of a ligand for cells displaying L-selectin is directly related to its valency. Increasing the valency from 35 monomer units to 150 resulted in an increase in the relative ratio from 1.1 to nearly 5 copies of L-selectin. The functional affinity of the interaction improved 10-fold. These results suggest that the adhesive strength of L-selectin is related to the stoichiometry of the selectin–ligand complex.

Intriguingly, these polymers not only bind L-selectin but also promote its proteolytic release, or shedding, from the cell surface.[256,257] It appears that cell signaling is important for triggering the release of L-selectin:[165,258] it is possible that clustering L-selectin activates the signaling cascade that leads to its cleavage; or perhaps physiological L-selectin ligands also influence L-selectin levels in vivo. These results taken together suggest that the stoichiometry of L-selectin–ligand interactions is an important determinant of both the adhesive and signaling functions of this protein.

5. Summary and Outlook

Cell-surface receptors mediate the essential tasks of cell adhesion and signaling. In these roles receptors are rarely left to function as isolated entities. Rather, they collaborate as constituents of higher order macromolecular assemblies. Understanding the mechanisms underlying the function of these assemblies is critical. Multivalent ligands can serve as powerful tools for the deconvolution of complex multireceptor networks. The use of synthetic multivalent ligands is complementary to other approaches; therefore, they provide the means to address important new questions.

In addition to utility as agents for examining receptor function, synthetic multivalent ligands have potential applications in the treatment of disease. Multivalent ligands can participate in binding mechanisms that are not available to small molecules. For example, Whitesides, Collier, and coworkers took advantage of this unique aspect of multivalent ligands to generate potent polyacrylamide-based multivalent ligands that function as inhibitors of the anthrax toxin.[259] The success of these and other[260,261] in vivo applications of multivalent ligands indicates that they may function not only as probes of biological processes but even as therapeutic agents. In addition to their potential uses as inhibitors, multivalent ligands can mediate the clustering of cell-surface proteins and thereby function as effectors. While many small-molecule inhibitors are known, it is typically more difficult to find small molecules that serve as activators of signal transduction. The ability of multivalent ligands to activate signal transduction pathways suggest that they may have complementary therapeutic applications.

Multireceptor complexes are the requisite entities that convert extracellular stimuli into appropriate cellular responses. Communication and coordination between receptors provides a means to amplify, integrate, and process signals. Understanding how these processes occur at a molecular level is crucial to illuminating the function of biological *systems*. While monovalent ligands are powerful tools for disrupting such complexes, they cannot be used to examine the importance of the formation of complexes. Multivalent ligands have the necessary attributes to direct the formation of multiprotein complexes and/or control the localization of multiple proteins within the cell. We envision that such ligands, which can be used in a similar manner as small molecules for temporal control, will illuminate how protein assembly and/or protein localization direct cellular responses.

In this Review, we have provided an overview of some of the uses of synthetic multivalent ligands as probes. Additional advances in target-oriented and diversity-oriented syntheses of multivalent ligands will afford novel compounds that address increasingly complex biological questions. Such investigations demand a multidisciplinary approach that combines chemical and biological concepts to yield, ultimately, a coherent understanding of the molecular mechanisms governing cellular systems.

Received: August 7, 2005

[1] J.-P. Chaneux, J. Thiéry, Y. Tung, C. Kittel, *Proc. Natl. Acad. Sci. USA* **1966**, *57*, 335.
[2] C.-H. Heldin, *Cell* **1995**, *80*, 213.
[3] J. Schlessinger, *Trends Biochem. Sci.* **1988**, *13*, 443.
[4] J. D. Klemm, S. L. Schreiber, G. R. Crabtree, *Annu. Rev. Immunol.* **1998**, *16*, 569.
[5] H. Metzger, *J. Immunol.* **1992**, *149*, 1477.
[6] J. C. Sacchettini, L. G. Baum, C. F. Brewer, *Biochemistry* **2001**, *40*, 3009.
[7] F. D. Smith, J. D. Scott, *Curr. Biol.* **2002**, *12*, R32.
[8] A. Weiss, J. Schlessinger, *Cell* **1998**, *94*, 277.
[9] J. T. Groves, *Angew. Chem.* **2005**, *117*, 3590; *Angew. Chem. Int. Ed.* **2005**, *44*, 3524.
[10] M. Mellado, J. Rodríguez-Frade, A. J. Vila-Coro, S. Fernández, A. Martín de Ana, D. R. Jones, J. L. Toran, C. Martínez-A, *EMBO J.* **2001**, *20*, 2497.
[11] H. D. Madhani, *Cell* **2001**, *106*, 9.
[12] D. J. Riese II, D. F. Stern, *BioEssays* **1998**, *20*, 41.
[13] M. L. Dustin, A. C. Chan, *Cell* **2000**, *103*, 283.
[14] D. Bray, *Annu. Rev. Biophys. Biomol. Struct.* **1998**, *27*, 59.
[15] S. Tsunoda, J. Sierralta, Y. Sun, R. Bodner, E. Suzuki, A. Becker, M. Socolich, C. S. Zuker, *Nature* **1997**, *388*, 243.
[16] E. Stein, A. A. Lane, D. P. Cerretti, H. O. Schoecklmann, A. D. Schroff, R. L. Van Etten, T. O. Daniel, *Genes Dev.* **1998**, *12*, 667.
[17] M. N. Levit, Y. Liu, J. B. Stock, *Biochemistry* **1999**, *38*, 6651.
[18] M. N. Teruel, T. Meyer, *Cell* **2000**, *103*, 181.
[19] D. A. Lauffenburger, *Proc. Natl. Acad. Sci. USA* **2000**, *97*, 5031.
[20] M. B. Kennedy, *Science* **2000**, *290*, 750.
[21] J. H. Kim, R. L. Huganir, *Curr. Opin. Cell Biol.* **1999**, *11*, 248.
[22] R. N. Germain, *Curr. Biol.* **1997**, *7*, R640.
[23] L. Matsuuchi, M. R. Gold, *Curr. Opin. Immunol.* **2001**, *13*, 270.
[24] A. van der Flier, A. Sonnenberg, *Cell Tissue Res.* **2001**, *305*, 285.
[25] T. S. Shimizu, N. Le Novére, M. D. Levin, A. J. Beavil, B. J. Sutton, D. Bray, *Nat. Cell Biol.* **2000**, *2*, 792.
[26] D. Bray, M. D. Levin, C. J. Morton-Firth, *Nature* **1998**, *393*, 85.
[27] P. T. Martin, *Glycobiology* **2002**, *12*, 1R.
[28] S. Damjanovich, R. Gaspar, Jr., C. Pieri, *Q. Rev. Biophys.* **1997**, *30*, 67.

 © 2006 Wiley-VCH Verlag GmbH & Co. KGaA, Weinheim

[29] D. Holowka, B. Baird, *Annu. Rev. Biophys. Biomol. Struct.* **1996**, *25*, 79.
[30] P. W. Janes, S. C. Ley, A. I. Magee, P. S. Kabouridis, *Semin. Immunol.* **2000**, *12*, 23.
[31] A. Cherukuri, M. Dykstra, S. K. Pierce, *Immunity* **2001**, *14*, 657.
[32] D. A. Brown, E. London, *Annu. Rev. Cell Dev. Biol.* **1998**, *14*, 111.
[33] C. Langlet, A.-M. Bernard, P. Drevot, H.-T. He, *Curr. Opin. Immunol.* **2000**, *12*, 250.
[34] M. Edidin, *Curr. Opin. Struct. Biol.* **1997**, *7*, 528.
[35] E. D. Sheets, D. Holowka, B. Baird, *Curr. Opin. Chem. Biol.* **1999**, *3*, 95.
[36] T. E. Hebert, M. Bouvier, *Biochem. Cell Biol.* **1998**, *76*, 1.
[37] T. Bartfai, J. L. Benovic, J. Bockaert, R. A. Bond, M. Bouvier, A. Christopoulos, O. Civelli, L. A. Devi, S. R. George, A. Inui, B. Kobilka, R. Leurs, R. Neubig, J. P. Pin, R. Quirion, B. P. Roques, T. P. Sakmar, R. Seifert, R. E. Stenkamp, P. G. Strange, *Nat. Rev. Drug Discovery* **2004**, *3*, 574.
[38] P. R. Gouldson, C. R. Snell, R. P. Bywater, C. Higgs, C. A. Reynolds, *Protein Eng.* **1998**, *11*, 1181.
[39] J. R. Maddock, L. Shapiro, *Science* **1993**, *259*, 1717.
[40] C. C. Yin, F. A. Lai, *Nat. Cell Biol.* **2000**, *2*, 669.
[41] L. Pellegrini, D. F. Burke, F. von Delft, B. Mulloy, T. L. Blundell, *Nature* **2000**, *407*, 1029.
[42] J. Schlessinger, *Cell* **2000**, *103*, 211.
[43] T. Brümmendorf, V. Lemmon, *Curr. Opin. Cell Biol.* **2001**, *13*, 611.
[44] C. Chan, A. J. T. George, J. Stark, *Proc. Natl. Acad. Sci. USA* **2001**, *98*, 5758.
[45] A. D. Douglass, R. D. Vale, *Cell* **2005**, *121*, 937.
[46] J. E. Gestwicki, L. L. Kiessling, *Nature* **2002**, *415*, 81.
[47] D. J. Irvine, A. M. Mayes, L. G. Griffith, *Biomacromolecules* **2001**, *2*, 85.
[48] I. Markovic, E. Leikina, M. Zhukovsky, J. Zimmerberg, L. V. Chernomordik, *J. Cell Biol.* **2001**, *155*, 833.
[49] A. H. Elcock, J. A. McCammon, *Proc. Natl. Acad. Sci. USA* **2001**, *98*, 2990.
[50] T. E. Hébert, M. Bouvier, *Biochem. Cell Biol.* **1998**, *76*, 1.
[51] M. K. Dean, C. Higgs, R. E. Smith, R. P. Bywater, C. R. Snell, P. D. Scott, G. J. G. Upton, T. J. Howe, C. A. Reynolds, *J. Med. Chem.* **2001**, *44*, 4595.
[52] D. L. Milligan, D. E. Koshland, Jr., *Science* **1991**, *254*, 1651.
[53] S. Terrillon, M. Bouvier, *EMBO Rep.* **2004**, *5*, 30.
[54] V. Sourjik, H. C. Berg, *Nature* **2004**, *428*, 437.
[55] S. W. Fesik, *Cell* **2000**, *103*, 273.
[56] H. Wu, *Cell Surf. Recept.* **2004**, *68*, 225.
[57] J. J. Skehel, D. C. Wiley, *Annu. Rev. Biochem.* **2000**, *69*, 531.
[58] E. W. Yu, D. E. Koshland, Jr., *Proc. Natl. Acad. Sci. USA* **2001**, *98*, 9517.
[59] T. L. Blundell, D. F. Burke, D. Chirgadze, V. Dhanaraj, M. Hyvonen, C. A. Innis, E. Parisini, L. Pellegrini, B. L. Sayed, *Biol. Chem.* **2000**, *381*, 955.
[60] P. J. Gardina, M. D. Manson, *Science* **1996**, *274*, 425.
[61] I. Tatsuno, M. Homma, K. Oosawa, I. Kawagishi, *Science* **1996**, *274*, 423.
[62] P. Ames, C. A. Studdert, R. H. Resier, J. S. Parkinson, *Proc. Natl. Acad. Sci. USA* **2002**, *99*, 7060.
[63] S.-H. Kim, W. Wang, K. K. Kim, *Proc. Natl. Acad. Sci. USA* **2002**, *99*, 11611.
[64] P. A. Thomason, P. M. Wolanin, J. B. Stock, *Curr. Biol.* **2002**, *12*, R399.
[65] A. Ullrich, J. Schlessinger, *Cell* **1990**, *61*, 203.
[66] F. Alderton, S. Rakhit, K. C. Kong, T. Plamer, B. Sambi, S. Pyne, N. J. Pyne, *J. Biol. Chem.* **2001**, *276*, 28578.
[67] F. Liu, Q. Wan, Z. B. Pristupa, Y. T. Yu, H. B. Niznik, *Nature* **2000**, *403*, 274.
[68] C. C. Garner, J. Nash, R. L. Huganir, *Trends Cell Biol.* **2000**, *10*, 274.
[69] T. Pawson, P. Nash, *Science* **2003**, *300*, 445.
[70] M. Sheng, C. Sala, *Annu. Rev. Neurosci.* **2001**, *24*, 1.
[71] S. N. Gomperts, *Cell* **1996**, *84*, 659.
[72] K. E. Prehoda, W. A. Lim, *Curr. Opin. Cell Biol.* **2002**, *14*, 149.
[73] W. A. Lim, *Curr. Opin. Struct. Biol.* **2002**, *12*, 61.
[74] P. Friedl, A. T. den Boer, M. Gunzer, *Nat. Rev. Immunol.* **2005**, *5*, 532.
[75] M. F. Krummel, M. M. Davis, *Curr. Opin. Immunol.* **2002**, *14*, 66.
[76] R. N. Germain, I. Stefanova, *Annu. Rev. Immunol.* **1999**, *17*, 467.
[77] E. O. Long, *Annu. Rev. Immunol.* **1999**, *17*, 875.
[78] M. L. Hermiston, Z. Xu, R. Majeti, A. Weiss, *J. Clin. Invest.* **2002**, *109*, 9.
[79] L. Tuosto, I. Parolini, S. Schröder, M. Sargiacomo, A. Lanzavecchia, A. Viola, *Eur. J. Immunol.* **2001**, *32*, 345.
[80] P. A. van der Merwe, S. J. Davis, A. S. Shaw, M. L. Dustin, *Semin. Immunol.* **2000**, *12*, 5.
[81] A. Viola, S. Schroeder, Y. Sakakibara, A. Lanzavecchia, *Science* **1999**, *283*, 680.
[82] S. K. Bromley, W. R. Burack, K. G. Johnson, K. Somersalo, T. N. Sims, C. Sumen, M. M. Davis, A. S. Shaw, P. M. Allen, M. L. Dustin, *Annu. Rev. Immunol.* **2001**, *19*, 375.
[83] Y. M. Vyas, K. M. Mehta, M. Morgan, H. Maniar, L. Butros, S. Jung, J. K. Burkhardt, B. Dupont, *J. Immunol.* **2001**, *167*, 4358.
[84] L. L. Kiessling, J. E. Gestwicki, L. E. Strong, *Curr. Opin. Chem. Biol.* **2000**, *4*, 696.
[85] J. I. Healy, C. C. Goodnow, *Annu. Rev. Immunol.* **1998**, *16*, 645.
[86] A. R. Asthagiri, D. A. Lauffenburger, *Annu. Rev. Biomed. Eng.* **2000**, *2*, 31.
[87] T. Ideker, T. Galitski, L. Hood, *Annu. Rev. Genomics Hum. Genet.* **2001**, *2*, 343.
[88] S. Krauss, M. D. Brand, *FASEB J.* **2000**, *14*, 2581.
[89] J. Matko, M. Edidin, *Methods Enzymol.* **1997**, *278*, 444.
[90] C. Philipona, Y. Chevolot, D. Léonard, H. J. Mathieu, H. Sigrist, F. Marquis-Weible, *Bioconjugate Chem.* **2001**, *12*, 332.
[91] J. Zhang, R. E. Campbell, A. Y. Ting, R. Y. Tsien, *Nat. Rev. Mol. Cell Biol.* **2002**, *3*, 906.
[92] J. Lippincott-Schwartz, E. Snapp, A. Kenworthy, *Nat. Rev. Mol. Cell Biol.* **2001**, *2*, 444.
[93] F. S. Wouters, P. J. Verveer, P. I. H. Bastiaens, *Trends Cell Biol.* **2001**, *11*, 203.
[94] Y. Liu, L. Xu, N. Opalka, J. Kappler, H.-B. Shu, G. Zhang, *Cell* **2002**, *108*, 383.
[95] D. C. Tully, J. M. J. Fréchet, *Chem. Commun.* **2001**, 1229.
[96] R. Roy, *Curr. Opin. Struct. Biol.* **1996**, *6*, 692.
[97] N. V. Bovin, *Glycoconjugate J.* **1998**, *15*, 431.
[98] J. J. Lundquist, E. J. Toone, *Chem. Rev.* **2002**, *102*, 555.
[99] R. Roy, D. Page, S. F. Perez, V. V. Bencomo, *Glycoconjugate J.* **1998**, *15*, 251.
[100] M. Mammen, S.-K. Choi, G. M. Whitesides, *Angew. Chem.* **1998**, *110*, 2908; *Angew. Chem. Int. Ed.* **1998**, *37*, 2754.
[101] L. L. Kiessling, L. E. Strong, *Top. Organomet. Chem.* **1998**, *1*, 199.
[102] T. Kenakin, *FASEB J.* **2001**, *15*, 598.
[103] M. D. Carrithers, M. R. Lerner, *Chem. Biol.* **1996**, *3*, 537.
[104] M. B. Macek, L. C. Lopez, B. D. Shur, *Dev. Biol.* **1991**, *147*, 440.
[105] H. Schneider, W. Chaovapong, D. J. Matthews, C. Karkaria, R. T. Cass, H. J. Zhan, M. Boyle, T. Lorenzini, S. G. Elliot, L. B. Giebel, *Blood* **1997**, *89*, 473.
[106] D. Somjen, Y. Amirzaltsman, B. Gayer, G. Mor, N. Jaccard, Y. Weisman, G. Barnard, F. Kohen, *J. Endocrinol.* **1995**, *145*, 409.
[107] I. A. Graef, L. J. Holsinger, S. Diver, S. L. Schreiber, G. R. Crabtree, *EMBO J.* **1997**, *16*, 5618.
[108] C. Torigoe, J. K. Inman, H. Metzger, *Science* **1998**, *281*, 568.

 © 2006 Wiley-VCH Verlag GmbH & Co. KGaA, Weinheim

[109] H. Nishizumi, K. Horikawa, I. Mlinaric-Rascan, T. Yamamoto, *J. Exp. Med.* **1998**, *187*, 1343.
[110] D. Wright, L. Usher, *Curr. Org. Chem.* **2001**, *5*, 1107.
[111] Y. Liu, X. Hong, J. Kappler, L. Jiang, R. Zhang, L. Xu, C.-H. Pan, W. Martin, R. C. Murphy, H.-B. Shu, S. Dai, G. Zhang, *Nature* **2003**, *423*, 49.
[112] H. M. Kim, K. S. Yu, M. E. Lee, D. R. Shin, Y. S. Kim, S.-G. Paik, O. J. Yoo, H. Lee, J.-O. Lee, *Nat. Struct. Biol.* **2003**, *10*, 342.
[113] R. Sasisekharan, G. Venkataraman, *Curr. Opin. Chem. Biol.* **2000**, *4*, 626.
[114] J. D. Esko, U. Lindahl, *J. Clin. Invest.* **2001**, *108*, 169.
[115] L. L. Kiessling, L. E. Strong, J. E. Gestwicki, *Annu. Rep. Med. Chem.* **2000**, *35*, 321.
[116] P. A. Clemons, *Curr. Opin. Chem. Biol.* **1999**, *3*, 112.
[117] P. S. Portoghese, *J. Med. Chem.* **2001**, *44*, 2259.
[118] D. L. Boger, J. Goldberg, *Bioorg. Med. Chem.* **2001**, *9*, 557.
[119] H. E. Blackwell, P. A. Clemons, S. L. Schreiber, *Org. Lett.* **2001**, *3*, 1185.
[120] M. Pattarawarapan, K. Burgess, *Angew. Chem.* **2000**, *112*, 4469; *Angew. Chem. Int. Ed.* **2000**, *39*, 4299.
[121] J. Goldberg, Q. Jin, S. Satoh, J. Desharnais, K. Capps, D. L. Boger, *J. Am. Chem. Soc.* **2002**, *124*, 544.
[122] M. J. Krantz, N. A. Holtzman, C. P. Stowell, Y. C. Lee, *Biochemistry* **1976**, *15*, 3963.
[123] Y. C. Lee, C. P. Stowell, M. J. Krantz, *Biochemistry* **1976**, *15*, 3956.
[124] E. Gillitzer, D. Willits, M. Young, T. Douglas, *Chem. Commun.* **2002**, 2390.
[125] Q. Wang, T. Lin, L. Tang, E. Johnson, M. G. Finn, *Angew. Chem.* **2002**, *114*, 477; *Angew. Chem. Int. Ed.* **2002**, *41*, 459.
[126] T. L. Schlick, Z. Ding, E. W. Kovacs, M. B. Francis, *J. Am. Chem. Soc.* **2005**, *127*, 3718.
[127] G. Maheshwari, G. Brown, D. A. Lauffenburger, A. Wells, L. G. Griffith, *J. Cell Sci.* **2000**, *113*, 1677.
[128] N. Paran, B. Geiger, Y. Shaul, *EMBO J.* **2001**, *20*, 4443.
[129] N. Horan, L. Yan, H. Isobe, G. M. Whitesides, D. Kahne, *Proc. Natl. Acad. Sci. USA* **1999**, *96*, 11782.
[130] C. S. Chen, M. Mrksich, S. Huang, G. M. Whitesides, D. E. Ingber, *Biotechnol. Prog.* **1998**, *14*, 356.
[131] B. T. Houseman, M. Mrksich, *Angew. Chem.* **1999**, *111*, 876; *Angew. Chem. Int. Ed.* **1999**, *38*, 782.
[132] M. Mrksich, *Chem. Soc. Rev.* **2000**, *29*, 267.
[133] E. A. Smith, W. D. Thomas, L. L. Kiessling, R. M. Corn, *J. Am. Chem. Soc.* **2003**, *125*, 6140.
[134] D. Lévy, A. Bluzat, M. Seigneuret, J.-L. Rigaud, *Biochim. Biophys. Acta* **1990**, *1025*, 179.
[135] F. M. Menger, J. S. Keiper, *Curr. Opin. Chem. Biol.* **1998**, *2*, 726.
[136] E. K. Woller, M. J. Cloninger, *Org. Lett.* **2002**, *4*, 7.
[137] Y. Kim, S. C. Zimmerman, *Curr. Opin. Chem. Biol.* **1998**, *2*, 733.
[138] Y. Aoyama, *Chem. Eur. J.* **2004**, *10*, 588.
[139] M. J. Cloninger, *Curr. Opin. Chem. Biol.* **2002**, *6*, 742.
[140] W. B. Turnbull, S. A. Kalovidouris, J. F. Stoddart, *Chem. Eur. J.* **2002**, *8*, 2988.
[141] T. K. Lindhorst, *Host-Guest Chem.* **2002**, *218*, 201.
[142] C.-H. Lin, G.-J. Shen, E. Garcia-Junceda, C.-H. Wong, *J. Am. Chem. Soc.* **1995**, *117*, 8031.
[143] N. V. Bovin, H.-J. Gabius, *Chem. Soc. Rev.* **1995**, *24*, 413.
[144] J. D. Reuter, A. Myc, M. M. Hayes, Z. Gan, R. Roy, D. Qin, R. Yin, L. T. Piehler, R. Esfand, D. A. Tomalia, J. R. Baker, Jr., *Bioconjugate Chem.* **1999**, *10*, 271.
[145] K. Matyjaszewski, J. Xia, *Chem. Rev.* **2001**, *101*, 2921.
[146] D. J. Irvine, A.-V. G. Ruzette, A. M. Mayes, L. G. Griffith, *Biomacromolecules* **2001**, *2*, 545.
[147] B. R. Griffith, B. L. Allen, A. C. Rapraeger, L. L. Kiessling, *J. Am. Chem. Soc.* **2004**, *126*, 1608.
[148] V. Ladmiral, E. Melia, D. M. Haddleton, *Eur. Polym. J.* **2004**, *40*, 431.
[149] H. D. Maynard, S. Y. Okada, R. H. Grubbs, *J. Am. Chem. Soc.* **2001**, *123*, 1275.
[150] T. M. Trnka, R. H. Grubbs, *Acc. Chem. Res.* **2001**, *34*, 18.
[151] M. Kanai, K. H. Mortell, L. L. Kiessling, *J. Am. Chem. Soc.* **1997**, *119*, 9931.
[152] A. D. Schlüter, J. P. Rabe, *Angew. Chem.* **2000**, *112*, 860; *Angew. Chem. Int. Ed.* **2000**, *39*, 864.
[153] J. K. Pontrello, M. J. Allen, E. S. Underbakke, L. L. Kiessling, *J. Am. Chem. Soc.* **2005**, *127*, 14536.
[154] L. E. Strong, L. L. Kiessling, *J. Am. Chem. Soc.* **1999**, *121*, 6193.
[155] D. D. Manning, L. E. Strong, X. Hu, P. J. Beck, L. L. Kiessling, *Tetrahedron* **1997**, *53*, 11937.
[156] H. Arimoto, K. Nishimura, T. Kinumi, I. Hayakawa, D. Uemura, *Chem. Commun.* **1999**, 1361.
[157] V. C. Gibson, E. L. Marshall, M. North, D. A. Robson, P. J. Williams, *Chem. Commun.* **1997**, 1095.
[158] K. H. Mortell, R. V. Weatherman, L. L. Kiessling, *J. Am. Chem. Soc.* **1996**, *118*, 2297.
[159] D. M. Lynn, B. Mohr, R. H. Grubbs, *J. Am. Chem. Soc.* **1998**, *120*, 1627.
[160] E. L. Dias, S. T. Nguyen, R. H. Grubbs, *J. Am. Chem. Soc.* **1997**, *119*, 3887.
[161] C. Fraser, R. H. Grubbs, *Macromolecules* **1995**, *28*, 7248.
[162] K. H. Mortell, M. Gingras, L. L. Kiessling, *J. Am. Chem. Soc.* **1994**, *116*, 10253.
[163] S. Iyer, S. Rele, G. Grasaa, S. Nolan, E. L. Chaikof, *Chem. Commun.* **2003**, 1518.
[164] D. A. Mann, M. Kanai, D. J. Maly, L. L. Kiessling, *J. Am. Chem. Soc.* **1998**, *120*, 10575.
[165] E. J. Gordon, W. J. Sanders, L. L. Kiessling, *Nature* **1998**, *392*, 30.
[166] C. W. Cairo, J. E. Gestwicki, M. Kanai, L. L. Kiessling, *J. Am. Chem. Soc.* **2002**, *124*, 1615.
[167] J. E. Gestwicki, C. W. Cairo, L. E. Strong, K. A. Oetjen, L. L. Kiessling, *J. Am. Chem. Soc.* **2002**, *124*, 14922.
[168] S. L. Schreiber, *Science* **2000**, *287*, 1964.
[169] W. J. Hoekstra, B. L. Poulter, *Curr. Med. Chem.* **1998**, *5*, 195.
[170] S. R. Wilson, A. W. Czarnik, *Combinatorial Chemistry: Synthesis and Applications*, Wiley, New York, **1997**.
[171] K. C. Nicolaou, J. A. Pfefferkorn, *Biopolymers* **2001**, *60*, 171.
[172] J. A. Ellman, M. A. Gallop, *Curr. Opin. Chem. Biol.* **1998**, *2*, 317.
[173] M. A. Shogren-Knaak, P. J. Alaimo, K. M. Shokat, *Annu. Rev. Cell Dev. Biol.* **2001**, *17*, 405.
[174] V. Wittmann, S. Seeberger, *Angew. Chem.* **2000**, *112*, 4508; *Angew. Chem. Int. Ed.* **2000**, *39*, 4348.
[175] L. L. Kiessling, N. L. Pohl, *Chem. Biol.* **1996**, *3*, 71.
[176] W. P. Jencks, *Proc. Natl. Acad. Sci. USA* **1981**, *78*, 4046.
[177] P. I. Kitov, J. M. Sadowska, G. Mulvey, G. D. Armstrong, H. Ling, N. S. Pannu, R. J. Read, D. R. Bundle, *Nature* **2000**, *403*, 669.
[178] Z. Zhang, E. A. Merritt, M. Ahn, C. Roach, Z. Hu, C. L. M. J. Verlinde, W. G. J. Hol, E. Fan, *J. Am. Chem. Soc.* **2002**, *124*, 12991.
[179] E. Fan, Z. Zhang, W. E. Minke, Z. Hou, C. L. M. J. Verlinde, W. G. J. Hol, *J. Am. Chem. Soc.* **2000**, *122*, 2663.
[180] A. L. Banerjee, D. Eiler, B. C. Roy, X. Jia, M. K. Haldar, S. Mallik, D. K. Srivastava, *Biochemistry* **2005**, *44*, 3211.
[181] S. Howorka, J. Nam, H. Bayley, D. Kahne, *Angew. Chem.* **2004**, *116*, 860; *Angew. Chem. Int. Ed.* **2004**, *43*, 842.
[182] M. Mammen, G. Dahmann, G. M. Whitesides, *J. Med. Chem.* **1995**, *38*, 4179.
[183] M. P. Sheetz, D. P. Felsenfeld, C. G. Galbraith, *Trends Cell Biol.* **1998**, *8*, 51.
[184] M. A. Schwartz, *Trends Cell Biol.* **2001**, *11*, 466.

 © 2006 Wiley-VCH Verlag GmbH & Co. KGaA, Weinheim

[185] S. M. Schoenwaelder, K. Burridge, *Curr. Opin. Cell Biol.* **1999**, *11*, 274.
[186] D. Bouvard, C. Brakebusch, E. Gustafsson, A. Aszódi, T. Bengtsson, A. Berna, R. Fässler, *Circ. Res.* **2001**, *89*, 211.
[187] R. O. Hynes, *Cell* **2002**, *110*, 673.
[188] R. H. Li, N. Mitra, H. Gratkowski, G. Vilaire, R. Litvinov, C. Nagasami, J. W. Weisel, J. D. Lear, W. F. DeGrado, J. S. Bennett, *Science* **2003**, *300*, 795.
[189] D. M. Spencer, T. J. Wandless, S. L. Schreiber, G. R. Crabtree, *Science* **1993**, *262*, 1019.
[190] I. A. Graef, F. Chen, A. Kuo, G. R. Crabtree, *Cell* **2001**, *105*, 863.
[191] A. S. Yap, W. M. Brieher, M. Pruschy, B. M. Gumbiner, *Curr. Biol.* **1997**, *7*, 308.
[192] S. K. Muthuswamy, M. Gilman, J. S. Brugge, *Mol. Cell. Biol.* **1999**, *19*, 6845.
[193] J. F. Amara, T. Clackson, V. M. Rivera, T. Guo, T. Keenan, S. Natesan, R. Pollock, W. Yang, N. L. Courage, D. A. Holt, M. Gilman, *Proc. Natl. Acad. Sci. USA* **1997**, *94*, 10618.
[194] P. A. Clemons, B. G. Gladstone, A. Seth, E. D. Chao, M. A. Foley, S. L. Schreiber, *Chem. Biol.* **2002**, *9*, 49.
[195] T. Hato, N. Pampori, S. J. Shattil, *J. Cell Biol.* **1998**, *141*, 1685.
[196] N. J. Boudreau, P. L. Jones, *Biochem. J.* **1999**, *339*, 481.
[197] E. R. Welsh, D. A. Tirrell, *Biomacromolecules* **2000**, *1*, 23.
[198] D. G. Stupack, E. Li, S. A. Silletti, J. A. Kehler, R. L. Geahlen, K. Hahn, G. R. Nemerow, D. A. Cheresh, *J. Cell Biol.* **1999**, *144*, 777.
[199] S. R. George, B. F. O'Dowd, S. P. Lee, *Nat. Rev. Drug Discovery* **2002**, *1*, 808.
[200] M. Mellado, J. Rodríguez-Frade, S. Mañes, C. Martínez-A, *Annu. Rev. Immunol.* **2001**, *19*, 397.
[201] R. H. Kramer, J. W. Karpen, *Nature* **1998**, *395*, 710.
[202] G. D. Glick, P. L. Toogood, D. C. Wiley, J. J. Skehel, J. R. Knowles, *J. Biol. Chem.* **1991**, *266*, 23660.
[203] B. P. England, P. Balasubramanian, I. Uings, S. Bethell, M.-J. Chen, P. J. Schatz, Q. Yin, Y.-F. Chen, E. A. Whitehorn, A. Tsavaler, C. L. Martens, R. W. Barrett, M. McKinnon, *Proc. Natl. Acad. Sci. USA* **2000**, *97*, 6862.
[204] Y. He, J. W. Karpen, *Biochemistry* **2001**, *40*, 286.
[205] J. M. Paar, N. T. Harris, D. Holowka, B. Baird, *J. Immunol.* **2003**, *169*, 856.
[206] D. Chan, L. Gera, J. Stewart, B. Helfrich, M. Verella-Garcia, G. Johnson, A. Baron, J. Yang, J. P. Bunn, *Proc. Natl. Acad. Sci. USA* **2002**, *99*, 4608.
[207] R. G. Bhushan, S. K. Sharma, Z. Xie, D. J. Daniels, P. S. Portoghese, *J. Med. Chem.* **2004**, *47*, 2969.
[208] M. Miyazaki, H. Kodama, I. Fujita, Y. Hamasaki, S. Miyazaki, M. Kondo, *J. Biochem.* **1995**, *117*, 489.
[209] K. Yano, S. Kimura, Y. Imanishi, *Eur. J. Pharm. Sci.* **1998**, *7*, 41.
[210] L. He, J. Fong, M. von Zastrow, J. L. Whistler, *Cell* **2002**, *108*, 271.
[211] M. L. Dustin, *J. Clin. Invest.* **2002**, *109*, 155.
[212] W. W. A. Schamel, I. Arechaga, R. M. Risueno, H. M. van Santen, P. Cabezas, C. Risco, J. M. Valpuesta, B. Alarcon, *J. Exp. Med.* **2005**, *202*, 493.
[213] J. J. Boniface, J. D. Rabinowitz, C. Wülfing, J. Hampl, Z. Reich, J. D. Altman, R. M. Kantor, C. Beeson, H. M. McConnell, M. M. Davis, *Immunity* **1998**, *9*, 459.
[214] J. R. Cochran, D. Aivazian, T. O. Cameron, L. J. Stern, *Trends Biochem. Sci.* **2001**, *26*, 304.
[215] J. R. Cochran, L. J. Stern, *Chem. Biol.* **2000**, *7*, 683.
[216] S. Miyamoto, S. K. Akiyama, K. M. Yamada, *Science* **1995**, *267*, 883.
[217] J. A. Hubbell, *Curr. Opin. Biotechnol.* **1999**, *10*, 123.
[218] B. Lowin-Kropf, V. S. Shapiro, A. Weiss, *J. Cell Biol.* **1998**, *140*, 861.
[219] C. R. F. Monks, B. A. Freiberg, H. Kupfer, N. Sciaky, A. Kupfer, *Nature* **1998**, *395*, 82.
[220] J. Stock, M. Levit, *Curr. Biol.* **2000**, *10*, R11.
[221] G. L. Hazelbauer, H. C. Berg, P. Matsumura, *Cell* **1993**, *73*, 15.
[222] J. J. Falke, R. B. Bass, S. L. Butler, S. A. Chervitz, M. A. Danielson, *Annu. Rev. Cell Dev. Biol.* **1997**, *13*, 457.
[223] R. Jasuja, Y. Lin, D. R. Trentham, S. Khan, *Proc. Natl. Acad. Sci. USA* **1999**, *96*, 11346.
[224] A. M. Stock, *Proc. Natl. Acad. Sci. USA* **1999**, *96*, 10945.
[225] J. P. Armitage, C. J. Dorman, K. Hellingwerf, R. Schmitt, D. Summers, B. Holland, *Mol. Microbiol.* **2003**, *47*, 583.
[226] X. Feng, J. W. Baumgartner, G. L. Hazelbauer, *J. Bacteriol.* **1997**, *179*, 6714.
[227] B. A. Mello, Y. Tu, *Proc. Natl. Acad. Sci. USA* **2003**, *100*, 8223.
[228] J. E. Gestwicki, A. C. Lamanna, R. M. Harshey, L. L. McCarter, L. L. Kiessling, J. Adler, *J. Bacteriol.* **2000**, *182*, 6499.
[229] K. K. Kim, H. Yokota, S. H. Kim, *Nature* **1999**, *400*, 787.
[230] J. E. Gestwicki, C. W. Cairo, D. A. Mann, R. M. Owen, L. L. Kiessling, *Anal. Biochem.* **2002**, *305*, 149.
[231] V. Sourjik, *Trends Microbiol.* **2004**, *12*, 569.
[232] R. S. Syed, S. W. Reid, C. Li, J. C. Cheetham, K. H. Aoki, B. Liu, H. Zhan, T. D. Osslund, A. J. Chirino, J. Zhang, J. Finer-Moore, S. Elliott, K. Sitney, B. A. Katz, D. J. Matthews, J. J. Wendoloski, J. Egrie, R. M. Stroud, *Nature* **1998**, *395*, 511.
[233] J. E. Dueber, B. J. Yeh, R. P. Bhattacharyya, W. A. Lim, *Curr. Opin. Struct. Biol.* **2004**, *14*, 690.
[234] M. Beyermann, S. Rothemund, N. Heinrich, K. Fecher, J. Furkert, M. Dathe, R. Winter, E. Krause, M. Bienert, *J. Biol. Chem.* **2000**, *275*, 5702.
[235] D. Qin, R. Sullivan, W. F. Berkowitz, R. Bittman, S. A. Rotenberg, *J. Med. Chem.* **2000**, *43*, 1413.
[236] S. H. Park, A. Zarrinpar, W. A. Lim, *Science* **2003**, *299*, 1061.
[237] P. Hasler, M. Zouali, *FASEB J.* **2001**, *15*, 2085.
[238] H. M. Dintzis, R. Z. Dintzis, B. Vogelstein, *Proc. Natl. Acad. Sci. USA* **1976**, *73*, 3671.
[239] R. Z. Dintzis, B. Vogelstein, H. M. Dintzis, *Proc. Natl. Acad. Sci. USA* **1982**, *79*, 884.
[240] B. Sulzer, A. S. Perelson, *Mol. Immunol.* **1997**, *34*, 63.
[241] P. K. A. Mongini, C. A. Blessinger, P. F. Highlet, J. K. Inman, *J. Immunol.* **1992**, *148*, 3892.
[242] G. Ragupathi, L. Howard, S. Capello, R. R. Koganty, D. Qiu, B. M. Longnecker, M. A. Reddish, K. O. Lloyd, P. O. Livingston, *Cancer Immunol. Immunother.* **1999**, *48*, 1.
[243] R. Z. Dintzis, M. Okajima, M. H. Middleton, G. Greene, H. M. Dintzis, *J. Immunol.* **1989**, *143*, 1239.
[244] R. P. McEver, K. L. Moore, R. D. Cummings, *J. Biol. Chem.* **1995**, *270*, 11025.
[245] S. R. Hasslen, U. H. von Andrian, E. C. Butcher, R. D. Nelson, S. L. Erlandsen, *Histochem. J.* **1995**, *27*, 547.
[246] S. R. Hasslen, A. R. Burns, S. I. Simon, W. Smith, K. Starr, A. N. Barclay, S. A. Michie, R. D. Nelson, S. L. Erlandsen, *J. Histochem. Cytochem.* **1996**, *44*, 1115.
[247] S. D. Rosen, *Annu. Rev. Immunol.* **2004**, *22*, 129.
[248] E. E. Simanek, G. J. McGarvey, J. A. Jablonowski, C.-H. Wong, *Chem. Rev.* **1998**, *98*, 833.
[249] G. Thoma, R. O. Duthaler, J. L. Magnani, J. T. Patton, *J. Am. Chem. Soc.* **2001**, *123*, 10113.
[250] G. Thoma, J. T. Patton, J. L. Magnani, B. Ernst, R. Ohrlein, R. O. Duthaler, *J. Am. Chem. Soc.* **1999**, *121*, 5919.
[251] D. D. Manning, X. Hu, P. Beck, L. L. Kiessling, *J. Am. Chem. Soc.* **1997**, *119*, 3161.
[252] W. J. Sanders, E. J. Gordon, O. Dwir, P. J. Beck, R. Alon, L. L. Kiessling, *J. Biol. Chem.* **1999**, *274*, 5271.
[253] R. Stahn, H. Schäfer, F. Kernchen, J. Schreiber, *Glycobiology* **1998**, *8*, 311.
[254] R. M. Owen, J. E. Gestwicki, T. Young, L. L. Kiessling, *Org. Lett.* **2002**, *4*, 2295.

 © 2006 Wiley-VCH Verlag GmbH & Co. KGaA, Weinheim

[255] E. J. Gordon, J. E. Gestwicki, L. E. Strong, L. L. Kiessling, *Chem. Biol.* **2000**, *7*, 9.
[256] E. J. Gordon, L. E. Strong, L. L. Kiessling, *Bioorg. Med. Chem. Lett.* **1998**, *8*, 1293.
[257] P. Mowery, Z. Q. Yang, E. J. Gordon, O. Dwir, A. G. Spencer, R. Alon, L. L. Kiessling, *Chem. Biol.* **2004**, *11*, 725.
[258] E. J. Gordon, L. E. Strong, L. L. Kiessling, *Bioorg. Med. Chem.* **1998**, *6*, 1293.
[259] M. Mourez, R. S. Kane, J. Mogridge, S. Metallo, P. Deschatelets, B. R. Sellman, G. M. Whitesides, R. J. Collier, *Nat. Biotechnol.* **2001**, *19*, 958.
[260] L. Bracci, L. Lozzi, A. Pini, B. Lelli, C. Falciani, N. Niccolai, A. Bernini, A. Spreafico, P. Soldani, P. Neri, *Biochemistry* **2002**, *41*, 10194.
[261] G. W. Byrne, A. Schwarz, J. R. Fesi, P. Birch, A. Nepomich, I. Bakaj, M. A. Velardo, C. Jiang, A. Manzi, H. Dintzis, L. E. Diamond, J. S. Logan, *Bioconjugate Chem.* **2002**, *13*, 571.
[262] Y. Minamoto, T. Hato, S. Nakatani, S. Fujita, *Thromb. Haemost.* **1996**, *76*, 1072-1079.
[263] J. E. Gestwicki, L. L. Kiessling, unpublished results.

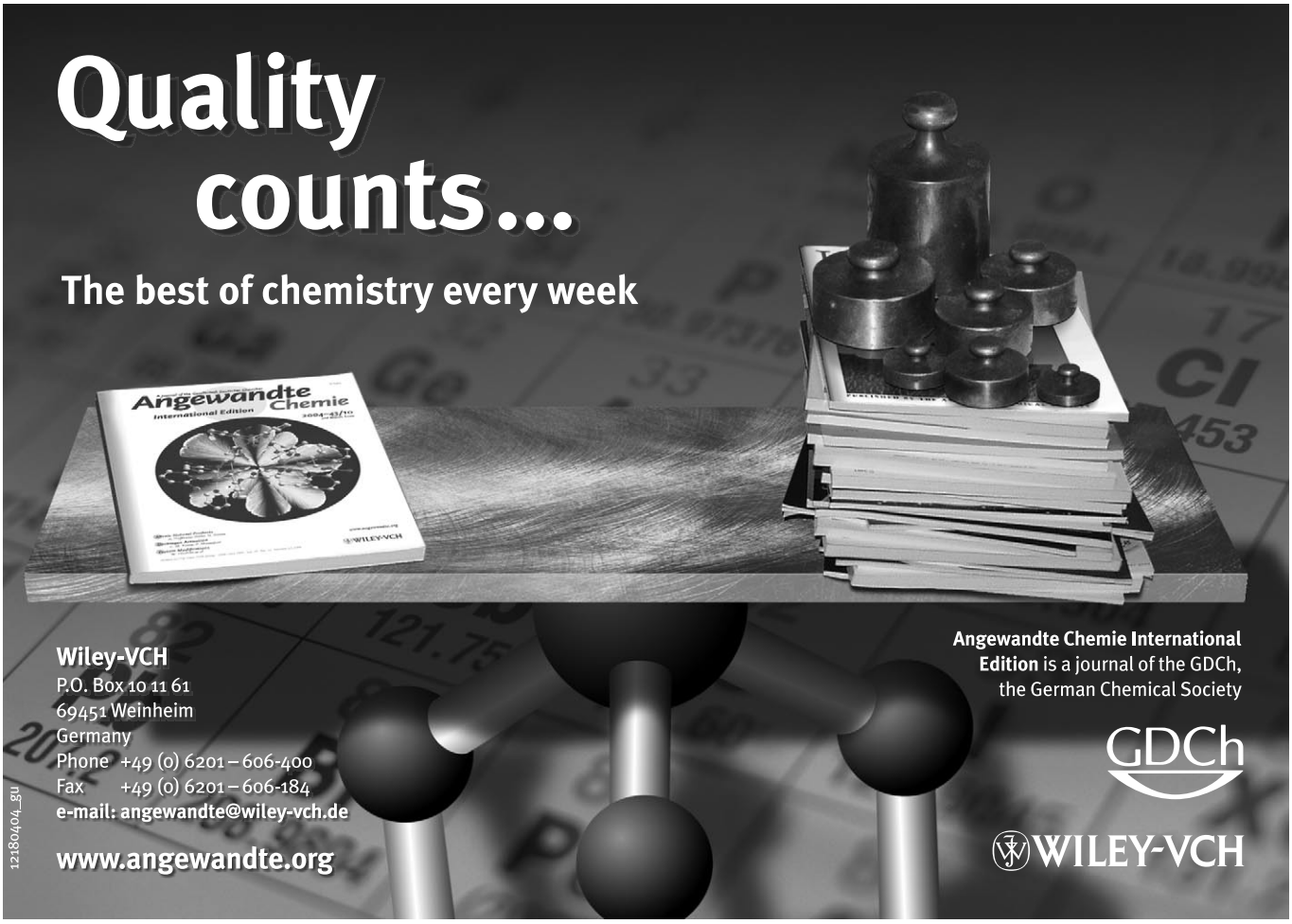

 © 2006 Wiley-VCH Verlag GmbH & Co. KGaA, Weinheim

Communications

DOI: 10.1002/anie.200503202

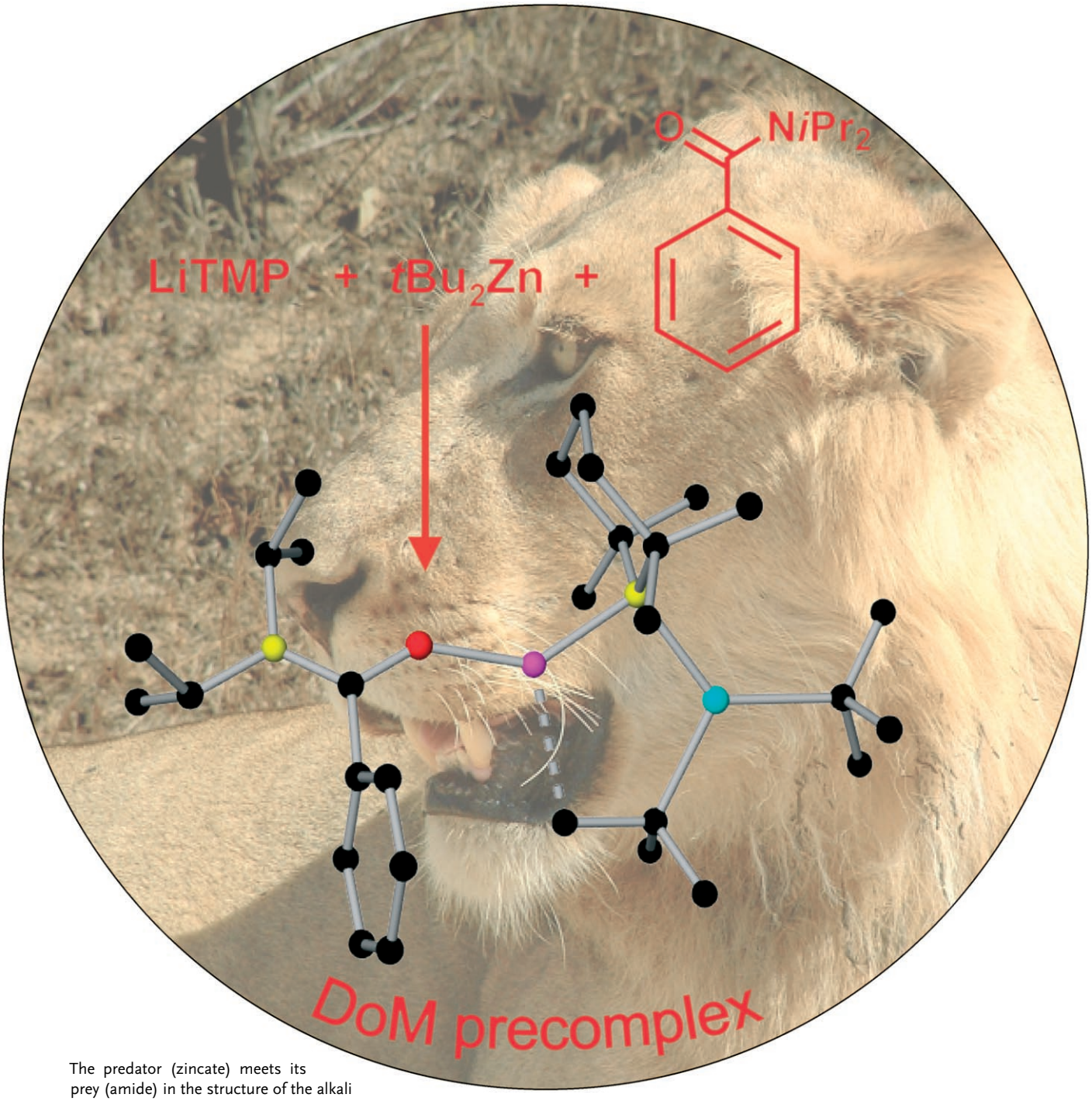

The predator (zincate) meets its prey (amide) in the structure of the alkali metal zincate shown. The compound includes an aromatic amide "precomplex" for directed *ortho*-metalation (DoM) that exists prior to the devouring (*ortho*-zincation) of the amide by the hungry zincate. For more information on this chemical feast see the Communication by R. E. Mulvey and co-workers on the following pages.

WILEY InterScience DISCOVER SOMETHING GREAT
© 2006 Wiley-VCH Verlag GmbH & Co. KGaA, Weinheim

ortho-Metalation (1)

DOI: 10.1002/anie.200503202

Pre-Metalation Structural Insights into the Use of Alkali-Metal-Mediated Zincation for Directed *ortho*-Metalation of a Tertiary Aromatic Amide**

*William Clegg, Sophie H. Dale, Eva Hevia, Gordon W. Honeyman, and Robert E. Mulvey**

We recently coined the phrase "alkali-metal-mediated zincation" to describe a special type of metalation reaction which is unequivocally a zincation (a zinc–hydrogen interconversion) but one which proceeds only in the presence of an alkali-metal compound, in other words a mixed-metal-induced "synergic metalation". This effect was demonstrated[1] by the success of the sodium dialkyl amidozincate reagent [(tmeda)Na(μ-*t*Bu)(μ-tmp)Zn(*t*Bu)] (**1**) in metalating benzene to generate the phenyl product [(tmeda)Na(μ-Ph)(μ-tmp)Zn(*t*Bu)] (**2**) and the failure of tBu_2Zn in the absence of NaTMP to react with benzene (Scheme 1: TMEDA is *N*,*N*,*N*′,*N*′-tetramethylethylenediamine; TMP is 2,2,6,6-tetramethylpiperidide). With zincate chemistry attracting appreciable attention at present,[2] it is not surprising that other researchers are discovering examples of alkali-metal-mediated zincation too, though usually the reactions reported are not explicitly interpreted in terms of alkali-metal-mediated zincation. In a case where the synergic element to the metalating ability of a related lithium TMP–zincate reagent is fully recognized, Kondo states that "precomplexation of lithium TMP and tBu_2Zn is essential for successful metalation".[3] While this important reagent, empirically formulated by Kondo as **3**, has been established as a highly chemoselective base for directed *ortho*-metalation of alkyl benzoates and dialkyl benzamides, hitherto little was known about this zincate in its own right except for a ^{13}C NMR spectrum recorded in $[D_8]$THF solution. Herein we remedy this situation by presenting detailed structural information. Thus, from crystallographic data we are able to reveal one possible structure of the reagent itself in [(thf)Li(μ-tmp)(μ-*t*Bu)Zn(*t*Bu)] (**4**), which contains the three components of the experimental solution mixture, in a result that adds considerable support to Kondo's precomplexation proposition. In a significant implication for the mechanism of directed *ortho*-metalation[4] generally and in TMP–zincate chemistry specifically, we also report the synthesis and crystal structure of the tertiary aromatic amide-complexed [{(*i*Pr)$_2$NC(Ph)(=O)}Li(μ-tmp)(μ-*t*Bu)Zn(*t*Bu)] (**5**), which can be formally regarded as a possible representative complex of the "complex-induced proximity effect" type[5] involved in the *ortho*-zincation of *N*,*N*-diisopropylbenzamide.[6]

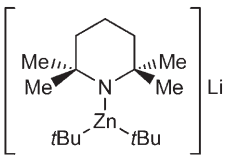

3

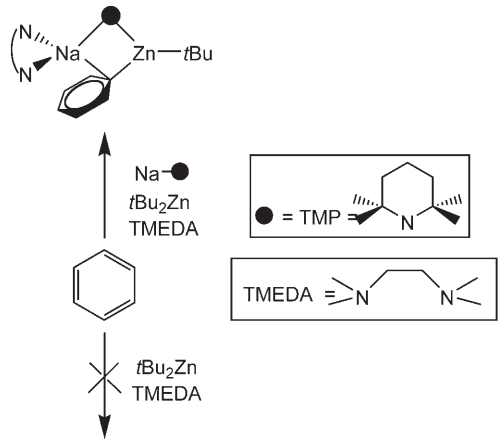

Scheme 1. Illustration of the mixed-metal synergic effect required for the zincation of benzene.

In Kondo and co-workers' original preparation of **3**,[3] tBu_2Zn is added to lithium TMP in neat THF solution at −78 °C, and the mixture warmed to room temperature then utilized as is (in situ) in a metalation application with a protic substrate. Under these conditions, the polar solvent THF undoubtedly solvates lithium, and the "precomplex" **3** (which strictly should include THF in its formulation) is most certainly highly soluble in the vast excess of polar solvent. To reduce solubility and increase the opportunity for crystal growth, we adapted this procedure by performing the reaction in bulk nonpolar hydrocarbon (hexane) solution to which only one molar equivalent (per lithium) of THF was added. Room temperature was maintained throughout until the reaction solution was placed in a freezer at −20 °C. This adapted procedure successfully produced colorless crystalline **4**, which itself is highly soluble in hydrocarbon solvents even though its lithium center is solvated by only one THF ligand. The composition of **4** was first deduced from solution NMR spectroscopic studies (see Experimental Section). Following this same procedure but replacing THF by *N*,*N*-diisopropylbenzamide afforded colorless crystals of **5**, which were also characterized spectroscopically (see Experimental Section).

Determined by X-ray crystallography, the strikingly similar molecular structures of **4**[7] (Figure 1) and **5**[8] (Figure 2) could be described as ion-contacted zincates. Comprising one TMP and two *t*Bu ligands, the distorted trigonal planar zincate anion contacts the lithium cation primarily through the TMP nitrogen atom (the Zn-N-Li bridge is modestly shorter at the lithium end by a mean value

[*] Dr. E. Hevia, Dr. G. W. Honeyman, Prof. R. E. Mulvey
WestCHEM
Department of Pure and Applied Chemistry
University and Strathclyde
Glasgow, G1 1XL (UK)
Fax: (+44) 141-552-0876
E-mail: r.e.mulvey@strath.ac.uk
Prof. W. Clegg, Dr. S. H. Dale
School of Natural Sciences (Chemistry)
University of Newcastle
Newcastle upon Tyne, NE1 7RU (UK)

[**] This work was supported by the UK Engineering and Physical Science Research Council through grant award No. GR/R81183/01 and by the EU through a Marie Curie Fellowship to E.H.

 © 2006 Wiley-VCH Verlag GmbH & Co. KGaA, Weinheim

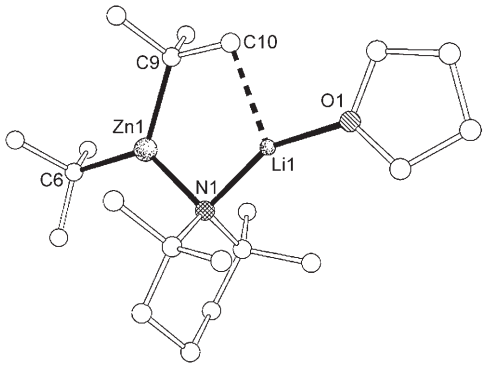

Figure 1. Molecular structure of **4** (hydrogen atoms and minor disorder component are omitted for clarity). The agostic contact is denoted by a hatched line. Selected bond lengths [Å] and angles [°]: Zn1–N1 2.0741(19), Zn1–C6 2.058(2), Zn1–C9 2.072(2), Li1–N1 1.973(5), Li1–O1 1.921(5), Li1–C10 2.410(6); N1-Zn1-C6 128.03(9), N1-Zn1-C9 111.72(9), C6-Zn1-C9 120.25(10), N1-Li1-O1 153.2(3), Zn1-N1-Li1 100.27(16).

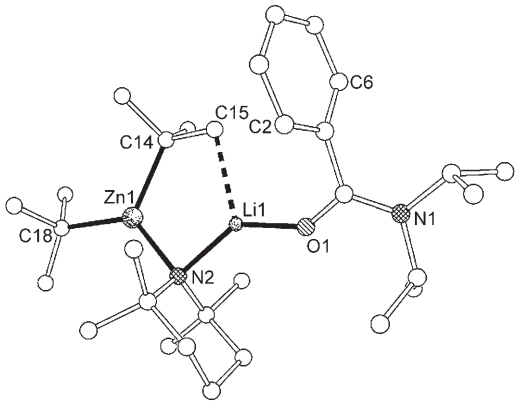

Figure 2. Molecular structure of **5** (hydrogen atoms are omitted for clarity). The agostic contact is denoted by a hatched line. Selected bond lengths [Å] and angles [°]: Zn1–N2 2.0741(14), Zn1–C14 2.0819(17), Zn1–C18 2.0705(17), Li1–N2 1.968(3), Li1–O1 1.851(3), Li1–C15 2.425(4); C14-Zn1-C18 118.57(7), C14-Zn1-N2 112.90(6), C18-Zn1-N2 128.44(6), O1-Li1-N2 138.88(19), Zn1-N2-Li1 97.59(11).

of 0.103 Å over both structures). However, there is a weak secondary "agostic" contact,[9] Li1···C10 (2.410(6) Å) in **4** and Li1···C15 (2.425(4) Å) in **5**, involving one Me arm of the *t*Bu bridge (the second *t*Bu ligand is terminally bound to the zinc center), to close a five-membered (LiNZnCC) ring. To engineer this contact the μ-*t*Bu ligand has to tilt perceptibly towards lithium as gauged by the narrowing of the C9-Zn1-N1 (111.72(9)° in **4**) and C14-Zn1-N2 (112.90(6)° in **5**) bond angles from those involving the terminal *t*Bu-Zn bond (i.e., C6-Zn1-N1 in **4**, 128.03(9)°; C18-Zn1-N2 in **5**, 128.44(6)°). Neutral oxygen ligands, THF in **4** and the benzamide in **5**, attach terminally to the lithium center to complete the structures, with the benzamide approaching more closely (Li1–O1, 1.921(5) Å in **4**, 1.851(3) Å in **5**) in keeping with the highly basic nature of amide oxygen atoms. The structure of the sodium zincate **1** bears a strong resemblance to those of **4** and **5**, though it may be significant that the corresponding Na···C(H_3) agostic contact which closes a (NaNZnCC) ring is substantially longer at 2.750(10) Å and that the corresponding tilt angle is wider at 116.9(3)°. A more fundamental distinction of **1** is the bidentate chelation of sodium by TMEDA.

Precedents for crystallographically characterized structures with metal-coordinated, neutral, tertiary aromatic amide ligands appear limited to the simple trialkylgallium [*t*Bu_3Ga{O=C(Ph)NMe_2}].[10] This situation means that there are no examples at all of crystal structures in which these neutral ligands[11] coordinate to an organolithium reagent such as *n*BuLi or *s*BuLi. Structures of this composition could be viewed as the substrate–organometallic precomplexes that are thought to direct (or help to direct in combination with the inductive, acidifying effect of the electron-withdrawing substituents) subsequent *ortho*-metalation of the substrate, that is Directed *ortho*-Metalation (DoM) precomplexes. There is good IR spectroscopic and kinetic evidence that substrate–alkyllithium precomplexes also play a prominent role in the mechanisms of α-lithiation reactions of substrates containing similar amide functional groups.[12] Assuming DoM precomplexes are also involved in alkali-metal-mediated zincation, then the structure of **5** can be considered a valuable guide to the nature of a DoM precomplex itself or at least to a key intermediate in the reaction pathway to *ortho*-zincated *N,N*-diisopropylbenzamide.[6] Experimentally we explored this possibility by subjecting a solution of **5** (on the basis of the appearance of NMR spectroscopic data its structure remains intact when dissolved) to one molar equivalent of TMEDA, and the result was immediate *ortho*-zincation, manifested in the unexpected bis(amide) [(tmeda)Li{2-[1-C(O)N(*i*$Pr)_2$]C_6H_4}$_2$Zn(*t*Bu)].[6] It is tempting to state that this is irrefutable evidence that **5** actually is a genuine DoM precomplex; however, doubts must remain in the absence of corroborative kinetic information as Collum and co-workers have cautioned through a thought-provoking study of the *ortho*-lithiation of anisole by *n*BuLi/TMEDA that suggests that methoxy–lithium interactions are negligible in the rate-limiting transition structure.[13]

Interpreting **5** as a DoM precomplex, the structure establishes that the first point of coordination of the substrate remains the alkali metal (as it is in conventional directed *ortho*-lithiation) even though the ensuing metalation is strictly a zincation. This fact alone justifies describing such bimetallic deprotonations as alkali-metal-mediated zincations. In conventional directed *ortho*-lithiation, the rate of lithiation is fastest if the amide N–C=O group and the Ph ring approach coplanarity,[13,14] a disposition that allows the lithium to interact strongly with the oxygen atom, and its attached carbanion to lie close to the *ortho* hydrogen atom about to be removed. The situation in alkali-metal-mediated zincation must be fundamentally different as it is zinc, not lithium, which ultimately ends up bound to an *ortho* carbon atom. As a working hypothesis based on the clues provided by the elucidation of the structures of **4** and **5**, two distinct transition states on the path to *ortho*-metalation can be envisaged (Scheme 2). The first involves a nine-membered (LiOCCCHCZnN) ring and leads to alkane elimination; whereas, the second involves a seven-membered (LiOCCCHN) ring and leads to amine elimination. On balance, the first mechanism looks more plausible as the

 © 2006 Wiley-VCH Verlag GmbH & Co. KGaA, Weinheim

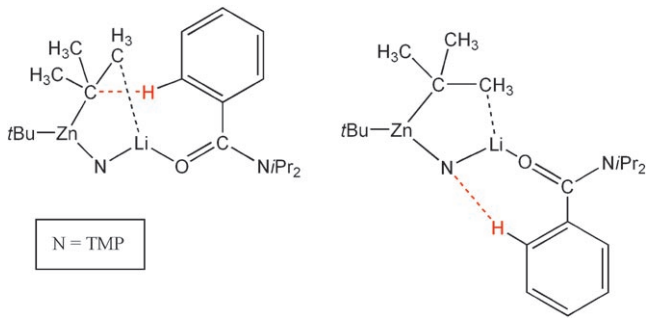

Scheme 2. Two possible alternative transition structures involved in *ortho*-zincation of the aromatic amide by the LiTMP–zincate base. The agostic contact is denoted by a hatched black line and the developing C–H and N–H bonds are denoted by hatched red lines.

TMP binds strongly to both lithium and zinc in **4** and **5**, in contrast to the μ-*t*Bu ligand which binds strongly to zinc alone, is more sterically accessible, and is oriented towards the Ph ring through the weak, but significant agostic Li···C(H_3) interaction (which appears to remain intact in **5** in solution). Supporting this view, the μ-*t*Bu ligand lies closer than the TMP nitrogen atom to the *ortho* carbon atoms in **5** in which the shortest contact involves the agostic Me group (C15···C6, 3.590(3) Å), not the tertiary carbon (C14···C6, 5.109(3) Å), though the shortest contact to a nitrogen atom (N2···C2, 5.526(3) Å) is longer still. However, such comparative reasoning must be qualified by the fact that **5** requires TMEDA to promote metalation. Thus the implication must be that addition of TMEDA to **5**, in increasing the coordination number and steric bulk about lithium, must push the Ph group even closer towards the μ-*t*Bu ligand. While this might reasonably explain the initial elimination of alkane, it would appear that subsequently amine is also eliminated as the final product is the bis(benzamide) [(tmeda)Li{2-[1-C(O)N(*i*Pr)$_2$]C$_6$H$_4$}$_2$Zn(*t*Bu)].[6] Clearly, these mixed-metal, mixed-ligand bases are highly complicated systems and much mechanistic/structural work remains to be done before the intricacies of their chemistry can be fully unraveled.

Experimental Section

4: A solution of *t*Bu$_2$Zn (0.36 g, 2 mmol) in hexane (5 mL) was transferred by cannula to a solution of LiTMP [prepared in situ by reaction of BuLi (1.25 mL of a 1.6 M solution in hexane, 2 mmol) and TMP(H) (0.34 mL, 2 mmol)]. The colorless solution was allowed to stir for 10 min and THF (0.16 mL, 2 mmol) was then introduced. The solution was concentrated by removing some solvent under vacuum and placed in the freezer (−20 °C). A crop of colorless crystals was deposited overnight (0.54 g, 67 %). ^{1}H NMR (400 MHz, 25 °C, [D$_8$]THF): δ = 3.69 (m, 4H, OCH_2, THF), 1.79 (m, 4H, CH_2, THF), 1.66 (m, 2H, H$_\gamma$ TMP), 1.20 (m, 4H, H$_\beta$, TMP), 1.01 (s, 12H, CH_3-TMP), 0.90 ppm (s, 18H , CH_3, *t*Bu). ^{13}C{^{1}H} NMR (100.63 MHz, 25 °C, [D$_8$]THF): δ = 68.39(OCH_2, THF), 53.10 (C$_\alpha$, TMP), 41.57 (C$_\beta$, TMP), 36.39 (CH_3, *t*Bu), 34.87 (CH_3-TMP), 26.39 (CH_2,THF), 22.02 (C(CH_3)$_3$, *t*Bu), 20.40 ppm (C$_\gamma$ TMP). ^{7}Li NMR (155.50 MHz, 25 °C, [D$_8$]THF, reference LiCl in D$_2$O at 0.00 ppm): δ = 2.86 ppm.

5: Following the same procedure described above for **4**, a solution of *t*Bu$_2$Zn (0.36 g, 2 mmol) in hexane (5 mL) was transferred by cannula to a solution of LiTMP (2 mmol). The colorless solution was allowed to stir for 10 min and then *N*-diisopropylbenzamide (0.41 g, 2 mmol) was introduced. The solution changed from colorless to bright yellow. The solution was concentrated by removing some solvent under vacuum and placed in the freezer (−20 °C). A crop of colorless crystals was deposited overnight (0.79 g, 74 %). FT-IR (nujol): $\tilde{\nu}$ = 1595 cm^{-1}($\nu_{C=O}$). ^{1}H NMR (400 MHz, 25 °C, C$_6$D$_6$): δ = 7.04 (m, 3H, H_{meta} and H_{para} Ph), 6.87 (m, 2H, H_{ortho} Ph), 3.42 (m, 1H, C*H*, *i*Pr), 3.01 (m, 1H, C*H*, *i*Pr), 1.83 (m, 2H, H$_\gamma$ TMP), 1.59 (s, 9H, *t*Bu), 1.36, 1.34 (2s [partially overlapped], 15H, 9H of *t*Bu and 6H of CH_3-TMP), 1.29 (d, 6H , CH_3, *i*Pr), 1.15 (m, 4H, H$_\beta$, TMP), 1.10 (s, 6H, CH_3-TMP), 0.51 ppm (d, 6H , CH_3, *i*Pr). ^{13}C{^{1}H} NMR (100.63 MHz, 25 °C, C$_6$D$_6$): δ = 173.13 (*C*=O), 137.60 (C_{ipso}), 130.23 (C_{para}), 129.50 (C_{meta}), 125.33 (C_{ortho}), 52.60 (*C*H, *i*Pr) 52.50 (C$_\alpha$, TMP), 46.90 (*C*H, *i*Pr), 40.11 (C$_\beta$, TMP), 36.64 (*C*H$_3$, *t*Bu), 35.65, 35.26 (*C*H$_3$, *t*Bu and *C*H$_3$-TMP), 34.31 (*C*H$_3$-TMP), 20.24 (*C*(CH$_3$)$_3$, *t*Bu), 20.74 (*C*H$_3$, *i*Pr), 20.58 (*C*(CH$_3$)$_3$, *t*Bu), 20.31 (C$_\gamma$ TMP), 20.16 ppm (*C*H$_3$, *i*Pr). ^{7}Li NMR (155.50 MHz, 25 °C, C$_6$D$_6$, reference LiCl in D$_2$O at 0.00 ppm): δ = 1.33 ppm.

Received: September 8, 2005
Revised: November 8, 2005
Published online: March 2, 2006

Keywords: alkali metals · amides · complex-induced proximity effect · metalation · zinc

[1] P. C. Andrikopoulos, D. R. Armstrong, H. R. L. Barley, W. Clegg, S. H. Dale, E. Hevia, G. W. Honeyman, A. R. Kennedy, R. E. Mulvey, *J. Am. Chem. Soc.* **2005**, *127*, 6184.

[2] For recent examples see M. Westerhausen, T. Bollwein, N. Makropoulos, H. Piotrowski, *Inorg. Chem.* **2005**, *44*, 6439; F. F. Kneisel, M. Dochnahl, P. Knochel, *Angew. Chem.* **2004**, *116*, 1032; *Angew. Chem. Int. Ed.* **2004**, *43*, 1017; D. R. Gauthier, Jr., R. H. Szumigala, Jr., P. G. Dormer, J. D. Armstrong III, R. P. Volante, P. J. Reider, *Org. Lett.* **2002**, *4*, 375; M. Kobayashi, Y. Matsumoto, M. Uchiyama, T. Ohwada, *Macromolecules* **2004**, *37*, 4339; S. Nakamura, M. Uchiyama, T. Ohwada, *J. Am. Chem. Soc.* **2004**, *126*, 11146; H. R. L. Barley, W. Clegg, S. H. Dale, E. Hevia, G. W. Honeyman, A. R. Kennedy, R. E. Mulvey, *Angew. Chem.* **2005**, *117*, 6172; *Angew. Chem. Int. Ed.* **2005**, *44*, 6018.

[3] Y. Kondo, M. Shilai, M. Uchiyama, T. Sakamoto, *J. Am. Chem. Soc.* **1999**, *121*, 3539.

[4] For key reviews of Directed *ortho*-Metalation (DoM) see "The Directed *ortho*-Metalation-Cross Coupling Nexus. Synthetic Methodology for the Aryl-Aryl and Aryl-Heteroatom-Aryl Bonds": E. Anctil, V. Snieckus in *Metal-Catalyzed Cross-Coupling Reaction*, *2nd ed.* (Eds.: F. Diederich, A. de Meijere), Wiley-VCH, Weinheim, **2004**, pp. 761–813; "The Directed *ortho*-Metalation Reaction. A Point of Departure for New Synthetic Aromatic Chemistry": C. G. Hartung, V. Snieckus in *Modern Arene Chemistry* (Ed.: D. Astruc), Wiley-VCH, New York, **2002**, pp. 330–367.

[5] P. Beak, A. I. Meyers, *Acc. Chem. Res.* **1986**, *19*, 356; P. Beak, J. E. Hunter, Y. M. Jun, *J. Am. Chem. Soc.* **1983**, *105*, 6350.

[6] W. Clegg, S. H. Dale, R. W. Harrington, E. Hevia, G. W. Honeyman, R. E. Mulvey, *Angew. Chem.* **2006**, *118*, 2434; *Angew. Chem. Int. Ed.* **2006**, *45*, 2374.

[7] Crystal data for **4**: C$_{21}$H$_{44}$LiNOZn, M_r = 398.9, orthorhombic, space group *Pnma*, a = 19.608(3), b = 10.0108(9), c = 11.8225(8) Å, V = 2320.7(4) Å^3, Z = 4 (the molecule lies on a mirror plane), ρ_{calcd} = 1.142 g cm^{-3}, μ(Mo$_{K\alpha}$) = 1.07 mm^{-1}, T = 150 K, R = 0.031 ($F^2 > 2\sigma$), R_w = 0.073 (for all F^2 values) for 2785 data and 140 refined parameters; final difference synthesis within ±0.41 e Å^{-3}. One THF C atom is disordered on both sides of the mirror plane to give the usual nonplanar ring. H atoms were constrained with a riding model.

 © 2006 Wiley-VCH Verlag GmbH & Co. KGaA, Weinheim

[8] Crystal data for **5**: $C_{30}H_{55}LiN_2OZn$, $M_r = 532.1$, triclinic, space group $P\bar{1}$, $a = 10.4011(9)$, $b = 13.0653(13)$, $c = 13.599(2)$ Å, $\alpha = 68.288(8)$, $\beta = 68.361(10)$, $\gamma = 85.470(8)°$, $V = 1592.4(3)$ Å^3, $Z = 2$, $\rho_{calcd} = 1.110$ g cm^{-3}, $\mu(Mo_{K\alpha}) = 0.79$ mm^{-1}, $T = 150$ K, $R = 0.036$ ($F^2 > 2\sigma$), $R_w = 0.088$ (for all F^2 values) for 7211 data and 330 refined parameters; final difference synthesis within ± 0.55 e Å^{-3}. CCDC 283194 and CCDC 283195 contain the supplementary crystallographic data for this paper. These data can be obtained free of charge from The Cambridge Crystallographic Data Centre via www.ccdc.cam.ac.uk/data_request/cif.

[9] K. W. Klinkhammer, *Chem. Eur. J.* **1997**, *3*, 1418.

[10] A. Keys, T. J. Barbarich, S. G. Bott, A. R. Barron, *J. Chem. Soc. Dalton Trans.* **2000**, 577.

[11] There are two reported crystal structures in which related but anionic, tertiary aromatic amide ligands with an ethyl substituent on the aromatic ring have been lithiated laterally at the ethyl site, see: D. R. Armstrong, J. Clayden, R. Haigh, D. J. Linton, P. Schooler, A. E. H. Wheatley, *Chem. Commun.* **2003**, 1694; D. R. Armstrong, S. R. Boss, J. Clayden, R. Haigh, B. A. Kirmani, D. J. Linton, P. Schooler, A. E. H. Wheatley, *Angew. Chem.* **2004**, *116*, 2187; *Angew. Chem. Int. Ed.* **2004**, *43*, 2135.

[12] M. Al-Aseer, P. Beak, D. Hay, D. J. Kempf, S. Mills, S. G. Smith, *J. Am. Chem. Soc.* **1983**, *105*, 2080; D. R. Hay, Z. Song, S. G. Smith, P. Beak, *J. Am. Chem. Soc.* **1988**, *110*, 8145.

[13] S. T. Chadwick, R. A. Rennels, J. L. Rutherford, D. B. Collum, *J. Am. Chem. Soc.* **2000**, *122*, 8640.

[14] Note that the dihedral twist angle between the amide N–C=O and Ph planes in **5** is 75.64(11)°.

 © 2006 Wiley-VCH Verlag GmbH & Co. KGaA, Weinheim

ortho-Metalation (2)

DOI: 10.1002/anie.200503213

Post-Metalation Structural Insights into the Use of Alkali-Metal-Mediated Zincation for Directed *ortho*-Metalation of a Tertiary Aromatic Amide**

*William Clegg, Sophie H. Dale, Ross W. Harrington, Eva Hevia, Gordon W. Honeyman, and Robert E. Mulvey**

Introduced in 1999 by Kondo et al.,[1] lithium di-*tert*-butyltetramethylpiperidinozincate (LiTMP-zincate) is a highly chemoselective base for directed *ortho*-metalation (DoM) of alkyl benzoates, alkyl benzamides, and related aza-aromatics.[2,3] This important reagent is but one of a growing number of alkali-metal zincate compounds that are attracting much attention from synthetic chemists in respect of their often special reactivities/selectivities,[4] and in certain cases, catalytic action[5] towards organic substrates. Much of our knowledge of these synthetic applications comes at the end of the reaction sequence, when all active metal–organic materials have been exhausted,[6] and is usually derived from isolated, metal-free products obtained by the in situ interception of metalated intermediates by electrophilic quenching. Scheme 1 illustrates this method for the sequential *ortho*-

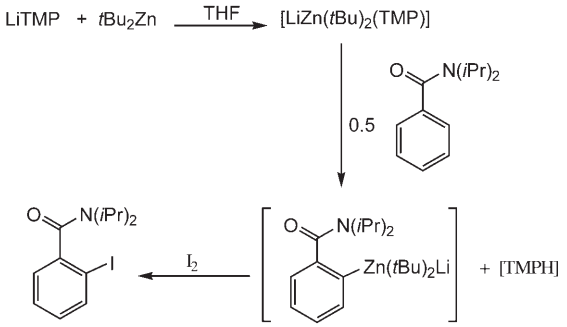

Scheme 1. Synthesis of *N*,*N*-diisopropyl-2-iodobenzamide by a standard metalation/electrophilic-interception strategy.

metalation/iodination of *N*,*N*-diisopropylbenzamide by a LiTMP–zincate/I_2 combination,[1] a reaction sequence that is relevant to the present study. In general, surprisingly little well-defined information exists on the chemistry taking place "at the coalface", that is, about the natures of the starting alkali-metal zincate reagents themselves and the metalated intermediates they generate prior to the final, electrophilic quenching, step. To fully understand this chemistry and develop it rationally, such information is indispensable, particularly in the case of LiTMP–zincate and related ambident reagents which in theory could exhibit either alkyl or amido (or both) reactivity towards organic substrates. In the preceding Communication in this issue we discussed the structures of the TMP–zincate reagent [(thf)Li(μ-tmp)(μ-*t*Bu)Zn(*t*Bu)] and the related tertiary aromatic amide complex [{(*i*Pr)$_2$NC(Ph)(=O)}Li(μ-tmp)(μ-*t*Bu)Zn(*t*Bu)], thus providing valuable structural information on zincate bases prior to them taking part in metalation reactions.[7] Herein, in reporting the first application of a sodium TMP-zincate reagent in directed *ortho*-metalation, we shed light on the selective ligand transfer effecting *ortho*-metalation of *N*,*N*-diisopropylbenzamide, by successfully isolating and crystallographically characterizing the *ortho*-metalated "intermediate". Furthermore, by similarly elucidating the *ortho*-metalated structure generated by the analogous lithium TMP–zincate system (not the original Kondo reagent but a new TMEDA-complexed variant), we have uncovered an intriguing "alkali-metal effect", as it transpires that the sodium zincate and lithium zincate reagents behave differently towards the aromatic tertiary amide. We also discuss how these mixed-metal *ortho*-metalated structures deviate in

[*] Dr. E. Hevia, Dr. G. W. Honeyman, Prof. R. E. Mulvey
WestCHEM
Department of Pure and Applied Chemistry
University of Strathclyde
Glasgow, G1 1XL (UK)
Fax: (+44) 141-552-0876
E-mail: r.e.mulvey@strath.ac.uk
Prof. W. Clegg, Dr. S. H. Dale, Dr. R. W. Harrington
School of Natural Sciences (Chemistry)
University of Newcastle
Newcastle upon Tyne, NE1 7RU (UK)

[**] This work was supported by the UK Engineering and Physical Science Research Council through grant award no. GR/R81183/01 and by the EU through a Marie Curie Fellowship to E.H.

InterScience
© 2006 Wiley-VCH Verlag GmbH & Co. KGaA, Weinheim

many key respects from the few recorded structures of related *ortho*-lithiated aromatic amides.

Both alkali-metal zincate reagents, previously known [(tmeda)Na(μ-tmp)(μ-*t*Bu)Zn(*t*Bu)] (**1**)[8] and the previously unknown lithium congener [(tmeda)Li(μ-tmp)(μ-*t*Bu)Zn(*t*Bu)] (**2**) were generated in situ in hexane solution by treating NaTMP and LiTMP, respectively, with equimolar amounts of tBu_2Zn then TMEDA. The formulation of **1** as written was established earlier by X-ray crystallography,[8] supporting Kondo's view that "precomplexation of MTMP and tBu_2Zn is essential for successful metalation". Subsequent reaction of **1** with one molar equivalent of *N*,*N*-diisopropylbenzamide yielded the colorless crystalline *ortho*-zincated product [(tmeda)Na(tmp){2-[1-C(O)N(*i*Pr)$_2$]C$_6$H$_4$}Zn(*t*Bu)] (**3**; Scheme 2). The retention of TMP within this

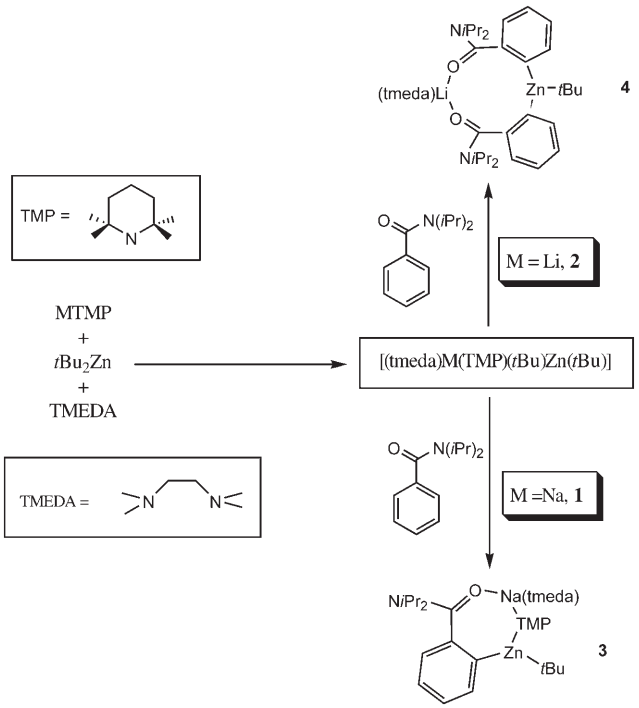

Scheme 2. The distinct reaction pathways followed by sodium zincate **1** and lithium zincate **2** towards *N*,*N*-diisopropylbenzamide.

metalation product indicates that at least in part, and possibly in whole, sodium zincate **1** functions as an alkyl base towards the aromatic amide. This finding is consistent with the reported metalating behavior of **1** towards benzene;[8] but contrasts with the amido basicity exhibited by LiTMP–zincate in its reaction with this amide[1] (Scheme 1) which, it should be stressed, was carried out in neat THF solution. In the light of these precedents, the outcome of the corresponding reaction between the suspension of TMEDA-complexed lithium zincate **2** and the amide is wholly surprising. Either [(tmeda)Li(tmp){2-[1-C(O)N(*i*Pr)$_2$]C$_6$H$_4$}Zn(*t*Bu)] (by analogy with **3**) or [(tmeda)Li(*t*Bu){2-[1-C(O)N(*i*Pr)$_2$]C$_6$H$_4$}Zn(*t*Bu)] (by analogy with the LiTMP–zincate reaction) could have been the product expected, but in practice neither is found, and instead, unexpectedly, the bis(amide) [(tmeda)Li{2-[1-C(O)N(*i*Pr)$_2$]C$_6$H$_4$}$_2$Zn(*t*Bu)] (**4**) is produced. NMR spectroscopic data suggest that production of **4** is accompanied by a significant quantity of residual **2**, out of step with the 1:1 stoichiometry of reactants employed in the experiment. It was then reasoned that **2** could be exhibiting dual alkyl and amido basicity towards the aromatic amide, and thus that only 0.5 molar equivalents would be needed to convert all of the amide into the *ortho*-metalated form, with the co-products being *t*BuH and TMPH. This idea was duly confirmed on repeating the reaction with a 1:2 stoichiometry of zincate **2**: aromatic amide as the yield of isolated, crystalline **4** obtained increased from 38% to 72%. Furthermore, TMP(H) was found to be the predominant component of the filtrate following removal of **4**. For stoichiometric efficiency **2** is therefore the reagent solution of choice in this case, though it is noted that four times as much TMEDA-free LiTMP-zincate was employed in the aforementioned original reaction[1] (Scheme 1), that is, a 2:1 as opposed to a 1:2 base:amide stoichiometry. No explanation was given for using excess base.

Retaining the "{(tmeda)Na(μ-TMP)Zn(*t*Bu)}" backbone of the reactant zincate **1**, the molecular structure of **3**[9] (Figure 1) is completed by the *ortho*-metalated benzamide

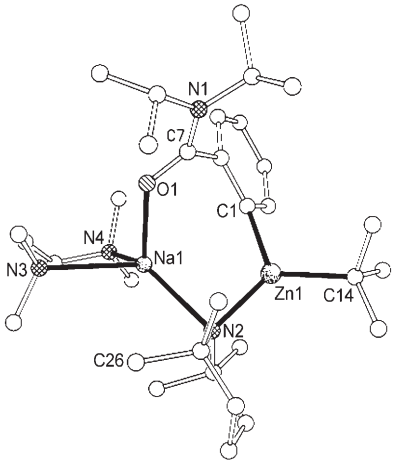

Figure 1. Molecular structure of **3** (hydrogen atoms and minor disorder component are omitted for clarity). Selected interatomic distances [Å] and angles [°]: Zn1–C1 2.077(3), Zn1–C14 2.055(3), Zn1–N2 2.018(2), Na1···C1 3.032(3), Na1···C7 3.102(3), Na1–O1 2.258(2), Na1–N2 2.435(3), Na1–N3 2.576(3), Na1–N4 2.493(3), C7–O1 1.245(3); C1-Zn1-C14 113.66(12), C1-Zn1-N2 115.73(10), C14-Zn1-N2 130.14(11), O1-Na1-N2 112.94(9), O1-Na1-N3 90.41(9), O1-Na1-N4 111.44(9), N2-Na1-N3 127.85(9), N2-Na1-N4 128.71(10), N3-Na1-N4 75.32(10).

fragment which bridges asymmetrically through its oxygen and *ortho*-carbon atoms to the sodium and zinc centers, respectively. This results in a seven-membered, five-element (NaNZnCCCO) ring. In contrast, having two *ortho*-metalated benzamide bridges with the same chemoconnectivity (O to alkali metal; *ortho*-C to Zn), **4** exhibits a larger 10-membered [Li(OCCC)$_2$Zn] ring within its molecular structure[10] (Figure 2), which is completed by terminal TMEDA (*N*,*N*′-attached) and *t*Bu (tertiary C-attached) ligands on lithium and zinc, respectively. A pseudo C_2 axis runs through the LiZnCC(H)$_3$ plane. Further to providing the first insights into

 © 2006 Wiley-VCH Verlag GmbH & Co. KGaA, Weinheim

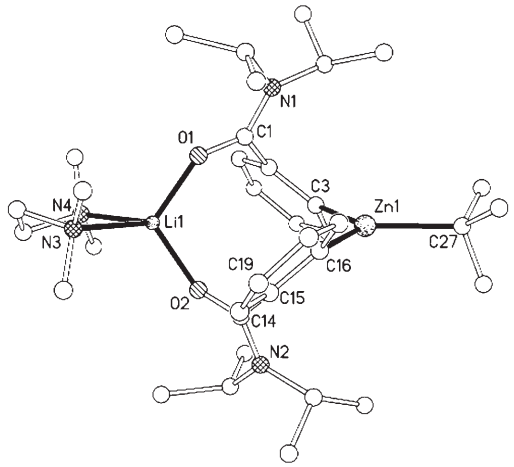

Figure 2. Molecular structure of **4** (hydrogen atoms are omitted for clarity). Selected bond lengths [Å] and angles [°]: Zn1–C3 1.934(2), Zn1–C16 1.971(2), Zn1–C27 2.255(3), Li1–O1 1.881(4), Li1–O2 1.891(4), Li1–N3 2.200(5), Li1–N4 2.185(5), O1–C1 1.280(3), O2–C14 1.250(3); C3-Zn1-C16 111.76(10), C3-Zn1-C27 122.61(11), C16-Zn1-C27 125.59(10), O1-Li1-O2 112.0(2), O1-Li1-N3 114.58(18), O1-Li1-N4 115.7(2), O2-Li1-N3 117.1(2), O2-Li1-N4 116.83(19), N3-Li1-N4 76.61(15).

the products of tertiary amide-directed *ortho* metalation[11] promoted by alkali-metal zincate reagents, the structures of **3** and **4** enable comparisons with the few known examples of analogous *ortho*-lithiated (homometallic) structures. All three such compounds reported, namely, *N*,*N*-diisopropyl-2-lithiobenzamide·Et_2O,[12] *N*,*N*-diisopropyl-2-lithionaphthamide·THF and *N*,*N*-diisopropyl-2-ethyl-6-lithiobenzamide·THF[13] adopt essentially the same dimeric, *trans* 5.4.5 fused-ring, arrangement with a central $(LiC)_2$ ring and LiOCCC outer rings (**5**; Figure 3)—a motif markedly distinct to that of either **3** or **4**. The salient feature of **5** is that lithium binds simultaneously to both the carbonyl oxygen atom (a contact assumed to be important mechanistically in terms of the "complex-induced proximity effect")[7,14] and the *ortho*-carbon anion. This is a key distinction in comparison to the situation in **3** and **4**, where the alkali-metal binds to the carbonyl oxygen atom but is distant from the *ortho*-carbon anion. In **4**, where a direct comparison is possible, the mean Li–O (carbonyl) length (1.886 Å) is significantly shorter than those in each structure of **5** (1.936(3), 1.974(4), and 1.972(5) Å, respectively).[11,12] Aided by zinc, lithium can approach the carbonyl oxygen atom more closely than its counterparts in **5** and at the same time zinc can engage in shorter and stronger bonds with the *ortho*-carbon anion (mean length in **4**, 1.953 Å; in **3**, 2.077 Å: the significant lengthening of the latter bond could be due to the presence of the bulky TMP co-ligand on this zinc atom), than the lithium atoms can achieve in **5** (mean length over the three structures, 2.280 Å). Thus the metalation process generating **3** and **4** is best viewed as an "alkali-metal-mediated zincation",[15] and the synergic bimetallic component of the bonding within the products appears to lead to an extra stabilization in comparison to the situation in the single-metal, *ortho*-lithiated products. However, whether the synergic bonding would have a similar beneficial effect on the stability of the transition states and on the reaction rates of these *ortho*-metalation processes remains an open question. In the report of aforementioned *N*,*N*-diisopropyl-2-lithiobenzamide·Et_2O[11] it was noted that the dihedral angle of the amide N–C=O and aromatic Ph planes (57° in the parent amide)[16] had to lessen to 46.8° to allow coordination of lithium to the amide C=O group; interestingly the situation is reversed in **3** and **4** as this twist angle increases to 63.24(17)° and 76.24(13)°, respectively. These increases may reflect the fact that there is no longer a requirement for the alkali metal to interact simultaneously with the *ortho*-carbon anion, though caution is required in attempting to rationalize differences in any bond angle in isolation as the global stereochemistries of **3**, **4**, and **5**, are markedly different in each case. *ortho*-Lithiation reactions utilizing *s*BuLi as the base are sensitive to the twist angle of the amide, with coplanarity (twist angle, 0°) leading to the fastest rates.[16] Whether the same correlation would hold true in the case of alkali-metal zincate bases that give rise to metalated products with unique structures distinct from those of *ortho*-lithiated products remains to be ascertained.

It is worth emphasizing that *t*Bu_2Zn, a feeble deprotonating agent on its own, is incapable of directly zincating tertiary aromatic amides.[17] Hence, the description of the new reactions outlined herein as "alkali-metal-mediated zincations" is both accurate and apt. These results also establish that the identity of the alkali metal can have a profound effect on the outcome of a zincate reaction, ruling out the possibility that mechanistically the zincate reagents react as solvent-separated ion pairs $[M\cdot(solvent)_x]^+[Zn(tmp)(tBu)_2]^-$, which would be expected to yield equivalent $[ZnR_3]^-$ products. Moreover, this study reinforces the added value of studying the reactive metallo intermediates, because quenching the reaction solutions of **3** or **4** with an electrophile such as I_2 would give the same set of organic products and the distinction between the lithium and sodium systems would have remained invisible.

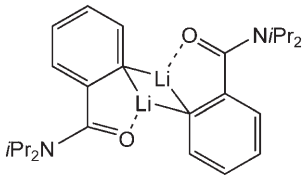

5

Figure 3. Representative structure of the *trans* 5.4.5 fused-ring arrangement found in *ortho*-lithiated aromatic amides.

Experimental Section

All reactions were carried out under a protective argon atmosphere.

3: A solution of *t*Bu_2Zn (0.358 g, 2 mmol) in hexane (10 mL) was transferred by cannula to a suspension of NaTMP in hexane [prepared in situ by reaction of BuNa (0.16 g, 2 mmol) with TMP(H) (0.34 mL, 2 mmol)]. Subsequently a molar equivalent of TMEDA (2 mmol, 0.30 mL) was added. The resulting suspension was heated gently to form a yellow solution which was allowed to cool to ambient temperature before the addition of a molar equivalent (2 mmol, 0.41 g) of *N*,*N*-diisopropylbenzamide, forming a brightly

 © 2006 Wiley-VCH Verlag GmbH & Co. KGaA, Weinheim

colored yellow solution. The solution was transferred to the freezer to aid crystallization. A crop (0.48 g, 40%) of transparent crystals formed in solution that were suitable for X-ray crystallographic analysis. FT-IR (nujol): $\tilde{\nu} = 1598\ cm^{-1}$ ($\nu_{C=O}$). ^1H NMR (400 MHz, 25 °C, C_6D_6): $\delta = 7.98$ (d, 1H, H_{meta} Ar′), 7.21 (t, 1H, H_{para} Ar′), 7.02 (t, 1H, H_{meta*} Ar′), 6.95 (d, 1H, H_{ortho*} Ar′), 4.17 (m, 1H, C*H*, *i*Pr, Ar′), 3.08 (m, 1H, C*H*, *i*Pr, Ar′), 1.98 (m, 6H, broad, 2H of γ-TMP and 4H of β-TMP), 1.79 (s, 4H, CH_2 TMEDA), 1.71 (s, 12H, CH_3 TMEDA), 1.56 (s, 9H, *t*Bu), 1.54, 1.51, 1.30, 1.20 (s, 3H each, CH_3-TMP), 1.48, 1.39, 0.91, 0.81 ppm (d, 3H each, CH_3, *i*Pr, Ar′). $^{13}C\{^1H\}$ NMR (100.63 MHz, 25 °C, [D$_6$]benzene): $\delta = 179.22$ (*C*=O), 169.15 (C_{ortho}), 148.06 (C_{ipso}), 142.26 (C_{meta}), 127.23 (C_{meta*}), 124.04 (C_{para}), 123.84 (C_{ortho*}), 57.94 (CH_2, TMEDA), 53.55, 53.23 (α-TMP), 52.00, 46.22 (*C*H, *i*Pr), 46.32 (CH_3, TMEDA), 41.18, 40.29 (β-TMP), 37.83, 36.16, 35.34, 34.87 (CH_3-TMP), 36.64 (CH_3, *t*Bu), 22.89, 21.97 (CH_3, *i*Pr), 21.03 (γ-TMP), 20.70 ppm ($2 \times CH_3$, *i*Pr and $C(CH_3)_3$, *t*Bu). Figure 4 shows the labeling scheme of benzamide (Ar′).

Ar′ =

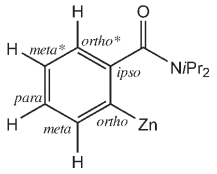

Figure 4. Atom-labeling scheme used in the NMR assignments of the *ortho*-zincated benzamide structures.

4: A solution of tBu_2Zn (0.358 g, 2 mmol) in hexane (10 mL) was transferred by cannula to a solution of LiTMP in hexane [prepared in situ by reaction of BuLi (1.25 mL of a 1.6 M solution in hexane, 2 mmol) with TMP(H) (0.34 mL, 2 mmol)]. The addition of TMEDA (0.30 mL, 2 mmol) to the resulting pale yellow solution was accompanied by the precipitation of a white solid. *N*,*N*-diisopropylbenzamide (0.34 mL, 2 mmol) was then introduced. A bright yellow solution is obtained which was stirred for 30 min at room temperature. Toluene (2 mL) was added to the solution that was slightly cloudy, obtaining a transparent bright yellow solution that was placed in the freezer at −20 °C. A crop of cubic colorless crystals was obtained (0.51 g, 38%); one of these crystals was used for an X-ray crystallography experiment. FT-IR (nujol): $\tilde{\nu} = 1603\ cm^{-1}$ ($\nu_{C=O}$). ^1H NMR (400 MHz, 25 °C, C_6D_6): $\delta = 8.26$ (d, 2H, H_{meta} Ar′), 7.29 (t, 2H, H_{para} Ar′), 7.10 (t, 2H, H_{meta*} Ar′), 6.84 (d, 2H, H_{ortho*} Ar′), 4.23 (m, 2H, C*H*, *i*Pr, Ar′), 3.02 (m, 2H, C*H*, *i*Pr, Ar′), 1.89 (24H, CH_2 and CH_3 TMEDA), 1.80 (s, 9H, *t*Bu), 1.25, 1.15, 1.10, 0.67 ppm (d, 6H each, CH_3, *i*Pr, Ar′). $^{13}C\{^1H\}$ NMR (100.63 MHz, 25 °C, [D$_6$]benzene): $\delta = 179.01$ (*C*=O), 169.27 (Zn-C_{ortho}), 146.78 (C_{ipso}), 141.77 (C_{meta}), 126.13 (C_{meta*}), 123.52 (C_{para}), 122.26 (C_{ortho*}), 57.58 (CH_2, TMEDA), 51.27 (*C*H, *i*Pr), 46.43 (CH_3, TMEDA), 45.82 (*C*H, *i*Pr), 36.31 (CH_3, *t*Bu), 22.87 ($C(CH_3)_3$, *t*Bu), 21.32, 20.85, 20.83, 20.51 ppm (CH_3, *i*Pr). ^7Li NMR (155.50 MHz, 25 °C, C_6D_6, reference LiCl in D_2O at 0.00 ppm): 0.12 ppm.

Received: September 9, 2005
Revised: November 8, 2005
Published online: March 2, 2006

Keywords: alkali metals · amides · directing groups · metalation · zinc

[1] Y. Kondo, M. Shilai, M. Uchiyama, T. Sakamoto, *J. Am. Chem. Soc.* **1999**, *121*, 3539.
[2] T. Imahori, M. Uchiyama, T. Sakamoto, Y. Kondo, *Chem. Commun.* **2001**, 2450.
[3] M. Uchiyama, T. Miyoshi, Y. Kajihara, T. Sakamoto, Y. Otani, T. Ohwada, Y. Kondo, *J. Am. Chem. Soc.* **2002**, *124*, 8514.
[4] W. Tückmantel, K. Oshima, H. Nozaki, *Chem. Ber.* **1986**, *119*, 1581; T. Harada, T. Katsuhira, A. Osada, K. Iwazaki, K. Maejima, A. Oku, *J. Am. Chem. Soc.* **1996**, *118*, 11377; M. Uchiyama, M. Koike, M. Kameda, Y. Kondo, T. Sakamoto, *J. Am. Chem. Soc.* **1996**, *118*, 8733; Y. Kondo, N. Takazawa, C. Yamazaki, T. Sakamoto, *J. Org. Chem.* **1994**, *59*, 4717; M. Uchiyama, S. Furumoto, M. Saito, Y. Kondo, T. Sakamoto, *J. Am. Chem. Soc.* **1997**, *119*, 11425; M. Uchiyama, M. Kameda, O. Mishima, N. Yokoyama, M. Koike, Y. Kondo, T. Sakamoto, *J. Am. Chem. Soc.* **1998**, *120*, 4934.
[5] F. F. Kneisel, M. Dochnahl, P. Knochel, *Angew. Chem.* **2004**, *116*, 1032; *Angew. Chem. Int. Ed.* **2004**, *43*, 1017; L.-Z. Gong, P. Knochel, *Synlett* **2005**, 267.
[6] For an NMR spectroscopic structural determination of organozincate reagents see: T. A. Mobley, S. Berger, *Angew. Chem.* **1999**, *111*, 3256; *Angew. Chem. Int. Ed.* **1999**, *38*, 3070.
[7] W. Clegg, S. H. Dale, E. Hevia, G. W. Honeyman, R. E. Mulvey, *Angew. Chem.* **2006**, *118*, 2430–2434; *Angew. Chem. Int. Ed.* **2006**, *45*, 2371.
[8] P. C. Andrikopoulos, D. R. Armstrong, H. R. L. Barley, W. Clegg, S. H. Dale, E. Hevia, G. W. Honeyman, A. R. Kennedy, R. E. Mulvey, *J. Am. Chem. Soc.* **2005**, *127*, 6184.
[9] Crystal data for **3**: $C_{32}H_{61}N_4NaOZn$, $M_r = 606.2$, monoclinic, space group $P2_1/n$, $a = 14.946(3)$, $b = 15.913(3)$, $c = 15.158(3)$ Å, $\beta = 90.18(3)°$, $V = 3605.1(12)$ Å^3, $Z = 4$, $\rho_{calcd} = 1.117\ g\,cm^{-3}$, μ($Mo_{K\alpha}$) $= 0.72\ mm^{-1}$, $T = 150$ K, $R = 0.053$ ($F^2 > 2\sigma$), $R_w = 0.107$ (for all F^2 values) for 6942 data and 398 refined parameters; final difference synthesis within $\pm 0.41\ e\,Å^{-3}$. The *t*Bu group is disordered over two orientations. H atoms were constrained with a riding model.
[10] Crystal data for **4**: $C_{36}H_{61}LiN_4O_2Zn$, $M_r = 654.2$, monoclinic, space group $P2_1/n$, $a = 14.192(4)$, $b = 17.825(5)$, $c = 15.641(5)$ Å, $\beta = 90.041(7)$, $V = 3957(2)$ Å^3, $Z = 4$, $\rho_{calcd} = 1.098\ g\,cm^{-3}$, μ($Mo_{K\alpha}$) $= 0.65\ mm^{-1}$, $T = 150$ K, $R = 0.034$ ($F^2 > 2\sigma$), $R_w = 0.091$ (for all F^2 values) for 8018 data and 413 refined parameters; final difference synthesis within $\pm 0.52\ e\,Å^{-3}$. CCDC 283196 and CCDC 283197 contain the supplementary crystallographic data for this paper. These data can be obtained free of charge from The Cambridge Crystallographic Data Centre via www.ccdc.cam.ac.uk/data_request/cif.
[11] For a minireview on how homo- and hetero-aggregation can affect directed *ortho*-lithiation see: R. A. Gossage, J. T. B. H. Jastrzebski, G. van Koten, *Angew. Chem.* **2005**, *117*, 1472; *Angew. Chem. Int. Ed.* **2005**, *44*, 1448.
[12] J. Clayden, R. P. Davies, M. A. Hendy, R. Snaith, A. E. H. Wheatley, *Angew. Chem.* **2001**, *113*, 1282; *Angew. Chem. Int. Ed.* **2001**, *40*, 1238.
[13] D. R. Armstrong, S. R. Boss, J. Clayden, R. Haigh, B. A. Kirmani, D. J. Linton, P. Schooler, A. E. H. Wheatley, *Angew. Chem.* **2004**, *116*, 2187; *Angew. Chem. Int. Ed.* **2004**, *43*, 2135.
[14] P. Beak, A. I. Meyers, *Acc. Chem. Res.* **1986**, *19*, 356; P. Beak, J. E. Hunter, Y. M. Jun, *J. Am. Chem. Soc.* **1983**, *105*, 6350.
[15] For an example of alkali-metal-mediated magnesiation see: P. C. Andrikopolous, D. R. Armstrong, D. V. Graham, E. Hevia, A. R. Kennedy, R. E. Mulvey, C. T. O'Hara, C. Talmard, *Angew. Chem.* **2005**, *117*, 3525; *Angew. Chem. Int. Ed.* **2005**, *44*, 3459.
[16] P. Beak, S. T. Kerrick, D. J. Gallagher, *J. Am. Chem. Soc.* **1993**, *115*, 10628.
[17] For the use of a mixed LiTMP–nBu_2Zn system in the direct zincation of ferrocene see: H. R. L. Barley, W. Clegg, S. H. Dale, E. Hevia, G. W. Honeyman, A. R. Kennedy, R. E. Mulvey, *Angew. Chem.* **2005**, *117*, 6172; *Angew. Chem. Int. Ed.* **2005**, *44*, 6018.

 © 2006 Wiley-VCH Verlag GmbH & Co. KGaA, Weinheim

Nanostructures

DOI: 10.1002/anie.200503565

A Water-Soluble Titanium Complex for the Selective Synthesis of Nanocrystalline Brookite, Rutile, and Anatase by a Hydrothermal Method**

*Koji Tomita, Valery Petrykin, Makoto Kobayashi, Motoo Shiro, Masahiro Yoshimura, and Masato Kakihana**

In recent years considerable interest has been devoted to the synthesis and structural characterization of water-soluble titanium(IV) compounds[1–4] with the aim of developing convenient, nontoxic titanium compounds that can be used as environmentally benign precursors for the solution-based synthesis of titanium oxide and multicomponent inorganic materials containing titanium. This need is dictated by the increasing importance of nanoscale materials, in particular nanosized TiO_2, which can be used for UV-protective and self-cleaning coatings,[5,6] as an electrode material in dye-sensitized solar cells,[6,7] and as a photocatalyst for removal of harmful organic compounds.[6,8] Conventional solid-state syntheses cannot provide the required particle size, morphology, and homogeneity, thus chemical reaction routes (chimie douce) are being considered for their synthesis. However, common titanium compounds are inadequate for these advanced solution synthesis methods due to their fast hydrolysis, toxicity, and formation of corrosive by-products.

Perhaps the most remarkable progress has been made in the synthesis of titanium dioxide nanopowders in the form of rutile and anatase by solution methods.[9,10] However, the preparation of fine brookite powders remains a serious challenge,[10] and most of the attempts to obtain brookite by chimie douce techniques have yielded mixtures of brookite and rutile. The preparation procedures usually rely on thermolysis of alcohol solutions[11] and strongly acidic aqueous solutions[10] of $TiCl_4$, or controlled hydrolysis of titanium acetylacetonate in ethylene glycol under solvothermal conditions.[12] As mentioned above, most samples contain brookite and the rutile form of TiO_2. This outcome is believed to result from a competing reaction that yields rutile, as both rutile and anatase can form under similar hydrothermal conditions.

Water-soluble complexes of titanium have proved to be very promising reagents from an environmental point of view for the preparation of titanium-containing functional materials by solution (water-based) synthesis methods.[13] Therefore, the main incentive of this work was to broaden the range of water-soluble titanium compounds, in particular with a lower content of carbon per titanium atom, that are suitable for the fabrication of oxide materials. With this in mind we decided to use glycolic acid ($HOCH_2COOH$), which is the simplest hydroxycarboxylic acid. Glycolic acid is also favorable as an industrial reagent due to its availability and low toxicity. Herein, we report the synthesis and crystal structure of the new compound $(NH_4)_6[Ti_4(C_2H_2O_3)_4(C_2H_3O_3)_2(O_2)_4O_2]\cdot 4H_2O$ (**1**). The unexpected stability of this complex over a broad range of pH values and temperatures allows tailoring of the hydrothermal treatment procedures and the selective synthesis of brookite, rutile, and rutile–anatase nanopowders.

Single crystals of **1** were obtained by slow evaporation of an aqueous solution containing the water-soluble titanium complex $(NH_4)_6[Ti_4(C_2H_2O_3)_4(C_2H_3O_3)_2(O_2)_4O_2]$ (**1a**), prepared from titanium powder, hydrogen peroxide, NH_3(aq), and glycolic acid. The synthetic procedures can be summarized by the chemical equations (1) and (2).

$$Ti + 3H_2O_2 + NH_3 \rightarrow [Ti(OH)_3O_2]^- + 2H_2O + NH_4^+ \quad (1)$$

$$4[Ti(OH)_3O_2]^- + 6C_2H_4O_3 + 2H_2O \rightarrow [Ti_4(C_2H_2O_3)_4(C_2H_3O_3)_2(O_2)_4O_2]^{6-} + 10H_2O + 2H_3O^+ \quad (2)$$

The prepared titanium complex is stable and does not undergo hydrolysis in aqueous solution under ambient conditions, and single crystals of the ammonium salt form upon gradual evaporation of the water. The crystals were separated from the solution and analyzed by TG-DTA, elemental analysis (see Experimental Section), FTIR spectroscopy (see Supporting Information), and single-crystal X-ray diffraction. Elemental analysis suggested the most likely chemical formula to be $(NH_4)_3[Ti_2C_6H_7O_{14}]\cdot 2H_2O$, although a more accurate chemical formula for this complex that reflects the structural information determined from the X-ray diffraction data is $(NH_4)_6[Ti_4(C_2H_2O_3)_4(C_2H_3O_3)_2(O_2)_4O_2]\cdot 4H_2O$.[14]

Figure 1 presents a stereoview of the anion of complex **1a** (see Supporting Information for an ORTEP view). This anion contains four titanium atoms, each of which is coordinated in a didentate fashion to one molecule of glycolic acid with deprotonated carboxy and hydroxy groups. This fragment forms a five-membered ring that is essential for the stability of compound **1**, similar to the case of the citrate[1–3] and lactate complexes.[4] In addition, the deprotonated hydroxy group of the glycolic acid acts as a bridging group to the neighboring Ti atom to give two sets of almost equal Ti–O bonds (Ti1–

[*] Dr. K. Tomita, Dr. V. Petrykin, M. Kobayashi, Prof. Dr. M. Kakihana
Institute of Multidisciplinary Research for Advanced Materials
Tohoku University
1,1 Katahira, 2-Chome, Aobaku, Sendai 980-8577 (Japan)
Fax: (+81) 22-217-5649
E-mail: kakihana@tagen.tohoku.ac.jp
Dr. M. Shiro
X-ray Research Laboratory
Rigaku Corporation
3-9-12 Matsubara-cho, Akishima-shi, Tokyo (Japan)
Prof. Dr. M. Yoshimura
Materials and Structures Laboratory
Tokyo Institute of Technology
4259 Nagatsuta, Midori, Yokohama 226-8503 (Japan)

[**] This work was financially supported by CREST/JST, the Nippon Sheet Glass Foundation for Materials Science, and the Engineering and Collaborative Research Project of the Materials and Structures Laboratory of the Tokyo Institute of Technology.

Supporting Information for this article is available on the WWW under http://www.angewandte.org or from the author.

InterScience
© 2006 Wiley-VCH Verlag GmbH & Co. KGaA, Weinheim

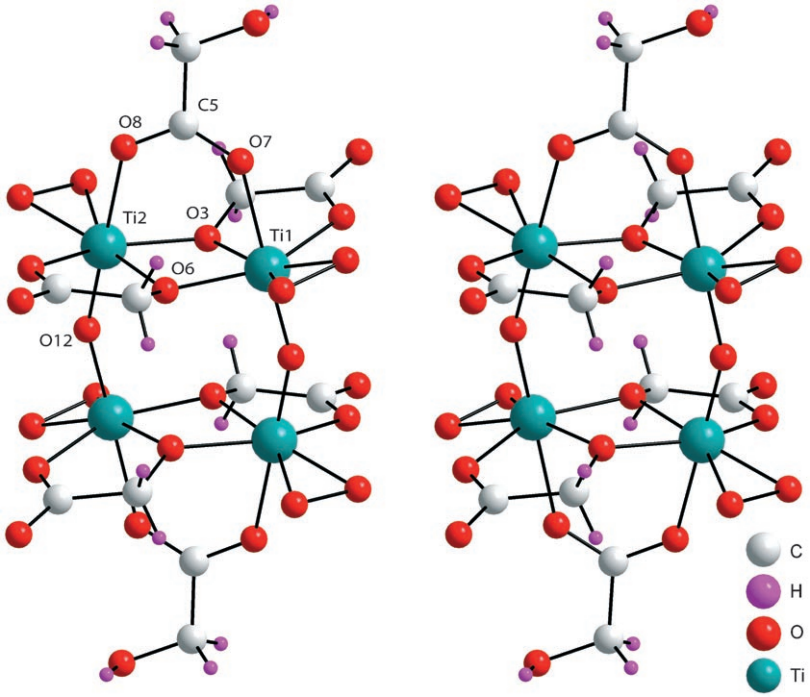

Figure 1. Stereoview of the structure of the anion in **1a**.

O3 2.055, Ti1–O6 1.993, Ti2–O3 2.026, Ti2–O6 2.041 Å). One more glycolic acid molecule does not lose the proton of its OH group and coordinates both Ti1 and Ti2 through the bridging carboxylic group O7-C5-O8. A peroxo group occupies one site in the coordination environment of Ti, similar to the citratoperoxo complex,[1,2] with corresponding Ti–O bond lengths of 1.922–1.947 Å and O–O distances of 1.473 and 1.48 Å. Two of these dimer fragments are connected to each other through the bridging oxygen atom O12, with relatively short Ti–O distances (Ti1–O12 1.830 and Ti2–O12 1.815 Å) and a Ti-O-Ti angle of 155°. A calculation of the bond-valence sum[17] for this oxygen atom yields a value of approximately −2, which indicates a reasonable coordination sphere of O12.

One particularly intriguing possibility was to conduct hydrothermal experiments with this newly synthesized titanium complex at relatively high pH because conventional titanium compounds are stable only in a strongly acidic environment which is usually considered as the main limitation for the synthesis of brookite.[10,12] Therefore, aqueous solutions of complex **1** were treated under hydrothermal conditions in the temperature range 160–200 °C for 24 h. The pH of the solutions was adjusted to 3, 6, and 10 by addition of glycolic acid or ammonia. The obtained precipitates were separated with a centrifuge and characterized by XRD and TEM. As can be seen from the XRD data in Figure 2a and the TEM image in Figure 3a, samples heated at 200 °C and pH 10 yielded single-phase brookite nanorods. At 200 °C and pH 6 nanorods of rutile formed as the only phase (Figure 2b and Figure 3b), while at pH 3 rutile is accompanied by nanoparticles of anatase (Figure 2c and Figure 3c). The formation of anatase became more pronounced as the synthesis temperature was lowered (Figure 2d and Figure 3d).

We believe that the formation of single-phase brookite from the new complex is not accidental and is not exclusively related to the stability of **1** in aqueous solutions at higher pH values. It can easily be seen that the complex anion structure closely resembles the architecture of brookite. Figure 4 presents a possible scheme for brookite formation from complex **1** under hydrothermal conditions. During the first step, the anion in **1a** loses a peroxo group to yield free oxygen. The empty site in the coordination environment is then filled by the oxygen of a bridging oxo group and the oxygen atoms of an axial carboxylic group, as shown in Figure 4a, to yield a dimer (Figure 4b), which can grow further, as hydrolysis and decomposition of peroxo groups occur, to produce stripes of $Ti_{4n}O_{14n+4}$ (Figure 4c). During the next step, the stripes are arranged into the brookite structure (Figure 4d) as a result of oxolation and, possibly, further hydrolysis. In contrast, at low pH the bridging oxo group should be protonated and the dominating species in the solution would

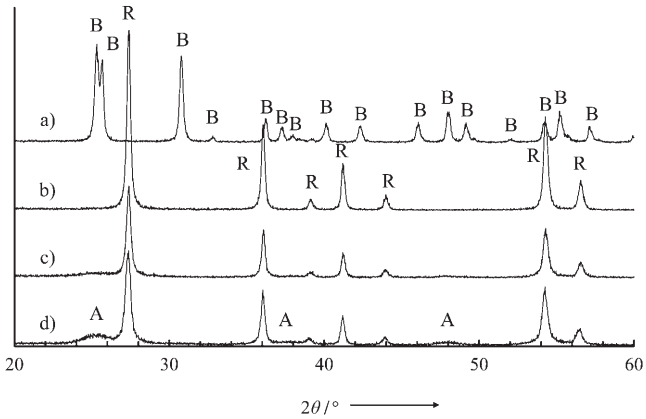

Figure 2. XRD patterns of TiO_2 prepared by hydrothermal treatment of complex **1** under the following conditions: a) pH 10, 200 °C for 24 h; b) pH 6, 200 °C for 24 h; c) pH 3, 200 °C for 24 h; d) pH 6, 160 °C for 24 h. A = anatase, B = brookite, R = rutile.

then be dimeric complex anions. These species cannot effectively build a brookite lattice although they are suitable building blocks for the rutile lattice.

This example illustrates a more general principle, namely that metastable phases often crystallize first in chimie douce methods at low temperatures because their nucleolus may require lower supersaturation to form in the nucleation-controlled regime. In this regard, the structural similarity between the dissolved molecules and the nuclei of the solid phase is of great importance. Once the nucleation of the phase (brookite in our case) has occurred, the growth of the crystallites needs a lower activation energy than nucleation of another phase.

 © 2006 Wiley-VCH Verlag GmbH & Co. KGaA, Weinheim

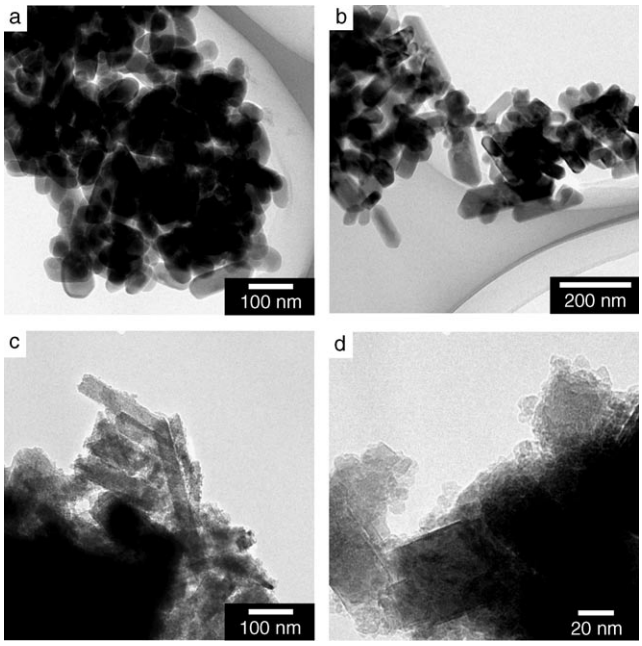

Figure 3. TEM images of TiO_2 prepared by hydrothermal treatment of **1** under the following conditions: a) pH 10, 200 °C for 24 h (brookite); b) pH 6, 200 °C for 24 h (rutile); c) pH 3, 200 °C for 24 h (rutile and anatase); d) pH 6, 160 °C for 24 h (rutile and anatase).

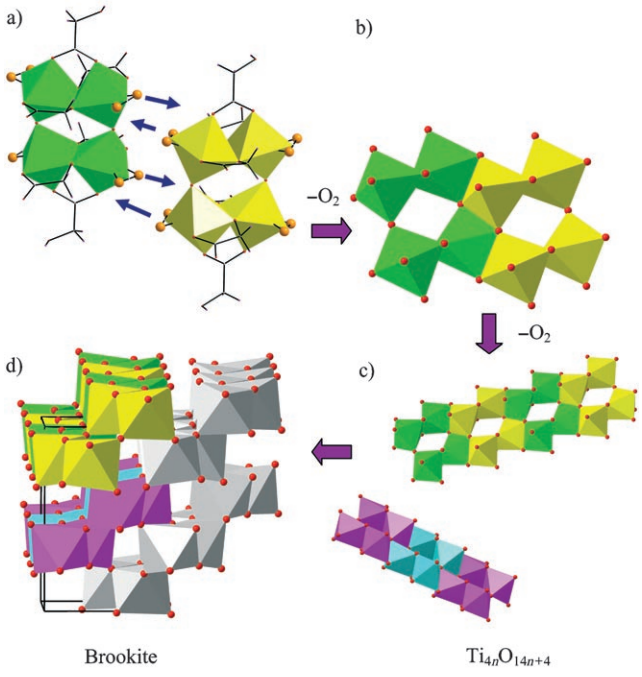

Figure 4. Possible mechanisn of formation of brookite from **1a** anions in the solution at pH 10 under hydrothermal conditions. See text for details.

To summarize, hexaammonium hexaglycolatodioxotetraperoxotetratitanate(IV) tetrahydrate (**1**) has been obtained for the first time and its structure has been determined by single-crystal X-ray diffraction techniques. The complex anion is composed of four titanium ions coordinated by glycolic acid and peroxo groups in a dimer-like structure that is connected to another dimer through bridging oxo groups. The complex is stable in the pH range between strongly acidic and weakly basic. Hydrothermal treatment of this complex allows the selective preparation of nanopowders of single-phase brookite and rutile, and a rutile–anatase mixture. The formation of brookite from this titanium complex is related to the inherent structure of the complex anion and its similarity to the brookite architecture. The proposed scheme for brookite formation gives rise to one interesting question: is it possible to tailor the synthesis of other, perhaps unknown, forms of TiO_2 by using different water-soluble complexes of titanium?

Experimental Section

1: Titanium powder (Furuuchi Chemical Co., Tokyo; 10 mmol) was dissolved in an ice-cooled solution of 30% H_2O_2 (40 mL; Kanto Chemicals Co. Inc., Tokyo) and 28% NH_3 (10 mL; Kanto Chemicals Co. Inc., Tokyo). After 2 h, glycolic acid (27 mmol; Kanto Chemicals Co. Inc., Tokyo) was added to this solution, and the mixture was heated for one day at 80 °C until an orange gel formed. The obtained gel was dissolved in water and kept for about one week to give transparent, orange crystals. Single crystals of this complex fully decompose in four steps up to 520 °C to produce 32% of TiO_2 (see Supporting Information for TG-DTA data). Elemental analysis: calcd (%) for $(NH_4)_3[Ti_2C_6H_7O_{14}]\cdot 2H_2O$: C 14.74, H 4.74, N 8.59, ash calcd (TiO_2) 32.67; found: C 14.27, H 4.59, N 8.32. This composition was used further for structure solution.[14]

Nanocrystalline TiO_2: The powder of **1** was dissolved in distilled water (Ti concentration approximately 0.25 M). Three specimens were used for hydrothermal synthesis: the original solution (pH 6), a solution adjusted to pH 3 by addition of glycolic acid, and a solution adjusted to pH 10 by addition of ammonia solution. A 20-mL portion of one of these solutions was placed into the Teflon reactor of a stainless-steel autoclave, which was heated to 200 °C for 24 h and then allowed to cool. Hydrothermal treatment of the solution at pH 6 was also carried out at 160 °C. The resulting titanium dioxide powders were separated in a centrifuge and washed three times with water. The obtained specimens were dried under ambient conditions.

Powder X-ray diffraction (XRD) analysis: The diffraction patterns were collected in the Bragg–Brentano configuration using $Cu_{K\alpha}$ radiation with a RINT2000 (Rigaku Co.) diffractometer operating at 40 kV and 30 mA. The scanning speed was 4° min^{-1} with a scanning step, $\Delta 2\Theta$, of 0.02°.

Thermogravimetric–differential thermal analysis (TG-DTA): TGA analysis was conducted with a Type-2020, MAC Science Co. thermal analyzer. The sample (10 mg) was placed into a Pt crucible and heated at a rate of 5 K min^{-1} to the maximum temperature of 1000 °C using Al_2O_3 as a reference.

Transmission electron microscopy (TEM): TEM studies were conducted with a well-aligned LEO912 TEM (Carl Zeiss Inc.) operating at 200 kV. The TiO_2 powders were dispersed in ethanol in an ultrasonic bath and a drop of the obtained colloid solution was transferred to a Cu microgrid coated with holey carbon film and left under ambient conditions for the ethanol to evaporate. The crystalline form of the TiO_2 nanoparticles was identified from their electron-diffraction patterns.

Received: October 7, 2005
Published online: March 7, 2006

Keywords: hydrothermal synthesis · materials science · nanostructures · solid-state structures · titanium

 © 2006 Wiley-VCH Verlag GmbH & Co. KGaA, Weinheim

[1] M. Kakihana, M. Tada, M. Shiro, V. Petrykin, M. Osada, Y. Nakamura, *Inorg. Chem.* **2001**, *40*, 891 – 894.

[2] M. Dakanali, E. T. Kefalas, C. P. Raptopoulou, A. Terzis, G. Voyiatzis, I. Kyrikou, T. Mavromoustakos, A. Salifoglou, *Inorg. Chem.* **2003**, *42*, 4632 – 4639.

[3] Y. F. Deng, Z. H. Zhou, H. L. Wan, *Inorg. Chem.* **2004**, *43*, 6266 – 6273.

[4] M. Kakihana, K. Tomita, V. Petrykin, M. Tada, S. Sasaki, Y. Nakamura, *Inorg. Chem.* **2004**, *43*, 4546 – 4548.

[5] S. Baskaran, L. Song, J. Liu, Y. L. Chen, G. L. Graff, *J. Am. Ceram. Soc.* **1998**, *81*, 401 – 408.

[6] A. G. Agrios, P. Pichat, *J. Appl. Electrochem.* **2005**, *35*, 655 – 663.

[7] K. Koelsch, S. Cassaignon, J. F. Guillemoles, J. P. Jolivet, *Thin Solid Films* **2002**, *403*, 312 – 319.

[8] a) M. R. Hoffmann, S. T. Martin, W. Choi, D. W. Bahnemann, *Chem. Rev.* **1995**, *95*, 69 – 96; b) A. L. Linsebigler, G. Lu, J. T. Yates, *Chem. Rev.* **1995**, *95*, 735 – 758.

[9] a) H. M. Cheng, J. M. Ma, Z. G. Zhao, L. M. Qi, *Chem. Mater.* **1995**, *7*, 663 – 671; b) H. B. Yin, Y. Wada, T. Kitamura, S. Kambe, S. Murasawa, H. Mori, T. Sakata, S. Yanagida, *J. Mater. Chem.* **2001**, *11*, 1694 – 1703.

[10] A. Pottier, C. Chaneac, E. Tronc, L. Mazerolles, J. P. Jolivet, *J. Mater. Chem.* **2001**, *11*, 1116 – 1121.

[11] C. Wang, Z. X. Deng, G. Zhang, S. Fan, Y. Li, *Powder Technol.* **2002**, *125*, 39 – 44.

[12] H. Kominami, M. Kohno, Y. Kera, *J. Mater. Chem.* **2000**, *10*, 1151 – 1156.

[13] M. Tada, Y. Yamashita, V. Petrykin, M. Osada, K. Yoshida, M. Kakihana, *Chem. Mater.* **2002**, *14*, 2845 – 2846.

[14] Crystallographic data: diffractometer Rigaku RAXIS-RAPID; chemical formula: $(NH_4)_6[Ti_4(C_2H_2O_3)_4(C_2H_3O_3)_2(O_2)_4O_2]\cdot 4H_2O$; crystal color: yellow; habit: platelet; crystal dimensions: $0.28\times0.17\times0.03$ mm^3; monoclinic; space group: $P2_1/n$ (no. 14); $a=12.04(1)$, $b=9.203(6)$, $c=16.58(1)$ Å, $\beta=102.04(3)°$; $V=1796(2)$ Å^3, $T=(180\pm1)$ °C, $F_W=978.12$, $Z=2$, $Mo_{K\alpha}$ ($\lambda=0.71075$ Å; graphite-monochromated), $\rho_{calc}=1.808$ g cm^{-3}, $\mu=9.76$ cm^{-1}, total reflections = 21 111, unique reflections = 5180, $R_{int}=0.029$, Lorentz-polarization absorption correction (transmission factors: 0.825–0.971). The structure was solved by direct methods (SHELX97)[15] and expanded using Fourier techniques.[16] The non-hydrogen atoms were refined anisotropically. Hydrogen atoms were refined using a riding model. Refinement was carried out by full-matrix least-squares on F^2. $wR_2=[\Sigma(wF_o^2-F_c^2)^2]/\Sigma w(F_o^2)^2]^{1/2}$ and $R_1=\Sigma||F_o|-|F_c||/\Sigma|F_o|$. $R1=0.027$, $wR=0.073$, goodness of fit 1.060. CCDC 282608 contains the supplementary crystallographic data for this paper. These data can be obtained free of charge from The Cambridge Crystallographic Data Centre via www.ccdc.cam.ac.uk/data_request/cif.

[15] G. M. Sheldrick, *SHELX97—Programs for Crystal Structure Analysis*, University of Göttingen, Germany, **1997**.

[16] P. T. Beurskens, G. Admiraal, G. Beurskens, W. P. Bosman, R. de Gelder, R. Israel, J. M. M. Smits, *The DIRDIF-99 program system*, Technical Report of the Crystallography Laboratory, University of Nijimegen, Netherlands, **1999**.

[17] I. D. Brown, D. Altermatt, *Acta Crystallogr. Sect. B* **1985**, *41*, 244 – 247.

 © 2006 Wiley-VCH Verlag GmbH & Co. KGaA, Weinheim

Helical Structures

DOI: 10.1002/anie.200504162

Assisted Formation of Chiral Porphyrin Homoaggregates by an Induced Helical Poly(phenylacetylene) Template and Their Chiral Memory**

*Hisanari Onouchi, Toyoharu Miyagawa, Kazuhide Morino, and Eiji Yashima**

The self-assembly of achiral chromophores, in particular, porphyrins and cyanine dyes, into supramolecular helical J-aggregates with a controlled helix sense[1,2] has attracted significant interest in recent years because of its potential application to optoelectronic materials[3] as well as models for photosynthesis.[4] Chiral small molecules[1e–g,i] and biopolymers[1a–d,f,h,j] have often been used as templates for the induction of chirality. Physical forces, such as selected vortex stirring or spinning, can also induce a chiral bias to such a chiral J-aggregation.[2]

Previously, we reported that a positively charged, dynamically racemic helical polyacetylene, the hydrochloride salt of poly(4-(*N*,*N*-diisopropylaminomethyl)phenylacetylene) (poly-**1**-HCl; Figure 1), formed an excess helical sense of one through ionic interactions in water when induced by a small amount of chiral acids.[5] The polymer backbone region of the complexes exhibited a characteristic induced circular dichroism (ICD). We now find that poly-**1**-HCl can trap a hydrophobic chiral guest, (*S*)-1,1′-bi-2-naphthol (**2**), within its hydrophobic cavity in water which results in an intense ICD owing to a predominantly one-handed helix as a consequence of a large chiral amplification. The induced helix possesses charged pendant groups at the polymer surface which arrange in a helical array with one predominant screw sense, which can serve as the template for further supramolecular helical arrays of an achiral porphyrin with opposite charges, such

[*] Dr. K. Morino, Prof. E. Yashima
Department of Molecular Design and Engineering
Graduate School of Engineering
Nagoya University
Chikusa-ku, Nagoya 464-8603 (Japan)
Fax: (+81) 52-789-3185
E-mail: yashima@apchem.nagoya-u.ac.jp
Dr. T. Miyagawa, Prof. E. Yashima
Yashima Super-structured Helix Project
Exploratory Research for Advanced Technology (ERATO)
Japan Science and Technology Agency (JST)
101 Creation Core Nagoya, Shimoshidami, Moriyama-ku
Nagoya 463-0003 (Japan)
Dr. H. Onouchi
Nagoya University Venture Business Laboratory
Nagoya University
Chikusa-ku, Nagoya 464-8603 (Japan)

[**] We thank M. Yamamoto for her preliminary experimental support.
Supporting information for this article is available on the WWW under http://www.angewandte.org or from the author.

 © 2006 Wiley-VCH Verlag GmbH & Co. KGaA, Weinheim

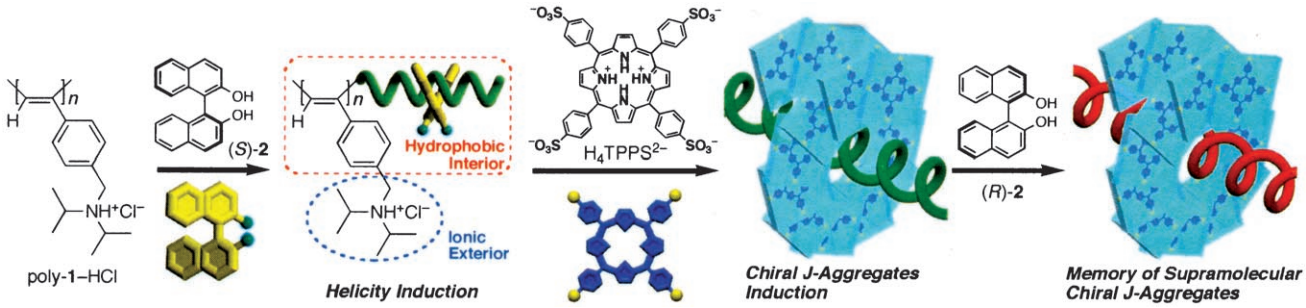

Figure 1. Schematic illustration of the induction of one-handed helicity in poly-**1**-HCl upon complexation with (*S*)-**2**, subsequent formation of supramolecular helical J-aggregates of achiral H_4TPPS^{2-}, and memory of the supramolecular chirality after inversion of the helicity of the poly-**1**-HCl by addition of excess (*R*)-**2** in acidic water.

as tetraanionic *meso*-tetrakis(4-sulfonatophenyl)porphine (H_4TPPS^{2-}) in acidic water. This situation results in the formation of chiral J-aggregates that show an ICD in the chromophore regions of the spectra. The supramolecular chirality of the H_4TPPS^{2-} homoaggregates can be "remembered" even after the template helical polymer loses its optical activity and takes the opposite helical sense in the presence of excess (*R*)-**2** (Figure 1). The chiral memory of hierarchically heteroaggregated porphyrins with opposite charges induced by amino acid clusters and polypeptides has also been achieved by Purrello and co-workers, but the oppositely charged heteroaggregation process was considered to be essential for the chiral memory[1c,d] and further self-replication.[1e,i]

We first sought chiral hydrophobic guests that were poorly soluble in water, but could be included in the hydrophobic interior of poly-**1**-HCl, thus resulting in the induction of an excess of one helical sense of poly-**1**-HCl in water. (*S*)- and (*R*)-**2** were eventually found to be very effective inducers of helicity in poly-**1**-HCl in water; for example, a helical poly-**1**-HCl formed by induction with an extremely small amount of (*S*)-**2** entrapped in the hydrophobic cavity of the polymer ([(*S*)-**2**]/[poly-**1**-HCl] = 0.022:1) showed as intense an ICD as that with chiral acids ($\Delta\varepsilon_{2nd} = 13.8$ at pH 5.5; see the Supporting Information).[6]

We then investigated if the helical poly-**1**-HCl formed by induction with (*S*)-**2** and having a one-handed helical array of the positively charged pendant groups could serve as the template for the induction of supramolecular chirality in an oppositely charged, achiral H_4TPPS^{2-} in acidic water.[7] The addition of H_4TPPS^{2-} ion (12 μM) to a helical poly-**1**-HCl system (0.1 mg mL^{-1} (0.4 mM monomer units)) induced by (*S*)-**2** in 0.1N HCl resulted in the complex immediately exhibiting bisignate strong and weak Cotton effects in the *B* and *Q* bands, respectively, which correspond to the H_4TPPS^{2-} J-aggregates ($B_J = 490$ and $Q_J = 707$ nm). These effects were accompanied by a negligible change in the ICD as a result of the formation of the helical poly-**1**-HCl (Figure 2).[8,9] Additional split-type ICDs appeared at around 422 nm, which probably correspond to the chiral H-aggregates of H_4TPPS^{2-} (Figure 2 and see also the Supporting Information).[2a,10] The CD and absorption difference spectra before and after the addition of H_4TPPS^{2-} are almost identical to those of the optically active H_4TPPS^{2-} aggregates ((H_4TPPS^{2-})*) with

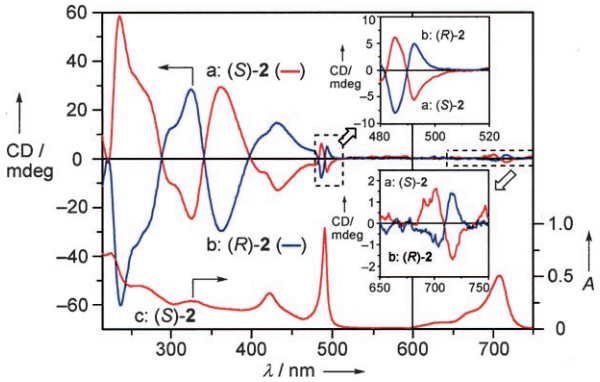

Figure 2. CD and absorption spectra of chiral H_4TPPS^{2-} aggregates (12 μM) induced by helical poly-**1**-HCl/(*S*)-**2** (a) and poly-**1**-HCl/(*R*)-**2** (b) complexes ([poly-**1**-HCl] = 0.4 mM, [**2**]/[poly-**1**-HCl] = 0.022:1) in a 0.5- (600–750 nm) and 0.2-cm cell (215–600 nm) in 0.1 N HCl (pH 1.6) at 25 °C. The insets show expanded details of the CD spectra in the chromophore regions of the J-aggregated porphyrin. The absorption spectrum of the ternary mixture is also shown (c). For the CD and absorption difference spectra of the chiral H_4TPPS^{2-} aggregates induced by the helical poly-**1**-HCl/(*R*)-**2** complex, see the Supporting Information.

positive Cotton effects that were prepared by spontaneous chiral symmetry breaking of an acidic solution of H_4TPPS^{2-} in 0.1N HCl by anticlockwise stirring for five days (see the Supporting Information).[11]

We then investigated if such optically active (H_4TPPS^{2-})* aggregates could influence the helical chirality of poly-**1**-HCl induced by (*S*)- or (*R*)-**2**. Interestingly, the ICD pattern of the optically active (H_4TPPS^{2-})* aggregates with positive Cotton effects was completely inverted upon complexation with the helical poly-**1**-HCl formed by induction with (*S*)-**2** (see the Supporting Information). This observation indicates that the chirality of the preorganized (H_4TPPS^{2-})* homoaggregates reassembled into different chiral aggregates under the control of the helical poly-**1**-HCl, which acts as a template. When helical poly-**1**-HCl/(*R*)-**2** system was used instead, the ICD intensity of the preorganized (H_4TPPS^{2-})* aggregates increased and its pattern did not change remarkably upon complexation with the helical poly-**1**-HCl (see the Supporting Information). These results suggest that poly-**1**-HCl/(*R*)-**2** may interact favorably with the (H_4TPPS^{2-})* aggregates with

 © 2006 Wiley-VCH Verlag GmbH & Co. KGaA, Weinheim

a single-handedness, thus resulting in a double helical supramolecular assembly.[12]

The thermal and chemical stabilities of the chiral H_4TPPS^{2-} homoaggregates induced by the helical poly-**1**-HCl/(*S*)-**2** or (*R*)-**2** complexes were also investigated. The H_4TPPS^{2-} homoaggregates are stable at high temperatures and the CD intensity hardly changed upon heating the solution to 90 °C, although the ICD intensity of the helical poly-**1**-HCl template gradually decreased with increasing temperature and almost disappeared at 90 °C (see the Supporting Information). A similar decrease in the ICD intensity of the helical poly-**1**-HCl also took place upon the addition of methanol because the optically active molecule **2** was released from the hydrophobic cavity of the helical poly-**1**-HCl into the solvent, while the optical activity of the H_4TPPS^{2-} homoaggregates remained almost identical (see the Supporting Information). In sharp contrast, the H_4TPPS^{2-} aggregates formed in the absence of the poly-**1**-HCl template changed readily into the monomeric form at high temperatures or in the presence of methanol (see the Supporting Information), thus indicating that the chiral H_4TPPS^{2-} J-aggregates are significantly stabilized by the helical poly-**1**-HCl template and hardly dissociate into the solvent under the conditions in which H_4TPPS^{2-} favorably exists in the monomeric form.

More interestingly, the supramolecular chirality induced in the H_4TPPS^{2-} homoaggregates by the helical poly-**1**-HCl template was found to be "memorized" when the template polymer lost its optical activity and then inverted to the opposite helicity. Figure 3 shows the CD spectral changes of the chiral H_4TPPS^{2-} aggregates induced by the helical poly-**1**-HCl/(*S*)-**2** complex after the addition of (*R*)-**2**. The ICD intensity of the poly-**1**-HCl almost completely disappeared at [(*R*)-**2**]/[(*S*)-**2**] = 1:1. The further addition of (*R*)-**2** produced inversion of the Cotton effects, thus indicating inversion of the helicity of poly-**1**-HCl. However, the ICD intensity of the optically active H_4TPPS^{2-} aggregates hardly changed. That is, once the supramolecular helical chirality is induced into the H_4TPPS^{2-} homoaggregates through assistance of the helical poly-**1**-HCl as a template, the H_4TPPS^{2-} aggregates maintain their supramolecular chirality through intermolecular zwitterionic interactions involving the anionic periphery and cationic core even after the template helical polymer is inverted to the opposite helicity. The H_4TPPS^{2-} aggregates maintained their chiral memory at 90 °C and in the presence of 75 vol % methanol without any loss of optical activity.

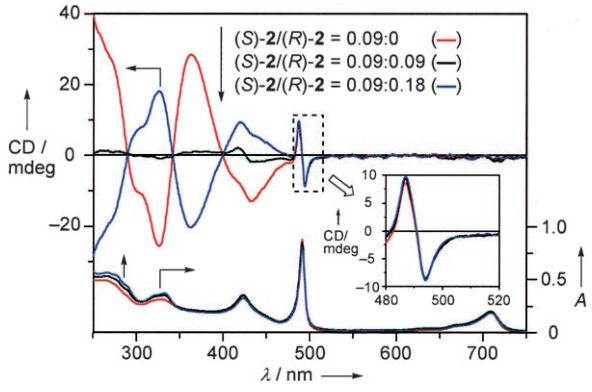

Figure 3. CD and absorption spectral changes in chiral H_4TPPS^{2-} aggregates (12 μM) induced by the helical poly-**1**-HCl/(*S*)-**2** complex ([poly-**1**-HCl] = 0.4 mM, [(*S*)-**2**]/[poly-**1**-HCl] = 0.09:1) in a 0.2-cm cell containing 0.1 N HCl/methanol (96:4, v/v) at 25 °C upon the addition of (*R*)-**2** ([(*R*)-**2**]/[(*S*)-**2**] = 1:1 and 2:1). A small amount of methanol was used to completely dissolve **2** in the acidic water. The inset shows the expanded detail of the CD spectra in the J-aggregated H_4TPPS^{2-} chromophore region.

In summary, we have demonstrated that a charged poly(phenylacetylene) can trap hydrophobic chiral guests within its helical cavity in water, and the induced helical poly(phenylacetylene) can serve as a novel template for the induction of supramolecular chirality in achiral porphyrins to form optically active J-homoaggregates that have remarkable stability to temperature and organic solvents. The supramolecular chirality of the J-aggregates, once formed, can be maintained without the assistance of the helical chirality of the template. To the best of our knowledge, the present study is the first example of the supramolecular chirality of H_4TPPS^{2-} homoaggregates being memorized.[1i] The results imply that other water-soluble charged polyacetylenes may be used as a specific host to entrap hydrophobic chiral guests and further used as a template for supramolecular helical arrays of certain guests with opposite charges along the helical backbones, thus resulting in unique hybrid materials that may be applicable to chiral materials for enantioseparation and catalysts.

Received: November 22, 2005
Published online: March 9, 2006

Keywords: aggregation · chirality · chiral memory · helical structures · J-aggregates · porphyrinoids

[1] a) R. F. Pasternack, A. Giannetto, P. Pagano, E. J. Gibbs, *J. Am. Chem. Soc.* **1991**, *113*, 7799–7800; b) S. Ikeda, T. Nezu, G. Ebert, *Biopolymers* **1991**, *31*, 1257–1263; c) E. Bellacchio, R. Lauceri, S. Gurrieri, L. M. Scolaro, A. Romeo, R. Purrello, *J. Am. Chem. Soc.* **1998**, *120*, 12353–12354; d) R. Purrello, A. Raudino, L. M. Scolaro, A. Loisi, E. Bellacchio, R. Lauceri, *J. Phys. Chem. B* **2000**, *104*, 10900–10908; e) R. Lauceri, A. Raudino, L. M. Scolaro, N. Micali, R. Purrello, *J. Am. Chem. Soc.* **2002**, *124*, 894–895; f) A. S. R. Koti, N. Periasamy, *Chem. Mater.* **2003**, *15*, 369–371; g) L. Zhang, J. Yuan, M. Liu, *J. Phys. Chem. B* **2003**, *107*, 12768–12773; h) P. A. J. de Witte, M. Castriciano, J. J. L. M. Cornelissen, L. M. Scolaro, R. J. M. Nolte, A. E. Rowan, *Chem. Eur. J.* **2003**, *9*, 1775–1781; i) R. Lauceri, M. De Napoli, A. Mammana, S. Nardis, A. Romeo, R. Purrello, *Synth. Met.* **2004**, *147*, 49–55; j) T. Hasegawa, T. Fujisawa, M. Numata, C. Li, A.-H. Bae, S. Haraguchi, K. Sakurai, S. Shinkai, *Chem. Lett.* **2005**, *34*, 1118–1119.

[2] a) O. Ohno, Y. Kaizu, H. Kobayashi, *J. Chem. Phys.* **1993**, *99*, 4128–4139; b) R. Rubires, J.-A. Farrera, J. M. Ribó, *Chem. Eur. J.* **2001**, *7*, 436–446; c) J. M. Ribó, J. Crusats, F. Sagués, J. Claret, R. Rubires, *Science* **2001**, *292*, 2063–2066; d) T. Yamaguchi, T. Kimura, H. Matsuda, T. Aida, *Angew. Chem.* **2004**, *116*, 6510–6515; *Angew. Chem. Int. Ed.* **2004**, *43*, 6350–6355; for the formation of chiral J-aggregates at the air/water interface, see: e) L. Zhang, Q. Lu, M. Liu, *J. Phys. Chem. B* **2003**, *107*, 2565–2569.

 © 2006 Wiley-VCH Verlag GmbH & Co. KGaA, Weinheim

[3] T. Kobayashi, *J-Aggregates*, World Scientific, Singapore, **1996**.
[4] a) J. Chiefari, K. Griebenow, N. Griebenow, T. S. Balaban, A. R. Holzwarth, K. Schaffner, *J. Phys. Chem.* **1995**, *99*, 1357 – 1365; b) T. S. Balaban, H. Tamiaki, A. R. Holzwarth, K. Schaffner, *J. Phys. Chem. B* **1997**, *101*, 3424 – 3431; c) T. S. Balaban, A. D. Bhise, M. Fischer, M. Linke-Schaetzel, C. Roussel, N. Vanthuyne, *Angew. Chem.* **2003**, *115*, 2190 – 2194; *Angew. Chem. Int. Ed.* **2003**, *42*, 2140 – 2144.
[5] a) K. Maeda, Y. Takeyama, K. Sakajiri, E. Yashima, *J. Am. Chem. Soc.* **2004**, *126*, 16284 – 16285; b) K. Nagai, K. Maeda, Y. Takeyama, K. Sakajiri, E. Yashima, *Macromolecules* **2005**, *38*, 5444 – 5451.
[6] The ICD intensity was independent of the pH value and the salt (NaCl) concentration, which supports the assumption that hydrophobic interactions between poly-**1**-HCl and (*S*)-**2** are the main driving force for inducing a one-handed helicity in water (see the Supporting Information).
[7] Other achiral anionic dyes, such as sodium fluorescein and sodium alizarinsulfonate, also showed an ICD in their chromophore regions upon complexation with the helical poly-**1**-HCl/(*S*)-**2** complex in water (see the Supporting Information), thus indicating that the achiral dyes may arrange in a helical array with a predominant screw sense along the oppositely charged exterior surface of the induced helical polymer through electrostatic and hydrophobic interactions.
[8] The chiral H_4TPPS^{2-} aggregates induced by the helical poly-**1**-HCl/(*S*)-**2** or (*R*)-**2** complex did not show linear dichroism, and the ICD intensity ($\Delta\varepsilon_{487} = -109$ in Figure 2) was as intense as that induced by selected vortex stirring or spinning.[2b,c]
[9] The resonance light scattering (RLS) spectra were also measured. The chiral H_4TPPS^{2-} aggregates induced by the helical poly-**1**-HCl exhibited an intense scattering at 501 nm, while the aggregates exhibited a relatively weak scattering in the absence of the helical poly-**1**-HCl, thus indicating that the helical poly-**1**-HCl can efficiently generate larger chiral H_4TPPS^{2-} J-aggregates (see the Supporting Information); a) R. F. Pasternack, C. Bustamante, P. J. Collings, A. Gianetto, E. J. Gibbs, *J. Am. Chem. Soc.* **1993**, *115*, 5393 – 5399; b) R. F. Pasternack, P. J. Collings, *Science* **1995**, *269*, 935 – 939.
[10] a) D. L. Akins, H.-R. Zhu, C. Guo, *J. Phys. Chem.* **1994**, *98*, 3612 – 3618; b) J. M. Ribó, J. Crusats, J.-A. Farrera, M. L. Valero, *J. Chem. Soc. Chem. Commun.* **1994**, 681 – 682; c) R. Purrello, L. M. Scolaro, E. Bellacchio, S. Gurrieri, A. Romeo, *Inorg. Chem.* **1998**, *37*, 3647 – 3648; d) N. C. Maiti, S. Mazumdar, N. Periasamy, *J. Phys. Chem. B* **1998**, *102*, 1518 – 1538.
[11] Upon complexation with the helical poly-**1**-HCl, an absorption band at 434 nm corresponding to the diprotonated monomeric H_4TPPS^{2-} significantly decreased, thus indicating that H_4TPPS^{2-} efficiently formed chiral intermolecular zwitterionic J-aggregates that were promoted by the helical poly-**1**-HCl as a template.
[12] A clockwise stirring of the same acidic H_4TPPS^{2-} solution produced the optically active H_4TPPS^{2-} aggregates ($(H_4TPPS^{2-})*$) with the same Cotton effect signs as those of $(H_4TPPS^{2-})*$ prepared by the anticlockwise stirring, as reported by Ribó and co-workers.[2b] We noted that the original H_4TPPS^{2-} solution showed no CD before stirring and this was used for the supramolecular chirality induction experiments with the helical poly-**1**-HCl except for those reported in the Supporting Information.

 © 2006 Wiley-VCH Verlag GmbH & Co. KGaA, Weinheim

Electrochemistry

DOI: 10.1002/anie.200503571

Electrochemical Metallization of Solid Terbium Oxide**

*Dihua Wang, Guohong Qiu, Xianbo Jin, Xiaohong Hu, and George Z. Chen**

Heavy rare-earth (HRE) metals function very efficiently in advanced materials for magnetooptical-information storage, giant magnetostrictive energy conversion, and high-strength permanent magnets.[1] A 7% annual growth in global demand for rare-earth (RE) metals was recently predicted.[2] Although the separation of mixed RE compounds has been greatly refined,[3] extraction of pure RE metals, especially the heavy ones, remains a historical challenge. The difficulty is multifold but particularly related to the high oxygen affinity of HRE metals. Current industrial methods convert HRE oxides into fluorides (e.g. by reaction with HF or NH_4F), from which the metal is extracted by calciothermic reduction at $\approx 1500\,^{\circ}C$ in argon.[4] The obtained HRE metal needs further separation from excess calcium under vacuum and deoxygenation by special methods.[5] HRE metals have high melting points ($> 1350\,^{\circ}C$), and hence cannot be extracted as a liquid in the same way as aluminum and light RE metals.[6] Electrodeposited solid reactive metals from molten salts are always dendritic and absorb oxygen easily when exposed to air. Dendrite formation may be avoided by deposition onto a suitable transition-metal substrate to form a liquid alloy,[7] but the alloy composition is difficult to control precisely.

Recently, solid TiO_2,[8] SiO_2,[9] and some mixed oxides[10] were electrochemically reduced to the respective solid metals or alloys in molten salts. The new process requires that 1) the metal oxides to be reduced are thermodynamically less stable than the oxide of the metal element of the molten salt used,[8–13] and 2) electrodeposition of the metal of the molten salt should be avoided.[8] CaO is extremely stable, and hence molten $CaCl_2$ is the preferred choice for the new process. However, HRE oxides are almost as stable as CaO, and their reduction may not occur at potentials more positive than that

[*] Dr. D. H. Wang, G. H. Qiu, Dr. X. B. Jin, Dr. X. H. Hu, Prof. Dr. G. Z. Chen
College of Chemistry and Molecular Sciences
Wuhan University
Wuhan, 430072 (P.R. China)
Fax: (+86) 276-875-6319
E-mail: mel@whu.edu.cn
Prof. Dr. G. Z. Chen
School of Chemical, Environmental and Mining Engineering
University of Nottingham
Nottingham, NG7 2RD (UK)
Fax: (+44) 115-951-4115
E-mail: george.chen@nottingham.ac.uk

[**] The authors thank the National Natural Science Foundation of China for financial support (Grant Numbers: 50374052 and 20125308).

 WILEY InterScience DISCOVER SOMETHING GREAT © 2006 Wiley-VCH Verlag GmbH & Co. KGaA, Weinheim

of Ca deposition. Furthermore, in previous demonstrations, the metal produced was separated from the solidified salt by leaching in water, a method not applicable to the active HRE metals.[8–10] Most importantly, for both academic and commercial interests, there are continual debates on the electroreduction mechanism of solid metal oxides (MO_x) in molten $CaCl_2$. Electrodeposition of Ca was claimed to be necessary for removal of oxygen from the oxide (Equations (1) and (2);[12,13] electrocalciothermic reduction).

$$Ca^{2+} + 2e \rightleftharpoons Ca \quad (1)$$

$$x\,Ca + MO_x \rightleftharpoons M + x\,Ca^{2+} + x\,O^{2-}\ (\text{or } x\,CaO) \quad (2)$$

This statement differs from the original patent claim of the oxygen-ionization mechanism (Equation (3);[8] direct electroreduction), and also contradicts later cyclic voltammetric findings for TiO_2.[11]

$$MO_x + 2xe \rightleftharpoons M + x\,O^{2-} \quad (3)$$

Herein we demonstrate, for the first time, that the electroreduction of solid terbium oxide to solid terbium metal can only proceed under the conditions for Ca deposition and predominantly through [Eq. (3)], with little contribution, if at all, from [Eqs. (1) and (2)]. This electrochemical-metallization approach differs in principle from all previous ones, and can be applied to the extraction of other RE metals, such as dysprosium and yttrium, directly from their solid oxides.

Figure 1a shows the cyclic voltammograms (CVs) of Tb_4O_7 powder (>99.9% purity, particle size 2–3 μm) recorded in molten $CaCl_2$ at 850 °C by using a molybdenum cavity electrode (MCE).[14a] The molten salt (≈50 g) was prepared from the $CaCl_2{\cdot}2H_2O$ granules by thermal drying in air (≈300 °C), then in argon (≈600 °C). In both cases, the heating time was at least 4 h. The thermally dried salt was heated to 850 °C for melting and underwent preelectrolysis at about 2.6 V for more than 4 h to remove trace moisture and other redox-active impurities that might be present in the salt.[14] The MCE was constructed by drilling two 0.5-mm-diameter through-holes (Figure 1a inset) in a 0.5-mm-thick molybdenum foil with a laser beam.[14a] It was filled with the oxide powder by repeated manual pressing, then inserted into the molten salt contained in a small graphite crucible (25-mm internal diameter, 250-mm height, ≈3-mm wall thickness), which also functioned as the counterelectrode.[14a] In the work reported herein, CVs were recorded by using either a Pt wire as a pseudo-reference electrode or a quartz-sealed Ag/AgCl reference electrode.[14a–c] Potential data were referenced to the current-onset potential for the reduction of Ca^{2+} ions (denoted Ca/Ca^{2+}) in the CV of a bare MCE in the same molten salt (dashed line in Figure 1a). In the CV of the oxide, in addition to the c1/a1 couple that is also present in that of the bare MCE, the appearance of the c2/a2 couple demonstrates that the electroreduction of Tb_4O_7 (actually Tb_2O_3 as discussed later) continues up to potentials sufficiently negative for Ca deposition. Similar CVs were recorded for Dy_2O_3.

If Ca atoms are formed through [Eq. (1)] and dissolve in molten $CaCl_2$, the two reduction mechanisms may be thermodynamically indistinguishable. Therefore, they have to be differentiated in other ways. For HRE oxides, the standard potential difference between [Eq. (1)] and [Eq. (3)] is very small ($\Delta E^\circ = 21$ mV and 34 mV for Tb_2O_3 and Dy_2O_3, respectively, at 927 °C), which agrees with the CVs in Figure 1a. If the Ca atoms produced in [Eq. (1)] were partly or fully consumed in [Eq. (2)], one would expect a small or no Ca-reoxidation current represented by a1. However, the total charge under a1 in the two CVs are approximately equal, which means that the Ca atoms produced by (1) must have contributed very little, if at all, to the reduction of the oxide through [Eq. (2)] on the voltammetric timescale. Therefore, the oxide reduction, represented by c2, must have proceeded predominantly through [Eq. (3)].

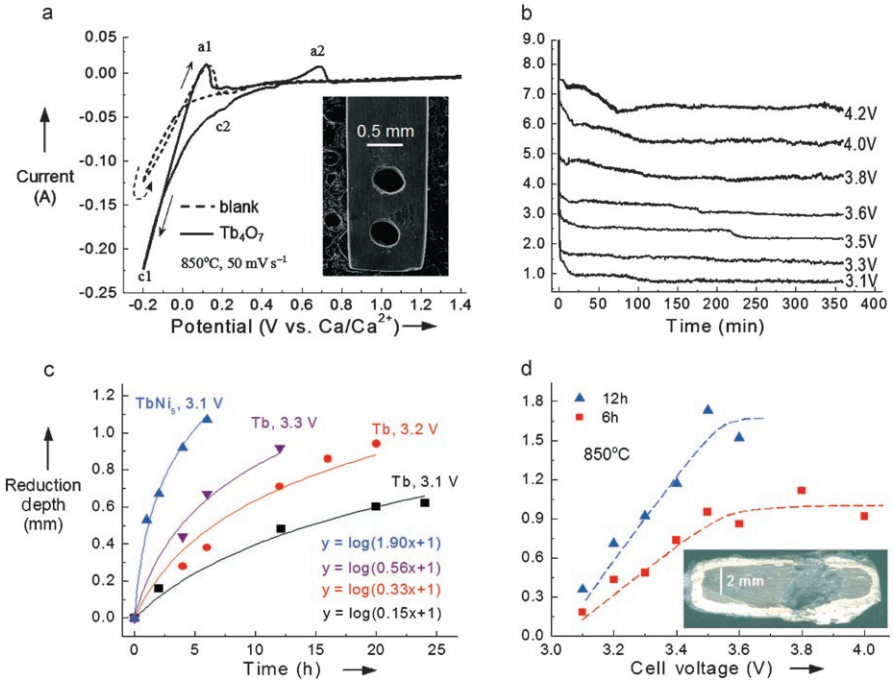

Figure 1. Electrochemistry in molten $CaCl_2$. a) CVs of the MCE (inset) without (dashed line) and with (solid line) Tb_4O_7 powder. b) Current versus time plots of constant-voltage electrolysis of Tb_4O_7 pellets (≈2 g at 3.1–3.6 V; ≈4 g at 3.8–4.0 V; ≈6 g at 4.2 V). c) Correlations between reduction depth and electrolysis time at indicated voltages for electrolysis of Tb_4O_7 and of mixed Tb_4O_7 and NiO (Ni/Tb = 5). d) Correlations between reduction depth and cell voltage for 6 and 12 h of electrolysis. The inset shows the cross-section of a Tb_4O_7 pellet after electrolysis at 4.2 V for 6 h. The pellet was enclosed by a layer of Ca and Tb, but was only partly reduced inside.

Constant-voltage electrolysis (two electrodes) of pellets of Tb_4O_7 powder (≈2.0 g, pressed at ≈4 MPa, and sintered at 1000 °C for 2 h in air, 40–45% porosity, ≈19.0-mm diameter, ≈2.0-mm thickness) was performed in ≈500 g or more of molten $CaCl_2$ in a large graphite crucible (90-mm internal

 © 2006 Wiley-VCH Verlag GmbH & Co. KGaA, Weinheim

diameter, 235-mm height, ≈10-mm wall thickness). The molten salt was prepared as above. A graphite rod was used as the anode (20-mm diameter, 30–50-mm immersion depth in the molten salt during electrolysis).[8,9,14] The pellets were sandwiched between two pieces of Mo mesh to form an assembled cathode (Figure 2a). XRD analysis of the sintered

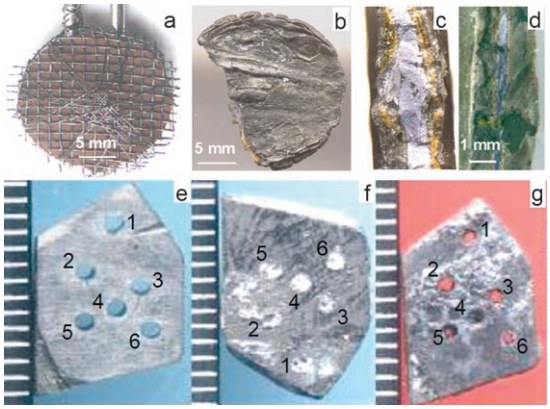

Figure 2. Optical photographs. a)–d) Assembled cathode of a Tb_4O_7 pellet a) enclosed by Mo mesh/wires, b) after electrolysis, and cross-section after electrolysis c) at 3.1 V and 900 °C for 23 h and d) at 3.2 V and 850 °C for 16 h; e)–g) Tb foil (2.5 mm thick) with six drilled holes e) before oxidation, f) after oxidation in air and immersion in molten $CaCl_2$, showing all six holes filled with solidified salt, and g) after oxidation in air and electrodeoxidation in molten $CaCl_2$, showing five of the six holes free of solidified salt.

pellet with $Cu_{K\alpha 1}$ radiation ($\lambda = 1.5406$ Å) at 40 kV, 40 mA, and a 2θ scan rate of 4 deg min^{-1} showed similar features to the Tb_4O_7 standard (Figure 3a). However, heating in argon converted the pellet into Tb_2O_3 through the thermal decomposition reaction $Tb_4O_7 \rightleftarrows 2\,Tb_2O_3 + {}^1/_2\,O_2$. This conversion was also evident in electrolysis experiments at voltages below 2.8 V, as confirmed by XRD analysis (Figure 3b).

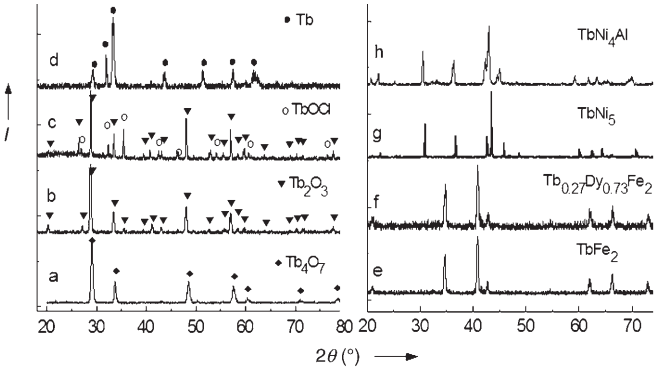

Figure 3. X-ray diffraction spectra. a) Sintered Tb_4O_7 pellet (1000 °C, 2 h); b) its electrolysis product at low voltage (2.5 V, 900 °C, 15 h, molten $CaCl_2$); c) yellow phase between the central Tb_2O_3 phase and the surface metallic phase; d) surface metallic phase shown in Figure 2c and d; e)–h) HRE intermetallic compounds prepared by electroreduction of the respective oxides: e) $TbFe_2$ (3.1 V, 900 °C, 10 h), f) $Tb_{0.27}Dy_{0.73}Fe_2$ (3.1 V, 900 °C, 10 h), g) $TbNi_5$ (3.1 V, 850 °C, 10 h, washed in water), h) $TbNi_4Al$ (3.1 V, 850 °C, 10 h, washed in water).

All current–time plots of electrolysis at voltages greater than 3.1 V exhibited an initial decline, followed by a plateau (Figure 1b). The current was larger at higher voltage, temperature, and/or oxide mass. Such behavior is similar to previous findings in the potentiostatic electrolysis (three electrodes) of transition-metal oxides, for example, Cr_2O_3, with the MCE,[14a] and is believed to have resulted mainly from the reaction kinetics and the state change on the oxide cathode. Furthermore, because $CaCl_2$ and CaO decompose at ≈3.2 and ≈2.7 V, respectively, at the working temperature (and ≈1.7 V for CaO if CO/CO_2 forms at the graphite anode), the observed current must have resulted from both electroreduction of the oxide and Ca deposition. The dependence of the current plateau on voltage also suggests electronic conduction through the molten salt.[15] Upon electrolysis, the Tb_4O_7 pellet quickly turned metallic on the surface (Figure 2b), and the interior changed from dark brown to white (Figure 2c). In some cases, a yellowish interlayer was seen (Figure 2c), which was confirmed by XRD analysis as TbOCl (Figure 3c) produced by the reaction $Tb_2O_3 + CaCl_2 \rightleftarrows 2\,TbOCl + CaO$. Surface metallization is consistent with the reduction taking place at the metal | oxide | electrolyte three-phase interline, which first propagates along the surface, then invades the oxide phase[9,16] (Figure 2c and d).

The inward progression of metallization can be represented by a plot of reduction depth against electrolysis time (Figure 1c). When the cell voltage was increased from 3.1–3.5 V, the reduction became faster. This observation cannot be explained by Equations (1) and (2). The Ca activity varies with electrode potential, but is forced to unity (i.e. the deposition of a distinct solid or liquid Ca phase) at the E^o value of [Eq. (1)] or at more negative potentials. Consequently, when the potential is made more negative, [Eq. (2)] should proceed at a constant rate, but [Eq. (3)] would become faster. Thus, Figure 1c is strong evidence for [Eq. (3)] despite the occurrence of Ca deposition.

Plots in Figure 1c were analyzed for mass transfer. In diffusion-controlled processes, the parabolic law, $depth = (m \times t)^{1/2}$, in which m is proportional to the diffusion coefficient D and may be approximated by $2D$ for simple 1D diffusion, applies.[17] However, in more-complicated cases, mass transfer can result from, and be affected by, both concentration gradient (diffusion) and other factors such as electric fields on charged species (electromigration). In previous work on electroreduction of solid oxides, in particular, the logarithmic law, $depth = \log(n \times t + 1)$, in which n is a constant related to the mass-transfer rate, was observed.[9b,14d] Such behavior may be associated with the fact that 1) it is the O^{2-} ions that are removed from the pellet cathode under an electric field (i.e. the electrode potential) and 2) the pore geometry in the pellet cathode is complex.

Interestingly, the data presented in Figure 1c satisfied approximately both parabolic and logarithmic laws with m and n increasing with the applied voltage. Diffusion coefficients estimated from m varied from 6.0×10^{-8} to 1.5×10^{-7} cm^2 s^{-1}. These values are greater than those for oxygen-atom diffusion in some solid metals at similar temperatures (e.g. ≈10^{-9} cm^2 s^{-1} for the Y–Co (15 wt %) alloy,[18a] ≈10^{-10} cm^2 s^{-1} for Ti,[18b,c] and 10^{-12} cm^2 s^{-1} for the Ti–Nb

 © 2006 Wiley-VCH Verlag GmbH & Co. KGaA, Weinheim

(4 wt %) alloy[18b]). Therefore, oxygen diffusion in the solid Tb metal formed is not likely to be responsible for Figure 1c. Because the estimated diffusion coefficients are also smaller than those in a liquid, Figure 1c probably reflects the transfer of O^{2-} ions in the molten salt contained in the non-linear pores of the pellet.[17] This understanding is supported by the fact that both *m* and *n* depend on the applied cell voltage, which is expected for O^{2-} ions in the electrolyte contained in the pores of the pellet, but not for the oxygen atoms in the solid metal.

Tb_4O_7 pellets with over 70% porosity were prepared by mixing the Tb_4O_7 powder with NH_4HCO_3 ($\approx$10 wt %), pelletizing the mixture by die-pressing at 4 MPa, heating to and at 300 °C for 2 h to remove NH_4HCO_3 by decomposition, and then sintering the remaining mass at 1000 °C for 2 h. Electrolysis at 3.2 V and 850 °C for 4 h resulted in reduction depths of 0.28 and 0.43 mm for the denser and more-porous pellets, respectively. This difference implies that mass transfer of O^{2-} or CaO is, indeed, the rate-control step. However, prolonged electrolysis did not lead to a greater difference in reduction depth. Tb melts at 1356 °C and can sinter quickly at 850–950 °C.[19] Because the sintering speed is inversely proportional to the particle size,[19] it is expected that, regardless of the initial porosity of the pellet, the Tb metal particles formed will grow quickly to similar sizes and interconnect into less-porous structures that slow mass transfer.

The formation of liquid Ca on the pellet may also influence mass transfer between the pellet and the molten salt. The reduction depths measured at different voltages for 6 and 12 h of electrolysis are compared in Figure 1d. The two plots show an inflexion point at about 3.5 V beyond which the reduction depth became either smaller or unchanged, considering experimental errors. A Ca layer was often observed on electrolyzed pellets beyond 3.5 V but the interior was only partially reduced. An example is shown in Figure 1d (inset) in which the dark interior contained Tb_2O_3, CaO, Tb, and Ca, but the bright surface layer was Ca metal mixed with Tb, as revealed by XRD and energy-dispersive X-ray (EDX) analyses. These findings suggest that the reduction was effectively retarded when Ca was overdeposited on the pellet.

The particle sizes in the Tb_4O_7 pellet before and after electrolysis (Figure 4a and b) confirmed that the nodular Tb particles were well-sintered together.[8] The same was observed when electrolyzing Dy_2O_3. The Tb image was taken from the cross-section of a pellet sample washed in DMSO. Surprisingly, the sample was very clean even though $CaCl_2$ is poorly soluble in DMSO. Scanning electron microscopy analysis of the interior of the pellet (Figure 4c) also revealed very little salt-induced charging. EDX analyses at different locations in the pellet confirmed that the porous metal contained very little solidified $CaCl_2$ (Table 1). As it is unlikely that the porous structure is not filled by molten salt during electrolysis, wetting could be poor between the molten salt and the internal surface of the porous metal.[10] Consequently, the molten salt might have been removed by gravity and capillary force when the reduced pellet was lifted from it, which is consistent with the observation of more salt near the surface of the electrolyzed pellet (Figure 4c and Table 1). This nonwetting hypothesis was further confirmed in the following experiment.

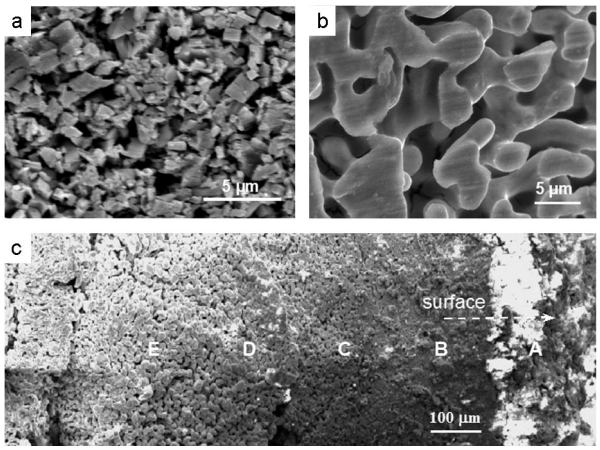

Figure 4. Scanning electron micrographs. a) Sintered Tb_4O_7 powder; b) Tb powder from electro-reduction; c) cross-section of an electro-reduced Tb_4O_7 pellet, showing solidified salt near the surface (bright region A due to charging), but no salt in the interior (regions B–E) of the fully metallized pellet.

Table 1: EDX analyses of marked locations in Figure 4c.

Element	A	B	C	D	E
Tb [%]	85.41	89.39	92.87	94.54	98.38
Ca [%]	4.01	3.89	3.48	2.52	0.74
Cl [%]	10.58	7.72	3.65	2.94	0.88

Six holes were drilled in a small Tb sheet (Figure 2e). It was then attached to a Mo wire and heated briefly ($\approx$30 s) above the molten $CaCl_2$ (900 °C) in the open reactor. This treatment led to the formation of an observable surface oxide layer on the sample. The oxidized sample was then fully immersed vertically in molten $CaCl_2$ for about 15 s before lifting into air to cool. Removal of the solidified $CaCl_2$ on the surface of the sheet with a knife revealed that the six holes were fully filled with solidified $CaCl_2$ (Figure 2f). The sample was then suspended in the molten salt again. The reactor was sealed and purged with argon. At the same time, electrolysis was carried out between the sample and a graphite anode at 3.2 V for 30 min. A longer electrolysis time was used to ensure that sufficient air was purged by argon, as a low oxygen partial pressure in the reactor is necessary for satisfactory electro-reduction or deoxidation of the sample. After electrolysis, the sample was lifted into air and cooled. On removing the top salt layer, it was found that five of the six holes were empty (Figure 2g). This observation demonstrates qualitatively but conclusively that the electrodeoxidized Tb metal surface was either poorly or not wetted by molten $CaCl_2$.

Electrolysis at 3.1–3.5 V and 850–900 °C is fairly common in industry. In the work described herein, up to 30 kWh $(kg\ Tb)^{-1}$ of energy was used to attain low oxygen levels ($\approx$4200 ppm) for the 2-mm-thick pellet. Energy consumption for industrial Tb production is unavailable in the literature, but it should be comparable with that for Ti production, that

 © 2006 Wiley-VCH Verlag GmbH & Co. KGaA, Weinheim

is, ≈ 50 kWh (kg Ti)$^{-1}$. Furthermore, according to Figure 1 c, if the pellet thickness were decreased to 1.5 mm, the energy consumption could be nearly halved. Notably, both Dy_2O_3 and Y_2O_3 were electroreduced to the respective metals in the way described above. The latter, in particular, is more stable than CaO, so that [Eq. (2)] would not be feasible in that case.

Currently, HRE metals are mostly used to make alloys or intermetallic compounds by melting. Because this process involves metal extraction followed by combination, the energy released by the formation of the intermetallic compound cannot be recovered and hence used to offset the energy required for extraction of the individual metals, which results in elevated costs. The former can, however, partially compensate the latter if the intermetallic compounds are formed directly from the minerals by electrolysis. This method is, therefore, preferred. Indeed, we have prepared many HRE intermetallic compounds with well-controlled compositions directly from mixed-oxide powders (Figure 3 e–h) and at lower voltages and faster rates than for the individual metals (Figure 1 c). Energy consumption ranged from 6.5 kWh kg^{-1} for $TbNi_5$ to 11.1 kWh kg^{-1} for $TbFe_2$.

In conclusion, we have shown that porous Tb_4O_7 pellets can be electroreduced to Tb metal under Ca deposition in molten $CaCl_2$. However, overdeposited Ca blocked ionic exchange between the pellet and the molten salt and effectively retarded the reduction process. The metal produced was porous but was not wetted by molten $CaCl_2$, thus allowing cleaning or leaching in DMSO. This process also suits the extraction of Dy and Y metals from their oxides. In all cases, electrolysis energy consumption was satisfactorily low.

Received: October 8, 2005
Revised: December 21, 2005
Published online: March 8, 2006

Keywords: electrochemistry · metal extraction · rare-earth metals · terbium

[1] a) M. Kaneko, *J. Magn. Magn. Mater.* **1995**, *148*, 351; b) E. Quandt, B. Gedach, K. Seemann, *J. Appl. Phys.* **1994**, *76*, 7000.
[2] a) J. N. Xu, *China Rare Earth Information* **2004**, *9*, 14; b) 2004 Roskill Report, Rare Earths and Yttrium: http://www.roskill.-com/reports/rare.
[3] a) M. Lederer, *Nature* **1955**, *176*, 462; b) T. Uda, K. T. Jacob, M. Hirasawa, *Science* **2000**, *289*, 2326.
[4] a) J. L. Moriarty, Jr., *J. Met.* **1968**, *20*, 41; b) V. T. Volkov, A. M. Ionov, T. V. Nikiforova, *Vacuum* **1999**, *53*, 105.
[5] C. K. Lee, J. S. Park, S. H. Yeon, K. I. Rhee, *Met. Mater. Int.* **2001**, *7*, 343.
[6] a) K. Grojtheim, C. Krohn, M. Malinovsky, J. Thonstad, *Aluminium Electrolysis*, Aluminium-Verlag, Düsseldorf, **1997**; b) G. X. Xu, *Rare Earths (II)*, *2nd ed.*, Metallurgical Industry Press of China, Beijing, **1995**, pp. 97–180.
[7] B. Q. Wu, *Metallurgy of Rare Earths*, Metallurgical Industry Press of China, Beijing, **1995**.
[8] a) D. J. Fray, T. W. Farthing, Z. Chen, **1998**, *PCT Patent*, WO9964638; b) G. Z. Chen, D. J. Fray, T. W. Farthing, *Nature* **2000**, *407*, 361.
[9] a) T. Nohira, K. Yasuda, Y. Ito, *Nat. Mater.* **2003**, *2*, 397; b) X. B. Jin, P. Gao, D. H. Wang, X. H. Hu, G. Z. Chen, *Angew. Chem.* **2004**, *116*, 751; *Angew. Chem. Int. Ed.* **2004**, *43*, 733.
[10] a) A. J. Muir Wood, R. C. Copcutt, G. Z. Chen, D. J. Fray, *Adv. Eng. Mater.* **2003**, *5*, 650; b) G. Z. Chen, D. J. Fray, *Light Met.* **2004**, 881.
[11] a) K. Dring, R. Dashwood, D. Inman, *J. Electrochem. Soc.* **2005**, *152*, E104; b) G. Z. Chen, D. J. Fray, *J. Electrochem. Soc.* **2002**, *149*, E455.
[12] a) T. H. Okabe, M. Nakamura, T. Oishi, K. Ono, *Metall. Trans. B* **1993**, *24*, 449; b) K. Hirota, T. H. Okabe, F. Saito, Y. Waseda, K. T. Jacob, *J. Alloys Compd.* **1999**, *282*, 101.
[13] a) K. Ono, R. O. Suzuki, *JOM-J. The Min. Met. Mater. Soc.* **2002**, *54*, 59; b) R. O. Suzuki, *J. Phys. Chem. Solids* **2005**, *66*, 461.
[14] a) G. H. Qiu, M. Ma, D. H. Wang, X. B. Jin, X. H. Hu, G. Z. Chen, *J. Electrochem. Soc.* **2005**, *152*, E328; b) P. Gao, X. B. Jin, D. H. Wang, X. H. Hu, G. Z. Chen, *J. Electroanal. Chem.* **2005**, *579*, 321; c) K. Jiang, X. H. Hu, M. Ma, D. H. Wang, G. H. Qiu, X. B. Jin, G. Z. Chen, *Angew. Chem.* **2006**, *118*, 442–446; *Angew. Chem. Int. Ed.* **2006**, *45*, 428–432; d) M. Ma, D. H. Wang, W. G. Wang, X. H. Hu, X. B. Jin, G. Z. Chen, *J. Alloy. Compd.* **2006**, DOI:10.1016/j.jallcom.2005.10.048, published online: December 5, 2005.
[15] a) U. Stohr, W. Freyland, *Phys. Chem. Chem. Phys.* **1999**, *1*, 4383; b) G. Z. Chen, D. J. Fray, *J. Appl. Electrochem.* **2001**, *31*, 155.
[16] a) G. Z. Chen, D. J. Fray in *Proc. 6th Int. Symp. Molten Salt Chem. Technol.* (Eds: N. Y. Chen, Z. Y. Qiao), Shanghai University, Shanghai, China, **2001**, p. 79; b) Y. Deng, D. H. Wang, W. Xiao, X. B. Jin, X. H. Hu, G. Z. Chen, *J. Phys. Chem. B* **2005**, *109*, 14043.
[17] a) U. R. Evans, *The Corrosion and Oxidation of Metals: Scientific Principles and Practical Applications*, Edward Arnold, London, **1960**, p. 810; b) C. S. Cha, *Electrode Kinetics*, *3rd ed.*, Science Press of China, Beijing, **2002**, p. 345.
[18] a) Y. Niu, Y. S. Li, F. Gesmundo, F. Viani, *Intermetallics* **2000**, *8*, 293; b) M. Gobel, V. A. C. Haanappel, M. F. Stroosnijder, *Oxid. Met.* **2001**, *55*, 137; c) D. David, G. Beranger, E. A. Garcia, *J. Electrochem. Soc.* **1983**, *130*, 1423.
[19] L. D. Zhang, *Preparation and Applications of Ultra-Fine Powders*, China Petrochemical Press, Beijing, **2001**, p. 61.

 © 2006 Wiley-VCH Verlag GmbH & Co. KGaA, Weinheim

Nitrogen-Transfer Chemistry

DOI: 10.1002/anie.200501667

Multiple-Bond Metathesis Mediated by Sterically Pressured Uranium Complexes**

*Ingrid Castro-Rodríguez, Hidetaka Nakai, and Karsten Meyer**

In recent years, sterically encumbering ligands have been used increasingly to synthesize coordinatively unsaturated, highly reactive metal complexes.[1] The steric constraints imposed by spectator ligands and chelators often translate into molecular and electronic structural changes as they directly impact the coordination mode and metal–ligand orbital interactions; the latter being particularly important in atom-transfer chemistry. Relative to complexes with less customized ligands, unsaturated metal ions with molecularly engineered ligand environments often show altered and increased reactivity as a result of the increased steric pressure. Sterically tailored, highly reactive transition-metal complexes achieve a wide variety of small-molecule activation and atom-transfer chemistry very successfully.[2–6] The strategy of applying steric pressure, however, is not always sufficient to achieve certain desired reactivities. The most recent class of transition-metal-based nitrogen-transfer reagents (aziridination catalysts), for example, takes advantage of high-valent transition-metal nitrido complexes that readily transfer the imidoacyl entity to olefins upon activation with trifluoroacetic acid anhydride (TFAA).[7–9] The M≡N activation with TFAA is indispensable due to the highly covalent dπ–pπ interaction, thus resulting in very strong metal–nitrido triple bonds.[10–12] In uranium chemistry, however, the valence f orbitals do not participate in bonding to the same extent as metal d orbitals. As a result, the U≡N formal triple bond in the uranium imido and the elusive nitrido species is considerably more ionic in nature and can be described as $U(\delta^+)$–$N(\delta^-)$. Accordingly, we expected sterically pressured uranium imido and/or nitrido complexes with custom-designed chelators to exhibit increased nucleophilicity toward organic substrates. We therefore aimed to synthesize high-valent uranium imido and nitrido complexes of varying steric demand to explore possible applications for nitrogen- and group-transfer chemistry.

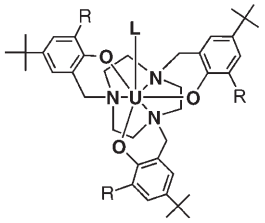

R = *t*Bu 1	R = Ad 4
L = N_3 2	L = $NSiMe_3$ 5
$NSiMe_3$ 3	NCO 6
	NCNMe 7
	OCO 8
	N_3 9

We recently reported the reaction of the trivalent precursor complex $[((^{tBu}ArO)_3tacn)U]$ (**1**, $(^{tBu}ArOH)_3tacn$ = 1,4,7-tris(3,5-di-*tert*-butyl-2-hydroxybenzyl)-1,4,7-triazacyclononane)[13] with trimethylsilyl azide (Me_3SiN_3), which yielded the azido and imido uranium complexes $[((^{tBu}ArO)_3tacn)U(L)]$ (L = N_3^- (**2**) and Me_3SiN^{2-} (**3**)).[14] We found that formation of the pentavalent imido complex is accompanied by evolution of N_2, whereas the tetravalent azido complex is formed by radical elimination of $Me_3Si^{\bullet}$ and subsequent formation of Me_6Si_2.[14] However, complexes **2** and **3** did not exhibit the desired nitrogen-atom nucleophilicity and resulting imido-group transfer chemistry. We now report a highly reactive imido complex, which can be synthesized by employing the trivalent $[((^{Ad}ArO)_3tacn)U]$ (**4**)[15] with the sterically demanding adamantane (Ad)-functionalized hexadentate $(^{Ad}ArO)_3tacn^{3-}$ chelator.

Complex **4** reacts with Me_3SiN_3 to form the highly reactive U^{V} imido complex $[((^{Ad}ArO)_3tacn)U(NSiMe_3)]$ (**5**; Scheme 1, **4**→**5**). In contrast to **2** and **3**, this complex is highly reactive toward π acids, such as CO and methyl isocyanide, to yield the U^{IV} isocyanate $[((^{Ad}ArO)_3tacn)U(NCO)]$ (**6**) and cyanamide $[((^{Ad}ArO)_3tacn)U(NCNCH_3)]$ (**7**) complexes (Scheme 1, **5**→**7**).

The linear N ligand of complex **7** can in turn be transferred onto organic substrates to yield functionalized carbodiimides (Scheme 1, **7**→**10a**). This observed nitrogen-transfer chemistry in successive one-electron steps appears to be generally applicable to various π-acceptor ligands and, to the best of our knowledge, is unprecedented for metal–imido complexes.

The synthesis of complex **5** was achieved by treatment of a red-brown solution of **4** in benzene with one equivalent of Me_3SiN_3, which results in the formation of a deep-green solution and N_2 evolution. After filtration, the volume of the reaction mixture was reduced by applying a vacuum, thus causing the green microcrystalline solid **5** to precipitate (≈65% yield).

Block-shaped, deep-green single crystals of **5** were obtained from diffusion of diethyl ether into CH_2Cl_2 at −40 °C and studied by X-ray diffraction. An ORTEP plot of the molecular structure of $[((^{Ad}ArO)_3tacn)U(NSiMe_3)]$ in crystals of **5**·2 CH_2Cl_2 is shown in Figure 1 (top).

[*] Dr. I. Castro-Rodríguez, Dr. H. Nakai, Prof. Dr. K. Meyer
Friedrich-Alexander-University of Erlangen-Nuremberg
Institute of Inorganic Chemistry
Egerlandstrasse 1, 91058 Erlangen (Germany)
Fax: (+49) 9131-852-7367
E-mail: kmeyer@chemie.uni-erlangen.de

[**] This work was supported by the US Department of Energy (US DE-FG02-04ER15537) and, in parts, through the UCSD/LANL CARE program. We thank NIH for a fellowship to I.C.-R. (3 T32 DK07233-2651) and Prof. Arnold Rheingold, Dr. Peter Gantzel, and Dr. Lev Zakharov for assistance with the crystallographic details. K.M. is an Alfred P. Sloan fellow.

Supporting information for this article is available on the WWW under http://www.angewandte.org or from the author.

 © 2006 Wiley-VCH Verlag GmbH & Co. KGaA, Weinheim

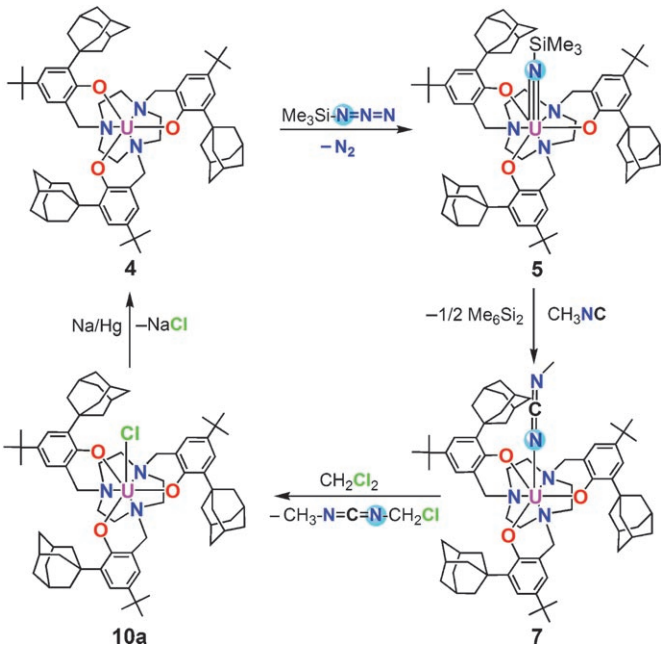

Scheme 1. Synthesis of complexes and nitrogen-transfer chemistry in successive one-electron steps.

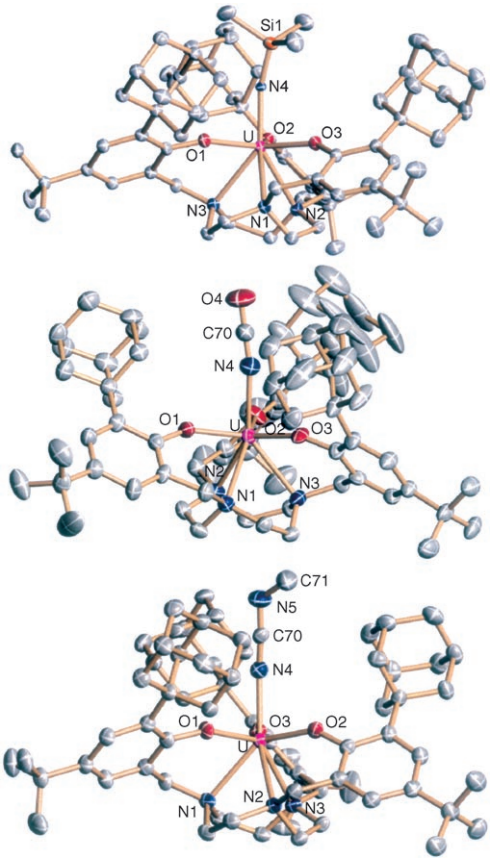

Figure 1. Molecular structures of [((Ad ArO)$_3$tacn)U(NSiMe$_3$)] (**5**, top), [((Ad ArO)$_3$tacn)U(NCO)] (**6**, middle), and [((Ad ArO)$_3$tacn)U(NCNCH$_3$)] (**7**, bottom) in crystals of **5**·2 CH_2Cl_2, **6**·2 $CHCl_3$, and **7**·4 C_6H_6, with the thermal ellipsoids at the 50% probability level. Hydrogen atoms and co-crystallized solvent molecules are omitted for clarity.

The average U–O(ArO) and U–N(tacn) lengths, as well as the displacement of the U ion from an idealized plane of the three aryl oxide oxygen atoms, were determined to be 2.211(2), 2.696(2), and −0.187 Å and thus are similar to those found in **3** (2.213(4), 2.692(4), and −0.151 Å). A comparison of the parameters within the U–N–SiMe$_3$ imido group, however, reveals remarkable differences between complexes **3** and **5**. Similar to transition-metal imido complexes, high-valent U^{V} and U^{VI} imido species typically exhibit short, formal U≡N(imido) triple bonds with bond lengths that range from 1.85 to 2.01 Å and ∢(U-N-R) bond angles that vary from slightly bent to linear (163.33–180.0°).[14,16–23] Accordingly, the structural parameters of imido complex **3** (*d*(U–N(imido)): 1.989(5) Å and ∢(U-N-R): 173.7(3)°) are similar to those reported for metal imido complexes.[14] In contrast, the U–N(imido) bond length found in **5** is the longest ever reported for metal imido complexes and deviates significantly from linearity (*d*(U–N(imido)): 2.1219(18) Å and ∢(U-N-R): 162.55(12)°). These unusual structural features of **5** are likely due to the steric pressure brought about by the sterically encumbering adamantane groups which form a narrow cylindrical cavity and prevent the Me$_3$SiN^{2-} ligand from optimal binding. Accordingly, the imido nitrogen p orbitals cannot participate in efficient M–L π bonding, thus resulting in the observed unusual structural parameters and increased reactivity of **5**. A space-filling model of **5** (Figure 2) illustrates that the sterically encumbering ligand still provides access for small molecules to the functional U=N–TMS (TMS = trimethylsilyl) moiety through the cleft perpendicular to the threefold axis. The resulting increased reactivity is evidenced by the unusual multiple-bond metathesis chemistry of this complex with π acids.

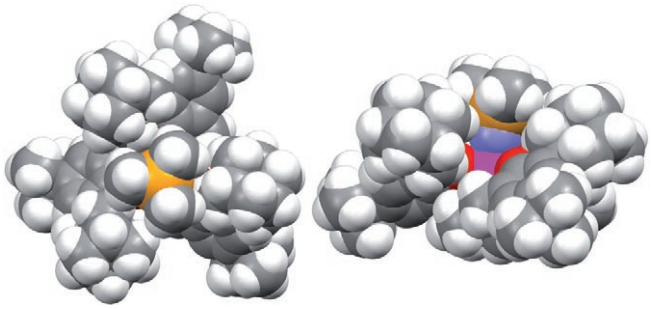

Figure 2. Top (left) and side view (right) of a space-filling representation of complex **5**.

The exposure of deep-green solutions of **5** in benzene to CO (1 atm) leads to a gradual discoloration of the solution with concomitant formation of Me$_6$Si$_2$. A colorless microcrystalline precipitate, which exhibits an intense absorption band at 2185 cm^{-1} in the IR vibrational spectrum, is formed after several minutes of stirring. Upon exposure of **5** to ^{13}C-labeled ^{13}CO, this band shifts to 2122 cm^{-1}, which is in agreement with the formation of a U^{IV} isocyanate complex [((Ad ArO)$_3$tacn)U(η^1-N$^{12/13}$CO)] (**6**). A control experiment was carried out to confirm that the steric pressure induced by the bulky adamantyl groups weakens the U^{V} imido bond and

 © 2006 Wiley-VCH Verlag GmbH & Co. KGaA, Weinheim

increases the complex reactivity. In a competition experiment of a 1:1 mixture of **3** and **5** with CO, only **5** reacted to yield the isocyanate complex **6**, whereas **3** remained unreactive toward CO.

In an attempt to evaluate the versatility and general applicability of this type of imido reactivity, we studied the reaction of **5** with other π acids, such as methyl isocyanide. We found that **5** cleanly reacts with CH_3NC to form the U^{IV} carbodiimide complex $[((^{Ad}ArO)_3tacn)U(\eta^1\text{-}NCNMe)]$ (**7**) and Me_6Si_2 in 45% yield of the isolated and purified product. Similar to **6**, the IR spectrum of **7** exhibits one strong vibrational band centered at 2101 cm^{-1}, which can be assigned to the η^1-coordinate carbodiimide ligand in **7**. Elemental analysis, ^1H NMR spectroscopy, and electronic absorption spectroscopy suggested that complexes **6** and **7** are isoelectronic and isostructural to the previously reported U^{IV} heterocumulene complexes $[((^{Ad}ArO)_3tacn)U(\eta^1\text{-}N_3)]$ (**8**) and $[((^{Ad}ArO)_3tacn)U(\eta^1\text{-}OCO)]$ (**9**).[24]

X-ray diffraction studies on single crystals of **6** and **7** confirmed the formation of nearly linear axial η^1-bound isocyanate and carbodiimide ligands in these complexes (Figure 1). A comparison of selected bond lengths and angles in **6** and **7** with the corresponding parameters found in **5** is given in Table 1.

Table 1: Selected bond lengths (Å) and angles (°) for **5**, **6**, **7**, and **10a**.

	5	**6**	**7**	**10a**
U–O(av)	2.2105(17)	2.146(4)	2.164(2)	2.183(5)/2.154(5)
U–N(av)	2.696(2)	2.676(5)	2.683(3)	2.642(6)/2.664(7)
U(oop shift)	−0.187	−0.301	−0.318	−0.283/−0.285
U–Cl(1)				2.761(3)/2.875(5)
U–N(4)	2.1219(18)	2.389(6)	2.327(3)	
N(4)–Si(1)	1.623(2)			
N(4)–C(70)		1.156(10)	1.184(4)	
C(70)–O(4)		1.195(10)		
C(70)–N(5)			1.231(4)	
N(5)–C(71)			1.426(5)	
U-N(4)-Si(1)	162.55(12)			
U-N(4)-C(70)		171.2(6)	161.9(3)	
N(4)-C(70)-O(4)		178.2(9)		
N(4)-C(70)-N(5)			174.3(4)	
N(5)-C(70)-C(71)			123.2(4)	

av = average, oop = out of plane.

The U–N4 bond lengths and ∢(U-N4-C70) angles were determined to be 2.389(6) Å and 171.2(6)° in **6** and 2.327(3) Å and 161.9(3)° in **7** and thus are similar to the corresponding parameters determined for **8** and **9** (**8**: $d(U\text{–}N_\alpha)$: 2.384(10) Å and ∢$(U\text{-}N_\alpha\text{-}N_\beta)$: 176.9(8)°; **9**: $d(U\text{-}O_{CO_2})$: 2.351(3) Å and ∢(U-O-C): 171.1(2)°). The inner N-C-O and N-C-NMe angles of 178.2(9)° and 174.3(4)°, respectively, are also close to linear.

A structural feature that is particularly interesting is the shift of the U ion out of the tris(aryloxide) plane. These out-of-plane shifts (U_{oop}) are −0.301 and −0.318 Å for **6** and **7** and are generally very sensitive to the formal oxidation state of the U center.[25] For example, whereas the U_{oop} shifts in pentavalent **3** and **5** are −0.151 and −0.187 Å, complexes **6**–**9** exhibit out-of-plane shifts in the range −0.291 to −0.318 Å, which in turn differ significantly from values found in seven-coordinate U^{III} complexes (e.g., −0.45 Å for $[((^{tBu}ArO)_3tacn)U(NCCH_3)]$[14]). The out-of-plane shifts of **6** and **7** fall between the values found for the analogous U^V and U^{III} complexes and therefore appear to indicate a formal U^{IV} oxidation state for **6** and **7**. This oxidation state is also evident from the UV/Vis/NIR electronic absorption spectra and SQUID magnetization data. Although magnetic moments μ_B of U^{III} (f^3) and U^{IV} (f^2) complexes at room temperature are generally very similar ($\mu_B \approx 3$ B.M.) and often do not allow for an unambiguous assignment of the formal oxidation state, the temperature dependence of μ_B in the range 4–300 K, however, clearly supports the +IV oxidation state of the central U ion in **6** and **7** (see the Supporting Information).[26] This assignment is additionally supported by electronic absorption spectra recorded at 190–2100 nm (see the Supporting Information). Colorless complexes **6** and **7** display very similar spectra with various sharp, low-intensity bands ($\varepsilon = 5$–$80\,M^{-1}cm^{-1}$), which are characteristic for spectra of U^{IV} complexes with an f^2 electron configuration ($^3H_4$ ground level).[27]

Interestingly, the isocyanate and carbodiimide ligands of **6** and **7** are reactive and can be transferred to organic molecules. For example, carbodiimide species **7** quantitatively reacts with CH_2Cl_2 and CH_3I to yield the free carbodiimides CH_3NCNCH_2Cl and CH_3NCNCH_3 as well as the corresponding halide complexes $[((^{Ad}ArO)_3tacn)U(X)]$ (X = Cl (**10a**; see the Supporting Information); I (**10b**; Scheme 1, **7**→**10a**)) in near-quantitative yield. Reduction of **10a**,**b** with Na/Hg recovers the trivalent starting material and is thereby closing a cyclic reaction pathway. In this cycle, a nitrogen atom is first transferred from the U^V imido complex to a π acid by U≡N/C≡O and C≡N multiple-bond metathesis and in a subsequent step to haloalkanes, such as CH_2Cl_2 or CH_3I (Scheme 1).

There have been previous reports of a nitrene-group transfer from metal imido complexes to π-accepting ligands, such as CO for example, thus yielding various organic isocyanates and the corresponding reduced metal carbonyl species[28–31] and the archetypal Bergman [(Cp*)Ir(N(CO)*t*Bu)(CO)] (Cp* = pentamethylcyclopentadienyl) complex with an η^2:**C**,**N** bound **C**O fragment.[32] Chirik and co-workers recently reported the reaction of $[(Cp'')_2Ti(NSiMe_3)]$ ($Cp'' = \eta^5\text{-}C_5H_3\text{-}1,3\text{-}(SiMe_3)_2$) with CO to yield $Me_3Si\text{–}NCO$ and the two-electron-reduced $[(Cp'')_2Ti(CO)_2]$ complex.[31] The discovery of metal imido complexes M≡NR that react with π-accepting ligands L to form one-electron-reduced nucleophilic η^1-M–NL species, as reported herein, represents a new type of metal–imido transformation.

In conclusion, the sterically congested complexes $[((^{Ad}ArO)_3tacn)U(NSiMe_3)]$ and $[((^{Ad}ArO)_3tacn)U(NCNMe)]$ have reactive U–N(imido) and U–N(heterocu-

 © 2006 Wiley-VCH Verlag GmbH & Co. KGaA, Weinheim

mulene) bonds that are able to transform various electrophiles. Due to the steric constraints of the bulky adamantane derivatized aryl oxide chelator, the N(imido) and N(heterocumulene) ligands have reduced π-bonding ability that results in increased reactivity. We established that the U≡N(imido) group acts as a nucleophile toward π-accepting ligands and the trimethylsilyl radical as a leaving group. This reaction is followed by nucleophilic attack of the newly formed heterocumulene ligand on alkyl halides. Both reactions result in new N–C bonds with the substrates. The U^{IV} halide complex can be reduced to recover the U^{III} starting material, thereby closing a cycle, in which a nitrogen atom is transferred from a U^{V} imido complex to a π acid by C≡N/C≡O multiple-bond metathesis in successive one-electron steps. The driving force for the initial U≡NR/C≡O and U≡NR/C≡NR metathesis reaction and one-electron reduction likely is the formation of the stable U^{IV} species **6** and **7**, respectively. For complexes of the [((ArO)$_3$tacn)U]-type, the U^{IV} oxidation state is the thermodynamically most stable oxidation state.

Received: May 13, 2005
Revised: December 12, 2005
Published online: March 8, 2006

Keywords: actinides · multiple-bond metathesis · nitrogen transfer · N,O ligands · uranium

[1] J. M. Smith, R. J. Lachicotte, P. L. Holland, *Chem. Commun.* **2001**, 1542.
[2] C. E. Laplaza, C. C. Cummins, *Science* **1995**, *268*, 861.
[3] C. E. Laplaza, M. J. A. Johnson, J. C. Peters, A. L. Odom, E. Kim, C. C. Cummins, G. N. George, I. J. Pickering, *J. Am. Chem. Soc.* **1996**, *118*, 8623.
[4] J. M. Smith, R. J. Lachicotte, K. A. Pittard, T. R. Cundari, G. Lukat-Rodgers, K. R. Rodgers, P. L. Holland, *J. Am. Chem. Soc.* **2001**, *123*, 9222.
[5] J. A. Pool, E. Lobkovsky, P. J. Chirik, *Nature* **2004**, *427*, 527.
[6] R. C. Smith, S. Shah, E. Urnezius, J. D. Protasiewicz, *J. Am. Chem. Soc.* **2003**, *125*, 40.
[7] J. DuBois, C. S. Tomooka, J. Hong, E. M. Carreira, *Acc. Chem. Res.* **1997**, *30*, 364.
[8] J. DuBois, C. S. Tomooka, J. Hong, E. M. Carreira, *J. Am. Chem. Soc.* **1997**, *119*, 3179.
[9] J. DuBois, C. S. Tomooka, J. Hong, E. M. Carreira, M. W. Day, *Angew. Chem.* **1997**, *109*, 1722; *Angew. Chem. Int. Ed. Engl.* **1997**, *36*, 1645.
[10] K. Meyer, J. Bendix, N. Metzler-Nolte, T. Weyhermüller, K. Wieghardt, *J. Am. Chem. Soc.* **1998**, *120*, 7260.
[11] J. Bendix, R. J. Deeth, T. Weyhermüller, E. Bill, K. Wieghardt, *Inorg. Chem.* **2000**, *39*, 930.
[12] J. P. F. Cherry, A. R. Johnson, L. M. Baraldo, Y. C. Tsai, C. C. Cummins, S. V. Kryatov, E. V. Rybak-Akimova, K. B. Capps, C. D. Hoff, C. M. Haar, S. P. Nolan, *J. Am. Chem. Soc.* **2001**, *123*, 7271.
[13] I. Castro-Rodriguez, K. Olsen, P. Gantzel, K. Meyer, *Chem. Commun.* **2002**, 2764.
[14] I. Castro-Rodriguez, K. Olsen, P. Gantzel, K. Meyer, *J. Am. Chem. Soc.* **2003**, *125*, 4565.
[15] H. Nakai, X. L. Hu, L. N. Zakharov, A. L. Rheingold, K. Meyer, *Inorg. Chem.* **2004**, *43*, 855.
[16] R. E. Cramer, K. Panchanatheswaran, J. W. Gilje, *Angew. Chem.* **1984**, *96*, 88; *Angew. Chem. Int. Ed. Engl.* **1984**, *23*, 912.
[17] J. G. Brennan, R. A. Andersen, *J. Am. Chem. Soc.* **1985**, *107*, 514.
[18] A. Zalkin, J. G. Brennan, R. A. Andersen, *Acta Crystallogr. Sect. C* **1988**, *44*, 1553.
[19] C. J. Burns, W. H. Smith, J. C. Huffman, A. P. Sattelberger, *J. Am. Chem. Soc.* **1990**, *112*, 3237.
[20] D. S. J. Arney, C. J. Burns, *J. Am. Chem. Soc.* **1993**, *115*, 9840.
[21] D. S. J. Arney, C. J. Burns, *J. Am. Chem. Soc.* **1995**, *117*, 9448.
[22] B. P. Warner, B. L. Scott, C. J. Burns, *Angew. Chem.* **1998**, *110*, 1005; *Angew. Chem. Int. Ed.* **1998**, *37*, 959–960.
[23] J. L. Kiplinger, D. E. Morris, B. L. Scott, C. J. Burns, *Chem. Commun.* **2002**, 30.
[24] I. Castro-Rodriguez, H. Nakai, L. N. Zakharov, A. L. Rheingold, K. Meyer, *Science* **2004**, *305*, 1757.
[25] I. Castro-Rodriguez, K. Meyer, *J. Am. Chem. Soc.* **2005**, *127*, 11242.
[26] J. L. Stewart, R. A. Andersen, *New J. Chem.* **1995**, *19*, 587.
[27] J. J. Katz, L. R. Morss, G. T. Seaborg, *The Chemistry of the Actinide Elements*, Chapman Hall, New York, **1980**.
[28] D. J. Mindiola, G. L. Hillhouse, *Chem. Commun.* **2002**, 1840.
[29] D. M. Jenkins, T. A. Betley, J. C. Peters, *J. Am. Chem. Soc.* **2002**, *124*, 11238.
[30] S. D. Brown, T. A. Betley, J. C. Peters, *J. Am. Chem. Soc.* **2003**, *125*, 322.
[31] T. E. Hanna, I. Keresztes, E. Lobkovsky, W. H. Bernskoetter, P. J. Chirik, *Organometallics* **2004**, *23*, 3448.
[32] D. S. Glueck, J. X. Wu, F. J. Hollander, R. G. Bergman, *J. Am. Chem. Soc.* **1991**, *113*, 2041.

 © 2006 Wiley-VCH Verlag GmbH & Co. KGaA, Weinheim

Protein Recognition

DOI: 10.1002/anie.200503760

Selective Protein Capture by Epitope Imprinting**

*Hidekazu Nishino, Chin-Shiou Huang, and Kenneth J. Shea**

General methods for the selective recognition of specific peptide sequences and/or proteins remain a significant challenge. Such substances have important applications for separations,[1–3] for use in biosensors,[4] and for the development of biomedical diagnostics.[5] The nonbiological approach

[*] Dr. H. Nishino, Prof. Dr. K. J. Shea
Department of Chemistry
University of California Irvine
Irvine, CA 92697 (USA)
Fax: (+1) 949-824-2210
E-mail: kjshea@uci.edu
Dr. C.-S. Huang
Aspira Biosystems, Inc.
849 Mitten Road, Suite 101, Burlingame, CA 94010 (USA)

[**] We are grateful for financial support from Aspira Biosystems, Inc. and in part, the National Institutes of Health. The peptides were synthesized by Peptide Support Ltd. (Kyushu Institute of Technology, Japan). We also wish to acknowledge Meri Gruber and Rich Ellison (Aspira Biosystems), and Professor Pierre Baldi for helpful discussions.

WILEY InterScience DISCOVER SOMETHING GREAT
© 2006 Wiley-VCH Verlag GmbH & Co. KGaA, Weinheim

of molecular imprinting creates populations of specific recognition sites in robust network polymers by polymerization of cross-linking and functional monomers in the presence of an imprint molecule.[6,7] The imprint molecule is either the intended target or some fragment of it. Successful examples of protein imprinting are very limited and specialized.[8,10–12] Herein we report a general procedure for creating synthetic receptors for proteins by using molecular imprinting. An exposed domain (epitope) of the target protein (a unique nine amino acid sequence) was used to imprint the capture sites. The peptide epitope was covalently attached to a glass or silicon surface. Monomers were then polymerized on these surfaces to produce a molecularly imprinted polymer (MIP) film. Following separation from the functionalized surface, the polymer film bound and captured the target protein from protein mixtures. The capture was achieved under native conditions.

Biological macromolecules, such as proteins and DNA, are essential for every life form on earth. Studies of these molecules have been dependent on our ability to selectively capture these molecules from complex biological mixtures. Base-pair complementarity provides a robust and powerful tool for selectively isolating and purifying DNA and RNA molecules with desired sequences. This tool will remain instrumental in virtually all aspects of molecular biology research. Antibodies have been the most widely used for selective protein capture and are used for industrial protein purification, basic biomedical research, and clinical diagnostics. However, antibodies exhibit characteristics that limit their applications. These proteins are large ($M_r \approx 150$ K), complex molecules that need to be stored carefully. As antibodies are produced by living cells, it is sometimes difficult to control their quality. Furthermore many proteins are known to be difficult to raise antibodies against. An ideal protein-capture agent should have high specificity and be composed of a stable, robust, nonbiological material.

Molecular imprinting is one of the few general, nonbiological methods for creating molecular receptors.[6] Most successful applications of this strategy target low molecular weight, organic-soluble molecules. The resulting molecularly imprinted polymers (MIPs) can function as the recognition element for drugs, environmental pollutants, and other toxic substances. Peptide and protein targets, on the other hand, present greater challenges due, in part, to their structural complexity and the incompatibility of these targets with organic solvents that are typically used for imprinting. Furthermore, as most molecularly imprinted polymers use target molecules as templates, it is critical to remove all template molecules before their use. This concern can be overcome by the use of template molecules that differ from the target. Specifically, the use of an epitope from the target would eliminate this potential problem. Minoura and coworkers first demonstrated this approach for peptide recognition.[13] Herein, we utilize "exposed" epitopes of proteins to imprint the capture site. Proteins with exposed C-termini were selected as this site is a less frequent target for post-translational modification.[14,15] Nonapeptides were chosen as the sequence length as it represents a near-unique code in unstructured domains for the identification of a specific protein.[16,17] The choice of short epitopes focuses on developing capture agents for the primary structure of the peptide rather than the more-complex secondary and tertiary structures of a target proteins, and is similar to the use of peptide fragments to generate epitope selective antibodies and synthetic materials.[18,19] Furthermore, the capture conditions were designed to be compatible with the native protein structure.

Three protein targets that conformed to the above criteria were chosen for these studies, cytochrome *c* (Cyt c), alcohol dehydrogenase (ADH), and bovine serum albumen (BSA). The peptide sequences corresponding to the C-terminus domains of these proteins (Cyt c from bovine-heart amino acids 97–104, AYLKKATNE; ADH from yeast amino acids 339–347, GRYVVDTSK; and BSA amino acids 599–607, VVSTQTALA) were used as the imprinting peptides. Each nonapeptide was chemically synthesized. The nonapeptide corresponding to the nine amino acid sequence of the C-terminus of ADH was attached through an eight-carbon tether to a glass or oxidized silicon surface through the N-terminal amino acid. In the case of Cyt c and BSA, attachment can be through either the N-terminal amino acid and/or the unprotected side-chain amine of the lysine residue of the peptide. The attachment protocol for N-terminal attachment is outlined in Figure 1 A. Clean-glass and silica surfaces were treated with 7-octenyltrichlorosilane. The olefin functionality was oxidized to the carboxylic acid with a buffered solution (pH 7.5) of $KMnO_4$, $NaIO_4$, and K_2CO_3 for 1 h then rinsed and dried. The monolayer, with terminal carboxylic acid groups, was activated with 1-ethyl-3-(3-dimethylaminopropyl)carbodiimide (EDC)/*N*-hydroxylsuccinimde (NHS) for 1 h. The peptide epitopes were subsequently attached to the substrate, through the N-terminus, in a phosphate buffer solution (pH 7.3). The surface was quenched with NH_4OH and dried with a stream of N_2. Contact-angle measurements confirmed each step in the surface modification, alkylation ($82.7° \pm 2$), oxidation ($22.0° \pm 4$), and peptide immobilization ($27.4° \pm 6$).[9] Washing with aqueous base (0.1 M NaOH) after the oxidation step further reduced the contact angle to $4° \pm 1$, which is consistent with a hydrophilic surface terminated with COOH groups. The composition of the glass surface after each step was also measured by X-ray photoelectron spectroscopy (XPS). For untreated and silane-treated glass plates, typical Si_{2p}, Si_{2s}, O_{1s}, O_{KLL}, and Ca_{2p} signals were detected (a trace amount of a possible Rh impurity was also detected). For alkyl silane-treated glass plates, an additional carbon signal (C_{1s}) from the alkyl chain and a fluorine signal (F_{KLL}, F_{1s}), possibly from the Teflon container used for the surface treatment, was also detected. Following the oxidation step, the presence of an additional contribution at ≈ 289.7 eV suggests the presence of carboxylic acid functionalities. The peptide-coupled sample shows the presence of nitrogen (i.e. amine, amide functionalities) together with an increased concentration of carbon. Concomitantly, oxygen and silicon concentrations decrease most likely owing to attenuation by the "peptide" overlayer. The carbon spectrum of the sample shows the increased presence of oxygenated carbons at approximately 286.5 eV (possibly together with amine functionalities). It also shows an additional contribution at

 © 2006 Wiley-VCH Verlag GmbH & Co. KGaA, Weinheim

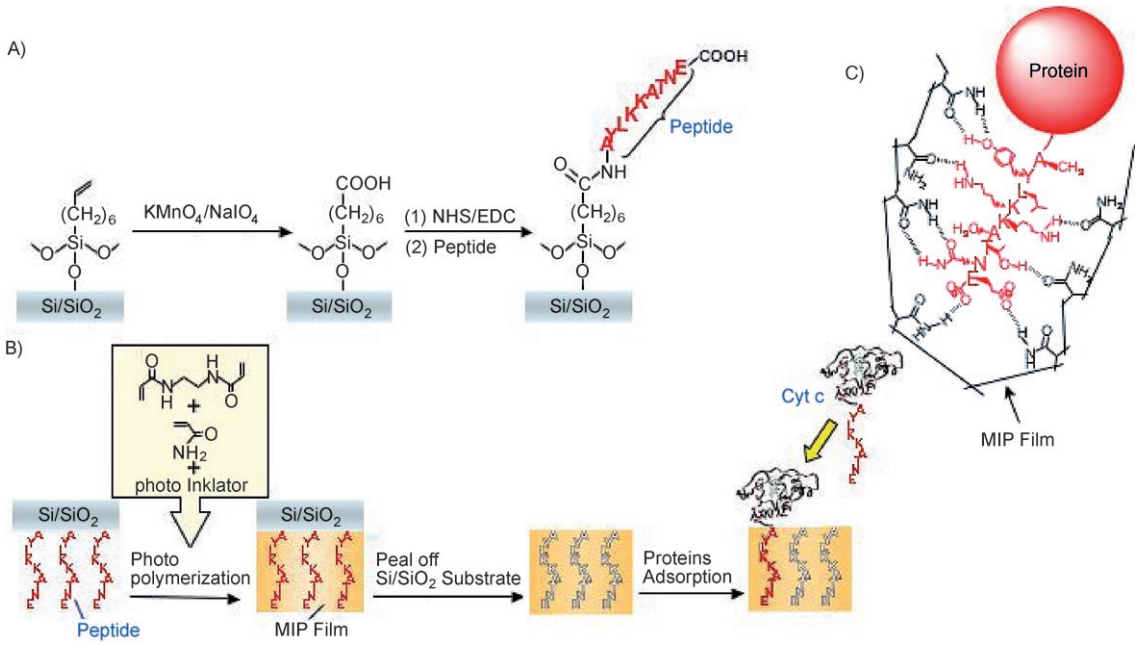

Figure 1. Protocol for template imprinting with protein epitopes. A) Method for glass modification and peptide attachment. The vinylsilane surface was oxidized with $KMnO_4$ (0.5 mM), $NaIO_4$ (19.5 mM), and K_2CO_3 (1.8 mM; pH 7.5). The carboxylic acid-terminated monolayer was activated with NHS/EDC. The peptide epitopes were subsequently attached to the substrate in a solution (0.25 mg mL^{-1}) of phosphate buffer (10 mM; pH 7.3) and NaCl (140 mM). The attachment protocol is illustrated only for N-terminal attachment. B) Illustration outlining MIP film fabrication and evaluation. The C-terminus nonapeptide epitope is attached through a tether to a glass or oxidized silicon surface by the N-terminal amino acid of the peptide. Monomers are photochemically cross-linked with a UV lamp (21 700 $\mu W cm^{-2}$) for 10 min while remaining in contact with the peptide modified surface. Following polymerization, the glass substrate and/or silicon wafer was removed by soaking the film and substrate in buffer overnight at 4 °C, whereupon the film and substrate spontaneously separated. C) Proposed mechanism for the target protein recognition of C-terminus peptide-sequence-imprinted surfaces. A nanocavity-bound target protein is caused by many cooperative weak interactions, involving hydrogen bonds and hydrophobic interactions.

≈288.4 eV, which suggests the presence of amide functionalities.

Synthesis of the imprinted polymer was achieved as outlined in Figure 1B. The functionalized surfaces were exposed to a monomer solution (degassed with dry N_2) consisting of acrylamide (20%), *N*,*N*-ethylene-bis-acrylamide (10%),[20,21] and polyethylene glycol 200-diacrylate (0.1 mol%) in buffer solution containing 2-hydroxy-4′-(2-hydroxyethoxy)-2-methylpropiophenone (0.2%) as a photoinitiator. The monomer solution was poured between the peptide containing substrates that were separated by a thin Teflon spacer. The monomers were photochemically polymerized with a UV lamp while remaining in contact with the surface. After polymerization, the glass substrate and/or silicon wafer was removed by soaking the film and substrate overnight in buffer solution at 4 °C, whereupon the film and substrate spontaneously separated. Polymers were washed with phosphate buffer solution providing a continuous opaque film of approximately 520 μm. Control films were prepared in a similar manner by using the carboxylic acid-terminated monolayer surface.

Protein affinity was established by incubating the MIP films (approximately 4 cm^2) in a buffer solution containing five proteins (BSA, ADH, carbonic anhydrase (CA; from bovine erythrocytes, C-terminus NRQVRGFPK), trypsine inhibitor (T.I.; from soybean, C-terminus FQKLDKESL), and Cyt c). The samples were gently mixed and incubated overnight. Films were washed with phosphate buffer (10 mM; pH 7.6) to remove material that was nonspecifically bound. After washing, the bound protein was eluted from both the imprinted MIP (Cyt c) and the control films by washing in three separate steps. The supernatants from the extractions were combined and lyophilized. The residue was analyzed by SDS-PAGE (gels: 12.5% SDS-PAGE, staining: CBB (Coomassie Brilliant Blue); Figure 2). Cyt c was present in the extract of the MIP film imprinted with the Cyt c epitope (Figure 2A). The four mismatched proteins were, in general, below the detection limits of the experiment. In a similar manner, films that were imprinted with the ADH C-terminus epitope sequence (GRYVVDTSK) selectively captured ADH from the same protein mixture, and the BSA C-terminus epitope (sequence VVSTQTALA) imprinted film captured BSA (Figure 2b and c). In each case, the dominant protein that was captured corresponded to the peptide epitope that was used as the surface-attached imprint.

The identity of the protein bound to the imprinted polymer film in the uptake studies was confirmed by mass spectrometry (MALDI-TOF). Each target protein (ADH and Cyt c) was extracted from the protein band of the SDS-PAGE gel and modified with iodoacetamide.[22] From the protein band eluted from the film imprinted with Cyt c, two peaks were identified as modified apo-Cyt c (observed M_r = 11728.1, calculated M_r = 11727.1 $[M+K]^+$) and modified Cyt c (observed M_r = 12306.9, calculated M_r = 12305.6 $[M+$

 © 2006 Wiley-VCH Verlag GmbH & Co. KGaA, Weinheim

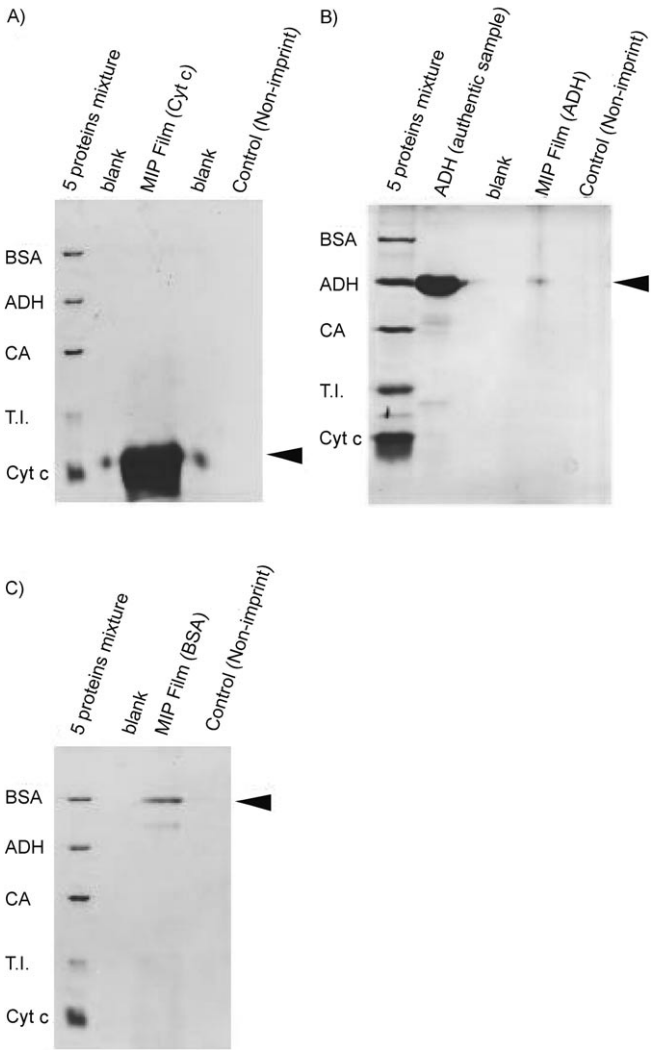

Figure 2. Analysis of protein uptake by MIP films. Each peptide imprinted MIP film(≈4 cm^2) was incubated with a solution containing five proteins (50 $\mu g\,mL^{-1}$ of BSA, ADH, CA, T.I., and Cyt c solutions). After incubation, the films were washed with phosphate buffer (10 mM; pH 7.6) and the bound proteins were extracted with FAIW (formic acid/acetonitrile/isopropanol/water (20:25:15:40)), acetonitrile/TFA aq. (50:1) and acetonitrile solution (80%), respectively. The extracts were combined and lyophilized. The residue was dissolved in phosphate buffer (10 mM; pH 7.6) and 2×SDS gel sample buffer (5 μL) and analyzed by SDS-PAGE (gels: 12.5% SDS-PAGE, Staining: CBB (Coomassie Brilliant Blue)). A) MIP film (Cyt c), B) MIP film (ADH) and MIP film (Non-imprint), C) MIP film (BSA).

Heme]$^+$). MS analysis of the single-peak protein band that was eluted from the ADH-imprinted film was identified as modified ADH (observed M_r: 37096.9, calculated M_r: 37098.4 $[M+7]^+$ acetamide modified with a Cys residue).

Hydrogen bonding is essential for molecular recognition of biological systems in aqueous media. We attribute the binding specificity of the epitope-imprinted polymers to collective hydrogen bonding. When the target protein contacts a complementary domain, multiple hydrogen bonds are formed between the oriented groups within the polymer domain and the target protein's C-terminus sequences (Figure 1C). These cooperative, multivalent interactions can lead to specific protein binding. Because the array of hydrogen bonds is based on sequence complementarity, the number of hydrogen bonds between a specific polymer domain and a nontarget protein is small. Consequently, the binding strength is low and nonspecific protein binding is inhibited.

To obtain more-quantitative information regarding protein binding to the imprinted polymer film, a protein adsorption isotherm was constructed (Figure 3). A film imprinted with the C-terminus sequence of Cyt c was

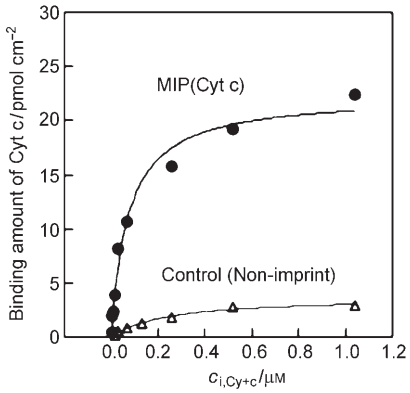

Figure 3. Binding isotherms for Cyt c to a MIP film prepared with AYLKKATNE as the template peptide. The amount of protein bound to the film was measured by using NanoOrange. An increase in Cyt c capacity was found for the Cyt c imprinted MIP film. Binding to the non-imprint MIP film was minimal. $c_{i,Cyt\,c}$ = initial concentration of Cyt c.

incubated with a buffered solution (1 mL) of protein over a concentration range of 0 to 12.8 $\mu g\,mL^{-1}$. Each sample was gently mixed overnight at room temperature to ensure equilibrium. The film was then removed, washed, and extracted by using the protocol described above. The amount of protein bound to the film was quantified by using NanoOrange.[23] The average K_d for Cyt c binding was calculated to be 72.3 nM. Binding to a non-imprinted control polymer film is also shown in Figure 3. The epitope-imprinted film reveals a significantly higher affinity and capacity for the target protein (Cyt c) over other sequences examined; the non-imprinted film has a low affinity for the protein. From the binding curve at the point of saturation, we estimated the degree of Cyt c coverage of the MIP film. This value was determined by assuming a protein area of 5.6 nm^2 (estimated from X-ray crystallography structural data). Assuming a flat surface, a Cyt c "monolayer" film of 1 cm^2 was comprised of approximately 30 $pmol\,cm^{-2}$. The amount of Cyt c bound to the MIP film was estimated at 22.4 $pmol\,cm^{-2}$, which corresponds to approximately 75% coverage of 1 cm^2 of the MIP film surface. Surface roughness would significantly reduce this value. The sensitivity of this method can also be determined by examining the tolerance to single amino acid mismatches in the target. Interestingly, the selectivity of the imprinted MIP film for BSA is diminished by a single amino acid substitution in most of the cases (Figure 4). In this experiment, the native C-terminus of BSA (STQ**T**ALA)] and four single amino acid (STQ**A**ALA, STQ**L**ALA, STQ**E**ALA and STQ**Y**ALA) mutations of template peptides were synthesized

 © 2006 Wiley-VCH Verlag GmbH & Co. KGaA, Weinheim

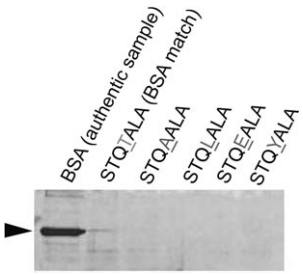

Figure 4. SDS-PAGE analysis of the uptake of films imprinted with the C-terminus nonapeptide of BSA or single amino acid substitutions at the 4th position. The imprinted films have a very low tolerance for even a single amino acid mismatch between the epitope and target.

and imprinted. The sequences differed only at position four from the C-terminus sequence of BSA (STQ**T**ALA). The imprinted polymer films prepared from these mutant peptides had dramatically lowered binding of BSA relative to the film imprinted with the correct peptide sequence.

In summary, we have developed a general protocol for creating macromolecular receptors for proteins by using molecular imprinting. Unlike many approaches that employ affinity ligands for protein isolation and purification (i.e., His_6 tag), the current method focuses on capture of native proteins. It utilizes the sequences of exposed epitopes based on known or predicted protein structures. This method requires only the peptide sequence of a small portion of the target protein for the template molecule, it does not use or need whole proteins. As such, this approach provides opportunities for the capture of target proteins based only on genomic information.

Received: October 24, 2005
Revised: January 9, 2006
Published online: March 9, 2006

Keywords: imprinting · molecular recognition · protein epitopes · protein recognition · proteins

[1] D. E. Meyer, A. Chilkoti, *Nat. Biotechnol.* **1999**, *17*, 1112 – 1115.
[2] H. Kanoh, K. Honda, S. Simizu, M. Muroi, H. Osada, *Angew. Chem.* **2005**, *117*, 3625 – 3628; *Angew. Chem. Int. Ed.* **2005**, *44*, 3559 – 3562.
[3] N. Shimizu, K. Sugimoto, J. Tang, T. Nishi, I. Sato, M. Hiramoto, S. Aizawa, M. Hatakeyama, R. Ohba, H. Hatori, T. Yoshikawa, F. Suzuki, A. Oomori, H. Tanaka, H. Kawaguchi, H. Watanabe, H. Handa, *Nat. Biotechnol.* **2000**, *18*, 877 – 881.
[4] K. Tomizaki, K. Usui, H. Mihara, *ChemBioChem* **2005**, *6*, 782 – 799.
[5] G. A. Michaud, M. Salcius, F. Zhou, R. Bangham, J. Bonin, H. Guo, M. Snyder, P. F. Predki, B. I. Schweitzer, *Nat. Biotechnol.* **2003**, *21*, 1509 – 1512.
[6] a) *Molecularly Imprinted Materials, Science and Technology* (Eds: M. Yan, O. Ramstrom), Marcel Dekker, New York, **2005**; b) G. Wulff, *Angew. Chem.* **1995**, *107*, 1958 – 1979; *Angew. Chem. Int. Ed. Eng.* **1995**, *34*, 1812.
[7] K. Haupt, K. Mosbach, *Chem. Rev.* **2000**, *100*, 2495 – 2504.
[8] H. Shi, W.-B. Tsai, M. D. Garrison, S. Ferrari, B. D. Ratner, *Nature* **1999**, *398*, 593 – 597.
[9] S.-S. Cheng, D. A. Scherson, C. N. Sukenik, *Langmuir* **1996**, *12*, 1190 – 1195.
[10] M. Kempe, M. Glad, K. Mosbach, *J. Mol. Recognit.* **1995**, *8*, 35 – 39.
[11] J. Rick, T.-C. Chou, *Anal. Chim. Acta* **2005**, *542*, 26 – 31.
[12] D.-F. Tai, C.-Y. Lin, T.-Z. Wu, L.-K. Chen, *Anal. Chem.* **2005**, *77*, 5140 – 5143.
[13] A. Rachkov, N. Minoura, *J. Chromatogr. A* **2000**, *889*, 111 – 118.
[14] B. Polevoda, F. Sherman, *J. Biol. Chem.* **2000**, *275*, 36479 – 36482.
[15] B. Polevoda, F. Sherman, *J. Biol. Chem.* **2001**, *276*, 20154 – 20159.
[16] S. Sudarsanam, *Proteins* **1998**, *30*, 228 – 232.
[17] I. A. Wison, D. H. Haft, E. D. Getzoff, J. A. Tainer, R. A. Lerner, S. Brenner, *Proc. Natl. Acad. Sci. USA* **1985**, *82*, 5255 – 5259.
[18] M. H. V. Regenmortel, *J. Immunoassay* **2000**, *21*, 85 – 108.
[19] A. Rachkov, N. Minoura, *Biochim. Biophys. Acta* **2001**, *1544*, 255 – 266.
[20] B. R. Hart, K. J. Shea, *J. Am. Chem. Soc.* **2001**, *123*, 2072 – 2073.
[21] B. R. Hart, K. J. Shea, *Macromolecules* **2001**, *34*, 6192 – 6201.
[22] S. Cohen, B. T. Chait, *Anal. Biochem.* **1997**, *247*, 257 – 267.
[23] L. J. Jones, R. P. Haugland, V. L. Singer, *BioTechniques* **2003**, *34*, 850 – 861.

 © 2006 Wiley-VCH Verlag GmbH & Co. KGaA, Weinheim

Nanomaterials

DOI: 10.1002/anie.200504158

Secondary Structure Dependent Self-Assembly of β-Peptides into Nanosized Fibrils and Membranes**

*Tamás A. Martinek, Anasztázia Hetényi, Lívia Fülöp, István M. Mándity, Gábor K. Tóth, Imre Dékány, and Ferenc Fülöp**

Life relies on polymers that are able to form a well-defined hierarchy of self-assembling structural levels. For a long time,

[*] Dr. T. A. Martinek, A. Hetényi, I. M. Mándity, Prof. Dr. F. Fülöp
Institute of Pharmaceutical Chemistry
University of Szeged
Eötvös u. 6, 6720 Szeged (Hungary)
Fax: (+36) 62-545-564
E-mail: fulop@pharm.u-szeged.hu
Dr. L. Fülöp, Dr. G. K. Tóth
Department of Medical Chemistry
University of Szeged
Dóm tér 8, 6720 Szeged (Hungary)
Dr. I. Dékány
Nanostructured Materials Research Group,
Hungarian Academy of Sciences, University of Szeged
Aradi vértanúk tere 1, 6720 Szeged (Hungary)

[**] This work was supported by the Hungarian Research Foundation (OTKA F038320 and TS04888) and the National Research and Development Office, Hungary (OMFB-0066/2005-DNT and GVOP-311-2004-05-0255/3.0). T.A.M. acknowledges the award of a János Bolyai scholarship from the Hungarian Academy of Sciences.

Supporting information for this article is available on the WWW under http://www.angewandte.org or from the author.

WILEY InterScience DISCOVER SOMETHING GREAT
© 2006 Wiley-VCH Verlag GmbH & Co. KGaA, Weinheim

only biopolymers (proteins, RNA, and DNA) were known to have such properties. However, an increasing amount of evidence demonstrates that biomimicking β-amino acid sequences (β-peptide foldamers) are also fully capable of forming residue-controlled and biologically active secondary structures, such as various types of helices, strands, and loops.[1–8] A major challenge in foldamer chemistry is to prove that higher-order structural levels are available for β-peptides and that their formation can be tailored by the β-amino acid sequence. The construction of tertiary structures through the building of protein-sized β-peptide sequences is a formidable task because of synthetic difficulties. However, the synthesis of a 20-residue-long helical chain was recently accomplished.[9] Through observation of the packing of the secondary structural units in the solid state, tertiary structural motifs potentially available for β-peptides were identified; X-ray crystallographic studies revealed a H14 helix-bundle motif[10] and a polar pleated sheet.[3] As a further step towards tertiary structures, designed β-peptide helices have been observed to exhibit self-association in solution,[11–14] but the creation of distinct tertiary structures with specific morphologies still remains a challenge.

Herein, we followed the paradigm of the controlled, specific self-association of β-peptide secondary structural units in solution to construct supramolecular structures in which self-organization is governed by the forces of the repeating tertiary structural motifs (helix bundles and nonpolar pleated sheets). Designed β-peptide oligomers were utilized and, depending on the nature of the secondary structure (controlled by the relative configuration of the β-peptide backbone), the self-assembly of pleated-sheet sandwich motifs and helix-bundle membranes could be induced, thus leading to nanosized fibrils and vesicles, respectively.

The building blocks of choice were the homo-oligomers of cyclic β-amino acid residues prepared in various chain lengths by using published protocols: *cis*-(1*R*,2*S*)-ACPC$_n$ (**1**–**4**; ACPC = *cis*-2-aminocyclopentanecarboxylic acid) and *trans*-(1*S*,2*S*)-ACHC$_m$ (**5**–**7**; ACHC = *trans*-2-aminocyclohexanecarboxylic acid; Figure 1), which are known to form a nonpolar strand and a self-stabilizing helix in solution, thus resembling the β strand and the α helix of α-peptides, respectively.[6,13] As a consequence of their dissimilar secondary structures, essentially different modes of packing can be anticipated if self-association is intrinsically possible for these β-peptides in solution. Helix units **5**–**7** are amphiphilic in nature as a result of their protonatable N termini and the strongly hydrophobic helix surface. Accordingly, the oligomer-sized hydrodynamic radius found earlier, even at low concentrations,[13] renders hydrophobically driven helix-bundle formation likely, but the morphology of the assemblies has not been investigated thus far.

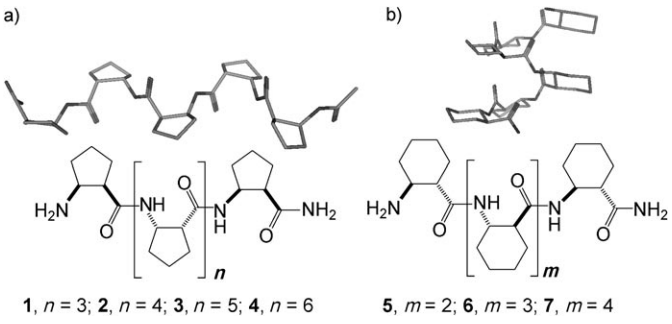

Figure 1. Chemical structures and the known secondary structures of the studied *cis*-ACPC$_n$ (**1**–**4**) and *trans*-ACHC$_m$ (**5**–**7**) oligomers.

NMR measurements have revealed that the peptide-bond NH/ND exchange rate strongly decreases as the concentration of strand **3** increases (see the Supporting Information). These observations can not be explained purely within the framework of extremely stable secondary structures, and they therefore oriented our attention to self-association phenomena. On the other hand, natural and designed peptidic sequences with hydrophobic side chains with a propensity to fold into a β strand generally form twisted amyloid fibrils or lamellar ribbons, in which the core structure is uniformly a cross β-pleated sheet (Figure 2).[15–18] These facts, together with the proven β-strand-like nonpolar strand secondary structure of **1**–**4**, presage fibril formation.

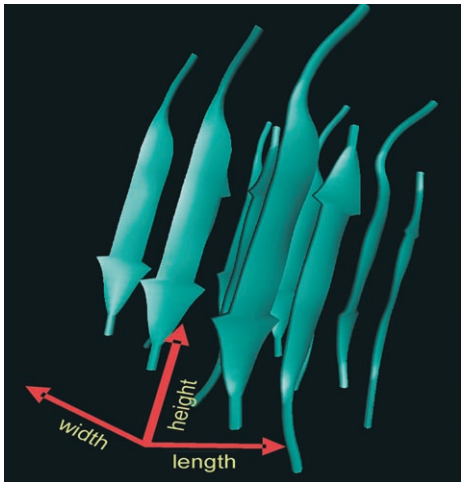

Figure 2. Schematic representation of the cross-β-sheet structure of the amyloid-type fibrils.

First and most importantly, the morphology of the self-assembling structures was established by using transmission electron microscopy (TEM; see the Supporting Information) with negative staining (uranyl acetate). The time-dependent nature of the supramolecular structure formation was followed by means of particle-size measurements. Dynamic light scattering (DLS) experiments were conducted in back-scattering mode to gain a picture of the particle-size distribution in the solvent over a wide diameter range. The DLS autocorrelation data were analyzed by utilizing the CONTIN[19] algorithm with the maximum-entropy regularization implemented in the program SEDFIT.[20] The ζ potential was measured as well in the same experimental setup. A diffusion NMR method (DOSY), previously described,[13] was applied to monitor self-assembly at the oligomer level (diameter: < 10 nm), at which the DLS method may be unreliable because of the concomitant larger particles. The diffusion-based particle-size measurements, such as DLS, utilize a spherical approximation, and therefore these measurements do not give exact radii for the fibrillar assemblies

 © 2006 Wiley-VCH Verlag GmbH & Co. KGaA, Weinheim

above the oligomer size range. However, the time dependence of the approximate size distribution can be readily monitored, and the spherical approximation causes less error in the oligomer size range at which DOSY NMR spectroscopic analysis is effective.

The TEM images clearly show ribbonlike fibrils for the strand units **2**–**4** in methanol after incubation of the 1 mM samples for 1 week at room temperature (Figure 3). Fibril

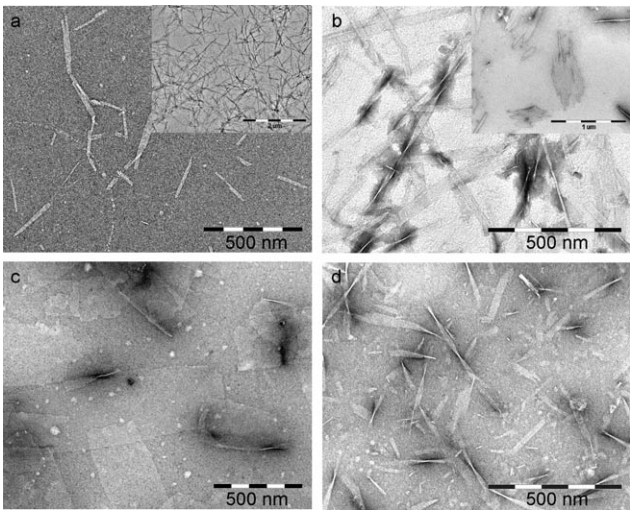

Figure 3. TEM images of 1 mM *cis*-ACPC$_n$ **2**–**4** fibrils after 1 week in MeOH for a) **2** (inset: longer fibrils in the same sample), b) **3** (inset: fibrils and sheets of **3** measured in water), c) **4**, and d) **3** after 1 day.

formation could not be detected in **1** under the experimental conditions applied, which is in good accord with the lower overall hydrophobic nature of the pentamer strand unit. The lengths of the ribbons are uniformly in the micrometer range. The geometry of the ribbons exhibits a strong chain-length dependence; the widths are in the ranges 12–32, 30–50, and 100–400 nm for **2**–**4**, respectively. The ribbons can likewise be recognized in water but are considerably wider, with sheet formation being observed (Figure 3b, inset). A very interesting feature of the ribbonlike fibrils is the random occurrence of helical twists. The helical twists observed for **3** and **4** allow an estimation of the ribbon height, which is 2–3 nm. Unfortunately, the limit of resolution in the TEM protocol applied does not permit observation of the minute changes in ribbon height caused by the different chain length; nevertheless, the estimated value corresponds closely to the length of a single β-peptide oligomer in its nonpolar strand conformation. The process was sampled for **3** after 1 day, when considerably shorter fibril fragments were seen (50–400 nm; Figure 3d), to test the time-dependent nature of the self-association. The solvent- and time-dependent size and morphology strongly support the self-assembling process.

Whereas the DLS data for **1** in methanol do not exhibit any nanometer-sized particles that corroborate the TEM results, **3** unequivocally reveals an increasing trend for the particle diameter (see the Supporting Information). Particles in the micrometer range could be detected after one week, with the scattering intensity tapering off because of the sedimentation of the macroscopic species. The samples exhibit scattering intensity in the monomer/oligomer size range; nevertheless, the apparent hydrodynamic diameter was estimated by using diffusion NMR spectroscopic analysis, which is more accurate in this domain. The apparent hydrodynamic diameters determined at a concentration of 1 mM in methanol after one week were 1.54, 4.69, 5.72, and 3.61 nm for **1**–**4**, respectively. Only monomers were observed in each case immediately after dissolution at a concentration of 1 mM. The oligomerization measured without delay after sample preparation displayed a concentration dependence (see the Supporting Information), which points to a concentration-dependent self-association rate. The NMR gradient echo intensity did not exhibit a multiexponential decay, thus suggesting relatively fast *cis*-ACPC$_n$ exchange between the dissolved monomers and the oligomers. The ζ potential of the nanoribbons was 34 mV, which proves that the free N termini of the *cis*-ACPC$_n$ strands are situated on the surface and are partially protonated. The significant ζ potential endows the fibrils with stability, thus preventing coagulation.

It may be concluded that the predicted formation of pleated-sheet fibrils occurs for the studied β-peptide strands. From the measured nanoribbon dimensions and the known high-resolution structure of the similar-behaving amyloid-type fibrils,[21,22] the construction of the ribbon model is rather straightforward. The ribbon height of 2–3 nm corresponds to the distance between the N and C termini of a single *cis*-ACPC$_n$ strand. The ribbon width increased with the oligomer size and solvent polarity, which strongly indicates that the ribbons are organized by hydrophobic forces between the side chains in the corresponding dimension, thereby leading to a continuous pleated-sheet sandwich tertiary structural motif. The supramolecular structure is organized by the interstrand hydrogen bonds formed by the peptide moieties parallel to the long fibril axis. Ab initio calculations on the H-bond-stabilized and fully protonated parallel and antiparallel dimers of the *cis*-ACPC$_7$ strands at the HF/3-21G level prove that the pleated sheet is stable (Figure 4a); furthermore, there is no steric repulsion and the stabilization energy in vacuo is estimated to be 40–50 kcal mol^{-1} (see the Supporting Information). The antiparallel pleated sheet is approximately 20 kcal mol^{-1} more stable than the parallel arrangement. In accordance with the above findings, the molecular model of the fragment of the *cis*-ACPC$_7$ nanoribbon was built up with antiparallel strand orientations. Minimization and subsequent long-term molecular dynamics (MD) simulations (3 ns) were run with explicit water, the periodic boundary conditions, and the MMFF94[23] force field implemented in the molecular operating environment of the Chemical Computing Group. The ribbon model converged to a stable energy level; only side-chain vibrations were observed. Interestingly, the model structure displays signs of the helical twist along the axis parallel to the peptide bonds (Figure 4).

The TEM images of helices **5**–**7** after 1 day at a concentration of 1 mM in either methanol (Figure 5) or water demonstrated the formation of spherical objects in the cases of **6** and **7**. Only oligomer-sized aggregates were visible with **5**; sphere formation could be detected after 1 week (Figure 5a). The lower association rate observed for **5** may be explained by its shorter chain length, the conformational behavior estab-

 © 2006 Wiley-VCH Verlag GmbH & Co. KGaA, Weinheim

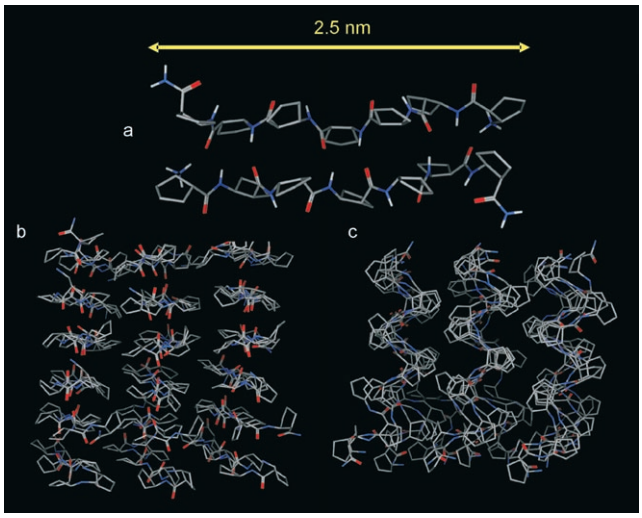

Figure 4. Molecular model of *cis*-ACPC$_7$ fibrils. a) Ab initio (HF/3-21G) model of an antiparallel β-peptide sheet. b) Side view of a fibril-fragment model after 3-ns MD simulation (explicit solvent not displayed). c) Top view of a fibril-fragment model after 3-ns MD simulation.

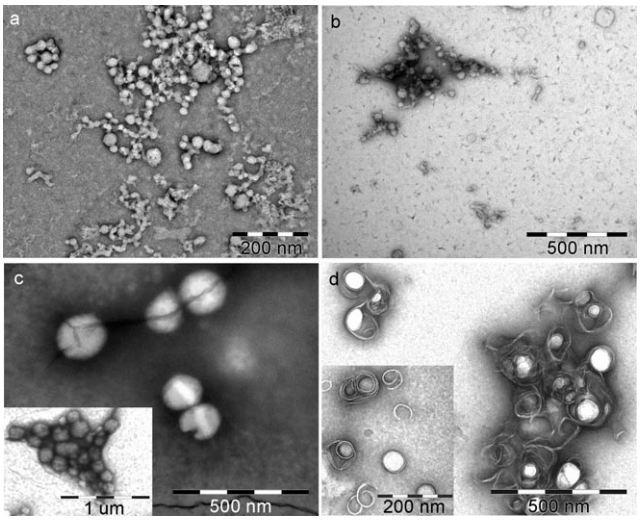

Figure 5. TEM images of 1 mM *trans*-ACHC$_m$ vesicles after 1 day in MeOH for a) **5**, b) **6**, and c) **7** (inset: coagulated vesicles observed for **7**). d) Disintegrated multilamellar vesicles and membranes measured after sonication of sample **7**.

lished earlier being different from that for **6** and **7**.[13] The sphere diameters were in the range 20–180 nm for all the chain lengths, and both the shape and the size of the spheres remained constant, apart from a significant coagulation (Figure 5a–c, inset). The spherical species built up from the vertically amphiphilic helix units are phenomenologically very similar to vesicles of amphiphiles in both shape and size.[24,25] Following the hypothesis that the spheres behave like mono- or multilamellar vesicles, samples were sonicated for 15 min (35 kHz, 34 W), which should disclose any membranelike fine structure. After the treatment, the TEM images undoubtedly exhibited partially disintegrated vesicles built up from predominantly multilamellar walls (Figure 5d). Importantly, the vesicles reassembled 1 day after the sonication, thus proving the self-assembly process. The unilamellar wall thickness at the narrowest edges was approximately 2 nm, which is equal to twice the length of a helical unit.

The results of the DLS measurements supported the TEM observations; the size-distribution curve for **7** indicated particles in the range 10–200 nm, with a trend towards larger diameters in accordance with the coagulation (see the Supporting Information). The scattering intensity disappeared within a few days as a result of the sedimentation. The size distribution of **5** after 1 day clearly showed no scattering intensity above 5 nm, which corroborates the TEM results on the slower vesicle formation for the shorter chain length. The population observed in the monomer/oligomer size range by DLS is supported by the diffusion NMR spectroscopic finding of apparent hydrodynamic diameters of 3.03, 3.58, and 4.07 nm for **5**–**7**, respectively.[13] The oligomerization was independent of the concentration; the average diameter decreased only at a concentration of 0.05 mM (see the Supporting Information). ζ-Potential measurements furnished a value of 13 mV. It may be concluded that, despite the identical sample preparation protocol, the surface concentration of the basic N-terminal nitrogen atoms was much lower than that of the *cis*-ACPC$_n$ ribbons. The low ζ potential explains the increased coagulation propensity as well.

In regard to the observed membranes with a wall thickness of approximately 2 nm and the low ζ potential, we hypothesize head-to-head (Figure 6a) and head-to-tail (Figure 6b) contacts of the helices within the membrane. Such a dimerization could not be detected by observation of the NOE interactions, which furnish information on the oligomers only visible by NMR spectroscopy. The proposed bilayer corresponds to the experimentally estimated membrane thickness, and the fact that the buried N termini is in good accord with the low ζ potential. Ab initio calculations resulted in stable helix dimers in vacuo (the implicit solvent

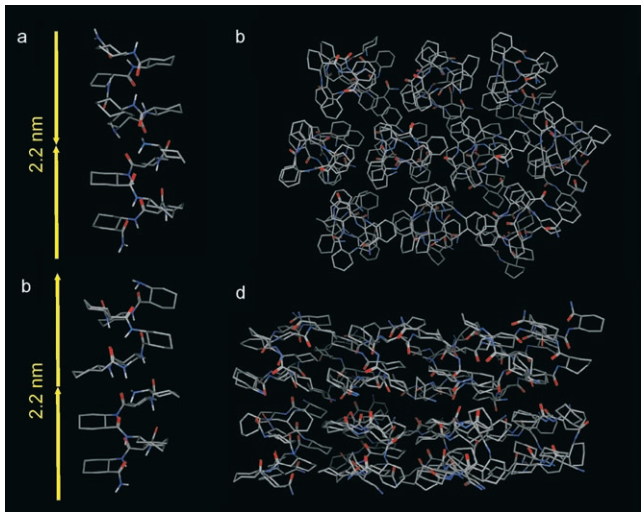

Figure 6. Molecular model of *trans*-ACHC$_6$ membranes. a) Ab initio (HF/3-21G) model of head-to-head helix dimer. b) Ab initio (HF/3-21G) model of head-to-tail helix dimer. c) Top view of helix-bundle membrane fragment model after 3-ns MD simulation (explicit solvent not displayed). d) Side view of helix-bundle membrane-fragment model after 3-ns MD simulation.

 © 2006 Wiley-VCH Verlag GmbH & Co. KGaA, Weinheim

drastically decreased the stabilization energy) for both contact types. These hydrogen bonds can probably exert their stabilizing effect only when the terminal nitrogen atom is deprotonated and are shielded from the solvent within the membrane bilayer. Finally, it is safe to assume that the helix surface forms a hydrophobic surface sufficiently large to facilitate the solvent-driven association into a continuous helix-bundle motif. Similar packing was observed in the solid phase by using X-ray crystallography.[10] The cog-wheel-like mutual fit of the helix side chains further increases the stabilizing hydrophobic surface (Figure 6). The *trans*-$ACHC_6$ membrane segment was constructed by following the above lines and a 3-ns MD simulation was run with the same setup as that used for the nanoribbon model. The simulation revealed a stable membrane bilayer with side-chain vibrations.

We can conclude that the designed β-peptide secondary structural units are intrinsically capable of forming self-assembling supramolecular structures: fibrils of pleated-sheet sandwiches and helix-bundle membranes. Tuning of the relative configurations of the β-peptide backbone allows control not only of the secondary structure, but also of the self-assembly pattern, and consequently the morphology on the nanometer scale. The specific β-peptide self-assembly presented herein can contribute to the design principles of future distinct β-peptide (or β-protein?) tertiary structures. We also believe that such newly generated nanostructured materials may gain applications in the fields of nano- and biotechnology[26–28] and may contribute to a deeper understanding of the molecular mechanism of protein misfolding diseases.

Received: November 22, 2005
Published online: March 9, 2006

Keywords: beta-peptides · foldamers · nanomaterials · peptide mimetics · self-assembly

[1] B. L. Iverson, *Nature* **1997**, *385*, 113.
[2] D. H. Appella, L. A. Christianson, D. A. Klein, D. R. Powell, X. L. Huang, J. J. Barchi, S. H. Gellman, *Nature* **1997**, *387*, 381 – 384.
[3] D. Seebach, S. Abele, K. Gademann, B. Jaun, *Angew. Chem.* **1999**, *111*, 1700 – 1703; *Angew. Chem. Int. Ed.* **1999**, *38*, 1595 – 1597.
[4] D. Seebach, J. L. Matthews, *Chem. Commun.* **1997**, 2015 – 2022.
[5] E. A. Porter, X. Wang, H. S. Lee, B. Weisblum, S. H. Gellman, *Nature* **2000**, *404*, 565 – 565.
[6] T. A. Martinek, G. K. Tóth, E. Vass, M. Hollósi, F. Fülöp, *Angew. Chem.* **2002**, *114*, 1794 – 1797; *Angew. Chem. Int. Ed.* **2002**, *41*, 1718 – 1721.
[7] R. P. Cheng, S. H. Gellman, W. F. DeGrado, *Chem. Rev.* **2001**, *101*, 3219 – 3232.
[8] D. Seebach, A. K. Beck, D. J. Bierbaum, *Chem. Biodiversity* **2004**, *1*, 1111 – 1239.
[9] D. Seebach, R. I. Mathad, T. Kimmerlin, Y. R. Mahajan, P. Bindschadler, M. Rueping, B. Jaun, *Helv. Chim. Acta* **2005**, *88*, 1969 – 1982.
[10] D. H. Appella, L. A. Christianson, I. L. Karle, D. R. Powell, S. H. Gellman, *J. Am. Chem. Soc.* **1999**, *121*, 6206 – 6212.
[11] T. L. Raguse, J. R. Lai, P. R. LePlae, S. H. Gellman, *Org. Lett.* **2001**, *3*, 3963 – 3966.
[12] R. P. Cheng, W. F. DeGrado, *J. Am. Chem. Soc.* **2001**, *123*, 11564 – 11565.
[13] A. Hetényi, I. M. Mándity, T. A. Martinek, G. K. Tóth, F. Fülöp, *J. Am. Chem. Soc.* **2005**, *127*, 547 – 553.
[14] P. Chakraborty, U. Diederichsen, *Chem. Eur. J.* **2005**, *11*, 3207 – 3216.
[15] M. Sunde, L. C. Serpell, M. Bartlam, P. E. Fraser, M. B. Pepys, C. C. F. Blake, *J. Mol. Biol.* **1997**, *273*, 729 – 739.
[16] S. B. Malinchik, H. Inouye, K. E. Szumowski, D. A. Kirschner, *Biophys. J.* **1998**, *74*, 537 – 545.
[17] M. S. Lamm, K. Rajagopal, J. P. Schneider, D. J. Pochan, *J. Am. Chem. Soc.* **2005**, 127, 16692 – 16700.
[18] L. Fulop, M. Zarandi, Z. Datki, K. Soos, B. Penke, *Biochem. Biophys. Res. Commun.* **2004**, *324*, 64 – 69.
[19] S. W. Provencher, *Comput. Phys. Commun.* **1982**, *27*, 213 – 227.
[20] P. Schuck, *Biophys. J.* **2000**, *78*, 1606 – 1619.
[21] C. Soto, *Nat. Rev. Neurosci.* **2003**, *4*, 49 – 60.
[22] C. Branden, J. Tooze, *Introduction to Protein Structure*, Garland, New York, **1998**.
[23] T. A. Halgren, *J. Comput. Chem.* **1996**, *17*, 490 – 519.
[24] P. L. Luisi, P. Stano, S. Rasi, F. Mavelli, *Artif. Life* **2004**, *10*, 297 – 308.
[25] B. M. Discher, Y.-Y. Won, D. S. Ege, J. C.-M. Lee, F. S. Bates, D. E. Discher, D. A. Hammer, *Science* **1999**, *284*, 1143 – 1146.
[26] P. Ball, *Nanotechnology* **2005**, *16*, R1 – R8.
[27] J. D. Hartgerink, E. Beniash, S. I. Stupp, *Science* **2001**, *294*, 1684 – 1688.
[28] G. A. Silva, C. Czeisler, K. L. Niece, E. Beniash, D. A. Harrington, J. A. Kessler, S. I. Stupp, *Science* **2004**, *303*, 1352 – 1355.

 © 2006 Wiley-VCH Verlag GmbH & Co. KGaA, Weinheim

Living Polymerization

DOI: 10.1002/anie.200600027

Discrete, Multiblock Isotactic–Atactic Stereoblock Polypropene Microstructures of Differing Block Architectures through Programmable Stereomodulated Living Ziegler–Natta Polymerization**

*Matthew B. Harney, Yonghui Zhang, and Lawrence R. Sita**

The past two decades have witnessed dramatic advances in the development of well-defined transition-metal complexes that can function as catalysts for the stereoselective Ziegler–

[*] M. B. Harney, Dr. Y. Zhang, Prof. L. R. Sita
Department of Chemistry and Biochemistry
University of Maryland
College Park, MD 20742 (USA)
Fax: (+1) 301-314-9121
E-mail: lsita@umd.edu

[**] Funding for this work was provided by the NSF (CHE-0092493). We wish to thank the ACS Division of Organic Chemistry for a graduate fellowship (to M.B.H.) sponsored by Proctor & Gamble.

Supporting information for this article is available on the WWW under http://www.angewandte.org or from the author.

WILEY InterScience DISCOVER SOMETHING GREAT
© 2006 Wiley-VCH Verlag GmbH & Co. KGaA, Weinheim

Natta polymerization of propene.[1] Indeed, the manipulation of the microstructure of polypropene through modifications of the catalyst ligand has provided a wealth of new thermoplastic materials, ranging from stiff plastics to elastomers.[2–4] In this regard, Natta first proposed nearly half a century ago a new class of thermoplastic elastomer based on an isotactic–atactic stereoblock polypropene (i-a sb-PP) microstructure (see Scheme 1).[5] Subsequent academic and commercial

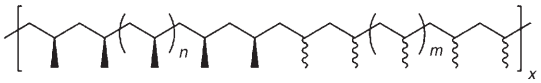

Scheme 1. Representation of a generic isotactic–atactic stereoblock polypropene microstructure.

efforts to obtain such materials under controlled conditions resulted in the production of elastomers that were determined, on the basis of then state-of-the-art spectroscopic and physical analyses, to have an isotactic–atactic stereoblock microstructure.[6] However, owing to the probabilistic way in which the microstructure evolves in these polymerizations, all the i-a sb-PP materials reported to date are actually stereochemically heterogeneous in nature; that is, the collection of polymer chains in the sample represents a distribution of stereochemical microstructures.[2] Indeed, some of these i-a sb-PP elastomers can be solvent-fractionated into multiple components, each of which exhibits different physical properties as a result of different isotactic contents.[6a,c] Further, the true nature of their microstructures and the mechanisms by which they are presumed to arise still remain unclear.[7] As a consequence, it has not yet been possible to systematically categorize, and thereby potentially improve upon, elastomeric properties for this class of material.

Herein, we introduce a new class of polypropene material in the form of discrete, multiblock, isotactic–atactic stereoblock polypropene microstructures in which the molecular weight and the number, length, and placement of each stereoblock type can be programmed as desired to provide a wide range of specifically designed stereoblock architectures (e.g., di-, tri-, and tetrablocks) that are uniform amongst all polymer chains. Importantly, this new class of polypropene has already yielded several new structurally distinct thermoplastic elastomers, thereby allowing a direct comparison of the consequences of the isotactic–atactic stereoblock architecture on elastomeric behavior.

As presented in Figure 1, we have established that propene can be polymerized in either atactic or highly isotactic fashion by simply adjusting the stoichiometric amount of the borate, $[PhNHMe_2][B(C_6F_5)_4]$ (**1**), that is used to effect protonolysis of the methyl group of $Cp^*ZrMe_2[N(Et)C(Me)N(t\mathrm{Bu})]$ (**2**; $Cp^* = \eta^5\text{-}C_5Me_5$) which results in the in situ generation of the active cationic initiator, $[Cp^*ZrMe\{N(Et)C(Me)N(t\mathrm{Bu})\}][B(C_6F_5)_4]$ (**3**).[8–10] More specifically, polymerization of propene with an initial equimolar ratio of **1**:**2** produced highly isotactic polypropene, with stereocontrol attained under exclusive enantiomorphic site control ($mmmm = 0.71$, $\sigma = 0.94$).[2,8] This high degree of isoselectivity for propene enchainment initiated by **3** is among

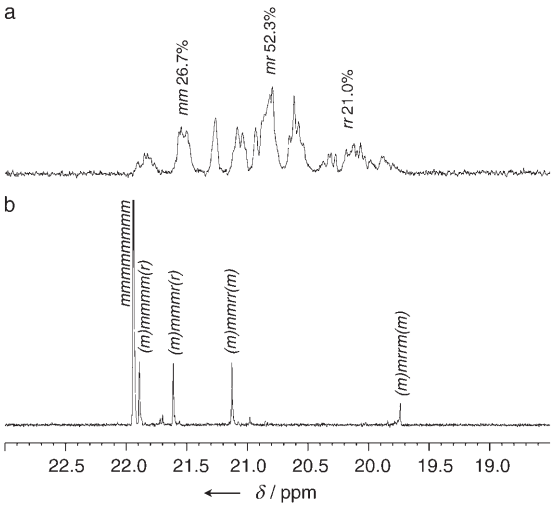

Figure 1. $^{13}C\{^1H\}$ NMR spectra (125 MHz, 1,1,2,2-$C_2D_2Cl_4$, 70 °C) of polypropene samples highlighting the methyl regions of a) atactic polypropene prepared using a ratio of 0.5 of **1**:**2** with triad distribution, and b) isotactic polypropene prepared using a ratio of 1.0 of **1**:**2** with stereo-errors labeled at the heptad level of analysis (conditions: 34.5 kPa propene, −10 °C, C_6H_5Cl). *m* and *r* denote *meso* and racemic (*rac*) stereochemical relationships, respectively, between adjacent stereocenters of the polymer backbone.[2]

the highest recorded for the living polymerization of propene.[11] To the best of our knowledge, **3** is the first initiator of a stereoselective living Ziegler–Natta polymerization that does not require significant ligand modification to achieve a broad monomer specificity that ranges from propene to higher α-olefins to α,ω-unconjugated dienes.[9] On the other hand, polymerization of propene with an initial ratio of **1**:**2** of 0.5 resulted in the production of an atactic microstructure as a result of propagation taking place through a recently discovered degenerative-transfer (DT) living Ziegler–Natta polymerization process that proceeds through a rapid and reversible transfer of methyl groups between active (cationic) and dormant (neutral) propagating centers.[10,12] Owing to a dormant state that is configurationally unstable with respect to a metal-centered epimerization that proceeds much faster than propagation, an atactic microstructure is produced, although it still reveals a narrow polydispersity D ($D = M_w/M_n$). For both atactic and isotactic polypropene, ^{13}C NMR spectroscopy established that propagation occurs through 1,2-insertion of propene with less than 0.5% of 2,1-insertion regio-errors observed, and ^1H NMR spectroscopy revealed the absence of any vinyl resonances that could be attributed to termination by β-hydrogen transfer processes. Final confirmation that propene polymerizations under both DT and non-DT conditions occur in living fashion was provided by kinetic analyses that documented that the number-average molecular weight index, M_n, of the polymer increases in a strictly linear fashion as a function of time, as a result of the number of propagating centers remaining constant—a true signature of a living system.[8,13] Finally, under both DT and non-DT conditions polydispersity values of all polypropene samples were $D = 1.18$, which indicates that for degenerative

 © 2006 Wiley-VCH Verlag GmbH & Co. KGaA, Weinheim

group exchange the relative magnitudes of the rate constants for exchange and propagation are $k_{exc} \gg k_p$.[8,14]

By modulating living DT Ziegler–Natta polymerization "on" for one amount of monomer, and then "off" for another, we previously prepared well-defined atactic–isotactic stereoblock diblock polyolefins of uniform molecular weight and block length from higher α-olefins.[10a] The synthesis of discrete, multiblock stereoblock architectures through programmed stereomodulation of living, or "controlled", polymerizations, however, presents an enormous challenge; to the best of our knowledge, it has not yet been achieved for any class of polymerization type (e.g., anionic, Ziegler–Natta, or atom transfer radical (ATRP)).[15,16] In the present study, the principle obstacle to overcome was how to turn DT back "on" after it has been "off" by introducing methyl groups back into the system through methylation of cationic propagating centers in such a way that will not introduce a new species that is deleterious to either DT or subsequent non-DT living polymerizations. After considerable evaluation and optimization, it was determined that compound **4**[17] is ideally suited for this task.[18] Owing to the significant intrinsic steric strain that is released, **4** engages in irreversible methyl group transfer with **3** or with cationic propagating centers derived from it (see Scheme 2), as determined by NMR spectroscopy.

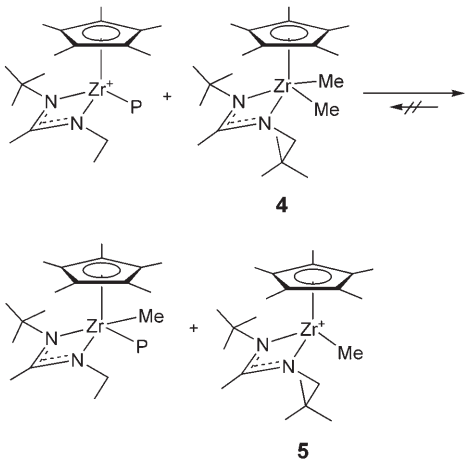

Scheme 2. Methylation of cationic zirconium propagating centers. P = polymer chain; the borate counterion is not shown.

Furthermore, the new cationic species **5** that is produced after methyl group transfer was determined to be completely inactive for olefin polymerizations, presumably due to substantial steric crowding about the metal center.[17]

With all the elements in hand, the programmed synthesis of several different discrete, multiblock, i-a sb-PP architectures proved to be a straightforward task. In practice, polymerization time is used to define block length. As the polymerization of propene is living at −10 °C, the type of stereoblock can be switched as many times as desired from being initially atactic (**1**:**2** = 0.5) by simply interrupting the propene feed, adding either 0.5 equivalents of **1** (for a→i) or 0.5 equivalents of **4** (for i→a), and then resuming polymerization with the reintroduction of propene. Unequivocal proof that sharp block boundaries exist in the final i-a sb-PP materials was obtained by introducing a 99% ^{13}C-labeled methyl group at the beginning of the growth of the polymer chain using ^{13}C-labeled **2**. Aliquots were then taken after the synthesis of each new block and difference (next block−last block) ^{13}C NMR spectra were produced as shown in Figure 2,

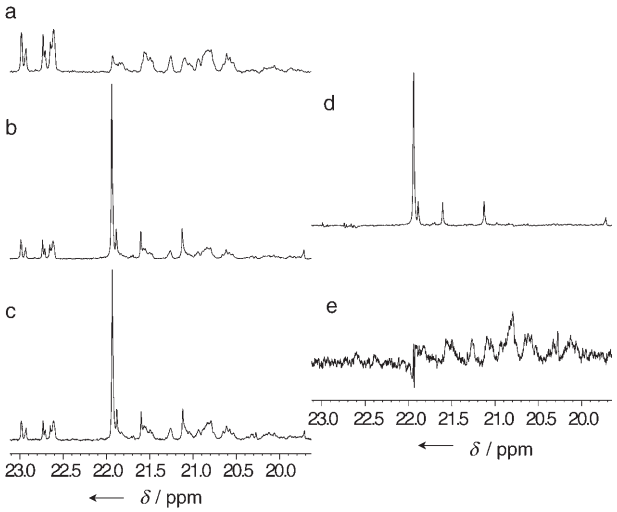

Figure 2. ^{13}C{^{1}H} NMR spectra (125 MHz, 1,1,2,2-$C_2D_2Cl_4$, 70 °C) highlighting the methyl regions of aliquots taken during the synthesis of triblock a-i-a sb-PP prepared with a ^{13}C-labeled methyl end group (note that the resonances for this end group appear between $\delta = 22.5$–23.0 ppm and are used as the internal reference to generate difference spectra). a) Atactic block aliquot; b) atactic–isotactic diblock aliquot; c) final atactic–isotactic–atactic triblock; d) difference spectrum between (a) and (b); note that polymerization has switched from being purely atactic to highly isotactic; and e) difference spectrum between (c) and (b); note that polymerization has switched back from being highly isotactic to being purely atactic.

using the resonance of the ^{13}C-labeled methyl end group as an internal reference, that confirmed that each new block added was either strictly isotactic or atactic as programmed. This detailed spectroscopic analysis then also served to validate the routine use of the *mmmm* index from ^{13}C NMR pentad analysis of aliquots to unequivocally establish the compositional block structure of each new i-a sb-PP material that was synthesized.[9] Importantly, in this regard, as we did not attempt to rigorously compensate for changes in mass transfer of propene and viscosity effects that can occur as a function of polymerization time, or to a lesser extent in temperature and concentration, quantitative block lengths within a target i-a sb-PP multiblock structure were observed to vary slightly from run to run (e.g., a/i/a ratio of 1.0:1.2:0.8 observed for a target 1:1:1 a-i-a sb-PP triblock). Also note that while multiblock architectures commencing first with an isotactic block (i.e., an i-a-i sb-PP triblock) can be synthesized, the resulting isolated materials also have relative block lengths that deviate from those expected, owing to problems associated with sometimes undesired precipitation of the pure isotactic block. Further optimization of the polymerization conditions are currently in progress to ameliorate these technical issues.

 © 2006 Wiley-VCH Verlag GmbH & Co. KGaA, Weinheim

As an initial probe of structure–property relationships, three different i-a sb-PP stereoblock architectures, a 60:40 a-i diblock, a 30:40:30 a-i-a triblock, and a 30:20:30:20 a-i-a-i tetrablock, were synthesized, keeping the molecular weight and total isotactic content constant ($M_n \approx 170000$, $mmmm \approx 0.32$ (or 40% isotactic); see Figure 3).[8] Gratifyingly, testing of the tensile properties of as-prepared standard dog-bone-shaped samples (ASTM D 412-98a; thickness: 0.5 mm) demonstrated a clear dependency of the elastomeric properties on the stereoblock architecture (Figure 4). The triblock displayed the highest ultimate elongation to break of 1530% (70% recovery after break) relative to either the diblock at 1325% (84%) or the tetrablock at 1227% (91%). Furthermore, from stress–strain hysteresis curves for 10 cycles, the tetrablock a-i-a-i sb-PP material proved to be an exceptional elastomer after initial strain-induced annealing (2 cycles), with virtually no further irreversible deformation taking place within subsequent stress–strain cycles involving an initial maximum strain of 300% (see Figure 4b).

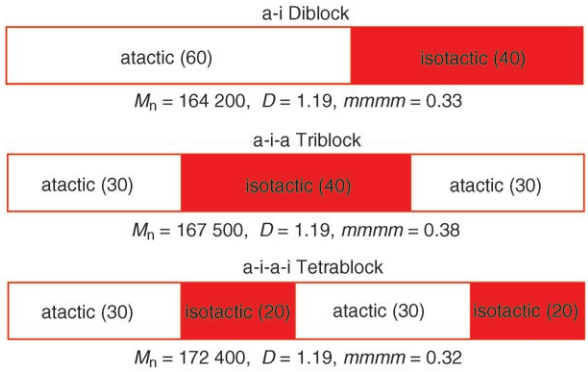

Figure 3. Representation of three different i-a sb-PP stereoblock architectures (di-, tri-, and tetrablock) polypropene samples prepared. The molecular weight and total isotactic content is constant ($M_n \approx 170000$, $mmmm \approx 0.32$ (or 40% isotactic)).

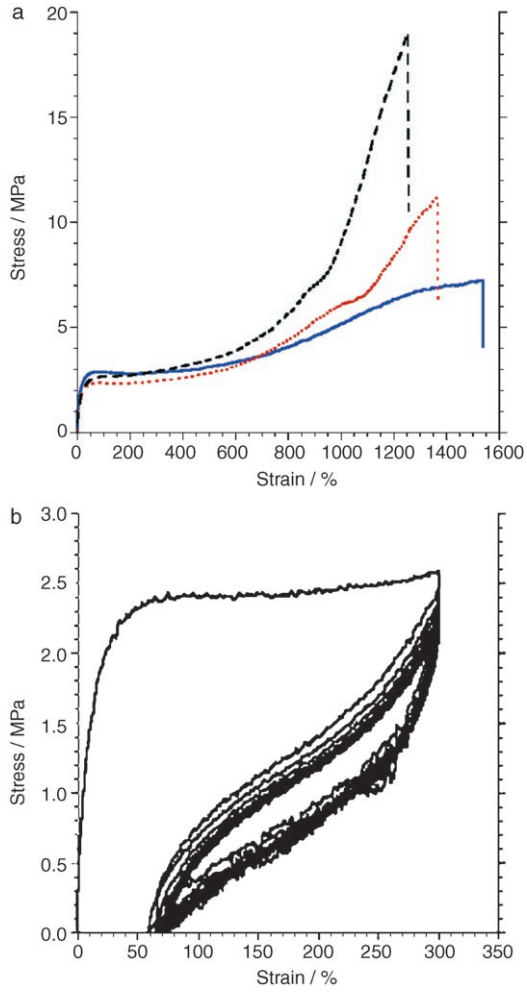

Figure 4. a) Stress–strain curves showing ultimate elongation to break for the 30–40–30 a-i-a triblock (solid line), the 60–40 a-i diblock (dotted line), and the 30–20–30–20 a-i-a-i tetrablock (dashed line). b) Strain hysteresis curves (10 cycles) for a fresh, as-prepared sample of the a-i-a-i tetrablock sb-PP.

In conclusion, a new class of polypropene material, namely discrete, multiblock i-a sb-PP, has been prepared for the first time. The ability to synthesize an almost unlimited variety of new stereoblock architectures for this class of material in which molecular weight and the number, length, and placement of each stereoblock type can be programmed as desired, coupled with clear evidence that subtle differences in polymer chain dynamics that are governed by stereoblock architecture can play major roles in determining physical properties, now sets the stage for a potentially rich new area of discovery that might serve to further extend the useful range of polypropene-based products.

Received: January 3, 2006
Published online: March 9, 2006

Keywords: polymerization · polypropylene · tacticity

[1] a) H. H. Brintzinger, D. Fischer, R. Mülhaupt, B. Rieger, R. M. Waymouth, *Angew. Chem.* **1995**, *107*, 1255; *Angew. Chem. Int. Ed. Engl.* **1995**, *34*, 1143; b) G. W. Coates, *Chem. Rev.* **2000**, *100*, 1223; c) V. C. Gibson, *Chem. Rev.* **2003**, *103*, 283.
[2] L. Resconi, L. Cavallo, A. Fait, F. Piemontesi, *Chem. Rev.* **2000**, *100*, 1253.
[3] C. De Rosa, F. Auriemma, A. Di Capua, L. Resconi, S. Guidotti, I. Camurati, I. E. Nifant'ev, I. P. Lashevtsev, *J. Am. Chem. Soc.* **2004**, *126*, 17040.
[4] G. Müller, B. Rieger, *Prog. Polym. Sci.* **2002**, *27*, 815.
[5] G. Natta, *J. Polym. Sci.* **1959**, *34*, 531.
[6] See, for instance: a) J. W. Collette, C. W. Tullock, R. N. MacDonald, W. H. Buck, A. C. L. Su, J. R. Harrell, R. Mülhaupt, B. C. Anderson, *Macromolecules* **1989**, *22*, 3851; b) D. T. Mallin, M. D. Rausch, Y. G. Lin, S. Dong, J. C. W. Chien, *J. Am. Chem. Soc.* **1990**, *112*, 2030; c) G. W. Coates, R. M. Waymouth, *Science* **1995**, *267*, 217.
[7] a) J. W. Gauthier, S. Collins, *Macromolecules* **1995**, *28*, 3779; b) V. Busico, V. v. A. Castelli, P. Aprea, R. Cipullo, A. Segre, G. Talarico, M. Vacatello, *J. Am. Chem. Soc.* **2003**, *125*, 5451.
[8] Details are provided in the Supporting Information.
[9] a) K. C. Jayaratne, L. R. Sita, *J. Am. Chem. Soc.* **2000**, *122*, 958; b) K. C. Jayaratne, R. J. Keaton, D. A. Henningsen, L. R. Sita, *J. Am. Chem. Soc.* **2000**, *122*, 10490; c) R. J. Keaton, K. C.

 © 2006 Wiley-VCH Verlag GmbH & Co. KGaA, Weinheim

Jayaratne, D. A. Henningsen, L. A. Koterwas, L. R. Sita, *J. Am. Chem. Soc.* **2001**, *123*, 6197.
[10] a) Y. Zhang, R. J. Keaton, L. R. Sita, *J. Am. Chem. Soc.* **2003**, *125*, 9062; b) Y. Zhang, L. R. Sita, *J. Am. Chem. Soc.* **2004**, *126*, 7776.
[11] a) V. Busico, R. Cipullo, N. Friederichs, S. Ronca, G. Talarico, M. Togrou, B. Wang, *Macromolecules* **2004**, *37*, 8201; b) A. F. Mason, G. W. Coates, *J. Am. Chem. Soc.* **2004**, *126*, 16326.
[12] A. H. E. Müller, R. Zhuang, D. Yan, G. Litvinenko, *Macromolecules* **1995**, *28*, 4326.
[13] a) M. Szwarc, M. van Beylen, *Ionic Polymerization and Living Polymers*, Chapman & Hall, New York, **1993**; b) K. Matyjaszewski, *J. Phys. Org. Chem.* **1995**, *8*, 197; c) K. Matyjaszewski, S. Gaynor, D. Greszta, D. Mardare, T. Shigemoto, *J. Phys. Org. Chem.* **1995**, *8*, 306.
[14] It is important to point out that if the rate of polymerization of propene is now equal or greater in magnitude to the rate of methyl group exchange between active and dormant sites or the rate of epimerization of the dormant site, that is, $R_p \geq R_{exc}$ or $R_p \geq R_{epi}$, then an atactic microstructure will not be formed under DT conditions. Furthermore, under DT conditions the value of D is approximately given by $1 + k_p/k_{exc}$, so narrow polydispersities for the final polypropene materials will result only if the rate constants for methyl group exchange and propagation are on the order of $k_{exc} \gg k_p$.[12]
[15] For the synthesis of diblock stereoblock polymers, see, for instance: a) A. D. Bolig, E. Y.-X. Chen, *J. Am. Chem. Soc.* **2002**, *124*, 5612; b) J.-F. Lutz, D. Neugebauer, K. Matyjaszewski, *J. Am. Chem. Soc.* **2003**, *125*, 6986; c) K. Nishii, T. Shiono, T. Ikeda, *Macromol. Rapid Commun.* **2004**, *25*, 1029.
[16] Coates and co-workers have recently succeeded in producing a triblock regioblock polypropene material consisting of isotactic, regioregular blocks and atactic, regioirregular blocks in which temperature was used to switch between block types; see: A. E. Cherian, J. M. Rose, E. B. Lobkovsky, G. W. Coates, *J. Am. Chem. Soc.* **2005**, *127*, 13770.
[17] D. A. Kissounko, J. C. Fettinger, L. R. Sita, *Inorg. Chim. Acta* **2003**, *345*, 121.
[18] The task of finding a suitable methylating reagent is complicated by the need to avoid the introduction of solvents, such as diethyl ether or tetrahydrofuran, that can serve as strong complexing σ donors to the cationic metal centers. Dimethylzinc was unfortunately not effective in this role.

 © 2006 Wiley-VCH Verlag GmbH & Co. KGaA, Weinheim

Dendrimers

DOI: 10.1002/anie.200600063

Palladium-Catalyzed Convergent Synthesis and Properties of Conjugated Dendrimers Based on Triarylethene Branching**

Kenichiro Itami, Keisuke Tonogaki, Toshiki Nokami, Youichi Ohashi, and Jun-ichi Yoshida**

Dendrimers are molecular architectures that offer an enormous opportunity for creating new functional materials.[1] Their highly branched, globular architectures give rise to a number of interesting properties that contrast with those of linear polymers. Although a number of dendrimers exist that are based on various core and branching units, the development of new core and branching units should pave the way for a generation of new functional materials.[1] In particular, the evolution of novel and effective π-branching units is necessary in the emerging field of π-conjugated dendrimers,[2–6] because most of the branches of known π-conjugated dendrimers are based on benzene structures with 1,3,5-linkages, which considerably interrupt any interbranch π conjugation.

Triggered by the tremendous progress in the field of stilbenoid compounds, and in particular the oligophenylenevinylenes,[7] the development of electroactive and light-emitting stilbenoid dendrimers is of great interest to many researchers. However, all the stilbenoid dendrimers reported to date are based on 1,3,5-benzene branching and thereby suffer from disrupted interbranch conjugation (Figure 1).[8]

Over the last few years, we have explored the chemistry of extended π systems based on highly substituted C=C cores (i.e., triarylethene- and tetraarylethene-based extended π systems) which has involved methodological challenges associated with selective synthesis and the potential application of these compounds as functional materials.[9] We

[*] Prof. K. Itami
Research Center for Materials Science, Nagoya University
and PRESTO, Japan Science and Technology Agency (JST)
Chikusa-ku, Nagoya 464-8602 (Japan)
Fax: (+81)52-788-6098
E-mail: itami@chem.nagoya-u.ac.jp
K. Tonogaki, Dr. T. Nokami, Y. Ohashi, Prof. J. Yoshida
Department of Synthetic Chemistry and Biological Chemistry
Graduate School of Engineering
Kyoto University
Nishikyo-ku, Kyoto 615-8510 (Japan)
Fax: (+81)75-383-2727
E-mail: yoshida@sbchem.kyoto-u.ac.jp

[**] This work was supported in part by a Grant-in-Aid for Scientific Research from the Ministry of Education, Culture, Sports, Science, and Technology, Japan. K.T. is a recipient of the JSPS Predoctoral Fellowships for Young Scientists. We thank Dr. Atsushi Wakamiya and Professor Shigehiro Yamaguchi (Nagoya University) for valuable discussions.

Supporting information for this article is available on the WWW under http://www.angewandte.org or from the author.

WILEY InterScience DISCOVER SOMETHING GREAT
© 2006 Wiley-VCH Verlag GmbH & Co. KGaA, Weinheim

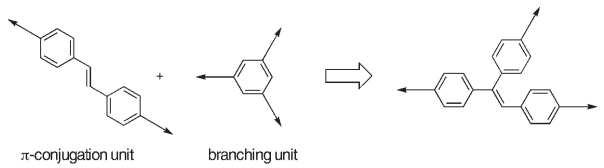

Figure 1. Triarylethene (right) as a π-conjugated branching unit for conjugated dendrimers.

envisaged that a strategic modification of our triarylethene synthesis would lead to the generation of novel conjugated dendrimers that incorporate the triarylethene structure as a new π-conjugated branching unit (Figure 1). We expected such dendrimers to be different from previous stilbenoid dendrimers with respect to their properties, which reflect the effective delocalization of the π electrons as well as their unique structure. Herein, we describe the convergent synthesis of novel triarylethene-based conjugated dendrimers using palladium-catalyzed iterative triarylation of vinylboronate esters. The results of preliminary examinations of the photophysical properties of the dendrimers are also described.

We previously reported the rapid synthesis of triarylethenes using a catalytic one-pot triarylation on the C=C core of vinylboronate pinacol ester CH_2=CHB(pin) (**1**).[10] Under the influence of a Pd catalyst and an amine, **1** undergoes a double Mizoroki–Heck-type arylation[11,12] with two equivalents of aryl halides to generate β,β-diarylated vinylboronates Ar_2C=CHB(pin). The subsequent Suzuki–Miyaura coupling[13] of the resultant boronates with aryl halides rapidly affords triarylethenes Ar_2C=CHAr.[10] We envisaged that a convergent synthesis of triarylethene-based dendrimers would be possible by using these aryl-assembling reactions (i.e., double C–H arylation and C–B arylation) with the strategic use of di- and trifunctional aryl units (aryl dihalides and trihalides). Our strategy that employs aryl dihalides is shown in Scheme 1.

The treatment of vinylboronate **1** with two equivalents of aryl halides **2** in the presence of a Pd catalyst and amine afforded β,β-diarylated vinylboronates **3** (step A, a double Mizoroki–Heck arylation).[10] Although the subsequent double cross-coupling of **3** with aryl dihalides produced the 2:1 coupling adduct **G1**, the selective mono-cross-coupling at either of the Ar–X bonds of the aryl dihalides produced the 1:1 coupling adduct with unreacted Ar–X (step B, selective mono-cross-coupling). This simple sequence allowed us to quickly prepare π-extended aryl halides **2**. Thus, the repetition of the sequence of steps A and B resulted in the production of highly π-extended alkenylboronates **3**. In each cycle, the boronates **3** were doubly cross-coupled with aryl dihalides (step C, double cross-coupling) to produce triarylethene-based dendrimers **G*n*** (where *n* is the generation number) in a convergent manner. The power of this synthetic strategy is apparent, as all of these dendrimers are prepared from common reagents using standard reactions.

A representative synthesis of **4-G*n*** ($n = 1$–3) dendrimers, which include triphenylethene branching units, is shown in Scheme 2. The use of the highly active [Pd(P*t*Bu$_3$)$_2$] catalyst[14] in combination with *i*Pr$_2$NH was useful in the double Mizoroki–Heck arylation (step A in Scheme 1). These conditions were particularly effective for the selective arylation of C–H over C–B, which is otherwise favorable (Suzuki–Miyaura coupling). For selective mono-cross-coupling reactions (step B in Scheme 1), the use of 1-bromo-4-iodobenzene as the aryl dihalide under the catalytic influence of moderately active [Pd(PPh$_3$)$_4$] was effective. When a highly active catalyst such as [Pd(P*t*Bu$_3$)$_2$] was used, then double cross-coupling often took place to afford **4-G1** (see Figure 2) in high yields. Therefore, we used [Pd(PPh$_3$)$_4$] for mono-cross-coupling reactions (step B) and [Pd(P*t*Bu$_3$)$_2$] for the final double cross-coupling reactions (step C).[15] Gratifyingly, the third generation dendrimer **4-G3** was obtained in reasonable overall yield upon repeating these reactions.

When the double cross-coupling reactions (step C, Scheme 1) were performed at earlier stages, such as, with **3-G1** and **3-G2**, then lower generation dendrimers **4-G1** and **4-G2**, respectively, were obtained in good yields (Scheme 2). The application of various core units in the final double cross-coupling rapidly afforded various conjugated dendrimers in a convergent manner (Figure 2). When Mizoroki–Heck arylations (step A) were conducted in a mono fashion, then dendrimers with fewer branches, such as **12**, were easily prepared. Such dendrimers are useful for elucidating the effect of branching of the dendrimers on their properties.

Our strategy could be extended to the synthesis of conjugated dendrimers with mixed branching units by

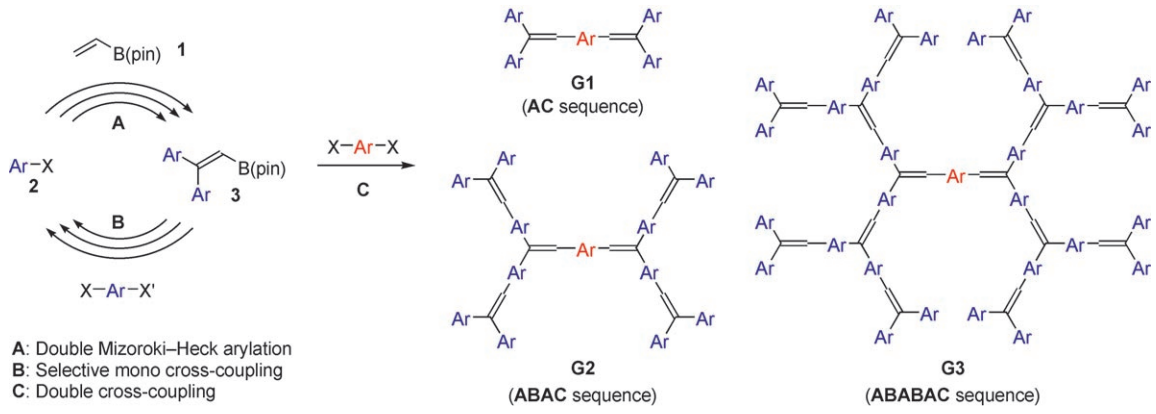

Scheme 1. Convergent synthesis of triarylethene-based conjugated dendrimers. pin = pinacolyl.

 © 2006 Wiley-VCH Verlag GmbH & Co. KGaA, Weinheim

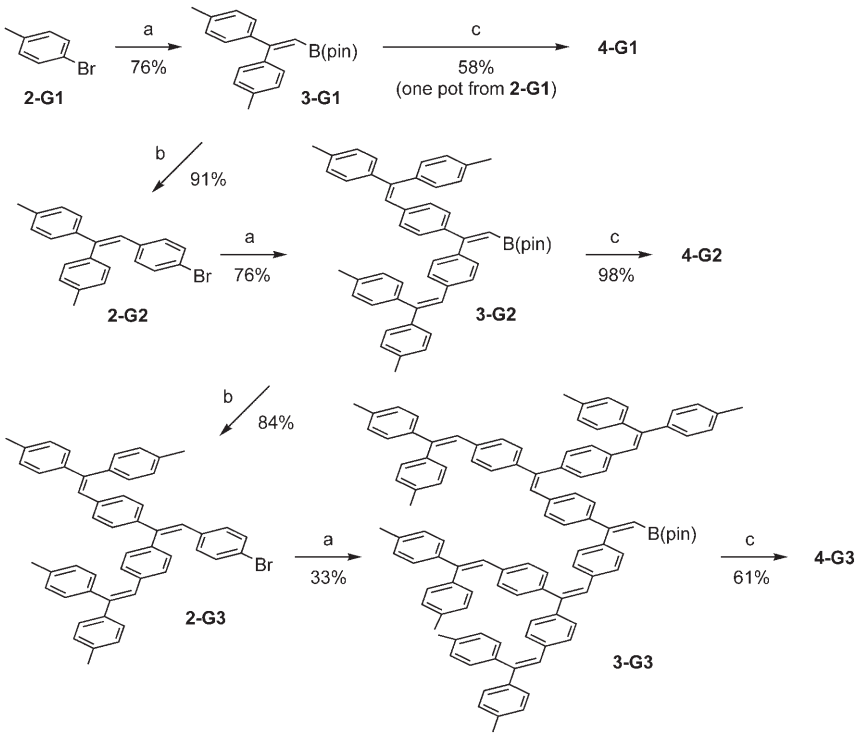

Scheme 2. Synthesis of triarylethene-based dendrimers **4-G*n*** ($n = 1$–3). a) **1**, [Pd($Pt Bu_3$)$_2$], iPr_2NH, toluene, 80 °C; b) 1-bromo-4-iodobenzene, [Pd(PPh_3)$_4$], aq. Cs_2CO_3, toluene, 90 °C; c) 1,4-diiodobenzene, [Pd($Pt Bu_3$)$_2$], NaOH, H_2O, toluene, 90 °C.

simply applying aryl trihalides in place of the aryl dihalides in the reaction scheme described in Scheme 1. For example, when 1,3,5-tribromobenzene was used as a trifunctional unit, then the highly branched dendrimer **13**, which contains triphenylethene and benzene branching units (Figure 2), was obtained in high yield (Scheme 3).

Most of the dendrimers prepared were soluble in common organic solvents and, thus, allowed us to characterize them using standard methods such as ^{1}H NMR and ^{13}C NMR spectroscopy and high-resolution FAB mass spectrometry (HRMS). In many cases, the methyl groups at the surface of the dendrimers were well distinguished (although not fully) in the ^{1}H and ^{13}C NMR spectra. In addition, analysis of the samples by gel permeation chromatography showed that all the dendrimers were monodispersed, as would be expected from their well-ordered construction.

Interestingly, many of the conjugated dendrimers prepared emitted fluorescence in both solution and the solid state. The photophysical properties (UV/Vis and fluorescence) of these conjugated dendrimers in chloroform are listed in Table 1. As expected, the wavelength of the emission maximum (λ_{em}) increases with increasing dendrimer generation (i.e., λ_{em}(**4-G3**) > λ_{em}(**4-G2**) > λ_{em}(**4-G1**)) and is ascribed to the extension of the π conjugation. We also found that the quantum yield of fluorescence (Φ_F) also increased with increasing dendrimer generation (Φ_F(**4-G1**) = 0.024, Φ_F(**4-G2**) = 0.58, Φ_F(**4-G3**) = 0.62). Note the 24-fold increase from **4-G1** to **4-G2**. Such a dramatic effect of the dendrimer generation in the color and efficiency of the fluorescence emission has not been reported for 1,3,5-benzene-branched stilbenoid dendrimers. We believe that the enhanced emission of the higher generation dendrimers is attributable to their unique structure. Owing to the sterically congested environment, the higher dendrimers such as **4-G2** probably adopt a nonplanar structure, which reduces the probability of effective intermolecular fluorescence-quenching interactions and molecular motions that may trigger radiationless transitions, thereby enhancing the overall fluorescence efficiency.[16]

To examine the effect of branching on the properties of these dendrimers, the less-branched dendrimer **12** was prepared as a reference for **4-G2**. As the absorption and emission maxima and emission color of **12** are similar to those of **4-G2**, it is reasonable to assume that the extent of the π conjugation seen in **4-G2** is already established in the substructure **12** and that the remaining four *p*-tolyl branches in **4-G2** contribute to its enhanced fluorescence efficiency (Φ_F(**12**) = 0.32 vs Φ_F(**4-G2**) = 0.58).

Moreover, the solubility of these π systems was found to generally increase as the degree of branching increases. For example, the solubility of **4-G2** in chloroform (61.4 mM) and benzene (63.8 mM), as saturated solutions, is 6–10 times higher than that of **12** in the same solvents (11.3 and 6.7 mM, respectively). The increased solubility of **4-G2** is also thought to be attributable to its unique nonplanar structure, which reduces intermolecular interactions and thereby facilitates solvation. The current focus of research into oligophenylenevinylenes and stilbenoid dendrimers lies in enhancing their solubility and processability while preserving the planarity and rigidity of the phenylenevinylene unit, which is responsible for their unique functional properties. Therefore, the exploitation of π branching as observed in our work may be a useful approach toward this goal.

The photophysical properties of the dendrimers were found to depend significantly on the nature of the core structure. For example, the second generation dendrimers based on 1,2- and 1,3-benzene cores (**5** and **6**) emitted blue light with a low efficiency, which was significantly different to the yellow light emitted by **4-G2** with $\Phi_F = 0.58$. The low emissions of the "half-dendrimer" **7** and dendrimer **8** with a nonconjugated core also support the importance of the core structure with regard to the fluorescence properties. Such "core-tuning" is also useful in the generation of materials with interesting properties. For example, the second generation dendrimer **9** with a fluorene core emitted yellow light with an extremely high quantum yield ($\Phi_F = 0.82$). The finding of a hydrocarbon that strongly emits yellow light is of great interest. Moreover, the replacement of the above core structure with bithiophene to give **10** and fluorenone to give **11** gives rise to orange and red light emissions, respectively.

 © 2006 Wiley-VCH Verlag GmbH & Co. KGaA, Weinheim

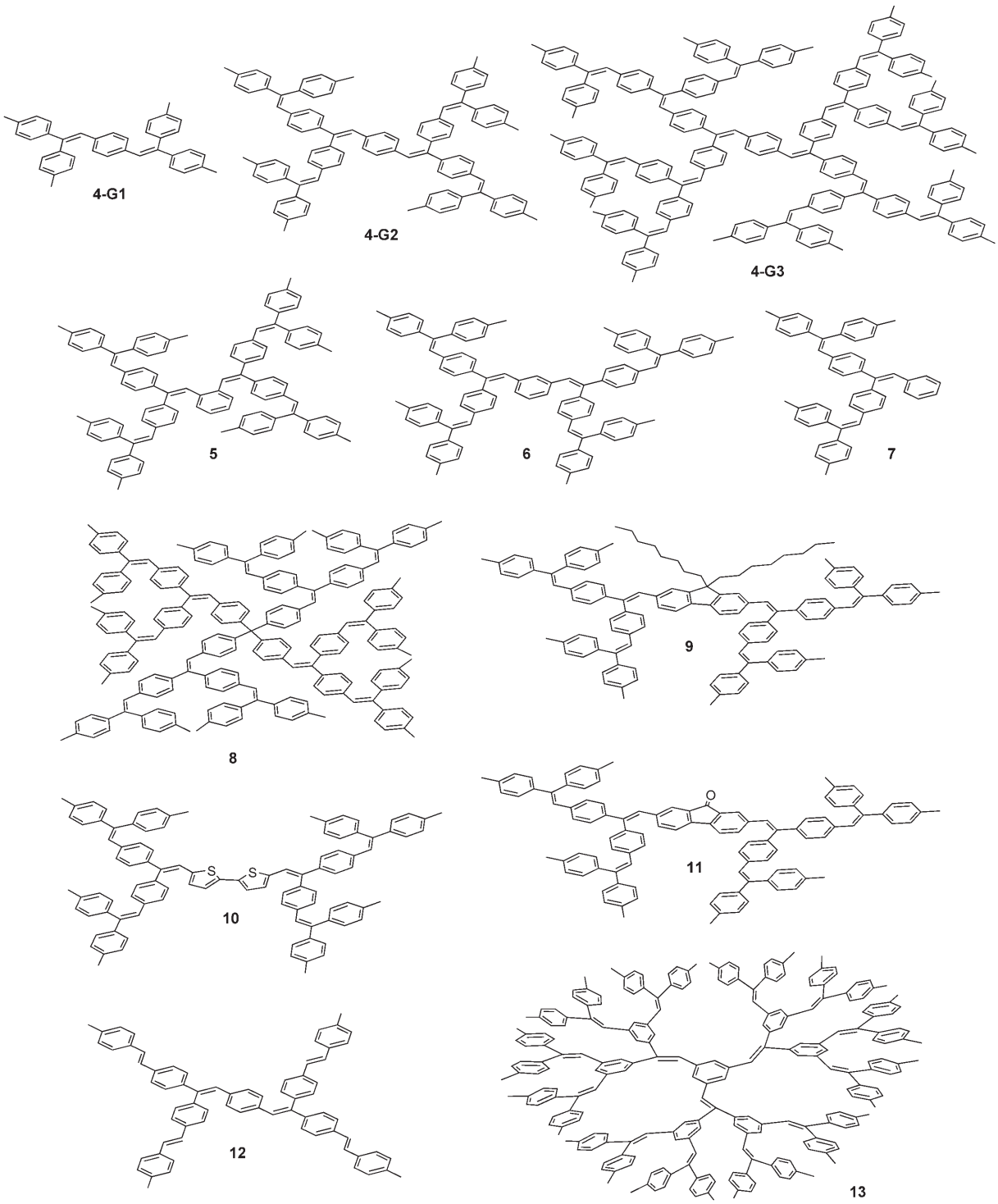

Figure 2. Various conjugated dendrimers prepared in this study.

These results clearly show that the photophysical properties can be conveniently tuned at the final double cross-coupling stage (step C in Scheme 1) rather than at the earlier stages.

In summary, we have developed an extremely useful and flexible method for the convergent synthesis of novel conjugated dendrimers based on triarylethene branching. A simple yet powerful strategy using common reagents (aryl halides) and reactions (Pd-catalyzed arylations) allowed us to quickly and systematically prepare various fluorescent dendrimers. Moreover, our highly branched dendrimers revealed both a high efficiency of fluorescence emission and high solubility in common organic solvents, which are useful attributes for future applications. This branching effect may find many uses in the emerging field of stilbenoid materials[7,8]

 © 2006 Wiley-VCH Verlag GmbH & Co. KGaA, Weinheim

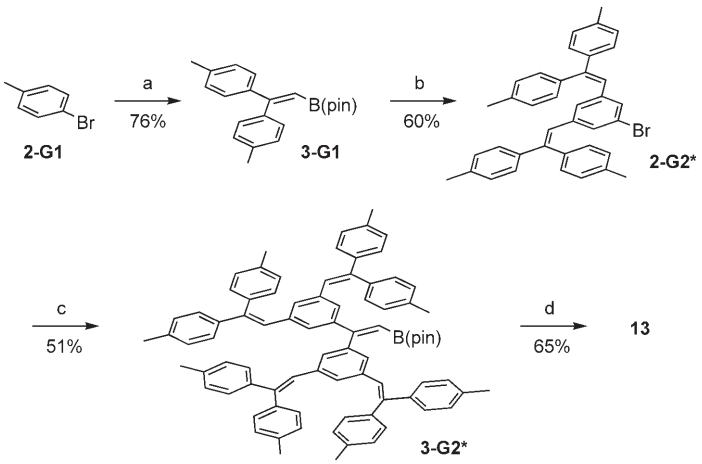

Scheme 3. Synthesis of conjugated dendrimer **13** with mixed branching units. a) **1**, [Pd(P*t*Bu$_3$)$_2$], *i*Pr$_2$NH, toluene, 80 °C; b) 1,3,5-tribromobenzene, [Pd(PPh$_3$)$_4$], NaOH, H$_2$O, toluene, 90 °C; c) **1**, [Pd(P*t*Bu$_3$)$_2$], *i*Pr$_2$NH, toluene, reflux; d) 1,3,5-tribromobenzene, [Pd(P*t*Bu$_3$)$_2$], NaOH, H$_2$O, toluene, 90 °C. Compounds **2-G2*** and **3-G2*** are related to **2-G2** and **3-G2**, respectively (see Scheme 2).

Table 1: Photophysical properties of conjugated dendrimers.

Compounds	UV/Vis data[a]	Fluorescence data[a]		
	λ_{max} [nm], (log ε)	λ_{em} [nm]	Color	Φ_F[b]
4-G1	359 (4.56)	473	blue	0.024
4-G2	402 (4.72), 343 (4.86)	518	yellow	0.58
4-G3	343 (5.20), 248 (5.13)	520	yellow	0.62
5	340 (5.00)	492	blue	0.15
6	340 (5.00)	489	blue	0.050
7	340 (4.71)	471	blue	0.015
8	345 (5.31)	484	blue	0.099
9	406 (4.89), 340 (4.92)	497	yellow	0.82
10	451 (4.72), 335 (4.79)	559	orange	0.17
11	473 (3.97), 388 (4.88), 332 (4.97)	616	red	0.010[c]
12	344 (5.03)	511	yellow	0.32

[a] Measured in chloroform, unless otherwise stated. [b] Determined with reference to 9,10-diphenylanthracene (λ_{exc} = 350 nm), unless otherwise stated. [c] Determined with reference to fluorescein in ethanol (λ_{exc} = 400 nm).

as well as in the development of novel functional materials, where there remain problems with respect to solubility and undesirable intermolecular interactions (aggregation) of the currently used materials.

Received: January 7, 2006
Published online: March 9, 2006

Keywords: C–C coupling · dendrimers · fluorescence · homogeneous catalysis · palladium

[1] a) S. M. Grayson, J. M. Fréchet, *Chem. Rev.* **2001**, *101*, 3819; b) *Dendrimers V: Functional and Hyperbranched Building Blocks, Photophysical Properties, Applications in Materials and Life Sciences* (Eds.: C. A. Schalley, F. Vögtle), Springer, Berlin, **2003**; c) *Dendrimers II: Architecture, Nanostructure and Supramolecular Chemistry* (Ed.: F. Vögtle), Springer, Berlin, **2000**.

[2] Early important conjugated dendrimers based on 1,3,5-benzene branches: a) T. M. Miller, T. X. Neenan, *Chem. Mater.* **1990**, *2*, 346; b) T. M. Miller, T. X. Neenan, R. Zayas, H. E. Bair, *J. Am. Chem. Soc.* **1992**, *114*, 1018; c) J. Zhang, J. S. Moore, Z. Xu, R. A. Aguirre, *J. Am. Chem. Soc.* **1992**, *114*, 2273; d) Z. Xu, J. S. Moore, *Angew. Chem.* **1993**, *105*, 1394; *Angew. Chem. Int. Ed. Engl.* **1993**, *32*, 1354.

[3] Selected recent examples of conjugated dendrimers based on benzene branches: a) C. D. Simpson, G. Mattersteig, K. Martin, L. Gherghel, R. E. Bauer, H. J. Räder, K. Müllen, *J. Am. Chem. Soc.* **2004**, *126*, 3139; b) X. Shen, D. M. Ho, R. A. Pascal, Jr., *J. Am. Chem. Soc.* **2004**, *126*, 5798; c) T. W. Kwon, M. M. Alam, S. A. Jenekhe, *Chem. Mater.* **2004**, *16*, 4657; d) D. Liu, S. D. Feyter, M. Cotlet, A. Stefan, U.-M. Wiesler, A. Herrmann, D. Grebel-Koehler, J. Qu, K. Müllen, F. C. De Schryver, *Macromolecules* **2003**, *36*, 5918; e) J. S. Melinger, Y. Pan, V. D. Kleiman, Z. Peng, B. L. Davis, D. McMorrow, M. Lu, *J. Am. Chem. Soc.* **2002**, *124*, 12002.

[4] Conjugated dendrimers based on enediyne branches: G. T. Hwang, H. S. Son, J. K. Ku, B. H. Kim, *J. Am. Chem. Soc.* **2003**, *125*, 11241.

[5] Conjugated dendrimers based on phenylazomethine branches: M. Higuchi, K. Yamamoto, *Bull. Chem. Soc. Jpn.* **2004**, *77*, 853.

[6] Conjugated dendrimers based on truxene branches: X.-Y. Cao, X.-H. Liu, X.-H. Zhou, Y. Zhang, Y. Jiang, Y. Cao, Y.-X. Cui, J. Pei, *J. Org. Chem.* **2004**, *69*, 6050.

[7] a) A. Kraft, A. C. Grimsdale, A. B. Holmes, *Angew. Chem.* **1998**, *110*, 416; *Angew. Chem. Int. Ed.* **1998**, *37*, 402; b) H. Meier, *Angew. Chem.* **1992**, *104*, 1425; *Angew. Chem. Int. Ed. Engl.* **1992**, *31*, 1399.

[8] Stilbenoid dendrimers based on 1,3,5-benzene branches: a) S. K. Deb, T. M. Maddux, L. Yu, *J. Am. Chem. Soc.* **1997**, *119*, 9079; b) H. Meier, M. Lehmann, *Angew. Chem.* **1998**, *110*, 666; *Angew. Chem. Int. Ed.* **1998**, *37*, 643; c) M. Halim, J. N. G. Pillow, I. D. W. Samuel, P. L. Burn, *Adv. Mater.* **1999**, *11*, 371; d) J. N. G. Pillow, M. Halim, J. M. Lupton, P. L. Burn, I. D. W. Samuel, *Macromolecules* **1999**, *32*, 5985; e) J. N. G. Pillow, P. L. Burn, I. D. W. Samuel, M. Halim, *Synth. Met.* **1999**, *102*, 1468; f) H. Meier, M. Lehmann, U. Kolb, *Chem. Eur. J.* **2000**, *6*, 2462; g) E. Díez-Barra, J. C. García-Martínez, J. Rodríguez-López, R. Gómez, J. L. Segura, N. Martín, *Org. Lett.* **2000**, *2*, 3651; h) J. L. Segura, R. Gómez, N. Martín, D. M. Guldi, *Org. Lett.* **2001**, *3*, 2645; i) E. Díez-Barra, J. C. García-Martínez, S. Merino, R. del Ray, J. Rodríguez-López, P. Sánchez-Verdú, J. Tejeda, *J. Org. Chem.* **2001**, *66*, 5664; j) D. Ma, J. M. Lupton, R. Beavington, P. L. Burn, I. D. W. Samuel, *Adv. Funct. Mater.* **2002**, *12*, 507; k) S. Sengupta, S. K. Sadhukhan, R. S. Singh, N. Pal, *Tetrahedron Lett.* **2002**, *43*, 1117; l) A. R. Cano-Marín, E. Díez-Barra, J. Rodríguez-López, *Tetrahedron* **2005**, *61*, 395.

[9] a) K. Itami, K. Mitsudo, T. Kamei, T. Koike, T. Nokami, J. Yoshida, *J. Am. Chem. Soc.* **2000**, *122*, 12013; b) K. Itami, T. Nokami, J. Yoshida, *J. Am. Chem. Soc.* **2001**, *123*, 5600; c) K. Itami, T. Nokami, Y. Ishimura, K. Mitsudo, T. Kamei, J. Yoshida, *J. Am. Chem. Soc.* **2001**, *123*, 11577; d) K. Itami, Y. Ushiogi, T. Nokami, Y. Ohashi, J. Yoshida, *Org. Lett.* **2004**, *6*, 3695; e) K. Itami, M. Mineno, N. Muraoka, J. Yoshida, *J. Am. Chem. Soc.* **2004**, *126*, 11778; f) K. Itami, Y. Ohashi, J. Yoshida, *J. Org. Chem.* **2005**, *70*, 2778.

[10] K. Itami, K. Tonogaki, Y. Ohashi, J. Yoshida, *Org. Lett.* **2004**, *6*, 4093.

 © 2006 Wiley-VCH Verlag GmbH & Co. KGaA, Weinheim

[11] Reviews on the Mizoroki–Heck reaction: a) I. P. Beletskaya, A. V. Cheprakov, *Chem. Rev.* **2000**, *100*, 3009; b) A. de Meijere, F. E. Meyer, *Angew. Chem.* **1994**, *106*, 2473; *Angew. Chem. Int. Ed. Engl.* **1994**, *33*, 2379.
[12] Multiple Mizoroki–Heck reaction: a) S. Bräse, A. de Meijere in *Handbook of Organopalladium Chemistry for Organic Synthesis* (Ed.: E. Negishi), Wiley, New York, **2002**, p. 1179; b) P. Nilsson, M. Larhed, A. Hallberg, *J. Am. Chem. Soc.* **2001**, *123*, 8217; c) see Reference [9].
[13] Review on Suzuki–Miyaura couplings: N. Miyaura, A. Suzuki, *Chem. Rev.* **1995**, *95*, 2457.
[14] Use of Pd/P(tBu)$_3$ as a catalyst for Mizoroki–Heck reactions: a) A. F. Littke, G. C. Fu, *J. Am. Chem. Soc.* **2001**, *123*, 6989; b) K. Itami, D. Yamazaki, J. Yoshida, *Org. Lett.* **2003**, *5*, 2161; c) see Reference [9].
[15] Use of Pd/P(tBu)$_3$ as a catalyst for Suzuki–Miyaura couplings: a) A. F. Littke, C. Dai, G. C. Fu, *J. Am. Chem. Soc.* **2000**, *122*, 4020; b) K. Itami, T. Kamei, J. Yoshida, *J. Am. Chem. Soc.* **2003**, *125*, 14670.
[16] It may also be possible that irradiation of the sample during spectroscopy induces electrocyclization to give partially cyclized products that are highly emissive. However, we could not detect such products in the samples by UV or NMR spectral analysis after irradiation.

 © 2006 Wiley-VCH Verlag GmbH & Co. KGaA, Weinheim

Nanobiotechnology

DOI: 10.1002/anie.200600061

DNA Polymerization on Gold Nanoparticles through Rolling Circle Amplification: Towards Novel Scaffolds for Three-Dimensional Periodic Nanoassemblies**

Weian Zhao, Yan Gao, Srinivas A. Kandadai, Michael A. Brook, and Yingfu Li**

Recent years have witnessed an explosion of interest in the use of DNA–nanoparticle bioconjugates for programmed nanostructures, 1D or 2D nanoparticle arrays, nanoelectronics, and biosensing and biodiagnostics.[1–9] DNA was chosen as a polymeric material in these studies owing mainly to the specificity of DNA base-pairing, the predictability of inter- or intramolecular interactions, its physicochemical stability, and mechanical rigidity. In addition, DNA can be manipulated and modified by a wide range of enzymes, including DNA polymerase, ligase, and restriction endonucleases. The powerful, convenient, and specific enzymatic manipulations make DNA a highly desirable building block for the construction of various nanostructures. In the current study, we set out to investigate whether we can perform rolling circle amplification (RCA) between a DNA oligonucleotide tethered to gold nanoparticles (AuNPs) as the primer and a single-stranded circular DNA as a template, catalyzed by a special DNA polymerase known as ϕ29 DNA polymerase (ϕ29DNAP).

RCA is a powerful but simple biochemical method that can be used to generate long single-stranded DNA (ssDNA) with a repeating sequence unit.[10–11] In a typical RCA process, a DNA polymerase, such as ϕ29DNAP, which has a strong ability to displace newly synthesized DNA strands, makes continuous nucleotide additions to a growing DNA chain over a short circular single-stranded DNA as the template under isothermal conditions. As a result, long, linear tandemly repetitive single strands of DNA are produced. As the synthesized long DNA molecules contain many repeating sequence motifs, RCA coupled with ensuing hybridization with fluorescent DNA probes has been used as an on-chip signal-amplification tool for sensitive biosensing.[12–16] Recently, it has been shown that long DNA molecules from RCA can be used as scaffolds for assembling nanoparticles to form 1D nanoparticle arrays.[17–18] However, to our knowledge, performing the RCA reaction on gold nanoparticles and using the resultant special DNA–AuNP assemblies to form 3D nanoparticle array have not been demonstrated.

Figure 1 schematically illustrates the RCA process on gold nanoparticles and its scaffolding for 3D periodical nanoassemblies. Gold nanoparticles of 15 nm diameter were first prepared by the classical citrate reduction route. Thiol-modified DNA primers (41 nucleotides) were then functionalized onto the nanoparticles following Mirkin's approach.[5] The concentration of DNA primers on the gold nanoparticles, referred to hereafter as primer–Au, was determined using UV/Vis spectroscopy by measuring the amount of DNA in solution before and after coupling; each primer–Au contained approximately 230 DNA primer strands. A 63-nucleotide-long circular DNA template was then annealed with the DNA-functionalized gold nanoparticles. The hybridization efficiency, as examined by measuring the radioactivity on the gold nanoparticles and in solution after annealing with a radiolabeled circular DNA template, was estimated to be approximately 30%, which is consistent with a previous study.[19] A control experiment in which a non-complementary radiolabeled circular DNA template was annealed with primer–Au showed negligible non-specific binding.

To achieve the best RCA performance, we optimized the experimental conditions. Our foremost concern was the stability of primer–Au in the presence of dithiothreitol (DTT). Primer–Au nanoparticles underwent irreversible aggregation in the presence of 4 mM DTT (a condition recommended by the manufacturer of ϕ29DNAP) at 30 °C in

[*] W. Zhao, Dr. Y. Gao, Prof. Dr. M. A. Brook, Prof. Dr. Y. Li
Department of Chemistry
McMaster University
1280 Main St., W. Hamilton, ON L8N 3Z5 (Canada)
Fax: (+1) 905-522-9033
E-mail: mabrook@mcmaster.ca
liying@mcmaster.ca
Dr. S. A. Kandadai, Prof. Dr. Y. Li
Department of Biochemistry and Biomedical Sciences
McMaster University
1280 Main St., W. Hamilton, ON L8N 3Z5 (Canada)

[**] The authors wish to thank Andy M. Duft for help with AFM measurements. Financial support was provided by the Natural Sciences and Engineering Research Council of Canada (NSERC) and the Canadian Institutes for Health Research (CIHR). Y.L. holds a Canada Research Chair.

 © 2006 Wiley-VCH Verlag GmbH & Co. KGaA, Weinheim

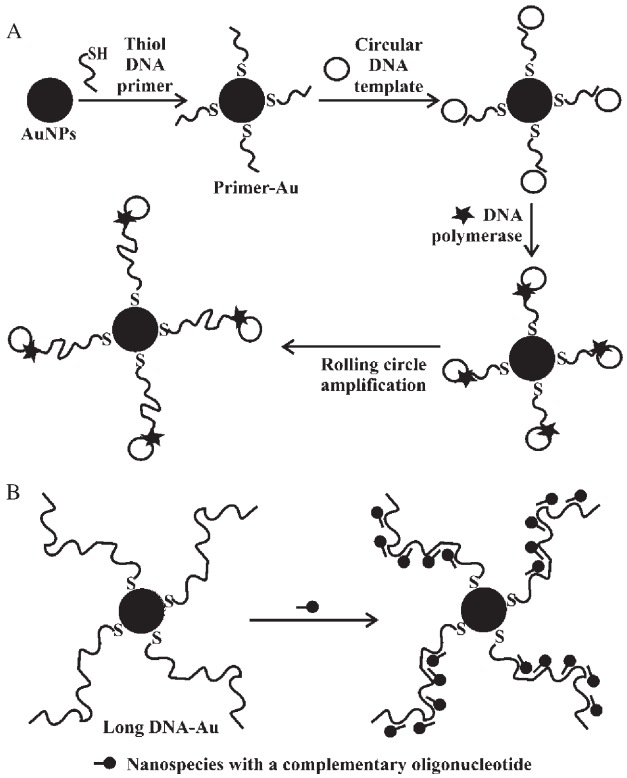

Figure 1. A) Schematic illustration of RCA on gold nanoparticles (AuNPs). B) DNA–Au conjugates produced by RCA as a scaffold for the formation of 3D nanostructures.

30 min. As ϕ29DNAP was supplied in a stock solution containing 1 mM DTT that was critical to the storage of the enzyme, we next performed the RCA reaction using diluted conditions (50 μM DTT and 5 units of ϕ29DNAP in 10 μL reaction solution). At this concentration of DTT, primer–Au was found to be stable (no detectable color change and no aggregation). Note that further dilution of the ϕ29DNAP stock solution produced an ineffective enzyme concentration for RCA. The second point of concern was the effect of the concentration of primer–Au conjugates on the performance of ϕ29DNAP. To investigate this issue, we conducted the RCA reaction in solution in the presence of T_{20}–Au (gold nanoparticles functionalized with DNA oligonucleotides containing 20 thymine bases) and found that these nanoparticles, particularly at high concentration (typically over 3 nM), significantly inhibited the activity of ϕ29DNAP (data not shown) presumably because some enzymes were nonspecifically adsorbed and denatured by the gold nanoparticles. On the basis of these results, we subsequently carried out the RCA reaction at relatively low concentrations of primer–Au (ca. 0.67 nM) and over a relatively short period (30 min), considering the high efficiency of DNA polymerase. The reaction temperature was fixed at 30 °C, as recommended by the manufacturer.

The resultant DNA was displaced from the surface of the gold nanoparticles by incubation with 250 mM mercaptoethanol at 37 °C overnight. The band obtained at the top of a 10% PAGE gel (Figure 2, lane 1) indicated that a large amount of high-molecular-weight DNA product was formed by RCA on

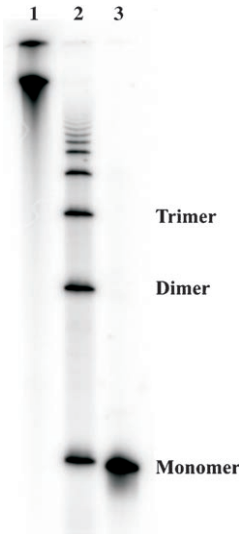

Figure 2. 10% denaturing polyacrylamide gel electrophoresis (PAGE) for the product obtained by RCA and synthesized from radiolabeled dNTPs (lane 1), the product obtained after digestion by Taq I (lane 2), and a 63-nt-long linear DNA oligonucleotide (lane 3).

the gold nanoparticles. As a critical test of the rolling circle amplification, a restriction endonuclease digestion experiment was performed. Each repetitive DNA unit contained a TCGA site that can be digested by the endonuclease Taq I. In the presence of Taq I, the long DNA molecules were indeed converted into much shorter DNA fragments (monomer, dimer, trimer, etc.) after 2 h digestion (lane 2 of Figure 2). It was difficult to determine precisely the length of the DNA produced by RCA; however, we estimated (based on the counting of DNA fragments as the marker in lane 2 of Figure 2) that the DNA molecules produced on the gold nanoparticles were significantly larger than 1000 nt (nt = nucleotide).

The long-DNA–Au conjugates were also directly investigated by atomic force microscopy (AFM). A DNA brush conformation, in which long DNA (typically hundreds of nanometers to microns in length) grafted from gold nanoparticles by RCA, was clearly observed (Figure 3, A and B). The long ssDNA, unlike rigid double-stranded DNA (dsDNA), cannot be fully stretched; that is, some of the

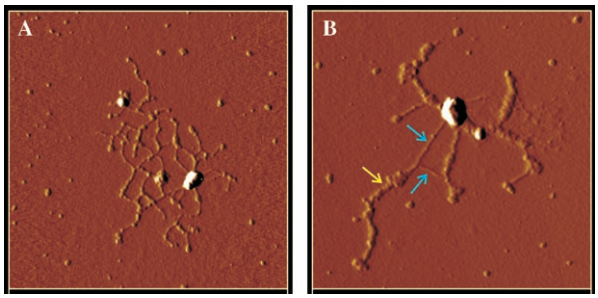

Figure 3. Tapping mode AFM images (amplitude mode) for long-DNA–Au conjugates obtained through RCA with gold nanoparticles. Scale: A) 1000×1000 nm^2; B) 800×800 nm^2. In (B), the blue arrows indicate ssDNA strands, and the yellow arrow indicates dsDNA-like structures.

 © 2006 Wiley-VCH Verlag GmbH & Co. KGaA, Weinheim

ssDNA may stick together and condense into globular structures. Indeed, in some cases, two ssDNA (Figure 3B, blue arrow) appeared to merge into dsDNA-like structures (Figure 3B, yellow arrow). It was a surprise that there were only tens or less of ssDNA grafted from each gold nanoparticle, considering that there were about 230 primers on each nanoparticle. Such a low graft density may be attributed to the fact that 1) the hybridization efficiency of the circular DNA template and primer–Au was poor (ca. 30%), 2) the DTT present (even at a low concentration) could displace the primer from the surface by thiol exchange, or 3) the DNA polymerase could be inhibited by the Au surface due to enzyme denaturation and steric effects. Note also that the size of these gold nanoparticles as measured by AFM was larger than those of both unfunctionalized "bare" gold nanoparticles and primer–Au (AFM data not shown), which is a typical phenomenon when one uses AFM to characterize a rigid nanoparticle core with polymer brushes collapsed on the surface.[20]

We next tested the capabilities of the DNA–Au nanoparticle conjugates, referred to as long-DNA–Au, to act as 3D scaffolds for further nanoassemblies by incubating long-DNA–Au with 5-nm gold nanoparticles that were modified with a 25-nt antisense oligonucleotide overnight. The resultant long-DNA–Au/5-nm-AuNP complexes were isolated by centrifugation at a relatively low speed (5000 rpm for 10 min) and analyzed by transmission electron microscopy (TEM).

A typical nanoassembled superstructure (Figure 4A) showed that 5-nm gold nanoparticles appeared only in the area (typically a few hundred nanometers in diameter) surrounding the 15-nm gold nanoparticles, indicating that these complexes were formed specifically by Watson–Crick base pairing. The average number of assembled 5-nm gold nanoparticles on each long-DNA–Au conjugate was approximately 26, as obtained statistically from 157 individual nanoassembled architectures. Remarkably, the distance between 5-nm gold nanoparticles along the long DNA (to clarify, attempts were made to trace DNA; see Figure 4B, red line) in most cases was in good agreement with the theoretical distance (ca. 21 nm), given that the distance between 5-nm gold nanoparticles is identical to the length of the 63-nucleotide-long DNA template and the separation between base pairs in a typical B-form dsDNA helix is 0.34 nm. These data strongly suggest that the nanoassembly events occurred in a well-defined, periodic manner along these long DNA. This conclusion was further confirmed by AFM studies in which the successful periodical assembly of 5-nm gold nanoparticles along these long DNA surrounding the 15-nm gold nanoparticles was clearly observed (Figure 4C). Control experiments in which 5-nm gold nanoparticles that were not functionalized with antisense DNA were incubated with long-DNA–Au, did not show any well-defined superstructures (data not shown). Indeed, neither long-DNA–Au nanoparticles nor 5-nm gold nanoparticles could be spun down by using the same centrifugation speed (5000 rpm for 10 min).

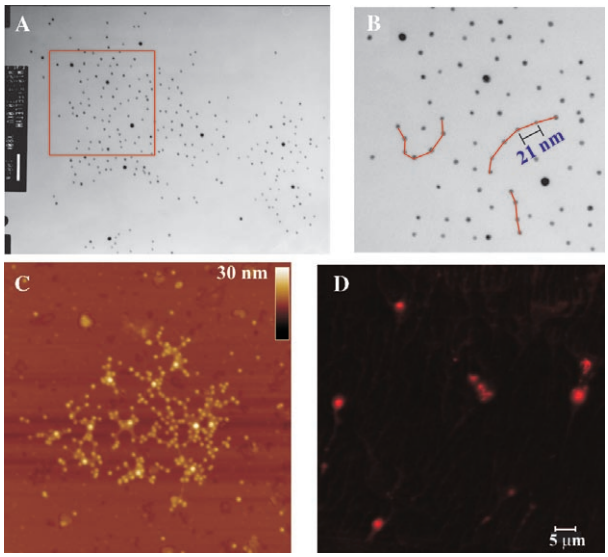

Figure 4. A) TEM images of nanoassembled superstructures prepared from 5-nm gold nanoparticles modified with antisense DNA and long-DNA–Au scaffolds. Scale bar: 100 nm. The red box was zoomed in to obtain the image shown in part (B). C) Height-mode AFM image of nanoassembled superstructures constructed from long-DNA–Au and 5-nm gold nanoparticles. The brighter and bigger dots correspond to the 15-nm gold nanoparticles. Scale: 2000×2000 nm^2. D) Confocal microscopy images of long-DNA–Au decorated with complementary DNA-capped Alexa 647. Scale bar: 5 μm.

The long-DNA–Au conjugates were also investigated as scaffolds that could be decorated with dyes (Alexa 647) modified with antisense DNA. After incubation, the complex was isolated, purified by centrifugation, and analyzed by confocal microscopy. Bright fluorescent dots, with diameters of hundreds of nanometers to microns, were clearly observed (Figure 4D). In contrast, the control experiment in which Alexa 647 modified with non-complementary DNA was used did not show any fluorescence (data not shown). Given that the RCA process itself is a signal-amplification tool and is widely used for microarray-based biodetections,[12–16] the adaptation of RCA on nanoparticles can potentially open a new avenue for ultrasensitive nanoparticle-based biosensing. This application may be particularly useful when the unique properties of nanoscaled materials are incorporated.

In conclusion, we have demonstrated that long single-stranded DNA can be grafted directly from gold nanoparticles and the resultant DNA–AuNP assemblies can be further used as a unique scaffold that may find a number of applications in nanotechnology and biodiagnostics. The envisioned applications include the design of well-ordered 3D nanoparticle arrays, nanocomputing devices, nanophotonics and electronics, bioimaging tools, and ultrasensitive biosensors. While there are still some drawbacks (e.g. high polydispersity of DNA polymers synthesized by RCA, thiol exchange by DTT, etc.) associated with this strategy that need to be overcome, the scaffolding on the basis of this long DNA–Au scaffold has several significant advantages: 1) The assembly events are performed in a three-dimensional and periodic manner, given that these DNA polymer brushes containing repetitive sequences are grafted from a gold nanoparticle core. 2) This assembly is fully controllable, that is, the distance between assembled nanospecies can be readily varied by adjusting the length of the circular DNA template. 3) The assembly is entirely reversible owing to the nature of

 © 2006 Wiley-VCH Verlag GmbH & Co. KGaA, Weinheim

DNA base pairing. 4) Multiple assemblies, wherein two or more nanospecies are constructed simultaneously, can be readily achieved simply by assembling different species functionalized with different antisense DNA or by performing different RCA process on each single nanoparticle.

Experimental Section

15-nm gold nanoparticles were prepared following the reported approach with minor modifications.[5] Trisodium citrate (Sigma; 25 mL, 38.8 mM) was added to a boiling solution of $HAuCl_4$ (Sigma; 250 mL, 1 mM). Within several minutes, the color of the solution changed from pale yellow to deep red. The mixture was allowed to heat under reflux for another 30 min to ensure complete reduction, before it was slowly cooled to room temperature, and the nanoparticles were filtered through a 200-nm filter.

Primer–Au conjugates were prepared according to a published method.[5] Briefly, 5′-thiol-modified DNA primers (5′-thiol-TTTTTTTTTTTTTTTTTTTTGGCGAAGACAGGTGCTTAGTC, Keck Biotechnology Resource Laboratory, Yale University; 5.6 μL, 70 μM) were mixed with H_2O (25 μL) and then added to the gold nanoparticles (50 μL, 13.4 nM). The solution was aged overnight and then added to phosphate buffer (10 mM, pH 7, NaCl, 0.1 M) and aged for another 12 h. NaCl (0.3 M) and phosphate (10 mM, pH 7) were then added to the mixture and the solution was allowed to stand for another 12 h. The resultant solution was centrifuged, and the particles were washed once with sodium phosphate buffer (200 μL, 0.3 M, pH 7). The primer–Au conjugates were then redispersed in water (50 μL).

The circular DNA template was prepared according to a procedure adapted from a published protocol.[21] First, linear DNA (5′-TGTCTTCGCCTTCTTGTTTCCTTTCCTTGAAACTTCTTCC-TTTCTTTCTTTCGACTAAGCACC, Central Facility, McMaster University; 16.3 μL, 30.6 μM) was phosphorylated by T4 polynucleotide kinase (MBI Fermentas) using the manufacturer-supplied protocol. The enzyme was denatured by heating at 90 °C for 5 min. This solution was used directly for DNA ligation in the presence of ligation templates (5′-GGCGAAGACAGGTGCTTAGTC, Central Facility, McMaster University; 7.6 μL, 78.5 μM) and T4 DNA ligase (MBI Fermentas) at room temperature overnight. The circular DNA was purified by 10% PAGE and redispersed in water.

RCA on the gold nanoparticles was performed as follows: First, the circular DNA template was annealed with primer–Au. In a typical experiment, a solution of the primer–Au (4 μL, ca. 13.4 nM) and an excess of the circular template were mixed in RCA buffer solution (50 mM Tris-HCl, 10 mM $MgCl_2$, 10 mM $(NH_4)_2SO_4$, pH 7.5, 20 μL). This mixture was heated at 60 °C for 5 min and then annealed at room temperature for 30 min. Two centrifugation/redispersion cycles were applied to get rid of the non-specifically bound circular template by RCA buffer solution (50 μL), and the final product was redispersed in RCA buffer solution (20 μL). ϕ29 DNA polymerase (NEB, 4 μL, 40 units) and dNTPs (dATP, dTTP, dCTP, dGTP; MBI Fermentas, 4 μL, 1 mM) were added to the above solution, and the final volume was brought to 80 μL with RCA buffer solution. For the synthesis of radioactive RCA product, [α-^{32}P]-dGTP (Amersham Biosciences; 2 μL, specific activity: 20 μCi) was incorporated. The reaction was performed at 30 °C for 30 min. The product (long-DNA–Au) was washed twice with RCA buffer (50 μL) and H_2O (50 μL) using centrifugation and redispersed in water (20 μL). For AFM experiments, the solution of long-DNA–Au was diluted 10-fold and 30 μL of the resultant solution was spin-coated (3500 rpm) onto a freshly cleaved mica surface and investigated by AFM (Digital Instruments Nanoscope II). For gel electrophoresis experiments, the resultant DNA was displaced from the surface of the gold nanoparticles by treating with a solution of mercaptoethanol (Sigma, 250 mM) at 37 °C overnight. Endonuclease digestion was performed by Taq I (MBI Fermentas) using conditions recommended by the manufacturer, and the resultant DNA fragments were analyzed by 10% denaturing PAGE.

To form the assembly with 5-nm gold nanoparticles, 5′-biotinylated oligonucleotide (5′-biotin-CCTTGAAACTTCTTCCTTT-CTTTCT, Keck Biotechnology Resource Laboratory, Yale University; 2.5 μL, 91.8 μM) was incubated with streptavidin-capped 5-nm gold nanoparticles (Canemco Inc & Marivac Inc; 50 μL) in a buffer solution (20 mM Tris-HCl, 20 mM EDTA, 300 mM NaCl, pH 7.5, 300 μL) at room temperature for 30 min. The resultant antisense-DNA–AuNP complex was washed twice with RCA buffer (200 μL) using centrifugation and redispersed in RCA buffer solution (20 μL). Long-DNA–Au in RCA buffer solution (20 μL) was then added. The mixture was frozen in a bath of dry ice and propan-2-ol and then thawed at room temperature overnight, an approach known to facilitate the hybridization of DNA-attached gold nanoparticles.[5] The nanoassembled complex was isolated by centrifugation at 5000 rpm for 10 min and redispersed in RCA buffer. The TEM sample was prepared by dropping this solution (5 μL) onto a copper-coated grid. After 5 min, the solution was wicked from the edge of the grid with a piece of filter paper. TEM images were measured with a JEOL 1200EX transmission electron microscope.

To prepare the fluorophore-functionalized nanoparticles, oligonucleotide modified at the 5′ position with Alexa 647 (5′-Alexa 647-TGAAACTTCTTCCTTTCTTTCTTTC, Invitrogen; 0.5 μL, 90 μM) and long-DNA–Au (10 μL) were added to RCA buffer (10 μL). The mixture was heated at 65 °C for 5 min and then annealed at room temperature for 15 min. The resultant complex was washed twice with RCA buffer (50 μL), isolated by centrifugation, and analyzed by confocal microscopy (SLM 8100 spectrofluorimeter, Spectronic Instruments, Rochester, NY).

Received: January 6, 2006
Published online: March 9, 2006

Keywords: DNA · DNA amplification · gold · nanotechnology · self-assembly

[1] a) B. Samorì, G. Zuccheri, *Angew. Chem.* **2005**, *117*, 1190 – 1206; *Angew. Chem. Int. Ed.* **2005**, *44*, 1166 – 1181; b) E. Katz, I. Willner, *Angew. Chem.* **2004**, *116*, 6166 – 6235; *Angew. Chem. Int. Ed.* **2004**, *43*, 6042 – 6108.
[2] N. L. Rosi, C. A. Mirkin, *Chem. Rev.* **2005**, *105*, 1547 – 1562.
[3] S. Brakmann, *Angew. Chem.* **2004**, *116*, 5851 – 5855; *Angew. Chem. Int. Ed.* **2004**, *43*, 5730 – 5734.
[4] C. A. Mirkin, R. L. Letsinger, R. C. Mucic, J. J. Storhoff, *Nature* **1996**, *382*, 607 – 609.
[5] R. Elghanian, J. J. Storhoff, R. C. Mucic, R. L. Letsinger, C. A. Mirkin, *Science* **1997**, *277*, 1078 – 1080.
[6] D. Zanchet, C. M. Micheel, W. J. Parak, D. Gerion, A. P. Alivisatos, *Nano Lett.* **2001**, *1*, 32 – 35.
[7] C. Sönnichsen, B. M. Reinhard, J. Liphardt, A. P. Alivisatos, *Nat. Biotechnol.* **2005**, *23*, 741 – 745.
[8] J. Liu, Y. Lu, *J. Am. Chem. Soc.* **2004**, *126*, 12298 – 12305.
[9] T. Niazov, V. Pavlov, Y. Xiao, R. Gill, I. Willner, *Nano Lett.* **2004**, *4*, 1683 – 1687.
[10] A. Fire, S. Xu, *Proc. Natl. Acad. Sci. USA* **1995**, *92*, 4641 – 4645.
[11] D. Liu, S. L. Daubendiek, M. A. Zillman, K. Ryan, E. T. Kool, *J. Am. Chem. Soc.* **1996**, *118*, 1587 – 1594.
[12] P. M. Lizardi, X. Huang, Z. Zhu, P. Bray-Ward, D. C. Thomas, D. C. Ward, *Nat. Genet.* **1998**, *19*, 225 – 232.
[13] B. Schweitzer, S. Wiltshire, J. Lambert, S. O'Malley, K. Kukanskis, Z. Zhu, S. F. Kingsmore, P. M. Lizardi, D. C. Ward, *Proc. Natl. Acad. Sci. USA* **2000**, *97*, 10113 – 10119.

 © 2006 Wiley-VCH Verlag GmbH & Co. KGaA, Weinheim

[14] B. Schweitzer, S. Roberts, B. Grimwade, W. Shao, M. Wang, Q. Fu, Q. Shu, I. Laroche, Z. Zhou, V. T. Tchernev, J. Christiansen, M. Velleca, S. F. Kingsmore, *Nat. Biotechnol.* **2002**, 20, 359 – 365.
[15] Y. Chen, M. R. Shortreed, D. Peelen, M. Lu, L. Smith, *J. Am. Chem. Soc.* **2004**, *126*, 3016 – 3017.
[16] E. J. Cho, L. Yang, M. Levy, A. D. Ellington, *J. Am. Chem. Soc.* **2005**, *127*, 2022 – 2023.
[17] S. Beyer, P. Nickels, F. C. Simmel, *Nano lett.* **2005**, *5*, 719 – 722.
[18] Z. Deng, Y. Tian, S. Lee, A. E. Ribbe, C. Mao, *Angew. Chem.* **2005**, *117*, 3648 – 3654; *Angew. Chem. Int. Ed.* **2005**, *44*, 3582 – 3585.
[19] L. M. Demers, C. A. Mirkin, R. C. Mucic, R. A. Reynolds, R. L. Letsinger, R. Elghanian, G. Viswanadham, *Anal. Chem.* **2000**, *72*, 5535 – 5541.
[20] J. Pyun, T. Kowalewski, K. Matyjaszewski, *Macromol. Rapid Commun.* **2003**, *24*, 1043 – 1059.
[21] L. P. Billen, Y. Li, *Bioorg. Chem.* **2004**, *33*, 582 – 598.

 © 2006 Wiley-VCH Verlag GmbH & Co. KGaA, Weinheim

Nanostructures

DOI: 10.1002/anie.200504098

Size-Selectivity in the Oxidation Behaviors of Au Nanoparticles**

*Dong Chan Lim, Ignacio Lopez-Salido, Rainer Dietsche, Moritz Bubek, and Young Dok Kim**

The interaction of oxygen with metal and the subsequent oxidation has been one of the most widely studied subjects in chemistry and physics as a result of its implication for corrosion processes and heterogeneous catalysis.[1–7] For example, oxide shells formed on metallic entities can show high catalytic activities towards the oxidation of CO.[8] The metal–oxygen interaction can change as a function of the particle size at the nanoscale, which can cause an interesting size selectivity in a heterogeneously catalyzed reaction.[2–7] Among the various metals, Au has been attracting particular attention because of the strong size selectivity observed in various catalytic reactions.[2,4–7] The interaction of oxygen with Au nanoparticles has been the subject of many previous studies.[7]

In the present study, Au nanoparticles of different sizes were supported on silica surfaces and oxidized in atomic oxygen environments. Au nanoparticles of different sizes were prepared by depositing various amounts of Au at room temperature on the surfaces of Si wafers, which were covered by thin silica layers. This kind of particle synthesis generally gives a broad distribution of particle sizes rather than a perfectly monodisoperse surface, which can be achieved by other techniques, such as the mass-selected cluster deposition or micellar technique.[3,9] The intensity of the Au 4f peak with respect to the Si peak in the XPS spectra decreases with decreasing Au coverage (Figure 1 a–g).[10] Positive shifts in the core level can also be observed with decreasing Au coverage: the Au 4f peaks of the sample with the lowest Au coverage show a positive shift in the core level of 0.8 eV with respect to the bulk values (Figure 1 g). The gradual shifts of the Au 4f states to the higher binding energy region with decreasing Au coverage confirms that the particle size decreases as the Au coverage decreases (Figure 1 a–g).[11–16] The particle sizes of three samples estimated by scanning tunneling microscopy (STM) are also suggestive of reduced particle size with decreasing Au coverage (Figure 2).

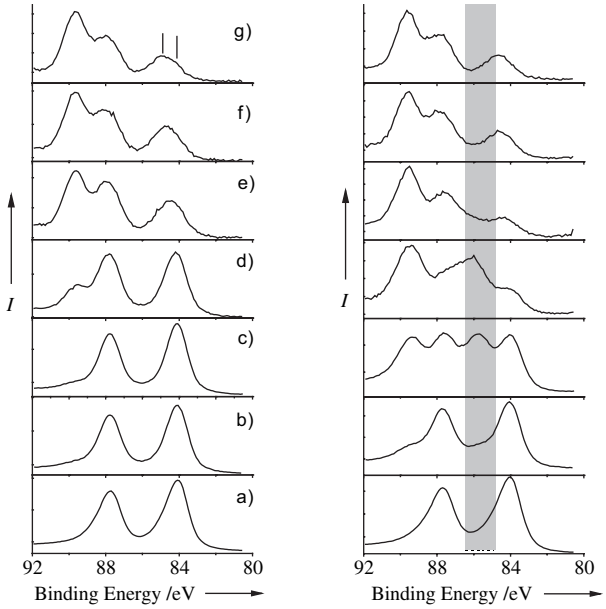

Figure 1. Left panel: XPS spectra of the Au 4f states for Au nanoparticles grown on SiO_2/Si. a–g) The Au coverage is reduced, that is, the average particle size decreases, from (a) to (g). For (a), (b), and (e), the average particle heights (widths) estimated on the basis of the STM data in Figure 2 are approximately 4 (<10), 1 (<3), and 0.7 (<1.5) nm, respectively. Right panel: XPS spectra of the Au 4f states of the samples shown in the left panel after exposing them to the atomic oxygen atmosphere. The shoulders in the higher binding energy region correspond to the formation of Au_2O_3 (marked by the gray bar).

Additional peaks in the higher binding energy region with respect to the metallic Au 4f state appears in the XPS spectra upon treatment of most of the samples examined (Figure 1) with atomic oxygen. This result can be attributed to the

[*] D. C. Lim, I. Lopez-Salido, R. Dietsche, M. Bubek, Prof. Dr. Y. D. Kim
Fachbereich Physik
Universität Konstanz
Universitätsstrasse 10, 78457 Konstanz (Germany)
Fax: (+49) 7531-883-888
E-mail: young.kim@uni-konstanz.de
Prof. Dr. Y. D. Kim
Division of Nanosciences and Department of Chemistry
Ewha Womans Univeristy
11-1 Daehyun-Dong, Seodaemun-Gu, Seoul, 120-750 (Korea)

[**] The German Research foundation is acknowledged for financial support within the SFB 513 program, project number A15. Gerd Ganteför is acknowledged for fruitful discussions.

 © 2006 Wiley-VCH Verlag GmbH & Co. KGaA, Weinheim

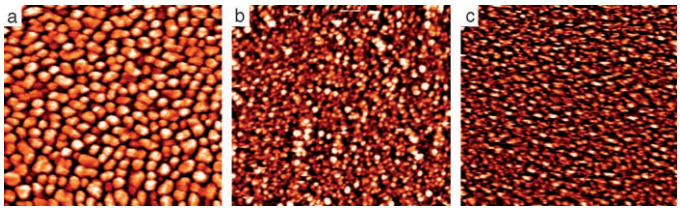

Figure 2. STM images: a) 193 nm × 193 nm, 2 V, 0.1 nA, b) 124 nm × 124 nm, 4.7 V, 0.1 nA, and c) 123 nm × 123 nm, 4.7 V, 0.1 nA corresponding to the XPS spectra (a), (b), and (e) in Figure 1.

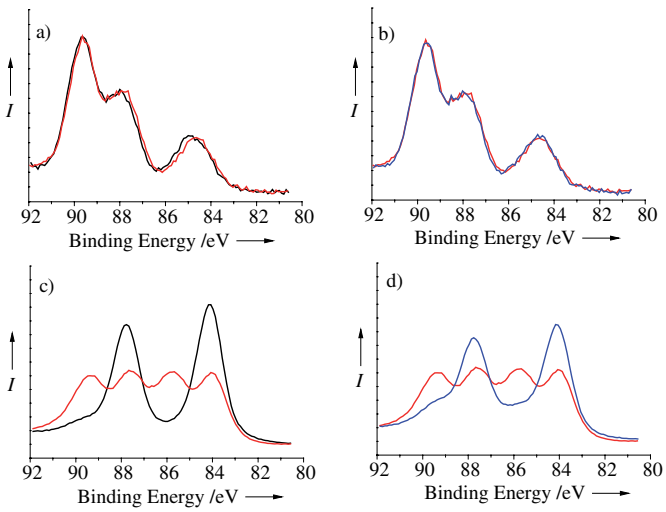

Figure 3. a) The sample of Figure 1 g was exposed to the atomic oxygen atmosphere, and the Au 4f spectra were recorded before (black) and after (red) exposure to atomic oxygen. A small shift of the Au 4f state can be observed upon treatment with atomic oxygen. b) The sample of Figure 1 g exposed to atomic oxygen (red) was further exposed to 3000 L CO (blue). No change can be seen after exposure to CO. c) The sample of Figure 1 c was exposed to the atomic oxygen atmosphere, and the Au 4f spectra were recorded before (black) and after exposure to atomic oxygen (red). d) The sample of Figure 1 c exposed to atomic oxygen (red) was further exposed to 3000 L CO (blue).

formation of Au_2O_3.[3] The relative intensity of the Au_2O_3 peak compared to the respective metallic Au peak increases when the mean height of the particles decreases from 4 nm to about 0.7 nm. This observation can be explained by an increased surface/volume ratio with decreasing particle size, that is, the surface layers of the nanoparticles are oxidized and form core(metallic)/shell(oxidic)-type particles. In contrast, when the mean height of the particles is lower than about 0.7 nm, the Au_2O_3 peak becomes less pronounced with decreasing particle size (Figure 1). The sample with the smallest mean particle size does not show Au_2O_3 peaks in the XPS spectrum after reaction under atomic oxygen conditions, whereas the Au 4f peaks are shifted to a lower binding energy by approximately 0.3 eV (Figures 1, 3). It should be noted that the accuracy of the determination of the binding energies is better than 0.1 eV. All the Au nanoparticles studied here show some changes upon exposure to atomic oxygen, which implies that none of the Au nanoparticles studied here are completely inert towards oxygen uptake, which has been previously suggested to be the case for the Au_{55} cluster.[3] We cannot synthesize a monodisperse surface consisting of only the magic Au_{55} clusters by using our particle preparation method. With the exception of Au_{55}, all other Au particles were shown to be able to form Au_2O_3, which disagrees with our data.[3] The difference in the results can most likely be rationalized by taking into account the different oxidation conditions used by the two different research groups: oxygen plasma was used by Boyen et al.,[3] whereas we have used atomic oxygen created by a hot Pt filament, which may provide a milder oxidizing environment than the oxygen plasma.

Reduction of Au_2O_3 could be observed by exposure of the Au nanoparticles treated with atomic oxygen (to form the Au_2O_3) to 3000 L ($1\,L = 1 \times 10^{-6}$ torr for 1 s) of CO at room temperature (Figure 3). The Au^{III} species are not completely removed by the CO, most likely because of the fact that not only are the topmost Au layers oxidized, but deeper layers are also oxidized, which cannot be reduced efficiently by CO. No change could be observed in the Au 4f level when the small Au nanoparticles that showed only a negative shift in the Au 4f state without appearance of the Au_2O_3 peak upon treatment with atomic oxygen were exposed to CO, thus demonstrating that different oxygen species with various characteristics in X-ray photoelectron spectroscopy (XPS) show dissimilar chemical properties.

Au nanoparticles were prepared on a heavily sputtered HOPG surface to shed light on the oxidation behaviors of the very small Au nanoparticles on highly ordered pyrolytic graphite (HOPG) surfaces (Figure 4).[17] No reasonable STM images could be obtained for Au nanoparticles smaller than 3 nm in diameter on HOPG because of the very weak metal–support interactions, which can cause tip-induced movements of the nanoparticles on the surface. However, the XPS data clearly show that the particles in the sample (Figure 4) should be much smaller than 3 nm in diameter: when the particles are larger than 3 nm, shifts of the Au 4f level with respect to

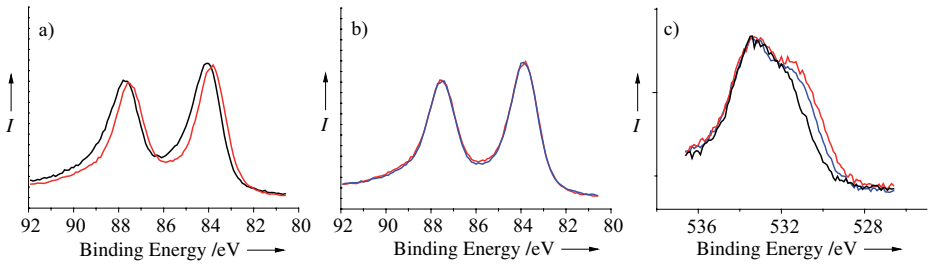

Figure 4. a) Au 4f spectra of Au nanoparticles on HOPG before (black) and after (red) exposure to atomic oxygen. b) The Au particles treated with atomic oxygen (red) were subsequently exposed to CO (blue). c) The O 1s spectra were collected for the Au nanoparticles on HOPG exposed to atomic oxygen (red), and subsequently to CO (blue). For comparison, the O 1s spectrum of a bare sputtered HOPG surface exposed to the similar amount of atomic oxygen is shown (black).

 © 2006 Wiley-VCH Verlag GmbH & Co. KGaA, Weinheim

the bulk value are at most 0.1 eV, whereas a shift in the Au 4f core level of 0.3 eV could be observed for the sample in Figure 4.[17] When this sample was treated with atomic oxygen, no Au_2O_3 shoulder could be observed in the higher binding energy region, whereas the Au 4f peaks were only shifted to lower binding energies, similar to the behaviors of the small Au nanoparticles on SiO_2/Si (Figure 1g).

When the Au nanoparticles were on a SiO_2/Si surface, the O 1s signal from the substrate (SiO_2) is much larger than that of oxygen atoms bound to Au nanoparticles, thus preventing a clear discrimination of the O/Au signals by XPS. In contrast, this problem does not arise with HOPG substrates because of their very low oxygen uptake (Figure 4c). Exposure of the Au nanoparticles on HOPG (Figure 4) to atomic oxygen resulted in an additional state at about 531 eV in the O 1s spectrum, which can be attributed to the oxygen species bound to Au (Figure 4c). The O 1s signal from Au nanoparticles on HOPG decreases in intensity by about 30% upon exposure to 3000 L of CO. Since Au oxide species formed on Au particles larger than 20 nm can be nearly completely removed by 1000 L CO at room temperature, the atomic oxygen species on smaller Au nanoparticles are much less reactive for the CO oxidation at room temperature.[17] The average CO/CO_2 conversion probability of the oxygen species bound to very small Au particles is estimated on the basis of data in Figure 4 to be at most 0.01%. This result also confirms that the negative shifts in the Au 4f level of smaller Au particles upon treatment with atomic oxygen are not simply a consequence of the structural change of the Au nanoparticles (for example, sintering) without formation of an Au–O bond, but from the adsorption/absorption of oxygen on the Au nanoparticles.

It is worth mentioning that the formation of oxygen species that are inactive for the oxidation of CO has been suggested for Au/TiO_2 systems, which implies that the unique behavior of the small Au nanoparticles seems to be independent of the substrate.[18]

It has been previously suggested that the activation of oxygen molecules on Au nanoparticles is the key to the increased catalytic activities of Au: once oxygen molecules are dissociated on Au nanoparticles, they can readily react with CO to form CO_2 well below room temperature.[19] In the present study, in contrast, we found oxygen species formed by deposition of atomic oxygen on Au nanoparticles that hardly react with CO at room temperature. As already mentioned, the mean CO/CO_2 conversion probability of this oxygen species is at most 0.01%, which is at least one order of magnitude smaller than those of Au oxide or oxygen atoms chemisorbed on top of bulklike Au surfaces.[17,20] This less reactive oxygen species for the oxidation of CO is tentatively assigned to either the subsurface oxygen or surface oxygen species, which are not active for CO oxidation (either they occupy the same adsorption sites as CO, thus preventing CO chemisorption on Au nanoparticles, or the Au–O interaction is too strong).[18] Further theoretical studies may shed light on the nature of the inactive oxygen species on small Au nanoparticles. It is likely that the oxygen species found in the present study also exist on the Au nanoparticles used in catalysis, and therefore, consideration of these oxygen species can provide a complete understanding of Au nanocatalysis.

Experimental Section

Two ultrahigh vacuum (UHV) chambers were used for the STM and XPS studies. A sample could be transferred between the two chambers by using a portable UHV system. The polycrystalline Si wafer samples with native oxide layers were inserted into the UHV system and degassed at about 800 K, which also reduced the amount of carbon impurities. The cleanliness of the Si wafers was confirmed by using XPS (X-ray source: $Al_{K\alpha}$, photon energy = 1486.6 eV). Au nanoparticles were grown by evaporating an Au rod (purity 99.999% from Alfa Aesar) through heating either resistively or using an electron bombardment heater. The preparation of the Au/HOPG systems and details of the oxidation/reduction experiments can be found elsewhere.[17]

Received: November 17, 2005
Published online: March 7, 2006

Keywords: gold · nanostructures · oxidation · oxygen · X-ray photoelectron spectroscopy

[1] H. Over, A. P. Seitsonen, *Science* **2002**, *297*, 2003–2005.
[2] M. Valden, X. Lai, D. W. Goodman, *Science* **1998**, *281*, 1647–1650.
[3] H.-G. Boyen, G. Kästle, F. Weigl, B. Koslowski, C. Dietrich, P. Ziemann, J. P. Spatz, S. Riethmüller, C. Hartmann, M. Möller, G. Schmid, M. G. Garnier, P. Oelhafen, *Science* **2002**, *297*, 1533–1536.
[4] M. S. Chen, D. W. Goodman, *Science* **2004**, *306*, 252–255.
[5] B. Yoon, H. Häkkinen, U. Landman, *J. Phys. Chem. A* **2003**, *107*, 4066–4071.
[6] M. Haruta, S. Tsubota, T. Kobayashi, H. Kageyama, M. J. Genet, B. Delmon, *J. Catal.* **1993**, *144*, 175–192.
[7] R. Meyer, C. Lemire, Sh. K. Shaikhutdinov, H.-J. Freund, *Gold Bull.* **2004**, *37*, 72–124.
[8] J. Aßmann, D. Crihan, M. Knapp, E. Lundgren, E. Löffler, M. Muhler, V. Narkhede, H. Over, M. Schmid, A. P. Seitsonen, P. Varga, *Angew. Chem.* **2005**, *117*, 939–942; *Angew. Chem. Int. Ed.* **2005**, *44*, 917–920.
[9] B. Yoon, H. Häkkinen, U. Landman, A. S. Wörz, J. Antonietti, S. Abbet, K. Judai, U. Heiz, *Science* **2005**, *307*, 403–407.
[10] J. F. Moulder, W. F. Stickle, P. E. Sobol, K. D. Bomben, *Handbook of X-ray Photoelectron Spectroscopy, Physical Electronics*, Inc., Minnesota, USA **1995**.
[11] G. K. Wertheim, S. B. DiCenzo, S. E. Youngquist, *Phys. Rev. Lett.* **1983**, *51*, 2310–2313.
[12] W. Eberhardt, P. Fayet, D. M. Cox, Z. Fu, A. Kaldor, R. Sherwood, D. Sondericker, *Phys. Rev. Lett.* **1990**, *64*, 780–783.
[13] P. Zhang, T. K. Sham, *Phys. Rev. Lett.* **2003**, *90*, 245502.
[14] B. Richter, H. Kuhlenbeck, H.-J. Freund, P. S. Bagus, *Phys. Rev. Lett.* **2004**, *93*, 026805.
[15] V. Vijayakrishnan, A. Chainani, D. D. Sarma, C. N. R. Rao, *J. Phys. Chem.* **1992**, *96*, 8679–8682.
[16] K. Luo, X. Lai, C.-W. Yi, K. A. Davis, K. K. Gath, D. W. Goodman, *J. Phys. Chem. B* **2005**, *109*, 4064–4068.
[17] D. C. Lim, I. Lopez-Salido, Y. D. Kim, *Surf. Sci.* **2006**, *600*, 517–523.
[18] T. S. Kim, J. D. Stiehl, C. T. Reeves, R. J. Meyer, C. B. Mullins, *J. Am. Chem. Soc.* **2003**, *125*, 2018–2019.
[19] N. Lopez, J. K. NØrskov, *J. Am. Chem. Soc.* **2002**, *124*, 11262–11263.
[20] J. M. Gottfried, K. J. Schmidt, S. L. M. Schroeder, K. Christmann, *Surf. Sci.* **2003**, *525*, 197–206.

 © 2006 Wiley-VCH Verlag GmbH & Co. KGaA, Weinheim

Asymmetric Catalysis

DOI: 10.1002/anie.200504561

Copper–Phthalocyanine Conjugates of Serum Albumins as Enantioselective Catalysts in Diels–Alder Reactions**

Manfred T. Reetz and Ning Jiao*

Anchoring ligand-bound transition metals to proteins covalently or noncovalently provides conjugates that are of potential interest as enantioselective hybrid catalysts in organic synthesis.[1] Although a number of studies regarding this concept have appeared, examples of truly high enantioselectivity (> 90 % *ee*) are rare. Indeed, pronounced degrees of asymmetric induction cannot be expected just because the protein environment is chiral. Herein we report Cu^{II}-catalyzed Diels–Alder reactions of azachalcones **1a**–**e** with cyclopentadiene (**2**) in an aqueous medium in the presence of appropriate proteins, leading to products **3** [Eq. (1)] with

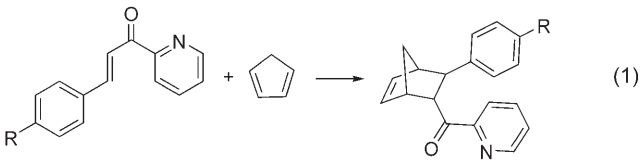

(1)

1a R = H
b R = CH_3
c R = OCH_3
d R = NO_2
e R = Cl

2

3

surprisingly high enantiopurities (85–98 % *ee*). The first transition-metal-catalyzed asymmetric Diels–Alder reactions in water were reported by Engberts and co-workers, who performed the cycloaddition of **1a** with **2** in the presence of water-soluble Cu^{II} complexes of chiral α-amino acids (up to 74 % *ee* of the major *endo* product **3a**).[2] More recently Roelfs and Feringa carried out the same reaction also in water with Cu^{II} conjugates of DNA, resulting in a maximum of 53 % *ee* for *endo*-**3a** (*endo*/*exo* 91:9).[3] Moreover, *endo*/*exo* selectivity of certain Diels–Alder reactions is known to be influenced by the presence of Baker's yeast,[4] and in another study Colonna et al. showed that enantioselectivity up to 38 % *ee* can be achieved upon adding bovine serum albumin (BSA) to the aqueous medium.[5] Highly stereoselective Diels–Alder reactions in water were reported to be catalyzed by Diels–Alderases,[6] catalytic antibodies,[7] and ribozymes.[8]

In our study we chose the commercially available water-soluble amphiphilic phthalocyanine–copper complex **4** as the achiral catalyst and various serum albumins as the protein hosts.

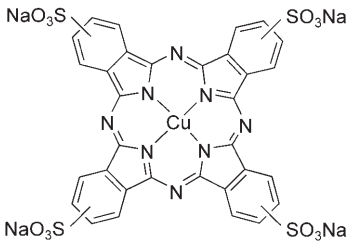

4

Serum albumins are proteins present at high concentrations in blood plasma, functioning as transport carriers for a wide variety of compounds, including fatty acids, bile acids, bilirubin, and hemin.[9] They are generally robust, readily accessible, and easy to handle. The decision to choose these proteins in our study was also influenced by several previous reports.[5,10,11] Kokubo et al. demonstrated that a 1:1 complex of an osmate ester and bovine serum albumin (BSA) functions as a catalyst in the *cis* dihydroxylation of alkenes (up to 68 % *ee*).[10] In a novel and systematic study Mahammed and Gross anchored certain water-soluble sulfonylated Fe^{III}– and Mn^{III}–corroles to serum albumins and used the conjugates as catalysts in the H_2O_2-based asymmetric sulfoxidation of prochiral thioethers (up to 74 % *ee*).[11] Previous to the latter study it had been reported that the sodium salts of di-, tri-, and tetrasulfonic acid derivatives of porphyrins, phthalocyanines, and corroles bind strongly to serum albumins in a noncovalent manner, although the exact position of anchoring in the proteins was not elucidated with absolute certainty in all cases.[12] An example of unambiquous assignment was recently reported by Curry and co-workers, who showed that iron–protoporphyrin dimethyl ester binds in the subdomain IB of human serum albumin (HSA) and that weak axial coordination by Tyr161 contributes to the binding.[13]

Exploratory experiments were carried out with BSA under various conditions (Table 1). A formate buffer (pH ≈ 4) was found to be optimal. Remarkably, **4**–BSA turned out to be a highly selective catalyst for the reaction of **1a** with **2**. The *endo*/*exo* ratio was 96:4, and the enantioselectivity of the major *endo* diastereomer was 93 % *ee* under optimized conditions with only 2 mol % of the catalyst (Table 1, entry 6). The *endo* selectivity is not influenced significantly by the presence of BSA, as **4** alone leads to a 95:5 ratio. The observed enantioselectivity is, of course, a result of the protein environment. Upon increasing the scale of the reaction by a factor of 20 (0.4 mM of **1a**), 89 % *ee* was attained (*endo*/*exo* 93:7; 85 % yield of isolated product **3a** after 3.5 days at 5 °C). To rule out possible catalysis by BSA alone, the Diels–Alder reaction was repeated in the absence of the Cu^{II} complex **4**. Under otherwise identical conditions only

[*] Prof. Dr. M. T. Reetz, Dr. N. Jiao
Max-Planck-Institut für Kohlenforschung
Kaiser-Wilhelm-Platz 1, 45470 Mülheim an der Ruhr (Germany)
Fax: (+49) 208-306-2985
E-mail: reetz@mpi-muelheim.mpg.de

[**] Generous support from the Fonds der Chemischen Industrie is gratefully acknowledged. N.J. thanks the Alexander von Humboldt-Stiftung for a research fellowship.

Supporting information for this article is available on the WWW under http://www.angewandte.org or from the author.

InterScience
© 2006 Wiley-VCH Verlag GmbH & Co. KGaA, Weinheim

Table 1: Optimization of the Diels–Alder reaction of **1a** with **2** in the presence of Cu^{II} salts and BSA.[a]

Entry	Cu^{II} salt	Buffer (pH)	Conv. [%]	*endo*/*exo*	*ee* [%] (*endo*-**3a**)
1	**4** (crude)[b]	MOPS (6.5)[c]	30	92:8	64
2	**4** (crude)	acetate (5.0)	74	86:14	81
3	**4** (crude)	formate (4.5)	74	93:7	82
4	**4** (crude)	formate (4.0)	80	96:4	93
5	**4** (crude)[d]	formate (4.0)	80	95:5	89
6	**4**[e]	formate (4.0)	78	96:4	93

[a] Purchased from Sigma [A-6793/Fraction 5]; **1**/**2**/BSA/Cu^{II} = 50:300:1.2:1 (20-μmol scale), [BSA] = 0.3 mM in buffer (30 mM), 3 °C, 3 days. [b] Purchased from Aldrich [27360-85-6] as a mixture of regioisomeric tetrasulfonic acid sodium salts. [c] MOPS = (3-[*N*-morpholino]propane sulfonic acid). [d] Reaction performed at 5 °C. [e] Complex **4** was purchased from Aldrich [123439-80-5] as the 3,4′,4″,4‴-tetrasulfonic acid sodium salt.

4% conversion was observed, the *endo*/*exo* ratio was 72:28, and the major product was essentially racemic. Moreover, BSA–$Cu(NO_3)_2$, BSA–$CuCl_2$, BSA–$Cu(OTf)_2$, and BSA–$Cu(BF_4)_2$ led to essentially racemic product **3a** (< 4% *ee*), which is the result of indiscriminate binding of these Cu^{II} salts throughout the protein[14] and/or failure to cause asymmetric induction in reactions of the respective Cu^{II}–**1a** complexes.

Upon subjecting the other chalcones **1b–e** to the Diels–Alder reaction with cyclopentadiene (**2**) under the optimized conditions, we discovered that the asymmetric cycloaddition works consistently well (Table 2). Enantioselectivities of 85–98% *ee* were observed, the nitro derivative **1d** leading to the maximum *ee* value (Table 2, entry 4).

Table 2: Diels–Alder reaction of **1b–e** with **2** in the presence of **4**–BSA.[a]

Entry	Chalcone	Conv. [%]	*endo*/*exo*	*ee* [%] (*endo*-**3**)
1	**1b**	84	93:7	87
2	**1c**	71	95:5	88
3	**1d**	90	93:7	90
4	**1d**[b]	91	91:9	98
5	**1e**[b]	89	95:5	85

[a] Same conditions as in the case of **1a** described in Table 1 unless otherwise noted. [b] **4**–BSA: 10 mol%; CH_3CN: 0.06 M.

We then tested other commercially available serum albumins, specifically HSA, porcine serum albumin (PSA), rabbit serum albumin (RSA), sheep serum albumin (SSA), and chicken-egg serum albumin (CSA) in the reaction of **1a** with **2**. Table 3 shows that RSA and CSA lead to poor results (Table 3, entries 3 and 5), whereas HSA, PSA, and SSA perform reasonably well (Table 3, entries 1, 2, and 4).

HSA and especially BSA constitute the best hosts for the present Cu^{II}-catalyzed cycloaddition. At this stage we refrain from speculating about the reason(s) for the observed high enantioselectivities. However, some preliminary observations are worthy of mention. As shown in Figure 1, the rate of the Diels–Alder reaction of **1a** with **2** is considerably higher when the Cu complex **4** is used alone as the catalyst in the absence of BSA. In this case *endo* selectivity is the same, but the

Table 3: Diels-Alder reaction of **1a** with **2** in the presence of **4** and various serum albumins.[a]

Entry	Serum albumin	Conv. [%]	*endo*/*exo*	*ee* [%] (*endo*-**3**)
1	HSA	89	91:9	85
2	PSA	87	89:11	68
3	RSA	69	88:12	7
4	SSA	76	87:13	75
5	CSA	72	78:22	1

[a] Same conditions as in Table 1.

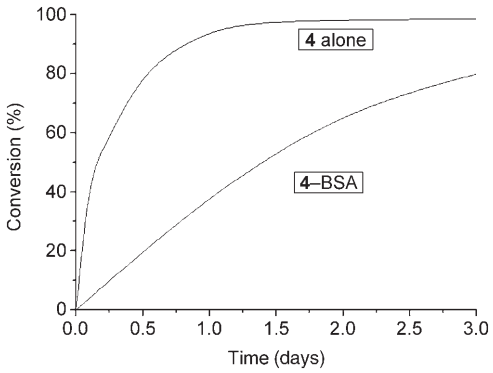

Figure 1. Rates of Diels–Alder reaction of **1a** with **2** catalyzed by **4** alone and by the conjugate **4**–BSA.

product **3a** is, of course, racemic. This rate difference, taken together with the high enantioselectivity induced by the conjugate **4**–BSA, indicates that the amphiphilic Cu^{II} complex **4** is indeed strongly anchored to the protein. Evidence for binding was obtained by the MALDI mass spectrum of **4**–BSA which displays the parent peak without sodium at *m*/*z* 67322.35 (calcd 67323). Moreover, the reaction of BSA or HSA with **4** resulted in a new and strong UV/Vis absorption band at $\lambda = 680$ nm, while the peak at $\lambda = 630$ nm diminished somewhat. In the case of RSA and CSA this effect is very small which may be an indication that binding is less strong, leading to lower *ee* values.

In the case of HSA, which has high homology with BSA, binding probably occurs in the IB subdomain analogous to the known behavior of Fe-containing porphyrin derivatives (hemin).[13] We have used the crystallographic data of hemin–HSA[13a] to obtain a model of **4**–HSA (Figure 2), indicating where catalysis probably occurs.

In their study of the Diels–Alder reaction of **1a** with **2** in water catalyzed by chiral α-amino acid complexes of Cu-$(NO_3)_2$, Engberts and co-workers showed that Cu^{II} undergoes bidentate coordination to the carbonyl oxygen atom and the nitrogen atom of the pyridyl moiety in **1a**.[2] In our case bidentate complexation on one face of the phthalocyanine-bound Cu^{II} center would involve a highly distorted octahedral complex. Currently we cannot eliminate this (unlikely?) possibility, but monodentate complexation at the carbonyl function alone would likewise induce lowering of the LUMO and therefore activation of **1a**. This would also allow axial complexation of Cu^{II} on the opposite face of the phthalocya-

 © 2006 Wiley-VCH Verlag GmbH & Co. KGaA, Weinheim

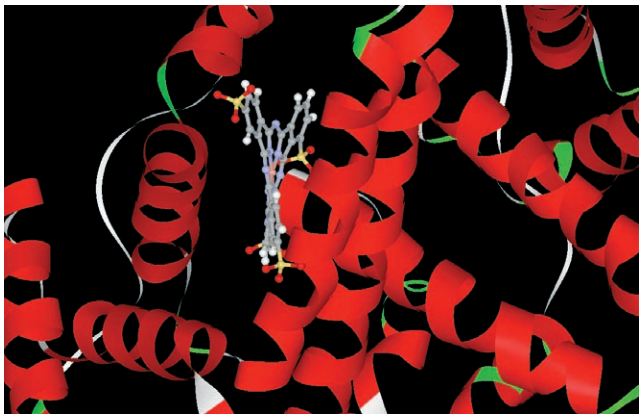

Figure 2. Model of **4**–HSA based on the X-ray crystal structure of hemin–HSA.[13a,15]

nine by an amino acid of BSA. We therefore tested the **4**–BSA-catalyzed reaction of chalcone **5**, which lacks a pyridine moiety [Eq. (2)]. The reaction with **2** proved to be considerably slower and less enantioselective than that of the pyridyl

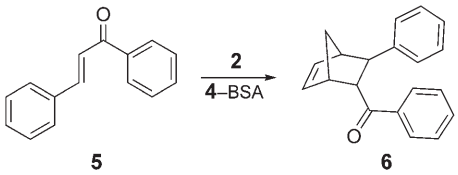

5 **6** (2)

analogue **1a**. Under the usual conditions (**4**–BSA (2 mol%), formate buffer, 5 °C, 3 days) product **6** was formed in only 5% yield with 56% *ee*. Thus, either bidentate activation of **1a** does, in fact, occur in the original reaction, or the nitrogen atom in the pyridyl moiety plays a different role, possibly undergoing protonation and/or hydrogen bonding with the protein. Detailed mechanistic investigations are necessary to clarify these and other questions.[16]

In summary, we have shown that protein conjugates, which are easily prepared by treating serum albumins BSA or HSA with the phthalocyanine–Cu^{II} complex **4**, provide Lewis acidic catalysts for highly enantioselective Diels–Alder reactions of azachalcones **1a**–**e** (85–98% *ee*). This opens the door for other types of enantioselective Lewis acid catalyzed reactions with these cheap hybrid catalysts, but also for the analogous use of porphyrins and/or corroles bearing Cu^{II} or other Lewis acidic transition metals. Our primary interest is to exploit this system in the quest to put our previously proposed concept of directed evolution of hybrid catalysts[11f,17] into practice, that is, to produce thousands of mutant proteins by gene mutagenesis/expression, followed by mass covalent or noncovalent attachment of metal–ligand moieties and finally by screening for the most active and enantioselective variant in a catalytic reaction. If necessary further cycles can be performed to exert evolutionary pressure. Specific noncovalent anchoring of the metal, as in the present case, is particularly convenient and readily amenable to parallelization. An expression system for recombinant HSA (in *Pichia pastoris*) is a prerequisite for this endeavor and is already available.[18]

Received: December 22, 2005
Published online: March 10, 2006

Keywords: asymmetric catalysis · copper · cycloaddition · phthalocyanines · proteins

[1] a) M. E. Wilson, G. M. Whitesides, *J. Am. Chem. Soc.* **1978**, *100*, 306–307; b) C.-C. Lin, C.-W. Lin, A. S. C. Chan, *Tetrahedron: Asymmetry* **1999**, *10*, 1887–1893; c) J. Collot, J. Gradinaru, N. Humbert, M. Skander, A. Zocchi, T. R. Ward, *J. Am. Chem. Soc.* **2003**, *125*, 9030–9031; d) T. R. Ward, *Chem. Eur. J.* **2005**, *11*, 3798–3804; e) G. Klein, N. Humbert, J. Gradinaru, A. Ivanova, F. Gilardoni, U. E. Rusbandi, T. R. Ward, *Angew. Chem.* **2005**, *117*, 7942–7945; *Angew. Chem. Int. Ed.* **2005**, *44*, 7764–7767; f) M. T. Reetz, M. Rentzsch, A. Pletsch, M. Maywald, *Chimia* **2002**, *56*, 721–723; g) D. Qi, C.-M. Tann, D. Haring, M. D. Distefano, *Chem. Rev.* **2001**, *101*, 3081–3111; h) M. Ohashi, T. Koshiyama, T. Ueno, M. Yanase, H. Fujii, Y. Watanabe, *Angew. Chem.* **2003**, *115*, 1035–1038; *Angew. Chem. Int. Ed.* **2003**, *42*, 1005–1008; i) J. R. Carey, S. K. Ma, T. D. Pfister, D. K. Garner, H. K. Kim, J. A. Abramite, Z. Wang, Z. Guo, Y. Lu, *J. Am. Chem. Soc.* **2004**, *126*, 10812–10813; j) B. G. Davis, *Curr. Opin. Biotechnol.* **2003**, *14*, 379–386; k) T. Ueno, T. Koshiyama, M. Ohashi, K. Kondo, M. Kono, A. Suzuki, T. Yamane, Y. Watanabe, *J. Am. Chem. Soc.* **2005**, *127*, 6556–6562; l) C. A. Kruithof, M. A. Casado, G. Guillena, M. R. Egmond, A. van der Kerk-van Hoof, A. J. R. Heck, R. J. M. Klein Gebbink, G. van Koten, *Chem. Eur. J.* **2005**, *11*, 6869–6877; m) See also: D. Hilvert, E. T. Kaiser, *Biotechnol. Genet. Eng. Rev.* **1987**, *4*, 297–318; n) E. T. Kaiser, *Angew. Chem.* **1988**, *100*, 945–955; *Angew. Chem. Int. Ed. Engl.* **1988**, *27*, 913–922.

[2] a) S. Otto, J. B. F. N. Engberts, *J. Am. Chem. Soc.* **1999**, *121*, 6798–6806; b) S. Otto, G. Boccaletti, J. B. F. N. Engberts, *J. Am. Chem. Soc.* **1998**, *120*, 4238–4239.

[3] G. Roelfes, B. L. Feringa, *Angew. Chem.* **2005**, *117*, 3294–3296; *Angew. Chem. Int. Ed.* **2005**, *44*, 3230–3232.

[4] K. R. Rao, T. N. Srinivasan, N. Bhanumathi, *Tetrahedron Lett.* **1990**, *31*, 5959–5960.

[5] a) S. Colonna, A. Manfredi, R. Annunziata, *Tetrahedron Lett.* **1988**, *29*, 3347–3350; for other types of reactions in the presence of BSA, see: b) R. Annunziata, S. Banfi, S. Colonna, *Tetrahedron Lett.* **1985**, *26*, 2471–2474; c) S. Colonna, A. Manfredi, M. Spadoni, *Tetrahedron Lett.* **1987**, *28*, 1577–1580; d) S. Colonna, N. Gaggero, M. Leone, *Tetrahedron* **1991**, *47*, 8385–8398; e) for a review on stereoselective oxidations and reductions catalyzed by nonredox proteins, see: S. V. Dzyuba, A. M. Klibanov, *Tetrahedron: Asymmetry* **2004**, *15*, 2771–2777.

[6] a) A. Ichihara, H. Oikawa, *Curr. Org. Chem.* **1998**, *2*, 365–394; b) G. Pohnert, *ChemBioChem* **2001**, *2*, 873–875; c) G. Pohnert, *ChemBioChem* **2003**, *4*, 713–715; d) E. M. Stocking, R. M. Williams, *Angew. Chem.* **2003**, *115*, 3186–3223; *Angew. Chem. Int. Ed.* **2003**, *42*, 3078–3115; e) J. Kennedy, K. Auclair, S. G. Kendrew, C. Park, J. C. Vederas, C. R. Hutchinson, *Science* **1999**, *284*, 1368–1372; f) K. Auclair, A. Sutherland, J. Kennedy, D. J. Witter, J. P. Van den Heever, C. R. Hutchinson, J. C. Vederas, *J. Am. Chem. Soc.* **2000**, *122*, 11519–11520; g) H. Oikawa, K. Watanabe, K. Yagi, S. Ohashi, T. Mie, A. Ichihara, M. Honma, *Tetrahedron Lett.* **1999**, *40*, 6983–6986; h) H. Oikawa, *Bull. Chem. Soc. Jpn.* **2005**, *78*, 537–554.

[7] a) F. E. Romesberg, B. Spiller, P. G. Schultz, R. C. Stevens, *Science* **1998**, *279*, 1929–1933; b) A. Heine, E. A. Stura, J. T. Yli-

 © 2006 Wiley-VCH Verlag GmbH & Co. KGaA, Weinheim

Kauhaluoma, C. Gao, Q. Deng, B. R. Beno, K. N. Houk, K. D. Janda, I. A. Wilson, *Science* **1998**, *279*, 1934 – 1940.
[8] a) B. Seelig, S. Keiper, F. Stuhlmann, A. Jäschke, *Angew. Chem.* **2000**, *112*, 4764 – 4768; *Angew. Chem. Int. Ed.* **2000**, *39*, 4576 – 4579; b) F. Stuhlmann, A. Jäschke, *J. Am. Chem. Soc.* **2002**, *124*, 3238 – 3244; c) A. Serganov, S. Keiper, L. Malinina, V. Tereshko, E. Skripkin, C. Höbartner, A. Polonskaia, A. Tuân Phan, R. Wombacher, R. Micura, Z. Dauter, A. Jäschke, D. J. Patel, *Nat. Struct. Mol. Biol.* **2005**, *12*, 218 – 224.
[9] a) T. Peters, *All about Albumin: Biochemistry, Genetics and Medical Applications*, Academic Press, San Diego, **1996**; b) for a recent study of O_2- and CO-binding properties of artificial hemoproteins formed by complexing Fe–protoporphyrin IX with HSA mutants, see: T. Komatsu, N. Ohmichi, A. Nakagawa, P. A. Zunszain, S. Curry, E. Tsuchida, *J. Am. Chem. Soc.* **2005**, *127*, 15933 – 15942, and references therein.
[10] T. Kokubo, T. Sugimoto, T. Uchida, S. Tanimoto, M. Okano, *J. Chem. Soc. Chem. Commun.* **1983**, 769 – 770.
[11] A. Mahammed, Z. Gross, *J. Am. Chem. Soc.* **2005**, *127*, 2883 – 2887.
[12] a) A. Mahammed, H. B. Gray, J. J. Weaver, K. Sorasaenee, Z. Gross, *Bioconjugate Chem.* **2004**, *15*, 738 – 746, and references therein; b) T. G. Gantchev, R. Ouellet, J. E. van Lier, *Arch. Biochem. Biophys.* **1999**, *366*, 21 – 30; c) S. Chatterjee, T. S. Srivastava, *J. Porphyrins Phthalocyanines* **2000**, *4*, 147 – 157; d) Y. Ding, B. Lin, C. W. Huie, *Electrophoresis* **2001**, *22*, 2210 – 2216; e) U. Kragh-Hansen, V. T. G. Chuang, M. Otagiri, *Biol. Pharm. Bull.* **2002**, *25*, 695 – 704.
[13] a) P. A. Zunszain, J. Ghuman, T. Komatsu, E. Tsuchida, S. Curry, *BMC Struct. Biol.* **2003**, *3*, 6; See also: b) M. Wardell, Z. Wang, J. X. Ho, J. Robert, F. Ruker, J. Ruble, D. C. Carter, *Biochem. Biophys. Res. Commun.* **2002**, *291*, 813 – 819; c) M. Dockal, D. C. Carter, F. Rüker, *J. Biol. Chem.* **1999**, *274*, 29303 – 29310.
[14] J. C. Cassatt, *J. Biol. Chem.* **1973**, *248*, 6129 – 6134, and references therein.
[15] We thank K. Angermund for generating Figure 2.
[16] The absolute configuration of **3a** was not determined by earlier researchers,[2,3] which means that this task is also necessary before a detailed discussion of the source of enantioselectivity is possible.
[17] a) M. T. Reetz, *Tetrahedron* **2002**, *58*, 6595 – 6602; b) M. T. Reetz, *Proc. Natl. Acad. Sci. USA* **2004**, *101*, 5716 – 5722; c) M. T. Reetz, DE-A 101 29 187.6, **2001**.
[18] a) K. A. Barr, S. A. Hopkins, K. Sreekrishna, *Pharm. Eng.* **1992**, *12*, 48 – 51; b) W. Ohtani, Y. Nawa, K. Takeshima, H. Kamuro, K. Kobayashi, T. Ohmura, *Anal. Biochem.* **1998**, *256*, 56 – 62.

 © 2006 Wiley-VCH Verlag GmbH & Co. KGaA, Weinheim

Natural Product Synthesis

DOI: 10.1002/anie.200504015

A Flexible Strategy for the Synthesis of Tri- and Tetracyclic Lupin Alkaloids: Synthesis of (+)-Cytisine, (±)-Anagyrine, and (±)-Thermopsine**

*Diane Gray and Timothy Gallagher**

The lupin alkaloids, which comprise a varied range of primarily bi-, tri-, and tetracyclic molecules based on a quinolizidine core, represent an increasingly important group of natural products that exhibit a diverse array of properties.[1] (−)-Cytisine (**1**),[2,3] which is a potent and α4β2 subtype-selective partial agonist at nicotinic acetylcholine receptors, was recently exploited successfully by Coe, O'Neill et al. as the natural product lead for the discovery of varenicline.[4] In a quite different realm, the potential (and also limitations) of (−)-sparteine (**2**) as a reagent and ligand for asymmetric synthesis are now well established.[5–7] Many key structural relationships between important members of the lupin alkaloids are known.[1] For example, reduction of (+)-anagyrine (**3**) gives (−)-sparteine (**2**), while reduction of (−)-thermopsine (**4**), the C11 epimer of anagyrine, leads to

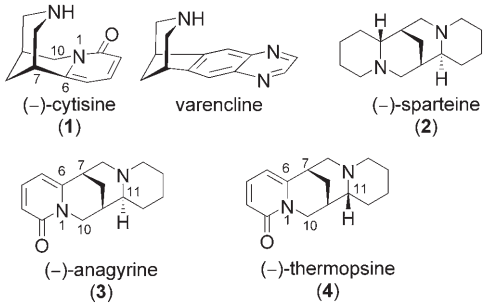

(−)-α- and (+)-β-isosparteine. Given this background, the development of general and therefore flexible synthetic entries to key lupin alkaloid targets becomes an attractive challenge; earlier contributions in this area by van Tamelen and Baran[3a,d] are of particular note.

We previously reported a novel approach to (±)-cytisine.[8a] Although highly convergent, this chemistry had limitations in terms of its broader utility.[8b] Herein, we

[*] D. Gray, Prof. T. Gallagher
School of Chemistry
University of Bristol
Bristol BS81TS (UK)
Fax: (+44) 117-929-8611
E-mail: t.gallagher@bristol.ac.uk

[**] We thank Dr. Ernest Boehm (Apin Chemicals Ltd.) for an authentic sample of natural anagyrine and the EPSRC for financial support.

Supporting information for this article is available on the WWW under http://www.angewandte.org or from the author.

© 2006 Wiley-VCH Verlag GmbH & Co. KGaA, Weinheim

report a second-generation approach that provides both a more efficient and also an asymmetric entry to cytisine. Furthermore, the core strategy focuses on establishing both N1–C10 and C6–C7 bond constructions, which are not only suited to cytisine (**1**) but also encompass a broader range of lupin alkaloids. The more general applicability of our approach is demonstrated here by the synthesis of both anagyrine (**3**) and thermopsine (**4**).

Our approach to cytisine (**1**) is shown in Scheme 1 and involves the efficient enzymatic resolution of ester **5**,[8,9] which

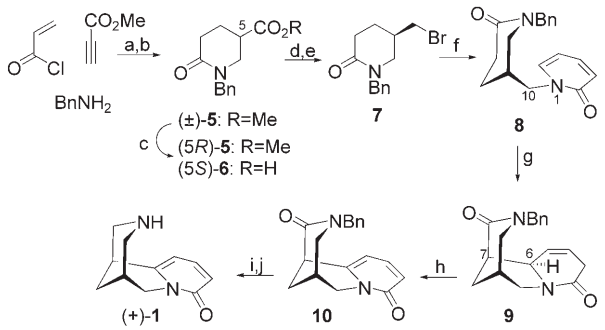

Scheme 1. Synthesis of (+)-cytisine ((+)-**1**). a) See Ref. [9], 56%; b) 10% Pd/C, H_2 (1 atm), Na_2CO_3, EtOH, 95%; c) α-chymotrypsin, 0.1 M phosphate buffer, acetone, pH 7.4, (5*R*)-**5** (42% yield, >98% *ee*) and (5*S*)-**6** (48% yield, 64% *ee* after derivatization to its methyl ester for HPLC analysis); d) $LiAlH_4$, THF; e) PBr_3, toluene, 57% overall yield from (5*R*)-**5**; f) 2-pyridone, K_2CO_3, Bu_4NBr, H_2O, PhMe, reflux, 66% (+15% of the corresponding 2-alkoxypyridine); g) LHMDS (2 equiv), THF, 70 °C, sealed tube, 15 h, 94%; h) MnO_2, CH_2Cl_2, 79%; i) BH_3·THF, 0 °C→RT; j) $Pd(OAc)_2$, H_2 (1 atm), MeOH, HCl, 60% overall from **10**. Bn = benzyl; LHMDS = lithium hexamethyldisilazide.

is readily available in a two-pot operation from simple and commercially available starting materials. Resolution of **5** was achieved using α-chymotrypsin to give (5*R*)-**5** in 42% isolated yield and with over 98% *ee* (as determined by chiral HPLC).[10] The acid (5*S*)-**6** was obtained in 48% yield in 64% *ee*, and the absolute configuration of (5*R*)-**5** was established by its conversion into (+)-cytisine[3j] (the non-natural enantiomer). Reduction of ester (5*R*)-**5** and bromination provided (5*R*)-**7** (57% overall), and reaction of **7** with 2-pyridone under basic conditions gave the N-alkylated adduct **8** (66%), so establishing the N1–C10 linkage.

The second key feature of our strategy is formation of the C6–C7 bond, which is a structural feature common to many lupin alkaloids. Previously, this bond was set using a Pd^0-mediated intramolecular α-arylation of the lactam unit,[8] but the same C6–C7 linkage can now be made more simply. Exposure of lactam **8** to LHMDS (or LDA) led to smooth cyclization to give the internal 1,6-addition adduct **9** as a single diastereomer (and alkene regioisomer) in 94% yield, with the stereochemistry at C6 of **9** confirmed by NOE studies.[12] Intramolecular 1,6-additions to 2-pyridone have not previously been reported, and indeed there are only a few examples known of the corresponding intermolecular process.[11] Mild oxidation of **9** gave lactam **10** in 79% yield, which was then converted through two steps[8] into (+)-cytisine by reduction of the lactam and debenzylation (60% yield over two steps). In this way, non-natural (+)-cytisine ((+)-**1**)[13] was obtained in 10 steps in 3.7% overall yield from commercially available materials and also allowed us to assign the absolute stereochemistry of both (5*R*)-**5** and (5*S*)-**6** as indicated in Scheme 1.

The broader applicability of this synthetic strategy is exemplified for two representative tetracyclic lupin alkaloids, anagyrine (**3**)[14,15] and its C11 epimer thermopsine (**4**),[15,16] as shown in Scheme 2 and Scheme 3. Anagyrine (**3**) was first isolated in 1895 from *Anagyris foetida*, and previous syntheses of anagyrine were reported by van Tamelen and Baran,[3d] Goldberg and Lipkin,[14a] and most recently by Padwa et al.[14b] Our approach to **3** is shown in Scheme 2, and again it targeted the N1–C10 and C6–C7 bonds as the key disconnections, requiring the quinolizidine-based bromide **13**[17,18] as a substrate for alkylation of 2-pyridone. Bromide **13** was

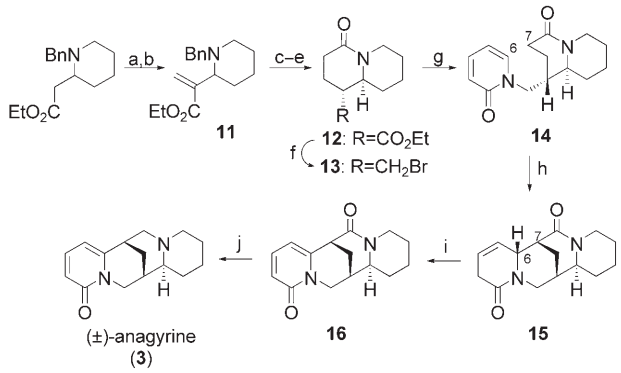

Scheme 2. Synthesis of (±)-anagyrine (**3**). a) LHMDS, $EtOCH_2Cl$, THF, −78 °C→RT, 87%; b) KO*t*Bu, THF, −78 °C, 84%; c) $MeCO_2tBu$, LDA, −78 °C, THF, 68%; d) 10% Pd/C, H_2 (1 atm), 100%; e) AcOH, toluene, reflux, 73%; f) $LiAlH_4$, THF, then PBr_3, toluene, 70% overall yield; g) 2-pyridone, K_2CO_3, Bu_4NBr, H_2O, toluene, reflux, 66% (+14% of the corresponding 2-alkoxypyridine); h) LDA (2 equiv), THF, room temperature, 3 h, 44%; i) MnO_2, CH_2Cl_2, 76%; j) BH_3·THF, 0 °C→RT, 85%. LDA = lithium diisopropylamide; AcOH = acetic acid.

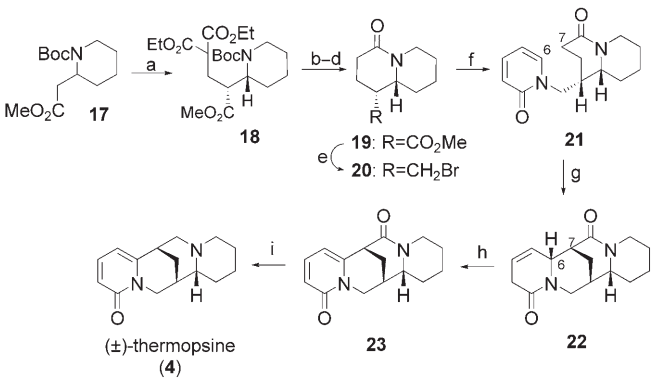

Scheme 3. Synthesis of (±)-thermopsine (**4**). a) LHMDS, $(EtO_2C)_2C{=}CH_2$, THF, −78 °C→RT, 79%; b) TFA, CH_2Cl_2, THF, 0 °C, 100%; c) AcOH, toluene, reflux, 89%; d) NaCl, H_2O, DMSO, 130 °C, 72 h, 72%; e) $LiAlH_4$, THF, then PBr_3, toluene, 72% overall yield; f) 2-pyridone, K_2CO_3, Bu_4NBr, H_2O, toluene, reflux, 71% (+12% of the corresponding 2-alkoxypyridine); g) LDA (2 equiv), THF, room temperature, 2.5 h, 26%; h) MnO_2, CH_2Cl_2, 70%; i) BH_3·THF, 0 °C→RT, 57%. TFA = trifluoroacetic acid; DMSO = dimethyl sulfoxide.

 © 2006 Wiley-VCH Verlag GmbH & Co. KGaA, Weinheim

prepared through diastereoselective 1,4-addition[19] of the enolate derived from *tert*-butyl acetate to the α,β-unsaturated ester **11**, which was available in two steps from racemic ethyl *N*-benzyl homopipecolate. N-Debenzylation of the 1,4-addition adduct and then acid-mediated cyclization led to **12**, and reduction of the ester and bromination provided the requisite bromide **13**. Again, this intermediate underwent clean N-alkylation with 2-pyridone, and cyclization of **14** under basic conditions proceeded to give **15** in 44% yield. This step serves to complete the tetracyclic core of anagyrine as a single diastereomer, with the relative stereochemistry at C6 that corresponds to that required for sparteine, as again determined by NOE studies.[20] Oxidation of **15**, followed by selective reduction of lactam **16** then gave (±)-anagyrine (**3**), which we were able to compare directly with an authentic sample of the natural product.[21]

The synthesis of (±)-thermopsine (**4**) was achieved by application of the same strategy. The only significant requirement here was for the epimeric quinolizidine derivative **20**,[17,18] which was prepared efficiently as shown in Scheme 3. The key stereocenters were established by addition of the enolate derived from (±)-**17** to freshly prepared diethyl methylenemalonate to give adduct **18** as a single diastereomer. The stereochemical outcome of this key step was consistent with that reported for the corresponding allylation reaction, as reported by Knight and co-workers.[22] Cleavage of the Boc residue from **18** and thermally induced cyclization were followed by selective ester cleavage and decarboxylation to give **19**, the structure and relative stereochemistry of which was confirmed by single-crystal X-ray analysis.[23] Conversion of **19** into bromide **20** followed by N-alkylation of 2-pyridone gave **21**. This intermediate underwent base (LDA)-induced cyclization to provide **22** in 26% yield.[24,25] In the same fashion as described for anagyrine, oxidation of **22** and subsequent reduction of the lactam in **23** gave (±)-thermopsine (**4**). Although an authentic sample of thermopsine was not available, we were able to compare spectroscopic data for our synthetic material with that available in the literature[15c,d] and our crystallographic assignment of ester **19** underpins this conclusion.

In summary, we have disclosed a synthetic strategy that is broadly applicable to representative lupin alkaloids, with syntheses of anagyrine (**3**) and thermopsine (**4**) also constituting formal routes to sparteine (**2**) and α- and β-isosparteines, respectively. More significantly, however, the chemistry that we have described is highly convergent, concentrating as it does on two key and common bonds within the core of these target structures. This approach also offers new opportunities to develop novel and significantly different variants of important targets, including both cytisine and sparteine, which will complement currently available methods. Our primary objective has been to validate the viability of the basic synthetic strategy, but asymmetric entries are also important and are being pursued.[18] However, the cornerstone of this new approach is the intramolecular 1,6-addition of a mono- or bicyclic lactam enolate to an N-alkylated pyridone as exemplified by **8**→**9** (94%), **14**→**15** (44%), and **21**→**22** (26%). Such 1,6-addition processes are without direct precedent, and this step needs to be examined in more detail as it is clearly sensitive to the steric environment of the substrate.[25] This type of process has applications elsewhere, and further studies to understand more fully, optimize, and extend the scope of this process are underway.[26]

Received: November 11, 2005
Published online: March 7, 2006

Keywords: alkaloids · cyclization · natural products · nucleophilic addition · synthetic methods

[1] N. J. Leonard in *The Alkaloids*, *Vol. 3* (Eds: R. H. F. Manske, H. L. Holmes), Academic Press, New York, **1953**, p. 120; H. C. S. Wood, R. Wrigglesworth in *Rodd's Chemistry of Carbon Compounds*, *Vol. IV*, part H (Ed: S. Coffey), Elsevier, Amsterdam, **1978**, chap. 38, p. 285; K. A. Aslanov, Y. K. Kushmuradov, A. S. Sadykov in *The Alkaloids*, *Vol. 31* (Ed: A. Brossi), Academic Press, New York, **1997**, p. 117.

[2] H. Ing, *J. Chem. Soc.* **1932**, 2778; A. Partheil, *Arch. Pharm.* **1894**, *232*, 161. For a recent overview of nicotinic pharmacology relevant to cytisine, see: A. A. Jensen, B. Frølund, T. Lijefors, P. Krogsgaard-Larsen, *J. Med. Chem.* **2005**, *48*, 4705.

[3] For previous syntheses of cytisine, see ref. [8] and: a) E. E. van Tamelen, J. S. Baran, *J. Am. Chem. Soc.* **1955**, *77*, 4944; b) F. Bohlmann, A. English, N. Ottawa, H. Sander, W. Weise, *Chem. Ber.* **1956**, *89*, 792; c) T. R. Govindachari, S. Rajadurai, M. Subramanian, B. S. Thyagarajan, *J. Chem. Soc.* **1957**, 3839; d) E. E. van Tamelen, J. S. Baran, *J. Am. Chem. Soc.* **1958**, *80*, 4659; e) B. T. O'Neill, D. Yohannes, M. W. Bundesmann, E. P. Arnold, *Org. Lett.* **2000**, *2*, 4201; f) J. W. Coe, *Org. Lett.* **2000**, *2*, 4205; g) P. Nshimyumukiza, D. Cahard, J. Rouden, M. C. Lasne, J. C. Plaquevent, *Tetrahedron Lett.* **2001**, *42*, 7787; h) D. Stead, P. O'Brien, A. J. Sanderson, *Org. Lett.* **2005**, *7*, 4459; for asymmetric routes to cytisine, see: i) B. Danieli, G. Lesma, D. Passarella, A. Sacchetti, A. Silvani, A. Virdis, *Org. Lett.* **2004**, *6*, 493; for the synthesis of (+)-cytisine, see: j) T. Honda, R. Takahashi, H. Namiki, *J. Org. Chem.* **2005**, *70*, 499.

[4] a) J. W. Coe, M. G. Vetelino, C. G. Bashore, M. C. Wirtz, P. R. Brooks, E. P. Arnold, L. A. Lebel, C. B. Fox, S. B. Sands, T. I. Davis, D. W. Schulz, H. Rollema, F. D. Tingley, B. T. O'Neill, *Bioorg. Med. Chem. Lett.* **2005**, *15*, 2974; b) J. W. Coe, P. R. Brooks, M. G. Vetelino, M. C. Wirtz, E. P. Arnold, J. H. Huang, S. B. Sands, T. I. Davis, L. A. Lebel, C. B. Fox, A. Shrikhande, J. H. Heym, E. Schaeffer, H. Rollema, Y. Lu, R. S. Mansbach, L. K. Chambers, C. C. Rovetti, D. W. Schulz, F. D. Tingley, B. T. O'Neill, *J. Med. Chem.* **2005**, *48*, 3474. Varenicline (Champix) has recently been granted a priority review by the US FDA and is currently in late-stage clinical trials as a smoking cessation agent.

[5] a) D. Hoppe, T. Hense, *Angew. Chem.* **1997**, *109*, 2376; *Angew. Chem. Int. Ed. Engl.* **1997**, *36*, 2283; b) T. Schutz, *Synlett* **2003**, 901.

[6] For the synthesis, evaluation, and computational aspects of sparteine mimics, see: a) M. J. Dearden, C. R. Firkin, J. P. R. Hermet, P. O'Brien, *J. Am. Chem. Soc.* **2002**, *124*, 11870; b) M. J. Dearden, M. J. McGrath, P. O'Brien, *J. Org. Chem.* **2004**, *69*, 5789; c) P. O'Brien, K. B. Wiberg, W. F. Bailey, J. P. R. Hermet, M. J. McGrath, *J. Am. Chem. Soc.* **2004**, *126*, 15480; d) P. W. Phuan, J. C. Ianni, M. C. Kozlowski, *J. Am. Chem. Soc.* **2004**, *126*, 15473.

[7] For asymmetric syntheses of sparteine, see: a) B. T. Smith, J. A. Wendt, J. Aube, *Org. Lett.* **2002**, *4*, 2577; b) J. P. R. Hermet, M. J. McGrath, P. O'Brien, D. W. Porter, J. Gilday, *Chem. Commun.* **2004**, 1830; a number of approaches to racemic sparteine have also been reported; see: T. Buttler, I. Fleming, S. Gonsior, B. H.

 © 2006 Wiley-VCH Verlag GmbH & Co. KGaA, Weinheim

Kim, A. Y. Sung, H. G. Woo, *Org. Biomol. Chem.* **2005**, *3*, 1557, and references therein.

[8] a) C. Botuha, C. M. S. Galley, T. Gallagher, *Org. Biomol. Chem.* **2004**, *2*, 1825; b) We have already examined the feasibility of extrapolating this first-generation synthetic approach to thermopsine (**4**). However, problems were encountered in both the N-alkylation of 6-bromo-2-pyridone using bromide **20** to establish the N1–C10 linkage: O-alkylation predominated. This result provided the motivation to find more straightforward solutions to the formation of the N1–C10 and C6–C7 bonds.

[9] G. R. Cook, L. G. Beholz, J. R. Stille, *J. Org. Chem.* **1994**, *59*, 3575.

[10] Felluga et al. reported the enzymatic resolution of a series of N-substituted pyrrolidinone analogues of **5**: F. Felluga, G. Pitacco, M. Prodan, S. Pricl, M. Visintin, E. Valentin, *Tetrahedron: Asymmetry* **2001**, *12*, 3241. The enantiomeric excess of ester (5*R*)-**5** was determined by chiral HPLC (Chiralcel OJ column) using racemic **5** as a standard. The enantiomeric excess of acid (5*S*)-**6** was determined by its conversion into ester (5*S*)-**5** using HCl in MeOH. We have observed the same sense of asymmetric differentiation, that is, selective hydrolysis of (5*S*)-**5** to (5*S*)-**6**, as seen by Felluga et al. in the five-membered lactam series.

[11] For rare examples of intermolecular 1,6-additions of alkyl lithium derivatives to 2-pyridones that lack additional activating (electron-withdrawing) substituents, see: a) P. Meghani, J. A. Joule, *J. Chem. Soc. Perkin Trans. 1* **1988**, 1; b) E. W. Thomas, *J. Org. Chem.* **1986**, *51*, 2184; an interesting photochemical 1,6-addition to 2-pyridone has been suggested to involve electron transfer and radical coupling; see: N. Sakurai, S. Ohmiya, *J. Chem. Soc. Chem. Commun.* **1993**, 297.

[12] Characterization data for all compounds reported herein are available in the Supporting Information. NOE experiments were carried out to determine the stereochemistry of **9**. Irradiation of C6-*H* showed an enhancement of both C8-H_{ax} (2.8%) and C10-H_{ax} (6.2%). Irradiation of C8-H_{ax} showed an enhancement of both C6-*H* (9.1%) and C10-H_{ax} (4.8%).

[13] Natural (−)-cytisine is commercially available, and we used a commercial sample of it to compare with our synthetic material. A lack of information in the literature as to the pharmacological profile of (+)-cytisine[26] prompted our interest in this enantiomer as our initial target, and (+)-cytisine is currently under evaluation as a nicotinic ligand. Optical rotation data for synthetic (+)-cytisine were recorded: $[\alpha]_D^{20} = +120$ ($c = 0.1$, EtOH); (literature values: for (−)-**1** $[\alpha]_D = -110$ ($c = 0.5$, EtOH)[13a]; for (+)-**1** $[\alpha]_D = +113.5$ ($c = 0.3$, EtOH)[3j]). a) Y.-H. Wang, J.-S. Li, H. Kubo, K. Higashiyama, H. Komiya, S. Ohmiya, *Chem. Pharm. Bull.* **1999**, *47*, 1308.

[14] The first synthesis of anagyrine was reported by van Tamelen and Baran,[3d] who exploited related chemistry to synthesise cytisine[3a-d] and thermopsine[3d]. For later routes to anagyrine, see: a) S. I. Goldberg, A. H. Lipkin, *J. Org. Chem.* **1972**, *37*, 1823; b) A. Padwa, T. M. Heidelbaugh, J. T. Kuethe, *J. Org. Chem.* **2000**, *65*, 2368.

[15] The crystal structure reported supposedly for anagyrine (A. U. Rahman, A. Pervin, M. I. Choudhary, N. Hasan, B. Sener, *J. Nat. Prod.* **1991**, *54*, 929) corresponds, in fact, to thermopsine, and this has been the subject of a query note placed on the file in the Cambridge Crystallographic Data Centre. The authors of the original paper, however, have not commented on this apparent error. There has been some dispute over the stereochemical assignments of anagyrine and thermopsine; for a discussion of the issues involved, see: a) D. S. Rycroft, D. J. Robins, I. H. Sadler, *Magn. Reson. Chem.* **1991**, *29*, 936; b) Z. M. Liu, L. Yang, Z. J. Jia, J. H. Chen, *Magn. Reson. Chem.* **1992**, *30*, 511. This problem has since been resolved and the original assignments confirmed: c) D. J. Robins, D. S. Rycroft, *Magn. Reson. Chem.* **1992**, *30*, 1125; d) B. Mikhova, H. Duddeck, *Magn. Reson. Chem.* **1998**, *36*, 779. Mikhova and Duddeck[15d] report a comprehensive listing of ^{13}C NMR data for lupin alkaloids, including both anagyrine and thermopsine.

[16] Earlier syntheses of thermopsine were reported by van Tamelen and Baran[3d] and Bohlmann et al. (F. Bohlmann, E. Winterfeldt, H. Overwien, H. Pagel, *Chem. Ber.* **1962**, *95*, 944).

[17] A number of different approaches to racemic quinolizidines esters and halides **12**/**19** and **13**/**20**, respectively, have already been reported[17a–h], but attempts to produce asymmetric variants of these have had limited success.[17h] New synthetic approaches to both **12** and **19** have been outlined herein (Schemes 2 and 3) with the longer term aim of using these routes to provide enantiomerically pure substrates. These studies are currently underway.[18] a) F. Bohlmann, E. Winterfeldt, H. Laurent, W. Ude, *Tetrahedron* **1963**, *19*, 195; b) T. Kappe, *Monatsh. Chem.* **1967**, *98*, 1852; c) B. Lal, D. N. Bhedi, H. Dornauer, N. J. De Souza, *J. Heterocycl. Chem.* **1980**, *17*, 1073; d) M. L. Bremmerr, S. M. Weinreb, *Tetrahedron Lett.* **1983**, *24*, 261; e) M. Ihara, T. Kirihara, K. Fukumoto, T. Kametani, *Heterocycles* **1985**, *23*, 1097; f) M. Ihara, T. Kirihara, A. Kawaguchi, M. Tsuruta, K. Fukumoto, *J. Chem. Soc. Perkin Trans. 1* **1987**, 1719; g) T. Nagasaka, H. Yamamoto, H. Hayashi, H. Kato, M. Kawaida, K. Yamaguchi, F. Hamaguchi, *Heterocycles* **1989**, *29*, 1209; h) M. J. Wanner, G. J. Koomen, *Tetrahedron* **1991**, *47*, 8431; i) E. D. Edstrom, *Tetrahedron Lett.* **1991**, *32*, 5709.

[18] Methyl homopipecolate, the starting material used in Schemes 2 and 3, is now available in enantiomerically pure form by either an efficient homologation process[18a] or by enzymatic resolution.[18b] a) D. Gray, C. Concellón, T. Gallagher, *J. Org. Chem.* **2004**, *69*, 4849; b) C. Pousset, R. Callens, M. Haddad, M. Larchevêque, *Tetrahedron: Asymmetry* **2004**, *15*, 3407.

[19] O'Brien and co-workers reported a related diastereoselective 1,4-addition reaction in their synthesis of (+)-sparteine.[7b] This reaction used an *N*-α-methylbenzyl moiety to induce a very modest level of diastereoselectivity in a cyclization reaction leading to the piperidine ring. For a related alkylative cyclization strategy also based on *N*-α-methylbenzyl as a chiral-directing group that generates a very similar intermediate to that used by O'Brien and co-workers, see: D. N. A. Fox, D. Lathbury, M. F. Mahon, K. C. Molloy, T. Gallagher, *J. Am. Chem. Soc.* **1991**, *113*, 2652.

[20] NOE experiments were carried out to determine the stereochemistry of **15**. Irradiation of C6-*H* showed an enhancement of C10-H_{ax} (3.9%). Enhancement of C8-H_{ax} was also observed but was complicated because this signal overlapped with C13-H_{ax} and C13-H_{eq}. As a result, selective irradiation of C8-H_{ax} was not possible. Irradiation of C10-H_{ax} showed an enhancement of both C6-*H* (7.9%) and C8-H_{ax}, although the latter enhancement could not be quantified.

[21] A sample of natural anagyrine was kindly provided by Dr. Ernest Boehm (Apin Chemicals Ltd.) and used for comparison purposes (^{1}H and ^{13}C NMR spectroscopic data and TLC). We were able to correlate ^{1}H and ^{13}C NMR data for synthetic anagyrine (and synthetic thermopsine) with that reported by Robins et al.,[15a,c] and Mikhova and Duddeck.[15d] The region of the ^{13}C NMR spectra[15d] displaying the resonances for C7–C15 for these two isomers is quite distinct, and full details are available in the Supporting Information.

[22] C. Morley, D. W. Knight, A. C. Share, *J. Chem. Soc. Perkin Trans. 1* **1994**, 2903; for related diastereoselective alkylations involving *N*-benzyl piperidines, see: S. Ledoux, J. P. Célérier, G. Lhommet, *Tetrahedron Lett.* **1999**, *40*, 9019; S. Ledoux, E. Marchalant, J. P. Célérier, G. Lhommet, *Tetrahedron Lett.* **2001**, *42*, 5397.

[23] Crystal data for lactam **19**: $C_{11}H_{17}NO_3$, $M_r = 211.26$, colorless plate, $0.50 \times 0.50 \times 0.10$ mm^3, $Mo_{K\alpha}$ radiation ($\lambda = 0.71073$ Å) was used, and intensity data were collected as ω scans (frames, 0.3° width, $2\theta_{max} = 50°$); a multiscan absorption correction (G. M.

 © 2006 Wiley-VCH Verlag GmbH & Co. KGaA, Weinheim

Sheldrick, SADABS v2.03, University of Göttingen, Germany, **2003**) was applied, ($\mu = 0.094$ mm^{-1}, $T_{max} = 1.00$, $T_{min} = 0.94$), the structure was solved and refined by standard techniques (G. M. Sheldrick, SHELXS-97, University of Göttingen, Germany, **1990**; G. M. Sheldrick, SHELXL-97, University of Göttingen, Germany, **1997**); triclinic crystal system, $a = 9.3234(19)$, $b = 10.175(2)$, $c = 11.724(2)$ Å, $\alpha = 88.69(3)$, $\beta = 75.71(3)$, $\gamma = 88.28(3)°$, $V = 1077.2(4)$ Å^3, $\rho = 1.303$, $T = 173(2)$ K, space group $P\bar{1}$, $Z = 4$, $R_{int} = 0.0456$ (for 10271 measured reflections), 273 parameters were used in the refinement, hydrogen atoms were constrained to ideal geometries and refined with displacement parameters equal to 1.5 times (methyl H atoms) or 1.2 times (all other H atoms) U_{eq} of their parent atom; largest difference electron density map features were $+0.192$, -0.191 eÅ^{-3}, $R_1 = 0.0423$ [for 2532 unique reflections with $> 2\sigma(I)$], $wR_2 = 0.0994$ (for all 3787 unique reflections). CCDC 289282 contains the supplementary crystallographic data for this paper. These data can be obtained free of charge from the Cambridge Crystallographic Data Centre via www.ccdc.cam.ac.uk/data request/cif.

[24] NOE experiments were carried out to determine the stereochemistry of **22**. Irradiation of C6-*H* showed an enhancement of both C8-H_{ax} (2.2%) and C10-H_{ax} (3.4%). Irradiation of C10-H_{ax} showed an enhancement of both C6-*H* (4.4%) and C8-H_{ax} (3.2%).

[25] For cyclization to occur, there is a requirement that the enolates derived from bicyclic lactams **14** and **21** maintain the pyridone substituent associated with C1 (quinolizidine numbering) in an axial environment. Interestingly, the crystal structure of bicyclic lactam **19** (see Supporting Information) shows the CO_2Me substituent at C1 to be orientated in a pseudoequatorial environment, and, significantly, the cyclization of **21** (derived from **19** and which leads to thermopsine) is the least efficient of those we have examined to date. However, at this time, the factors that moderate the efficiency and scope of this reaction have not yet been defined, and the processes reported here remain unoptimized.

[26] Note added in proof: The activity of (+)-cytisine at the α4β2* nicotine acetylcholine receptor labeled with [^{3}H]-epibatidine has been determined: $K_i = 0.79 \pm 0.30$ μM for (+)-cytisine versus $K_i = 3.0 \pm 0.65$ nM for (−)-cytisine. This low level of activity could also be attributed to a small (ca. 0.4%) level of contamination by (−)-cytisine as a consequence of the kinetic resolution step involved. We thank Professor Susan Wonnacott and Neal Innocent (University of Bath) for this determination.

 © 2006 Wiley-VCH Verlag GmbH & Co. KGaA, Weinheim

Mixture Synthesis

DOI: 10.1002/anie.200600041

Solution-Phase Mixture Synthesis with Fluorous Tagging En Route: Total Synthesis of an Eight-Member Stereoisomer Library of Passifloricins**

Dennis P. Curran, Gustavo Moura-Letts, and Matthias Pohlman*

Fluorous mixture synthesis is a new solution-phase technique that permits the synthesis of mixtures of compounds—with the attendant savings in effort—but at the same time provides for the isolation of individual, pure products through a sorting process called demixing.[1,2] This symphony of reactions and separations is orchestrated by fluorous tags, which are typically attached to substrates in the guise of protecting groups bearing a homologous series of perfluoroalkyl groups ($-(CF_2)_nCF_3$). A mixture of compounds encoded with different fluorous tags can be kept together or pulled apart (demixed) during a separation depending on whether a fluorous or a non-fluorous separation method is used. Demixing is generally accomplished by chromatography over fluorous silica gel.[3]

Fluorous tags have been used to encode enantiomers[1c] (so-called quasiracemic synthesis), diastereomers,[1c] and analogues.[1b] While limitless in principle, the number of fluorous tags is limited in practice by the availability of suitable fluoroalkyl precursors and more importantly by the increasing molecular weights and unusual properties that very large fluorous groups confer on molecules that bear them. It is thus an important goal to leverage available tags by developing tagging methods in which the number of tagged compounds exceeds the number of tags.[4]

We report herein the total synthesis of an eight-member stereoisomer library of passifloricins[5–7] in which the stereocenters are introduced and tagged en route during the synthesis. The library comprises the enantiomer of passifloricin A and all seven epimers at C5, C7, and C9. The synthesis contrasts with all prior mixture work, in which building blocks with coded stereocenters were premade and pretagged. Further, the total fluorine content of each tagged molecule is defined by two tags, whereas a lone fluorous tag has been used in all prior work.

[*] Prof. Dr. D. P. Curran, G. Moura-Letts, Dr. M. Pohlman
Department of Chemistry
University of Pittsburgh
Pittsburgh, PA 15260 (USA)
Fax: (+1) 412-624-9861
E-mail: curran@pitt.edu

[**] We thank the National Science Institutes of Health (Institute for General Medical Sciences) for funding this study, the German Academic Exchange Organization (DAAD) for a fellowship (M.P.), and Prof. J. A. Marco for providing the samples.

Supporting information for this article is available on the WWW under http://www.angewandte.org or from the author.

© 2006 Wiley-VCH Verlag GmbH & Co. KGaA, Weinheim

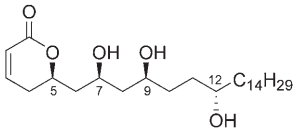

passifloricin A
(5*R*,7*S*,9*S*,12*S*)-**1**

The en route approach is doubly attractive because it saves steps over serial or parallel approaches and because it naturally enables the use of fewer fluorous tags than the number of stereoisomers in the library. These two points are illustrated by the synthetic pathway diagrams in Figure 1. In the traditional serial or parallel synthesis of stereoisomer libraries, the reaction products must be divided into two parts prior to the introduction of each new stereocenter and then carried along separately. The unavoidable doubling of work that attends the introduction of each stereocenter explains why stereoisomer libraries have received little attention to date.

In fluorous mixture synthesis, the division and complementary reactions to introduce a new stereocenter in both possible configurations are followed by tagging and remixing. Thus, the synthesis never diverges if there are sufficient tags to accommodate the isomers. Further, whereas two new tags are needed to encode the first stereocenter, only one new tag is needed for each of the successive stereocenters. Thus, a library of n molecules is uniquely encoded with $2/n + 1$ tags. The pairwise combination of tags T^1–T^3 provides four products with differing numbers of fluorine atoms provided only that T^1, T^2, and T^3 have a different fluorine content. One of the tags does not need to have any fluorine atoms, thereby further economizing the available perfluoroalkyl groups. If the effect of the fluorine content of the tags is additive on fluorous chromatography, then these products can be unambiguously demixed and their configurations decoded.

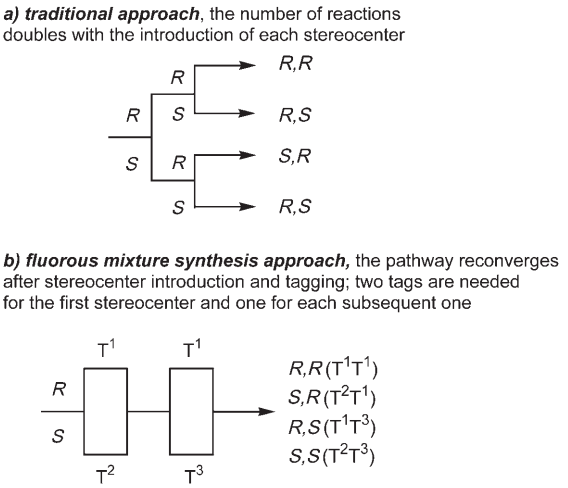

Figure 1. Strategies for the synthesis of stereoisomer libraries with the formation of stereocenters en route. Each branch represents the division of a product and introduction of a new stereocenter in both possible configurations.

The synthesis of the passifloricin stereoisomer library follows in the footsteps of syntheses of individual passifloricins by Marco[6a,b,7] and Cossy[6c,d] and is summarized in Scheme 1. The reaction path involves three similar iterative cycles of 1) oxidation to an aldehyde, 2) division and reagent-controlled asymmetric allylation of the aldehyde with both enantiomers of the Duthaler–Hafner reagent (hereafter called the DH reagent),[6c,d,8] 3) fluorous tagging of the isomeric products, and 4) remixing. We chose to make the enantiomer of passifloricin A because Marco and co-workers had already prepared natural passifloricin A and three

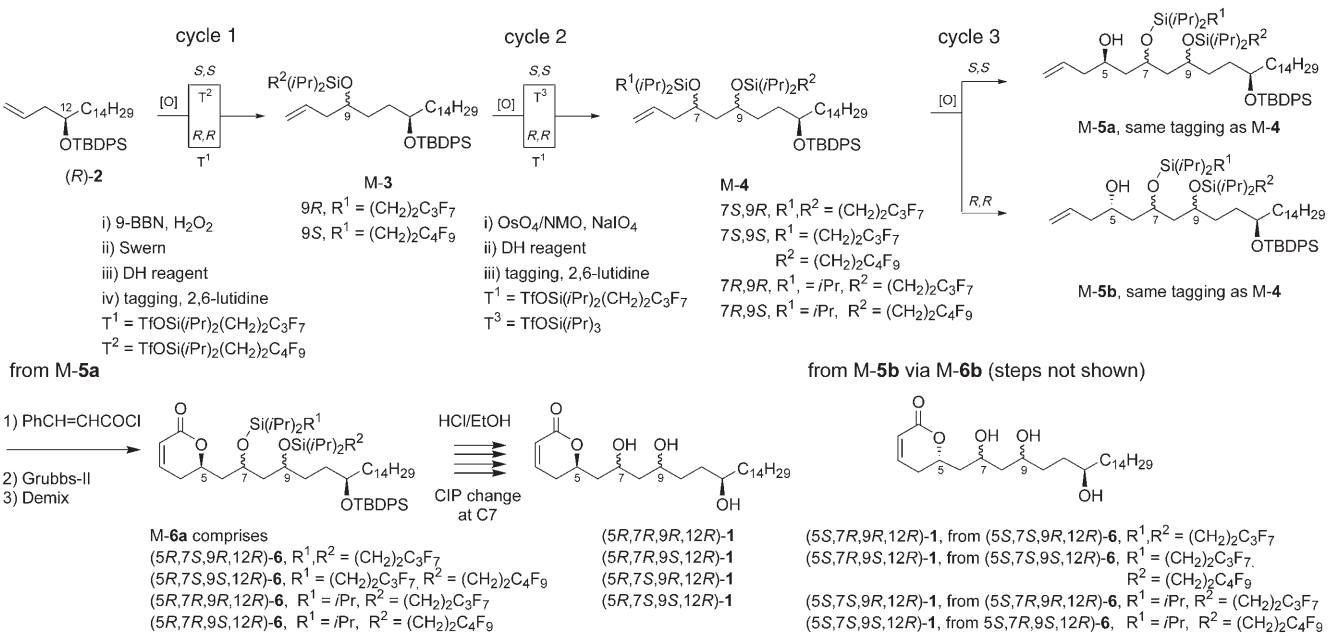

Scheme 1. Synthesis of passifloricins. 9-BBN = 9-borabicyclo[3.3.1]nonane, TBDPS = *tert*-butyldiphenylsilyl.

 © 2006 Wiley-VCH Verlag GmbH & Co. KGaA, Weinheim

isomers.[7] These four compounds served as controls for the success of our exercise.

Enantiopure allyl silyl ether (*R*)-**2** (>99% *ee*) was subjected to a sequence of hydroboration and oxidation. Half of the resulting aldehyde was treated with the (*R*,*R*)-DH reagent, and the resulting alcohol (82%, d.r. = 98:2) was tagged with fluorous triisopropylsilyl trifluoromethanesulfonate (^{F}TIPSOTf) bearing a C_4F_9 group (81%).[9] The other half was treated with the (*S*,*S*)-DH reagent, and the alcohol (83%, d.r. = 2:98) was tagged with the ^{F}TIPS group bearing C_3F_7 (95%). The resulting quasi-diastereomers were mixed to make M-**3** for the second cycle.

The terminal carbon atom of the allyl group is not needed in cycle 2, so the aldehyde was generated by oxidative cleavage (OsO_4/*N*-methylmorpholine *N*-oxide (NMO), then $NaIO_4$, 73%) of M-**3**. Now division and allylation as above (91 and 88%, respectively) were followed by tagging; the product from the (*R*,*R*)-DH reagent received the new "null" (non-fluorous) TIPS tag (90%), and the product from the (*S*,*S*)-DH reagent received the repeat C_3F_7 tag. The resulting pair of two-compound mixtures was mixed to make a four-compound mixture of quasi-diastereomers M-**4** in preparation for cycle 3.

Cycle 3 was identical to cycle 2 through oxidation (73%) and allylation (93 and 80%) but was then interrupted to complete the synthesis. The resulting two mixtures of four compounds M-**5a**,**b** were acylated with cinnamoyl chloride (83 and 78%), and the crude products were directly subjected to ring-closing metathesis with the second-generation Grubbs catalyst[6,7] (85 and 92%). This process provided the full stereoisomer library of protected passifloricins as two mixtures of four compounds M-**6a**,**b**.

The product structures and retention times for the preparative demixing of M-**6a** are shown in Scheme 2. The

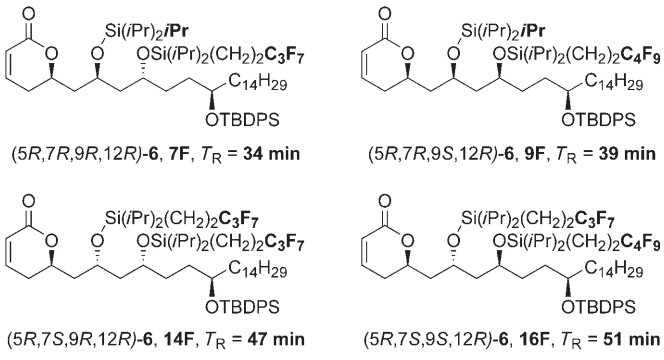

Scheme 2. Demixing of M-**6a** by fluorous HPLC: the quasi-diastereomers emerge in order of increasing total fluorine content.

samples were injected on a PF-C8 fluorous HPLC column,[9] which was eluted over 60 minutes with a gradient from 80% MeCN/water to 100% MeCN. The approximate additivity of the fluorine content of the tags was indeed observed, with the quasi-isomer of **6** bearing 7 fluorine atoms emerging first, followed in turn by those with 9, 14, and 16 fluorine atoms. These four major fractions were collected and concentrated to provide the four individual, protected quasi-isomers of passifloricin. Demixing of M-**6b** provided the other four isomers (not shown). All eight isomers of **6** were deprotected individually by exposure to 3 N HCl in EtOH. Products **1** were purified by flash chromatography and normal-phase HPLC to provide the eight-member library including (*ent*)-passifloricin A (5*S*,7*R*,9*R*,12*R*-**1**) and its seven diastereomers with *R* configurations at C12 and all the possible configurations at C5, C7, and C9.[10]

Unlike previous libraries that we have made with remote stereocenters,[1c] each member of this library exhibited unique ^{1}H and ^{13}C NMR spectra. Samples of passifloricin and three isomers from Marco and co-workers[7b] were identical to the four expected products **1** in our library, thus demonstrating that the tagging and demixing process was successful. The exercise confirms the stereostructure of passifloricin by rigorously proving that it is not any of the other seven possible stereoisomers.

This strategy of fluorous mixture synthesis with the introduction and tagging of stereocenters en route is a powerful new approach to making stereoisomer libraries with significant savings in effort. The mixture synthesis phase of this work required only 18 chemical reactions, whereas the same synthesis conducted in serial fashion would have required 44 reactions. The route also economizes tags, as four pairs of isomers were made by using three tags, only two of which were fluorous. Eight isomers could be made in a single mixture with five tags, 16 isomers with 9 tags, and so on. Central to this approach is the approximate additivity of the fluorine content of the tags as expressed by elution order in the demixing. Although demonstrated in an en route setting, the tactic of using multiple tags is equally applicable in settings in which pretagged building blocks are assembled.[11]

Received: January 4, 2006
Published online: March 9, 2006

Keywords: allylation · asymmetric synthesis · fluorous tags · mixture synthesis · separation tags

[1] a) Z. Luo, Q. Zhang, Y. Oderaotoshi, D. P. Curran, *Science* **2001**, *291*, 1766–1769; short reviews: b) W. Zhang, *Arkivoc* **2004**, 101–109; c) Q. Zhang, D. P. Curran, *Chem. Eur. J.* **2005**, *11*, 4866–4880.

[2] a) D. P. Curran, T. Furukawa, *Org. Lett.* **2002**, *4*, 2233–2235; b) W. Zhang, Z. Luo, C. H.-T. Chen, D. P. Curran, *J. Am. Chem. Soc.* **2002**, *124*, 10443–10450; c) Q. Zhang, H. Lu, C. Richard, D. P. Curran, *J. Am. Chem. Soc.* **2004**, *126*, 36–37; d) S. Dandapani, M. Jeske, D. P. Curran, *Proc. Natl. Acad. Sci. USA* **2004**, *101*, 12,008–12,012; e) S. Manku, D. P. Curran, *J. Comb. Chem.* **2005**, *7*, 63–68.

[3] D. P. Curran in *The Handbook of Fluorous Chemistry* (Eds.: J. A. Gladysz, D. P. Curran, I. T. Horváth), Wiley-VCH, Weinheim, **2004**, pp. 101–127; and D. P. Curran in *The Handbook of Fluorous Chemistry* (Eds.: J. A. Gladysz, D. P. Curran, I. T. Horváth), Wiley-VCH, Weinheim, **2004**, pp. 128–156.

[4] a) Redundant tagging: S. Manku, D. P. Curran, *J. Org. Chem.* **2005**, *70*, 4470–4473; b) double tagging with fluorous and oligoethylene glycol tags: C. S. Wilcox, V. Gudipati, H. Lu, S. Turkyilmaz, D. P. Curran, *Angew. Chem.* **2005**, *117*, 7098–7100; *Angew. Chem. Int. Ed.* **2005**, *44*, 6938–6940.

 © 2006 Wiley-VCH Verlag GmbH & Co. KGaA, Weinheim

[5] Isolation, activity: a) F. Echeverri, V. Arango, W. Quinones, F. Torres, G. Escobar, Y. Rosero, R. Archbold, *Phytochemistry* **2001**, *56*, 881 – 885; b) W. Cardona, W. Quinones, F. Echeverri, *Molecules* **2004**, *9*, 666 – 672.
[6] Syntheses of regioisomers: a) J. Murga, J. García-Fortanet, M. Carda, J. A. Marco, *Tetrahedron Lett.* **2003**, *44*, 7909 – 7912; b) J. García-Fortanet, J. Murga, M. Carda, J. A. Marco, *Org. Lett.* **2003**, *5*, 1447 – 1449; c) J. Cossy, S. BouzBouz, M. Popkin, *C. R. Chim.* **2003**, *6*, 547 – 552; d) S. BouzBouz, J. Cossy, *Tetrahedron Lett.* **2003**, *44*, 4471 – 4473; e) ^{13}C NMR spectroscopic analysis: G. Bifulco, L. Gomez-Paloma, R. Riccio, *Tetrahedron Lett.* **2003**, *44*, 7137 – 7141.
[7] Synthesis of passifloricin: J. Murga, J. García-Fortanet, M. Carda, J. A. Marco, *J. Org. Chem.* **2004**, *69*, 7277 – 7283.
[8] A. Hafner, R. O. Duthaler, R. Marti, G. Rihs, P. Rothe-Streit, F. Schwarzenbach, *J. Am. Chem. Soc.* **1992**, *114*, 2321 – 2336.
[9] Reagents and fluorous silica products were purchased from Fluorous Technologies, Inc; D.P.C. holds an equity interest in this company.
[10] Note the change in Cahn–Ingold–Prelog (CIP) priorities at C7 between **6** and **1**.
[11] The Supporting Information contains copies of the NMR spectra for all of the eight isomers of **6** and **1**.

 © 2006 Wiley-VCH Verlag GmbH & Co. KGaA, Weinheim

Allylation

DOI: 10.1002/anie.200504432

Catalytic Enantioselective and Catalyst-Controlled Diastereofacial-Selective Additions of Allyl- and Crotylboronates to Aldehydes Using Chiral Brønsted Acids**

*Vivek Rauniyar and Dennis G. Hall**

Despite the extensive efforts of numerous research groups over the course of more than two decades, there is still no methodology for the allylation of aldehydes that possesses all of the following attributes: mildness and chemoselectivity, substrate generality (for both the allyl–metal reagent and aldehyde substrate), high levels of diastereo- and enantioselectivity, and high practicality (ease of use, low cost, nontoxicity, and low environmental impact).[1] Very importantly, the ideal enantioselective allylation methodology would circumvent the use of a chiral auxiliary through a simple and efficient chiral catalyst.[2] The recent discovery of Lewis and Brønsted acid catalyzed allylboration manifolds[3] has opened doors towards an ideal methodology for the allylation of carbonyl compounds. Indeed, pinacol allylboronates are air- and water-stable nontoxic reagents whose additions to aldehydes are characterized by very high levels of chemo-, regio-, and diastereoselectivity. Efforts by us and others[3b] to develop catalytic enantioselective additions with chiral Lewis acids have led only to low levels of enantioselectivity in model allylborations of aldehydes. Herein, following our recent report of Brønsted acid catalyzed allylborations,[3e] we demonstrate that the use of the Yamamoto chiral diol–$SnCl_4$ complexes[4] (Scheme 1) provides a significant advance towards a general catalytic enantioselective allylboration process. The current conditions are particularly advantageous in promoting efficient diastereofacial control in additions to α-chiral aldehydes.

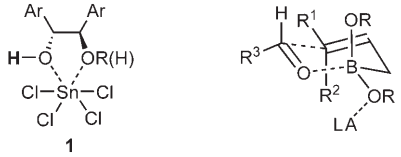

Scheme 1. Left: diol–$SnCl_4$ chiral Brønsted acid complex **1**.[4] Right: Proposed transition state in the Lewis acid (LA) catalyzed allylboration.[5]

Mechanistic studies of the Lewis acid catalyzed allylboration point to a cyclic bimolecular transition state with boronate activation through coordination of an oxygen atom of the hindered pinacolate to the metal center (Scheme 1).[5] In this perspective, the use of a smaller activator, a proton, seemed ideal and prompted us to investigate a number of chiral Brønsted acid catalysts.[6] Among several systems tested for the model reaction between hydrocinnamaldehyde and pinacol allylboronate at −78 °C, the concept of "Lewis acid assisted Brønsted acidity" with diol–$SnCl_4$ complexes, developed by Yamamoto and co-workers,[4] was found to be the most promising (Scheme 2).

As shown in Table 1, basic 1,2-diphenyl-1,2-ethanediol (**1a**) provided product **4a** with 37% *ee* (entry 1). Further optimization of the diol, catalyst stoichiometry, and additives led to the current optimal conditions shown in entry 12 with commercially available (*R*,*R*)-(+)-1,2-di(1-naphthyl)-1,2-ethanediol (**1j**). No other diol derivatives, including electronically modulated diaryl glycols (**1e**,**f** and **1i**) and various mono-O-alkylated diols (**1b**,**c**), led to higher enantioselectivities.[7] In all cases, the *ee* values were slightly higher in anhydrous toluene than in dichloromethane. Interestingly, $SnCl_4$ alone promotes an allylboration at a comparable rate, although in a non-enantioselective fashion. Thus, the use of a slight excess of diol was found to be desirable (compare

[*] V. Rauniyar, Prof. D. G. Hall
Department of Chemistry
Gunning-Lemieux Chemistry Centre
University of Alberta
Edmonton, Alberta, T6G 2G2 (Canada)
Fax: (+1) 780-492-8231
E-mail: dennis.hall@ualberta.ca

[**] Acknowledgment for financial support is given to the Natural Sciences and Engineering Research Council (NSERC) of Canada (Discovery Grant to D.G.H.), the Donors of the American Chemical Society Petroleum Research Funds (PRF-AC Grant to D.G.H.), and the University of Alberta. V.R. thanks the Alberta Ingenuity Foundation for a Graduate Scholarship. The authors are grateful to Glen Bigam and Mark Miskolzie for help in the variable-temperature NMR studies.

Supporting information for this article is available on the WWW under http://www.angewandte.org or from the author.

InterScience
© 2006 Wiley-VCH Verlag GmbH & Co. KGaA, Weinheim

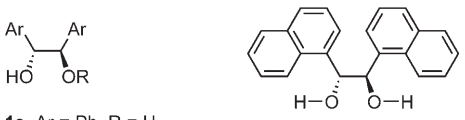

1a Ar = Ph, R = H
1b Ar = Ph, R = Me
1c Ar = Ph, R = Bn
1d Ar = 3,5-$(CH_3)_2$-C_6H_3, R = H
1e Ar = 3,5-$(CF_3)_2$-C_6H_3, R = H
1f Ar = 4-CH_3O-C_6H_4, R = H
1g Ar = 2-CH_3-C_6H_4, R = H
1h Ar = 2-Ph-C_6H_4, R = H
1i Ar = 2-CH_3-4-CH_3O-C_6H_3, R = H

Scheme 2. Chiral *R,R* diols evaluated in the enantioselective allylboration catalyzed by diol–$SnCl_4$ complexes.

Table 1: Optimization of the diol–$SnCl_4$ catalyst system.[a]

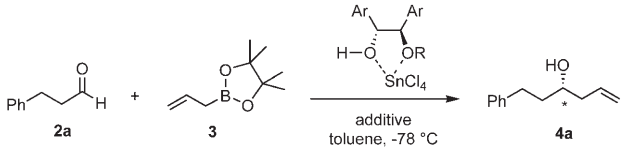

Entry	Diol [mol%]	$SnCl_4$ [mol%]	Additive	*ee* [%][b]
1	**1a** (11)	(10)	Na_2CO_3	37
2	**1b** (11)	(10)	none	34
3	**1c** (11)	(10)	Na_2CO_3	62
4	**1c** (10)	(20)	Na_2CO_3	0
5	**1d** (11)	(10)	Na_2CO_3	38
6	**1e** (11)	(10)	Na_2CO_3	34
7	**1f** (11)	(10)	Na_2CO_3	45
8	**1g** (11)	(10)	Na_2CO_3	69
9	**1h** (11)	(10)	Na_2CO_3	33
10	**1i** (11)	(10)	Na_2CO_3	74
11	**1j** (11)	(10)	none	70
12	**1j** (11)	(10)	Na_2CO_3	78
13	**1j** (11)	(10)	Ag_2CO_3	75
14	**1j** (11)	(10)	K_2CO_3	74

[a] Conditions: all reactions were performed with aldehyde **2a** (0.25 mmol), allylboronate **3** (0.275 mmol), *R,R* diol **1** (0.0275 mmol), $SnCl_4$ (0.025 mmol), Na_2CO_3 (0.05 mmol), and 4-Å molecular sieves (50 mg) in toluene (1 mL) at −78 °C for 12 h. [b] The absolute configuration was determined by comparison with known compounds;[7] all *ee* values were measured through the formation of Mosher esters and ^{19}F NMR spectroscopic analysis.[7]

entries 3 and 4). Because of worries that adventitious HCl (e.g., residual HCl in commercial $SnCl_4$) could lead to an erosion of the stereoselectivity, mildly basic additives were tested as precautionary HCl scavengers (entries 11–14). The use of Na_2CO_3, insoluble in toluene, afforded the highest enantioselectivity.[8] Other allylboronic esters, such as those made from 1,2-cyclohexanediol, 1,2-cyclopentanediol, and tetraphenylethanediol, provided much lower enantioselectivities, even with the optimal diol **1j** (results not shown[7]).

The substrate scope of the catalytic enantioselective allylborations was studied with a panel of model aldehydes under the optimal conditions of Table 1[7] (the results are summarized in Table 2). In contrast with several other reported catalytic allylation systems,[1] aliphatic aldehydes give higher enantioselectivities in the current allylboration process. Whereas aromatic and unsaturated aldehydes gave

Table 2: Enantioselective additions of allyl- and crotylboronates.[a]

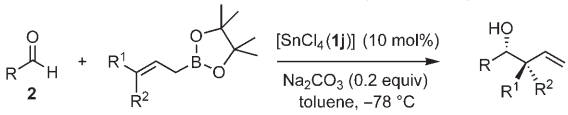

3 R^1, R^2 = H
5 R^1 = Me, R^2 = H
7 R^1 = H, R^2 = Me

4a R = $Ph(CH_2)_2$, R^1, R^2 = H
4b R = $CH_3(CH_2)_8$, R^1, R^2 = H
4c R = C_6H_{11}, R^1, R^2 = H
4d R = TBDPSO$(CH_2)_2$, R^1, R^2 = H
4e R = Ph, R^1, R^2 = H
4f R = PhCH=CH, R^1, R^2 = H
4g R = $CH_3(CH_2)_4CC$, R^1, R^2 = H
6a R = $Ph(CH_2)_2$, R^1 = Me, R^2 = H
6b R = $CH_3(CH_2)_8$, R^1 = Me, R^2 = H
8a R = $Ph(CH_2)_2$, R^1 = H, R^2 = Me
8b R = $CH_3(CH_2)_8$, R^1 = H, R^2 = Me

Entry	Aldehyde (R)	Boronate	Product	Yield [%][b]	e.r.[c]
1	**2a** $PhCH_2CH_2$	**3**	**4a**	85	89:11
2	**2b** $CH_3(CH_2)_8$	**3**	**4b**	76	90:10
3	**2c** C_6H_{11}	**3**	**4c**	90	85:15
4	**2d** TBDPSO$(CH_2)_2$	**3**	**4d**	90	83:17
5	**2e** Ph	**3**	**4e**	99	55:45
6	**2f** PhCH=CH	**3**	**4f**	72	60:40
7	**2g** $CH_3(CH_2)_4CC$	**3**	**4g**	99	56:44
8	**2a** $PhCH_2CH_2$	**5**	**6a**	99	86:14
9	**2b** $CH_3(CH_2)_8$	**5**	**6b**	70	86:14
10	**2a** $PhCH_2CH_2$	**7**	**8a**	87	70:30
11	**2b** $CH_3(CH_2)_8$	**7**	**8b**	70	73:27

[a] Reaction conditions: all entries were performed with aldehyde (0.25 mmol), allylboronate (0.275 mmol), **1j** (0.0275 mmol), $SnCl_4$ (0.025 mmol), Na_2CO_3 (0.05 mmol), and 4-Å molecular sieves (50 mg) in toluene (1 mL) at −78 °C for 12 h (entries 1–7) or 24 h (entries 8–11). [b] The yields are for the isolated product and are an average of two runs. [c] All the e.r. values were measured by chiral HPLC (Chiralcel OD), except for entries 3, 7, 9, and 11, which were measured through the formation of Mosher esters and ^{19}F NMR spectroscopic analysis.[7] TBDPS = *tert*-butyldiphenylsilyl.

modest selectivities (entries 5–7), the enantiomeric ratio in allylations of aliphatic aldehydes rose to 90:10 (80% *ee*; entry 2). The e.r. values of prototypic crotylborations (entries 8–11) were slightly lower than those obtained in the simple allylborations, with *trans*-crotyl reagent **5** giving higher selectivities. The diastereoselectivities of the crotylations are very high (> 98:2 d.r.) and consistent with the corresponding uncatalyzed allylborations.

Uncatalyzed additions of pinacol allylboronates are known to proceed very slowly at −78 °C. Nonetheless, we carried out control experiments with hydrocinnamaldehyde (**2a**), which confirmed the lack of a background reaction (namely, < 2% conversion) in the absence of the diol–$SnCl_4$ catalyst. The addition of allylboronate **3** to aldehyde **2a** in the presence of 100 mol% of [$SnCl_4$(**1j**)] led only to a modest improvement, from 78 (10 mol% [$SnCl_4$(**1j**)]) to 83% *ee*. These observations suggest that in the case of aliphatic aldehydes the current level of enantioselectivity is not limited by a competitive racemic background reaction, thus superior diols could possibly be found. Satisfactorily, the current conditions were found to be effective for the diastereocontrolled additions of allyl- and crotylboronates to chiral α-methyl aldehyde **9**, thus providing the very useful propionate units of **10** and **11** and dipropionate "triads" of types **12** and **13**

 © 2006 Wiley-VCH Verlag GmbH & Co. KGaA, Weinheim

[Eqs. (1) and (2)]. There has been huge interest in the construction of these units for applications in the total synthesis of bioactive polypropionate natural products.[9] Current methods, however, require chiral allylation reagents to effect a high diastereofacial selective addition (namely, double diastereoselection).[10] Herein, we have demonstrated that diol–$SnCl_4$ catalysis of allylations and *cis*-crotylations of chiral aldehydes can be successfully employed with convenient, stable achiral pinacolate esters. The catalyst was found to exert a strong influence on the diastereofacial selectivity. In both the allylation [Eq. (1)] and *cis*-crotylation with **9** [Eq. (2)], the [$SnCl_4$(**1j**)] catalyst system improved the

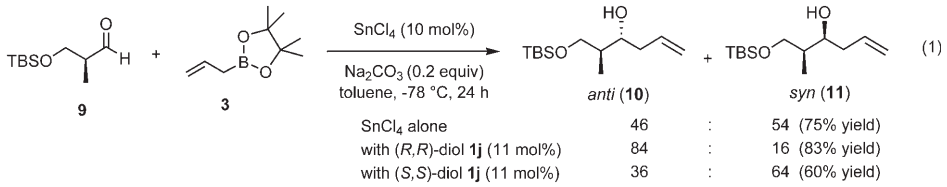

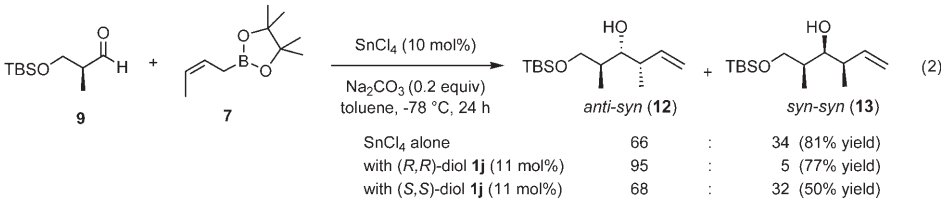

intrinsic selectivity preference of the $SnCl_4$-catalyzed reactions in the matched combination, and even improved the selectivity of the disfavored diastereomer when using the antipode of diol **1j**. For example, selectivity in favor of the *anti–syn* unit **12** was improved from a modest 2:1 ratio to 19:1 using [$SnCl_4${(*R*,*R*)-**1j**}] [Eq. (2)]. For reasons not yet understood, the *trans* crotylations with **5** were less successful, thus giving low conversions, even after 24 h. The [$SnCl_4$(**1j**)]-catalyzed additions of **3** and **7**, however, are particularly impressive considering that pinacol allyl- and crotylboronates react very slowly and unselectively in the absence of a catalyst.[10] Combined with the commercial availability of diol **1j**, this new system is operationally simple and could find immediate use in the diastereoselective construction of several types of propionate units found in bioactive natural products.

The unusual conditions of this allylation system using an insoluble basic additive (Na_2CO_3) warrant a brief mechanistic discussion. We believe that catalysis is due to Brønsted acid activation and not through a Lewis acid activation mechanism, which could possibly occur by the base-promoted formation of tin alkoxides.[11] Indeed, structural studies of the [$SnCl_4$(**1a**)] and [$SnCl_4$(**1j**)] complexes by variable temperature (VT) NMR spectroscopic analysis reveal the same species at −78 °C with or without added Na_2CO_3.[7] This tin(IV) complex does show the presence of activated hydroxy protons and, according to ^{119}Sn NMR shift data, is unambiguously hexacoordinated. The enantioselectivities in the absence of Na_2CO_3 tend to be lower and irreproducible. A soluble base, such as Et_3N, however, shuts down the activating effect of the catalyst. These observations are consistent with a passive role in which the basic additive Na_2CO_3 simply acts as a scavenger of adventitious HCl, which is likely a strong but non-enantioselective activator of this reaction.

This novel chiral Brønsted acid catalyzed enantioselective allylation system constitutes the most efficient catalytic enantioselective allylboration reported thus far. It represents a significant advance that demonstrates the great potential of chiral Brønsted acid catalysis towards the development of an ideal methodology for the allylation of carbonyl compounds. The current diol–$SnCl_4$ catalyst system is readily applicable to catalyst-controlled double diastereoselective allylations to access, with improved selectivities, polypropionate units of the type found in a large number of bioactive natural products.

Received: December 13, 2005
Published online: March 9, 2006

Keywords: allylation · asymmetric synthesis · Brønsted acids · enantioselective catalysis · stereoselectivity

[1] a) S. E. Denmark, N. G. Almstead in *Modern Carbonyl Chemistry* (Ed.: J. Otera), Wiley-VCH, Weinheim, **2000**, chap. 10, pp. 299–402; b) J. W. J. Kennedy, D. G. Hall, *Angew. Chem.* **2003**, *115*, 4880–4887; *Angew. Chem. Int. Ed.* **2003**, *42*, 4732–4739.
[2] S. E. Denmark, J. Fu, *Chem. Rev.* **2003**, *103*, 2763–2793.
[3] Lewis acid catalysis: a) J. W. J. Kennedy, D. G. Hall, *J. Am. Chem. Soc.* **2002**, *124*, 11586–11587; b) T. Ishiyama, T.-a. Ahiko, N. Miyaura, *J. Am. Chem. Soc.* **2002**, *124*, 12414–12415; c) H. Lachance, X. Lu, M. Gravel, D. G. Hall, *J. Am. Chem. Soc.* **2003**, *125*, 10160–10161; d) R. Wada, K, Oisaki, M. Kanai, M. Shibasaki, *J. Am. Chem. Soc.* **2004**, *126*, 8910–8911; Brønsted acid catalysis: e) S. H. Yu, D. G. Hall, *J. Am. Chem. Soc.* **2005**, *127*, 12808–12809.
[4] a) K. Ishihara, M. Kaneeda, H. Yamamoto, *J. Am. Chem. Soc.* **1994**, *116*, 11179–11180; b) S. Nakamura, M. Kaneeda, K. Ishihara, H. Yamamoto, *J. Am. Chem. Soc.* **2000**, *122*, 8120–8130; c) K. Ishihara, S. Nakamura, M. Kaneeda, H. Yamamoto, *J. Am. Chem. Soc.* **1996**, *118*, 12854–12855; d) K. Ishihara, S. Nakamura, H. Yamamoto, *J. Org. Chem.* **1998**, *63*, 6444–6445; e) K. Ishihara, D. Nakashima, Y. Hiraiwa, H. Yamamoto, *J. Am. Chem. Soc.* **2003**, *125*, 24–25.
[5] V. Rauniyar, D. G. Hall, *J. Am. Chem. Soc.* **2004**, *126*, 4518–4519.
[6] a) P. M. Pihko, *Angew. Chem.* **2004**, *116*, 2110–2113; *Angew. Chem. Int. Ed.* **2004**, *43*, 2062–2064; b) C. Bolm, T. Rantanen, I. Schiffers, L. Zani, *Angew. Chem.* **2005**, *117*, 1788–1793; *Angew. Chem. Int. Ed.* **2005**, *44*, 1758–1763.
[7] See the Supporting Information for the full experimental details and spectroscopic data.
[8] The use of several other additives, such as $Ag(SbF_6)$, $AgBF_4$, Cs_2CO_3, $NaHCO_3$, phenol, 2,6-dimethylphenol, and 2,6-diphenylphenol, was attempted but provided a lower selectivity.
[9] I. Paterson, *Pure Appl. Chem.* **1992**, *64*, 1821–1830.
[10] W. R. Roush, A. D. Palkowitz, M. A. Palmer, *J. Org. Chem.* **1987**, *52*, 316–318.
[11] F. Iwasaki, T. Maki, W. Nakashima, O. Onomura, Y. Matsumura, *Org. Lett.* **1999**, *1*, 969–972.

 © 2006 Wiley-VCH Verlag GmbH & Co. KGaA, Weinheim

Oligosaccharide Analysis

DOI: 10.1002/anie.200503168

Identification of a High-Affinity-Binding Oligosaccharide by (+) Nanoelectrospray Quadrupole Time-of-Flight Tandem Mass Spectrometry of a Noncovalent Enzyme–Ligand Complex**

*F. Henning Cederkvist, Alina D. Zamfir, Sven Bahrke, Vincent G. H. Eijsink, Morten Sørlie, Jasna Peter-Katalinić, and Martin G. Peter**

Oligosaccharides are of current interest as targets for the development of novel pharmaceuticals and plant-growth regulators.[1] For example, so-called heterochitooligosaccharides, which are composed of *N*-acetylglucosamine (GlcNAc or A) and glucosamine (GlcN or D), exhibit various biological activities, such as promotion of chondrocyte growth in cell culture, morphogenetic activity in vertebrates, and elicitor action in plants.[2] The entities used for biological studies are usually prepared by enzymatic hydrolysis of the aminoglucan chitosan, clearly yielding intractable, complex mixtures of aminoglucan oligomers. These oligomers differ in their degree of polymerization (DP; number of monomer units), as well as in the mole fraction of A residues (that is, homologues) and in the sequences of D and A residues (that is, isomers).

Despite the fact that several protein–ligand complexes containing GlcNAc homooligomers or enzyme inhibitors have been investigated by protein crystallography[2,3] and ^{1}H NMR spectroscopy,[4] the molecular mechanisms of the biological actions of heterochitooligosaccharides remain essentially unknown as a result of a lack of structural information and the fact that pure ligands are not available. One option for obtaining more information is the use of mass spectrometry (MS), which may be employed for the detection and chemical/structural analysis of noncovalent protein–carbohydrate complexes. In principle, MS-based techniques could provide information on binding stoichiometry and identification of the ligand by fragmentation.[5,6]

We observed earlier that mixtures of A_nD_m heterochitooligosaccharides with a mole fraction of A units (F_A) of 0.5 and a DP of 5 or 6 contain inhibitory compounds with high affinity for the chitinolytic enzyme chitinase B (ChiB), from the soil bacterium *Serratia marcescens*.[5] The apparent IC_{50} value (inhibitory concentration 50%) was about 15 μM, with $(GlcNAc)_2$-4-methylumbelliferone (A_2-MU) as the substrate (Michaelis constant of A_2-MU, $K_m = 30$ μM[7]). Assuming that not all components are inhibitors, the IC_{50} value of the active component must indeed be lower, possibly in the sub-μmol range. The challenge was now to identify a high-affinity binding ligand from a complex oligosaccharide mixture.

Herein, we report on the specificity and stoichiometry of enzyme–ligand recognition, by using (+) nanoelectrospray ionization (nanoESI) MS for analysis of the formation of a noncovalent protein–ligand complex. A novel method based on nanoESI quadrupole time-of-flight collision-induced dissociation tandem mass spectrometry (nanoESI-QTOF-CID MS/MS) was employed for top-down sequencing of the complex-generating fragment ions of the bound ligand. The MS-based method provides an excellent tool for the study of biological complexes,[6,8,9] especially when protein crystallography or NMR spectroscopy cannot be applied.

The choice of nanoESI-QTOF MS was guided by the advantage of using low flow rates for sample infusion[10] in a hybrid system, which combines the simplicity of a quadrupole for precursor-ion selection with the ultrahigh efficiency of an orthogonal acceleration TOF mass analyzer. This system is capable of the simultaneous detection of all analyte (MS mode) and fragment ions (MS/MS mode) across the full mass range with a resolution above 5000 (FWHM). Unlike scanning instruments, the TOF spectrometer performs parallel detection of all masses within a spectrum at high sensitivity and high acquisition rates. This characteristic is important for following the kinetics of noncovalent interactions, as each spectrum is representative of the composition of the infused sample at that point in time.

A fraction of heterochitooligosaccharides was separated by gel-permeation chromatography from an enzymatic hydrolyzate of chitosan, as described previously.[11] Analysis by (+) nanoESI MS revealed a mixture of nine components, which were oligomers and homologues (Figure 1 and Table 1). Major components were D_1A_3 and D_2A_3, while the remaining components were present in minor amounts (<10%). In fact, the mixture is even more complex, as any of the heterooligomers could contain different isomers.

The (+) nanoESI-QTOF mass spectrum of ChiB (Figure 2) revealed the presence of four pseudomolecular ions at charges 13–16, which confirmed, after deconvolution, a molecular weight[12] of 55338.36 ± 2.07 Da. Oligomerization of the protein was not observed in the nanoESI mass spectrum.

The mass spectrum recorded after incubation of ChiB with the chitooligosaccharide mixture for 5 min revealed, besides ChiB, two additional molecular species at charge states 13–15, shifted to masses of 56285.05 Da (major) and

[*] S. Bahrke, Prof. Dr. M. G. Peter
Institut für Chemie
Universität Potsdam
Postfach 601553, 14415 Potsdam (Germany)
Fax: (+49) 331-977-5300
E-mail: peter@chem.uni-potsdam.de
F. H. Cederkvist,[+] Prof. Dr. V. G. H. Eijsink, Dr. M. Sørlie
Department of Chemistry, Biotechnology, and Food Science
Norwegian University of Life Sciences
P.O. Box 5003, 1432 Ås (Norway)
Dr. A. D. Zamfir,[+] Prof. Dr. J. Peter-Katalinić
Institut für Medizinische Physik und Biophysik
Universität Münster
Robert-Koch-Strasse 31, 48149 Münster (Germany)
[+] These authors contributed equally.

[**] This work was supported by the Deutsche Forschungsgemeinschaft (Sonderforschungsbereich 492, project Z2 to J.P.K. and grant Pe 264/18-1 to M.G.P.) and by the Norwegian Research Council (grant 140497/420 to M.S. and V.G.H.E.)

Supporting information for this article is available on the WWW under http://www.angewandte.org or from the author.

 © 2006 Wiley-VCH Verlag GmbH & Co. KGaA, Weinheim

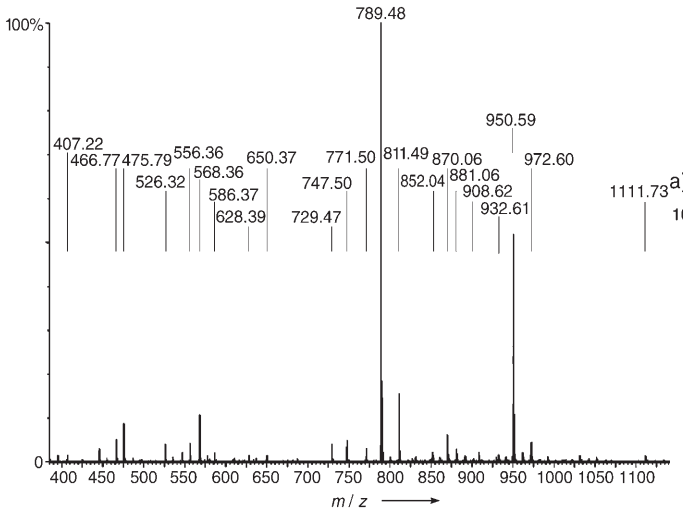

Figure 1. (+) NanoESI-QTOF MS of the chitooligosaccharide fraction used for incubation with ChiB. Solvent: 10 mM ammonium acetate/formic acid (pH 6.0); average sample concentration: 2 pmol μL^{-1}; capillary nanoESI voltage: 900 V; sampling cone potential: 30–40 V.

Table 1: Oligomers and homologues present in the heterochitooligosaccharide fraction.

m/z	Assignment[a]
407.22 $[M-H_2O+2H]^{2+}$	A_4
526.32 $[M-H_2O+2H]^{2+}$	D_4A_2
586.37 $[M+H]^+$; 608.46 $[M+Na]^+$	D_1A_2
628.39 $[M+H]^+$; 650.37 $[M+Na]^+$	A_3
747.50 $[M+H]^+$; 729.47 $[M-H_2O+H]^+$	D_2A_2
789.48 $[M+H]^+$; 811.49 $[M+Na]^+$	D_1A_3
908.62 $[M+H]^+$; 890.73 $[M-H_2O+H]^+$	D_3A_2
950.59 $[M+H]^+$; 972.60 $[M+Na]^+$;	D_2A_3
475.79 $[M+2H]^{2+}$; 466.77 $[M-H_2O+2H]^{2+}$	
1111.73 $[M+H]^+$; 556.36 $[M+2H]^{2+}$	D_3A_3

[a] A: 2-acetamido-2-deoxy-D-glucopyranosyl monosaccharide unit; D: 2-amino-2-deoxy-D-glucopyranosyl monosaccharide unit in chitooligosaccharides.

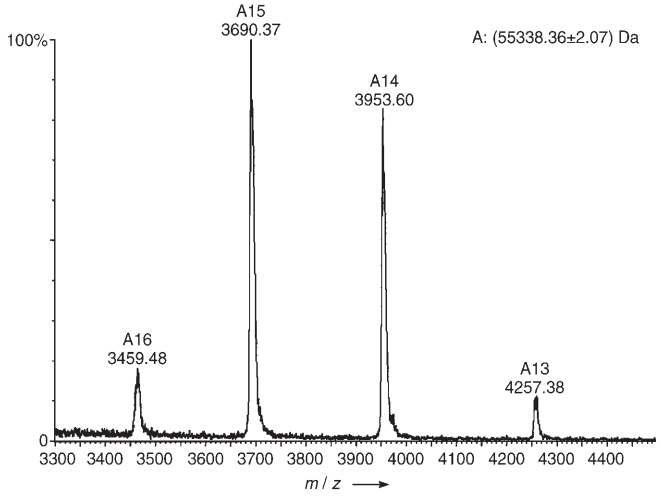

Figure 2. (+) NanoESI-QTOF MS of ChiB. Solvent: 10 mM ammonium acetate/formic acid (pH 6.0); concentration: 3 pmol μL^{-1}; capillary nanoESI voltage: 1 kV; sampling cone potential: 80–100 V; A*n*: $[M+nH]^{n+}$ ion of ChiB.

56124.25 Da (minor) (Figure 3a), which indicates complexation of ChiB with the oligomers D_2A_3 and D_1A_3, respectively. Figure 3b shows a spectrum of the complex measured after incubation for 90 min, in which a third peak appeared at

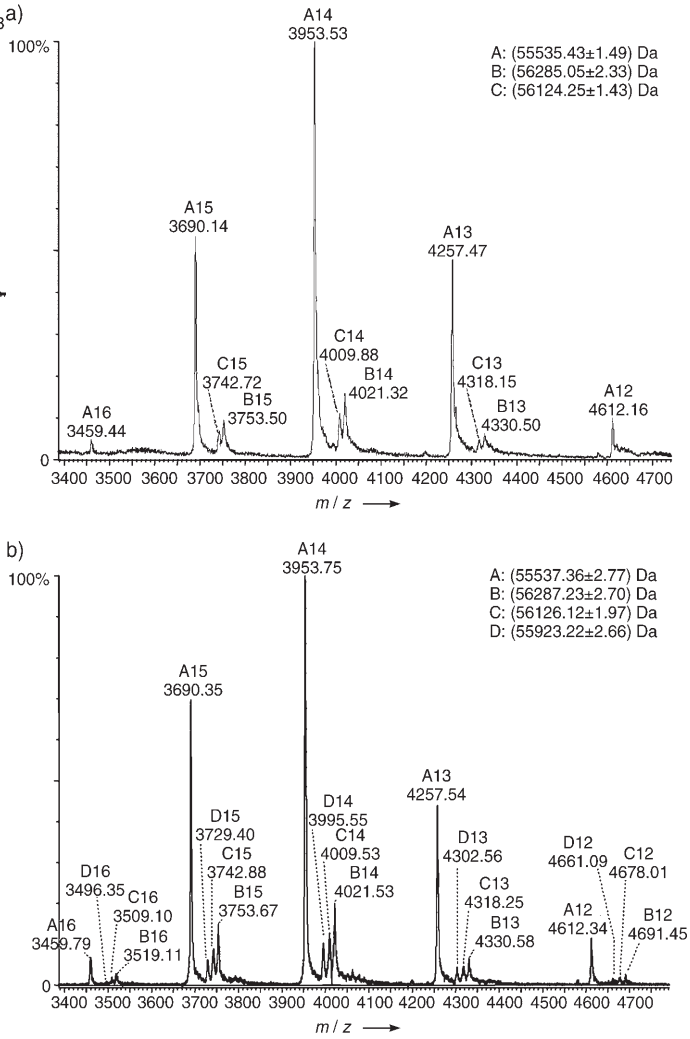

Figure 3. (+) NanoESI-QTOF MS of the ChiB/chitooligosaccharide incubation mixture. Solvent: 10 mM ammonium acetate/formic acid (pH 6.0); capillary nanoESI voltage: 1.0 kV; sampling cone potential: 100 V; incubation at 37°C. a) After 5 min incubation; b) after 90 min incubation. A*n* = $[M+nH]^{n+}$ ion of ChiB (calculated mass of A: 55338.1 Da); B*n* = $[M+nH]^{n+}$ ion of ChiB-D_2A_3 (calculated mass of B: 56287.5 Da); C*n* = $[M+nH]^{n+}$ ion of ChiB-D_1A_3 (calculated mass of C: 56128.6 Da); D*n* = $[M+nH]^{n+}$ ion of ChiB-D_1A_2 (calculated mass of D: 55923.3 Da).

55923.22 Da corresponding to the ChiB-D_1A_2 complex. The mass spectrum recorded after incubation of ChiB with the chitooligosaccharide mixture for 180 min revealed that the relative ion abundance of the complexes did not change, thus documenting a kinetic equilibrium of the species in the solution. The binding of the trisaccharide D_1A_2 to ChiB is interesting, as this compound was present at low levels ($\leq 5\%$) in the original mixture (Figure 1 and Table 1).

A CID experiment was carried out on the ChiB–D_2A_3 complex, with the B^{14+} molecular ion at *m/z* 4021.51 as a

 © 2006 Wiley-VCH Verlag GmbH & Co. KGaA, Weinheim

precursor (Figure 4a). Two events, namely the breakdown of the protein–sugar complex and the fragmentation of the released D_2A_3 pentasaccharide ligand, took place (Figure 4a).

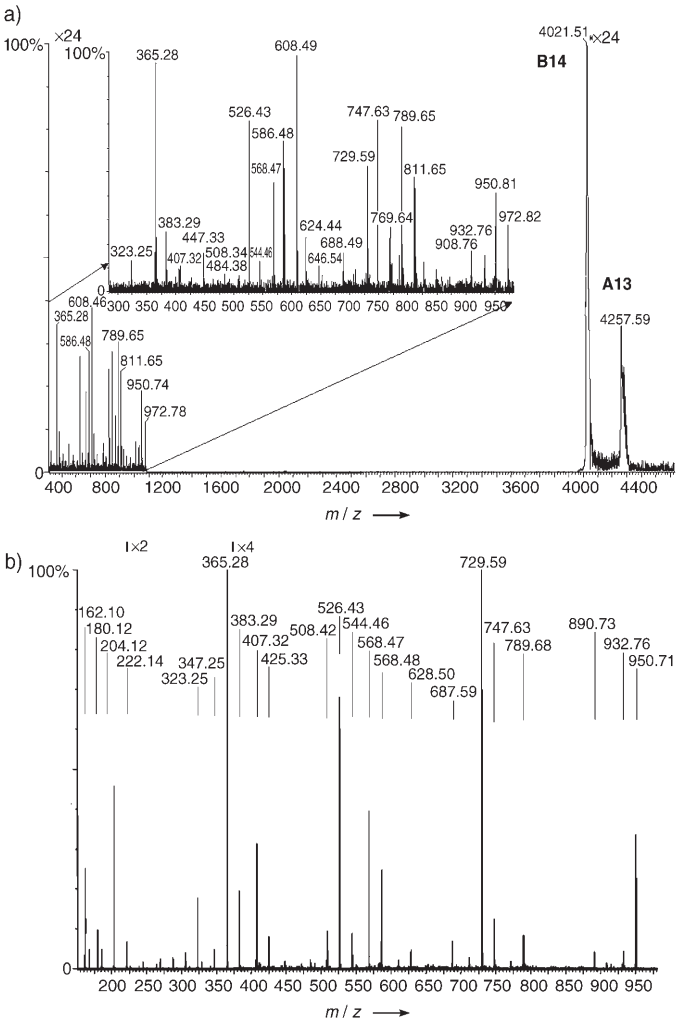

Figure 4. a) CID MS/MS analysis of the ChiB–D_2A_3 noncovalent complex detected as the $[M+14\,H]^{14+}$ ion at m/z 4021.51. Solvent: 10 mM ammonium acetate/ammonia (pH 6.0); incubation: 90 min at 37 °C; capillary nanoESI voltage: 1.0 kV; sampling cone potential: 100 V; signal acquisition: 100 min, 2850 scans over collision energies between 8 and 15 eV; collision-gas pressure $P_{lab}=10$–12 psi. Inset: zoom out of the 350–975 m/z range. b) CID MS/MS of the singly charged ion at m/z 950.71 of D_2A_3 present in the original heterooligosaccharide mixture. Solvent: 10 mM ammonium acetate/formic acid (pH 6.0); concentration: 2 pmol μL^{-1}; capillary nanoESI voltage: 900 V; sampling cone potential: 30 V; collision energy: 30–50 eV; collision-gas pressure $P_{lab}=15$ psi.

Permutation of the monosaccharide units in the D_2A_3 pentamer shows that ten isomeric sequences exist (Table 2). CID MS/MS provided diagnostic fragment ions (Table 3), which can be used to deduce the sequence of the pentameric ligand that was stably bound to ChiB. According to the fragmentation pattern obtained in the top-down experiment, sequences 1 and 3 must be excluded, as no A_3 triad fragment ions were obtained in the top-down spectrum. In contrast, the

Table 2: The ten possible sequences of D_2A_3.

Identification number	Sequence	Identification number	Sequence
1	AAADD	6	AADDA
2	DAAAD	7	DAADA
3	DDAAA	8	ADADA
4	AADAD	9	ADDAA
5	ADAAD	10	DADAA

A_3 fragment ion and its dehydrated counterpart are present in the MS/MS spectrum of D_2A_3 in the heterosaccharide mixture (Figure 4b and Table 3). This result strongly suggests that the enzyme selectively binds from the mixture a D_2A_3 isomer that does not contain the AAA sequence. Sequence 2 is excluded because D_2A_1 and D_2A_2 fragment ions cannot arise from this isomer. The presence of the highly abundant fragment ion at m/z 526.43 corresponding to D_2A_1 excludes the sequences 5 and 7. Furthermore, D_1A_3 cannot be formed from the sequences 6, 8, and 9.

The ion at m/z 323.25 could principally be formed as a dyad D_2 from sequences 1, 3, and 9. However, comparison of Figure 4a and b shows that in the top-down spectrum this ion has low abundancy and, unlike the pentamer sequenced from the mixture, it is not accompanied by further loss of H_2O. This feature, along with the clear-cut exclusion of the sequences 1, 3, and 9, demonstrates that the D_2 fragment is generated in the top-down experiment either by the loss of an acetyl group from other fragment ions, for example from the abundant D_1A_1 ion, or by cleavage of the 0–4 ring bond of the DA fragment in either of the monosaccharides. The sequences 4 and 10 are indistinguishable by MS/MS as no diagnostic fragment ion supporting one or the other can be obtained. However, detailed studies of the degradation of chitosans by ChiB have shown that isomer sequence 4 is an excellent substrate for ChiB (cleavage between AA and DAD),[13] thus leading to the conclusion that the pentamer that is stably bound to ChiB must be the pentasaccharide DADAA (sequence 10).

The first investigation of a noncovalent enzyme–oligosaccharide complex by ESI MS was reported by Ganem for lysozyme and the GlcNAc homohexamer.[14] In the present study, complex mixtures of chitooligosaccharides were analyzed with respect to their binding to the chitinolytic enzyme ChiB. The structure and mechanism of catalysis of this chitinase are known in detail. The enzyme is a family 18 *exo*-glycosidase, which contains three sugar-binding sites, numbered −1 to −3, at the glycon side.[3a,15] Hydrolysis of GlcNAc homooligomers yields A_2 (substrate DP = 4) and A_3 (substrate DP = 4), the latter being cleaved further into A_1 and A_2.[7,16] Catalysis proceeds through anchimeric nucleophilic assistance of the acetyl group to give an oxazolinium ion as the crucial intermediate. Therefore, the presence of an A residue at the −1 glycon subsite of the fissile bond was shown to be required for an efficient hydrolysis.[3a,13,16] No exclusive structural requirement is posed for the first aglycon subsite (+1), whereas the −2 glycon subsite has a strong but not absolute preference for an A residue.[13]

The K_m values of chitinases have been determined with A_n homooligomers in a few cases. They are generally in the

 © 2006 Wiley-VCH Verlag GmbH & Co. KGaA, Weinheim

Table 3: Assignment of peaks [*m*/*z*] detected in the CID MS/MS analyses of the ChiB–D_2A_3 complex and the original D_2A_3 fraction (see Figures 4a and b, respectively).

Fragment	In top-down CID MS/MS	In CID MS/MS of original D_2A_3
D	not considered	162.10 $[D-H_2O+H]^+$; 180.12 $[D+H]^+$
A	not considered	204.12 $[A-H_2O+H]^+$; 222.14 $[A+H]^+$
D_2	323.25	323.25 $[D_2-H_2O+H]^+$; 305.48 $[D_2-2H_2O+H]^+$
D_1A_1	365.28; 383.29	347.25 $[D_1A_1-2H_2O+H]^+$; 365.28 $[D_1A_1-H_2O+H]^+$; 383.29 $[D_1A_1+H]^+$
A_2	407.32; 447.33 $[A_2+Na]^+$	407.32 $[A_2-H_2O+H]^+$; 425.33 $[A_2+H]^+$
D_2A_1	508.34; 526.43	508.42 $[D_2A_1-2H_2O+H]^+$; 526.43 $[D_2A_1-H_2O+H]^+$; 544.46 $[D_2A_1+H]^+$
D_1A_2	568.47; 586.48; 608.49 $[D_1A_2+Na]^+$	568.47 $[D_1A_2-H_2O+H]^+$; 586.48 $[D_1A_2+H]^+$
A_3	absent	628.50 $[A_3+H]^+$; 610.46 $[A_3-2H_2O+H]^+$
D_2A_2	688.49 $[D_2A_2-HOAc+H]^+$; 729.59; 747.63; 769.64 $[D_2A_2+Na]^+$	687.59 $[D_2A_2-HOAc+H]^+$; 729.59 $[D_2A_2-H_2O+H]^+$; 747.63 $[D_2A_2+H]^+$
D_1A_3	789.65; 811.65 $[D_1A_3+Na]^+$	789.68 $[D_1A_3+H]^+$
D_2A_3	908.76 $[M-HOAc+H]^+$; 932.76; 950.81; 972.82 $[M+Na]^+$	890.73 $[M-H_2O-HOAc+H]^+$; 932.76 $[M-H_2O+H]^+$; 950.71 $[M+H]^+$

low μmol range for the hexamer of GlcNAc and roughly one order of magnitude higher for the lower oligomers.[17] The K_m value of heterochitooligosaccharides is not known for any chitinases. In our study, we found that ChiB binds particular components out of a complex mixture of chitooligosaccharides. The results allow conclusions on the specificity of ligand selection from complex mixtures and on the stoichiometry of binding. The formation of noncovalent complexes occurs fast with the tetra- and pentamers D_1A_3 and D_2A_3, whereas binding of the trimer D_1A_2 is observed only after prolonged incubation. A priori, this finding is expected as, in general, the affinity of polysaccharide-cleaving enzymes for oligosaccharides increases with the chain length.[18] Nevertheless, detection of the D_1A_2 complex is surprising, as the trimer would bind with lower affinity than the higher oligomers.

Most likely, the concentration of D_1A_2 could be increased during the incubation because of productive binding of other oligomers and even of DADAA (sequence 10), which could be cleaved very slowly at the fissile A–D glycosidic bond (Scheme 1). On the other hand, the high-affinity, nonproductive binding of sequence 10 (occupying subsites −3 to +2, that is, with a D position in the crucial −1 subsite and a highly favorable A position in the subsite −2) would result in the observed[5] competitive enzyme inhibition, because the crucial oxazolinium ion intermediate cannot be formed.

In summary, we have shown that: 1) a carbohydrate-binding enzyme selects ligands binding with high affinity from a complex mixture of closely related oligosaccharides; 2) identification of a heterooligosaccharide in a noncovalent protein–ligand complex is feasible by top-down sequencing in combination with sequence analysis of the components present in the original complex mixture; and 3) the mechanism of enzyme inhibition can be conclusively deduced by combination of knowledge on the mechanism of catalysis and structure identification of an oligosaccharide ligand binding with high affinity. NanoESI MS and fragmentation of the

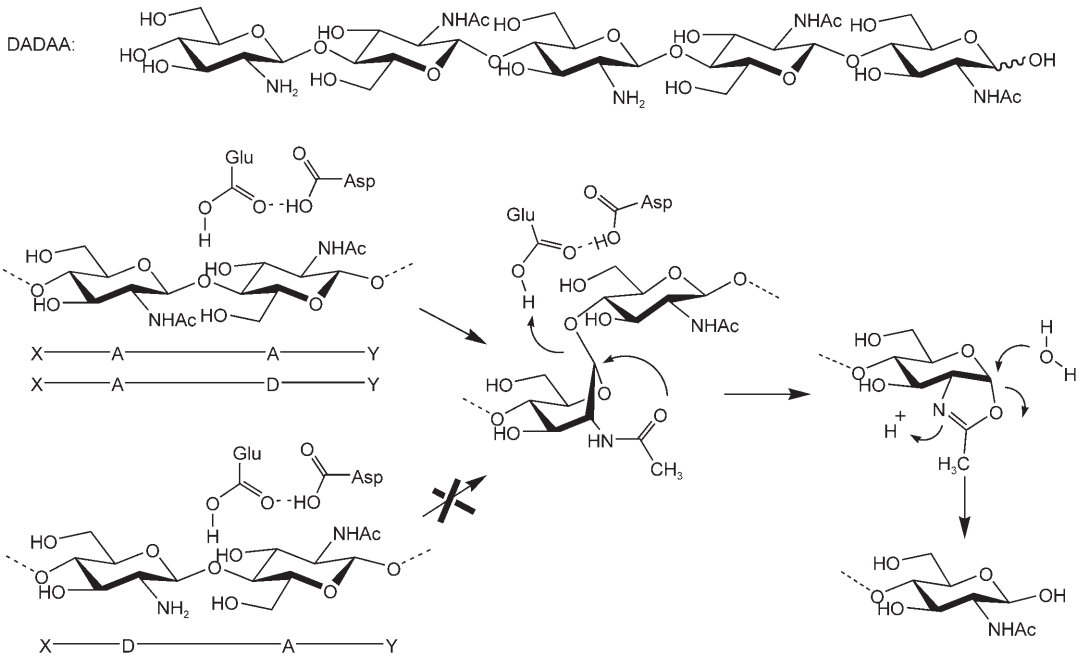

Scheme 1. Structure of DADAA (sequence 10), mechanism of glycoside bond hydrolysis by a family of 18 chitinases, and competitive inhibition by nonproductive binding of sequence 10.

 © 2006 Wiley-VCH Verlag GmbH & Co. KGaA, Weinheim

specific sequence of the bound ligand by CID MS/MS is presented as a powerful tool of general applicability in functional proteomics and glycomics.

Experimental Section

For preparation of the chitooligosaccharides, the lyophilized product (F_A 0.63; 2.16 g) of an enzymatic hydrolyzate of chitosan[11] was dissolved in ammonium acetate buffer (0.05 M, 180 mL, pH 4.2). The solution was filtered sequentially through 0.8- and 0.2-μm cellulose acetate membranes (Schleicher & Schuell) and a 3000-Da cut-off membrane (Amicon), and the filtrate was lyophilized. The residue was subjected to gel-permeation chromatography (GPC) on a 5 × 200-cm Biogel P4 column (fine grade; BioRad) with ammonium acetate buffer (0.05 M, adjusted to pH 4.2 with 0.23 M acetic acid) as the mobile phase (flow rate 60 mL h^{-1}) and refractive index detection (Shimadzu RID 6A). Collected fractions (20 mL) were appropriately combined, then concentrated to a small volume by rotary evaporation, and finally lyophilized.

Wild-type ChiB from *Serratia marcescens* was overexpressed in *Escherichia coli* and purified as described elsewhere.[7] The protein was > 95% pure, as determined by SDS-PAGE. Stock solutions of ChiB and heterochitooligosaccharides were mixed and diluted with stirring at 800 rpm and 37 °C to give final concentrations of 3.0 pmol μL^{-1} of protein and 60 pmol μL^{-1} of oligosaccharide in ammonium acetate buffer (10 mM, pH 6.0). The oligosaccharide concentrations were calculated by using an average molecular mass of 1000 Da. Aliquots were collected after 5, 30, 90, and 180 min and kept on ice prior to MS analysis. Calibration of mass spectra was achieved with a mixture of dextran oligomers, obtained from the Department of Physical Chemistry, University of Wageningen, The Netherlands. The reference sample provided ions over a broad m/z range, as required for MS and CID MS/MS top-down analysis.

MS experiments were conducted in the positive-ion mode on an orthogonal hybrid QTOF mass spectrometer (QTOF Micromass, Manchester, UK) equipped with a nanoESI ion source positioned in the Micromass Z-spray geometry. The QTOF mass spectrometer was interfaced to a personal computer running the MassLynx software to control the instrument, and to acquire, process, and deconvolute the mass spectra. The ESI capillary, sampling cone potentials, and desolvation gas were optimized to promote efficient ionization, hinder the in-source fragmentation, and ensure maximal ion transfer into the MS quadrupole analyzer. For all experiments the ion-source temperature was set at 80 °C and the desolvation gas was used at a flow rate of 50 L h^{-1}. The ESI-QTOF MS system was programmed to record the MS and MS/MS signals at a scan speed of one scan per 2.1 s.

Top-down analysis of the protein–ligand complex was performed by CID at low energy, with argon as collision gas. The experiment started by tuning the instrument for assessing the possibility of isolating the precursor ion: the low- and high-mass resolution of the quadrupole for isolation were set to 6 and 8, respectively; the ion acceleration voltage and collision gas pressure were set to 0. Ten MS/MS scans were acquired under these conditions, and the ion at m/z 4021.51 was detected as a single peak in the tandem mass spectrum. For fragmentation, the gas pressure was set to 10 psi and the ion acceleration energy was increased stepwise during continuous signal acquisition. The spectra combined across the total ion current recorded for different energies below 7–8 eV show that no complex dissociation occurred. At a collision energy of 8 eV in the product ion spectrum the abundant $[M+14\,H]^{14+}$ precursor ion at m/z 4021.51, the low abundant $[M+13\,H]^{13+}$ protein ion at m/z 4257.59, and peaks at low m/z values corresponding to the detached intact D_2A_3, in its sodiated and dehydrated forms, were detected. The sequencing of the ligand was obtained by adjusting the gas pressure to 12 psi (P_{lab}), with long (2850 scans) signal acquisition at 9–10 eV for generating large (tetramer) and medium-sized (trimer) fragment ions, and shorter signal acquisition (approximately 50 scans) at 15 eV to induce severe fragmentation for generating dimer fragments. By summing all 2850 scans acquired at collision energies between 8 and 15 eV and 10–12 psi Ar pressure, all fragment ions generated by the succession of induced dissociation events were displayed in a single spectrum (Figure 4a).

Received: September 6, 2005
Revised: January 10, 2006
Published online: March 9, 2006

Keywords: enzymes · hydrolases · mass spectrometry · oligosaccharides · sequence determination

[1] *Carbohydrates in Chemistry and Biology*, *Part II*, *Vol. 4: Lectins and Saccharide Biology* (Eds.: B. Ernst, G. W. Hart, P. Sinaÿ), Wiley-VCH, Weinheim, **2002**.
[2] For a review, see: M. G. Peter in *Biopolymers*, *Vol. 6: Polysaccharides II* (Ed.: A. Steinbüchel), Wiley-VCH, Weinheim, **2002**, pp. 481–574.
[3] a) D. M. F. van Aalten, D. Komander, B. Synstad, S. Gaseides, M. G. Peter, V. G. H. Eijsink, *Proc. Natl. Acad. Sci. USA* **2001**, *98*, 8979–8984; b) Y. Papanikolau, G. Prag, G. Tavlas, C. E. Vorgias, A. B. Oppenheim, K. Petratos, *Biochemistry* **2001**, *40*, 11338–11343; c) D. R. Houston, K. Shiomi, N. Arai, S. Omura, M. G. Peter, A. Turberg, B. Synstad, V. G. H. Eijsink, D. M. F. van Aalten, *Proc. Natl. Acad. Sci. USA* **2002**, *99*, 9127–9132; d) E. Bokma, H. J. Rozeboom, M. Sibbald, B. W. Dijkstra, J. J. Beintema, *Eur. J. Biochem.* **2002**, *269*, 893–901; e) F. V. Rao, D. R. Houston, R. G. Boot, J. Aerts, S. Sakuda, D. M. F. van Aalten, *J. Biol. Chem.* **2003**, *278*, 20110–20116; f) D. R. Houston, A. D. Recklies, J. C. Krupa, D. M. F. van Aalten, *J. Biol. Chem.* **2003**, *278*, 30206–30212; g) G. Vaaje-Kolstad, A. Vasella, M. G. Peter, C. Netter, D. R. Houston, B. Westereng, B. Synstad, V. G. H. Eijsink, D. M. F. van Aalten, *J. Biol. Chem.* **2004**, *279*, 3612–3619.
[4] a) T. Ikegami, T. Okada, M. Hashimoto, S. Seino, T. Watanabe, M. Shirakawa, *J. Biol. Chem.* **2000**, *275*, 13654–13661; b) A. Germer, C. Mügge, M. G. Peter, A. Rottmann, E. Kleinpeter, *Chem. Eur. J.* **2003**, *9*, 1964–1973.
[5] M. C. Letzel, B. Synstad, V. G. H. Eijsink, J. Peter-Katalinić, M. G. Peter, *Adv. Chitin Sci.* **2000**, *4*, 545–552.
[6] W. Wang, E. N. Kitova, J. S. Klassen, *Anal. Chem.* **2003**, *75*, 4945–4955.
[7] M. B. Brurberg, I. F. Nes, V. G. H. Eijsink, *Microbiology* **1996**, *142*, 1581–1589.
[8] S. A. Hofstadler, R. H. Griffey, *Chem. Rev.* **2001**, *101*, 377–390.
[9] A. J. R. Heck, R. H. H. van der Heuvel, *Mass Spectrom. Rev.* **2004**, *23*, 368–389.
[10] K. Benkestock, G. Sundqvist, P. O. Edlund, J. J. Roeraade, *J. Mass Spectrom.* **2004**, *39*, 1059–1067.
[11] S. Bahrke, J. M. Einarsson, J. Gislason, S. Haebel, M. C. Letzel, J. Peter-Katalinić, M. G. Peter, *Biomacromolecules* **2002**, *3*, 696–704.
[12] M. B. Brurberg, V. G. H. Eijsink, A. J. Haandrikman, G. Venema, I. F. Nes, *Microbiology* **1995**, *141*, 123–131.
[13] A. Sørbotten, S. J. Horn, V. G. H. Eijsink, K. M. Vårum, *FEBS Lett.* **2005**, *579*, 538–549.
[14] B. Ganem, *J. Am. Chem. Soc.* **1991**, *113*, 7818–7819.
[15] D. M. F. van Aalten, B. Synstad, M. B. Brurberg, E. Hough, B. W. Riise, V. G. H. Eijsink, R. K. Wierenga, *Proc. Natl. Acad. Sci. USA* **2000**, *97*, 5842–5847.
[16] K. Suzuki, N. Sugawara, M. Suzuki, T. Uchiyama, F. Katouno, N. Nikaidou, T. Watanabe, *Biosci. Biotechnol. Biochem.* **2002**, *66*, 1075–1083.

 © 2006 Wiley-VCH Verlag GmbH & Co. KGaA, Weinheim

[17] a) E. Bokma, T. Barends, A. C. Terwisscha van Scheltinga, B. W. Dijkstra, J. J. Beintema, *FEBS Lett.* **2000**, *478*, 119–122; b) T. Hollis, Y. Honda, T. Fukamizo, E. Marcotte, P. J. Day, J. D. Robertus, *Arch. Biochem. Biophys.* **1997**, *344*, 335–342.
[18] E. W. Thomas, J. F. McKelvy, N. Sharon, *Nature* **1969**, *222*, 485–486.

 © 2006 Wiley-VCH Verlag GmbH & Co. KGaA, Weinheim

Monodispersed Materials

DOI: 10.1002/anie.200503253

Particle-Size Control and Surface Structure of the Cubic Mesocaged Material AMS-8**

Alfonso E. Garcia-Bennett, Kristina Lund, and Osamu Terasaki*

Mesoporous materials,[1] which are ordered porous structures with siloxane-bridged amorphous walls, are a family of nanoporous solids with several extremely attractive features that allow them to host molecules of various shapes, sizes, and functionalities.[2] Much research effort has been devoted to extending the number of available mesostructures by varying the templating surfactant and synthetic conditions as well as to extending their compositional range and surface functionality.[3–5] Only recently, and as a result of the numerous potential applications that have been reported for these versatile silicates, has attention shifted towards the control of morphological features, which can be achieved through an understanding of crystal-growth mechanisms.

It has already been shown that the shape and form of nanoparticles often determine their function and utility, often with extreme changes in physicochemical properties.[6] Mesoporous silica morphologies that have been obtained include fibers, toroids, spiral shapes, discoids, gyroids, and hollow and solid spheres.[7] It has recently been beautifully demonstrated by Lin et al.[8] that the cubic morphology of mesocaged solid SBA-1 can be varied from cubes to rhombic dodecahedra and spheres simply by controlling the hydrolysis and condensation rates of the silica source under acid conditions in an aqueous synthesis. El-Safty and Hanaoka[9] have also reported the synthesis of large-pore (ca. 10 nm), monolithic mesostructures, whilst thin films of mesoporous materials have been prepared by the use of evaporation-induced self-assembly (EISA) methods by Sanchez and co-workers.[10]

A novel synthetic route to mesoporous silicates using anionic surfactants derived from *N*-acylamino acids has been reported that involves the use of the co-structure-directing agents (CSDA) *N*-trimethoxysilylpropyl-*N*,*N*,*N*-trimethylammonium chloride (TMAPS) and (3-aminopropyl)trimethoxysilane (APS) under alkaline conditions.[11] These mesoporous structures are synthetically interesting not only due to the interaction between the surfactants' carboxylic acid moiety and the CSDA, but also for their structural diversity, chiral properties, and the opportunity to functionalize the pore surface by removing the surfactant by solvent extraction.[12–14] This family of materials has been named AMS-*n* (anionic-templated mesoporous silicas). The mechanism has been generalized as $S^-N^+ \approx I^-$, where S^- is the surfactant, N^+ represents the positively charged amine moiety in the aminosilane group, and I^- the condensing silica framework. Several novel mesocaged structures have also been prepared using the surfactant *N*-lauroylglutamic acid (C12GlutA), whose large headgroup area favors the formation of spherical micelles. The structure of the cubic mesocaged material AMS-8 can be described as composed of bimodal spherical cages arranged with $Fd\bar{3}m$ symmetry. Both large and small cages are interconnected by small connecting windows, which makes them ideal for the confinement of guest compounds.[15]

The control of morphology in mesoporous materials is thought to be governed by kinetic effects as the self-assembly of surfactant molecules and nucleation processes occur simultaneously as a result of the hydrolysis of the silica source, usually tetraethyl orthosilicate (TEOS), into small silicate oligomers. The particle-growth process is dominated by the condensation of these oligomers. Co-condensation with organic functional groups in the form of organoalkoxysilanes has been identified as an important parameter in the formation of different particle morphologies in MCM-41, and a proposed mechanism based on the intercalation of the hydrophobic groups of organoalkoxysilanes between the micellar headgroups has been proposed.[16] We recently suggested that this proposed mechanism can be extended to explain the structural transformations observed on addition of increasing amounts of co-condensing agents and on delayed addition of the silica source with respect to the organoalkoxysilanes.[14,17]

Alternative explanations for time-dependent structural changes have been formulated that take into account depletion or reduction in the concentration of co-surfactant (co-structure-directing agents) in the synthesis gel not incorporated into the growing mesophase.[18] A double surfactant system made up of a cationic and a nonionic polymeric surfactant has been used by Imai et al.[19] for the controlled growth of silica particles but resulted in poorly defined morphologies and agglomerates. In the present study we attempt to control the diffusion of these silicate oligomers in

[*] Dr. A. E. Garcia-Bennett,[+] K. Lund, Prof. O. Terasaki
Structural Chemistry
Arrhenius Laboratory, Stockholm University
10691 Stockholm (Sweden)
E-mail: alfonso.garcia@angstrom.uu.se

[+] Present address: Nanotechnology and Functional Materials
Department of Engineering Sciences
The Ångström Laboratory
Uppsala University
Box 534, 75121 Uppsala (Sweden)
Fax: (+46) 1850-0131

[**] We are grateful to Dr. Mika Linden for helpful discussions. This work was partly supported by the Swedish Science Council (VR) and Core Research for Evolutional Science and Technology (CREST) of JST and BNRI, Japan (O.T.).

Supporting Information for this article is available on the WWW under http://www.angewandte.org or from the author.

InterScience
© 2006 Wiley-VCH Verlag GmbH & Co. KGaA, Weinheim

the synthesis gel by addition of a triblock copolymer surfactant (P123) at temperatures above its cloud point, where interaction with silicate species is not expected. This polymer acts by dispersing the nucleation sites and therefore limits the diffusion of silicate oligomers through the synthesis gel. The structural and morphological properties of the mesoporous materials prepared are discussed in terms of the "crystal" growth mechanism and surface structure of the cubic mesocaged solid.

Table 1: Structural and porous properties of AMS-8(x) mesocaged solids.

AMS-8(x) $x=$	Unit-cell parameter [Å][a]	Unit-cell parameter [Å][b]	Pore-size distribution [Å][c]	Total pore volume [$cm^3 g^{-1}$]	Surface area [$m^2 g^{-1}$]	Average particle size [nm]
0	162.6	154.9	40.3	0.57	687.0	–
70	151.7	148.4	40.3	0.51	623.8	1300
12.5	150.0	151.3	40.3	0.73	603.7	700
9	154.5	151.6	40.3	0.83	684.3	100
6	153.3	154.8	40.3	1.03	720.0	15

[a] Determined by TEM. [b] Determined by XRD. [c] Determined by DFT.

The samples in this report are denoted AMS-8(x), where x is the C12GlutA/P123 molar ratio in the synthesis gel. Powder X-ray diffraction (XRD) patterns of calcined AMS-8 and AMS-8(x) samples are shown in Figure 1. All spectra contain

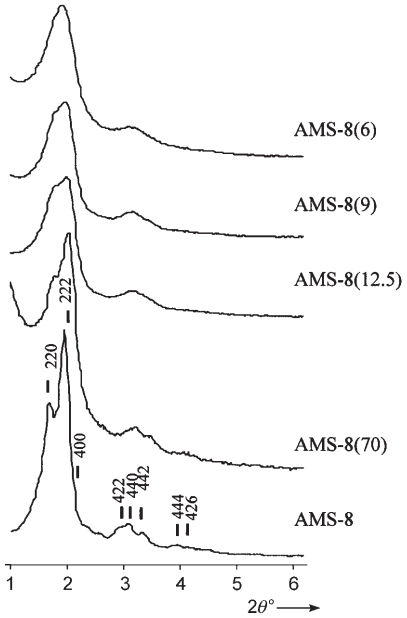

Figure 1. XRD patterns of calcined samples of mesocaged silicate AMS-8 prepared by addition of different amounts of P123 triblock copolymer to the synthesis gel.

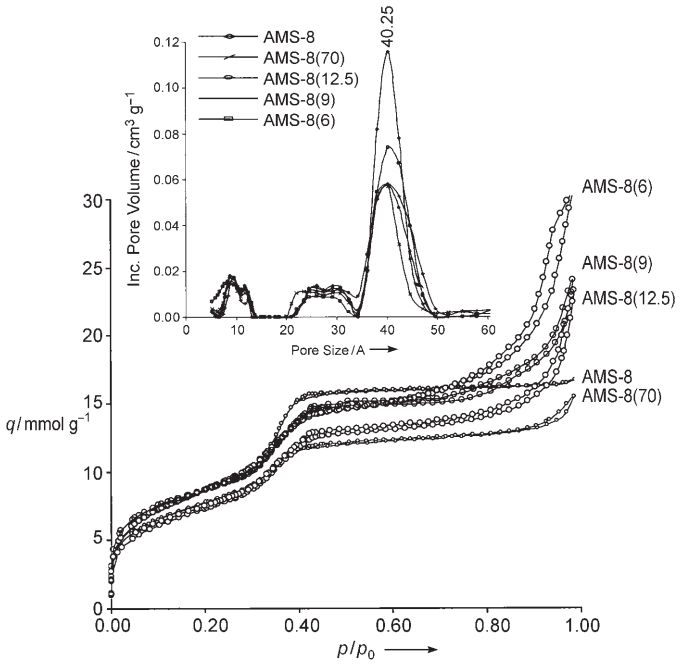

Figure 2. Nitrogen adsorption–desorption isotherms of calcined cubic mesocaged material and related structures synthesized by addition of P123. Pore-size distribution curves (inset; plotted against the increase in pore volume) were derived with the NLDFT software provided by Micromeritics and by assuming the Tarazona model for spherical cavities.[20]

peaks at low angles consistent with a mesoscopic order. The patterns can be indexed on the basis of a cubic unit cell with $Fd\bar{3}m$ symmetry; however, it is evident that on addition of further P123 surfactant the peaks broaden considerably and less-resolved patterns are obtained. There is no apparent variation in the unit-cell parameters on addition of further surfactant, as calculated directly from the 222 reflection in the XRD pattern. The structural and porous parameters of the samples are summarized in Table 1.

Nitrogen adsorption–desorption isotherms of AMS-8 and AMS-8(x) samples are shown in Figure 2. All curves are type-IV isotherms typical of mesoporous materials and are characterized by a sharp capillary condensation step as a result of filling of the mesocages in the relative pressure range $p/p_0 = 0.3$–0.4. There is no evidence of microporosity from the t-plot curves (not shown).

Pore-size-distribution curves, as derived by the NLDFT method, show that there is little change in cage size on addition of the polymeric surfactant P123 to the synthesis gel. The BET surface areas for these materials are typical of mesocaged solids, with the highest (720.0 $m^2 g^{-1}$) being that of AMS-8(6) (Table 1). There is only a small increase in BET specific surface area on addition of increased amounts of P123 to the synthesis gel; the increase for AMS-8(6) corresponds to 5.0% relative to conventional AMS-8. However, there are marked differences in the total pore volume (V_{tot}) adsorbed, as can be seen by the sharp, hysteretic rise in nitrogen uptake for AMS-8(x) in comparison with conventional AMS-8 (Figure 2). Samples synthesized in the presence of P123 show a lower initial nitrogen uptake in the pressure range $p/p_0 = 0.2$–0.6, followed by a rise in adsorption at higher pressures, presumably as a result of adsorption in cavities or pores between the particles. An increase of 40.6% in V_{tot} is

 © 2006 Wiley-VCH Verlag GmbH & Co. KGaA, Weinheim

observed for AMS-8(6) in comparison to conventional AMS-8.

transmission electron microscopy (TEM) images of calcined samples of AMS-8(12.5), AMS-8(9), and AMS-8(6) are shown in Figure 3. All samples, except AMS-8(6), consist of highly ordered monodispersed particles. The Fourier transform diffractograms (not shown) confirm the structure and symmetry of the samples as cubic $Fd\bar{3}m$. The unit-cell parameters derived from the TEM data are consistent with those estimated from small-angle powder XRD patterns. The average particle size, estimated from TEM observations, decreased with increasing addition of P123 to the synthesis gel. Monodispersed facetted particles, with an average particle size of 100 nm, can be observed in sample AMS-8(9). Particles with some degree of structural defects associated with the AMS-8 cubic $Fd\bar{3}m$ structure were observed for all samples (see Figure 3). However, high mesoscopic order is observed to the very edge of the particle. As the particle size decreases, the structural "origins" of these defects can be clearly observed by TEM analysis. Figure 3C shows a TEM image recorded along the [110] direction of AMS-8(9). Structural defects of the stacking-fault type that result in surface-morphology features parallel to the (110) plane are indicated by arrows.

More interestingly, the stacking faults in this and other particles can be traced to structural units consistent with a different cubic structure (see legend for details), which can be assumed to have $Pm\bar{3}n$ symmetry. The implications of this for the growth mechanism are discussed below. Indeed, a few particles have been obtained from these syntheses that show an intergrowth structure composed of these two mesostructures (Figure 3B). From these, it can be deduced that the [110] and [100] directions of cubic $Fd\bar{3}m$ and $Pm\bar{3}n$ mesostructures are crystallographically related and may grow epitaxially in this system. More specifically, the (00*l*) planes in the $Fd\bar{3}m$ and $Pm\bar{3}n$ structures are equivalent, whilst the (*hk*0) and (0*k*0) planes grow perpendicular to these for the $Fd\bar{3}m$ and $Pm\bar{3}n$ phases, respectively. The size and connectivity of the cages in both structures is different, and such an intergrowth material is likely to possess an interesting cage network. Further studies to determine the precise phase relationship are underway.

AMS-8(6) shows a disordered intraparticle arrangement of pores that is consistent with the large overall adsorption capacity of this sample. The point-group symmetry for mesostructured particles observed in samples of AMS-8(12.5) and AMS-8(9) is not consistent with that expected for the $Fd\bar{3}m$ space group, that is $m\bar{3}m$, where a 2*mm* plane-group symmetry is expected along the [110] direction. A model depicting the $m\bar{3}m$ point-group symmetry and a typical particle of AMS-8(9) is shown in Figure 4.

Surprisingly, the particle displays a deviation from twofold symmetry when viewed along the [110] axis. We propose an explanation for this based on the presence of stacking faults

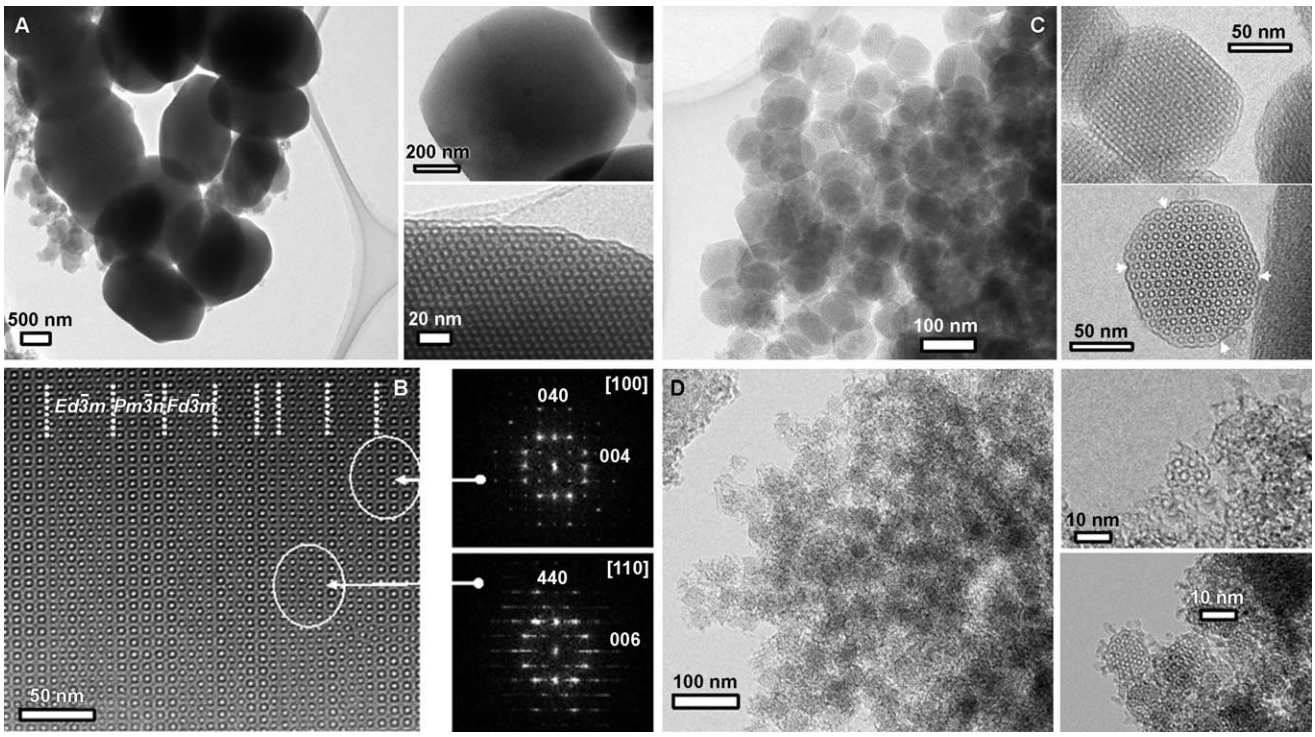

Figure 3. High-resolution TEM (HRTEM) images recorded at different magnifications of calcined AMS-8(12.5) (A and B), AMS-8(9) (C), and AMS-8(6) (D). The images show typical particle morphologies and sizes obtained on addition of increasing quantities of P123 surfactant to the synthesis gel. The images in (C) show facetted particles along the [211] and [110] orientations (top and bottom, respectively). Four stacking faults, which result in steps in the surface of the particle, can be observed along the [110] direction. These are highlighted in the image. The images in (B) show an HRTEM image of calcined AMS-8(12.5) with a repetitive series of stacking faults and intergrowths of $Pm\bar{3}n$ *and* $Fd\bar{3}m$ structures viewed along the [100] and [110] directions, respectively. The fast Fourier transform (FFT) diffractograms taken from selected areas are also shown and prove conclusively that these two structures grow epitaxially along these directions.

 © 2006 Wiley-VCH Verlag GmbH & Co. KGaA, Weinheim

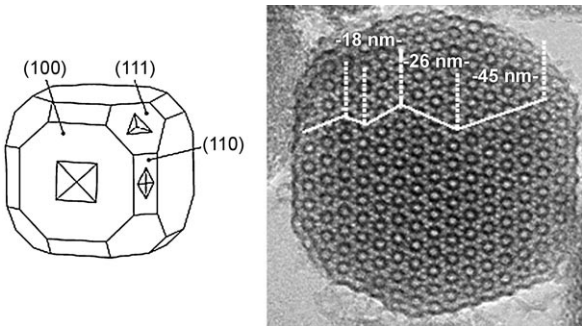

Figure 4. A model of the expected morphology for a cubic particle with point-group symmetry $m\bar{3}m$ (left). The TEM image is taken along [110], which is a twofold symmetry axis in the space group. The crystal morphology does not show the expected symmetry because of the existence of planar faults, as observed in a typical AMS-8(9) particle (right).

and the layered growth of particles in this system. Figure 5 shows a speculative model of the self-assembly mechanism occurring during the synthesis of AMS-8 nanoparticles. For

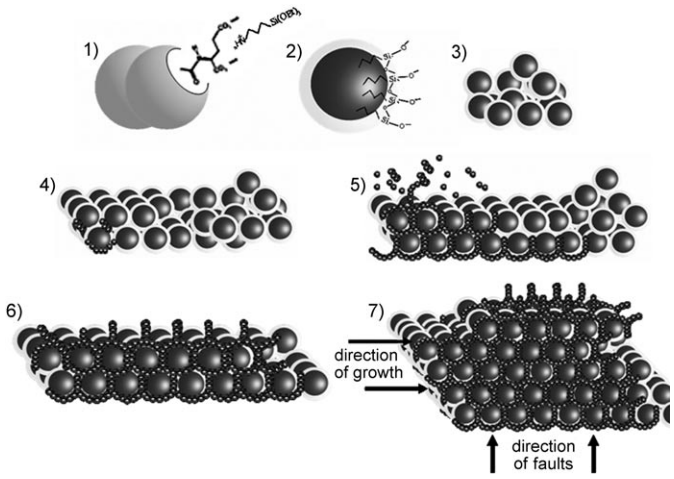

Figure 5. A model of the self-assembly mechanism observed in the preparation of AMS-8 nanoparticles. The different stages include: 1) surfactant–CSDA interaction, 2) partial hydrolysis of the CSDA surrounding the micelle to form a silica shell, 3) and 4) self-assembly of surfactant–CSDA units caused by TEOS hydrolysis and formation of silica oligomers (small spheres), 5) TEOS hydrolysis and growth of a silica wall around the nucleation sites, and 6) and 7) layered growth and formation of surface features as a result of structural defects.

the purpose of this discussion, a typical TEM image of a calcined sample of AMS-8(70) prepared with a synthesis time of only 12 h at 80 °C is shown in Figure 6. The self-assembly mechanism is thought to proceed in five stages. First (stage 1 in Figure 5), the amine moiety of the alkoxysilane CSDA interacts electrostatically with the acid groups on the surface of the micelle. Even though the hydrolysis rate of the CSDA is relatively slow as a result of the presence of an organic group bonded to the silica, under these synthetic conditions (pH of about 9) partial hydrolysis and condensation of the groups surrounding the micelle will occur. This leads to a negatively charged, shell-like silica layer at the micelle–water interface

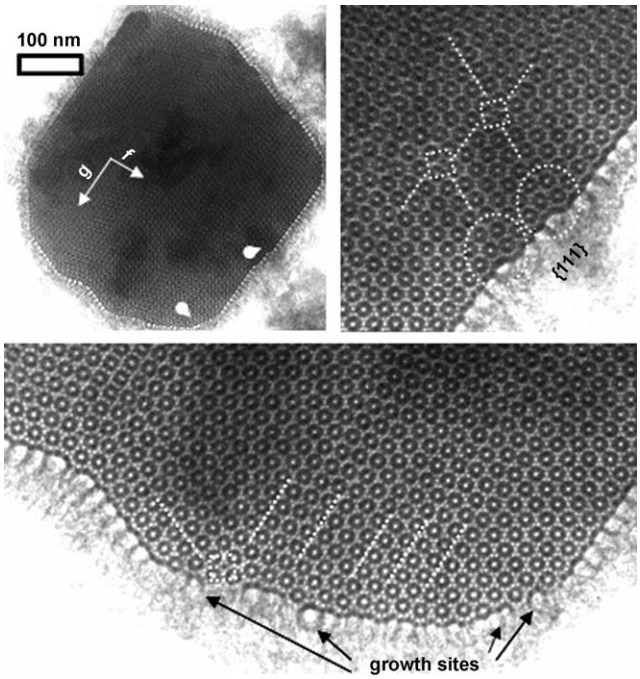

Figure 6. HRTEM image and enlarged areas of a typical particle obtained from a calcined sample of AMS-8(70). The images were recorded along the [110] orientation of AMS-8 and show the distinct "rugged" {111} surface and features such as surface nucleation sites in the form of follicle-like silica hairs surrounding the particle, growth sites of different maturity, recurrent stacking faults and twinning (dashed lines), surface termination sites (dashed circles), and $Pm\bar{3}n$ units (dashed squares). The direction of growth (*g*) is observed to be perpendicular to the stacking-fault planes (*f*).

(stage 2 in Figure 5) and to an extension of the effective headgroup area in the micelle. By considering the micelle-packing parameter, *g*, the large repulsive headgroup, and the headgroup separations at the micelle surface, it can be concluded that spherical micelles must form in the CSDA–surfactant system.[21] Self-assembly of spherical micelles will then occur (stages 3 and 4). The formation of silicate oligomers is well known under the synthetic conditions employed here. Interaction with the micelle-surface oligomeric silica units will further self-assemble the CSDA–surfactant and provide nucleation sites for further growth (stage 5).

Overall, particle growth in this system appears to proceed in a preferred direction perpendicular to the stacking-fault planes and at the {111} surface, which accounts for the elongation of the particles in this direction observed in the TEM images shown in Figure 6. This is consistent with a layered growth of particles where nucleation occurs at a surface and growth proceeds along it. Indeed, several growth sites and follicle-type surface features that can be interpreted as nucleation sites on the surface can be seen and have been highlighted in Figure 6. The formation of stacking faults in this system is complex, and with the available data we can only assume that they occur as a result of slight variations in concentration, shape, and local environment of the CSDA–surfactant micelle units, which aggregate and self-assemble in the presence of silica oligomers on the growing surface at a

 © 2006 Wiley-VCH Verlag GmbH & Co. KGaA, Weinheim

nucleation point. From the images shown it can be seen that these features are more prominent perpendicular to the fault-twin planes on the particle. This is depicted in stages 6 and 7 in Figure 5. Hence, when the particle size is small (below 200 nm), the rate of nucleation is faster perpendicular to the (111) plane. Stacking faults are clearly responsible for the morphology features observed and for the corresponding loss of point-group symmetry by directing the growth of the particle. Nonequilibrium growth is clearly visible in these nanoparticles. However, with time, and hence with larger particles, this effect disappears, that is, the growth of these particles reaches equilibrium and the $m\bar{3}m$ point-group symmetry is restored.

Monodispersed samples of AMS-8 mesocaged material have been prepared using the polymeric surfactant P123 to control the growth of the nanoparticles. These particles are facetted and show structural and surface characteristics that are typical of cubic AMS-8, as well as an increased adsorption capacity as a result of the formation of intraparticle spaces. Indeed, almost as much nitrogen is adsorbed at low pressures in-between particles for this sample as there is within the mesocages. However, unexpectedly, there is only a small increase in surface area.

It is evident from this study that the addition of P123 surfactant under basic conditions at temperatures above the cloud point of the polymeric surfactant has the effect of controlling the size of the mesoporous particles. We suggest that P123 acts as a dispersant of nucleation sites in the synthesis of AMS-8. It can be seen from the TEM images that the growth of this mesocaged solid occurs via a layered-growth mechanism and that stacking faults and other structural defects play a decisive role in the final nanoparticle morphology and surface structure.

Further studies are being conducted in order to determine the degree of control that can be achieved using this procedure in the synthesis of different AMS-*n* type mesostructures as well as with different polymeric surfactants.

Received: September 13, 2005
Revised: January 9, 2006
Published online: March 9, 2006

Keywords: electron microscopy · materials science · nanostructures · surface analysis · surfactants

[1] C. T. Kresge, M. E. Leonowicz, W. J. Roth, J. C. Vartuli, J. S. Beck, *Nature* **1992**, *359*, 710.
[2] F. Schüth, W. Schmidt, *Adv. Mater.* **2002**, *14*, 629.
[3] D. Y. Zhao, J. Feng, Q. Huo, N. Melosh, G. H. Fredrickson, B. F. Chmelka, G. D. Stucky, *Science* **1998**, *279*, 548.
[4] P. T. Tanev, T. J. Pinnavaia, *Chem. Mater.* **1996**, *8*, 2068.
[5] Q. Hou, J. Feng, B. F. Chmelka, G. D. Stucky, *J. Am. Chem. Soc.* **1998**, *120*, 6024.
[6] M. Antonietti, G. A. Ozin, *Chem. Eur. J.* **2004**, *10*, 28.
[7] H. Yang, G. Vovk, N. Coombs, I. Sokolov, G. A. Ozin, *J. Mater. Chem.* **1998**, *8*, 743.
[8] M.-C. Chao, H.-P. Lin, D.-S. Wang, C.-Y. Mou, *Chem. Lett.* **2004**, *33*, 374.
[9] S. A. El-Safty, T. Hanaoka, *Chem. Mater.* **2004**, *16*, 384.
[10] C. Sanchez, J. D. Galo, A. A. Soler-Illia, F. Ribot, D. Grosso, *C. R. Chim.* **2003**, *6*, 1131.
[11] S. Che, A. E. Garcia-Bennett, T. Yokoi, K. Sakamoto, H. Kunieda, O. Terasaki, T. Tatsumi, *Nat. Mater.* **2003**, *2*, 801.
[12] A. E. Garcia-Bennett, S. Che, T. Tatsumi, O. Terasaki, *Chem. Mater.* **2004**, *16*, 813.
[13] S. Che, Z. Liu, T. Ohsuna, K. Sakamoto, O. Terasaki, T. Tatsumi, *Nature* **2004**, *429*, 281.
[14] A. E. Garcia-Bennett, N. Kupferschmidt, Y. Sakamoto, S. Che, O. Terasaki, *Angew. Chem.* **2005**, *117*, 5451; *Angew. Chem. Int. Ed.* **2005**, *44*, 5317.
[15] A. E. Garcia-Bennett, S. Che, K. Miyasaka, O. Terasaki, *Chem. Mater.* **2004**, *16*, 3597.
[16] S. Huh, J. W. Wiench, J.-C. Yoo, M. Pruski, V. S.-Y. Line, *Chem. Mater.* **2003**, *15*, 4247.
[17] R. P. Hodgkins, A. E. Garcia-Bennett, P. A. Wright, *Microporous Mesoporous Mater.* **2005**, *79*, 241.
[18] J. Patarin, B. Lebeau, R. Zana, *Curr. Opin. Colloid Interface Sci.* **2002**, *7*, 107.
[19] K. Suzuki, K. Ikari, H. Imai, *J. Am. Chem. Soc.* **2004**, *126*, 462.
[20] P. I. Ravikovitch, D. Wei, W. T. Chueh, G. L. Haller, A. V. Neimark, *J. Phys. Chem. B* **1997**, *101*, 3671; P. I. Ravikovitch, A. V. Neimark, *Langmuir* **2002**, *18*, 1550; P. I. Ravikovitch, A. V. Neimark, *Langmuir* **2000**, *16*, 2419.
[21] S. Manne, T. E. Schäffer, Q. Huo, P. K. Hansma, D. E. Morse, G. D. Stucky, I. A. Aksay, *Langmuir* **1997**, *13*, 6382.

 © 2006 Wiley-VCH Verlag GmbH & Co. KGaA, Weinheim

Intermolecular Bonding

DOI: 10.1002/anie.200504486

Relative Strengths of the O–H···Cl and O–H···F Hydrogen Bonds**

Walther Caminati, Sonia Melandri, Assimo Maris, and Paolo Ottaviani*

Hydrogen bonding involves many scientific areas and is invoked to explain the energetic and structural features of inorganic, organic, and biological chemical systems.[1,2] Herein, we show that a water molecule in a solvent-free environment prefers to form a hydrogen bond with a Cl atom rather than with a F atom. For this purpose, several isotopologues of chlorofluoromethane/water were studied by molecular-beam Fourier transform rotational spectroscopy.

[*] Prof. W. Caminati, Dr. S. Melandri, Dr. A. Maris, Dr. P. Ottaviani
Dipartimento di Chimica "G. Ciamician" dell'Università
Via Selmi 2, 40126 Bologna (Italy)
Fax: (+39) 051-209-9456
E-mail: walther.caminati@unibo.it

[**] We thank the Ministero dell'Istruzione, dell'Università e della Ricerca (MIUR, PRIN 2004) and the University of Bologna (ex 60% and funds for special topics) for financial support.

Supporting information for this article is available on the WWW under http://www.angewandte.org or from the author.

InterScience
© 2006 Wiley-VCH Verlag GmbH & Co. KGaA, Weinheim

The most important molecule involved in hydrogen bonding is water. The structural and energetic features of hydrogen bonding between water and organic molecules were recently investigated in detail by high-resolution spectroscopic analysis of hydrogen-bonded complexes.[3] The O–H···O, O–H···N, O–H···S, and N–H···O interactions were characterized through rotational-spectroscopic studies of molecular complexes of water with ethers,[4] amines,[5] diazines,[6] thioethers,[7] and imino groups inserted into aromatic rings;[8] all of those represent relatively strong hydrogen bonds, with energies in the range 15–25 kJ mol^{-1}. The O–H···F interaction was investigated with this technique as well, through analysis of the rotational spectrum of the complex of freon-32 (difluoromethane) with water.[9] The dissociation energy of this complex (ca. 8 kJ mol^{-1}) is considerably lower than those of the above mentioned systems and includes a contribution from secondary C–H···O interactions. This energy is similar to the values obtained for other molecular complexes stabilized by a few—typically three—weak C–H···O (or C–H···F) interactions.[10] For example, the difluoromethane[11] and dimethyl ether dimers,[12] the adducts between trifluoromethane and oxirane, or fluoromethane[13] have interaction energies of about 6 kJ mol^{-1}, which can be attributed to three C–H···F and/or C–H···O weak hydrogen-bonding interactions, with an approximate energy contribution of 2 kJ mol^{-1} for each bond. From these data one can extrapolate an energy of approximately 4 kJ mol^{-1} for the C–H···F hydrogen bonding. No data are available for complexes of water with organic molecules containing a Cl atom, that is, regarding the O–H···Cl hydrogen bonding. If such data were available, it would be possible to compare the O–H···F and O–H···Cl energies. More direct and easy-to-compare information should come from the investigation of a complex of water with a molecule containing both a F or Cl atom. The simplest molecule containing a Cl and F atom, ClF, turned out to react with water. However, by using a fast-mixing nozzle, Legon and coworkers observed an adduct with no hydrogen bonding, H_2O···ClF, which displayed an O···Cl interaction.[14] The same effect, but with an O···F interaction, was observed for H_2O···F_2.[14]

Unlike H_2O···F_2, the adduct H_2O···F_2CH_2 displayed an O–H···F hydrogen bond; for this reason, we thought that the study of the rotational spectrum of an adduct of water with an aliphatic molecule containing both Cl and F atoms would give direct evidence about which of the two atoms is favored in the interaction with the water molecule. The prototype molecule with these requisites is freon-31, chlorofluoromethane (CFM). Herein, we report the results of the investigation of the CFM/H_2O complex.

Before collecting the rotational spectra, we ran some theoretical calculations at the MP2/6-311++G(d,p) and MP2/aug-cc-pVTZ levels.[15] Four stationary points, which lie in a very small energy range (ca. 70 cm^{-1}), were found (Table 1). Two conformers (I and IV) display an O–H···F interaction, whereas the other two display an O–H···Cl hydrogen bond. One pair of conformers presents a plane of symmetry (II and IV) and an inertial defect as small as that of the CFM monomer, and the other pair has a higher inertial defect and no symmetry element.

Table 1: Ab initio spectroscopic parameters of the plausible conformers of CFM/H_2O.[a]

		Conformer			
		I	II	III	IV
ΔE [cm^{-1}] values from MP2 calculations at various levels of theory[b]					
6-311++G(d,p)	n.c.	0[c]	19	23	71
	CP	0[d]	67	75	7
	CP and ZPE	96[e]	71	139	0[e]
aug-cc-pVTZ	n.c.	42	0[f]	22	65
	CP	50	0[g]	39	61
Spectroscopic constants calculated at the MP2/aug-cc-pVTZ level					
A [MHz]		9698.0	6708.7	5988.8	17922.9
B [MHz]		2153.5	2725.9	2769.3	1825.6
C [MHz]		1901.0	1962.9	2005.4	1674.8
Δ_c [uÅ^2]		−20.9	−3.27	−14.9	−3.27
μ_a [D]		1.1	2.6	−1.6	−2.1
μ_b [D]		0.2	0.1	0.2	−0.2
μ_c [D]		0.2	0.0	−0.3	0.0
χ_{aa} [MHz]		−28.0	26.9	27.1	−66.1
χ_{bb} [MHz]		16.4	−62.9	−50.0	−29.6
χ_{cc} [MHz]		11.6	36.1	23.0	36.4
χ_{ab} [MHz]		−35.7	11.8	18.8	−4.1
χ_{ac} [MHz]		−4.4	0.0	4.1	0.0
χ_{bc} [MHz]		−16.8	0.0	−8.9	0.0

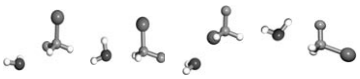

[a] μ_g and χ_{gg} (g = *a*, *b*, *c*) are the dipole-moment components and the ^{35}Cl quadrupole coupling constants, respectively. [b] n.c. = no correction; CP = counterpoise corrections; ZPE = zero-point energy corrections. [c] $E/H_a = -674.7860506$. [d] $E/H_a = -674.7838540$. [e] $E/H_a = -674.7782936$. [f] $E/H_a = -674.9989467$. [g] $E/H_a = -674.9981354$.

A counterpoise correction[16] to the MP2/6-311++G(d,p) calculated energies was performed that showed that the global minimum remains the same but the relative energies of the other conformers are interchanged. With the larger aug-cc-pVTZ Dunning basis set,[17] the position of the global minimum is changed as well. We found with a frequency calculation (harmonic approximation) that conformer IV is slightly nonplanar. We applied zero-point energy corrections to the smaller basis values of the other three. The four sets of relative energies and spectroscopic constants are collected in Table 1.

Only one rotational spectrum, which corresponds to species II of Table 1, was observed and assigned. The first lines to be observed were the $2_{1,2}$–$1_{1,1}$, $2_{0,2}$–$1_{0,1}$, and $2_{1,1}$–$1_{1,0}$ rotational transitions of the ^{35}Cl isotopomer. Each of them appeared as multiplets of lines because of the nuclear quadrupole moment of the ^{35}Cl nucleus and the doubling of lines (see below) caused by the tunneling of water. Figure 1 shows these details for the $2_{0,2}$–$1_{0,1}$ transition. The six hyperfine component lines that result from the ^{35}Cl nuclear spin coupling with the overall rotation are further split into two lines, with an intensity ratio of about 1:3, which corresponds to the statistical weight for the 0^+ and 0^- states of the internal rotation of the water moiety. In addition, each line appears as a doublet because of the Doppler effect (see Experimental Section).

 © 2006 Wiley-VCH Verlag GmbH & Co. KGaA, Weinheim

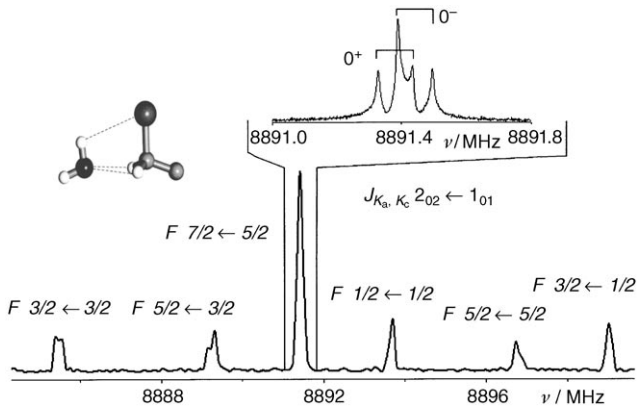

Figure 1. ^{35}Cl hyperfine structure and 0^+ and 0^- component lines of the 2_{02}–1_{01} μ_a transition of the observed conformer of CFM/H_2O.

The line frequencies (see Supporting Information) were used to determine the spectroscopic constants reported in Table 2. The fit was performed with a Pickett-type coupled Hamiltonian,[18] given here in a simple form [Eq. (1)]:

$$H = H_R(0^+) + H_R(0^-) + H_{CD} + H_Q \quad (1)$$

$H_R(0^+)$ and $H_R(0^-)$ represent the rigid rotational parts of the Hamiltonian for the 0^+ and 0^- states, respectively. The centrifugal distortion contributions (analyzed using the S reduction and I^r representation[19]) are represented by H_{CD} and were assumed to be the same in both states. H_Q is the operator associated with the interaction of the ^{35}Cl (or ^{37}Cl) nucleus electric quadrupole moment with the electric field gradient at the Cl nucleus.[20]

After progressive partial structural adjustments, we searched for and assigned the spectra of the ^{37}Cl, D_2O, HOD, DOH, and $H_2{}^{18}O$ isotopomers. They were fitted with the same procedures as described for the normal species. However, the mono and bideuterated species did not show any doubling that resulted from the water motion, either because of a symmetry breakdown or the H→D isotopic effects. Measured transitions are given in the Supporting Information, and the spectroscopic parameters are shown in Table 2.

The first piece of information on the conformation of the observed complex is readily deduced from the value of the defect of inertia Δ_c, which gives a measure of the extension of the atomic masses out of the inertial planes of the complex. The experimental value (−3.34 uÅ^2) matches the theoretical values only for species II and IV (see Tables 1 and 2). The discrimination between these two species is given by the r_s substitution coordinates[21] of the Cl, O, and water H atoms (Table 3). One can readily see that the experimental data only fit the MP2/aug-cc-pVTZ values for species II. These data supply a reliable O···Cl r_s distance. The observed conformer is shown in Figure 2, with some structural parameters used in the text.

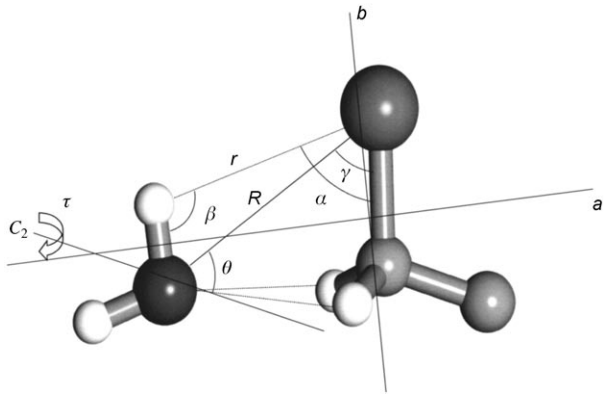

Figure 2. The observed conformer of CFM/H_2O displays one O–H···Cl and two weak C–H···O hydrogen bonds. Some structural parameters used in the text are shown.

A partial r_0 structure was calculated from the six sets of available experimental rotational constants (see Table 2), with the geometries of CFM and H_2O fixed as in the isolated molecules. We first calculated the r_0 structure of CFM from

Table 2: Spectroscopic constants of all measured isotopomers of CFM/H_2O.[a]

Constant	$CH_2{}^{35}ClF\cdots H_2O$		$CH_2{}^{37}ClF\cdots H_2O$		$CH_2ClF\cdots DOH$	$CH_2ClF\cdots D_2O$	$CH_2ClF\cdots HOD$	$CH_2ClF\cdots H_2{}^{18}O$	
	0^+[b]	0^-	0^+[b]	0^-				0^+[b]	0^-
A [MHz]	6613.0779(10)[b]	6612.6886(10)	6415.565(2)	6415.214(2)	6627.42(14)	6587.60(9)	6577.8(2)	6560.516(16)	6560.125(16)
B [MHz]	2599.5241(4)	2599.5009(4)	2597.8594(13)	2597.8465(13)	2526.715(3)	2389.411(2)	2452.248(5)	2431.5841(5)	2431.5704(5)
C [MHz]	1889.3205(3)	1889.3696(3)	1871.9406(13)	1871.9859(12)	1852.1739(12)	1774.3707(18)	1807.7017(16)	1795.0131(3)	1795.0622(3)
Δ_c [uÅ^2]	−3.34	−3.35	−3.34	−3.35	−3.41	−3.40	−3.35	−3.33	−3.34
χ_{aa} [MHz]	30.190(2)		23.863(3)		29.788(7)	30.141(9)	30.502(8)	30.603(2)	
χ_{bb} [MHz]	−67.615(2)		−53.354(6)		−67.276(17)	−67.72(2)	−67.97(2)	−68.032(4)	
χ_{cc} [MHz]	37.425(3)		29.491(6)		37.488(18)	37.58(2)	37.47(2)	37.429(4)	
χ_{ab} [MHz]	11.6(8)		9.66[c]		11.6[d]	11.6[d]	11.6[d]	9.8(4)	
D_J [kHz]	4.009(7)		3.931(10)		3.50(18)	3.30(5)	3.2(2)	3.692(12)	
D_{JK} [kHz]	24.42(8)		23.89(15)		21.7(8)	21.2(11)	23.7(9)	24.01(7)	
d_1 [kHz]	1.310(9)		0.70(6)		0.97(13)	1.05(3)	0.82(19)	1.169(11)	
d_2 [kHz]	0.285(10)		−2.4(3)		0.285[d]	0.285[d]	0.285[d]	0.325(7)	
N[e]	123		57		23	42	31	94	
σ [kHz]	2.2		3.7		3.8	9.4	8.6	4.1	

[a] The species containing mono- or bideuterated water do not show water-inversion splittings. [b] Uncertainties (in parentheses) are expressed in units of the last digit. [c] Fixed to the value obtained for $CH_2{}^{35}ClF\cdots H_2O$, corrected by the $^{37}Cl/^{35}Cl$ ratio of the electric nuclear quadrupole moment Q. [d] Fixed to the value obtained for normal species. [e] Number of transitions in the fit.

 © 2006 Wiley-VCH Verlag GmbH & Co. KGaA, Weinheim

Table 3: Structural parameters r_s and r_0 of CFM/H_2O.

Atom		Experimental	MP2/aug-cc-pVTZ Conformer II	MP2/aug-cc-pVTZ Conformer IV
r_s coordinates of substituted atoms[a] ($\|c\| = 0.0$)				
Cl	$\|a\|$ [Å]	0.250(6)[a]	0.207	1.791
	$\|b\|$ [Å]	1.099(2)	1.100	0.204
O	$\|a\|$ [Å]	2.6115(6)	2.528	2.918
	$\|b\|$ [Å]	0.590(3)	0.634	0.454
H_{free}	$\|a\|$ [Å]	3.4202(5)	3.489	3.879
	$\|b\|$ [Å]	0.673(3)	0.674	0.426
$H_{H\ bond}$	$\|a\|$ [Å]	2.3749(7)	2.321	2.645
	$\|b\|$ [Å]	0.417(4)*i*	0.307	0.470
Partial r_0 geometry				
Fitted parameters:			Derived parameters:[c]	
r(Cl···O) [Å]		3.36(1)	r [Å]	2.655
∢CCl···O [°]		65.2(2)	α [°]	77.8
∢Cl···HO [°]		37(6)	β [°]	135.8
			r(O···HC) [Å]	2.777

[a] r_s(Cl···O) = 3.323(8) Å, obtained from the r_s coordinates. [b] Uncertainties (in parentheses) are expressed in units of the last digit. [c] See Figure 2.

the available rotational constants,[22] thus obtaining the values given in the Supporting Information. After, we calculated the r_0 values of three parameters required to determine the structure of the molecular complex, for example, the set r(Cl···O), ∢CCl···O, and ∢Cl···HO. Alternative parameters, such as r, α, and β of Figure 2 and the O···HC distance, which appear more meaningful with respect to the characterization of the hydrogen bond, have also been derived from this partial r_0 structure. All r_0 parameters are reported at the bottom of Table 3.

We estimated the stretching-force constant (k_s) by approximating the molecular complex to a pseudodiatomic molecule according to Equation (2):[23]

$$k_s = 16\pi^4 (\mu R_{CM})^2 [4B^4 + 4C^4 - (B-C)^2(B+C)^2]/(h D_J) \quad (2)$$

B and C are the rotational constants and μ, R_{CM} (3.436 Å, obtained from the r_0 geometry), and D_J are the reduced mass, the distance between the centers of mass, and the first-order centrifugal distortion constant, respectively. The value $k_s = 8.6\ N\,m^{-1}$, which corresponds to a harmonic stretching frequency of 102 cm^{-1}, was obtained.

Assuming a Lennard–Jones potential, the dissociation energy (E_D) can be evaluated by using the approximated equation [Eq. (3)]:

$$E_D = 1/72\, k_s R_{CM}^2 \quad (3)$$

The result ($E_D = 8.5\ kJ\,mol^{-1}$) is similar to the corresponding values for the difluoromethane/water adducts ($E_D = 7.5\ kJ\,mol^{-1}$ [9]), thus confirming that the interaction energies of aliphatic Cl and F atoms are very similar to each other, although the present work shows the former to be slightly higher.

The differences between the rotational constants of the two states supply the information needed to obtain the energetic shape of the tunneling pathway for the internal rotation of water by using the one-dimensional, flexible Meyer model.[24] We calculated the rotational and vibrational wavefunctions and eigenvalues, and therefore the vibrational spacings. The following potential-energy function, suitable for two equivalent periodic minima, has been adopted [Eq. (4)]:

$$V(\tau) = V_2[1-\cos(2\tau)] \quad (4)$$

Here, V_2 and τ are the barrier and the internal-rotation coordinate, respectively (in our case, τ represents the rotation of water around its symmetry axis), and $\tau = 0$ is the equilibrium value, with H_2O lying in the ClCF plane. MP2/aug-cc-pVTZ calculations indicated that three parameters undergo a considerable structural relaxation upon the internal rotation of water: R, α, and θ of Figure 2. These relaxations within the flexible model were accounted for as described in the Supporting Information.

The results for the fitted shifts in the rotational constants are reported in Table 4. A barrier of $V_2 = 336\ (10)\ cm^{-1}$ was obtained, which is very similar to the value of $V_2 = 340\ (10)\ cm^{-1}$ for difluoromethane/H_2O.[9]

Table 4: Flexible model results and potential-energy parameters for the internal rotation of water in CFM/H_2O.

Parameter	Experimental	Calculated
ΔA [MHz]	−0.389	−0.393
ΔB [MHz]	−0.023	−0.002
ΔC [MHz]	0.049	0.022
ΔE [MHz]	–	823
Determined parameter:[a] $V_2 = 336(10)\ cm^{-1}$[b]		

[a] Structural relaxations fixed at the ab initio values (see Supporting Information). [b] Uncertainties (in parentheses) are given in units of the last digit.

We believe that the obtained results have a general chemical interest because 1) they show that the O–H···Cl hydrogen-bonding interaction is preferred to the O–H···F interaction; 2) freon/water adducts can be formed in the upper atmosphere and can have a relevant role in the decompositions of freons.

Experimental Section

The Fourier-transform microwave (FT-MW) spectrometer is described elsewhere.[25] It has been updated recently with the FT-MW++ set of programs.[26] A mixture of 2% CFM in He was flown over water at room temperature and expanded to about 10^{-5} mbar. Each rotational transition is split by the Doppler effect, enhanced by the molecular-beam expansion in the coaxial arrangement of the supersonic jet and resonator axes. The rest frequency is calculated as the arithmetic mean of the frequencies of the Doppler components. The estimated accuracy of frequency measurements is better than 3 kHz, and lines separated by more than 7 kHz are resolvable.

Received: December 17, 2005
Published online: March 7, 2006

 © 2006 Wiley-VCH Verlag GmbH & Co. KGaA, Weinheim

Keywords: hydrogen bonding · molecular complexes · molecular dynamics · rotational spectroscopy · supersonic jets

[1] G. A. Jeffrey, *An Introduction to Hydrogen Bonding*, Oxford University Press, New York, **1997**.
[2] S. Scheiner, *Hydrogen Bonding*, Oxford University Press, New York, **1997**.
[3] S. E. Novick, *Bibliography of Rotational Spectra of Weakly Bound Complexes*, **2005**, available at http://www.wesleyan.edu/chem/faculty/novick/vdw.html.
[4] W. Caminati, A. Dell'Erba, S. Melandri, P. G. Favero, *J. Am. Chem. Soc.* **1998**, *120*, 5555; U. Spoerel, W. Stahl, W. Caminati, P. G. Favero, *Chem. Eur. J.* **1998**, *4*, 1974; W. Caminati, P. Moreschini, I. Rossi, P. G. Favero, *J. Am. Chem. Soc.* **1998**, *120*, 11144; P. Ottaviani, M. Giuliano, B. Velino, W. Caminati, *Chem. Eur. J.* **2004**, *10*, 538; M. Becucci et al., *J. Chem. Phys.* **2004**, *120*, 5601; B. M. Giuliano, W. Caminati, *Angew. Chem.* **2005**, *117*, 609; *Angew. Chem. Int. Ed.* **2005**, *44*, 603.
[5] W. Caminati, A. Dell'Erba, G. Maccaferri, P. G. Favero, *J. Am. Chem. Soc.* **1998**, *120*, 2616.
[6] W. Caminati, L. B. Favero, P. G. Favero, A. Maris, S. Melandri, *Angew. Chem.* **1998**, *110*, 852; *Angew. Chem. Int. Ed.* **1998**, *37*, 792; W. Caminati, P. Moreschini, P. G. Favero, *J. Phys. Chem. A* **1998**, *102*, 8097; S. Melandri, M. E. Sanz, W. Caminati, P. G. Favero, Z. Kisiel, *J. Am. Chem. Soc.* **1998**, *120*, 11504.
[7] M. E. Sanz et al., *J. Phys. Chem. A* **1999**, *103*, 5285.
[8] S. Blanco, J. C. Lopez, J. L. Alonso, P. Ottaviani, W. Caminati, *J. Chem. Phys.* **2003**, *119*, 880; T. M. Korter, D. W. Pratt, J. Küpper, *J. Phys. Chem. A* **1998**, *102*, 7211.
[9] W. Caminati, S. Melandri, I. Rossi, P. G. Favero, *J. Am. Chem. Soc.* **1999**, *121*, 10098.
[10] G. R. Desiraju, T. Steiner, *The Weak Hydrogen Bond*, Oxford University Press, Oxford, **1999**; P. Hobza, Z. Havlas, *Chem. Rev.* **2000**, *100*, 4253.
[11] W. Caminati, S. Melandri, P. Moreschini, P. G. Favero, *Angew. Chem.* **1999**, *111*, 3105; *Angew. Chem. Int. Ed.* **1999**, *38*, 2924.
[12] Y. Tatamitani, B. Liu, J. Shimada, T. Ogata, P. Ottaviani, A. Maris, W. Caminati, J. L. Alonso, *J. Am. Chem. Soc.* **2002**, *124*, 2739.
[13] J. L. Alonso, S. Antolínez, S. Blanco, A. Lesarri, J. C. López, W. Caminati, *J. Am. Chem. Soc.* **2004**, *126*, 3244; W. Caminati, J. C. López, J. L. Alonso, J.-U. Grabow, *Angew. Chem.* **2005**, *117*, 3908; *Angew. Chem. Int. Ed.* **2005**, *44*, 3840.
[14] S. A. Cooke, G. Cotti, C. M. Evans, J. H. Holloway, Z. Kisiel, A. C. Legon, J. M. A. Thumwood, *Chem. Eur. J.* **2001**, *7*, 2295.
[15] Gaussian 03 Revision B.04, M. J. Frisch et al., Gaussian, Inc., Pittsburgh PA, **2003**.
[16] S. F. Boys, F. Bernardi, *Mol. Phys.* **1970**, *19*, 553.
[17] D. E. Woon, T. H. Dunning, Jr., *J. Chem. Phys.* **1993**, *98*, 1358.
[18] H. M. Pickett, *J. Mol. Spectrosc.* **1991**, *148*, 371.
[19] J. K. G. Watson in *Vibrational Spectra and Structure*, *Vol. 6* (Ed.: J. R. Durig), Elsevier, New York, **1977**, p. 1.
[20] J. K. Bragg, *Phys. Rev.* **1948**, *74*, 533.
[21] J. Kraitchman, *Am. J. Phys.* **1953**, *21*, 17.
[22] S. Blanco, A. Lesarri, J. C. López, J. L. Alonso, A. Guarnieri, *J. Mol. Spectrosc.* **1995**, *174*, 397.
[23] W. G. Read, E. J. Campbell, G. Henderson, *J. Chem. Phys.* **1983**, *78*, 3501.
[24] R. Meyer, *J. Mol. Spectrosc.* **1979**, *76*, 266.
[25] W. Caminati, A. Millemaggi, J. L. Alonso, A. Lesarri, J. C. Lopez, S. Mata, *Chem. Phys. Lett.* **2004**, *392*, 1.
[26] J.-U. Grabow, Habilitationsschrift, Universität Hannover, Hannover **2004**, http://www.pci.uni-hannover.de/≈lgpca/spectroscopy/ftmw.

 © 2006 Wiley-VCH Verlag GmbH & Co. KGaA, Weinheim

Mixed-Metal Oxides

DOI: 10.1002/anie.200503730

Hydrothermal Synthesis of a Cerium(IV) Pyrochlore with Low-Temperature Redox Properties**

*Christopher S. Wright, Janet Fisher, David Thompsett, and Richard I. Walton**

Oxides containing Ce^{IV} are extensively investigated for their many applications in catalysis. Current interest in these materials arises from their use in solid-oxide fuel cells[1] and depollution catalysts, particularly for automotive exhausts.[2,3] The key to their catalytic activities is the ability of Ce^{IV} to be reversibly reduced to Ce^{III} at moderate temperatures (less than 500 °C). This property is associated with considerable oxide-ion mobility in the solid state.[4] In the three-way catalytic converters used in automotive exhausts, such materials play the role of oxygen-level buffers and also act as catalysts for the water gas shift reaction, converting carbon monoxide and water into carbon dioxide and hydrogen gas.[5] Doped ceria (the parent material, ceria (CeO_2), adopts the fluorite structure) is often the material of choice in these applications, and much recent work has been undertaken to prepare ceria-based materials with controlled levels of dopants to tune the redox properties of the solids. Ceria–zirconia mixed oxides have now established themselves as among the most active and versatile materials for three-way catalytic converters, and their development and properties have recently been reviewed.[6,7] The preparation of materials with high surface areas and porosities has also been focused upon to optimize catalytic activity, and soft chemical routes have recently been employed to achieve this aim. For example, Li et al. prepared nanocrystalline $Ce^{IV}_{1-x}Y^{III}_{x}O_{2-x/2}$ ($x \leq 0.35$) by coprecipitation.[8] Deshpande et al. also used coprecipitation to form nanoparticles of ceria–zirconia ($Ce^{IV}_{1-x}Zr^{IV}_{x}O_2$) with a small particle size distribution,[9] and

[*] Dr. R. I. Walton
Department of Chemistry, The Open University
Walton Hall, Milton Keynes, MK7 6AA (UK)
Fax: (+44) 190-885-8327
E-mail: r.i.walton@open.ac.uk
C. S. Wright
The Geoffrey Pope Building, University of Exeter
Stocker Road, Exeter, EX4 4QD (UK)
Dr. J. Fisher, Dr. D. Thompsett
Johnson Matthey Technology Centre
Sonning Common, Reading, RG4 9NH (UK)

[**] The authors thank Johnson Matthey plc for provision of a CASE studentship to C.S.W., Alex Hannon of the Rutherford Appleton Laboratory for assistance with the density measurement, the CCLRC for beam time at the Daresbury SRS, and the University of Exeter for providing laboratory space prior to the closure of its Chemistry Department.

Supporting information for this article is available on the WWW under http://www.angewandte.org or from the author.

WILEY InterScience DISCOVER SOMETHING GREAT
© 2006 Wiley-VCH Verlag GmbH & Co. KGaA, Weinheim

Inomata and co-workers used hydrothermal synthesis to dope Fe^{III} ions into nanoscale ceria.[10]

Hydrothermal synthesis is perhaps best known for its use in the preparation of zeolites and other nanoporous solids. The method also has considerable utility in the preparation of dense phases (which are otherwise usually synthesized by the high-temperature ceramic methods of solid-state chemistry), and has historically been used for the growth of large quartz crystals[11] and mixed-metal fluorides.[12] Hydrothermal synthesis also offers some distinct advantages in the preparation of complex transition-metal oxides: the use of low temperatures (typically less than 250 °C) may allow access to metastable phases not observed at high temperatures, and the use of a solvent permits some control over particle size and morphology.[13,14] Herein, we demonstrate how hydrothermal synthesis, with the addition of an appropriate oxidizing agent to control the metal oxidation state in the product, allows the one-step preparation of a cerium(IV) titanate that has not been accessible by conventional oxide synthesis methods. This novel compound has favorable redox activity in the solid state.

The material $(Na_{1/3}Ce_{2/3})_2Ti_2O_7$ was prepared from a mixture of $CeCl_3{\cdot}7H_2O$:2.5 TiF_3:50 H_2O_2:20 NaOH:470 H_2O (H_2O_2 may be replaced by 2.5 equivalents per Ce atom of $NaBrO_3$, a more conveniently handled solid oxidant). Typically, a reaction mixture based on 0.37 g of $CeCl_3{\cdot}7H_2O$ was sealed in a 25-mL teflon-lined autoclave after stirring for 30 minutes, but we successfully scaled up the reaction to mixtures based on 15 g of $CeCl_3{\cdot}7H_2O$ in 2-L reaction vessels. Hydrothermal reaction at 240 °C for 5 hours yielded a pale-yellow solid product, which was isolated by filtration, washed thoroughly with warm distilled water, and dried in air at 50 °C. The oxidant (H_2O_2 or $NaBrO_3$) is vital for the synthesis of the new phase: if it is omitted from the reaction mixture, the perovskite $NaCe^{III}Ti_2O_6$ is produced,[15] and if less than 5 equivalents of H_2O_2 as oxidant are used, a mixture of the perovskite and the new $(Na_{1/3}Ce^{IV}_{2/3})_2Ti_2O_7$ phase is formed. If NaOH is replaced by another base (such as KOH or an alkylammonium hydroxide), then the material isolated is amorphous; this observation indicates that NaOH plays the role of a reagent, rather than solely that of a mineralizer.

Powder X-ray diffraction (XRD) reveals that $(Na_{1/3}Ce_{2/3})_2Ti_2O_7$ crystallizes in the space group $Fd\bar{3}m$ with $a = 10.120(9)$ Å and is isostructural with the cubic pyrochlore $Y_2Ti_2O_7$.[16] Thermogravimetric analysis (TGA; performed under static air, while heating from room temperature to 900 °C at 10 °C min^{-1}) shows that the as-made material contains approximately 7.8 % water (and/or surface hydroxide ions) by mass (see Supporting Information), which corresponds to approximately two equivalents of water (and/or surface hydroxide ions) per formula unit (that is, $(Na_{1/3}Ce_{2/3})_2Ti_2O_7{\cdot}\sim 2H_2O$). Inductively coupled plasma (ICP) analysis of the metals confirms that the pyrochlore phase has the composition $(Na_{1/3}Ce_{2/3})_2Ti_2O_7$. The general formula of the pyrochlore oxides is $A_2B_2O_7$, where A and B are cations occupying eight- and six-coordinate sites in the structure, respectively. Thus, in $(Na_{1/3}Ce_{2/3})_2Ti_2O_7$, the A site should be occupied by 2/3 Ce^{IV} and 1/3 Na^+ on average. This model provides an excellent match to the observed peak intensities in the powder XRD pattern, and also satisfies charge balance. The radius ratio of the metals in the A and B sites, r_A/r_B, is 1.59 (taking the weighted average of the radii of Ce^{IV} and Na^+ as the A-site radius). This value is consistent with $(Na_{1/3}Ce_{2/3})_2Ti_2O_7$ adopting the cubic pyrochlore structure, on the basis of trends between radius ratios and structure types that have been established for $A_2B_2O_7$ materials containing a variety of combinations of metal ions.[17] The measured density (obtained using micropycnometry with He as the working fluid) of a sample dried at 100 °C for several days was 5.4(1) g cm^{-3}, in good agreement with the value of 5.30 g cm^{-3} calculated from our structural model.

The powder XRD pattern of $(Na_{1/3}Ce_{2/3})_2Ti_2O_7$ exhibits severe peak broadening, which is only slightly reduced by firing the sample at 900 °C (Figure 1). Scherrer analysis of the

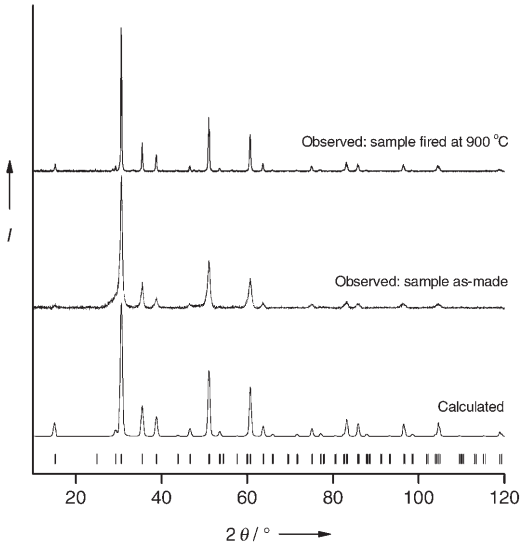

Figure 1. Experimental powder XRD patterns ($Cu_{K\alpha1/K\alpha2}$ radiation) for a sample of $(Na_{1/3}Ce_{2/3})_2Ti_2O_7$ fired at 900 °C (top), and for the as-made $(Na_{1/3}Ce_{2/3})_2Ti_2O_7$ material (middle). Calculated pattern for the $Y_2Ti_2O_7$-type model of $(Na_{1/3}Ce_{2/3})_2Ti_2O_7$ (bottom). Vertical bars indicate the Bragg peak positions for a face-centered cubic unit cell with $a = 10.120(9)$ Å ($Fd\bar{3}m$). See text for details.

data shows that the crystallites in the as-made sample have an average diameter of 20 nm. Transmission electron microscopy (TEM) confirms that the spherical particles have an average diameter of 20 nm, although particle sizes of 10–30 nm are typically found (Figure 2a). The surface area of the powder, measured by BET nitrogen sorption, was found to be 150 $m^2 g^{-1}$, consistent with the small particle size of the material. Upon firing the sample, the small particles tend to fuse to produce agglomerates (Figure 2b), but no phase separation is detected by powder XRD for samples fired at 900 °C.

To confirm the assignment of oxidation states in the new material, we collected X-ray absorption near-edge structure (XANES) spectra at the Ce L_{III} and Ti K edges. When compared to reference materials containing the metals in known oxidation states, the characteristic edge shifts and near-edge structures of the XANES spectra allow the

 © 2006 Wiley-VCH Verlag GmbH & Co. KGaA, Weinheim

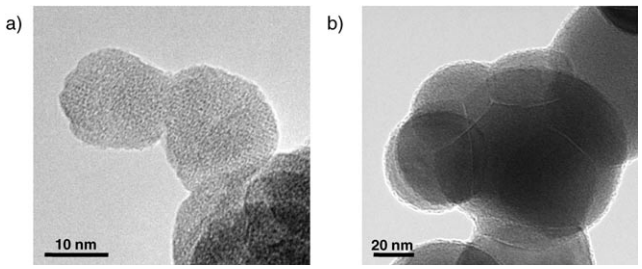

Figure 2. TEM images of typical particles found in a) the as-made $(Na_{1/3}Ce_{2/3})_2Ti_2O_7$ material, and b) a sample of $(Na_{1/3}Ce_{2/3})_2Ti_2O_7$ fired at 900 °C.

oxidation states of the metals to be inferred (Figure 3).[15] These results corroborate our formulation of the pyrochlore as $(Na_{1/3}Ce^{IV}{}_{2/3})_2Ti^{IV}{}_2O_7$. A full analysis of the Ti K edge extended X-ray absorption fine structure (EXAFS) spectrum shows that the local environment of the Ti atom is consistent with the pyrochlore structure (see Supporting Information). $(Na_{1/3}Ce^{IV}{}_{2/3})_2Ti_2O_7$ is the first example of a pyrochlore that contains solely Ce^{IV}; the only other Ce^{IV}-containing materials with related structures belong to the family $(Ce^{III}{}_{1-x}Ce^{IV}{}_x)_2Zr_2O_{7+x}$ $(x < 0.36)$, produced by the oxidation of the stoichiometric parent phase $Ce^{III}{}_2Zr_2O_7$ through the intercalation of interstitial oxide ions.[18]

To assess the catalytic properties of $(Na_{1/3}Ce_{2/3})_2Ti_2O_7$, we used temperature-programmed reduction/oxidation (TPR/TPO) as a diagnostic test of redox activity (Figure 4).[19] The

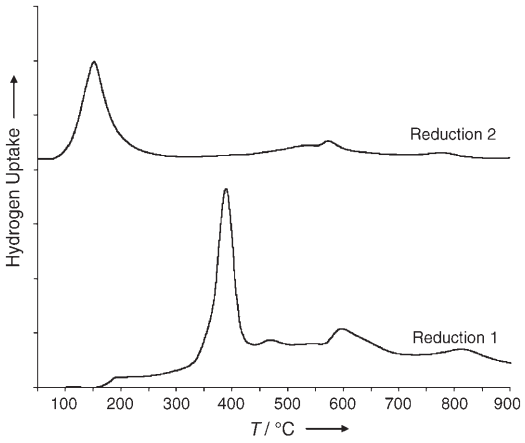

Figure 4. TPR data for $(Na_{1/3}Ce_{2/3})_2Ti_2O_7$. After an initial cycle of reduction (bottom) and low-temperature re-oxidation, the temperature of reduction decreases in the second (top) and subsequent cycles. The curves are vertically offset for clarity.

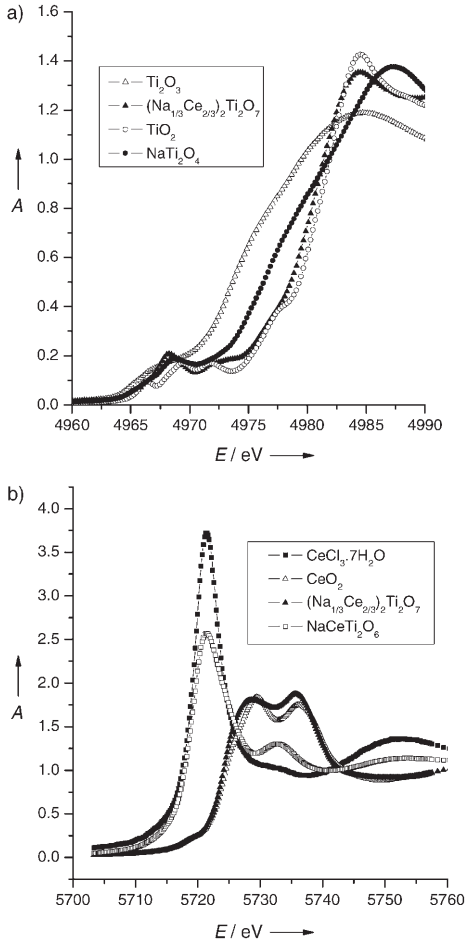

Figure 3. Normalized XANES spectra for $(Na_{1/3}Ce_{2/3})_2Ti_2O_7$ and reference compounds at a) the Ti K edge, and b) the Ce L_{III} edge.

reduction of the sample was carried out using 10% H_2 in N_2, while heating from 50–500 °C at 10 °C min^{-1}, and the subsequent re-oxidation was carried out using 5% O_2 in Ar, while heating from 30–250 °C. In the initial redox cycle, the majority of the Ce^{IV} is reduced to Ce^{III} at 375 °C. After re-oxidation of the sample, the material undergoes reduction over the strikingly low temperature range 100–250 °C in the second cycle. This low-temperature reduction is reproducible and also occurs in the third and subsequent redox cycles, with no apparent loss in activity. The initial activation step could be explained by the loss of surface water, as detected in the TGA experiment, but some ceria–zirconia materials undergo a similar activation after a cycle of reduction followed by low-temperature re-oxidation.[20] During the reduction steps, the hydrogen uptake by $(Na_{1/3}Ce_{2/3})_2Ti_2O_7$ is 1.8 mmol [H] g^{-1}, which corresponds to a reduction of not more than 50% of the Ce^{IV}. In situ XANES experiments, under a flow of 5% H_2 in N_2 , while heating from 25–500 °C, confirm that close to 50% of the Ce^{IV} in $(Na_{1/3}Ce_{2/3})_2Ti_2O_7$ is reduced to Ce^{III} during the process (Figure 5), and furthermore provide no evidence for the reduction of Ti^{IV}. The in situ XANES experiments also demonstrate that the Ce^{III} is rapidly and fully re-oxidized (in a matter of minutes) to Ce^{IV}, upon exposure to air at room temperature.

The temperature of reduction of $(Na_{1/3}Ce_{2/3})_2Ti_2O_7$ is considerably lower than is typically observed for ceria-based solids. Ceria itself undergoes reduction at 500 °C, and only when activated with a precious metal, such as Rh, undergoes a low-temperature reduction at less than 200 °C.[21] The best unactivated ceria–zirconia catalysts typically exhibit a low-temperature reduction characterized by a broad TPR signal from 200–350 °C.[6,7,20] The pyrochlore structure may be

 © 2006 Wiley-VCH Verlag GmbH & Co. KGaA, Weinheim

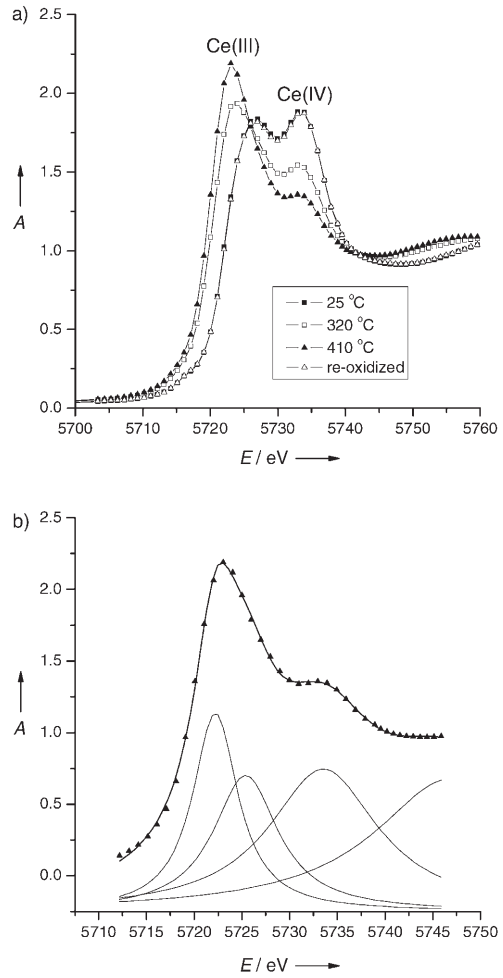

Figure 5. a) Selected in situ Ce L_{III} edge XANES spectra of $(Na_{1/3}Ce_{2/3})_2Ti_2O_7$ recorded under a flow of 5% H_2 in N_2 at temperatures of 25, 320, and 410°C. The re-oxidized sample was obtained by exposing the sample to air. b) Deconvolution of the 410°C spectrum by Lorentzian fitting, illustrating how the relative amounts of Ce^{IV} and Ce^{III} are quantified (by comparison to the spectra of reference materials, not shown).

thought of as a distorted, anion-deficient version of the fluorite structure; it is, therefore, probable that oxide-ion mobility in $(Na_{1/3}Ce_{2/3})_2Ti_2O_7$ is enhanced over that of fluorite-type ceria-based solids. In the pyrochlore structure, there are two sites for oxide ions, the O site (48*f*), which bridges the A (16*c*) and B (16*d*) metal sites, and the O′ site (8*a*), which is only associated with the A metal sites; thus, the structural formula of pyrochlores can also be written as $A_2B_2O_6O'$. The A metals and the O′ oxide ions reside in channels running through the network of linked $\{TiO_6\}$ octahedra (Figure 6). Considering the structure of the material, as well as the TPR and XANES results, we therefore propose that, during the redox process, the reaction described by Equation (1) takes place. It is conceivable that the presence of Na^+ prevents further reduction of the Ce^{IV} ions.

$$(Na_{1/3}Ce^{IV}{}_{2/3})_2Ti_2O_6O' + 1/3\,H_2 \leftrightarrow (Na_{1/3}Ce^{IV}{}_{1/3}Ce^{III}{}_{1/3})_2Ti_2O_6O'_{2/3} + 1/3\,H_2O \quad (1)$$

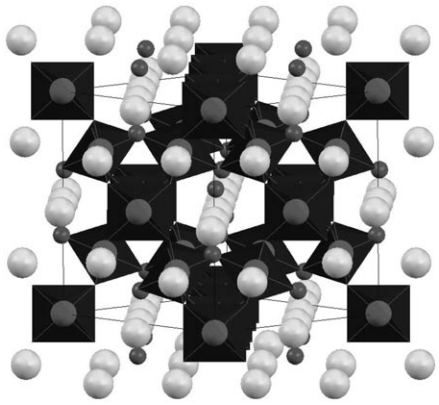

Figure 6. The pyrochlore-type structure of $(Na_{1/3}Ce_{2/3})_2Ti_2O_7$. Channels running through the network of linked $\{TiO_6\}$ octahedra (black) contain A (Na/Ce; large pale spheres) and O′ (small dark spheres) sites. The unit cell is indicated.

Interestingly, it has recently been suggested that the presence of pyrochlore-type phases under reducing conditions is important in determining the redox behavior of ceria–zirconia mixed oxides.[22] The high surface area of $(Na_{1/3}Ce_{2/3})_2Ti_2O_7$ might also contribute to its ease of reduction, as reported for CeO_2 samples.[23] However, we have discovered that amorphous cerium(IV) titanates with similar surface areas (approximately 100 m^2g^{-1}) isolated from hydrothermal reactions performed at $T < 200$°C do not exhibit the same low-temperature reduction properties as the crystalline $(Na_{1/3}Ce_{2/3})_2Ti_2O_7$ phase, and in fact are almost inactive towards reduction. EXAFS analysis of one of these amorphous materials showed that the component Ti atoms do not have the same local environment as found in the pyrochlore structure (see Supporting Information). We, thus, propose that the atomic order of the pyrochlore structure is largely responsible for the low-temperature reduction of Ce^{IV} in $(Na_{1/3}Ce_{2/3})_2Ti_2O_7$, and that the small particle size, although advantageous, is not the main origin of the material's remarkable redox activity.

In summary, we have demonstrated that mild hydrothermal synthesis provides a one-step route to a quaternary oxide that has not been isolated by other synthetic methods, in nanoparticulate form. By means of oxidizing conditions in the hydrothermal autoclave, we can isolate a Ce^{IV}–Ti^{IV} oxide, rather than phases containing the metals in lower oxidation states. Thus, we have gained some synthetic control over the oxidation levels of the constituent metals in a complex oxide.

Experimental Section

XAFS spectra were collected on Station 7.1 of the Daresbury SRS at the Ce L_{III} and Ti K edges in transmission mode for samples diluted with approximately 80% by mass of BN and pressed into self-supporting pellets. The station is equipped with a harmonic-rejecting double-crystal Si(111) monochromator, the second crystal of which allows sagittal focusing of the X-ray beam. Harmonic rejection was set to 50% for all experiments, by detuning the second crystal to 50% of the maximum X-ray intensity. Data were also measured simultaneously from a 5-μm Ti foil placed between the second and third ionization chambers to provide an edge-shift calibration for the

 © 2006 Wiley-VCH Verlag GmbH & Co. KGaA, Weinheim

XANES data. Data were collected in three regions: 1) the pre-edge region, with a step size of 10 eV to allow a pre-edge background calculation and subtraction, 2) the XANES region from 30 eV below the absorption edge to 50 eV above the edge, with a step size of 0.2 eV, and 3) the EXAFS region, up to an energy of $k = 13$ Å^{-1}. In situ XANES experiments were performed from room temperature to 500 °C under a flow of 5 % H_2 in N_2 over pellets of the sample diluted with BN. In separate experiments, data were measured at the Ce L_{III} and Ti K edges every 4 min, using a Quick-EXAFS scanning double-crystal monochromator. The XANES data for the Ce L_{III} edge were deconvoluted by fitting a series of Lorentzian functions to the near-edge region. The average oxidation state of Ce under reducing conditions was determined by comparing the near-edge features to those of a reference series of physical mixtures of $CeCl_3 \cdot 7H_2O$ and CeO_2.

Received: October 20, 2005
Published online: March 9, 2006

Keywords: cerium · hydrothermal synthesis · oxides · reduction · X-ray absorption spectroscopy

[1] H. Yokokawa, N. Sakai, T. Horita, K. Yamaji, M. E. Brito, *MRS Bull.* **2005**, *30*, 591.
[2] A. Trovarelli, C. de Leitenburg, M. Boaro, G. Dolcetti, *Catal. Today* **1999**, *50*, 353.
[3] *Catalysis by Ceria and Related Materials* (Ed.: A. Trovarelli), Imperial College Press, London, **2002**.
[4] M. Ozawa, C.-K. Loong, *Catal. Today* **1999**, *50*, 329.
[5] H.-W. Jen, G. W. Graham, W. Chun, R. W. McCabe, J.-P. Cuif, S. E. Deutsch, O. Touret, *Catal. Today* **1999**, *50*, 309.
[6] R. D. Monte, J. Kašpar, *Catal. Today* **2005**, *100*, 27.
[7] R. D. Monte, J. Kašpar, *J. Mater. Chem.* **2005**, *15*, 633.
[8] J. G. Li, T. Ikegami, Y. R. Wang, T. Mori, *J. Solid State Chem.* **2002**, *168*, 52.
[9] A. D. Deshpande, N. Pinna, P. Beato, M. Antonietti, M. Niederberger, *Chem. Mater.* **2004**, *16*, 2599.
[10] G. Li, R. L. Smith, H. Inomata, *J. Am. Chem. Soc.* **2001**, *123*, 11091.
[11] R. A. Laudise, *Chem. Eng. News* **1987**, *65*, 30.
[12] M. Leblanc, G. Férey, R. De Pape, *Mater. Res. Bull.* **1984**, *19*, 1581.
[13] G. Demazeau, *J. Mater. Chem.* **1999**, *9*, 15.
[14] R. I. Walton, *Chem. Soc. Rev.* **2002**, *31*, 230.
[15] C. S. Wright, R. I. Walton, D. Thompsett, J. Fisher, *Inorg. Chem.* **2004**, *43*, 2189.
[16] O. Knop, F. Brisse, L. Castelliz, *Can. J. Chem.* **1969**, *47*, 971.
[17] F. Brisse, D. J. Stewart, V. Seidel, O. Knop, *Can. J. Chem.* **1972**, *50*, 3648.
[18] J. B. Thomson, A. R. Armstrong, P. G. Bruce, *Chem. Commun.* **1996**, 1165.
[19] S. Bernal, G. Blanco, J. J. Calvino, J. M. Gatica, J. A. P. Omil, J. M. Pintado, *Top. Catal.* **2004**, *28*, 31.
[20] R. T. Baker, S. Bernal, G. Blanco, A. M. Cordón, J. M. Pintado, J. M. Rodríguez-Izquierdo, F. Fally, V. Perrichon, *Chem. Commun.* **1999**, 149.
[21] M. Boaro, M. Vicario, C. de Leitenburg, G. Dolcetti, A. Trovarelli, *Catal. Today* **2003**, *77*, 407.
[22] T. Montini, M. A. Banares, N. Hickey, R. D. Monte, P. Fornasiero, J. Kăpar, M. Graziani, *Phys. Chem. Chem. Phys.* **2004**, *6*, 1.
[23] V. Perrichon, A. Laachir, G. Bergeret, R. Frety, L. Tournayan, O. Touret, *J. Chem. Soc. Faraday Trans.* **1994**, *90*, 773.

 © 2006 Wiley-VCH Verlag GmbH & Co. KGaA, Weinheim

Synthetic Methods

DOI: 10.1002/anie.200504050

Nickel-Catalyzed Three-Component [3+2+2] Cocyclization of Ethyl Cyclopropylideneacetate and Alkynes—Selective Synthesis of Multisubstituted Cycloheptadienes**

*Shinsuke Komagawa and Shinichi Saito**

Transition-metal-catalyzed multicomponent-assembling reactions are useful methods in organic synthesis.[1] Selective synthesis of cyclic compounds by short routes is an especially important issue.[2] Although numerous examples of transition-metal-catalyzed [2+2+2] cocyclization reactions for the synthesis of benzene derivatives have been reported,[2,3] few examples of [3+2+2] cocyclization reactions leading to seven-membered rings are available.[4,5] Examples of intermolecular three-component cocyclization reactions are particularly rare, and in many cases, an equivalent of metal complex is used.[6] We have recently reported that a new intermolecular [3+2+2] cycloaddition reaction of ethyl cyclopropylideneacetate (**1**) with alkynes proceeded in the presence of a Ni^0/PPh_3 catalyst, and the formation of cycloheptadiene derivatives was observed.[4] In this reaction, two molecules of alkyne were incorporated into a seven-membered ring. Subsequently, we examined the possibility of the three-component reaction involving **1** and two different alkynes occurring in the presence of nickel catalysts. Herein, we describe a new nickel-catalyzed three-component [3+2+2] cocyclization of **1** and alkynes (Scheme 1).

We examined the reaction of **1**, trimethylsilylacetylene (**2a**), and various alkynes (**3**) in the presence of 10 mol% "$Ni(PPh_3)_2$", which was prepared in situ from $[Ni(cod)_2]$ (cod = 1,5-cyclooctadiene) and PPh_3.[7] Surprisingly, the formation of only one isomer (**4**) was observed, and other regioisomers were not identified. The best yields were obtained by the use of one equivalent of **1**, four equivalents of **2a**, and one equivalent of **3**. The yield decreased when a smaller amount of **2a** or a larger amount of **3** was used.[8] Among the phosphine ligands we examined, PPh_3 proved to be the most efficient. The reaction proceeded smoothly in dry toluene or DMF, but lower yields were observed when the

[*] S. Komagawa, Prof. Dr. S. Saito
Department of Chemistry
Faculty of Science
Tokyo University of Science
Kagurazaka, Shinjuku, Tokyo 162-8601 (Japan)
Fax: (+81) 3-3235-2214
E-mail: ssaito@rs.kagu.tus.ac.jp

[**] We thank the Tokyo University of Science (Special Grants), the Mitsubishi Chemical Corporation Fund, the Saneyoshi Scholarship Foundation, and The Kurata Memorial Hitachi Science and Technology Foundation for financial support.

Supporting information for this article is available on the WWW under http://www.angewandte.org or from the author.

WILEY InterScience DISCOVER SOMETHING GREAT
© 2006 Wiley-VCH Verlag GmbH & Co. KGaA, Weinheim

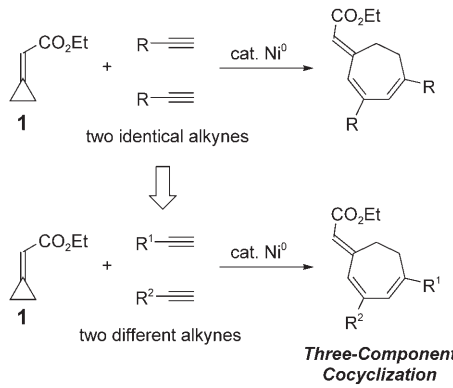

Scheme 1. Three-component [3+2+2] cocyclization of **1** and two different alkynes.

reaction was carried out in dry THF, diethyl ether, or CH_2Cl_2.[9]

The results of the three-component coupling reactions of **1**, **2a**, and alkynes **3a–h** are shown in Table 1. A variety of

Table 1: Nickel-catalyzed three-component cycloaddition of **1**, **2a**, and alkynes **3a–h**.[a]

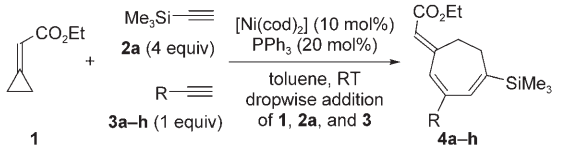

Entry	Compound	R	Yield of **4** [%][b]
1	**3a**	$MeOCH_2$	69 (**4a**)[c]
2	**3b**	$tBuMe_2SiOCH_2$	67 (**4b**)
3	**3c**	$PhCH_2$	66 (**4c**)
4	**3d**	n-C_6H_{13}	68 (**4d**)
5	**3e**	Ph	56 (**4e**)
6[d]	**3e**	Ph	72 (**4e**)
7	**3f**	p-$MeOC_6H_4$	65 (**4f**)
8	**3g**	p-$CF_3C_6H_4$	74 (**4g**)
9	**3h**	$HO(CH_3)_2C$	69 (**4h**)

[a] Reaction conditions: A solution of **1** (1 mmol), **2a** (4 mmol), and **3** (1 mmol) in toluene (0.5 mL) was added dropwise over 5 h to a mixture of $[Ni(cod)_2]$ (0.1 mmol) and PPh_3 (0.2 mmol) in dry toluene (0.5 mL) at room temperature under Ar. The mixture was then stirred overnight. [b] Yields of isolated product. [c] Essentially the same yields were obtained for three experiments. [d] A larger amount of **3e** (1.2 equiv) was used.

alkynes could be used in this three-component cocyclization. For example, the reactions with propargyl ethers (Table 1, entries 1 and 2) and propargylbenzene (Table 1, entry 3) gave cycloheptadiene derivatives **4a–c** in good yields. Terminal aliphatic alkynes such as 1-octyne (**3d**) were also good substrates for this reaction (Table 1, entry 4). Phenylacetylene derivatives **3e–g** reacted with **1** and **2a**, and the corresponding cycloheptadiene derivatives were isolated in yields of 56–74% (Table 1, entries 5–8). In the case of the reaction of phenylacetylene (**3e**), the yield of **4e** improved when 1.2 equivalents of **3e** were used (Table 1, entry 6). Variation of the substituents on the aromatic rings at the *para* position did not significantly influence the yields (Table 1, entries 7,8). The reaction of propargyl alcohol **3h** also occurred, and compound **4h** was isolated in 69% yield (Table 1, entry 9). The structure of the cycloheptadiene derivative **4d** was confirmed by NOESY experiments (see the Supporting Information).

We previously reported that the use of bulky terminal alkynes led to the regioselective formation of cycloheptadienes, while less-congested terminal alkynes gave regioisomers of cycloheptadienes.[4] In contrast, the selective cycloaddition reactions proceeded smoothly even when these three-component reactions were carried out with **2a** and less-congested alkynes (**3a–d**, Table 1, entries 1–4).

Subsequently, we examined the reaction of various bulky alkynes **2** with **1** and **3** (Table 2). (*tert*-Butyldimethylsilyl)-

Table 2: Nickel-catalyzed three-component cycloaddition of **1** and alkynes.[a]

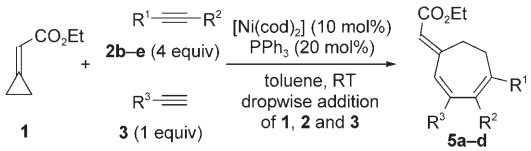

Entry	R^1, R^2	R^3	Yield of **5** [%][b]
1	$tBuMe_2Si$, H (**2b**)	$MeOCH_2$ (**3a**)	66 (**5a**)
2	$PhCH_2Me_2Si$, H (**2c**)	Ph (**3e**)	58 (**5b**)
3	tBu, H (**2d**)	$MeOCH_2$ (**3a**)	50 (**5c**)
4	nPr, nPr (**2e**)	$MeOCH_2$ (**3a**)	46 (**5d**)

[a] Reaction conditions: A solution of **1** (1 mmol), **2** (4 mmol), and **3** (1 mmol) in toluene (0.5 mL) was added dropwise over 5 h to a mixture of $[Ni(cod)_2]$ (0.1 mmol) and PPh_3 (0.2 mmol) in dry toluene (0.5 mL) at room temperature under Ar. The mixture was then stirred overnight. [b] Yields of isolated product.

acetylene (**2b**) reacted in a similar way with **1** and **3a** (Table 2, entry 1) as **2a** did. (Benzyldimethylsilyl)acetylene (**2c**) could also be used (Table 2, entry 2). Since vinyl(benzyl)dimethylsilanes have been reported to be good substrates for the fluoride-promoted cross-coupling reaction with aryl iodides in the presence of a Pd catalyst,[10] compound **5c** would be a promising substrate for the synthesis of complex cycloheptane derivatives. *tert*-Butylacetylene (**2d**) also gave the corresponding cycloaddition product in moderate yield (Table 2, entry 3). The reaction of **1** and **3a** with an internal alkyne such as 4-octyne (**2e**) occurred, and the cycloheptadiene **5d** was obtained in 46% yield (Table 2, entry 4).

A proposed mechanism of this three-component reaction is shown in Scheme 2. Initially, two molecules of different alkynes **2** and **3** coordinate to a nickel complex, and a nickelacyclopentadiene complex **6** is formed. The selective formation of **6** has been predicted theoretically, and supporting experimental evidence has been reported.[6a,11,12] Stockis and Hoffmann predicted the selective formation of metallacyclopentadiene complexes similar to **6** on the basis of calculations of the molecular orbitals.[12] The preferential formation of a complex similar to **6** has also been indicated in the three-component [2+2+2] cocycloaddition reaction

 © 2006 Wiley-VCH Verlag GmbH & Co. KGaA, Weinheim

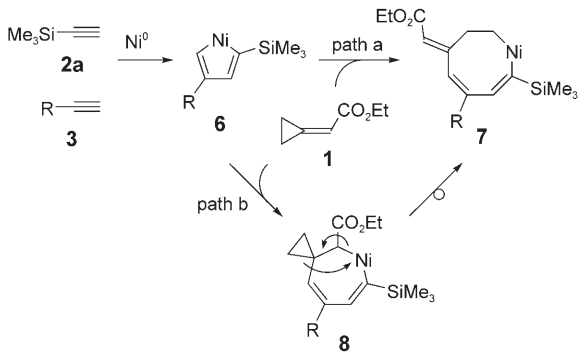

Scheme 2. Proposed mechanism of the three-component cocyclization of **1** and alkynes.

reported by Ikeda and co-workers.[6a,13,14] The presence of a larger amount of the less reactive **2a** prevents the formation of the nickelacyclopentadiene complex that would be formed by two molecules of **3** with the Ni catalyst. Furthermore, the slow addition of the substrates to the nickel catalyst also facilitates the formation of **6**. A nickelacyclooctadiene complex **7** is formed by the insertion of a C–C σ bond (path a) or the C–C π bond (path b) of **1** into **6**.[15–17] The direct insertion of the C–C bond proximal to the C–C double bond of the methylenecyclopropane fragment might proceed (path a).[17] Alternatively, a nickelacycloheptadiene intermediate **8**, which is formed by the reaction of **1** and **6**, could undergo cyclopropylmethyl–butenyl rearrangement (path b).[16,18] The selective insertion of **1** into **6** would proceed because of the presence of the bulky trimethylsilyl group and the electronic configuration of the C–Ni bond.[11,15] Finally, reductive elimination of the nickel catalyst gives the cycloheptadiene derivative.[19]

In conclusion, we have developed a new three-component assembling reaction which gave polysubstituted seven-membered carbocycles. This [3+2+2] cocyclization reaction proceeded in good yields, and the chemo- and regioselective formation of cycloheptadienes was observed. The wide scope of the reaction with various terminal alkynes is a characteristic of this reaction.

Received: November 15, 2005
Revised: January 6, 2006
Published online: March 9, 2006

Keywords: alkynes · cycloaddition · cycloheptadienes · nickel · synthetic methods

[1] Reviews: a) D. J. Ramón, M. Yus, *Angew. Chem.* **2005**, *117*, 1628 – 1661; *Angew. Chem. Int. Ed.* **2005**, *44*, 1602 – 1634; b) S. Ikeda, *Acc. Chem. Res.* **2000**, *33*, 511 – 519; c) A. Dömling, I. Ugi, *Angew. Chem.* **2000**, *112*, 3300 – 3344; *Angew. Chem. Int. Ed.* **2000**, *39*, 3168 – 3210; d) G. Balme, E. Bossharth, N. Monteiro, *Eur. J. Org. Chem.* **2003**, 4101 – 4111.

[2] For recent reviews of transition-metal-catalyzed cycloaddition reactions, see: a) J. Montgomery, *Angew. Chem.* **2004**, *116*, 3980 – 3998; *Angew. Chem. Int. Ed.* **2004**, *43*, 3890 – 3908; b) J. A. Varela, C. Saá, *Chem. Rev.* **2003**, *103*, 3787 – 3801; c) S. Saito, Y. Yamamoto, *Chem. Rev.* **2000**, *100*, 2901 – 2915; d) V. Gevorgyan, Y. Yamamoto, *J. Organomet. Chem.* **1999**, *576*, 232 – 247; e) M. Lautens, W. Klute, W. Tam, *Chem. Rev.* **1996**, *96*, 49 – 92; f) N. E. Schore, *Chem. Rev.* **1988**, *88*, 1081 – 1119; g) K. P. C. Vollhardt, *Angew. Chem.* **1984**, *96*, 525 – 541; *Angew. Chem. Int. Ed. Engl.* **1984**, *23*, 539 – 556.

[3] For reviews of the nickel-catalyzed oligomerization of alkynes, see: a) "Cyclooligomerization and Cycloisomerization of Alkenes and Alkynes": S. Saito in *Modern Organonickel Chemistry* (Ed.: Y. Tamaru), Wiley-VCH, Weinheim, **2005**, pp. 171 – 204; b) "Nickel Catalyzed Oligomerization of Alkynes and Related Reactions": P. W. Jolly in *Comprehensive Organometallic Chemistry*, *Vol. 8* (Eds.: G. Wilkinson, F. G. A. Stone, E. W. Abel), Pergamon, Oxford, **1982**, pp. 649 – 670.

[4] S. Saito, M. Masuda, S. Komagawa, *J. Am. Chem. Soc.* **2004**, *126*, 10540 – 10541.

[5] For examples of [3+2+2] cocyclization, see: a) K. E. Schwiebert, J. M. Stryker, *J. Am. Chem. Soc.* **1995**, *117*, 8275 – 8276; b) N. Etkin, T. K. Dzwiniel, K. E. Schweibert, J. M. Stryker, *J. Am. Chem. Soc.* **1998**, *120*, 9702 – 9703; c) J. Barluenga, R. Vicente, P. Barrio, L. A. López, M. Tomás, J. Borge, *J. Am. Chem. Soc.* **2004**, *126*, 14354 – 14355; d) P. Binger, U. Schuchardt, *Chem. Ber.* **1980**, *113*, 1063 – 1071.

[6] For examples of intermolecular three-component cocyclization, see: a) N. Mori, S. Ikeda, Y. Sato, *J. Am. Chem. Soc.* **1999**, *121*, 2722 – 2727; b) T. Takahashi, Z. Xi, A. Yamazaki, Y. Liu, K. Nakajima, M. Kotora, *J. Am. Chem. Soc.* **1998**, *120*, 1672 – 1680; c) T. Takahashi, F. Tsai, Y. Li, H. Wang, Y. Kondo, M. Yamanaka, K. Nakajima, M. Kotora, *J. Am. Chem. Soc.* **2002**, *124*, 5059 – 5067; d) L. Deng, A. J. Giessert, O. O. Gerlitz, X. Dai, S. T. Diver, H. M. L. Davies, *J. Am. Chem. Soc.* **2005**, *127*, 1342 – 1343; e) N. Mori, S. Ikeda, K. Odashima, *Chem. Commun.* **2001**, 181 – 182; f) Y. Wakatsuki, K. Aoki, H. Yamazaki, *J. Am. Chem. Soc.* **1979**, *101*, 1123 – 1130; g) G. Chouraqui, M. Petit, C. Aubert, M. Malacria, *Org. Lett.* **2004**, *6*, 1519 – 1521.

[7] The yield was reduced (58%) and the starting material **1** was not consumed when the reaction was carried out in the presence of 5 mol% of catalyst.

[8] The reaction of **1** with a smaller amount of **2a** (2 equiv) and **3a** (1 equiv) proceeded in 61% yield. When a larger amount of **3a** (1.2 equiv) was used, the product was observed in 62% yield.

[9] The three-component coupling of 1-cyclopropylidenepropan-2-one, trimethylsilylacetylene, and methyl propargyl ether also occurred, albeit in low yield.

[10] a) S. E. Denmark, S. A. Tymonko, *J. Am. Chem. Soc.* **2005**, *127*, 8004 – 8005; b) S. E. Denmark, R. F. Sweis, D. Wehrli, *J. Am. Chem. Soc.* **2004**, *126*, 4865 – 4875.

[11] a) Y. Wakatsuki, O. Nomura, K. Kitaura, K. Morokuma, H. Yamazaki, *J. Am. Chem. Soc.* **1983**, *105*, 1907 – 1912; b) J. J. Eisch, G. A. Damasevitz, *J. Organomet. Chem.* **1975**, *96*, C19 – C22.

[12] S. Stockis, R. Hoffmann, *J. Am. Chem. Soc.* **1980**, *102*, 2952 – 2962.

[13] In our study, the formation of a nickelacyclopentadiene complex **6** from **2a** and **3e** is controlled by the slow addition of **3e** to maintain a low concentration of **3e** in the reaction mixture. The lower concentration of **3** suppresses the formation of an alternative nickelacyclopentadiene complex resulting from two molecules of the more reactive **3**.

[14] We assume that an equilibrium exists between **6** and **6′**, and the more reactive (sterically less congested) **6** would selectively react with **1**.

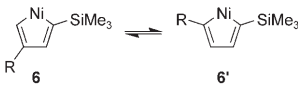

 © 2006 Wiley-VCH Verlag GmbH & Co. KGaA, Weinheim

[15] For reviews of transition-metal-catalyzed cycloadditions of methylenecyclopropanes, see: a) P. Binger, H. M. Büch, *Top. Curr. Chem.* **1987**, *135*, 77–151; b) "Metal-Catalyzed Cycloadditions of Methylenecyclopropanes": P. Binger, T. Schmidt in *Methods of Organic Chemistry (Houben-Weyl)*, *Vol.E17b* (Ed.: A. de Meijere), Thieme, Stuttgart, **1997**, pp. 2217–2294.

[16] For examples of transition-metal-catalyzed reactions of methylenecyclopropanes and vinylcyclopropanes, which involve similar reactions of the cyclopropylmethyl–butenyl rearrangement, see: a) T. Kawasaki, S. Saito, Y. Yamamoto, *J. Org. Chem.* **2002**, *67*, 4911–4915; b) P. Binger, P. Müller, S. Podubrin, S. Albus, C. Krüger, *J. Organomet. Chem.* **2002**, *656*, 288–298; c) H. Nüske, M. Noltemeyer, A. de Meijere, *Angew. Chem.* **2001**, *113*, 3509–3511; *Angew. Chem. Int. Ed.* **2001**, *40*, 3411–3413; d) P. A. Wender, G. G. Gamber, R. D. Hubbard, L. Zhang, *J. Am. Chem. Soc.* **2002**, *124*, 2876–2877; e) P. A. Wender, H. Takahashi, B. Witulski, *J. Am. Chem. Soc.* **1995**, *117*, 4720–4721.

[17] For reviews of transition-metal-catalyzed carbon–carbon bond-cleavage reactions, see: a) B. Rybtchinski, D. Milstein, *Angew. Chem.* **1999**, *111*, 918–932; *Angew. Chem. Int. Ed.* **1999**, *38*, 870–883; b) K. C. Bishop, *Chem. Rev.* **1976**, *76*, 461–486; c) R. H. Crabtree, *Chem. Rev.* **1985**, *85*, 245–269.

[18] The cyclopropylmethyl–butenyl rearrangement has been reported, and related intermediates were isolated; see: P. Binger, M. J. Doyle, R. Benn, *Chem. Ber.* **1983**, *116*, 1–10.

[19] An alternative mechanism might be possible. At first, a nickelacyclopentene intermediate **9** is formed from **1** and the less-congested alkyne **3**.[6a,9–12] The insertion of the bulky alkyne **2a** then occurs to give **8**. A nickelacyclohexene intermediate **10** could also be formed from **9** by rearrangement, but currently, we assume that compound **10** would undergo facile reductive elimination to provide the corresponding cyclopentane derivative, and the further insertion of the alkyne is less likely to occur.

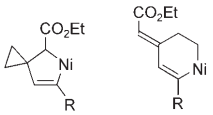

9 **10**

 © 2006 Wiley-VCH Verlag GmbH & Co. KGaA, Weinheim

Chiral Resolution

DOI: 10.1002/anie.200504116

A Practical Approach to the Resolution of Racemic *N*-Benzyl α-Amino Acids by Liquid–Liquid Extraction with a Lipophilic Chiral Salen–Cobalt(III) Complex**

Toby B. Reeve, Jean-Philippe Cros, Cesare Gennari, Umberto Piarulli,* and Johannes G. de Vries*

The development of chiral hosts for the enantioselective recognition and separation of α-amino acids and their derivatives represents an open challenge as a method for the production of enantiopure compounds. A simultaneous binding of both the amino and the carboxylic group is usually required to achieve chiral discrimination,[1] which makes metal ions modified with a chiral ligand ideal species for such selection. In fact, transition-metal complexes have been used in several such molecular-recognition studies,[2] including the selective crystallization from a racemic mixture of a complex of one enantiomer bound to the chiral selector.[3] Molecular recognition involving chiral transition-metal complexes has also been demonstrated in various practical methods for the separation of enantiomers including chiral HPLC,[4] transport across a liquid membrane,[5] micelle-enhanced ultrafiltration,[6] and co-micellar systems with two aqueous phases.[7]

In the cases described above the complexes were usually based on the coordination of ligands derived from amino acids or amines to Cu^{II} ions,[3–7] although enantioselective complexes of other metal ions, such as Co^{II} and Ni^{II}, have also

[*] Dr. T. B. Reeve, Dr. J.-P. Cros, Prof. Dr. C. Gennari
Dipartimento di Chimica Organica e Industriale
Centro di Eccellenza C.I.S.I.
Università degli Studi di Milano
Istituto di Scienze e Tecnologie Molecolari (ISTM) del CNR
Via G. Venezian, 21, 20133 Milano (Italy)
Fax: (+39) 02-5031-4072
E-mail: cesare.gennari@unimi.it

Prof. Dr. U. Piarulli
Dipartimento di Scienze Chimiche e Ambientali
Università degli Studi dell'Insubria
Via Valleggio, 11, 22100 Como (Italy)
Fax: (+39) 031-238-6449
E-mail: umberto.piarulli@uninsubria.it

Prof. Dr. J. G. de Vries
DSM Pharma Chemicals—Advanced Synthesis, Catalysis & Development
P.O. Box 18, 6160 MD Geleen (The Netherlands)

[**] We thank the European Commission for financial support (IHP Network grant "Enantioselective Recognition: Towards the Separation of Racemates" HPRN-CT-2001-00182) and for postdoctoral fellowships to J.-P.C. and T.B.R. We would also like to thank "Merck Research Laboratories" (Merck's Academic Development Program Award to C.G.) for financial support. Salen = *N*,*N*′-bis(salicylidene)ethylenediamine dianion.

Supporting information for this article is available on the WWW under http://www.angewandte.org or from the author.

© 2006 Wiley-VCH Verlag GmbH & Co. KGaA, Weinheim

been reported.[2,3a] In one notable case, a chiral cobalt(II) complex derived from ligand **1** (Scheme 1), namely [Co^{II}(**1**)], was used in an enantioselective resolution of *N*-benzylalanine (*N*-Bn-Ala).[8] Treating [Co^{II}(**1**)] with two equivalents of

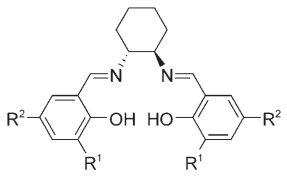

(*R*,*R*)-**1** $R^1 = R^2 = H$
(*R*,*R*)-**2** $R^1 = CH_3$, $R^2 = H$
(*R*,*R*)-**3** $R^1 = R^2 = t$Bu

Scheme 1. Chiral salen ligands.

racemic *N*-Bn-Ala in MeOH/H_2O (5:1), followed by extraction with $CHCl_3$/H_2O led to enantiomeric excesses of 94% (*R*) and 93% (*S*) for the complexed ([Co^{III}(**1**)(*N*-Bn-Ala)]) and the uncomplexed amino acid, respectively.[9] The major drawback of this approach resided in the necessity to use rather harsh conditions (reduction with $NaBH_4$) to release the complexed amino acid.

A promising methodology is the enantiomeric separation of racemic mixtures of hydrophilic substrates by liquid–liquid extraction.[10] This method involves the extraction of one enantiomer into an organic phase by selective coordination to a hydrophobic selector (for example, a chiral metal complex) to leave the uncomplexed enantiomer in an aqueous phase. The attraction of this method is that it circumvents the use of excessive handling of solids, which is associated with classical resolution by crystallization of diastereomeric salts; on a production scale this is often the slowest step in the process.

Herein we report a novel approach to the resolution of racemic *N*-benzyl α-amino acids by liquid–liquid extraction, using the lipophilic chiral salen–cobalt(III) complex [Co^{III}(**3**)(OAc)] (Scheme 2), in excellent yield and enantioselectivity. As a result of the resolution by extraction, one enantiomer of the *N*-benzyl amino acid predominates in the aqueous phase, while the other enantiomer is driven into the organic phase by complexation to the cobalt center. The complexed amino acid can then be released by a reductive (Co^{III}→Co^{II}) counter-extraction into an aqueous phase. The original chiral Co^{III} complex can be regenerated and reused with essentially no loss of reactivity or selectivity. Enantiomerically pure *N*-benzyl α-amino acids have found various important synthetic applications,[11] and can be easily transformed into α-amino acids by hydrogenolysis.[12]

As a preliminary investigation, we dissolved [Co^{II}(**1**)] (1 equiv) in dichloromethane and stirred this phase with an aqueous solution of racemic *N*-benzylalanine (2 equiv). As expected, the interaction of [Co^{II}(**1**)] with *N*-benzylalanine induced the air oxidation of the metal ion to cobalt(III) with concurrent formation of the cobalt(III) complex [Co^{III}(**1**)(*N*-Bn-Ala)]. This complex was isolated in nearly quantitative yield (99%) and was characterized by HRMS (ESI) as well as IR, ^{1}H and ^{13}C NMR spectroscopy. The absolute configuration (*S*) and the *ee* value of uncomplexed *N*-Bn-Ala (55.8% *ee*) were determined by HPLC analysis of the aqueous phase (Table 1, entry 1);[13] reduction of the Co^{III} complex with $NaBH_4$ led to the recovery of (*R*)-*N*-Bn-Ala with a consistent *ee* value. An extraction using the methyl-substituted analogue [Co^{II}(**2**)] under the same conditions again led to the formation of a cobalt(III) species, [Co^{III}(**2**)(*N*-Bn-Ala)], through air oxidation of the metal. In this case *N*-benzylalanine was also extracted in high yield (96%), however decreased enantioselectivity (38.9% *ee*) was observed in the unbound *N*-benzylalanine (Table 1, entry 2). The possibility of releasing the coordinated amino acid by using different reductive (Na_2SO_3, $Na_2S_2O_4$, $Na_2S_2O_3$, Na_2S, $NaBH_4$) or hydrolytic (HCl, CF_3COOH, CF_3SO_3H) methods was investigated; in general, no reaction occurred except by the above-mentioned reduction with $NaBH_4$.

Table 1: Extraction of racemic *N*-Bn-Ala using chiral salen–cobalt(II) and –cobalt(III) complexes at 10°C.

Entry	Host complex	Product	Equiv extracted	*ee* [%][a]
1	(*R*,*R*)-[Co^{II}(**1**)]	[Co^{III}(**1**)(*N*-Bn-Ala)]	0.99[b]	55.8[c]
2	(*R*,*R*)-[Co^{II}(**2**)]	[Co^{III}(**2**)(*N*-Bn-Ala)]	0.96[b]	38.9
3	(*R*,*R*)-[Co^{II}(**3**)]		0[b]	
4	(*R*,*R*)-[Co^{III}(**1**)(OAc)]	[Co^{III}(**1**)(*N*-Bn-Ala)]	0.92	54.8
5	(*R*,*R*)-[Co^{III}(**2**)(OAc)]	[Co^{III}(**2**)(*N*-Bn-Ala)]	0.99[d]	53.6
6	(*R*,*R*)-[Co^{III}(**3**)(OAc)]	[Co^{III}(**3**)(*N*-Bn-Ala)]	**0.99**	**93.0**
7	(*R*,*R*)-[Co^{III}(**3**)(OAc)][e]	[Co^{III}(**3**)(*N*-Bn-Ala)]	**0.98**	**93.0**
8	(*R*,*R*)-[Co^{III}(**3**)(OTf)]	[Co^{III}(**3**)(*N*-Bn-Ala)]	0.92	85.5
9	(*R*,*R*)-[Co^{III}(**3**)(PF_6)]	[Co^{III}(**3**)(*N*-Bn-Ala)]	0.92	87.8

[a] Determined on uncomplexed (*S*)-*N*-Bn-Ala by chiral HPLC analysis of the aqueous phase (see the Supporting Information). [b] Extractions were run at room temperature. [c] For a comment, see Ref. [13]. [d] Extraction time of 48 h was necessary, compared to 24 h in all other cases. [e] Second cycle: (*R*,*R*)-[Co^{III}(**3**)(OAc)] was obtained from [Co^{III}(**3**)-(*N*-Bn-Ala)] after reductive cleavage and reoxidation (see text and the Supporting Information).

Chiral ligand **3** is known for its selectivity in several asymmetric processes such as epoxidation, epoxide opening, and kinetic resolution.[14] It

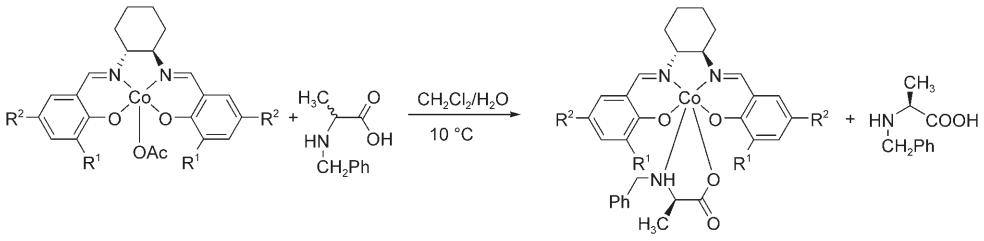

[Co^{III}(**1**)(OAc)] $R^1 = R^2 = H$
[Co^{III}(**2**)(OAc)] $R^1 = CH_3$, $R^2 = H$
[Co^{III}(**3**)(OAc)] $R^1 = R^2 = t$Bu

[Co^{III}(**1**)(*N*-Bn-Ala)]
[Co^{III}(**2**)(*N*-Bn-Ala)]
[Co^{III}(**3**)(*N*-Bn-Ala)]

Scheme 2. Resolution of a racemic mixture of *N*-benzylalanine by liquid–liquid extraction using salen–cobalt(III) complexes.

 © 2006 Wiley-VCH Verlag GmbH & Co. KGaA, Weinheim

can be easily prepared by a high-yielding one-pot method,[15] or is commercially available on a large scale along with its cobalt(II) complex [Co^{II}(**3**)]. However, disappointing results were obtained when complex [Co^{II}(**3**)] was employed in the extraction of *N*-benzylalanine by using our procedure: no oxidation of cobalt occurred, and no extraction of *N*-benzylalanine into the organic phase was observed.

These results indicated that formation of a cobalt(III) complex was necessary for obtaining both a high yield *and* enantioselectivity in the extraction. The increased stability of [Co^{II}(**3**)] towards oxidation led us to believe that a ternary complex [Co^{III}(**3**)(*N*-Bn-AA)] (AA = α-amino acid) might have an increased susceptibility towards reduction back to cobalt(II), thus facilitating an extraction/counterextraction cycle. With this in mind, salen–cobalt(III) acetate complexes [Co^{III}(**1**–**3**)(OAc)] (Scheme 2) were tested in our extraction procedure. These complexes were readily prepared from complexes [Co^{II}(**1**–**3**)], by oxidation with air in the presence of acetic acid.[16] It became apparent during the course of our investigation that there was a significant correlation between temperature and enantioselectivity, with extractions performed at 10 °C giving the optimal results.[17,18] The results of extractions using one equivalent of complexes [Co^{III}(**1**–**3**)(OAc)] with two equivalents of racemic *N*-benzylalanine under thermostated conditions at 10 °C are summarized in Table 1. In all cases, extraction of *N*-benzylalanine was very efficient and the cobalt(III)/amino acid complexes were isolated from the organic phase in near-quantitative yields. Enantioselectivities were moderate to high, with the *tert*-butyl-substituted ligand **3** giving the best results (93.0% *ee*, Table 1, entry 6). In addition, similar results were obtained when extractions were conducted with cobalt(III) complexes [Co^{III}(**3**)(X)] bearing alternative counterions (X = OTf, PF_6; Table 1, entries 8, 9).

The significance of the substituents on the salen ligand became further apparent when the counterextraction of complexed *N*-benzylalanine from ternary complex [Co^{III}(**3**)(*N*-Bn-Ala)] was investigated. We found that by vigorously mixing a solution of the complex in dichloromethane with an aqueous solution containing excess sodium dithionite (10 equiv),[19] the bound *N*-benzylalanine was cleaved from the complex and recovered in the aqueous phase in quantitative yield (Scheme 3). The *ee* value of this counterextracted *N*-benzylalanine was consistent with the expected value based on the *ee* value of the *N*-benzylalanine which remained in the aqueous phase after the initial extraction step. Furthermore, cobalt(III) was reduced back to cobalt(II) during the cleavage of complex [Co^{III}(**3**)(*N*-Bn-Ala)]; after separation, the pure [Co^{II}(**3**)] complex could be isolated from the organic phase by simple evaporation of dichloromethane, trituration in methanol, and filtration (78% recovered yield).[20] In contrast, complexes [Co^{III}(**1**)(*N*-Bn-Ala)] and [Co^{III}(**2**)(*N*-Bn-Ala)] were not reduced under these conditions.

The recovered [Co^{II}(**3**)] was then reoxidized with air in the presence of acetic acid, and the cobalt(III) acetate thus formed was reused in a second extraction with no loss of activity or enantioselectivity (Table 1, entry 7). It should be noted that in the case of [Co^{III}(**3**)(*N*-Bn-Ala)], the amino acid release/cobalt(II) complex recovery was not successful by using the previously reported[8] $NaBH_4$-reduction method.[21]

Preliminary studies into the scope of this methodology have been conducted with particular interest in adapting the procedure to substrates of varying hydrophilicity relative to *N*-benzylalanine. The results of extractions of a range of racemic *N*-benzyl amino acids using complex [Co^{III}(**3**)(OAc)] are summarized in Table 2. The extraction of water-soluble *N*-benzylthreonine proceeded in near quantitative yield (94%) and with high *ee* values (96.3%), thus leaving uncomplexed (*S*)-*N*-benzylthreonine in the aqueous phase (Table 2, entry 1). Extractions of racemic mixtures of *N*-benzylvaline, *N*-benzylleucine, and *N*-benzylphenylalanine were also investigated (Table 2, entries 2–4). These substrates, with increased lipophilicity compared to *N*-benzylalanine, are essentially insoluble in both neutral water and dichloromethane. In the cases of *N*-benzylvaline and *N*-benzylleucine, however, all of the substrate was drawn into solution to form

Table 2: Resolution of racemic *N*-Bn-amino acids using (*R*,*R*)-[Co^{III}(**3**)(OAc)] at 10 °C.

Entry	Substrate	Meth.[a]	Product	Equiv extracted	*ee* [%][b]
1	*N*-Bn-Thr	A	[Co^{III}(**3**)(*N*-Bn-Thr)]	0.94	96.3[c]
2	*N*-Bn-Val	A	[Co^{III}(**3**)(*N*-Bn-Val)]	0.98	90.1
3	*N*-Bn-Leu	A	[Co^{III}(**3**)(*N*-Bn-Leu)]	0.99	99.0
4	*N*-Bn-Phe	B	[Co^{III}(**3**)(*N*-Bn-Phe)]	0.99	93.3
5	*N*-Bn-Val	C	[Co^{III}(**3**)(*N*-Bn-Val)]	0.99	94.2
6	*N*-Bn-Phe	C	[Co^{III}(**3**)(*N*-Bn-Phe)]	0.98	92.7
7	*N*-Bn-Ala	C	[Co^{III}(**3**)(*N*-Bn-Ala)]	0.98	16.3
8	*N*-Bn-Ala	C	[Co^{III}(**3**)(*N*-Bn-Ala)]	0.98[d]	65.8

[a] Method A: biphasic water/dichloromethane extraction; method B: biphasic water/dichloromethane treatment and recovery of the uncomplexed amino acid by filtration; method C: stirring a suspension of the racemic *N*-Bn-amino acid with a solution of (*R*,*R*)-[Co^{III}(**3**)(OAc)] in dichloromethane and recovery of the uncomplexed amino acid by filtration. [b] Determined on the uncomplexed (*S*)-*N*-Bn-amino acid by chiral HPLC analysis. [c] Determined by chiral HPLC analysis on (*R*)-*N*-Bn-Thr, following treatment of [Co^{III}(**3**)(*N*-Bn-Thr)] with aqueous sodium dithionite. [d] Performed at −10 °C; a reaction time of 72 h was necessary, compared to 24 h in all other cases.

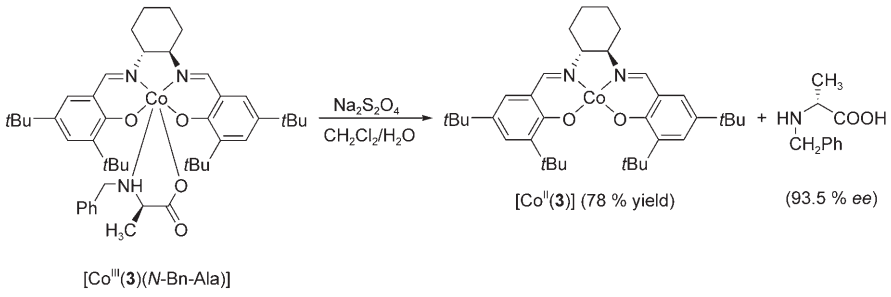

Scheme 3. Reductive cleavage of the cobalt(III) complex [Co^{III}(**3**)(*N*-Bn-Ala)].

 © 2006 Wiley-VCH Verlag GmbH & Co. KGaA, Weinheim

two clear phases over the course of the extraction. One equivalent was extracted into the dichloromethane phase to form the complexes [Co^{III}(**3**)(*N*-Bn-AA)], while the second equivalent was dissolved in the aqueous phase where the *ee* values were found to be 90.1 and 99.0% in favor of (*S*)-*N*-benzylvaline and (*S*)-*N*-benzylleucine, respectively (Table 2, entries 2, 3). The extraction of *N*-benzylphenylalanine under the same conditions also proceeded in high yield with one equivalent of substrate extracted into the organic phase through formation of [Co^{III}(**3**)(*N*-Bn-Phe)] (Table 2, entry 4). The unbound substrate, (*S*)-*N*-benzylphenylalanine remained as a suspension and could be isolated by filtration or dissolved into the aqueous phase by treatment with NaOH. Again, a high *ee* value was observed (93.3% *ee*). Treatment of the complexes [Co^{III}(**3**)(*N*-Bn-AA)] with aqueous sodium dithionite released the opposite enantiomer in quantitative yield and with consistent *ee* values (see the Supporting Information).

Resolution of racemic *N*-benzyl amino acids using only dichloromethane and no water was also attempted (Table 2, entries 5–8, method C). In all cases, one equivalent of the substrate was complexed by [Co^{III}(**3**)(OAc)] and dissolved into the dichloromethane phase, while the uncomplexed solid material could be isolated simply by filtration. Enantioselectivities of 94.2 and 92.7% *ee* were observed for the recovered *N*-benzylvaline and *N*-benzylphenylalanine, respectively (Table 2, entries 5, 6). Thus, method C represents a more practical procedure for less hydrophilic amino acids with no loss of enantioselectivity. Conversely, and surprisingly, *N*-benzylalanine showed only poor enantioselectivity by this method (Table 2, entry 7), which could be somewhat improved by lowering the temperature, with 65.8% *ee* obtained at −10°C (Table 2, entry 8).

In conclusion, we have developed a novel approach to the resolution of racemic *N*-benzyl α-amino acids in excellent yields and enantiomeric excesses by using the lipophilic chiral salen–cobalt(III) complex [Co^{III}(**3**)(OAc)]. The complexed amino acid can then be released by a reductive ($Co^{III}\rightarrow Co^{II}$) counterextraction with aqueous sodium dithionite. The original chiral cobalt(III) complex can be regenerated and reused with essentially no loss of reactivity and selectivity. We are actively investigating the scope of this methodology using different substrates as well as its large-scale application in an industrial environment.

Received: November 18, 2005
Published online: March 10, 2006

Keywords: amino acids · chiral resolution · cobalt · molecular recognition · N,O ligands

[1] a) P. Breccia, M. Van Gool, R. Perez-Fernandez, S. Martin-Santamaria, F. Gago, P. Prados, J. De Mendoza, *J. Am. Chem. Soc.* **2003**, *125*, 8270–8284; b) X. X. Zhang, J. S. Bradshaw, R. M. Izatt, *Chem. Rev.* **1997**, *97*, 3313–3361.

[2] a) P. D. Knight, P. Scott, *Coord. Chem. Rev.* **2003**, *242*, 125–143, and references therein; b) H.-J. Kim, R. Asif, D. S. Chung, J.-I. Hong, *Tetrahedron Lett.* **2003**, *44*, 4335–4338; c) H.-J. Kim, W. Kim, A. J. Lough, B. M. Kim, J. Chin, *J. Am. Chem. Soc.* **2005**, *127*, 16776–16777.

[3] a) R. R. Fenton, F. S. Stephens, R. S. Vagg, P. A. Williams, *Inorg. Chim. Acta* **1995**, *236*, 109–115; b) J. Chin, S. S. Lee, K. J. Lee, S. Park, D. H. Kim, *Nature* **1999**, *401*, 254–257.

[4] a) W. Linder, J. N. LePage, G. Davies, D. E. Seitz, B. L. Karger, *J. Chromatogr.* **1979**, *185*, 323–344; b) E. Gil-Av, A. Tishbee, P. E. Hare, *J. Am. Chem. Soc.* **1980**, *102*, 5115–5117; c) E. Armani, L. Barazzoni, A. Dossena, R. Marchelli, *J. Chromatogr.* **1988**, *441*, 287–298, and references therein; d) T. Arai, H. Koike, K. Hirota, H. Oizumi, *J. Chromatogr.* **1988**, *448*, 439–444; e) N. Ôi, H. Kitahara, R. Kira, *J. Chromatogr.* **1992**, *592*, 291–296; f) N. Ôi, H. Kitahara, F. Aoki, *J. Chromatogr. A* **1995**, *707*, 380–383; g) G. Galaverna, R. Corradini, A. Dossena, E. Chiavaro, R. Marchelli, F. Dallavalle, G. Folesani, *J. Chromatogr. A* **1998**, *829*, 101–113.

[5] a) P. Scrimin, U. Tonellato, N. Zanta, *Tetrahedron Lett.* **1988**, *29*, 4967–4970; b) P. Scrimin, P. Tecilla, U. Tonellato, *Tetrahedron* **1995**, *51*, 217–230; c) P. J. Pickering, J. B. Chaudhuri, *J. Membr. Sci.* **1997**, *127*, 115–130; d) B. Baragaña, A. G. Blackburn, P. Breccia, A. P. Davis, J. de Mendoza, J. M. Padrón-Carrillo, P. Prados, J. Riedner, J. G. de Vries, *Chem. Eur. J.* **2002**, *8*, 2931–2936; e) J. D. Clark, B. Han, A. S. Bhown, S. R. Wickramasinghe, *Sep. Purif. Technol.* **2005**, *42*, 201–211.

[6] T. J. M. De Bruin, A. T. M. Marcelis, H. Zuilhof, L. M. Rodenburg, H. A. G. Niederländer, A. Koudijs, P. E. M. Overdevest, A. van der Padt, E. J. R. Sudhölter, *Chirality* **2000**, *12*, 627–636.

[7] A. L. Creagh, B. B. E. Hasenack, A. van der Padt, E. J. R. Sudholter, K. van't Riet, *Biotechnol. Bioeng.* **1994**, *44*, 690–698.

[8] Y. Fujii, M. Matsufuru, A. Saito, S. Tsuchiya, *Bull. Chem. Soc. Jpn.* **1981**, *54*, 2029–2038.

[9] The opposite enantiomer (*S*,*S*) of ligand **1** was actually used in the study by Fujii et al.: treatment of [Co^{II}(ent-**1**)] with 2 equiv of a racemic mixture of *N*-Bn-Ala in MeOH/H_2O (5:1), followed by extraction with $CHCl_3$/H_2O led to enantiomeric excesses of 94% (*S*) and 93% (*R*) for the complexed ([Co^{III}(ent-**1**)(*N*-Bn-Ala)]) and the uncomplexed amino acid, respectively (see Ref. [8]).

[10] a) T. Takeuchi, R. Horikawa, T. Tanimura, *Anal. Chem.* **1984**, *56*, 1152–1155; b) T. Takeuchi, R. Horikawa, T. Tanimura, Y. Kabasawa, *Sep. Sci. Technol.* **1990**, *25*, 941–951; c) H. Nishizawa, K. Tahara, A. Hayashida, Y. Abe, *Anal. Sci.* **1993**, *9*, 611–615; d) H. Tsukube, J. Uenishi, T. Kanatani, H. Itoh, O. Yonemitsu, *Chem. Commun.* **1996**, 477–478; e) H. Tsukube, S. Shinoda, J. Uenishi, T. Kanatani, H. Itoh, M. Shiode, T. Iwachido, O. Yonemitsu, *Inorg. Chem.* **1998**, *37*, 1585–1591; f) S. E. Snyder, J. R. Carey, W. H. Pirkle, *Tetrahedron* **2005**, *61*, 7562–7567.

[11] a) For a single-step synthesis of cyclopropanols (EtMgBr, cat. Ti(O*i*Pr)$_4$), see: I. L. Lysenko, O. G. Kulinkovich, *Russ. J. Org. Chem.* **2001**, *37*, 1238–1243; b) for the preparation of enzyme inhibitors, see: C. T. Supuran, A. Scozzafava, *Eur. J. Pharm. Sci.* **2000**, *10*, 67–76; c) for the synthesis of 2,3,4-trisubstituted piperidines, see: S. Laschat, R. Fröhlich, B. Wibbeling, *J. Org. Chem.* **1996**, *61*, 2829–2838; d) for the synthesis of statine and hydroxymethylene dipeptide isosteres, see: A. McCluskey, J. Garner, D. J. Young, S. Caballero, *Tetrahedron Lett.* **2000**, *41*, 8147–8151.

[12] S. N. N. Babu, G. R. Srinivasa, D. C. Santhosh, D. C. Gowda, *J. Chem. Res. Synop.* **2004**, 66–67.

[13] This experiment (a real biphasic liquid–liquid extraction) differs substantially from the conditions used by Fujii et al. (a homogeneous MeOH/H_2O solution (5:1), see Refs. [8,9]). The results obtained by Fujii et al. could be nicely reproduced by performing this separation under the original conditions.

[14] J. R. Larrow, E. N. Jacobsen, *Top. Organomet. Chem.* **2004**, *7*, 123–152.

 © 2006 Wiley-VCH Verlag GmbH & Co. KGaA, Weinheim

[15] T. V. Hansen, L. Skattebøl, *Tetrahedron Lett.* **2005**, *46*, 3829–3830.
[16] S. E. Schaus, B. D. Brandes, J. F. Larrow, M. Tokunage, K. B. Hansen, A. E. Gould, M. E. Furrow, E. N. Jacobsen, *J. Am. Chem. Soc.* **2002**, *124*, 1307–1315.
[17] For example, the enantioselectivity of the extraction of *N*-benzylalanine using [Co^{III}(**3**)(OAc)] improved from 75.0% to 93.0% *ee* when the temperature was lowered from 25 °C to 10 °C. Extractions run at room temperature (not thermostated) gave erratic results (83 ± 10% *ee*).
[18] The variation of other parameters (stirring speed, concentrations, type of reaction vessel) did not significantly affect the extraction results (yields and enantioselectivities). Once the extraction was complete, the enantiomeric excesses did not vary over additional time.
[19] E. V. Kudrik, S. V. Makarov, A. Zahl, R. van Eldik, *Inorg. Chem.* **2003**, *42*, 618–624.
[20] Optimization of the [Co^{II}(**3**)] recovery process is under active investigation in our laboratories.
[21] Reaction of [Co^{III}(**3**)(*N*-Bn-Ala)] with $NaBH_4$ (1 equiv) in $MeOH/H_2O$ gave quantitative release of *N*-benzylalanine but a very poor recovery (< 10%) of [Co^{II}(**3**)].

 © 2006 Wiley-VCH Verlag GmbH & Co. KGaA, Weinheim

Self-Assembly

DOI: 10.1002/anie.200504447

Choices of Iron and Copper: Cooperative Selection during Self-Assembly**

*David Schultz and Jonathan R. Nitschke**

The technique of subcomponent self-assembly is emerging at the intersection of dynamic covalent[1] and metallo-supramolecular[2] chemistry. In subcomponent self-assembly two hierarchical self-assembly reactions[3] occur as parts of the same overall process: Intraligand (generally C=N) bonds form at the same time as metal–ligand bonds, thus bringing molecular and supramolecular structures into being at the same time.[4]

The use of subcomponents rather than presynthesized ligands in programmed self-assembly presents a particular challenge to the "programmer/chemist": for a given level of structural complexity, one must employ subcomponents that contain more self-assembly information than presynthesized ligands, since "assembly instructions" for both the ligands and supramolecular structure must be included. This problem becomes acute when sets of "non-orthogonal" subcomponents are employed, for example, two amines that could condense with two different aldehydes to give a dynamic library[5] of four imines, with the size of this library growing for larger collections or multivalent starting materials.

We have previously described a system consisting of a set of ligand components that combine together in all possible ways in the absence of copper(I) ions, but which undergo a thermodynamic self-sorting process in the presence of the metal ion, thereby eliminating all mixed ligands from the system [Eq. (1)].[6]

$$a + b + c \longrightarrow ab + ac + ab_2 + abc + ac_2 \xrightarrow{Cu^{I}} [Cu^{I}(ab_2)] + [Cu^{I}(ac_2)] \quad (1)$$

Herein, we describe a more-complex self-organizing system,[7] in which a larger dynamic library collapses during the simultaneous formation of iron(II) and copper(I) complexes [Eq. (2)]. Each one of the six initially present chemical species was directed to its place in one of the two product complexes by the dynamic interplay of steric and electronic factors on both covalent and coordinative levels. We are not aware of another example of a clean sorting of chemically non-orthogonal components into two well-separated "baskets". The driving forces behind this selectivity were examined individually, and it was found that selection preferences expressed by the two metals acted in concert to deconvolute the initial library of ligands. Although these preferences do not lead to quantitative selection in the absence of one of the metals, they reinforce each other in the full mixture to select the observed products from all the possible products. Although this model system consists of only two mononuclear complexes, the methodology demonstrated here may thus prove useful in the development of hierarchically self-assembled systems of greater complexity and function.

$$a + b + c + d \longrightarrow \begin{matrix} ac + ac_2 + ac_3 \\ ad + ad_2 + ad_3 \\ acd + ac_2d + acd_2 \\ bc + bd \end{matrix} \xrightarrow[Fe^{II}]{Cu^{I}} [Fe^{II}(ac_3)] + [Cu^{I}(bd)] \quad (2)$$

Mixing pyridine-2-carbaldehyde (**A**, 3 equiv), 6-methylpyridine-2-carbaldehyde (**B**, 3 equiv), tris(2-aminoethyl)amine (**C**, 1 equiv), and ethanolamine (**D**, 3 equiv) in aqueous solution affords a dynamic library of imines (Scheme 1) in equilibrium with the starting materials, as observed by ESI-MS and NMR spectroscopy. The addition of copper(I) tetrafluoroborate (1.5 equiv) and iron(II) sulfate (1 equiv) resulted in the dynamic library of imines collapsing within 12 h at 323 K to leave **1** and **2** as the sole products. This sorting process is thermodynamic in nature. NMR spectra of the reaction mixture during the hours following the addition of the metals revealed the presence of kinetic products, which disappeared during equilibration.

Certain factors play a clear role in winnowing down the number of observed product structures: The template effect[8]

[*] D. Schultz, Dr. J. R. Nitschke
Department of Organic Chemistry
University of Geneva
30 Quai Ernest Ansermet, 1211 Genève 4 (Switzerland)
Fax: (+41) 22-379-3215
E-mail: jonathan.nitschke@chiorg.unige.ch

[**] This work was supported by the Swiss National Science Foundation. We thank Profs. A. Hauser, J. Lacour, and C. Piguet for critical comments on the manuscript, and P. Perrottet for mass spectrometric analyses.

Supporting information for this article (the syntheses of **1**, **2**, and **3**, as well experimental details for the reactions shown) is available on the WWW under http://www.angewandte.org or from the author.

 © 2006 Wiley-VCH Verlag GmbH & Co. KGaA, Weinheim

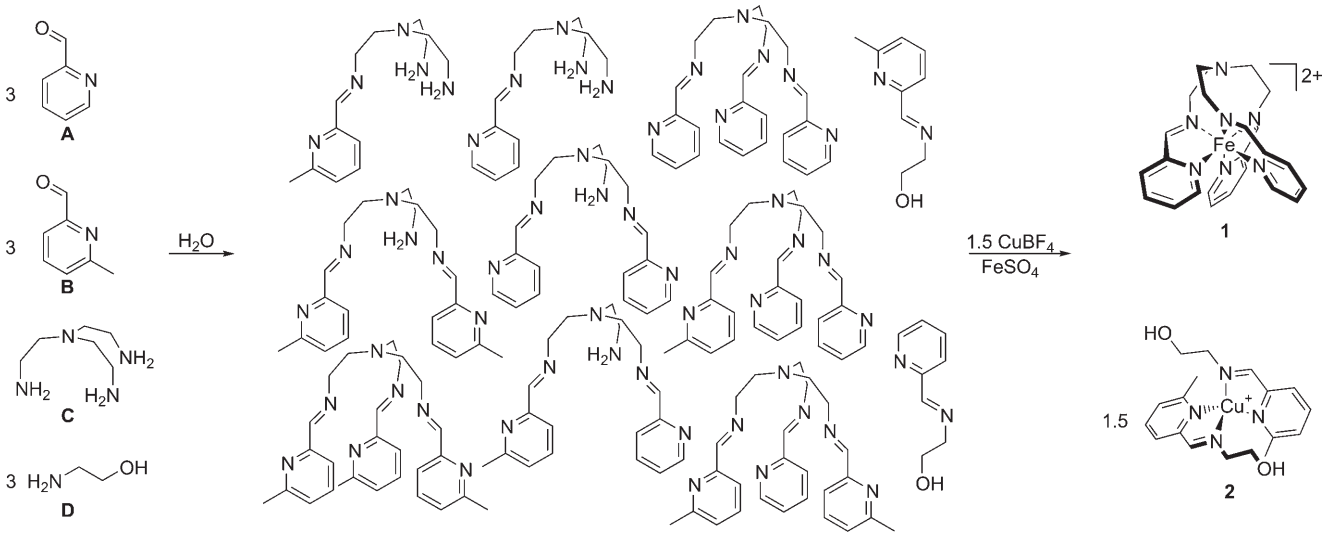

Scheme 1. The formation of a dynamic combinatorial library of ligands, and the collapse of this library following addition of Cu^{I} and Fe^{II} ions.

should eliminate all partially formed ligands and ligand subcomponents from the mixture, the chelate effect[9] should favor structures containing ligands that bear the highest number of bound donor atoms possible, and the iron(II) and copper(I) ions should be bound to six and four donor atoms, respectively. Within these limits, a variety of different product structures might nonetheless be envisaged. We discuss herein our investigations of three distinct preferences exhibited by copper(I) and iron(II) ions. These preferences act in concert to select **1** and **2** alone as the products of the reaction shown in Scheme 1.

Firstly, copper(I) ions formed complexes that incorporated methylated aldehyde **B** in preference to **A**. ESI-MS analysis of the reaction mixture following the addition of copper(I) tetrafluoroborate (1 equiv) to an aqueous mixture of aldehydes **A** and **B** as well as amine **D** (2 equiv each) showed the presence of all the three possible products shown in Scheme 2. We were not able to quantify them by NMR spectroscopic analysis because of overlapping signals, however the concentrations of the free aldehydes **A** and **B** could be quantified. Aldehydes **A** and **B** were incorporated into the product mixture in a ratio of 30:70, which indicates a slight (ca. 6.3 kJ mol^{-1}) thermodynamic preference (assuming an equilibrium of the type $[Cu(\mathbf{B})_2]+2\mathbf{A}\rightleftharpoons[Cu(\mathbf{A})_2]+2\mathbf{B}$) for the incorporation of **B**. This preference may be attributed to the presence of an electron-donating methyl group on **B**, which allows the ligands to better stabilize the cationic copper(I) center.

Secondly, iron(II) ions were observed to form pseudo-octahedral complexes that incorporate triamine **C** in preference to monoamine **D**. Complex **1** and amine **D** were the only products observed by NMR spectroscopy and ESI-MS when complex **3**, prepared as a mixture of *fac* and *mer* isomers, was mixed with an equimolar amount of triamine **C** in aqueous solution (Scheme 3). On the basis of the sensitivity of the

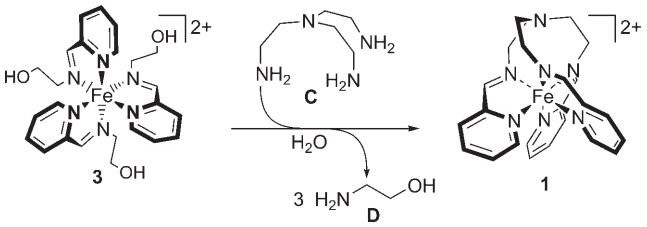

Scheme 3. The choice of iron: the entropically driven displacement of monoamine **D** by triamine **C**.

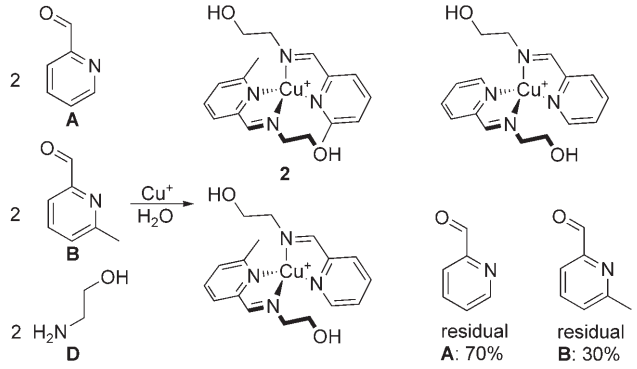

Scheme 2. The choice of copper: aldehyde **B** was incorporated in preference to **A** during the formation of **2** in aqueous solution.

NMR spectrometer at the concentration studied (63 mM), we concluded that **C** and **3** were present at concentrations of less than 1%. We estimate therefore that the energetic driving force for this reaction is greater than 22 kJ mol^{-1} (assuming an equilibrium of the type $[Fe(\mathbf{D})_3]+\mathbf{C}\rightleftharpoons[Fe(\mathbf{C})]+3\mathbf{D}$). The chelate effect[9] may be understood to drive this substitution: The incorporation of one equivalent of amine **C** results in the liberation of three equivalents of amine **D**, which provides the entropic driving force for this reaction.

A third driving force for the observed selectivity, complementing and amplifying the choice of the copper center for **B** over **A**, is the preference of iron(II) ions to incorporate aldehyde **A** instead of **B** into complexes of type **1**. As shown

 © 2006 Wiley-VCH Verlag GmbH & Co. KGaA, Weinheim

in Scheme 4, the addition of iron(II) ions (1 equiv) to a mixture of triamine **C** (1 equiv) and aldehydes **A** and **B** (3 equiv of each) gave a product mixture in which free **A** and **B** were present in a 3:97 ratio following equilibration at 323 K

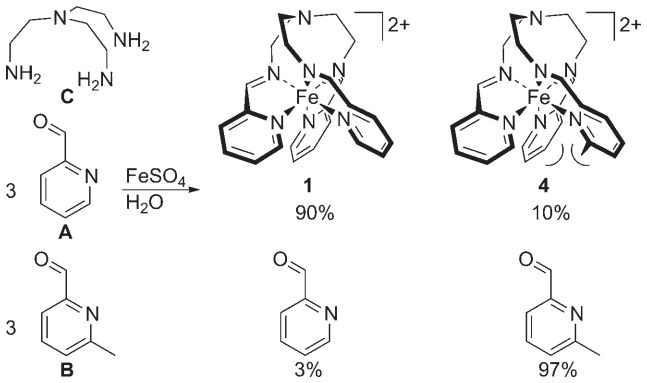

Scheme 4. The choice of iron: the preferential incorporation of the less-hindered aldehyde **A** into **1** and **4**. The steric clash between methyl group and ring is shown for **4**.

over 4 days. This ratio suggests that the incorporation of aldehyde **A** over **B** was favored by about 14.1 kJ mol^{-1} (assuming an equilibrium of the type $[Fe(\mathbf{A})_3]+\mathbf{B}\rightleftharpoons[Fe(\mathbf{A})_2(\mathbf{B})]+\mathbf{A}$). The broad NMR and the ESI-MS spectra of the product mixture were assigned to a mixture of **1**, incorporating uniquely aldehyde **A**, and **4**, incorporating two equivalents of **A** and one equivalent of **B**. The reaction shown in Scheme 4 deviates substantially from a statistical mixture of products; indeed, only two of the expected four products are observed to form. No evidence was found of complexes incorporating two or three equivalents of **B**.

Mixtures of products were obtained when either cobalt(II) or zinc(II) sulfate was used in place of the iron(II) salt in the reactions shown in Schemes 1 or 4. The crystal structures show that the iron(II) ion is bound more tightly in **1** (mean $r_{Fe\text{-}N}=1.95$ Å)[10] than is the cobalt(II) ion (mean $r_{Co\text{-}N}=2.15$ Å)[10] or zinc(II) ion (mean $r_{Zn\text{-}N}=2.18$ Å)[10] in complexes with the same ligand. This observation correlates with the finding that the Fe^{II} ion is the only divalent first-row transition metal to have a low-spin ground state with this ligand.[10] The research groups of Drago,[11] Hendrickson,[12] and Hauser[13] have investigated the magnetic behavior of **1** and **4** as well as the other two congeners incorporating two and three equivalents of **B**, respectively. They determined that although **1** remains in the low-spin $^1A_1$ state over the temperature range 30–450 K,[12,13] the complexes containing **B** subcomponents undergo spin crossover to the high-spin $^5T_2$ state as the temperature increases. The more **B** subcomponents a complex contains, the lower the temperature at which it undergoes spin crossover. A steric clash between the methyl groups and the facing pyridyl rings, as shown in Scheme 4, appears to destabilize the low-spin state relative to the high-spin state by elongating the Fe–N bonds.

The strong thermodynamic preference of iron(II) ions to incorporate aldehyde **A** in preference to **B** during the formation of **1** might thus be attributed to the high energy penalty paid for a steric clash in iron(II) complexes of this type. Since the presence of high-spin iron(II) centers may be inferred in complexes incorporating one or more **B** subcomponent, one might also invoke the possibility of a "spin-selection" phenomenon, whereby the formation of short, strong bonds between low-spin iron(II) centers and sp^2 nitrogen atoms serves as a thermodynamic driving force for the preferential incorporation of sterically unhindered **A**.

In summary, we have examined individually the factors leading to the observed high degree of selectivity in this simple model system. The preference for iron(II) complexes to incorporate triamine **C** in preference to monoamine **D** may be considered as "strong"—in excess of 22 kJ mol^{-1}. The preferences of copper for subcomponent **B** (ca. 6.3 kJ mol^{-1}) and iron for subcomponent **A** (ca. 14.1 kJ mol^{-1}) were both weaker, but these preferences complemented each other and reduced the concentrations of mixed products to undetectable levels (estimated to be $<1\%$, based on ESI-MS and NMR spectroscopic measurements).

This deconvolution methodology may prove useful in determining the thermodynamic preferences of other systems incorporating mixed sets of subcomponents, particularly in cases where selective self-assembly is desired. The concurrent formation of complexes **1** and **2** might also be harnessed to drive the self-assembly of larger, more complex structures: the covalent attachment of other self-assembling groups to **A**, **B**, **C**, or **D** could allow the self-assembly "program" that generates **1** and **2** to be used as a "subroutine" within the assembly of a superstructure incorporating **1** and **2** as subunits.

Received: December 14, 2005
Published online: March 9, 2006

Keywords: coordination modes · copper · dynamic combinatorial chemistry · iron · self-assembly

[1] a) S. J. Rowan, S. J. Cantrill, G. R. L. Cousins, J. K. M. Sanders, J. F. Stoddart, *Angew. Chem.* **2002**, *114*, 938–993; *Angew. Chem. Int. Ed.* **2002**, *41*, 898–952; b) S. Otto, *J. Mater. Chem.* **2005**, *15*, 3357–3361; c) R. Cacciapaglia, S. Di Stefano, L. Mandolini, *J. Am. Chem. Soc.* **2005**, *127*, 13666–13671; d) F. Arico, T. Chang, S. J. Cantrill, S. I. Khan, J. F. Stoddart, *Chem. Eur. J.* **2005**, *11*, 4655–4666; e) T. Ono, T. Nobori, J.-M. Lehn, *Chem. Commun.* **2005**, 1522–1524.

[2] a) C. J. Baylies, T. Riis-Johannessen, L. P. Harding, J. C. Jeffery, R. Moon, C. R. Rice, M. Whitehead, *Angew. Chem.* **2005**, *117*, 7069–7072; *Angew. Chem. Int. Ed.* **2005**, *44*, 6909–6912; b) B. J. Holliday, C. A. Mirkin, *Angew. Chem.* **2001**, *113*, 2076–2097; *Angew. Chem. Int. Ed.* **2001**, *40*, 2022–2043; c) C. Piguet, G. Bernardinelli, G. Hopfgartner, *Chem. Rev.* **1997**, *97*, 2005–2062; d) W.-Y. Sun, M. Yoshizawa, T. Kusukawa, M. Fujita, *Curr. Opin. Chem. Biol.* **2002**, *6*, 757–764; e) D. L. Caulder, K. N. Raymond, *Acc. Chem. Res.* **1999**, *32*, 975–982; f) F. A. Cotton, C. Lin, C. A. Murillo, *Acc. Chem. Res.* **2001**, *34*, 759–771; g) M. Albrecht, *J. Inclusion Phenom. Macrocyclic Chem.* **2000**, *36*, 127–151; h) S. R. Seidel, P. J. Stang, *Acc. Chem. Res.* **2002**, *35*, 972–983; i) B. Linton, A. D. Hamilton, *Chem. Rev.* **1997**, *97*, 1669–1680; j) M. Albrecht, *Chem. Rev.* **2001**, *101*, 3457–3497; k) J. C. G. Bunzli, C. Piguet, *Chem. Rev.* **2002**, *102*, 1897–1928.

 © 2006 Wiley-VCH Verlag GmbH & Co. KGaA, Weinheim

[3] a) M. Albrecht, S. Mirtschin, M. de Groot, I. Janser, J. Runsink, G. Raabe, M. Kogej, C. A. Schalley, R. Froehlich, *J. Am. Chem. Soc.* **2005**, *127*, 10371 – 10387; b) V. Berl, M. J. Krische, I. Huc, J.-M. Lehn, M. Schmutz, *Chem. Eur. J.* **2000**, *6*, 1938 – 1946.
[4] a) L. Hogg, D. A. Leigh, P. J. Lusby, A. Morelli, S. Parsons, J. K. Y. Wong, *Angew. Chem.* **2004**, *116*, 1238 – 1241; *Angew. Chem. Int. Ed.* **2004**, *43*, 1218 – 1221; b) D. A. Leigh, P. J. Lusby, S. J. Teat, A. J. Wilson, J. K. Y. Wong, *Angew. Chem.* **2001**, *113*, 1586 – 1591; *Angew. Chem. Int. Ed.* **2001**, *40*, 1538 – 1543; c) H. Houjou, A. Iwasaki, T. Ogihara, M. Kanesato, S. Akabori, K. Hiratani, *New J. Chem.* **2003**, *27*, 886 – 889; d) L. J. Childs, N. W. Alcock, M. J. Hannon, *Angew. Chem.* **2002**, *114*, 4418 – 4421; *Angew. Chem. Int. Ed.* **2002**, *41*, 4244 – 4247; e) J. Hamblin, L. J. Childs, N. W. Alcock, M. J. Hannon, *J. Chem. Soc. Dalton Trans.* **2002**, 164 – 169; f) J. R. Nitschke, D. Schultz, G. Bernardinelli, D. Gérard, *J. Am. Chem. Soc.* **2004**, *126*, 16538 – 16543; g) J. R. Nitschke, J.-M. Lehn, *Proc. Natl. Acad. Sci. USA* **2003**, *100*, 11970 – 11974; h) J. R. Nitschke, M. Hutin, G. Bernardinelli, *Angew. Chem.* **2004**, *116*, 6892 – 6895; *Angew. Chem. Int. Ed.* **2004**, *43*, 6724 – 6727; i) S. Brooker, S. J. Hay, P. G. Plieger, *Angew. Chem.* **2000**, *112*, 2044 – 2046; *Angew. Chem. Int. Ed.* **2000**, *39*, 1968 – 1970; j) K. S. Chichak, S. J. Cantrill, A. R. Pease, S.-H. Chiu, G. W. V. Cave, J. L. Atwood, J. F. Stoddart, *Science* **2004**, *304*, 1308 – 1312.
[5] a) S. G. Telfer, X. J. Yang, A. F. Williams, *Dalton Trans.* **2004**, 699 – 705; b) K. Severin, *Chem. Eur. J.* **2004**, *10*, 2565 – 2580; c) S. Otto, R. L. E. Furlan, J. K. M. Sanders, *Science* **2002**, *297*, 590 – 593; d) R. Nguyen, I. Huc, *Chem. Commun.* **2003**, 942 – 943; e) J.-M. Lehn, A. V. Eliseev, *Science* **2001**, *291*, 2331 – 2332; f) F. Hof, C. Nuckolls, J. Rebek, Jr., *J. Am. Chem. Soc.* **2000**, *122*, 4251 – 4252; g) M. Albrecht, I. Janser, J. Runsink, G. Raabe, P. Weis, R. Froehlich, *Angew. Chem.* **2004**, *116*, 6832 – 6836; *Angew. Chem. Int. Ed.* **2004**, *43*, 6662 – 6666.
[6] D. Schultz, J. R. Nitschke, *Proc. Natl. Acad. Sci. USA* **2005**, *102*, 11191 – 11195.
[7] a) A. X. Wu, L. Isaacs, *J. Am. Chem. Soc.* **2003**, *125*, 4831 – 4835; b) M. Schmittel, V. Kalsani, R. S. K. Kishore, H. Colfen, J. W. Bats, *J. Am. Chem. Soc.* **2005**, *127*, 11544 – 11545.
[8] T. J. Hubin, D. H. Busch, *Coord. Chem. Rev.* **2000**, *200*, 5 – 52.
[9] G. Schwarzenbach, *Helv. Chim. Acta* **1952**, *35*, 2344 – 2363.
[10] R. M. Kirchner, C. Mealli, M. Bailey, N. Howe, L. P. Torre, L. J. Wilson, L. C. Andrews, N. J. Rose, E. C. Lingafelter, *Coord. Chem. Rev.* **1987**, *77*, 89 – 163.
[11] M. A. Hoselton, L. J. Wilson, R. S. Drago, *J. Am. Chem. Soc.* **1975**, *97*, 1722 – 1729.
[12] A. J. Conti, C. L. Xie, D. N. Hendrickson, *J. Am. Chem. Soc.* **1989**, *111*, 1171 – 1180.
[13] S. Schenker, A. Hauser, W. Wang, I. Y. Chan, *J. Chem. Phys.* **1998**, *109*, 9870 – 9878.

 © 2006 Wiley-VCH Verlag GmbH & Co. KGaA, Weinheim

Natural-Gas Hydrates

DOI: 10.1002/anie.200504366

n-Pentane and *n*-Hexane as Coguests in Structure-H Hydrates in Mixtures of 2,2-Dimethylbutane and Methane

*Jong-won Lee, Hailong Lu, Igor L. Moudrakovski, Christopher I. Ratcliffe, and John A. Ripmeester**

Gas hydrates are icelike solid materials formed when small molecules are captured in the cavities of ordered three-dimensional hydrate frameworks.[1] As a large amount of the Earth's natural gas supply is known to be trapped in hydrate deposits that occur globally under the permafrost and in marine sediment on the continental margins,[2] intensive research has been performed to explore and assess this potential new energy source for eventual utilization. It is well known that gas hydrates are classified into three main structures, known as cubic structure I (sI), cubic structure II (sII), and hexagonal structure H (sH). Amongst hydrocarbon molecules, methane and ethane form sI or sII hydrates, whereas C3 and C4 hydrocarbons, often in the presence of C1 and C2 hydrocarbons, form sII hydrates.[1] The sH hydrate, identified by Ripmeester et al. in 1987, can accommodate heavier hydrocarbons up to C8, such as cycloalkanes, methylcycloalkanes, and methyl-substituted *n*-alkanes, in the largest cavity ($5^{12}6^8$) of the structure.[3,4] For sH hydrates, it is necessary to fill the small cavities (5^{12}, $4^3 5^6 6^3$) with an help gas, such as methane, to form a stable structure. However, *n*-alkanes with five or more carbon atoms were identified as not being able to stabilize the sH hydrate, and it was conjectured that they may not fill the large cage efficiently.[4] Because the amount, and location, of natural gas stored in hydrate form strongly depends on the nature of the hydrate, the structural, compositional, and stability characteristics of the hydrate become critical in evaluating a hydrate for its potential as an energy source and climate-change agent. So far, analysis of natural-gas hydrate samples has shown that most natural hydrates formed from gas of biogenic origin are the sI form, whereas sII and sH hydrates have been conjectured to form from thermogenic gases[5] on the basis of gas analysis;[6] a sII hydrate has been identified directly only once. Accordingly, though the existence of sI and sII hydrates in nature has already been verified, it is thought that an sH hydrate can only exist in a laboratory environment.[7] Recently, according to the compositional analysis of natural-gas hydrate samples recovered from Cascadia, there was evidence of hydrates that contained heavier hydrocarbons, including *n*-pentane and *n*-

[*] Dr. J.-w. Lee, Dr. H. Lu, Dr. I. L. Moudrakovski, Dr. C. I. Ratcliffe, Dr. J. A. Ripmeester
Steacie Institute for Molecular Sciences
National Research Council of Canada
100 Sussex Drive, Ottawa, ON, K1A OR6 (Canada)
Fax: (+1) 613-998-7833
E-mail: john.ripmeester@nrc.ca

WILEY InterScience DISCOVER SOMETHING GREAT
© 2006 Wiley-VCH Verlag GmbH & Co. KGaA, Weinheim

hexane. However, as the latter were not considered to be hydrate formers,[1,8] their presence in the natural hydrate[9] suggests that they may in fact contribute to hydrate formation in the presence of other sH-hydrate formers.

2,2-Dimethylbutane is one of the well-known sH-hydrate formers, and its phase equilibria with CH_4 gas have been reported under various conditions.[7] When 2,2-dimethylbutane is allowed to react with CH_4 individually or as a mixture with *n*-pentane or *n*-hexane, gas hydrates are formed successfully in each case. To verify the structure of the synthetic samples, powder X-ray diffraction (XRD) measurements were performed (Figure 1). Table 1 shows the observed 2θ values for each sample along with the corresponding Miller indices. All of the patterns have reflections in common, although some reflections are unique to each sample. The lattice parameters, obtained from a fit of the reflections indexed according to the sH-hydrate structure (*P6/mmm*), are $a = 12.2664$ and $c = 10.0667$ Å for the 2,2-dimethylbutane + CH_4 hydrate, $a = 12.1597$ and $c = 10.0731$ Å for the 2,2-dimethylbutane + *n*-pentane + CH_4 hydrate, and $a = 12.2667$ and $c = 10.0754$ Å for the 2,2-dimethylbutane + *n*-hexane + CH_4 hydrate. These values correspond to unit-cell volumes of 1311.75, 1289.85, and 1312.96 Å^3 for 2,2-dimethylbutane + CH_4, 2,2-dimethylbutane + *n*-pentane + CH_4, and 2,2-dimethylbutane + *n*-hexane + CH_4 hydrates, respectively. The unit-cell volumes of 2,2-dimethylbutane + CH_4 and 2,2-dimethylbutane + *n*-hexane + CH_4 hydrates are almost identical, whereas the value is slightly decreased by the addition of *n*-pentane to the system.

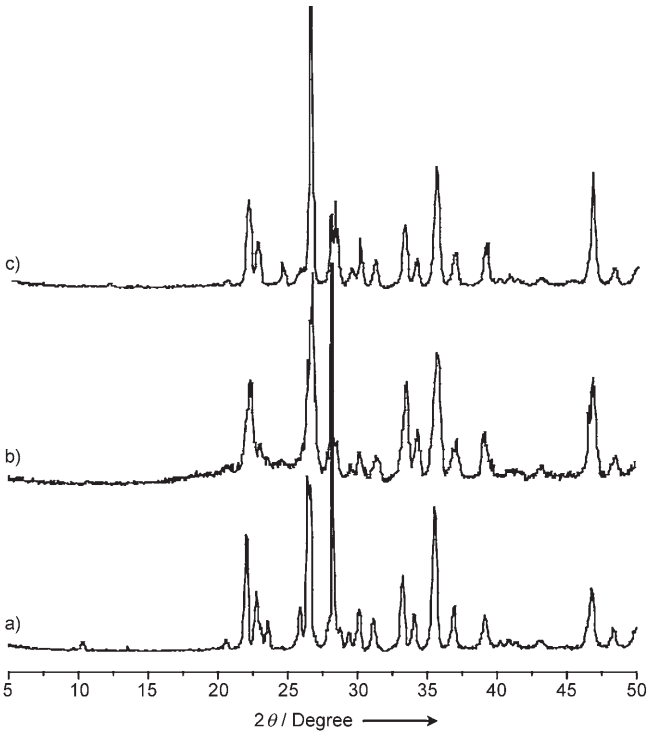

Figure 1. Powder XRD patterns of a) 2,2-dimethylbutane + CH_4, b) 2,2-dimethylbutane + *n*-pentane + CH_4, and c) 2,2-dimethylbutane + *n*-hexane + CH_4 hydrates at 85 K.

Table 1: Miller indices and observed angles [°] of powder XRD patterns for the synthesized sH hydrate samples.

hkl	Hydrate		
	2,2-Dimethylbutane + CH_4	2,2-Dimethylbutane + *n*-pentane + CH_4	2,2-Dimethylbutane + *n*-hexane + CH_4
0 0 1	10.27		
0 0 2	20.47		20.42
2 0 1	21.99	22.36	21.95
1 0 2	22.70		22.65
2 1 0	25.79		25.68
2 1 1			27.86
2 0 2			28.33
3 0 0	29.27	29.58	29.35
3 0 1	31.04	31.40	31.05
2 1 2	33.09	33.47	33.11
2 2 0	33.91	34.38	33.99
1 1 3			35.42
3 1 0	35.41	35.74	
2 0 3	36.76	36.81	36.71
3 1 1		37.09	
2 2 2	40.11		39.92
2 1 3	40.65	40.74	40.66
3 1 2	41.20	41.48	41.21
1 0 4	42.90	42.98	42.91
3 0 3		43.18	
2 2 3		46.84	
3 2 2	48.14	48.33	48.15

The composition of the hydrate samples and their structures can be identified using cross-polarization/magic-angle-spinning (CP/MAS) ^{13}C NMR spectroscopy. All of the spectra were consistent with the presence of an sH hydrate (Figure 2), with a CH_4 peak at $\delta = -4.50$ ppm, which arises from CH_4 in the 5^{12} and $4^3 5^6 6^3$ cavities of the hydrate phase. This observation agrees with the structural identification from powder XRD studies. In the downfield region of the spectra, four sharp peaks ($\delta = 8.66$ (C_δ), 29.31 (C_α), 30.28 (C_β), and 36.90 ppm (C_γ) for ($C_\alpha H_3$)$_3$-C_β-$C_\gamma H_2$-$C_\delta H_3$) are observed, which represent the four ^{13}C NMR resonances in 2,2-dimethylbutane. However, when *n*-pentane and *n*-hexane are added to the system, three additional peaks appear. Because the melting points of *n*-pentane and *n*-hexane are 143 and 178 K, respectively, CP/MAS NMR spectroscopy will not detect these hydrocarbons if they are not present in the solid hydrate, as the liquid phase is invisible with this technique. Hence, we can conclude that the additional peaks in the mixed hydrates can indeed be assigned to *n*-pentane and *n*-hexane in the hydrate cages.

NMR spectra for pure *n*-pentane and *n*-hexane at 200 K are shown (Figure 3). As mentioned earlier, these chemicals exist as liquids at this temperature, and the NMR spectra were obtained with a high-power decoupling (HPDEC) method. Three sharp peaks are observed for each hydrocarbon. The observed chemical shifts of *n*-pentane ($\delta = 14.89$ (C_α), 23.95 (C_β), and 35.54 ppm (C_γ) for $C_\alpha H_3$-$C_\beta H_2$-$C_\gamma H_2$-$C_\beta H_2$-$C_\alpha H_3$) are slightly different from those of *n*-hexane ($\delta = 14.11$ (C_α), 23.22 (C_β), and 32.28 ppm (C_γ) for $C_\alpha H_3$-$C_\beta H_2$-$C_\gamma H_2$-$C_\gamma H_2$-$C_\beta H_2$-$C_\alpha H_3$). Figure 4 shows a comparison between the spectra of the 2,2-dimethylbutane + *n*-hexane + CH_4 hydrate obtained by the two NMR methods from solid

 © 2006 Wiley-VCH Verlag GmbH & Co. KGaA, Weinheim

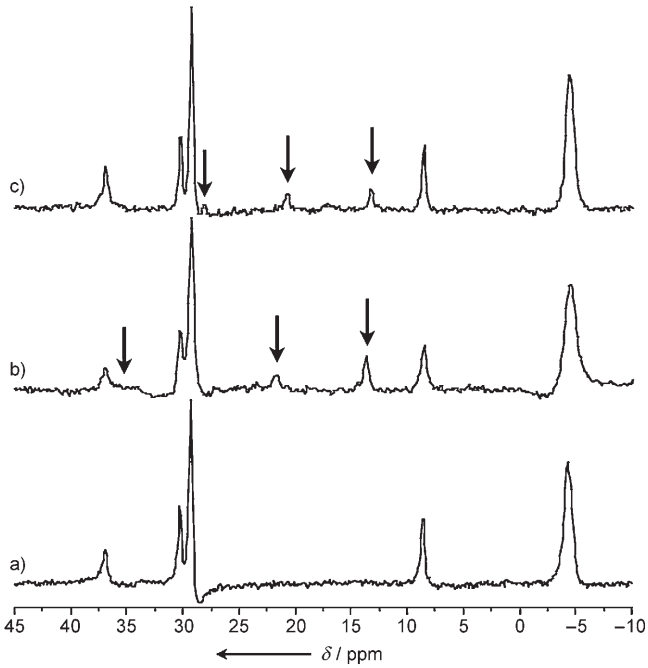

Figure 2. CP/MAS ^{13}C NMR spectra of a) 2,2-dimethylbtuane + CH_4, b) 2,2-dimethylbutane + *n*-pentane + CH_4, and c) 2,2-dimethylbutane + *n*-hexane + CH_4 hydrates at 200 K. The arrows in (b) and (c) indicate the additional peaks assigned to *n*-pentane or *n*-hexane, respectively, in the hydrate cages.

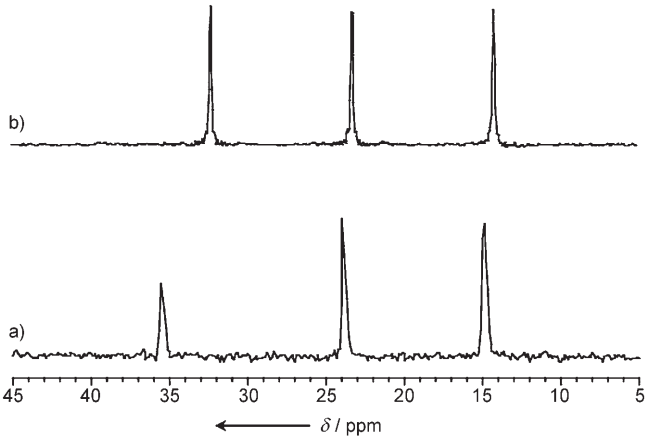

Figure 3. HPDEC ^{13}C NMR spectra of a) *n*-pentane and b) *n*-hexane at 200 K.

samples. As expected, the HPDEC method shows other peaks in addition to the seven obtained by the CP method, as now both the peaks for the solid and liquid phases become apparent. The three extra peaks at $\delta = 14.70$, 23.66, and 32.81 ppm represent liquid *n*-hexane in the samples, as excess *n*-hexane was used for their preparation. The other extra peak at $\delta = 9.24$ ppm indicates liquid 2,2-dimethylbutane in the sample, which means not all of the hydrocarbon mixture was converted into the hydrate. We note that the use of these two methods in obtaining the spectra is essential in this case, as we need to distinguish the enclathrated form from the liquid guest.

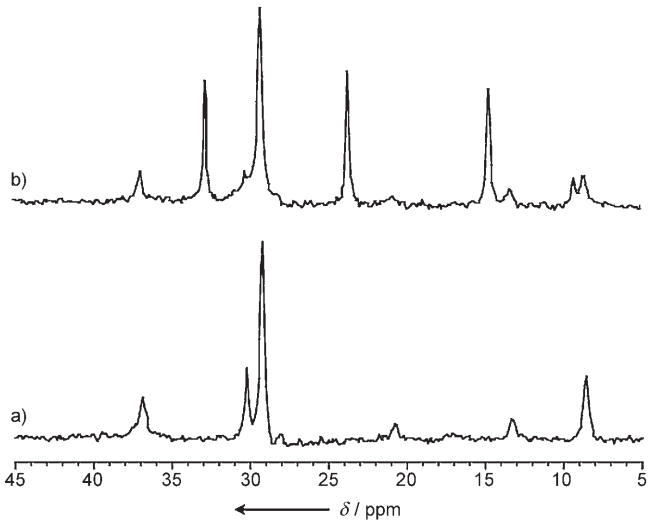

Figure 4. ^{13}C NMR spectra for 2,2-dimethylbutane + *n*-hexane + CH_4 hydrate at 200 K by a) CP/MAS and b) HPDEC methods at 200 K.

Based on the peak areas of the CP/MAS NMR spectra obtained, the amount of *n*-pentane and *n*-hexane in the large ($5^{12}6^8$) cavity of the sH hydrate was calculated. *n*-Pentane represents about 15.7 mol% of the heavy hydrocarbons in the hydrate phase of the 2,2-dimethylbutane + *n*-pentane + CH_4 hydrate, whereas *n*-hexane represents about 8.3 mol% of the heavy hydrocarbons in the 2,2-dimethylbutane + *n*-hexane + CH_4 hydrate. Assuming that the total large-cage occupancies of the large cavity are almost the same for both samples, the calculated values agree with the fact that *n*-hexane has a longer carbon chain, that is, it is more difficult for a larger molecule to enter the sH hydrate.[1] Hydrocarbons with five or more carbon-atom chains extended in an all-*trans* chain conformation are likely to be too large to fit in the large cages (8.62 Å) of an sH hydrate, although in other conformations, such as methylcyclohexane in which there is one gauche interaction, the five-carbon chain fits quite comfortably. This behavior is also reflected in the unit-cell volumes, for which the volume is somewhat smaller for the pentane-containing inclusion than for the other two compounds studied. In the case of *n*-hexane, it is likely that the encaged conformer will have more than one gauche interaction to fit into the cage. We note that at this stage it is not possible to say whether the compositions are determined by thermodynamics (overall stability) or kinetics (rate at which the right conformer presents itself for inclusion). Certainly, one can assume that even if the *n*-alkanes were able to form thermodynamically stable sH compounds without coguests, nucleation might be a problem as the concentration of the correct conformers may well be too low.

It is clear that special attention must be paid to sH hydrates made from hydrocarbon mixtures as it is not necessarily obvious which guest molecules may be found in the hydrate lattice. This observation is also true for phase equilibrium studies—only a direct measurement will confirm which hydrocarbons are present as guests.

 © 2006 Wiley-VCH Verlag GmbH & Co. KGaA, Weinheim

Experimental Section

Sample preparation: ice (5.0 g) was ground into a fine powder and placed in a high-pressure cell (internal volume: approximately 20.0 cm^3) with either a pure 2,2-dimethylbutane (1.0 g) or a liquid mixture of 2,2-dimethylbutane and *n*-pentane or *n*-hexane (1 mL). To prevent the ice powders from melting, the liquid mixture was cooled in a freezer at 253.15 K before addition. After filling the cell with ice and the liquid mixture, the cell was kept in a water bath kept at a constant temperature of 271.15 K. Then, CH_4 gas was slowly introduced up to 30.0 bar so as not to form pure CH_4 hydrate from the reaction between the ice and CH_4 gas. When the pressure drop because of the hydrate formation was observed after 1 day, the temperature was increased to 274.15 K to promote the conversion of water into hydrate. To convert additional water into hydrate, this thermal cycling procedure was performed twice.

Structural identification of the prepared samples was carried out on a Rigaku powder X-ray diffractometer equipped with an Anton Paar low-temperature controller. This apparatus has a maximum capacity of 12 kW and can be operated down to 83 K. $Co_{K\alpha}$ with a wavelength of 1.79021 Å was used as the radiation source and reflections were collected from 5.0 to 50.0° with a step size of 0.05° and a step time of 5 s. During the diffraction measurements, the experimental temperature was kept at about 85 K using liquid nitrogen. For compositional investigations, ^{13}C NMR spectra were obtained at 200 K by packing the hydrate samples in a 7-mm diameter Zirconium rotor, which was loaded into the variable temperature (VT) probe of a Bruker DSX400 solid-state NMR spectrometer. All spectra were recorded at a Larmor frequency of 100.6 MHz with magic angle spinning (MAS) at 2.0 kHz with cross-polarization (CP) or from single-pulse free induction decays with ^1H decoupling. The ^{13}C NMR resonance peaks of adamantane, with assigned chemical shifts of $\delta = 38.56$ and 29.50 ppm at 298 K were used as the external chemical-shift reference.

Received: December 8, 2005
Published online: March 7, 2006

Keywords: alkanes · clathrates · hydrates · natural gas · NMR spectroscopy

[1] E. D. Sloan, *Clathrate Hydrates of Natural Gas*, 2nd ed., Marcel Dekker, New York, **1998**.
[2] K. A. Kvenvolden, *Chem. Geol.* **1988**, *71*, 41; K. A. Kvenvolden, *Org. Geochem.* **1995**, *23*, 997; D. Grauls, *Mar. Pet. Geol.* **2001**, *18*, 519.
[3] J. A. Ripmeester, J. S. Tse, C. I. Ratcliffe, B. M. Powell, *Nature* **1987**, *325*, 135; K. A. Udachin, C. I. Ratcliffe, G. D. Enright, J. A. Ripmeester, *Supramol. Chem.* **1997**, *8*, 173.
[4] J. A. Ripmeester, C. I. Ratcliffe, *J. Phys. Chem.* **1990**, *94*, 8773.
[5] J. M. Brooks, M. C. Kennicutt, R. R. Fay, T. J. McDonald, R. Sassen, *Science* **1984**, *225*, 409.
[6] R. Sassen, I. R. MacDonald, *Org. Geochem.* **1994**, *2*, 1029; D. W. Davidson, S. K. Garg, S. R. Gough, Y. P. Handa, C. I. Ratcliffe, J. A. Ripmeester, J. S. Tse, W. F. Lawson, *Geochim. Cosmochim. Acta* **1986**, *50*, 619.
[7] A. P. Mehta, E. D. Sloan, *J. Chem. Eng. Data* **1993**, *38*, 580.
[8] A. P. Mehta, Ph.D. thesis, Colorado School of Mines (USA), **1996**.
[9] A. P. Mehta, J. A. Ripmeester, *Proc. 4th Int. Conf. Gas Hydrates*, Yokohama, Japan, **2002**, p. 580.

 © 2006 Wiley-VCH Verlag GmbH & Co. KGaA, Weinheim

Synthetic Methods

DOI: 10.1002/anie.200600300

Metal-Catalyzed [2+2+1] Cycloadditions of 1,3-Dienes, Allenes, and CO**

Paul A. Wender, Mitchell P. Croatt, and Nicole M. Deschamps*

Step economy is a preeminent goal of synthesis.[1] It influences the length, efficiency, cost, time, separation, and environmental impact of a synthesis. Step economy is favored by the use of single, serial, or multicomponent reactions that proceed in one operation with a great increase in target revelant complexity. The design or discovery of such reactions is thus critical to extending the practical reach of organic synthesis. Toward this end, we have directed effort at the identification of new metal-catalyzed reactions, especially those which are forbidden or difficult to achieve in the absence of a catalyst. This program has thus far produced several new two-, three-, and four-component reactions, including [4+4],[2] [4+2],[3] [5+2],[4] [6+2],[5] [5+2+1],[6] [2+2+1],[7] [4+2+1],[7a] and [5+1+2+1][8] cycloadditions. Herein, we report the first examples of the [2+2+1] cycloaddition reaction of diene–allenes and CO and preliminary examples of acceleration of this process by Brønsted acids.

This investigation originated from our studies on the first metal-catalyzed intramolecular [4+2] cycloadditions of dienes and alkynes [Eq. (1)].[3,9] We recognized that the

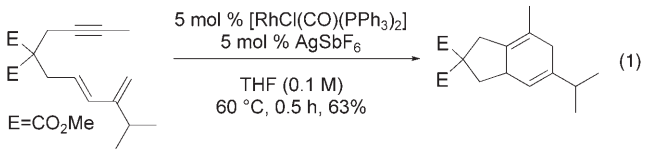

(1)

metallacyclic intermediates in this process could be intercepted by an additional component to produce three-component cycloadducts. With CO as the trapping agent, this approach indeed proved effective, thus resulting in the first examples of an intramolecular dienyl Pauson–Khand reaction [Eq. (2)] and a new [4+2+1] cycloaddition (not shown).[7a,10] Significantly, the diene was found to facilitate the reaction relative to an alkene [cf. Eqs. (2) and (3)].[7a,b] In the case of

[*] Prof. P. A. Wender, M. P. Croatt, N. M. Deschamps
Department of Chemistry
Stanford University
Stanford, CA 94305-5080 (USA)
Fax: (+1) 650-725-0259
E-mail: wenderp@stanford.edu

[**] This research was supported by the National Science Foundation (CHE-040638). Fellowship support from Eli Lilly and Company (M.P.C. and N.M.D.) is gratefully acknowledged.

Supporting information for this article is available on the WWW under http://www.angewandte.org or from the author.

© 2006 Wiley-VCH Verlag GmbH & Co. KGaA, Weinheim

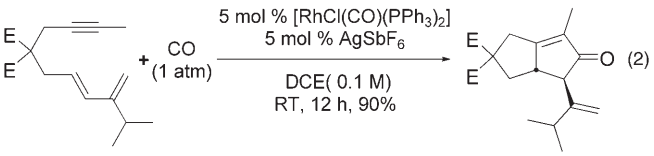

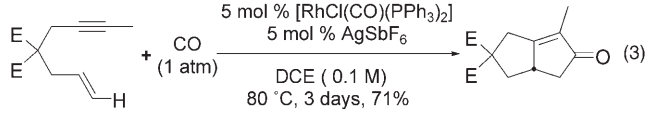

the [2+2+1] cycloaddition reaction of diene-enes, the presence of the diene enabled the reaction to occur, as these reactions do not proceed with simple bisalkenes.[7c] We expected that dienes could be used as two-carbon-atom components to enhance or enable other reactions because of their special reactivity. For example, although many impressive cases of the [2+2+1] cycloaddition reaction of alkyne–allenes (the allenic Pauson–Khand reaction) have been reported,[11] there have been no analogous reactions described for simple alkene–allenes. In fact, Brummond[12] and Itoh[13,14] found independently that simple alkene–allenes prefer to undergo efficient Rh^I-catalyzed cycloisomerizations to seven-membered rings rather than [2+2+1] cycloaddition reactions (even in the presence of CO; Scheme 1).[13,14] We have now

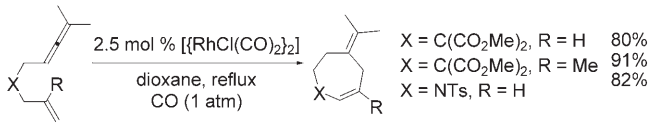

Scheme 1. Rh^I-catalyzed cycloisomerization reaction of alkene–allenes. Ts = tosyl.

found that if a diene–allene is used instead of an alkene–allene, a new [2+2+1] cycloaddition reaction is achievable, often in high yield.

Under the optimal conditions found for the analogous [2+2+1] cycloaddition reaction of diene-enes,[7c] diene–allene **1** provides the [2+2+1] and the [4+2] cycloadducts **2** and **3** upon treatment with a catalytic amount of a Rh^I complex in 1,2-dichloroethane (DCE) at 80 °C under one atmosphere of CO (Scheme 2). It is noteworthy that diene–allenes give high yields of the [4+2] product in the absence of CO.[15] Exploration of the reaction conditions revealed that a decrease in reaction temperature from 80 °C to room temperature led to the exclusive formation of the [2+2+1] product **2**, which was structurally assigned by X-ray crystallographic analysis.

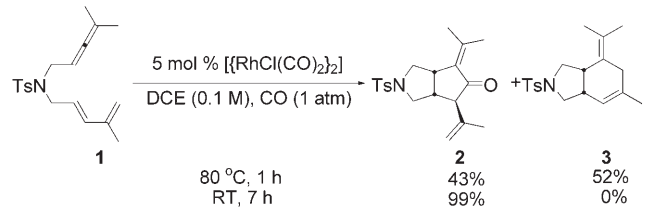

Scheme 2. Initial results and temperature effects for the competing [2+2+1] and [4+2] cycloaddition reactions.

A brief survey of different Rh^I complexes indicated that $[\{RhCl(CO)_2\}_2]$ is the best catalyst of those examined (Table 1, entries 1–3). The nature of the solvent had a substantial effect on the efficiency of the reaction. Poor-to-moderate yields were obtained and long reaction times were required when toluene, dioxane, and acetonitrile were used, whereas excellent yields were obtained when the reaction was carried out in either DCE, methanol, or 2,2,2-trifluoroethanol (TFE; entries 1, 4–8). Significantly, a dramatic increase in the reaction rate was observed with TFE.[16] Gratifyingly, when the catalyst loading was lowered to 0.1 mol % and the concentration in TFE was increased to 0.5 M, an excellent yield of **2** was obtained (entry 9).

Table 1: Optimization of the [2+2+1] cycloaddition of **1**.[a]

Entry	Catalyst	Solvent	*t* [h]	Yield of **2** [%][b]
1	$[\{RhCl(CO)_2\}_2]$	DCE	7	99
2	$[Rh(naph)(cod)]SbF_6$	DCE	1.5	32
3	$[\{RhCl(dppb)\}_2]$	DCE	32	80
4	$[\{RhCl(CO)_2\}_2]$	toluene	24.5	38
5	$[\{RhCl(CO)_2\}_2]$	dioxane	21.5	64
6	$[\{RhCl(CO)_2\}_2]$	CH_3CN	45	77
7	$[\{RhCl(CO)_2\}_2]$	MeOH	12	96
8	$[\{RhCl(CO)_2\}_2]$	TFE	0.25	92
9	$[\{RhCl(CO)_2\}_2]$	TFE[c]	8	97

[a] Rhodium (10 mol %), 0.1 M, RT, 1 atm CO. [b] Yield of isolated product. [c] Catalyst (0.1 mol %), 0.5 M. cod = 1,5-cyclooctadiene, naph = napthalene, and dppb = 1,4-bis(diphenylphosphino)butane.

Intrigued by the rate enhancement observed with TFE, we wondered whether this effect could be due to the acidity of the solvent, as the observed trend correlates poorly with the corresponding dielectric constants or dipole moments of the solvents used. To test this hypothesis, the effect of adding acids to the [2+2+1] cycloaddition reaction of **1** was investigated (Table 2).[17] This study revealed that the addition of acid provides a rate enhancement and, with the exception of *para*-toluenesulfonic acid (TsOH; the most acidic of the acids surveyed), has a negligible effect on the yield of the [2+2+1] cycloaddition reaction. The fastest reactions were obtained when the reaction was carried out in DCE in the presence of 14 equivalents of phenol (entry 7) or in TFE (entry 2). For practical reasons, including avoiding the need to

Table 2: Effect of acid on reaction time for diene–allene **1**.[a]

Entry	Solvent	Acid (equiv)	*t* [h]	Yield [%]
1	DCE	none	7	99
2	TFE	none	0.25	92
3	DCE	TsOH (0.05)	1.3	81
4	DCE	AcOH (6)	4	93
5	DCE	AcOH (100)	2.5	96
6	AcOH	none	2	93
7	DCE	PhOH (14)	0.25	94
8	DCE	TFE (14)	2	95

[a] $[\{RhCl(CO)_2\}_2]$ (5 mol %), 0.1 M, RT, CO (1 atm).

 © 2006 Wiley-VCH Verlag GmbH & Co. KGaA, Weinheim

separate phenol from the product at the end of the reaction, TFE was chosen as the solvent in the initial studies on the scope of this new [2+2+1] cycloaddition.

The [2+2+1] cycloaddition reaction of diene–allenes that vary in diene and allene substitution and type of tether was examined next (Table 3). In all cases, reaction at the proximal double bond of the allene was observed. Me, H, and *i*Pr substitution at the 2-position of the diene is well tolerated; however, approximately 10–25% of the olefin isomer was observed for H substitution.[18] Entries 1–3 indicate that the presence of heteroatoms in the tether has no deleterious effect on the efficiency of the reaction. The [2+2+1] cycloaddition reaction of substrate **9**, which has a terminally methyl-substituted allene, gave both diastereomers **10** and **11**. When this reaction was carried out in TFE, only a 39% overall yield was obtained (entry 5); however, a much cleaner and higher-yielding process (81%) was obtained when the reaction was carried out in DCE at a concentration of 0.05 M (entry 6). The [2+2+1] cycloaddition reaction of **12**, which is substituted with the larger *t*Bu group, can be carried out in TFE in an excellent overall yield of 94% (entry 7). Initial attempts to carry out the [2+2+1] cycloaddition reaction of diene–allene **15** in either TFE or DCE were unsuccessful. It was found that when the temperature and CO pressure were increased and the concentration in DCE was decreased, a 43% yield of the [2+2+1] product and a 19% yield of the [4+2] product (entry 8) were obtained.

Table 3: Substrate scope for the diene–allene [2+2+1] cycloaddition reaction.

Entry	Diene–allene	Conditions[a]	*t* [h]	Product	Yield
1	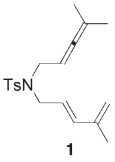 **1**	A	8	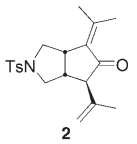 **2**	97
2	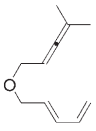 **4**	B	1.5	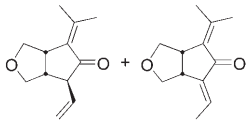 **5** **6**	97 (2.9:1)
3	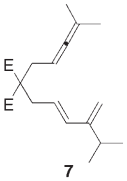 **7**	C	0.3	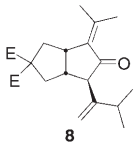 **8**	92
4	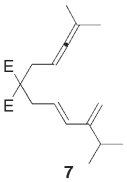 **7**	D	1.5	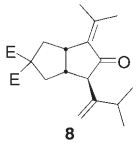 **8**	81
5	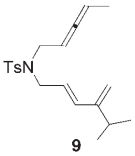 **9**	E	16	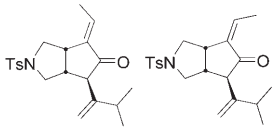 **10** **11**	39 (4.6:1)
6	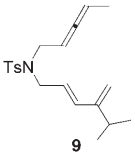 **9**	F	24	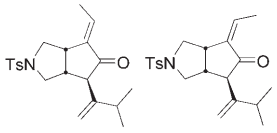 **10** **11**	81 (1.2:1)
7	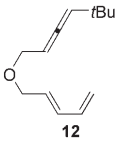 **12**	B	24	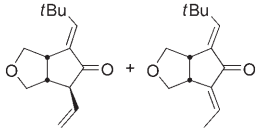 **13** **14**	94 (7.5:1)
8	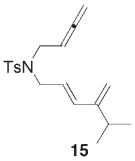 **15**	G	1.5	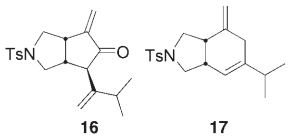 **16** **17**	62 (2.3:1)

[a] Conditions: A: [{RhCl(CO)$_2$}$_2$] (0.1 mol%), TFE (0.5 M), RT, CO (1 atm); B: [{RhCl(CO)$_2$}$_2$] (2.5 mol%), TFE (0.1 M), RT, CO (1 atm); C: [{RhCl(CO)$_2$}$_2$] (1 mol%), TFE (0.1 M), RT, CO (1 atm); D: [{RhCl(CO)$_2$}$_2$] (5 mol%), DCE (0.1 M), RT, CO (1 atm); E: [{RhCl(CO)$_2$}$_2$] (2.5 mol%), TFE (0.5 M), RT, CO (1 atm); F: [{RhCl(CO)$_2$}$_2$] (1 mol%), DCE (0.05 M), RT, CO (1 atm); G: [{RhCl(CO)$_2$}$_2$] (5 mol%), DCE (0.01 M), 60°C, CO (4 atm).

In conclusion, the first examples of the diene–allene [2+2+1] cycloaddition reaction are reported, thus providing an efficient, selective, and operationally facile route (room temperature, 1 atm CO) to highly substituted alkylidenyl cyclopentanones. The reaction is chemoselective with respect to the allene as the proximal olefin is targeted. The use of the diene leads exclusively to the [2+2+1] cycloadduct instead of the product from the carbocyclization reaction, which has been reported with alkene–allenes (Scheme 1), thus resulting in a process of mechanistic and synthetic utility. An additional point of significance is that the reaction is accelerated in several cases when performed in TFE or in the presence of certain Brønsted acids, thus suggesting cocatalysis possibly involving CO protonation in the migratory-insertion step. Further investigations on this and other [$m+n+$o] cycloaddition reactions of dienes are ongoing.[19]

 © 2006 Wiley-VCH Verlag GmbH & Co. KGaA, Weinheim

Experimental Section

Typical procedure: Preparation of the catalyst solution: [{RhCl(CO)$_2$}$_2$] was weighed into an oven-dried test tube equipped with a magnetic stir bar, and TFE was added by syringe to make a 0.005 M solution. The test tube was capped with a septum, and the solution was stirred under a balloon of CO vented to a bubbler for 45 min.

Diene–allene **1** (21 mg, 0.063 mmol) was weighed into an oven-dried test tube equipped with a magnetic stir bar, TFE (0.114 mL) was added by syringe, and the test tube was capped with a rubber septum. The solution was stirred under a balloon of CO vented to a bubbler for 30 min. The catalyst solution ([{RhCl(CO)$_2$}$_2$]; 0.0127 mL, 0.000063 mmol) was added by syringe, and the reaction mixture was stirred under a balloon of CO for 8 h. The solution was concentrated by rotary evaporation, and the residue was purified by column chromatography on silica gel (EtOAc/CH_2Cl_2 2:98). The product-containing fractions were combined and concentrated to give **2** (20.6 mg, 97%) as a white solid; the compounds were chromatographically homogeneous.

Received: January 24, 2006
Published online: March 9, 2006

Keywords: allenes · cycloaddition · dienes · Pauson–Khand reaction · rhodium

[1] a) P. A. Wender, F. C. Bi, G. G. Gamber, F. Gosselin, R. D. Hubbard, M. J. C. Scanio, R. Sun, T. J. Williams, L. Zhang, *Pure Appl. Chem.* **2002**, *74*, 25 – 31; b) P. A. Wender, S. T. Handy, D. L. Wright, *Chem. Ind. (London)* **1997**, 765; c) P. A. Wender, B. L. Miller, *Organic Synthesis: Theory and Applications*, *Vol. 2* (Ed.: T. Hudlicky, JAI, Greenwich, **1993**, p. 27.

[2] a) P. A. Wender, N. C. Ihle, *J. Am. Chem. Soc.* **1986**, *108*, 4678 – 4679; b) P. A. Wender, N. C. Ihle, C. R. D. Correia, J . *Am. Chem. Soc.* **1988**, *110*, 5904 – 5906.

[3] For the first examples, see: a) P. A. Wender, T. E. Jenkins, *J. Am. Chem. Soc.* **1989**, *111*, 6432 – 6434; b) P. A. Wender, T. E. Jenkins, S. Suzuki, *J. Am. Chem. Soc.* **1995**, *117*, 1843 – 1844.

[4] For the first examples, see: a) P. A. Wender, H. Takahashi, B. Witulski, *J. Am. Chem. Soc.* **1995**, *117*, 4720 – 4721; b) P. A. Wender, H. Rieck, M. Fuji, *J. Am. Chem. Soc.* **1998**, *120*, 10976 – 10977; for the most recent, see: c) P. A. Wender, T. J. Williams, *Angew. Chem.* **2002**, *114*, 4732 – 4735; *Angew. Chem. Int. Ed.* **2002**, *41*, 4550 – 4553; d) P. A. Wender, J. A. Love, T. J. Williams, *Synlett* **2003**, 1295 – 1298.

[5] P. A. Wender, A. G. Correa, Y. Sato, R. Sun, *J. Am. Chem. Soc.* **2000**, *122*, 7815 – 7816.

[6] a) For the first report with alkynes, vinylcyclopropanes, and CO; see: P. A. Wender, G. G. Gamber, R. D. Hubbard, L. Zhang, *J. Am. Chem. Soc.* **2002**, *124*, 2876 – 2877; b) for the first report with allenes, vinylcyclopropanes, and CO; see: H. A. Wegner, A. de Meijere, P. A. Wender, *J. Am. Chem. Soc.* **2005**, *127*, 6530 – 6531.

[7] a) For the first report of a diene-yne [4+2+1] and dienyl Pauson–Khand reaction, see: P. A. Wender, N. M. Deschamps, G. G. Gamber, *Angew. Chem.* **2003**, *115*, 1897 – 1901; *Angew. Chem. Int. Ed.* **2003**, *42*, 1853 – 1857; b) for the first intermolecular dienyl Pauson–Khand reaction, see: P. A. Wender, N. M. Deschamps, T. J. Williams, *Angew. Chem.* **2004**, *116*, 3138 – 3141; *Angew. Chem. Int. Ed.* **2004**, *43*, 3076 – 3079; c) for the first [2+2+1] cycloaddition reaction of diene-enes and CO, see: P. A. Wender, M. P. Croatt, N. M. Deschamps, *J. Am. Chem. Soc.* **2004**, *126*, 5948 – 5949; d) Y. K. Chung, S. I. Lee, J. H. Park, S.-G. Lee, *J. Am. Chem. Soc.* **2004**, *126*, 10190 (Y. K. Chung, S. I. Lee, J. H. Park, S.-G. Lee, *J. Am. Chem. Soc.* **2004**, *126*, 2714 – 2715).

[8] P. A. Wender, G. G. Gamber, R. D. Hubbard, S. M. Pham, L. Zhang, *J. Am. Chem. Soc.* **2005**, *127*, 2836 – 2837.

[9] For the first example of a Rh^{I}-catalyzed [4+2] cycloaddition reaction of diene-ynes and diene-enes, see: R. S. Jolly, G. Luedtke, D. Sheehan, T. Livinghouse, *J. Am. Chem. Soc.* **1990**, *112*, 4965 – 4966.

[10] For a [4+2+2] cycloaddition reaction of diene-ynes and alkynes, see: S. R. Gilbertson, B. DeBoef, *J. Am. Chem. Soc.* **2002**, *124*, 8784 – 8788.

[11] For a recent review featuring work by Brummond, Narasaka, Cazes, Livinghouse, Alcaide, Mukai, Cook, and Shibata, see: B. Alcaide, P. Almendros, *Eur. J. Org. Chem.* **2004**, 3377 – 3383.

[12] K. M. Brummond, H. Chen, B. Mitasev, A. D. Casarez, *Org. Lett.* **2004**, *6*, 2161 – 2163.

[13] T. Makino, K. Itoh, *J. Org. Chem.* **2004**, *69*, 395 – 405.

[14] Only the vinylsilane substrate below reacted in a [2+2+1] fashion:

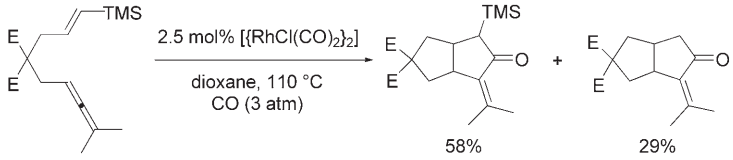

[15] For the first example of a metal-catalyzed intramolecular diene–allene [4+2] cycloaddition reaction, see: P. A. Wender, T. E. Jenkins, S. J. Suzuki, *J. Am. Chem. Soc.* **1995**, *117*, 1843 – 1844.

[16] A similar rate enhancement was observed for the intermolecular [5+2] cycloaddition reaction of vinyl cyclopropanes and alkynes, see: P. A. Wender, C. M. Barzilay, A. J. Dyckman, *J. Am. Chem. Soc.* **2001**, *123*, 179 – 180.

[17] Although protic acids accelerate the [2+2+1] cycloaddition reaction, the Lewis acid $MgBr_2(OEt_2)$ does not have the same effect in this case.

[18] Similar isomerizations are observed in the [2+2+1] cycloaddition reaction of diene-enes and CO; ref. [7c].

[19] Full procedural details and characterization data are given in the Supporting Information.

 © 2006 Wiley-VCH Verlag GmbH & Co. KGaA, Weinheim

Chip Laboratories

DOI: 10.1002/anie.200504205

Enantioselective Catalysis and Analysis on a Chip**

Detlev Belder, Martin Ludwig, Li-Wen Wang, and Manfred T. Reetz**

The application of microsystems technology to chemistry enables miniaturization of chemical processes on so-called microfluidic chips, where reactions are performed in micro channels and cavities rather than in flasks and tubes. The ambitious aim is to shrink chemical laboratories to so called lab-on-a-chip systems. Besides the advantages of miniaturization, such as improved portability, safety, and reduced reagent consumption, one of the most promising features of integrated palmtop laboratories is the accelerated speed of reaction and analysis,[1] with corresponding potential for high-throughput screening. While the introduction of classical high-throughput screening systems based on robotics and massive parallelization has revolutionized chemical synthesis, miniaturization and integration on chip size would constitute a quantum leap.

Currently, significant progress is being made in microfluidics and its application for down-sizing chemical reactors.[2] One of the most successful applications of microfluidics in analytical chemistry is microchip electrophoresis (MCE), which can be regarded as a miniaturized version of classical capillary electrophoresis. One of the most prominent features of MCE is the extraordinary high speed of analysis, which could also be successfully applied to the separation of enantiomers by us[3] and others.[4] By applying MCE to the enantioselective separations of amino acids in less than a second we have already reported the fastest chiral separation.[5] In previous work we laid the foundation for the general applicability of chip electrophoresis to chiral high-throughput screening of enantioselective catalysts.[6]

The ultimate potential of chip technology in chemistry can only be exploited fully by the integration of chemical synthesis and analysis. While complex integrated lab-on-a-chip systems have recently been described for biochemical applications, such as genetic analysis of the influenza virus,[7] similar achievements remain to be made in synthetic chemistry. Recently, a miniaturized T-reactor was impressively applied in asymmetric synthesis, chiral analysis of the reaction products was, however, performed offline utilizing traditional GC/MS.[8]

We have now implemented a novel integrated approach which combines a microfluidic reactor and analysis unit on a single device. We have utilized this reaction/analysis chip for testing the enantioselectivity of enzyme mutants created by directed evolution of the enzymes.[9] As a model system, the epoxide hydrolase catalyzed hydrolytic kinetic resolution of glycidyl phenyl ether[10] was integrated with chiral electrophoresis on a chip.

The working principle of the chip we developed for this purpose is shown in Figure 1. Substrate and catalyst are placed in respective microvials on the chip. Upon applying pressure or electrical fields, enzyme and substrate solutions are merged through microfluidic channels, the mixing and reaction are aided by means of a meandering channel. The reaction products are then guided to the separation channel by applying a voltage-controlled pinched injection.[11] The actual electrophoretic separation of products and educts occurs in an electrical field in the separation channel.

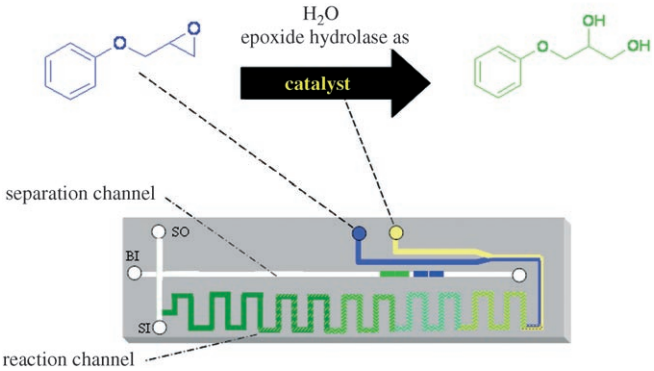

Figure 1. Schematic drawing of the working principle of the integrated catalysis/analysis chip. SO: sample outlet, SI: alternative sample inlet, BI: buffer outlet.

A photo of such a microfluidic chip made from fused-silica[12] together with a typical example of a separation of (+/−) substrate and (+/−) product is shown in Figure 2. This prototype contains four microvials for dispensing different substrates or catalysts, enabling, for example, three catalysts acting on one substrate to be tested in a single set of experiments.

For separation of the compounds a 50 mmol L^{-1} borate buffer at pH 8.5 containing 15 mmol L^{-1} heptakis-6-sulfato-β-cyclodextrin as a chiral selector was utilized. Under these conditions product and educt can simultaneously be separated into the respective enantiomers in less than 90 seconds (Figure 2). For the detection of the analytes we applied native fluorescence detection, using a deep-UV laser (Nd:YAG, $\lambda =$ 266 nm); a technique that we only recently introduced in chip analysis[13] and which requires UV-transparent fused-silica chips, rather than the commonly applied borofloat glass as chip material.

This new system was successful in testing the enantioselectivity of new enzyme mutants created by directed evolu-

[*] Dr. D. Belder, Dr. M. Ludwig, L.-W. Wang, Prof. Dr. M. T. Reetz
Max-Planck-Institut für Kohlenforschung
Kaiser-Wilhelm-Platz 1
45470 Mülheim an der Ruhr (Germany)
Fax: (+49) 208-306-2982
E-mail: belder@mpi-muelheim.mpg.de

[**] We acknowledge financial support from the Fonds der Chemischen Industrie and the DFG (SSP1170) and L.-W. Wang acknowledges support from the DAAD for a doctoral stipend.

© 2006 Wiley-VCH Verlag GmbH & Co. KGaA, Weinheim

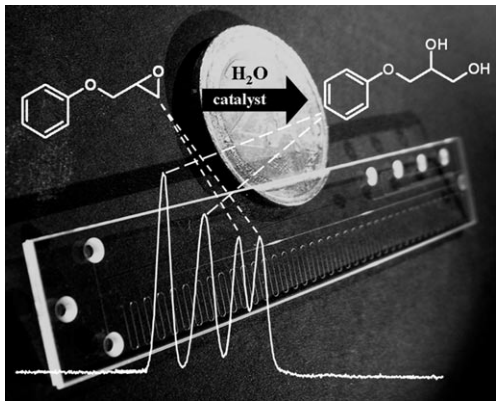

Figure 2. Photo of the microfluidic chip in comparison with a 2-Euro coin together with the reaction scheme (top) and the electrophoretic data (bottom) of the separated enantiomers of product and precursor.

tion. The data of on-chip electrophoretic separations after on-chip reaction of different epoxide hydrolase mutants[10b] from *Aspergillus niger*, as well as from the wild type,[10a] are shown in Figure 3. Reaction on-chip was possible using purified

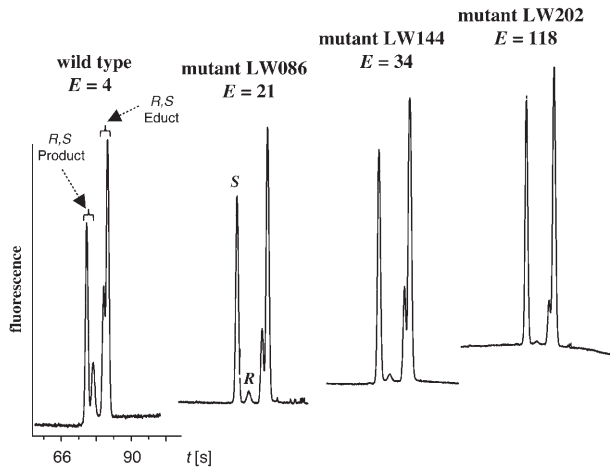

Figure 3. Application of the system for testing the wild type as well as different epoxide hydrolase mutants created by directed evolution. Electrophoretic separation of product and educt enantiomers after on-chip catalysis. The *E* values were calculated from the corresponding single measurements.

enzymes in the case of the wild type or cell lysates and with whole cells. No interfering signals for the enzymes or cell lysates or cells where obtained under the experimental conditions employed. As reaction medium a 10 millimolar phosphate buffer at pH 7.2 containing 7.5 % (v/v) acetonitrile was employed. With this approach it is possible to reliably differentiate the enzymes with respect to their selectivities, (Figure 3). While a selectivity factor[14] of $E = 4$ was obtained for the wild type, an *E* value of 118 was determined for the best mutant LW202 in the respective single measurements.

The results obtained with the miniaturized catalysis/analysis chip were compared with those determined by the traditional procedure, namely reaction on bench-scale format and subsequent analysis of the supernatant with conventional chiral HPLC (Table 1). The agreement is good, which shows in principle the applicability of our miniaturized integrated system. The data for the chip experiments in Table 1 are mean values of triplicate determinations. The relative standard

Table 1: Comparison of experimental results for determination of conversion, enantiomeric excess (*ee*), and *E* value obtained with the catalysis/analysis chip or with conventional reaction in bench-scale format and subsequent HPLC-Analysis.[a]

Enzyme	Method	Conv [%]	*ee* diol [%]	*E*
wild type	chip	38	49	4
	bench-scale/HPLC	18	58	4
LW080	chip	22	90	23
	bench-scale/HPLC	23	82	13
LW086	chip	43	84	21
	bench-scale/HPLC	40	84	20
LW144	chip	28	93	37
	bench-scale/HPLC	37	89	29
LW202	chip	41	95	101
	bench-scale/HPLC	48	95	115

[a] The data are mean values from triplicate experiments.

deviations (RSD) are in a quite acceptable range, especially in view of the fact that these are data from a prototype. For the *ee* value determinations we obtained RSDs of 1–3 % and for the *E* values RSD of 3–21 % were determined. Although the RSDs for the *E* values are somewhat high, unequivocal identification of the best mutants is still possible.

In the experiments described above the mixing process and reaction of substrates and enzymes occurred in microfluidic channels on a chip. The liquids were forced through the reaction channel by the application of vacuum; alternatively this was also carried out by applying an electrical field. Due to the long channel geometry the voltage driven reaction step was, however, more time consuming (about 25 min) than the vacuum transport (10 min). By integration of a more effective and faster micromixer it can be expected that the reaction and mixing times can be reduced considerably.[15]

Instead of merging substrate and enzyme in a microfluidic channel, mixing and reaction can be performed much faster and straightforward by pipetting the compounds together in a microvial. The reaction will then start instantly, which however may be disadvantageous for testing large libraries of catalysts because different conversions are then to be expected. On the other hand, this instant-start effect can be exploited to study the conversion and selectivity in real time by utilizing the fast and integrated analysis part of the chip. This approach can be put into practice by pipetting substrate and enzyme into the microvial labeled BI (Figure 1) and applying a so-called gated injection[16] by repetitive switching between defined electrical potentials. This results in sequential injections of reactants into the separation channel from a continuous sample flow. As a result stacked electropherograms are obtained which can be used to follow the kinetics of the reaction. (Figure 4).

The respective data together with the extracted values of conversion and *E* value are displayed in Figure 5. These experiments were carried out with 10 μL of a 0.02 mg mL^{-1}

 © 2006 Wiley-VCH Verlag GmbH & Co. KGaA, Weinheim

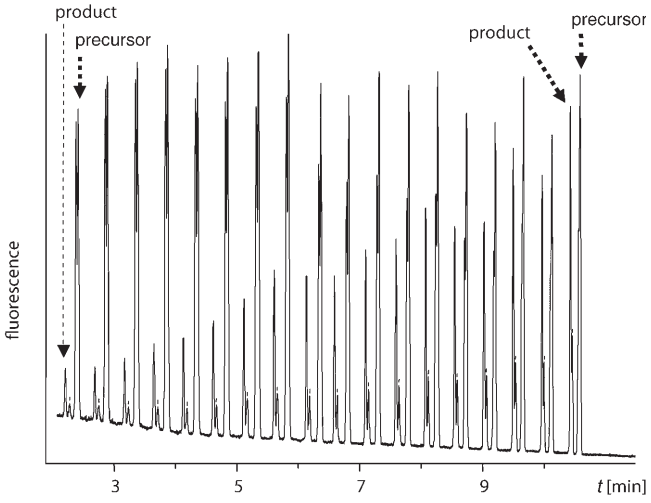

Figure 4. Monitoring reaction kinetics with stacked electropherograms. For this purpose the wild-type enzyme and substrate were pipetted together in a microvial on a chip and repetitive chiral separations were preformed.

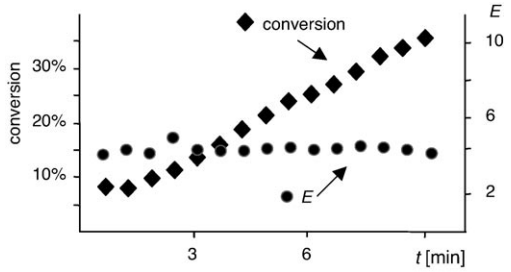

Figure 5. Slope for conversion and *E* value, derived from data of stacked electropherograms in Figure 4.

solution of epoxide hydrolase of the wild-type enzyme and with 10 μL of 0.75 mmol L^{-1} of epoxide solution.

Herein we have demonstrated the first example of an integrated chip-based system applied in synthetic chemistry and catalysis which integrates a microfluidic reactor with chemical analysis. In this initial study the device was successfully applied for testing enantioselective biocatalysts created by directed evolution of enzymes; the device also has great potential for high-throughput screening. Integration of chemical reaction and analysis on a chip results in reduced reagent consumption and allows the speed of the whole screening process to be increased considerably. Further improvement of the system, with regard to high-throughput appears possible by implementing faster and more effective micromixers, by parallelization of the microfluidic separation and reaction channels and/or by coupling with microdroplet devices as previously suggested.[17]

Received: November 25, 2005
Published online: January 27, 2006

Keywords: directed evolution · electrophoresis · enantiomer separation · high-throughput screening · microreactors

[1] A. Manz, J. C. T. Eijkel, *Pure Appl. Chem.* **2001**, *73*, 1555 – 1561.
[2] a) J. Atencia, D. J. Beebe, *Nature* **2005**, *437*, 648 – 655; b) V. Hessel, H. Löwe, *Chem. Eng. Technol.* **2005**, *28*, 267 – 284; c) J. Kobayashi, Y. Mori, K. Okamoto, R. Akiyama, M. Ueno, T. Kitamori, S. Kobayashi, *Science* **2004**, *304*, 1305 – 1308; d) S. J. Haswell, R. J. Middleton, B. O'Sullivan, V. Skelton, P. Watts, P. Styring, *Chem. Commun.* **2001**, *5*, 391 – 398; e) D. Erickson, D. Li, *Anal. Chim. Acta* **2004**, *507*, 11 – 26; f) M. Tokeshi, Y. Kikutani, A. Hibara, K. Sato, H. Hisamoto, T. Kitamori, *Electrophoresis* **2003**, *24*, 3583 – 3594; g) T. Vilkner, D. Janasek, A. Manz, *Anal. Chem.* **2004**, *76*, 3373 – 3385; h) M. Brivio, R. H. Fokkens, W. Verboom, D. N. Reinhoudt, N. R. Tas, M. Goedbloed, A. van den Berg, *Anal. Chem.* **2002**, *74*, 3972 – 3976; i) P. S. Dittrich, P. Schwille, *Anal. Chem.* **2003**, *75*, 5767 – 5774; j) K. Jähnisch, V. Hessel, H. Löwe, M. Baerns, *Angew. Chem.* **2004**, *116*, 410 – 453; *Angew. Chem. Int. Ed.* **2004**, *43*, 406 – 446; k) F. Schönfeld, V. Hessel, C. Hofmann, *Lab Chip* **2004**, *4*, 65 – 69; l) A. E. Guber, M. Heckele, D. Herrmann, A. Muslija, V. Saile, L. Eichhorn, T. Gietzelt, A. Hoffmann, P. C. Hauser, J. Tanyanyiwa, A. Gerlach, N. Gottschlich, G. Knebel, *Chem. Eng. J.* **2004**, *101*, 447 – 453; m) M. Kakuta, F. G. Bessoth, A. Manz, *Chem. Rec.* **2001**, *1*, 395 – 405; n) C. Erbacher, F. G. Bessoth, M. Busch, E. Verpoorte, A. Manz, *Mikrochim. Acta* **1999**, *131*, 19 – 24; o) M. Grumann, A. Geipel, L. Riegger, R. Zengerle, J. Ducrée, *Lab Chip* **2005**, *5*, 560 – 565.
[3] a) D. Belder, M. Ludwig, *Electrophoresis* **2003**, *24*, 2422 – 2430; b) M. Ludwig, F. Kohler, D. Belder, *Electrophoresis* **2003**, *24*, 3233 – 3238; c) D. Belder, M. Ludwig, *Electrophoresis* **2003**, *24*, 3595 – 3606; d) D. Belder, A. Deege, M. Maass, M. Ludwig, *Electrophoresis* **2002**, *23*, 2355 – 2361.
[4] a) L. D. Hutt, D. P. Glavin, J. L. Bada, R. A. Mathies, *Anal. Chem.* **1999**, *71*, 4000 – 4006; b) S. R. Wallenborg, I. S. Lurie, D. W. Arnold, C. G. Bailey, *Electrophoresis* **2000**, *21*, 3257 – 3263; c) I. Rodriguez, L. J. Jin, S. F. Y. Li, *Electrophoresis* **2000**, *21*, 211 – 219; d) H. Wang, Z. P. Dai, L. Wang, J. L. Bai, B. C. Lin, *Chin. J. Anal. Chem.* **2002**, *30*, 665 – 669; e) M. A. Schwarz, P. C. Hauser, *J. Chromatogr. A* **2001**, *928*, 225 – 232; f) E. Ölvecka, M. Masar, D. Kaniansky, M. Jöhnck, B. Stanislawski, *Electrophoresis* **2001**, *22*, 3347 – 3353; g) S. Il Cho, K. N. Lee, Y. K. Kim, J. H. Jang, D. S. Chung, *Electrophoresis* **2002**, *23*, 972 – 977; h) B. F. Liu, M. Ozaki, Y. Utsumi, T. Hattori, S. Terabe, *Anal. Chem.* **2003**, *75*, 36 – 41.
[5] N. Piehl, M. Ludwig, D. Belder, *Electrophoresis* **2004**, *25*, 3848 – 3852.
[6] M. T. Reetz, K. M. Kühling, A. Deege, H. Hinrichs, D. Belder, *Angew. Chem.* **2000**, *112*, 4049 – 4052; *Angew. Chem. Int. Ed.* **2000**, *39*, 3891 – 3893.
[7] R. Pal, M. Yang, R. Lin, B. N. Johnson, N. Srivastava, S. Z. Razzacki, K. J. Chomistek, D. C. Heldsinger, R. M. Haque, V. M. Ugaz, P. K. Thwar, Z. Chen, K. Alfano, M. B. Yim, M. Krishnan, A. O. Fuller, R. G. Larson, D. T. Burke, M. A. Burns, *Lab Chip* **2005**, *5*, 1024 – 1032.
[8] C. I. Jönsson, S. Lundgren, S. J. Haswell, C. Moberg, *Tetrahedron* **2004**, *60*, 10515 – 10520.
[9] a) Review articles on directed evolution of enantioselective enzymes: M. T. Reetz, *Proc. Natl. Acad. Sci. USA* **2004**, *101*, 5716 – 5722; M. T. Reetz in *Advances in Catalysis, Vol. 49* (Eds.: B. C. Gates, H. Knözinger), **2005**, pp. 1 – 70; b) review on high-throughput-screening systems for evaluation of enantioselective catalysts and enzymes: M. T. Reetz, *Angew. Chem.* **2001**, *113*, 292 – 320; *Angew. Chem. Int. Ed.* **2001**, *40*, 284 – 310; c) reviews on directed evolution: *Directed Enzyme Evolution*: *Screening and Selection Methods, Vol. 230* (Eds. F. H. Arnold, G. Georgiou), Humana Press, Totowa, NJ, **2003**; d) *Directed Molecular Evolution of Proteins (or How to Improve Enzymes for Biocatalysis)* (Eds.: S. Brakmann, K. Johnsson), Wiley-VCH,

 © 2006 Wiley-VCH Verlag GmbH & Co. KGaA, Weinheim

Weinheim, **2002**; e) *Enzyme Functionality*: *Design*, *Engineering*, *and Screening* (Ed.: A. Svendsen), Marcel Dekker, New York, **2004**; f) *Evolutionary Methods in Biotechnology*: *Clever Tricks for Directed Evolution* (Eds. S. Brakmann, A. Schwienhorst), Wiley-VCH, Weinheim, **2004**.

[10] a) M. T. Reetz, C. Torre, A. Eipper, R. Lohmer, M. Hermes, B. Brunner, A. Maichele, M. Bocola, M. Arand, A. Cronin, Y. Genzel, A. Archelas, R. Furstoss, *Org. Lett.* **2004**, *6*, 177 – 180; b) M. T. Reetz, L.-W. Wang, M. Bocola, *Angew. Chem.* **2006**, *118*, 1258 – 1263; *Angew. Chem. Int. Ed.* **2006**, *45*, 1236 – 1241; c) reviews on epoxide hydrolases: K. Faber, R. V. A. Orru in *Enzyme Catalysis in Organic Synthesis* (Ed.: K. Drauz, H. Waldmann), Wiley-VCH, Weinheim, **2002**, pp. 579 – 608; d) C. Morisseau, B. D. Hammock, *Annu. Rev. Pharmacol. Toxicol.* **2005**, *45*, 311 – 333; e) A. Archelas, R. Furstoss, *Curr. Opin. Chem. Biol.* **2001**, *5*, 112 – 119; f) further literature on directed evolution of enantioselective epoxide hydrolases: B. van Loo, J. H. L. Spelberg, J. Kingma, T. Sonke, M. G. Wubbolts, D. B. Janssen, *Chem. Biol.* **2004**, *11*, 981 – 990; g) L. Y. Rui, L. Cao, W. Chen, K. F. Reardon, T. K. Wood, *Appl. Environ. Microbiol.* **2005**, *71*, 3995 – 4003.

[11] S. C. Jacobson, R. Hergenröder, L. B. Koutny, R. J. Warmack, J. M. Ramsey, *Anal. Chem.* **1994**, *66*, 1107 – 1113.

[12] Manufactured by Micronit (Enschede, The Netherlands).

[13] P. Schulze, M. Ludwig, F. Kohler, D. Belder, *Anal. Chem.* **2005**, *77*, 1325 – 1329.

[14] The *E* values were calculated according to the equation introduced by Sih: C.-S. Chen, Y. Fujimoto, G. Girdaukas, C. J. Sih, *J. Am. Chem. Soc.* **1982**, *104*, 7294 – 7299.

[15] Reviews on micromixers: a) N.-T. Nguyen, Z. Wu, J. *Micromech. Microeng.* **2005**, *15*, R1 – R16; b) J. M. Ottino, S. Wiggins, *Philos. Trans. R. Soc. London Ser. A* **2004**, *362*, 923 – 935.

[16] S. C. Jacobson, L. B. Koutny, R. Hergenröder, A. W. Moore, J. M. Ramsey, *Anal. Chem.* **1994**, *66*, 3472 – 3476.

[17] D. Belder, *Angew. Chem.* **2005**, *117*, 3587 – 3588; *Angew. Chem. Int. Ed.* **2005**, *44*, 3521 – 3522.

 © 2006 Wiley-VCH Verlag GmbH & Co. KGaA, Weinheim

Synthetic Methods

DOI: 10.1002/anie.200503945

Enantioselective Modular Synthesis of 2,4-Disubstituted Cyclopentenones by Iridium-Catalyzed Allylic Alkylation**

*Mathias Schelwies, Pierre Dübon, and Günter Helmchen**

Cyclopentenones are important structural motifs of natural products and pharmaceuticals.[1] Their stereoselective synthesis remains a challenge because of the numerous possible substitution patterns.[2] Here we report a new enantioselective method for the synthesis of 2,4-disubstituted cyclopentenones and its application in the synthesis of some interesting targets. Cyclopentenones are also of interest as intermediates, because of their suitability for reactions at position 3 with nucleophiles and at position 5 with electrophiles; thus, numerous further functionalizations are possible (Scheme 1).[3]

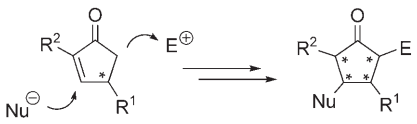

Scheme 1.

The new method is based on the following concept (Scheme 2): a) Iridium-catalyzed allylic alkylation using the enolate of amide **1**, a new prenucleophile, leads to a new chirality center having an adjacent vinyl group with high enantioselectivity.[4] b) The Weinreb-type[5] amide group allows facile conversion of the alkylation product into an enone. c) Finally, the enone can be cyclized by Ru-catalyzed ring-closing metathesis (RCM).[6] The combination of metal-catalyzed allylic alkylation and ring-closing metathesis is already known as a method for the construction of cyclic compounds;[4f,7] however, it has not yet found broad application in organic synthesis.

Over the last few years iridium-catalyzed allylic alkylation has evolved into a reliable method for enantioselective C–C bond formation.[4] The phosphorus amidite ligands, introduced by Alexakis and Feringa,[4g,8] have proved to be

[*] M. Schelwies, P. Dübon, Prof. Dr. G. Helmchen
Organisch-Chemisches Institut der Universität Heidelberg
Im Neuenheimer Feld 270, 69120 Heidelberg (Germany)
Fax: (+49) 6221-544-205
E-mail: g.helmchen@oci.uni-heidelberg.de

[**] This work was supported by the Deutsche Forschungsgemeinschaft (SFB 623), the Degussa Stiftung, and the Studienstiftung des deutschen Volkes. We thank Sandra Dreisigacker for her assistance, Dr. K. Ditrich (BASF AG) for enantiomerically pure 1-arylethylamines, and Dr. G. Egri (Reuter Chemischer Apparatebau KG) for a sample of (*S*)-binol.

 InterScience © 2006 Wiley-VCH Verlag GmbH & Co. KGaA, Weinheim

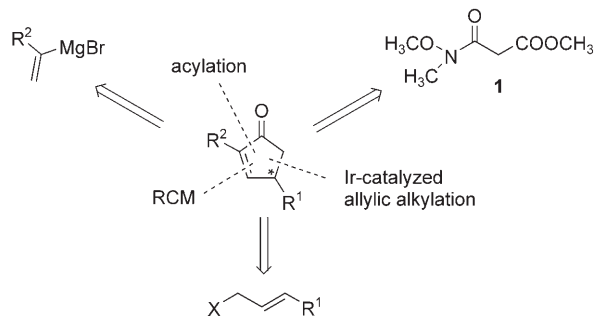

Scheme 2. Retrosynthetic concept.

particularly well suited for these reactions. Catalysts prepared by reaction of [{Ir(cod)Cl}$_2$] (cod = cyclooctadiene) with **L1** or **L2** and base (Scheme 3) induce very high activity and

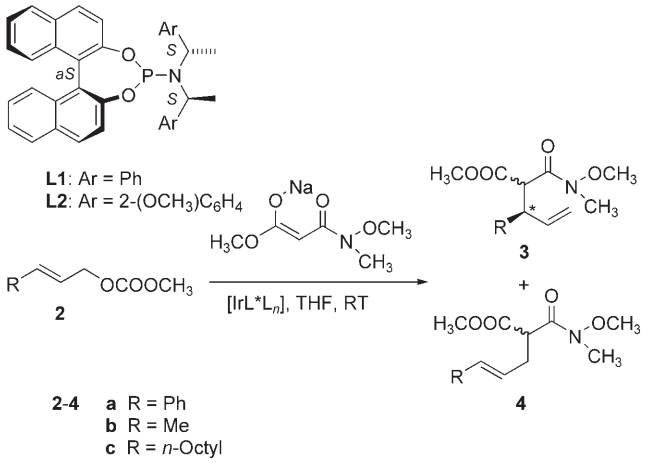

Scheme 3. Allylic substitution using a malonic amide of the Weinreb-type derived from dimethyl malonate.

selectivity (see Experimental Section). In these reactions, iridacycles are formed by C–H activation.[4d,9] We applied this method to study allylic alkylations with the enolate of compound **1** as a new nucleophile (Scheme 3). Absolute configurations of the products were assigned in analogy to the results of previously investigated substitutions with malonates and amides as nucleophiles. To date, the steric course of all substitutions yielding a product with known absolute configuration was found to be independent of the nucleophile.[10]

The results displayed in Table 1 demonstrate that the alkylations were fast as well as highly regio- and enantioselective. The enolate of **1** shows reactivity and selectivity similar to that of enolates of malonic esters, which are the standard nucleophiles employed in allylic alkylations. Products **3** were formed as 1:1 mixtures of diastereoisomers, which were neither separated nor characterized because of facile equilibration through enolization of the malonic amide part of the molecule. Enantiomeric excesses were found to be in the range of 95–99% *ee* and regioselectivities, in the range of **3**/**4** = 83:17 to 98:2.

The mixtures of the substitution products **3** and **4** could be smoothly converted in three steps into the corresponding 2,4-disubstituted cyclopentenones in overall yields of >50% (Scheme 4, Table 2). Saponification/decarboxylation gave the amides **5**, and in the next step, reaction with Grignard reagents, the enones **6** were obtained with various substituents in position 2. Subsequent ring-closing metathesis using Grubbs' second-generation catalyst[11] afforded cyclopentenones **7**–**11** (Table 2); side products formed from regioisomers **4** could be separated off easily. The enantiomeric excesses of compounds **3** and those of the corresponding cyclopentenones were identical to within the accuracy of measurement; in other words, the ring-closing metathesis proceeds without

Table 1: Iridium-catalyzed allylic alkylation of carbonates **2a**–**c** according to Scheme 3 (cf. Experimental Section).

Entry	Substr.	L*	t[a] [h]	Yield **3**+**4** [%][b]	**3**/**4**[c]	*ee* (**3**) [%][d] (abs. config.)
1	**2a**	**L1**	1	89	>98:2	96 (*R*)
2[e]	**2a**	**L2**	0.5	88	>98:2	98 (*R*)
3[e]	**2b**[f]	**L1**	3	83	94:6	95 (*R*)
4	**2b**[f]	**L2**	2	76	94:6	95 (*R*)
5	**2c**[f]	**L1**	18	89	83:17	96 (*R*)
6[e]	**2c**[f]	**L2**	5.5	62	84:16	99 (*R*)

[a] Reaction time. [b] Yield of the isolated mixture of the regioisomeric products **3** and **4**. [c] Determined by ^{1}H NMR spectroscopy. [d] Determined by HPLC on a chiral column (Daicel Chiralcel AD-H, 250×4.6 mm, 5 μm with guard cartridge AD-H, 10×4 mm, 5 μm, 0.5 mL min^{-1}). In all cases the branched compounds **3** were obtained as 1:1 mixtures of diastereoisomers; therefore, in each case the chromatograms displayed four peaks. All given absolute configurations refer to the starred chirality center in Scheme 3. Compounds **4** were racemic. Chromatographic conditions and results (*n*-hexane/isopropyl alcohol 95:5, 20°C, 210 nm): t_R[(*S*)-**3a**] = 28 min/37 min, t_R[(*R*)-**3a**] = 33 min/47 min, t_R[**4a**] = 39 min/42 min; (*n*-hexane/isopropyl alcohol 99:1, 20°C, 210 nm): t_R[(*R*)-**3b**] = 36 min/43 min, t_R[(*S*)-**3b**] = 41 min/47 min, t_R[**4b**] = 58 min/64 min; (*n*-hexane/isopropyl alcohol 99:1, 20°C, 220 nm): t_R[(*R*)-**3c**] = 26 min/28 min, t_R[(*S*)-**3c**] = 27 min/32 min, t_R[**4c**] = 31 min/32 min. [e] Reaction was conducted with 0.02 equiv of the Iridium catalyst. [f] The substrate contained 2–3% of the *cis* diastereoisomer.

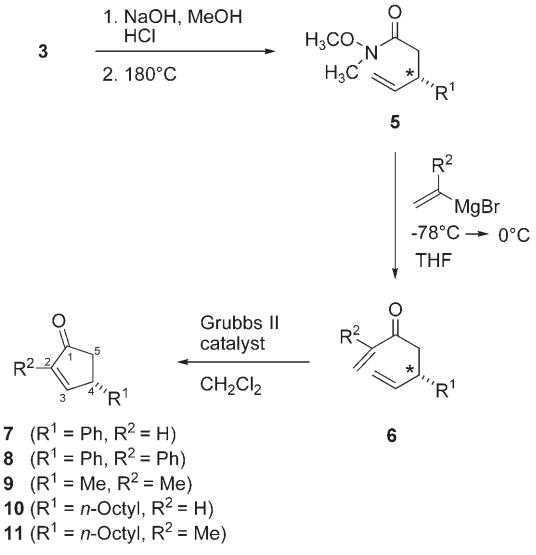

Scheme 4. Synthesis of chiral cyclopentenones.

 © 2006 Wiley-VCH Verlag GmbH & Co. KGaA, Weinheim

Table 2: Synthesis of cyclopentenones according to Scheme 4.

Entry	Substr.	R^1	R^2	Yield [%][a]	Product	*ee* [%][b]
1	(*R*)-**3a**	Ph	H	66	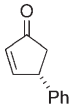 (–)-(*S*)-**7**	97
2	(*R*)-**3a**	Ph	Ph	55	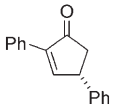 (–)-(*S*)-**8**	96
3	(*R*)-**3b**	Me	Me	44[c]	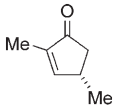 (–)-(*S*)-**9**	95
4	(*R*)-**3c**	*n*-Octyl	H	56	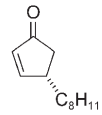 (–)-(*S*)-**10**	96
5	(*R*)-**3c**	*n*-Octyl	Me	56	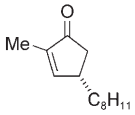 (–)-(*S*)-**11**	n.d.

[a] Starting from **3** + **4**. [b] Determined by HPLC on a chiral column; in each case synthesis of both enantiomers. [c] Volatile substance.

racemization. With respect to R^2, there is the limitation that with sterically demanding substituents, such as $Si(CH_3)_3$, the ring closure by metathesis is currently not possible.

Of the examples presented in Table 2, compounds **9** and **10** deserve special comment. Enone **9** has been identified as a volatile flavor component of dried fish.[12] A synthesis of the nonracemic compound has not yet been described to the best of our knowledge.

Compound **10** (entry 4 in Table 2) is a particularly interesting target in the area of synthesis of biologically active compounds as it offers a fast access to the prostaglandin analogue *TEI-9826*, a 5-alkylidene-4-alkyl-2-cyclopentenone that displays high anticancer activity against cisplatin-resistant tumors (Scheme 5).[13] Enone **10** has already been synthesized as a racemate and as an enantiomerically pure compound starting from (*S*)-but-3-yn-2-ol (> 98% *ee*), which was obtained by resolution.[14] In our synthesis, the mixture of the regioisomers **3c**/**4c**, which was obtained by allylic alkylation (Table 1, entry 3), was transformed directly into cyclopentenone **10** (cf. Scheme 4). This was obtained in 56% overall yield with an enantiomeric purity of 96% *ee*. The

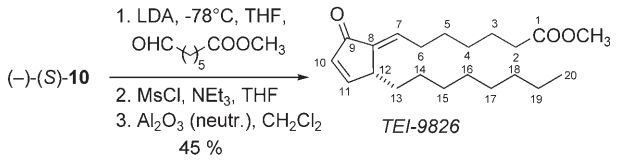

Scheme 5. Synthesis of *TEI-9826* from (–)-(*S*)-**10**. LDA = lithium diisopropylamide, Ms = methanesulfonyl.

subsequent aldol condensation was carried out according to a procedure described by Kobayashi et al.[2d] and yielded the desired prostaglandin analogue *TEI-9826* with 95% *ee* (Scheme 5).

Finally, we want to direct attention to the chiral 2-substituted cyclopentenones listed in Table 2. In prostaglandin and carbonucleoside chemistry these compounds are of interest as intermediates for the synthesis of analogues.[15]

Experimental Section

General procedure for the iridium-catalyzed allylic alkylation: A solution of the nucleophile was prepared by the dropwise addition of malonic amide **1** (1.3 mmol) to a suspension of NaH (1.3 mmol) in anhydrous THF (4.0 mL) (solution A).

Under an argon atmosphere, a solution of $[\{Ir(cod)Cl\}_2]$ (13.4 mg, 0.02 mmol) and **L1** or **L2** (0.04 mmol) in anhydrous THF (1.0 mL, content of water $< 50\ \mu g\,mL^{-1}$, Karl Fischer titration) was treated with tetrahydrothiophene (18 μL, 0.20 mmol) and 1,5,7-triazabicyclo-[4.4.0]dec-5-ene (TBD, 11.1 mg, 0.08 mmol), and the mixture was stirred for 2 h. Then substrate **2** (1.0 mmol), CuI (38 mg, 0.20 mmol), and solution A were added, and the mixture was stirred for the time given in Table 1; conversion was monitored by thin-layer chromatography. After complete conversion had been reached, Et_2O (5 mL) and saturated NH_4Cl solution (5 mL) were added, and the aqueous phase was extracted with Et_2O (2×20 mL). The combined organic phases were washed with brine (20 mL), dried over Na_2SO_4, filtered, and concentrated in vacuo. The crude product was analyzed with respect to the ratio **3**/**4** by ^1H NMR spectroscopy and then subjected to flash column chromatography (silica, petroleum ether/ethyl acetate).

Physical data of selected compounds: **10**: $[\alpha]_D^{24} = -129$ ($c = 0.50$, $CHCl_3$) (96% *ee*); ^1H NMR (300 MHz, $CDCl_3$): $\delta = 0.87$ (t, $^3J = 6.5$ Hz, 3H, CH_3), 1.19–1.44 (m, 13H, $CH_{2(n\text{-octyl})}$), 1.45–1.68 (m, 1H, $CH_{2(n\text{-octyl})}$), 1.99 (dd, $^2J_{5a,5b} = 18.8$, $^3J_{5a,4} = 2.1$ Hz, 1H, 5-H_a), 2.52 (dd, $^2J_{5b,5a} = 18.8$, $^3J_{5b,4} = 6.3$ Hz, 1H, 5-H_b), 2.86–2.96 (m, 1H, 4-H), 6.13 (dd, $^3J_{2,3} = 5.7$, $J = 2.0$ Hz, 1H, CH=), 7.63 ppm (dd $^3J_{3,2} = 5.6$, $J = 2.4$ Hz, 1H, CH=); ^{13}C NMR (75 MHz, $CDCl_3$): $\delta = 14.22$ (q, CH_3), 22.78, 27.75, 29.36, 29.58, 29.73, 31.97, 34.89 (7 t, $CH_{2(n\text{-octyl})}$), 41.20 (t, C-5), 41.63 (d, C-4), 133.68, 168.82 (2 d, C-2, C-3), 210.23 ppm (s, C-1).

TEI-9826: $[\alpha]_D^{20} = -121$ ($c = 0.58$, $CHCl_3$) (95% *ee*); ^1H NMR (500 MHz, $CDCl_3$): $\delta = 0.87$ (t, $^3J_{20,19} = 7.1$ Hz, 3H, 20-H), 1.18–1.33 (m, 12H, CH_2), 1.34–1.42 (m, 2H, CH_2), 1.45–1.55 (m, 3H, CH_2), 1.58–1.68 (m, 2H, CH_2), 1.75–1.85 (m, 1H, CH_2), 2.18–2.32 (m, 4H, 2-H, 6-H), 3.46 (m, 1H, 12-H), 3.66 (s, 3H, OCH_3), 6.32 (dd, $^3J_{10,11} = 6.0$, $^4J_{10,12} = 2.0$ Hz, 1H, 10-H), 6.51 (t, $^3J_{7,6} = 7.8$ Hz, 1H, 7-H), 7.53 ppm (dd, $^3J_{11,10} = 6.0$, $^3J_{11,12} = 2.0$ Hz, 1H, 11-H); ^{13}C NMR (125 MHz, $CDCl_3$): 14.22 (q, C-20), 22.77, 24.86, 26.01, 28.48, 29.04, 29.05, 29.36, 29.58, 29.91, 31.97, 32.61, 34.04 (12 t, C-2, C-3, C-4, C-5, C-6, C-13, C-14, C-15, C-16, C-17, C-18, C-19), 43.46 (d, C-12), 51.63 (q, OCH_3), 134.92 (d, C-10), 135.33 (d, C-7), 138.25 (s, C-8), 162.12 (d, C-11), 174.17, 197.11 ppm (2s, C-1, C-9).

Received: November 7, 2005
Published online: March 9, 2006

Keywords: allylic substitution · cyclopentenones · enantioselectivity · iridium · ring-closing metathesis

[1] a) S. M. Roberts, M. G. Santoro, E. S. Sickle, *J. Chem. Soc. Perkin Trans. 1* **2002**, 1735–1742; b) M. Iqbal, P. Evans, A. Lledó, X. Verdaguer, M. A. Pericàs, A. Riera, C. Loeffler, A. K. Sinha, M. J. Mueller, *ChemBioChem* **2005**, *6*, 276–280; c) A. Rossi, P. Kapahi, G. Natoli, T. Takahashi, Y. Chen, M. Karin, M. G. Santoro, *Nature* **2000**, *403*, 103–108.

 © 2006 Wiley-VCH Verlag GmbH & Co. KGaA, Weinheim

[2] a) Review: S. E. Gibson, S. E. Lewis, N. Mainolfi, *J. Organomet. Chem.* **2004**, *689*, 3873 – 3890; b) K. Tanaka, G. C. Fu, *J. Am. Chem. Soc.* **2002**, *124*, 10296 – 10297; c) X. Shi, D. J. Gorin, F. D. Toste, *J. Am. Chem. Soc.* **2005**, *127*, 5802 – 5803; d) Y. Kobayashi, M. G. Murugesh, M. Nakano, E. Takahisa, S. B. Usmani, T. Ainai, *J. Org. Chem.* **2002**, *67*, 7110 – 7123; e) C. Schultz-Fademrecht, M. A. Tius, S. Grimme, B. Wibbeling, D. Hoppe, *Angew. Chem.* **2002**, *114*, 1610 – 1612; *Angew. Chem. Int. Ed.* **2002**, *41*, 1532 – 1534; f) C. P. Davie, R. L. Danheiser, *Angew. Chem.* **2005**, *117*, 6017 – 6020; *Angew. Chem. Int. Ed.* **2005**, *44*, 5867 – 5870.

[3] a) H. Grebe, A. Lange, H. Riechers, K. Kieslich, W. Viergutz, P. Washausen, E. Winterfeldt, *J. Chem. Soc. Perkin Trans. 1* **1991**, 2651 – 2655; b) M. Suzuki, Y. Morita, H. Koyano, M. Koga, R. Noyori, *Tetrahedron* **1990**, *46*, 4809 – 4822.

[4] a) B. Bartels, G. Helmchen, *Chem. Commun.* **1999**, 741 – 742; b) B. Bartels, C. Garcia-Yebra, F. Rominger, G. Helmchen, *Eur. J. Inorg. Chem.* **2002**, 2569 – 2586; c) B. Bartels, C. Garcia-Yebra, G. Helmchen, *Eur. J. Org. Chem.* **2003**, 1097 – 1103; d) G. Lipowsky, N. Miller, G. Helmchen, *Angew. Chem.* **2004**, *116*, 4695 – 4698; *Angew. Chem. Int. Ed.* **2004**, *43*, 4595 – 4597; e) A. Alexakis, D. Polet, *Org. Lett.* **2004**, *6*, 3529 – 3532; f) S. Streiff, C. Welter, M. Schelwies, G. Lipowsky, N. Miller, G. Helmchen, *Chem. Commun.* **2005**, 2957 – 2959; g) D. Polet, A. Alexakis, *Org. Lett.* **2005**, *7*, 1621 – 1624.

[5] S. Nahm, S. M. Weinreb, *Tetrahedron Lett.* **1981**, *22*, 3815 – 3818.

[6] For the construction of cyclopentenones from enones by RCM see: a) A. K. Chatterjee, J. P. Morgan, M. Scholl, R. H. Grubbs, *J. Am. Chem. Soc.* **2000**, *122*, 3783 – 3784; b) A. Wrobleski, K. Sahasrabudhe, J. Aubé, *J. Am. Chem. Soc.* **2004**, *126*, 5475 – 5481; c) F. A. Davis, Y. Wu, *Org. Lett.* **2004**, *6*, 1269 – 1272; d) C. L. Chandler, A. J. Phillips, *Org. Lett.* **2005**, *7*, 3493 – 3495.

[7] a) Pd: B. M. Trost, C. Jiang, *Org. Lett.* **2003**, *5*, 1563 – 1565; b) Rh: P. A. Evans, L. J. Kennedy, *Tetrahedron Lett.* **2001**, *42*, 7015 – 7018; c) Cu: K. Tissot-Croset, D. Polet, A. Alexakis, *Angew. Chem.* **2004**, *116*, 2480 – 2482; *Angew. Chem. Int. Ed.* **2004**, *43*, 2426 – 2428.

[8] a) B. L. Feringa, *Acc. Chem. Res.* **2000**, *33*, 346 – 353; b) K. Tissot-Croset, D. Polet, S. Gille, C. Hawner, A. Alexakis, *Synthesis* **2004**, 2586 – 2590.

[9] C. A. Kiener, C. Shu, C. Incarvito, J. F. Hartwig, *J. Am. Chem. Soc.* **2003**, *125*, 14272 – 14273.

[10] R. Weihofen, A. Dahnz, O. Tverskoy, G. Helmchen, *Chem. Commun.* **2005**, 3541 – 3543.

[11] M. Scholl, S. Ding, C. W. Lee, R. H. Grubbs, *Org. Lett.* **1999**, *1*, 953 – 956.

[12] I. Yajima, M. Nakamura, H. Sakakibara, J. Ide, T. Yanai, K. Hayashi, *Agric. Biol. Chem.* **1983**, *47*, 1755 – 1760.

[13] S. Fukushima, Y. Takeuchi, S. Kishimoto, S. Yamashita, K. Uetsuki, S. Shirakawa, M. Suzuki, K. Furuta, R. Noyori, H. Sasaki, Y. Kikuchi, T. Kita, T. Yamori, J. Sawada, M. Kojima, A. Hazato, S. Kurozumi, M. Fukushima, *Anti-Cancer Drugs* **2001**, *12*, 221 – 234.

[14] a) Racemate: M. Iqbal, P. Evans, *Tetrahedron Lett.* **2003**, *44*, 5741 – 5745; b) Compound with >98% *ee*: R. Weaving, E. Roulland, C. Monneret, J.-C. Florent, *Tetrahedron Lett.* **2003**, *44*, 2579 – 2581.

[15] Y. Che, J. B. Gloer, D. T. Wicklow, *J. Nat. Prod.* **2002**, *65*, 399 – 402.

 © 2006 Wiley-VCH Verlag GmbH & Co. KGaA, Weinheim

Enzyme Catalysis

DOI: 10.1002/anie.200503280

Control of Stereoselectivity in an Enzymatic Reaction by Backdoor Access**

*Richard Wombacher, Sonja Keiper, Sandra Suhm, Alexander Serganov, Dinshaw J. Patel, and Andres Jäschke**

The ability of biopolymers to discriminate between optical isomers is vital for living systems, and the selective formation of only one product stereoisomer from achiral substrates is one of the most sophisticated tasks for enzymes. Using a Diels–Alder ribozyme as an example, we demonstrate here that by a simple strategy a biocatalyst can be used to selectively synthesize both product stereoisomers in one catalytic pocket, namely, by controlling access to the active site from opposite directions through different "doors". While substrates tethered to the catalyst were used to observe this phenomenon, we propose that nature may use conformational gating to control the stereoselectivity of enzymatic reactions.

Since the importance of stereoselective recognition to biology was realized, the structural and mechanistic basis underlying these phenomena has become the subject of intensive research.[1–4] Enzymatic reactions provide the basis of cellular biochemistry and typically display high stereoselectivity. Enzyme engineering and in vitro evolution not only aid in understanding the structural basis of stereoselectivity but they also provide tools to manipulate this property.[5–7] The standard view of an enzyme's active site is that of a pocket with an opening on one side and an array of functional groups that precisely match molecular features of the reaction's transition state. Recent results, however, indicate that many enzymes contain more than one possible entrance to the active site, but the function of these "alternative entrances" or "backdoors" remains unclear.[8–10] They have been implicated in controlling substrate entrance, product egress, removal of bound water, cofactor binding, and proton

[*] Dr. R. Wombacher, Dr. S. Keiper, S. Suhm, Prof. Dr. A. Jäschke
Institute of Pharmacy and Molecular Biotechnology
University of Heidelberg
69120 Heidelberg (Germany)
Fax: (+49) 6221-546-430
E-mail: jaeschke@uni-hd.de

Dr. A. Serganov, Prof. Dr. D. J. Patel
Structural Biology Program
Memorial Sloan-Kettering Cancer Center
New York, NY 10021 (USA)

[**] We gratefully acknowledge support by the Bundesministerium für Bildung und Forschung (BioFuture program), the Deutsche Forschungsgemeinschaft, and the Human Frontiers Science Program (A.J.), and by the NIH, the DeWitt Wallace Foundation, and the Abby Rockefeller Mauze Trust (D.J.P.).

Supporting information for this article is available on the WWW under http://www.angewandte.org or from the author.

© 2006 Wiley-VCH Verlag GmbH & Co. KGaA, Weinheim

shuttling.[11,12] The stereochemical consequences of having multiple-access pathways to one stereoselective catalytic center, however, have not been investigated so far.

Our laboratory previously discovered an RNA enzyme (ribozyme) that catalyzes the formation of carbon–carbon bonds by a Diels–Alder reaction between an anthracene diene and a maleimide dienophile (Figure 1a).[13] This reaction type is of great relevance in organic chemistry,[14] and candidates for catalyzing the Diels–Alder reaction in nature are currently under intensive investigation.[15–17] This ribozyme was the first RNA enzyme to catalyze a bond-forming reaction enantioselectively,[18] and substrate-specificity studies suggested a simple and convincing structural model for the stereoselectivity (Figure 1b).[19] The size of the diene's substituent was identified as the major determinant of stereoselectivity (see the table in Figure 1), and the diene was thought to enter the catalytic pocket with the sterically less demanding edge first, then react with the maleimide bound in one fixed orientation (Figure 1b, left model), while the opposite orientation of the anthracene (right model) was found to be disfavored.

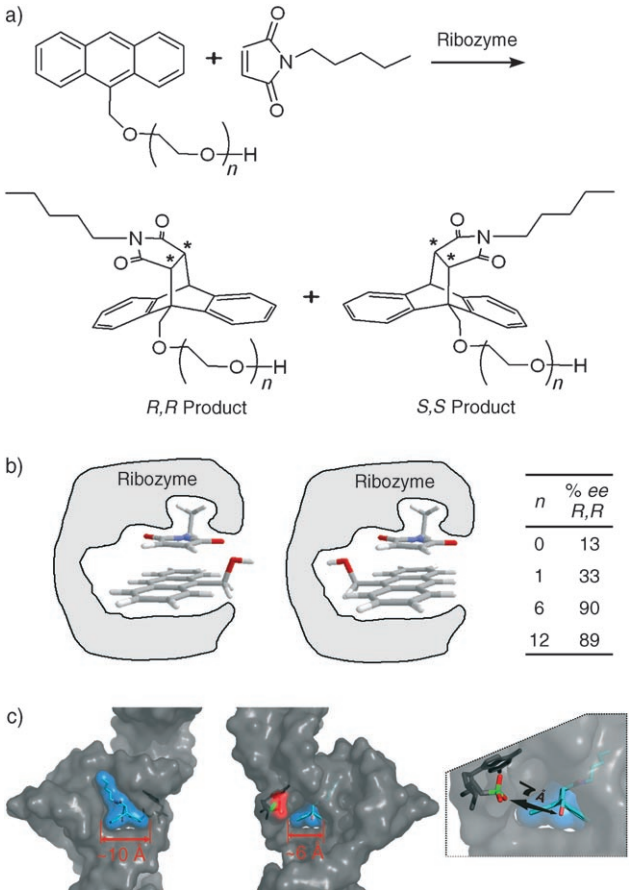

Figure 1. Ribozyme-catalyzed Diels–Alder reactions. a) Bimolecular reaction between oligo(ethylene glycol)anthracene derivatives and *N*-pentylmaleimide catalyzed by a ribozyme. Enantioselectivity is controlled by the ethylene glycol substituent of the anthracene substrate. *R*,*R* and *S*,*S* denote the stereochemical configuration at the carbon atoms with asterisks. b) Model for the stereoselection in the RNA-catalyzed reaction with free substrates; O atoms in red, N atoms in blue. Preferred orientation (left), disfavored orientation (right). The chart on the right shows the *ee* values for the enantioselective formation of *R*,*R* product with different substituents on the anthracene unit. c) Surface representation of the Diels–Alder ribozyme crystal structure; P atom in green, O atoms in red; view from the front side (left), view from the back side (middle), enlarged picture of the backdoor with assigned distance between the G1-phosphate group and the Diels–Alder product inside the pocket.

Rather than a typical enzyme pocket, the recent X-ray crystal structure of the ribozyme/Diels–Alder product complex surprisingly featured a catalytic center accessible from both front and back sides, with two openings of different sizes. In fact, the reaction product was bound inside the pocket with the sterically more demanding side first, contrary to what had been expected (Figure 1c).[20] The only difference between these and the previous experiments was that the substrate specificity was investigated using free substrates (true catalysis, Figure 2a, I), while for co-crystallization, the Diels–Alder product was covalently linked to the ribozyme by an 18-atom flexible tether (reaction with a tethered substrate, Figure 2a, II) which was attached to the RNA close to the backdoor. This raised the question whether restriction of the substrate's translational and rotational mobility by tethering could force it to enter the catalytic pocket through the narrower, disfavored backdoor and thus influence the stereochemistry of the reaction. Our investigation of this phenomenon provides direct chemical evidence that in the true catalytic reaction and the tethered version, the substrates use different approaches to the catalytic pocket, bind in different orientations, and are converted to yield the opposite product enantiomers.

To study the influence of tethering on stereoselectivity, a chromatographic assay was established. A Diels–Alder reaction of *N*-pentylmaleimide with anthracene attached to the ribozyme's 5′-end by a hexa(ethylene glycol) tether was carried out, and the reaction products were digested by snake venom phosphodiesterase I to liberate the hexa(ethylene glycol)-tethered reaction product(s). In parallel, the reaction mixture for the true catalysis reaction derived from chemically identical hexa(ethylene glycol)anthracene, *N*-pentylmaleimide, and ribozyme, as well as an uncatalyzed background reaction (hexa(ethylene glycol)anthracene + *N*-pentylmaleimide) were investigated under otherwise identical conditions. The resulting product mixtures were then analyzed by HPLC on a chiral stationary phase (Figure 2a,b).[18] While the background reaction gave the racemic mixture (Figure 2b, black curve), both catalyzed reactions produced one product in large excess (over 90% *ee*). Whereas the true catalytic reaction produced predominantly the *R*,*R* enantiomer (blue curve), the product of the tethered version was found to be the *S*,*S* enantiomer (red curve), thereby supporting our initial assumption.

According to the crystal structure, the attachment site of the tether is located directly behind the backdoor, and measured through the door, the distance between 5′-phosphate and anthracene's 9′-O is only 7 Å. Diene binding through the frontdoor by folding the tether around the ribozyme's backbone would require a tether length of ≈35 Å to reach the pocket. As the length of a hexa(ethylene glycol) tether in a fully stretched conformation is only 21 Å, these data imply that in the tethered version, the tether must be

 © 2006 Wiley-VCH Verlag GmbH & Co. KGaA, Weinheim

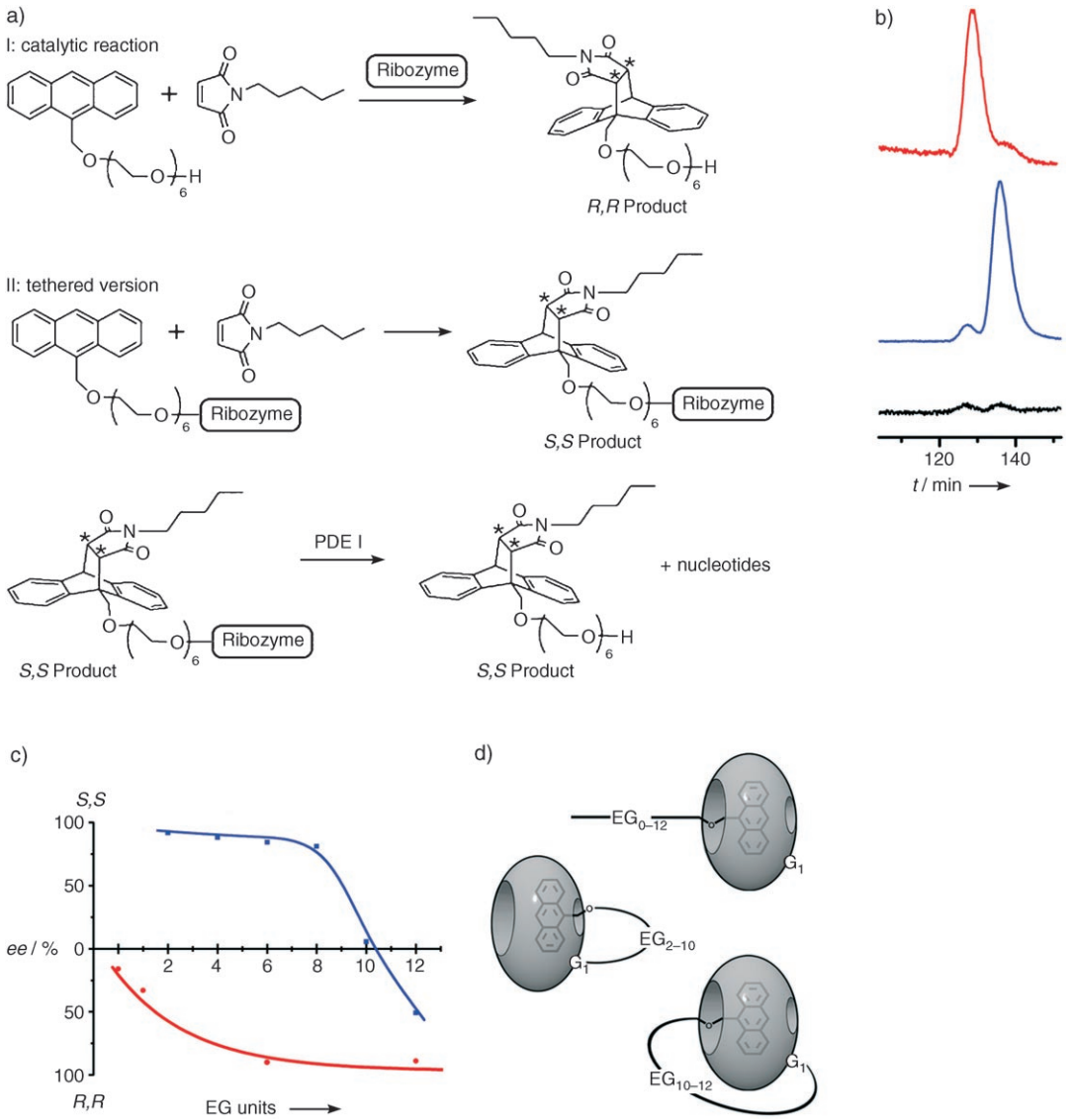

Figure 2. Investigation of the ribozyme's stereoselectivity in a true catalytic reaction (I) and in a reaction with a tethered substrate (II). a) Reaction scheme. b) HPLC chromatograms of the reaction mixture: background reaction without ribozyme (black), reaction with anthracene covalently attached to the Diels–Alder ribozyme by a hexa(ethylene glycol) tether (blue), and catalytic reaction of the free substrates in presence of the Diels–Alder ribozyme (red). c) Dependence of the ribozyme's stereoselectivity on the number of ethylene glycol (EG) units in the tethered version (blue) and in the catalytic reaction (red). d) Models for the mechanism of stereoselection. For experimental details, see the Supporting Information.

threaded through the backdoor, leading to the orientation observed in the crystal structure. According to this hypothesis, the preference for the frontdoor over the backdoor should depend on the tether length, and Figure 2c shows the systematic investigation of both reaction formats for tether lengths between 0 and 12 ethylene glycol units.

EG_0 (no tether; 9-hydroxymethylanthracene directly esterified with the RNA 5′-phosphate) is not accepted as a substrate, as the diene is apparently unable to reach the catalytic center. Between EG_2 and EG_8, the tethered version always gives *ee* values between 90 and 95% in favor of the *S*,*S* enantiomer, consistent with the assumption of threading through the backdoor (Figure 2C, blue curve). At EG_{10} (extended tether length: 35 Å), the *ee* value drops to 6% (*S*,*S*), while at EG_{12} (extended tether length: 42 Å) the stereoselectivity is inverted (51%, in favor of the *R*,*R* enantiomer). Apparently, the tether is now long enough for the anthracene to reach the frontdoor which is preferred owing to the larger size of its opening.[21] For the true catalytic reaction (Figure 2c, red curve), however, the *R*,*R* product is always favored, and the selectivity increases with the the size of the substituent.[22]

These data imply the following mechanism of stereoselection (Figure 2d):

- In the true catalytic reaction, the free diene enters the catalytic pocket with the sterically less demanding side first through the wide frontdoor (longest dimension: ≈10 Å), as proposed previously,[18,19] resulting in the formation of the *R*,*R* enantiomer.

 © 2006 Wiley-VCH Verlag GmbH & Co. KGaA, Weinheim

- If the diene is attached to the RNA by a short tether, this tether threads through the smaller door in the back of the pocket (longest dimension: ≈6 Å), giving rise to the opposite product enantiomer. The mechanism by which the tethered anthracene (shortest dimension: ≈7 Å) gets through the narrow hole is currently unknown; most likely dynamic opening and closing of the ribozyme's tertiary base pairs enlarges the door and facilitates threading.[23]
- If the tether is long enough (35 Å), it folds around the RNA backbone and the diene binds like in the true catalytic reaction. It has been shown previously for tethered ligand–receptor pairs that even nearly stretched tether conformations lead to productive binding events if sufficient sampling time is permitted.[24]

The most important aspect of this investigation is the finding that one evolved enzyme active site can be used for the selective synthesis of both product enantiomers, depending on which entrance to the catalytic center the substrate is permitted to use.[25] Although the situation created for observing this phenomenon (covalent tethering of catalyst and substrate) is an artificial one, this discovered mechanism of stereoselection raises the question whether nature might use similar strategies for "dual use" of active sites, providing controlled synthesis of both product enantiomers using only one enzyme. Alternative access pathways and backdoors have been suggested in key enzymes of metabolism (cytochrome P450s),[9] signal transduction (acetylcholine esterase),[26] and muscle action (myosin).[27] The regulation of different access pathways to the active center might be achieved by conformational changes or by binding of effectors, which are both standard gating mechanisms, or in the case of multienzyme complexes, alternative substrate channeling strategies might be used, thereby allowing for adaptation to changing metabolic needs. Like enzymes that catalyze different reactions ("catalytic promiscuity")[28] or carry out completely different functions ("moonlighting"),[29,30] the regulated synthesis of different stereoisomers may provide an evolutionary more simple and economic strategy than the de novo evolution of a new catalyst.[31–33]

Received: September 15, 2005
Revised: December 14, 2005
Published online: March 10, 2006

Keywords: cycloaddition · enantioselectivity · enzyme catalysis · ribozymes

[1] E. Fischer, *Ber. Dtsch. Chem. Ges.* **1894**, *27*, 2985.
[2] A. G. Ogston, *Nature* **1948**, *162*, 963.
[3] A. D. Mesecar, D. E. Koshland, Jr., *Nature* **2000**, *403*, 614.
[4] R. S. Shallenberger, T. E. Acree, *Nature* **1967**, *216*, 480.
[5] M. T. Reetz, *Proc. Natl. Acad. Sci. USA* **2004**, *101*, 5716.
[6] F. H. Arnold, *Nature* **2001**, *409*, 253.
[7] O. May, P. T. Nguyen, F. H. Arnold, *Nat. Biotechnol.* **2000**, *18*, 317.
[8] R. C. Wade, B. A. Luty, E. Demchuk, J. D. Madura, M. E. Davis, J. M. Briggs, J. A. McCammon, *Nat. Struct. Biol.* **1994**, *1*, 65.
[9] K. Schleinkofer, Sudarko, P. J. Winn, S. K. Lüdemann, R. C. Wade, *EMBO Rep.* **2005**, *6*, 584.
[10] R. G. Yount, D. Lawson, I. Rayment, *Biophys. J.* **1995**, *68*, 44S.
[11] A. Ostermann, R. Waschipky, F. G. Parak, G. U. Nienhaus, *Nature* **2000**, *404*, 205.
[12] G. Koellner, G. Kryger, C. B. Millard, I. Silman, J. L. Sussman, T. Steiner, *J. Mol. Biol.* **2000**, *296*, 713.
[13] B. Seelig, A. Jäschke, *Chem. Biol.* **1999**, *6*, 167.
[14] K. C. Nicolaou, S. A. Snyder, T. Montagnon, G. Vassilikogiannakis, *Angew. Chem.* **2002**, *114*, 1747; *Angew. Chem. Int. Ed.* **2002**, *41*, 1668.
[15] E. M. Stocking, R. M. Williams, *Angew. Chem.* **2003**, *115*, 3186; *Angew. Chem. Int. Ed.* **2003**, *42*, 3078.
[16] T. Ose, K. Watanabe, T. Mie, M. Honma, H. Watanabe, M. Yao, H. Oikawa, I. Tanaka, *Nature* **2003**, *422*, 185.
[17] C. R. Guimaraes, M. Udier-Blagovic, W. L. Jorgensen, *J. Am. Chem. Soc.* **2005**, *127*, 3577.
[18] B. Seelig, S. Keiper, F. Stuhlmann, A. Jäschke, *Angew. Chem.* **2000**, *112*, 4764; *Angew. Chem. Int. Ed.* **2000**, *39*, 4576.
[19] F. Stuhlmann, A. Jäschke, *J. Am. Chem. Soc.* **2002**, *124*, 3238.
[20] A. Serganov, S. Keiper, L. Malinina, V. Tereshko, E. Skripkin, C. Höbartner, A. Polonskaia, A. T. Phan, R. Wombacher, R. Micura, Z. Dauter, A. Jäschke, D. J. Patel, *Nat. Struct. Mol. Biol.* **2005**, *12*, 218.
[21] Competition experiments clearly support the intramolecular nature of the reaction with the tethered substrate. Addition of 2, 4, and 8 equiv of ribozyme to 1 equiv of anthracenehexa(ethylene glycol)–ribozyme had no effect on the initial rate of the Diels–Alder reaction.
[22] Calculation of the differences in free activation energy ($\Delta\Delta G^{\#}$) from the measured *ee* values lead to the expected small values typical for enantiodifferentiations (< 2 kcal mol^{-1}).
[23] T. Hermann, P. Auffinger, E. Westhof, *Eur. Biophys. J.* **1998**, *27*, 153.
[24] C. Jeppesen, J. Y. Wong, T. L. Kuhl, J. N. Israelachvili, N. Mullah, S. Zalipsky, C. M. Marques, *Science* **2001**, *293*, 465.
[25] It should be noted that this situation provides strong experimental support for the four-location model of stereoselective recognition by Mesecar and Koshland (see Ref. [3]).
[26] M. K. Gilson, T. P. Straatsma, J. A. McCammon, D. R. Ripoll, C. H. Faerman, P. H. Axelsen, I. Silman, J. L. Sussman, *Science* **1994**, *263*, 1276.
[27] J. D. Lawson, E. Pate, I. Rayment, R. G. Yount, *Biophys. J.* **2004**, *86*, 3794.
[28] U. T. Bornscheuer, R. J. Kazlauskas, *Angew. Chem.* **2004**, *116*, 6156; *Angew. Chem. Int. Ed.* **2004**, *43*, 6032.
[29] Y. Shi, *Trends Genet.* **2004**, *20*, 445.
[30] D. R. Klopfenstein, R. D. Vale, S. L. Rogers, *Cell* **2000**, *103*, 537.
[31] G. J. Bartlett, N. Borkakoti, J. M. Thornton, *J. Mol. Biol.* **2003**, *331*, 829.
[32] L. C. James, D. S. Tawfik, *Protein Sci.* **2001**, *10*, 2600.
[33] P. J. O'Brien, D. Herschlag, *Chem. Biol.* **1999**, *6*, 91.

 © 2006 Wiley-VCH Verlag GmbH & Co. KGaA, Weinheim

Fullerene-Like Molecules

DOI: 10.1002/anie.200503511

Spherical Cluster Comprising a Four- and Six-Membered-Ring Motif**

*Brian P. Johnson, Fabian Dielmann, Gábor Balázs, Marek Sierka, and Manfred Scheer**

Dedicated to Professor Malcolm Chisholm on the occasion of his 60th birthday

The synthesis, structures, and properties of giant spherical molecules make up a challenging field in contemporary chemistry, which unifies all fields of organic/supramolecular, inorganic, and coordination chemistry as well as organometallic chemistry. The seminal discovery of buckminsterfullerene C_{60}[1,2] not only established a new carbon allotrope but also unveiled a novel mode of icosahedral symmetry in three-dimensional carbon-based molecules. This generated a theoretical discussion and experimental search for additional fullerenes and fullerene-type molecules that exhibit modes of high symmetry. Theoretical calculations predicted that, except for C_{50}, C_{60}, and C_{70}, stable fullerenes C_n ($n = 20$–70) would generally be expected to exhibit low symmetry.[3] For smaller fullerenes C_n ($n < 60$), C_{32} was predicted by Kroto as one of the few fullerenes displaying exceptional stability in this series, and thus, 32 represents one of the so-called "magic numbers."[4] However, for C_{32}, only low symmetry can be envisioned for molecules that contain few or no four-membered rings,[5] which contribute in fullerene chemistry to high strain energy and render their cage compounds too unstable for formation and isolation. For the most highly symmetric version of C_{32} with O_h symmetry, eight four-membered rings are required.[6]

Our group has been interested in employing P_n-ligand complexes for the synthesis of 1D and 2D coordination polymers as well as spherical molecules. We recently reported the use of $[Cp^*Fe(\eta^5\text{-}P_5)]$ ($Cp^* = \eta^5\text{-}C_5Me_5$) in the synthesis of the soluble, fullerene-like cage compounds $[\{Cp^*Fe(\eta^5{:}\eta^1{:}\eta^1{:}\eta^1{:}\eta^1{:}\eta^1\text{-}P_5)\}_{12}\{CuX\}_{10}\{Cu_2X_3\}_5\{Cu(CH_3CN)_2\}_5]$ (**1a**: X = Cl;[7] **1b**: X = Br[8]), which each possess a 90-atom core consisting entirely of inorganic atoms. Herein, we report the synthesis and characterization of $[\{Cp''Ta(CO)_2(\eta^4{:}\eta^1{:}\eta^1{:}\eta^1{:}\eta^1\text{-}P_4)\}_6\{CuCl\}_8]$ (**2**) ($Cp'' = \eta^5\text{-}C_5H_3tBu_2$) as the first spherical molecule which is based on four- and six-membered rings and possesses 32 inorganic core atoms. The core of compound **2** exhibits O_h-like symmetry, which has not yet been attained in fullerene chemistry.

We have shown that the P_n-ligand complexes $[\{CpMo(CO)_2\}_2(\mu,\eta^2\text{-}P_2)]$ and $[Cp^*Fe(\eta^5\text{-}P_5)]$ can be employed as connecting moieties between late-transition-metal cations to form extended structures. Reactions of the former complex with copper(I) and silver(I) centers result in the formation of straight-chain or zigzag polymeric structures,[9,10] while reactions of the latter with copper(I) halides form linear polymers of the type $[CuCl\{Cp^*Fe(\eta^5{:}\eta^1{:}\eta^1\text{-}P_5)\}]_\infty$ as well as two-dimensional polymers of the type $[CuX\{Cp^*Fe(\eta^5{:}\eta^1{:}\eta^1{:}\eta^1\text{-}P_5)\}]_\infty$ (X = Br, I).[11] We found that tweaking the reaction conditions and stoichiometry of the $[Cp^*Fe(\eta^5\text{-}P_5)]$ systems led to the formation of soluble, supramolecular assemblies, as evidenced by the isolation of **1**. As a continuation of these investigations, we have now incorporated the *cyclo*-P_4 complex $[Cp''Ta(CO)_2(\eta^4\text{-}P_4)]$ (**3**)[12] to examine whether a *cyclo*-P_4 unit can serve as a viable source of stable four-membered phosphorus rings for building spherical molecules.

Upon layering a solution of CuCl in a mixture of MeCN and CH_2Cl_2 onto a yellow solution of **3** in CH_2Cl_2 (CuCl/**3** in 4:3 stoichiometric ratio), the nearly immediate formation of **2** as bright-orange microcrystals was observed. After about five days, the diffusion was complete, and **2** could be isolated in analytically pure form in 66% yield. To obtain larger cubic crystals of **2** suitable for single-crystal X-ray analysis, slower diffusion techniques were applied (see Experimental Section). Compound **2** crystallizes with one molecule of CH_2Cl_2 per formula unit in the trigonal space group $R\bar{3}$.[13] In the molecular structure (Figure 1a), the P atoms of each *cyclo*-P_4 ring are coordinated to the Cu atoms in a 1,2,3,4 mode, and each {CuCl} unit is bound by three $\{Cp''Ta(CO)_2(\eta^4\text{-}P_4)\}$ units with each Cu atom in approximate tetrahedral geometry.

The overall structure resembles an extended cube in which the six faces are represented by the *cyclo*-P_4 rings, and the twelve edges are replaced by six-membered Cu_2P_4 rings in boat conformation, thus resulting in a closed-cage framework consisting exclusively of alternating four- and six-membered rings. The structural motif of the core in **2** parallels that of the T_d-symmetrical cages considered by theoretical calculations of the Group 13/15 oligomers $[HMEH]_{16}$ (M = B, Al, Ga, In; E = N, P, As),[14] but to our knowledge, no such motif has been observed in an isolated compound.

In the crystal structure, **2** is centered on the crystallographic C_3 axis, which extends through two opposing {CuCl} units and through the center of the inner cavity. A view of the structure along this axis is shown in Figure 1b. The symmetry of the core is distorted-octahedral, whereby a slight deviation from this symmetry arises from the small variations in P–P

[*] B. P. Johnson, F. Dielmann, Dr. G. Balázs, Prof. Dr. M. Scheer
Institut für Anorganische Chemie der Universität Regensburg
93040 Regensburg (Germany)
Fax: (+49) 941-943-4439
E-mail: mascheer@chemie.uni-regensburg.de
Dr. M. Sierka
Institut für Chemie der Humboldt-Universität zu Berlin
Unter den Linden 6
10099 Berlin (Germany)
Fax: (+49) 30-2093-7136
E-mail: marek.sierka@chemie.hu-berlin.de

[**] This work was comprehensively supported by the Deutsche Forschungsgemeinschaft and the Fonds der Chemischen Industrie. We thank Prof. Dr. H. Eckert (Univ. Münster) for recording the ^{31}P MAS NMR spectrum of the title compound. M. Sierka gratefully acknowledges Prof. Joachim Sauer and the Humboldt-Universität zu Berlin for providing computing facilities.

Supporting information for this article is available on the WWW under http://www.angewandte.org or from the author.

 © 2006 Wiley-VCH Verlag GmbH & Co. KGaA, Weinheim

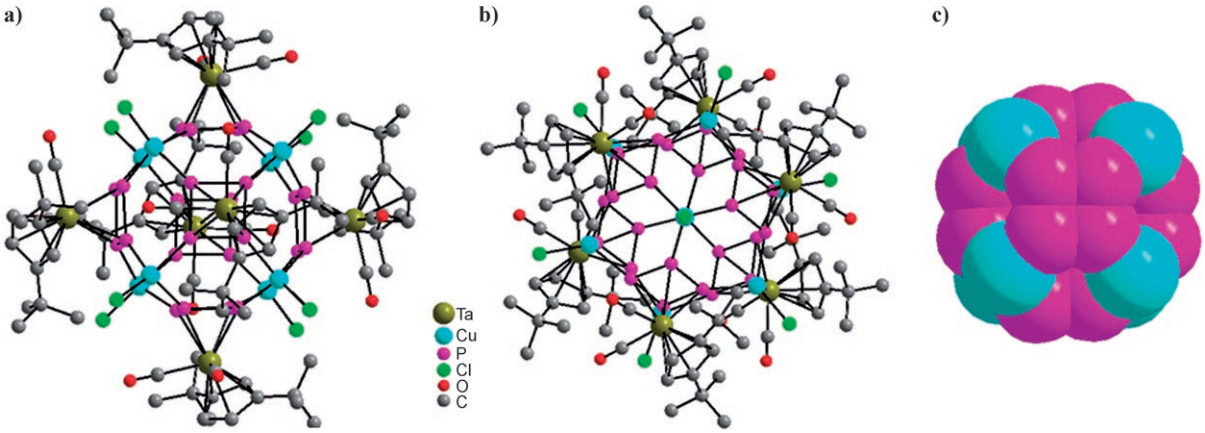

Figure 1. a) Molecular structure of **2**. b) View of **2** along the crystallographic C_3 axis. c) Space-filling model of the core of **2**. The H atoms (a, b) as well as the $Cp''Ta(CO)_2$ fragments and Cl atoms (c) have been omitted.

bond lengths within each *cyclo*-P_4 ligand. The planar *cyclo*-P_4 ligands in the free complex **3** are found in approximate kite geometry (d(P–P) = 2.162 Å (av)). In **2**, the *cyclo*-P_4 ligands remain planar (maximal deviation of the atoms from the best plane: 0.02 Å), and the kite conformation is maintained. All the P–P bonds are slightly elongated in comparison to those in the free complex **3**, thus resulting in an average P–P bond length in **2** (d(P–P) = 2.174 Å (av)) that is over 0.01 Å longer than that in **3**. The P-P-P bond angles in **2** show only minor changes from complex **3**. The inner cavity of **2** possesses an approximate cube shape, with the Cu atoms representing the corners and the *cyclo*-P_4 ligands representing the faces. This cavity possesses a diagonal of 0.60 nm (Cu to Cu) and a distance of 0.44 nm between the opposing faces (P to P).[15] The maximum outside diameter of 2.19 nm reflects the bulkiness of the *t*Bu groups of the Cp″ rings. The spherical cluster core of 32 atoms (space-filling model in Figure 1c) possesses an outer diameter of 1.16 nm. For comparison, the fullerene cage C_{60} carries outer dimensions of 0.7 nm, while the nanoball **1a** has an inner-cavity diameter of 1.25 nm and an outer diameter of 2.13 nm.

Compound **2** is insoluble in common organic solvents, including more polar solvents such as acetonitrile, acetone, THF, DME, and 1,2-dichlorobenzene. Attempts to dissolve **2** in DMF resulted in decomposition of the spherical structure to yield free **3**, as evidenced by ^{1}H and ^{31}P NMR spectroscopy. In the IR spectrum of **2**, the CO stretching frequencies display a significant shift to higher wave numbers (**3**: 1952, 1983 cm^{-1}; **2**: 1974, 2040 cm^{-1}), which can be attributed to the more rigid nature of the overall structure. The ESI mass spectrum[16] shows only partially maintained coordination fragments consisting of the $[\{Cp''Ta(CO)_2(\eta^4\text{-}P_4)\}_2Cu]^+$ and $[\{Cp''Ta(CO)_2(\eta^4\text{-}P_4)\}_2Cu_2Cl]^+$ cations as well as the disproportionation fragment $[\{Cp''Ta(CO)_2(\eta^4\text{-}P_4)\}_4Cu]^+$.

Density functional theory (DFT) calculations were performed to address the origin of distortion of the core of **2** from perfect octahedral symmetry. Calculations on the O_h-symmetric cation $[\{Ta(\eta^4{:}\eta^1{:}\eta^1{:}\eta^1\text{-}P_4)\}_6\{CuCl\}_8]^{6+}$, neutral $[\{Ta(\eta^4{:}\eta^1{:}\eta^1{:}\eta^1\text{-}P_4)\}_6\{CuCl\}_8]$, and $[\{ClCo(\eta^4{:}\eta^1{:}\eta^1{:}\eta^1\text{-}P_4)\}_6\{CuCl\}_8]$, in which Cp″ and $Ta(CO)_2$ are replaced by Cl and Co, respectively, yield in all cases nondegenerate ground states. This result suggests that the first-order Jahn–Teller effect is an unlikely reason for the distortion. To investigate the influence of the ligand arrangement on the structure of **2**, we performed calculations on the original complexes **3** and **2**, as well as on a series of model complexes (see the Supporting Information). For **3**, the optimized structure shows a staggered orientation of the *cyclo*-P_4 and CO ligands, in agreement with experimental data. This orientation and the kite distortion of the *cyclo*-P_4 ligand from square geometry are a result of orbital interactions similar to those discussed by Chu and Hoffmann for *cyclo*-C_4H_4 complexes.[17] This interpretation is confirmed by our calculations on the hypothetical complex $[Cp^*Co(\eta^4\text{-}P_4)]$, in which Cp* and P_4 rings are oriented parallel and the *cyclo*-P_4 ligand shows almost perfect square geometry (d(P–P): 2.185 Å, ∢(P-P-P): 89.6° and 90.4°). From calculations on model complexes, we have also found that the {CuCl} units provide quite flexible linking between the *cyclo*-P_4 rings. Calculations on complexes in which the Cp″ ligands in **3** and **2** are replaced by Cp (hypothetical complexes **3′** and **2′**) leave the structure of the *cyclo*-P_4 rings and of the core of **2** virtually unchanged. However, in **2′**, the less bulky **3′** units can be rotated by 90° around the axes perpendicular to the P_4 units, thus leading to two D_{3d}-symmetric isomers **2′a** and **2′b**. The isomers are only 7 and 25 kJ mol^{-1}, respectively, less stable than **2′**, but the kite geometry of the P_4 rings and their mutual arrangement with the CO and Cp ligands are preserved. Thus, the Cu–P linkages are flexible enough to adjust to the rotation of the relatively stiff *cyclo*-P_4 units, and essentially preserve the shape of the building units of **2′**.

The results have shown that $[Cp''Ta(CO)_2(\eta^4\text{-}P_4)]$ (**3**) can be employed in the coordination chemistry with copper(I) halides for the assembly of inorganic, spherical molecules, thus producing a novel 32-atom core. The use of the P_4 ligands offers a stable source of four-membered rings for the formation of spherical aggregates, whereas no precedence has been found for high-symmetry carbon structures bearing four-membered rings. The distorted-octahedral structure of **2** is a result of the nonparallel arrangement of the Cp″ and CO ligands relative to the *cyclo*-P_4 ligands, as well as the flexibility of the {CuCl} linkages.

 © 2006 Wiley-VCH Verlag GmbH & Co. KGaA, Weinheim

Experimental Section

All reactions were performed under dry argon with standard vacuum, Schlenk, and glove-box techniques. Solvents were purified and degassed by standard procedures. Commercial-grade chemicals were used without further purification. Complex **3** was prepared by a literature method.[12]

2: A Schlenk tube was charged with a solution of **3** (70 mg, 0.13 mmol) in CH_2Cl_2 (2 mL). Onto this solution was layered a mixture of CH_2Cl_2/MeCN (4 mL/2 mL)and subsequently a solution of CuCl (17 mg, 0.17 mmol) in CH_2Cl_2/MeCN (1 mL/1 mL). The doubly layered system was allowed to stand in an undisturbed area, and orange crystals of **2** formed within 24 h. The mixture was allowed to stand 5 days to ensure thorough diffusion, and the mother liquor was decanted away. The crystals were washed once with MeCN (2 mL) and twice with CH_2Cl_2 (2 mL), and dried under vacuum. Yield: 59 mg (66%); m.p. 196°C (decomp., discoloration to black); IR (KBr pellet): $\tilde{\nu}_{CO} = 2040$ (vs, br), 1974 cm^{-1} (sh); MS (ESI, DMF): *m/z* (%): 2215.4 (99) $[\{Cp''Ta(CO)_2P_4\}_4Cu]^+$, 1239.0 (9.0) $[\{Cp''Ta(CO)_2P_4\}_2Cu_2Cl]^+$, 1139.1 (100) $[\{Cp''Ta(CO)_2P_4\}_2Cu]^+$. Elemental analysis (%) calcd for $C_{91}H_{128}O_{12}Cl_{10}Cu_8P_{24}Ta_6$ (4105.89): C 26.62, H 3.14; found: C 26.74, H 3.19.

DFT calculations were performed by using the TURBOMOLE program package.[18] The BP86 exchange-correlation functional[19] was used along with the triple-zeta plus polarization (TZVP) basis set on all atoms.[20] To speed up the calculations, the Coulomb part was evaluated by using the MARI-J method[21] and the triple-zeta plus double set of polarization functions (TZVPP) auxiliary basis sets on all atoms.[22] Quasi-relativistic pseudopotentials were used for Ta.[23]

Received: October 4, 2005
Published online: March 10, 2006

Keywords: cluster compounds · density functional calculations · fullerenes · phosphorus · tantalum

[1] *Fullerenes: Chemistry, Physics and Technology* (Eds.: K. M. Kadish, R. S. Ruoff), Wiley, New York, **2000**.
[2] A. L. Balch, M. M. Olmstead, *Chem. Rev.* **1998**, *98*, 2135–2165.
[3] B. L. Zhang, C. Z. Wang, K. M. Ho, C. H. Xu, C. T. Chan, *J. Chem. Phys.* **1992**, *97*, 5007–5011.
[4] H. W. Kroto, *Nature* **1987**, *329*, 529–531.
[5] Y. D. Gao, W. C. Herndon, *J. Am. Chem. Soc.* **1993**, *115*, 8459–8460.
[6] For comparison of the stability of C_{60} and C_{32} (O_h) by ab initio methods: F. L. Gu, Q. S. Li, A. Q. Tang, *Acta Chim. Sin.* **1995**, *53*, 942–946.
[7] J. Bai, A. V. Virovets, M. Scheer, *Science* **2003**, *300*, 781–783.
[8] M. Scheer, J. Bai, B. P. Johnson, R. Merkle, A. V. Virovets, C. E. Anson, *Eur. J. Inorg. Chem.* **2005**, 4023–4026.
[9] J. Bai, E. Leiner, M. Scheer, *Angew. Chem.* **2002**, *114*, 820–823; *Angew. Chem. Int. Ed.* **2002**, *41*, 783–786.
[10] M. Scheer, L. Gregoriades, J. Bai, M. Sierka, G. Brunklaus, H. Eckert, *Chem. Eur. J.* **2005**, *11*, 2163–2169.
[11] J. Bai, A. V. Virovets, M. Scheer, *Angew. Chem.* **2002**, *114*, 1808–1811; *Angew. Chem. Int. Ed.* **2002**, *41*, 1737–1740.
[12] O. J. Scherer, R. Winter, G. Wolmershäuser, *Z. Anorg. Allg. Chem.* **1993**, *619*, 827–835.
[13] The crystal structure analysis of **2** was performed on a STOE IPDS diffractometer with $Mo_{K\alpha}$ radiation ($\lambda = 0.71073$ Å). The structure was solved by direct methods with the program SHELXS-97,[24a] and full-matrix least-squares refinement on F^2 in SHELXL-97[24b] was performed with anisotropic displacements for non-H atoms. The H atoms were fixed at idealized positions and refined isotropically by using the riding model. The solvent molecules are disordered and fill the space between the clusters of **2**. The carbon atom of the CH_2Cl_2 molecule (C16) occupies one position on the crystallographic threefold-symmetry axis, whereas each chlorine atom is disordered over three positions. The additional symmetry operations for the chlorine atoms of the dichloromethane molecule were defined by the EQIV instruction. The U_{ij} components of C16, Cl3, and Cl4 were restrained by the SIMU instruction, and the C–Cl distances were fixed to 1.65 Å by the DFIX instruction. A free refinement of the occupancy of C16, Cl3, and Cl4 converged to a value of 0.16667, at which they were fixed. To calculate the H-atoms on C16, the symmetry-generated chlorine atoms were freed from C16 by the FREE instruction. **2**·CH_2Cl_2: $C_{91}H_{128}Cl_{10}Cu_8O_{12}P_{24}Ta_6$, $M_r = 4105.73$, crystal dimensions $0.08 \times 0.08 \times 0.04$ mm^3, trigonal, space group $R\bar{3}$ (No. 148); $a = b = 22.845(3)$, $c = 22.658(5)$ Å, $T = 150(1)$ K, $Z = 3$, $V = 10241(3)$ $Å^3$, $\rho_{calcd} = 1.997$ $Mg\,m^{-3}$, $\mu(Mo_{K\alpha}) = 6.526$ mm^{-1}, 22248 reflections collected, 4007 unique reflexes ($R_{int} = 0.0756$, $2\theta_{max} = 50°$), 3285 observed with $F_o = 4\sigma$ (F_o); 250 parameters, $R_1 = 0.0365$, wR_2(all data) = 0.0854. CCDC-281812 contains the supplementary crystallographic data for this paper. These data can be obtained free of charge from The Cambridge Crystallographic Data Centre via www.ccdc.cam.ac.uk/data_request/cif.
[14] a) A. Y. Timoshkin, *Inorg. Chem. Commun.* **2002**, *5*, 274–277; b) A. Y. Timoshkin, H. F. Schaefer III, *J. Am. Chem. Soc.* **2004**, *126*, 12141–12154; c) A. Y. Timoshkin, H. F. Schaefer III, *Inorg. Chem.* **2005**, *44*, 843–845.
[15] The inner diameters are calculated as geometrically opposing atomic distances, minus the following van der Waals radii: P, 0.18 nm; Cu, 0.14 nm. The outer diameter is taken as twice the largest distance from the theoretical center of the molecule to the *t*Bu hydrogen atoms, plus twice the van der Waals radius for H (2×0.12 nm). For the inner cavity, the term "diameter" is defined here as the diameter of the largest spherical form that is geometrically allowed inside the cavity by the given atoms.
[16] a) From freshly prepared DMF solutions; b) In the ^{31}P MAS NMR spectrum of **2** at room temperature, a broad, unresolved signal is observed at $\delta = -70$ ppm, which is broadened as a result of the P,P and in particular the P,Cu coupling.
[17] S.-Y. Chu, R. Hoffmann, *J. Phys. Chem.* **1982**, *86*, 1289–1297.
[18] a) R. Ahlrichs, M. Bär, M. Häser, H. Horn, C. Kölmel, *Chem. Phys. Lett.* **1989**, *162*, 165–169; b) O. Treutler, R. Ahlrichs, *J. Chem. Phys.* **1995**, *102*, 346–354.
[19] a) A. D. Becke, *Phys. Rev. A* **1988**, *38*, 3098–3100; b) S. H. Vosko, L. Wilk, M. Nusair, *Can. J. Phys.* **1980**, *58*, 1200–1211; c) J. P. Perdew, *Phys. Rev. B* **1986**, *33*, 8822–8824; erratum: J. P. Perdew, *Phys. Rev. B* **1986**, *34*, 7406.
[20] F. Weigend, R. Ahlrichs, *Phys. Chem. Chem. Phys.* **2005**, *7*, 3297–3305.
[21] a) K. Eichkorn, O. Treutler, H. Öhm, M. Häser, R. Ahlrichs, *Chem. Phys. Lett.* **1995**, *242*, 652; b) M. Sierka, A. Hogekamp, R. Ahlrichs, *J. Chem. Phys.* **2003**, *118*, 9136–9148.
[22] K. Eichkorn, F. Weigend, O. Treutler, R. Ahlrichs, *Theor. Chem. Acc.* **1997**, *97*, 119–124.
[23] D. Andrae, U. Häußermann, M. Dolg, H. Stoll, H. Preuss, *Theor. Chim. Acta* **1990**, *77*, 123–141.
[24] a) G. M. Sheldrick, SHELXS-97, University of Göttingen, **1997**; b) G. M. Sheldrick, SHELXL-97, University of Göttingen, **1997**.

 © 2006 Wiley-VCH Verlag GmbH & Co. KGaA, Weinheim